TMS 2018

147th Annual Meeting & Exhibition

SUPPLEMENTAL PROCEEDINGS

TMS

Springer

The Minerals, Metals & Materials Series

The Minerals, Metals & Materials Society
Editor

TMS 2018
147th Annual Meeting & Exhibition Supplemental Proceedings

TMS

Springer

Editor
The Minerals, Metals & Materials Society
Pittsburgh, PA
USA

ISSN 2367-1181 ISSN 2367-1696 (electronic)
The Minerals, Metals & Materials Series
ISBN 978-3-319-72525-3 ISBN 978-3-319-72526-0 (eBook)
https://doi.org/10.1007/978-3-319-72526-0

Library of Congress Control Number: 2017963376

Printed on acid-free paper

This Springer imprint is published by the registered company Springer International Publishing AG part of Springer Nature
The registered company address is: Gewerbestrasse 11, 6330 Cham, Switzerland

The TMS 2018 Annual Meeting Supplemental Proceedings is a collection of papers from the TMS 2018 Annual Meeting & Exhibition, held March 11–15 in Phoenix, Arizona, USA. The papers in this volume represent 37 symposia from the meeting. This volume, along with the other proceedings volumes published for the meeting, and TMS archival journals, represents the available written record of the 92 symposia held at TMS 2018.

Contents

Part I
2018 Symposium on Functional Nanomaterials: Discovery and Integration of Nanomaterials

2-D Nanosheets and Rod-Like WO_3 Obtained via Chemical Precipitation Method for Detecting Formaldehyde

HuiMin Yu and JianZhong Li

Abstract In this paper, WO_3 nanosheets and rod-like were successfully prepared via chemical precipitation method for efficient sensing of formaldehyde gas at low working temperature. The structure and morphology of the precursors and the calcined products in air were characterized X-ray diffraction (XRD) and scanning electron microscopy (SEM). XRD analyses confirmed that the precursors were compound of monoclinic structure WO_3 and orthorhombic structure $WO_3 \cdot 0.33H_2O$, whereas monoclinic structure WO_3 were obtained by calcining at 450 °C for 2 h. Sensors fabricated by calcined WO_3 exhibited a quick response (5 s)/recovery (15 s) characteristic. The gas sensing texts showed the response value (Ra/Rg = 16.5) to 100 ppm HCHO at the optimum temperature of 300 °C. The possible oxidation-reduction reaction mechanism of HCHO molecule on the sensor surface were researched and discussed too. WO_3 could be a promising sensing materials for detecting organic pollutants.

Keywords WO_3 · Formaldehyde · Gas sensing

Introduction

Formaldehyde as a kind of poisonous pollutant gas widely exists in building decoration materials, such as paint, wooden floor, and furniture, which can pose a threat to the health of human body such as respiratory system, immune system, and even increase the risk of cancer [1]. Therefore, the real-time detection of formaldehyde is extremely vital, and the study of formaldehyde gas sensitive material is also an urgent problem for scientists. Various methods have been used to detect formaldehyde, such as spectrophotometry, potentiometric, mid-IR difference-frequency generation,

H. Yu (✉) · J. Li
Northeastern University, Shenyang, China
e-mail: 18842433651@163.com

J. Li
e-mail: lijz@mail.neu.edu.cn

The Minerals, Metals & Materials Society, *TMS 2018 147th Annual Meeting & Exhibition Supplemental Proceedings*, The Minerals, Metals & Materials Series,
https://doi.org/10.1007/978-3-319-72526-0_1

electrochemical biosensors, piezoelectric sensors, amperometric, optical methods and filter color testing methods [2]. But these methods are inconvenient and complicated in practice so far. Owing to high sensitivity, quick response time and low cost, semiconductor gas sensor has been greatly developed in recent years to detect formaldehyde and is widely used in practice. Among these semiconductor materials, gas sensors based on SnO_2 [3], ZnO [4], NiO [5] and WO_3 [6] have attracted great attention from scientists due to its simple production, low cost, convenient portability and excellent gas sensitive performance, which has been widely studied.

WO_3 is an n-type semiconductor with wide bandgap of 2.6–2.7 eV, has been evoke in a lot of interest in the scientific area. In the existing research, WO_3 has been used to detect various gases such as H_2S, NO_X, H_2, ethyl, NH_3, volatile organic compounds (VOC_S), etc. [7]. Various methods are used to prepare WO_3 such as hydrothermal method, chemical precipitation method, chemical vapor deposition method and solid phase method, a variety of morphology products are prepared, such as 1-D, 2-D, 3-D including nanowires, nanotubes, nanosheets, nanoflower, porous spheres, and hierarchical structure was composed of nanosheets by self-assembly. How to obtain high sensitivity and selectivity to formaldehyde for WO_3 sensors is still a challenge.

In this paper, two-dimensional (2-D) sheets with high electron conductivity, high specific surface area were obtained via a simple chemical precipitation method to improve the sensing properties of the WO_3 gas sensor, structure and morphology of sensing materials were characterized using X-ray diffraction (XRD) and field emission scanning electron microscopy (FESEM). In the end, the sensors to detect HCHO was investigated.

Experiment

Chemical Reagents

All the chemical reagents were analytical grade and used as purchased without further purification. Deionized water was used throughout the experiments. Chemicals including sodium tungstate, Poly-vinyl pyrrolidone (PVP-K30), formalin solution and sulfuric acid were purchased from Sinopharm Chemical Reagents Co., Ltd.

Preparation of WO_3 Material

The WO_3 sheets were prepared via chemical precipitation method as follows:

Na_2WO_4 (0.02 mmol) was dissolved in 100 ml deionized water with magnetic stirring to form a homogeneous solution, 30 min later, H_2SO_4 (0.5 mol L^{-1}) was dropwise added until the pH value of the mixture reach to 1.0. 30 ml PVP-K30 (1 mol L^{-1}) added into above solution subsequently, the resulted emulsion lasted for 30 min under magnetic stirring. Then the resulted precipitates were collected by centrifugation and washed with deionized water and ethanol for several times alternately before drying at 80 °C for 12 h. Finally the dried products were annealed in muffle furnace at 450 °C for 2 h in air atmosphere.

Characterization

The WO_3 samples were characterization by the X-ray diffraction (Smart Lab, 9KW, Japan) using CuKα1 radiation ($\lambda = 0.15406$ nm) at a scanning rate of 6°/min in the range of 10°–85°. The morphology and structure of the samples were obtained by scanning electron microscopy (JSM-7800F, Japan).

Fabrication of Gas Sensor

To fabricate gas sensor to detect formaldehyde gas based on calcined WO_3, the as-obtained product were mixed with a small quantity deionized water and ethyl to form paste. Then the resulting paste was coated uniformly onto the surface of a cleaned alumina tube by small brush after grinding for 20 min. After the coating was dried in air, the Al_2O_3 microtubules were sintered at 400 °C for 1 h to remove the ethanol and increase the contact between particles so as to improve the stability and repeatability of sensors. Waited until the ceramic tubes cool to room temperature, a Ni-Cr alloy coil passed through the ceramic tube as a heater to adjusting operating temperature of sensors. The working temperature of the gas sensor was adjusted by varying the heating resistor. The circuit voltage was constant ($V_c = 5$ V) and the output voltage (V_{out}) was the terminal voltage of the load resistor ($R_L = 10$ kΩ). By monitoring V_{out}, the resistance change of the gas sensor in air or the target gases could be measured ($R_s = (V_c - V_{out})\, R_L/V_{out}$), working circuit was shown in Fig. 1, and the surface reaction diagrammatic figure was shown in and Fig. 2. Subsequently, welded to a pedestal with four Pt wires attached on two Au electrons.

Sensing Measurements

The as-prepared gas sensors were all aged on an aging equipment for three days to enhance long-term stability and repeatability before gas sensing measurement.

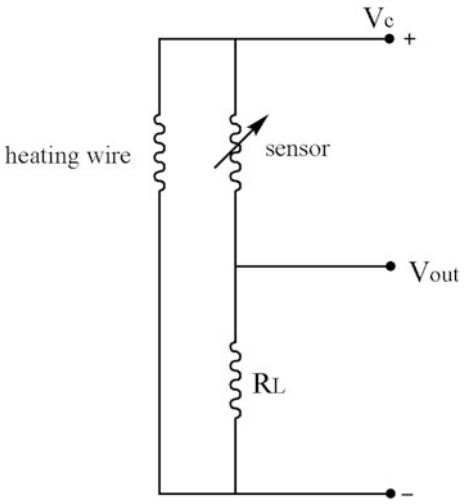

Fig. 1 The working circuit of texting system

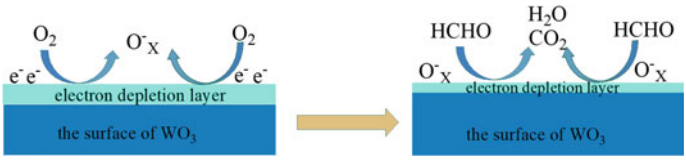

Fig. 2 The surface reaction diagrammatic figure

To guarantee the results of gas sensing text maintain the margin of error, all sensors were fabricated by the same method.

The desired concentration HCHO gas was obtained by injecting corresponding formalin solution micro-syringe onto the crucible heater which settled in texting chamber. The solution was evaporated by heater, one air fan installed in chamber made the target gas homogeneous. For a target concentration, the volume of formalin solution needed could be calculated as follows in formula (1):

$$V = \frac{V_B \cdot c \cdot M}{22.4 \cdot \rho \cdot \omega\%} \tag{1}$$

where V_B, c, M, ρ, ω denoted the volume of texting chamber, HCHO concentration (ppm), molecular weight (g/mol), density of formalin solution (g/cm^3) and purity of formalin liquid (37%), respectively.

The response value (S) of sensors in this paper was defined as S = Ra/Rg, where Ra, Rg was the resistance of sensor in air and in target gas respectively. The response time was defined as the time to reach 90% of the final equilibrium value

when sensors were exposed to target gas, and the recovery time was the time to decrease 10% of the final equilibrium value when sensors exposed in air regain.

Results and Discussion

Crystal Structure and Morphology

The X-ray powder diffraction of as-prepared precipitate products were shown in Fig. 3. XRD analyses confirmed that the precursors were compound of monoclinic structure WO_3 and orthorhombic structure $WO_3 \cdot 0.33H_2O$. The diffraction peaks of (002), (200), (220), (111) and (020) crystal planes were sharp and intense, indicating their high crystallization. The diffraction pattern for sintered product shown in Fig. 4 exhibited peaks at 23.1°, 23.6°, 24.3°, 26.6°, 28.6°, 28.9°, 33.3°, 34.2°, 41.9°, 49.9° and 55.9°, corresponding to (002), (020), (200), (120), (−112), (112), (022), (202), (222), (400), and (420) of WO_3 (PDF 72-0677), respectively. The sintering process converted crystal phase of samples into monocline. Figure 5a presented SEM images of obtained precipitate products, indicating that the resultant particles were piled up by positive hexagonal plates which were about 200 nm in thickness. Figure 5b–d showed the precipitate products sintered in muffle under various temperature. It's obvious from the SEM photograph that sheets transformed into rod-like or capsule-like particles after sintering.

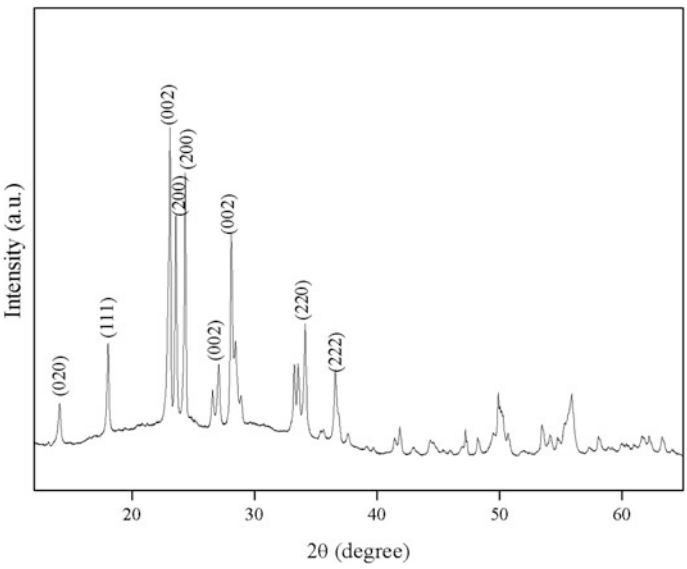

Fig. 3 The XRD pattern of as-prepared precipitate products

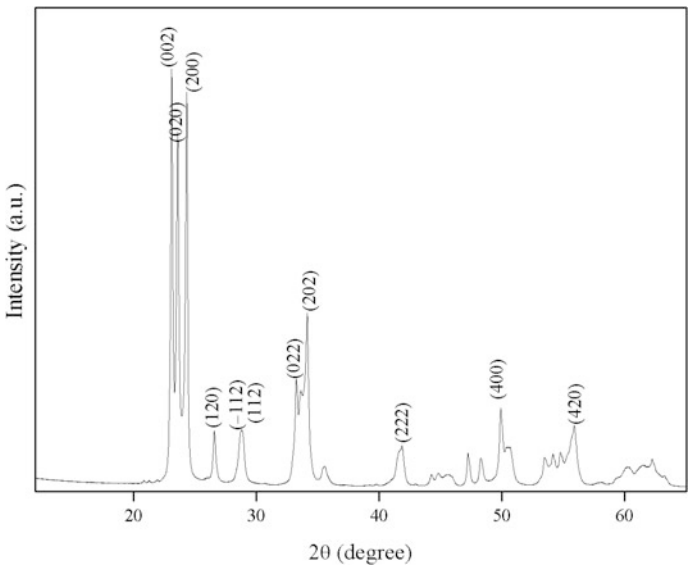

Fig. 4 The XRD pattern of sintered products

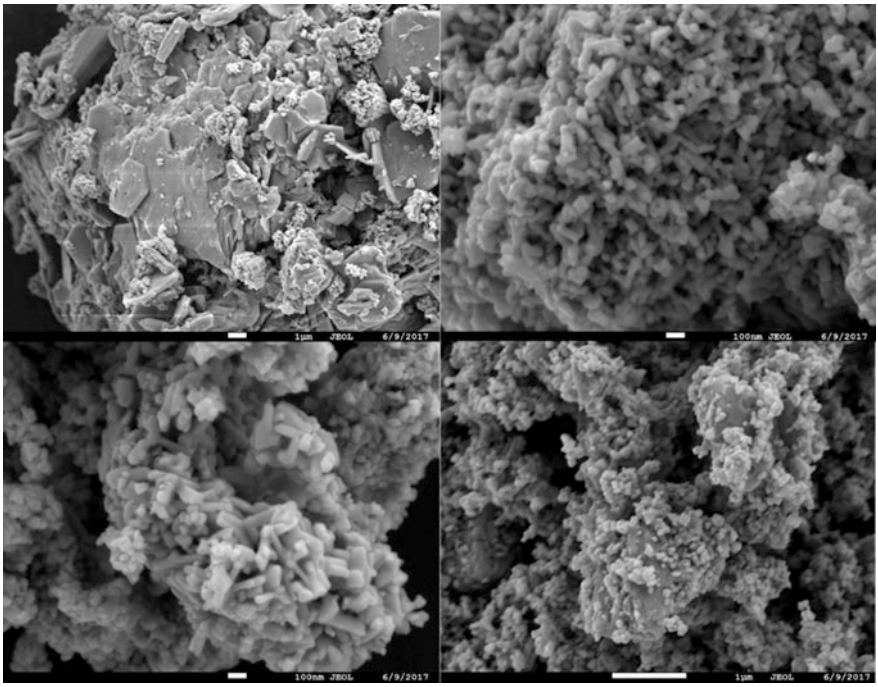

Fig. 5 SEM images of precipitate and sintered products

Formaldehyde Sensing Properties

The formaldehyde sensing performance of WO_3 sensors were examined by placing them into texting chamber, the desired concentration HCHO were obtained by injecting formalin solution. Here, the sensing properties of WO_3 for HCHO were investigated. Figure 6 presented the response to 100 ppm HCHO at 300 °C, it could be observed that the response increased and reached its maximum in 5 s, the sensor exhibited maximum response of 16.5–100 ppm HCHO, and the recovery time was also short to 15 s. The sensors based on WO_3 had almost real-time monitoring for formaldehyde gas.

Mechanism of Sensing Properties

The working mechanism of the gas sensors relies on electron transport caused by oxidation and reduction reaction on surface of sensors thin films. The gas sensing response was reflected by the change of resistance when their exposed to target gas, target gas and chemisorbed oxygen species leaded to change in charge. When sensors were exposed in air atmosphere, oxygen species absorbed on surface or inner of samples would trap electrons from conduction band and then created chemisorbed oxygen species for instance O_2^-, O^-, O^{2-}, the reaction were shown as Eqs. (2)–(5). These reactions would produce an electron depletion layer causing in a high resistance for sensors.

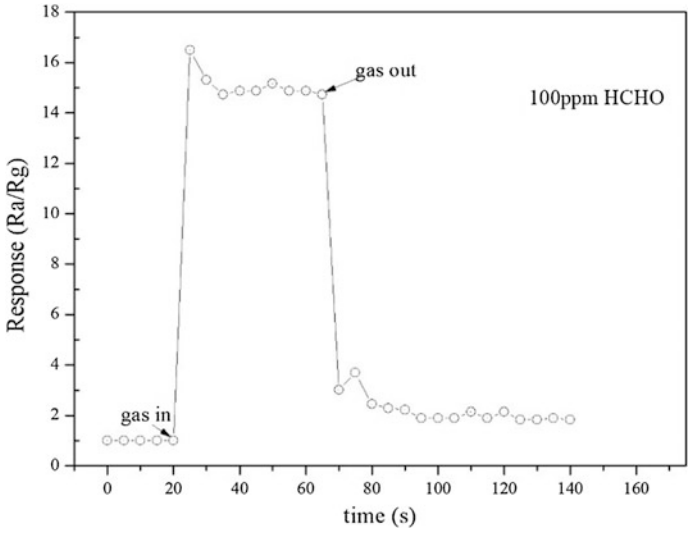

Fig. 6 100 ppm formaldehyde response characteristic of sintered WO_3 at 300 °C

$$O_{2(gas)} \rightarrow O_{2(ads)} \tag{2}$$

$$O_{2(ads)} + e^- \rightarrow O^-_{2(ads)} \tag{3}$$

$$O^-_{2(ads)} + e^- \rightarrow O^-_{(ads)} \tag{4}$$

$$O^-_{(ads)} + e^- \rightarrow O^{2-}_{(ads)} \tag{5}$$

When gas sensors were exposed to HCHO gas, the gas chemisorbed oxygen species would react with HCHO molecules and trapped electrons would be released to conduction band. Thus, the thickness of electrons depletion layer decreased, causing to an enhancement on conductivity of the materials. The possible chemical reaction process was shown as Eqs. (6) and (7). Response of materials for detecting HCHO gas could be reflected by output voltage of the load resistor in text circuit.

$$HCHO_{(gas)} \rightarrow HCHO_{(ads)} \tag{6}$$

$$HCHO_{(ads)} + 2O^-(ads) \rightarrow CO_2 + H_2O + 2e^- \tag{7}$$

In the whole process, we could find that the operating temperature which affected the process of chemisorption and desorption played a critical role, it could influence the quantity of chemisorbed oxygen species and also affect the adsorption as well as desorption rate of detected gas on sensing thin films surface.

Conclusion

In conclusion, sheet and rod-like WO_3 have been successfully synthesized by a simple chemical precipitation route combined with a subsequent sintering process. XRD characterization showed the sintered products were monocline phase WO_3. SEM results demonstrated that as-obtained precipitate products were piled up by slices and transformed into rod-like particles after calcining. Gas sensing texts exhibited the obtained samples have excellent HCHO sensing performance especially in rate of response and recovery. The materials have a distinctive response to 100 ppm HCHO with very short time (5 s) and recovery time (15 s). These results mean that the WO_3 could be a candidate material for detecting HCHO gas in real-time.

References

1. Zhang YM, Lin YT, Chen JL, Zhang J, Zhu ZQ, Liu QJ (2014) A high sensitivity gas sensor for formaldehyde based on silver doped lanthanum ferrite. Sens Actuators B: Chem 190:171–176
2. Li YX, Chen N, Deng DY, Xing XX, Xiao XC, Wang YD (2017) Formaldehyde detection: SnO_2 microspheres for formaldehyde gas sensor with high sensitivity, fast response/recovery and good selectivity. Sens Actuators B: Chem 238:264–273
3. Tan RQ, Guo YQ, Zhao JH, Li Y, Xu TF, Song WJ (2011) Synthesis, characterization and gas-sensing properties of Pd-doped SnO_2 nano particles. Trans Nonferrous Met Soc China 21 (7):1568–1573
4. Dong CJ, Liu X, Han BQ, Deng SJ, Xiao XC, Wang YD (2016) Nonaqueous synthesis of Ag-functionalized In_2O_3/ZnO nanocomposites for highly sensitive formaldehyde sensor. Sens Actuators B: Chem 224:193–200
5. Li P, Tang ZA, Yu J, Zhang FT, Wei GF, Huang ZX, Hu YN (2008) Study on a micro-gas sensor with SnO_2-NiO sensitive film for indoor formaldehyde detection. Sens Actuators B Chem 132(1):74–80
6. Cai ZX, Li HY, Ding JC, Guo X (2017) Hierarchical flowerlike WO_3 nanostructures assembled by porous nanoflakes for enhanced NO gas sensing. Sens Actuators B: Chem 246:225–234
7. Li F, Guo SJ, Shen JL, Shen L, Sun DM, Wang B, Chen Y, Ruan SP (2017) Xylene gas sensor based on Au-loaded $WO_3 \cdot H_2O$ nanocubes with enhanced sensing performance. Sens Actuators B: Chem 238:364–373

Electrochemical Fabrication of Micro/Nanoporous Copper by Electrosynthesis-Dealloying of Cu–Zn Alloy in Deep Eutectic Solvent

Shujuan Wang, Xingli Zou, Xueliang Xie, Xionggang Lu, Yinshuai Wang, Qian Xu, Chaoyi Chen and Zhongfu Zhou

Abstract The electrodeposition of Cu–Zn alloy films on a Ni substrate from CuO and ZnO precursors in choline chloride (ChCl)/urea (1:2 molar ratio) based deep eutectic solvent (DES) was firstly carried out. Then, micro/nanoporous Cu films were fabricated by further electro-dealloying of the synthesized Cu–Zn alloy films. XRD analysis indicates that the phase compositions of the deposited Cu–Zn alloys are Cu_5Zn_8 and $CuZn_5$. Further investigation shows that the more-active component Zn would be dissolved during the electro-dealloying process, and porous Cu can be obtained. The result reveals that the electrosynthesis-dealloying process may provide a promising strategy for the production of micro/nanoporous Cu at low temperature.

Keywords Porous copper · Electrosynthesis · Dealloying · Cu–zn alloy Deep eutectic solvent

S. Wang · X. Zou (✉) · X. Xie · X. Lu (✉) · Y. Wang · Q. Xu · Z. Zhou
State Key Laboratory of Advanced Special Steel and Shanghai Key Laboratory of Advanced Ferrometallurgy and School of Materials Science and Engineering, Shanghai University, Shanghai 200072, China
e-mail: xlzou@shu.edu.cn

X. Lu
e-mail: luxg@shu.edu.cn

X. Zou
Center for Electrochemistry Department of Chemistry, The University of Texas at Austin, Austin, TX 78712, USA

C. Chen
School of Materials and Metallurgy, Guizhou University, Guiyang 550025, China

Z. Zhou
Institute of Mathematics and Physics, Aberystwyth University, Aberystwyth SY23 3BZ, UK

The Minerals, Metals & Materials Society, *TMS 2018 147th Annual Meeting & Exhibition Supplemental Proceedings*, The Minerals, Metals & Materials Series,
https://doi.org/10.1007/978-3-319-72526-0_2

Introduction

Due to high surface areas, micro/nanoporous metals with superior physical and chemical properties have drawn broad attention in various applications, including catalysis, sensors, actuators, fuel cells, and batteries, etc. [1–4]. Several approaches have been proposed to fabricate micro/nanoporous metals, such as covering casting, melt gas injection, thermal evaporation, sputter deposition, vapor deposition technique, electrochemical methods, and dealloying [5, 6]. Among these techniques, the dealloying technique that refers to selective dissolution of one or more components from an alloy has attracted wide attention and becomes a promising process to produce micro/nanoporous metals. In addition, electrochemical dealloying method exhibits a relatively versatile superiority to prepare various micro/nanoporous metals, *e.g.*, gold, platinum, silver, nickel, tungsten, copper, and so on [7–9]. In recent year, nanoporous Cu with a relatively low cost and several exceptional features, such as low density, high modulus of elasticity and reaction activity, shows a promising application prospect [6]. However, the electrochemical fabrication of micro/nanoporous metals are usually carried out in acidic or alkaline media, which commonly involves the chemical/electrochemical etching of the substrate surface [10].

Room-temperature ionic liquids (RTILs) generally possess many distinct advantages such as extremely low vapor pressure, high ionic conductivity, wide electrochemical windows, high solubility of metal salts, and thermal stability [11, 12]. In particular, RTILs have gained considerable attention in comparison with aqueous solutions. In various kinds of RTILs, deep eutectic solvents (DESs) have been considered as the potential alternatives sharing most of physical and chemical properties of conventional RTILs [13]. Practically considering the cost and handling ionic liquids, DESs are obtained primitively by mixing quaternary ammonium salts with hydrogen-bond donors such as alcohols, amides, and acids [14, 15]. Moreover, the other merits of rifeness include low cost, nontoxicity and more accessible synthesis with high purity, make them attractive solvents for large-scale technological applications.

In this work, we report the electrosynthesis-dealloying of Cu–Zn alloy from CuO and ZnO precursors in DES on a Ni substrate. Moreover, the fabrication process for the micro/nanoporous copper is discussed.

Experimental

Electrolyte Preparation

Choline chloride [$HOC_2H_4N(CH_3)_3Cl$] (ChCl) (Aldrich 99%), urea [NH_2CONH_2] (Aldrich > 99%), ZnO (Aldrich > 99%) and CuO (Aldrich > 99%) were used as received. To remove the water residue and trapped air, ChCl and urea were dried

under vacuum at 333–363 K for at least 12 h. The eutectic mixture in the molar proportion of ChCl: urea = 1:2 was stirred under argon atmosphere using a polytetrafluoroethylene(PTFE)-coated magnetic stir bar in a beaker at 353 K until a homogeneous and colorless solution was formed. Thereafter, 0.01 M CuO and 0.1 M ZnO were dissolved in the ChCl-urea DES at 343 K and stirred until the blue transparent electrolyte was obtained.

Electrodeposition and Dealloying Experiments

Electrodeposition experiments were performed in a three-electrode system, consisting of a Ni foil (1 cm^2) as the working electrode, a platinum plate (0.6 cm^2) as the counter electrode, and a silver wire (99.995%, 1.0 mm in diameter) as the reference electrode. Approximately 50 mL of the ChCl-urea DES containing 0.01 M CuO and 0.1 M ZnO was used as the electrolyte for the electrodeposition experiments. The experimental device is shown in Fig. 1. Mirror polishing with 0.5 μm alumina paste, washing with 10 vol% H_2SO_4, degreasing with acetone, and rinsing with deionized water constitute the sequence in surface pretreating for the Ni substrate. Subsequently, the electrodeposition of alloy films on the Ni substrate was carried out at three different potentials (−1.1,−1.15 and −1.2 V versus Ag) by using chronoamperometry (CA) electrodeposition in the electrolytic cell at 343 K for 2 h. In order to minimize the water ingress into the electrolyte, all the electrodeposition experiments were conducted in a sealed cell. All final products were taken out from the cell, followed washing with distilled water and anhydrous alcohol, and then dried.

After the electrodeposition, the formed Cu–Zn alloy films were then dealloyed in the same system as the electrodeposition experiments at room temperature at −0.5 V verus Ag for a certain time (from 100 to 900 s). The dealloying potential was chosen from the cyclic voltammetry curve, and more negative than which will result in the dissolution of copper and more positive than which will lead to the dissolution of zinc [16]. Then, the as-prepared samples were removed from the solvent, carefully washed with anhydrous alcohol and distilled water, and dried finally by N_2 gas stream. The whole simplified process of electrodeposition and electrosynthesis-dealloying is shown in Fig. 2.

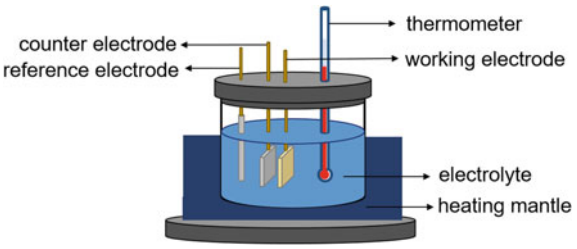

Fig. 1 Schematic illustration of the experimental device for the electrodeposition and dealloying processes

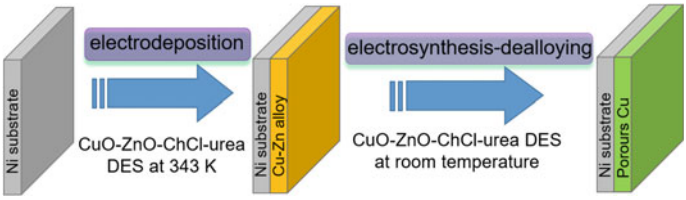

Fig. 2 Schematic illustration of the electrodeposition and electrosynthesis-dealloying processes

The microstructure of the electrodeposited Cu–Zn alloy films and the dealloyed products were examined with scanning electron microscope (SEM, JEOL JSM-6700F). The corresponding phase structures were analyzed by X-ray diffraction (XRD, Bruker-AXS D8Advance) with Cu-Kα radiation at a scan rate of $5° \text{ min}^{-1}$.

Results and Discussion

Electrodeposition of Cu–Zn Alloy Films

Chronoamperometry experiments were carried out in the potential range of −1.1 to −1.2 V. Typical current-time transient curves recorded in the ChCl-urea DES containing 0.01 M CuO and 0.1 M ZnO at 343 K for 2 h are shown in Fig. 3. From the enlarged part of Fig. 2, the drastically negative increasing of the initial current (A → B) may be caused by the double layer charging [17]. Then, as a result of the formation and growth of Cu-Zn alloy nuclei, the current (B → C) gradually shifts positively until a steady value (C → D). Compare the current-time curves recorded

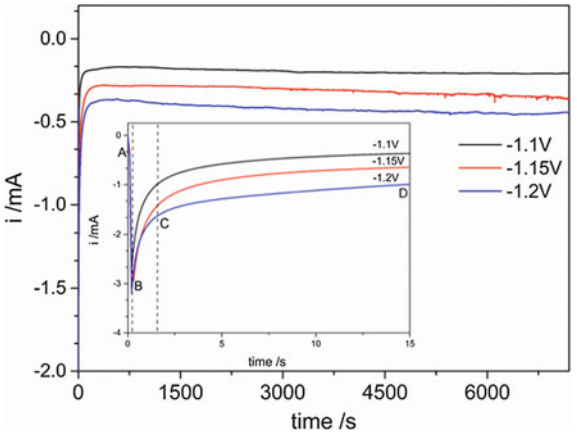

Fig. 3 Current-time curve of the electrodeposition process on a Ni substrate in ChCl-urea DES containing 0.01 M CuO and 0.1 M ZnO at different potentials from −1.1 to −1.2 V at 343 K for 2 h

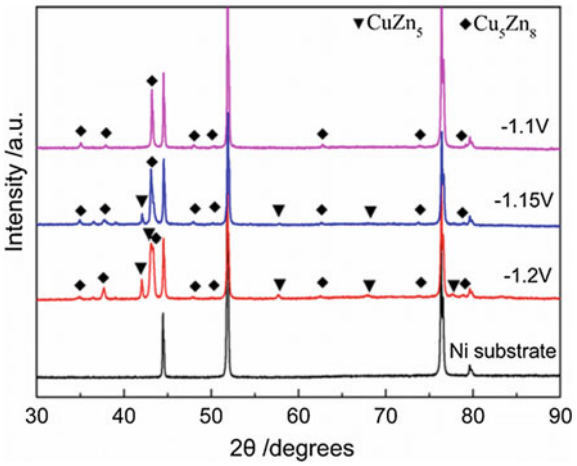

Fig. 4 XRD patterns of the electrodeposited Cu–Zn alloy films on a Ni substrate in ChCl-urea DES containing 0.01 M CuO and 0.1 M ZnO at different potentials and 343 K for 2 h

at different potentials, it is obvious that the final stable current increases with more negative potential.

Copper and zinc co-deposition was performed on a nickel foil at a constant potential, and the as-deposited samples were examined by XRD and SEM analysis. Figure 4 shows the XRD patterns the Cu–Zn alloy films electrodeposited at different potentials and 343 K for 2 h. The characteristic diffractions are attributed to Ni, $CuZn_5$ and Cu_5Zn_8 phases. Cu_5Zn_8 phase was produced at −1.1 V. As the potential becomes more negative, $CuZn_5$ electrodeposition becomes more distinct, owing to the increasing of the Zn electrodeposition rate at more negative potentials (−1.15 and −1.2 V) [18].

The corresponding SEM images of the samples electrodeposited at different potentials are shown in Fig. 5a–c. It can be observed that the particle size of the electrodeposits is approximately 800 nm (Fig. 5a). The pure Cu_5Zn_8 film electrodeposited at −1.1 V is uniform. As the electrodeposition potential increases to −1.15 V, the Cu–Zn alloy film is consisted of flower-shaped clusters (Fig. 5b). With further increasing the electrodeposition potential to −1.2 V, the Cu_5Zn_8 and

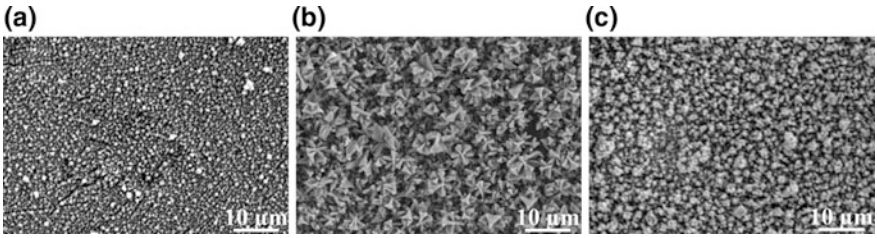

Fig. 5 SEM images of the electrodeposited Cu–Zn alloy films on a Ni substrate in ChCl-urea DES containing 0.01 M CuO and 0.1 M ZnO at different potentials: **a** −1.1 V, **b** −1.15 V, **c** −1.2 V at 343 K for 2 h

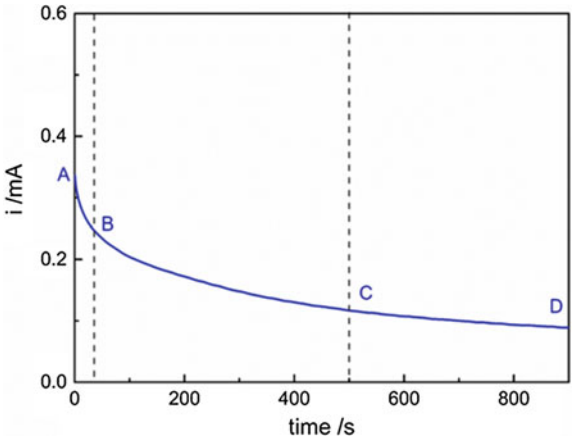

Fig. 6 Anodic stripping current-time curve of the dealloying of the formed Cu–Zn alloy film at −0.5 V and room temperature

$CuZn_5$ alloy films with conglobating structure are observed, owing to the Zn electrodeposition rate increases with more negative potential (Fig. 5c).

Synthesis of Porous Copper

The current-time curve recorded during the dealloying process of the Cu-Zn alloy film is shown in Fig. 6. The Cu-Zn film was firstly prepared on a Ni substrate in ChCl-urea DES containing 0.01 M CuO and 0.1 M ZnO at −1.15 V and 343 K for 2 h, then the electrochemical dealloying process was carried out at −0.5 V verus Ag and room temperature. As shown in Fig. 6, there are three stages in the anodic stripping current-time curve. The initial part (A → B) of the dealloying current decreases sharply, which is related to the quick dissolution of outmost zinc from the uppermost surface. The corresponding SEM examination of the film (Fig. 7b) shows that the flower-shaped clusters were gradually disappeared. As time goes by (B → C, C → D), the current decreases slowly and eventually stabilizes, implying more Zn atoms were dissolved (Fig. 7c–d, then porous Cu was obtained. The EDS spectrum confirms that the dealloyed product is Cu.

Conclusions

The electrochemical fabrication of micro/nanoporous copper films has been investigated by electrochemical alloying/dealloying of Cu-Zn alloy films in the ChCl/urea-based DES. It is suggested that the formation of Cu-Zn alloys including Cu_5Zn_8 and $CuZn_5$ alloy depends on the cathodic electrodeposition potential. More negative potential can contribute to the increasing of Zn electrodeposition rate.

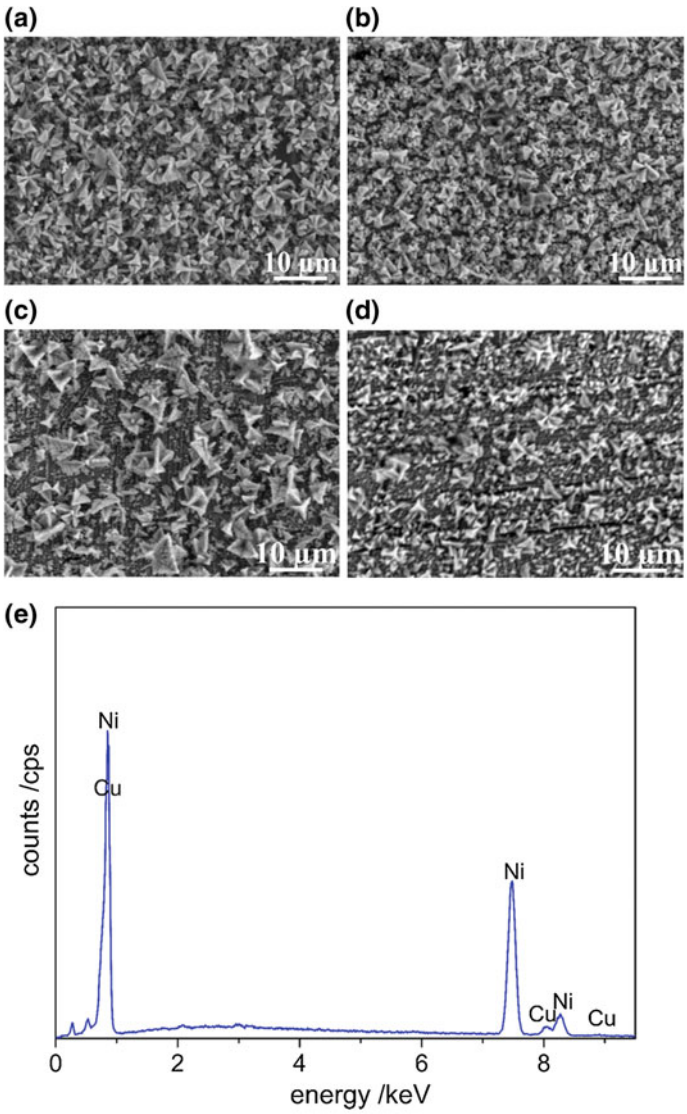

Fig. 7 SEM images of the electrodeposited Cu–Zn alloy films after being dealloyed for different times: **a** 0 s, **b** 70 s, **c** 400 s, **d** 900 s. and **e** EDS spectrum of after being dealloyed for 900 s

Comparing to the traditional acidic or alkaline solutions, the method of preparing micro/nanoporous copper in DES on the Ni substrate is more environmentally sustainable and recyclable, and spends less time (less than 1 h) in lower temperature. Moreover, this method may also have implications for the production of other porous metal materials.

Acknowledgements The authors thank the National Natural Science Foundation of China (No. 51574164) and the National Basic Research Program of China (No. 2014CB643403) for financial support. We also thank the Instrumental Analysis and Research Center of Shanghai University for materials characterization.

References

1. Noh J, Park S, Boo H, Kim HC, Chung TD (2011) Nanoporous platinum solid-state reference electrode with layer-by-layer polyelectrolyte junction for pH sensing chip. Lab Chip 11:664
2. Ding Y, Erlebacher J (2003) Nanoporous metals with controlled multimodal pore size distribution. J Am Chem Soc 125:7772–7773
3. Imokawa T, Williams KJ, Denuault G (2006) Fabrication and characterization of nanostructured Pd hydride pH microelectrodes. Anal Chem 78:265
4. Erlebacher J, Aziz MJ, Karma A, Dimitrov N, Sieradzki K (2001) Evolution of nanoporosity in dealloying. Nature 410:450–453
5. Huang JF, Sun IW (2005) Fabrication and surface functionalization of nanoporous gold by electrochemical alloying/dealloying of Au-Zn in an Ionic Liquid, and the self-assembly of L-cysteine monolayers. Adv Funct Mater 15:989–994
6. Tuan NT, Park J, Lee J, Gwak J, Lee D (2014) Synthesis of nanoporous Cu films by dealloying of electrochemically deposited Cu-Zn alloy films. Corros Sci 80:7–11
7. Thorp JC, Sieradzki K, Tang L, Crozier PA, Misra A, Nastasi M, Mitlin D, Picraux ST (2006) Formation of nanoporous noble metal thin films by electrochemical dealloying of Pt_xSi_{1-x}. Appl Phys Lett 88:1107
8. Chen LY, Yu JS, Fujita T, Chen MW (2009) Nanoporous copper with tunable nanoporosity for SERS applications. Adv Funct Mater 19:1221–1226
9. Liu F, Yamazaki T, Shen YB, Meng D, Kikuta T, Nakatani N, Kawabata T (2008) Dealloying derived synthesis of W nanopetal films and their transformation into WO_3. J Phys Chem C 112:1391–1395
10. Zhang Q, Abbott A, Yang C (2015) Electrochemical fabrication of nanoporous copper films in choline chloride-urea deep eutectic solvent. Phys Chem Chem Phys 17:14702–14709
11. Hartley J, Ip C, Forrest G, Singh K, Gurman S, Ryder K, Abbott A, Frisch G (2014) EXAFS study into the speciation of metal salts dissolved in ionic liquids and deep eutectic solvents. Inorg Chem 53:6280–6288
12. Endres F, Abbott AP, Macfarlane DR (2008) Electrodeposition from ionic liquids. Wiley-VCH 70:729–754
13. Wagle DV, Zhao H, Baker GA (2014) ChemInform Abstract: Deep eutectic solvents: sustainable media for nanoscale and functional materials. Acc Chem Res 47:2299
14. Abbott A, Boothby D, Capper G, Davies D, Rasheed R (2004) Deep eutectic solvents formed between choline chloride and carboxylic acids: versatile alternatives to ionic liquids. J Am Chem Soc 126:9142
15. Abbott A, Capper G, Davies D, Rasheed R, Tambyrajah V (2002) Novel solvent properties of choline chloride/urea mixtures. Chem Commun 9:70–71
16. Xie X, Zou X, Lu X, Xu Q, Lu C, Chen C, Zhou Z (2017) Electrodeposition behavior and characterization of copper-zinc ally in deep eutectic solvent. J Appl Electrochem 47:679–689
17. Li RQ, Chu QW, Liang J (2015) Electrodeposition and characterization of Ni–SiC composite coatings from deep eutectic solvent. RSC Adv 5:44933–44942
18. Juškėnas R, Karpavičienė V, Pakštas V, Selskis A, Kapočius V (2007) Electrochemical and XRD studies of Cu–Zn coatings electrodeposited in solution with D-mannitol. J Electroanal Chem 602:237–244

Electrosynthesis of CuNPs from e-Waste

M. Islas Hernández, P. A. Ramírez Ortega, L. García Hernández and U. M. Flores Guerrero

Abstract Currently, e-waste, such as integrated circuits or microprocessors, has been increasing, due to the development of new technologies that make them obsolete. Therefore, to minimize the impact of this type of waste and recover the valuable metals present in them. In this work, copper nanoparticles (CuNPs) were synthesized from e-waste by electrochemical techniques. The voltammetric studies were performed in a typical electrode cell of three electrodes, as a working electrode was used a stainless steel plate, as a counter electrode a dimensionally stable anode (DSA) and as a reference electrode a saturated calomel electrode (SCE). The voltammetric studies allowed to determine the interval attributed to the reduction of the ionic copper species, the chronopotentiometric studies allowed to obtain homogeneous deposits on the surface of the working electrode, which was characterized by scanning electron microscopy (SEM-EDS) showing a morphology spherical type with sizes between 5 and 13 nm. On the other hand the studies by the technique of galvanostatic pulses allowed the obtaining of CuNPs, which were characterized by SEM-EDS and UV-Vis spectroscopy.

Keywords e-Waste · Copper · Nanotechnology · Electrochemistry Synthesis

Introduction

Globalization has increased the demand for electronic equipment; this causes companies in the sector to adopt increasingly aggressive strategies for product innovation, especially those related to information technologies. This has resulted in

M. Islas Hernández (✉) · P. A. Ramírez Ortega · L. García Hernández
U. M. Flores Guerrero
Centro de Desarrollo En Nanotecnología, Área Electromecánica Industrial,
Universidad Tecnológica de Tulancingo, Camino a Ahuehuetitla no. 301
Colonia Las Presas Hidalgo, Tulancingo 43642, Mexico
e-mail: 110519@utec-tgo.edu.mx

The Minerals, Metals & Materials Society, *TMS 2018 147th Annual Meeting & Exhibition Supplemental Proceedings*, The Minerals, Metals & Materials Series,
https://doi.org/10.1007/978-3-319-72526-0_3

shorter life cycles for electronic products and consequently a significant increase in the volume of e-waste that can cause serious environmental problems due to the toxicity of some of its products components. Electronic or e-waste is one of several categories of Waste Electrical and Electronic Equipment (WEEE) that includes several products that have recyclable components including ferrous metals and non-ferrous metals. Despite growing international attention on the subject of electronic waste, Mexico still does not have a specific plan for the management of this waste, since within the comprehensive plan of the Ministry of Environment and Natural Resources it is not clear whether waste should be considered dangerous or special handling. This problem has attracted the attention of governments, companies and consumers looking to design strategies for the control and proper disposal of these wastes in an effort to protect the environment [1]. Printed Circuit Board (PCB) is the basis of the electronics industry. The composition of PCBs is made of non-metallic materials (polymers and ceramics). Heavy metals in e-waste become contaminants if they are altered by anthropogenic activities. Toxic metals can be Cadmium, Mercury, Lead, Selenium and Arsenic which are highly polluting for the environment and human health. Similarly, e-waste is composed of metals such as Copper, Tin, Iron, Nickel, Silver, Gold and Palladium [2]. For some materials, a recycling system can not be implemented spontaneously with high effectiveness, which makes it an issue that concerns technology, planning and economic and environmental regulation. Due to the increasing severity of recycling policies, countries such as China, Japan, Taiwan and South Korea, including the European Union and some US states, have established standards for the management and regulation of e- waste). Accordingly, strategies for the implementation of an appropriate recycling system should be based on three points: (i) technical feasibility; (ii) economic sustainability of the process; and (iii) a high and real level of social support for the program [3].

The antimicrobial property of Copper has been demonstrated in microbial agents such as Staphylococcus aureus, Escherichia coli 0157: H7, Pseudomonas aeruginosa, Enterobacter aerogenes, Listeria Monocytogenes, Enteric salmonella, Campylobacter jejuni, Legionella pneumophila, Clostridium difficile and Mycobacterium tuberculosis, based on EPA criteria (Environmetal Protection Agency). Studies by Michels et. al. show that the antimicrobial action on the copper surface is exerted with the same efficiency at different temperatures (35–22 °C) and in different relative humidity conditions (between 90 and 20% ranges). Other metals such as silver, which also have antibacterial properties, are only active in high temperature and humidity environments. Copper's antimicrobial mechanisms are complex and occur in different forms, both within cells and interstitial spaces between cells. One factor responsible for the antimicrobial properties of copper is the ability of this metal to easily accept or donate its electrons (i.e copper has a high oxidation and high reduction potential). This chemical property allows Copper ions to alter the proteins inside the cells of the microbes so that the proteins can no

longer perform their normal functions [4]. Nanotechnology is a subclassification of technology in the fields of biotechnology, physics, chemistry and other scientific domains. The National Nanotechnology Initiative (NNI) of the United States defines nanotechnology as the understanding and control of matter in dimensions from 1 to 100 nm, where unique phenomena that allow the development of new applications for the materials. The concept of nanotechnology was first mentioned by physicist Richard Feynman (Nobel Prize in Physics in 1965). In 1974, Professor Norio Taniguchi of the University of Science in Tokyo in an article published, titled, "On the Basic Concept of Nanotechnology" states that nanotechnology consists of the processes of separation, consolidation and deformation of matter atomic or molecular levels [5]. There are techniques and methods for the synthesis of nanoparticles both physical and chemical, one that stands out for its versatility and reliability. Electrochemistry, for its part, consists of applying a potential difference between two electrodes inside a conductive solution (electrolytic solution) in order to generate the chemical reaction known as Redox, ie, oxidation-reduction. Electrochemistry is a branch of physicochemistry, which studies the chemical changes produced by the electric current and the production of electricity through chemical reactions. All electrochemical reactions involve the transfer of electrons and are therefore oxidation-reduction reactions. Oxidation and reduction occur simultaneously and takes place at the interface, between the electrolyte and the electrodes (cathode and anode), which are shown separated from each other, so that oxidation occurs at the anode and the reduction in the cathode [6]. Therefore, this work proposes the recovery of copper under non-aggressive chemical means, supplemented with electrochemical techniques for the exchange of ionic Cu to metallic Cu, being deposited on a stainless steel substrate, monitoring kinetics of solution concentration by the technique of spectroscopy After obtaining this procedure, the synthesis of Cu nanoparticles is sought for its possible application in the wastewater treaty and in the industrial sector, maintaining a minimum and economically accessible environmental impact for a larger scale, obtaining a viable methodology with an industrial technological impact.

Methodological Framework

Strategy

Figure 1 represents the block diagram for methodological development.

Figure 2 shows the scheme of the synthesis process by means of electrochemical techniques to obtain CuNPs from electronic waste.

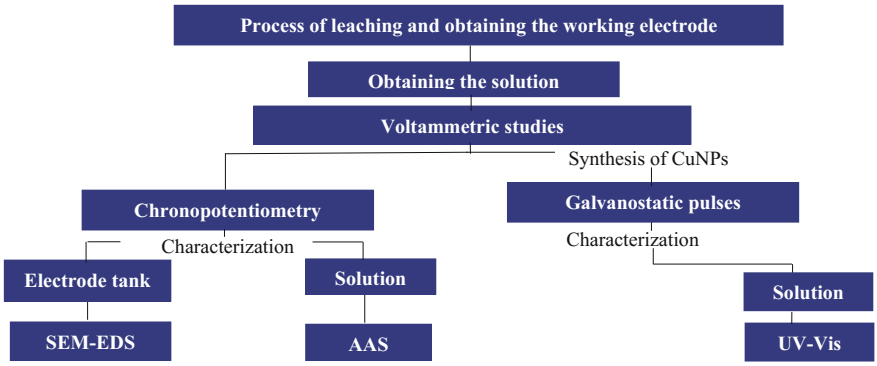

Fig. 1 Block diagram for the synthesis of CuNPs

Methodology

Experimental Characteristics

(a) Cyclic voltammetry

The Voltamperometric (CV) studies were carried out within a typical three-cell electrode with a capacity of 100 m. As a working electrode (WE) a stainless steel sheet was used, as against electrode (CE), a mesh type DSA and, as reference electrode (RE), a Saturated Calomel electrode (SCE). The potential window was −0.65 to 0.7 V versus ECS, and a scanning rate of 15 mVs-1 was used.

(b) Chronopotentiometric techniques

For the application of the chronopotentiometric technique, an experimental arrangement of two electrodes (WE-stainless steel and CE-DSA) immersed in the solution were used inside a cell with a capacity of 100 mL. The study was carried out for 21600 s applying the potentials obtained from the CV technique.

(c) Galvanostatic pulses

Galvanostatic pulses (GP) with an experimental arrangement of two electrodes (WE-stainless steel and RE-DSA) were used inside a cell with a capacity of 100 mL. The duration of the technique was 20 s with a separation time of 0.00007 s between pulses in the presence of ultra sound. The working electrodes were polished. For the synthesis of nanoparticles an ultrasonic Autoscience model AS2060B.

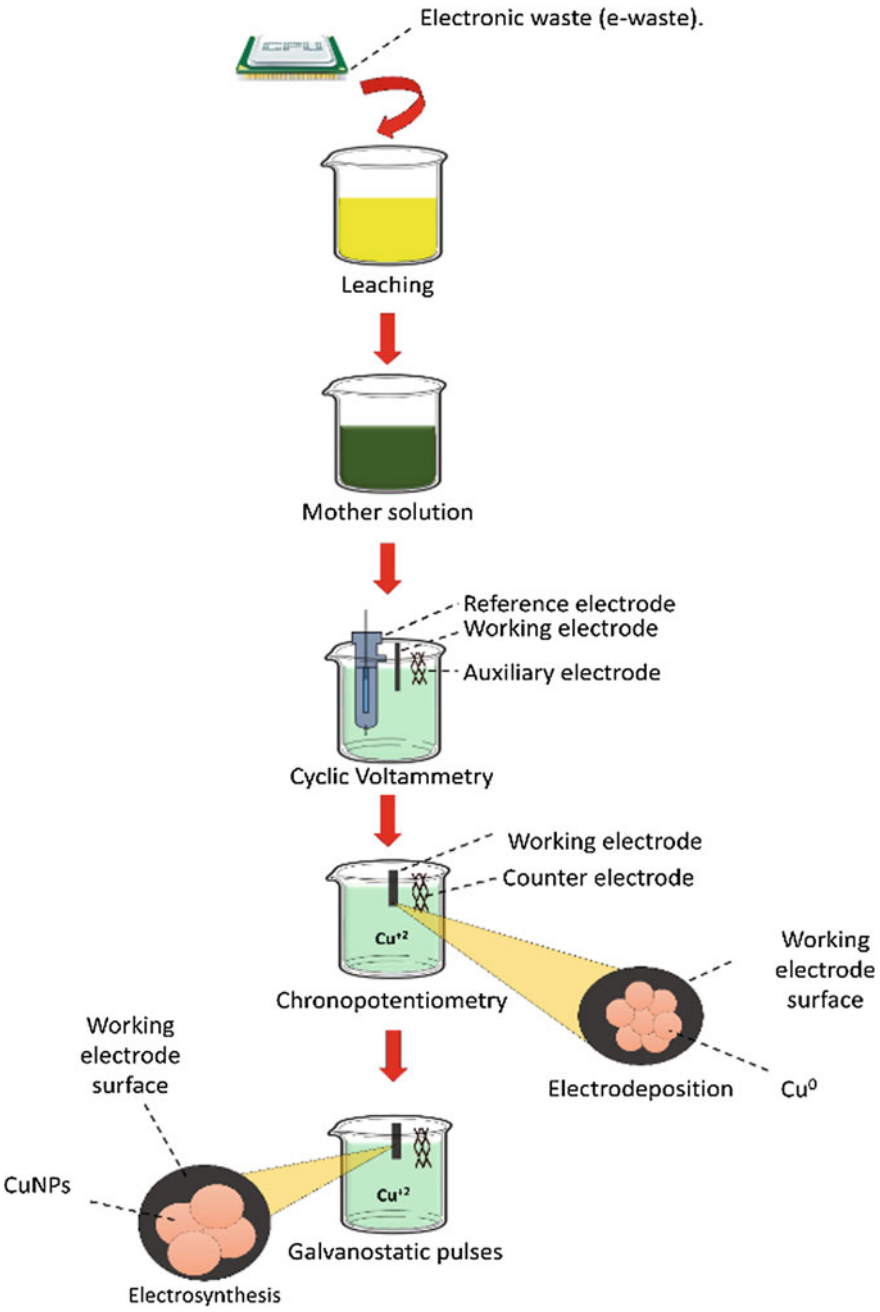

Fig. 2 Process by means of electrochemical techniques to obtain CuNPs from electronic waste

Both the techniques of cyclic voltammetry, chronopotentiometries and galvanostatic pulses were carried out in a galvanostat potentiostat Princeton Applied Research model VersaSTAT4

Characterization

The characterization of the deposits obtained on the stainless steel electrode was performed in a Scanning Electron Microscope coupled to a JEOL EDD model: JSM-6701F. The concentration monitoring of Cu^{+2} was obtained in a PerkinElmer Atomic Absorption Spectroscopy (AAnalyst200) model. The characterization of the solution after the galvanostatic pulses technique was performed was performed in a PerkinElmer model Lambda 35 UV-VIS spectrophotometer.

Analysis and Interpretation of Results

Voltammetric Studies

Figure 3 shows the voltamperogram of the target on the stainless steel working electrode in the potential window −0.7 to 0.5 V versus SCE on a stainless steel working electrode at a scanning speed of 15 mVs^{-1}. In Fig. 3 it can be seen that in

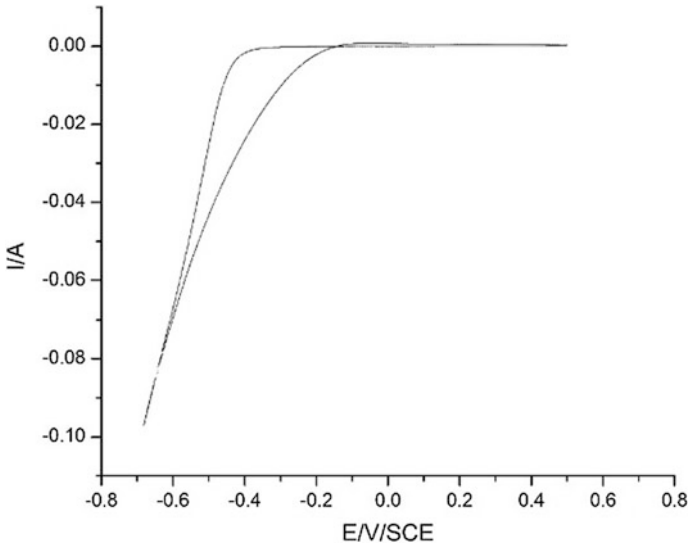

Fig. 3 Voltamperogram of the solution on the stainless steel electrode in the window from −0.7 to 0.5 V and a scanning speed of 15 mVs^{-1}

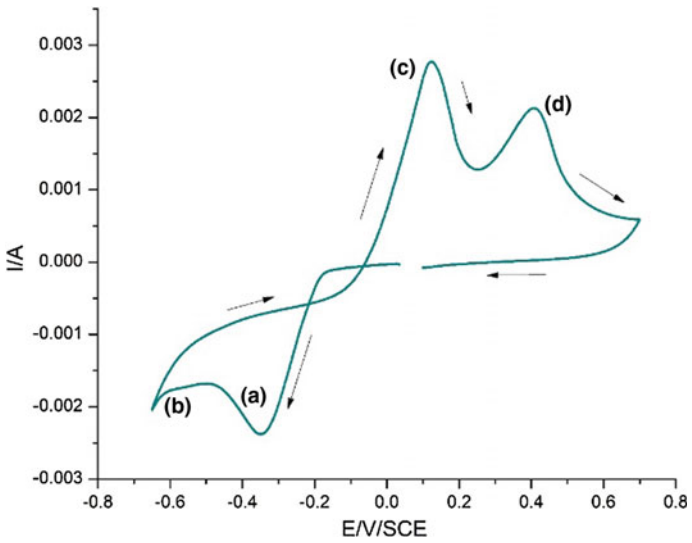

Fig. 4 Voltamperogram of the solution on the stainless steel electrode in the window from −0.65 to 0.7 V and a scanning speed of 15 mVs^{-1}

the window of potential studied there is a reduction process, which starts at a potential of −0.2 V versus SCE and is attributed to the reduction of the medium, although the inverse sweep does not appreciates no oxidation process.

Figure 4 shows the voltamperogram of the electrolytic solution rich in copper ions on the stainless steel working electrode in the potential window of −0.65 to 0.7 V versus SCE at a scanning speed of 15 mVs^{-1}. In Fig. 4 shows two reduction processes, the first in the range of −0.0002 to −0.0023 A (potential range −0.16 to −0.5 V versus SCE), which is attributed to the reduction of ionic species of copper (a); and the second starting at −0.00163 A, which is attributed to the reduction of the medium (b). Similarly, in the reverse sweep two peaks are observed, the first in the range of −0.000532 to 0.00132 A (potential range −0.2 to 0.24 V versus SCE) and the second in the range of 0.00132–0.00054 A (potential range 0.24–0.7 V versus SCE), which are attributed to the oxidation of the ionic species of copper (c) and of the medium (d), respectively. The obtainment of the reduction interval of the ionic copper species allowed to perform the chronopotentiometric studies.

Chronopotentiometric Studies

Chronopotentiometry is a galvanostatic technique in which a current is passed through the working electrode, recording the change of potential with respect to the electrolysis time. Figure 5 shows the results of the chronopotentiometric study in

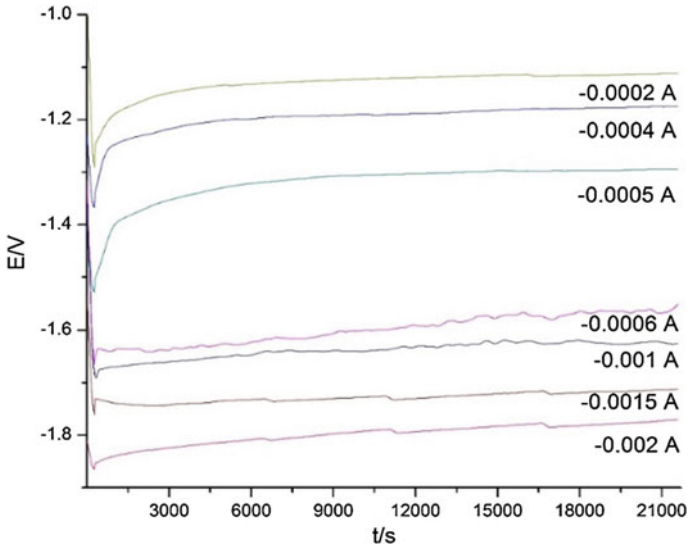

Fig. 5 Cronopotentiograms of the reduction of the ionic species of copper on the stainless steel electrode, in the range of −0.0002 to −0.002 A in a time of 21600 s (360 min) without stirring

the range of −0.0002 to −0.002 A. The macroelectrolysis was carried out for 21600 s (360 min) without agitation.

In Fig. 5 it can be seen that in the range of currents studied as the current takes more cathodic values the potential is more negative; Likewise, it can be seen that the potential takes more positive values as the electrolysis time increases. Likewise, it can be seen that each galvanostatic transient presents practically the same slope which indicates that the reduction of the ionic copper species is being carried out on the surface of the working electrode (stainless steel).

When comparing the behavior of the different deposits during the chronopotentiometric studies, it was possible to identify the current that generated a homogeneous deposit on the working electrode, being this −0.0005 A.

After the application of chronopotentiometric techniques, the deposits obtained on the surface of the stainless steel electrode were analyzed by USB microscope, to observe the surface of the electrode and the generated deposit. This was to determine which of the streams had generated a homogeneous deposit on the stainless steel surface.

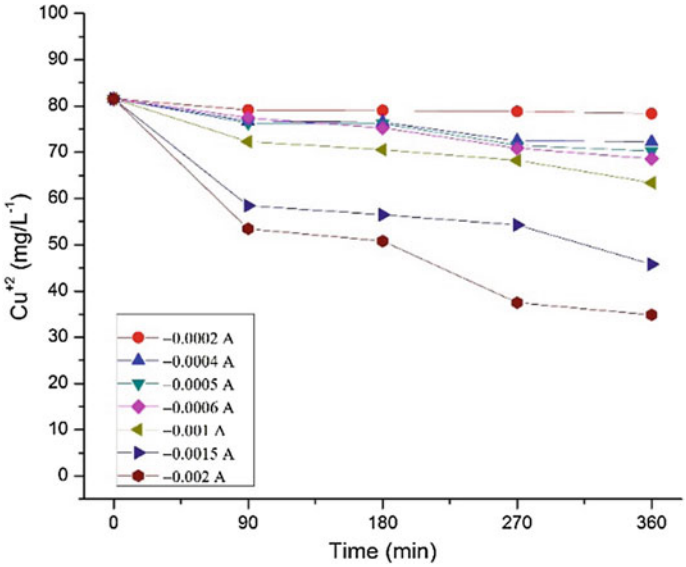

Fig. 6 AAS performed at 7 different currents, used for chronopotentiometric studies, monitoring copper reduction during 360 min

Analysis by Atomic Absorption Spectroscopy

To confirm the reduction of the ionic copper species in the electrolytic solution, a study was carried out by AAS, for which during the chronopotentiometric experiments samples were taken every 90 min throughout the electrolysis time.

Figure 6 shows the variation of the concentration of the ionic copper species present in the electrolytic solution with respect to the electrolysis time by AAS for each of the chronopotentiometric studies carried out on the stainless steel working electrode in the current range of −0.0002 A at −0.002 A for 21600 s (360 min) without stirring.

In Fig. 6 it can be seen that in the entire range of imposed currents (0.0002 A to −0.002 A) the concentration of the electroactive copper species decreases throughout the electrolysis time.In addition, as the current takes more cathodic current values the reduction of the copper ion species decreases in the electrolytic solution, which indicates that a larger amount of copper deposit is generated on the surface of the stainless steel electrode. The current that showed a higher deposit was −0.002 A, which is demonstrated by observing the change of concentration in Fig. 6. In order to know the composition and morphology of the deposits obtained by the chronopotentiometric technique, the characterization was performed by Scanning Electron Microscopy and Energy Dispersive Spectroscopy

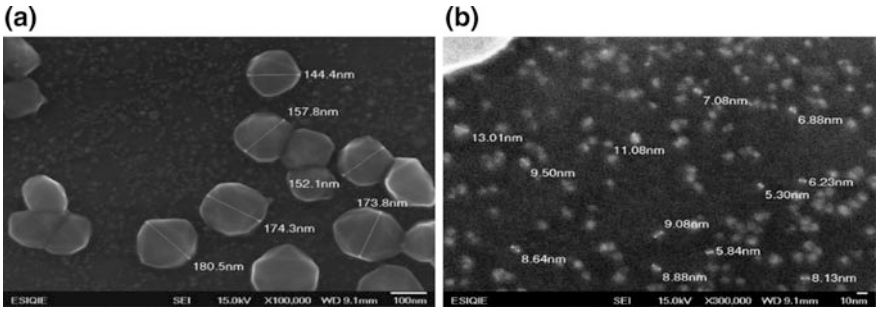

Fig. 7 Micrographs obtained by the SEM mark JOEL model: JSM-6701F from the deposit obtained on the surface of the stainless steel electrode, after which the study was performed by chronopotentiometric technique of the solution in a time of 360 min

Analysis by Scanning Electron Microscopy

Figure 7a shows the micrograph obtained by SEM at 100,000× of the deposit obtained on the surface of the stainless steel electrode by imposing a current of −0.0005 A during a time of electrolysis of 360 min. In said micrograph, particles deposited on the electrode with sizes between 180 and 144 nm with a spheroidal type morphology can be observed.

On the other hand, the formation of particles between 5.3 and 13 nm with a spheroidal morphology is observed in Fig. 7b on the same deposit at 300,00×.

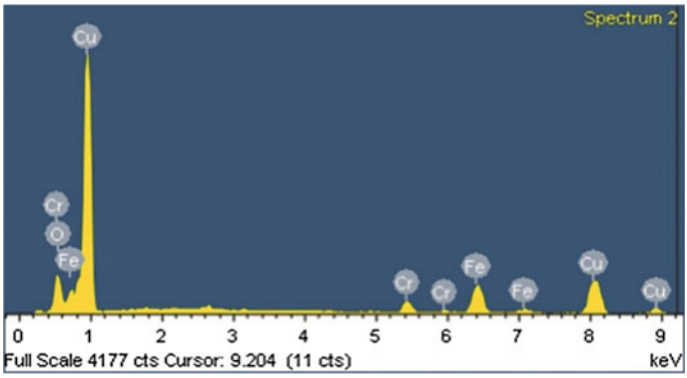

Fig. 8 EDS spectra of the Cu^0 tank on stainless steel at a current −0.0005 A to 360 min

Analysis by Energy Dispersive Spectroscopy

Figure 8 shows the spectrum obtained by energy dispersive spectroscopy (EDS) of the deposit generated on the surface of the stainless steel electrode at a current of −0.0005 A, during a time of electrolysis of 360 min. This study revealed the nature of the deposit, which corresponds to Cu and the remaining elements correspond to the substrate (stainless steel).

Study by Galvanostatic Pulses

For the synthesis of copper nanoparticles the technique of galvanostatic pulses was used with the current that generated a homogeneous deposit and presented a more stable behavior, which was of −0.0005 A during 20 s to 100 cycles; Also, a 100 mL capacity cell was used with a two-electrode array (ET-stainless steel, E-DSA). This study showed that the current of −0.0005 A, used in chronopotentiometric studies, is feasible for the synthesis of CuNPs by means of the galvanostatic pulses technique.

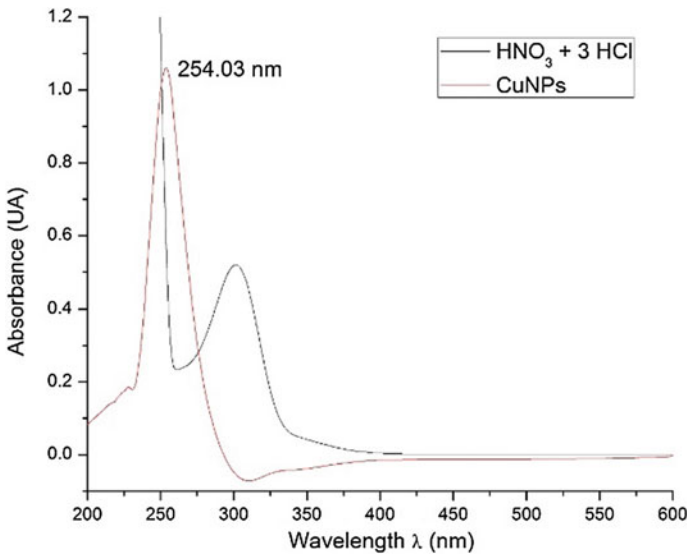

Fig. 9 UV-VIS spectrogram for a sample of colloidal CuNPs obtained by galvanostatic pulses

Analysis by UV-Vis Spectroscopy

Next, the UV-Vis spectrogram is presented for colloidal CuNPs obtained by means of the galvanostatic pulses technique. Wavelength against absorbance is plotted (Fig. 9).

When analyzing the target it is observed that it has absorbance attributed to the double bonds present in the acidic solution under study, then it is compared with the spectrum of the solution obtained from the technique of galvanostatic pulses. The absorbance plasmon is observed at a wavelength of 230–310 nm, whose maximum absorbance is at 254 nm. Also, the band width is associated with an almost uniform distribution in the size of the nanoparticles obtained. The presence of CuNPs is checked since the plasmon is within the characteristic range for said nanoparticles ranging from 250–350 nm.

Conclusion

Applying the technique of cyclic voltammetry to the solution from the stock solution on the stainless steel electrode the peaks of the redox pair were observed. In the area of reduction, a peak of −0.00023 to −0.002 A (potential range −0.16 to −0.5 V versus SCE) was present, which is attributed to the reduction of the ionic species of copper (a), and the second starting at −0.00163 A, which is attributed to the reduction of the medium (b). Similarly, in the reverse sweep two peaks are observed, the first in the range of −0.000532 to 0.00132 A (potential range −0.2 to 0.24 V versus SCE) and the second in the range of 0.00132–0.00054 A (potential range 0.24–0.7 V versus SCE), which are attributed to the oxidation of the ionic species of copper (c) and of the medium (d), respectively. Chronopotentiometric studies allowed the identification of the current where a homogeneous Cu deposit was present on the stainless steel electrode, which was −0.0005 A. The analysis by AAS shows that as current values tend to be more cathode in a range of −0.0002 to −0.002 A, the copper concentration in the solution actually decreases. The micrographs obtained by SEM showed the morphology of the deposit obtained on the stainless steel electrode; in addition, particles of approximately 180–144 nm and 13 to 5.3 nm of spheroidal shape were observed in some sites. Spectra by EDS revealed that the nature of the deposit obtained on the stainless steel electrode is Copper. It was demonstrated by means of UV-Vis Spectroscopy that the synthesis of CuNP's is viable by the galvanostatic pulse technique as well as the chronopotentiometric studies carried out throughout this work.

References

1. Arroyo López P, Villanueva Bringas M, Gaytán Iniestra J, García Vargas M (2014) Contaduría y Administración, Vol 59, pp 9–41
2. Chmielewski AG, Urbański TS, Migdał W (1997) Separation technologies for metals recovery from industrial wastes. Hydrometallurgy 45(3):333–344
3. Zhou Yihui, Qiu Keqiang (2009) A new technology for recycling materials from waste printed circuit boards 175:1–2
4. Michels HT, Noyce JO, Keevil CW (2009) Effects of temperature and humidity on the effcacy of methicillinresistant Staphylococcus aureus challenged antimicrobial materials containing silver and copper, Vol 49, pp 191–195
5. Ramos del Valle LF (2006) Nanotecnologia, Vol 9
6. Garritz A, Chamizo JA (1994) QUÍMICA. Addison-Wesley Iberoamericana S.A., Wilmington, Delawer, E.U.A, pp. 856

Experimental Investigation of the Effect of ZnO-*Citrus sinensis* Nano-additive on the Electrokinetic Deposition of Zinc on Mild Steel in Acid Chloride

Oluseyi O. Ajayi, Olasubomi F. Omowa, Olugbenga A. Omotosho, Oluwabunmi P. Abioye, Esther T. Akinlabi, Stephen A. Akinlabi, Abiodun A. Abioye, Felicia T. Owoeye and Sunday A. Afolalu

Abstract This work investigated the effect of ZnO-*Citrus sinensis* nano-additive on the electrokinetic deposition of Zinc on mild steel in acid chloride. Fifty-four plates of (100 × 10 × 3) mm^3 mild steel samples were cut, cleaned with dilute H_2SO_4 solution, rinsed in water and dried. The nano-additive was produced by infusing 30 ml Orange Juice extract in Zinc Oxide solution. The acid chloride electrolyte consisting of 71 g ZnCl, 207 g KCl and 35 g H_3BO_3 in 1 l of distilled water was divided into six portions. The nano-additive with different molar concentrations 0(0.2)1.0 was added to each portion of the acid chloride. Nine plates of mild steel samples were electroplated with zinc as the anode in each of the six prepared electrolyte solution and plated at different times (three plates each at 10, 15 and 20 min). The effects of electroplating on the average weights were measured and the results from the experiment showed the optimal nano-additive concentration and electroplating time.

Keywords Nano-additive · Nanotechnology · Corrosion protection Deposition · Mild steel

O. O. Ajayi (✉) · O. F. Omowa · O. A. Omotosho · O. P. Abioye
A. A. Abioye · S. A. Afolalu
Department of Mechanical Engineering, Covenant University,
Canaan Land, Ota, Ogun State, Nigeria
e-mail: oluseyi.ajayi@covenanatuniversity.edu.ng

E. T. Akinlabi
Department of Mechanical Engineering Science, University of Johannesburg,
Johannesburg, South Africa

S. A. Akinlabi
Department of Mechanical and Industrial Engineering Technology,
University of Johannesburg, Johannesburg, South Africa

F. T. Owoeye
Chemistry Department, Covenant University, Canaan Land, Ota, Ogun State, Nigeria

The Minerals, Metals & Materials Society, *TMS 2018 147th Annual Meeting & Exhibition Supplemental Proceedings*, The Minerals, Metals & Materials Series,
https://doi.org/10.1007/978-3-319-72526-0_4

Introduction

Steel has found various applications in the industries because of their excellent properties. It is reasonable in cost, longer life, and variability in strength levels and also very adaptable to corrective rework [1]. These properties made steel to meet the ever increasing stringent engineering needs in the industries. Steel is a major material in automative and other sectors majorly because of corrosion resistance with zinc coatings, ease of joining, recyclability and good crash energy absorption [2–4].

In most manufacturing sectors and industries chloride solutions are used as cleaning agents and other function but steel being widely used in such industries are affected by the action of chloride solutions [5]. Electrodeposited steel can be made to withstand and reduce aggrieved strength of chloride as a medium [6, 7]. Different methods have been employed for corrosion protection but zinc coating is the major method used in industrial sectors as protective coating for large quantities of products and other fabricated ferrous metal parts [5, 8–13]. The addition of agents to aqueous electroplating baths plays an important role because of the important effects they produce on the growth, structure and glossiness of deposits [12, 13]. Additives have different benefits which include reduction in grain size and tendency to tree, improve mechanical and physical properties, reduces stress and pitting, increase current density range and promote levelling and brightening of deposit. In this investigation, the effect of orange nanoparticle additive on the surface morphology of the substrate performance was studied to determine the optimal nano-additive concentration and electroplating time.

Experimental Method

Samples of mild steel plates were cut into various pieces with the dimension 100 × 10 × 3 mm. Surface preparation was done using polishing machine with different grades of emery papers. The pickling of the mild steel was done for 15 min using dilute H_2SO_4 of 120 ml of H_2SO_4 in 1litre of water. The samples were rinsed, dried and stored in a desiccator. The percentage chemical composition of the mild steel substrate was analysed using Optical Emission Spectrometer as showed in Table 1.

Orange nanoparticle supernatant was used for this experiment. The additive was prepared by infusion of 30 ml of orange juice in zinc oxide solution of varying concentrations 0.2, 0.4, 0.6, 0.8 and 1 M. The mixtures were left to react for 48 h. The reacted mixture were centrifuged at 4500 rpm for 15 min. The supernant were then, decanted from the mixture. The nano particle suspension was transferred to watch glass, after which it was air dried and stored in sample bottles at room temperature. The acid chloride bath for this experiment contained zinc chloride, boric acid and potassium chloride. The acid chloride solution was prepared by

Table 1 Chemical composition of the mild steel substrate

Elements	% Composition
Si	0.131
Mn	0.3042
Ni	0.0071
Mo	0.0007
C	0.057
Sn	0.005
Co	0.0013
Al	0.0257
Cu	0.0029
P	0.0144
Fe	Bal

Table 2 The additives concentration and electroplating time

Additive	Concentration (M)	Time (Min)
Control	0	10, 15, 20
ZnO-*Citrus sinensis* nano-additives	0.2	10, 15, 20
	0.4	10, 15, 20
	0.6	10, 15, 20
	0.8	10, 15, 20
	1	10, 15, 20

dissolving 71 g of zinc chloride, 207 g of potassium chloride and 35 g of boric acid in 1 l of distilled water. This solution was filtered to remove any form of impurity.

The mild steel to be electroplated (cathode) and two zinc anodes were partially immersed in 150 ml of acid chloride bath. The cathode was connected to the negative terminal while the zinc anodes were connected to the positive terminal of the direct current (DC) power supply, current was set to 0.8 A. The additives concentrations and plating time were varied as shown in Table 2. The weight of the mild steel was measured before and after the plating to determine the mass deposited. The experiment was replicated to arrive at an average coherent value.

Results and Discussion

Effect of Electrodeposition Time

The result of the electro deposition experiment revealed the different mass addition of zinc on mild steel substrate in the bath for varying orange zinc oxide nanoparticle

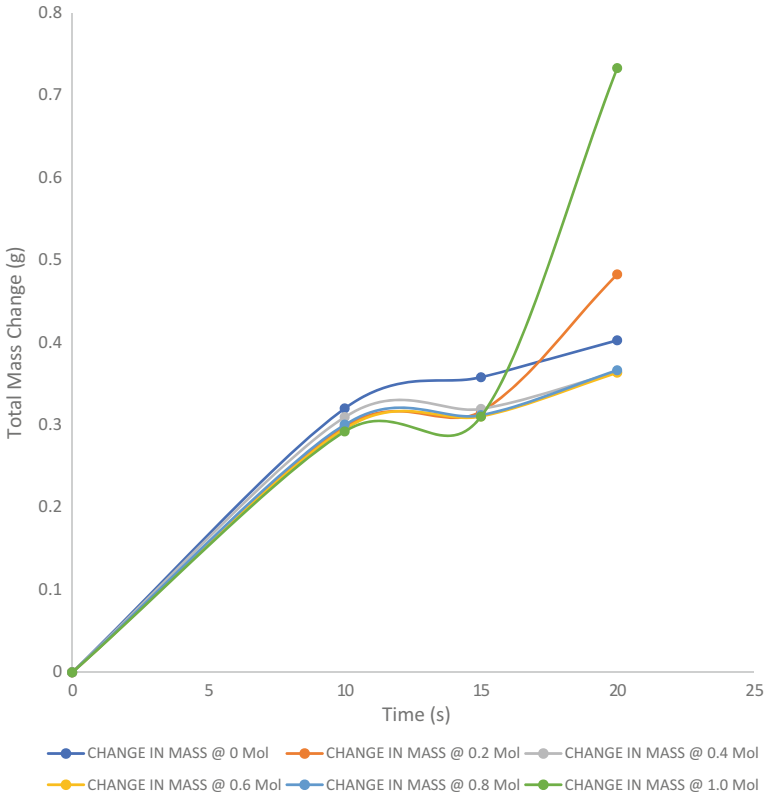

Fig. 1 A graph of the change in mass against deposition time for 0, 0.2, 0.4, 0.6, 0.8 and 1.0 M additive concentration

additive concentrations. The results obtained were for plating time of 10, 15 and 20 min. Figure 1 showed the graph of the change in mass against time at 0, 0.2, 0.4, 0.6, 0.8 and 1.0 M additive concentrations. A steady increase in total mass change was observed as the electrodeposition time increased for all the additive concentration used. Thus, irrespective of the additive concentration, the total mass change increases with electrodeposition time.

*Effect of the ZnO-*Citrus Sinensis *Nano-additive*

Figure 2 shows the effect of ZnO-*Citrus sinensis* nano-additive on the electrodeposition of Zinc on steel at different deposition time. For deposition done at 10 and 15 min, there was no significant impact of the additive concentration on the mass change. However, at 20 min electrodeposition time, a significant increase in total mass changed was observed at 1 M additive concentration.

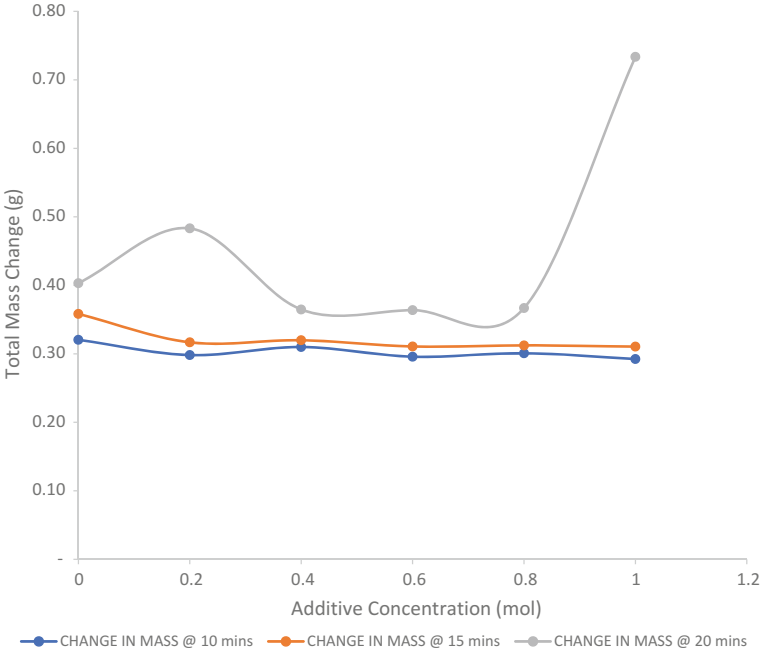

Fig. 2 A graph of the change in mass against the additive concentration at different electrodeposition time

Conclusion

Nanodeposition of zinc on steel in acid chloride environment with ZnO-*Citrus sinensis* nano-additive increases with electrodeposition time.

Moreover, physical examination of the zinc deposited mild steel shows a smoother surface finish with an increase in the concentration of ZnO-*Citrus sinensis* as nano-additive in the electrolyte solution.

Also, the study of the effect of ZnO-*Citrus sinensis* nano-additive on the mass change shows that optimum combination of factors to yield optimum deposition of zinc on mild steel occurred at the additive concentration of 1 M when electroplated for the period of 20 min.

References

1. Singh MK (2016) Application of Steel in Automotive Industry. Int J Emerg Technol Adv Eng 6(7):2250–2459
2. DeCicco JM (2005) Steel and iron technologies for automotive light weighting. Environ Defense

3. Ultralight Steel Auto Body (1998) Final report. American Iron and Steel Institute, Southfield, MI. March
4. Opbroek E, Weissert U (1998) Ultralight steel auto closures project. SAE Paper No. 982308
5. Popoola API, Fayomi OS (2011) Performance evaluation of zinc deposited mild steel in chloride medium. Int J Electrochem Sci 6(2011):3254–3263
6. Fang F, Brown B, Nesic S (2010) Corr Sci Sect 67:1–12
7. Abdullah M, Fouda AS, Shama SA, Afifi EA (2008) Africa J Pure Appl Chem 2(2008):83–91
8. Donald RA (1994) The science and engineering of materials. PWS Publishing Company, Washington, p 8
9. Joo YL, Joe WK, Min KL, Hyun TK, Su-moon P (2004) J Electrochem Soc 151:C25–C31
10. de Pedro N, Adriana N, Correia P, Walney SA (2007) J Braz Chem Soc 18:1164–1175
11. Shivakumara S, Manohar U, Arthoba Naik Y, Venkatesha Enkatesha TU (2007) Influence of additives on electrodeposition of bright Zn–Ni alloy on mild steel from acid sulphate bath. Bull Mater Sci 30(5):455–462. © Indian Academy of Sciences
12. Popoola API, Fayomi OSI (2011) Effect of some process variables on zinc coated low carbon steel substrates. Sci Res Essays 6(20):4264–4272, 19 Sept 2011. https://doi.org/10.5897/sre11.777. ISSN 1992-2248 ©2011 Academic Journals
13. Hague IU, Ahmad N, Akhan Jour A (2005) Chem Soc Pak 27:307–311
14. Field S, Weil AD (1951) Electroplating. Sir Isaac Pitman & Sons Ltd., London, p 136
15. Dini JW (1993) Electrodeposition—the materials science of coatings and substrates. Noyes Publications, New Jersey, USA, p 195

Obtaining of Iron Nanoparticles (Fe NP's) for Treatment of Water Contaminated with As

D. Barrón-Romero, L. García-Hernández, P. A. Ramírez-Ortega, I. A. Reyes-Domínguez, M. U. Flores Guerrero, M. J. Ivey Cruz and M. N. Hernández Escamilla

Abstract Iron nanoparticles exhibit interesting properties that can be exploited in a variety of applications such as mitigation of wastewaters. For the development of this project a typical cell of three electrodes was used, an iron working electrode was used against a ruthenium oxide mesh as dimensional stable anode and as reference electrode a saturated calomel electrode. The electrochemical techniques used were: cyclic voltammetry, chronopotentiometry and galvanostatic pulses. The characterization of the solution treated by the galvanostatic pulses technique was performed by UV-Vis, where it was possible to observe the characteristic band of iron nanoparticles. The materials deposited on the electrode were characterized by SEM-EDS to observe the size of the particles obtained by the cronopotentiometrys. To study the affinity of the iron nanoparticles on heavy metals, a solution containing arsenic was prepared; the reduction of arsenic was studied by AAS, calculating the concentration of arsenic ions contained in the solution.

Keywords Synthesis · Iron nanoparticles · Affinity · Arsenic mitigation

Introduction

In many parts of the world, potable water is contaminated with arsenic. This element is eliminated by mining, chemical industries and refineries, etc. [1]. The presence of arsenic in groundwater can also be natural due to the leaching of rocks

D. Barrón-Romero (✉) · L. García-Hernández · P. A. Ramírez-Ortega · M. U. Flores Guerrero · M. J. Ivey Cruz · M. N. Hernández Escamilla
Electromechanics Industrial Area, Tulancingo Technological University, Road to Ahuehuetitla, No. 301 Col. Las Presas, 43642 Tulancingo, Hidalgo, Mexico
e-mail: barrron.romero.daniel@gmail.com

I. A. Reyes-Domínguez
Institute of Metallurgy, Autonomous University of San Luis Potosí, Av. Sierra Leona No. 550, Lomas 2nd Section, 78210 San Luis Potosi, S. L. P., Mexico

The Minerals, Metals & Materials Society, *TMS 2018 147th Annual Meeting & Exhibition Supplemental Proceedings*, The Minerals, Metals & Materials Series,
https://doi.org/10.1007/978-3-319-72526-0_5

and sediments containing this element [2]. This groundwater contains large amounts of arsenic and are consumed by millions of people around the world in countries like Bangladesh, Cambodia, China, India, Laos, Myanmar, Nepal, Pakistan and Vietnam in Asia [3]. This problem is also present in the American continent, in countries such as Argentina, Mexico, Chile, Peru, the United States, Brazil and Canada [4, 5]. For these reasons, the US Environmental Protection Agency has established the amount of 10 μg L^{-1} as the maximum contamination level allowed in drinking water [6]. Therefore, several alternatives have been studied to solve this problem. An alternative is nanotechnology with the use of compounds based on zero-valent iron and iron oxide. The surface area presented by nanostructured materials is a good alternative to be able to mitigate the highest amount of arsenic contained in different aqueous environments.

Materials and Methodology

For the development of this project a typical cell of three electrodes was used, an iron working electrode against a mesh of ruthenium oxide and as reference electrode a saturated calomel electrode (SCE); taking the reported by Fajaroh et al. [7] and modifying certain variables of the process. The ferric sulfate solution was prepared using analytical grade chemicals and deionized water. The electrochemical techniques used were: cyclic voltammetry, chronopotentiometry and galvanostatic pulses, all the techniques were performed in a Princeton Applied Research Potentiostat-Galvanostat model VersaSTAT 4. The characterization of the solution treated by the galvanostatic pulses technique was performed by UV-vis and the materials deposited on the electrode by SEM-EDS.

To study the affinity of the iron nanoparticles on heavy metals, a solution with at a certain concentration was prepared using a standard of arsenic with an initial concentration of 1000 ppm. The reduction of arsenic has been studied by AAS by calculating the concentration of arsenic ions contained in the solution. Studies on the affinity of nanoparticles were carried out by adding the nanoparticles obtained through the deposition, controlling temperature, concentration and agitation. Subsequently the studies with the nanoparticles obtained by galvanostatic pulses followed the same procedure controlling the aforementioned variables.

Results and Discussion

Cyclic Voltammetry

Figure 1 shows the cyclic voltamperogram of the ferric sulfate electrolytic solution on the iron working electrode in the potential window of −1 to −1.5 V versus ECS

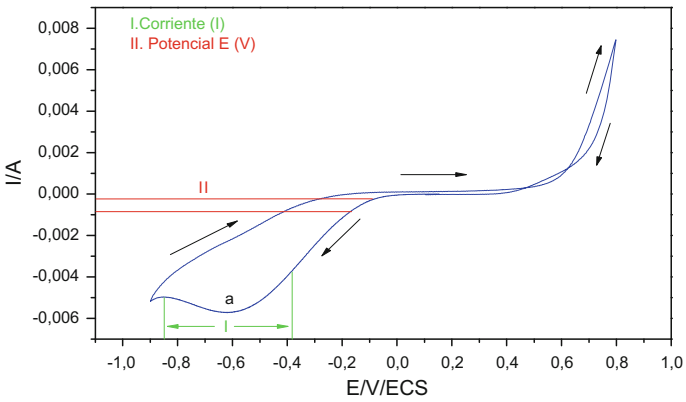

Fig. 1 Voltamperogram of the ferric sulfate solution on the iron electrode in the window from −1 to −1.5 V versus ECS at a scanning rate of 15 mV/s

at a scanning rate of 15 mV/s. A reduction of the ionic species can be observed from −0.382 to −0.847 mV. The information obtained from the peak of reduction was used to determine the potentials to be used in the chronopotentiometries for the electrodeposition on the working electrode.

Chronoamperometry

Chronopotentiometric studies served to know the most stable potentials. Figure 2 shows the chronamperometric analysis on an iron electrode. The macro electrolysis was carried out for 10800 S with stirring in the solution. Figure 2 shows the galvanic transient contained on the iron electrode in a current range of -2.45×10^{-5} to -5.6×10^{-3} A.

Electrodeposition

A coating was made to the anode of iron by immersing it in the cell, with solution of ferric sulphate and controlling the current and the electrical tension to cover or deposit a layer. As a result a very fine black powder was obtained, washed with deionized water and dried in a muffle at 170 °C until all traces of moisture were removed. Subsequently, it was analyzed by SEM to know the particle size and EDS to know the composition of the results obtained.

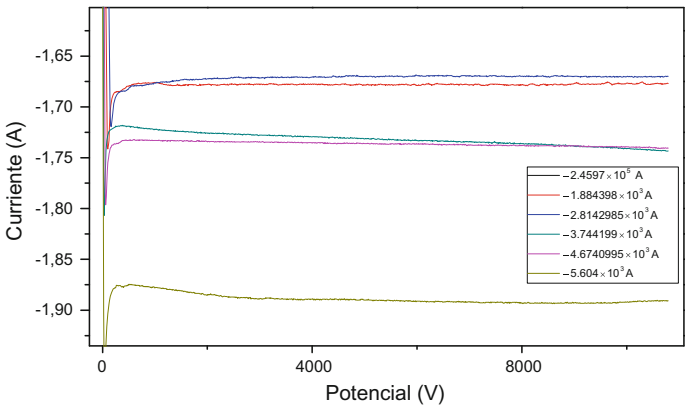

Fig. 2 Chronopotentiograms of the reduction of Fe^0 on the iron electrode, in the range of −0.000145 to −0.002 A current of -2.45×10^{-5} to -5.6×10^{-3} A without agitation

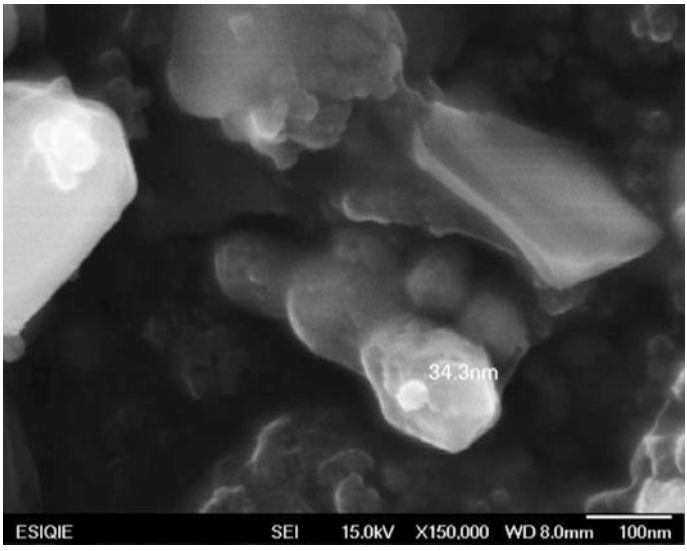

Fig. 3 Micrograph obtained by MEB from the coating made on the anode

SEM-EDS

The powder obtained by electrochemical deposition was analyzed by scanning electron microscopy, which shows the iron NPs, which have a size between 40 and 60 nm (Fig. 3).

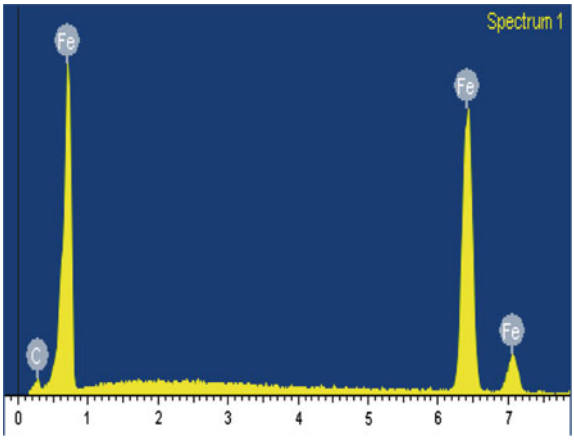

Fig. 4 EDS where the presence of iron oxide is confirmed

X-ray dispersive energy spectroscopy (EDS) confirmed the presence of iron in the reservoir, which is considered to be zero-valent iron because no oxygen is present in the EDS spectrum (Fig. 4).

UV-VIS

Next, the UV-Vis spectrogram for colloidal Fe NP's obtained by means of the galvanostatic pulses technique is presented. Wavelengths are plotted against absorbance. It is possible to observe an absorbance band from 250 to 330 nm attributed to Fe colloidal nanoparticles. Due to the lack of uniformity at the absorbance band it is speculated the presence of a variety of sizes and different iron oxides.

Studies of the Affinity of Arsenic with Synthetized Iron Nanoparticles

Due to the small amount of powder obtained during th electrodeposition it was decided to continue the studies only with the nanoparticles synthetized by the galvonostatic pulses. For the following studies, a solution with arsenic was prepared, later, colloidal iron nanoparticles obtained by galvanostatic pulses were added. The results presented below show a small decrease in the concentration of the arsenic ions contained in the solution (Fig. 5). The contaminated solution was

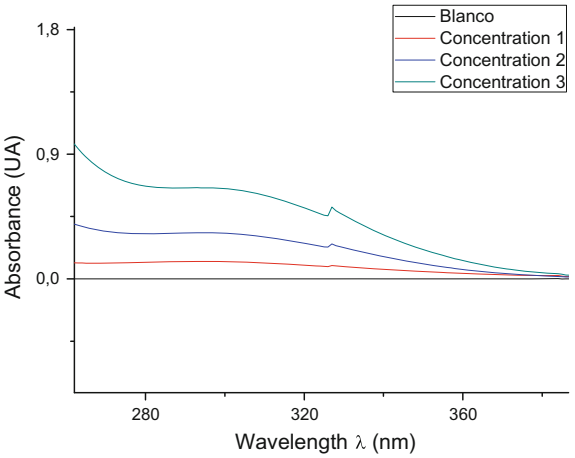

Fig. 5 UV-Vis spectrogram for the sample of colloidal Fe NP's obtained by the galvanostatic pulses

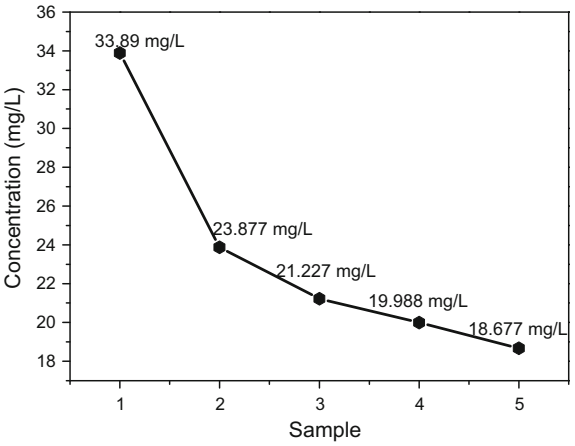

Fig. 6 Graphic made from the results obtained by AAS to know the concentration of arsenic after adding Fe NP's obtained by galvanostatic pulses

heated to 60 °C with constant magnetic stirring. During one hour, every 10 min 2 mL of the solution was added with iron nanoparticles. It's estimated that the reduction of arsenic ions in the solution is close to 40% (Fig. 6).

Conclusion

According to the results of cyclic voltammetry, the current and potential ranges were obtained where the reduction of the ionic species of iron takes place. By means of the chronopotentiometries an iron deposit was obtained on the surface of the working electrode, characterized by scanning electron microscopy (SEM-EDS), the technique of galvanostatic pulses allowed to obtain iron NPs that were

characterized by UV-vis. The result showed the obtaining of spherical nanoparticles of sizes ranging from 20 to 60 nm, grouped in agglomerates, throughout the electrode. The presence of iron and the absence of oxygen have been verified through EDS, suggesting that nanoparticles of zero-valent iron have been obtained. The results obtained by AAS showed that a considerable amount of arsenic was removed from the solution; a later characterization by TEM would confirm the absorption of arsenic by the nanoparticles synthetized.

References

1. Korngold E, Belayev LA (2001) Removal of arsenic from drinking water by anion exchangers. Desalination 141:81
2. Choong TSY, Chuah TG, Robiah Y, Lé Gregory Koay F, Azni I (2007) Arsenic toxicity, health hazards and removal techniques from water: an overview. Desalination 217:139–166
3. Santra SC, Samal AC, Bhattacharya P, Banerjee S, Biswas A, Majumdar J (2017) Arsenic in foodchain and community healt risk: a study in gangetic west bengal. Procedia Environ Sci 18:2–13
4. Mandal BK, Suzuki KT (2002) Arsenic around the world: a review. Talanta 58:201–235
5. Ning RY (2002) Arsenic removal by reverse osmosis. Desalination 143:237
6. EPA (2002) EPA Office of groundwater and drinking water. Implementation guidance for the arsenic rule. Report-816-D-02-005, Cincinnati, USA
7. Fajaroh F, Widiyastuti H, Winardi S (2012) Synthesis of magnetite by surfactant-free electrochemical method in aqueous system. Adv Powder Technol 23:328–333

Synthesis of Gold Nanoparticles Using the Extract of *Sedum praealtum* and Its Deposition on a Ceramic Substrate

L. García-Hernández, B. Aguilar-Pérez, J. Ramírez-Castro, P. A. Ramírez-Ortega, M. U. Flores-Guerrero and D. Arenas-Islas

Abstract In the present research the synthesis of gold nanoparticles (AuNPs) was established using the extract of *Sedum praealtum*. It should be pointed out that the conditions of synthesis directly influence the size, morphology, stability and physicochemical properties of the nanoparticles obtained. The extract of the plant was characterized by FTIR spectroscopy finding groups N-H, C-OH, who are credited with the reducing capacity of the ions AU^{+3}. The AuNP's obtained were characterized by UV-visible spectroscopy, observing plasmones absorbance between 530 and 550 nm characteristic of these nanoparticles, moreover they were characterized by SEM and was observed the nanometric sizes, the reduction capacity of the extract was evaluated by voltammetric study, observing the intervals of the processes of reducing and oxidation of the ionic species. Additionally, it was done the deposition of nanoparticles synthesized on a ceramic substrate in order to achieve its stabilization and then the nanocomposite was analyzed by SEM.

Keywords *Sedum praealtum* · Nanocomposite · Gold nanoparticles Synthesis

L. García-Hernández (✉) · B. Aguilar-Pérez · J. Ramírez-Castro · P. A. Ramírez-Ortega · M. U. Flores-Guerrero
Área de Electromecánica, Universidad Tecnológica de Tulancingo,
Camino a Ahuehuetitla no. 301 Colonia Las Presas, C.P. 43645 Tulancingo, Hidalgo, Mexico
e-mail: laura.garcia@utec-tgo.edu.mx; laura.garcia@utectulancingo.edu.mx

B. Aguilar-Pérez
e-mail: 1715110396@utec-tgo.edu.mx

J. Ramírez-Castro
e-mail: 1715110294@utec-tgo.edu.mx

D. Arenas-Islas
OceanogrSynthesis of Goldaphy/FCM-UABC, Carretera Ensenada-Tijuana no. 3917,
Fraccionamiento Playitas, 22860 Ensenada, Baja California, Mexico

The Minerals, Metals & Materials Society, *TMS 2018 147th Annual Meeting & Exhibition Supplemental Proceedings*, The Minerals, Metals & Materials Series,
https://doi.org/10.1007/978-3-319-72526-0_6

Introduction

There are several methods of synthesis of nanoparticles, however, most have negative effects on the environment, that is why they developed a discipline that is eco-friendly and economic, also has the same effectiveness as conventional physical and chemical methods; this is the green chemistry. This discipline has as main objective to promote the development and use of innovative chemical technologies that reduce or eliminate the use or generation of harmful substances in the design, manufacture and use of chemical products [1].

Through the control of biological molecules, green chemistry offers the synthesis of nanoparticles, several studies have reported the synthesis of metallic nanoparticles using plant species as reducing agents of ions. Nanoparticles of noble metals, and especially gold nanoparticles (AuNP's), are of great interest because they possess optical, electrical and conductive properties, properties which are suitable for application in controlled release of drugs, in therapeutic macromolecules, in gene therapy, biosensors, etc. [2].

Recently interest in AuNPs has been strengthened because of the physical behaviors they exhibit intrinsic to size; among them are the enhancement of the Raman dispersion by surfaces, magnetization and Resonance of surface Plasmons. This property occurs when the particle is smaller than the incident wavelength in the sample; the oscillating electric field induces an electric dipole, thus generating a negative charge on one side of the particle [3].

Different biological means are known to synthesize nanoparticles through green chemistry, among which are viruses, bacteria, yeasts, fungi and plants; those that possess greater potential to accumulate heavy metals have better ability to synthesize nanoparticles. Plants have been considered as the most eco-friendly route for the synthesis of metallic nanoparticles; its extracts contain bioactive alkaloids, phenolic acids polyphenols, proteins, sugars and terpenoids that play an important role in the reduction of metal ions and subsequent stabilization of the nanoparticles [4].

Nanoparticles are synthesized from all parts of the plant such as seeds, stem, flowers, leaves and skin of fruits, although the properties of the particles vary due to the change in concentration of the reducing agents through the plant [5]. The size of AuNPs governs its properties and the applications for which they are used: small size (2–15 nm) has applications such as immunohistochemistry, microscopy and biomarkers; medium-sized (20–60 nm) are used in the detection and purification of the environment, drug delivery, biomarkers, chemical sensors, DNA detection; while the large ones (80–250 nm) are used in forensic science, electronic devices, manufacturing, etc. [6]. The AuNPs were tested in the first room for the color changes of the colloidal solutions, ranging from purple to brown and the appearance of absorbance bands in the range of 510–550 nm, a result obtained by UV- Vis;

a shift of the bands towards larger wavelengths is associated with an increase in the size of the nanoparticles while the spreading indicates a greater distribution of such sizes and shapes.

In metallic colloids there is no well-defined metal-metal bond with a certain nuclearity, but they are agglomerates of atoms. An important aspect is the stabilization of NPs to maintain their size and shape as a function of time; in the absence of repulsive forces the particles tend to coagulate and subsequently precipitate. To counteract this problem, the use of stabilizing agents such as fatty acids, amines and polymers is used, which absorb on the surface of the newly formed nanoparticle and prevent aggregation [7]. Sometimes the plant species plays the role of stabilizer, however, there are other methods to achieve a more lasting stability, for example a deposition of the nanoparticles on a substrate; in this case a nanocomposite material is obtained.

Among the species reported with potential for the synthesis of nanoparticles is the species *Sedum praealtum*. It is native to Mexico and is distributed from the center of the country to Central America. It grows in semi-warm, semi-dry, temperate or cold climates, in humid stony soils. It tends to be associated with disturbed vegetation of xerophytic scrub, and oak and pine forest. The flowering period occurs between the periods from winter to spring. It resists temperatures of up to −3 °C and survives in full sunlight, for cultivation, can be watered once a week in spring and summer and once a month during the winter. This plant is multiplied by cuttings of leaves or stem in late spring or summer [8]. Herbaceous of long stems, reaches about 50 cm or more, the branch is basipeta and presents knots light brown color to reddish and white in terminal zones. Knots are associated to buds of leaf which have auxiliary yolks. The leaves emerge in clusters and later they become ramifications. The buds are arranged vertically in 6-leaf fascicles at an early stage, increasing the number of leaves as it grows. The leaves are green, fleshy, thick, spatulate with whole margin and reticulated venation in color light green, the apex is reddish, truncated when they are young and as they grow rounded. The base of the leaves is acuminate, sessile and without petiole. As they grow they leave the stem naked so that they are accumulated in the terminal part of it. The size of the leaves can reach up to 5 cm in length in the observed specimen. Yellow inflorescences have been observed in pinnate panicle cluster. Following the dichotomous key given by Rzedowski and Calderón, the described specimen was identified as *Sedum praelatum* belonging to the family Crassulaceae, considering the traits of shrub, glabra erecta with stems branched from the base, numerous leaves in basal rosette imbricated and flat, thick stems of woody appearance, yellow petals with non-exfoliating bark [9]. An image of the specimen used is shown in Fig. 1.

Fig. 1 *Sedum praealtum* specie

Experimental

Preparation of *Sedum praealtum* leaves extract

The extract was prepared from green leaves of the plant, washed with running water and then with distilled water. It weighed 1.25 g of the leaf and were maintained at 80 °C for 10 min in deionized water with Bath Maria. Once the extract was cold, it was leaked.

Characterization by of Sedum praealtum leaves extract

FTIR analysis

The leaves of *Sedum praealtum* were characterized by the technique Fourier-transform infrared spectroscopy (FTIR) to identify the main functional groups present. The sample was prepared by cutting the blade into small pieces.

Cyclic voltammetric study

As a working electrode (ET) a Pt electrode was used, as a counter electrode (CE) a type DSA mesh and as reference electrode (ER) a Calomel saturated electrode SCE. The sweep speed was 12 mVs^{-1}. In the first place the extract was analyzed and later the solution after the synthesis. The analysis was conducted in a galvanostat potentiostat Princeton Applied Research model VersaSTAT4.

Synthesis of gold Nanoparticles

To obtain nanoparticles, an ion Au^{+3} solution was used as a precursor agent at different concentrations (5, 10, 20 and 30 mgL^{-1}). The concentration of the extract used was 1.25%. The synthesis was made with Bath Maria at 80° C adding 10 mL of the precursor solution in aliquots of 2 ml every 10 min.

Characterization of gold nanoparticles

Characterization by UV-Vis

The samples obtained were analyzed in a UV-Visible spectrophotometer Perkin Elmer Lambda 35 double beam using 1 cm quartz cells of optical pathway in the

range of 200–800 nm λ, in order to identify the resonance band of the plasmon surface characteristic of the gold nanoparticles.

Preparation of the substrate

A ceramic substrate was used, obtained from natural source. The ceramic was washed with running water and cleaned manually. It was subsequently washed with deionized water. For drying, it was left under sunlight for 5 h. Past this time they proceeded with grinding in an agate mortar. The dust obtained was then dried in a flask at 100° C for 1 h and then sieved to obtain grains with a diameter of less than 38 microns.

Deposition of gold nanoparticles

The synthesis was carried out using a concentration of 1.25% of the plant and the precursor 30 mg L^{-1}, since under these conditions there was less precipitation. The ceramic matrix powder was added to the extract to make the deposition and later the synthesis was performed. After the 50 min of synthesis, the final solution was decanted and finally filtered using paper filtering, in this way, to separate from the solution the substrate with the nanoparticles. The paper filters obtained were introduced in a desiccator to later characterize the nanocomposite.

Characterization of the nanocomposite

SEM analysis:

The powder deposited on the filter paper was used for analysis by Scanning Electronic Microscope on an equipment JOEL model JSM-6701F.

X-ray Difraction:

The ceramic matrix with was deposited nanoparticles was dried with filter paper and subsequently analyzed by XRD.

Results and Discussion

Characterization of *Sedum praealtum* leaves extract

FTIR analysis

The characterization of the leaves of *Sedum praealtum* by FTIR was performed to know the main functional groups present in the extract of the plant. The Fig. 2 shows the obtained spectrum. The FTIR spectrum shows a pronounced peak in the 3400 cm^{-1} which is associated with the N-H band of amino groups or the hydroxyl group (−OH). The band in the 2908 cm^{-1} is attributed to alkanes groups (H-CH) or carboxylic acids (O-h). The band found in the 2843 cm^{-1} can be produced by alkanes groups or by the presence of acids (O-H). The band located at 1603 cm^{-1} denotes the presence of aldehydes (= C = O) or primary amides. The band at 1435 cm^{-1} may occur due to the presence of amino groups (N-H) or alcohols (C-OH). Likewise, the peaks in 1075 and 672 cm^{-1} denote the presence of amines and alquinos respectively. The reducing power of the ions Au^{+3} was attributed to the acid groups and OH.

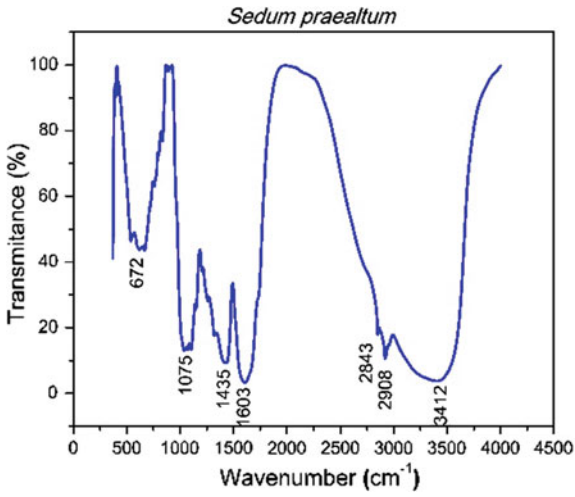

Fig. 2 Analysis by FTIR of *Sedum praealtum* leaves extract

Ciclic voltammetric study

In Fig. 3 is shown the Voltammogram obtained when analyzing (a) the extract of *Sedum praealtum* and (B) The solution of colloidal AuNPs after 50 min of synthesis. In the Voltamperograma (a) no peaks of oxidation and reduction are observed while in the Voltamperograma obtained from the synthesis of AuNPs is appreciated a peak reduction in the range of potential from −0.2 to −0.3 V which is attributed to the reduction of the ions Au^{+3} over Titanium electrode; Likewise, a second peak starts at −0.33 V, associated with the reduction of the medium. By compared both voltammograms is evidenced the ability of the species Sedum raealtum to reduce the ions Au^{+3} in Au^{0} and thus obtain nanoparticles; However, the reduction peak corresponds to Au^{+3} ions still present in the solution.

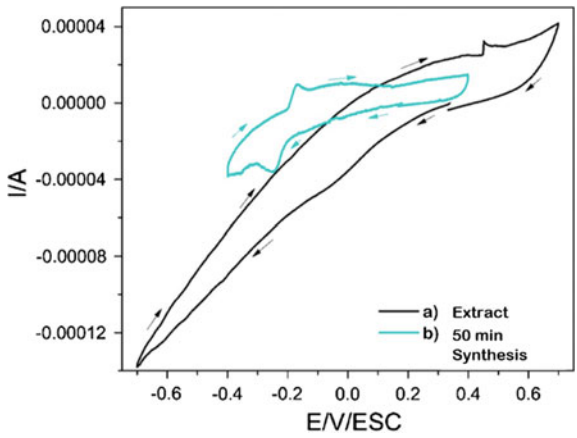

Fig. 3 Cyclic voltammetry performed on a Pt V vs ECS Electrode and an contra-electrode DSA, at a sweeping speed of 12 mVs^{-1}, for **a** the extract of *Sedum praealtum*, with a potential window of −0.7 to 0.7 V, and **b** colloidal nanoparticles solution 50 min of synthesis with a potential window of −0.4 to 0.4 V

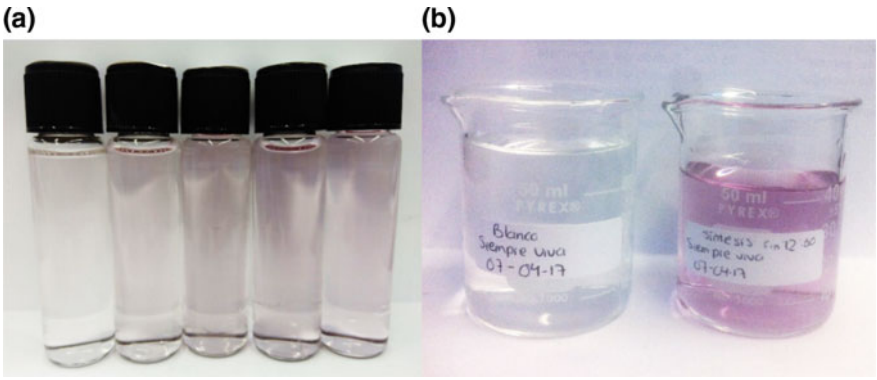

Fig. 4 **a** samples to different reaction time of colloidal AuNPs starting from a precursor with ion Au^{+3} concentration with initial concentration of 30 mgL^{-1} and extract to 1.25% of *Sedum praealtum* and **b** extract before and after adding the precursor ion solution Au^{+3}

Visual observation

The synthesis of AuNPs can be evidenced by the change of colouring of the colloidal solutions obtained. By adding the precursor agent of the Au^{+3} ions to the extract of *Sedum praealtum*, an immediate color change was presented, obtaining solutions with violet pink tones as shown in Fig. 4. A change in pH value of 7–2 was presented when synthesis was performed.

Characterization of gold nanoparticles

Characterization by UV-Vis

Figure 5 shows the spectrogram obtained for different synthesis of nanoparticles using the extract at 1.25% but varying the concentration of the precursor. In all the studies, the extract was analyzed and it was found that no plasmons of absorbance were present in the area of interest; later, it was compared with the synthesis of AuNPs. In the spectrogram, a plasmon of absorbance is observed in the region of 480–720 nm, which denotes obtaining AuNPs. In all the graphs it is observed that the band of the Plasmon suffers a shift towards greater wavelengths as the time of synthesis elapses, as well as to increase the concentration of the precursor agent, which is associated to the increase of the size of the Nanoparticles. Similarly, the Plasmon resonance band is widened proportionately to the increase in the concentration of the precursor, due to an increase in the variety of nanoparticle sizes. Compared to the obtained spectra, it is observed that using the extract of the plant with concentration of 1.25% and the precursor to 30 mgL^{-1} the plasmon corresponding the highest absorbance is presented, i.e. the highest number of AuNPs synthesized.

Characterization of the nanocomposite

SEM analysis

The MEB image of Fig. 6 corresponds to the nanocomposite whose matrix was prepared from ceramic matrix. Micrographs were obtained at different

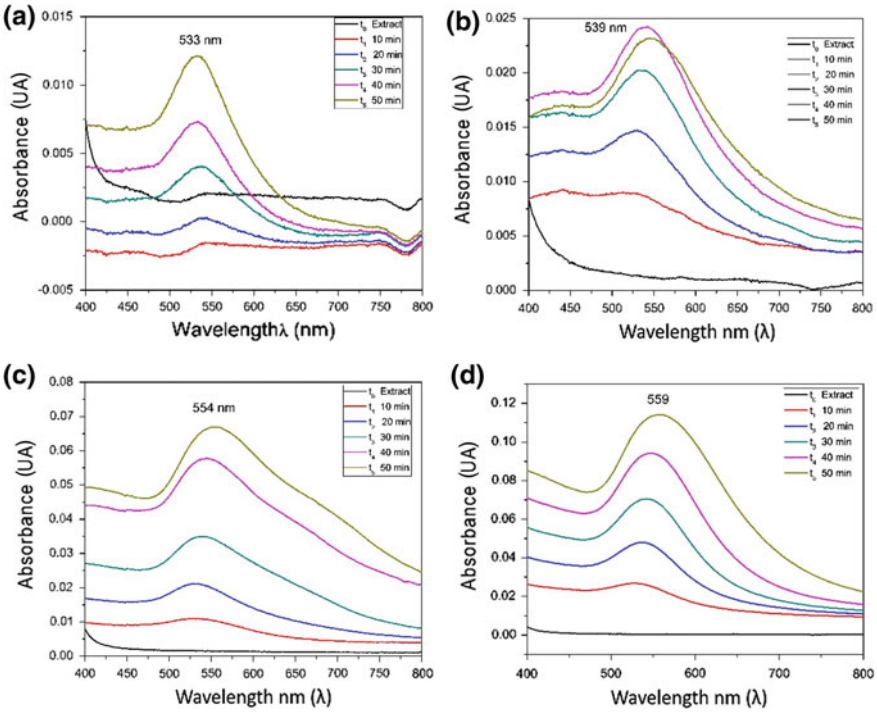

Fig. 5 UV-Vis spectrogram for a sample of colloidal AuNPs obtained from an Au^{+3} precursor agent with an initial concentration of 5 mgL^{-1} and the *Sedum praealtum* extract at 1.25%

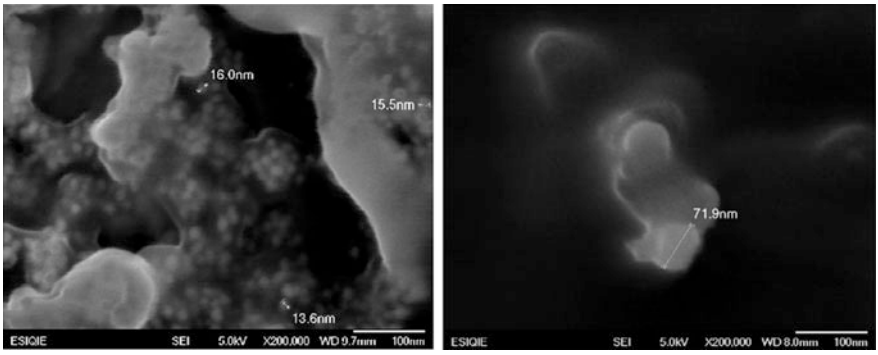

Fig. 6 MEB image of the Nanocompósito synthesized using as ceramic matrix

magnifications. Observing the micrographs shown, it is observed that some of the synthesized nanoparticles show a tendency towards rounded shapes; however, the greatest number of them do not exhibit a defined form. The average size of nanoparticles have in a range of 13.8–71.9 nm.

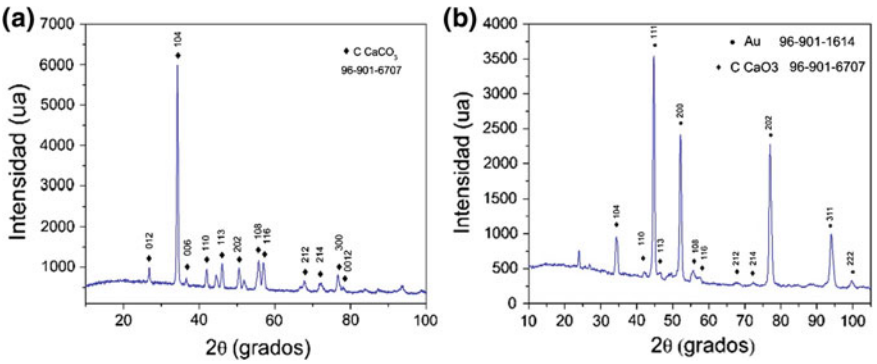

Fig. 7 Diffractogram obtained for **a** ceramic matrix and **b** nanocomposite obtained using ceramic-matrix-AunNP's

X-ray Difraction

Figure 7a shows the diffractogram obtained from the characterization of the eggshell while the Diffractogram of (b) belongs to the same substrate with the deposited nanoparticles.

In the diffractrogram observed in Fig. 7 are presented peaks located at angles 27, 34, 36, 42, 46, 51, 55, 57, 68, 72 and 77 in 2 θ, which correspond to the planes (012), (104), (006), (110), (113), (202), (108), (116), (212), (214), (300), (0012), indicators of calcite, the main component of ceramic matrix. On the other hand the diffractogram corresponding to the Nanocompósito shows peaks at angles 45°, 52°, 77°, 94° and 99° in 2 θ representing the planes (111), (200), (202), (311) and (222), which indicate the presence of metallic gold in the sample. The remaining peaks belong to the planes (104), (110), (113), (108), (116), (212) and (214), which correspond to the composition of the Matrix (calcite), however, the intensity of these peaks is lower compared to the first diffractogram, which is because the structure of the calcite was modified to a lesser extent when depositing the nanoparticles.

Conclusions

According to the analyzes shown, it is established that the aqueous extract of the species *Sedum praealtum* has the ability to reduce the Au^{+3} ions to Au^{0} to synthesize nanoparticles due to the macromolecules present in the extract. Initially, the presence of AuNPs was estimated by visual analysis, with changes in the coloration of the solution during synthesis; subsequently through UV-Vis spectroscopy its existence was corroborated due to the appearance of plasmas of absorbance in characteristic wavelengths of this metal.

It was taken into account that the AuNP's synthesized have little stability, since they tend to precipitate, reason why a deposition on a ceramic substrate was realized, being effective. The AuNP's powders were analyzed by XRD, SEM and EDS, observing through XRD the presence of Au in small amounts.

It was observed by SEM that the AuNPs synthesized have sizes that fluctuate within 13–70 nm and the micrographs of the obtained nanocomposite show that the AuNPs are deposited on the substrate, anchored to the grains.

References

1. Meléndez Pizarro CO, Camacho Dávila AA (2008) Química verde, la química del nuevo milenio. Facultad de Ciencias Químicas, Universidad Autónoma de Chihuahua, Aventuras del pensamiento
2. Dávila JL, Galeas VH, Pontón P, Rosas NM, Sotomayor V, Valdivieso C (2011) Nuevos materiales: Aplicaciones Estructurales e Industriales. imprefepp
3. Quintana MH (2008) Nanopartículas, principios y aplicaciones. http://www.cyd.conacyt.gob.mx/221/Articulos/Nanoparticulas/Nano1.html. Accessed 15 Apr 2017
4. Ahmed S, Saifullah Ahmad M, Lal Swami B, Ikram S (2016) Green synthesis of silver nanoparticles using Azadirachta indica aqueous leaf extract. J Radiat Res Appl Sci 1–7. http://dx.doi.org/10.1016/j.jrras.2015.06.006
5. Saranyaadevi K, Subha V, Ernest RR, Renganathan S (2014) Synthesis and characterization of copper nanoparticle using Capparis Zeylanica leaf extract. Int J ChemTech Res 4533–4541
6. Nalawade P, Mukherjee T, Kapoor S (2013) Green synthesis of gold nanoparticles using glycerol as a reducing agent. Adv Nanopart 2:78–86. https://doi.org/10.4236/anp.2013.22014
7. Rodríguez Llamazares SM (2007) Obtención de nanopartículas y nano-ordenamientos metálicos empleando la química de los compuestos de inclusión. Universidad de Chila, Facultad de Ciencias Químicas y Farmacéuticas
8. Estrada E (2009) Biblioteca digital de la medicina tradicional mexicana. http://www.medicinatradicionalmexicana.unam.mx/monografia.php?l=3&t=&id=7495. Accessed 10 Jan 2017
9. Rzedowski GC, de Rzedowski y J (2005) Colaboradores, Flora fanerogámica del Valle de México 2a. ed., 1a reimp., Instituto de Ecología, A.C. y Comisión Nacional para el Conocimiento y Uso de la Biodiversidad, Pátzcuaro (Michoacán), 1406 pp

Part II
Accident Tolerant Fuels for Light Water Reactor

Effects of Ce Addition on the Microstructure and Mechanical Properties of Accident-Tolerance Fe-Cr-Al Fuel Cladding Materials

Naimeng Liu, ZhongWu Zhang, Yang Zhang, Ye Cui, Dan Chen, Yu Zhao, SongSong Xu and Hao Guo

Abstract Fe-Cr-Al alloys are promising materials for accident-tolerance fuel cladding applications due to their excellent performance of oxidation and corrosion resistance under elevated temperature. In this study, effects of the addition of a small neutron absorption cross section rare-earth element Cerium (Ce) on the microstructure and mechanical properties of Fe-Cr-Al alloys with 0–0.1 wt% Ce have been investigated. As Ce content increased, the grains became size-refining obviously and number of precipitates increased. The results of EDS showed that the precipitates were mainly consisted of intermetallic compounds. Notably, the ultimate tensile strength and elongation reached the optimized values when the content of Ce was 0.02 wt%. However, the tensile properties decreased when Ce content was above 0.05 wt%, which may be due to the excess of intermetallic compounds.

Keywords Fe-Cr-Al alloys · Cerium · Grain refinements · Incoherency Mechanical properties

Introduction

FeCrAl ferritic alloys are highly considered as optional accident-tolerance fuel cladding materials due to their more outstanding oxidation and corrosion resisting ability exhibited under elevated temperatures compared to Zr-based alloys, which may even cause hydrogen gas generation under the condition of losing coolant accidents [1, 2]. Currently, the investigation focused on FeCrAl alloy is usually based on developing the composition to optimize the mechanical properties as well as maintaining adequate oxidation and corrosion resisting performance [1, 3–7].

N. Liu · Z. Zhang (✉) · Y. Zhang · Y. Cui · D. Chen · Y. Zhao · S. Xu · H. Guo
Key Laboratory of Superlight Materials and Surface Technology,
Ministry of Education, College of Materials Science and Chemical Engineering,
Harbin Engineering University, Harbin 150001, China
e-mail: zwzhang@hrbeu.edu.cn

The Minerals, Metals & Materials Society, *TMS 2018 147th Annual Meeting & Exhibition Supplemental Proceedings*, The Minerals, Metals & Materials Series,
https://doi.org/10.1007/978-3-319-72526-0_7

The rare earth element Cerium (Ce) is one of those alternative choices for improving the compositions of FeCrAl alloys when considering the contribution of addition of elements on both grain-refinement and neutron absorption cross sections [8, 9]. Applications of Cerium in recent years are basically on stainless steels as well as twinning induced plasticity (TWIP) steels [10, 11]. The results showed that Cerium played a role of refining the size of grains by means of formatting the globular inclusions, which act as nucleation sites or obstacles against the grain growth. However, the interactions between intermetallic inclusions and size refinement on grains and the effects of them on mechanical properties on room temperature have not been fully investigated.

It is the purpose of this work to enlighten the internal laws and the effects of various contents of Cerium addition (0–0.1 wt%) on the grain sizes, the distribution of inclusions and tensile properties at room temperature. The relationships between those compositions designed and the performance shown on both microstructure and mechanical properties are also discussed.

Experimental Methods

Four FeCrAl-RE alloys containing 0, 0.02, 0.05 and 0.1 wt% Ce (denoted as 0 Ce, 0.02 Ce, 0.05 Ce and 0.1 Ce, respectively) were cast in an arc-melting furnace in the atmosphere of Argon, and their compositions are showed in Table 1. The as-cast ingots were hot rolled at 950 °C with a total reduction of 70%. After hot rolling, four specimens were cold-rolled with a total reduction of 10%. The as-rolled alloys were then annealed at 550 °C for 0.5 h.

The grain size, shape and the distribution of precipitation of all alloys produced in this work were properly etched, observed and measured on a Carl Zeiss optical microscopy (OM). The distribution of elements corresponded to the microstructure were undertaken by an Oxford scanning electron microscopy (SEM) equipped with energy spectrum analysis (EDS). Tensile tests were carried out with the loading axis parallel to the rolling direction. Tensile testing specimens were shaped according to ASTM standards shown in Fig. 1, and were tested at room temperature (25 °C) with a tensile test machine.

Table 1 Nominal compositions of FeCrAl-RE alloys produced in this work (wt%)

Designation	Fe	Cr	Al	Y	Ce	C
0-Ce	Bal.	12	4.4	0.2	0	≤0.02
0.02-Ce	Bal.	12	4.4	0.2	0.02	≤0.02
0.05-Ce	Bal.	12	4.4	0.2	0.05	≤0.02
0.1-Ce	Bal.	12	4.4	0.2	0.1	≤0.02

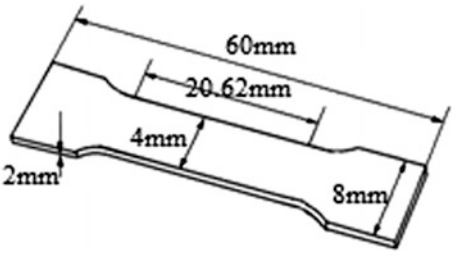

Fig. 1 Tensile testing specimens processed according to GB/T228.1-2010 standards

Results and Discussion

Microstructure

Microstructure of Hot-Rolled Specimens

Figure 2 exhibits microstructures of 950 °C hot- rolled specimens with various content of Ce. The as-rolled specimen showed a mainly coarse columnar grain structure surrounded by some small-sized equiaxed grains, and some of the inclusions are observed. Statistic analysis is performed for the results of average diameters of the grains, showing those specimens get their grains refined comparing to the Fe-12Cr-4.4Al-0.2Y one (Fig. 2a), as shown in Table 2. The distribution of the inclusions is also corresponded with the different content of Ce, as the inclusions dispersed when Ce is doped less than 0.02 wt%, and have a trend of

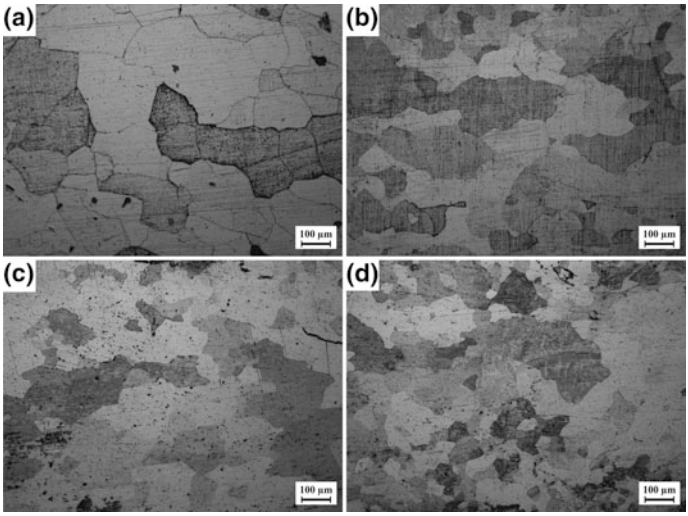

Fig. 2 Microstructures of 950 °C hot- rolled **a** 0-Ce, **b** 0.02-Ce, **c** 0.05-Ce and **d** 0.1-Ce specimens

Table 2 Values of average grain sizes on various hot-rolled specimens

Designation	0-Ce	0.02-Ce	0.05-Ce	0.1-Ce
Average grain size (μm)	161 ± 0.5	121 ± 0.5	116 ± 0.5	106 ± 0.5

centralizing on grain boundaries when Ce is doped more than 0.05 wt%. Almost no inclusions are exhibited in Fe-12Cr-4.4Al-0.2Y specimens.

Microstructure of Cold-Rolled and Annealed Specimens

The microstructures of all four specimens after cold-rolling and annealing at 550 °C for 0.5 h are shown in Fig. 3. As the statistic results shown in Table 3, the average grain size becomes smaller than hot-rolled specimens, because the cold rolling procedure came after hot rolling, making it a larger reduction in total. These results also show a similar trend on grain sizes corresponded to the content of Ce as the results on hot-rolled specimens have shown. The inclusions distribute in the matrix, and appear near grain boundaries when Ce content is more than 0.02 wt%. The size of inclusions is less than 2 μm.

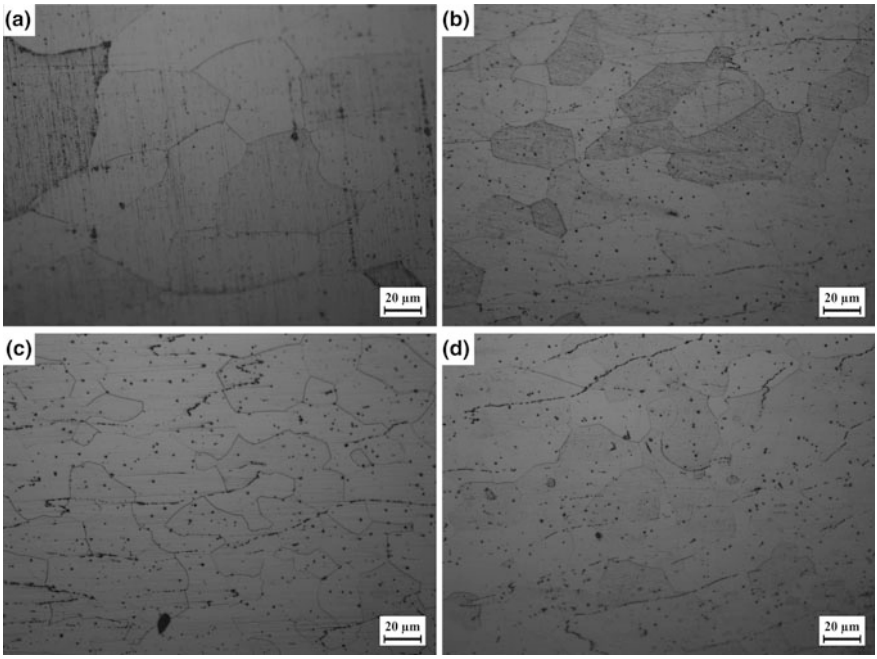

Fig. 3 Microstructures of cold-rolled and annealed **a** 0-Ce, **b** 0.02-Ce, **c** 0.05-Ce and **d** 0.1-Ce specimens

Table 3 Values of average grain sizes on various cold-rolled and annealed specimens

Designation	0-Ce	0.02-Ce	0.05-Ce	0.1-Ce
Average grain size (μm)	94 ± 2.3	81 ± 2.3	76 ± 2.3	71 ± 2.3

Mechanical Properties

Tensile Test Results of Hot-Rolled Specimens

Figure 4 and Table 4 show the results of tensile tests at room temperature on all specimens after 950 °C hot-rolling with various Cerium contents. Each of the samples shown represents the average of three samples. Composition dependence can be illustrated from the engineering stress-strain curves, as total elongation values increase when the content of Ce is between 0.02 and 0.05 weight percent, and reduce immediately when adding 0.1 wt% of Ce. For the magnitude of yield strength (YS) and ultimate tensile strength (UTS) shown in Table, no distinct dependence can be observed as their differences are less than 30 MPa.

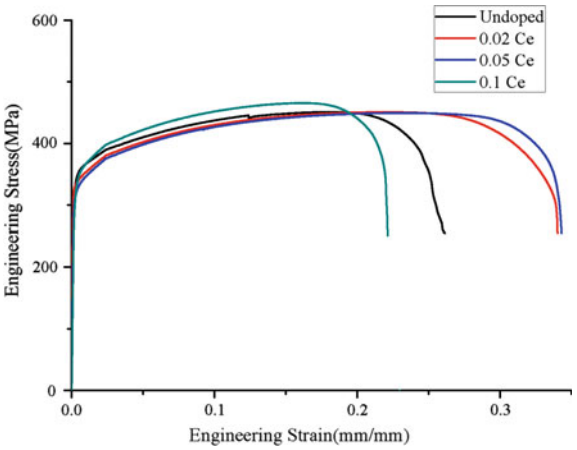

Fig. 4 Engineering stress-strain curves of various hot-rolled specimens tested at room temperature

Table 4 Values of tensile properties of various hot-rolled specimens tested at room temperature

Designation	0-Ce	0.02-Ce	0.05-Ce	0.1-Ce
Yield strength (MPa)	350.85	335.23	321.80	348.15
Ultimate tensile strength (MPa)	451.06	450.96	449.47	465.72
Elongation (%)	26.8	36.2	31.9	21.8

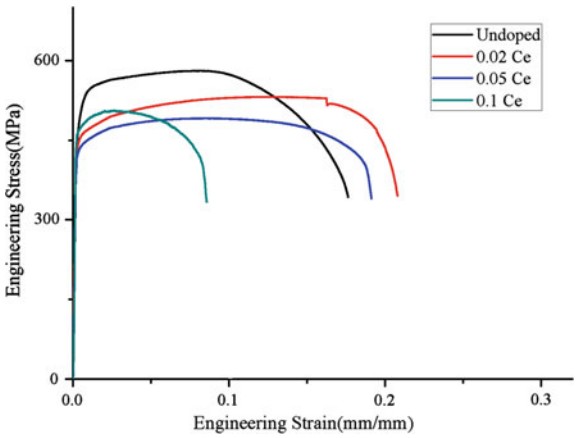

Fig. 5 Engineering stress-strain curves of various cold-rolled and annealed specimens tested at room temperature

Tensile Test Results of Cold-Rolled and Annealed Specimens

Tensile curves and magnitudes of YS, UTS and total elongation of cold-rolled and annealed specimens are depicted in Fig. 5 and Table 5. When the specimens get cold-rolled, their yield strength and ultimate tensile strength go upward, as their values advanced 40–150 MPa, approximately. An analogous trend as hot-rolled specimens on total elongation values can be shown, as they are on the increase when the content of Ce is between 0.02 and 0.05 weight percent, and decrease immediately when adding 0.1 wt% of Ce. However, it can be appreciated that the ultimate tensile strength values decline continuously as the content of Ce increases. Their largest disparity can be as many as 75.11 MPa. Nevertheless, their strength values go up while elongations reduce as a consequence of work hardening.

Analysis on Distribution of Elements

In addition to pervious research, the present work has also taken a research on the distribution of elements on both the matrix and the inclusions, in order to find their regularities in more detail. Figure 6 and Table 6 shows the SEM image and EDS analysis on the matrix of all specimens with various contents of Cerium. The

Table 5 Values of tensile properties of various cold-rolled and annealed specimens tested at room temperature

Designation	0-Ce	0.02-Ce	0.05-Ce	0.1-Ce
Yield strength (MPa)	532.63	455.86	433.21	459.84
Ultimate tensile strength (MPa)	581.20	531.87	491.53	506.09
Elongation (%)	21.4	21.6	21.3	12.1

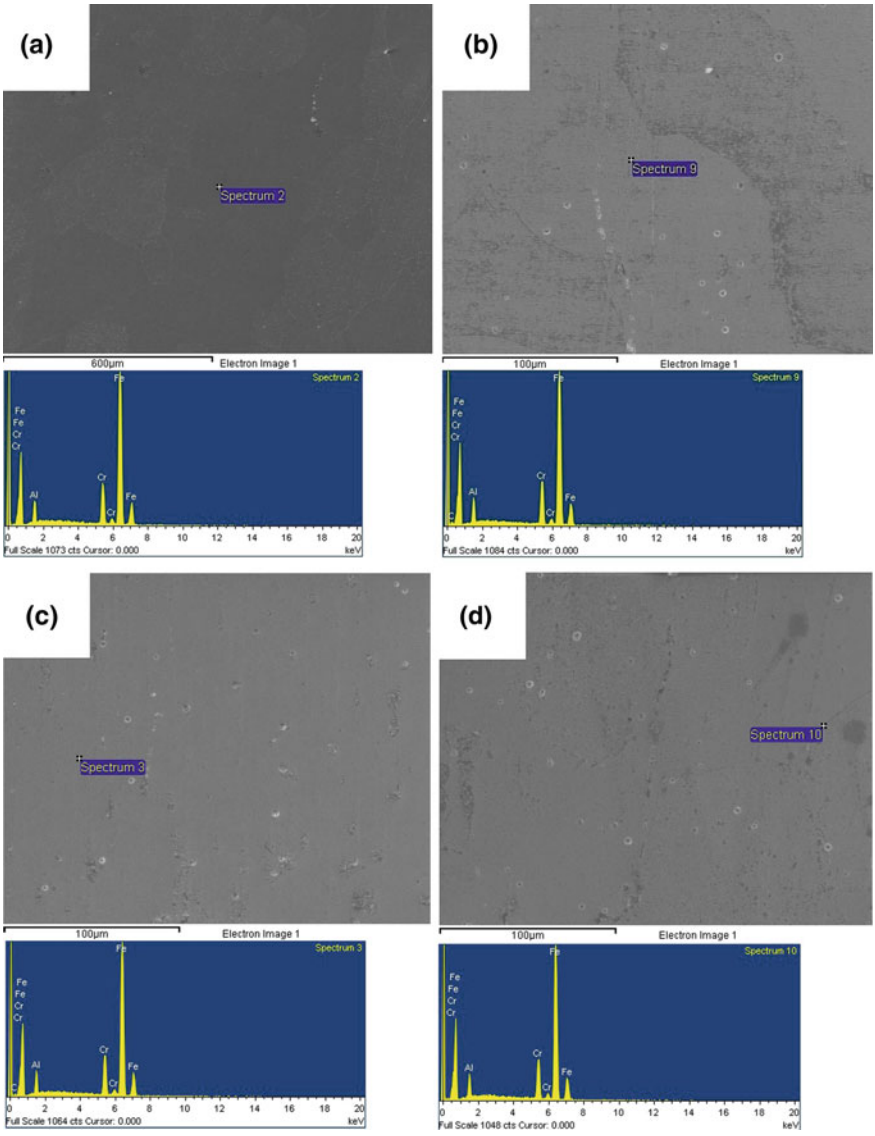

Fig. 6 SEM image and EDS analysis on the matrix of **a** 0-Ce, **b** 0.02-Ce, **c** 0.05-Ce and **d** 0.1-Ce specimens

analysis of energy spectrum shows that there is little component difference between specimens when taking Fe, Cr and Al into consideration, as the original proportion of these elements is equal.

Figure 7 and Table 7 presents the SEM image and EDS analysis on the inclusions of all Ce-doped specimens. It is Fe, Cr and Al constitute the main contents

Table 6 Values of contents in the matrix of all specimens analyzed by EDS (wt%)

Composition	Fe	Cr	Al	C
0-Ce	82.86	12.69	4.46	–
0.02-Ce	78.79	13.03	4.30	Detectable
0.05-Ce	81.50	12.07	4.31	Detectable
0.1-Ce	83.13	12.35	4.52	–

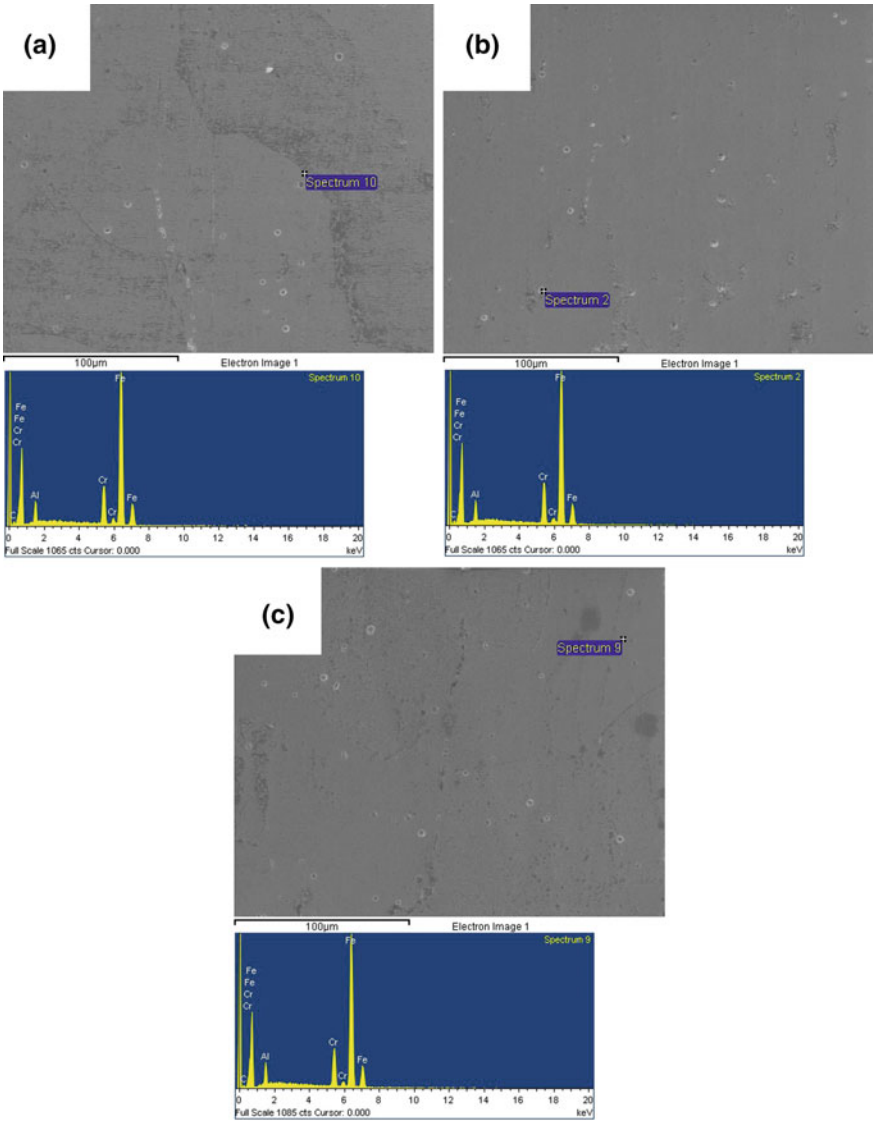

Fig. 7 SEM image and EDS analysis on the inclusions of **a** 0.02-Ce, **b** 0.05-Ce and **c** 0.1-Ce specimens

Table 7 Values of contents in the inclusions of all Ce-doped specimens analyzed by EDS (wt%)

Composition	Fe	Cr	Al	C
0.02-Ce	79.74	12.47	4.09	Detectable
0.05-Ce	79.92	12.37	4.17	Detectable
0.1-Ce	80.92	12.42	4.32	Detectable

and some peaks of C are observed, indicating that there could be some metallic carbides like $M_{23}C_6$, M_7C_3 or M_6C [12, 13], which have the proportion close to the results.

Discussion on Relationships Between Inclusions and Mechanical Performance

As described above, the mechanical properties of the present Fe-12Cr-4.4Al-0.2Y alloys are modified by the increase of inclusions related to the content of Ce, indicating the presence of the optimum range of Ce content. In particular, the inclusions change from uniformly distributed to a trend of segregating to grain boundaries, and their numbers are also boosted as the doping of Ce gets excessive.

The effects of Ce on refining have been investigated by Y. –U. Heo et al. who put the refining effect as a consequence of the dragging force of the Ce-rich compounds against the coalescence of the columnar grains [14]. Similar results on average grain sizes can also be observed as it shown above. According to the formula of Hall-Petch, the grain diameter has an inversely proportional effect on the yield strength of the specimens. The yield strength is improved as the grains get finer. Grain refining has a positive effect on improving the ductility as there are a growing number of grains per unit volume. As a result, the deformation can be dispersed to more grains, making it a homogeneous process preventing stress concentration locally, and retarding the crack initiation eventually. However, as the addition of Ce increases continuously, the size of inclusions are getting larger and the distribution of inclusions changed to a state of segregation, thus degrading the coherency of grain boundaries. Accordingly, their positions can be potential for crack initiation. As a result, the mechanical performance on both strengths and elongations reduced gradually when adding excessive Cerium.

Conclusion

Effects of Ce contents on both the microstructure and mechanical properties of FeCrAl fuel cladding materials were investigated, and the following conclusions were obtained:

(1) The average grain size of Fe-12Cr-4.4Al-0.2Y alloy was remarkably refined as the content of Ce increased. At the same time, intermetallic inclusions gradually occurred, and their distribution changed from dispersing on the matrix to a trend of segregating on grain boundaries when the addition of Ce was more than 0.05 wt%.
(2) As the content of Ce increased, composition dependence can be illustrated on the tensile properties of hot-rolled specimens, as total elongation values increase when the content of Ce is between 0.02 and 0.05 weight percent, and reduce immediately when adding 0.1 wt% of Ce. No distinct dependence can be observed from the magnitude of yield strength and ultimate tensile strength as their differences were within the margin of error. Analogous trend can also be exhibited on the results of cold-rolled and annealed tensile specimens, as the elongations are on the increase when the content of Ce is between 0.02 and 0.05 weight percent, and decrease immediately when adding 0.1 wt% of Ce. However, the margins on both the yield strength and the ultimate tensile strength values declined continuously as the content of Ce increased.
(3) The addition of Ce had effects on both grain refining and inclusion modifications, and the mechanical performance got affected as a consequence. When the doping of Ce was less than 0.02 wt%, the yield strength got improved due to fine-grain strengthening and the ductility was also optimized as the concentration of stress was avoided. However, when the doping of Ce was more than 0.05 wt%, the inclusions were in the state of incoherence with the matrix due to their larger size and segregating distribution, and reduced the tensile properties values eventually.

Acknowledgements This work was supported by the Fundamental Research Funds for the Central Universities (HEUCFJ171005, HEUCFJ171001 and HEUCFP201703), NSFC Funding (51371062 and U1460102), NSFHLJ (JC2017012). This paper is funded by the International Exchange Program of Harbin Engineering University for Innovation-oriented.

References

1. Yamamoto Y, Pint BA, Terrani KA, Field KG, Yang Y, Snead LL (2015) J Nucl Mater 467:703–716
2. Gussev MN, Field KG, Yamamoto Y (2017) Mater Des 129:227–238
3. Gamble KA, Barani T, Pizzocri D, Hales JD, Terrani KA, Pastore G (2017) J Nucl Mater 491:55–66
4. Field KG, Briggs SA, Sridharan K, Yamamoto Y, Howard RH (2017) J Nucl Mater 495:20–26
5. Field KG, Littrell KC, Briggs SA (2018) Scripta Mater 142:41–45
6. Briggs SA, Edmondson PD, Littrell KC, Yamamoto Y, Howard RH, Daily CR, Terrani KA, Sridharan K, Field KG (2017) Acta Mater 129:217–228
7. Field KG, Briggs SA, Sridharan K, Howard RH, Yamamoto Y (2017) J Nucl Mater 489:118–128

8. Coury FG, Botta WJ, Bolfarini C, Kiminami CS, Kaufman MJ (2015) Acta Mater 98:221–228
9. Liu P, Jiang H, Cai Z, Kang Q, Zhang Y (2016) J Magnes Alloys 4:188–196
10. Kim SM, Kim JS, Kim KT, Park K-T, Lee CS (2013) Mater Sci Eng A 573:27–36
11. Zhang Shaohua Yu, Yanchong WS, Hao L (2017) J Rare Earths 35(5):518–524
12. Xu Y-W, Song S-H, Wang J-W (2015) Mater Lett 161:616–619
13. Jie Z, Xianjun L (1995) Mater Mech Eng 19(5):14–16
14. Heo Y-U, Lee S-Y, Cho J-W (2016) Nam Hoe Heo. Mater Charact 120:234–243

Part III
Additive Manufacturing of Metals: Fatigue and Fracture

Evaluation of the Mechanical Properties of 15Cr-5Ni Stainless Steel Produced by Direct Metal Laser Sintering

Davoud M. Jafarlou, Victor K. Champagne and Ian R. Grosse

Abstract This research work examines the mechanical behavior of 15Cr-5Ni stainless steel parts produced by direct metal laser sintering (DMLS). The main objective of this research is to identify the influence of low-temperature precipitation hardening on tensile properties and fracture toughness of DMLS fabricated specimens. Test specimens were fabricated according to ASTM E8/M8 and ASTM E399 standards using EOS M290 laser sintering machine. Following DMLS specimens were subjected to precipitation hardening for an hour at a temperature of 486 °C. To evaluate the influence of heat treatment on mechanical properties of the DMLS produced parts, tension tests and linear-elastic plane-strain fracture toughness tests were performed at the room temperature. Furthermore, microscopic observation of fractured surface was performed to study the failure mechanisms in more detail. The outcomes indicated that the post-DMLS heat treatment improves mechanical properties in the terms of yield stress, Young's modulus, and ultimate tensile strength. However, this process has a negligible negative effect on the ductility. Moreover, the fracture toughness test results indicated ductile fracture mechanism in the DMLS produced specimens while the specimens were subjected to precipitation hardening demonstrates brittle fracture.

Keywords Additive manufacturing · 15Cr-5Ni stainless steel
Precipitation hardening · Tensile properties · Fracture toughness

D. M. Jafarlou (✉) · I. R. Grosse
Department of Mechanical and Industrial Engineering,
University of Massachusetts at Amherst, Amherst, MA, USA
e-mail: jafarlou@umass.edu

I. R. Grosse
e-mail: grosse@ecs.umass.edu

V. K. Champagne
US Army Research Laboratory, Aberdeen, USA
e-mail: vchampag@arl.army.mil

The Minerals, Metals & Materials Society, *TMS 2018 147th Annual Meeting & Exhibition Supplemental Proceedings*, The Minerals, Metals & Materials Series,
https://doi.org/10.1007/978-3-319-72526-0_8

Introduction

Precipitation-hardening (PH) stainless steels have found an extensive range of applications in the aerospace, marine, chemical and petrochemical industries due to the promising combination of high strength, relatively good ductility, exceptional corrosion resistance and weldability [1]. In recent years some grades of stainless steel are widely used in powder-based layer additive manufacturing (AM) [2]. Among powder-based systems, the direct metal laser sintering (DMLS) attracts considerable attention due to the capability for rapid tooling and rapid prototyping of geometrically complex metallic parts with short lead-times [3].

Components produced by DMLS exhibit significant variability in the values obtained when measuring mechanical properties which are associated with a build direction and layers orientation [2]. Furthermore, each location in an object produced through the sintering process experiences a different thermal history due to the rapid melting and solidification. This nonuniformity in temperature distribution leads to a nonhomogeneous microstructure, residual stresses, and anisotropy in mechanical properties [4, 5]. One study of the mechanical properties of stainless steel 316L parts produced by DMLS indicated that the build direction significantly affects the bending strength and the elongation with no effect on the tensile strength [6]. In addition, the authors found that an increase in layer thickness reduced the tensile strength and elongation without compromising bending strength. Chatterjee et al. [7] studied the effects of layer thickness and hatching distance on the density and hardness of low carbon steel produced by DMLS and concluded that increasing later thickness and hatching distance have a detrimental effect on density and hardness because of pore formation.

One of the major issues in DMLS is the oxidation of sintered layers which degrades interlayer bonding and causes problems such as balling effect (agglomeration of molten metal) and pore formation. Sintering in a vacuum or protective atmosphere is the most popular technique to minimize oxidation, providing good wetting and successful layer by layer fusion [8]. Gu and Shen [9] associated balling defect to non-uniform heat distribution due to the low laser power and high scan speed during DMLS of stainless steel 316L. They showed that increasing volumetric density of input energy, decreasing layer thickness and adding deoxidant reduce the tendency of metal agglomeration. Moreover, to minimize this problem an active control scheme and two beam approaches were developed to provide the constant temperature at the beam focus and around the actual sintering area [10].

It is well established that accumulation of residual stresses in the metal components produced by DMLS negatively affect their mechanical properties [11] and dimensional tolerance [12]. These residual stresses are originated in parts due to the temperature gradient and the cooldown phase of the molten top layer [13]. A number of researches have been carried out to minimize residual stress by selecting suitable exposure parameters [14, 15], layer thickness and build plate geometry [13], laser path optimization and preheating [12] and build plate heating and reheating of melt pool [16].

Although the optimization of the DMLS process parameters mitigates the potential defects in some extent, growing importance for producing fully functional parts necessitate the application of post-processing of DMLS parts. Thermal treatment is one of the most common ex situ methods for microstructure tailoring and relieving residual stresses of DMLS produced parts [17]. Simchi et al. [18] have shown that heat treatment of a sintered iron-based part in 1260 °C for 30 min improves microstructure homogeneity and density of a DMLS produced artifact. In another study, Shiomi et al. [19] indicated that stress relieving heat treatment effectively reduces the residual stress of SLM produced chrome molybdenum steel parts by about 70%. The post-processing of DMLS produced components using hot isostatic pressing (HIP) is also used as an effective method for densifying sintered parts and minimizing tensile residual stresses [20].

In this research work we evaluated the mechanical properties of 15Cr-5Ni stainless steel (15-5 PH SS) produced by DMLS using EOS M290 standard machine. Tensile properties and fracture toughness of as-printed specimens were measured based on ASTM E8/M8 and ASTM E399 standards. Subsequently, as-printed specimens were subjected to low-temperature heat treatment for an hour at a temperature of 486 °C to study the influence of precipitation hardening on the mechanical properties of DMLS produced specimens.

Materials and Methods

Material

The base material utilized in the current research for fabrication of test specimens is pre-alloyed 15-5 PH SS powder. This steel powder is manufactured by EOS GmbH and has a spherical morphology and particle size distribution of 20–63 μm. The chemical composition of 15-5 PH SS (in weight %: 15Cr, 5Ni, 4Cu, 1Mn, 1Si, 0.5Mo, 0.2Nb, 0.07C, balance Fe) is in accordance with the composition of DIN 1.4540 and UNS S15500.

Specimen Preparation

In this study, the influence of low-temperature heat treatment on the tensile strength and plane strain fracture toughness of 15-5 PH SS was investigated. Therefore, two categories of test specimens including as-printed and heat treated were prepared for experimental examination. Test specimens were fabricated at the UMass AddFab Laboratory using an EOS M290 standard machine. The machine is equipped with 400 W Yb (Ytterbium) fiber laser source operating at a wavelength of 1060–1100 nm. The process parameters including layer thickness, hatch spacing,

Fig. 1 A typical batch of tensile and fracture toughness specimens produced by DMLS

laser spot size, and exposure speed were selected as 0.02 mm, 0.1 mm, 100 μm and 1000 mm/s, respectively. The build chamber was purged using nitrogen gas, and the build plate was preheated to 100 °C. The fabrication of test specimens (Fig. 1) was performed in XY-plane considering Z-axis as a build direction. The precipitation hardening of as-printed specimens was carried out at 486 °C for an hour and air cooled after removing the specimens from the build plate to avoid as much as possible non-uniform heat absorption.

Experimental Procedure

Tension and fracture toughness tests were conducted in accordance with ASTM standards E8/E8M [21] and E399 [22], respectively using a 50 kN Instron 3369 universal test machine at ambient temperature. Measurement of tensile properties carried out in displacement control mode, producing constant strain rate of approximately 10^{-3}/s in the specimen's gage section. The linear-elastic fracture toughness was performed using compact tension C(T) specimens. A fatigue pre-crack in C(T) specimens was produced by cyclically loading the notch specimens using 10 kN Instron E10000 at stress ratio ($R = \sigma_{min}/\sigma_{max}$) of R = −1 at the frequency of 10 Hz to give a fatigue pre-crack length of almost 1.3 mm.

Results and Discussion

Tensile Properties

Representative engineering stress-strain curves for the as-printed and heat-treated specimens are given in Fig. 2. As-printed specimens represent well-defined yield stress (σ_y) of approximately 810 MPa, Young's modulus (E) of 165 GPa and average ultimate tensile strength (σ_u) of 1223 MPa. Implementation of heat treatment after DMLS improved the values of yield stress and Young's modulus by factor of 1.4. However, in terms of ultimate tensile strength (σ_u) slight improvement of 8% was measured for heat treated specimens. Moreover, the results did not indicate the notable difference in ductility between as-printed and heat-treated specimens. An average strain to failures (ε_u) of 19% and 18% were measured in the as-printed and heat-treated specimens, respectively.

An optical microscope was used to study the fractured surface of the as-printed specimens (Fig. 3). As-printed specimens demonstrated ductile fracture mode by showing "cup and cone" failure mode where shearing occurs at almost 45°. As evident in these figures formation of large cracks which initiated at the core of the specimens and from the surface of the specimens led to the fracture. Moreover, the magnified view of fracture surfaces indicated that fracture initiated by the coalescence of micro-voids and micro-cracks. The occurrence of these defects was correlated to the presence of defects in the surface of parts during sintering [23], porous nature of DMLS produced parts and delamination of layers due to the lack of fusion [8]. Furthermore, it is worth mentioning that skin and core strategy has been used to produce the specimens. The varying laser parameters used for core and skin of the specimens can act as a source of crack initiation.

The tensile fracture surface of heat treated specimens (Fig. 4) demonstrate the wide difference in the terms of micropores, number of cracks, size of cracks, and crack nucleation origin in comparison to the as-printed specimens (Fig. 3). Like as-printed specimens, the fracture surface of heat treated specimens is characterized

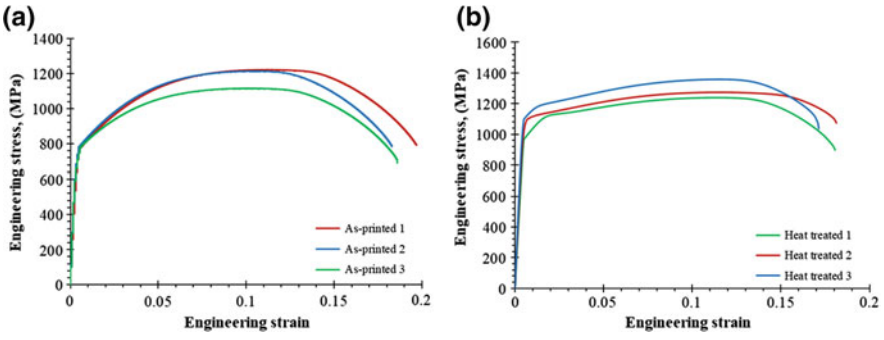

Fig. 2 Measured room-temperature tensile deformation behavior of **a** as-printed and **b** heat treated specimens

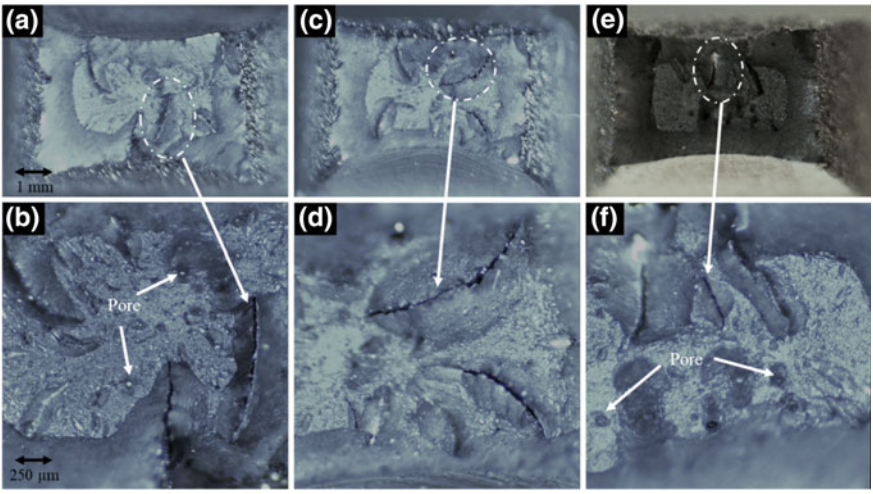

Fig. 3 Overall and magnified views of the tensile fracture surface of as-printed specimens **a**, **b** specimen 1, **c**, **d** specimen 2, and **e**, **f** specimen 3

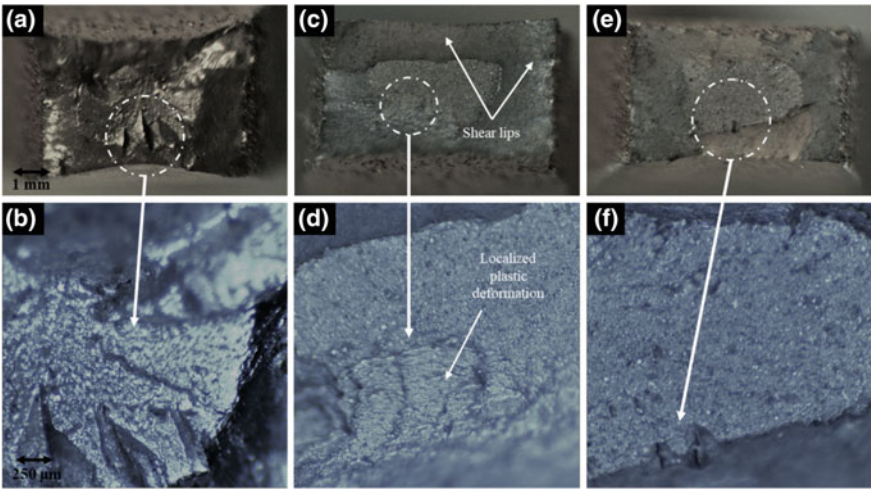

Fig. 4 Overall and magnified views of the tensile fracture surface of heat-treated specimens **a**, **b** specimen 1, **c**, **d** specimen 2, and **e**, **f** specimen 3

by ductile fracture with the formation of shear lips. However, the heat-treated specimens fracture surfaces showed highly localized plastic deformation regions and appearance of quasi-cleavage facets with ductile tear ridges. The differences measured in the mechanical properties are consistent with the differences observed in the tensile fracture surfaces.

Work Hardening Behavior

As can be seen from the engineering stress-strain curve, both as-printed and heat-treated specimens demonstrated significant plastic deformation zone which is expressed by Hollomon's equation for $\sigma \leq \sigma_y$ as [24]:

$$\sigma = k\epsilon^n \tag{1}$$

where σ is the true stress, ϵ is the true strain, n is the strain hardening exponent, and K is the strength coefficient. To calculate the n and k values, the true strain-stress curves were obtained and these values were calculated using following equations [24]:

$$n = \frac{N\sum_{i=1}^{N}(\log\ \epsilon_i \log \sigma_i) - \left(\sum_{i=1}^{N} \log\ \epsilon_i\right)\left(\sum_{i=1}^{N} \log \sigma_i\right)}{N\sum_{i=1}^{N}(\log\ \epsilon_i)^2 - \left(\sum_{i=1}^{N} \log\ \epsilon_i\right)^2} \tag{2}$$

$$\log k = \frac{\sum_{i=1}^{N}(\log \sigma_i) - n\sum_{i=1}^{N} \log \epsilon_i}{N} \tag{3}$$

where N is the number of data pairs. The average values of n were calculated as 0.19 and 0.11 for as-printed and heat-treated specimens, respectively. The evaluated average k values were 1798 MPa for as-printed specimens and 1810 MPa for and heat-treated specimens. It is well understood that upon aging treatment of PH stainless steel (15-5 and 17-4 PH stainless steel) in the temperature above 400 °C formation of Cu-enriched strengthening participants occurs in the martensite matrix of basal materials. This process takes place through a transformation of bcc to fcc structure through the intermediate twinned-9R structure by subsequent untwining and formation of 3R structure (bcc → twinned 9R → 3R → fcc) [25]. This hardening mechanism explains the improvement in yield stress, ultimate strength, and strength coefficient as well as a decrease in the ductility and the work hardening exponent.

Fracture Toughness

To determine fracture toughness (K_{IC}), the load-displacement curves for the as printed and heat-treated specimens were determined as presented in Fig. 5. The load-displacement curve of as-printed specimens (Fig. 5a) demonstrated ductile fracture mechanisms owing to the important influence of strain hardening (the work hardening exponent of 0.19 was measured for as-printed specimens) on crack extension behavior during the loading procedure. However, the pre-cracked heat-treated specimens resembled brittle fracture mechanism.

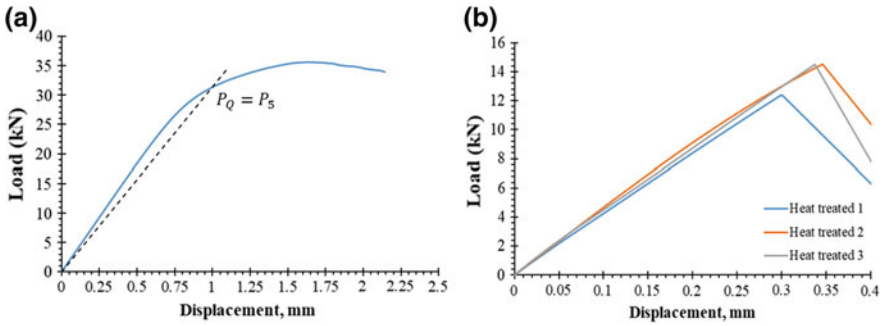

Fig. 5 Load-displacement curves of **a** as-printed and **b** heat treated specimens to determine P_Q and fracture toughness

The value of conditional fracture toughness (K_Q) was calculated using the following equation [22]:

$$K_Q = \frac{P_Q}{B\sqrt{W}} \frac{(2+\alpha)[0.886 + 4.64\alpha - 13.32\alpha^2 + 14.72\alpha^3 - 5.6\alpha^4]}{(1-\alpha)^{3/2}} \tag{4}$$

where P_Q is the critical load (obtained by 5% secant method), B is the specimen thickness and W is the specimen width. The value of α in this equation is determined as the ratio of the crack length (a) to specimen width (W). As-printed specimens indicated invalid K_{IC} values as the calculated K_Q did not fulfill the plane-strain requirements according to ASTM E399 [22]:

$$2.5\left(K_Q/\sigma_y\right)^2 \leq B \, and \, (W-a) \tag{5}$$

and

$$\frac{P_{max}}{P_Q} \leq 1.10 \tag{6}$$

where P_{max} indicates the maximum force. The average conditional fracture toughness (K_Q) of 62 MPa$\sqrt{m}$ was measured for the heat-treated specimens. The plane strain condition according to Eqs. 5 and 6 was fulfilled for the heat-treated specimens. Therefore, this value was considered as the fracture toughness (K_{IC}) of heat treated specimens. The fracture toughness test results indicated that precipitation hardening of DMLS-produced 15-5 PH SS part alters the fracture mechanism from ductile to brittle.

Conclusion

In this research work, the influence of low temperature precipitation-hardening treatment on mechanical properties of 15Cr-5Ni stainless steel produced by the direct metal laser sintering (DMLS) was studied. The research outcomes are summarized as follows:

- The tension test outputs showed that the precipitation hardening at temperature of 486 °C for an hour improves the yield stress and Young's modulus of the DMLS-produced specimens by factor of 1.4. Indeed, slight improvement of approximately 8% was observed in ultimate tensile strength.
- The results also signified that precipitation hardening has a slight detrimental effect on ductility of the DMLS-produced specimens. Moreover, work hardening exponent of heat-treated specimens decreased by 42% in comparison to the with as-printed ones.
- The microscopic observation demonstrated the wide difference between fractured surfaces of the as-printed and heat-treated specimens in the terms of micropores, number of cracks, size of cracks, and crack nucleation origin.
- An average fracture toughness (K_{IC}) of $62\,\mathrm{MPa}\sqrt{m}$ was measured for heat-treated specimens. However, the value of conditional fracture toughness for as-printed specimens demonstrated ductile fracture mechanism which demonstrate ductile to brittle transition due to the low temperature heat treatment.

Acknowledgements The authors gratefully acknowledge the financial support of the U.S. Army Research Laboratory, Aberdeen, MD. The authors would also like to acknowledge the Advanced Digital Design and Fabrication (ADDFab) laboratory in Life Science Laboratory, Amherst, MA for providing the necessary facilities and resources for this research.

References

1. Lo KH, Shek CH, Lai J (2009) Recent developments in stainless steels. Mater Sci Eng: R: Rep 65:39–104
2. Frazier WE (2014) Metal additive manufacturing: a review. J Mater Eng Perform 23: 1917–1928
3. Kumar S (2003) Selective laser sintering: a qualitative and objective approach. JOM 55:43–47
4. Carroll BE, Palmer TA, Beese AM (2015) Anisotropic tensile behavior of Ti–6Al–4V components fabricated with directed energy deposition additive manufacturing. Acta Mater 87:309–320
5. Zhu Y, Tian X, Li J, Wang H (2015) The anisotropy of laser melting deposition additive manufacturing Ti–6.5 Al–3.5 Mo–1.5 Zr–0.3 Si titanium alloy. Mater Des 67:538–542
6. Delgado J, Ciurana J, Rodrguez CA (2012) Influence of process parameters on part quality and mechanical properties for DMLS and SLM with iron-based materials. Int J Adv Manuf Technol 60:601–610

7. Chatterjee AN, Kumar S, Saha P, Mishra PK, Choudhury AR (2003) An experimental design approach to selective laser sintering of low carbon steel. J Mater Process Technol 136: 151–157
8. Das S (2003) Physical aspects of process control in selective laser sintering of metals. Adv Eng Mater 5:701–711
9. Gu D, Shen Y (2009) Balling phenomena in direct laser sintering of stainless steel powder: metallurgical mechanisms and control methods. Mater Des 30:2903–2910
10. Benda J (1994) Temperature controlled selective laser sintering, vol 5, pp 277–284
11. Amon CH, Beuth JL, Weiss LE, Merz R, Prinz FB (1998) Shape deposition manufacturing with microcasting: processing, thermal and mechanical issues. Trans-Am Soc Mech Eng J Manuf Sci Eng 120:656–665
12. Klingbeil NW, Beuth JL, Chin RK, Amon CH (2002) Residual stress-induced warping in direct metal solid freeform fabrication. Int J Mech Sci 44:57–77
13. Mercelis P, Kruth J (2006) Residual stresses in selective laser sintering and selective laser melting. Rapid Prototyping J 12:254–265
14. Wu AS, Brown DW, Kumar M, Gallegos GF, King WE (2014) An experimental investigation into additive manufacturing-induced residual stresses in 316L stainless steel. Metall Mater Trans A 45:6260–6270
15. Zaeh MF, Branner G (2010) Investigations on residual stresses and deformations in selective laser melting. Prod Eng Res Devel 4:35–45
16. Vasinonta A, Beuth JL, Griffith M (2007) Process maps for predicting residual stress and melt pool size in the laser-based fabrication of thin-walled structures. J Manuf Sci Eng 129:101–109
17. Agarwala M, Bourell D, Beaman J, Marcus H, Barlow J (1995) Post-processing of selective laser sintered metal parts. Rapid Prototyping J 1:36–44
18. Simchi A, Rota A, Imgrund P (2006) An investigation on the sintering behavior of 316L and 17-4PH stainless steel powders for graded composites. Mater Sci Eng A 424:282–289
19. Shiomi M, Osakada K, Nakamura K, Yamashita T, Abe F (2004) Residual stress within metallic model made by selective laser melting process. CIRP Ann Manuf Technol 53:195–198
20. Kruth J, Mercelis P, Van Vaerenbergh J, Froyen L, Rombouts M (2005) Binding mechanisms in selective laser sintering and selective laser melting. Rapid Prototyping J 11:26–36
21. ASTM Standard E8/E8M (2016) Standard test methods for tension testing of metallic materials. http://www.astm.org
22. ASTM Standard E399 (2012) Standard test methods for linear-elastic plane-strain fracture toughness KIC of metallic materials. http://www.astm.org
23. Mower TM, Long MJ (2016) Mechanical behavior of additive manufactured, powder-bed laser-fused materials. Mater Sci Eng A 651:198–213
24. ASTM Standard E646 (2016) Standard test method for tensile strain-hardening exponents (n-Values) of metallic sheet materials. http://www.astm.org
25. Monzen R, Iguchi M, Jenkins ML (2000) Structural changes of 9R copper precipitates in an aged Fe-Cu alloy. Philos Mag Lett 80:137–148

Creep and Thermomechanical Fatigue of Functionally Graded Inconel 718 Produced by Additive Manufacturing

V. A. Popovich, E. V. Borisov, V. Heurtebise, T. Riemslag, A. A. Popovich and V. Sh. Sufiiarov

Abstract Inconel 718 is a nickel-based superalloy commonly used in aircraft engine and nuclear applications, where components experience severe mechanical stresses. Due to the typical high temperature applications, Thermo-Mechanical Fatigue (TMF) and creep tests are common benchmarks for such applications. Additive manufacturing offers a unique way of manufacturing Inconel 718 with high degree of design freedom. However, limited knowledge exists regarding the resulting high temperature properties. The objective of this work is to evaluate creep and TMF behaviour of Inconel 718, produced by selective laser melting (SLM). A novel microstructural design, allowing for grain size control was employed in this study. The obtained functionally graded Inconel 718, exhibiting core with coarse and outside shell with fine grained microstructure, allowed for the best trade-off between creep and fatigue performance. The post heat-treatment regimens and resulting microstructures are also evaluated and its influence on creep and TMF is discussed.

Keywords Additive manufacturing · Inconel 718 · Functional grading Creep · Thermo-mechanical fatigue

V. A. Popovich (✉) · T. Riemslag
Department of Materials Science and Engineering,
Delft University of Technology, Delft, The Netherlands
e-mail: v.popovich@tudelft.nl

E. V. Borisov · A. A. Popovich · V. Sh.Sufiiarov
Peter the Great Saint-Petersburg Polytechnic University, Saint Petersburg, Russia

V. Heurtebise
SIGMA Clermont, Cedex, France

The Minerals, Metals & Materials Society, *TMS 2018 147th Annual Meeting & Exhibition Supplemental Proceedings*, The Minerals, Metals & Materials Series,
https://doi.org/10.1007/978-3-319-72526-0_9

Introduction

Inconel 718 is a precipitate strengthened nickel-based superalloy, which is commonly used in aerospace applications, where severe mechanical and thermal stresses are induced on a component. Inconel 718 is characterized by high strength, excellent creep, oxidation and corrosion resistance up to 700 °C, making it suitable for turbine, jet engine and nuclear reactor applications [1–3].

Conventional manufacturing routes of nickel-based alloys include casting, forging and powder metallurgy. However, near net shaping of complex components is difficult using such methods [4]. Recently, additive manufacturing (AM), such as selective laser melting (SLM), received a lot of attention, as it allows for several advantages compared to conventional technologies, like reduction of production steps, high flexibility, low material consumption and, most importantly, the possibility to manufacture parts with high geometrical complexity and dimensional accuracy [5, 6].

It is known, that the grain size is a typical way of controlling mechanical properties, including those of Inconel alloy 718 [7, 8], where coarser grained microstructure is favoured for creep strength and crack-growth resistance, while finer-grained structure for better fatigue life and tensile yield strength. In our previous study [9], a novel functionally graded Inconel 718 was produced with local functionalities via crystallographic texture, grain size and anisotropy optimization. It was shown that the grain structure and crystallographic texture of Inconel 718 can be changed during SLM processing by adapting the scanning strategy and the local solidification conditions. Furthermore, the effect of heat treatment has been investigated [10] and the results showed the capability of the SLM process to produce parts with mechanical properties better than conventional Inconel material.

The aim of this study is to investigate high temperature mechanical behaviour, such as creep and thermo-mechanical fatigue in order to fully explore the benefits of microstructural design in SLM Inconel 718. The effect of heat treatment on microstructure and high temperature mechanical behaviour is also evaluated and compared with conventional wrought Inconel 718.

Experimental Details

Materials and Heat Treatment

For manufacturing of the SLM specimens, (see Table 1 for process parameters) an SLM 280^{HL} facility (SML Solutions Group AG, Germany) featuring two YLR-lasers with a wavelength of 1070 nm and a maximum output power of 400 and 1000 W was employed. Laser power of 250 and 950 W was used to produce different areas within functionally graded cylindrical rods of 140 mm × Ø 14 mm (Fig. 1), further referred as FGM samples. The Z-axis was defined parallel to the

Table 1 Process parameters applied for SLM fabrication of specimens [10]

Laser power (W)	Laser scanning speed (mm/s)	Hatch distance (mm)	Layer thickness (μm)	Volume energy density (J/mm^3)
250	700	0.12	50	59.5
950	320	0.5	100	59.4

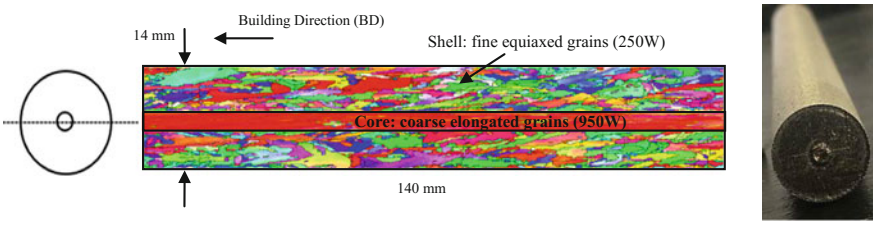

Fig. 1 SLM fabricated functionally graded Inconel 718 using a variation of 250 and 950 W laser sources

building direction, whereas each layer was deposited parallel to the XY-plane with the laser scanning at 45° between X and Y.

Post heat treatment was applied to examine the effect on microstructure and mechanical properties of Inconel 718 with tailored microstructure. The samples were investigated under "as-processed" and "heat treated (HT)" conditions, complying with AMS 5664E requirements [11] (see Table 2 for heat treatment details). In order to avoid contamination with oxygen, all heat treatments were conducted in argon atmospheres.

Samples of each of the heat treated conditions taken from YZ and XY planes were prepared for microstructural examination by grinding and polishing down to 1 μm. In order to reveal grain size and morphology, the specimens were etched in Glyceregia reagent (15 ml HCl, 10 ml glycerol and 5 ml HNO_3). Optical microscopy was carried out on a Keyence VHX-5000 for microstructure and porosity

Table 2 Designation of specimens and heat treatment parameters used for Inconel 718

Designation	Heat treatment	Details
As-processed (AP)	–	250, 950 W or Functionally Graded (FGM), see Fig. 1
Heat treated (HT)	Annealing + Aging	• Annealed at 850 °C, 2 h (air cooling) • Aged for 8 h at 720 °C, furnace cooling to 621 °C and holding for 8 h followed by air cooling
Wrought Inconel 718 (Wrought)	Annealing + Aging	• Solution annealed at 955 °C (1 h) • Aged for 8 h at 720 °C and furnace cooling to 621 °C and holding for 8 h followed by air cooling

investigation. A JEOL JSM 6500F scanning electron microscope (SEM) with energy-dispersive spectroscopy was used for fracture surface analysis. Vickers hardness profile measurements were performed under 3 kg force (further denoted as HV_3). X-ray diffraction (XRD) patterns were obtained using Brukker D8 diffractometer with CoK_α radiation ($\lambda = 1.79020$ Å). Diffraction patterns were recorded within the 2θ range from 10° to 120° with a step size of 0.035°. The X-ray beam was collimated to a spot size of 3 mm in diameter on the sample surface.

Creep and Thermomechanical Fatigue Testing

For creep and Thermo-Mechanical Fatigue (TMF) testing the round dogbone specimens were machined parallel to building direction as shown in Fig. 2a. Creep rupture and TMF testing were conducted on a servo hydraulic MTS 858 Table Top System, where induction heating and forced air cooling are used in order to cycle the temperature, Fig. 2b. During the tests the temperature was controlled by three thermocouples, which were in contact with the gauge of the specimen. The strain was monitored by the ceramic rod extensometer.

Creep rupture tests were performed at a constant tensile stress of 690 MPa and temperature of 650 °C, according to ASTM E139 standard [12]. Average creep properties were calculated based on 3 samples tested per process condition. After creep rupture the samples were prepared for fractography analysis.

Strain controlled in-phase thermo-mechanical fatigue (IP-TMF) tests were performed with temperature cycling between 350 and 650 °C at a frequency $R = \varepsilon_{min}/\varepsilon_{max} = -1$ and a strain amplitude of ±0.45%. Strain was measured by an axial extensometer and all tests were done in mechanical strain control (i.e. with a fixed total strain range compensated for thermal expansion $\Delta\varepsilon = \varepsilon_{max} - \varepsilon_{min}$). TMF testing was performed per process condition at a cooling and heating rate of 1 °C/s with a holding time at T_{max} of 300 s.

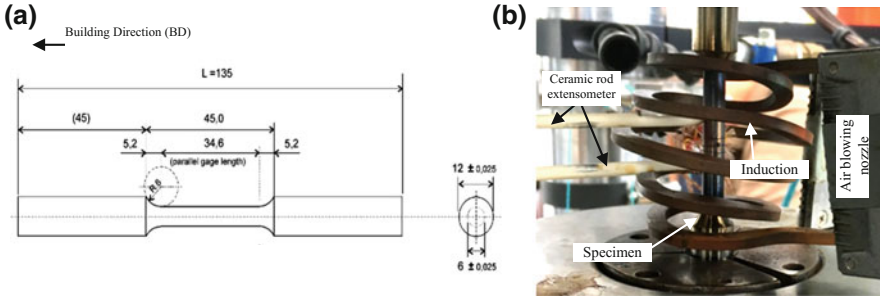

Fig. 2 Schematic of the creep and TMF test specimen and high frequency setup

Results and Discussion

Microstructural Characterization

Figure 3 shows optical microscopy images of the microstructure of Inconel 718 samples processed with the 950 and 250 W laser sources, further referred to as 950 and 250 W samples. As can be seen, the 250 W samples show a finer grained microstructure compared to the samples processed with the higher energy laser (Fig. 3a and b). Furthermore the microstructure of the part built with the 950 W laser (Fig. 3b) shows the formation of large columnar grains, primarily aligned along the building Z-axis with long axes approach the millimetre length range. In our previous study it was shown that columnar grained region has elongated grains with a (001) orientation with respect to building direction, i.e. the direction of predominant heat flux during processing. The observed microstructural differences were used to develop functional materials by modulating the laser scan strategy and process parameters [9] and resulting in a material featuring the core produced with coarse grains, while shell with fine grained microstructure (Fig. 3e, top view).

As previously shown, there is a formation of NbC and Laves-phase particles in the as-processed material [10]. Laves usually forms in heavily segregated regions and is known to reduce the mechanical properties of Inconel 718 through several mechanisms with the most dominant being brittle fracture of the phase, that provides the conditions for nucleation and crack growth. The presence of Laves phase in as-processed condition was further confirmed in this study by XRD, see Fig. 4.

In order to avoid the occurrence of such undesired microstructural features, post-processing heat treatment in a form of solution treatment and double aging were performed. The microstructure after heat treatment (see Fig. 3c, d, f) maintained its columnar nature and traces of layered build up. Furthermore, as can be seen in Fig. 3d, 950 W condition shows considerably larger process induced defects. The Laves phases on the other hand seem to transform into a needle-like Ni_3Nb-δ precipitates [10], which in this study is supported by XRD spectrum shown in Fig. 4.

Porosity measured by optical metallographic method showed that there is four times more porosity in 950 W samples (~4.5%) as compared to 250 W ones (~1.1%), which is considered as process induced defects and its detrimental effect on mechanical performance will be discussed in the next section.

Creep and Thermomechanical Fatigue Testing

Creep, porosity and hardness results for all tested materials are shown in Table 3, where t_f is the final time of fracture, ε_f is fracture strain and ε'_s is steady state creep rate. As expected [13, 14], the coarse grained microstructure is more creep resistant with respect to fracture strain (by a factor of three for heat treated condition).

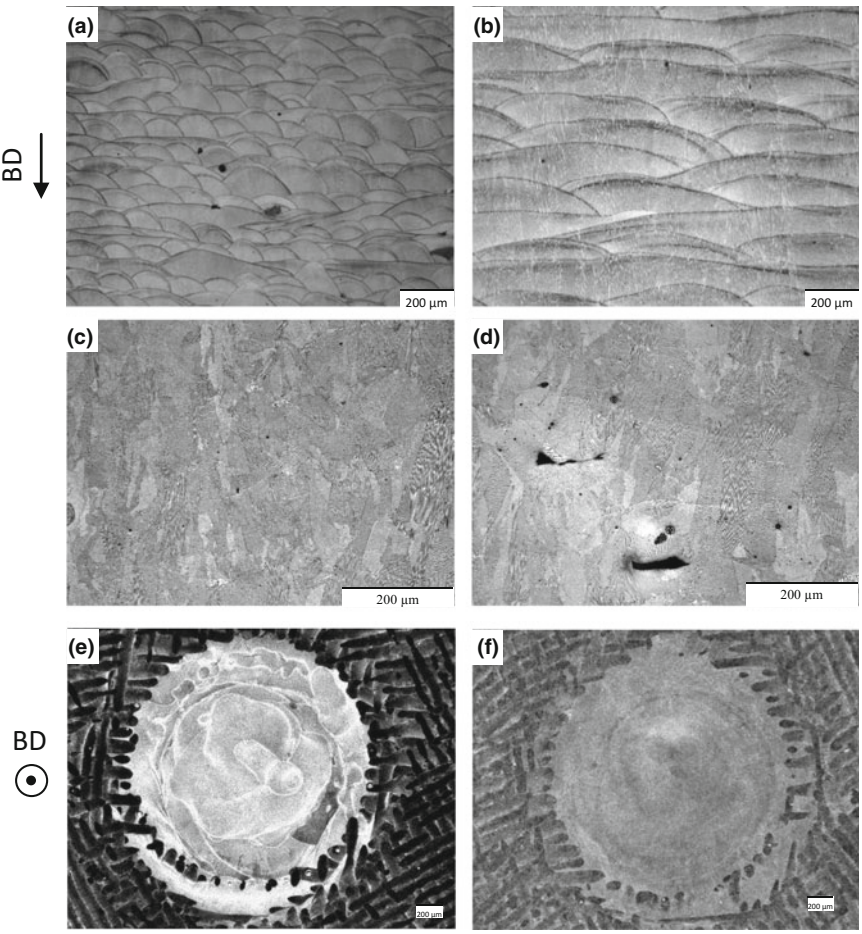

Fig. 3 Optical micrographs of SLM Inconel 718 specimens: **a** and **b** as-processed 250 and 950 W; **c** and **d** heat treated 250 and 950 W; **e** and **f** as-processed and heat treated functionally graded material. Images (**a**)–(**d**) depict top YZ plane, while images (**e**)–(**f**) show top XY plane, with 950 W zone located in the core

However, due to high scatter in results no clear conclusions can be drawn regarding the other creep parameters, such as creep life. It is believed that the high scatter is caused by the larger amount of process induced defects (porosity) observed in 950 W samples. The other explanation could be that in this temperature and stress range there is no grain size effect and a further research at lower stress and temperature level is recommended in order to evaluate the possible threshold level.

As can be seen, heat treatment substantially improves creep properties of SLM produced material. An increase of hardness by 40% for the as-heat treated condition is most likely attributable to precipitation hardening by plates of δ-phase (see Fig. 4 and [10]), which acts as a barrier for dislocation motion, thus improving hardness

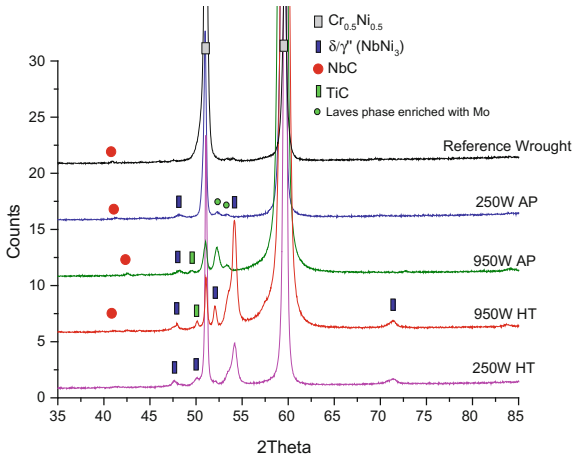

Fig. 4 XRD patterns showing reference wrought Inconel 718, as-processed (AP) and heat treated (HT) Inconel 718 produced via SLM with 250 and 950 W laser sources

Table 3 Creep results for 650 °C at a stress of 690 MPa

Specimen	t_f (h)	ε_f (%)	ε'_s (1/h)	Porosity (%)	Hardness, HV_3 250 W/950 W
250 W–AP	0.04 ± 0.04	15.6 ± 0.067	3.984 ± 2.70	1.1	303
250 W–HT	1.43 ± 0.58	4.0 ± 0.006	0.014 ± 0.006	1	446
950 W–AP	Fractured before reaching maximum stress of 690 MPa			4.5	290
950 W–HT	1.23 ± 0.80	12.3 ± 0.057	0.031 ± 0.034	4.1	415
FGM–AP	0.17 ± 0.18	17.3 ± 0.062	1.596 ± 1.491	0.3	312/294
FGM–HT	0.53 ± 0.23	9.0 ± 0.014	0.071 ± 0.031	0.4	449/426
Wrought	25.27 ± 10.32	18.8 ± 0.066	0.004 ± 0.001	0.2	424

and creep properties. Conversely, a significant reduction in creep fracture strain, can be explained by the presence of large carbides. As discussed in work [15], at this high temperature level, creep properties of Inconel alloy rather depend on applied stress than the grain size. Hence, for these testing conditions, heat treatment seems to be the most dominant factor controlling the creep life of SLM produced material. Furthermore, when compared with the reference wrought Inconel, it is evident that the lifetime of AM material should be significantly improved, which might be possible by reducing process induced defects. Hence, for final application of the higher energy laser source it is required to further optimize processing parameters and/or apply post processing hot isostatic pressing in order to reduce porosity.

Fracture surface of crept specimens is shown in Fig. 5. As can be seen, wrought Inconel exhibits ductile fracture with characteristic dimpled fracture and typical microvoid coalescence (Fig. 5a and b). SLM Inconel produced with 250 W

(fine grained microstructure) shows signs of ductile fracture with areas of cleavage planes associated with the location of brittle Laves phases (Fig. 5c and d). Inconel produced with 950 W (coarse grained microstructure) failed before reaching maximum stress level. Fracture surface of this material exhibits process induced pores and defects, which serve as stress concentrations inducing premature failure and thus resulting in interrupted creep test and thus p its poor creep properties (Fig. 5e and f).

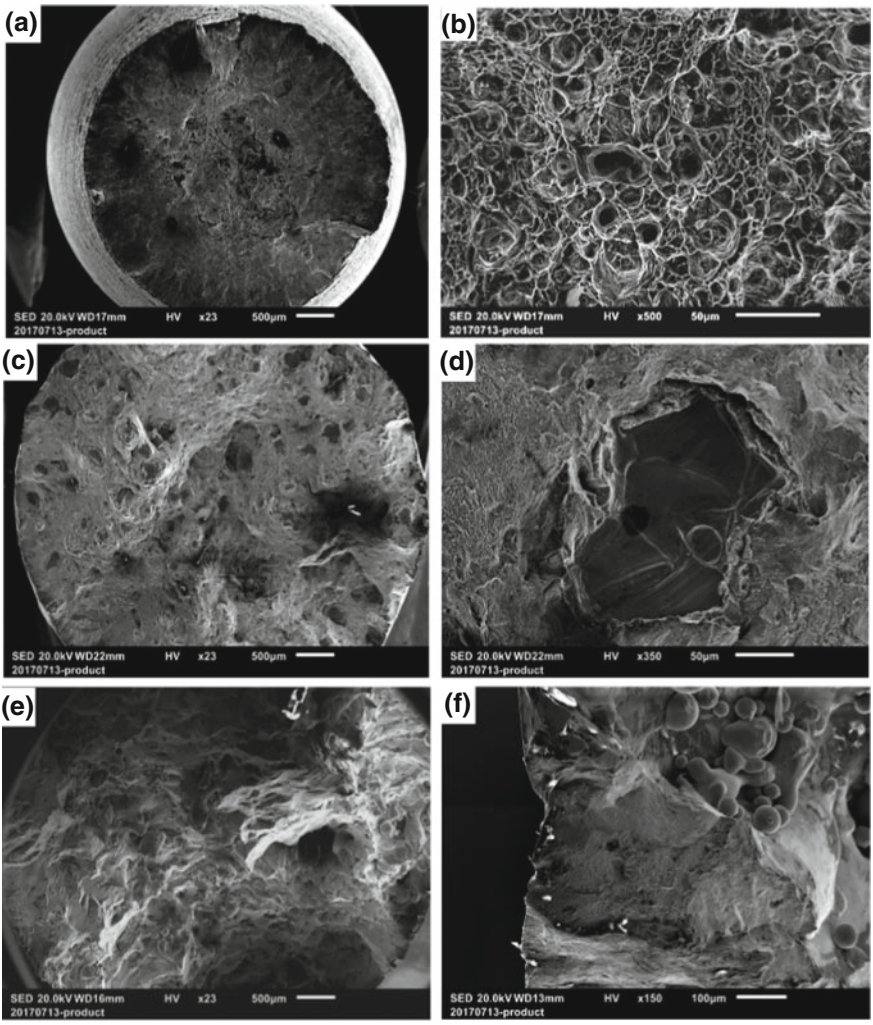

Fig. 5 Fracture surface of Inconel 718 after creep test at 650 °C and 690 MPa: **a** and **b** Wrought Inconel; **c** and **d** SLM produced with 250 W; **e** and **f** SLM produced with 950 W

Fractographic images of heat treated and FGM samples are shown in Fig. 6. One can see that 250 W (fine graded microstructure) has intergranular fracture with secondary cracks initiating at the grain boundaries (Fig. 6a and b). Parallel slips appearing within the same grain and cracks visible near the boundary (Fig. 5b) confirm a typical appearance of pure creep fracture surfaces. Contrary to 250 W specimens, 950 W condition shows microvoid coalescence indicating ductile mode, which might be attributed to the high density of process induced defect, resulting in insufficient time for creep mechanisms initiation. It should also be noted, that 950 W specimens have a coarse grained microstructure with grain orientation parallel to loading direction and there might be no grain boundaries present in the highest stress area (corresponding to pores and inclusions, see Fig. 7b). This observation is further confirmed in FGM samples (Fig. 6e–g), showing a clear transition, indicated by the black dashed line, from intergranular fracture (outside shell corresponding to 250 W) to ductile fracture (core corresponding to 950 W). A cross sectional investigation of crept specimens cut along the loading direction is advised for future work in order to get a deeper understanding of creep damage mechanisms acting in SLM processed material.

Thermomechanical fatigue (TMF) testing was performed in order to get closer to the actual turbine blades operational conditions. Thermomechanical fatigue crack

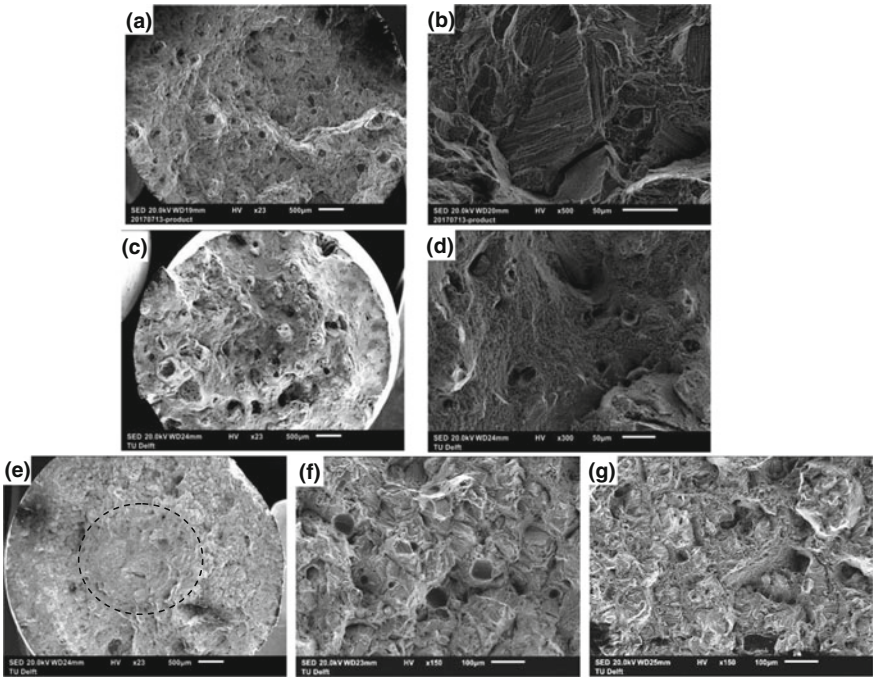

Fig. 6 Fracture surface of heat treated SLM produced Inconel 718 after creep testing at 650 °C and 690 MPa: **a** and **b** 250 W; **c** and **d** 950 W; **e** and **f** Functionally graded with core 950 W

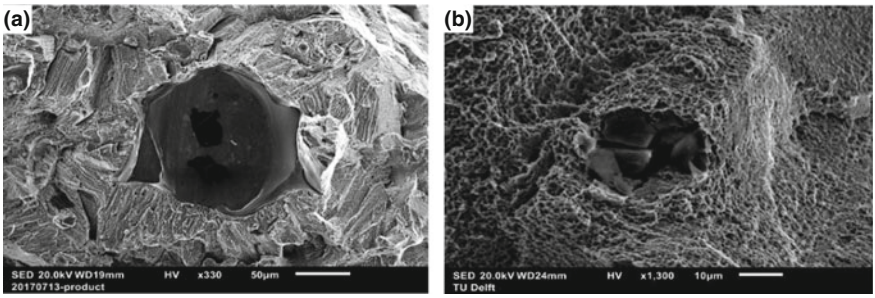

Fig. 7 Fracture surface of heat treated SLM produced Inconel 718, depicting **a** intergranular fracture around inclusion for 250 W and **b** ductile fracture around inclusion for 950 W

growth is more complicated than pure fatigue crack growth because it includes time dependent material behaviour characteristics such as creep and oxidation. Increasing temperature will activate specific mechanisms that can cause more damage than what would be expected by the individual contributions acting alone [15].

TMF results for fine and coarse grained SLM Inconel are shown in Table 4. As expected, samples produced with 950 W show short fatigue lifes as a result of large surface pores serving as crack initiation points. Cracks initiated at the surface pores result in a sudden force drop and final premature failure. On the other hand, samples produced with 250 W exhibit better TMF properties, which is explained by the small grain size and lower porosity. It should also be noted, that as heat-treated condition shows substantial increase in fatigue life. This lifetime increase can be explained by the dissolution of brittle Laves phase as well as the presence of the δ-phase at the grain boundaries, which provide restrictions to the grain boundary movement such as sliding [16]. Hence, grain boundary phases precipitated by heat treatment act as a barrier for dislocation motion, thus improving the high temperature properties of SLM built material.

An interesting observation was found for functionally graded material (FGM). As can be seen (Table 4), as-processed FGM samples show similar to pure matrix 250 W fatigue life properties, which indicates that outside shell (produced with fine grained 250 W) is the main microstructural zone controlling fatigue crack initiation

Table 4 In-phase thermomechanical fatigue (IP-TMF) data conducted between 350 and 650 °C

Specimen	Time until failure (h)	Cycles until failure	Porosity (%)
250 W–AP	103.3	621	1.1
250 W–HT	207.6	1246	1
950 W–AP	0.7	2	4.5
950 W–HT	45.7	275	4.1
FGM–AP	98.5	608	0.3
FGM–HT	407.2	2244	0.4

and growth and thus fatigue lifetime. A different fracture (crack growth) development has been observed for heat treated FGM sample, which shows superior to both 250 and 950 W lifetime properties. For this condition, during the initial 6 h under TMF loading, a pronounced decrease in developed tensile load levels has been observed, with a subsequent stabilisation. The load drop is indicating on specimen stiffness decrease due to the development of a TMF crack, whereas the load stabilization could be a result of possible crack arrest. Previous studies of nickel-based superalloys [17] showed that cracks which propagate along tortuous paths exhibit longer fatigue life than cracks with lesser deviation. Hence, obstructions such as grain boundaries, precipitates or graded interfaces may assist crack deflections into positions that cause crack arrest. This theory can explain behaviour of functionally graded material, where cracks that deviate into positions perpendicular to the loading direction (hence to core 950 W) no longer have a driving force to cause crack extension. Hence, instead of pure mode one loading of a crack growing perpendicular to the loading direction, small deviations create a mixed mode condition, decreasing the driving force, and slowing the crack growth rate. The proposed theory of crack arrest at graded interphase should be further investigated via fracture surface analysis and expended TMF testing. Furthermore, TMF testing of wrought Inconel should be performed in order to assess the possible benefits of AM functional grading.

Conclusions

A study of creep and thermomechanical fatigue of Inconel 718 produced by additive manufacturing has led to the following conclusions:

- *Post-processing heat treatment* in a form of solution treatment and double aging resulted in transformation of brittle Laves phase into a needle-like Ni_3Nb-δ precipitates.
- *Creep properties* of SLM produced Inconel do not show significant grain size effect, which might be attributed to high scatter in results caused by process induced pores observed in 950 W samples. Heat treatment, on the other hand, substantially improves creep properties, which is related to dissolution of Laves phase and precipitation hardening by plates of δ-phase, acting as a barrier for dislocation motion.
- There are two different *fracture mechanisms* observed in crept specimens: ductile fracture for 950 W and intergranular fracture for 250 W. It is suggested, that there is insufficient time for creep mechanisms initiation in 950 W samples exhibiting high density of process induced defects.
- *Thermomechanical fatigue* life of 950 W is lower than that of 250 W, which is due to larger grains and surface pores serving as crack initiation points. Heat treatment increases fatigue life by a factor of two.

- As-processed *functionally graded material* shows similar to pure matrix 250 W fatigue life, indicating that outside shell (produced with fine grained 250 W) is the main fatigue crack controlling zone.
- A substantial increase in *TMF lifetime* (by a factor of 4) is observed for *heat treated FGM condition*. A theory is proposed where functionally graded interface allows cracks to deviate into positions perpendicular to the loading direction (hence to core 950 W) thus reducing the driving force for further crack extension.

Further investigations of fracture surfaces as well as expended TMF testing will be performed in order to fully assess the possible benefits of AM functional grading.

References

1. Akca E, Gursel A (2015) A review on superalloys and IN718 nickel-based INCONEL superalloy. Periodicals Eng Nat Sci 3(1)
2. Azadian S, Wei LY, Warren R (2004) Delta phase precipitation in Inconel 718. Mater Charact 53(2004):7–16
3. Guedou J-Y et al (2008) Development of a new fatigue and creep resistant PM nickel-base superalloy for disk applications. In: Reed RC et al (eds) Superalloys 2008, TMS, Warrendale, PA, USA, pp 21–30
4. Murr LE, Gaytan SM et al (2012) Metal fabrication by additive manufacturing using laser and electron beam melting technologies. J Mater Sci Technol 28:1–14
5. Song B, Zhao X, Li Sh et al (2015) Differences in microstructure and properties between selective laser melting and traditional manufacturing for fabrication of metal parts: a review. Front. Mech. Eng. 10(2):111–125
6. Sames WJ, List FA, Pannala S, Dehoff RR, Babu SS (2016) The metallurgy and processing science of metal additive manufacturing. Int Mater Rev
7. Petch NJ (1953) J Iron Steel Inst 174:25
8. Moiz M (2013) The influence of grain size on the mechanical properties of Inconel 718. Linköping University, Sweden
9. Popovich VA, Borisov EV et al (2017) Functionally graded Inconel 718 processed by additive manufacturing: crystallographic texture, anisotropy of microstructure and mechanical properties. Mater Des 114:441–449
10. Popovich VA, Borisov EV et al (2017) Impact of heat treatment on mechanical behaviour of Inconel 718 processed with tailored microstructure by selective laser melting. Mater Des 131:12–22
11. AMS5664E Nickel Alloy, Corrosion and Heat Resistant, Bars, Forgings, and Rings 52.5Ni - 19Cr - 3.0Mo - 5.1Cb - 0.90Ti - 0.50Al - 18Fe Consumable Electrode or Vacuum Induction Melted 1950 °F (1066 °C) Solution Heat Treated, Precipitation Hardenable (2006)
12. E139 – 11, Standard Test Methods for Conducting Creep, Creep-Rupture, and Stress-Rupture Tests of Metallic Materials (2011)
13. Thébaud L et al (2015) Relationships between microstructural parameters and time-dependent mechanical properties of a new nickel based superalloy AD730™. In: Superalloys 2016, Wiley, pp 877–886
14. Reed RC (2006) The superalloys: fundamentals and applications. Cambridge University Press, Cambridge, UK

15. Zhang P, Zhu Q et al (2015) Review on thermo-mechanical fatigue behavior of nickel-base superalloys. Mater Trans 56(12):1930–1939
16. Baufeld B (2012) Mechanical properties of INCONEL 718 parts manufactured by shaped metal deposition (SMD). J Mater Eng Perform 21(7):1416–1421
17. Boyd-Lee AD (1999) Fatigue crack growth resistant microstructures in polycrystalline Ni-base superalloys for aeroengines. Int J Fatigue 21(4):393–405

Part IV
Additive Manufacturing: Building the Pathway towards Process and Material Qualification

Defect Detection in LENS AM Using In Situ Thermal Camera Process Monitoring

Tom Stockman, Judith Schneider, Cameron Knapp, Kevin Henderson and John Carpenter

Abstract This study utilizes in situ thermal imaging to monitor the melt pool during a LENS additive manufacturing (AM) process. A software tool is created which gathers metrics for each frame and summarizes them over every build. Plotted metrics allow a user to visually inspect the data, but the software tool also automatically identifies anomalies and flags them for further review. Anomalies are then correlated to physical locations in the build which are inspected for defects. This type of process monitoring could lead to fast detection of defects during a build, thus increasing the confidence in production quality and eliminating the acceptance of parts with abnormalities. An anomalous event was identified by the software tool and investigated with X-ray computed tomography. Defects were observed in the location identified by the software tool.

Keywords Process monitoring · LENS · Additive manufacturing

Introduction

AM is rapidly being integrated into production environments where parts must not only conform to specific geometrical tolerances but also perform structurally under significant stress and fatigue. Such a shift from prototyping to end-use products has increased demand for rigorous quality control [1]. The aerospace industry, for example, has begun adoption of AM parts into rocket engines where constant vibration makes fatigue a critical component to part performance. Such performance requirements mean that defects within the part can be detrimental. The term

T. Stockman (✉) · J. Schneider
University of Alabama in Huntsville, Huntsville, USA
e-mail: tom.j.stockman@gmail.com

J. Schneider
e-mail: jas0094@uah.edu

C. Knapp · K. Henderson · J. Carpenter
Los Alamos National Laboratory, Los Alamos, USA

The Minerals, Metals & Materials Society, *TMS 2018 147th Annual Meeting & Exhibition Supplemental Proceedings*, The Minerals, Metals & Materials Series,
https://doi.org/10.1007/978-3-319-72526-0_10

"defect" refers to a wide range of features that can be used to describe an anomaly in a build which would likely reduce its structural performance. Such defects could include, but are not limited to, lack of fusion, delamination, surface roughness, and unusually large or misshapen porosity [2]. This study focuses on Laser Engineered Net Shaping (LENS) which is a freeform AM process in which metallic powder is blown through nozzles into the path of a laser forming a melt pool.

In this study, the process is monitored using a camera with a two-color pyrometer to detect changes in the melt pool temperature profile during a build. As the metal is deposited onto a build plate, the camera records the temperature distribution within the melt pool region. Each frame from the camera is analyzed looking for anomalous behavior which is correlated to a location in the build. That location is then scanned using X-ray Computed Tomography (XCT) to investigate the abnormality.

Uses of high speed cameras, with framerates on the order of 5000 Hz, have been reported for in-situ process monitoring of AM processes [3, 4]. This study, however, uses a very low framerate (9.310 Hz) in an attempt to explore solutions which would be more readily accepted into a production environment. This lower framerate allows rapid processing of the data and extraction of a wide range of features from each frame without significant computational burden. By correlating the data obtained with defects in actual parts, the combination of metrics gathered from each frame can be identified as signatures of particular defect type. Although it is possible to miss defects with signatures on a timescale or length scale small enough to fit between frames. Continued in-situ and ex-situ analysis are needed to determine the false positive and false negative rates of any software tool developed.

Experimentation

The LENS machine used in this study was an Optomec LENS MR-7 [5] which is a blown powder system with 3 axis control housed within a glovebox as shown in Fig. 1. The base moves in X and Y while the deposition head moves in Z. The MR-7 is equipped with a 1 kW IPG fiber laser in an enclosed argon atmosphere (<10 ppm O_2). Several diagnostic tools have been installed in the machine, including a ThermalViz camera system used in this study. The camera uses a two-color pyrometer with 950 and <950 nm wavelengths, overlaying two discreet sensors to correct for emissivity. A tungsten filament is used to calibrate the temperature measurements with a linear temperature-radiance ratio. The data was sampled at 9.310 Hz, the maximum rate of the camera, with an exposure time of 20 ms. The pyrometer looks directly down onto the build plate coaxial with the laser.

The power delivered from the MR-7 LENS laser was 808 W focused at a distance of 0.9525 cm and with a powder feed rate of 33.7 g/min. Powders used were 304L with an average size of 100 μm. The dwell time for the laser starting each pass was 20 ms, and the travel speed of the table was 101.6 cm/min. The length of each pass was 5.08 cm with a 0.102 cm hatch spacing for the second pass

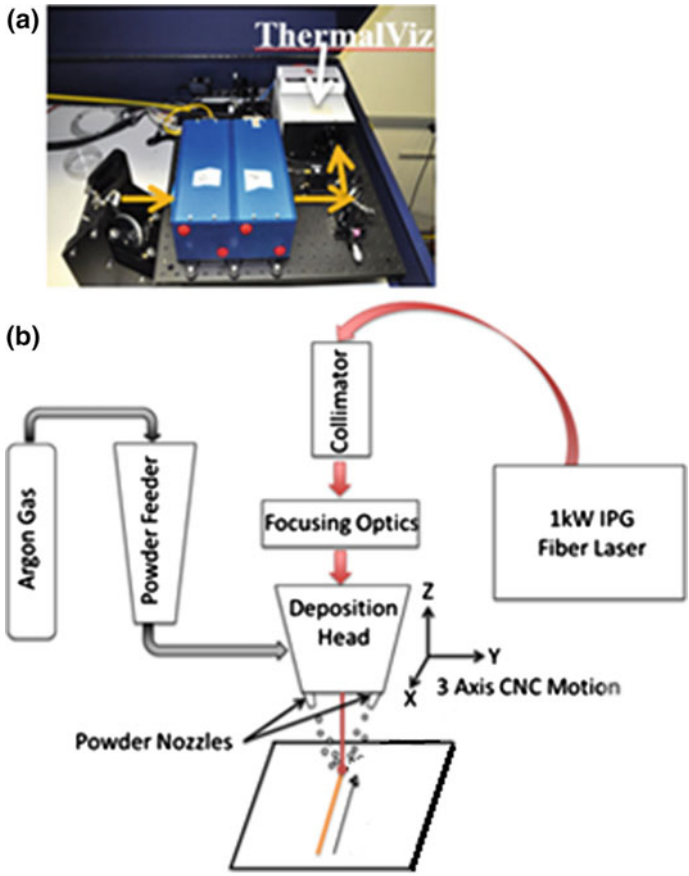

Fig. 1 **a** Shows the ThermalViz pyrometer looking down coaxial with the laser. **b** Shows the MR-7 schematic

deposited next to the first as illustrated in Fig. 2. Parameters were selected to create a fully dense deposit with no effort made to 'insert' a known population of defects. The print geometry used in this study was 5.08 cm long by 0.102 cm wide and 0.076 cm high.

In Situ Analysis

ThermalViz software was used to convert the data files from the camera into comma separated value (CSV) format. A custom Python script was used to process the CSVs. For each frame, a "summary image" is generated which compiles four different views of the data as shown in Fig. 3: (a) a colorized heat map, (b) the melt pool isolated with several features drawn on top of it, (c) a contoured heat map, and

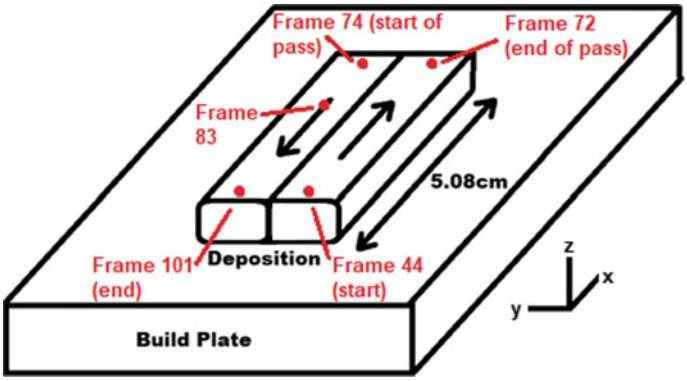

Fig. 2 Deposition plan used, 5.08 cm long, 2 layers deposited in alternating directions spaced 0.1016 cm apart

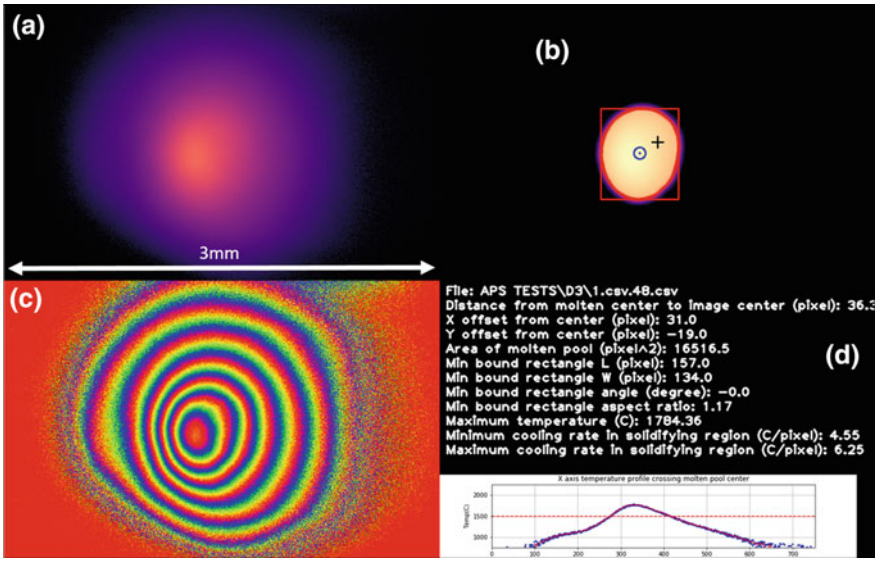

Fig. 3 A typical "Summary Image". **a** heat map, **b** molten pool, **c** contoured heat map, **d** frame metrics. The scale shown in (**a**) is the same for (**b**) and (**c**)

(d) a listing of several metrics recorded from that frame with an X direction plot of the temperature profile through the center of the melt pool (the blue circle in (b)) (Fig. 3). The contours are interpreted using the "prism" scale shown in Fig. 4.

The melt pool is generated by thresholding the original image to only pixels above a certain temperature value. In this case 1500 °C was chosen as the threshold temperature. This is slightly above the 1340 °C melting temperature of 304L which was chosen to ensure the identified region was molten. It is worth noting that the

Fig. 4 Matplotlib color map "prism" set to repeat approximately every 150 °C. The maximum temperature recorded in Fig. 3c was 1784 °C and can be seen visually by the number of repeating color bands across the contours to the final red color in the center of the molten pool

collection of these metrics from the melt pool region are not necessarily meant to be physically significant. The purpose of the analysis is to spatially resolve the location of anomalies and outliers; thus only consistency is required.

Once thresholded, the molten pool area is blurred. Unlike the colorized contour plot, a blur is required so that the software can draw a defined solid line around the region of interest. From the blurred molten pool the following metrics are gathered: center of mass, area, minimum bounding rectangle. These metrics are determined using the python library OpenCV and are summarized in Table 1.

Table 1 Metrics gathered from each frame with a brief description, typical measured values, and anomalous frame values

Metric	Description	Mean	St Dev	Frame 83	Difference from 83 to mean (%)
Distance (pixels)	Distance from molten pool CoM to pixel center of image	26.10	8.36	21.47	−17.80
X offset (pixels)	X direction component of distance	20.68	9.76	19.00	−8.10
Y offset (pixels)	Y direction component of distance	−13.98	6.36	−10.00	−28.50
Area (pixels^2)	Sum of molten pixel areas	*16767.41*	*3644.96*	*3587.00*	*−78.60*
Length (pixels)	Length of smallest bounding rectangle around molten pool	*166.96*	*16.69*	*107.35*	*−35.70*
Width (pixels)	Width of smallest bounding rectangle around molten pool	*126.66*	*19.28*	*48.66*	*−61.60*
Aspect ratio (Length/Width)	Length/Width parameters specified above	*1.34*	*0.19*	*2.21*	*64.70*
Max Temp (°C)	Maximum temperature in image	*1717.03*	*78.74*	*1540.18*	*−10.30*
Heating Rate (°C/pixel)	Temperature rate of change on leading edge of molten pool	*4.04*	*0.76*	*1.67*	*−58.70*
Cooling Rate (°C/pixel)	Temperature rate of change on trailing edge of molten pool	*5.84*	*1.43*	*2.08*	*−64.40*

Two metrics are gathered from the area just outside the molten pool which are called the "Heating Rate" and "Cooling Rate". These are created by thresholding the original image to isolate pixels in the temperature range of 1450–1500 °C. The range of 50 °C was selected to be broad enough to be significant, but narrow enough that temperature profile in this range would be linear. This 50 °C band around the melt pool is blurred so that contours can be drawn, and the thickness of the contour measured on both the leading and trailing edge of the molten pool. The pixel thickness of each is then divided by the temperature span of 50 °C to get a cooling rate in °C/pixel. This can later be converted to °C/m using the actual length of the image pixels and then into °C/s using the m/s table travel speed. An algorithm was developed to determine the direction of travel which was used to differentiate the "Heating Rate" from the "Cooling Rate".

In this study potential defects are identified by searching for statistical anomalies in the recorded metrics. After metrics are gathered for each frame, they are plotted and outliers are identified. For this initial study, anomalies are identified relative only to the data set of the current build. For each metric summarized in Table 1, the data is first analyzed while looking for data points which are more than four standard deviations from the mean. The frame location of these outliers is recorded, and those data points are removed from the data set. After the removal of extremes, the mean and standard deviations are recalculated, and any data points outside two standard deviations are also recorded. If a frame is identified as an outlier in more than three metrics, it is automatically flagged as an anomaly. Frames which are flagged as anomalies are then correlated to a location in the build so that XCT scans can be performed to look for defects. Figure 5 shows an example plot of the processed data with lines drawn to show one and two standard deviations away from the mean. Similar plots were generated for every metric gathered.

To guide the XCT scans, the location of the captured frame to a location in the build must be identified. However the LENS machine does not timestamp the frames thus there is no time/position data recorded. To provide this correlation, a combination of build path parameters and signatures in the thermal data are used to make an appropriate correlation. The passes in each build alternate in the negative and positive X directions as illustrated in Fig. 2. There is a brief pause between these passes while the machine adjusts in the Y direction. The pause is long enough to generate several dark frames in the data. Thus whenever two to three frames are missing this marks the beginning of a new pass which is assigned a pass number. To determine the position of the frame within that pass, a camera framerate of 9.310 Hz is used. Thus by counting the number of frames from the start of the pass, and knowing the travel speed of the table, the distance traveled can be calculated.

Because the time since the start of a pass is being used to calculate the position, any uncertainty in the time also propagates into the position. Two sources of uncertainty were quantified. First there is a uniformly distributed uncertainty about the start time of the build. Although the time associated with the laser on is unknown, it occurs sometime between the first frame where it is visible and the frame immediately prior. This uncertainty will be present regardless of the framerate of the camera, but the associated uncertainty scales inversely with the

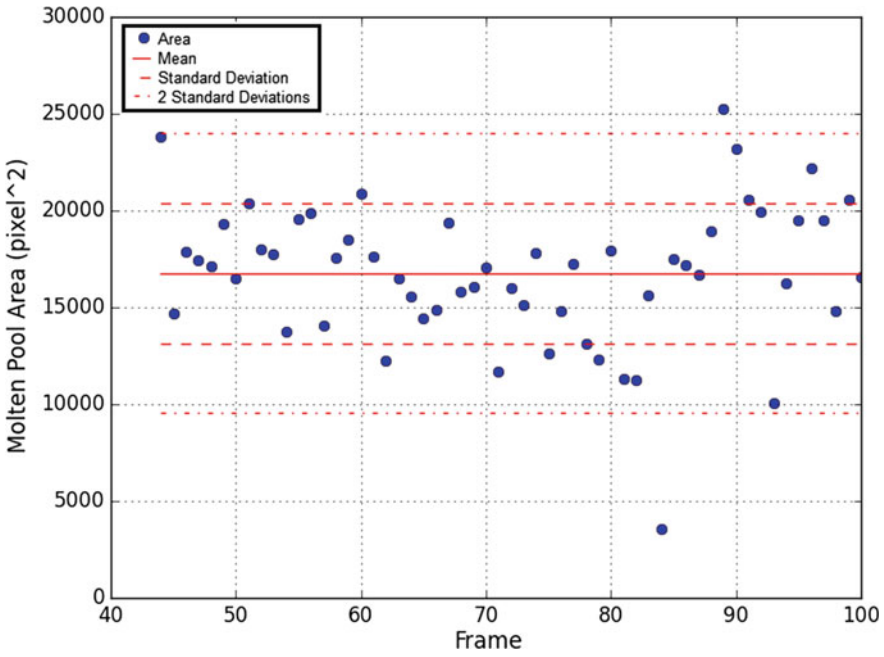

Fig. 5 Molten pool area (pixels^2) in each frame. Note that frame 83 falls outside of the standard deviation range. Frame 48 (marked by an arrow) represents the average frame used for comparison of melt pool size in Fig. 7

framerate. The second source of uncertainty is on the framerate itself. ThermalViz reports the framerate at the end of a build as an average of the number of frames taken over the total time it was running, but there is no information available on the consistency of that framerate. A normal distribution with a 1% standard deviation was assumed for the time between each frame meaning that this component of the uncertainty grows with each consecutive frame after a new pass has begun. This growth is modeled by a normal distribution about the sum of its constituent means and with a variance equal to the sum of its constituent distribution variances [6]. However because the position of the start of each pass is known from the coding input to the LENS machine, the growing component of the uncertainty can be reset to 0 at the start of each pass, hence referred to as a baseline event. Figure 6 plots the sum of these two uncertainties converted from time uncertainty to position uncertainty by multiplying by the travel speed. The travel speed is assumed constant with expected uncertainty of less than 1%. The three lines show three different confidence levels which were considered when identifying the location of particular frames.

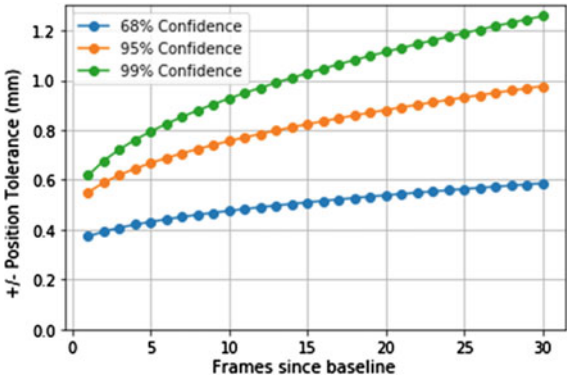

Fig. 6 Quantified positional uncertainty in the X direction at three confidence levels. Frame 83 from Fig. 5 is 10 frames since baseline. The position of this frame is known to within ±0.75 mm with a 95% confidence

Anomaly Detection Results

The analysis method used in this study identified two frames as anomalous: Frames 44 and 83. Frame 44 was omitted from further investigation as the camera is turned on for some time before the build actually begins, and the 44th frame from the camera initialization is the start of the build. The reason this frame flagged as unusual is that unlike subsequent frames, the current frame was symmetrical because the base plate had not yet begun to move. This made the shape, area, and position of the melt pool flag as outliers in the analysis. Thus it is not recommend to use the first frame of a build for outlier analysis.

Figure 7 shows the melt pools from summary image of Frame 83 which was considered for further analysis and Frame 48 which is representative of the rest. Frame 83 was flagged as an outlier in seven metrics: area, length, width, aspect ratio, maximum temperature, heating rate, and cooling rate. Table 1 shows some quantification of the metrics averaged over the whole build along with the specific values of frame 83. Frames which flagged as outliers are italicized. A typical frame

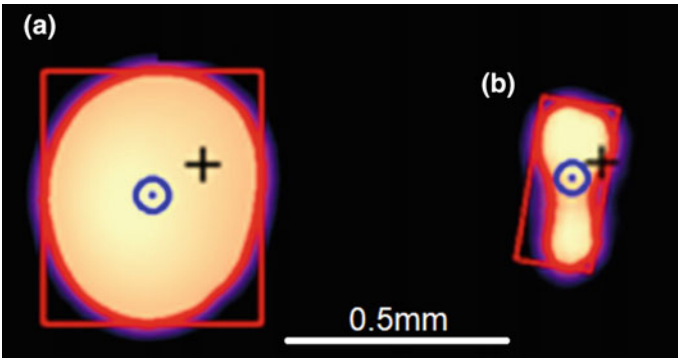

Fig. 7 Melt pools for **a** a normal frame (as seen in Fig. 3) and **b** Frame 83

is shown in Fig. 7a in contrast with frame 83 shown in Fig. 7b. The molten pool is visibly smaller and misshapen. Thus type of fluctuation could be due to anomalies in powder flow or laser power. Changes in these critical parameters could cause defects.

Ex-Situ Measurement

After the build was completed, it was inspected using an Xradia Micro Computed Tomography (XCT) machine. The X-ray source was a Micro Focus Hamamatsu operated at 40–150 kV acceleration voltage, 10 W total power, and 5 μm spot. The detector was a 2048 × 2048 pixel camera coupled with a scintillator crystal lens. The voxel dimension was 5 μm corresponding to a detectable defect size. The TXMReconstructor software package (Carl Zeiss Microscopy, Inc.) was utilized for tomogram reconstructions.

Figure 8 shows a lower density region or defect located near the identified area for Frame 83 but outside of expected location uncertainty bounds. The image shown is in the pass directly next to the location corresponding to Frame 83. Further testing of the part is needed to determine if the abnormality detected affects the structural property of the component.

Future Work

This study is on-going to identify abnormalities in the melt pool during a build. Initially the data obtained will be evaluated with respect to an individual build. The ability of the analysis tool developed demonstrated the ability to measure and calculate several metrics from the acquired frames. The metrics were used to

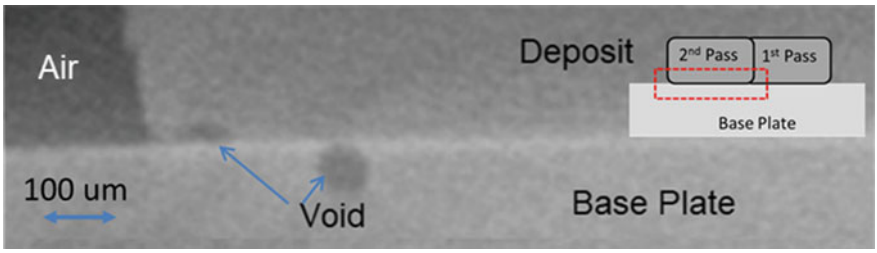

Fig. 8 Density difference observed in XCT scan in area near location identified as Frame 83. Dark gray areas marked as 'voids' indicate where density is lower than expected. The very dark area to the top left is open air not inside the material. Both voids are ~100 μm in diameter and, when summed, are 40% of the normal melt pool diameter seen in Fig. 7

identify anomalous behavior in a particular frame which can be correlated to a specific location in the build.

As the database of abnormalities are continued to be collected and correlated with impact on material properties this will provide a training dataset for subsequent analysis. Using this training set, more sophisticated methods can be developed to identify critical signatures in the data. Narrowing the required number of metrics would allow for faster processing thereby facilitating real time analysis. If an abnormality can be detected, the build can be terminated to reduce time in obtaining an acceptable quality build.

This type of data processing would benefit from AM equipment equipped with a time stamp. Although extrapolation of the position from the number of frames is possible, accuracy would be improved by having a timestamp directly correlated to a position within the build.

References

1. NIS (2013) Measurement science roadmap for metal-based additive manufacturing. Energetics Incorporated
2. Frazier WE (2014) Metal additive manufacturing: a review. J Mater Eng Perform 23(6): 1917–1928
3. Berumen S, Bechmann F, Linder S, Kruth J-P, Craeghs T (2010) Quality control of laser and powder bed-based additive manufacturing (AM) technologies. Phys Procedia 5:617–622
4. Furumoto T, Ueda T, Alkahari MR, Hosokawa A (2013) Investigation of laser consolidation process for metal powder by two-color pyrometer and high-speed cideo camera. CIRP Ann Manuf Technol 62(1):223–226
5. Optomec. www.optomec.com/wp-content/uploads/2014/04/LENS_MR-7_Datasheet_WEB_0816.pdf. Accessed 10 Sept 2017
6. Eisenburg B, Sullivan R (2008) Why the sum of independent normal random variables is normal. Math Mag 81:362–366

Part V
Advanced High-Strength Steels

Studying Hydrogen Embrittlement in Nano-twinned Polycrystalline Fe-12.5Mn-1.2C Austenitic Steel

Mahmoud Khedr, Wei Li and Xuejun Jin

Abstract Embedding austenitic structures with nano-twinned grains is a promising technique to enhance its strength and ductility, nano twins can be introduced via thermo-mechanical processing or via electro-deposition. In the current study, ternary Fe-Mn-C austenitic steel was cold rolled then subjected to flash annealing to keep some nano twins within the matrix. It was found that, the nano twinned condition showed better resistance to Hydrogen embrittlement (HE) than the as received state. In addition, notched samples charged with hydrogen were tensile tested to investigate the contribution of the nano-twinned grains in impeding cracks initiation/propagation, it was concluded that the prior twins distributed homogeneously the internal stresses inside the austenitic grains during the plastic deformation, which prevented cracks propagation at earlier strain level, and this delayed time till fracture happened.

Keywords Hydrogen embrittlement · Austenitic steels · Pre-induced twins

Introduction

Austenitic steels are famous with its usages in the applications related to serving in hydrogen environment, however, improving its resistance to hydrogen embrittlement(HE) is very important issue [1]. According to the literatures [2, 3], the HE resistance of austenitic steels was improved by decreasing grains sizes or alloying with Al. The target of the current work is to provide a new method to enhance the

M. Khedr (✉) · W. Li · X. Jin
School of Materials Science and Engineering, Institute of Advanced Steels and Materials, Shanghai Jiao Tong University, Shanghai 200240, China
e-mail: mahmoud.khedr.mk@gmail.com

M. Khedr · X. Jin
Collaborative Innovation Center for Advanced Ship and Deep-Sea Exploration, Shanghai Jiao Tong University, Shanghai 200240, China

The Minerals, Metals & Materials Society, *TMS 2018 147th Annual Meeting & Exhibition Supplemental Proceedings*, The Minerals, Metals & Materials Series,
https://doi.org/10.1007/978-3-319-72526-0_11

HE resistance of coarse grained high C-Mn steel via embedding the structure with nano-scale twins.

Nanos-scale twins can be introduced to FCC structures via thermo-mechanical processing or by electro-deposition [4, 5]. The nano-twinned structures showed enhanced strength and ductility, in addition to retarding cracks propagation compared with the not twinned grains [6], since that, twin boundaries are considered as planar defects which can hinder dislocations mobility [7]. On the other hand, existing of internal defects such as twins, work as hydrogen trapping sites, and it may affect hydrogen diffusivity [2].

Experimental Work

Materials

In the current work, commercial Hadfield steel containing Fe, 1.15 wt% C and 12.45 wt% Mn was investigated, it contains single phase of austenite. The as received condition was prepared by hot rolling followed by water quenching.

Introducing Nano Twin Plates via Cold Rolling then Heat-Treating

To embed the austenite phase with deformation twins, cold rolling was performed. The cold rolled specimens showed ductility less than 4% [8], so that, it was annealed at 915 °C for 90 s, in order to reduce the micro-strains, while the short time of annealing was selected to keep some nano twins within the structure, and to avoid de-twinning associated with long holding time. The heat-treated samples are named CR90.

Hydrogen Charging and Tensile Testing

Hydrogen charging was carried out via electro-chemical charging in aqueous solution of 3% NaOH and 3 g/l NH_4SCN with 16.8 mA/cm^2 current density, for 24 h at 80 °C. A platinum wire was used as a counter electrode.

Samples for tension test were prepared according to the ASTM standard (E 8M-03) with gauge dimensions of 25 × 6 × 1 mm^3, tested at slow strain rate (SSRT) of 4×10^{-5} s^{-1}. Using of the notched specimens during the tension test is an indicator of crack initiation and propagation sites [9]. Details about notch dimensions were presented elsewhere [10].

Characterization

The characterizations of the microstructure of Hadfield steel imply using of optical microscopy via (OM, Zeiss), and to get more details about twins structures, thin foils with diameter of 3 mm for transmission electron microscopy (TEM) were prepared by using ion beam polishing system (Gatan 691). Scanning electron microscopy (SEM) was performed by a JEOL JSM7600F. After tension test, samples within the gauge area were selected to measure it hardness according to Vickers scale (HV) under load of 100 g for 10 s as a penetration holding time.

Results and Discussion

Tension Test Results

Table 1 summarizes the results of the tension tests of the as received and cold rolled then heat-treated samples (CR90) with and without H charging. The mechanical behavior of the CR90 is better than the as received condition. After H-charging, yield strength of the as received was slightly decreased, while in the CR90 it was nearly not affected.

The Microstructure of the Gauge Area After Tension Test

Figure 1 shows the microstructure in the gauge area after fracture in both the as received and CR90 conditions, with and without hydrogen. Generally, the amounts of twin boundaries are higher in the CR samples. it seems that, the existence of hydrogen affected the process of initiating mechanical twins intensively in the as received condition, which may be related to dislocations cross slipping enhanced by hydrogen [1], and consequently the amount of induced twins were negatively affected.

Table 1 The mechanical properties of the as received and CR90 before and after H-charging

Condition	As received		CR90	
	Without H	With H	Without H	With H
YS (MPa)	361.2	353.6	374.3	373.9
UTS (MPa)	840.5	718.2	1028.4	973.1
Elongation (%)	29.2	23.1	41.1	39.3
Loss in UTS due to H-charging (%)	15.3		2.7	
Loss in Elongation due to H-charging (%)	22.5		6.1	

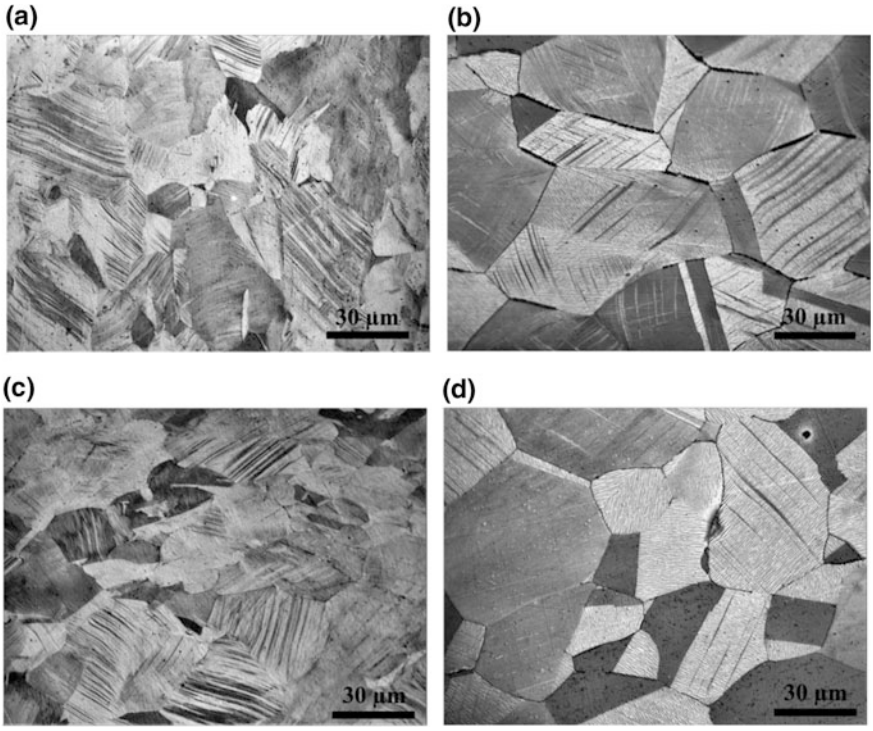

Fig. 1 The micrographs after tension test through the gauge area, at the CR90 (**a**, **c**), and as received condition (**b**, **d**), without H (**a**, **b**), and with H (**c**, **d**)

Notched Samples

Figure 2 shows a longitudinal section of the notched specimens at the two sides with hydrogen, in both as received and cold rolled conditions. Usually cracks are formed in the two sides of the notches during the tension test, while due to strain localization in Hadfield steel [11], fracture will start from one side then it will propagate to the other side [12]. Nevertheless, as shown in Fig. 2a, in the as received condition that was charged with hydrogen, only one crack was initiated and then propagated to the other side, which is an indicator of slip localization due to existence of hydrogen [13, 14]. On the other hand, in the CR90 condition that was charged with hydrogen, many cracks were initiated together due to the existence of the pre-induced twins in both 3% and 5% strain as shown in Fig. 2b and c. The pre-induced twins enhanced the homogeneous distribution of internal stresses during the plastic deformation, and this prevented crack propagation in an early stage of strain compared with the as received condition. Moreover, twins assisted crack propagation along grain boundaries at the interception with twin tips [1]. Cracks were propagated at around 3% strain in the as received condition,

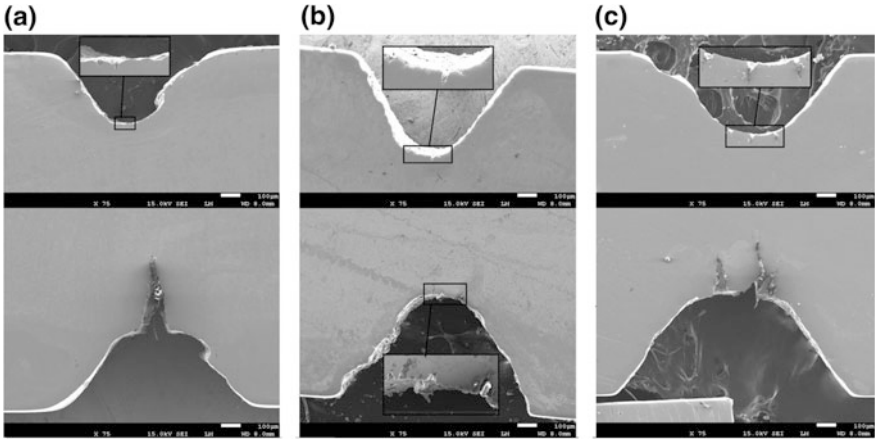

Fig. 2 Cracks initiation and propagation in the notched tension test specimens after H-charging, as received condition at 3% strain (**a**), and cold rolled at 3% and 5.5% strain respectively (**b**, **c**)

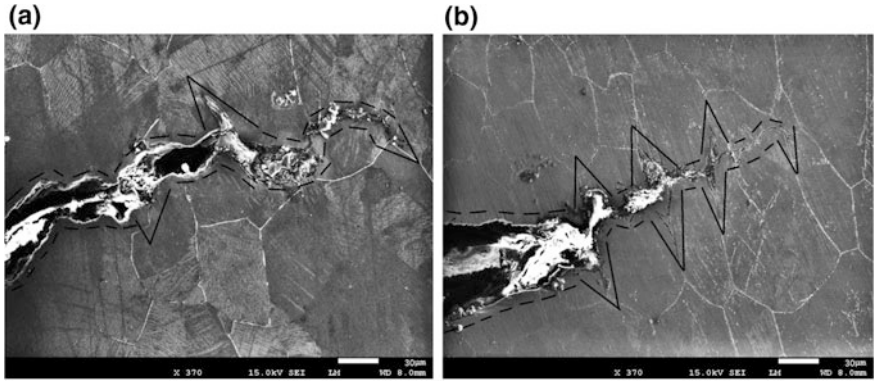

Fig. 3 The microstructure of the notched samples showing cracks paths, **a** the as received and **b** cold rolled conditions. The dotted lines show the crack propagation path, and the solid lines show the cracks initiation sites

while it propagated at 5.5% strain in the cold rolled samples. It worth mention that, the number of cracks in the notched area at the cold rolled condition are more than the as received.

Figure 3 shows the microstructure of the notched specimens under SEM after etching with Nital, in order to spot more light on the crack initiation and propagation in the as received and cold rolled samples. It is clear that the cracks are distributed homogeneously in the cold rolled samples, in addition, cracks were initiated from grain boundaries [12] during its propagation.

Table 2 Variation of hardness values in the as received and CR90 samples with and without hydrogen

Condition	As received		CR90	
	Without H	With H	Without H	With H
$HV_{0.1}$	445 ± 14	374.7 ± 30	502.1 ± 14	490.7 ± 13

Hardness Results

It was reported that, hardness values are dependent of the twins volume fraction in austenitic steels [15], so that hardness was measured in the gauge area after tension test. Table 2 shows the results of hardness on Vickers scale. The results show that, the cold rolled samples are having higher hardness values, and this may refer to more twin plates, but it will be better to enhance it with TEM.

TEM Results

Figure 4 shows the TEM results of the as received and CR90 conditions charged with hydrogen. As shown in Fig. 4a, it is clear that the initial nano twins introduced in the CR90 worked as barriers to dislocations movements and resulted in forming of very twin plates in spite of existing of hydrogen. On the other hand, as shown in Fig. 4b, twins were relatively thicker after H-charging, and it may be related to

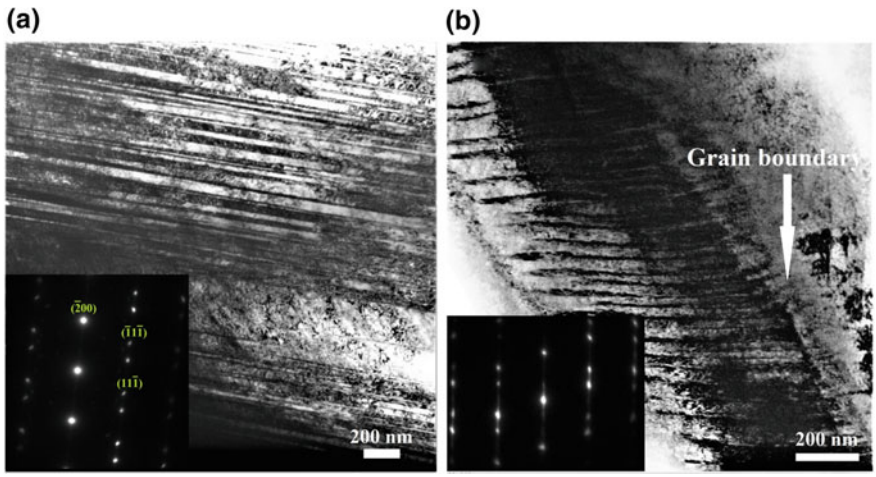

Fig. 4 TEM results using [110] zone axis after tension test of specimens charged with hydrogen. CR90 at (**a**), and as received at (**b**)

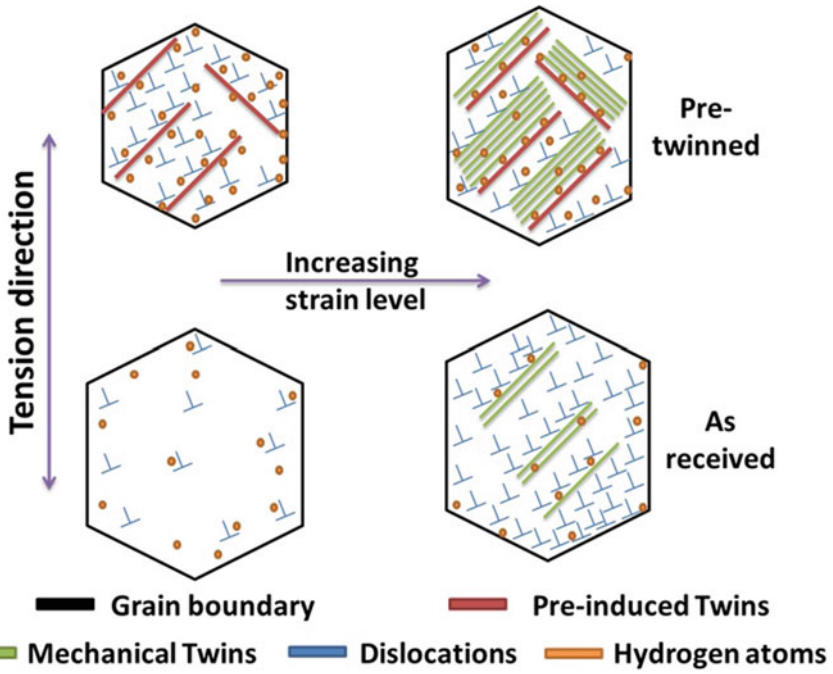

Fig. 5 Graphical illustration showing the effect of the pre-induced twins on preventing dislocations slip after H-charging in the cold rolled sample and consequently inducing more mechanical twins, while in the as received sample mechanical twinning was limited (For interpretation of the references to color in this figure legend, the reader is referred to the web version of this article.)

pilling up of the enhanced dislocations mobility on grain boundaries due to hydrogen entry, and it can refer to promoting more trans-granular fracture in the fracture surface revealed by Michler et al. [13].

Figure 5 shows illustration graph of the effect of the pre-induced twins in inhibiting dislocations slip after H-charging, and consequently increasing dislocations dissociation rate to form mechanical twins and distributing the internal stress homogeneously. Nevertheless, at the not-twinned sample, the amount of mechanical twins at fracture are lower than the pre-twinned sample due to dislocations mobility enhanced by hydrogen atoms, while there was no more obstacles to these dislocations like the pre-twinned sample, in addition, dislocations were accumulated on grain boundaries causing local stress concentrations that resulted in inter-granular fracture [13]. Moreover, it is important to note that the twin boundaries in Hadfield steel are containing tremendous amounts of dislocations [16].

Conclusion

Embedding coarse grained austenitic steel with nano twin plates resulted in increasing hydrogen embrittlement resistance of Hadfield steel. Moreover, notched samples confirmed that, the internal stresses were homogeneously distributed through the austenite matrix.

Acknowledgements The authors are grateful to the financial support of the National Key R&D Program of China (No. 2016YFB0300601), National Natural Science Foundation of China (U1564203, Nos. 51571141 and 51201105).

References

1. Koyama M, Akiyama E, Lee YK, Raabe D, Tsuzaki K (2017) Overview of hydrogen embrittlement in high-Mn steels. Int J Hydrog Energy 42:12706–12723
2. Park I, Jeong K, Jung J, Lee C, Lee Y (2012) The mechanism of enhanced resistance to the hydrogen delayed fracture in Al-added Fee18Mne0.6C twinning-induced plasticity steels. Int J Hydrog Energy 37:9925–9932
3. Ryu JH, Kim SK, Lee CS, Suh DW, Bhadeshia HKDH (2013) Effect of aluminium on hydrogen-induced fracture behaviour in austenitic Fe–Mn–C steel. Proc R Soc A 496:1–14
4. Yan FK, Liu GZ, Tao NR, Lu K (2012) Strength and ductility of 316L austenitic stainless steel strengthened by nano-scale twin bundles. Acta Mater 60:1059–1071
5. Lu K, Lu L, Suresh S (2009) Strengthening materials by engineering coherent internal boundaries at the nanoscale. Science 324:349–352
6. Chowdhury P, Sehitoglu H, Rateick R (2016) Recent advances in modeling fatigue cracks at microscale in the presence of high density coherent twin interfaces. Curr Opin Sol State Mater Sci 20:140–150
7. Greer JR (2013) It's all about imperfections. Nat Mater 12:689–690
8. Khedr M, Li W, Jin X (2016) The effect of deformation twins induced previously by cold rolling on the mechanical behavior of Hadfield steel. Paper presented at the 1st ICAS and 3rd HMnS, Cheng Du, China, 16–18 Nov 2016
9. Wang M, Akiyama E, Tsuzuki K (2007) Effect of hydrogen on the fracture behavior of high strength steel during slow strain rate. Corr Sci 49:4081–4097
10. Zhu X, Li W, Zhao H, Wang L, Jin X (2014) Hydrogen trapping sites and hydrogen-induced cracking in high strength quenching & partitioning (Q&P) treated steel. Int J Hydrog Energy 39:13031–13040
11. Canadinc D, Efstathiou C, Sehitoglu H (2008) On the negative strain rate sensitivity of Hadfield steel. Scr Mater 59:1103–1106
12. Koyama M, Akiyama E, Tsuzaki K, Raabe D (2013) Hydrogen-assisted failure in a twinning-induced plasticity steel studied under in situ hydrogen charging by electron channeling contrast imaging. Acta Mater 61:4607–4618
13. Michler T, Marchi CS, Naumann J, Weber S, Martin M (2012) Hydrogen environment embrittlement of stable austenitic steels. Int J Hydrog Energy 37:16231–16246
14. Nagumo M (2004) Hydrogen related failure of steels—a new aspect. Mater Sci Tech 20: 940–950

15. Tewary NK, Ghosh SK, Bera S, Chakrabarti D, Chatterjee S (2014) Influence of cold rolling on microstructure, texture and mechanical properties of low carbon high Mn TWIP steel. Mater Sci Eng A 615:405–415
16. Idrissi H, Renard K, Schryvers D, Jacques PJ (2010) On the relationship between the twin internal structure and the work-hardening rate of TWIP steels. Scr Mater 63:961–964

Non-metallic Inclusion and Their Effect on Fatigue Strength for Case-Hardened Carbon Steel in Gears

Izudin Dugic, Robin Berndt, Simon Josefsson and Martin Hedström

Abstract Steel is a very essential structural material and its production worldwide has shown significant increase over the last years. In steels there always exist a large number of inclusions which can have a degrading effect on the fatigue properties. This study is focused on the link between the characteristics of non-metallic inclusions and how they affect fatigue strength of the standardized case-hardened carbon steel 20MnCr5 and a version of this steel with a more favorable inclusion distribution, a so-called Clean steel. For the evaluation of the mechanical properties the test result from rotary bending tests are compared and an improvement by 37.5% in fatigue strength can be noted between the different steels. The new performed ultrasonic tests illustrate the difference in the size of defects in materials with different manufacturing processes and degree of reduction. By studying international and European standards for non-destructive testing and investigation of alloy compounds, the current material specification can be adjusted.

Keywords Steel · Clean-steel · Inclusions · Mechanical properties
Ultrasonic test · Standard

Introduction

The cleanliness in a steel is of great importance for the strength in general and the fatigue strength in particular. Non-metallic inclusion is a recurring problem in the production and casting of steel. Variation from specification in respect to inclusion distribution inevitable leads to costly reparations, downgrading or recycling of large quantities of material. There are different types of inclusions present in steel which

I. Dugic (✉) · R. Berndt · S. Josefsson
Faculty of Technology, Department of Mechanical Engineering, Linnaeus University, Växjö, Sweden
e-mail: Izudin.dugic@lnu.se

M. Hedström
China Euro Vehicle Technology AB, Göteborg, Sweden

The Minerals, Metals & Materials Society, *TMS 2018 147th Annual Meeting & Exhibition Supplemental Proceedings*, The Minerals, Metals & Materials Series,
https://doi.org/10.1007/978-3-319-72526-0_12

depends strongly on the production route, alloy composition and technical conditions of the process [1, 2].

The influence on the mechanical properties of inclusions is decided by the size, thermal expansion coefficient, modulus of elasticity and the deformability of said defects. A greater inclusion size in general leads to lowered mechanical properties. If the thermal expansion coefficient is greater than that of the metal, it will shrink more in the solidifying process leading to compressive residual stresses around said defect. If on the other hand the thermal expansion coefficient is lower than that of the metal, it will shrink less in the solidifying process, leading to tensile residual stress around the defect [2].

When it comes to dynamic loaded parts such as engines, gears, shafts and turbines the most occurring cause of failure today is material fatigue due to the many load cycles associated with parts such as there [3].

The purpose of fatigue tests with cycles between 10^6 and 10^7 is to statistically map the mean value and spread of the fatigue limit. There are different models developed and available for gathering data and calculation of the fatigue limit where the most common is the staircase-method, also known as the up and down method [4–8].

The data collected with the staircase method can through the "Dizon-Mood"-equations be used to calculate a mean value, $\hat{\mu}$ (Eq. 1) and a standard deviation, $\hat{\sigma}$ (Eq. 2) for the fatigue limit (Sn) [4–8].

$$\hat{\mu} = S_0 + s \times (B/A \pm 0.5)\ [\text{MPa}] \tag{1}$$

$$\hat{\sigma} = 1.62 \times s \times (A \times C - B^2/A^2 + 0.029)\ [\text{MPa}] \tag{2}$$

With the results from Eqs. (1–2), a 99.9% confidence limit is calculated:

$$\hat{\mu} - 3.291 \times \hat{\sigma}\sqrt{N} = 99.9\%\ \textit{confidence limit} \tag{3}$$

Currently, there exist two general methods for computation of the allowed fatigue stress for gears in accordance with ISO 6336 called method A and method. The method which is used for computation of the nominal stress value with respect to bending ($\sigma_{F\,lim}$) and contact fatigue for gears ($\sigma_{H\,lim}$) is the method B. Method B is comprised of different ways to compute and estimate the maximum bending and contact stress at the gear root and tooth flank of said gear [9].

For calculation of the nominal stress value for bending, the following steps can be used. The value for the confidence limit is used as the allowable stress number (σ_{FE}). The nominal stress value can consequently be calculated with the Eq. (4). The stress correction factor (Y_{ST}) needs to be decided and used. A reference gear in according to ISO 6336 should be manufactured with a value of 2.0.

$$\sigma_{F\,lim} = \sigma_{FE}/Y_{ST}\ [\text{MPa}] \tag{4}$$

Standardized values for the allowed nominal stress value for bending and contact fatigue can further be calculated with the use of Eq. (5) where the factors A and B can be found in the standard. The value of x is the surface hardness, which based on the type of material has a specified maximum value used for calculation [9].

$$\begin{cases} \sigma_{H\,lim} \\ \sigma_{F\,lim} \end{cases} = A \times x + B\,[\mathrm{MPa}] \tag{5}$$

Experimental

Materials

The Company produces several different components to the automotive industry. The European standard EN 10084 (DIN reference number 1.7149) has the status of the Company standard for Steel 20MnCrS5 used for construction of gears. The Company has some additional requirements regarding the chemical composition as shown in Table 1 [10].

The extent of micro inclusions (oxides) in the steel is referred to DIN 50602-1985, method K. Materials with a diameter less than 50 mm should be rated to K4 with a maximum allowed score of at most 30 and materials with a diameter above 50 mm must also be rated with K4 with a total score of at most 40. The K value defines the minimum size in width and length of inclusions used for purity evaluation. The value defined after K4 (40/30) is based on a scoring system where a major defect gets a higher factor. Number of defects multiplied by factor for individual defect forms a score. The total score is converted to an average for a certain area [11].

For the in line ultrasound inspection the acceptance criteria shall be in accordance to EN 10308, Table 2 as follows:

- diameter $\leq$ 100 mm: quality class 4,
- diameter $>$ 100 mm: quality class 3 [12].

In order to investigate the size of non-metallic inclusions in the steel, a series of ultrasonic testing were made on the standardized case-hardened carbon steel

Table 1 Chemical composition of 20MnCrS5 steel

Chemical composition in % (mass fraction)										
C	Si max	Mn	P max	S	Cr	Mo max	Ni max	Al	Cu max	N
0.16–0.22	0.025	1.10–1.35	0.025	0.020–0.035	1.00–1.30	0.08	0.25	0.015–0.050	0.25	0.080–0.014

Table 2 Chemical compositions of the evaluated steels

Steel	Chemical composition in % (mass fraction)								
	C	Si	Mn	P	S	Cr	Mo	Ni	Al
A	0.16–0.22	max 0.25	1.10–1.35	max 0.025	0.020–0.035	1.00–1.30	max 0.08	max 0.25	0.015–0.050
B	0.17–0.22	max 0.40	1.10–1.40	max 0.025	max 0.035	1.00–1.30	–	–	–
C	0.17–0.22	max 0.40	1.10–1.40	max 0.025	max 0.035	1.00–1.30	–	–	–
D	0.15–0.18	0.20–0.35	0.50–0.60	max 0.015	0.008–0.015	1.50–1.80	0.25–0.35	1.50–1.70	–
E	0.15–0.21	max 0.40	0.50–0.90	max 0.025	max 0.035	1.50–1.80	0.25–0.35	1.40–1.70	–
F	0.17–0.22	0.20–0.35	1.10–1.40	max 0.025	0.015–0.025	1.10–1.30	max 0.08	max 0.025	0.020–0.040

20MnCrS5 manufactured with continuous casting (in this work called Steel A) and the results are compared with earlier ultrasonic testing of 20MnCr5 manufactured with ingot casting (in this work called Steel B) and on the cleaner variant of 20MnCr5 manufactured with ingot casting (in this worked called Steel C). The chemical compositions of the evaluated steels are shown in Table 2.

For the evaluation of the mechanical properties the data on previously performed tests from rotary bending testing are compared. The materials evaluated are Steel 18CrNiMo7-6 manufactured with continuous casting (in this work called Steel D), Steel 18CrNiMo7-6 manufactured with ingot casting (in this work called Steel E) and Steel 20MnCr5 manufactured with ingot casting (in this work called Steel F). The chemical compositions of the evaluated steels are shown in Table 2.

Ultrasonic Testing

The machine which conducted the ultrasonic testing was an USIP 20, manufactured by Krautkramer Branson, equipped with a 10 MHz probe, calibrated to a FBH of 0.2 mm. The machine is calibrated using a reference peace of steel with a height of 60 mm and a diameter of 30 mm where a hole with the diameter 0.2 mm has been drilled to a depth of 1 mm. The reference steel is further scanned and the drilled hole acts as a reference for the size of defects that the machine is designed to find and indicate.

The conducted tests of steel A is made through preparing 5 cylindrical samples with a length of 250 mm and diameter of 80 mm. The material is delivered in soft annealed condition but gets normalized through annealing in 920 °C for 1 h after which it cools off before processing. The normalization process is carried out to minimize acoustic abnormalities before the ultrasonic testing. The material is milled

Fig. 1 Scanning of test material

10 mm on two opposite sides to achieve correct thickness of 60 mm and a plane surface for testing. The material is placed in a water tank and the 10 MHz probe scans the 5 samples, see Fig. 1. A graphical image is presented showing the size and distribution of detected inclusions present in the samples.

The data gathered from previously conducted tests are compiled and analyzed. The data consists of protocols from 5 samples of steel B and 2 samples from steel C.

Mechanical Testing

The data presented is the result of fully reversed rotational bending fatigue testing conducted with an Amsler UBM 200. All tests are conducted with specimens designed with a great radius to minimize the influences of stress concentrations. The tests are furthermore conducted and analyzed using a staircase method with stress levels varying with 25 (MPa). All samples are prepared from the transverse

direction, in through hardened condition with a smoothness of maximum 0.3 Ra. Each specimen is measured on the thinnest section and the load is modified to ensure a precise value for the effective stress the specimen is subjected to.

From the conducted tests 9 values for steel D, 5 values for steel E and 11 values for steel F can be used for calculation of the nominal stress value.

Results and Discussion

Ultrasonic Testing

The results from ultrasonic testing are shown in Table 3.

Mean value of defects in the weight of 10 kg for Steel A is 109.5 and the mean value for number of defects > 0.2 mm FBH/dm^3 is 9.6. These results for Steel A are shown as graphical images in Fig. 2.

Tests results for the five test specimens of Steel A shows 14 defects which are equal to or greater than the reference hole, 15 defects are in the range 50–99% of the reference hole, 17 defects in the range 30–49%, and 8 defects between 25 and 29% of the reference hole. In total a number of 54 defects are noticeable which corresponds to 25% or greater than the reference hole. The defects appear as white dots in the blue fields for each test piece. The results for Steel B and C show no noticeable defects which are greater than 25% of the reference hole.

After examining and evaluation of the ultrasonic tests, a clear difference in size and frequency of defects associated with the two process routes between the materials can be clearly distinguished.

Table 3 Results from ultrasonic tests

	Weight kg	25–29%	30–49%	50–99%	≥	Weighted value for each 10 kg	Number of defects > 0.2 mm FBH/dm^3
Steel A	2.27	2	1	5	3	125.6	10.3
	2.36	0	4	0	0	16.9	0
	2.24	3	9	4	9	285.7	31.3
	2.29	0	1	0	0	4.4	0
	2.35	3	2	6	2	114.9	6.6
Steel B	1.7	0	0	0	0	0	0
	1.88	0	0	0	0	0	0
	1.77	0	0	0	0	0	0
	1.84	0	0	0	0	0	0
	1.84	0	0	0	0	0	0
Steel C	2.88	0	0	0	0	0	0
	2.90	0	0	0	0	0	0

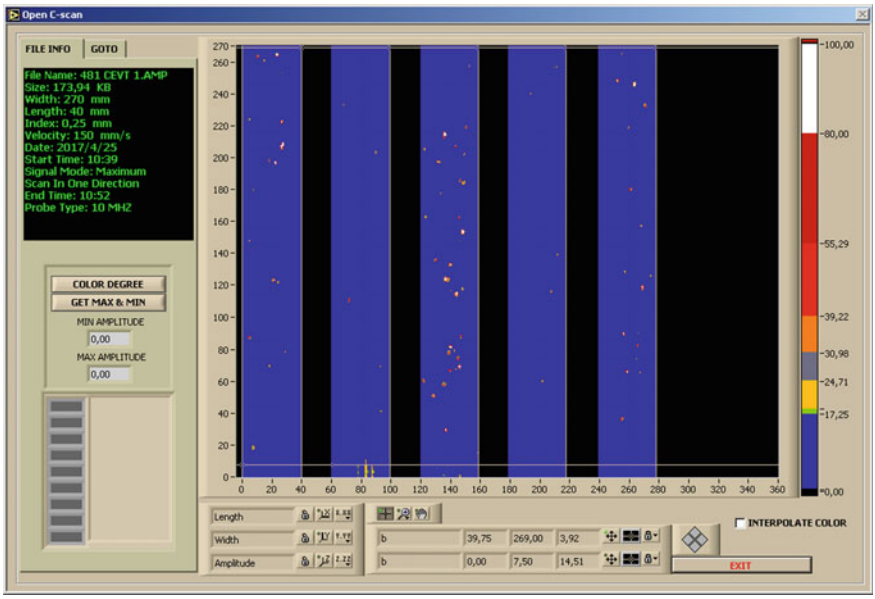

Fig. 2 Results from the ultrasonic test for steel A

The tests performed and evaluated cohere with the theory of what a 10 MHz probe can detect when only defects down to the size of 120 µm could be notated. When increasing the frequency up to 25 MHz, the effective thickness of material being tested is reduced from 60 to 25 mm as the size of defects that can be found is reduced to 50–100 µm. The possibility of removing slag in the bottom of the ladle by unloading some of the melted steel prior to casting and the possibility of a higher degree of reduction of a steel has an effect on how large inclusions a steel possesses proved to be true in the examination of the ultrasonic tests. A steel which is continuous casted are less likely to achieve as high reduction degree as an ingot casted steel and thus generally consist of an increased size of inclusions.

Mechanical Testing

Results of the calculations using Eqs. (1–3) on all materials which have been tested for bending fatigue can be seen in Table 4.

From the performed test, nine values could be used to calculate a nominal stress value for Steel D, see Fig. 3.

From the performed test, five values could be used to calculate a nominal stress value for Steel E, see Fig. 4.

From the performed test 11 values could be used to calculate a nominal stress value for Steel F, see Fig. 5.

Table 4 Results from bending fatigue

Material	$\hat{\mu}$ [MPa]	$\hat{\sigma}$ [MPa]	Confidence limit (99.9%) [MPa]
Steel D	537.5	21.4	502.3
Steel E	779.2	41.7	690.5
Steel F	922.5	75.7	810.6

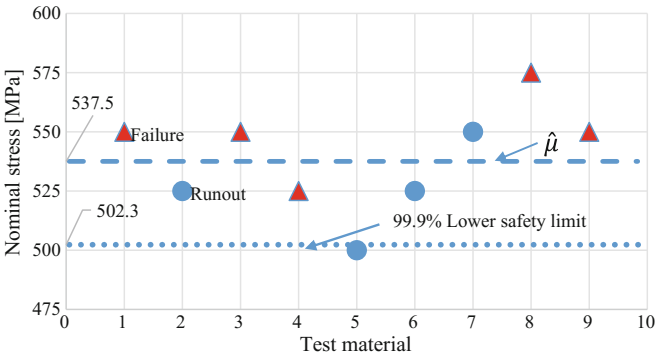

Fig. 3 Rotating bending test on Steel D

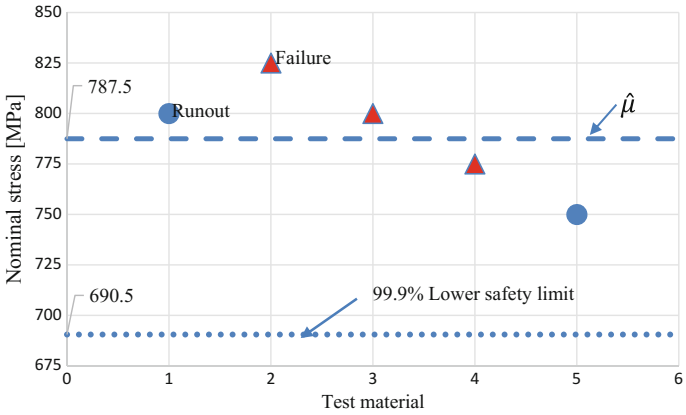

Fig. 4 Rotating bending test on Steel E

By using Eq. (4), nominal stress value for gears is calculated for the materials which the rotating bending test have been performed on. The result can be seen in Table 5.

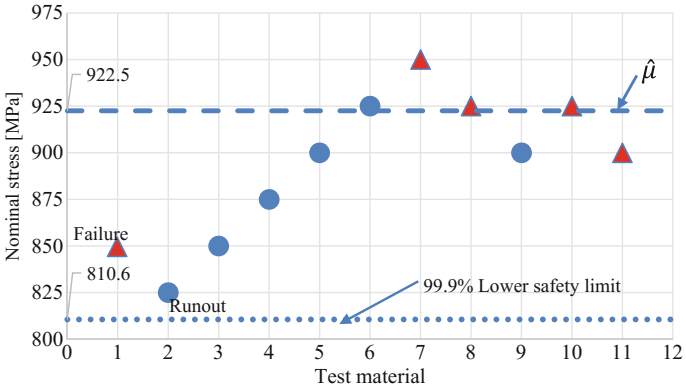

Fig. 5 Rotating bending test on Steel F

Table 5 Results of nominal stress values for bending fatigue

Material	Lower safety limit (99.9%) [MPa]	Nominal stress value for bending fatigue for gears ($\sigma_{F\,lim}$) [MPa]	Difference in stress value [%]
Steel D	502.3	251.2	0
Steel E	690.5	345.3	+37.5
Steel F	810.6	405.3	+61.4

Table 6 Results of comparison for 20MnCr5 steel

Material	Nominal stress value for bending fatigue for gear ($\sigma_{F\,lim}$) [MPa]	Difference in stress value [%]
Through hardened wrought steel (MQ)	340.0	0
Through hardened wrought steel (ME)	370.6	+9
Stell F	405.3	+19.2

By using Eq. (5) a comparison of the nominal stress value can be made between the steel 20MnCr5-IC and that from the standards for through hardened carbon steel in the classes ME and MQ [9]. The results can be seen in Table 6.

Conclusions

There is a clear difference in the distribution of defects between the two process routes continuous casting and ingot casting. Steel manufactured with ingot casting shows a significantly higher purity when performing ultrasound tests with a

10 MHz probe compared to that of a material manufactured with continuous casting.

The result shows a clear improvement in fatigue strength as the distribution of defects becomes more beneficial.

An improvement of fatigue strength for applications connected to power transmission can be proved by comparing results on rotating bending tests of the 18CrNiMo7-6 material in continuous casting versus ingot casting. To get an exact value which can be used in real applications e.g. strength calculations of gears a more applied test procedure such as a FZG-test or pulsator-test is recommended. This because of the uncertainty that occurs when transferring test data for bending stress between general fatigue strength and the value used to calculate fatigue strength of gears ($\sigma_{F\,lim}$).

To monitor the size and distribution of defects and ensure that steel with higher purity meets the requirements specified in the material specification, a lower K-value and score should be implemented when performing tests in accordance with DIN 50602. It should also be added that there are other standards for mapping and evaluating inclusions such as ASTM E45 and ISO 4967. To get a material specification that clearly describes and processes the defects in a material, an implementation of these, individually or in combination with each other, may be considered.

When verifying the distribution of defects with an ultrasonic test, a smaller FBH is recommended for calibration. Due to the decreased volume tested, per unit of time, when increasing the frequency for detection of smaller size defects, no increase in frequency is recommended at an initial stage. The fatigue strength which can be achieved with these implementations are based on the size of defects that can be found with a 10 MHz probe.

Acknowledgements The author would like to thank Linnaeus University, Faculty of Technology, Department of Mechanical Engineering, Växjö, Sweden and China Euro Vehicle Technology AB, Göteborg, Sweden.

References

1. Zhang L, Rietow B (2006) Large inclusions in plain-carbon steel ingots cast by bottom teeming. http://www.jstage.jst.go.jp/article/isijinternational/46/5/46_5_670/_article.pdf. Accessed 9 Apr 2017
2. Andrew B (2012) The effect of microstructure and induction processing on fatigue performance and crack initiation of induction hardened bar steel. http://dspace.library.colostate.edu/handle/11124/76674. Accessed 23 Mar 2017
3. Kamjou L, Hansson H (2015) Innovative steel design and gear machining of advanced engineering steel. AGMA technical paper
4. Lee Y, Pan J, Hathaway R (2004) Fatigue testing and analysis. Butterworth-Heinemann, USA
5. Pollak R (2005) Analysis of methods for determining high cycle fatigue strength of a material with investigation of Ti-6Al-4V gigacycle fatigue behavior. http://www.dtic.mil/dtic/tr/fulltext/u2/a441887.pdf. Accessed 23 Mar 2017

6. Nakazawa H, Kodama S (1987) Statistical S-N testing method with 14 specimens: JSME standard method for determination of S-N curves. In: Statistical research on fatigue and fracture
7. Dixon WJ, Mood AM (1948) A method for obtaining and analyzing sensitivity data. J Am Stat Assoc 43:109–126
8. Brian V, Ervin Z (2017) Rolling-element fatigue testing and data analysis—a tutorial. http://ntrs.nasa.gov/archive/nasa/casi.ntrs.nasa.gov/20110008238.pdf. Accessed 25 Apr 2017
9. International Organization of Standardization, ISO 6336:2006
10. EN 10084:2008-06: Case hardening steels—technical delivery conditions
11. DIN 50602-1985: Microscopic examination of special steels using standard diagrams to assess the content of non-metallic inclusions
12. European Standard EN 10308:2002: Non-destructive testing—ultrasonic testing of steel bars

Influence of Austenitizing Temperature and Time on Microstructure and Mechanical Properties of an YP460 Grade Crack Arrest Steel

Dan Chen, Wenqing Jiang, Songsong Xu, Naimeng Liu, Hao Guo, Ye Cui, Yang Zhang and Zhongwu Zhang

Abstract The influence of austenitizing temperature and austenitizing holding time on the microstructure and mechanical properties of a YP460 grade crack arrest steel was investigated. The first group specimens were austenitized at several temperatures ranging from 900 to 950 °C followed by water cooling. The second group specimens were austenitized at 900 °C with austenitizing holding time from 0.25 to 5 h followed by water cooling. Microstructure was characterized through optical microscopy. Tensile properties, hardness and plane strain fracture toughness of all these materials were determined and correlated with the microstructure. The results indicated that the austenitizing temperature influences the volume fraction of bainite and ferrite and then the mechanical properties. The volume fraction of bainite and ferrite and grain size are also affected by austenitizing time.

Keywords Crack arrest steel · Austenitizing temperature · Austenitizing holding time · Mechanical properties

Introduction

With the growth of world economy and transportation volume, the need for bigger sized container ships has been expanded for the purpose of cost reduction and better transportation efficiency. Therefore, the steel plate especially applied to the upper hull structure is getting thicker in order to ensure the required structural integrity due to its large cargo opening structure. Weight saving is strongly required to increase transportation efficiency of container ships. The higher strength steel plates with heavy thickness and excellent brittle crack arrestability should be developed in

D. Chen · W. Jiang · S. Xu · N. Liu · H. Guo · Y. Cui · Y. Zhang · Z. Zhang (✉)
Key Laboratory of Superlight Materials and Surface Technology, Ministry of Education, College of Materials Science and Chemical Engineering, Harbin Engineering University, Harbin 150001, China
e-mail: zwzhang@hrbeu.edu.cn

The Minerals, Metals & Materials Society, *TMS 2018 147th Annual Meeting & Exhibition Supplemental Proceedings*, The Minerals, Metals & Materials Series,
https://doi.org/10.1007/978-3-319-72526-0_13

Table 1 Chemical composition of investigated steels (wt%)

C	Mn	Si	Cr	Ni	Cu	Al	Nb	Ti	S	P
0.06	1	0.25	0.18	1	1	0.1	0.03	0.050	0.003	0.005

terms of the enlargement of the ship size and the liability against catastrophic brittle fracture [1–7].

In order to homogenize the microstructure and improve the mechanical properties of the YP460 grade steel, research about heat treatments are ordinarily required. However, there is few published literature on heat treatment of the YP460 grade steel. Therefore, it is very meaningful to investigate the effect of heat treatment temperatures and times on microstructures and mechanical properties of the YP460 grade steel.

Material and Experimental Procedures

The material used in this study is fabricated by 80 kg vacuum induction melting using high purity base materials and homogenized at 1200 °C for 2 h, followed by hot rolling into 20 mm thickness plate. The chemical composition of the steel is given in Table 1.

The specimens were divided into two groups. One group was subjected to austenitizing in the temperature range of 900–950 °C for 0.5 h followed by water cooling. The other group was carried out in the austenitizing holding time range of 0.25–5 h with the austenitizing temperature of 900 °C.

Mechanical properties were evaluated by tensile, hardness and Impact tests at the room temperature. The tensile Tests were performed on a UTM5105 testing machine according to standard procedures. The hardness of specimens was measured by Rockwell (Vickers) hardometer. Each value was the average of hardness values at ten points. Impact tests were performed on a JBW-300B testing machine. Optical microscopy were used to examine the microstructural features. The volume fraction of reversed austenite was determined from X-ray diffraction tests.

Results and Discussion

Preliminary Investigations

The A_{c1} and A_{c3} temperatures are important characteristic parameters of steel. Figure 1 shows the dilatometric curve of continuously heated specimen. In this figure, two tangent points on the curve represent starting and finishing temperature

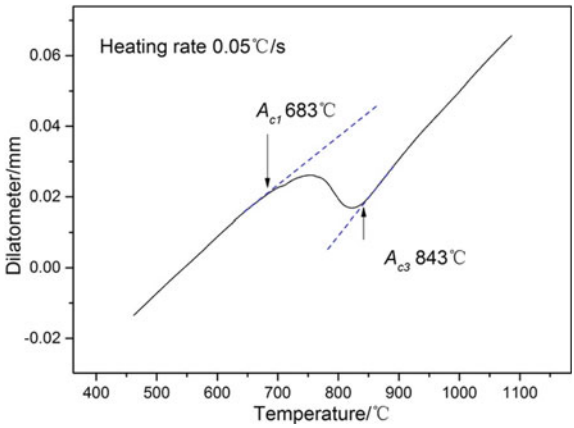

Fig. 1 Dilatometric curve of continuously heated specimen

of α to γ transformation. The A_{c1} and A_{c3} temperatures of this steel are 683 and 843 °C, respectively, when heating rate is 0.05 °C/s.

Effect of Austenitizing Temperature on Mechanical Properties

The results of the hardness, tensile and impact toughness tests on the water-quenched samples with different austenitizing temperature are shown in Figs. 2, 3 and 4, respectively. It can be seen that the effect of austenitizing temperature on the mechanical properties of the studied steels is not very complex. The hardness, tensile strength and yield strength increase slightly with increasing austenitizing temperature from 900 to 925 °C, while the elongation decreases significantly. With increasing the austenitizing temperature from 875 to 900 °C, the tempering process decreases the residual stress and dislocation density, which can be responsible for the slight decrease in the tensile strength and hardness [8, 9].

The plot of room temperature fracture toughness of the material against austenitizing temperature is shown in Fig. 5. With the austenitizing temperature increasing from 900 to 925 °C, the fracture toughness increases first and then increases.

Effect of Austenitizing Temperature on Microstructure

Figure 6a–c show the variation in the microstructures as the austenitizing temperature was increased from 900 °C to 950 °C, respectively. The microstructures of different austenitizing temperatures are similar consisting of ferrite and bainite. The

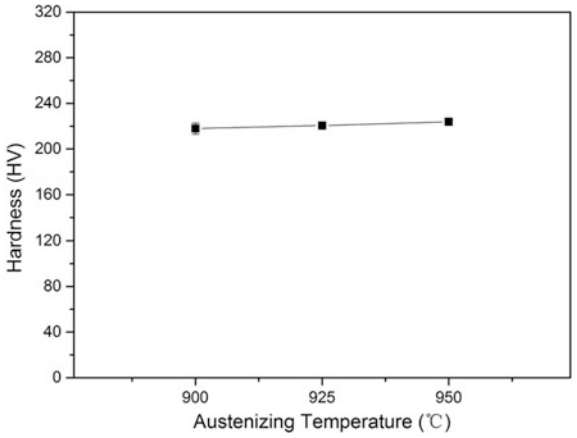

Fig. 2 Influence of austenitizing temperature on hardness

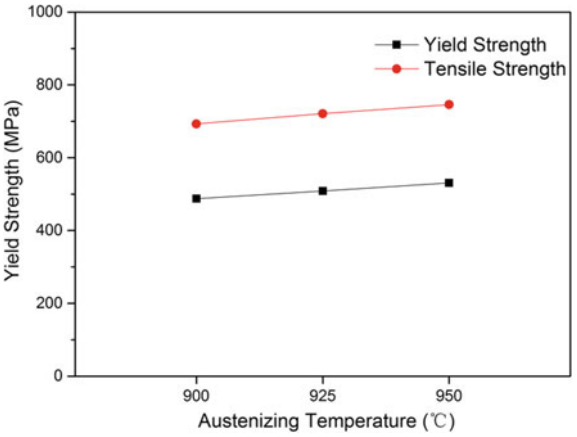

Fig. 3 Influence of austenitizing temperature on yield strength and tensile strength

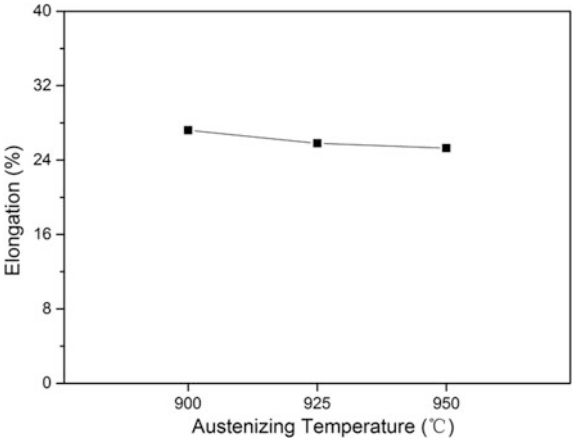

Fig. 4 Influence of austenitizing temperature on elongation (%)

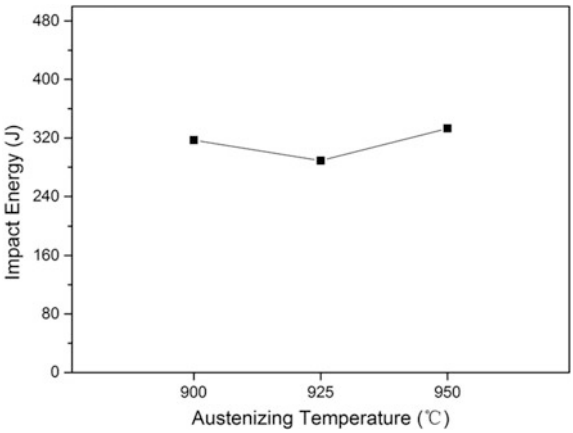

Fig. 5 Influence of austenitizing temperature on fracture toughness

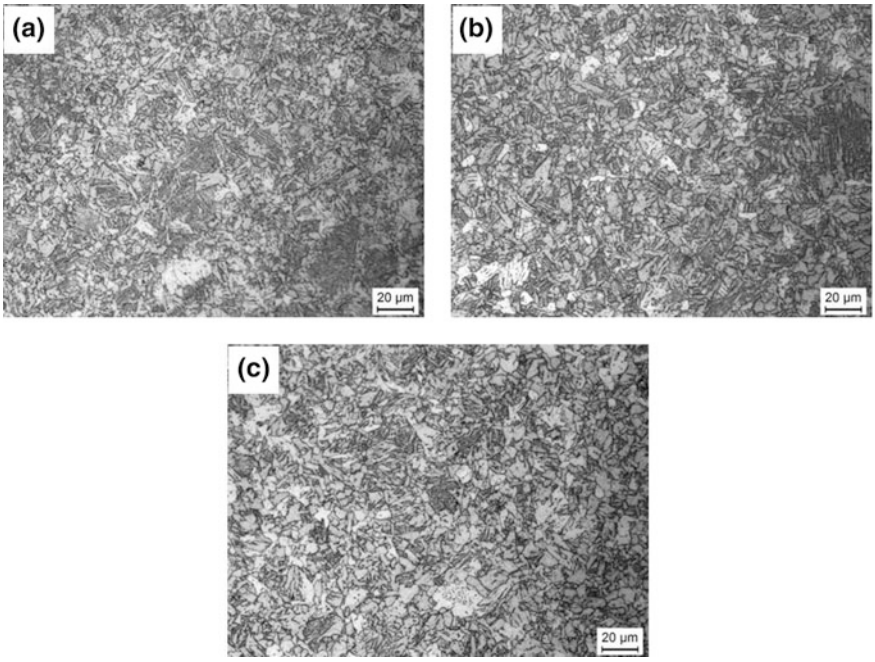

Fig. 6 Influence of austenitizing temperature on the volume fraction of austenite in the matrix

lower the austenite temperature is, the larger the volume fraction of bainite is. With the austenitizing temperature increasing, the volume fraction of ferrite increases, and the grain size increases.

Effect of Austenitizing Holding Time on Mechanical Properties

The effect of austenitizing time on tensile strength, yield strength, elongation and hardness are shown in Figs. 7, 8 and 9, respectively. With the extension of austenitizing holding time, the tensile strength, yield strength and hardness increase first and then decrease while the elongation decreasing first and then increasing. The tensile strength and yield strength reached the maximum 551 and 750 MPa, respectively, with the austenitizing holding time of 1 h and the hardness reached the maximum 234HV with the austenitizing holding time of 0.5 h. The initial increase of strength is induced by the dissolution of the interdendritic phases and the increase of solid solubility of matrix. Strength approaches the maximum value at 1 h, indicating that the interdendritic phases are dissolved sufficiently into the matrix at the temperature of 900.

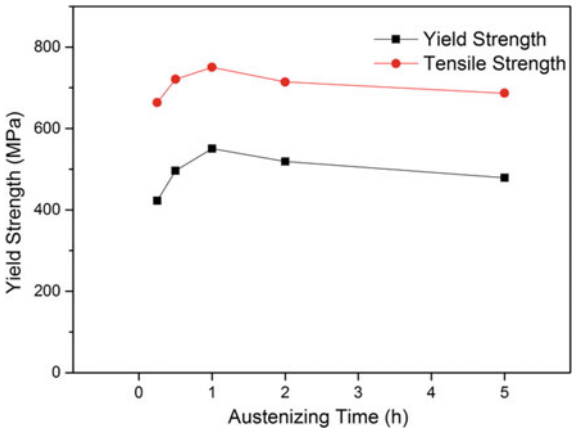

Fig. 7 Influence of austenitizing holding time on yield strength and tensile strength

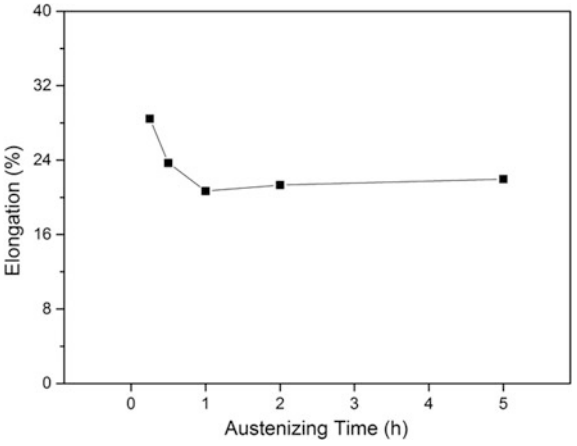

Fig. 8 Influence of austenitizing holding time on elongation (%)

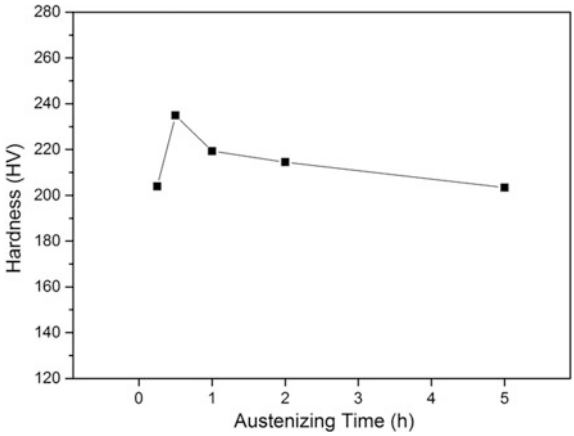

Fig. 9 Influence of austenitizing holding time on Microhardness

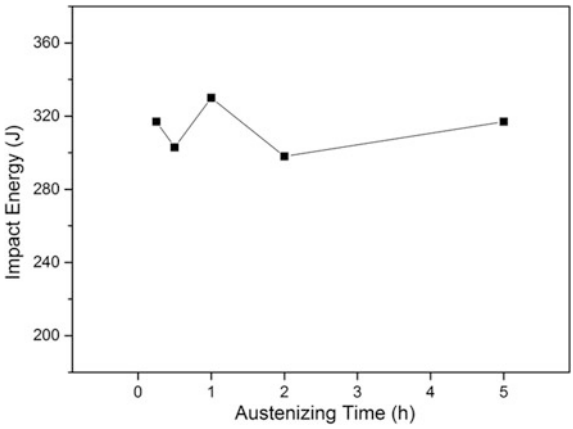

Fig. 10 Influence of austenitizing holding time on impact toughness

With the increase of the austenite holding time, the amount of alloying elements in the austenite increases resulting in solid solution strengthening, thus the strength and hardness of the material improving and the impact energy reducing. With the austenitizing holding time continues to increase, the solution of the alloying elements to further increase. The solution of excess alloying elements in austenite would improve the stability of austenite and the amount of retained austenite in microstructure increased which reducing the hardness and strength of the material. In addition, with increasing of the holding time, the distribution of carbon and alloying elements in the austenite is further homogenized and the segregation degree of the structure is reduced resulting in the impact energy of the material increasing.

The influences of austenitizing holding time on impact toughness is shown in Fig. 10. It can be seen that the effect of austenitizing holding time on impact toughness of the studied steels is very complex.

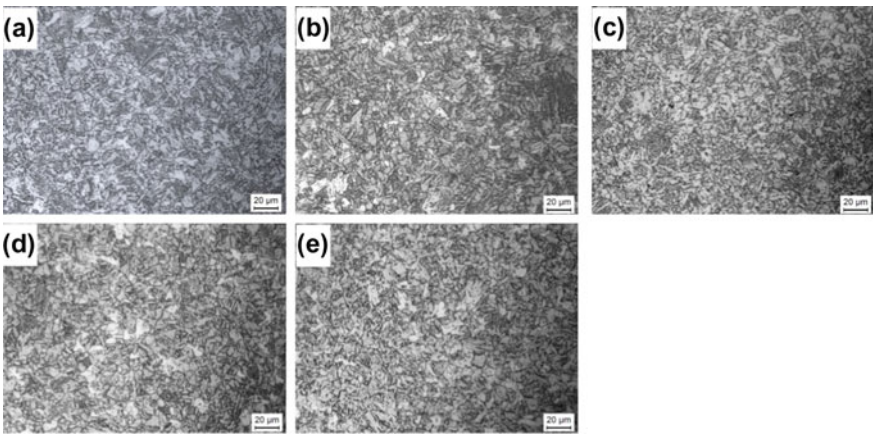

Fig. 11 Influence of austenitizing holding time on microstructure

Effect of Austenitizing Holding Time on Microstructure

Figure 11a–e show the variation in the microstructures as the austenitizing holding time was increased from 0.25 to 5 h with the austenitizing temperature of 900 °C, respectively. The microstructures of different austenitizing times are similar consisting of ferrite and bainite. With the austenitizing holding time increasing, the volume fraction of bainite decreased and the volume fraction of ferrite increased, Gradually. Moreover, The grain size increases slowly with the austenitizing holding time was increased from 0.25 to 5 h. This is mainly due to the addition of Nb and Ti to form Ti, Nb rich carbonitride particles and these can restrict austenite grain growth at high temperature [10–12].

Conclusions

The A_{c1} and A_{c3} temperatures were determined by dilatometric analysis as 683 and 843 °C, respectively.

Varying the austenitizing temperature in the range of 900–950 °C has no influence on the microstructure composition and only a slightly influence on the volume fraction of bainite and ferrite and mechanical properties. The best properties were obtained for the steel austenitized at 950 °C.

Varying the austenitizing holding time from 0.25 to 5 h with the austenitizing temperature of 900 °C has no influence on the microstructure composition and greater influence on the volume fraction of bainite and ferrite, grain size and mechanical properties. The best properties were obtained for the steel austenitized for 1 h.

Acknowledgements This work was supported by the Fundamental Research Funds for the Central Universities (HEUCFJ171005, HEUCFJ171001 and HEUCFP201703), NSFC Funding (51371062 and U1460102), NSFHLJ (JC2017012), the High-Tech Ship Research Projects Sponsored by MIIT and the International Exchange Program of Harbin Engineering University for Innovation-oriented.

References

1. Lee C-S, Kim S, Suh I-S, Um K-K, Kwon O (2011) High strength steel plates for large container ships. Int J Iron Steel Res 18:796–802
2. Choo W-Y, Suh I-S, Kim S, An G-B, Lee C-S (2011) High performance structural steels for shipbuilding and offshore structures. Int J Iron Steel Res 18:90–98
3. Kyokai NK (2009) Guidelines of the application of YP47 steel for hull structures of large container carriers
4. Wu W-M, Lin J-R (2015) Productivity growth, scale economies, ship size economies and technical progress for the container shipping industry in Taiwan. Transp Res Part E 73:1–16
5. UR S33, Requirements for use of extremely thick steel plates, Jan 2013
6. UR W31, Application of YP47 steel plates, Jan 2013
7. Murakami Y, Takeuchi Y, Hase K, Endo S (2014) Development of YP460 class steel plate with excellent brittle crack arrestability for large container ships. Int J Offshore Polar Eng 24 (4):286–291
8. Qin B, Wang ZY, Sun QS (2008) Effect of tempering temperature on properties of 00Cr16Ni5Mo stainless steel. Mater Charact 59(8):1096–1100
9. Zou D, Liu X, Han Y, Zhang W, Li J, Kun W (2014) Influence of heat treatment temperature on microstructure and property of 00Cr13Ni5Mo2 supermartensitic stainless steel. Int J Iron Steel Res 21(3):364–368
10. Craven AJ, He K, Garvie LAJ, Baker TN (2000) Complex heterogeneous precipitation in titanium-niobium microalloyed Al-killed HSLA steels—I. (Ti,Nb)(C,N) particles. Acta Mater 48:3857–3868
11. Kanasawa S, Nakashima A, Okamoto K, Kanaya K (1976) Improvement of weld fusion zone toughness by fine TiN. Trans Iron Steel Inst Japan 16:486
12. Wang GR, Lau TW, Weatherly GC, North TH (1989) Weld thermal cycles and precipitation effects in Ti-V-containing HSLA steels. Metall Trans 20A:2093–2100

The Evolution of Microstructure of an High Ni HSLA X100 Forged Steel Slab by Thermomechanical Controlled Processing

S. H. Mousavi Anijdan and M. Sabzi

Abstract An HSLA X100 steel was studied. After casting and forging to slab condition, thermomechanical controlled process was employed to produce steel sheet. Heat treatment was then employed to control the microstructure and optimize mechanical properties. Austenitization was performed at 950 °C followed by different quenching media. Samples were tempered from 500 to 750 °C. Mechanical testing and microstructural analyses were performed by Optical Microscopy, Scanning and Transmission Electron Microscopes. Results showed a complex microstructure of bainite, ferrite, martensite, retained austenite, and various carbides. High temperature tempering removed retained austenite from martensite lath providing a relatively high amount of toughness. A uniform distribution of carbides was detected in the tempered situations. Retained austenite was present in the quenched only samples. Low temperature tempering removed part of this retained austenite. Increasing the tempering temperature decreased the tensile properties and increased the toughness. Quenched samples showed inferior mechanical properties compared to the tempered ones.

Keywords HSLA X100 steel · Retained austenite · Bainite
Thermomechanical controlled process · Microstructure · Tempering

Introduction

High strength low alloy steel (HSLA) are a group of low carbon steels that small amounts of alloying elements are added to their composition to achieve yield strength level higher than 257 MPa in the normalized or rolled conditions [1]

S. H. Mousavi Anijdan (✉)
Young Researchers and Elites Club, Science and Research Branch,
Islamic Azad University, Tehran, Iran
e-mail: hashemmousavi@gmail.com; hashemmousavi@srbiau.ac.ir

M. Sabzi
Young Researchers and Elite Club, Dezful Branch, Islamic Azad University,
Dezful, Iran

The Minerals, Metals & Materials Society, *TMS 2018 147th Annual Meeting & Exhibition Supplemental Proceedings*, The Minerals, Metals & Materials Series,
https://doi.org/10.1007/978-3-319-72526-0_14

Compared with the rolled plain carbon steel, HSLA steels have superior mechanical properties and in some situations better corrosion resistance [2]. Though their corrosion resistance is inferior to that of stainless steels [3]. Additionally, as the HSLA steels can have high strength with low level of carbon, their weldability is comparable, and in some circumstances, better than the killed steels [4–6]. HSLA steels are formed as semi-finished products such as plate, strip, ingot etc. by hot rolling process. Usually, HSLA steels are hot rolled through controlled rolling to improve their mechanical properties [5–7] and used in such a condition as well. A combination of strength, hardness, formability, weldability and resistance to corrosion are required in designing the process route for these steels. These properties are obtained through careful addition of alloying elements and thermomechanical controlled processing, often containing, fasting cooling after hot rolling [6–11]. To control the properties of HSLA steels [10–14], a normal heat treatment of these steels contains a quenching step to obtain martensite followed by intermediate temperature tempering to improve toughness without significantly losing strength. Therefore, a fully martensitic structure is initially needed to obtain adequate level of strength. In that sense, a minimum quenching rate is required to prevent the austenite phase from transforming to phases such as ferrite, pearlite and bainite [10–16].

The effect of austenitization temperature on the properties of Nb-Ti microalloyed steel was already explored [17]. It was found that austenite coarsening temperature was close to 1000 °C. As well, the amount of ferrite was reduced by increasing austenitization temperature. A complex precipitation of Nb-Ti nature was detected in the HSLA steels [18]. Elevated temperature austenitization increases yield/tensile strengths and reduces elongation. Austenitization above 1100 °C also dissolves most of the prior precipitates, except for mostly rectangular Ti (C,N), and gives the possibility of re-precipitation during the hot rolling process to achieve precipitate size range below 100 nm. The effect of tempering on the microstructure and mechanical properties was also studied in these steels [19]. Tempering range between 450 and 650 °C at different soak times was investigated. They found that in tempering the quenched specimen at 500 °C, a martensitic morphology is preservable up to 24 h of soaking. A fast decrease of strength was reported in the first few hours of soaking, in mentioned HSLA steels with the elongation following the opposite trend. Dhua et al. [20] also studied the effect of tempering temperature on the properties of HSLA-100 steels containing copper with the chemistries similar to HSLA 100. The effect of the type of furnace for casting of these steels were investigated as well. Tempering temperature range of 400–700 °C for one hour was studied. Substantial improvement in in strength, YS-1024 and 1025 MPa; UTS-1079 and 1111 MPa for the two steels, was reported at the expense of impact toughness at the tempering temperature of 500 °C. This was related to the plentiful precipitation of Cu in these steels. The toughness value was substantially increased by increasing the tempering temperature up to 700 °C range which was related to the partially recovered matrix and the coarsened Cu precipitates.

In spite of a relatively large volume of research on typical HSLA steels, including some of the work of one of the current authors [21–24], the quenching

and tempering behavior of the high Ni HSLA 100 steel has not been studied. Therefore, it was one of the main objectives of the current article was to study microstructure and mechanical properties of this steel under the mentioned conditions.

Materials and Experimental Procedure

The steel used in this research was an high Ni HSLA X100 one. Samples with the thickness of 20 mm were prepared by thermomechanical controlled rolling process. The chemical composition of the samples prepared were analyzed by spectrophotometer model M7 based on four alloys of Fe, Cu, Al and Ni. The composition contained 0.057 wt%C-0.285Si-0.781Mn-0.626Cr-0.579Mo-3.48Ni-0.026Al-1.53Cu-0.01 W-0.04 Nb-0.04N-0.011Ti with balanced Fe.

For heat treatment purposes, the samples were austenitized at 950 °C for one hour per inch and then quenched in water and oil. The quenched samples were tempered at 550, 650 and 750 °C. The tempering time was one hour per inch of the samples. An electric furnace model F35L was used for these heat treatment processes. Specimens were cut from the heat treated and non-heat treated samples for microstructural analysis. Specimens were ground, polished and etched by common metallography procedure. Nital 2% was used to etch the specimens. Microstructural studies were performed by optical microscope, Scanning Electron Microscope (SEM), and Transmission Electron Microscope (TEM). Energy Dispersive Spectroscopy (EDS) analysis was also used to detect various precipitates.

Tensile specimens were prepared by CNC machine based on ASTM E8 standard [25]. Also, Charpy impact test samples were machined from the heat treated samples based on ASTM A370 standard [26]. Tensile tests were performed by a uniaxial SANTAM® instrument tensile tester ASTM-400 under the strain rate of 10^{-2} s^{-1}. As well, the Charpy impact tests were performed by a SANTAN® instrument at 20 °C with the capacity of 400 J.

Results and Discussion

Microstructural Observations

Figure 1 shows the optical micrograph, SEM micrograph and TEM micrograph of the high Ni HSLA X100 steel used in this study prior to the heat treatment process. As can be seen in this figure, the microstructure of this steel contains martensite lath together with the Cu precipitates distributed uniformly with almost similar sizes [6–10]. Small amount of bainite layers are also seen in the microstructure. Small amount of ferrite grain is observable in the structure. As well, almost no retained

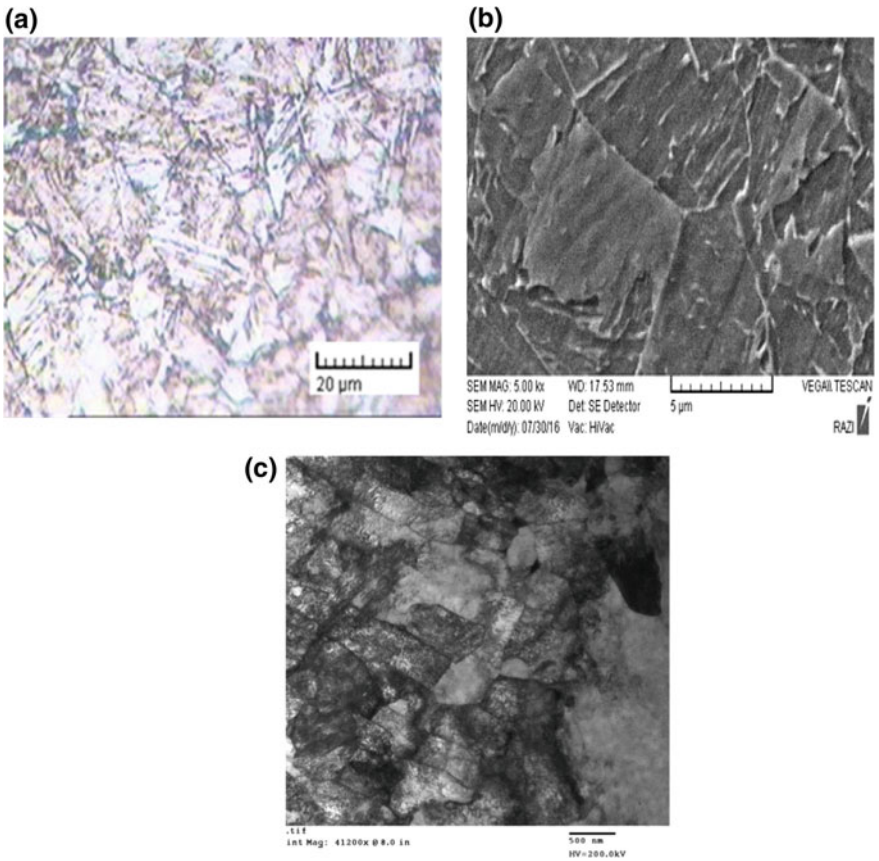

Fig. 1 Microstructure of the high Ni HSLA X100 steel under thermomechanical processing condition and prior to heat treatment process; **a** optical micrograph, **b** SEM micrograph, **c** TEM micrograph

austenite is observable in the structure which is an indication of high strength and toughness of the steel.

Figure 2 also shows the microstructures of the austenitized and quenched in water and oil samples together with a typical EDS analysis of the Cu precipitates. The microstructures in the quenched conditions contain martensite laths [14–19]. Small amount of retained austenite are observed between the martensite laths (bright areas in the SEM micrograph). As well, some inclusions are seen in the microstructure, which are most probably carbide precipitates [11–15]. It is important to mention that the microstructure of the samples quenched in water and oil are similar. The only difference is the smaller width of the martensite laths in the sample quenched in oil compared to the one quenched in water which is due to lower cooling rate in the former case. Also, more bainite layers are seen in the sample quenched in oil compared to the sample quenched in water. And lower

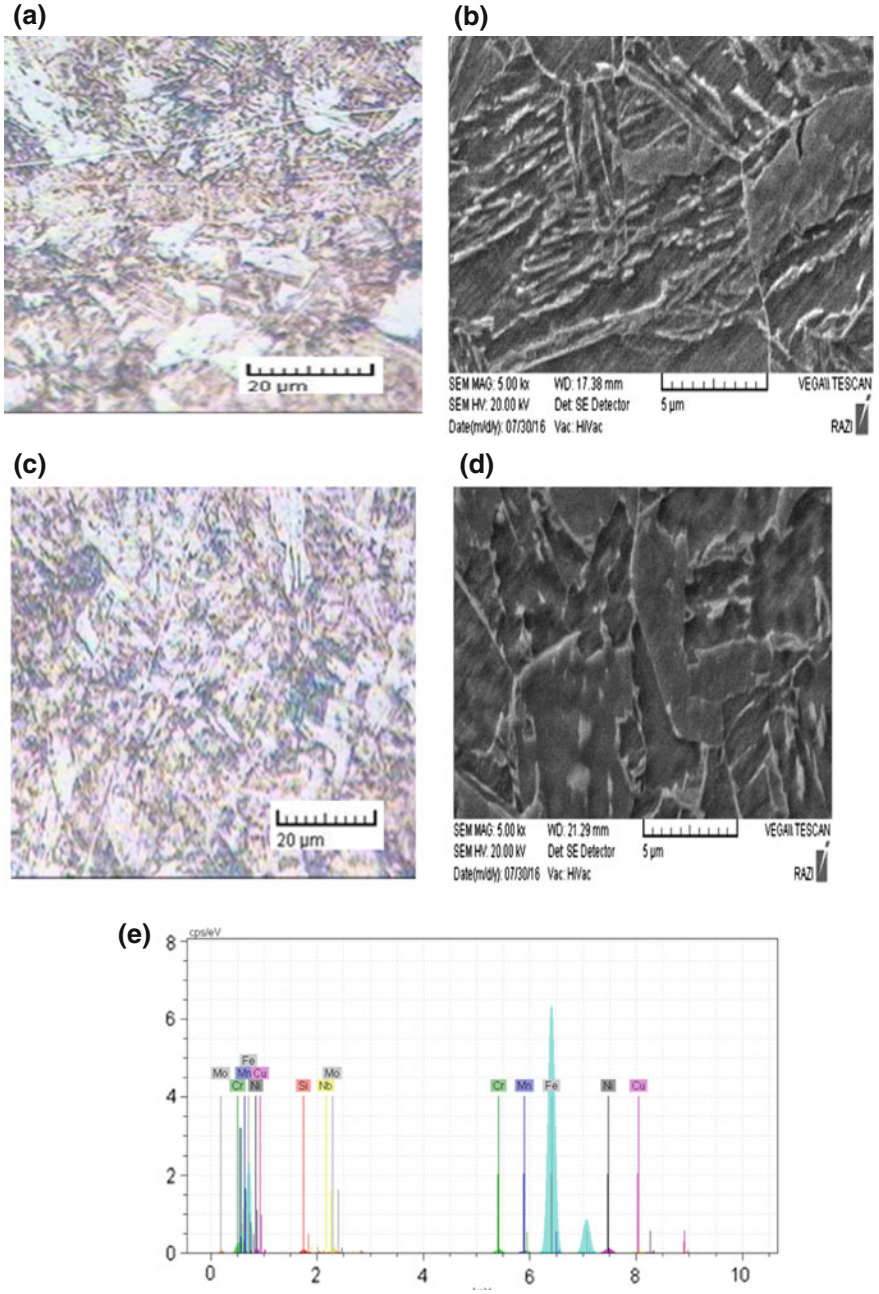

Fig. 2 Microstructures of the quenched samples; **a** and **b** in water, **c** and **d** in oil, **e** EDS analysis of the Cu precipitates

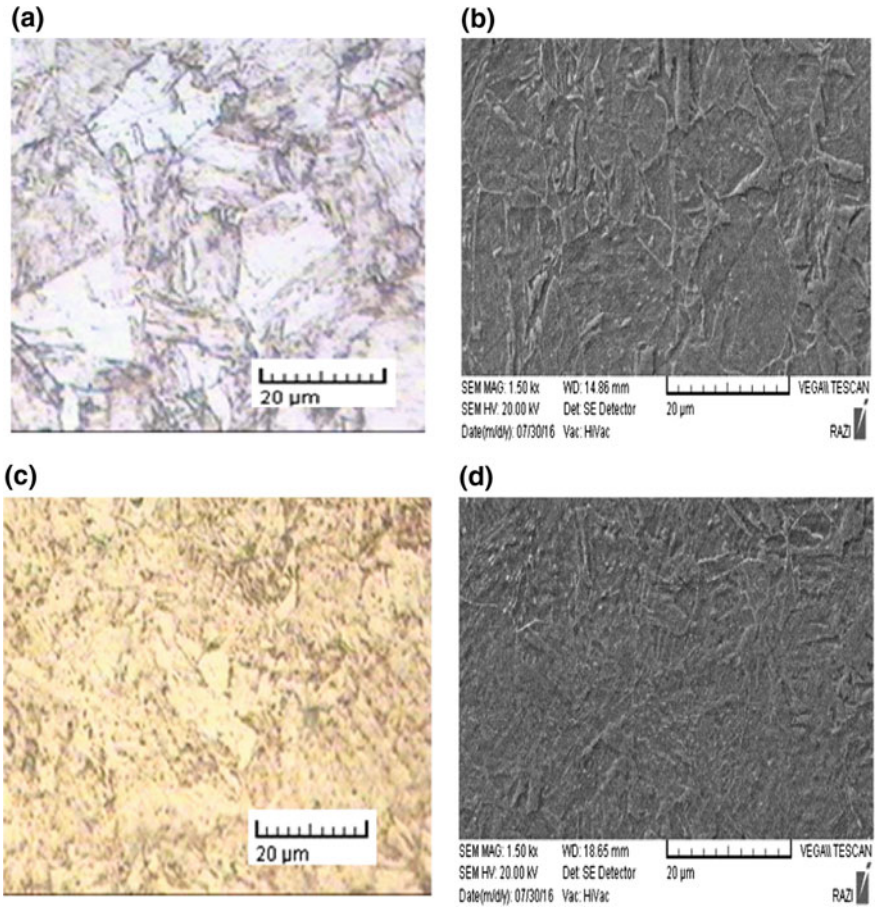

Fig. 3 Microstructures of the tempered samples at 550 °C under different quenching media: **a** and **b** in water; **c** and **d** in oil

amount of retained austenite and precipitates were observed in the sample quenched in water compared to the sample quenched in oil. Important to mention that austenite grain sizes are almost similar in these two cases.

Figure 3 shows the microstructures of the samples austenitized at 950 °C and quenched in water and oil, and tempered at 550 °C. The microstructures of these cases are very similar consisting of layers of lath martensite [15–19]. As well, clusters of Cu precipitates and layers of martensite grains are clearly seen in the structure. Comparing Figs. 2 and 3, it can be seen that the amount of retained austenite is lower inside the martensite grains of the tempered specimens compared with the quenched samples. The importance of tempering in this steel is due to the uniform distribution of Cu and other precipitates in the matrix in the form of

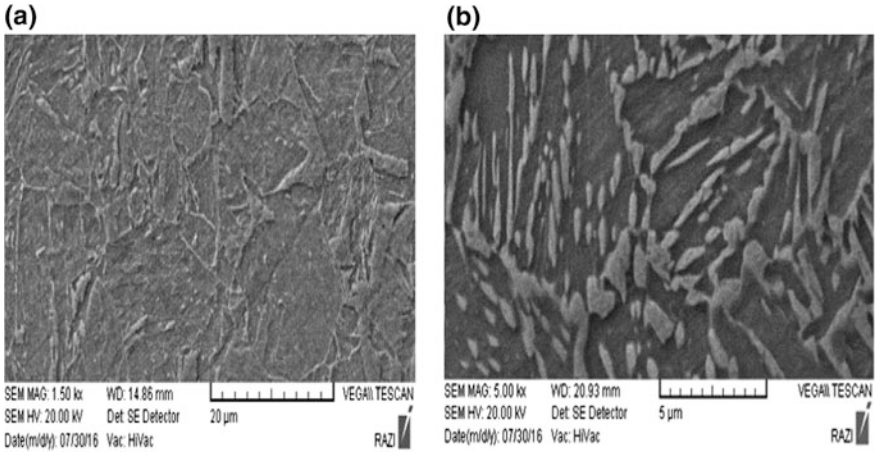

Fig. 4 SEM micrographs of the samples quenched in water and then tempered at; **a** 550 °C, **b** 750 °C

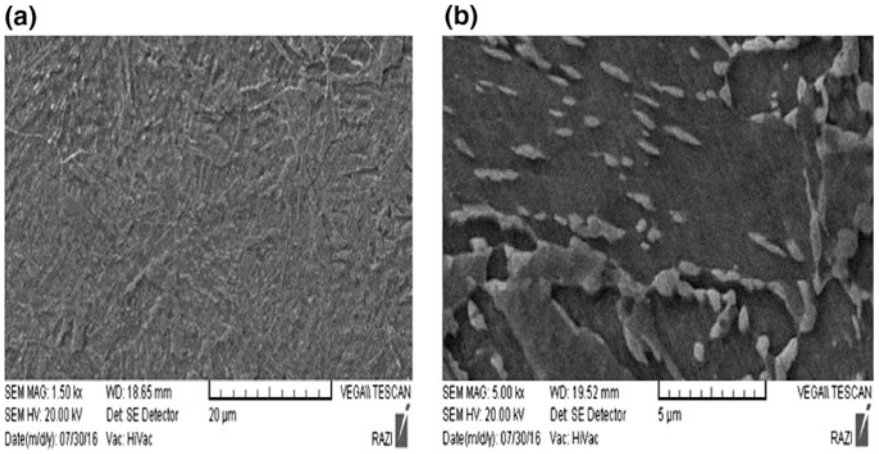

Fig. 5 SEM micrographs of the samples quenched in oil and then tempered at; **a** 550 °C, **b** 750 °C

spheres as opposed to the quenched conditions. This leads to an increase in the strength of the tempered samples compared with the quenched ones [7–11].

Figures 4 and 5 show microstructures of samples tempered at 550, and 750 °C after being quenched in water and oil. It can be seen in these figures that grain growth occurs with increasing the tempering temperature [15–20]. The microstructures of the samples contain bainite layer, martensite lath and also Cu precipitates. Other carbide precipitates can also be seen in the structure which are mainly in the form of bright points. It can also be seen in Figs. 4 and 5 that the

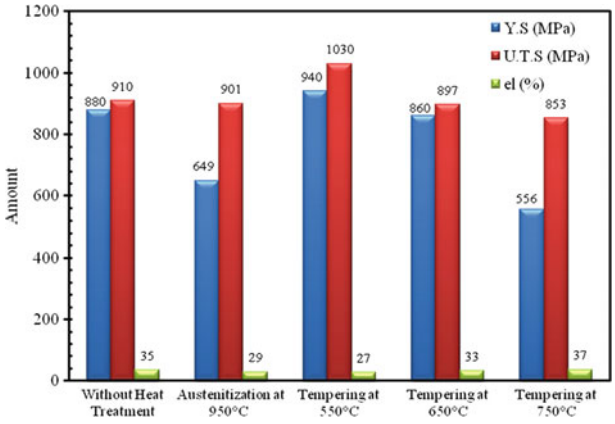

Fig. 6 Tensile test results for the non-heat treated, austenitized, quenched in water, and tempered at different temperatures

amount of retained austenite in the sample substantially decreases as the tempering temperature rises up hence for higher amount of smaller layer bainite. In fact, it can be seen in these figures that the amount of martensite and retained austenite decrease with increasing the tempering temperature. On the other hand, the amount of bainite increased in such a scenario.

Tensile test results

Figures 6 and 7 show tensile test results for this steel under different processing conditions. From the tensile tests, yield strength of 880 MPa and tensile strength of 910 MPa were obtained which are similar to the literature [20–24]. It is known that the mechanical properties of the HSLA steels are dependent on their initial austenite

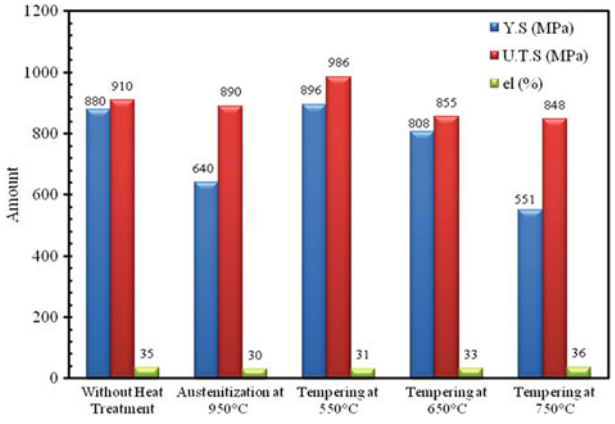

Fig. 7 Tensile test results for the non-heat treated, austenitized, quenched in oil, and tempered at different temperatures

grain size. Therefore, considering the microstructure of the non-heat treated samples, and the controlled rolling process (thermomechanically processed steel), the controlled deformation in the single austenite phase following with the fast quenching led to a significant grain refinement. This is expected to substantially increase the density of dislocations leading to such high values of yield/tensile strengths. Figures 6 and 7 also show that the yield strength and ductility of the samples that were austenitized and quenched, in water and oil, are lower compared with the non-heat treated cases. However, the tensile strength of the sample quenched in water was higher than the non-heat treated sample. As well, the yield and tensile strengths of the sample quenched in water was higher than the sample quenched in oil. From the microstructure of the quenched only sample that were not tempered, and given the results obtained from the tensile test, it could be said that these sample do not have proper mechanical properties.

Moreover, the results of Figs. 6 and 7 show that the yield/tensile strengths of the sample tempered at 550 °C is higher than the austenitized and non-heat treated samples. The values in this case is higher than the standard values. Tempering at 550 °C led to the presence of lower retained austenite in the microstructure compared to the austenitized sample. On the other hand, Cu precipitates and also other spherical precipitates are better distributed in the tempered situation leading to the presence of more obstacles for the movement of dislocations. This resulted in higher strength level [14–19]. Results also show that 550 °C is the optimum temperature for tempering in this steel. As the tempering temperature increases from 550 to 750 °C, the yield/tensile strengths of the steel substantially reduce. At the tempering temperatures higher than 550 °C, a significant grain growth occurs in the system. As well, some of the martensite in the matrix transform to bainite. A combination of these effects leads to a reduction in the strength.

Charpy impact test

Fracture resistance is one of the most important factors in using HSLA X100 steel in industry. Toughness is directly dependent on the initial austenite grain size, especially the ones with thick edges that are distributed throughout the matrix. Therefore, strength and toughness can be controlled with the control of the initial austenite grain size and the Cu precipitates. Most of the strengthening in the high Ni HSLA X100 is due to the clusters of BBC Cu where they exert compression force to the dislocations impeding their movement [15–19]. On the other hand, the interactions of the compression fields and increasing the number of dislocations prevents free movement of the dislocations and increases the toughness of the steel. When high Ni HSLA X100 steel is tempered at temperature higher than the optimum tempering temperature, strength substantially decreases while toughness improves. One of the main reasons for this behavior is the growth of the Cu precipitates. The size of the Cu precipitates is around 24 °A in optimum tempering condition. At higher temperatures, Cu precipitates size deviates from this optimum value and even reaches 40 °A. In such a condition, coherent BCC Cu precipitates transform to non-coherent FCC precipitates [18–23]. As well, the growth of the precipitates increases the distance between them reducing the interaction between

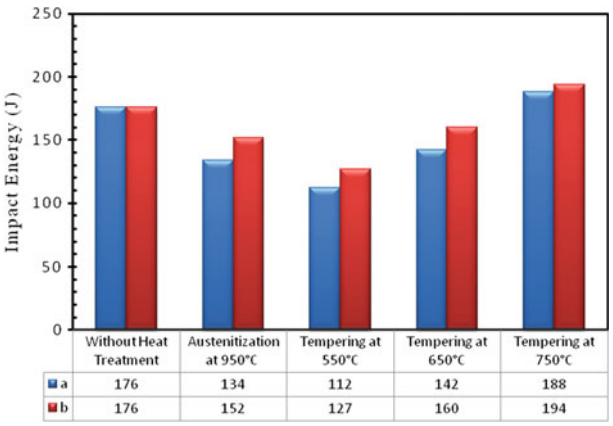

Fig. 8 Charpy impact test results of the high Ni HSLA X100 steel for samples non-heat treated, austenitized and quenched in oil/water and then tempered at different temperatures

the Cu precipitates and the dislocations. Indeed, an over-aged conditions is achieved in such a circumstances. The strength decrement and toughness increment due to the increase in tempering temperature is mainly due to the changing Cu precipitates shape from BBC to FCC and also the reduction of dislocation pile up [12–16].

Figure 8 show Charpy impact test results under different conditions of the hi Ni HSLA X100 steel. It can be seen in this figure that the fracture energy is the lowest at the tempering temperature of 550 °C. And as the tempering temperature increases, the fracture energy increases as such. At the tempering temperature of 750 °C, the fracture energy is the highest among the investigated cases.

Conclusions

A high Ni HSLA X100 steel was thermodynamically processed and its microstructures and mechanical properties were studied in different treatment conditions. The following results were obtained from conducting this research:

1. The results showed that the microstructure of the steel is a mix of ferrite, bainite, martensite, retained austenite and various carbides. Tempering at different temperatures removed retained austenite from the lath martensite and led to a relatively high amount of toughens. The carbides were also uniformly distributed in the tempered conditions. Low temperature tempering removed the retained austenite present in the quenched only conditions.
2. Tensile tests showed that austenitization reduces yield/tensile strengths of the high Ni HSLA X100 steel. Subsequent tempering improved these mechanical properties shortcomings. Results also showed that tempering at 550 °C gave the

highest yield/tensile strengths. Increasing tempering temperature from 550 to 750 °C reduced the strengths of this steel.

3. Charpy impact test results indicated that quenching substantially reduced impact energy of the high Ni HSLA X100 steel. Tempering recovered this property. Increasing the tempering temperature from 550 to 750 °C considerably increased fracture energy of the high Ni HSLA X100 steel.

References

1. Gladman T (1997) The physical matallurgy of microalloyed steels. The Institute of Materials, University Press, Cambridge
2. Mousavi Anijdan SH (2010) The effect of cool deformation on the microstructural evolution and flow strength of microalloyed steels. Ph.D. thesis. McGill University
3. Lavvafi H et al (2107) Effects of surface laser treatments on microstructure, tension, and fatigue behavior of AISI 316LVM biomedical wires. Mat Sci Eng A 688:101–113
4. Thompson SW (2013) Microstructural characterization of an as-quenched HSLA-100 plate steel via transmission electron microscopy. Mater Charact 77:89–98
5. Chae D, Koss DA (2004) Damage accumulation and failure of HSLA-100 steel. Mat Sci Eng A 366:299–309
6. Xue Q et al (2003) Constitutive response of welded HSLA 100 steel. Mat Sci Eng A 54:166–179
7. Das SK et al (2006) The effect of variation of microstructure on fracture mechanics parameters of HSLA-100 steel. Mat Sci Eng A 431:68–79
8. Tamura I, Sekine H, Tanaka T (1988) Thermomechanical processing of highstrength low-alloy steels. Elsevier, Butterworths, London
9. Mukherjee S et al (2004) Studies on low-energy nitrogen plasma immersion ion implantation on austenitic stainless steel and Cu-strengthened HSLA-100 steel. Surf Coat Technol 186:282–286
10. Shome M (2007) Effect of heat-input on austenite grain size in the heat-affected zone of HSLA-100 steel. Mat Sci Eng A 445–446:454–460
11. Martineau RL, Prime MB, Duffey T (2004) Penetration of HSLA-100 steel with tungsten carbide spheres at striking velocities between 0.8 and 2.5 km/s. Int J Impact Eng 30:505–520
12. Chattoraj I, Tarafder M, Das SK, Tarafder S (2003) Hydrogen induced brittle crack growth in Cu-strengthened HSLA-100 steels. Mat Sci Eng A 339:136–149
13. Densley JM, Hirth JP (1998) Mixed mode fracture of an HSLA-100 steel. Scripta Mater 39:881–885
14. Dai HL et al (2017) Investigation on the influence of damage to springback of U-shape HSLA steel plates. J Alloy Compd 708:575–586
15. Garcia CI (2017) High strength low alloyed (HSLA) steels. Autom Steels 145–167
16. Liu Y et al (2016) Effect of step quenching on microstructures and mechanical properties of HSLA steel. Mat Sci Eng A 675:371–378
17. Guiqin F, Duo J, Miaoyong Z (2015) Effect of austenitizing temperature on the microstructure and mechanical properties of steel. J Eng Sci Technol Rev 8:43–50
18. Mousavi Anijdan SH, Yue S (2012) The effect of cooling rate, and cool deformation through strain induced transformation, on microstructural evolution and mechanical properties of microalloyed steels. Metall Mat Trans A 43:1140–1162
19. Janjuševiæ Z et al (2014) Effect of tempering on mechanical properties and microstructure of a high-strength low-alloy steel. Metal Sci Heat Treat 56:81–83

20. Dhua SK, Ray A, Sarma DS (2001) Effect of tempering temperatures on the mechanical properties and microstructures of HSLA-100 type copper-bearing steels. Mat Sci Eng A 318:197–210
21. Mousavi Anijdan SH, Sediako D, Yue S (2012) Optimization of flow stress in cool deformed Nb-microalloyed steel by combining strain induced transformation of retained austenite, cooling rate and heat treatment. Acta Mater 60:1221–1229
22. Mousavi Anijdan SH, Yue S (2011) The necessity of dynamic precipitation for the occurrence of no-recrystallization temperature in Nb-microalloyed steel. Mat Sci Eng A 528:803–807
23. Mousavi Anijdan SH, Rezaeian A, Yue S (2012) The effects of chemical composition and austenite conditioning on the transformation behavior of microalloyed steels. Mat Charact 27–38
24. Mousavi Anijdan SH, Yue S (2010) Effect of cooling rate, and deformation in ferrite on the mechanical properties and microstructural evolution of microalloyed steels. Mat Sci Eng 1616–1626
25. Annual book of ASTM E8/ E8M-15a (2015) Standard test methods for tension testing of metallic materials. ASTM Int 03.01:1–8
26. Annual book of ASTM A370–14 (2014) Standard test methods and definitions for mechanical testing of steel products. ASTM Int 20–29:1–6

Effects of Matrix Microstructure on the Nanoscale Precipitation and Precipitation Strengthening in an Ultra-high Strength Steel

Songsong Xu, Hao Guo, Yu Zhao, Naimeng Liu, Dan Chen, Ye Cui, Yang Zhang and Zhongwu Zhang

Abstract Matrix microstructure and nanoscale clusters are the two main factors influencing the mechanical properties of nanocluster strengthened steels. Here, an ultra-high strength steel with a tensile strength of ~1.64 GPa and an elongation of ~14% has been developed through a combination of fine matrix microstructure and precipitation strengthening. Matrix microstructure was primarily controlled by annealing treatment. After annealing treatment at 750 °C for 1 h, the hot-rolled microstructure changes to the layered sorbite-like structure. The precipitation strengthening contributes a similar yield strength of ~494 MPa in both hot-rolled and annealed steels. The results indicate that there is no effect of matrix microstructure on the subsequent precipitation of nanoscale clusters and precipitation strengthening. The matrix microstructure and the precipitation of nanoscale clusters are independent and can be controlled separately.

Keywords Ultra-high strength steel · Matrix microstructure · Precipitation strengthening

Introduction

There has been an increasing demand of ultra-high strength steels (USS) with characteristics like high strength, good weldability and corrosion resistance due to the rapid economic development and fast growing national defense industry [1–4]. Precipitation strengthening plays an important role in the design and fabrication of USS with superior mechanical properties and strong resistance to radiation damage [5–12]. To obtain a good comprehensive properties, Cu and NiAl nanoparticles are two classes of effective strengthening phases among the various types of potential

S. Xu · H. Guo · Y. Zhao · N. Liu · D. Chen · Y. Cui · Y. Zhang · Z. Zhang (✉)
Key Laboratory of Superlight Materials and Surface Technology, Ministry of Education, College of Materials Science and Chemical Engineering, Harbin Engineering University, Harbin 150001, People's Republic of China
e-mail: zwzhang@hrbeu.edu.cn

The Minerals, Metals & Materials Society, *TMS 2018 147th Annual Meeting & Exhibition Supplemental Proceedings*, The Minerals, Metals & Materials Series,
https://doi.org/10.1007/978-3-319-72526-0_15

nanoparticles to be considered for precipitation hardening in steel [13, 14]. Jiao et al. [15] has found that Fe–Cu–Ni–Al-based steels with relatively low Ni/Cu and Al/Cu ratios, in which Cu nanoparticles are the dominant strengthening phase and NiAl nanoparticles provide a supplement strengthening effect. And if small variations in the Ni, Al and Cu contents, precipitation characteristics would have sensitive differences, including the composition, size and number density of the Cu and NiAl nanoparticles, thereby significantly influencing the degree of strengthening.

Although Cu-riched nanoscale precipitation appeared in the USS, can increase the mechanical properties and solve the problem of weldability [14, 16–19], the demand for the matrix microstructure in it is accordingly strict. Furthermore, the USS' matrix microstructure will be changed with the annealing treatment, variation of subsequent cooling rates, and alloy chemistry [14]. By austenite decomposing during continuous cooling rate, Thompson [20] has made the CCT diagram for the HSLA-80 steel and found that the austenite would transform to polygonal ferrite, widmanstatten ferrite, granular ferrite, acicular ferrite, upper bainite, lower bainite and martesite. By varying the continuous cooling rates and using three-dimensional electron backscatter diffraction and transmission electron microscopy, Kang [21] investigated that granular bainite, acicular ferrite and lath-type bainite will appear in the HSLA steel at the different cooling rates. However, understanding the relationship between annealing treatment and the precipitation of nanoscale clusters is the most important prerequisite for the preparation of nanocluster-strengthened steels with a combination of high strength and ductility.

In this paper, an experimental study is reported on for the precipitation strengthening in an ultra-high strength steel with different matrix microstructure. Combining the mechanical properties and matrix microstructure, the effect of matrix microstructure on the precipitation of nanoscale cluster was conducted.

Experimental Methods

A nanoprecipitates strengthened steel with a nominal composition of Fe-1.5Mn-2.5Cu-4Ni-1Al-0.005B-1.5Mo-0.05Nb-0.1Ti-1.5W-0.08C-0.5Si (wt%) was selected for the experimental investigation. The cast ingots with a weight of ~50 kg were obtained by vacuum induction melting with magnetic stirring to ensure homogeneous distribution of alloying elements. The cast ingots were rolled to a total reduction of 80% with a temperature of 800 °C through 8 passes. The final thickness of the as-rolled steel plate was 12 mm. The hot-rolled sample is labeled as HR. To identify the effects of annealing treatment on the precipitation of nanoscale clusters, HR steel was then annealing at 750 °C for 1 h after removing the surface oxides (labeled as 750AS). And then all the samples, HR and 750AS were aged at 525 °C for 2 h. The aged samples are labeled as HR-AG and 750AS-AG, respectively.

Hardness measurements were conducted on a Vickers tester with a load of 1 kg for 15 s. For each specimen, at least ten indents were measured to obtain an average value. The matrix microstructures were characterized using optical microscopy

(OM). The OM samples were polished to a final surface finish of 0.2 μm by standard mechanical polishing procedures, and then etched for approximate 5–15 s with a 4 vol.% Nital solution.

Tensile tests along the rolling direction of the samples were conducted on an Instron 5565 testing machine at a strain rate of 10^{-3} s^{-1}. The rod tensile samples were processed into the specimens with 5 mm in diameter and 25.4 mm in gauge length by numerically controlled lathe. Three specimens were tested in the same condition and the average values were reported. A contacting Instron extensometer was used to measure strain within the sample gauge upon loading. The yield strength was determined with the 0.2% offset plastic strain method.

Results and Discussion

Figure 1 shows the optical microstructures of HR and 750AS steels. The HR steel consists of the deformed original austenite and some recrystallized ferrites embedded in the deformed matrix (Fig. 1a), indicating that dynamic recovery/recrystallization is the predominant softening mechanism. After annealing at 750 °C for 1 h followed water quenching, the deformed fibrous structure of HR steel transformed into the layered sorbite due to recrystallization (in the Fig. 1b). And the layered sorbite were introduced long the rolling direction, the groups of sorbite were thin and homogeneous. The orientation of sorbite showed a symmetry

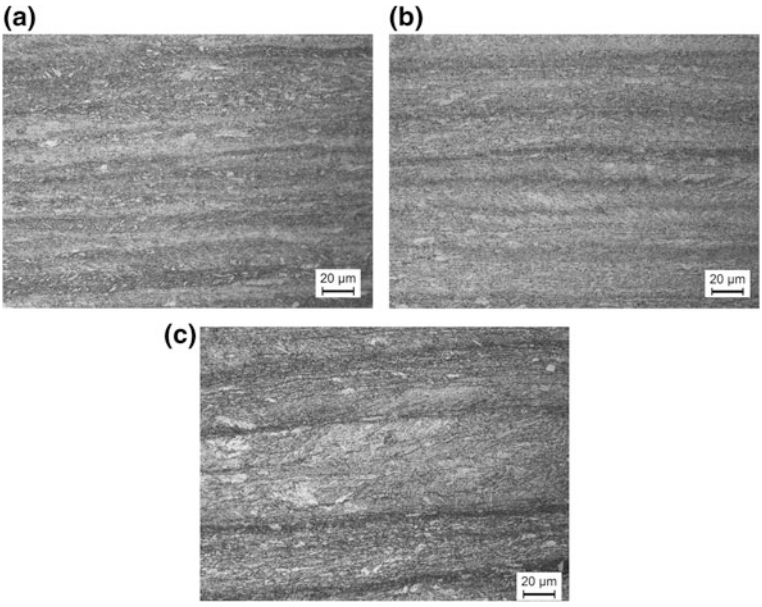

Fig. 1 The optical microstructures of **a** HR steel, **b** 750AS steel, **c** 750AS-AG steel

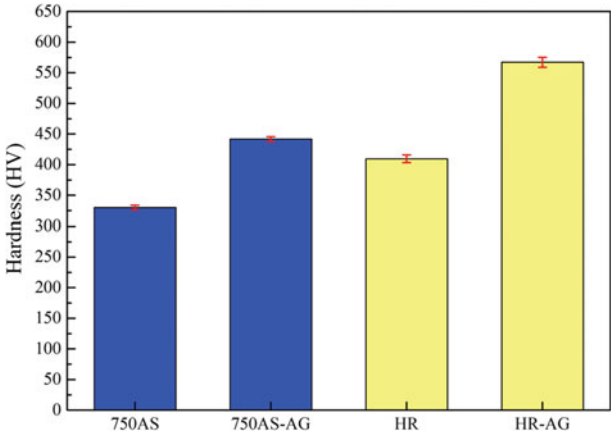

Fig. 2 Microhardness of HR and 750AS steels before and after aging treatment

along the boundary between the layers. With aging at 525 °C for 2 h, the 750AS-AG steel was also consisted of sorbite in the Fig. 1c. It confirms that aging treatment has no effect on the microstructure.

Microhardness measurements were conducted to evaluate the age hardening response of the HR and 750AS steels. The microhardness values were shown in Fig. 2. After aged at 525 °C for 2 h, the microhardness of HR and 750AS steels all has obviously increase due to the formation of nanoscale precipitates. The hardness increased significantly from 409 to 567 HV at an aging time of 2 h for HR steel, while 750AS steel has an increase of 111 HV. However, the hardness of 750AS steel has an obvious reduction than the HR steel due to the recrystallization. Aging treatment has no influence on the above results.

The engineering stress-strain curves were presented in Fig. 3. The HR steel showed a yield strength of ~1098 MPa and an ultimate tensile strength of

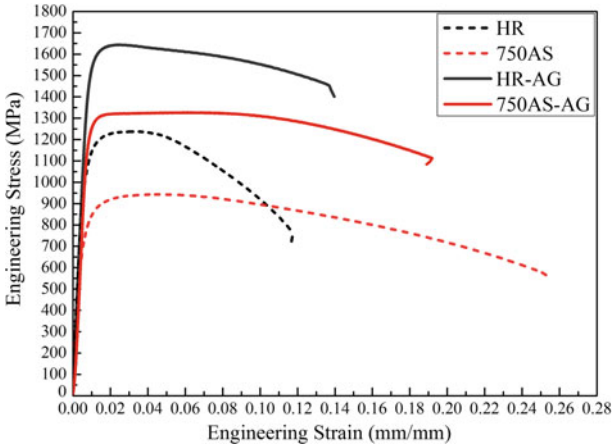

Fig. 3 Room-temperature tensile stress-strain curves of the steels

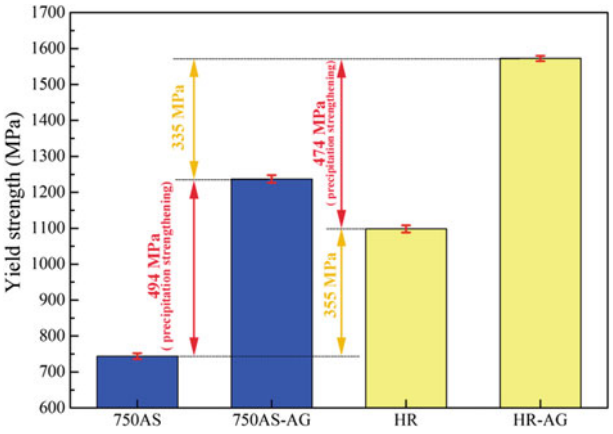

Fig. 4 Schematic diagram showing the effects of precipitation strengthening

~1237 MPa. As for HR-AG steel, the yield strength increased dramatically to ~1572 MPa with an elongation-to-failure 14%. Owing to the change of microstructure, the yield strength of 750SS steel has an obvious reduce from 1098 to 743 MPa comparing with HR steel. As for 750SS-AG steel, it has an increase of yield strength from 743 to 1237 MPa. As shown in Fig. 4, for all the two samples, HR and 750SS steels, the increments of yield strength induced by aging were very similar (474 MPa for HR steel, 494 MPa for 750SS steel). Owing to the different microstructure induced by different processing routes, matrix microstructure contributes different yield strength to HR and 750AS steels. However, the contributions of precipitation strengthening were similar for HR-AG and 750AS-AG steels. These results indicated that matrix microstructure had no effect on precipitation of the clusters and precipitation strengthening in the ultra-high strength steel.

As compared to the HR sample, the yield strength of 750AS decreased 355 MPa due to the change of matrix microstructure. However, the yield strength increment of HR and 750AS after aging were comparable though two sample have different matrix microstructure. These indicated that there was no effect of matrix microstructure on the precipitation of nanoscale clusters and precipitation strengthening, and the precipitation of nanoscale clusters and annealing treatment were independent. Our previous studies also confirmed this by in similar steels [9]. Local composition fluctuation would form Cu-enriched embryos and Cu-depleted regions, which are not rely on the matrix microstructure which was effected by the annealing treatment. The embryos become preferential sites for nucleation of nanoscale clusters when they reach a critical size.

Conclusion

In summary, the ultra-high strength steel with a tensile strength of 1.64 GPa and an elongation of ~14% have been successfully developed through a combination of fine matrix microstructure and nanoscale clusters. The matrix microstructure was controlled by the annealing treatment, which has no effect on the precipitation of nanoscale clusters. The matrix microstructure and the precipitation of nanoscale clusters are independent and can be controlled separately.

Acknowledgements This work was supported by the Fundamental Research Funds for the Central Universities (HEUCFJ171005, HEUCFJ171001 and HEUCFP201703), NSFC Funding (51371062 and U1460102), NSFHLJ (JC2017012), the Scientific Research Foundation for Returned Overseas Chinese Scholars (Heilongjiang Province), the Project for Innovative Talents of Science and Technology of Harbin (2014RFXXJ006) and the High-Tech Ship Research Projects Sponsored by MIIT (K24367). The neutron diffraction work at the China Academy of Engineering Physics (CAEP) is greatly appreciated. This paper is funded by the International Exchange Program of Harbin Engineering University for Innovation-oriented.

References

1. Kim SH, Kim H, Kim NJ (2015) Brittle intermetallic compound makes ultrastrong low-density steel with large ductility. Nature 518(7537):77
2. Jiao ZB, Luan JH, Miller MK, Chung YW, Liu CT (2016) Co-precipitation of nanoscale particles in steels with ultra-high strength for a new era. Mater Today
3. He BB, Hu B, Yen HW, Cheng GJ, Wang ZK, Luo HW, Huang MX (2017) High dislocation density-induced large ductility in deformed and partitioned steels. Science
4. Jiang S, Wang H, Wu Y, Liu X, Chen H, Yao M, Gault B, Ponge D, Raabe D, Hirata A, Chen M, Wang Y, Lu Z (2017) Ultrastrong steel via minimal lattice misfit and high-density nanoprecipitation. Nature 544(7651):460–464
5. Hättestrand M, Nilsson J-O, Stiller K, Liu P, Andersson M (2004) Precipitation hardening in a 12%Cr–9%Ni–4%Mo–2%Cu stainless steel. Acta Mater 52(4):1023–1037
6. Fine ME, Isheim D (2005) Origin of copper precipitation strengthening in steel revisite. Scr Mater 53(1):115–118
7. Raabe D, Ponge D, Dmitrieva O, Sander B (2009) Nanoprecipitate-hardened 1.5 GPa steels with unexpected high ductility. Scr Mater 60(12):1141–1144
8. Zinkle SJ, Busby JT (2009) Structural materials for fission and fusion energy. Mater Today 12 (11):12–19
9. Zhang ZW, Liu CT, Wang XL, Littrell KC, Miller MK, An K, Chin BA (2011) From embryos to precipitates: a study of nucleation and growth in a multicomponent ferritic steel. Phys Rev B 84(17)
10. Guo H, Cheng J, Yang S, He X (2013) Influence of combined Cu and Nb addition on the quenched microstructure and precipitation during tempering in ultra-low carbon steels. J Alloys Compd 577(Supplement 1):S619–S625
11. Jiao ZB, Luan JH, Zhang ZW, Miller MK, Liu CT (2014) High-strength steels hardened mainly by nanoscale NiAl precipitates. Scr Mater 87(4):45–48
12. Li XL, Lei CS, Deng XT, Wang ZD, Yu YG, Wang GD, Misra RDK (2016) Precipitation strengthening in titanium microalloyed high-strength steel plates with new generation-thermomechanical controlled processing (NG-TMCP). J Alloy Compd 689:542–553

13. Fine ME, Vaynman S, Isheim D, Chung Y-W, Bhat SP, Hahin CH (2010) A new paradigm for designing high-fracture-energy steels. Metall Mater Trans A 41(13):3318–3325
14. Mulholland MD, Seidman DN (2011) Nanoscale co-precipitation and mechanical properties of a high-strength low-carbon steel. Acta Mater 59(5):1881–1897
15. Jiao ZB, Luan JH, Miller MK, Liu CT (2015) Precipitation mechanism and mechanical properties of an ultra-high strength steel hardened by nanoscale NiAl and Cu particles. Acta Mater 97:58–67
16. Vaynman S, Isheim D, Kolli RP, Bhat SP, Seidman DN, Fine ME (2008) High-strength low-carbon ferritic steel containing Cu-Fe-Ni-Al-Mn precipitates. Metall Mater Trans A 39a(2):363–373
17. Trotter G, Rayner G, Baker I, Munroe PR (2014) Accelerated precipitation in the AFA stainless steel Fe–20Cr–30Ni–2Nb–5Al via cold working. Intermetallics 53:120–128
18. Vo NQ, Liebscher CH, Rawlings MJS, Asta M, Dunand DC (2014) Creep properties and microstructure of a precipitation-strengthened ferritic Fe–Al–Ni–Cr alloy. Acta Mater 71: 89–99
19. Huang S, Gao Y, An K, Zheng L, Wu W, Teng Z, Liaw PK (2015) Deformation mechanisms in a precipitation-strengthened ferritic superalloy revealed by in situ neutron diffraction studies at elevated temperatures. Acta Mater 83:137–148
20. Thompson SW (2013) Microstructural characterization of an as-quenched HSLA-100 plate steel via transmission electron microscopy. Mater Charact 77:89–98
21. Kang JS, Seol JB, Park CG (2013) Three-dimensional characterization of bainitic microstructures in low-carbon high-strength low-alloy steel studied by electron backscatter diffraction. Mater Charact 79(3):110–121

The Technology Study of Silicon Reduction of Chromite Powder in Microwave Field

Hua Liu, Shenghui Guo, Yu Duan, Jinhui Peng, Libo Zhang and Linqing Dai

Abstract Both chromite powder and ferrosilicon have good wave absorbing property in microwave field, the effects of reduction temperature, reduction time, microwave power, raw particle size and material height were investigated. The results from laboratorial experiments have shown that the particle size, microwave power and material layer height have obvious influence on the heating rate of the material. When the particle size is less than 74 μm, the material heating rate increased obviously and the conversion rate of chromium increased. With the particle size is less than 48 μm, chromium conversion rate is highest reaching 72.13%; when the microwave power from 1300 W, the heating rate increased

H. Liu · S. Guo · Y. Duan · J. Peng · L. Zhang · L. Dai (✉)
State Key Laboratory of Complex Nonferrous Metal Resources Clean Utilization, Kunming University of Science and Technology, Kunming, Yunnan 650093, China
e-mail: linqingdai@163.com

H. Liu
e-mail: lh07140927@163.com

S. Guo
e-mail: shguo78@hotmail.com

Y. Duan
e-mail: duan532952845@126.com

J. Peng
e-mail: jhuipeng78@163.com

L. Zhang
e-mail: libozhang77@163.com

H. Liu · S. Guo · Y. Duan · J. Peng · L. Zhang · L. Dai
Faculty of Metallurgical and Energy Engineering, Kunming University of Science and Technology, Kunming, Yunnan 650093, China

H. Liu · S. Guo · Y. Duan · J. Peng · L. Zhang · L. Dai
Key Laboratory of Unconventional Metallurgy, Ministry of Education, Kunming, Yunnan 650093, China

H. Liu · S. Guo · Y. Duan · J. Peng · L. Zhang · L. Dai
National Local Joint Laboratory of Engineering Application of Microwave Energy and Equipment Technology, Kunming, Yunnan 650093, China

The Minerals, Metals & Materials Society, *TMS 2018 147th Annual Meeting & Exhibition Supplemental Proceedings*, The Minerals, Metals & Materials Series,
https://doi.org/10.1007/978-3-319-72526-0_16

remarkable, the conversion rate of chromium is also increasing and also reduce the heating time and save energy, but the impact on the chromium conversion rate is not obvious; the reduction time and reduction temperature on conversion ratio of chromium effect is very obvious, with the temperature is higher than 1200 °C and the reduction time reduction of chromium is more favorable.

Keywords Microwave heating · Silicothermic reduction · Chromite Heating rate

Introduction

Chromite is the main form of chromium in nature. It is a kind of equiaxed mineral, which is composed of chromium oxides, iron oxides and other metal oxides. It is usually expressed in $(Mg, Fe^{2+})O(Cr, A1, Fe^{3+})_2O_3$ [1, 2]. Chromite has long been a shortage of mineral resources in China. The reserves are only 0.15 of the world, and the ore deposits are small in size, scattered in distribution and low in ore grade [3]. The dependence on imports of chromite in China is as high as 95% [4–6]. Chromite has a wide range of applications, mainly concentrated in metallurgy, refractory materials and chemical in these major areas [7, 8].

Chromite as an important strategic resource, mainly used in the production of ferrochrome, ferrochrome into high carbon ferrochrome, carbon ferrochrome, low carbon ferrochrome and low carbon ferrochrome with different carbon content, the carbon content is low, the added value is high. At present, low carbon ferrochrome smelting method in the traditional is mainly divided into two categories: oxygen blowing method and electric silicothermic method [9]. The former mainly exist in smelting high energy consumption, long process flow, equipment use short life shortcomings; the latter electrosilicothermic smelting low carbon ferrochromium slag, electrode contact or radiation from the work of electrodes of carbon particles are likely to enter the lead alloy carburizing.

According to the mechanism of the different heating methods of solid materials can be roughly divided into two categories [10]: one is the traditional heating methods, traditional heating mode is the mode of heat transfer by external heat by radiation and convection from the high temperature part of the transfer to the lower part, so has a certain temperature gradient, leading to the heating rate has been greatly restricted and can not too fast; the other is the microwave heating, which is different from the traditional heating method and is a new way of heating with clean and efficient, the heating mechanism is the microwave electromagnetic energy into heat and heat effect depends on the dielectric loss of material in microwave field and produce, there is a close relationship between polarization and molecular materials and as long as microwave energy and is absorbed through the material can achieve the purpose of heating [11, 12]. Microwave energy as a clean and efficient new heating energy [13, 14], its biggest advantage is that the powder material can be selectively heated [15–17]. Microwave heating of chromite ore powder with

silicon can combine the microwave heating characteristics with the self reduction characteristics of the chromite ore with silicon, and realize the simple and efficient use and disposal of the increasing chromite powder [18], but there is still a lack of research on its technology. Therefore, this paper explores key issues of chromite process control microwave field silicon thermal reduction, in-depth study of the main factors of raw material size, reduction time, reduction temperature, microwave power and the effect of material layer height on the heating up performance and Cr conversion rate of microwave reduced silicon chromite.

Experiment

Material Properties

The chromite powder used in the experiment was supplied by a company in Liaoning, Jinzhou, as a chromite in South Africa. The sample composition of chromite powder is shown in Table 1. The particle size composition is shown in Table 2. The trend of particle size distribution of chromite powder is shown in Fig. 1, and the XRD diagram is shown in Fig. 2.

Table 1 shows the content of Cr_2O_3 is 40.82%, the content of FeO is 14.10%, the ratio of chrome and iron (Cr_2O_3/FeO) is 1.69. Iron chromium (Cr_2O_3/FeO) refers to the Cr_2O_3 and FeO in chromite (the actual content of FeO and TFe are converted to the sum of FeO content), the same grade is an important index for evaluating the chromite deposits, for smelting ferrochrome alloy melting and reduction of chromite ore has certain reference evaluation function the. This experiment used the chromite powder not only content of Cr_2O_3 is higher, but also content of TFe is higher, so the material of the ferrochrome actually is lower, ferrochrome with the low ratio of chromite ore, even if the Cr_2O_3 grade is higher, it is not very easy to smelt high grade chrome alloy. Seeing from Table 1, Al_2O_3 and MgO are respectively 13.04% and 10.83% in chromite powder, has a high percentage, and Al_2O_3, MgO and composition of gangue minerals with high melting point which easy to cause the refractory ore, difficult reduction and also increase the difficulty of chromite reduction.

Although the chromite used in this experiment is powder, the particle size distribution of the chromite powder is unknown. Therefore, the particle size of chromite power is analyzed by laser particle size analyzer.

From the Fig. 1 and Table 2 analysis, D50 indicates the median size is 179.273 μm. That is to say, when the percentage of total particle size distribution of

Table 1 Main chemical composition of chromite powder %

Cr_2O_3	FeO	SiO_2	Al_2O_3	CaO	MgO	TFe	Cr_2O_3/FeO
40.82	14.10	5.02	13.04	2.4	10.83	19.85	1.69

Table 2 Particle size composition of chromite powder

D10	D50	D90	D97
25.707 μm	179.273 μm	362.236 μm	390.088 μm

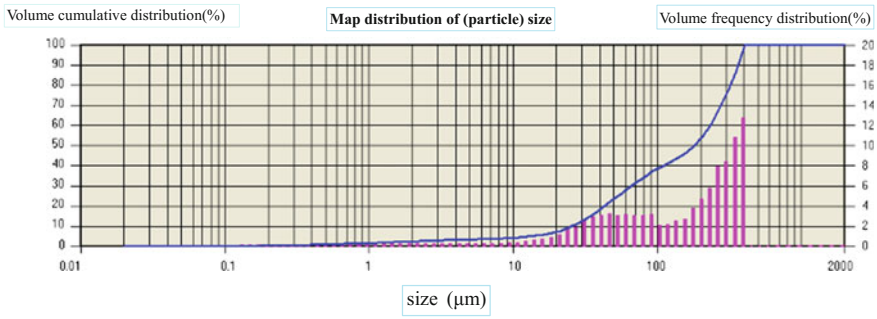

Fig. 1 Trend diagram of particle size distribution of chromite powder

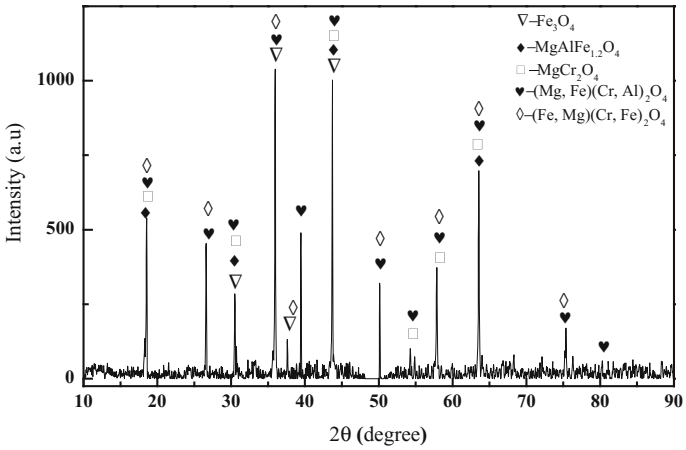

Fig. 2 XRD of chromite

Table 3 Main chemical composition of ferrosilicon powder (wt%)

Fe	O	Si	C	Ca	Mg	Cr	P	S	Al
50.13	38.48	6.65	2.82	0.48	0.48	0.07	0.03	0.02	0.26

chromite ore is 50%, the particle size is 179.273 μm, so the chromite powders used in the experiment with average particle size reach 179.273 μm, as if particle size is too big that not conducive to the reaction.

The results of XRD analysis of chromite samples shows that the main phase are (Mg, Fe) $(Cr, Al)_2O_4$ and (Fe, Mg) $(Cr, Fe)_2O_4$, secondary phase are Fe_3O_4, $MgCr_2O_4$ and $MgAlFe_{1.2}O_4$.

The reducing agent used in the laboratory is ferrosilicon powder. The results of industrial analysis and chemical composition of ash are shown in Table 3.

Microstructure of Chromite Powder

Figure 3 is the SEM of the chromite powder of different magnification under the condition of ore morphology, from the figure can be concluded that the reason why the chromite powder is hard to recover is that the surface is dense and smooth, and the crystalline degree of the mineral is good. Which also contribute to the traditional smelting temperature is generally higher than 1650 °C.

Microwave Heating Furnace

The experiment instrument is a self-developed good microwave metallurgical furnace with sealing performance of heating mixing material, the adjustable power range was 0–6 kW, and the microwave frequency was 2.45 GHz; with a tungsten rhenium thermocouple (measuring range: 0–1800 °C) measure the sample

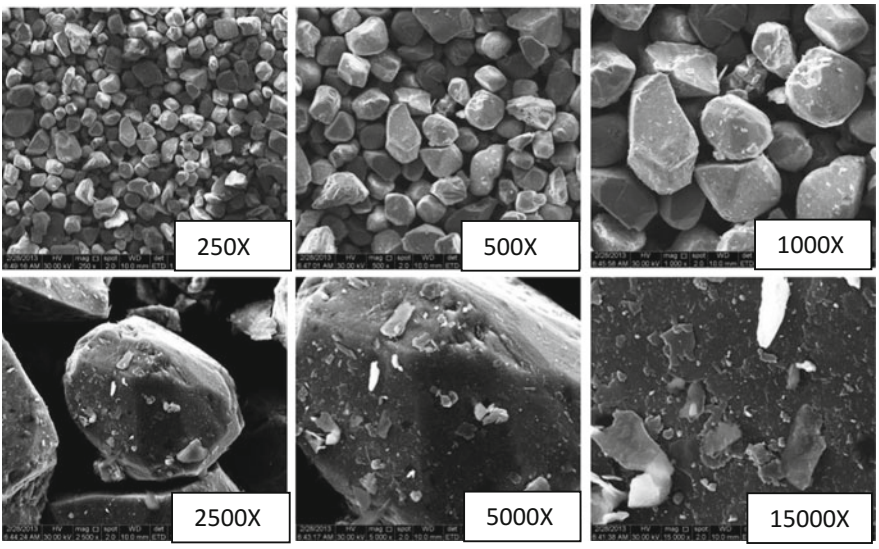

Fig. 3 SEM of chromite

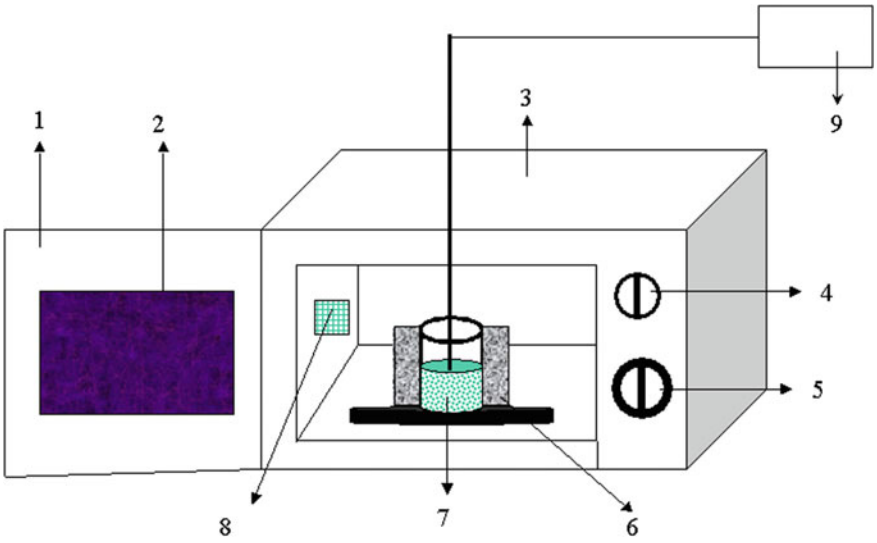

Fig. 4 Experiment setup in the microwave cavity. 1-Furnace door; 2-Port hole; 3-Microwave cavity; 4-Power switch; 5-Capacity control; 6-Insulation material; 7-Materials; 8-Exhaust hole; 9-The device of temperature measurement and control

temperature. Figure 4 shows the experiment setup in the microwave cavity, with a length of 400 mm, a width of 375 mm, a height of 235 mm.

The experimental materials were chromite powder from South Africa, ferrosilicon alloy powder as reducing agent, CaO powder (industrial pure) as flux, and their components were shown in Tables 1 and 3 respectively. The raw material was prepared by using the sample making mechanism, and the particle size was less than 74 μm (−200 mesh), according to the theoretical calculation proportion weighted and uniformly mixed into the Si chromite ore powder which could meet the smelting standard. By using Al_2O_3 crucible of 100 ml, after took a natural material and placed them in a microwave heating furnace (atmospheric pressure and atmosphere) and selected microwave heating power (1.5 kW) to heat up to the required temperature for microwave reduction.

After the reduction products were broken and prepared the sample, chemical phase analysis and XRD analysis were used to determine the content of chromium (*M* Cr) in the reduction products. The content of *T* Cr in the reducing sample was determined by the oxidation-reduction capacity method. The calculation method was as follows: [19].

$$\eta Cr = M\,Cr / T\,Cr,\ 100\%$$

In this formula, ηCr—Reduction rate of chromium metal, %; *M Cr*—Chromium content in reducing sample, %; *T Cr*—Content of total chromium in reducing sample, %.

Research on Wave Absorbing Property of Raw Materials

Taking chromite power and ferrosilicon powder as 50 g, researching the microwave absorbing property with microwave frequency of 2.45 GHz and power of 1.5 kW of in microwave oven was investigated. Figures 4 and 5 show the heating characteristic curves of chromite powder and ferrosilicon powder in the microwave field. It can be seen that the chromite powder was heated to 1200 °C about in 6 min, the heating rate was 200 °C/min, and the ferrosilicon powder was also heated up to 1200 °C approximately 6 min, the heating rate was around 200 °C/min. From heating rate, it can be concluded that chromite powder and ferrosilicon powder have good wave absorbing property (Fig. 6).

Results and Analysis

Effect of Particle Size on Temperature Rising Curve and Chromium Conversion

In the experiment, according to calculating, with 30% of the excess reducing agent (ferrosilicon powder), the flux of calcium oxide powder 30%, chromite powder 40%, the total amount of material of 96 g under the condition of different particle size on the temperature curve and explored the effect of chromium conversion.

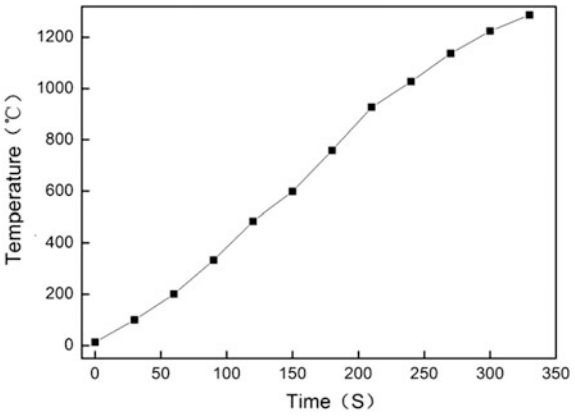

Fig. 5 Temperature rise characteristic curve in the microwave field of chromite

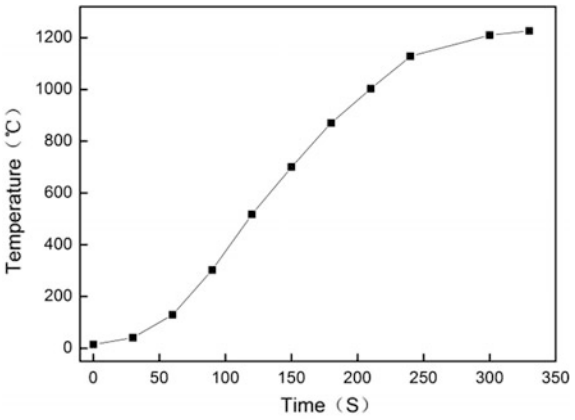

Fig. 6 Temperature rise characteristic curve in the microwave field of ferrosilicon

Mixture have been heated at 1200 °C, with microwave power 1500 W and the reduction time 60 min.

Figure 7 shows that with the decrease of the particle size, the heating rate is increasing and reduction time decreased, when the material size is less than −100 and −150, the heating rate does not appear too obvious difference. In other three sets of data, the particle size of −300 heating rate was the fastest, especially when after the heating time 12 min, rapidly heated up to 1200 °C, followed by −250 and −200, for the particle size of −300 and −200, the reduction time gap was 3–4 min. Table 4 shows that the smaller the particle size is, the higher the conversion rate of chromium. The conversion rate of chromium is the highest, with the particle size of −300, the conversion of chromium metal reaching 72.13%. Because the finer particle size of the mineral powder can help to increase the contact area between the materials, which is beneficial to the reaction.

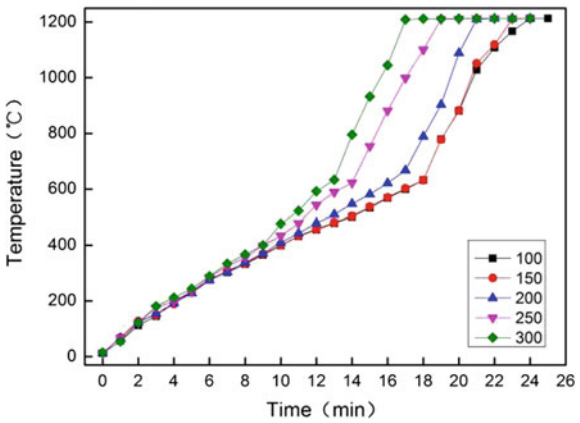

Fig. 7 Temperature rise characteristic curve in different particle size

Table 4 Conversion of chromium metal at different particle size

Size	−100	−150	−200	−250	−300
Conversion (%)	70.70	71.13	71.64	71.89	72.13

Effect of Microwave Power on Temperature Rising Curve and Chromium Conversion

In the experiment, based on calculating, with 30% of the excess reducing agent (ferrosilicon powder), the flux of calcium oxide powder 30%, chromite powder 40%, the total amount of material under the condition of 96 g of different microwave power and heating rates affect the conversion rate of chromium mixed material. The materials with different microwave power were heated to 1200 °C, the reduction time is 60 min, combined the size distribution of synthetic material and Table 4. The size of reaction material was −200 in this group.

Figure 8 shows that with the increase of microwave heating power, the heating time required to reach a reduction temperature of 1200 °C is gradually decreasing. There is no obvious difference in 12 min before heating rate of the five groups in the total material, after 12 min 1300 W and 1400 W heating rate relative to the other three groups was significantly increased, when the microwave power is 1400 W, about 19 min, the mixed material can be heated to 1200 °C. In the microwave power of 1000 and 1100 W, the heating rate is not as large as the overall difference.

As shown in Table 5, the conversion rate of Cr is different under different microwave heating power. The conversion rate of Cr increases with the increase of microwave power, and the range of increase is also increasing.

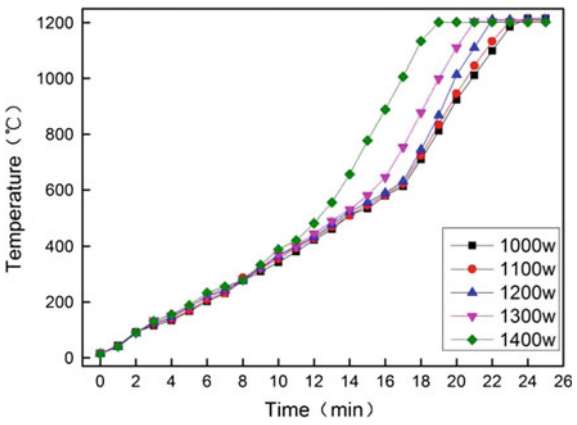

Fig. 8 Temperature rise characteristic curve in different microwave power

Table 5 Conversion of chromium metal at different microwave power

Power (W)	1000	1100	1200	1300	1400
Conversion (%)	70.16	70.34	70.53	70.83	71.29

Effect of Reduction Temperature on Chromium Conversion

In the experiment, according to calculating, with 30% of the excess reducing agent (ferrosilicon alloy powder), the flux of calcium oxide powder 30%, chromite powder 40%, the total amount of material under the condition of 96 g to explore the effect of reduction temperature on conversion rate of chromium, microwave power 1500 W, the reduction time is 60 min, size of material selection −200.

Figure 9 shows that chromium conversion rate increases with increasing reduction temperature, the initial stage of the growth rate was significantly increased, but the rate is more and more small, when the reduction temperature is 1400 °C, chromium conversion rate of 74.47%. Because the reduction of chromium minerals is a strong endothermic reaction, the higher the temperature, the more beneficial to the reduction of chromium.

Effect of Reduction Time on Chromium Conversion

In the experiment, according to calculating, with 30% of the excess reducing agent (ferrosilicon alloy powder) 30%, the flux of calcium oxide powder, chromite powder 40%, explored the effect of reduction time on chromium conversion rate of

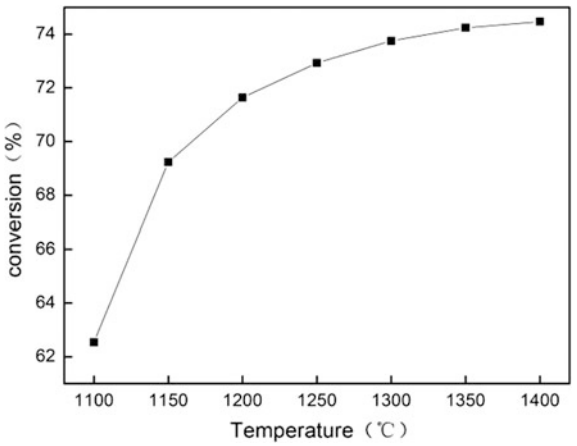

Fig. 9 Effect of reduction temperature on chromium conversion

total amount of material of 96 g under the condition of different microwave power material heated to 1200 °C, microwave power 1500 W, the reduction time is 30–180 min, the particle size of −200.

Figure 9 shows that the process of reduction time from 30 min to 180 min, the conversion rate of chromium has been increasing, but the rate of increase is more and more small, experiment, prolonged reduction time, basically has no obvious trend, the effect is not obvious. Therefore, the conversion of chromium will increase as the reduction time increases, but not the longer the reduction time, the better.

Effect of Material Height on Heating Rate and Chromium Conversion

In the experiment, the effects of the height of the five groups of 1.8 cm, 2.6 cm, 3.3 cm, 3.9 cm and 4.4 cm on the heating rate and Cr conversion rate of the mixed materials were investigated respectively. The corresponding alumina crucibles of 300, 200, 150, 100 and 50 ml were adopted in the experiment. The reduction temperature is 1200 °C, the microwave power is 1500 W, the reaction material granularity is −200, and the reduction time is 30 min (Fig. 11).

Combination with Fig. 10 and Table 6, the results show that with the decrease of the material height, the rate of heating rate is faster, but the influence on the conversion of chromium is not obvious. The problem with the experiment is that, in the two sets of 1.8 and 2.6 cm, the crucible is easy to break because of the high heating rate, so it is not as thin as possible.

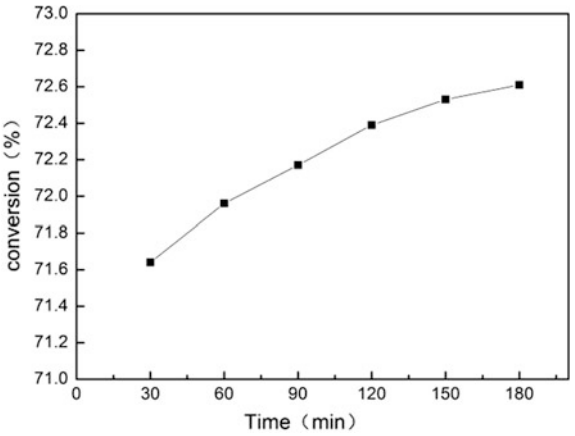

Fig. 10 Effect of reduction time on chromium conversion

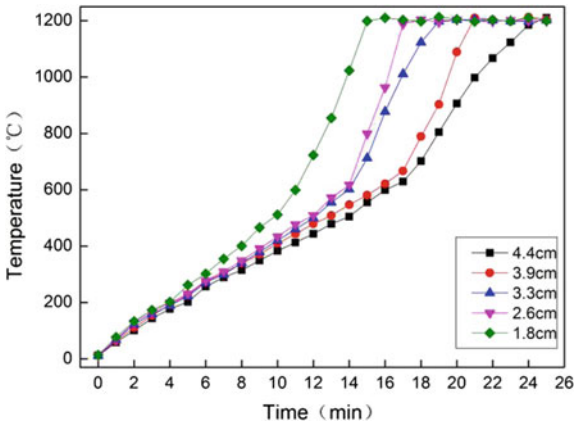

Fig. 11 Temperature rise characteristic curve of material height

Table 6 Material height of chromium conversion

Material height (cm)	1.8	2.6	3.3	3.9	4.4
Conversion (%)	71.29	71.32	71.33	71.34	71.34

Conclusions

1. The particle size, microwave power and material height have obvious influence on the rate of heating up. When the particle size is less than −200, the heating rate of the mixture increases obviously, and the conversion rate of chromium is the highest at −300, reaching 72.13%; when the microwave power starts from 1300 W, the heating rate increases obviously, and the conversion rate of chromium increases too. The decrease of material height also has obvious influence on the rate of heating up, but the influence on the conversion rate of chromium is not obvious.
2. The effect of reduction time and reduction temperature on the conversion of chromium is very obvious. When the temperature is higher than 1200 °C, prolonging the reduction time is more beneficial to the reduction of chromium.

Acknowledgements The authors are grateful for financial supported by the National Natural Science Foundation of China (Old No. 51504114 and New No. 51664035).

References

1. Zhao Q, Liu C, Jiang M et al (2013) Factors affecting the solid carbon reduction process of chromite. Sci Technol Rev 31(z1):40–43
2. Yan J, Chen J, Hu L (2007) J Chromium Metall

3. Kuilin W, Zhu H, Peng J et al (2014) Microstructure analysis of chromite chromite ore containing silicon by microwave heating reduction. J Electron Microsc 6:526–530
4. Zhu K, Qian Y (2006) New progress in chromite beneficiation. In: The ninth China mineral processing technology conference
5. Fang S (1998) An overview and grams of foreign chromite chromite mine. Geol Explor 2:16–18
6. Liu J (2005) Beneficiation of low grade chromite. Jiu Quan Steel Technol (2):4–9
7. Zhang F, Gao P, Chen J (2005) Analysis of future supply and demand situation and regulation policy of chromite in China. Contrib Geol Miner Resources Res 20(3):215–217
8. Liu Y (1996) Reasonable exploitation and utilization of chromite resources in Tibet. Eng Construct 5:9–13
9. Hu L (2010) Chromium resources and advanced chromium alloys. Chemical Industry Press
10. Qunying M, Li X (2004) Application and research progress of microwave heating technology. Physics 33(6):438–442
11. Atasoy A, Sale FR (2009) An investigation on the solid state reduction of chromite concentrate. Solid State Phenom 147–149:752–757
12. Cai W, Li H, Zhang Y (2005) Application of microwave technology in metallurgy. J Process Eng 5(2):228–232
13. Thostenson ET, Chou TW (1999) Microwave processing: fundamentals and applications. Compos A Appl Sci Manuf 30(9):1055–1071
14. Chen J, Liu L, Zeng Q et al (2004) Experimental study on reduction of iron ore containing carbon by microwave heating. J Steel 39(6):1–5
15. Hayashi M, Takeda K, Kashimura K et al (2013) Carbothermic reduction of hematite powders by microwave heating. ISIJ Int 53(7):1125–1130
16. Ren D, Wan T, Yuan Z et al (1990) Smelting of ferrochromium by shaft furnace with carbon bearing chrome-ore pellets. Ferro-Alloys
17. Ganesh I, Srinivas B, Johnson R et al (2004) Microwave assisted solid state reaction synthesis of $MgAl_2O_4$, spinel powders. J Eur Ceram Soc 24(2):201–207
18. Chen J, Zhang M, Zhao J et al (2008) Study on microstructure of carbon chromite ore by microwave heating reduction. J Electron Microsc 27(1):26–33
19. Li J (2017) Study on reduction characteristics of chromite pellets. Ferroalloy 48(2):19–22

Part VI
Advanced Magnetic Materials for Energy and Power Conversion Applications

Influence of Co-doping on the Crystal Structure, Magnetocaloric Properties and Elastic Moduli of the La(Fe, Si)$_{13}$ Compound

Dan Huang, Ronghui Kou, Jianrong Gao, Amanda Haglund, Jiaqiang Yan, Veerle Keppens, David Mandrus and Yang Ren

Abstract The La(Fe, Si)$_{13}$ compound shows a large magnetocaloric effect near room temperature. Partial substitution of Co for Fe can raise its Curie temperature and reduce the thermal hysteresis of its ferromagnetic transition. However, the influence of Co substitution on the crystal structure and magnetocaloric properties of La(Fe, Si)$_{13}$ is not well understood yet. In this work, we report a comparative study of the crystal structure, magnetocaloric effects and elastic moduli of polycrystalline $LaFe_{11.5}Si_{1.5}$ and $LaCoFe_{10.5}Si_{1.5}$ samples using synchrotron radiation X-ray diffraction, magnetic measurements and resonant ultrasound spectroscopy. Compared to the Co-free sample, the Co-doped sample shows a sluggish ferromagnetic transition and reduced volumetric expansion as well as softer elastic moduli at room temperature. The Co-doped sample also shows stronger temperature dependence of Fe-Fe distances in its ferromagnetic state. Such differences between the samples are explained by considering the influence of Co doping on ferromagnetic interactions and lattice entropy.

Keywords La(Fe, Si)$_{13}$ · Crystal structure · Elastic moduli · Magnetocaloric effect

D. Huang · R. Kou · J. Gao (✉)
Key Laboratory of Electromagnetic Processing of Materials (Ministry of Education), Northeastern University, Shenyang 110819, China
e-mail: jgao@mail.neu.edu.cn

D. Huang · A. Haglund · J. Yan · V. Keppens · D. Mandrus
Department of Materials Science and Engineering, University of Tennessee, Knoxville, TN 37996, USA

R. Kou · Y. Ren
Advanced Photon Source, Argonne National Laboratory, Argonne, IL 60439, USA

J. Yan · D. Mandrus
Oak Ridge National Laboratory, Oak Ridge, TN 37831, USA

The Minerals, Metals & Materials Society, *TMS 2018 147th Annual Meeting & Exhibition Supplemental Proceedings*, The Minerals, Metals & Materials Series,
https://doi.org/10.1007/978-3-319-72526-0_17

Introduction

In the past two decades, many intermetallic compounds [1–4] were found to show a large magnetocaloric effect (MCE), which can be used in room-temperature magnetic refrigeration. Among those compounds, the La(Fe, Si)$_{13}$ compound of a NaZn$_{13}$-type cubic structure has attracted much attention because of multiple advantages. Compared with other compounds, it shows a large MCE under a low magnetic field. It has a low cost of raw materials. It does not contain any toxic elements. However, it has disadvantages as well. For example, it appears difficult to prepare a single-phase material by ingot casting. The difficulty is related to the peritectic formation of La(Fe, Si)$_{13}$ following primary α-(Fe, Si) in casting [5]. The peritectic reaction is often incomplete leading to serious chemical segregation of as-cast ingots. Consequently, the ingots have to be annealed at high temperatures for a long time. Two novel methods were invented to shorten the time of annealing for preparation of the single phase material. One method combined rapid quenching to prepare the starting material [6], and the other method employed sintering of mixed powders [7]. Another disadvantage of La(Fe, Si)$_{13}$ is a low Curie temperature, T_C. Palstra et al. [8] showed many years ago that increasing Si concentration can increase the T_C of La(Fe, Si)$_{13}$ [4]. But, they did not investigate the effect of Co substitution on MCE. Hu et al. [9] found that partial substitution of Fe by Co can raise the T_C to room temperature without a significant decrease of the MCE. Fujita et al. [10] showed that introduction of interstitial hydrogen to the 1:13 phase can increase the T_C without reducing the MCE as well. Kim Anh et al. [11] showed that partial substitution of La by Nd increases the T_C at the cost of the MCE. In contrast, partial substitution of La by Ce or Pr [12, 13] lowers the T_C and increases the MCE. Such technical progress has made La(Fe, Si)$_{13}$ promising for room-temperature magnetic refrigeration applications.

Efforts were also made to understand the origin of the MCE of La(Fe, Si)$_{13}$. As usual, the MCE of La(Fe, Si)$_{13}$ can be related to a first-order ferromagnetic transition, which brings about a large change of the magnetization and thus a large change of magnetic entropy of the bulk material. Fujita et al. [14] related the MCE to an itinerant electron metamagnetic transition, which is of the first order and is accompanied by a large volumetric change. It is accepted that both transitions are important. Other studies were focused on a fundamental understanding of ferromagnetic interactions. Wang et al. [15] suggested a correlation between the lattice parameter and magnetic moments of Fe atoms after a neutron diffraction study of $LaFe_{11.4}Si_{1.6}$. Rosca et al. [16] investigated $LaFe_{11.31}Si_{1.69}$ and the $LaFe_{11.31}Si_{1.69}H_{1.45}$ using the neutron diffraction technique and suggested that increase of the T_C by introduction of interstitial hydrogen atoms is due to the increase of ferromagnetic interactions by the enlargement of Fe-Fe distances. Despite such progress, the relations between the crystal structure and the bulk magnetism of La(Fe, Si)$_{13}$-based compounds have not been well understood yet. In the present work, we carried out a comparative study of the thermally induced structure change, magnetism and elastic moduli of $LaFe_{11.5}Si_{1.5}$ and $LaFe_{10.5}CoSi_{1.5}$ for the purpose of

having insight into the mechanism of how Co substitution alters the T_C and the MCE of La(Fe, Si)$_{13}$.

Materials and Methods

Polycrystalline samples of $LaFe_{11.5}Si_{1.5}$ and $LaFe_{10.5}CoSi_{1.5}$ composition were prepared by melting of elemental materials in an arc-furnace under the protection of high-purity argon atmosphere. The purities of raw materials were 99.9% for La and 99.99% for Fe, Co and Si. An excess mass of elemental La, ~5%, was empirically added to the raw materials to compensate for its loss during melting. The samples were melted four times to ensure homogeneity. Individual samples had a mass of about 1.0 g after melting. They were sealed in an evacuated quartz tube and annealed at 1523 K for 4 h.

The crystal structure of the samples was studied in situ using high-energy X-ray diffraction (HEXRD) with a wavelength of $\lambda = 0.11725$ Å at the beam line ID-11-C of the Advanced Photon Source, Argonne National Laboratory. The samples were crushed into fine powders of approximately 45 μm in diameter and compacted into an epoxy resin pipe. In the measurements, the samples were heated to 400 K and then cooled down to 90 K in a step wise manner. The temperature of the samples was measured with an accuracy of ±1 K using a sensor placed close to the sample. At each temperature step, the samples were held for 3 min to achieve a thermally stabilized state. The diffraction rings of the samples were captured using a 2D detector and were integrated using the Fit-2D software. The lattice parameters and bond lengths of the samples were obtained by Rietveld refinement using the General Structure Analysis System (GSAS) software [17]. Small cubes were cut from the annealed bulk samples of $LaFe_{11.5}Si_{1.5}$ and $LaFe_{10.5}CoSi_{1.5}$ to perform mechanical measurements using a resonant ultrasonic spectroscopy (RUS) probe. The elastic moduli of the samples at room temperature were obtained by an analysis of resonant frequencies. The magnetization measurements were performed using a vibrating sample magnetometer (VSM) attached to Quantum Design Superconducting Quantum Interference Device (SQUID). Isothermal magnetization data were obtained crossing the Curie temperature with a step of 5 K under the magnetic field of 0-2 T.

Results

Figure 1 shows the HEXRD patterns of the $LaFe_{11.5}Si_{1.5}$ and $LaFe_{10.5}CoSi_{1.5}$ samples during cooling. The samples crystallize mainly into the $NaZn_{13}$-type cubic structure after the short time annealing. However, they contain a small amount of secondary phases, which were identified as LaFeSi and La(Fe, Co)Si of a tetragonal structure, respectively. When the samples are cooled, the diffraction peaks of the

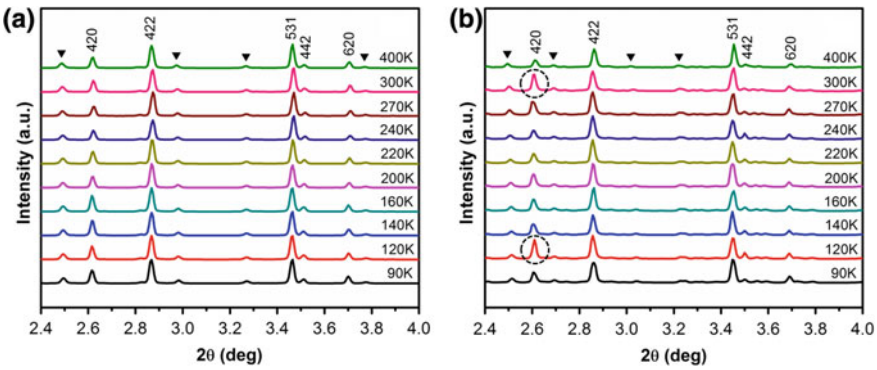

Fig. 1 Powder X-ray diffraction patterns of the polycrystalline samples of the $LaFe_{11.5}Si_{1.5}$ (**a**) and $LaFe_{10.5}CoSi_{1.5}$ (**b**) compounds during cooling. The dashed circles represent the (420) diffraction peak of $LaFe_{10.5}CoSi_{1.5}$ in which a higher intensity shows at the temperature of 300 and 120 K compared to other temperatures. (hkl) represents the 1:13 phase, ▼represents the secondary phase (1:1:1 phase)

cubic phase show an obvious shift due to thermal expansion. No new diffractions were detected during cooling, indicating that their crystal structures are not changed. The only difference is that the (420) diffraction peak of $LaFe_{10.5}CoSi_{1.5}$ shows a high intensity at the temperature of 300 and 120 K compared to other temperatures. This phenomenon implies that a temporary strain occurs to in the samples which results from the thermal stress during cooling.

Figure 2 shows temperature dependence of lattice parameters of the two samples during cooling. The lattice parameter of $LaFe_{11.5}Si_{1.5}$ shows normal contraction at temperatures above 240 K. A negative expansion phenomenon was observed in the temperature range 150–240 K. After cooling below 150 K, the lattice parameter shows little change with temperature. Such observations agree with neutron diffraction studies of similar materials by Wang et al. [15] and Rosca et al. [16]. However, the change of the lattice parameters of the present samples crossing the ferromagnetic transition is sluggish compared to observations of those studies. The negative expansion of $LaFe_{10.5}CoSi_{1.5}$ occurs at a higher temperature than that of the Co-free sample. Note that the lattice parameter and the unit cell volume of $LaFe_{10.5}CoSi_{1.5}$ are enlarged by 0.18% and 0.54%, respectively, compared to those of the Co-free sample. Such changes suggest that the partial substitution of Co for Fe reduces the negative thermal expansion.

Figure 3 shows variations of lengths of chemical bonds of the samples. Attention is paid to the interatomic distances between neighboring Fe atoms, which determine ferromagnetism of the bulk material. There are four kinds of Fe_2-Fe_2 bond lengths in the $La(Fe, Si)_{13}$ lattice. Two kinds lie in the same icosahedron (denoted as Fe_2-Fe_2_a and Fe_2-Fe_2_b), whereas the other kinds lie between neighboring icosahedra (denoted as Fe_2-Fe_2_c and Fe_2-Fe_2_d). As shown in Fig. 3a, the lengths of the four kinds of Fe_2-Fe_2 bonds show similar changes with

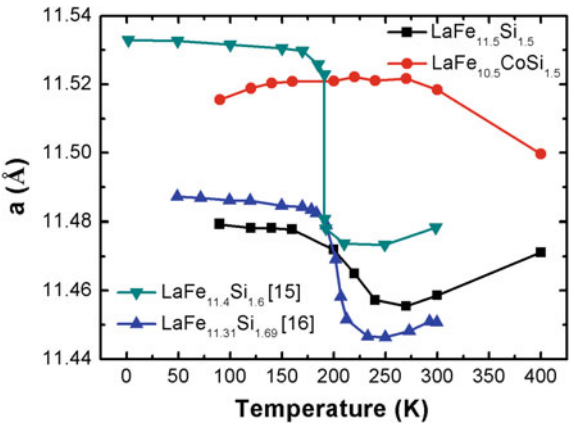

Fig. 2 Temperature dependence of lattice parameters of the $LaFe_{11.5}Si_{1.5}$, $LaFe_{10.5}CoSi_{1.5}$, $LaFe_{11.4}Si_{1.6}$ and $LaFe_{11.31}Si_{1.69}$ compounds during cooling

decreasing temperature. With the partial substitution of Co for Fe, the four kinds of Fe_2-Fe_2 bond lengths are increased by 0.52% relative to their values at room temperature. As shown in Fig. 3b, the variations of the lengths of the La-Fe_2 and Fe_1-Fe_2 bonds during cooling are similar to those of the lattice parameters. With the partial substitution of Co for Fe, both the La-Fe_2 and the Fe_2-Fe_2 bond lengths are increased by 0.52% relative to the Co-free sample at room temperature. Such changes are equivalent to those observed for the Fe_2-Fe_2 bonds.

Figure 4a and Figure 4b show isothermal magnetization curves of $LaFe_{11.5}Si_{1.5}$ and $LaFe_{10.5}CoSi_{1.5}$, respectively. At low temperatures, the curves display a characteristic ferromagnetic behavior. The magnetization is small when a low magnetic field is applied at temperatures above T_C. The magnetization increases with decreasing temperature. By integration of the measured data of isothermal magnetization, the maximum magnetic entropy changes of $LaFe_{11.5}Si_{1.5}$ and $LaFe_{10.5}CoSi_{1.5}$ were determined to be 7.85 and 5.14 J kg^{-1} K^{-1} for a change of the magnetic field of 2 T, respectively.

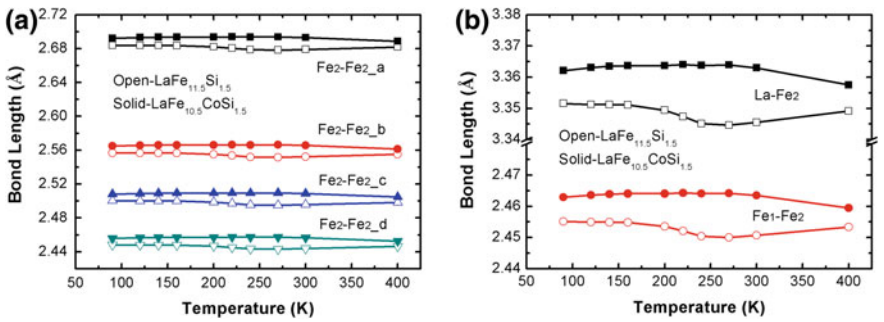

Fig. 3 Temperature dependence of **a** Fe_2-Fe_2 and **b** La-Fe_2, Fe_1-Fe_2 bond lengths of the $LaFe_{11.5}Si_{1.5}$ and $LaFe_{10.5}CoSi_{1.5}$ compounds during cooling

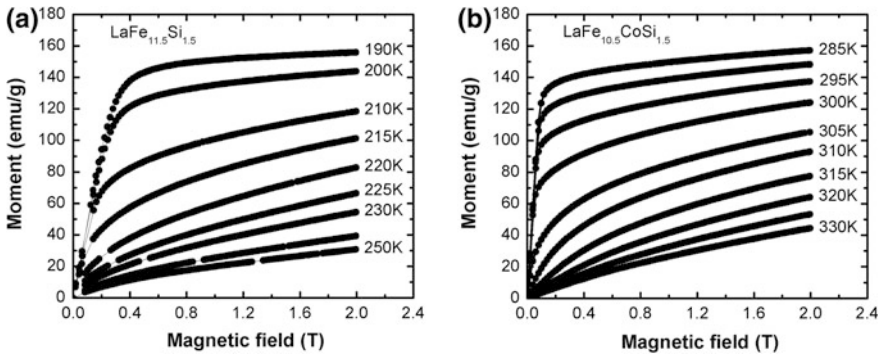

Fig. 4 The isothermal magnetization curves of **a** $LaFe_{11.5}Si_{1.5}$ and **b** $LaFe_{10.5}CoSi_{1.5}$ under the maximal magnetic field of 2 T

Table 1 Elastic moduli, Young's moduli and Poisson's ratio of $LaFe_{11.5}Si_{1.5}$ and $LaFe_{10.5}CoSi_{1.5}$ at room temperature

Sample	Longitudinal modulus (GPa)	Shear modulus (GPa)	Young's modulus (GPa)	Poisson's ratio
$LaFe_{11.5}Si_{1.5}$	134.53	44.05	110.70	0.257
$LaFe_{10.5}CoSi_{1.5}$	111.42	43.49	102.63	0.180

Table 1 shows the measured elastic moduli, Young's moduli and Poisson's ratio of $LaFe_{11.5}Si_{1.5}$ and $LaFe_{10.5}CoSi_{1.5}$. The Young's moduli and Poisson's ratio were calculated in terms of the measured longitudinal moduli and the shear moduli. The $LaFe_{10.5}CoSi_{1.5}$ sample shows soft elastic moduli at room temperature compared to the Co-free sample. This difference reflects a critical influence of the Co substitution for Fe on the lattice as discussed below.

Discussion

Sluggishness of Negative Thermal Expansion

The present results showed sluggish changes of the lattice parameter of $LaFe_{11.5}Si_{1.5}$ crossing its ferromagnetic transition compared with previous observations [15, 16]. This difference can be attributed to a difference in the sample preparation conditions. In this study, the annealing time is much shorter while the annealing temperature is higher. Although the present sample was determined to crystallize mainly into the $NaZn_{13}$-type cubic phase, diffusion of atoms may not be sufficient to achieve chemical homogeneity on a microscopic scale. It was shown elsewhere [5] that primary α-(Fe, Si) phase has a higher Si concentration than that

of the bulk material. Accordingly, the grains of La(Fe, Si)$_{13}$ have a lower Si concentration as a peritectic solidification product. During annealing, insufficient diffusion of Si atoms will bring about a gradient of the Si concentration inside the grains of La(Fe, Si)$_{13}$. In other words, some regions are rich in Si, whereas other regions are depleted in Si. This variation of local Si concentration can bring about a distribution of the ferromagnetic transition temperature. As a result, the negative thermal expansion crossing the ferromagnetic transition becomes sluggish. The same inhomogeneity of distribution of elemental Si may exist in the Co-doped sample. Thus, the slower increase of the negative thermal expansion is also expected. For this reason, the annealing time of the samples needs to be increased in order to ensure a chemical homogeneity on a scale of lattice parameters, i.e. on a nanometer scale.

Mechanism of the Influence of Co Doping on T_C

Observed effects of alloying elements on the T_C of La(Fe, Si)$_{13}$ were often correlated to enlargement or shrinkage of the cubic lattice. As shown in Fig. 5, this correlation is true for the T_C and lattice parameters of Co- or H-doped La(Fe, Si)$_{13}$ compounds as a function of doping amount [18–21]. However, the correlation fails between the T_C and lattice parameter of LaFe$_{13-x}$Si$_x$ [22, 23]. A high Si concentration increases the T_C but reduces the lattice parameter. Therefore, it is not reasonable to correlate the change of the T_C with the change of the lattice parameter. Rather, it is reasonable to correlate the increase of the T_C by chemical modification of La(Fe, Si)$_{13}$ to a change of Fe-Fe magnetic interactions [15, 16]. It is known that the Fe-Fe magnetic interactions depend critically on the distances between neighboring Fe atoms, i.e. the lengths of Fe-Fe bonds [24]. As the bond length is shorter than 2.45 Å, the anti-ferromagnetic coupling is stronger than the ferromagnetic coupling is. The ferromagnetic coupling becomes stronger if the bond length is larger than 2.45 Å. The present work showed that the partial substitution of Co for Fe elongates the Fe-Fe bond lengths. This structural change promotes the ferromagnetic coupling between Fe atoms leading to a more stable ferromagnetic phase. As a result, the T_C is increased.

Mechanism of the Influence of Co Doping on the MCE

According to the work by Jia et al. [25] and Mukherjee et al. [26], the experimentally observed magnetic entropy change, namely apparent magnetic entropy change, of a ferromagnetic material actually represents a sum of the net change of magnetic entropy and the change of the lattice entropy, if the electronic entropy can be ignored. Moreover, the lattice entropy change, arising from the change of lattice vibration at the ferromagnetic transition, is large and cancels out much of the magnetic entropy change of La(Fe, Si)$_{13}$ [25, 27]. It was determined that the

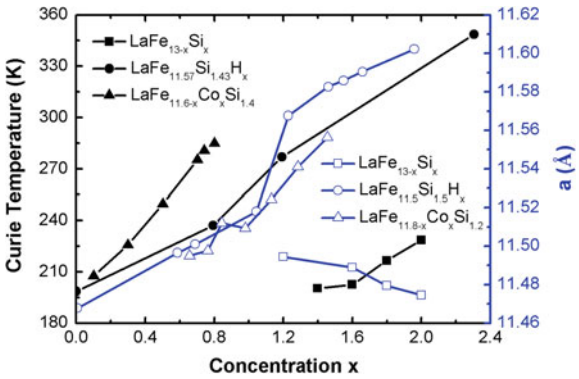

Fig. 5 Concentration dependence of Curie temperature and lattice parameters during cooling. The change of the Curie temperature of $LaFe_{13-x}Si_x$ ($1.4 \leq x \leq 2.0$), $LaFe_{11.57}Si_{1.43}H_x$ ($0 \leq x \leq 2.3$), $LaFe_{11.6-x}Co_xSi_{1.4}$ ($0.1 \leq x \leq 0.8$) compounds with concentration x. The lattice parameters of $LaFe_{13-x}Si_x$ ($1.2 \leq x \leq 2.0$), $LaFe_{11.5}Si_{1.5}H_x$ ($0 \leq x \leq 2.0$), $LaFe_{11.8-x}Co_xSi_{1.2}$ ($0.66 \leq x \leq 1.45$) compounds at room temperature. Data are taken from Refs. [17–22]

magnetic moments of Co and Fe atoms of La(Fe, Co, Si)$_{13}$ are 1.72 μ_B and 2.22 μ_B, respectively [18]. Thus, the magnetic entropy change decreases upon the substitution of Co for Fe. Balli et al. [28] reported that the magnetic entropy change is decreased by about 46% upon the substitution of 0.6 at.% Co for Fe. Similarly, the magnetic entropy change is decreased by about 34.5% in the present study. This decrease cannot be explained by considering the difference in the magnetic moments of Co and Fe atoms only. Apparently it is the influence of Co doping on the configurational entropy related to the microscopic chemical homogeneity that causes a more rapid decrease of the apparent magnetic entropy change. According to the present results, the doping of Co causes more inhomogeneous changes of bond lengths with declining temperature. In this sense, the doping of Co atoms may have enlarged the configurational entropy change leading to a larger reduction of the magnetic entropy change.

A linear decrease of Young's modulus with increasing temperature was observed for $LaFe_{10.54}Co_{1.43}Si_{1.03}$, and attributed to the increase of the thermal vibrations [29]. It was supposed that large vibrations of atoms increase the mean lattice parameter and thus weaken the bonding between magnetic atoms [29]. In this study, the lattice expansion and the softening of the elastic moduli were observed in the Co-doped sample at room temperature. Both changes may enlarge the thermal vibrations and therefore are responsible for the reduced magnetic entropy change of the Co-doped sample.

Conclusion

The crystal structure, magnetocaloric properties and elastic moduli of the $LaFe_{11.5}Si_{1.5}$ and $LaFe_{10.5}CoSi_{1.5}$ samples have been investigated. The $LaFe_{10.5}CoSi_{1.5}$ sample shows a higher T_C, a reduced MCE and softer room-temperature elastic moduli than those of the $LaFe_{11.5}Si_{1.5}$ sample. The higher T_C can be attributed to the increase of the Fe-Fe bond lengths by the Co substitution for Fe, which promotes the ferromagnetic coupling. On the other hand, the substitution of Co for Fe enlarges the configurational entropy of the cubic lattice and thus causes the rapid decrease of the MCE together with a magnetic diluting effect.

Acknowledgements This work is financially supported by the National Basic Research Program of China (2012CB619405) and by the National Natural Science Foundation of China (50671024). David Mandrus and Jiaqiang Yan acknowledge support from the National Science Foundation under Grant No. DMR-1410428. The authors thank Michael Koehler for his help in the RUS measurements. Dan Huang and Ronghui Kou thank the China Scholarship Council for granting a CSC fellowship. This research used resources of the Advanced Photon Source, a U.S. Department of Energy (DOE) Office of Science User Facility operated for the DOE Office of Science by Argonne National Laboratory under Contract No. DE-AC02-06CH11357.

References

1. Pecharsky VK, Gschneidner KA Jr (1997) Phys Rev Lett 78:4494
2. Wada H, Tanabe Y (2001) Appl Phys Lett 79:3302
3. Tegus O, Brück E, Buschow K, De Boer F (2002) Nature 415:150
4. Zhang XX, Wen GH, Wang FW, Wang WH, Yu CH, Wu GH (2000) Appl Phys Lett 77:3072
5. Niitsu K, Kainuma R (2012) Intermetallics 20:160
6. Liu XB, Altounian Z, Tu GH (2004) J Phys: Condens Matter 16:8043
7. Katter M, Zellmann V, Reppel GW, Uestuener K (2008) IEEE Trans Magn 44:3044
8. Palstra TTM, Mydosh JA, Nieuwenhuys GJ, Van der Kraan AM, Buschow KHJ (1983) J Magn Magn Mater 36:290
9. Hu FX, Shen BG, Sun JR, Wang GJ, Cheng ZH (2002) Appl Phys Lett 80:826
10. Fujita A, Fujieda S, Fukamichi K, Yamazaki Y, Iijima Y (2002) Mater Trans 43:1202
11. Kim Anh DT, Thuy NP, Duc NH, Nhien TT, Nong NV (2003) J Magn Magn Mater 262:427
12. Fujieda S, Fujita A, Fukamichi K, Hirano N, Nagaya S (2006) J Alloys Compd 408:1165
13. Fujieda S, Fujita A, Fukamichi K (2007) J Magn Magn Mater 310:e1004
14. Fujita A, Akamatsu Y, Fukamichi K (1999) J Appl Phys 85:4756
15. Wang FW, Wang GJ, Hu FX, Kurbakov A, Shen BG, Cheng ZH (2003) J Phys: Condens Matter 15:5269
16. Rosca M, Balli M, Fruchart D, Gignoux D, Hlil E-K, Miraglia S, Ouladdiaf B, Wolfers P (2010) J Alloys Compd 490:50
17. Toby BH (2001) J Appl Crystallogr 34:210
18. Chen X, Chen YG, Tang YB (2012) Bull Mater Sci 35:175
19. Lyubina J, Gutfleisch O, Kuz'min MD, Richter M (2009) J Magn Magn Mater 321:3571
20. Rosendahl Hansen B, Theil Kuhn L, Bahl CRH, Lundberg M, Ancona-Torres C, Katter M (2010) J Magn Magn Mater 322:3447
21. Jia L, Sun JR, Shen J, Gao B, Zhao TY, Zhang HW, Hu FX, Shen BG (2011) J Alloys Compd 509:5804

22. Phejar M, Paul-Boncour V, Bessais L (2010) Intermetallics 18:2301
23. Jia L, Sun JR, Zhang HW, Hu FX, Dong C, Shen BG (2006) J Phys: Condens Matter 18:9999
24. Li ZW, Morrish AH (1997) Phys Rev B 55:3670
25. Jia L, Liu GJ, Sun JR, Zhang HW, Hu FX, Dong C, Rao GH, Shen BG (2006) J Appl Phys 100:123904
26. Mukherjee T, Michalski S, Skomski R, Sellmyer DJ, Binek C (2011) Phys Rev B 83:214413
27. Gruner ME, Keune W, Cuenya BR, Weis C, Landers J, Makarov SI, Klar D, Hu MY, Alp EE, Zhao J, Krautz M, Gutfleisch O, Wende H (2015) Phys Rev Lett 114:057202
28. Balli M, Fruchart D, Gignoux D (2007) J Phys: Condens Matter 19:236230
29. Kaeswurm B, Barcza A, Vögler M, Geiger P, Katter M, Gutfleisch O, Cohen L (2017) J Alloys Compd 697:427

Part VII
Advanced Real Time Optical Imaging

Mass Transfer in High-Temperature Laser Confocal Microscopy

Stephano P. T. Piva, Dai Tang, Deepoo Kumar and Petrus Christiaan Pistorius

Abstract High-temperature laser confocal microscopy allows in situ observation of the sample surface while the temperature and gas atmosphere are controlled. Because of the relatively small sample size (diameter around 5 mm) mass transfer between the sample and the furnace atmosphere can be rapid. When studying liquid steel samples, evaporation from the steel surface can be sufficiently rapid to influence observations. In previous work, magnesium oxide inclusions (at the surface of liquid steel) were shown to shrink by dissolution, during observation by laser confocal microscopy. Inclusion dissolution was driven by evaporation of magnesium from the steel surface. In the work presented here, the rate of sample-gas mass transfer in a high-temperature confocal microscope was measured based on evaporation of manganese. The mass transfer rate can be estimated by simple static diffusion from the sample surface.

Keywords Confocal laser scanning microscopy · Mass transfer Evaporation · High temperature observation

Introduction

For more than two decades, groundbreaking research in Materials Science has used high-temperature confocal scanning laser microscopy (HT-CSLM). The technique enables in situ observation of materials up to 1700 °C with versatility of experimental design, permitting the use of different gaseous atmospheres and a wide range of possible sample heating and cooling rates. Assessing the possible phenomena occurring in a HT-CSLM experiment is necessary to critically interpret the outcomes and design new experiments.

S. P. T. Piva · D. Tang · D. Kumar · P. C. Pistorius (✉)
Department of Materials Science and Engineering, Center for Iron and Steelmaking Research, Carnegie Mellon University, 5000 Forbes Avenue, Pittsburgh, PA 15213, USA
e-mail: pistorius@cmu.edu

The Minerals, Metals & Materials Society, *TMS 2018 147th Annual Meeting & Exhibition Supplemental Proceedings*, The Minerals, Metals & Materials Series,
https://doi.org/10.1007/978-3-319-72526-0_18

HT-CSLM has been very important in the observation of non-metallic inclusions in steel and the behavior of these particles at a gas-liquid interface [1, 2]. Agglomeration and coarsening phenomena are of particular interest since the appearance of very large inclusions or clusters can induce mechanical failure by fatigue in parts made of steel [3] or cause clogging during continuous casting [4]. Their rate of removal also depends on their size distribution [5].

The large area-to-volume ratio of CSLM samples may cause rapid loss of solutes to the gas phase around the heated sample; this has been observed in previous work [6]. Another indication of mass transfer to the gas (in our laboratory) is the deposition of alloying elements, fumed from a molten high-alloy steel sample, on the CSLM chamber walls. In this paper, the gas mass transfer coefficient is quantified using molten manganese and iron-manganese alloys, measuring mass loss by evaporation.

Experimental Work

The high-temperature confocal laser scanning microscope setup used is shown in Fig. 1. The Fe-Mn alloys were pre-melted from electrolytic iron and electrolytic manganese in an induction furnace. Samples of pure manganese and Fe-Mn alloys were weighed and placed in dense alumina crucibles (9 mm outer diameter × 4 mm high). The crucible containing the metallic sample was placed on the B-type thermocouple sample holder inside the CSLM chamber; the chamber was evacuated and then backfilled with Cu and Mg-gettered Ar ($p_{O_2} \sim 10^{-20}$ atm). The volumetric flowrate of Ar at the inlet was maintained at 250 cm^3/min (for 25 °C and 1 atm), with an overpressure of 10 kPa inside the chamber. After stability of atmosphere oxygen content was reached (measured with an oxygen probe in the gas outlet; see Fig. 1), the sample was heated to a temperature above melting point at a heating rate of 500 K/min and then held at temperature for a defined time. After holding, heating was turned off and the samples were quenched by the Ar atmosphere. The weight of the resulting metal droplet was measured using a 0.0001 g resolution scale. The experiments are summarized in Table 1, also showing the calculated vapor pressures of Fe and Mn at the experimental temperatures [7].

Results

The results for weight loss in the HT-CSLM for each sample are listed in Table 2. The surface area of each sample was calculated assuming that the density of Mn is 5.95 g/cm^3 and that of the Fe-Mn alloys is 7 g/cm^3, when molten [8]. The samples were approximately hemispherical in shape.

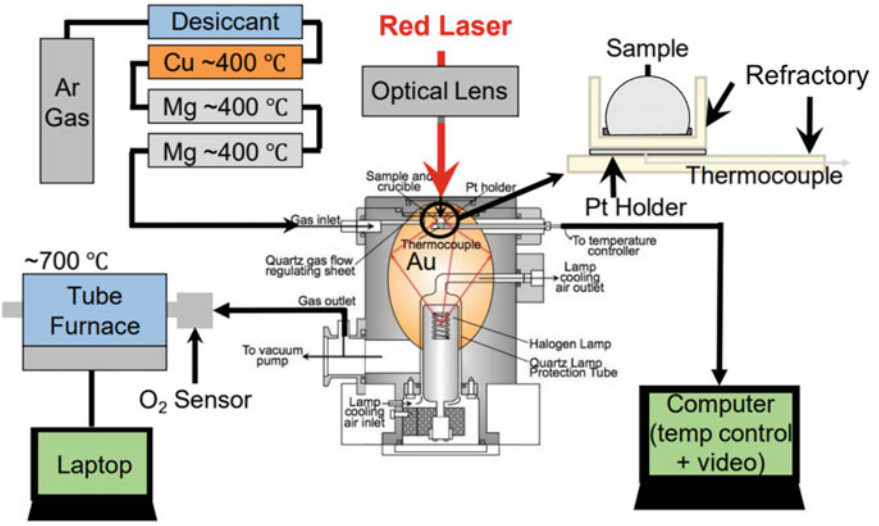

Fig. 1 Schematic of HT-CSLM used in the experiments

Table 1 Summary of specimens for Mn evaporation analysis in HT-CSLM

Sample	wt%Mn	Temperature (K)	Holding times (s)	p_{Mn} (Pa)	p_{Fe} (Pa)
Mn-100	100	1773	250, 375	2249	–
Mn-002	2	1823	1200	72	4
Mn-006	6	1823	600	217	4

Table 2 Manganese evaporation results from HT-CSLM

Sample	Initial mass (g)	Mass loss (g)	Surface area (cm^2)	Evaporative flux of Mn (10^{-3} mol/m^2s)
Mn-100-250 s	0.3395	0.0072	0.57	9.2
Mn-100-375 s	0.3323	0.0029	0.56	7.5
Mn-002-1200 s	0.3661	0.0013	0.54	0.4
Mn-006-600 s	0.3097	0.0018	0.48	1.1

The mass transfer expression for the rate of manganese loss due to evaporation from the surface of the molten metal can be written as in Eq. 1:

$$\frac{1}{A}\frac{dN}{dt} = k\left(\frac{p_{Mn}^{vap} - p_{Mn}^{atm}}{RT}\right) \tag{1}$$

In Eq. (1), A is the metal-gas area, N is moles of metal evaporating, k the mass transfer coefficient for gaseous mass transfer from the droplet surface, p_{Mn}^{vap} is the

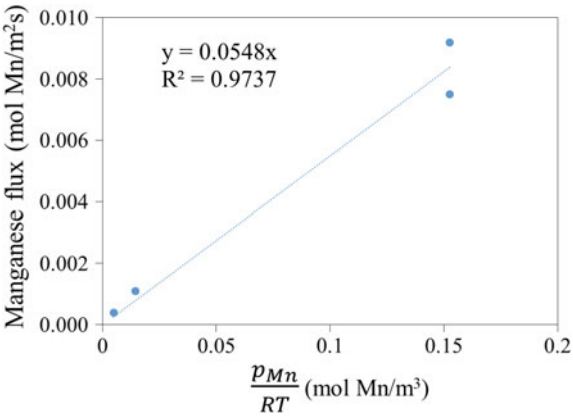

Fig. 2 Effect of equilibrium Mn concentration in gas on observed Mn flux

manganese vapor pressure at the droplet surface, $p_{\mathrm{Mn}}^{\mathrm{atm}}$ is the manganese pressure in the chamber, R is the ideal gas constant, and T is absolute temperature.

The concentration of metal in the chamber atmosphere is negligible, therefore $p_{\mathrm{Mn}}^{atm} = 0$. If it is assumed that the evaporation reaction is not rate determining (as shown in the next section), the experimental mass transfer coefficient for the gas phase can be obtained by a linear regression of the interfacial concentration of Mn given by its equilibrium vapor pressure and the observed molar flux of manganese. The obtained value of k_{gas} is 5.5×10^{-2} m/s (see Fig. 2).

Discussion

In the absence of mass transfer limitations, the maximum rate of evaporation as given by the Hertz-Knudsen equation [9] (Eq. 2):

$$\frac{1}{A}\frac{dN_{\mathrm{Me}}}{dt} = \frac{p_{\mathrm{Me}}^{vap}}{\sqrt{2\pi M_{\mathrm{Me}} RT}} \tag{2}$$

In Eq. 2, $p_{\mathrm{Me}}^{\mathrm{vap}}$ is the equilibrium vapor pressure of the evaporating metal, and M_{Me} its molar mass. For pure manganese (vapor pressure as in Table 1) the maximum evaporation rate is 31 mol/m^{2}s, which is several orders of magnitude larger than the experimental value. Therefore, mass transfer through the gas atmosphere from the droplet surface controls Mn removal.

The diffusivity of metallic atoms through argon were experimentally and theoretically assessed by Grieveson and Turkdogan [10, 11]. The Lennard-Jones potential parameters for metal vapor can be estimated using the molar volume and the boiling temperature [8, 12] of the liquid metal, using Eqs. 3 and 4 and the values in Table 3.

Table 3 Parameters used for Me-Ar binary diffusivity

Element	M[g/mol]	$V_m\left(\mathrm{cm^3 mol^{-1}}\right)$	$T_b(K)$	$\boldsymbol{\sigma}$[Å]	$\in/k$[K]
Ar	40.00	24.24	88	3.54	93
Mn	54.94	9.23	2235	2.44	2696
Fe	55.85	8.00	3023	2.33	3605

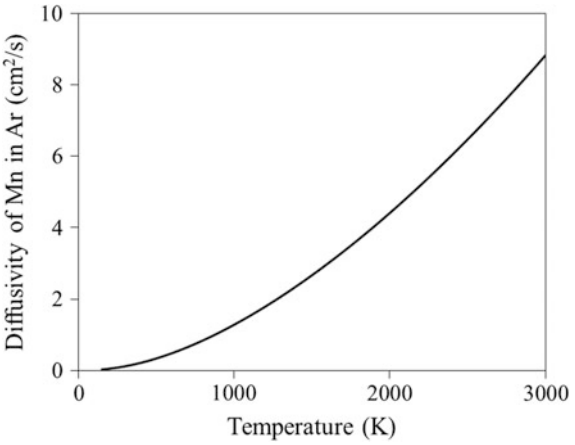

Fig. 3 Calculated binary diffusivity in Mn–Ar mixtures at different temperatures

$$\sigma = 1.166(V_m)^{1/3} \tag{3}$$

$$\frac{\in}{k} = 1.92(T_b) \tag{4}$$

Assuming that the enveloping gas is at 298 K and the droplet is at 1823 K, the diffusivity at the film temperature of 1061 K is estimated to be $1.3\,\mathrm{cm^2/s}$, or $1.3\times10^{-4}\,\mathrm{m^2/s}$. The droplet radius was 2.9 mm, so the characteristic length of the evaporating droplet was $d = 5.8\times10^{-3}$ m. The Sherwood number for mass transfer can be calculated using the experimental k_{gas}, calculated D_{Mn-Ar} and d (Fig. 3).

$$Sh = \frac{5.5\times10^{-2}\left[\frac{\mathrm{m}}{\mathrm{s}}\right]\times5.8\times10^{-3}[\mathrm{m}]}{1.3\times10^{-4}\left[\frac{\mathrm{m^2}}{\mathrm{s}}\right]} = 2.45 \tag{5}$$

The lower limit for the Sherwood number for spheres in a fluid is 2, which is the solution for the mass transfer differential equations of pure diffusion control in a static, infinite medium. Therefore, the gas regime surrounding the droplet in the confocal crucible must be close to stationary. The transversal cross-section of the ellipsoidal chamber in the position where the sample is maintained has a diameter

of 4 cm. In that region, the expected Reynolds number for Ar volumetric flowrate of 250 cm^3/min flowrate is 10, with an average velocity of 0.0033 m/s.

For a sphere, the Sherwood number can be calculated from the following Eq. [13]:

$$Sh = 2 + 0.552 Re^{1/2} Sc^{1/3} \tag{6}$$

For $Sh = 2.45$ and $Sc = 0.76$, the calculated Reynolds number is 0.8, which translates to an average velocity of 0.014 m/s. The creeping flow conditions found corroborates the case in which diffusion through the gas phase is the controlling factor for evaporation in HT-CSLM droplets.

Implications of Mass Transfer Phenomena in HT-CSLM Observations

There are several potentially reaction-limiting mechanisms of transport of chemical species in a HT-CSLM experiment, and they are represented in Fig. 4. Chemical reactions can be limited by transport through both boundary layers at an interface, or by transport of species in the bulk phases. Due to the high temperature, presence of both temperature and solutal gradients and large area-to-volume ratios of the materials employed in the experiment, transport in liquid can be controlled by convective and Marangoni flow, as experimentally assessed by Yin and Emi [14].

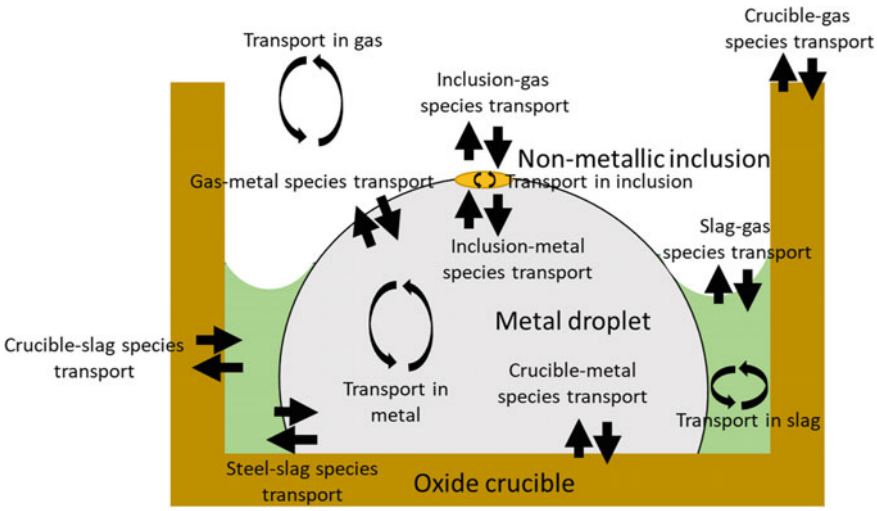

Fig. 4 Summary of transport mechanisms during a HT-CSLM experiment in the presence of a crucible containing a metal droplet and slag exposed to a gas atmosphere

Complex mass transfer effects have been reported in HT-CSLM observations. Mu et al. [6] discussed the dissolution of MgO inclusions in high-Al steels during in situ observation. In their study, Mg evaporation from the steel surface was relatively fast and Mg diffusion in steel (from dissolving MgO inclusions) was the rate-limiting step for inclusion disappearance. Crucible-steel reaction rates were insufficient to replenish Mg in steel to stabilize the MgO particles. In the presence of MgO-saturated slag, in a similar configuration to Fig. 4, MgO particles did not dissolve back, therefore reduction of Mg from slag by Al was fast enough to keep the steel saturated in Mg.

In another example of evaporation phenomena during HT-CSLM, Kumar and Pistorius [15] found MgO whisker growth at the top of the MgO crucible wall after melting Al-killed steel in contact with MgO-saturated slag. Evaporated Mg and trace O_2 in the gas reacted on the surface of slag droplets, with the slag acting as a catalyst that promoted directional growth of MgO crystals in the form of whiskers. As in the experiments of Mu et al., steel-slag reactions replenished Mg in steel while slag-crucible reactions maintained the slag MgO-saturated.

Story and Webler [16, 17] intentionally used mass transfer phenomena for in situ study of the effects of chemical composition and microstructure on high temperature oxidation of advanced high-strength steels (AHSS). This is an instance of gas-solid mass transfer effects, in which the partial pressure of oxygen was controlled using different gaseous mixtures of Ar-H_2-H_2O-(O_2). Gas flow over the surface of the samples did not generate a homogeneous oxide layer on the surface of the alloys, rather preferentially oxidizing the sharp edges of the sample where mass transfer is expected to be larger. However, a modified setup where the sample was placed inside a closed reaction tube provided a predictable parallel flow behavior over the surface of the sample disk, therefore eliminating gas-phase mass transfer as a rate-limiting step for surface oxidation. In this case, then, oxidation will be governed by transport of elements in the solid to the oxidation site.

Conclusions

Gas mass transfer can play a significant role during high-temperature confocal scanning laser microscopy. Evaporation experiments with manganese alloys show that a simple static-diffusion calculation can be used to estimate the gas mass transfer coefficient at the sample surface.

Acknowledgements We are grateful for support of this work by the industrial members of the Center for Iron and Steelmaking Research.

Financial support of Stephano P. T. Piva by CAPES under the process BEX 13379/13-5—Doutorado Pleno/Ciência sem Fronteiras is gratefully acknowledged.

References

1. Yin H, Shibata H, Emi T, Mikio S (1997) Characteristics of agglomeration of various inclusion particles on molten steel surface. ISIJ Int 37:946–955
2. Yin H, Shibata H, Emi T, Suzuki M (1997) "In-situ" observation of collision, agglomeration and cluster formation of alumina inclusion particles on steel melts. ISIJ Int 37:936–945
3. Murakami Y, Endo T (1980) Effects of small defects on fatigue strength of metals. Int J Fatigue 2:23–30. https://doi.org/10.1016/0142-1123(80)90024-9
4. Singh SN (1974) Mechanism of alumina buildup in tundish nozzles during continuous casting of aluminum-killed steels. Metall Trans 5:2165–2178. https://doi.org/10.1007/BF02643930
5. Suito H, Ohta H (2006) Characteristics of particle size distribution in early stage of deoxidation. ISIJ Int 46:33–41. https://doi.org/10.2355/isijinternational.46.33
6. Mu H, Zhang T, Yang L, Xavier RR, Fruehan RJ, Webler BA (2016) In situ observation of MgO inclusions in liquid iron-aluminum alloys. Metall Mater Trans B Process Metall Mater Process Sci 47:3375–3383. https://doi.org/10.1007/s11663-016-0794-7
7. Turkdogan ET, Fruehan RJ (1998) Ch. 2: Fundamentals of iron and steelmaking. In: The Making, Shaping and Treating of Steel, Steelmaking and Refining Volume, pp 13–157
8. Nasch PM, Steinemann SG (1995) Density and thermal expansion of molten manganese, iron, nickel, copper, aluminum and tin by means of the gamma-ray attenuation technique. Phys Chem Liq 29:43–58. https://doi.org/10.1080/00319109508030263
9. Hayes P (2013) Chemical reactions at moving surfaces: shape change, no phase change. In: Treatise on Process Metallurgy, pp 853–874
10. Grieveson P, Turkdogan ET (1964) Determination of interdiffusivities of argon and metal vapor mixtures at elevated temperatures. J Phys Chem 68:1547–1552
11. Turkdogan ET, Grieveson P, Darken LS, Edgar CU (1963) Enhancement of diffusion-limited rates of vaporization of metals. J Am Chem Soc 67:1647–1654. https://doi.org/10.1021/j100802a017
12. Ruben S (1985) Handbook of the elements
13. Froessling N (1938) Ueber die Verdunstung Fallender Tropfen (The Evaporation of Falling Drops). Gerlands Beitrage zur Geophys 52:107–216
14. Yin H, Emi T (2003) Marangoni flow at the gas/melt interface of steel. Metall Mater Trans B 34:483–493. https://doi.org/10.1007/s11663-003-0015-z
15. Kumar D, Pistorius PC (2017) Use of slag (CaO-Al_2O_3-SiO_2-MgO) droplet as a catalyst to grow MgO whiskers through VLS mechanism. Ceram Int 43:15478–15485. https://doi.org/10.1016/j.ceramint.2017.08.095
16. Story M, Webler B (2016) High-temperature oxidation of advanced high-strength steel. Paper presented in AISTech 2016, Pittsburgh, PA, 16–19 May 2016
17. Story M, Webler B (2017) Influence of microstructure on the kinetics of internal oxidation in a CMnSi advanced high-strength steel. Paper presented in AISTech 2017, Nashville, TN, 8–11 May 2017

Current State Art of Hot Thermocouple Technology—Novel Way for the Study of Mold Flux High-Temperature Properties

Lei Zhang, Wanlin Wang and Lejun Zhou

Abstract Hot Thermocouple Technology has been developed and approved to be a novel method to study the high-temperature related properties of molten slag. In this study, it will first give the development of Hot Thermocouple Technology, and its typical application to the mold flux. One example of crystallization process of the mold flux for casting low carbon (LC flux) and medium carbon steels (MC flux) were investigated by using Double Hot Thermocouple Technology (DHTT). The results of LC flux showed that, the glass phase firstly formed at the low temperature side; then, the fine crystals precipitated at the liquid/glass interface and grew toward glass and later on to liquid phase. However, the crystals directly formed at the low temperature side when MC flux was under cooling process and grew toward the high temperature side; which indicated the crystallization ability of MC flux was stronger than LC flux. Another crystallization sample of $CaO\text{-}SiO_2\text{-}B_2O_3$ based fluoride-free mold flux (F-free flux) was studied by using Single Hot Thermocouple Technology (SHTT), and the results showed the crystals first precipitated in the middle of sample and moved toward the thermocouple side, then the precipitated crystals grew up and new crystals formed in the middle of sample and moved toward the side, until the crystallization was completed and reached a steady state; the crystallization mechanism of the F-free flux was 1-dimensional growth.

Keywords Double hot thermocouple technology · Single hot thermocouple technology · Mold flux · Crystallization

Introduction

Mold flux plays an important role in the process of continuous casting, protecting the molten steel from oxidation, absorbing inclusions, providing the thermal insulation, lubricating the strand and controlling heat transfer between the mold and

L. Zhang · W. Wang (✉) · L. Zhou
School of Metallurgical Science and Engineering, Central South University, Changsha 410083, People's Republic of China
e-mail: Wanlin.Wang@gmail.com

The Minerals, Metals & Materials Society, *TMS 2018 147th Annual Meeting & Exhibition Supplemental Proceedings*, The Minerals, Metals & Materials Series,
https://doi.org/10.1007/978-3-319-72526-0_19

steel shell [1–4]. Among them, the heat transfer ability of mold flux directly determines the surface defects of as-cast slabs. Uneven heat transfer in the mold and rapid cooling can cause enormous thermal stress on the initial shell, introducing corner cracks, longitudinal face cracks, depressions, and other surface defects [5, 6]. In order to minimize stresses, the horizontal heat transfer from molten steel through mold flux film to water-cooled copper mold should be uniformly controlled to achieve a thin and uniform partially solidified shell. Mold flux crystallization is known to inhibit radiative heat from the steel and can create air gaps between the mold and partially solidified shell during the initial solidification of molten steel [7, 8], which increases the interfacial thermal resistance. Since a thick crystalline layer can resist the in-mold ferrostatic pressure [9]; it is usually achieved by improving the crystallization ability of mold flux to maintain a thick solid crystalline layer of slag film. Thus, the research on the crystallization of mold flux is a key parameter in the process of continuous casting.

A variety of methods have been used to determine crystallization property of mold flux. Differential Thermal Analysis (DTA) is the most common method for studying the crystallization of mold flux. In this case, the slag sample together with a reference substance is melted in a furnace and then cooled, the heat generation or heat absorption will take place when the sample occurs physiochemical reactions, then the temperature difference between the sample and the reference material will occur and be recorded. But, the method is limited to direct observation of the solidification phenomena and their accuracy as the heat change is easy to be affected by many environmental factors. Another technique is also frequently employed to determine the crystallization behavior of mold flux, which the slag sample is placed inside a metallic mold and heated at the temperature up to melting point of the mold flux for melting and then quenched [10–12]. After solidification, the sample can be tested at room temperature by Scanning Electron Microscope (SEM) and X-ray diffraction (XRD) to analyze the proportion of crystalline and the type of the crystalline phases. However, the technique also can not observe in situ the crystallization process of mold flux and does not provide a quantitative measurement to characterize the slag crystallization behavior.

To properly characterize the evolution process of crystallization, the crystal morphology and crystal growth rates, etc. The technique which combines hot thermocouple technique with video observation and image analysis was successfully developed in 1950s by Ordway [13] and Welch et al. [14]. Based on this, Ishii and Kashiwaya developed the double hot thermocouple method and applied to a microgravity experiment to determine the microstructural change of a superconducting oxide in 1992 [15–17]. And the double hot thermocouple technology first was applied in the research area of mold flux in 1995 [18, 19], from then it has been widely used to study the high-temperature properties of mold flux subsequently. In this paper, the crystallization process of mold flux for casting low carbon (LC flux) and medium carbon steels (MC flux) were investigated by using Double Hot Thermocouple Technology (DHTT) and the crystallization mechanism of the

CaO-SiO_2-B_2O_3 based fluoride-free mold flux (F-free flux) was also studied by Single Hot Thermocouple Technology (SHTT).

Experimental Apparatus and Method

Sample Preparation

The chemical compositions of the LC flux and MC flux and F-free flux are listed in Table 1. All samples were prepared from reagent grade chemicals of CaO, SiO_2, Li_2O, CaF_2, B_2O_3, and mechanical mixed prior to the placement inside the induction furnace, then it was heated to the melting point and held for 5 min to obtain a homogeneous melt. The molten slag was quickly poured onto a water-cooled copper plate to quench. The quenched samples were crushed and ground into powder samples for subsequent DHTT and SHTT experiments.

DHTT Experiments

The crystallization experiments of the mold flux for casting LC and MC steels were conducted by using DHTT, and the DHTT apparatus as shown in Fig. 1. Figure 1a is the illustration of DHTT, where is two B-type thermocouples (CH-1 and CH-2), and a desired temperature gradient between the two thermocouples can be achieved through controlling the temperature of each thermocouple separately. Meanwhile, the images of mold flux crystallization are observed through a microscope and recorded by a connected CCD onto a DVD.

For the DHTT experiments, the mold flux sample was first mounted on one of the two thermocouples; then, it was melted at 1773 K (1500 °C) with a rate of 15 K/s. After eliminating bubbles and homogenizing its chemical composition for 180 s, the mold flux was stretched to 2 mm by the two thermocouples. Then, the temperature of CH-2 was directly quenched with the maximum rate of 30 K/s to 1073 K (800 °C) to achieve the desired thermal gradient for the crystallization. The temperature controlling profile for the DHTT experiments is shown in Fig. 2.

Table 1 Chemical compositions of the mold fluxes after pre-melting (in Mass Pct)

	CaO/SiO_2 (C/S)	CaO	SiO_2	Na_2O	Li_2O	CaF_2	B_2O_3
LC flux	0.81	33.79	41.54	9.20	0.49	5.89	–
MC flux	1.32	43.51	32.86	5.11	0.5	3.92	–
F-free flux	1.15	41.80	36.38	7.97	2	–	5.83

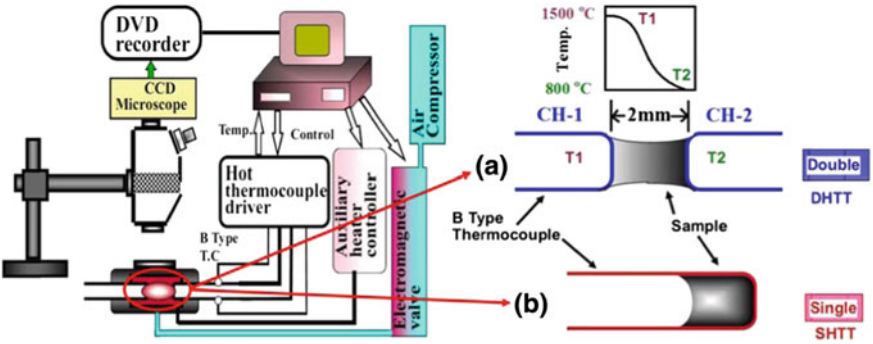

Fig. 1 The schematic of DHTT apparatus: **a** double and **b** single hot thermocouples

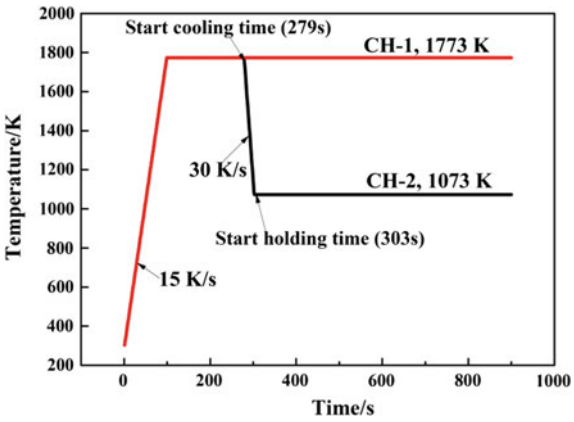

Fig. 2 The temperature controlling profile for DHTT experiments

SHTT Experiments

The crystallization mechanism of F-free flux was studied using SHTT, and the SHTT apparatus also as shown in Fig. 1. Figure 1b shows the schematic illustration of the SHTT, where is one of the two thermocouples, and the control of the temperature can be achieved through the corresponding auxiliary heater controller and its real-time temperature is recorded simultaneously. Also, the images of mold flux crystallization are observed through a microscope and recorded by a connected CCD onto a DVD.

For the SHTT experiments, the mold flux sample was first mounted on one thermocouple; and the sample was heated from room temperature to 1773 K at a rate of 15 K/s and held for 180 s to homogenize the chemical composition and minimize bubbles. Then, the molten slag was cooled at a rate of 30 K/s to various target temperatures to observe the isothermal crystallization for 600 s. The temperature controlling profile for the SHTT experiments is shown in Fig. 3.

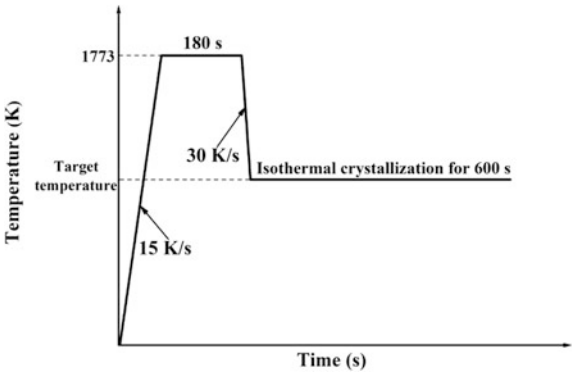

Fig. 3 The temperature controlling profile for SHTT experiments

Results and Discussion

The Evolution Crystallization Process of LC Flux and MC Flux for DHTT Experiments

Figure 4 shows the snapshots of the evolution crystallization process of LC flux for DHTT experiment. It can be seen that the mold flux is complete melted and is liquid when the two thermocouples are at 1773 K (Fig. 4a); then, the temperature of CH-1 thermocouple is kept 1773 K, while the temperature of CH-2 thermocouple is cooled to 1073 K with the rate of 30 K/s, this moment the mold flux near CH-1 side still as liquid and the mold flux near CH-2 side transform to glass phase (Fig. 4b); when the holding time reaches 82 s, some fine crystals precipitate at the liquid/glass interface, as shown in Fig. 4c; with time goes on, some dendritic crystals form in the middle of liquid mold flux and grow toward CH-1 side, as shown in Fig. 4d–g; when the holding time reaches 556 s, the crystallization is finished and the structure of the whole mold flux step into a relative steady state, where a little mold flux near CH-1 side is liquid and a little mold flux near CH-2 side is glassy phase and the others are crystal phase (Fig. 4h). It can be concluded from the whole process that the incubation time of the LC flux is about 82 s and the complete crystallization time is about 556 s.

The snapshots of the crystallization evolution process of MC flux for DHTT experiment are shown in Fig. 5. It can be observed that the whole mold flux as liquid when the both thermocouples are at 1773 K (Fig. 5a); then, the dendritic crystals begin to precipitate near the CH-2 side during the cooling process of CH-2 (Fig. 5b); later on, the crystals grow from the low temperature CH-2 side to high temperature CH-1 side, as shown in Fig. 5c–e; and some crystals precipitate near the CH-1 side and grow toward the middle (Fig. 5f–g); after the crystallization time keeps 49 s, the crystallization is completed and reaches a steady state, where a little liquid mold flux near CH-1 side and the others are crystal phase and no glass phase.

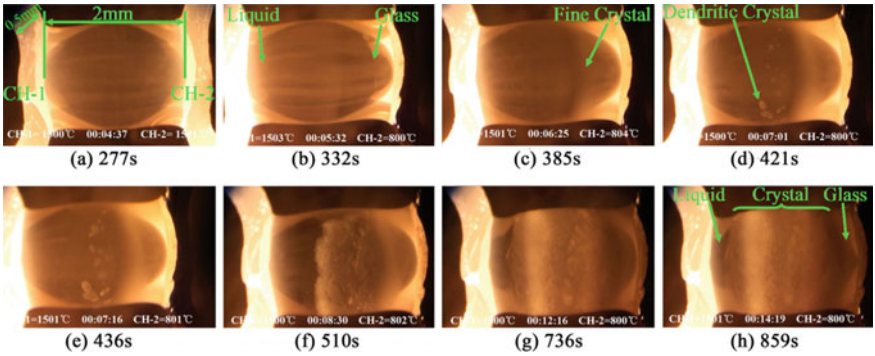

Fig. 4 The evolution process crystallization of LC flux for DHTT experiment [20]

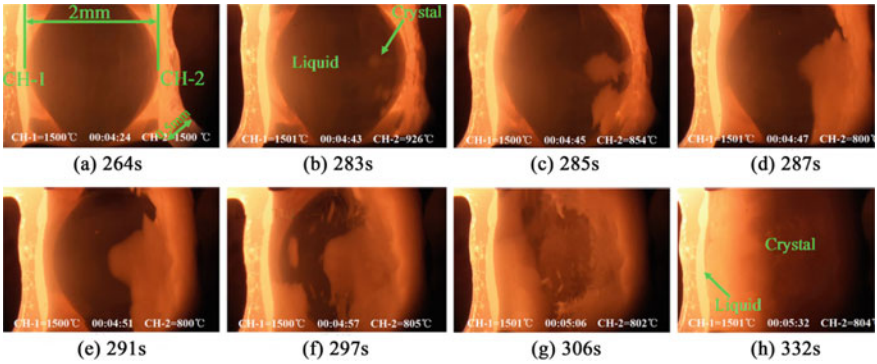

Fig. 5 The evolution process crystallization of MC flux for DHTT experiment [20]

It can be concluded from the whole process that the incubation time of the MC flux is about 0 s and the complete crystallization time is about 49 s.

Comparing with LC flux, the thickness of the MC flux crystal layer is thicker than LC flux, and the growth rate of MC flux crystal is much faster than LC flux. It indicates that the crystallization ability of MC flux is stronger than LC flux.

The Crystallization Mechanism of F-free Flux for SHTT Experiments

Figure 6 shows the snapshots of the evolution crystallization process of F-free flux at 1673 K (1400 °C) for isothermal crystallization using SHTT. It can be observed that the incubation time of F-free flux is 72 s and the complete crystallization time is about 156 s. The crystals first precipitate in the middle of sample and move

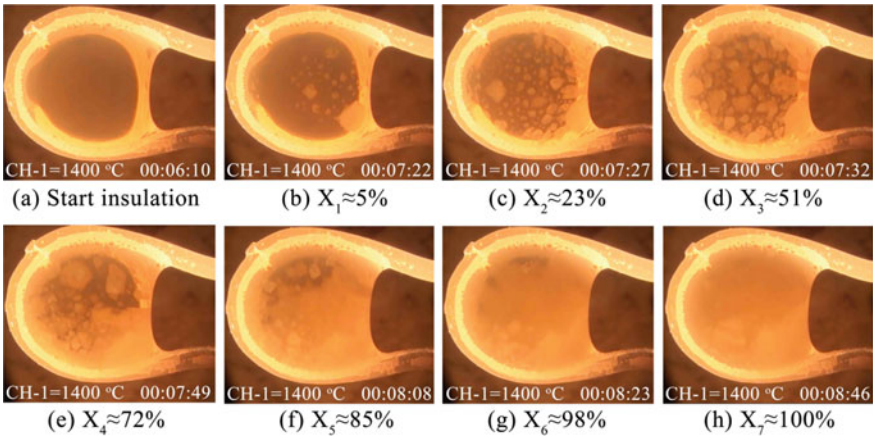

Fig. 6 The evolution process crystallization of F-free flux for SHTT experiment

toward the side. With the holding time goes on, the precipitated crystals grow up and meantime new crystals continue to precipitate in the middle and move toward the side of sample. Thus, the crystal volume fraction is becoming larger, until the crystallization is completed and reaches a steady state.

In order to study the crystallization mechanism of F-free flux, the Johnson-Mehl-Avrami (JMA) model [21, 22] need be applied in this work. According to the JMA model, the volume fraction of crystals (X) is given by

$$X = 1 - \exp\{-[k(t-\tau)]^n\} \tag{1}$$

where t is the crystallization time, τ is the incubation time, k is the constant of effective crystallization rate (including both nucleation and growth), and n is the Avrami exponent associated with nucleation and growth mechanism. The volume fraction of crystallization (X) obtained at a certain temperature was defined as $X = A_c/A_T$, where A_c is the area of the crystal and A_T is the total area of the mold flux. The values of X have been obtained by the above image analysis and shown in Fig. 6.

Therefore, the values of n and k can be determined according to the following equation by rearranging Eq. (1) into Eq. (2).

$$\ln\ln(1/1-X) = n\ln k + n\ln(t-\tau) \tag{2}$$

k and n can be acquired by plotting lnln(1/(1-X)) versus ln(t-τ), where n and k can be obtained from slope and intercept of the fitted line, respectively. The plots of ln [ln(1/(1-X))] as a function of ln(t-τ) and where n and k can be obtained are shown in Fig. 7. According to the corresponding relationship between n and the crystallization mechanism was given out by Christian [23], the value of n is about 1 indicates the crystallization mechanism of F-free flux is 1-dimensional growth.

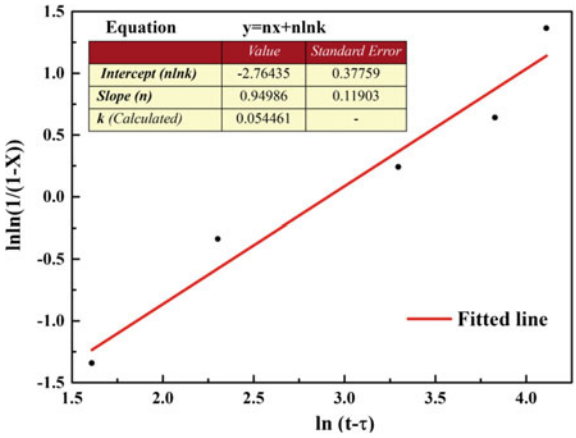

Fig. 7 The relation of crystal volume fraction evolution with function of time for F-free flux

Conclusions

In this paper, the development of Hot Thermocouple Technology has been introduced, and also crystallization process of the mold flux for casting low carbon (LC flux) and medium carbon steels (MC flux) by using Double Hot Thermocouple Technology (DHTT) and the crystallization mechanism of fluoride-free mold flux by using Single Hot Thermocouple Technology (SHTT) have been systematically studied. The main conclusions are summarized as follows:

(1) In the crystallization process of LC flux, the glass phase first formed when the CH-2 was quenched to 1073 K (800 °C) with the cooling rate of 30 K/s. Then, the fine crystal particles precipitated at the liquid/glass interface and grew toward the glass. The dendritic crystals later formed in the middle of the mold flux and grew toward the hot side. And the incubation time was about 82 s and the complete crystallization time was about 556 s.
(2) During the crystallization process of MC flux, the crystals formed directly near the CH-2 side during the cooling process of the CH-2 thermocouple. Then crystals began to precipitate near the CH-1 side and grew to the middle. The incubation time and the complete crystallization time was about 0 s and 49 s, individually. Comparing with LC flux, the thickness of the MC flux crystal layer was thicker than LC flux, and the growth rate of MC flux crystals was much faster than LC flux.
(3) The evolution crystallization process of F-free flux showed the crystals first precipitated in the middle of sample and moved toward the side, then the precipitated crystals grew up and new crystals formed and moved toward the side, until the crystallization was completed and reached a steady state. The results of crystallization kinetics indicated the crystallization mechanism of F-free flux was 1-dimensional growth.

References

1. Zhou LJ, Wang WL et al (2012) A kinetic study of the effect of basicity on the mold fluxes crystallization. Metall Mater Trans B 43(2):354–362
2. Mills KC, Fox AB, Li Z, Thackray RP (2005) Performance and properties of mould fluxes. Ironmak Steelmak 32(1):26–34
3. Wang WL, Cramb AW (2005) The observation of mold flux crystallization on radiative heat transfer. ISIJ Int 45(12):1864–1870
4. Yamauchi A, Sorimachi K, Sakuraya T, Fujii T (1993) Heat transfer between mold and strand through mold flux film in continuous casting of steel. ISIJ Int 33(1):140–147
5. Li C, Thomas BG (2004) Thermomechanical finite-element model of shell behavior in continuous casting of steel. Metall Mater Trans B 35(6):1151–1172
6. Sridhar S, Mills KC, Mallaband ST (2002) Powder consumption and melting rates of continuous casting fluxes. Ironmak Steelmak 29(3):194–198
7. Gu K, Wang WL, Zhou LJ et al (2012) The effect of basicity on the radiative heat transfer and interfacial thermal resistance in continuous casting. Metall Mater Trans B 43(4):937–945
8. Wang WL, Cramb AW (2010) Study of the effects of the mold surface and solid mold flux crystallization on radiative heat transfer rates in continuous casting. Steel Res Int 81 (6):446–452
9. Wei J, Wang WL et al (2014) Effect of Na_2O and B_2O_3 on the crystallization behavior of low fluorine mold fluxes for casting medium carbon steels. Metall Mater Trans B 45(2):643–652
10. Hering L, Heller HP, Fenzke HW (1992) Investigations for flux power selection in slab continuous-casting. Stahl Und Eisen 112(8):61–65
11. Sakai H, Kawashima T, Shiomi T, Watanabeand K, Iida T (1997) Molten the interface. In: The final step involves the dissolution of the Slags, Slags and Salts'97 Conference, Warrendale, PA
12. Bhamra M, Charlesworth M, Wong S, Sawyers VD, Cramb AW (1996). In: 54th Electric Furnace Conference, Dallas, TX, 9–12 Dec 1996
13. Ordway F (1952) Techniques for growing and mounting small single crystals of refractory compounds. National Bureau of Standards
14. Welch JH (1954) A simple microscope attachment for observing high-temperature phenomena. J Sci Instrum 31(12):458
15. Kuranaga T, Kashiwaya Y, Ishii K (1995). In: International Symposium on Advanced Materials and Technology for 2lst Century. JIM'95 Fall Meeting. Honolulu
16. Scholze H (1991) Glass: Nature. Structure and properties. Springer, Berlin
17. Uhlman DR (1983) Glass formation, a contemporary view. J Am Ceram Soc 66(2):95–100
18. Kashiwaya Y, Cicutti CE et al (1998) Development of double and for in situ observation and single hot thermocouple technique measurement of mold slag crystallization. ISIJ Int 38 (4):348–356
19. Kashiwaya Y, Cicutti CE, Cramb AW (1998) An investigation of the crystallization of a continuous casting mold slag using of the single hot thermocouple technique. ISIJ Int 38 (4):357–365
20. Zhou LJ, Wang WL, Huang DY et al (2012) In situ observation and investigation of mold flux crystallization by using double hot thermocouple technology. Metall Mater Trans B 43 (4):925–936
21. Sun NX, Liu XD, Lu K (1996) An explanation to the anomalous avrami exponent. Scripta Mater 34:1201–1207
22. Wang WL (2007) PhD thesis, Carnegie Mellon University
23. Christian JW (2002) The theory of transformations in metals and alloys, 3rd edn. Pergamon Press Ltd, London, UK

Part VIII
Algorithm Development in Materials Science and Engineering

Dislocation-Based Finite Element Modelling of Hydrogen Embrittlement in Steel Alloys

Amir Abdelmawla, Tarek M. Hatem and Nasr M. Ghoniem

Abstract Mechanical properties of many metals are greatly influenced by hydrogen solutes causing a well-known phenomenon of Hydrogen Embrittlement (HE). Hydrogen atoms affect the dislocation core, materials cohesion, and/or vacancies clustering causing the material capacity for plastic deformation to decrease. Such degradation in performance of metals leads to embrittlement resulting of catastrophic failure in structures. In this research, a physically-based constitutive model is developed to study hydrogen embrittlement in steel alloys. The developed model is an extension for Ghoniem-Matthews-Amodeo (GMA) dislocation-based model in order to predict the constitutive relation in the plastic regime for high strength steel alloys while considering hydrogen Effect on plasticity. The proposed physically-based dislocation-density model include the effect of hydrogen solute on dislocation mobility and interaction. The proposed model study the mechanical behavior of high-strength steel of HT-9 tensile test specimen.

Keywords Hydrogen embrittlement · Dislocation-based constitutive model Glide velocity

A. Abdelmawla · T. M. Hatem (✉)
Centre for Simulation Innovation and Advanced Manufacturing (SIAM), The British University in Egypt (BUE), El-Sherouk City, Cairo 11837, Egypt
e-mail: tarek.hatem@bue.edu.eg

A. Abdelmawla
e-mail: amir.abdelmawla@bue.edu.eg

T. M. Hatem
Microstructure Physics and Alloy Design Department, Max-Planck-Institut Fur Eisenforschung, 40237 Düsseldorf, Germany

N. M. Ghoniem
Department of Mechanical and Aerospace Engineering, University of California at Los Angeles (UCLA), 420 Westwood Plaza, Los Angeles, CA 90095-1597, USA
e-mail: ghoniem@ucla.edu

The Minerals, Metals & Materials Society, *TMS 2018 147th Annual Meeting & Exhibition Supplemental Proceedings*, The Minerals, Metals & Materials Series,
https://doi.org/10.1007/978-3-319-72526-0_20

Introduction

Hydrogen atoms are introduced inside the crystalline structure of materials as a result of processing and/or exposing of metals in hydrogen-rich environments. This introduction of hydrogen significantly impacts mechanical properties of metals and alloys through different embrittlement mechanisms. HE phenomena was firstly observed by Johnson more than a century ago when he studied the effect of the immersion in acids on the fracture properties of iron and steel [1]. Since then, many investigations have been conducting to well identify the HE phenomenon and its effect on the degradation of mechanical properties of materials. Such investigation are resulted in many published research articles such as the role of microstructure on HE [2], mechanisms of HE [3], and the hydrogen effect on mechanical properties and fracture behavior [4, 5]. Three mechanisms are adopted for explaining the degradation of materials in the presence of hydrogen atmosphere including, Stress-Induced Hydride Formation and Cleavage (SIHFC) [6, 7], Hydrogen Enhanced Localized Plasticity (HELP) and Hydrogen Induced Decohesion (HID) [5]. SIHFC embrittlement mechanism is observed in materials such as niobium and zirconium which hydrides can be easily formed at stress concentration zones such as crack tips. Such formation is accompanied by large amounts of plastic deformation. Thus, the phenomenon is characterized by a competition between plasticity, which is responsible for ductile fracture processes, and brittle fracture by stress-induced hydride formation and cleavage. As a consequence, hydrogen embrittlement by this mechanism is most severe at low strain rates and intermediate temperatures at which the mobility of hydrogen is sufficiently high such that hydrides can form and cleave faster than ductile fracture can occur because of the plastic deformation [6–9]. In systems that do not form hydrides, other mechanisms can lead the embrittlement process. In HELP mechanism, within certain range of temperatures and strain rates, the presence of hydrogen in solid solution decreases the barriers to dislocation motion, and such reduction in interaction energies between elastic stress centers impedes the dislocation mobility [10–14]. Sofronis and Birnbaum [12, 15] by analytical and numerical calculations showed that the interaction energies between dislocations and obstacles can be greatly reduced by the hydrogen atmospheres forming at the stress fields of the defects. These reduced interactions result in enhanced dislocation mobility, as has been supported by strong experimental evidence [12]. From a continuum mechanics point of view, enhanced dislocation mobility is associated with a reduced flow stress in the material [8]. HE through the decohesion mechanism is originally identified by Troiano [16]. The proposed H-enhanced decohesion mechanism states that hydrogen atoms are attracted to the crack tip, and this simply lowers the fracture energy by decreases the force required to separate the crystal along a crystallographic plane and ultimately the atomic bonding at the crack tip is weakened by the presence of hydrogen. As a results, the fracture toughness of steels is degraded and cleavage-like failure is encouraged [15]. However, this can occur only if the stress intensity for fracture is reduced below the value at which

dislocation emission occurs, which is the competing deformation mode that leads to crack blunting and defeats cleavage-like fracture [15]. This research mainly concerns with HELP mechanism and its effect on high strength steels. In this research, a comprehensive dislocation-based constitutive model for HE effects on material plasticity is developed. This model accounts for the effect hydrogen dislocations interactions and how the hydrogen affects the dislocation cores. A set of rate dependent ordinary differential equations are coupled with each other in order to develop a comprehensive model for HE in high strength steels. This includes, dislocation generation and multiplication, dislocation static and dynamic recovery rates, and the hydrogen effect on dislocation evaluation and mobility. The formulated model is then coupled with the ABAQUS CAE package through VUMAT user subroutine feature to simulate the plastic behavior of steel alloys at the continuum scale under the effect of HE. This paper is introduced in three sections such that the structure of the developed model is explained and presented in the second section, and the third section, meanwhile, presents the simulations and the associated results.

Methodology

Dislocation Generation and Interaction

The rates of mobile, immobile, and boundary dislocation densities that developed by Hatem and Zikry [17] and Ghoniem et al. [18]. Equations of mobile and immobile dislocation densities are reformulated to account for the dislocations interaction coefficients on the generalized model as well as to introduce the effect of hydrogen solutes on dislocation mobility. The evolution of mobile dislocation density during plastic deformation is proportional to the generation rate of dislocations minus the annihilation rate of dislocations due to dislocations interactions, the dynamic recovery, sub-boundary annihilation, and climb recovery. The mobile dislocations are generated due to dislocation forest sources which means the generation term is directly related to the immobile dislocations network. If the emitted dislocations from a source travel with a velocity v_g, the mobile dislocation generation rate is given by

$$\rho_{gen} = \varphi \, v_g \, \rho_{im}^{3/2} \tag{1}$$

where φ is a geometric parameter and ρ_{im} is the immobile dislocation density.

The dislocation density annihilation rates are related to the rate at which mobile segments are immobilized by interactions with dislocation densities during plastic deformation [19, 20]. The annihilation rate of dislocations depends on the interactions between mobile and immobile dislocation densities. The annihilation rates of mobile-mobile dislocations interaction and mobile-immobile dislocations

interaction depend on frequency with which mobile dislocations intersect mobile and immobile dislocations [21, 22] which are respectively given by the following formulas

$$\rho_{ann}^{+} = v_g \rho_m^2 g_{inter} \tag{2}$$

$$\rho_{ann}^{-} = v_g \rho_m \rho_{im} g_{inter} \tag{3}$$

It is shown in the previous equations, when a mobile dislocation interacts with an immobile dislocation to form a junction, this results in a rate of loss of mobile dislocation density and is the basis for the immobilization rate. It also results in a rate of loss of immobile dislocation density, in what follows, for a generalized recovery rate. The dynamic recovery rate ρ_{dyn} is also related to the frequency which immobile dislocations are intersected by mobile dislocations and the activation enthalpy H as well [17, 21, 22]. The activation enthalpy is related to the ratio of the immobile dislocation density to the saturation density. This can be recast as

$$\rho_{dyn} = v_g \rho_m \sqrt{\rho_{im}} \left[\exp\left(-\frac{H}{\kappa T} \left(1 - \sqrt{\frac{\rho_{im}}{\rho_{max}}} \right) \right) \right] \tag{4}$$

The dislocation annihilation rate at grain boundaries ρ_{subann} and rates of dislocation climb in bulk materials ρ_c and climb rate at walls ρ_{cw} are formulated by Ghoniem et al. [18] according to the following Eqs. (5)–(7)

$$\rho_{bouann} = \frac{v_g \rho_m}{R_{sb}} \tag{5}$$

$$\rho_c = \rho_m^{3/2} v_c \tag{6}$$

$$\rho_{cw} = \frac{v_{cw} \rho_{im}}{h} \tag{7}$$

where v_c is the dislocation climb velocity, v_{cw} is the dislocation climb velocity at wall, h is the spacing between dislocations at grain boundary, and R_{sb} is the radius of the grain. Dislocation climb velocity and climb velocity at barriers are given by the following equations

$$v_c = \left(\frac{2\pi}{b} \right) \left(\frac{\Omega \sigma_c}{\kappa T} \right) \left(e^{-\frac{\chi G \Omega}{\kappa T}} \right) \left(U_{so} e^{-\frac{U_s}{\kappa T}} \right) \left[\ln\left(\left(b^2 \rho_m \right)^{-0.5} \right) \right]^{-1} \tag{8}$$

$$v_{cw} = \left(\frac{2\pi}{b} \right) \left(\frac{\Omega \sigma_{cw}}{\kappa T} \right) \left(e^{-\frac{\chi G \Omega}{\kappa T}} \right) \left(U_{so} e^{-\frac{U_s}{\kappa T}} \right) \left[\ln\left(\left(\frac{b}{R_{sb}} \right)^{-0.5} \right) \right]^{-1} \tag{9}$$

where σ_c and σ_{cw} are the stresses that required for climb processes

$$\sigma_c = \frac{Gb\sqrt{\rho_m}}{\pi(1-\upsilon)} \tag{10}$$

$$\sigma_{cw} = \frac{Gb\sqrt{\rho_{im}}}{\pi(1-\upsilon)} \tag{11}$$

where G is the shear modulus, and b is the Burger vector.

Equations (2)–(11) are combined to obtain a coupled set of non-linear evolution equations for the mobile and immobile dislocation densities. To delineate dislocation activities such as generation, interaction, immobilization and annihilation, the evolution equations can be expressed as

$$\dot{\rho}_m = \rho_{gen} - \rho^{+}_{ann} - \rho^{-}_{ann} - \rho_{bouann} - \rho_c \tag{12}$$

$$\dot{\rho}_{im} = \rho^{+}_{ann} + \rho^{-}_{ann} + \rho_{dyn} + \rho_{bouann} - \rho_{cw} \tag{13}$$

Then, to calculate the rate of dislocation density at grain boundaries $\dot{\rho}_b$ and the nucleation rate of new grains $\dot{R}_{sb}$, Ghoniem et al. [18] proposed the following equations

$$\dot{\rho}_b = (1-2\zeta)\left[\frac{2v_{cw}\rho_{im}}{h}\right] \tag{14}$$

$$h = \frac{1}{\rho_s R_{sb}} \tag{15}$$

The rate of sub-grain radius is given by

$$\dot{R}_{sb} = \left[1 - 4N_p r_p^2 R_{sb}\right]^2 \left[\left(U_{so} e^{-\frac{U_s}{\kappa T}}\right)\left(\frac{G\Omega}{\kappa T}\right) R_{sb}^{-1}\right] - \left(\dot{\rho}_b R_{sb}\, \rho_s^{-1}\right) \tag{16}$$

The constitutive relation has been added to calculate stress as a function of the total strain and given by

$$\dot{\sigma} = E(\dot{\varepsilon} - \dot{\gamma}) \tag{17}$$

where $\dot{\varepsilon}$ is the strain rate and $\dot{\gamma}$ is the plastic share strain rate

Ultimately, Eqs. (12)–(14), (16), and (17) are gathered to shape a comprehensive physically-based constitutive model. Nevertheless, the effect of hydrogen is implemented in the dislocation glide velocity that formulate by Ghoniem et al. [18].

Dislocation Glide Velocity and Effect of Hydrogen Solutes

HE mainly results in drag effect on dislocation mobility and hydrogen induced stress due to lattice distortion when hydrogen diffuses inside the lattice, and hydrogen drag effect on dislocation mobility has the most dominant effect. In other words, hydrogen atmosphere mainly affects the dislocation core and this results in an additional frictional stress which shield (or weaken) the stress field of dislocations and effectively reduce their interactions with barriers. As a result, the dislocation glide motion is impeded. From the GMA model [18], the effective stress of the dislocation field is generally equal to the applied stress minus resistance stresses. The resistance stresses are caused by opposition to dislocation motion and there are many different processes responsible for their existence. One of these sources which opposes dislocation motion is due to the frictional resistance to glide from Cottrell atmosphere of solutes [15]. Therefore, the effective stress of dislocation can be constructed as a function of fractional stress exerted by hydrogen solute as follow

$$\sigma_e = \sigma_a - \sigma_{int} - \sigma_h \tag{18}$$

where σ_a is the applied stress, σ_{int} is the internal stress which arises from dislocation interaction with barriers, and σ_h is the hydrostatic stress in lattice due to the introduction of hydrogen atoms which is determined by the following equation

$$\sigma_h = -\frac{2EV_h(C_T - C_L)}{3(1-\upsilon)} \tag{19}$$

where V_h is the hydrogen partial molar volume which indicates the strained volume dilation in matrix due to the introduction of hydrogen, E is the Young's modulus, C_T is the hydrogen concentration in the trapped sites, C_L is the hydrogen concentration in lattice sites, and υ is the passion's ratio.

To calculate the hydrogen concentration in the dislocation core, Cottrell expression for solute atoms around dislocations is used, Eq. (20)

$$\frac{C_T}{1-C_T} = \frac{C_L}{1-C_L}\exp\left(-\frac{E_b}{\kappa T}\right) \tag{20}$$

where E_b is the binding energy between solute atoms and dislocations, κ is the Boltzmann constant, and T is the operating temperature.

The binding energy between hydrogen and defects is reduced by introduction of hydrogen in dislocation core [4]. The internal stress σ_{int} results due to dislocation-dislocation or dislocation-precipitate interactions which is defined by Ghoniem as follow

$$\sigma_{int} = \frac{Gb}{2\pi\lambda} \tag{21}$$

where λ is the spacing between dislocation and another dislocation or dislocation and precipitate, G is the shear modulus, and b is the magnitude of Burger vector. The spacing between dislocations through plastic deformation is stated by Ghoniem as follow

$$\frac{1}{\lambda} = \sqrt{\rho_m + \rho_{im}} + \sqrt{2N_p r_p} \tag{22}$$

where N_p and r_p are precipitate number and radius in the matrix respectively.

Two approaches are adopted to study the effect of HE mechanisms on plastic behavior of materials, open system and closed system and this research will only present the open system method. The open system approach is discussed by Hirth [4] which states that as long as the material exposed to hydrogen rich environment, the hydrogen will continue to enter into material lattice and diffuse to dislocation core. After filling dislocation core, the hydrogen then diffuses inside lattice sites of the material causing lattice distortion and exerts hydrostatic stress. Inside dislocation core, hydrogen increases the drag forces which reduces dislocation motion, interaction between mobile and immobile dislocations, and finally dislocation densities. This starts by defining the hydrogen concentration in lattice sites, C_L in ppm and the concentration in trapping sites, C_T is calculated from Eq. (20). The main effect of hydrogen solutes arises when solute atoms are trapped at the dislocation core which increases the drag effect on dislocation mobility. The glide velocity is formulated by Hirth [4] as follow

$$v_g = 2v_d \sinh\left(\frac{d_s b^2 \sigma_e}{\kappa T}\right)\left(e^{-\frac{E_g}{\kappa T}}\right) \tag{23}$$

where ν_d is the dislocation attempt frequency, d_s is the average distance between solute atoms inside the dislocation core, and E_g is the dislocation glide energy

The total hydrogen concentration, C_H, in open system is the summation of trapped and lattice concentrations

$$C_H = C_L + C_T \tag{24}$$

In this model, two limitations are introduced on the maximum and minimum number of hydrogen atoms inside the dislocation core and this is done based on the d_s parameter.

Results and Discussion

The developed model is implemented on both 1D and 3D analyses for both charged and uncharged high-strength steel tensile test specimen. 1D analysis is performed on an in-house code using 1D bar elements, while the 3D analysis is performed on Finite Element commercial package. Displacement boundary conditions are applied to count for the tensile load. Mesh convergence analysis and time step calculation were performed to insure numerical convergence and stability of the solution. The current study use the properties of HT-9 Martensitic High-Strength Steel Alloy as indicated in the Table 1.

Figure 1 presents the constitutive relation of the tested material in the presence and absence of hydrogen. It can be indicated that hydrogen atoms have a significant effect on the plastic behavior. A noticeable increase in the yield value of stress. Furthermore, as shown in Fig. 1, the slope of plastic part of the stress-strain curve in the charged specimen is lower than the uncharged specimen. The variation of hydrogen concentration inside the dislocation core with strain is plotted as presented in Fig. 2 which indicates the number of hydrogen atoms concentration that are trapped into dislocation core.

Table 1 Mechanical properties of HT-9 martensitic steel alloy

Parameter	Value
Young's modulus (GPa)	200
Poisson's ratio	0.30
Yield strength (MPa)	700
Burger's vector (m)	2.58E-10
Atomic volume (m)	1.19E-29

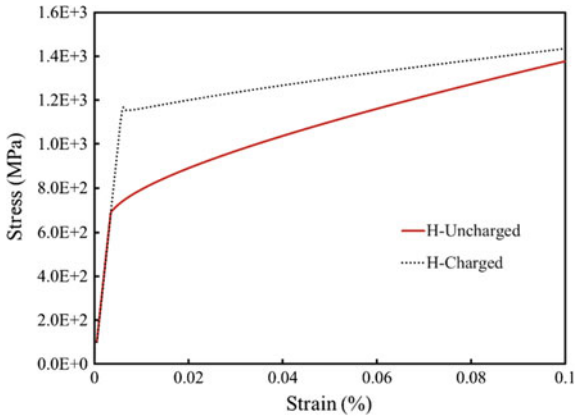

Fig. 1 Stress strain curve for charged and uncharged cases

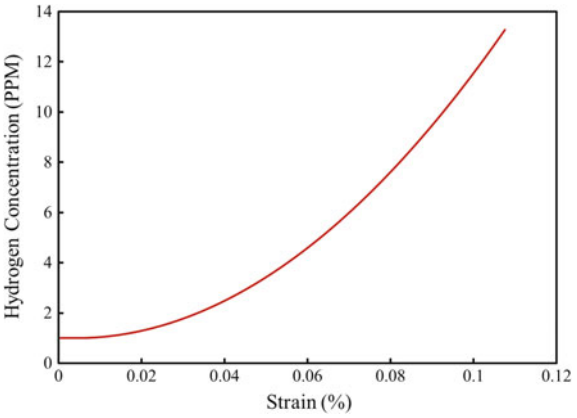

Fig. 2 Variation of hydrogen concentration inside the dislocation core

Inside the core, hydrogen increases the drag forces lead to a significant reduction in dislocation motion, interaction between mobile and immobile dislocations, and finally dislocation densities. During plastic deformation, the glide motion is inversely related to hydrogen concentration such that the more the hydrogen fill the dislocation core the lower the dislocation will slip.

Figures 3 and 4 present the mobile and immobile dislocation densities of the deformed specimen. It can be indicated that mobile and static dislocation densities are rapidly multiplied after the yield point.

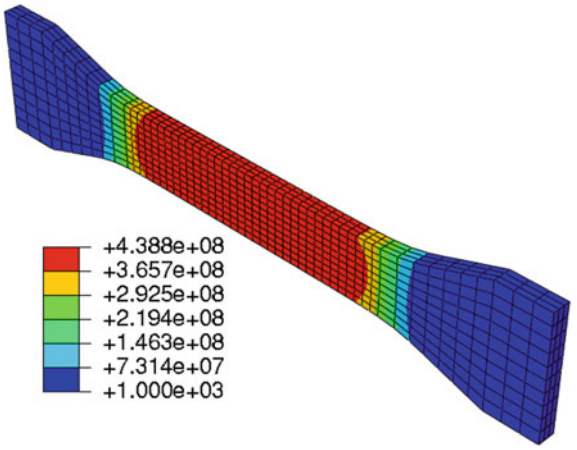

Fig. 3 Mobile dislocation density in hydrogen-charged tension specimen (mm^{-2})

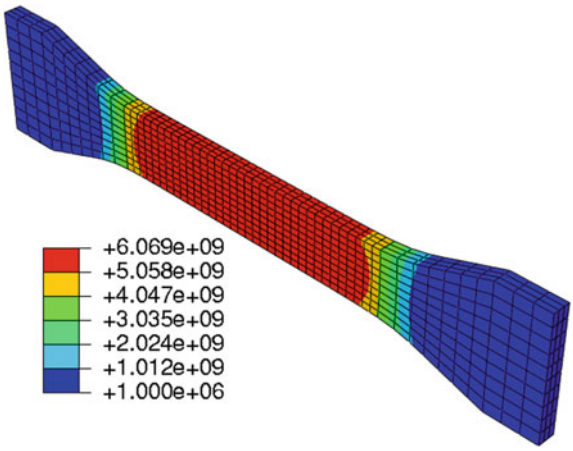

Fig. 4 Immobile dislocation density in hydrogen-charged tension specimen (mm^{-2})

Conclusion

A model for hydrogen effect on crystalline materials has been developed and presented in the current work. The model accounts for dislocations glide and climb as well as generation, interaction and annihilation. Furthermore, the model couples between mobile, immobile, and grain-boundaries dislocations as well as sub grain radius. The proposed physically-based dislocation-density model includes the effect of hydrogen solute on dislocation mobility and interaction.

The proposed model has been applied to study the mechanical behavior of high-strength steel of HT-9 tensile test specimen. The results show significant effect on the plastic behavior of the materials when hydrogen being introduced. An increase in the yield strength as well as a softer plastic behavior can both be noticed from the obtained results. Further comparison between the obtained behavior and experimental results shall be carried in future studies where parameters fitting will be necessary.

Acknowledgement This project is funded by the Academy of Scientific Research and Technology (ASRT) under Joint Collaborative Efforts of Egyptians Expatriates & Scientific Organizations towards Tackling R&D Challenges (JESOR), Contract No. 17.

References

1. Dadfarnia M, Nagao A, Wang S, Martin ML, Somerday BP, Sofronis P (2015) Recent advances on hydrogen embrittlement of structural materials. Int J Fract 196:223–243
2. Bernstein IM, Thompson AW (1984) The role of microstructure in hydrogen embrittlement. American Society for Metals, Metal Park, OH, pp 135–152
3. Hirth JP (1984) Theories of hydrogen induced cracking of steels. American Society for Metals, Metal Park, pp 29–41

4. Hirth JP (1980) Effects of hydrogen on the properties of iron and steel. Metall Trans A 11 (6):861–890
5. Hirth JP, Rice JR (1980) On the thermodynamics of adsorption at interfaces as it influences decohesion. Metall Trans A 11(9):1501–1511
6. Gahr S, Grossbeck ML, Birnbaum HK (1977) Hydrogen embrittlement of niobium—I. Macroscopic behavior at low temperatures. Acta Metall 25:125–134
7. Shih DS, Robertson IM, Birnbaum HK (1988) Hydrogen embrittlement of a titanium: in situ TEM studies. Acta Metall 36:111–124
8. Novak PM (2009) A dislocation-based constitutive model for hydrogen–deformation interactions and a study of hydrogen-induced intergranular fracture, University of Illinois at Urbana-Champaign
9. Hamza M, Hatem TM, Raabe D, El-Awady JA (2015) Hydrogen diffusion and segregation in alpha iron $\sum$ 3 (111) grain boundaries. In: ASME International Mechanical Engineering Congress and Exposition, Proceedings (IMECE), 9-2015
10. Song J, Curtin WA (2012) Atomic mechanism and prediction of hydrogen embrittlement in iron. Nat Mater. https://doi.org/10.1038/NMAT3479
11. Birnbaum HK, Sofronis P (1994) Hydrogen-enhanced localized plasticity—a mechanism for hydrogen-related fracture. Mater Sci Eng A 176(1–2):191–202
12. Gerberich WW, Marsh PG, Hoehn JW (1996) Hydrogen induced cracking mechanisms—are there critical experiments. TMS, Warrendale, PA, pp 539–551
13. Wagih MM, Tang Y, Hatem TM, El-Awady JA (2015) Discerning enhanced dislocation plasticity in hydrogen-charged α-iron nano-crystals. Mater Res Lett. https://doi.org/10.1080/21663831.2015.1052889
14. Hatem TM, Zikry MA (2011) A model for determining initial dislocation-densities associated with martensitic transformations. Mater Sci Technol 27(10):1570–1573
15. Sofronis P, Lianga Y, Aravas N (2001) Hydrogen induced shear localization of the plastic flow in metals and alloys. Eur J Mech A/Solids 20:857–872
16. Troiano AR (1960) The role of hydrogen and other interstitials in the mechanical behavior of metals. Trans Am Soc Metals 52:54–80
17. Hatem TM, Zikry MA (2009) Dislocation density crystalline plasticity modeling of lath martensitic microstructures in steel alloys. Philos Mag 89:3087–3109
18. Ghoniem NM, Matthews JR, Amodeo RJ (1990) A dislocation model for creep in engineering materials. Res Mechanica 29:197–219
19. Hatem TM, Zikry MA (2010) Dynamic shear-strain localization and inclusion effects in lath martensitic steels subjected to high pressure loads. J Mech Phys Solids 58(8):1057–1072
20. Hatem TM, Zikry MA (2009) Modeling of lath martensitic microstructure and failure evolution in steel alloys. J Eng Mater Technol—ASME 131(041207):1–10
21. Hatem TM, Zikry MA (2009) Shear pipes effect and shear-strain localization in martensitic steels. Acta Mater 57:4558–4567
22. Shanthraj P, Hatem TM, Zikry MA (2011) Microstructural modeling of failure modes in martensitic steel alloys. In: MRS Proceedings, vol 1296

Part IX
Biodegradable Materials for Medical Applications

Comparative Study on Corrosion Behavior of WE33 in Immersion and Polarization Influenced by Heat Treatment

Petra Maier, Maximilian Bechly, Benjamin Hess, Marino Freese and Norbert Hort

Abstract An extruded WE33 alloy is focus of this study. The influence of heat treatment on hardness and corrosion behavior is evaluated in immersion and polarization tests. Due to the application as a biodegradable implant, Ringer solution of 37 °C was chosen. As-extruded WE33 shows heterogeneous grain size distribution. Solution heat treatment (T4) causes significant grain growth with high variation in grain size with reduced hardness. Precipitation hardening (T6) causes reduced average grain size, mainly based on developing additional small grains. Hardness of T6 condition exceeds extruded material. The corrosion morphology is mostly described by the pitting factor. Corrosion behavior by corrosion rate (weight and cross-sectional area loss) and pitting factor of immersion are compared to polarization and shows the same trend: T6-condition shows lowest corrosion rate. On the other hand, T6-condition shows highest pitting corrosion tendency. Pitting factors evaluated in immersion tests are much higher than seen after polarization tests.

Keywords Magnesium · Voltammetry · Immersion · Morphology

Introduction

WE43 (Mg-4Y-3RE, where RE is a mixture of rare earth elements but contains mostly Ce and Nd; additionally, 0.5 Zr are present (all values in wt%)) is a high strength alloy with an acceptable biological response [1, 2]. A hot-extruded, only ternary Mg3.34Y3.43Nd alloy with a similar Y and Nd composition to WE43 alloy

P. Maier (✉) · M. Bechly · B. Hess · M. Freese
University of Applied Sciences Stralsund, Zur Schwedenschanze 15, 18435 Stralsund, Germany
e-mail: petra.maier@hochschule-stralsund.de

N. Hort
Helmholtz-Zentrum Geesthacht, Magnesium Innovation Center, Max-Planck-Straße 1, 21502 Geesthacht, Germany

The Minerals, Metals & Materials Society, *TMS 2018 147th Annual Meeting & Exhibition Supplemental Proceedings*, The Minerals, Metals & Materials Series, https://doi.org/10.1007/978-3-319-72526-0_21

is used in this study. The alloy contains other than the commercial WE43 [3] only Y and Nd. WE type alloys show a precipitation hardening response and are therefore conventionally used in the T6 condition. The intermetallic particles observed in these alloys are fully characterized [4–7]. Intermetallic particles $Mg_{12}Nd$, $Mg_{24}Y_5$ and $Mg_{14}Y_4Nd$ are observed in Mg-Y-Nd and the mechanical properties of the alloy depend strongly on the volume fraction and spatial distribution of these intermetallic phases. This work investigates the influence of solution heat treatment (T4) and precipitation hardening (T6) on the corrosion properties evaluated in immersion and polarization, its corrosion rate and corrosion morphology. Biomedical applications require an appropriately homogenous corrosion rate (CR) to avoid strong hydrogen evolution. Corrosion morphology is described by the pitting factor resulting from deep corrosion pits, the corroded surface area as well as the amount and shape of deep pits. Corrosion pits act as notches and can cause a strong reduction in the cross-sectional area resulting in increased stress intensity and should be avoided. Previous studies on pure Magnesium [8] have shown pitting factors of 1.76 in polarization tests, whereas the same material in immersion tests reaches pitting factors up to 22.3. An extruded WE32 alloy [9, 10] shows the highest CR in the T4 solution heat treated condition (25.2 mm/year) and the smallest after T6 precipitation hardening (5.3 mm/year), which on the other hand causes the highest pitting factor (up to 10.8) by similar deep pits (up to 1000 μm) in aged condition compared to as-extruded material (14.6 mm/year). Pitting factors of as-extruded and T4 are similar (between 3 and 4). The pitting factors evaluated in polarization do not exceed values of ~3 in all three conditions: as-extruded, T4 and T6.

Material and Experimental

Material and Processing: The ternary Mg3Y3Nd alloy was direct extruded at the Extrusion Research and Development Center TU Berlin at an overall temperature of 430 °C, a ram speed of 0.56 mm/s and an extrusion ratio of 84:1. The final diameter of the extrusion bars was 12 mm. A fine-grained microstructure developed as the result of recrystallization. The chemical composition was analyzed by the spark emission spectrometer Spectrolab M, Spectro, Germany, using the standard Mg10. Other than the commercial WE43 the alloy does not contain alloying elements like Zr. A solution heat treatment (T4) of 525 °C for 8 h has been applied, followed by quenching in water at a temperature of 55 °C according to the data sheet in [3], precipitation hardening was done at 250 °C for 8 h.

Experimental: Discs of a diameter of 12 mm for metallographic and hardness investigations were prepared according to Kree [11]. The grain size was determined by the line interception method. Vickers hardness was tested with a ZHU2.5 by Zwick with approximately 10 indents under a load of 1 kg (9.807 N) and the average value is reported.

Immersion tests were performed using 3 samples each. Cylinders had a diameter of 10 mm and a height of 15 mm, exposed to 500 ml Ringer solution at 37 °C for 7 days. Ringer solution, being more aggressive than HBSS or DMEM [8], has been chosen for corrosion tests. The solution was changed after 4 days to avoid an increase in pH value. The weight of the specimens was measured before testing and after removing the corrosion products with chromic acid to determine weight loss. The mean corrosion rate was calculated by using the following equation, where Δm is the weight change in g, A_s the surface area sample in cm^2, t the immersion time in h and ρ the density in g/cm^3.

$$CR_m = (8.76 \times 10\text{^}4 \times \Delta m)/(A_s \times t \times \rho)$$

The corrosion morphology is described according to ASTM G46-76 (standard visual chart for rating of pitting corrosion). The corroded samples were cut and ground down to half the cylinder (longitudinal cross-section) or 3D imaging was applied to evaluate pit shape and size. The deepest corrosion pit p, see Fig. 1, is used to calculate the pitting factor (PF), where p is divided by the average penetration d. The penetration d is either evaluated by weight loss (d_{CR}) or from the corroded area A_{corr} of the macrographic longitudinal cross-section, which is measured by light microcopy by taking the initial circumference of the cross-section (50 mm) into account ($d_{macrograph}$). A pitting factor of 1 indicates uniform corrosion, high pitting factors indicate a greater susceptibility to pitting corrosion. In addition, the length of corroded surface of the cross-section l_{corr} and the 10 deepest corrosion pits are measured to compare the depth and amount of deep pits among the material conditions.

Polarization tests were done on samples with a diameter of 12 mm and a height of 5 mm immediately after grinding with 600, 1200 and 2400-mesh paper, and cleaning in an ultrasonic bath in ethanol. A three-electrode flow cell (170 ml) using a counter electrode, an Argenthal reference electrode and the sample as the working electrode with a measurement area of ~95 mm^2 was used to measure polarization curves. To cause anodic corrosion, the curve was traced with a scan rate of 50 mV/min from a potential of −2000 to 500 mV. The electrolyte was circulating by a pump and had a temperature of 37 °C. An outer ring of initial surface is kept due to sealing ring and used as a reference, like seen in [8] and Fig. 2. The average

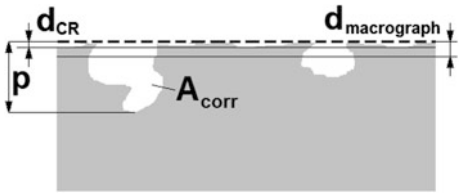

Fig. 1 Sketch with values to evaluate PF (longitudinal cross-section of immersion test samples): deepest pit p, corroded area A_{corr}, average penetration depth from CR d_{CR} and average penetration depth from A_{corr} $d_{macrograph}$

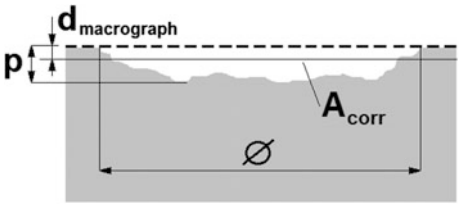

Fig. 2 Sketch with values to evaluate PF (cross-section of polarization test samples): deepest pit p, corroded area A_{corr}, diameter corroded area ∅, average penetration depth from A_{corr} $d_{macrograph}$

penetration depth $d_{macrograph}$ is calculated from the corroded area A_{corr} and the diameter of corroded area. Since voltammetry tests cause the sample to corrode by increasing voltage and the exposed area is much smaller, average penetration depth cannot be compared for the different corrosion methods, only the values among each other's material condition can be compared.

Results and Discussion

Composition: Table 1 shows the real composition. The values for Y and Nd are slightly above the nominal composition. As there is often a substantial burn-off (especially of RE [12]) normally more of these elements is added to the melt to compensate burn-off.

Grain size and hardness: The as-extruded WE33 bar has a fine-grained, homogeneous recrystallized microstructure, see cross-sectional macrograph in Fig. 3a, with slightly increasing transversal grain size towards the center of the sample (inner ring), see values in Table 2. The extrusion ratio of 84:1 is very high. Additionally, direct extrusion causes inhomogeneous materials flow at the interface of billed and die. Therefore, the stored energy will be different at the outside of the extrusion bar compared to the inside. Influenced by that non-uniform deformation stress, dynamic and static recrystallization causes an inhomogeneous microstructure. Table 2 presents a grain size of 13.1 µm for the outer ring and 14.5 µm for the inner ring, respectively. Longitudinal grain size agrees to transversal grain size. The hardness is, even in the opposite trend to the grain size, higher in the inner ring: 75.3 HV compared to 73.9 HV. A non-uniform contribution of alloying elements could be also an explanation. However, both grain size and hardness have relevant error bars.

During heat treatment the cross-sectional microstructure becomes more inhomogeneous: the inner ring grains grow during solution heat treatment (T4) very significant up to 173.4 µm, where the grains near the extrusion bar surface grow up to 136.0 µm, see Table 2. The reason for the high grain growth is, among others,

Table 1 Real composition (all values in wt%)

	Mg	Y	Nd	Fe	Cu	Ni
WE33	Bal	3.34	3.43	0.019	0.0037	0.0026

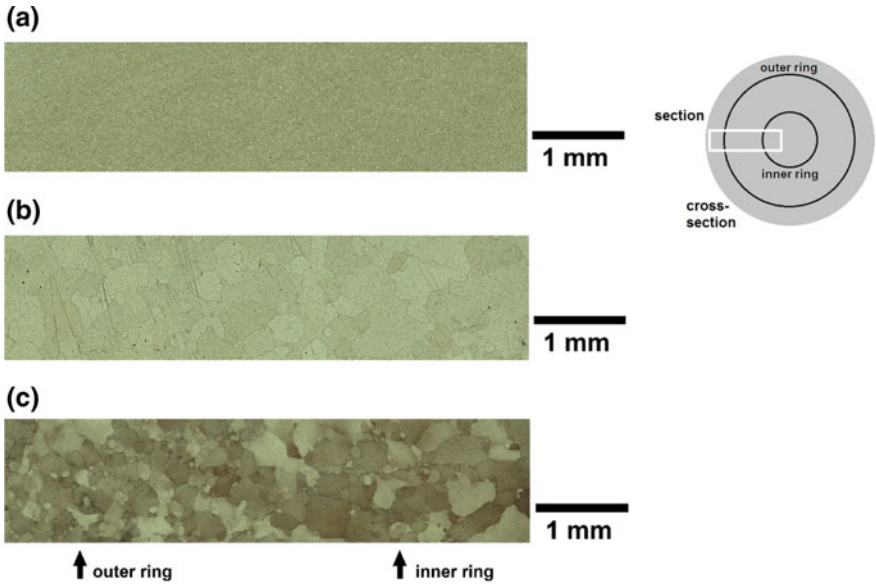

Fig. 3 Macrographs of **a** as-extruded WE33, **b** WE33-T4 and **c** WE33-T6

Table 2 Hardness and grain size of as-extruded WE33, WE33-T4 and WE33-T6

	HV1—outer ring	Grain size [µm]—outer ring	HV1—inner ring	Grain size [µm]—inner ring
as-extruded	73.9 ± 1.9	13.1 ± 6.0	75.3 ± 2.8	14.5 ± 6.4
T4	65.0 ± 3.9	136.0 ± 97.5	66.5 ± 6.7	173.4 ± 131.0
T6	91.6 ± 1.1	103.6 ± 66.5	97.2 ± 3.0	115.2 ± 75.6

the missing of alloying elements like Zr, Gd and Dy. The hardness is independent of the grain size: 65.0 and 66.5 HV, here determined by the solid solution strengthening—also showing inhomogeneous alloying element contribution: inner ring presumably slightly higher. Because of the high grain size, the hardness indent will most likely not cross more than one grain boundary. During precipitation hardening (T6) the grain size decreases and becomes more homogeneously: 103.6 µm at the outer ring and 115.2 µm at the inner ring. The error bars are still very high. The reason for the development of the smaller grain size is not part of this study and not completely understood yet, but new grains seem to start growing at grain boundaries. However, the reason for the hardness increase up to 97.2 HV, independent of the grain size for the same reason as mentioned above, is the formation of precipitates. The hardness, even with such a high grain size, exceeds the initial hardness of the extruded, fine grained microstructure.

Immersion: Figure 4 shows exemplary the visual appearance of a complete as-extruded WE33 sample after the immersion test after removing the corrosion

products. A non-uniform corrosion, identified by local corrosion pits, can be seen. The cross-sectional macrograph of a WE33-T4 sample is seen in Fig. 5, showing the deepest corrosion pit (983 µm). However, no pits are deeper than wider, so the stress intensity caused by the notch effect is within limits. Figure 6 shows the top view (Fig. 6a) and topography image (Fig. 6b) of the corrosion pits developed WE33-T6 (180 µm deep). A wide and shallow shape acts uncritically to stress increase.

Table 3 shows the evaluated parameter from the immersion tests. For WE33-T4 the mean corroded area A_{corr} reaches the highest value of 15.7 mm^2. That means that 10.5% of the longitudinal cross-sectional area (see Fig. 5) is corroded. The mean corroded areas agree with the mean corrosion rates CR: the lowest value of CR is found in WE33-T6 with 1.19 mm/year. The larger amount of finer precipitates effectively reduces the individual cathode surface area, which acts positive on forming a passive layer. WE33-T4, showing the highest corroded area and CR,

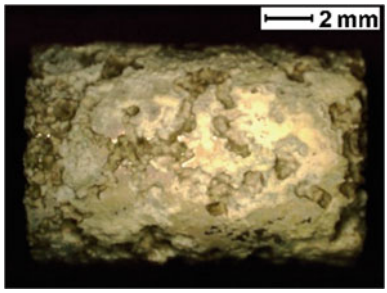

Fig. 4 Corroded sample after immersion of as-extruded WE33

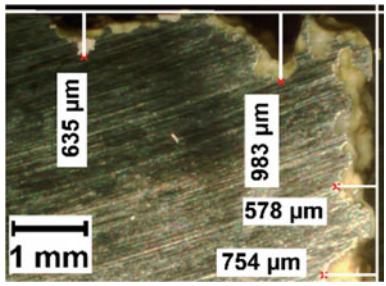

Fig. 5 Cross-section of corroded sample after immersion of WE33-T4

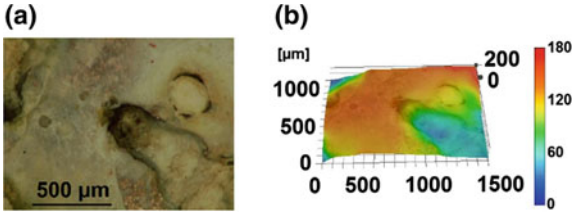

Fig. 6 Top view of corroded sample after immersion of WE33-T6: **a** photo and **b** 3D

Table 3 Evaluated parameter from immersion tests

	Mean A_{corr} (mm^2)	Mean l_{corr} (%)	Mean $d_{macrograph}$ (mm)	Deepest pit p (mm)	$PF_{macrograph}$	Mean CR (mm/year)	Mean d_{CR} (mm)	PF_{CR}
as-extruded	10.8	76.6	0.216	0.992	4.1	5.04	0.097	9.9
T4	15.7	91.8	0.310	0.983	3.2	7.78	0.149	6.2
T6	9.9	66.2	0.195	0.963	4.9	1.19	0.023	31.9

corrodes almost all over the surface: ~92% of the initial circumference of the longitudinal cross-section is corroded. Here all second phases are assumed to be dissolved in solid solution; alloying element Y has a potential very close to Mg. On the other hand, only ~66% of length (assuming surface area) is corroded in WE33-T6 and since the pits are almost as high as in the other two conditions the pitting factor reaches the highest value: 4.9 evaluated by the macrograph and 31.9 by the CR, which is too high. The passive layer is not dense and uniform enough to eliminate local corrosion. The highest corrosion rate in WE33-T4 with an almost all over the surface corrosion causes the smallest pitting factor of 3.2 taken from the macrographs and 6.2 from the CR, respectively. Pitting factors evaluated from CR are higher because the average penetrations d_{CR} is smaller; the corrosion rate takes the full sample surface into account, the longitudinal cross-section shows only one snapshot of the surface and has no information on the full 3D extent of the corroded parts. Up to our current knowledge the corrosion morphology seems to be independent of the grain size. Micrographs and their grain size distribution to evaluate the influence of grain size on corrosion morphology are under investigation.

To give some further information on the extent of pitting corrosion, the 12 deepest pits are measured (Fig. 7a) and sorted by the depth. It can be seen, that the pits in WE33-T4 start off at the highest values and stay there up to the 12th pit. With an exception of 2 pits (992 and 872 µm) in as-extruded WE33 no pits deeper than 700 µm could be found. The small grain size of less than 15 µm is responsible

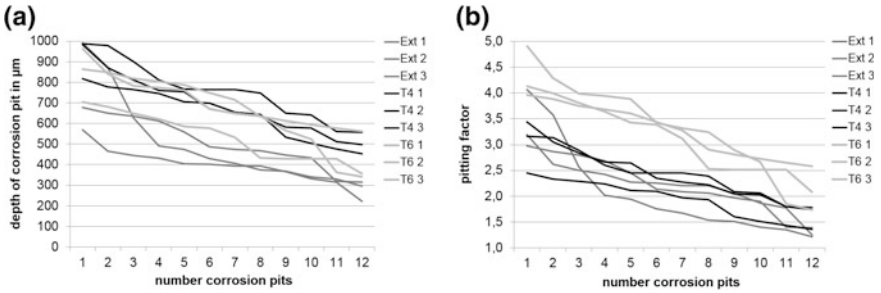

Fig. 7 Corrosion morphology of immersion samples of as-extruded WE33, WE33-T4 and WE33-T6 by **a** 12 deepest corrosion pits and **b** highest corrosion pits (determined with $d_{macrograph}$)

for a good relation of grain boundaries to inner grain areas inclusive the homogeneous distribution of second phases located depending on its size as grain boundary or inner grain precipitates. The following pit with the depth of 677 µm only results in a maximum pitting factor (taking $d_{macrograph}$ into account) of ~3, being less than in WE33-T4. The pits in WE33-T6 are in the middle range, but since the corroded area/average penetration and CR are the smallest, these pits lead to the highest pitting factors, see Fig. 7b. Even the larger amount of finer precipitates reduces effectively the corrosion rate, but the developed passive layer obviously still contains non-passivated small areas. Here the rather large grain size and precipitates mostly at the inner grain areas could be an explanation. The deepest pits in WE33-T4 get balanced by the highest average penetration, so the pitting factors move closer together. In relation to each other, pitting factors evaluated from the CR show the same picture as in Fig. 7b, but with a much bigger difference between WE33-T6 and the other two conditions extruded and T4.

Polarization: Figure 8 shows the influence of the material condition on the corrosion behavior, evaluated with potentiodynamic polarization (−2000 to 500 mV), where a representative curve of as-extruded WE33, WE33-T4 and WE33-T6 is seen. No significant difference in the anodic corrosion behavior can be seen. Even the curves of the heat treated materials become slightly unstable at 150 mV (27 mA/cm^2), there is no appearance of passivation. WE33-T4 reaches the highest current density at the potential of 500 mV. Comparing the three material conditions, as-extruded WE33 starts with the lowest current density and stays lowest.

Figure 9 show the macrographs of the corroded areas (cross-section) of the polarization tests. The initial surface is marked by a white line, connecting the non-corroded part of the sample, which is an outer ring sealed during the test. The area between the white line and the borderline metal—embedding resin is the corresponding corroded area. Since in polarization the anodic corrosion is increasing by increasing potential, pits may overlap and form a rough surface instead of deep shaped pits. The deepest corroded areas, here still called pits, are very wide and shallow forming a rather homogenous surface. The risk of stress increase when exposed to mechanical loading will be very small.

The highest corroded area and average penetration in WE33-T4 (Table 4) are in agreement to the highest anodic current density at 500 mV, see Fig. 8. As-extruded

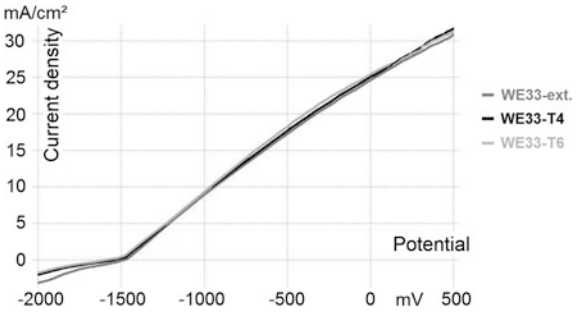

Fig. 8 Current density—potential curves (representative) of as-extruded WE33, WE33-T4 and WE33-T6

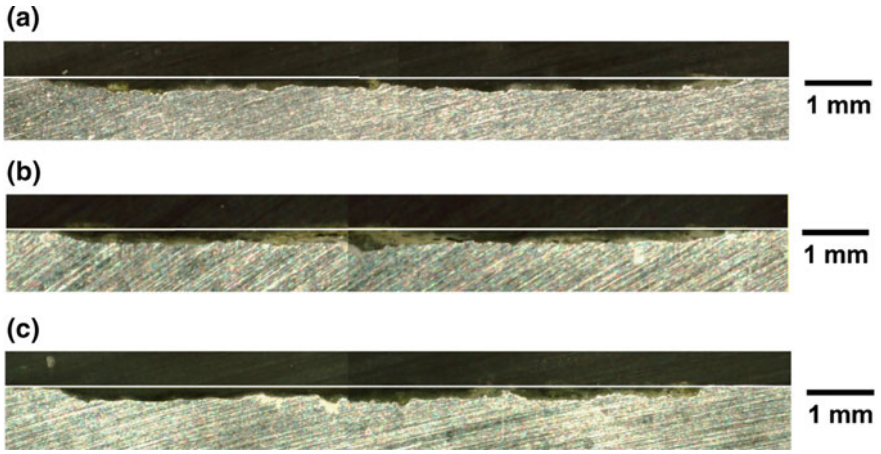

Fig. 9 Macrographs presenting the corroded areas of as-extruded WE33 (**a**), WE33-T4 (**b**) and WE33-T6 (**c**)

Table 4 Evaluated parameter from polarization tests

	Mean A_{corr} (mm^2)	Mean $d_{macrograph}$ (mm)	Deepest pit p (mm)	$PF_{macrograph}$
as-extruded	1.55	0.156	0.307	1.88
T4	1.79	0.175	0.327	1.85
T6	1.50	0.155	0.310	1.99

WE33 and WE43-T6 show smaller corroded areas and penetration depths similar to each other. As-extruded WE33 starts off with the smallest negative current density at −2000 mV. The deepest corrosion pits are found in WE33-T4, but since the average penetration is also high the pitting factor has the lowest level. However, no pitting factor exceeds a value of 2 and by the very wide shaped pits there is no harm expected when additionally exposed to mechanical load.

Figure 10 shows the 6 deepest pits measured (Fig. 7a) and sorted by the depth. Like seen in the immersion results (Fig. 7a) the pits in WE33-T4 start off at the highest values and remain up there. The pits found in as-extruded are at the lowest level up to sixth deep pit (due to the small grain size, see discussion of results of immersion tests). WE33-T6 pits are in the middle range and show the lowest difference between deepest and sixth deepest pit. Due to the overall less deep corrosion pits in relation to the average penetration depth the resulting pitting factors are smaller than in immersion (compare Fig. 10b to Fig. 7b). According to the ongoing anodic corrosion with a steady increase of current density seen in Fig. 8, no strong pitting is expected. Comparing with a previous study on pure Magnesium [8], where a mean corroded area of 1.44 mm^2 and a maximum pitting factor of 1.76 on a pit depth of 0.210 mm are found, the WE33 in this study does behave similar. Like seen in Fig. 7b, the T6 condition of WE33 corrodes also in

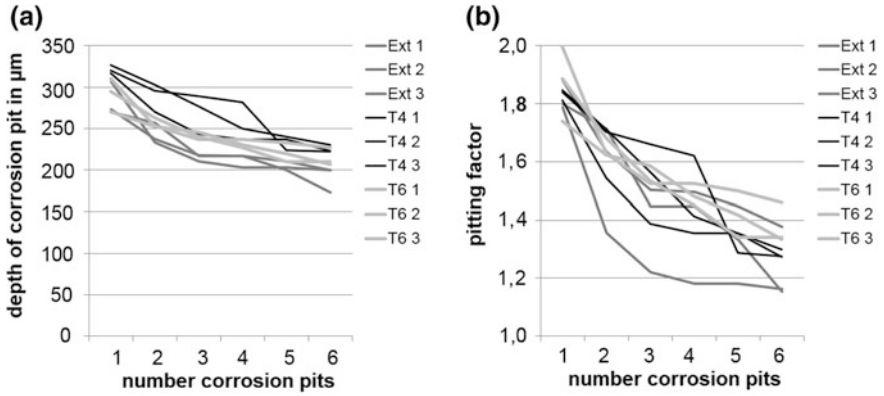

Fig. 10 Corrosion morphology of polarization test samples of as-extruded WE33, WE33-T4 and WE33-T6 by **a** 6 deepest corrosion pits and **b** highest corrosion pits

polarization with the highest pitting factor, once again because of the lowest "corrosion rate", here evaluated by mean corroded area/average penetration in combination with "middle range" corrosion.

Summary

The corrosion behavior of an extruded WE33 alloy in three different conditions was focus of this study: as-extruded, solution and precipitation heat treated. As-extruded WE33 shows a rather heterogeneous grain size distribution. Because of missing further alloying elements in the ternary Mg-Y-Nd system, heat treatment causes a significant grain growth. Furthermore, a development of an inhomogeneous microstructure has been found after heat treatment. Mechanical properties were evaluated by hardness measurements: solution heat treatment reduces hardness. The hardness in the precipitation hardened condition, even with such a high grain size, exceeds the initial hardness of the extruded, fine grained microstructure.

The corrosion rate and morphology, evaluated by immersion and polarization, were used to find out the influence of heat treatment on the corrosion behavior. Due to the application as a biodegradable implant, Ringer solution of 37 °C was chosen. The corrosion morphology is mostly described by the pitting factor. In immersion and polarization, the T6 condition shows lowest corrosion rate. On the other hand, the T6 condition shows the highest pitting corrosion tendency. Even the formation of a larger amount of finer precipitates during T6 reduces effectively the corrosion rate, the developed passive layer is obviously still not dense enough and contains non-passivated small areas. Here the rather large grain size might be responsible for that, showing that the mixture of rare earth elements (Nd and Ce) plus addition of Zr are needed to provide an acceptable corrosion behavior without pitting. Pitting factors evaluated in immersion tests are much higher than seen after polarization tests.

Acknowledgements This work is supported by Helmholtz Virtual Institute VH-VI-523. The material was extruded by the Extrusion Research and Development Center TU Berlin, the authors thank Sören Müller and Felix Gensch. The authors acknowledge the support Hartmut Habeck (UASS) for the voltammetry measurements.

References

1. Zheng YF, Gu XN, Witte F (2014) Mat Sci Eng R 77:1
2. Choudhary L, Singh Raman RK, Hofstetter J, Uggowitzer PJ (2014) Mater Sci Eng C 42:629–636
3. Magnesium Elektron UK, data sheet 467
4. Tolnai D, Mendis CL, Stark A, Szakács G, Wiese B, Kainer KU, Hort N (2013) Mater Lett 102–103:62
5. Smola B, Stulíková I, von Buch F, Mordike BL (2002) Mat Sci Eng A 324:113
6. Rokhlin LL, Dobatkina TV, Nikitina NI, Tarytina IE (2011) Met Sci Heat Treat 52:588
7. Kang YH, Wu D, Chen RS, Han EH (2014) J Magnes Alloys 2:109
8. Maier P, Gentsch L, Hort N (2017) Magnes Technol 2017:429–437
9. Maier P, Peters R, Mendis CL, Müller S, Hort N (2016) JOM 68(4):1183–1190
10. Maier P, Gonzalez J, Peters R, Feyerabend F, Ebel T, Hort N (2016) Eur Cells Mater 32(6):22
11. Kree V, Bohlen J, Letzig D, Kainer KU (2004) Pract Metallogr 41(5):233–246
12. Rokhlin LL (2003) Magnesium alloys containing rare earth metals. Taylor & Francis, London, UK

Metal Injection Molding (MIM) of Mg-Alloys

M. Wolff, J. G. Schaper, M. Dahms, T. Ebel, R. Willumeit-Römer and T. Klassen

Abstract MIM-technique possesses high potential for the SF_6 free near net shape mass production of small sized and complex shaped parts. Furthermore, MIM involves a high degree of freedom regarding individual alloy- and MMC-composition using the blended elemental (BE-route). Resent research has highlighted MIM of Mg-alloys as highly suitable for biomedical applications like screws, nails and bone-plates, as well as for commercial 3C applications. For prototyping and low quantities, the feedstock can be used for 3D-filament print, too. Hence, demonstrator parts and test specimen could be produced very successfully, ready for industrial upscaling. Increased mechanical properties of MIM dogbone tensile test specimen could be achieved using Mg-2.6Nd-1.3Gd-0.5Zr-0.3Zn alloy (EZK400, UTS: 164 MPa, YS: 123 MPa, ε_f: 3.4%) and AZ81-alloy for commercial applications (UTS: 240 MPa, YS: 118 MPa, ε_f: 4%). Thus, the mechanical properties are currently equivalent to those of as cast material and obtaining high development potential.

Keywords Metal injection molding · Magnesium · Sintering

M. Wolff (✉) · J. G. Schaper · T. Ebel · R. Willumeit-Römer
Div. Metallic Biomaterials, Helmholtz-Zentrum Geesthacht,
Centre for Materials and Coastal Research, Institute of Materials Research,
Max-Planck Str.1, 21502 Geesthacht, Germany
e-mail: martin.wolff@hzg.de

M. Dahms
University of Applied Sciences, HS-Flensburg,
Kanzleistr. 91-93, 24943 Flensburg, Germany

T. Klassen
Helmut Schmidt University, Holstenhofweg 85, 22043 Hamburg, Germany

The Minerals, Metals & Materials Society, *TMS 2018 147th Annual Meeting & Exhibition Supplemental Proceedings*, The Minerals, Metals & Materials Series,
https://doi.org/10.1007/978-3-319-72526-0_22

Introduction

Currently, Mg-alloys are becoming more and more attractive for consumer, lightweight [1–3] and biomedical application [4–11]. The new biodegradable and biocompatible Mg-based material shows mechanical properties matching those of cortical bone tissue [12–15]. However, commonly used casting and forging techniques require the use of sulfur hexafluoride (SF_6) as protective gas [16]. SF_6 is a 22800 times more active climate gas than CO_2 [17]. Hence, the use of SF_6 in cast-shops will be prohibited within the near future. In contrast, the powder-metallurgical (PM) processing route of metal injection molding (MIM) enable the economic near net shape mass production of complex shaped Mg-alloy parts. The MIM processing requires the manufacturing of a feedstock, consisting of Mg-alloy powder and different polymeric binder components. This feedstock can also be used for the manufacturing of filament, necessary for fused filament fabrication (FFF), commonly known as 3D-printing of filament material. Hence the material can be used for low batches up to high quantities (1piece—1mio. pc. and beyond).

However, sintering of Mg and its alloys was known as not feasible in literature because of a stable oxide layer, sticking on the particle surface and inhibiting the diffusion process, necessary for the sintering [18]. Recent work on sintering of Mg [19–21] and MIM of Mg [22–24] could overcome this major challenge. This study is focusing on the improvement of the full process chain of MIM of new Mg-alloys. In doing so, different test specimen, demonstrator parts and biomedical implant prototypes as shown in Fig. 1 were produces and tested successfully. Sufficient mechanical properties up to 240 MPa UTS, 118 MPa TYS and 4% elongation at fracture could be achieved.

- Right hand side components: feedstock granules made of Mg-alloy powder and binder components.

Fig. 1 Mg-alloy demonstrator parts and test specimens made by MIM of Mg at Helmholtz-Zentrum Geesthacht

- Upper part: implant screw demonstrator parts in the green and sintered condition (Mg-0.9Ca).
- Middle parts: dogbone tensile test specimen (EZK400) according to ISO 2740-B.
- Lower part: bookmark demonstrator parts (AZ81).

Materials and Methods

Powder, Feedstock and Green Part Production

For the green part preparation, commercial spherical gas atomized Mg-2.6Nd-1.3Gd-0.5Zr-0.3Zn alloy powder, in the following referred to as EZK400 (product name: MAP+21, Magnesium Elektron, UK) and Mg-8Al-1Zn alloy powder (AZ81, SFM, Martigny, Switzerland) were used for the specimen production. The feedstock was prepared using a binder system consisting of poly-propylene, stearic acid and paraffin wax. The components were blended at approx. 160 °C in a planetary mixer (Thinky ARE-250 planetary mixer, Japan) applying approx. 500G acceleration. To avoid any additional uptake of oxygen, powder handling took place under protective argon atmosphere in a glovebox system (Unilab, MBraun, Germany). Feedstock granules were produced using a cutting mill (Wanner B08.10F, Germany). The green part production of dogbone shape tensile test specimen (ISO 2740-B) and demonstrator parts as shown in Fig. 1 took place using an injection molding machine (Arburg Allrounder 320S) at up to 1500 bar injection pressure, 65 °C mold temperature and 135 °C feedstock temperature. Regarding the state of the art of sintering of magnesium, getter material inside of the labyrinth like crucible configuration has been used [19]. For this purpose, pure irregular coarse magnesium powder grit (Sigma Aldrich, USA) was applied.

Debinding and Sintering

Solvent debinding of stearic acid and organic wax components was done using hexane at 45 °C for 10–15 h (Lömi EBA50/2006, Germany). Thermal debinding of the backbone polymer and consolidation through sintering took place in a combined debinding and sintering hot wall furnace (MUT, Jena, Germany). Thermal debinding was performed in reactive Ar + 5% H_2 gas, using a flow of 1 L/min at 10–60 mbar. Corresponding to former studies about sintering Mg–Ca alloys [19–21], the sintering time was set to 64, 32, 16, 8, 3 and 1 h.

Evaluation of Optimal Sintering Time and Temperature

For evaluation of optimal sintering time and temperature of the new sinter material, DSC measurements served as a initial analysis (DSC2, Mettler Toledo, Switzerland). Because of the fact that the used MIM-binder-system and the injection molding process steps can influence the sintering performance of the new material, first sintering experiments were performed using the press and sinter (P+S) route to avoid any influences of binder components, debinding solvents and debinding gases. In doing so, the EZK400 powder was pressed to cylindrical compressive strength test specimen (diameter: 8.2 mm; length: 12.5 mm; according to DIN 50106) and micro-tensile test specimen green parts (according to DIN EN 6892-1:2009) using a manual mode press (Enerpac RC 55, USA, applied surface pressure: 100 MPa). To avoid any additional oxygen pick-up, the total powder and specimen handling took place in the glove box system under protective argon atmosphere.

Materials Characterization

The Archimedes method (Sartorius LA230S, Germany) was applied to measure the residual porosity of the sintered parts. Geometrical data calculation (Mahr 16EX, calliper, Germany) were performed to measure shrinkage and density, too. The microstructure was investigated, using SEM (Zeiss DSM 962, Germany) and EDS mapping. Compressive and tensile tests of sintered P+S as well as MIM specimens were performed using a Schenck Trebel RM100 materials testing machine.

Results and Discussion

Sintering Temperature and Time

The DSC-analysis of the commercial Mg-alloy powder EZK400 presented a liquidus temperature of approx. 635 °C (mean value of: 631–640 °C) as shown in the diagram in Fig. 2.

This first DSC result was used for the approximated setting of the initial sintering temperature. As a result, a sintering temperature of 635 °C was chosen as a good compromise in view of the following two aspects: The higher the sintering temperature, the exponentially higher is the diffusion activity between the particles. Hence, sintering time can be reduced drastically using marginal higher sintering temperature. On the other hand, the higher the sintering temperature, the higher is the amount of transient or permanent liquid phase in the compound. Hence, the part can lose its shape or liquid phase can pour out of the part. As mentioned above, first

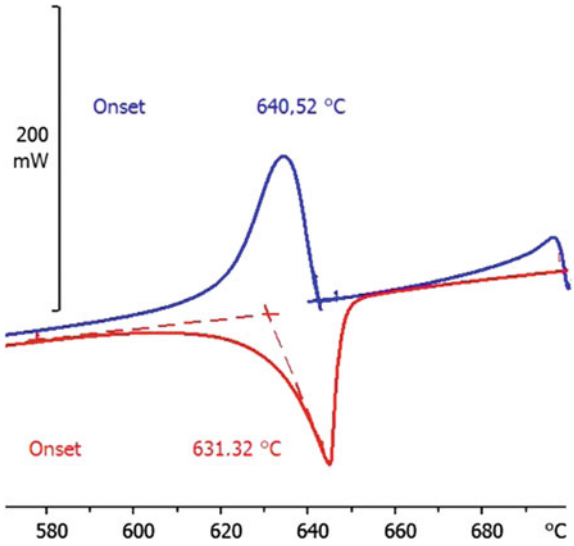

Fig. 2 DSC-analysis of EZK400 alloy powder using a heating rate of 5 K/min

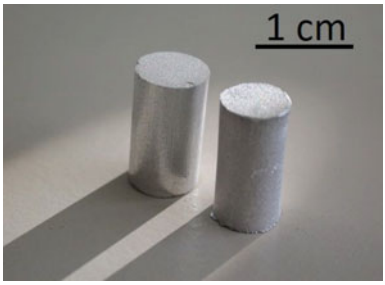

Fig. 3 Cylindrical compressive test specimen made of EZK400 in the green condition (left) and the as sintered condition (right) showing significant shrinkage

sintering experiments on cylindrical compressive test specimen as shown in Fig. 3 and micro-tensile test specimen were performed using binder free P+S technique.

The following diagram in Fig. 4 shows the micro-tensile test results of the first three sets of the P+S specimen sintered at 635 °C at different sintering times. The new EZK400 material is sintering with permanent liquid phase. Hence, the sintering time could be reduced significantly in comparison to former experiments using 64 h of sintering time.

The first set of columns in the diagram displays that 1 h of sintering time is insufficient for the nearly dense consolidation of the part. Only 1.1 ± 0.2% of elongation at fracture and 124 ± 6 MPa UTS were achieved. In contrast, using 16 h of sintering time, 188 ± 5 MPa UTS and 5.8% elongation at fracture could be

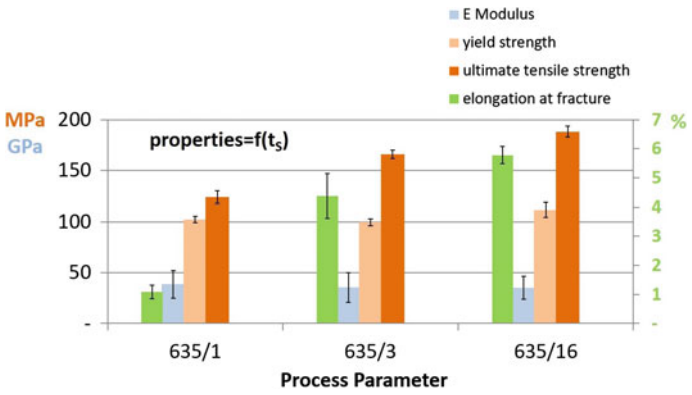

Fig. 4 Mechanical properties of micro-tensile test specimen produces by P+S, using a fixed sintering temperature of 635 °C and varying sintering time

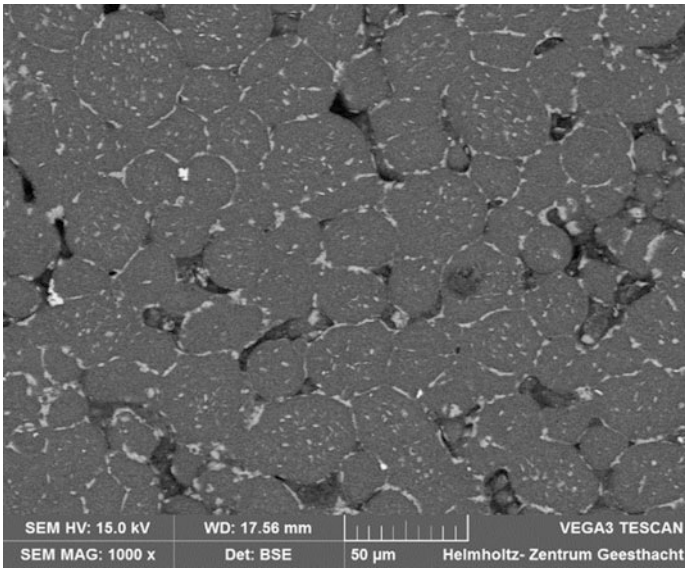

Fig. 5 SEM micrograph of the EZK400 alloy, sintered for 1 h

reached. Moreover, significant improvement of mechanical properties could be achieved even by use of an economic short sintering time of 3 h. The third set of columns displays sufficient material properties showing 4.4 ± 0.8% of elongation at fracture, and above 166 ± 4 MPa UTS. The following images in Figs. 5 and 6 shall give an overview about the microstructure of the material in the as sintered condition for the shortest chosen sintering time of 1 h as shown in Fig. 5 and the longest chosen sintering time of 64 h as shown in Fig. 6. The microstructure of the

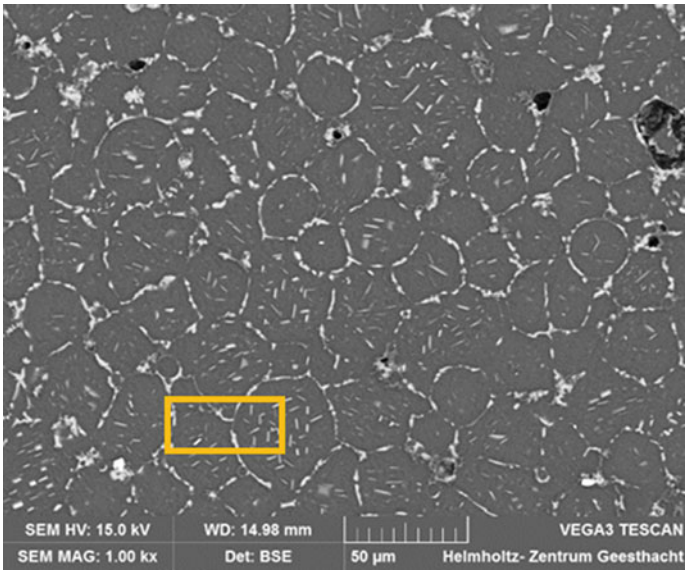

Fig. 6 SEM micrograph of the EZK400 alloy, sintered for 64 h

EZK400 material, sintered for 1 h, as show in Fig. 5 is in accordance to the mechanical properties, shown in the first set of columns of Fig. 4. It can be seen that the material is not fully consolidated, presenting a residual porosity of around 7%.

In contrast, the following Fig. 6 reveals the microstructure of the material, sintered for 64 h, which presents only 0.7 ± 0.1% of residual porosity.

Because of the fact that sintering time can influence the densification of the compound maximum in a linear behavior, a second set of sintering operations was done for further optimization of the sintering regime. In doing so, a fixed sintering time of 3 h and variation of the sintering temperature between 635 and 643 °C as shown in Fig. 7 were chosen. As a result, the mechanical properties of the material could be improved significantly using the economic sintering time of 3 h at 643 °C as shown in the third set of columns in Fig. 7. Hence, maximum UTS of 188 ± 4 MPa at 5 ± 1% of elongation at fracture and 122 ± 6 MPa yield strength were achieved.

Moreover, the sintering performance of the new EZK400 material was as good, that sintering could be performed without getter material inside of the crucible setup resulting in no significant loss of mechanical strength, as shown in the fourth set of columns in Fig. 7. This is in contrast to the state of the art for sintering of magnesium, where getter material inside the labyrinth-like crucible configuration has to be used [19]. The fast sintering performance of the EZK400 material might be explained on the ground of attendance of permanent rare earth rich liquid phase during sintering. The orange rectangle in Figs. 6 and 8A displays the area of an EDX-mapping analysis, performed on the EZK400 material, sintered for 64 h.

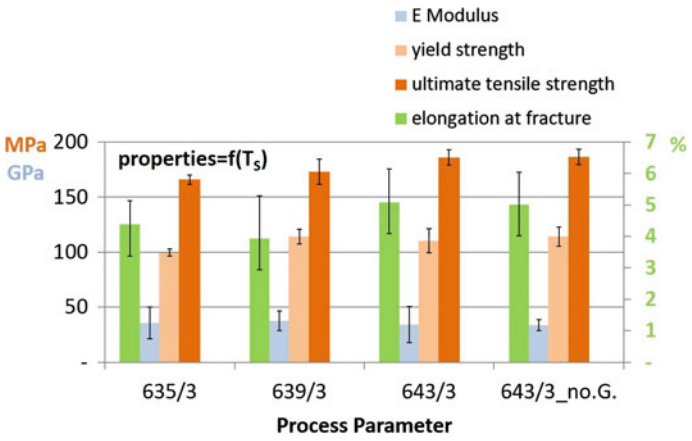

Fig. 7 Mechanical properties of micro-tensile test specimen produces by P+S, using a fixed sintering time of 3 h and variation sintering temperature

As shown in the SEM images and EDX mapping analyses in Fig. 8a–f, the former particle boundaries (yellow arrows) mainly consists of Gd-, Nd- and Zr-rich phases, combined with an increased level of oxygen (O). The needle shape bright crystal structure inside of the roundish particle structure (red arrows in Fig. 8a) can be allocated to Mg_5Gd and $MgNd_5$ intermetallic, as well as to mixed Mg-RE-oxides. In contrast, the bright secondary phases on the particle boundaries/ grain boundaries display additional zirconium (Zr) (Fig. 8a, e) and increased

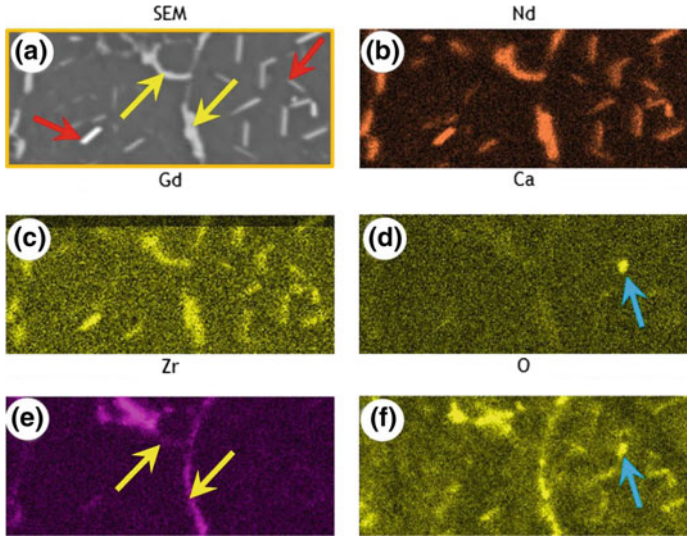

Fig. 8 SEM image and EDX mapping of the EZK400 material, sintered for 64 h

intensity of oxygen. The single bright oxygen dot inside of the roundish particle in Fig. 8d, f and a (blue arrow) can be identified as a CaO rich artefact onto the specimen's surface. However, for clear identification of these different phases in the as sintered EZK400 microstructure, nano-diffraction analysis, using synchrotron radiation might be a sufficient tool for further investigations.

How does the fast sintering of the EZK400 material occur? It can be assumed on the one hand that, if the powder particle surface is coated by magnesium oxide in the as received condition, the rare earth rich permanent liquid phases might be able to reduce this MgO-layer material in accordance to the relationship of Gibbs free energy of oxide formation. On the other hand, if rare earth rich oxides coat the particle surfaces of the used powder, Mg might be able to reduce these oxides, too. To answer this question in more detail, an adequate surface analysis of the particle surface, e.g. XPS, IR-spectroscopy or μ-XRF, in combination with DSC and XRD-analyses have to be done in future work. Regarding the sintering performance of Mg–Ca alloys, literature reveals that during magnesium oxide layer reduction as shown in the following Eq. 1:

$$\mathrm{MgO} + \mathrm{Ca} \leftarrow \rightarrow \mathrm{Mg} + \mathrm{CaO} \tag{1}$$

The shown redox reaction takes place, in dependency of element concentration, in both directions [25].

Sintering of MIM EZK400 Parts

In a further step, the sintering results of the prior chapter were adapted to the sintering of parts, produced by metal injection molding (MIM) as shown exemplary in Fig. 1 and the following Fig. 9. As shown in these images, the demonstrator parts and dogbone shape tensile test specimens exhibit significant shrinkage and a perfect smooth, silver shade surface. The tensile test results of the dogbone shape specimen, as shown in Fig. 1, reveal UTS of 161 MPa, yield strength of 123 MPa and elongation at fracture of 3.4%. The following diagram in Fig. 10 compares the

Fig. 9 Suture anchor implant screw demonstrator part made by MIM of EZK400 material. Design: ConMed, USA

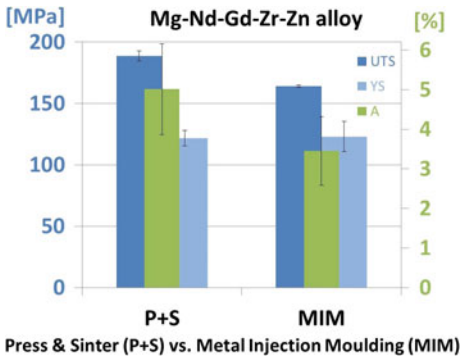

Fig. 10 Comparison of tensile test results of the EZK400 material using the P+S route in comparison to MIM

mechanical test results of EZK400 material of the P+S route to the MIM processed material.

The diagram points out that MIM processed material could achieve 87% of the UTS of the P+S processed material and 69% of the elongation at fracture of the P+S processed material. However, the yield strength of the MIM processed material is the same of the P+S processed material. The decrease in strength and ductility using the MIM-route in comparison to the P+S route can be explained by formation of additional needle shape crystals, forming a ring shape structure in the near grain boundary region of each grain/ancient powder particle in the microstructure, as shown in the following Fig. 11.

A feasible explanation of this phenomenon might be the formation of carbide phases during thermal debinding of the green part by chemical reaction of reactive, carbon rich debinding gases with rare earth alloying elements. Hence, this needle shape phase might consist of ZrC, or even Nd- and Gd-containing composite carbides. To avoid this weakening phenomenon of the material, different techniques can be used:

- The thermal debinding step has to be optimized. If it is possible to fulfill the binder decomposition in a certain temperature range in which carbide formation does not take place, the formation of this phase can be avoided.
- Thermal debinding in hydrogen atmosphere.
- Performing T4 solid solution and T6 ageing heat treatment to induce a homogeneous distribution of the new carbide phase in the microstructure.

If the second technique will be of success, even better mechanical properties in comparison to the P+S material could be achieved through precipitation hardening effects.

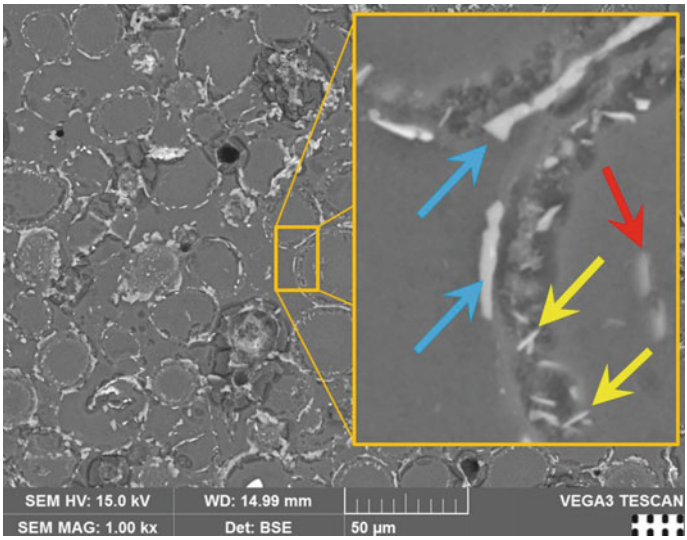

Fig. 11 Microstructure of MIM processed EZK400 showing secondary phases onto grain boundaries (blue arrows) and needle shape phases inside of the roundish grains (red arrow), as well as new near grain boundary needle shape phases (yellow arrows)

Sintering of MIM AZ81 Parts

Next to the EZK400 alloy powder, the commercial Mg-alloy powder AZ81 was tested, too. Dogbone shape tensile test specimens revealed UTS of 240 ± 6 MPa, yield strength of 118 ± 2 MPa and elongation at fracture of 5.1 ± 0.6%. The following Fig. 12 displays an SEM image of the microstructure of the as-sintered AZ81 material.

In comparison to the EZK400 material, the AZ81 material contained significantly less secondary phases being homogeneously distributed along the grain boundaries. Original powder particles, connected through liquid phase sintering, are still visible. The AZ81 could be sintered very successful achieving a residual porosity of 4.4% (see black dots).

Conclusions and Outlook

This study points out that Mg alloys like Mg-2.6Nd-1.3Gd-0.5Z-0.3Zn (EZK400) and AZ81 can be sufficiently sintered under SF_6-free and economic conditions. Before, this was known only for stainless steel, titanium alloys or hard metals. The optimal sintering regime for the novel EZK400 Mg-alloy powder could be found to be 643 °C for 3 h. Applying this parameter set and using pressed and sintered

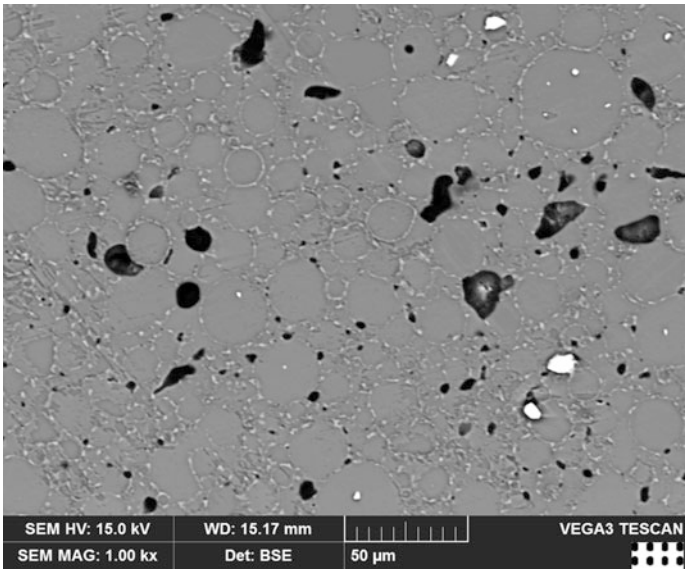

Fig. 12 Microstructure of MIM processed AZ81 showing 4.4% residual porosity and secondary phases on grain boundaries

(P+S) tensile test specimens, sound UTS of 188 MPa and 5% elongation at fracture could be achieved. Using MIM parts an UTS of 164 MPa and 3.4% elongation at fracture were determined. The discrepancy in UTS and elongation at fracture can be explained due to formation of additional secondary phases in the near grain boundary region. These phases are assumed to be carbides, formed during thermal debinding of the brown part. Further work shall identify these phases using adequate surface analysis technique of the particle surface, e.g. XPS, IR-spectroscopy and μ-XRF, in combination with DSC and XRD-analysis, as well as synchrotron based high-energy X-ray nano-diffraction. Moreover, this study discusses techniques to avoid these additional phases.

Furthermore, other Mg-alloy powders such as commercial AZ81 could be successfully processed by MIM, too, and an UTS of 240 MPa could be achieved. Generally, MIM processing of Mg-alloy powders implements economic and SF_6-free near net shape mass production of small sized complex Mg-alloy parts.

References

1. Friedrich HE, Mordike BL (2006) Springer, Berlin, Germany
2. Kainer KU (2010) Wiley-VCH, Weinheim, Germany
3. Dieringa H, Hort N, Kainer KU (2011) Proceedings of LMT 2011, vol. 690. Trans Tech Publications Ltd, Material Science Forum

4. Li Z, Gu X, Lou S, Zheng Y (2008) The development of binary Mg-Ca alloys for use as biodegradable materials within bone. Biomaterials 29:1329–1344
5. Staiger MP, Pietak AM, Huadmai J, Dias G (2006) Magnesium and its alloys as orthopaedic biomaterials- a review. Biomaterials 27:1728–1734
6. Witte F, Kaese V, Haferkamp H, Switzer E, Meyer-Lindenberg A, Wirth CJ, Windhagen H (2005) Biomaterials 26:3557–3563
7. Witte F, Reifenrath J, Müller PP, Crostack H-A, Nellesen J, Bach FW, Bormann D, Rudert M (2006) Materialwissenschaft und Werkstofftechnik 37:504–508
8. Witte F, Feyerabend F, Maier P, Fischer J, Störmer M, Blawert C, Dietzel W, Hort N (2007) Biomaterials 28:2163–2174
9. Witte F, Ulrich H, Rudert M, Willbold E (2007) J Biomed Mater Res 81A:748–756
10. Witte F, Fischer J, Nellesen J, Crostack HA, Kraese V, Pisch A, Beckmann F, Windhagen H (2006) Biomaterials 27:1013–1018
11. Witte F, Ulrich H, Palm C, Willbold E (2007) J Biomed Mater Res 81A:757–765
12. Poumarat G, Squire P (1993) Biomaterials 14:337–349
13. Cunha AR et al (2012) Int J Hypertens. Hindawi Publishing Co. Art. ID: 754250
14. Janning C, Willbold E, Vogt C, Nellesen J, Meyer-Lindenberg A, Windbergen H, Thorey F, Witte F (2010) Magnesium hydroxide temporarily enhancing osteoblast activity and decreasing the osteoclast number in peri-implant bone remodelling. Acta Biomaterialica 6:68–1861
15. Witte F, Fischer J, Nellesen J, Crostack HA, Kraese V, Pisch A, Beckmann F, Windhagen H (2006) In vitro and in vivo corrosion measurements of magnesium alloys. Biomaterials 27:1013–1018
16. Magnesium Taschenbuch (2000) Aluminium Verlag Düsseldorf, 1st edn, p 466ff. ISBN: 3-87017-264-9
17. Statistisches Bundesamt (2014) Erhebung bestimmter klimawirksamer Stoffe "Schwefelhexafluorid" (SF_6), Wiesbaden. www.destatis.de, Artikelnummer: 5332401-13700-4
18. Hort N, Dieringa H, Kumar ST, Kainer KU (2006) Magnesium matrix composites. Springer, Berlin, p 237
19. Wolff M, Dahms M, Ebel T (2010) Sintering of magnesium. Adv Eng Mater 12:829–836
20. Wolff M, Guelck T, Ebel T (2009) Sintering of Mg and Mg-Ca alloys for biomedical applications. Euro PM2009 Proceed 2:417–422
21. Wolff M, Bischof C, Dahms M, Ebel T, Klassen T (2012) 9th International conference on magnesium and their applications. Vancouver, Canada 8–12 July 2012, p 102
22. Wolff M, Schaper JG, Dahms M, Ebel T, Kainer KU, Klassen T (2014) Powder Metall 57 (5):331–340
23. Wolff M, Schaper JG, Suckert MR, Dahms M, Feyerabend F, Ebel T, Willumeit-Römer R, Klassen T (2016) Metal injection molding (MIM) of magnesium and its alloys. Metals 6(118). https://doi.org/10.3390/met6050118
24. Wolff M, Schaper JG, Suckert MR, Dahms M, Ebel T, Willumeit-Römer R, Klassen T (2016) Magnesium powder injection molding (MIM) of orthopedic implants for biomedical application. JOM 68(4). https://doi.org/10.1007/s11837-016-1837-x
25. Wiese B (2017) The effect of CaO on magnesium and magnesium calcium alloys. Universitätsbibliothek der TU Clausthal. https://doi.org/10.21268/-20170504133828

Microstructure and Mechanical Properties of Mg-Gd Alloys as Biodegradable Implant Materials

Yiyi Lu, Yuanding Huang, Frank Feyerabend, Regine Willumeit-Römer, Karl Urich Kainer and Norbert Hort

Abstract Mg alloys attract more and more attentions for biomedical applications. Mg-Gd alloys were designed as biodegradable implant materials which combine favorable mechanical and corrosion properties. In this work, the microstructure and mechanical properties of binary Mg-2Gd, ternary Mg-2Gd-(Ag, Ca) and quaternary Mg-2Gd-2Ag-0.4Ca alloys were investigated. The alloys were prepared by permanent mould casting. The results show that the additions of Ag and Ca had significant influences on the microstructure and mechanical properties of Mg-2Gd alloy. Ag and Ca additions affect the formation of second phases. A quaternary Mg-Gd-Ag-Ca second phase was found in the quaternary alloy. Both the hardness and tensile yield strength were improved by adding Ag and Ca to 2 wt% Gd-containing alloys due to grain refinement and formation of different intermetallic phases (IMPs). Furthermore, the addition of Ag and Ca can apparently enhance the age hardening of Mg-2Gd alloy.

Keywords Mg-2Gd-Ag-Ca alloys · Ageing treatment (T6) · Microstructure Mechanical properties

Introduction

Mg alloys as new biodegradable materials are attracting more and more attentions in the biological implant applications. Mg alloys are ideal for bone plate [1–3] due to their comparable density (about 1.75–1.85 g/cm^3) and Young's modulus (44 GPa) to that of human bone. Mg alloys have many advantages such as good mechanical compatibility, load-bearing ability, good degradability and excellent biocompatibility. However, they still exhibit some disadvantages such as a fast non-uniform degradation [1, 4] and a large amount of bubbles generated during

Y. Lu (✉) · Y. Huang · F. Feyerabend · R. Willumeit-Römer · K. U. Kainer · N. Hort
Institute of Materials Research, Helmholtz-Zentrum Geesthacht, Max-Planck-Strasse 1, 21502 Geesthacht, Germany
e-mail: yiyi.lu@hzg.de

The Minerals, Metals & Materials Society, *TMS 2018 147th Annual Meeting & Exhibition Supplemental Proceedings*, The Minerals, Metals & Materials Series,
https://doi.org/10.1007/978-3-319-72526-0_23

in vivo degradation. Moreover, the effects of alloying elements and intermetallic phases on degradation in biological environments present still many challenges. Therefore, it is necessary to further develop new biodegradable Mg alloys combining proper mechanical properties, controllable homogeneous degradation properties and good biocompatibility.

Mg-RE (rare earth) alloys show a good combination of increased mechanical properties and bio-corrosion resistance [5-10]. In biological medical application, RE elements were used in anticancer drugs due to their anti-carcinogenic properties [11, 12]. Gd has an acceptable biocompatibility and a high solid solubility in Mg. It was reported that Mg-Ag alloys showed improved ductility, a good biocompatibility and satisfactory antibacterial properties [13]. Ca as an essential element in human body is excellently biocompatible. Meanwhile, its small density (1.55 g/cm^3) makes the density of Mg alloys closer to that of human bone. Moreover, it plays an important role in physiological processes such as nerve, muscle stress, nerve impulse transmission, maintenance of the heart rhythm, blood coagulation, and cell adhesion, etc. Coexistence of Mg and Ca contributes to bone healing and preventing from stress shielding [14]. In addition, the addition of Ca can refine the microstructure of as-cast Mg alloys and improve their strength.

Alloying elements of RE, Ag and Ca can substitute the occupancies of Mg atoms to form solid solution. The additions of these alloying elements (RE, Ag, and Ca) provide both solution and precipitation strengthening depending on their contents. A maximum solubility is 23.49 wt% for Gd, 15.02 wt% for Ag and 1.34 wt% for Ca in Mg at the eutectic temperature [15]. It is not economical to use RE elements with their high contents owing to their high cost. Hence, the content of total alloying elements was limited (<5 wt%) to offset the cost without compromising the properties. In this work, the effects of Ag and Ca additions to Mg-2Gd alloy on microstructure, mechanical properties and ageing hardening effect were studied.

Experimental Procedure

Permanent mould casting [16] was used to prepare all the investigated alloys. High-purity Mg (MEL, UK, 99.95 wt%) was molten in a mild steel crucible (Fig. 1) under a protective atmosphere (Ar + 0.3% SF6). During melting, pure Gd (Grirem, China, 99.5 wt%) for binary Mg-2Gd and quaternary Mg-2Gd-2Ag-0.4Ca alloys, Mg-33.3Gd (wt%) master alloy for both ternary Mg-2Gd-2Ag and Mg-2Gd-0.8Ca alloys were used, respectively. Gd-containing mixtures together with pure silver Ag (99.99%, ESG Edelmetall-Handel GmbH & Co. KG, Germany) or/and pure Ca (Alfa Asear, Germany, 99.51 wt%) were added at a melt temperature of 720 °C. The melt was stirred at 200 rpm for 30 min. After that, the melt was poured into a mild steel mould (Fig. 2) preheated to 550 °C. A filter (Foseco SIVEX FC, Foseco GmbH, Borken, Germany) was used mainly to slow down the melt and to obtain lamella filling from the bottom of the mould. The filled mould was held at room temperature and afterwards the ingot was extracted from the mould after air cooling.

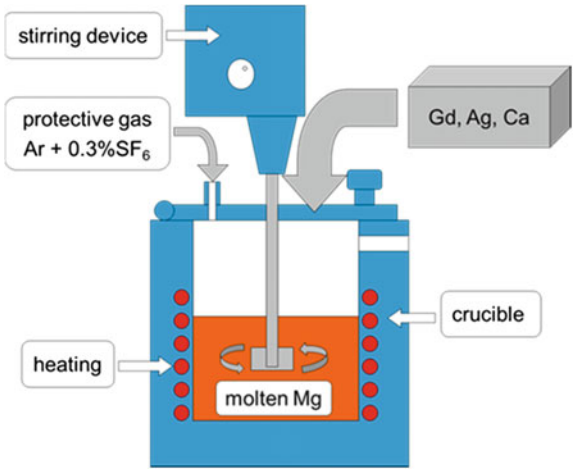

Fig. 1 Schematic sketch of the used melting furnace

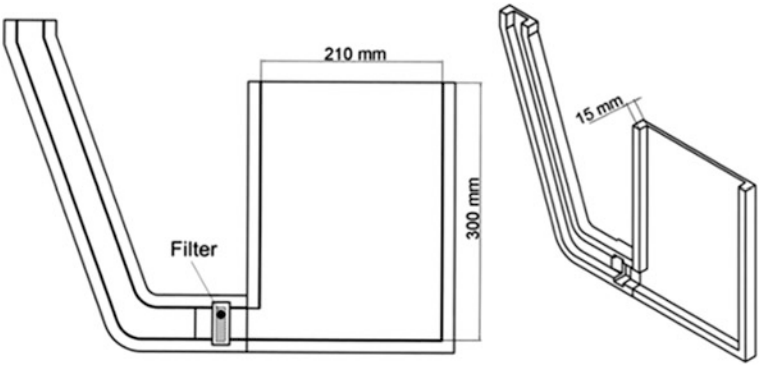

Fig. 2 Schematic sketch of one half part of mild steel mould [16]

The ingot was cuboid block with a size of 30 cm × 21 cm × 3 cm. All samples were not taken from the middle of plate ingot but from near-surface area. For each type of measurement, specimens were cut from the same position in ingots of different alloys. The contents of Gd, Ag and Ca were determined by X-ray fluorescence spectrometer (Bruker AXS S4 Explorer, Bruker AXS GmbH., Germany). The contents of Fe, Cu and Ni were determined by spark emission spectrometer (Spectrolab M, Spektro, Germany).

The grain size was measured using the line intercept methods with AnalySIS Pro software (Olympus Soft Imaging Solutions, Münster, Germany). The microstructure was investigated using VEGA3 TESCAN scanning electron microscope (SEM) equipped with energy-dispersive X-ray spectroscopy (EDS) at an accelerative voltage of 15 kV. The metallographic specimens for SEM were prepared by

grinding with SiC waterproof abrasive paper, polishing with a lubricant containing 1 μm diamond particles and 0.05 μm colloidal silica (OPS). The polished surface was finally cleaned using ethanol and dried under blowing hot air. The samples were finally covered with a conductive carbon adhesive (N650 Planocarbon). EDS was used to determine the local compositions by point and mapping analysis.

In order to investigate the influence of Ag and Ca additions on the mechanical properties, the hardness and tensile yield strength were investigated. Specimens for hardness tests were prepared by mounting and grinding with silicon carbide emery paper up to 2500 grit. The Vickers hardness measurements (HV5) were carried out using a standard microhardness tester (EMCOTEST M1C010 universal hardness tester) with a load of 5 kg and a dwell time of 10 s. An average of 10 measurements was made for each alloy. Strength and ductility of the tested alloys were measured by tension tests at room temperature. Universal testing machine Zwick Z050 (Zwick GmbH & Co., KG, Ulm, Germany) was used to conduct the quasi-static tensile tests. A strain rate of 0.001 s^{-1} was adopted for the tests. The tensile specimens have a diameter of 6 mm, a gauge length of 30 mm and threaded heads of 10 mm according to DIN 50125. The extensometers were used to measure the change of strain. 5 samples for each alloy for tension tests were conducted to avoid incidental errors or errors due to samples difference.

The ageing hardening of Mg-2Gd, Mg-2Gd-2Ag, and Mg-2Gd-0.8Ca alloys was investigated. The influences of 2 wt% Ag and 0.8 wt% Ca additions on the ageing hardening of Mg-2Gd alloy were also studied. Firstly, a solution treatment (T4) was performed at 510 °C for 48 h in a small resistance furnace (Vulcan™ A-550, DENTSPLY CERAMCO, USA), followed by water quenching. Afterwards, an ageing treatment (T6) was carried out at 200 °C for a period of time from 1 to 960 h, followed by air cooling.

Results and Discussion

Effects of Ag and Ca Additions on Microstructure

The real chemical compositions of all the investigated alloys are listed in Table 1. The accurate contents of Gd, Ag and Ca in alloys are little more or less than the

Table 1 Real chemical compositions (wt%) of the investigated alloys

Alloys	Gd	Ag	Ca	Cu	Fe	Ni	Mg
Mg-2Gd	1.80	–	–	0.0021	0.0054	<0.0100	Balance
Mg-2Gd-2Ag	2.12	2.47	–	0.0022	0.0020	<0.0027	Balance
Mg-2Gd-0.8Ca	2.21	–	0.75	0.0021	0.0018	<0.0027	Balance
Mg-2Gd-2Ag-0.4Ca	2.09	2.01	0.29	0.0020	0.0020	0.0081	Balance

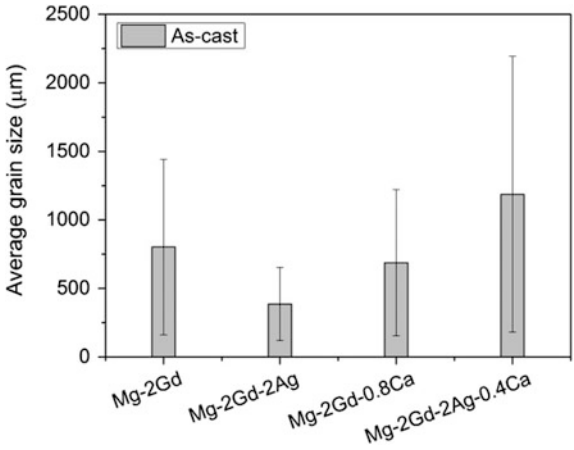

Fig. 3 Average grain size of Mg-2Gd-Ag-Ca alloys

normal chemical compositions, due to their burn off during casting. The amounts of impurities such as Cu, Fe, and Ni are quite small in ppm.

The average grain size of the as-cast binary Mg-2Gd, ternary Mg-2Gd-2Ag, Mg-2Gd-0.8Ca and quaternary Mg-2Gd-2Ag-0.4Ca alloys is shown in Fig. 3. The addition of 2 wt% Ag to Mg-2Gd alloy leads to not only an obvious reduction of grain size but also the improved homogeneous distribution of grains for Mg-2Gd-2Ag alloy. However, for Mg-2Gd-0.8Ca alloy, there is only little change of grain size by adding 0.8 wt% Ca to Mg-2Gd alloy. Moreover, the addition of small amount Ca to Mg-2Gd-2Ag ternary alloy results in a grain growth and inhomogeneous grain distribution.

Figure 4 shows SEM microstructures of the Mg-2Gd, Mg-2Gd-2Ag, Mg-2Gd-0.8Ca and Mg-2Gd-2Ag-0.4Ca alloys in the as-cast condition, respectively. Mg-2Gd alloy shows homogenous microstructure without dendrites. In contrast, after the respective additions of 2 wt% Ag and 0.8 wt% Ca to Mg-2Gd alloy, the microstructures are changed significantly and the morphologies of dendrites become very obvious. It reveals that the as-cast ternary Mg-2Gd-2Ag, Mg-2Gd-0.8Ca and quaternary Mg-2Gd-2Ag-0.4Ca alloys are mainly composed of continuous equiaxed dendrites with the segregation of solute atoms. The segregation mainly locates at dendritic boundaries.

The additions of Ag and Ca to Mg-2Gd alloy as well as the Ca addition to Mg-2Gd-2Ag alloy lead to very different formations of the IMPs. The size of IMPs becomes larger and their shape is changed significantly. The second phases in the ternary and quaternary alloys form a network-like structure. The volume fractions of both IMPs and segregation increase drastically, as compared with Mg-2Gd alloy. The IMP particles were analyzed by EDS point analysis, as shown in Fig. 5.

The microstructure of Mg-2Gd alloy shows the formation of few small bright particles. The IMP in Mg-2Gd alloy contains high contant of Gd,. which should be Mg_5Gd IMP. According to the EDS results, except Mg, the main IMP contains high Gd and Ag for Mg-2Gd-2Ag alloy, mainly high Ca for Mg-2Gd-0.8Ca alloy, and

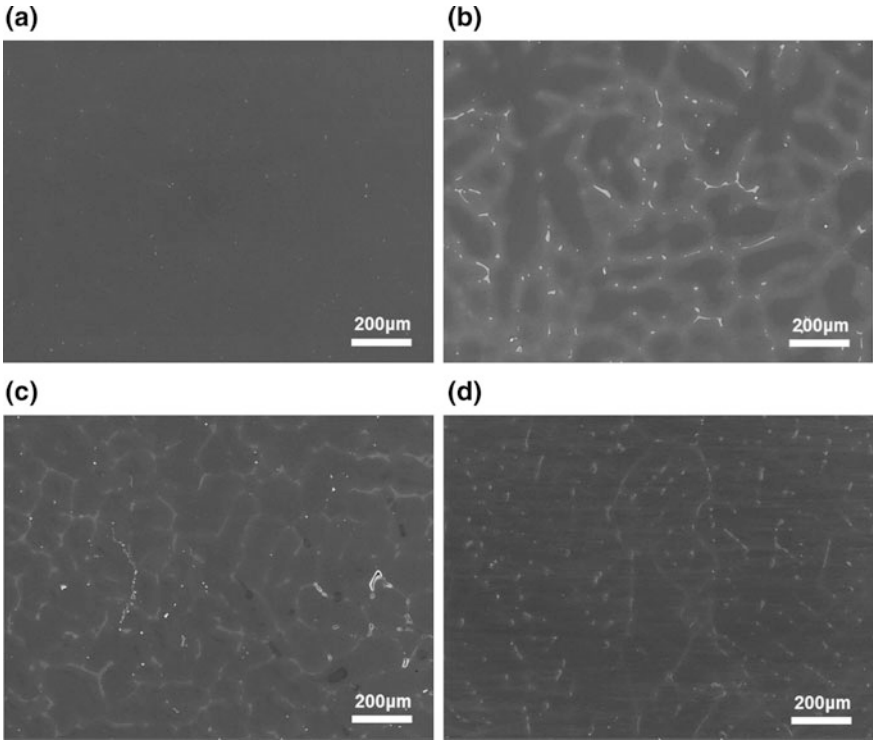

Fig. 4 SEM microstructures of as-cast Mg-2Gd (**a**), Mg-2Gd-2Ag (**b**), Mg-2Gd-0.8Ca (**c**) and Mg-2Gd-2Ag-0.4Ca (**d**) alloys

mainly high all these three alloying elements (Gd, Ag, Ca) for quaternary Mg-2Gd-2Ag-0.4Ca alloy. The second phases in these corresponding alloys are likely the MgGdAg ternary phase, Mg_2Ca binary phase and MgGdAgCa quaternary phase. It was reported that Mg-Gd and Mg-Ca alloys tend to contain Mg_5Gd and Mg_2Ca phase at an equilibrium state [17, 18]. A comparison of the main formed IMPs in these alloys is listed in Table 2.

Effects of Ag and Ca Additions on Mechanical Properties

The effects of Ag and Ca additions on hardness, tensile yield strength and ageing hardening were studied. Figure 6 shows Vickers hardness of the investigated as-cast alloys. The hardness is improved after adding 2 wt% Ag and 0.8 wt% Ca to Mg-2Gd alloy, respectively. The improvement of both ternary alloys is similar. The improved hardness is due to both grain refinement and more IMPs. With the addition of 0.4 wt% Ca to Mg-2Gd-2Ag alloy, the hardness is further improved.

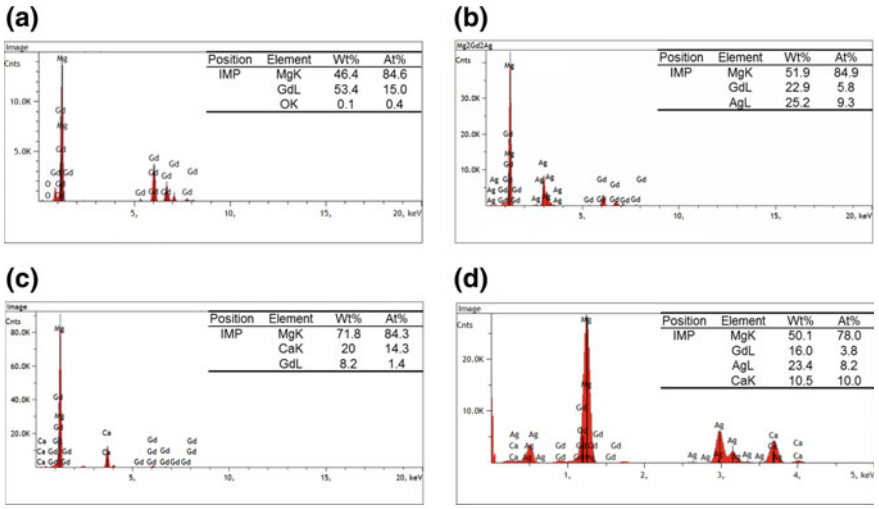

Fig. 5 EDS point analysis of the IMPs of as-cast Mg-2Gd (**a**), Mg-2Gd-2Ag (**b**), Mg-2Gd-0.8Ca (**c**) and Mg-2Gd-2Ag-0.4Ca (**d**) alloys

Table 2 Phase formation in the investigated alloys

Alloys	Main IMPs
Mg-2Gd	Mg_5Gd
Mg-2Gd-2Ag	Ternary MgGdAg phase
Mg-2Gd-0.8Ca	Mg_2Ca
Mg-2Gd-2Ag-0.4Ca	Quaternary MgGdAgCa phase

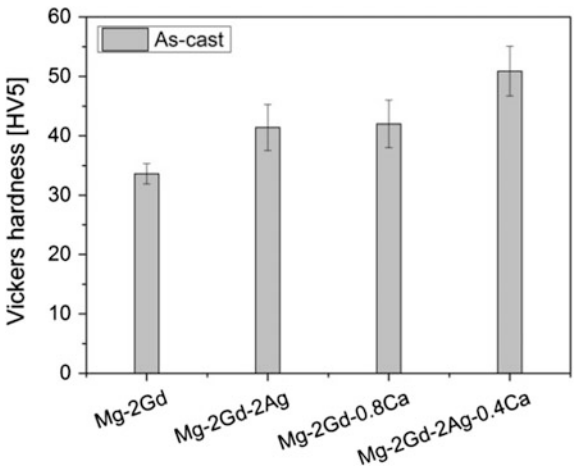

Fig. 6 Vickers hardness of Mg-2Gd-Ag-Ca alloys in the as-cast condition

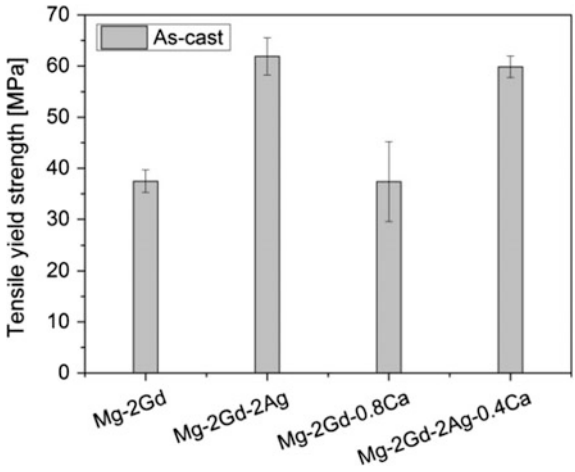

Fig. 7 Tensile yield strength of Mg-2Gd-Ag-Ca alloys in the as-cast condition

This is owing to the formation of more IMPs, even if the grain is coarsened in this quaternary alloy.

The tensile yield strength for these as-cast alloys is present in Fig. 7. The addition of 2 wt% Ag to Mg-2Gd alloy leads to a significant improvement of yield strength, due to the combined effects of grain refinement and second phase strengthening. However, the yield strength keeps no change by adding 0.8 wt% Ca to Mg-2Gd alloy, owing to the weak effects of both grain refinement and strengthening with brittle Mg_2Ca IMPs. The addition of 0.4 wt% Ca to Mg-2Gd-2Ag alloy shows no further enhancement of yield strength. This is mainly due to significant grain growth, which offsets the strengthening caused by the more formed second phases.

The age hardening response was measured for Mg-2Gd-(Ag, Ca) alloys at 200 °C. The relationship between hardness and aging time for Mg-2Gd-(Ag, Ca) alloys is shown in Fig. 8. Annealing at 200 °C, the hardness change is not apparent for Mg-2Gd alloy, while both Mg-2Gd-2Ag and Mg-2Gd-0.8Ca alloys show an obvious hardness change. Their hardness increases quickly in the initial period. It then increases gradually. A small plateau following the maximum hardness was observed. Further aging leads to a slow decrease in the hardness. Mg-2Gd-2Ag and Mg-2Gd-0.8 Ca alloys reach the peak hardness after 240 h and 480 h, respectively. The maximum hardness of both ternary alloys is about 60 HV. With addition of 2 wt% Ag or 0.8 wt% Ca to Mg-2Gd alloy, the age hardening is therefore apparent. The additions of both Ag and Ca are beneficial for enhancing the age hardening of Mg-2Gd alloy. According to the binary phase diagram of Mg-Gd alloys, the solubility of Gd is approximately 3 wt% at 200 °C [15]. This is why the binary Mg-2Gd alloy hardly has age hardening.

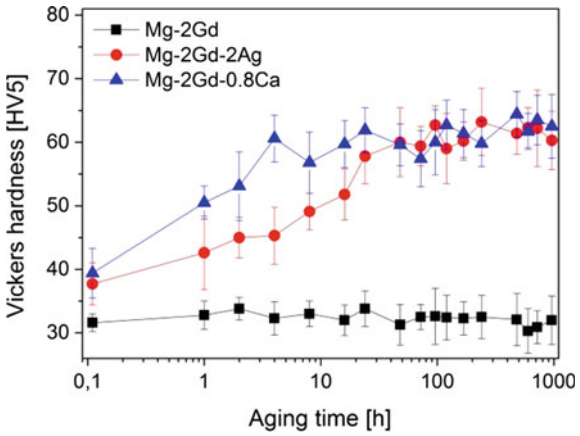

Fig. 8 Vickers hardness of Mg-2Gd-(Ag, Ca) alloys as a function of aging time at 200 °C

Conclusions

Effects of Ag and Ca additions on both the microstructure and mechanical properties of Mg-2Gd alloy were observed obviously.

The additions of Ag and Ca to Mg-2Gd alloy leads to a microstructural evolution including grain refinement and different IMP formations. Both hardness and tensile yield strength were improved by adding Ag and Ca to 2 wt% Gd-containing alloys due to grain refinement and formation of different second phases. Furthermore, the addition of Ag and Ca can apparently enhance the age hardening of Mg-2Gd alloy.

Acknowledgements This research was financially supported by the Helmholtz Virtual Institute VH-VI-523 (In vivo studies of biodegradable magnesium based implant materials).

References

1. Staiger MP, Pietak AM, Huadmai J, Dias G (2006) Magnesium and its alloys as orthopedic biomaterials: a review. Biomaterials 27:34-1728
2. Chen Y, Xu Z, Smith C, Sankar J (2014) Recent advances on the development of magnesium alloys for biodegradable implants. Acta Biomater 10:4561–4573
3. Li N, Zheng Y (2013) Novel magnesium alloys developed for biomedical application: a review. J Mater Sci Technol 29:489–502
4. Song GL (2007) Control of biodegradation of biocompatable magnesium alloys. Corros Sci 49:1696–1701
5. Yang L, Huang Y, Feyerabend F, Willumeit R, Mendis C, Kainer KU, Hort N (2013) Microstructure, mechanical and corrosion properties of Mg–Dy–Gd–Zr alloys for medical applications. Acta Biomater 9:8499–8508
6. Hou L, Li Z, Pan Y, Du L, Li X, Zheng Y, Li L (2014) In vitro and in vivo studies on biodegradable magnesium alloy. Prog Nat Sci Mater Int 24:466–471

7. Hänzi AC, Gunde P, Schinhammer M, Uggowitzer PJ (2009) On the biodegradation performance of an Mg–Y–RE alloy with various surface conditions in simulated body fluid. Acta Biomater 5:162–171
8. Gunde P, Hänzi AC, Sologubenko AS, Uggowitzer PJ (2011) High-strength magnesium alloys for degradable implant applications. Mater Sci Eng A 528:1047–1054
9. Feyerabend F, Fischer J, Holtz J, Witte F, Willumeit R, Drucker H, Vogt C, Hort N (2010) Evaluation of short-term effects of rare earth and other elements used in magnesium alloys on primary cells and cell lines. Acta Biomater 6:1834–1842
10. Atrens A, Liu M, Zainal Abidin NI (2011) 'Corrosion mechanism applicable to biodegradable magnesium implants. Mater Sci Eng B 176:1609–1636
11. Gu X-N, Zheng Y-F (2010) A review on magnesium alloys as biodegradable materials. Front Mater Sci Chin 4:111–115
12. Persaud-Sharma D, Mcgoron A (2012) Biodegradable magnesium alloys: a review of material development and applications. J Biomimetics, Biomater Tissue Eng 12:25–39
13. Tie D, Feyerabend F, Muller WD, Schade R, Liefeith K, Kainer KU, Willumeit R (2013) Antibacterial biodegradable Mg-Ag alloys. Eur Cells Mater 25:284–298
14. Salahshoor M, Guo Y (2012) Biodegradable orthopedic magnesium-calcium (Mg–Ca) alloys, processing, and corrosion performance. Materials 5:135–155
15. Nayeb-Hashemi AA, Clark JB (1998) Phase diagrams of binary magnesium alloys. ASM International, Metals Park, Ohio
16. Hort N, Huang Y, Fechner D, Stoermer M, Blawert C, Witte F, Vogt C, Druecker H, Willumeit R, Kainer KU, Feyerabend F (2010) Magnesium alloys as implant materials—Principles of property design for Mg–RE alloys. Acta Biomater 6:1714–1725
17. Peng Q, Ma N, Li H (2012) Gadolinium solubility and precipitate identification in Mg–Gd binary alloy. J Rare Earths 30:1064–1068
18. Chino Y, Kobata M, Iwasaki H, Mabuchi M (2002) Tensile properties from room temperature to 673 K of Mg–0.9 mass%Ca alloy containing lamella Mg_2Ca. Mater Trans 43:2643–2646

Study on Polylactide-Coconut Fibre for Biomedical Applications

O. P. Gbenebor, R. A. Atoba, E. I. Akpan, A. K. Aworinde, S. O. Adeosun and S. A. Olaleye

Abstract Polylactide (PLA) reinforced with 5 wt% coconut shell particles (CSp) were electrospun using 0.09–0.14 g/ml composite solutions in Dichloromethane (DCM) while keeping the spinneret angle to the collector at 30, 45 and 90°. The fibres produced were subjected to mechanical, microstructural and fluid absorption (in distilled water and phosphate buffer solution (PBS), at 31 and 70 °C) examinations. The results indicated that the fibres demonstrated improved mechanical properties due to the presence of intercalated structures and good alignment of reinforcement particles with the matrix fibre. A Young Modulus of 126.96 MPa was obtained at 0.1 g/ml composite concentration compared to 0.52 MPa for virgin PLA at the same concentration. At 0.11 g/ml composite concentration, the Young modulus was 121.61 MPa compared to 1.1 MPa virgin PLA at the same concentration. The addition of CSp to the PLA matrix increased the number of pores in the fibres matrix giving rise to a pore diameter of 30.3 μm at 0.1 g/ml composite concentration for 30° spinneret angle. The fluid absorption test showed that reinforced PLA has high affinity for water and PBS at test temperatures

O. P. Gbenebor (✉) · R. A. Atoba · S. O. Adeosun
Department of Metallurgical and Materials Engineering, University of Lagos, Lagos, Nigeria
e-mail: gbeneborphilips@yahoo.co.uk

R. A. Atoba
e-mail: atobaakorede@gmail.com

S. O. Adeosun
e-mail: samsonoluropo@yahoo.com

E. I. Akpan
Institut fur Verbundwerkstoffe GmbH, 67663 Kaiserslautern, Germany
e-mail: emma_eia@yahoo.com

A. K. Aworinde
Department of Mechanical Engineering, Covenant University, Ota, Nigeria
e-mail: abraham.aworinde@covenantuniversity.edu.ng

S. A. Olaleye
Department of Mechanical Engineering, University of Lagos, Lagos, Nigeria
e-mail: solaleye@unilag.edu.ng

The Minerals, Metals & Materials Society, *TMS 2018 147th Annual Meeting & Exhibition Supplemental Proceedings*, The Minerals, Metals & Materials Series,
https://doi.org/10.1007/978-3-319-72526-0_24

than virgin, while the latter and former are good water absorbers. The resulting fibres can therefore, be used as towels, diapers, wound dressers, filters and in tissue engineering.

Keywords Polylactide · Coconut shell particles · Composite fibre
Dichloromethane · Stiffness · Microstructure · Fluid absorption
Phosphate-buffer solution

Introduction

Most current studies on fibres and their reinforcements deal with organic polymers or biopolymers. On the other hand, because of some special requirements in applications such as high temperature or strong mechanical strength, inorganic filaments have also been attracting huge focus. These include carbon nanotubes on carbon fibres [1] and vanadium oxide whiskers on titanium oxide fibres [2]. The study of polymeric fibers containing strengthening agents such as carbon nanotubes [3–5], silica nanoclays [6–8] and graphite [9] etc., have been done with significant success.

However, there are studies on polymer fibres reinforced with agricultural wastes. Adeosun et al. [10] showed that the mechanical properties and biodegradability of rice-husk reinforced polylactide composites have substitution potentials to replace petroleum based polymeric-nano-fiber composites. In the plot study by Oksman et al. [11], the mechanical properties of PLA—flax fibre composites showed that, it is a candidate material for soft tissue engineering applications. Raju et al. [12] showed that the mechanical properties of vinyl ester improved with the use of groundnut shell particles. In this current study, coconut shell—an agricultural waste was used as a strengthening agent to improve the properties of Polylactide (PLA).

Materials and Methods

The PLA resin used in the fibre production is a product of NatureWorks obtained from China. The concentration of DCM as received from the dealer was 96% (v/v) with density measured to be 1.29 g/cm^3 at 27 °C. The reinforcement, CSp was milled to 53 μm at Federal Institute of Industrial Research Oshodi (FIIRO) Lagos, Nigeria, in a jaw crusher and completed in a ball mill for 72 h. PLA resins were weighed from 4.5–7.0 g at an interval of 0.5 g to produce six different weights of PLA. Each weight of the pure PLA was dissolved into 50 ml of DCM to give concentrations from 0.09–0.14 g/ml at 0.01 g/ml interval. These were kept in corked bottles for 3–4 h for proper dissolution of the PLA. Each solution was electrospun using a 20 ml syringe with a 1.2 mm nozzle needle diameter. This process was carried out at 30, 45 and 90° spinneret angles to the stationary

aluminium foil collector plate. A high voltage supply source of 50 kV, 2 mA, 100 W was used. The voltage source was connected to the tip of the nozzle to produce an electrostatic force, which resultantly spun the solution into fine thin fibres that were collected on a stationary aluminium foil. The distances between the nozzle and the collector are 75, 60 and 40 mm for 30, 45 and 90° respectively. Average of 12 ml of the solution was used to produce each sample spanning 12–15 min. A total of 18 samples were produced for unreinforced PLA with 6 for each spinneret angle.

The above procedures were repeated when the reinforcement was added to the solution. The PLA weights were reduced by 5 wt% and replaced with 5 wt% CSp to maintain concentrations of 0.09–0.14 g/ml when dissolved in 50 ml DCM. Although CSp did not dissolve in DCM, however, it blended with the solution on proper stirring. An average of 12 ml of composite solution was electrospun to produce fibre sample within 18–20 min. A total of 18 composite fibres were produced with 6 at each spinneret angle.

Sample Preparation for Characterization

The tensile test was carried out on 20 × 10 × 0.58 mm fibre specimens using an Instron Model 313 having Bluehill TM Version 1.00 analysis software at Centre for Energy Research and Development (CERD), Obafemi Awolowo University Ile-Ife, Osun State, Nigeria. The same dimension was also cut out from all the 36 samples four times and weighed out for fluid absorption test using distilled water and PBS at 31 and 70 °C in a Uniscope SM801A laboratory water bath. It was carried out for a period of 5 days and the samples were reweighed again to determine the rate of fluid absorption. The water absorption test was carried out in the Department of Metallurgical and Materials Engineering, University of Lagos, Nigeria.

Fibres specimens from the produced samples were subjected to Scanning Electron Microscopy (SEM) analysis. An ASPEX 3020 model variable pressure SEM operated with an electron intensity beam 15 kV and equipped with Noran-Voyager energy dispersive spectroscope located at Covenant University Ota, Ogun State, Nigeria was used to observe the morphological features of the fibres. The average diameter of fibres and pore sizes were determined from SEM microstructures obtained at a magnification of 1000 with a calibration of 80 μm. The 80 μm calibration on the picture was converted to its equivalent inches on the Microsoft word. Therefore, values of fibre and pores were measured in inches then converted to μm. For example, if 80 μm is equivalent to 1.07 inches and the value of fibre or pore diameter measured is 0.5 inch, then the fibre or pore diameter in μm will be given in Eq. 1.

$$X\,\mu m = 80\,\mu m \times \frac{0.5''}{1.07''} \quad (1)$$

Results and Discussion

Mechanical Properties

The ultimate tensile strength, UTS of the electrospun PLA and PLA-CSp fibres with respect to the spinneret angles are shown in Fig. 1. In Fig. 1a, the highest UTS were obtained at 0.14 g/ml (1.85 MPa), 0.12 g/ml (1.7 MPa) and 0.09 g/ml (0.8 MPa) for spinneret angles of 90°, 45° and 30° respectively. On the other hand, the lowest UTS (<0.2 MPa) was obtained at 0.1 g/ml for all the spinneret angles. From Fig. 1b, the highest UTS were obtained at 0.12 g/ml (1.0 MPa), 0.09 g/ml (1.3 MPa) and 0.11 g/ml (4.51 MPa) for spinneret angles of 90°, 45° and 30° respectively. On the other hand, the lowest UTS for the reinforced fibres were obtained at 0.13 g/ml (0.25 MPa) for 90° and 30° (0.5 MPa) and 0.1 g/ml (0.25 MPa) for 45°. The peak UTS for the reinforced fibre occurred at 0.11 g/ml with spinneret angle of 30° (4.51 MPa), while the least (0.19 MPa) occurred at 0.1 g/ml at spinneret angle of 45°. The inclusion of CSp increases the UTS of electrospun PLA until the peak value is attained. The irregularity observed in between the peak and the starting point is attributed to the nonalignment of the fibres collected on the plate owing to environmental impact. The reinforced fibres were better in strength than the unreinforced at 30° spinning within 0.1–0.11 g/ml and are thus recommended for use as it records strength increment of 1510.71–2646.67% over unreinforced.

The stiffness of electrospun PLA and PLA-CSp fibres are shown in Fig. 2. In Fig. 2a, the highest Modulus (18.45 MPa) was obtained at 0.14 g/ml for 90°

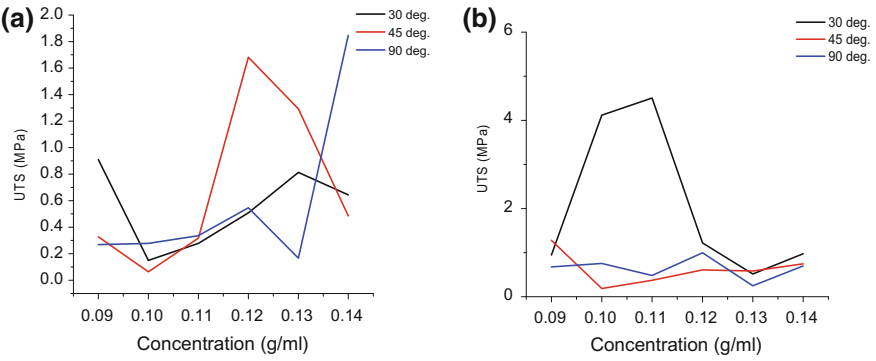

Fig. 1 Fibers ultimate tensile strengths of **a** PLA **b** PLA-CSp

spinning while it was a peak at 0.12 g/ml for 45° (25.33 MPa) and 30° (3.04 MPa) spinning. The least modulus (0.25 MPa) was obtained at 0.13 g/ml for 90° spinneret position while the minimum at 0.1 g/ml for 45° and 30° are 0.41 MPa and 0.52 MPa respectively. The Fig. 2b shows the highest stiffness at 0.11 g/ml for 90° and 45° with values of 24.96 MPa and 9.07 MPa respectively, while that at 30° with 0.1 g/ml was 126.96 MPa. The stiffness was least (0.63 MPa) at 0.13 g/ml for 90°, (2.8 MPa) at 0.1 g/ml for 45° and (5.12 MPa) at 0.09 g/ml for 30°. At 90° spinning, it was observed that the moduli of PLA-CSp are higher than that of pure PLA except at 0.14 g/ml. The CSp is responsible for the enhanced moduli. At 45°, the Young Modulus increased at four concentrations while at 0.12 g/ml and 0.13 g/ml, the pure PLA has higher stiffness than the reinforced PLA. At 30°, the inclusion of CSp tremendously increased the moduli of electrospun PLA to 126.96 MPa.

The elongations of electrospun PLA and PLA-CSp are presented in Fig. 3. The highest elongation (26.83 mm) was obtained at 0.13 g/ml for 90°, 12.25 mm at 0.09 g/ml for 45° and 13.53 mm at 0.14 g/ml for 30°. The lowest E was 1.98 mm at 0.11 g/ml for 90° and 45° and 3.62 mm at 0.12 g/ml for 30° (Fig. 3a). For PLA-CSp fibers, the highest E was 7.7 mm and 5.83 mm at 0.13 g/ml for both 90° and 45° respectively while 7 mm was obtained at 0.14 g/ml for 30° (Fig. 3b). The lowest E of 1.05 mm, 1.87 mm and 0.82 mm were obtained at 0.12 g/ml (90°), 0.1 g/ml (45°) and 0.13 g/ml (30°) respectively.

As observed from Figs. 1, 2 and 3 the inclusion of CSp improves the UTS and the Young Modulus of pure PLA. This high Young's modulus is attributed to the stiffening effect of the CSp filler. This agrees with the results of the micromechanical models [13, 14] and those of earlier studies [10, 12]. However, the ductility of the pure PLA was impaired.

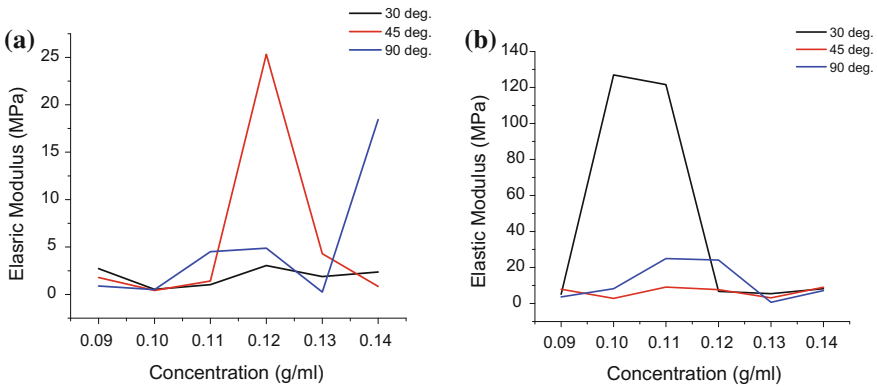

Fig. 2 Fibers stiffness strengths of **a** PLA **b** PLA-CSp

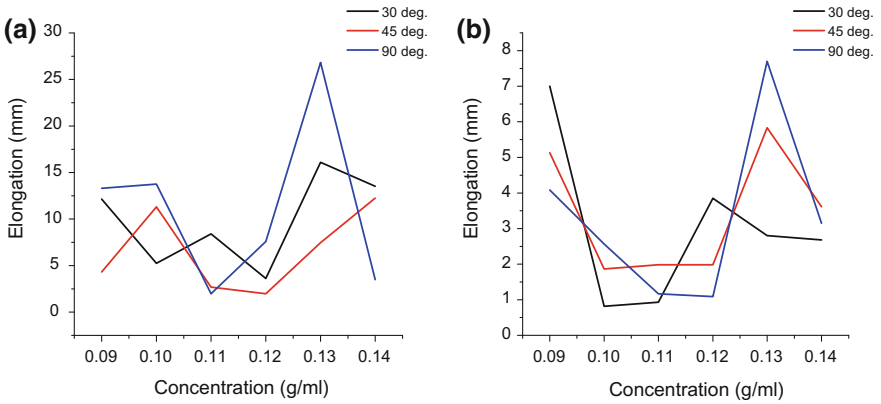

Fig. 3 Fibers elongation characteristics of **a** PLA **b** PLA-CSp

Fluid Absorption Characteristics PLA-CSp

Certain areas of application of PLA would require that its fluid absorption rate is ascertained. The degradation profile of PLA is affected by its fluid absorption propensity, which may positive or negative depending on the area of application [15]. The rate of water and PBS absorption of pure PLA and PLA-CSp at room temperature and 70 °C for a period of five days are shown in Fig. 4.

Unreinforced PLA absorbed more water than PBS both at room temperature and at 70 °C. The highest rate of absorption (0.38 g) was at 0.13 g/ml (Fig. 4a). Similarly, PLA-5 wt% CSp absorbed more water than PBS both at room temperature and at 70 °C with the highest (0.41 g) at 0.13 g/ml (Fig. 4b). The reinforced PLA also absorbs more of both water and PBS than the pure PLA at 90°. This is attributed to the amorphous content of the unprocessed CSp before use. The fluid loving constituents of CSp will thus attract more molecules into its matrix [16].

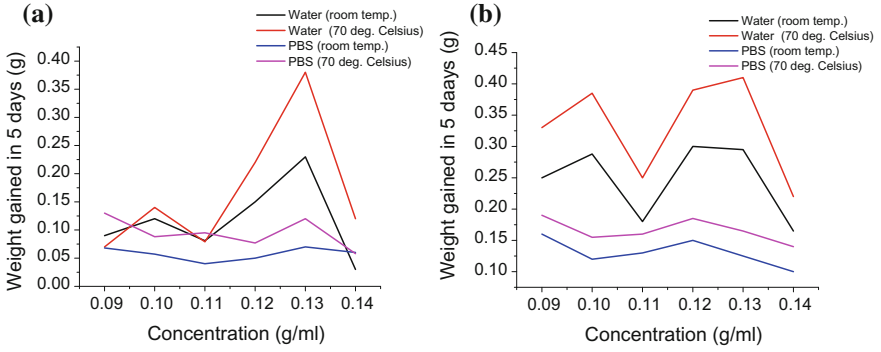

Fig. 4 Water and PBS absorption rate at 90° of **a** pure PLA **b** PLA-5 wt% CSp

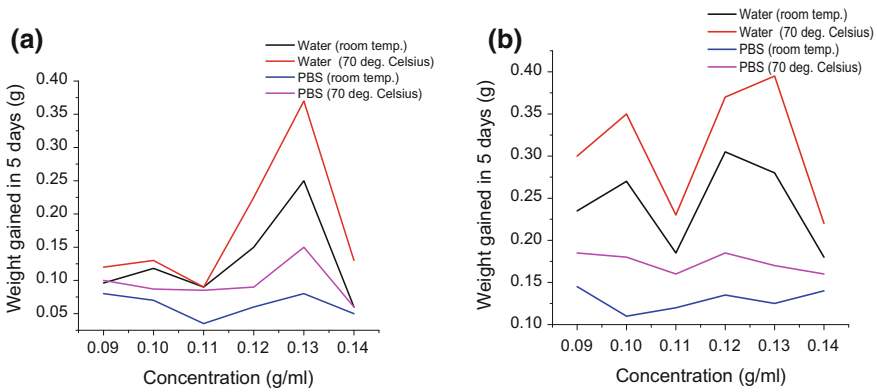

Fig. 5 Water and PBS absorption rate at 45° of **a** pure PLA **b** PLA-5 wt% CSp

In Fig. 5a the unreinforced PLA showed more affinity for water than PBS both at room temperature and at 70 °C. The highest rate of absorption (0.37 g) was at 0.13 g/ml). Similarly, PLA-5 wt% CSp absorbed more water than PBS both at room temperature and at 70 °C with the highest (0.395 g) at 0.13 g/ml (Fig. 5b). The reinforced PLA also absorbs more of both water and PBS than the pure PLA at 45°.

The study noticed that unreinforced PLA was more water loving than PBS both at room temperature and at 70 °C for 30° spinneret inclination. The highest rate of absorption (0.35 g) was at 0.12 g/ml (Fig. 6a). The PLA-5 wt% CSp followed a similar pattern with the unreinforced PLA as it absorbed more water than PBS both at room temperature and at 70 °C with the peak (0.39 g) at 0.12 g/ml (Fig. 6b). The affinity of reinforced PLA water and PBS was higher than unreinforced PLA. The increase in temperature increases the level of fluid absorption of the fibres. Thus, the addition of CSp to PLA at 0.12 g/ml concentration and at 70 °C significantly

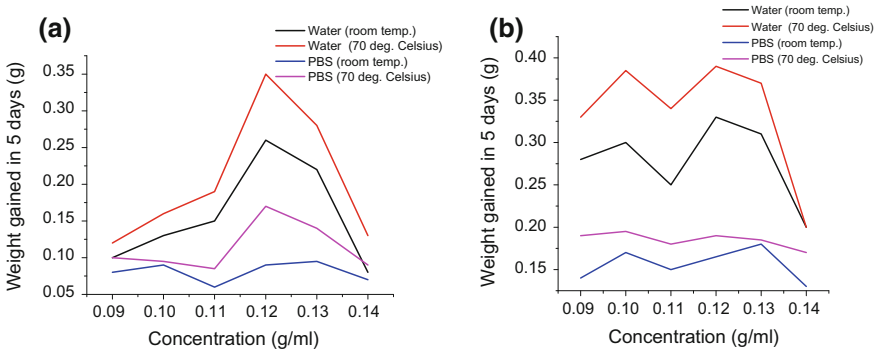

Fig. 6 Water and PBS absorption rate at 30° of **a** pure PLA **b** PLA-5 wt% CSp

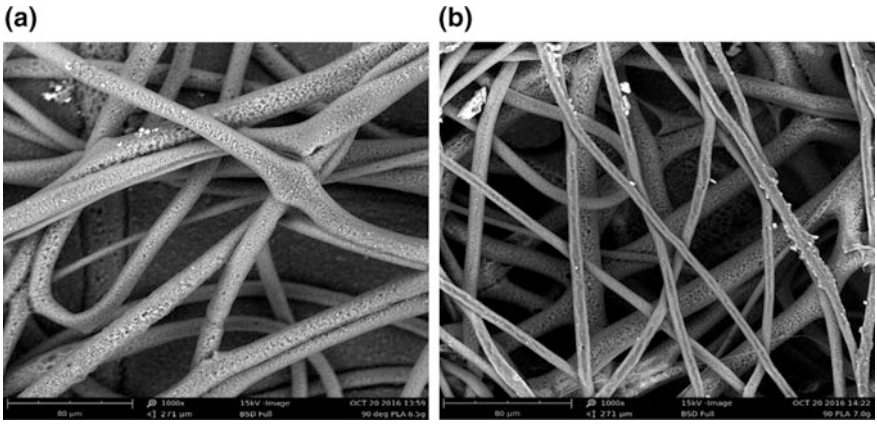

Fig. 7 Morphology of pure PLA for 90° spinning at **a** 0.13 g/ml **b** 0.14 g/ml

increased the water absorption level by 11.43% while the PBS absorption level was increased by 11.76%.

Morphological Analysis

Figures 7a and b are the morphological structures of pure PLA at 0.13 g/ml and 0.14 g/ml having ribbon-like shape fibres with embedded pores respectively. The mean fibre diameters were ~16346 nm and 10545 nm respectively.

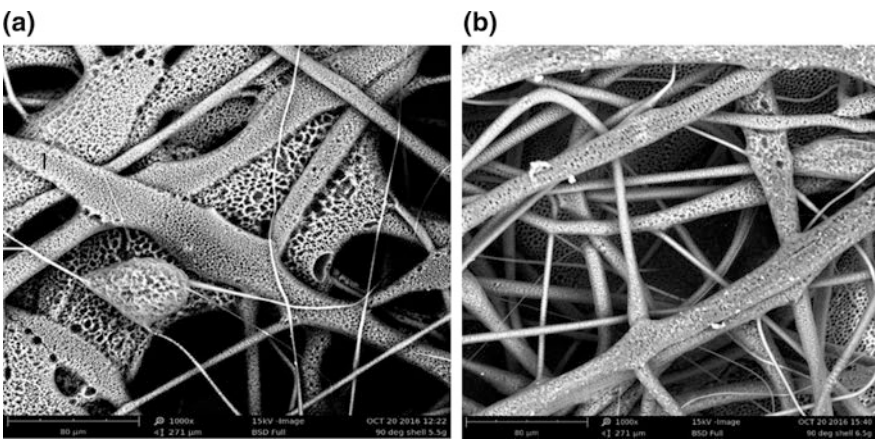

Fig. 8 Morphology of pure PLA-5 wt% CSp for 90° spinning at **a** 0.11 g/ml **b** 0.13 g/ml

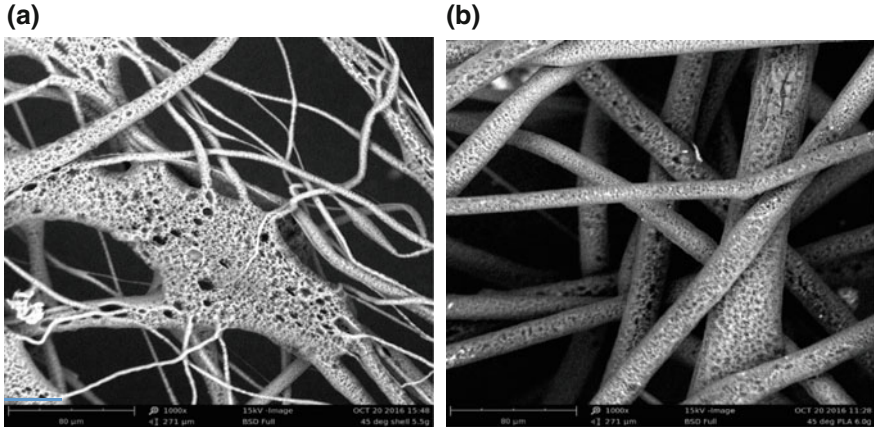

Fig. 9 Morphology of pure PLA-5 wt% CSp for 45° spinning at **a** 0.11 g/ml **b** 0.12 g/ml

Figure 8a and b show the morphological structure of PLA-5 wt% CSp at 0.11 g/ml and 0.13 g/ml respectively with large diameter pores having mean diameter of 14632 nm and 12148 nm respectively. These large diameter pores scattered over the fibre surface are attributed to the interaction between the particles and the matrix fibre. There is a kind of repulsion between the matrix and the filler resulting into pores formation [17].

Figure 9a shows the structure of PLA-5 wt% CSp at 0.11 g/ml and 45° spinneret angle. Large pores were found with an average diameter of ~16125 nm on the fibre surface and the fibres are irregularly arranged. The pores on the fibre surface are attributed to the presence of CSp in the PLA matrix. At 0.12 g/ml and 45°, a ribbon-like shape fibres with embedded pores were observed with a mean diameter of ~19685 nm (Fig. 9b).

Figure 10a shows PLA-5 wt% CSp fibre structure at 0.1 g/ml and 30° with pores of ~20162 nm mean diameter on fibre surface irregularly arranged with beads. Thus the large pores here are the cause of the large fibre diameter observed. This is in consonance with the findings of Zhu and Beyerlein [18], Rnjak et al. [19] and Eda and Shivkumar [20], where pore sizes were reported to have close and direct relation to the fibre diameter of electrospun mats. The pore size increases with the increase of the fibre diameter [21]. At 0.12 g/ml and 30° ribbon-like shape fibres with embedded pores with beads were observed (see Fig. 10b) having ~16456 nm diameter.

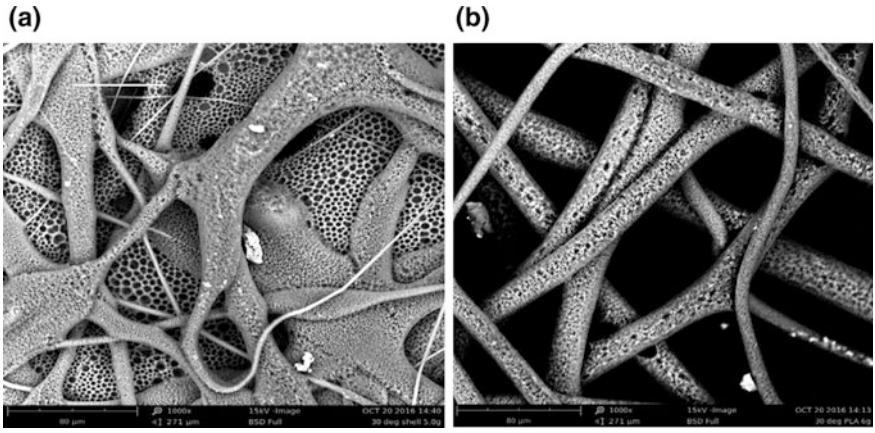

Fig. 10 Morphology of pure PLA-5 wt% CSp for 30° spinning at **a** 0.10 g/ml **b** 0.12 g/ml

Conclusion

In the characterization study of reinforced PLA, the addition of coconut shell particles produces a significant increase in the strength properties of the electrospun fibres and influences the production of pores in the fibres. This composite fibre may serve as wound dressers, moping materials for wet surfaces and can be impregnated with a drug for drug delivery.

References

1. Hou HQ, Reneker DH (2004) Carbon nanotubes on carbon nanofibers: a novel structure based on electrospun polymer nanofibers. Adv Mater 16(1):69–73
2. Ostermann R, Li D, McCann JT, Xia Y (2006) V_2O_5 nanorods on tio_2 nanofibers: a new class of hierarchical nanostructures enabled by electrospinning and calcination. Nano Lett 6 (6):1297–1302
3. Ko F, Gogotsi Y, Ali AA, Naguib N, Ye H, Yang G (2003) Electrospinning of continuous carbon nanotube-filled nanofiber yarns. Adv Mater 15:1161–1165
4. Seoul C, Kim YT, Baek CK (2003) Electrospinning of poly(vinylidene fluoride)/dimethylformamide solutions with carbon nanotubes. J Polym Sci Part B: Polym Phys 41:1572–1577
5. Sen R, Zhao B, Perea D, Itkis M, Hu H, Love J, Bekyarova E, Haddon RC (2004) Preparation of single-walled carbon nanotube reinforced polystyrene and polyurethane nanofibers and membranes by electrospinning. Nano Lett 4(3):459–464
6. Fong H, Liu W, Wang C, Vaia RA (2002) Generation of electrospun fibers of nylon 6 and nylon 6-montmorillonite nanocomposite. Polymer 43(3):775–780
7. Zhou HJ, Kim KW, Giannelis E, Joo YL (2006) Nanofibers from polylactic acid nanocomposites: effect of nanoclays on molecular structures. ACS Symp Ser 918:217–230
8. Ji Y, Li B, Ge S, Sokolov, JC Rafailovich MH (2006) Structure and nanomechanical characterization of electrospun ps/clay nanocomposite fibers. Langmuir 22:1321–1328

9. Mack JJ, Viculis LM, Ali A (2005) Graphite nanoplatelet reinforcement of electrospun polyacrylonitrile nanofibers. Adv Mater 17:77–80
10. Adeosun SO, Aworinde AK, Diwe IV, Olaleye SA (2016) Mechanical and microstructural characteristics of rice husk reinforced polylactide nanocomposite. West Indian J Eng 39:63–71
11. Oksman K, Skrifvars M, Selin JF (2003) Natural fibres as reinforcement in polylactic acid (PLA) composites. Compos Sci Technol 63:1317–1324
12. Raju GU, Kumarappa S, Gaitonde VN (2012) Mechanical and physical characterization of agricultural waste reinforced polymer composite. J Mater Environ Sci 3(5):907–916
13. Angelo GF, Mark TK, Ning Y (2006) Predicting the elastic modulus of natural fibre reinforced thermoplastics. Composites 37:1660–1671
14. Garesci F, Fliegener S (2013) Young's modulus prediction of long fiber reinforced thermoplastics. Compos Sci Technol 85:142–147
15. SuPing L, Darrel U (2009) Review degradability of polymers for implantable biomedical devices. Int J Mol Sci 10:4033–4065
16. Agunsoye JO, Talabi SI, Sanni OS (2012) Study of mechanical behaviour of coconut shell reinforced polymer matrix composite. J Miner Mater Charact Eng 11:774–779
17. Beard KW, Edwards AM (2012) Surface free energy based filled polymer microporous films. United States Patent Application Publication, pp 1–11
18. Zhu Y, Beyerlein I (2002) Bone-shaped short fiber composites—an overview. Mater Sci Eng A 326:27–208
19. Rnjak KJ, Wise SG, Li Z, Maitz PKM, Young CJ, Wang Y, Weiss AS (2011) Tailoring the porosity and pore size of electrospun synthetic human elastin scaffolds for dermal tissue engineering. Biomaterials 32(28):6729–6736
20. Eda G, Shivkumar S (2007) Bead-to-fiber transition in electrospun polystyrene. J Appl Polym Sci 106:475–487
21. Boland ED, Coleman BD, Barnes CP, Simpson DG, Wnek GE, Bowlin GL (2005) Electrospinning polydioxanone for biomedical applications. Acta Biomater 1:115–123

Visualization of Implant Failure by Synchrotron Tomography

Regine Willumeit-Römer, Julian Moosmann, Berit Zeller-Plumhoff, D. C. Florian Wieland, Diana Krüger, Björn Wiese, Ann Wennerberg, Niccolò Peruzzi, Silvia Galli, Felix Beckmann and Jörg U. Hammel

Abstract Magnesium (Mg) and its alloys degrade under physiological conditions. But how strong is the connection between the implant, the corrosion layer and the surrounding tissue, namely bone? Biomechanical tests like push-out tests have shown that a degraded Mg-pin is surprisingly well integrated with the bone "as reported by Castellani et al. (Acta Biomater 7(1):432–440, 2011) [1]". High-resolution synchrotron tomography offers a deep look into the microstructure of the material as well as of the bone during deformation until fracture happens. Here we present first data from an in situ tomography experiment of a

R. Willumeit-Römer (✉) · J. Moosmann · B. Zeller-Plumhoff · D. C. Florian Wieland · D. Krüger · B. Wiese
Division Metallische Biomaterialien, Institute for Materials Research, Helmholtz-Zentrum Geesthacht, Geesthacht, Germany
e-mail: regine.willumeit@hzg.de

J. Moosmann
e-mail: julian.moosmann@hzg.de

B. Zeller-Plumhoff
e-mail: berit.zeller-plumhoff@hzg.de

D. C. Florian Wieland
e-mail: florian.wieland@hzg.de

D. Krüger
e-mail: diana.krueger@hzg.de

B. Wiese
e-mail: bjoern.wiese@hzg.de

A. Wennerberg · S. Galli
Department of Prosthodontics, Faculty of Odontology, Malmö University, Malmö, Sweden
e-mail: ann.wennerberg@mah.se

S. Galli
e-mail: silvia.galli@mah.se

N. Peruzzi
Clinical Sciences, Lund University, 221 85 Lund, Sweden
e-mail: niccolo.peruzzi@med.lu.se

The Minerals, Metals & Materials Society, *TMS 2018 147th Annual Meeting & Exhibition Supplemental Proceedings*, The Minerals, Metals & Materials Series,
https://doi.org/10.1007/978-3-319-72526-0_25

biodegradable Mg-based implant under compressive load showing how Mg implants are incorporated into bone.

Keywords Magnesium (Mg) · Synchrotron tomography · Implant failure MicroCT · In situ biomechanical testing

Introduction

Aging populations, increasing obesity, and the rise in osteoporosis-related fractures will sustain a need for orthopedic intervention. In addition, juvenile patients and active adults exhibiting risky sporting activities also require perfect care. So far these indications are treated mainly with non-degradable metal implants or in some cases polymer implants. From the patient's point of view, degradable implants would clearly be preferred [2]. Here, degradable Magnesium based implants could become an alternative to permanent metallic implants which have to be removed after healing or to replace degradable polymers which do not always show the required mechanical properties.

Mg and its alloys degrade under physiological conditions. The great challenge is to tailor the degradation to be suitable for a biological environment. Fast or uncontrolled corrosion is associated with strong hydrogen and ion release and severe pH changes, which can lead to a fast loss of mechanical stability and undesirable biological reactions. Since these processes are highly complex in a living system and sufficient data describing the degradation in vivo is missing [3], it is very difficult to produce knowledge based new alloys. Therefore the development of new biodegradable Mg-based implants is strongly relying on the understanding of the degradation process in the living organism and the creation of an appropriate test system in vitro.

Of special importance is the question how the degrading implants interact with the surrounding tissue, namely bone, and how they behave under load during the degradation and healing process.

Bone healing and remodeling are highly complex biological processes which cannot be mimicked in vitro. They change the structural and mechanical properties of bone on all levels of the bone structure due to its hierarchical organization [4, 5]. Studies which analyze this in detail demonstrate that healing propagates in waves where first woven bone is formed followed by a reordering to a lamellar structure.

F. Beckmann · J. U. Hammel
Division Metallphysik, Institute for Materials Research, Helmholtz-Zentrum Geesthacht, Geesthacht, Germany
e-mail: felix.beckmann@hzg.de

J. U. Hammel
e-mail: joerg.hammel@hzg.de

On the micro-structural scale the hydroxyl apatite crystals first form thick particles with low orientation and an overall high degree of mineralization is observed [6, 7]. Subsequently, a transformation occurs and a decrease of the crystal size can be seen accompanied by a better alignment. As the orientation of the collagen matrix and the hydroxyl apatite crystals both play important roles, this observation is attributed to the low degree of orientation in these early bone structures. This fine-tuned orchestra can be easily disturbed when implants are positioned in the bone. This is even more important when the implant presents not only a mechanical but also a chemical disturbance to the microenvironment by releasing e.g. biologically active ions into the biological environment as Mg implants do.

For all types of implants osseointegration is a very important clinical issue. The success of the implantation is strictly related to the ability to be encapsulated by bone tissue. One of the biggest threats to this integration is the occurrence of micro-movements during the healing phase [8], while the implant is not yet bonded to the bone. This might be even more important for relatively fast degrading Mg implants (duration in the body 1–2 years, in some cases they can degrade within weeks) where a stable surface to which the bone cells can attach does not exist. However, not much is known about the interface between the bone, the corrosion layer, and the bulk metal and which forces are transferred from the metal to the bone or vice versa. Measuring push out forces showed that a degrading Mg implant is much stronger integrated into the bone than Ti or a polymer but the reason for this is unclear [1]. In situ synchrotron radiation tomography observing the structural changes within bone and corrosion layer during a push-out experiment will deliver the necessary data base which will allow us to simulate the force fields and thus to elucidate the mechanism of failure for this new class of implants.

Materials and Methods

Screws (4 mm long, 2 mm in diameter, thread M2 and a 0.5 × 0.5 mm slotted screw head) made of an alloy of Mg and Gadolinium (Gd) were prepared by permanent mold direct chill casting, solid solution heat treated (T4) and further processed by extrusion. Melting was performed using Ar + 3 vol% SF_6 as shielding gas in the induction furnace (Nabertherm) at a melding temperature of 700 °C. Gadolinium with 5 and 10 wt% were added to the magnesium melt. The melt was kept for 20 min and stirred with a rotation speed of 150 min^{-1}. Then the molten materials were poured into a permanent steel mold (diameter 110 mm, height 230 mm) which was preheated up to 680 °C. The melt was kept for 15 min at 680 °C in the mould. The cast ingots were cooled down to room temperature by water quenching [9]. The ingots were T4 heat treated at 525 °C for 6 h and cooled down by water quenching. The indirect extrusion was performed with an extrusion ratio of 84 to the final diameter of 12 mm. As extrusion parameter, a ram speed of 150 m/min and a temperate of 400 °C were used. With wire electrical discharge cutting, rods with a diameter of 3 mm were cut from the extruded bars. Their final

shape was machined by turning and for the head by milling. The screws were characterized with respect to their grain size and degradation behavior. Mg-5Gd exhibits an average grain size of 52.6 ± 15.3 μm, while the grains for the Mg-10Gd materials are smaller (25.9 ± 0.1 μm). Semi-static degradation tests over 1 month period were performed on Mg-5Gd and Mg-10Gd screws in order to examine the degradation behavior, in particular the degradation rate and degradation homogeneity. As degradation medium, mimicking biological conditions, α-Minimum Essential Medium (α-MEM; Thermo Fisher Scientific GmbH, Darmstadt, Germany) +10% Fetal Bovine Serum (FBS; PAA Laboratories, Linz, Austria) +1% Penicillin/Streptomycin (P/S; Thermo Fisher Scientific GmbH, Darmstadt, Germany) was used. The degradation medium was kept under cell culture conditions (37 °C, 5% CO_2, 20% O_2, 95% relative humidity). The degradation rate was determined at four time points (7, 14, 21, and 28th day of immersion) by using high-resolution synchrotron radiation computed tomography at the imaging beamline (IBL) P05 which is operated by the Helmholtz-Zentrum Geesthacht (HZG) at the PETRA III storage ring at the Deutsches Elektronen-Synchrotron (DESY), Hamburg [10–12]. The degradation rate was calculated as $\frac{\Delta V}{A \cdot t}$, where ΔV denotes the volume change detected by measuring the volume V from tomographic data before and after immersion, A the surface area before immersion, and t the time of immersion. From these four measurements, an average degradation rate of 0.30 ± 0.09 mm/year for both alloys was obtained which is acceptable for biodegradable implants [13]. The analysis showed that Mg-5Gd screws tend to degrade with localized pitting corrosion in the first week of immersion. Afterwards the corrosion layer starts to spread over the whole surface. In contrast, the primarily localized pitting corrosion of Mg-10Gd is not as pronounced; the degradation is more homogeneously distributed over a larger surface area (Fig. 1).

Screws made of Mg-5Gd and Mg-10Gd, and as reference materials, of polyether ether ketone (PEEK) and Titanium were implanted in the femur of Sprague Dawley rats for various healing times (4, 8, and 12 weeks). After the rats were sacrificed, cylindrical or box-shaped explants with a diameter/width of 5 mm were cut from

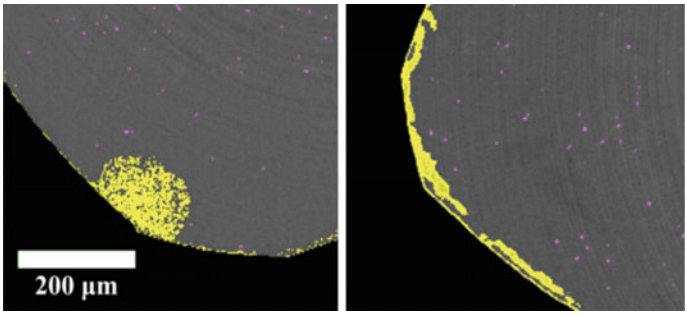

Fig. 1 Cross sectional slices of two screws after 1 week degradation. Left: Mg-5Gd, right: Mg-10Gd. Yellow colored areas represent corrosion layers and magenta colored dots represent Gd agglomerations

the rat's femur. The data presented in the following is from an explant of a Mg-10Gd screw implanted in a rat femur for 12 weeks.

In order to investigate the failure mechanisms and test the biomechanical properties of degraded Mg-based implants in situ, a load frame is used which allows the acquisition of a sequence of tomographic data sets under compressive load conditions [14]. Tomographic data sets employing conventional absorption contrast were acquired at IBL of PETRA III. A monochromatic X-ray beam with photon energy of 34 keV and a bandwidth of 10^{-4} was used. X-rays were detected with an indirect converting detector system consisting of a CCD camera, microscope optics, and a scintillator. The main components of the load frame are a motorized actuator delivering forces up to 1 kN, a load cell with an appropriately chosen sensitivity, and an X-ray transparent spacer made of polyether ether ketone (PEEK) ensuring force closure. Customized 3D printed sample mounts were used to support the explants and to ensure that the force is applied paraxially to the principal axis of the implant. Conventional absorption contrast tomography was employed with step-wise rotation, 1200 projection per tomogram, and a CCD camera with 3056 × 3056 pixels. At fivefold optical magnification, this resulted in an effective pixel size of 2.4 μm. A tomographic scan including acquisition of flat-and-dark-fields took about 80 min. A sequence of ten tomograms of an explant was acquired under increasing load conditions. Before the acquisition of each tomogram, the force applied onto the implant was successively increased by 2.5 N. The total range of forces probed was 0–24 N.

Results

In the following we present sections through the tomographic reconstructions of the data that was acquired under increasing load conditions as described above. Slices through the reconstructed volume along the principal axis of the implant are shown in Fig. 2. The top image in Fig. 2 was acquired before any load was applied to the screw, while for the bottom image the actuator was moved until a load of 24 N was reached before the tomographic scan was started. This force corresponds to roughly nine times the average body weight of a mature, male rat of about 275 g. Comparison of the top and bottom image in Fig. 2 clearly shows load-induced ruptures throughout the sample. Figure 3 depicts sequences of the regions which are indicated by the black squares in Fig. 2 where cracks occur, propagate, and expand in the course of increasing the load on the sample.

In Fig. 4 renderings of the cut-out explant, the corrosion layer, and the remaining bulk material of the corroded implant are depicted. The renderings are made from segmentations of the tomographic reconstruction which is shown in the top image in Fig. 2. Segmentation was done by simple thresholding. Prior to thresholding,

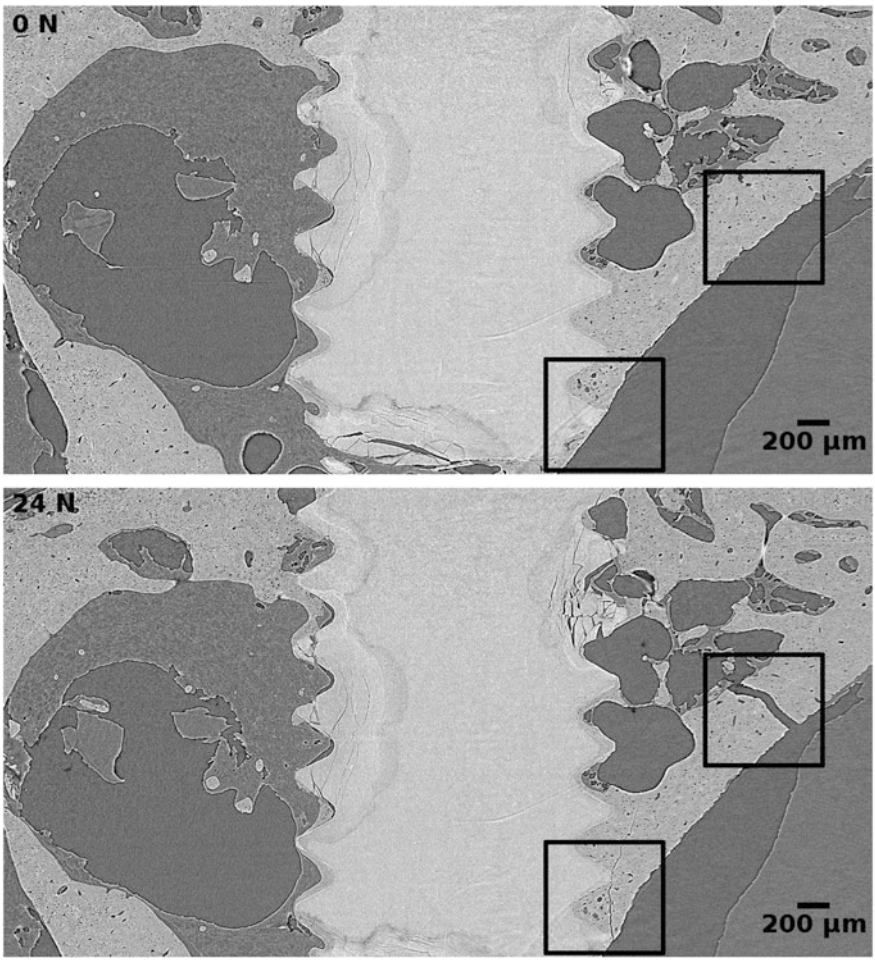

Fig. 2 Slices through the tomographic reconstructions of an explant along the principal axis of the implant. The top image (0 N) was acquired without load and the bottom image (24 N) under mechanical load. Images show a Mg-10Gd screw which was implanted in a rat femur for 12 weeks. Different layers of corrosion between implant and bone are distinguishable. In the bottom image load-induced ruptures are visible throughout the sample. The tomographic data during the load sequences was measured using conventional absorption contrast. After reconstruction images were twofold binned to a shape of 1096 × 592 pixels with a linear pixel size of 4.8 µm after binning

a phase-retrieval-filter (linearized transport-of-intensity/Paganin) was applied to the data in order to remove residual edge-enhancement and to enhance the density contrast in the reconstructions.

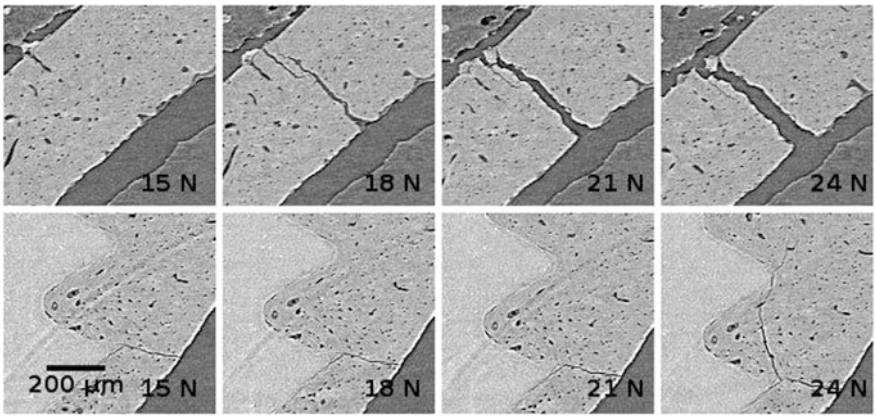

Fig. 3 Sequences of two enlarged regions in the slices through the tomographic reconstructions of an explant under increasing compressive load. The explant shown is a Mg-10Gd screw which was implanted in a rat femur for 12 weeks. The magnified details depicted in the image sequences refer to the two regions which are indicated in Fig. 2. The top row shows a region of cortical bone and the bottom row a region of the bone-to-implant interface as indicated by the top right and bottom left rectangle in Fig. 2, respectively. Before the acquisition of the tomographic scans was started, the force was set to 15 N, 18 N, 21 N, and 24 N, respectively. Images have a shape of 148 × 140 pixels with a linear pixel size of 4.8 µm

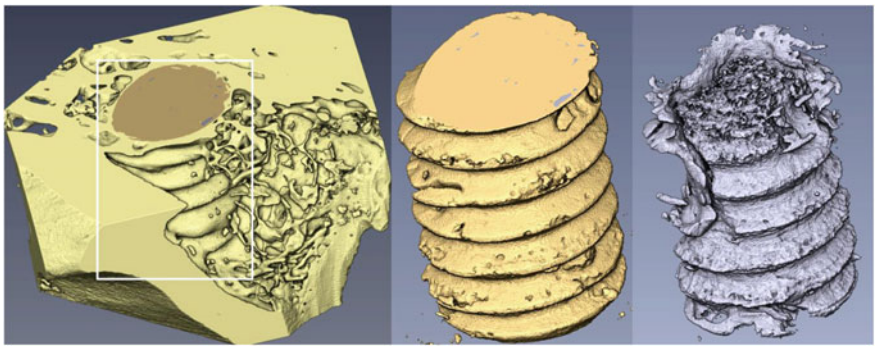

Fig. 4 Renderings of the explant (left), the corrosion layer (middle), and the remaining bulk material (right) of the corroded implant based on the reconstruction of the tomographic data. The middle and right images show the enlarged region as indicated by the rectangle in left image. Several layers of corrosion could be distinguished, but for the sake of a better visualization all layers are rendered as a single one

Discussion

The fragmentation of the implant material that can be seen in Fig. 2 in the areas where corrosion took place is not due to load, but a normal consequence of corrosion. It can also be observed in the corroded areas of screws that are not implanted but which have been immersed in a cell culture medium for about 1 week (Fig. 1). Ruptures in these fragmented areas increase under load, but do not seem to impair the stability of the implant. Note that the interface between implant material and bone does not exhibit a well-defined boundary surface. There is always an inhomogeneous corrosion layer in between bone and bulk material with a composition that is influenced by the bone. Considering the rupture lines in the image sequences of the magnified regions in Fig. 3 (which correspond to rupture planes in 3D), the propagation of these cracks does not seem to occur directly at the bone-to-implant interface. Instead, the first crack is at a 45° angle with respect to the direction of loading, which is the direction of maximum shear stress. Whilst this may indicate the strength of the osseointegration of the implant, it is more likely to be an artefact of the experimental setup, as the lower part of implant is integrated into the cortical bone which effectively results in a zero displacement boundary condition in the loading direction. To circumvent this artefact it is necessary to ensure that the implant has no interface with the cortical bone opposite the implantation site. Segmentations, as in Fig. 4, allow to calculate the contact area between bone and implant which is a means to assess the osseointegration and the bone formation around implants.

Conclusions

During tomography on a bone-implant sample biomechanical testing was performed in situ yielding four-dimensional image data showing implant failure. The reconstructed volumes allow to distinguish cortical and trabecular bone, osteocyte lacunae, Haversian canals, and bone marrow. The analyzed load sequence showed that the bone-to-implant interface remained intact under compression with up to 18 N, where the first breakage occurred. When implant failure took place within the sample, sites of fracture were distributed throughout the sample. However, ruptures do not seem to predominantly originate from or propagate along the bone-to-implant interface. Cracks within corroded areas of the implant, which are already present prior to load, increased under load. This does not seem to impair the stability of the implant as in these regions load induced rupture lines are not more frequent than in other. Moreover, the analyzed Mg-based implants show an excellent osseointegration. The data acquired in this first experiment under load conditions corroborates the idea to use biodegradable Mg-based screws for bone implants. In follow-up experiments a statistically significant number of implants will be considered and additional small angle X-ray scattering experiments will be

performed. This will give evidence on the performance of the employed implant material i.e. on integration and stability with respect to the employed material, healing times, and load conditions.

Acknowledgements This research was carried out within the SynchroLoad project (BMBF project number 05K16CGA) and the MgBone project (BMBF project number 05K16CGB) which are funded by the Röntgen-Ångström Cluster (RÅC), a bilateral research collaboration of the Swedish government and the German Federal Ministry of Education and Research (BMBF). We acknowledge provision of beamtime, related to the proposals I-20160658 and I-20160104, at beamline P05 at PETRA III at DESY, a member of the Helmholtz Association (HGF). We would like to thank Thomas Dose, Hilmar Burmester, and Jens Brehling for designing and constructing the load frame. We are also very grateful for the support by Fabian Wilde, Alexander Hipp, and Monika Luczak.

References

1. Castellani C, Lindtner RA, Hausbrandt P, Tschegg E, Stanzl-Tschegg SE, Zanoni G, Beck S, Weinberg A-M (2011) Bone-implant interface strength and osseointegration: biodegradable magnesium alloy versus standard titanium control. Acta Biomater 7(1):432–440
2. Mittal R, Morley J, Dinopoulos H, Drakoulakis EG, Vermani E, Giannoudis PV (2005) Use of bio-resorbable implants for stabilisation of distal radius fractures: the United Kingdom patients' perspective. Injury 36(2):333–338
3. Sanchez AHM, Luthringer BJC, Feyerabend F, Willumeit R (2015) Mg and Mg alloys: how comparable are in vitro and in vivo corrosion rates? a review. Acta Biomater 13:16–31
4. Hoerth RM, Seidt BM, Shah M, Schwarz C, Willie BM, Duda GN, Fratzl P, Wagermaier W (2014) Mechanical and structural properties of bone in non-critical and critical healing in rat. Acta Biomater 10(9):4009–4019
5. Liu Y, Manjubala I, Roschger P, Epari DR, Schell H, Lienau J, Bail HJ, Duda GN, Fratzl P (2009) The evolution of size and distribution of apatite mineral crystals during bone fracture healing in sheep. Bone 44:S271–S272
6. Liu Y, Roschger P, Manjubala I (2008) Characteristics of mineral particles in the callus during fracture healing in a sheep model. Calcif Tissue Int 82
7. Liu Y, Manjubala I, Schell H, Epari DR, Roschger P, Duda GN, Fratzl P (2010) Size and habit of mineral particles in bone and mineralized callus during bone healing in sheep. J Bone Miner Res 25(9):2029–2038
8. Szmukler-Moncler S, Salama H, Reingewirtz Y, Dubruille JH (1998) Timing of loading and effect of micromotion on bone–dental implant interface: review of experimental literature. J Biomed Mater Res 43(2):192–203
9. Peng Qiuming, Huang Yuanding, Zhou Le, Hort Norbert, Kainer Karl Ulrich (2010) Preparation and properties of high purity mg–y biomaterials. Biomaterials 31(3):398–403
10. Haibel A, Beckmann F, Dose T, Herzen J, Ogurreck M, Müller M, Schreyer A (2010) Latest developments in microtomography and nanotomography at PETRA III. Powder Diffr 25(2): 161–164
11. Haibel A, Ogurreck M, Beckmann F, Dose T, Wilde F, Herzen J, Müller M, Schreyer A, Nazmov V, Simon M, Last A, Mohr J (2010) Micro- and nano-tomography at the GKSS imaging beamline at PETRA III. In: Proceedings of SPIE, p 78040B
12. Wilde F, Ogurreck M, Greving I, Hammel JU, Beckmann F, Hipp A, Lottermoser L, Khokhriakov I, Lytaev P, Dose T, Burmester H, Müller M, Schreyer A (2016) Micro-CT at the imaging beamline P05 at PETRA III. In: AIP conference proceedings, vol 1741(1), p 030035

13. Wetterlöv Charyeva O (2015) Bioresorbable magnesium implants for bone applications. PhD thesis, Justus-Liebig-Universität
14. Moosmann J, Zeller-Plumhoff B, Wieland DCF, Galli S, Krüger D, Dose T, Burmester H, Wilde F, Bech M, Peruzzi N, Wiese B, Hipp A, Beckmann F, Hammel JU, Willumeit-Römer R (2017) Biodegradable magnesium-based implants in bone studied by synchrotron radiation microtomography. In: Proceedings of SPIE—developments in x-ray tomography XI, vol 10391–23

Part X
Biological Materials Science

3D Full-Field Mechanical Measurement of a Shoulder Bone Under Implant Loading

Yuxiao Zhou, Michael A. Hernandez Lamberty, Gregory S. Lewis, April D. Armstrong and Jing Du

Abstract The mechanics of shoulder bones under implant loading is important to the success of shoulder replacement surgery. This work presents the results of a noninvasive three-dimensional (3D) full-field mechanical measurement of implanted shoulder bones under various physiologically realistic loading conditions. A glenoid implant was cemented in a human cadaveric specimen by a shoulder surgeon and loaded in a mechanical tester coupled with micro X-ray computed tomography (micro-CT). The micro-CT images of the specimen was taken under no-load, eccentric loading, and concentric loading conditions, respectively. Using image processing technique and digital volume correlation, the 3D displacement field inside the shoulder bone were calculated. The results were displayed using 3D visualization tools. The clinical implications of the results are discussed for the improvement of total shoulder replacement.

Keywords Implant · Shoulder bone · Micro-CT · Digital volume correlation

Y. Zhou · J. Du (✉)
Department of Mechanical and Nuclear Engineering, Penn State University, 316B Leonhard Building, University Park, PA PA16802, USA
e-mail: jingdu@psu.edu

Y. Zhou
e-mail: yyz5239@psu.edu

M. A. Hernandez Lamberty
Department of Mechanical Engineering, University of Puerto Rico at Mayagüez, Mayagüez, PR, USA
e-mail: michael.hernandez15@upr.edu

G. S. Lewis · A. D. Armstrong
Department of Orthopaedics and Rehabilitation, Penn State College of Medicine and M.S. Hershey Medical Center, Hershey, PA, USA
e-mail: gsl120@psu.edu

A. D. Armstrong
e-mail: aarmstrong@hmc.psu.edu

The Minerals, Metals & Materials Society, *TMS 2018 147th Annual Meeting & Exhibition Supplemental Proceedings*, The Minerals, Metals & Materials Series,
https://doi.org/10.1007/978-3-319-72526-0_26

Introduction

Glenoid implant loosening is the most common complication in the total shoulder replacement surgery. After 5 years, radiographic loosening rates have been observed to be 15–44% [1–4]. Glenoid implant loosening is related to the mechanics in the implant-bone structure. There is a need to study the biomechanics of the shoulder bone when glenoid implants are under loading conditions.

Micro X-ray computed tomography (micro-CT) techniques were used in our prior study to explore the damage of bone and loosening of the implant [5]. Digital volume correlation (DVC) of micro-CT images can provide three-dimensional (3D) displacement and strain distribution. It was recently applied on the study of implant-bone biomechanics [6–8]. In this study, we used mechanical testing coupled with micro-CT scans and the DVC method to study the deformation of shoulder bone under various physiologically realistic loading conditions.

Materials and Method

Sample Preparation

A fresh-frozen shoulder bone specimen (glenoid) was obtained. The soft tissues were stripped off. A commercial shoulder implant (glenoid component) (Bigliani/Flatow, Zimmer Inc., Warsaw, IN) was placed into the shoulder bone, with bone cement (Surgical Simplex P, Stryker, Kalamazoo, MI) filling up the bone-implant interface. The surgical operation was performed by a senior shoulder surgeon. The implant is three-pegged. It is made of polyethylene, and has a dimeter of 46 mm. The metal pin in the central peg of glenoid implant was removed to reduce image artifact under micro-CT.

The shoulder bone was then embedded in polymethyl methacrylate (PMMA, Ortho-Jet BCA, Lang Dental, Wheeling, IL), and sectioned to approximately 40 × 40 × 60 mm in size to fit into the mechanical tester. The specimen was kept frozen until 12 h prior to the test, when it was thawed in a refrigerator.

In Situ Mechanical Testing

In situ mechanical testing of the implant in shoulder bone was performed using a mechanical tester (CT5000, Deben UK Limited, Suffolk, United Kingdom) coupled with micro-CT (Phoenix v|tome|x L300 multi-scale nano/microCT system, GE, Boston, MA) (Fig. 1). A compressive load was applied on the implant through a hemispherical polyoxymethylene indenter in order to mimic the contact loading from the humeral head.

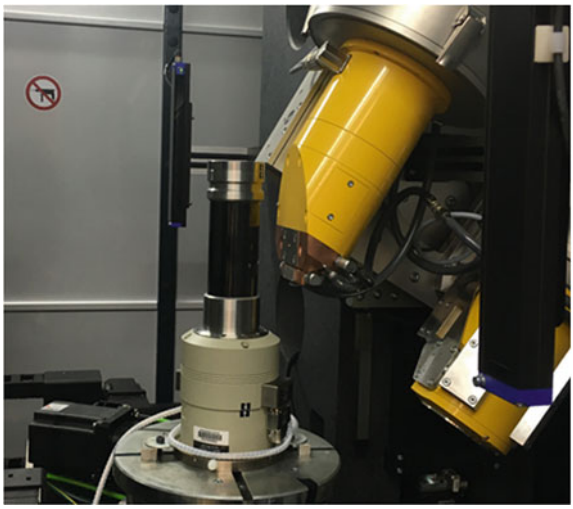

Fig. 1 The experimental setup for the mechanical testing coupled with micro-CT

The specimen was loaded at a displacement rate of 1 mm/min until the load reached 750 N. Then the load was maintained at this level for ~1 h for the specimen to almost fully relax. The compressive load was applied under three different conditions, where the glenoid component was aligned (1) 4 mm to the anterior side of the shoulder bone; (2) concentric to the shoulder bone and (3) 4 mm to the posterior side of the shoulder bone.

Micro-CT scans of the specimen were performed before the specimen was loaded and after the specimen was relaxed at the above-mentioned 3 loading conditions. A voltage of 150 kV and a current of 160 μA was used in the scans. Image sequences with sizes of ~2014 × 2014 × 2024 were obtained. The resolution of the images is 24 μm.

Image Segmentation and Registration

The micro-CT images were cropped in Avizo 3D analysis software (FEI Visualization Sciences Group, Burlington, MA) to obtain the images for the region of interest. They were then segmented using water-shed techniques in Avizo to several regions, including bone, implant and potting materials (Fig. 2). The images of bone were extracted for the following analysis. The images of bone were registered in Avizo to make the bottom 1/10 of the images aligned with each other.

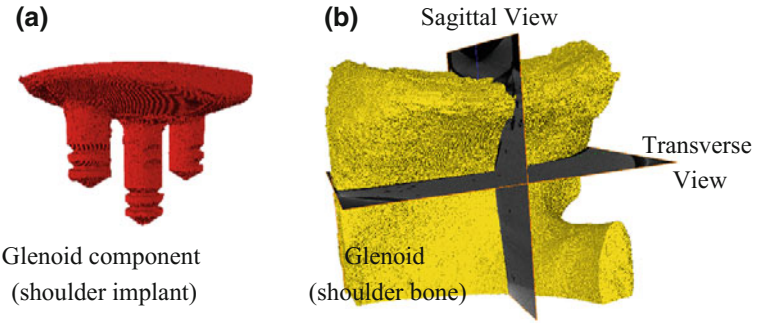

Fig. 2 Rendered 3D images of **a** implant and **b** bone obtained from segmentation of micro-CT images

Digital Volume Correlation (DVC)

Digital volume correlation (DVC) was performed in DaVis software (LaVision, Goettingen, Germany) on the extracted images of shoulder bone. The movements of each block of pixels were tracked by comparing the images at no-load and loaded states. A sequential correlation method was used. A coarser block size of 128 × 128 × 128 was used in the first trial to predict the movements. A block size of 64 × 64 × 64 was used in the second and also final step. The overlap ratio between adjacent blocks was chosen to be 50%. The deformation of shoulder bone was calculated for the above-mentioned 3 loading conditions.

Results and Discussion

Deformation Obtained from Image Registration

The registered images are displayed in Fig. 3, with the bottom 1/10 of the images at no-load and loaded conditions aligned together. It is consistent with the experimental setup, when the bottom of the specimens were fixed to the tester. The images at loaded conditions (yellow) was overlaid on the images at no-load condition (grey scale).

Deformation Obtained from DVC

The deformation of the shoulder bone along the loading direction was obtained from DVC. They are displayed in Fig. 4 on transverse cross-sections at ~2/3 of the specimen height. Negative sign is towards the loading direction.

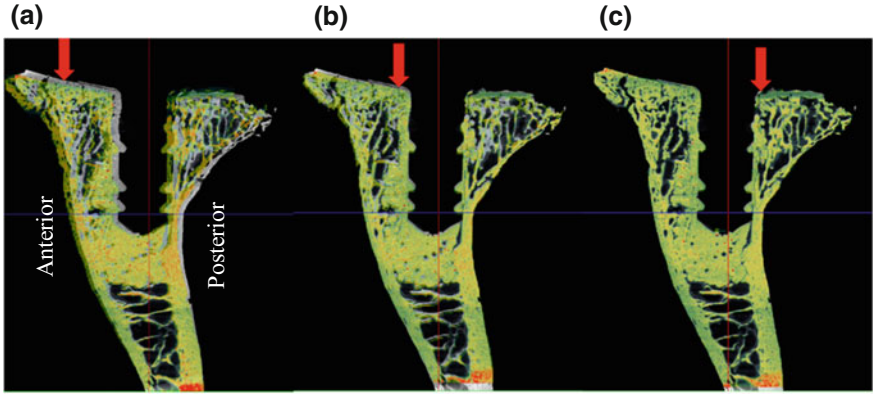

Fig. 3 Registered sagittal-views of shoulder bone with the bottoms aligned, for **a** eccentric loading to the anterior side, **b** concentric loading and **c** eccentric loading to the posterior side

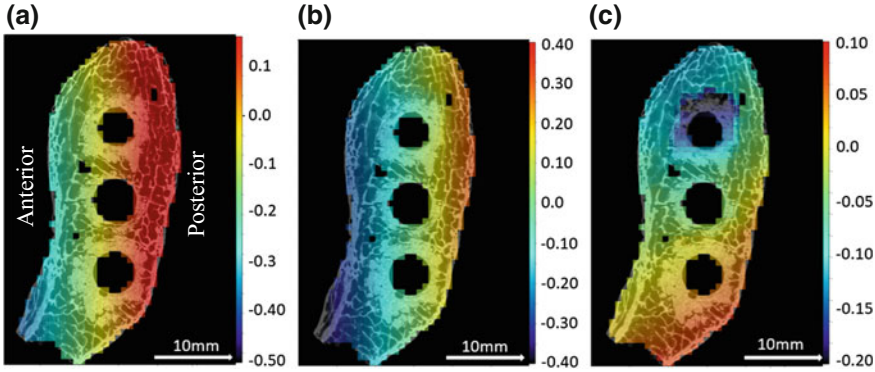

Fig. 4 Deformation of shoulder bone obtained from DVC for **a** eccentric loading to the anterior side, **b** concentric loading and **c** eccentric loading to the posterior side, displayed on a transverse cross-section. (unit: mm)

Discussion

The deformation fields obtained from image registration and DVC have good agreement with each other. The anterior side was pressed down in anteriorly eccentric loading and concentric loading conditions, while the posterior side rose up. In posteriorly eccentric loading conditions, the deformation was much smaller than that for the other two loading conditions. It can be attributed to the asymmetric geometry of shoulder bone.

Implications

The results show that the deformations of shoulder bone under various physiologically realistic loading conditions are different. They are different in the direction and in scale. In this particular specimen, it was more resistant to the posteriorly eccentric loading. Due to the limited sample size, it is just a proof-of-concept study. The results provide insights for the future improvement for the total shoulder replacement procedures.

It is needed to note that the DVC results in the cementing materials are not accurate. Future work are needed to improve the accuracy of the DVC in cement or to segment the images of cement from bone.

Conclusions

This paper presents the results of a study on the loading of shoulder glenoid implant. The deformation of a shoulder bone under various physiologically realistic loading conditions was measured in the in situ mechanical testing coupled with micro-CT. Image registration and digital volume correlation of the micro-CT images at no-load and loaded conditions provide the deformation of shoulder bone. The results obtained from the two methods have good agreement with each other. This particular shoulder bone specimen was more resistant to the posterior loading. Future directions include systematic studies of implant loading for more specimens under cyclic loading conditions.

Acknowledgements The project described was supported by the National Center for Advancing Translational Sciences, National Institutes of Health, through Grant UL1TR002014. The content is solely the responsibility of the authors and does not necessarily represent the official views of the NIH. The support was made available through Penn State Clinical and Translational Science Institute (CTSI). The authors are grateful to Dr. Timothy Ryan and Mr. Timothy Stecko at the Center for Quantitative Imaging (CQI) at Penn State University for technical support on micro-CT scans. Appreciation is also extended to Mr. Richard Prevost at LaVision for useful technical discussions.

References

1. Bohsali KI, Wirth MA, Rockwood CA (2006) Complications of total shoulder arthroplasty. J Bone Joint Surg Am 88(10):2279–2292
2. Torchia ME, Cofield RH, Settergren CR (1997) Total shoulder arthroplasty with the neer prosthesis: long-term results. J Shoulder Elb Surg 6(6):495–505
3. Sperling JW, Cofield RH, Rowland CM (2004) Minimum fifteen-year follow-up of neer hemiarthroplasty and total shoulder arthroplasty in patients aged fifty years or younger. J Shoulder Elb Surg 13(6):604–613

4. Nagels J, Valstar ER, Stokdijk M, Rozing PM (2002) Patterns of loosening of the glenoid component. J Bone Jt Surg [Br] 84–B:83–87
5. Lewis GS, Brenza JB, Paul EM, Armstrong AD (2015) Construct damage and loosening around glenoid implants: a longitudinal micro-CT study of five cadaver specimens. J Orthop Res no. June:1053–1060
6. Du J, Lee J, Jang AT, Gu A, Hossaini-Zadeh M, Prevost R, Curtis DA, Ho SP (2015) Biomechanics and strain mapping in bone as related to immediately-loaded dental implants. J Biomech
7. Zhu ML, Zhang QH, Lupton C, Tong J (2016) Spatial resolution and measurement uncertainty of strains in bone and bone-cement interface using digital volume correlation. J Mech Behav Biomed Mater 57, no. Dec 2015:269–279
8. Tozzi G, Dall'Ara E, Palanca M, Curto M, Innocente F, Cristofolini L (2017) Strain uncertainties from two digital volume correlation approaches in prophylactically augmented vertebrae: local analysis on bone and cement-bone microstructures. J Mech Behav Biomed Mater 67, no. Feb 2016:117–126

The Influence of Plastic Deformation Mechanisms on the Adhesion Behavior and Collagen Formation in Osteoblast Cells

B. Uzer, F. Monte, Kamal R. Awad, Pranesh B. Aswath, Venu G. Varanasi and D. Canadinç

Abstract In many of biomedical applications, the implant might get in direct contact with the bone tissue where the osteogenesis needs to be stimulated. If osteoblasts can not successfully attach on the implant surface, the bone might resorb and implant can fail. In the current study MC3T3 cells were cultured on the 316L stainless steel samples which were deformed up to four different strain levels (5, 15, 25 and 35%) to activate plastic deformation mechanisms (slip and twinning) in different volume fractions. Scanning electron microscopy (SEM) images showed that cells adhered and spread significantly on the 25 and 35% deformed samples owing to the greater surface roughness and energy provided by the increased density of micro-deformation mechanisms which promoted the formation of focal contacts. In addition, significant amount of collagen formation was observed on the sample deformed up to 25% of strain which can be due to the ideal match of the surface roughness and collagen molecules. Overall these results show that material's microstructure can be manipulated through plastic deformation mechanisms in order to enhance the cell response and collagen deposition. As a result long lasting implants could be obtained which would eliminate additional surgical interventions and provide a successful treatment.

B. Uzer (✉)
Department of Mechanical Engineering, Abdullah Gul University, 38080 Kayseri, Turkey
e-mail: benay.uzer@agu.edu.tr

B. Uzer · D. Canadinç
Advanced Materials Group (AMG), Department of Mechanical Engineering, Koç University, 34450 Sariyer, İstanbul, Turkey

F. Monte · K. R. Awad · P. B. Aswath · V. G. Varanasi
Department of Materials Science and Engineering, University of Texas at Arlington, Arlington, TX 76019, USA

K. R. Awad
Refractories, Ceramics and Building Materials Department, National Research Centre, Giza, Egypt

D. Canadinç
Koç University Surface Science and Technology Center (KUYTAM), 34450 Sariyer, İstanbul, Turkey

The Minerals, Metals & Materials Society, *TMS 2018 147th Annual Meeting & Exhibition Supplemental Proceedings*, The Minerals, Metals & Materials Series,
https://doi.org/10.1007/978-3-319-72526-0_27

Keywords Osteoblast · Collagen formation · Cell adhesion
Micro-deformation mechanisms · Slip · Twinning · Plastic deformation

Introduction

Metallic materials are widely utilized in biomedical applications including orthopedics, cardiology, cranioplasty and orthodontics [1, 2]. Orthopedic implants such as staples, screws, intramedullary nails or hip replacements involve direct interaction with bone [1, 3, 4]. In order to attain a successful treatment a complete fusion between the implant surface and bone tissue needs to be established by eliminating the attachment of epithelial or connective tissue cells that could lead to fibrous tissue interface and implant failure [3, 5, 6]. In addition, any inflammatory reaction or bacterial infections should also be prevented for optimal bone regeneration [5]. The initial interaction of the cell and the implant surface constitutes utmost importance and controls the further proliferation of the bone cells [2]. Osteoblast cells need to form direct focal contact points on the interface and adhesion should be promoted [6]. In consequence of a good cell adhesion, osteoblasts deposit collagen matrix on the implant surface which after 4–6 weeks is replaced with woven bone forming the connection between the implant and surrounding bone [6]. If osteoblasts can not successfully attach and proliferate on the implant surface the bone might resorb and implant can fail as a result of loosening [1]. Previous studies pointed out the essential role of material selection, and surface roughness, topography and energy on the osteoblast adhesion [3, 7, 8]. Recently improved brain tumor cell response was reported in parallel with the activation of plastic deformation mechanisms (i.e. slip and twinning) which provided high surface energy and catalyzed the formation of focal contacts [2]. This study showed the significant effect of plastic deformation mechanisms on the surface topography, roughness and energy which eventually led to increased cell adhesion and viability. Earlier, numerous surface modification techniques were utilized to improve material properties in order to obtain improved osteoblast cell response [4, 8–11]. These studies showed that cell adhesion and collagen production was promoted with the increase of the surface roughness and energy. However, they were confined with the modifications of the surface properties, and the influence of material's microstructural features (slip and twinning mechanisms) on the response of osteoblast cells and collagen formation has not been reported yet. The current study was carried out with this motivation to address this issue.

In the current study the MC3T3 cells were cultured on the 316L stainless steel samples which were deformed up to four strain levels (5, 15, 25 and 35%) to activate plastic deformation mechanisms (slip and twinning) in different volume fractions. SEM images showed that cell attachment improved significantly with the increase of the plastic deformation. Specifically, cells adhered and spread by forming filopodias significantly on the 25 and 35% deformed samples owing to the enhanced activity micro-deformation mechanisms. However, the formation of

collagen was mostly promoted on the sample deformed up to 25% of strain which was also confirmed with Raman spectroscopy and might be due to the ideal match of the proteins with the surface roughness of this sample. Overall these results showed that desired implant-tissue integration can be achieved by plastically deforming the material and manipulating its microstructure at an optimum level. In this way long lasting implants could be manufactured that would eliminate implant failure and additional surgical interventions.

Experimental

Austenitic stainless steel samples with the grade of 316L were utilized in the current study since mechanical properties and the microstructure of this metal is well known, as well as its interaction with the cells which has been subjected to numerous studies [1, 12, 13]. Initially dog bone shaped tensile test specimens with the dimensions of 20 × 10 × 1 mm were cut via electrical discharge machining (EDM) and both sides of the sample surface were ground with 600, 800 and 1200 grit SiC sandpapers and polished with the diamond abrasives which had the particle size of 6, 3 and 1 μm respectively. Uniaxial tensile test was carried out up to four strain levels: 5, 15, 25 and 35% which led to the activation of plastic deformation mechanisms (i.e. slip and twin) in gradually increasing volumetric fractions. Surface topography of the undeformed and deformed samples was analyzed via confocal laser scanning microscopy (CLSM) at a magnification of 50×. Average surface roughness (R_a) of each sample was evaluated by scanning 5 different regions with an area of 50 × 50 μm and taking the average value of these scans.

Dependence of cell adhesion and collagen formation on the plastic deformation mechanisms were evaluated by analyzing the response of the MC3T3-E4 cells cultured on the metal samples. 200,000 cells were seeded on the samples placed in 12 well plate using 200 μl of medium with 10% fetal bovine serum (FBS). Plate was placed in incubator (37 °C, >95% re., 5% CO_2) for 30 min for adequate cell attachment, after 1 ml of alfa-MEM + 1% P/S + 10% FBS were added per well. Cells were allowed to grow for 24 h, then they were synchronized with α-MEM 2% FBS and 1% penicillin-streptomycin (P/S) for 48 h. After synchronization, the medium was changed by differentiation medium formed by α-MEM + 10% FBS + 1% P/S and supplemented with ascorbic acid 50 ppm. Differentiation medium was changed every 2 days up to 21 days. Afterwards, the media was removed, samples were washed with PBS and prepared for Raman spectroscopy and scanning electron microscopy. The samples were fixed with glutaraldehyde 2.5% for 1 h, dehydrated with ethanol and allowed to air dry overnight.

Attachment, spreading and adhesion behavior of these cells, and collagen formation on the implant materials were observed via scanning electron microscopy (Hitachi S-3000 N Variable Pressure SEM). The images were obtained with secondary electron (SE) detector, under an accelerating voltage of 25 kV and at a magnification in the range of 1000–8000×. Chemical structure of the biological

molecules attached on material surface were detected using Microspot Raman Spectroscopy (DXR, Thermo Scientific, 10× objective) with 532 nm excitation laser at 10 mW, and 50 μm pinhole slit. The samples were photobleached for 4 min prior to spectra collection and 4 s exposure time was used. Thirty-two spectra per location were recorded between 600 and 2000 cm^{-1}.

Results and Discussion

Surface topography of each sample was analyzed via CLSM and the average surface roughness (R_a) values are presented in Table 1. The results showed that R_a increased in concomitant with the plastic deformation (Table 1) which constitutes importance because greater surface roughness was shown to have a positive effect on the cell adhesion [2, 9, 14, 15].

Adhesion and spreading behavior of the cells on the samples deformed up to different strain levels were analyzed with SEM. The images showed that osteoblast attachment increased significantly as the deformation level increased. For instance, cell adhesion on the undeformed and 35% deformed samples are presented in Fig. 1, and significant morphological differences can be observed. The osteoblast cells had round shape and sphere like surface evagination on the undeformed sample (Fig. 1a). They did not form filopodia, actin containing protrusions, which play critical role on cell adhesion, migration and formation of cell-cell contacts [16]. Filopodias are directly related with the surface adhesion of the cells because cell adhesion molecules are often found in the tips of these protrusions [17]. On the other hand, cells on the sample deformed up to 35% had a flattened and spread morphology (Fig. 1b) and they formed filopodias in multiple direction which help them to better adhere on the implant surface. In addition to that intercellular attachment was also prevalent on this sample which shows that the neighboring cells recognized one another through their membrane proteins and attached with their filopodias [2]. This enhanced cell response on this sample was explained with greater surface energy provided by the activation of slip and twinning mechanisms, and their interaction. Specifically, twins acted as barriers against dislocation motion which increased the stress concentration and further catalyzed the cell attachment on the samples with greater plastic deformation. These mechanisms also created groove like regions on the material surface which successively increased the surface roughness and eased the deposition of adhesion proteins [2]. Earlier studies on the interaction of osteoblast cells and the implant showed that surface roughness can significantly alter the cell response by affecting the cytokines and growth factor

Table 1 Average surface roughness (R_a) values of the samples deformed up to different strain levels (in μm)

Sample	Undeformed	5%	15%	25%	35%
R_a	0.069 ± 0.001	0.117 ± 0.003	0.350 ± 0.029	0.470 ± 0.024	0.690 ± 0.017

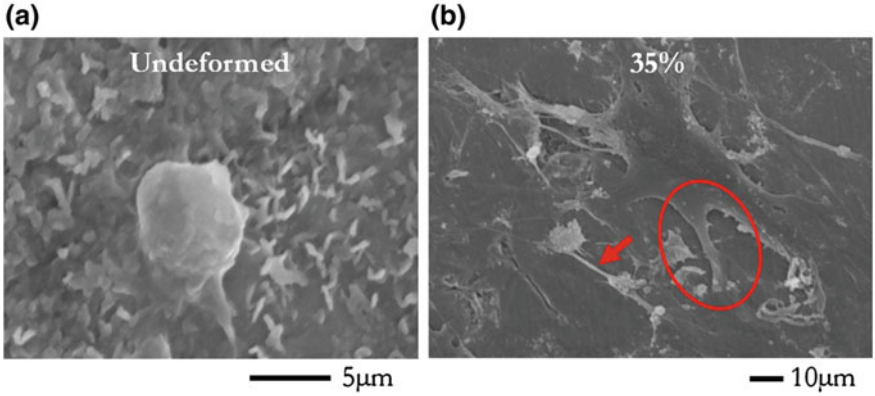

Fig. 1 Images showing the adhesion behavior of the cells cultured on the (**a**) undeformed and (**b**) 35% deformed samples. Collagen bundle is marked with red arrow and filopodia is encircled in red in figure (**b**)

production which directly affects the bone [18]. Thus, the increased surface roughness of this sample would result with improved cell response. It should be noted that the formation of filopodias was also observed densely on the sample deformed up to 25% of strain.

In addition to the above, collagen formation also plays critical role to achieve a successful treatment, and bone reformation which would have good quality and strength [19]. Studies also showed higher percentage of implant bone contact and increased bone formation was attained when the implant was covered with collagen membranes [20, 21]. Collagen fibers provide the ductility and ability to absorb energy [19]. Therefore its structure throughout the implant-tissue integration can significantly affect the mechanical properties of the bone and the treatment [19]. Collagen bundles on each sample were analyzed in detail via SEM. The image of cells cultured on the sample deformed up to 25% of strain showed the greatest density of collagen formation (Fig. 2). One of the reasons for this can be the optimal match between the extracellular matrix (ECM) molecules and the surface

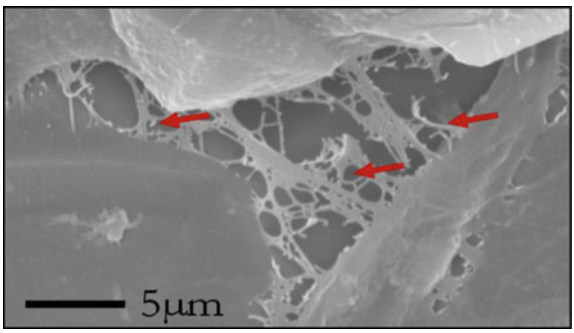

Fig. 2 Collagen formation in MC3T3 osteoblast cells cultured on the sample deformed up to 25% of strain

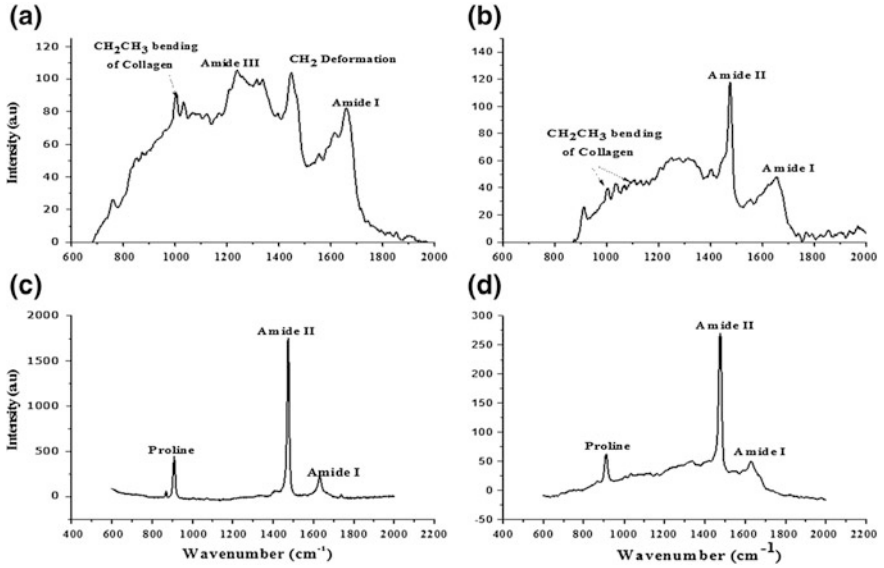

Fig. 3 Raman spectra of the samples deformed up to **a** 5, **b** 15, **c** 25 and **d** 35% of strain

roughness, such that in this sample the proteins responsible for the cell attachment might have deposited more easily by accumulating in these grooves.

Chemical structure of the molecules adhered on the material surface was analyzed via Raman spectroscopy. Raman spectra have been reported for all samples to present any mineral or matrix collagen deposition. Figure 3 shows the actual Raman spectra for the four deformed samples, it is clear that samples deformed up to 5 and 15% of strain show small intensive peak for amide I at 1660 cm^{-1} and peaks of CH_3-CH_2 bending mode of collagen at 1032 cm^{-1}. On the other hand, 25 and 35% deformed samples show very well defined and intensive peaks for amide I and II at 1660 cm^{-1} and 1480 cm^{-1}. By comparing the area under the peaks of amide I for all samples, it clear that the area increases from 409 cm^2 for 5% sample to reach to the highest value of 5796 cm^2 for sample 25%, which confirm the SEM results that this sample showed the greatest density of collagen formation. These results show that improved bone-implant integration can be achieved by selecting the sample deformed up to 25% of strain as the implant material. However, it should be noted that in order to better understand the exact interaction between implant surface and the proteins taking role in adhesion further qualitative and quantitative analyses need to be carried out through the immune labelling of the proteins. In this way implants with superior properties could be attained which would lead to acceleration of the healing and manufacturing of long-lasting implants without the occurrence of failure.

Conclusion

The results of this study confirm that, osteoblast cells show more spread behavior and improved cell adhesion in parallel with the increasing density of slip and twinning mechanisms. Significant filopodial formation was observed on the samples deformed up to 25 and 35% of strain owing to the higher activity of micro-deformation mechanisms. The collagen bundles were prevalent with the greatest density on the sample deformed up to 25% of strain which was also confirmed with the results of Raman spectroscopy. Overall the results of the current study show that by optimally manipulating the implant's microstructure utilizing the activation of micro-deformation mechanisms improved cell response can be achieved that would lead to a successful implant treatment.

Acknowledgements D. Canadinc acknowledges the financial support by the Turkish Academy of Sciences (TÜBA) within the Outstanding Young Scientist Program (GEBİP).

References

1. Chen Q, Thouas GA (2015) Mater Sci Eng R Reports 87:1–57
2. Uzer B, Toker SM, Cingoz A, Bagci-Onder T, Gerstein G, Maier HJ, Canadinc D (2016) J Mech Behav Biomed Mater 60:177–186
3. Anselme K (2000) Biomaterials 21:667–681
4. Le Guéhennec L, Soueidan A, Layrolle P, Amouriq Y (2007) Dent Mater 23:844–854
5. Linez-Bataillon P, Monchau F, Bigerelle M, Hildebrand HF (2002) Biomol Eng 19:133–141
6. Plecko M, Sievert C, Andermatt D, Frigg R, Kronen P, Klein K, Stübinger S, Nuss K, Bürki A, Ferguson S, Stoeckle U, Von Rechenberg B (2012) Bmc Musculoskelet Disord 1–12
7. Gronowicz G, McCarthy MB (1996) J Orthop Res 14:878–887
8. Deligianni DD, Katsala N, Ladas S, Sotiropoulou D, Amedee J, Missirlis YF (2001) Biomaterials 22:1241–1251
9. Qin L, Zeng Q, Wang W, Zhang Y, Dong G (2014) J Mater Sci 2662–2671
10. Meyer U, Büchter A, Wiesmann HP, Joos U, Jones DB (2005) Eur Cells Mater 9:39–49
11. Wexell CL (2013) Int J Biomater
12. Bordji K, Jouzeau JY, Mainard D, Payan E, Delagoutte JP, Netter P (1996) Biomaterials 17:491–500
13. Martinesi FBM, Bruni S, Stio M, Treves C, Bacci T (2006) J Biomed Mater Res A 81:131–145
14. Hayakawa T, Yoshida E, Yoshimura Y, Uo M, Yoshinari M (2012) Int J Biomaterials 1–7
15. Wu C, Chen M, Zheng T, Yang X (2015) Biomed Mat Eng 26:155–164
16. Arjonen A, Kaukonen R, Ivaska J (2011) Cell Adhes Migr 5:421–430
17. Mattila PK, Lappalainen P (2008) Nat Rev Mol Cell Biol 9:446–454
18. Kieswetter K, Schwartz Z, Hummert TW, Cochran DL, Simpson J, Dean DD, Boyan BD (1996) J Biomed Mater Res 32:55–63
19. Viguet-Carrin PDDS, Garnero P (2006) Osteoporos Int 17:319–336
20. Han J, Shin S, Herr Y, Kwon Y, Chung J (2011) Clin Oral Implant Res 1391–1398
21. De Barros RRM, Novaes AB Jr, Korn P, Queiroz A, De Almeida ALG, Hintze V, Scharnweber D, Bierbaum S, Stadlinger B (2013) Clin Implant Dent Relat Res 742–757

Part XI
Bulk Metallic Glasses XV

Probabilistic Modeling and Simulation of Microstructural Evolution in Zr Based Bulk Metallic Glass Matrix Composites During Solidification

Muhammad Musaddique Ali Rafique

Abstract Bulk metallic glass and their composites are unique new materials which have superior mechanical and structural properties as compared to existing conventional materials. However, their mechanical behavior is dubious, unpredictable and requires extensive experimentation to draw conclusive results. In present study, which is continuation of previous work of author, a non-linear one-dimensional iterative deterministic model is combined with two-dimensional probabilistic cellular automaton method to describe nucleation and growth of primary ductile phase from melt in glassy matrix during solidification. Preliminary methodology ad philosophy of model making is described with an aim to explain the grounds on which this approach is adopted. MATLAB® is chosen as programing platform. Results indicate that the effect of incorporating all heat transfer, mass transfer and diffusion coefficients with appropriate interpolation play a vital role in refining the model and bringing it closer to actual experimental observations. Two types of hypo and hyper eutectic systems were studied with different inoculants.

Keywords Cellular automaton · Solidification · Mass transfer coefficients Interpolation

Introduction

Bulk Metallic Glass Matrix Composites (BMGMC) have emerged as new materials of future bearing unique properties of strength, hardness and elastic strain limit [1] which are not observed in other conventional engineering materials. However, they suffer from lack of ductility and toughness which make them impracticable to be used in any structural engineering application [2]. They fail catastrophically under

M. M. A. Rafique (✉)
School of Engineering [Aerospace, Mechanical and Manufacturing],
RMIT University, City Campus, Carlton, VIC 3053, Australia
e-mail: s3469212@student.rmit.edu.au; ali.rafique@hotmail.com

The Minerals, Metals & Materials Society, *TMS 2018 147th Annual Meeting & Exhibition Supplemental Proceedings*, The Minerals, Metals & Materials Series,
https://doi.org/10.1007/978-3-319-72526-0_28

the application of external load without yielding. Due to this they have not been able to gain enough popularity and are still being investigated at laboratory scale. Various theories and thoughts exist which reinforce or cast doubts about their large scale manufacturing. Recently, a lot of attention has been diverted at making them useful for outer space and extreme environment conditions [3–6] such as windows of international space station (ISS) [5], gears of outer and deep space exploration missions and rovers [7, 8]. However, an in depth understanding of their microstructure evolution is still a gap in field of research. Various efforts have been made to address this problem such as use of container less levitation techniques [4], experiments in micro and zero gravity [4, 9] and use of synchrotron light [10, 11] but none has proved out to be satisfactory. In present study, an effort has been made to address this problem from modeling and simulation perspective. A detailed probabilistic iterative model is developed based on well-known theory of self-reproducing automata [12] which is based on authors earlier work [3] describing deterministic modeling and simulation in Zr based BMGMCs. Some of the salient features of model and approach are described below.

Model

It consists of making a detailed probabilistic model explaining two dimensional evolution of dendritic microstructure (e.g. B2 in CuZrAlCo and β-Zr CuZrAlNi) in a carefully selected simulation domain based on cellular automaton method [13]. Its features are:

1. It takes into account the use of transient thermal parameters (temperature, density, specific heat capacity, thermal conductivity) of actual Zr based BMGMCs [14], incorporate them in detailed heat transfer model in ABAQUS, generate temperature profile at each node of mesh in ABAQUS simulation geometry and finally use this temperature as input for CA simulation domain inside ABAQUS finite element (FE) grid [15]. In summary CA process [13] adopted here is:
    a. Determine phases to be evolved in a typical selected alloy system (based on literature).
    b. Determine their volume fraction (V_f) (based on literature).
    c. Select Representative Volume Element (RVE) in a test piece/coupon (in mm) (actual part—in present case rectangular block).
    d. Selection of simulation domain (Cartesian or point based grid) (e-g 300 × 300 [15]). This is performed in MATLAB.
    e. Select cell shape (square, hexagon, rectangle (based on literature)). This is done in MATLAB.

f. Select parameters to account for mesh anisotropy. This can be done by any of following

   i. Selection of modified square cell (decentred square algorithm (DCSA [16–19])) (most popular approach).
   ii. Refining of square cells e.g. limited angle method [15]
   iii. Refining of mesh (by decreasing it physical size from micron to nm) (usually not adopted—leads to increase of computational time and make process inefficient).

g. Select neighborhood transition rules [20] based on well-established CA pattern selected in step e above (These rules are well defined in literature e.g. Von Numen rules, Moore rules [21] (popular, accurate but computationally expensive), Solid/Liquid Interface generation and energy at tip) [22, 23].
h. Scan whole simulation domain/grid for "*n*" number of cells (300 × 300 [15]) and assign a random number r ($0 < r < 1$) to each cell [24–26].
i. Select physical appearance of next cells based on neighborhood transition rules of step g above.

Note: CA model is physical model as it gives interface curvature physically and plot it in a cell in terms of solid fraction in a 2D simulation domain/grid thus a visual/physical picture is obtained. (However, it depends on previous deterministic [3] and heat transfer model (as described above)).

Explanation

In essence, the model consists of calculating solid fraction in defined cell as a function of time. Once this solid fraction is calculated at a particular time, a random number is generated which is assigned to next growing grain/cell. Life or death of next cell is determined on the basis of this number. Similarly, growth (solid fraction) in next cell (Fig. 1a and b) is determined on the basis of its life/existence and the process continues.

It is primarily based on following fundamental studies [24, 27–29] whose origins goes back to welding process owing to similarities in features and characteristics as additive manufacturing process.

1. Nastac, L., *Numerical modeling of solidification morphologies and segregation patterns in cast dendritic alloys.* Acta Materialia, 1999. **47**(17): p. 4253–4262
2. Wei, Y.H., et al., *Numerical simulation of columnar dendritic grain growth during weld solidification process.* Science and Technology of Welding and Joining, 2007. **12**(2): p. 138–146

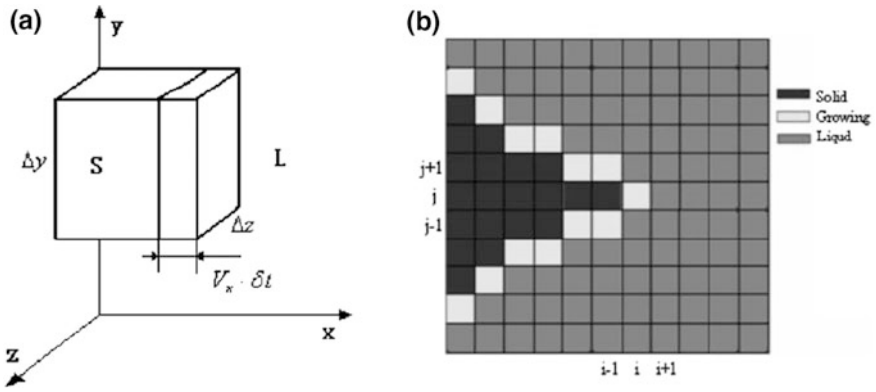

Fig. 1 **a** Schematic of growth in one cell **b** Schematic diagram of movement of dendrite tip in a grid of cells represented by change of state index of each cell [27]. (Reprinted with permission from Taylor and Francis Group)

3. Zhou, X., et al., *Simulation of microstructure evolution during hybrid deposition and micro-rolling process.* Journal of Materials Science, 2016. **51**(14): p. 6735–6749
4. Dezfoli, A.R.A., et al., *Determination and controlling of grain structure of metals after laser incidence: Theoretical approach.* Sci. Rep. 2017. **7**: p. 41527

Present study is focused on development of detailed theoretical model for BMGMCs. Coding, simulation results and their comparison with experimental values will be described in subsequent studies.

References

1. Zhang T et al (2014) Tensile mechanical behaviors of in situ metallic glass matrix composites at ambient temperature and in supercooled liquid region. Metallurg Mater Trans A 45(5): 2382–2388
2. Kruzic JJ (2016) Bulk metallic glasses as structural materials: a review. Adv Eng Mater 18 (8):1308–1331
3. Rafique MMA, Qiu D, Easton M (2017) Modeling and simulation of microstructural evolution in Zr based bulk metallic glass matrix composites during solidification. MRS Advanc:1–16
4. Hofmann DC, Roberts SN (2015) Microgravity metal processing: from undercooled liquids to bulk metallic glasses, vol 1, p 15003
5. Davidson M et al (2013) Investigating amorphous metal composite architectures as spacecraft shielding. Adv Eng Mater 15(1–2):27–33
6. Jiang J-Z et al (2015) Low-density high-strength bulk metallic glasses and their composites: a review. Adv Eng Mater 17(6):761–780
7. Hofmann DC et al (2016) Castable bulk metallic glass strain wave gears: towards decreasing the cost of high-performance robotics 6:37773

8. Hofmann DC et al (2017) Optimizing Bulk metallic glasses for robust, highly wear-resistant gears. Advanc Eng Mater 19(1):1600541-n/a
9. Zimmermann G et al (2011) Investigation of columnar-to-equiaxed transition in solidification processing of AlSi alloys in microgravity—the CETSOL project. J Phys Conf Ser 327(1): 012003
10. Guo G-Q et al (2015) Detecting structural features in metallic glass via synchrotron radiation experiments combined with simulations. Metals 5(4):2093
11. Guo G-Q et al (2015) How can synchrotron radiation techniques be applied for detecting microstructures in amorphous alloys? Metals 5(4):2048
12. Von Neumann J, Burks AW (1996) Theory of self-reproducing automata. University of Illinois Press Urbana
13. Reuther K, Rettenmayr M (2014) Perspectives for cellular automata for the simulation of dendritic solidification—a review. Comput Mater Sci 95:213–220
14. Wu K, Li R, Zhang T (2013) Crystallization and thermophysical properties of Cu46Zr47Al6Co1 bulk metallic glass. AIP Adv 3(11):112115
15. Liu S, Kouadri-Henni A, Gavrus A (2016) Modeling grain orientation of DP600 steel. In: MATEC Web of Conferences by Nd: YAG laser, EDP Sciences
16. Free ML, Siegmund AH (2013) EPD Congress 2013. Wiley
17. Tan W et al (2011) Multiscale modeling of transport phenomena and dendritic growth in laser cladding processes. Metallurg Mater Trans B 42(6):1306–1318
18. Rai A, Markl M, Körner C (2016) A coupled cellular automaton–lattice Boltzmann model for grain structure simulation during additive manufacturing. Comput Mater Sci 124(Suppl C):37–48
19. Krane MJM, Johnson DR, Raghavan S (2009) The development of a cellular automaton-finite volume model for dendritic growth. Appl Math Model 33(5):2234–2247
20. Zhou JX, Wu ST, Yin YJ (2014) Effect of neighbourhood configurations on grain structure in CA models. Mater Res Innov 18(Suppl 2):p S2-892–S2-897
21. Wei L et al (2012) A cellular automaton model for a pure substance solidification with interface reconstruction method. Comput Mater Sci 54(Suppl C):p 66–74
22. Sharifi H, Larouche D (2014) Numerical study of variation of mechanical properties of a binary aluminum alloy with respect to its grain shapes. Materials 7(4):3065
23. Sharifi H, Larouche D (2014) A numerical method for microstructure generation of a binary aluminum alloy and study of its mechanical properties using the finite element method. Metallurg Mater Trans A 45(13):5866–5875
24. Nastac L (1999) Numerical modeling of solidification morphologies and segregation patterns in cast dendritic alloys. Acta Mater 47(17):4253–4262
25. Laurentiu N, Doru MS (1997) Stochastic modelling of microstructure formation in solidification processes. Modell Simul Mater Sci Eng 5(4):391
26. Rappaz M, Gandin CA (1993) Probabilistic modelling of microstructure formation in solidification processes. Acta Metallurg Mater 41(2):345–360
27. Wei YH et al (2007) Numerical simulation of columnar dendritic grain growth during weld solidification process. Sci Technol Weld Join 12(2):138–146
28. Zhou X et al (2016) Simulation of microstructure evolution during hybrid deposition and micro-rolling process. J Mater Sci 51(14):6735–6749
29. Dezfoli ARA et al (2017) Determination and controlling of grain structure of metals after laser incidence: theoretical approach. vol 7: p 41527

Part XII
Computational Design and Simulation of Materials (CDSM 2018): Atomistic Simulations

The Adhesion Force in Nano-Contact During Approaching and Retrieving Processes

Biao Yang and Bailin Zheng

Abstract Atomistic simulations are used to test the continuum contact theories on the micro scale. Nominally spherical tips are pressed into a flat substrate. The force-displacement curves obtained contain information about the relationship between the adhesion force and the normal displacement. The indenter size is also taken into consideration. Snapshots of atomistic configurations are used to explain the results. Results show that the adhesion effects are different during the approaching and retrieving processes. Which means different effects of surface interaction and would give different solutions of continuum contact theories. What's more, the maximum normal displacement (D_{max}) has great impact on the pull-off force, accompanied with different dislocation nucleation, movements and annihilation. Also it is found that the position where the maximum pull-off force occurred is related to the maximum normal displacement and the indenter size. It happens earlier with decreased normal displacement and indenter size.

Keywords Adhesion force · Nano-contact · Molecular dynamic simulation

Introduction

Study on the contact mechanism in nanoscale is beneficial for the manufacture of many microfabricated devices. Literature depicting the contact mechanism between solids could be found since 1896 [1]. Nowadays with the rapid development in nano-technology and computer technology, experiments and simulations working on the nano-contact mechanism have become more and more popular [2–6], which facilitate better understanding of atomic-level mechanism of the contact problem. Contrasted with experiments, atomistic simulation provides invaluable physical insight to nano-contact for scientists to probe the contact behavior.

B. Yang · B. Zheng (✉)
School of Aerospace Engineering and Applied Mechanics, Tongji University, No.1239 Siping Road, Shanghai 200092, China
e-mail: blzheng@tongji.edu.cn

The Minerals, Metals & Materials Society, *TMS 2018 147th Annual Meeting & Exhibition Supplemental Proceedings*, The Minerals, Metals & Materials Series,
https://doi.org/10.1007/978-3-319-72526-0_29

It is well known that contact mechanism in small scale concerning the work of adhesion or not is totally different [7]. It might be Johnson and his cooperators who first consider the work of adhesion in contact in 1971 [8]. And Derjaguin et al. proposed another way to model the adhesive contact after 4 years [9]. Comparison between these theories have been done by Zhao et al. [10]. It is found that the JKR and DMT theories are suitable for different conditions as limiting cases of soft and hard contact, respectively [5]. However, as the size of contact regions approached atomic dimensions, continuum theories describing the contact between surfaces seem to be disabled [11]. Luan and Robbins discovered that the atomic scale roughness have profound effects on contact areas, local stresses and the work of adhesion by using the atomistic simulation [4, 11]. Although there are a few methods to simulate the nano-contact problem, it is arguably that the most appropriate numerical tool to study the adhesive contact at atomic scale is the classical molecular dynamics simulation [6]. Landman et al. first use MD to study the atomistic mechanisms of adhesion, contact formation and separation [12]. Yu and Polycarpou proposed a new method to determine the equilibrium distance of Lennard-Jones potential for reducing the computation error [13]. Si and Wang presented a simulation study of adhesion contact between a spherical tip and single asperities situated on a flat surface. Results showed that radii and heights of asperities have a great influence on the van der Waals force and the adhesive force [14]. Solhjoo and Vakis investigated the applicability of classical contact theories at nanoscale and elucidate the work of adhesion [6]. It could easily be found from the above literatures that when a spherical tip was pressed onto a flat substrate, the adhesive force between approaching and retrieving processes is different. But few works have been done to study the phenomenon which is critical to the problem of contact status.

In this paper, molecular dynamics simulation is employed to investigate the adhesion work during the nano-contact with the consideration of different normal displacement and indenter size. Emphases are paid on the difference of adhesion between approaching and retrieving processes with different normal displacement, aiming to better understanding the atomic-level mechanism of adhesion work. Section 2 introduces the simulation method employed in this work. Empirical potentials, computation models, temperature, boundary conditions and visualization techniques are given in this section. In Sect. 3, a detailed discussion is given to analyze the work of adhesion in the nano-contact problem. The comparison with the continuum theories and atomistic simulation is also discussed. Finally, it is the conclusion including the future prospects of this research.

Modeling and Simulation

In this work, the MD model consists of a nickel indenter and a flat nickel substrate. Figure 1 shows the sketch of the nano-contact model. The axis X, Y, Z represent for crystal orientation [100], [010], [001] respectively. The radius of the spherical

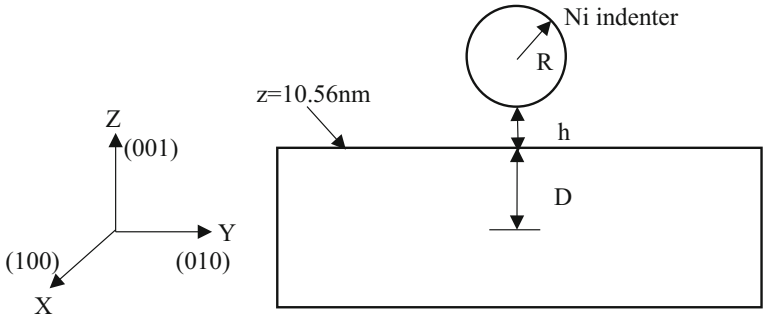

Fig. 1 Sketch of model

indenter is represented by R, which could be 12λ, 15λ and 15λ respectively, where λ is the lattice constant of Ni (λ = 0.352 nm). The size of the nickel substrate is 60λ × 60λ × 60λ. There are 56346 atoms and 871200 atoms in the indenter and the substrate(R = 15λ) respectively. The distance between the down point of the indenter and the up surface of the substrate is h while D represents the depth of the indenter displacement from the up surface of the nickel substrate. The simulation model are presented in Fig. 2. The bottom surface of the nickel substrate is fixed along [001] orientation to avoid rigid displacements. To eliminate the effect of boundary conditions on the side faces, periodic boundary condition is added along [010] and [100] orientation [15]. The model is divided into three layers as Newtonian, thermostat and rigid atoms along $[00\bar{1}]$ orientation. Since the influence of

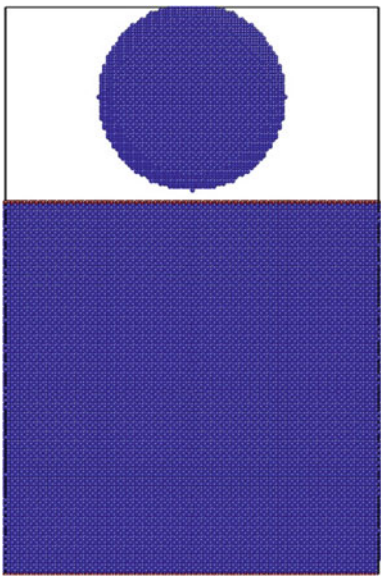

Fig. 2 The simulation model (R = 15λ)

temperature on dislocations is not considered in this work, microcanonical ensemble is taken in the simulation processes. And the temperature of thermostat atoms is controlled by rescaling the atoms velocities [16]. The initial temperature of the matrix is 1 K. The speed of indenter belongs to 1–100 m/s normally [17] and in this paper is defined as 20 m/s with the step time 2×10^{-15} s.

Interatomic interactions in classical molecular dynamics simulations are usually represented by empirical potentials. It's confirmed that the embedded-atom method (EAM) potential proposed by Foiles et al. [18] is appropriated for Ni-Ni.

Technique to selectively visualize interior defects is very important in the atomistic simulation of defect nucleation and evolution. Center symmetry parameter (CSP) was chosen in this paper which had been proven effective for the visualization of dislocation nucleation and evolution [19, 20]. For FCC crystals, the CSP value of each atom could be defined by formula (1):

$$\mathrm{CSP} = \sum_{i=1,6} |R_i + R_{i+6}|^2, \tag{1}$$

where R_i stands for the nearest-neighboring atoms and R_{i+6} stands for the opposite ones. If there exists a defect in a material, the CSP value of the atoms in the vicinity of the defects will be greater than the perfect ones. When the value is less than a cutoff value, which is equal to 0.4, the corresponding atom will be eliminated from visualizing the simulation results.

Discussion of Adhesive Force in Approaching and Retrieving Processes

It is suggested that the work of adhesion could be expressed as the external work done to separate unit area of the adhering surfaces [21, 22]. However, Fig. 3 shows that the work of adhesion could be different during the approaching and retrieving processes. The famous jump-to-contact phenomenon [12] was found when the indenter approached the substrate. The sudden rise of the force is due to the long-range interactions such as van der Waals forces. It began at $h = 0.479$ nm and developed to the maximum value 110.096 nN at $h = 0.169$ nm. The equilibrium distance at which the attractive force equals the repulsive force was $D = 0.059$ nN.

As shown in Fig. 3, there was a hysteresis in the force-displacement curve. The force would have a drop when the indenter stopped pressing and began to retrieve. It was easy to see that the force-displacements during the retrieving process were different. Firstly, the adhesion force during the retrieving process is dependent of the maximum normal displacement (D_{max}), which means the pull-off force (F_{pf}) differs with respect to the contact depth. As the contact depth increased, the pull-off force to separate the adhering surface became bigger. It only needed 117.321 nN, which is close to the maximum value of attractive force during the approaching process, to pull off the indenter from the substrate when $D_{max} = 0.1408$ nm. And it

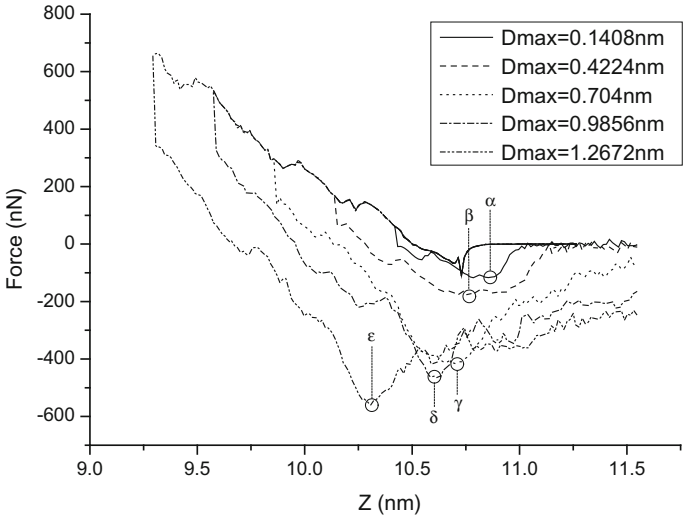

Fig. 3 The force-displacement curves with different maximum normal displacement (R = 15λ)

grew to −560.959 nN when D_{max} = 1.2672 nm. Secondly, the location of the pull-off force (h_{pf}) occurred was also related to the maximum normal displacement. Figure 4 gave the relationship between the D_{max} and h_{pf}. Note that $h_{pf} < 0$ means the location was under the up surface of the substrate while $h_{pf} > 0$ means the location was above the up surface. The D_{max}−h_{pf} curve indicated that the h_{pf} decreased as the D_{max} increased and even became negative when $D_{max} > 1.1$ nm.

The influence of the indenter radius was shown in Fig. 5. It is obvious that with bigger radius of indenter, the adhesion force became larger both in the approaching and retrieving processes. Also, the position where the maximum adhesion force

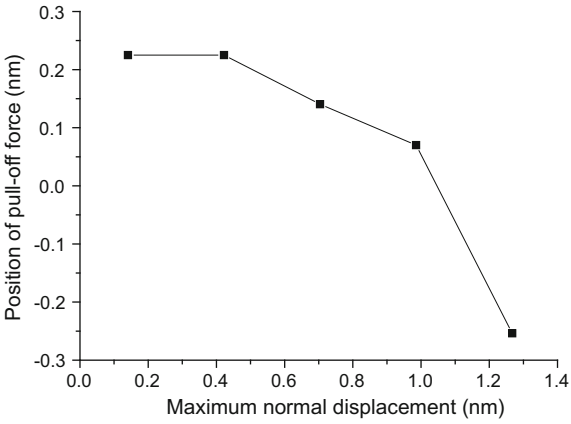

Fig. 4 The relationship between maximum normal displacement and position of pull-off force (R = 15λ)

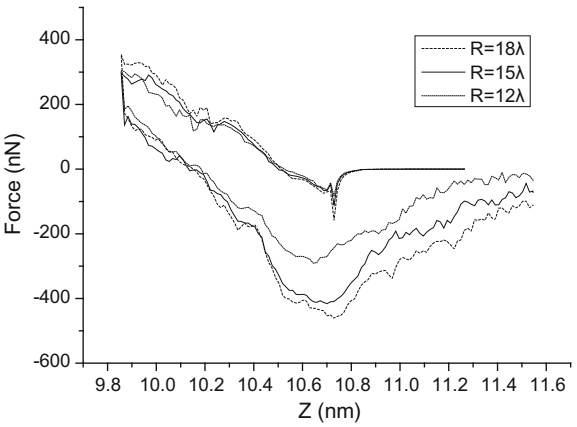

Fig. 5 The force-displacement curves with different indenter radius (R = 12λ, 15λ, 18λ)

occurred was different during the approaching and retrieving processes. It occurred earlier with smaller indenter size.

Snapshots of the atomistic structures at the instants marked by α-ε in Fig. 3 were given in Fig. 6 respectively. A neck was formed when the indenter was pulled off the surface due to the work of adhesion. It is easy to understand that the larger D_{max} would induce more nucleation of dislocation, as shown in Fig. 6. Moreover, the larger D_{max} also caused much more atoms on the surface of the substrate adhere to the surface of the indenter, which lead to larger pull-off force during separation. Clearly, it is the deformation of the substrate which lead to the difference of the adhesion force during the approaching and retrieving processes. The dislocation nucleation, movements and annihilation during the approaching and retrieving processes are responsible for the distinction of the force-displacement curves.

The effects of the maximum normal displacement on the work of adhesion are analyzed using the following formula [8]

$$\gamma = -\frac{2}{3}\frac{F_{pf}}{\pi R} \tag{2}$$

where γ is the work of adhesion. Using the JKR and DMT theories, which took adhesion into consideration, we could get the relationship between applied load (P) and contact radius (a). The formulas including the Hertz contact equations were given by

$$a_{JKR}^3 = \left(\frac{R}{K}\right)\left(\mathrm{P} + 3\pi\gamma\mathrm{R} + \sqrt{6\pi\gamma RP + (3\pi\gamma R)^2}\right) \tag{3}$$

$$a_{DMT}^3 = \left(\frac{R}{K}\right)(P + 2\pi\gamma R) \tag{4}$$

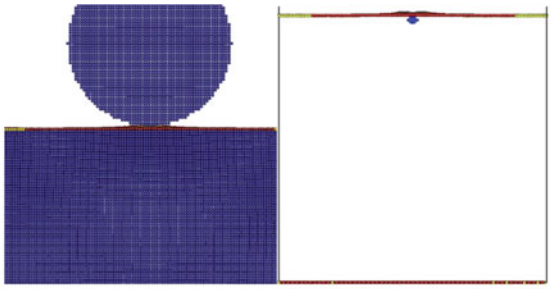

(a) D_{max}=0.1408 nm

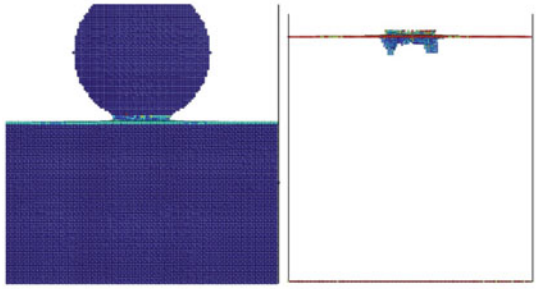

(b) D_{max}=0.4224 nm

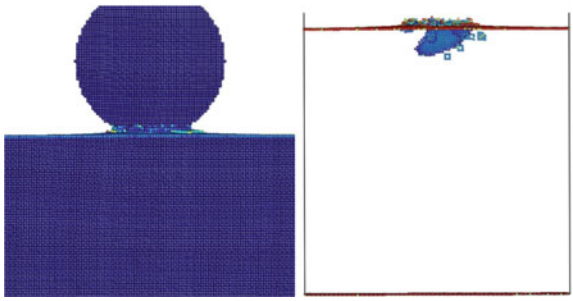

(c) D_{max}=0.704 nm

Fig. 6 Atomistic structures at the position where the maximum pull-off force occurred during retrieving processes with different D_{max}

$$a_{Hertz}^3 = \frac{RP}{K} \tag{5}$$

where K is the equivalent elastic modulus of the indenter and the substrate, given by

$$\mathrm{K} = \frac{4}{3}\left(\frac{1-\mu_1}{E_1} + \frac{1-\mu_2}{E_2}\right)^{-1} \tag{6}$$

where E and μ are the Young's modulus and the Poisson's ratio respectively, and subscripts 1 and 2 denote the indenter and substrate respectively. Figure 7 showed the Influence of the work of adhesion γ on the contact radius in both JKR, DMT and

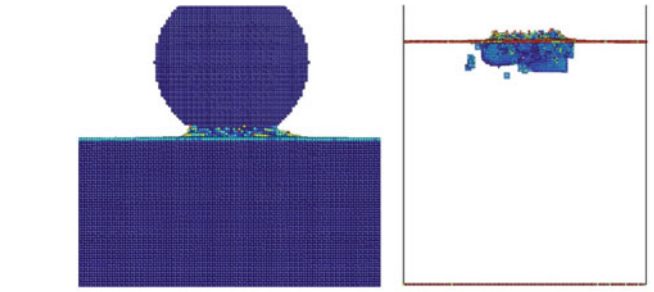

(d) D_{max}=0.9856 nm

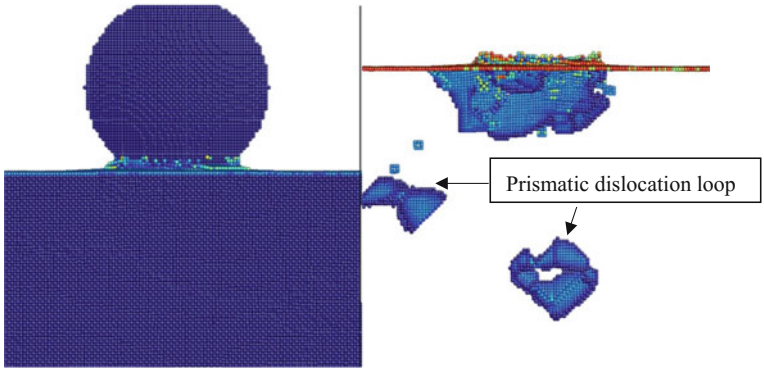

(e) D_{max}=1.2672 nm

Fig. 6 (continued)

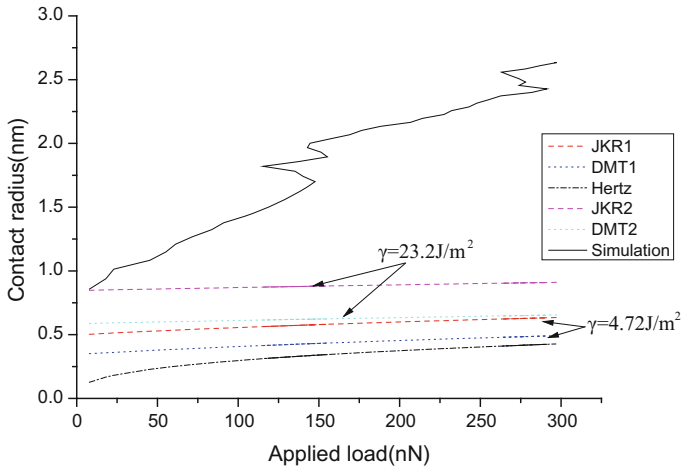

Fig. 7 Influence of the work of adhesion (γ) on the contact radius in both JKR, DMT and Hertz models, compared with the atomistic simulation

Hertz models, the results were compared with the atomistic simulation. The contact radius in the simulation work was calculated based on the following formula

$$a_{simulation} = \sqrt{2RD - D^2} \tag{7}$$

where D is the contact depth. It was suggested that the results of the atomistic simulation were only close to the continuum theories at the early stage of the contact process with shallow contact depth. And it seems that the value of γ is the key to the errors between the atomistic simulation and continuum theories. If the contact depth became deeper, there would be much deviation between the atomistic simulation and continuum theories. Because of the neglect of plastic deformation, all the continuum theories used in this paper might not be appropriate for the contact status with larger normal displacement situation. Also, the continuum theories might not take the work of dislocation nucleation, movements and annihilation into consideration.

Conclusion

In this work, the adhesion force in nano-contact during approaching and retrieving processes was studied and the continuum contact theories were compared with the atomistic simulation. The conclusions are listed as follows

1. The work of adhesion in approaching and retrieving were different.
2. The maximum normal displacement contributed a lot to the pull-off force. As the contact depth increased, the pull-off force to separate the adhering surface became bigger
3. The deviation between the atomistic simulation and the continuum contact theories was based on the value of γ, which was determined by the pull-off force. It does mean that the contact depth would affect the results.
4. It need to take the maximum normal displacement into consideration to develop a more accurate method to model the nano-contact situation. Especially, for the larger contact depth with plastic deformation.

Acknowledgements This work is supported by The National Natural Science Foundation of China (51210008).

References

1. Hertz H (1896) Miscellaneous papers. Macmillan, London, p 146
2. Leng Y, Yang G, Hu Y, Zheng L (2000) Computer experiments on nano-indentation: a molecular dynamics approach to the elasto-plastic contact of metal copper. Journal of materials science 35(8):2061–2067

3. Cha PR, Srolovitz DJ, Vanderlick TK (2004) Molecular dynamics simulation of single asperity contact. Acta Mater 52(13):3983–3996
4. Luan B, Robbins MO (2006) Contact of single asperities with varying adhesion: comparing continuum mechanics to atomistic simulations. Phys Rev E 74(2):026111
5. Efremov YM, Bagrov DV, Kirpichnikov MP, Shaitan KV (2015) Application of the Johnson–Kendall–Roberts model in AFM-based mechanical measurements on cells and gel. Colloids Surf B 134:131–139
6. Solhjoo S, Vakis AI (2015) Single asperity nanocontacts: Comparison between molecular dynamics simulations and continuum mechanics models. Comput Mater Sci 99:209–220
7. Giannakopoulos AE, Venkatesh TA, Lindley TC, Suresh S (1999) The role of adhesion in contact fatigue. Acta Mater 47(18):4653–4664
8. Johnson KL, Kendall K, Roberts AD (1971) Surface energy and the contact of elastic solids. Proc Royal Soc London A Math Phys Engineering Sci 324(1558):301–313
9. Derjaguin BV, Muller VM, Toporov YP (1975) Effect of contact deformations on the adhesion of particles. J Colloid Interface Sci 53(2):314–326
10. Zhao YP, Shi X, Li WJ (2003) Effect of work of adhesion on nanoindentation. Rev Advanc Mater Sci 5(4):348–353
11. Luan B, Robbins MO (2005) The breakdown of continuum models for mechanical contacts. Nature 435(7044):929
12. Landman U, Luedtke WD, Burnham NA, Colton R (1990) Atomistic mechanisms and dynamics of adhesion, nanoindentation, and fracture. Science, 248(4954):454–461
13. Yu N, Polycarpou AA (2004) Adhesive contact based on the Lennard-Jones potential: a correction to the value of the equilibrium distance as used in the potential. J Colloid Interface Sci 278(2):428–435
14. Si L, Wang X (2014) Nano-adhesion influenced by atomic-scale asperities: A molecular dynamics simulation study. Appl Surf Sci 317:710–717
15. Fang TH, Chang WY, Huang JJ (2009) Dynamic characteristics of nanoindentation using atomistic simulation. Acta Mater 57(11):3341–3348
16. Kramer B, Schreiber M, Hoffmann KH (1996) Computational physics. Springer
17. Lee Y, Park JY, Kim SY, Jun S, Im S (2005) Atomistic simulations of incipient plasticity under Al (111) nanoindentation. Mech Mater 37(10):1035–1048
18. Foiles SM, Baskes MI, Daw MS (1986) Embedded-atom-method functions for the fcc metals Cu, Ag, Au, Ni, Pd, Pt, and their alloys. Phys Rev B 33(12):7983
19. Lilleodden ET, Zimmerman JA, Foiles SM, Nix WD (2003) Atomistic simulations of elastic deformation and dislocation nucleation during nanoindentation. J Mech Phys Solids 51(5):901–920
20. Kelchner CL, Plimpton SJ, Hamilton JC (1998) Dislocation nucleation and defect structure during surface indentation. Phys Rev B 58(17):11085
21. Johnson KL (1998) Mechanics of adhesion. Tribol Int 31(8):413–418
22. Gao H, Yao H (2004) Shape insensitive optimal adhesion of nanoscale fibrillar structures. Proc Natl Acad Sci USA 101(21):7851–7856

Atomistic Simulations of Carbon Diffusion and Segregation in α-Iron Grain Boundaries

Mohamed Hendy, Tarek M. Hatem and Jaafar A. El-Awady

Abstract Polycrystalline materials' mechanical properties and failure modes depend on many factors that include segregation of different alloying elements as well as its grain boundaries (GBs) structure. Understanding the parameters affecting the diffusion and binding of alloying elements within GBs will allow enhancing the mechanical properties of the commercial engineering materials and developing interface dominant materials. In practice, the coincidence site lattice (CSL) GBs are experiencing deviations from their ideal configurations. Consequently, this will change the atomic structural integrity by superposition of sub-boundary dislocation networks on the ideal CSL interfaces. For this study, ideal $\sum 3$ GB structures and their angular deviations in BCC iron within the range of Brandon criterion will be studied comprehensively using molecular statics (MS) simulations. GB segregation energy and free surface segregation energies are calculated for carbon atoms. Rice-Wang model will be used to assess the embrittlement impact variation over the deviation angles.

Keywords Carbon · Grain boundary · Coincidence lattice

M. Hendy · T. M. Hatem (✉)
Department of Mechanical Engineering, The British University in Egypt,
El-Sherouk City 11837, Cairo, Egypt
e-mail: tarek.hatem@bue.edu.eg

M. Hendy
e-mail: mohamed.hendy@bue.edu.eg

T. M. Hatem
Microstructure Physics and Alloy Design Department, Max-Planck-Institut
Fur Eisenforschung, 40237 Düsseldorf, Germany

J. A. El-Awady
Department of Mechanical Engineering, Johns Hopkins University,
Baltimore, MD 21218, USA
e-mail: jelawady@jhu.edu

The Minerals, Metals & Materials Society, *TMS 2018 147th Annual Meeting & Exhibition Supplemental Proceedings*, The Minerals, Metals & Materials Series,
https://doi.org/10.1007/978-3-319-72526-0_30

Introduction

Mechanical properties and failure modes of steels depend on many factors that include segregation of different alloying elements as well as its grain boundaries (GBs) structure [1]. Understanding the parameters affecting the diffusion and binding of alloying elements within GBs will allow enhancing the mechanical properties of the commercial engineering steels and developing interface dominant materials [2]. Some of the elements dissolved in iron lead to enhancing the strength of steel, on the other hand others can degrade the toughness of steel significantly [3]. Being the main alloying element in steel, carbon segregation to different GBs is of ultimate importance.

Overall strength of steel can be greatly controlled through GB cohesion and strengthening. Several studies have been performed in this area. Many numerical studies indicated that carbon increases the cohesion at GB [4, 5]. It is of great importance to mention that the local structure within GB affects the segregation energy. First principle calculations have indicated that strong covalent bond is created between carbon and iron atoms at GB. Experiments showed that segregation of carbon to GBs of steel hinders grain coarsening and interface sliding leading to a steel alloy with ultrahigh strength of 7 GPa [6]. This is due to the role of carbon in decreasing GB energy that results in reducing the driving force for grain coarsening. Carbon segregation at nanocrystalline ferrite GBs, gives the material high thermal stability upon annealing.

Advancements in the field of grain boundary segregation engineering (GBSE) proved that GB segregation can be used as a microstructure design method since solutes affect the structure, phase state and atomic bonds within the steel interface [7]. Experiments in the field of GBSE indicated that deviated structures from coherency are common, even the most coherent GBs can contain deviated portions, where the alloying elements and impurities segregate and alter the GB mechanical properties. As a consequence, considering GB deviated and defected structures is of great importance since many cases ideal CSL GBs not formed; rather a deviation from the misorientation angle exists. Exponential property changes can occur if the GB plane is misaligned by only a few degrees from its most coherent position [7]. Deviant GBs are still considered CSL if the deviation angle is lower than a certain value for each $\sum$ indicated by Brandon [8]. The deviations introduce dislocation superimposing the GB and are associated with partial dislocations or elastic strain. Different deviation angle alters the trapping sites for impurities by changing the structural integrity of the grain boundary. This will affect segregation tendency of the impurity atoms to the grain boundary. It was showed experimentally using atom probe tomography that changing the deviation angle affects the carbon percentage segregated to the grain boundaries. It has been shown that the segregation values for $\Sigma 3$ (112) is sensitive to the angular deviations [6]. No prior atomistic study examined the effect of carbon segregation to deviated GB structures within Brandon criteria. This study aims to investigate the effect of deviation angles from the ideal CSL structure for three different common symmetrical tilt grain boundaries (STGB)

$\sum 3$ (111), $\sum 3$ (112) and $\sum 5$ (310) on carbon segregation and the cohesive energy changes due to carbon segregation to these interfaces.

Methodology

The concept of deviation from ideal CSL is shown in Fig. 1. Angle (Θ) represents the misorientation angle between the two grains. If the one of the two grains, forming the bi-crystal, is rotated relative to the other by a deviation angle (ϕ) around the Z-axis, the GB will still be regarded as CSL structure. Nevertheless, increasing ϕ above a certain limit causes the GB to lose its special character. In order to determine the deviation angles to be studied, it should be mentioned that Brandon criterion sets the maximum deviation angle from the ideal CSL configuration above which the structure no longer preserve the CSL structure. The maximum deviation angle can be calculated according to Brandon criterion through Eq. (1):

$$\theta_{\max} = \theta_{\circ} \sum^{-0.5} \tag{1}$$

where θ_{max} is Brandon limit, $\theta_{\circ}$ is Brandon limit constant approximately equals to 15° and $\sum$ is Reciprocal value of the CSL density, therefore the equation is function of $\sum$ only. For $\sum 3$ grain boundaries the Brandon limit is 8.66°. Hence the chosen deviation for $\sum 3$ grain boundaries are 5°, 9°, where 9° represents the extreme case of Brandon criteria.

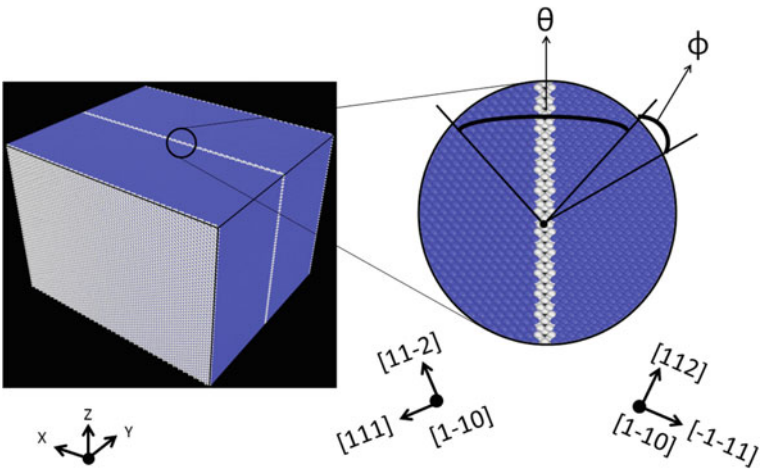

Fig. 1 Left: Bi-crystal simulation cell. Right: GB structure of ideal CSL sigma 3 (111) where Θ represents the misorientation angle between the two grains and ϕ is the deviation angle

Molecular statics (MS) simulations are performed using LAMMPS [9] with embedded atom method (EAM) potential developed by Veiga et al. [10]. The interatomic potential was developed to study of low concentrations of carbon in ferritic solid solution.. Bi-crystal cubic simulation cells are modeled with dimensions of 20 × 20 × 20 nm as shown in Fig. 1. Free surface boundary conditions were employed along the three-directions since the periodicity cannot be preserved for the deviated structures. For the current MS simulations, the simulation cells dimensions are sufficient to eliminate the free surface effect while computing the values of GB segregation energy. In order to define the two crystals geometrically, the first grain is defined with its GB plane normal and axis of rotation, then the second grain is rotated around this axis with angle equals to the sum of the misorientation angle (Θ) and the deviation angle (ϕ) as shown in Fig. 1. For ideal GB structures, deviation angle is 0°, while for the deviated structures, the deviation angle has values higher than 0° up to Brandon limit. In the cuurent simulations, GB plane normal is taken to be in the Y-direction, while the rotational axis in the Z-direction.

Carbon is inserted at distance 15 Angstrom from GB plane at the octahedral site, which is the most preferable interstitial site for carbon accommodation. At each certain distance from GB, the simulation is done many times with carbon at different position on X and Z directions to reduce the experimental error. The aim of MS technique is to minimize the potential energy of the system, though a numerical iterative process. In order to reach the minimum energy configuration, the coordinates of each atom are iteratively adjusted. The iterations are completed, when satisfying one of the ending criteria. The ending criteria chosen are either the change of the system energy is lower than 10^{-6} or it can be terminated after 10000 iterations. The minimization is done at 0 K using the conjugate gradient (CG) algorithm (Polak-Ribiere version).

As a result of the different orientation of the two grains intersecting at GB, many atoms overlap resulting in an unphysical system with high energy. In order to reach the optimum configuration of the system with global minimum energy, the overlapping atoms should be eliminated. Hence a certain cut off radius under which the close atoms are removed should be determined. A certain criterion [11] is to examine all the cut off radii between 0.0275α and -0.7α (where a is the lattice constant) with increment of 0.05 until reaching the most relaxed structure with minimum energy.

For each GB structure carbon segregation to GB and the surface corresponding to each GB are calculated. GB and surface segregation are required to be quantified to compare the preference of carbon segregation to grain boundary or surface. This will allow to determine the enhancing effect of carbon regarding each GB according to Rice-Wang model as it will discussed later. Eq. 2 is used to calculate GB segregation energy.

$$E^{\alpha}_{segGB} = (E^{\alpha}_{GB} - E_{GB}) - (E^{\alpha}_{bulk} - E_{bulk}) \quad (2)$$

where E^{α}_{segGB} is the GB segregation energy, E^{α}_{GB} is the total energy of the simulation cell with GB and carbon atom allocated at an interstitial octahedral site of the GB, E_{GB} without carbon, while the E^{α}_{bulk} and E_{bulk} are the total energy of the corresponding single crystal system with and without carbon respectively. The term $(E^{\alpha}_{bulk} - E_{bulk})$ represents the bulk segregation of carbon. It is put in the equation of grain boundary and surface segregation in order to measure all the segregation energy relative to the bulk segregation to allow for better comparison.

Carbon segregation to the free surface for each GB structure is also calculated. It is important to calculate the surface segregation as well as the GB segregation to establish the relation between the deviation angle and the change in the GB cohesive energy. Carbon tendency to bind with these free surfaces are calculated through determining the carbon free surface segregation energy using Eq. 3:

$$E^{\alpha}_{segFS} = (E^{\alpha}_{FS} - E_{FS}) - (E^{\alpha}_{bulk} - E_{bulk}) \quad (3)$$

E^{α}_{segFS} is the carbon free surface segregation energy, E^{α}_{FS} is the total energy of the free surface single crystal system with carbon atom allocated at an interstitial octahedral site and E_{FS} is the corresponding system without carbon addition.

Rice-Wang model will be adopted in order to compare quantitatively the effect of GB segregation of carbon to the different deviated structures from ideal CSL. Moreover, this model will allow predicting the change in cohesive energy for each GB structure due to carbon segregation. A positive change in the cohesive energy means a strengthening effect for carbon at this GB structure. Rice and Wang model describes intergranular embrittlement mechanism through the contest between brittle boundary separation and plastic crack blunting. According to Rice and Wang model [12], the ability of an impurity atom to reduce the Griffith work of a grain boundary is a linear function of the difference in the binding energies at the grain boundary and free surface of this impurity atom. Generally, if the impurity atom tends to segregate to free surface rather than the GB, the impurity atom will cause the embrittlement of the material and enhance the intergranular fracture. On the other hand, if the impurity atom tends to segregate to the grain boundary rather than the free surface, the impurity atom will enhance the cohesion of the grain boundary and as a consequence the strength of the material and the creep resistance will be enhanced. According to this model, The change in cohesive energy or embrittlement potency can be calculated as indicated by Eq. (4).

$$\begin{aligned} E^{\alpha}_{SE} &= (E^{\alpha}_{FS} - E_{FS}) - (E^{\alpha}_{GB} - E_{GB}) \\ &= E^{\alpha}_{segFS} - E^{\alpha}_{segGB} \end{aligned} \quad (4)$$

where E^{α}_{SE} is the change in cohesive energy or the strengthening energy due to segregation of one carbon atom to the GB and it is equal to the difference between

average GB segregation and average free surface segregation for carbon. If the value of E_{SE}^{α} is positive then the impurity atom enhance the cohesive strength of the grain boundary. This model will provide a powerful tool to compare the cohesive enhancement of each GB structure due to carbon segregation. Also, the effect of the deviation angles on the change in cohesive energy of those interfaces can be constructed easily.

Results

The GB segregation energy of carbon is calculated within the ideal and deviated GB structures using MS simulations. Extensive simulations have been made for these GB models over different distances from the GB plane. The results are summarized in Fig. (2) and statistical analysis has been made for segregation energy results at each distance level from the GB plane, where the mean of each data population is estimated at 95% confidence level. For $\sum 3(111)$ GB, All the segregation energy results among the tested deviation angles showed that GB is preferable location for segregation and binding since there is significant reduction in segregation energy as carbon atom position approaches a bulk site. In addition, the segregation behavior is affected by the angular deviations from the (111) ideal symmetry plane. For $\sum 3(112)$ GB, ideal and 5° deviated structure showed less preference for carbon, while 9° showed more binding sites.

In order to compare GB segregation of the different deviated structures from ideal CSL, average GB segregation energy is calculated by considering the values of segregation energy between −2 to + 2 Angstrom along the GB plane. The results show that angular deviation from the ideal symmetry plane has an observable effect on the segregation energy. The average GB segregation energy for the studied GBs and their deviations are shown in Fig. (3). For $\sum 3(111)$ GB, It is clear that the average GB segregation energy values increase as the deviation angle increases from 0° to 9° indicating less binding of carbon to GB region compared to the ideal one. Increasing the deviation angle to 9°, the average GB segregation energy decreases again with a value slightly lower than 5° structure. On the contrary, for $\sum 3(112)$ GB, it is observed that the average GB segregation energy value decrease as the deviation angle increases indicating a higher tendency for carbon to segregate to GB as the deviation increase. The most significant increase in GB segregation energy is for the 9° deviation configuration (slightly higher than Brandon limit) to reach −0.6 eV. GB segregation energy value at 9° is six times higher than the value for the ideal structure indicating that for $\sum 3(112)$ GB, exceeding Brandon limit alters the segregation properties considerably. Comparing the GB segregation values for $\sum 3(112)$ and $\sum 3(111)$ GBs, it is obvious that generally $\sum 3(111)$ GB is more preferred for carbon segregation than $\sum 3(112)$ GB within GB structures ranging from 0° to 5°. Deviated 9° is the only structure that GB segregation for $\sum 3(112)$ is lower than $\sum 3(111)$.

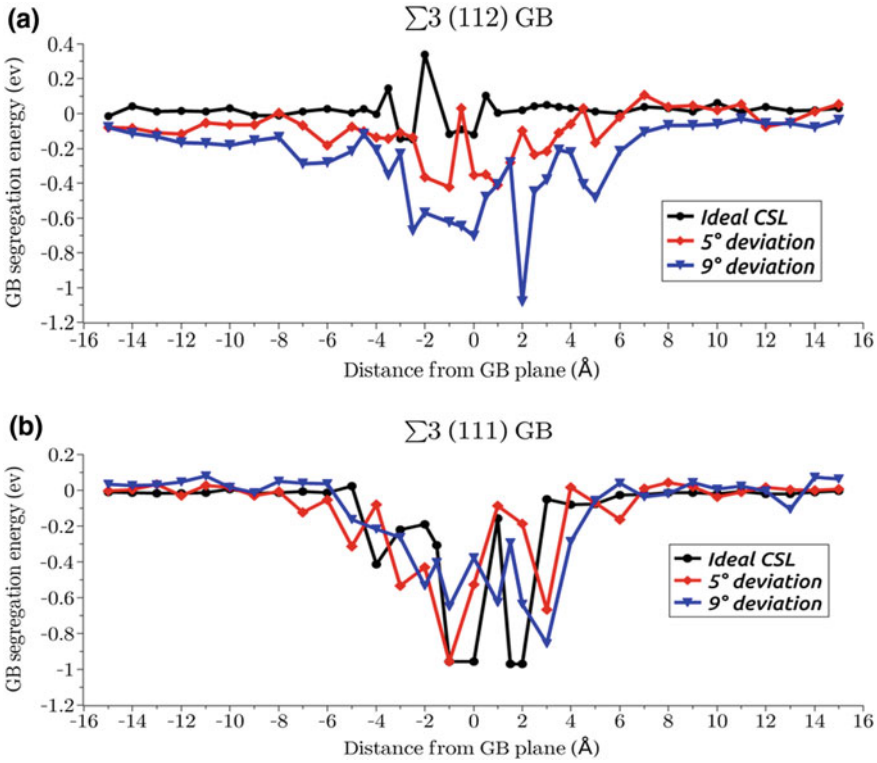

Fig. 2 GB segregation energy (ev) versus distance along GB plane (Angrstom) for the studied ideal and deviant structure showing less preference sites for carbon (higher segregation energy) for **a** $\sum 3(112)$ GB compared to **b** $\sum 3(111)$ GB

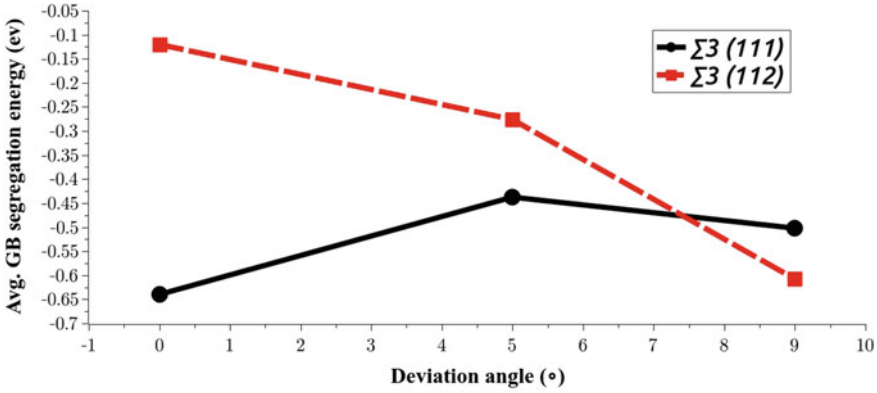

Fig. 3 Average GB segregation energy (ev) versus deviation angle showing decrease in avg. segregation energy for $\sum 3$ (111) and increase for $\sum 3$ (112) compared to ideal

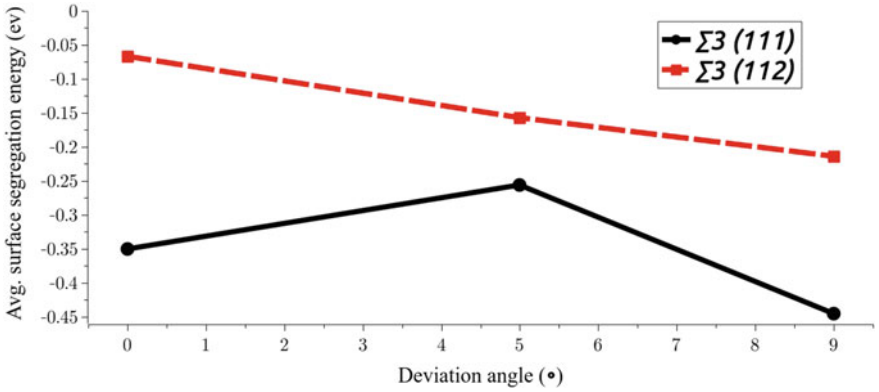

Fig. 4 Average surface segregation energy (ev) versus deviation angle showing decrease in avg. segregation energy for ∑3 (112) compared to ideal, for ∑3 (111) it shows increase at 5° then decrease at 9°

Due to the difference in the deviation angle for each GB structure, the orientation of the free surface laying in the orthogonal direction to GB plane varies over each GB structure. Hence, the carbon free surface segregation energy is calculated for ideal CSL structure as well as the other deviation angle structures. A single carbon atom at the octahedral site is placed near the free surface to calculate the free surface segregation energy. The positions are varied in different simulations to eliminate the statistical error. The results of the free surface segregation energy are shown in Fig. (4). For the free surface corresponding to $\sum 3(111)$ GB, It can be observed that the highest free surface segregation preference (lowest segregation energy) for carbon is to segregate to 9° deviation free surface, followed by the ideal free

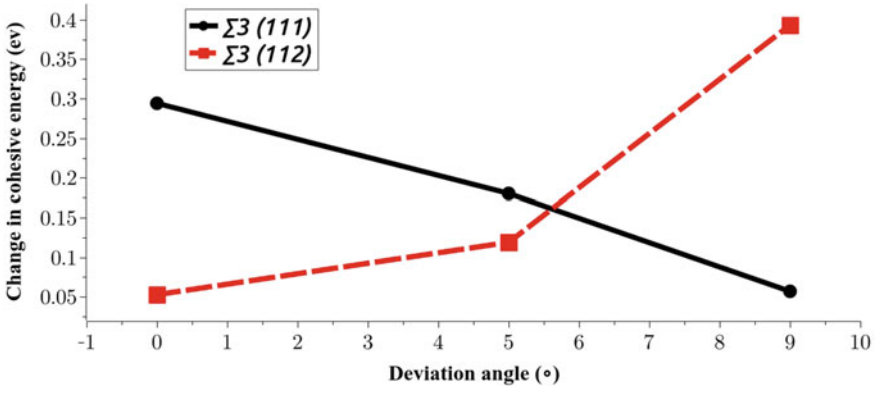

Fig. 5 Change in cohesive energy (strengthening energy) (eV) versus deviation angle showing decrease in strengthening energy for ∑3 (111) with increasing deviation angle, for ∑3 (112) strengthening energy increase with increasing deviation angle compared to ideal

surface. For the free surface corresponding to $\sum 3(112)$ GB, the value of the average free surface segregation corresponding to ideal is the highest. Upon increasing the deviation angle, free surface segregation energy decrease. The highest free surface segregation preference is observed for the free surface of 9° deviation GB similar to $\sum 3(111)$ GB. The results of the change in cohesive energy vs deviation angle is shown in Fig. (5). For $\sum 3$ (111), increasing the deviation angle showed a lower cohesive energy enhancement compared to the ideal, however still have a beneficial effect of GB structures. For $\sum 3$ (112) GB, all the deviant structure have higher strengthening energy compared to the ideal one. 9° deviant structure showed the highest beneficial effect.

Conclusion

Small deviation angle from the ideal misorientation angle of CSL configuration for $\sum 3(111)$ and $\sum 3(112)$ altered the segregation and binding of carbon to those GBs and their corresponding free surface. With the aid of Rice-Wang model, it was shown that carbon segregation to all the studied ideal and deviant structures has a beneficial effect on the cohesive energy of the GBs. Deviation angle has an observable effect on the strengthening energy of the GBs studied. $\sum 3(111)$ and $\sum 3(112)$ GB showed different responses to increasing the deviation angle. For $\sum 3(111)$, increasing the deviation angle resulted in decreased strengthening energy compared to the ideal structure. An opposite behavior is observed for $\sum 3(112)$ that increasing the deviation angle leaded to increased strengthening energy relative to the ideal structure.

Acknowledgment This project is funded by the Academy of Scientific Research and Technology (ASRT) under joint collaborative Efforts of Egyptians Expatriates & Scientific Organizations towards Tackling R&D Challenges (JESOR), Contract No. 17.

References

1. Wachowicz E, Kiejna A (2008) Effect of impurities on grain boundary cohesion in bcc iron. Comput Mater Sci 43:736–743
2. Hatem TM, Zikry MA (2009) Dislocation density crystalline plasticity modeling of lath martensitic microstructures in steel alloys. Philos Mag 89:3087–3109
3. Krasko GL, Olson GB (1990) Effect of boron, carbon, phosphorus and sulphur on intergranular cohesion in iron. Solid State Commun 76:247–251
4. Hatem TM, Zikry MA (2009) Shear pipe effects and dynamic shear-strain localization in martensitic steels. Acta Mater 57:4558–4567
5. Kontis P et al (2016) On the effect of boron on grain boundary character in a new polycrystalline superalloy. Acta Mater 103:688–699

6. Kuzmina M, Ponge D, Raabe D (2015) Grain boundary segregation engineering and austenite reversion turn embrittlement into toughness: example of a 9 wt.% medium Mn steel. Acta Mater 86:182–192
7. Raabe D et al (2014) Grain boundary segregation engineering in metallic alloys: a pathway to the design of interfaces. Curr Opin Solid State Mater Sci 18:253–261
8. Brandon DG (1969) The structure of high angle grain boundaries. Phys Status Solidi 31:193–201
9. Plimpton S (1995) Fast parallel algorithms for short-range molecular dynamics. J Comput Phys 117:1–19
10. Veiga RGA, Becquart CS, Perez M (2014) Comments on atomistic modeling of an Fe system with a small concentration of C. Comput Mater Sci 82:118
11. Solanki KN, Tschopp MA, Bhatia MA, Rhodes NR (2013) Atomistic investigation of the role of grain boundary structure on hydrogen segregation and embrittlement in α-Fe. *Metall*. Mater Trans A Phys Metall Mate Sci 44:1365–1375
12. Rice JR, Wang JS (1989) Embrittlement of interfaces by solute segregation. Mater Sci Eng, A 107:23–40

Part XIII
Computational Design and Simulation of Materials (CDSM 2018): Meso/Macroscale Simulations

Microstructure Prediction for TMW-4M3 During Heat Treatment

Takaaki Hara, Shinichi Kobayashi, Tomonori Ueno, Nobufumi Ueshima and Katsunari Oikawa

Abstract The alloy TMW-4M3 has been developed as a novel cast and wrought alloy based on a concept of combining Ni-base and Co-base superalloys. This alloy contains higher amounts of Co and Ti than Alloy 720Li. For practical applications, it is very important to control the size and distribution of γ' phase as an intended microstructure. However, precipitation behavior of this type of alloy greatly depends on heat treatment conditions. In this study, we made a modification to the thermodynamic database in order to obtain reasonable γ/γ' phase boundary in the range of high Co composition. By using it, both the nucleation rate calculation based on classical nucleation theory and the microstructure evolution prediction based on the phase field method were applied to the precipitation of intragranular γ' particles during the heat treatment process. The simulated microstructures under different temperature history conditions agree well with experiments in both the size and the morphology of γ' precipitates.

Keywords TMW-4M3 · Microstructure · Nucleation rate · Phase-field method · Gamma prime

T. Hara (✉) · S. Kobayashi · T. Ueno
Metallurgical Research Laboratory, Hitachi Metals, Ltd, 1240-2, Hashimacho, Yasugi, Shimane 692-8601, Japan
e-mail: takaaki.hara.zk@hitachi-metals.com

S. Kobayashi
e-mail: shinichi.kobayashi.ye@hitachi-metals.com

T. Ueno
e-mail: tomonori.ueno.hd@hitachi-metals.com

T. Hara · N. Ueshima · K. Oikawa
Department of Metallurgy Graduate School of Engineering, Tohoku University, Aoba-6-6-02, Aramaki, Aoba-Ku, Sendai 980-8579, Japan
e-mail: n-ueshima@material.tohoku.ac.jp

K. Oikawa
e-mail: k-oikawa@material.tohoku.ac.jp

The Minerals, Metals & Materials Society, *TMS 2018 147th Annual Meeting & Exhibition Supplemental Proceedings*, The Minerals, Metals & Materials Series,
https://doi.org/10.1007/978-3-319-72526-0_31

Table 1 Nominal compositions of TMW-4M3 and Alloy 720Li (wt%)

Alloy	Ni	Co	Cr	Mo	W	Ti	Al	C	B	Zr
TMW-4M3	Bal.	25.0	13.5	2.8	1.2	6.2	2.3	0.015	0.015	0.03
720Li	Bal.	15.0	16.0	3.0	1.3	5.0	2.5	0.015	0.015	0.03

Introduction

[1]TMW-4M3 is a Ni-Co base superalloy developed for applications of turbine disks and other components by the National Institute for Material Science in Japan [1]. As shown in Table 1, this alloy is similar to Alloy 720Li in composition, but has larger amounts of Co and Ti. Therefore, the control of γ' precipitates is very important in order to obtain the required mechanical properties. However, precipitation behavior of γ' precipitates in this alloy greatly depends on heat treatment conditions [2].

That is why it takes a long time to find the most appropriate manufacturing conditions for making an intended microstructure. In this work, we have suggested the numerical modelling of microstructure evolution for TMW-4M3 during heat treatment process to accelerate the alloy designing process. Both nucleation calculation based on classical nucleation theory (CNT) and microstructure prediction based on multi-phase-field model coupled with the calculation of phase diagram (CALPHAD) approach were applied to the evolution of γ' particles during heat treatment process [3–5]. First, the thermodynamic database was assessed for phase boundaries and driving force evaluation. In microstructure prediction, we have calculated nucleation various nucleation rates in accordance with different cooling conditions, and then γ' precipitation and its evolution have been numerically analyzed with them. The computed microstructures were compared with the experimental results.

Experiments

A heat treatment experiment was conducted to study precipitation behavior of γ' phase [2]. Test pieces were from forged disk of TMW-4M3. First, solution treatment (ST) under subsolvus condition was carried out with two different temperatures (1373.15 and 1408.15 K), and then two different cooling rates were applied. One is the rapid cooling condition (RC) and the other is slow cooling condition (SC). Finally, a double aging process followed (923.15 K/24 h + 1033.15 K/16 h). The microstructures after the heat treatment process are shown in Fig. 1. Larger particles are secondary γ' and smaller particles are tertiary γ'. These are all

[1]"TMW" is a trademark of National Institute for Materials Science registered in Japan.

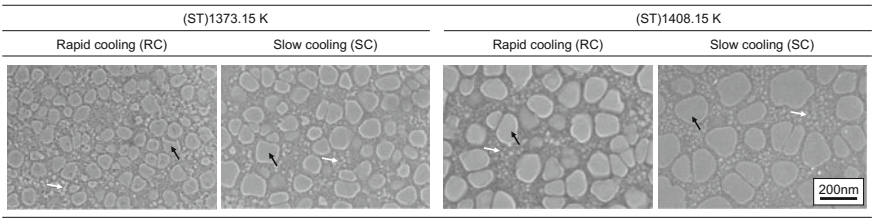

Fig. 1 Microstructures of TMW-4M3 after aging treatment. Bigger particles are secondary γ' (*black arrow*) and smaller particles are tertiary γ' (*white arrow*)

intragranular precipitates and have precipitation strengthening effect. The size of secondary γ' particle was larger with higher solution temperature and slower cooling rate.

Numerical Simulation and Results

Thermodynamic Database

For the calculation of the γ' precipitation behavior during cooling process, it is very important to know how much solute elements are contained in the γ matrix, which is defined by the heat treatment temperature and the γ' solvus temperature. Therefore, the thermodynamic database used for microstructure prediction is desired to reproduce the solvus temperature of γ' phase precisely. Under the metastable conditions, the computed γ' solvus temperature was 1485.15 K calculated by Thermo-Calc software and ThermoTech TTNI8 database [6, 7]. However, this is about 20 K higher than the experimental result. We assumed it is because TMW-4M3 has larger amount of Co and Ti than standard Ni base superalloys. From the comparison between the calculated Ni-Co-Ti ternary phase diagram at 900 °C and recent experiment data, we found that solubility of γ phase is narrow and phase boundary related to η phase is different from experiments [8]. In order to fill these gaps, modified formation energy of η and γ' phase and interaction energy of γ phase in Ni-Co-Ti systems were introduced to TTNI8. We can see that the calculated γ' solvus temperature of TMW-4M3 with the modified parameters shows

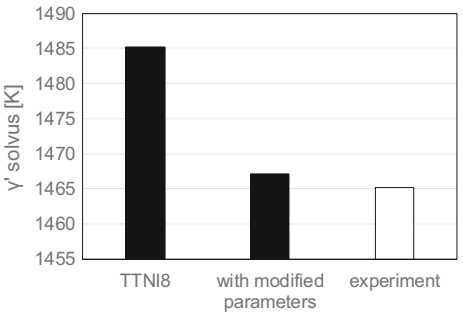

Fig. 2 Comparison of γ' solvus between calculation results (*black bar*) and experiment (*white bar*)

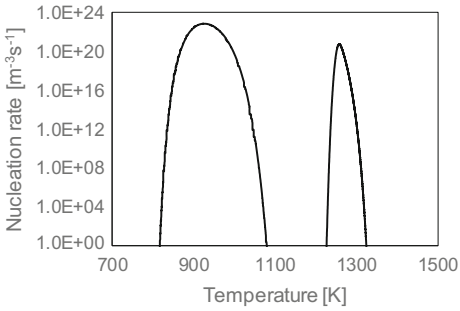

Fig. 3 Calculated nucleation rate of γ' precipitates during cooling process for ST1100 °C + RC

good agreements with experiments (see Fig. 2). The predicted γ' solvus of TMW-4M3 is 1467.15 K, which is quite close to experimental results.

Nucleation Rate Calculation

On the basis of classical nucleation theory, we predicted γ' nucleation behavior during cooling process after solution treatment. The calculated nucleation rate of γ' precipitates for the condition of (ST) 1373.15 K + RC is shown in Fig. 3. There are two peaks of nucleation. Precipitated γ' particles at high temperature easily grow up to large size because diffusion of solute elements would be faster. Therefore, first peak is corresponding to secondary γ', and then the second broad peak from 1100 K to 800 K is thought to be tertiary γ'. In this study, a two-dimensional calculation of microstructure prediction was applied to save computation time. Then, we converted the calculated three-dimensional nucleation rate to a two-dimensional value with the same average internuclear distance and applied it to a microstructure evolution simulation.

Microstructure Prediction

The precipitation strengthening effect in TMW-4M3 is mainly caused by secondary γ' precipitates [9]. Then, two-dimensional calculation by multi-phase-field model was applied to the evolution of secondary γ' precipitates during the heat treatment process with MICRESS software [10, 11]. We used the microscopic simulation domain of 600 nm square with grid size of 4 nm and interface width of 16 nm. All boundaries were periodical condition. The whole area was assumed as the single phase of the γ matrix in the initial condition. This is because secondary γ' particles appear among the intragranular area. As for γ/γ' interface, we introduced the Arrhenius type temperature dependent mobility considering the diffusion coefficient of Al in Ni [12]. The interface energy was also calculated on the basis of extended

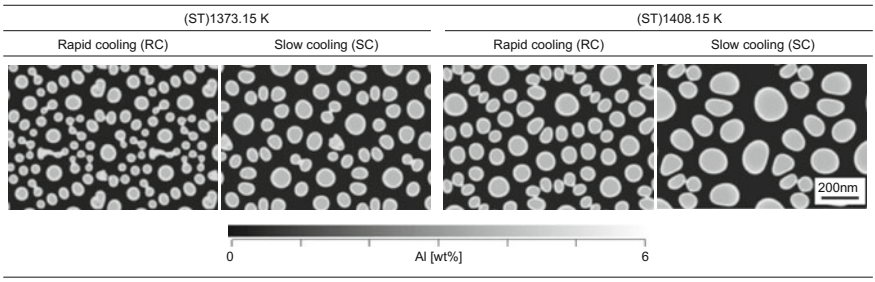

Fig. 4 Calculated microstructure after aging treatment (Al composition distribution)

Becker's model [13]. The predicted microstructures after aging treatment process are summarized in Fig. 4. Each feature of the γ' shape anisotropy tendencies were captured well in accordance with different heat treatment conditions. Moreover, the mean precipitate diameters of the γ' phase after aging treatment process were investigated. Each average particle size was calculated as an equivalent circle diameter. For all conditions, computed size of secondary γ' precipitates shows good agreement with an uncertainty of 10%.

Conclusion

To accelerate the alloy designing process, we have developed a technique to predict the γ' distribution of TMW-4M3 by using nucleation calculation on the basis of classical nucleation theory and microstructure evolution on the basis of the multi-phase-field method. As for thermodynamic database, modified parameters by reflecting large amount of Co and Ti were introduced, which lead to good prediction of γ' solvus temperature. Then, characteristic multimodal nucleation behavior during the cooling process can be predicted. Moreover, the simulated microstructures under different temperature history conditions agree well with experiments in both the size and the morphology of γ' precipitates. We can use this technique as a prior evaluation for trial production of actual alloys and expect alloy design processes to be accelerated.

References

1. Gu YF, Fukuda T, Cui C, Harada H, Mitsuhashi A, Yokokawa T, Fujioka J, Koizumi Y, Kobayashi T (2009) Comparison of mechanical properties of TMW alloys, new generation of cast-and-wrought superalloys for disk applications. Metall Mater Trans A 40(13):3047–3050
2. Kobayashi S, Ueno T, Ohno T, Harada H (2016) Relationship between the microstructure, low cycle and creep properties of a cast and wrought Ni-Co base superalloy TMW-4M3 disk. Superalloy 849–857

3. Kashchiev D (2000) Nucleation. Butterworth-Heinemann
4. Russell KC (1980) Nucleation in solids: the induction and steady state effects. Adv Colloid Interface Sci 13(3):205–318
5. Saunders N, Midownik AP (eds) (1998) CALPHAD calculation of phase diagrams: a comprehensive guide. Elsevier, New York
6. Andersson JO, Helander T, Höglund L, Shi P, Sundman B (2002) THERMO-CALC and DICTRA, computational tools for materials science. Calphad 26:273–312
7. Saunders N, Fahrmann M, Small CJ (2000) The application of CALPHAD calculation to Ni-based superalloys. Superalloys 803–811
8. Riani P, Sufryd K, Cacciamani G (2014) Critical assessment and experimental investigation of Co-Ni-Ti phase equilibria. Calphad 44:26–38
9. Osada T, Gu YF, Nagashima N, Yuan Y, Yokokawa T, Harada H (2013) Optimum microstructure combination for maximizing tensile strength in a polycrystalline superalloy with a two-phase structure. Acta Mater 61:1820–1829
10. Eiken J, Böttger B, Steinbach I (2006) Multiphase-field approach for multicomponent alloys with extrapolation scheme for numerical application. Phys Rev E 73(6)
11. MICRESS. http://web.micress.de/. Accessed 29 Aug 2017
12. Hillert M (1975) Diffusion and surface control of reactions in alloys. Metall Trans A 6:5–19
13. Becker R (1938) Die Keimbildung bei der Ausscheidung in metallischen Mischkristallen. Ann Phys 424:128–140

Study on the Effect of Die Coating Thickness on the Interfacial Heat Transfer Coefficient in Squeeze Casting of Aluminum Alloy

Feifan Wang, Xuyang Wang, Keyan Wu and Zhiqiang Han

Abstract The effect of die coating thickness on the heat transfer at the metal-die interface in squeeze casting process was studied, where the interfacial heat transfer coefficient (IHTC) was determined by applying an inverse approach based on the temperature measurements inside the mold. The acquired data were processed by a low pass filtering method based on Fast Fourier Transform (FFT). The die coating used in these experiments was water-based graphite which was sprayed onto the surface of the die cavity. The die coating thickness was measured by using TT260B coating thickness gauge. The results showed that the peak and average value of the IHTC increased with the increasing of the die coating thickness when the die coating thickness was less than 32 μm. When it was more than 32 μm, the peak and average value of the IHTC decreased with the increasing of the die coating thickness. Besides, the effect of the applied pressure on the IHTC was getting smaller as the die coating thickness increased.

Keywords Squeeze casting · Interfacial heat transfer coefficient
Pressure · Die coating thickness

Introduction

The application of lightweight components in the automotive industry contributes to reduce fuel consumption and CO_2 emissions. The utilization of lightweight components whose materials are mainly aluminum and magnesium alloys in the automotive industry has therefore significantly increased in past few years. However, there are many defects generated in castings during solidification, such as gas

F. Wang · X. Wang · K. Wu · Z. Han (✉)
School of Materials Science and Engineering, Tsinghua University, Beijing 100084, China
e-mail: zqhan@tsinghua.edu.cn

F. Wang · X. Wang · K. Wu · Z. Han
Key Laboratory for Advanced Materials Processing Technology (Ministry of Education), Tsinghua University, Beijing 100084, China

The Minerals, Metals & Materials Society, *TMS 2018 147th Annual Meeting & Exhibition Supplemental Proceedings*, The Minerals, Metals & Materials Series,
https://doi.org/10.1007/978-3-319-72526-0_32

pore, shrinkage and cold shut. These defects deteriorate the mechanical properties of the casting components, which limits the application of light-weight alloys. Thus, squeeze casting which is a casting technology of near net shape method has received more and more attentions due to the high integrity, fine grain size, and superior mechanical properties [1–3].

In casting, it is well established that the microstructure and the mechanical properties of solidified alloys depends on the rate of solidification. In squeeze casting process, heat removal from the molten alloy proceeds through a layer of solidified alloy, the casting-die interface and then through the die. With a metallic die, heat exchange effect is usually governed by the properties of the casting-die interface, which is characterized by the IHTC. In squeeze casting, the coating separates the die surface from the casting surface. As a result, the ejection of the casting after the completion of solidification can be done smoothly. Besides, the die coating is a thermal barrier which has an influence on the heat extraction during casting solidification. Because the thickness of coating is important, it should be one of the key parameters by which the IHTC is affected. Knowledge of the IHTC is of great benefit for simulating the solidification, understanding the effect of the process parameters and controlling the microstructure of castings [4–7].

It is known that a coating offers a resistance to heat transfer due to its thermal conductivity. The thermal resistance due to various coatings can be linked to their composition and thickness. An effort to estimate the effect of a coating on heat transfer requires a close examination of each of the aforementioned properties.

A few steady-state coating investigations provide some understanding of the effect of coating thickness and composition on the IHTC. Griffith and Hallam [8] and Broucaret et al. [9] found slight differences in IHTC between graphite-based coatings and those based on ceramic. Hamasaiid et al. [10] established the relationship of the heat flux, the peak value of the IHTC and the coating thickness. However, all the studies above focused on gravity die casting and high pressure die casting. For squeeze casting, the studies on the die coating has not been reported yet.

In present paper, the die coating used in the experiments was water-based graphite which was sprayed manually onto the surface of the die. As a result, the present paper mainly discussed the effect of coating thickness on the IHTC.

Experiment Procedure and Estimation of IHTC

Experiment Procedure

In these experiments, direct squeeze casting (DSC) process was adopted. The aluminum alloy casting was cast in H13 steel die. The dimension of this casting was 140 × 90 × 30 mm.

The interfacial heat transfer coefficient (IHTC) was estimated by using an inverse method. The accuracy of the estimated result is strongly dependent on the measured temperature, so the temperature measurement procedure must be well designed to meet the requirement of the accurate determination of the IHTC. In order to acquire accurate temperature readings, a special temperature sensor unit was designed in the present study. Six 1-mm-wide and 1-mm-deep grooves were machined in the sensor unit for the placement of the thermocouples. Each groove was machined to terminate at a particular distance (1, 3, and 6 mm) from the front end of the sensor unit. The thermocouple tip was welded to the end wall of the groove by stored-energy welding in order to maintain a perfect contact with the temperature measurement point. In order to prevent the welded thermocouples from falling off, high temperature resistant inorganic adhesive was filled in the grooves. The temperature sensor unit was manufactured using the same material as the die to ensure that the heat transfer process would not be distorted.

The die coating used in these experiments was water-based graphite which was sprayed onto the surface of the die cavity. The die coating thickness was measured by using TT260B coating thickness gauge. The die material was H13 steel. A data acquisition system manufactured by Integrated Measurement Corporation (IMC, Berlin, Germany) was used during the experiment with a sampling frequency of 200 Hz.

Before pouring, the dies were pre-heated to 483 K (210 °C) using four heat cartridges installed inside the lower die. The experimental procedure included spraying the die coating onto the die cavity surface, measuring the temperature of the molten aluminum alloy before pouring using a sheathed thermocouple, pouring the melt into the lower die, closing the dies, squeezing solidification with the applied pressure, opening the dies, and ejecting the casting.

Estimation of IHTC

Due to the high sampling frequency of the data acquisition system which was set as 200 Hz, the high-frequency noise components (usually 40–50 Hz) in the temperature and pressure measurements were also measured and inevitably included in the acquired data. In order to eliminate the negative effect of these high-frequency noise components on the analysis of the IHTC, a low pass filtering method based on Fast Fourier Transform (FFT) was adopted to process the data. The detail of the data processing method was discussed in Ref. [11].

Due to the fact that the thickness of the casting was relatively small than the other dimension of the casting (width and length), the following assumptions were made during the estimation procedure: (1) the heat transfer is one-dimensional; (2) the casting center is adiabatic; and (3) the initial temperature of the casting equals the melt temperature. As a result, the inverse method was adopt in this paper to estimate the IHTC. Detailed description of the inverse method can be found in Ref. [11].

Results and Discussion

In the experiments shown in Fig. 1, the castings in Case 1, 2 and 3 were solidified under applied pressure of 70, 46 and 23 MPa, respectively. The initial die temperature of Case 1 was 503 K (230 °C) and the initial die temperature of the other three cases was 523 K (250 °C). The pouring temperature of the three cases was 933 K (660 °C).

As shown in Fig. 1, before the pressure was applied, the IHTC of the three cases had little difference because of the same conditions for the solidification. At the beginning stage of the pressure applying, the IHTC of all the three cases with applied pressure underwent an abrupt increasing stage and reached their peak value, as shown in Fig. 1. The higher the applied pressure, the higher the peak value of the IHTC. Immediately after the pressure was applied, the IHTC decreased.

As shown in Fig. 1a, the IHTC profiles was sensitive to the variation of the applied pressure, when the die coating thickness was 32 μm. After the pressure was applied, there was a large difference in the profiles of the IHTC under different applied pressure. However, the sensitivity of the IHTC to the change of the applied pressure became very low, when the die coating thickness was 136 μm. The difference in the profiles of the IHTC under different applied pressure was almost eliminated, as shown in Fig. 1b. As shown in Fig. 2, when the die coating thickness reached 136 μm, the variation of the peak and the average value of the IHTC became smaller and smaller with the increasing of the die coating thickness.

In these experiments, the roughness of the die surface was about 25–50 μm. When the die coating was 32 μm, it was mainly used to fill the gap between the casting and die. This would enhance the heat transfer at the casting-die interface, as shown in Fig. 3b. However, when the die coating thickness was 136 μm, a thick coating layer was formed between the casting and die, as shown in Fig. 3c. Its thermal resistance became the dominant factor affecting the interfacial heat transfer.

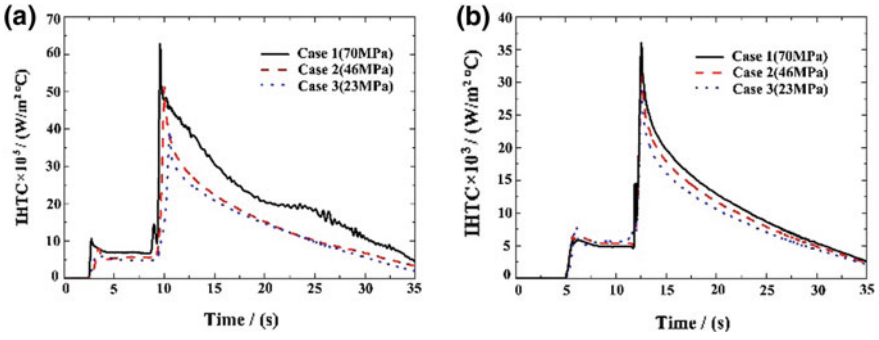

Fig. 1 IHTC under different pressure: **a** the die coating thickness was 32 μm; **b** the die coating thickness was 136 μm

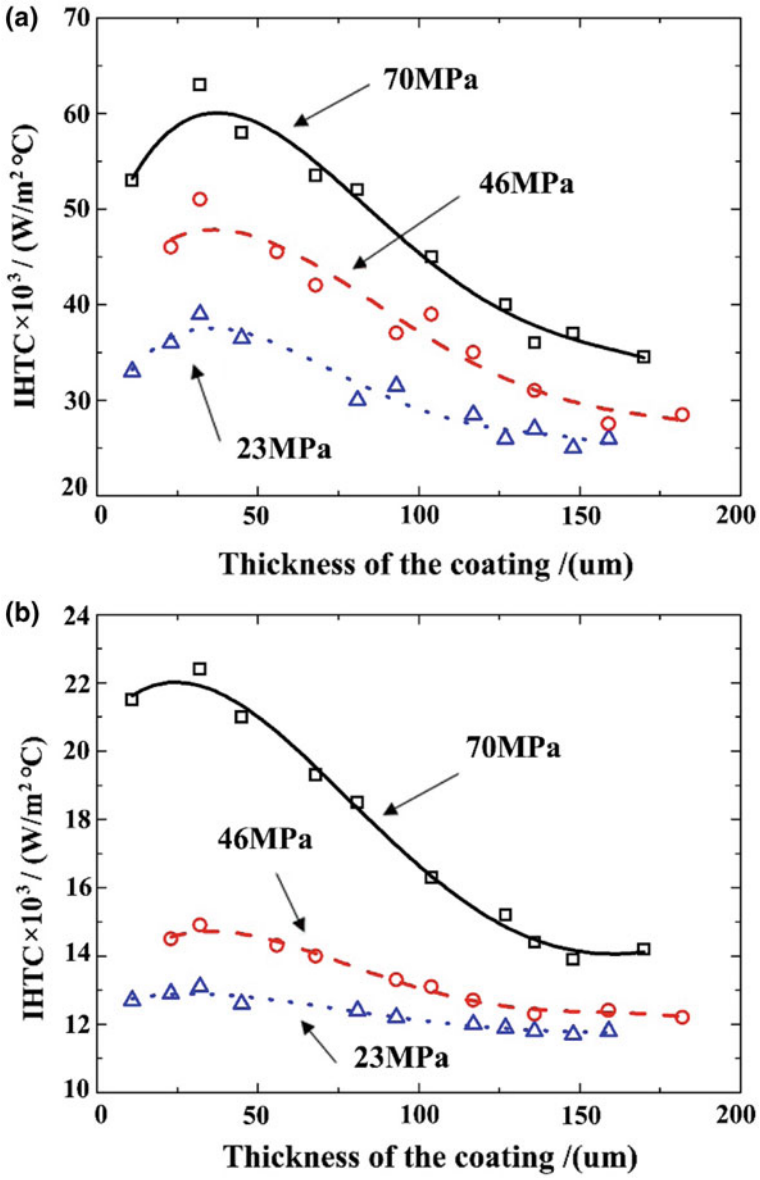

Fig. 2 **a** The peak value and **b** the average value of the IHTC under different condition of the die coating thickness

As shown in Fig. 2, the peak and average value of the IHTC increased with the increasing of the die coating thickness when the die coating thickness was less than 32 μm. When it was more than 32 μm, the peak and average value of the IHTC

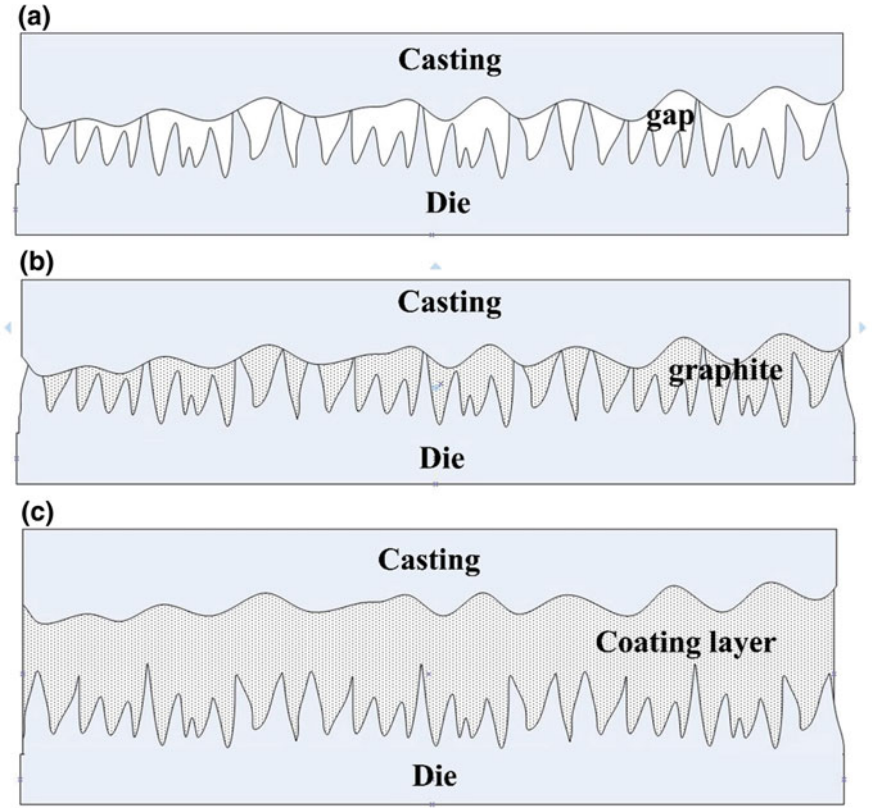

Fig. 3 Schematics of the casting-die interface: **a** no coating; **b** the die coating was thinner; **c** the die coating was thicker

decreased with the increasing of the die coating thickness. The peak and the average value of the IHTC reached their maximum value when the die coating was 32 μm. It meant that the heat exchange effect was the best when the die coating was 32 μm.

As shown in Fig. 3a, if the die coating was not used, the gap between the casting and die was fill with air. When the die coating was used in these squeeze casting experiments, the graphite was squeezed into the gap between the casting and die, as shown in Fig. 3b. As the conductivity of the graphite was much larger than air, the heat transfer effect of the casting-die interface was improved. When the die coating thickness was less than 32 μm, the thicker the die coating was, the more graphite was squeezed into the gap. As a result, the heat exchange effect was getting better. However, when the die coating thickness was more than 32 μm, the gap was almost full of graphite, the coating layer began to form. As the thickness of the coating layer increased, the contact status of the casting and die became worse and worse. The heat exchange effect became worse and worse.

Conclusions

1. The peak and average value of the IHTC increased with the increasing of the die coating thickness when the die coating thickness was less than 32 μm. When it was higher than 32 μm, the peak and average value of the IHTC decreased with the increasing of the die coating thickness.
2. The difference of the peak value of the IHTC under applied pressure of 70, 46 and 23 MPa was getting smaller as the die coating thickness increased.
3. When the die coating thickness was about 32 μm, the applied pressure had great influence on the average value of the IHTC and the one under applied pressure of 70 MPa was much higher than the ones under applied pressure of 46 and 23 MPa. As the die coating thickness increased, the difference of the average value of the IHTC under applied pressure of 70, 46 and 23 MPa was getting smaller.

Acknowledgements This work is funded by the National Key Research and Development Program of China (2016YFB0701204) and the National Science and Technology Major Project of China (2017ZX04080001).

References

1. Abou El-khair MT (2005) Microstructure characterization and tensile properties of squeeze-cast AlSiMg alloys. Mater Lett 59:894–900
2. Guo ZP, Xiong SM, Liu BC, Li M (2008) Determination of the heat transfer coefficient at metal—die interface of high pressure die casting process of AM50 alloy. Int J Heat Mass Trans 51:6032–6038
3. Han ZQ, Pan HW, Li YD (2015) Study on pressurized solidification behavior and microstructure characteristic of squeeze casting magnesium alloy AZ91D. Metall Mater Trans B 46:328–336
4. Yue TM, Chadwick GA (1996) Squeeze casting of light alloys and their composites. J Mater Process Technol 58:302–307
5. Lewis RW, Postek EW, Han ZQ (2006) A finite element model of the squeeze casting process. Int J Numer Method H 16:539–572
6. Han ZQ, Zhu W, Liu BC (2009) Thermomechanical modeling of solidification process of squeeze casting I. Mathematic model and solution methodology. Acta Metall Sin 45:356–362
7. Fardi Ilkhchy A, Jabbari M, Davam P (2012) Effect of pressure on heat transfer coefficient at the metal/mold interface of A356 aluminum alloy. Int Commun Heat Mass 39(5):705–712
8. Griffiths WD, Hallam CP (2004) A model of the interfacial heat-transfer coefficient for the aluminum gravity die-casting process. Metall Mater Trans 35B:721–733
9. Broucaret S, Michrafy A, Dour G (2001) Heat transfer and thermo-mechanical stresses in a gravity casting die. J Mater Process Technol 110:211–217
10. Hamasaiid A, Dargusch MS, Davidson CJ, Dour G (2007) Effect of mold coating materials and thickness on heat transfer in permanent mold casting of aluminum alloys. Metall Mater Trans 38A:1303–1316
11. Wang FF, Ma QX, Meng W, Han ZQ (2017) Experimental study on the heat transfer behavior and contact pressure at the casting-mold interface in squeeze casting of aluminum alloy. Int J Heat Mass Trans 112:1032–1043

Part XIV
Computational Design and Simulation of Materials (CDSM 2018): Computational Design of Materials

Study on the Effect of Applied Pressure on Directional Dendritic Growth by In-Situ Observation

Shan Shang, Keyan Wu, Leewei Kuo and Zhiqiang Han

Abstract A custom experimental apparatus was designed to realize the in-situ observation of dendritic growth under pressure in directional solidification of model material, succinonitrile. The evolution of dendritic growth under ambient pressure (P_0) and pressure of 3.0 MPa (P) was captured by a high-speed microscope and compared by analyzing qualitative distinctions in morphology and the quantitative ones in tip velocity and SDAS. Qualitatively, increased pressure promotes dendrite growth in directional solidification, elevating growth velocity and facilitating the burgeoning and growth of secondary arms, resulting in longer and more developed dendrites and much smaller SDAS. Quantitatively, the average tip velocities under P_0 and P are 14.5 μm/s and 29.8 μm/s, respectively, with 100% rise when growing under pressure P. Moreover, the SDAS is 50.3 μm and 30.2 μm, respectively, declining by 40% when solidified under pressure P. This phenomenon can be attributed to the effect of pressure on melting point and its destabilizing effect on S/L interface.

Keywords Pressure · Dendritic growth · In-situ observation
Directional solidification · Succinonitrile (SCN)

Introduction

Squeeze casting is an advanced near-net-shape materials processing technology, in which liquid metal solidifies under applied pressure, making products with excellent final microstructure and thus mechanical properties [1, 2]. It has been reported that in squeeze casting process, pressure has a great influence on dendritic growth,

S. Shang · K. Wu · L. Kuo · Z. Han (✉)
School of Materials Science and Engineering, Tsinghua University, Beijing 100084, China
e-mail: zqhan@tsinghua.edu.cn

S. Shang · K. Wu · L. Kuo · Z. Han
Key Laboratory for Advanced Materials Processing Technology (Ministry of Education), Beijing 100084, China

The Minerals, Metals & Materials Society, *TMS 2018 147th Annual Meeting & Exhibition Supplemental Proceedings*, The Minerals, Metals & Materials Series,
https://doi.org/10.1007/978-3-319-72526-0_33

such as growth velocity, secondary dendritic arm spacing (SDAS) and grain size [3–7].

It is of significant importance to understand the mechanism how pressure influences microstructure evolution. However, researches so far have not realized in-situ observation of dendritic growth of metals when solidified under pressure, due to the opacity of metal and limit of experimental approach available. Fortunately, transparent model materials, such as succinonitrile (SCN), has been selected as substitute to accomplish in-situ observation [8–10]. Koss et al. [11, 12] carried out a series of experiments to study the response of equiaxed dendritic growth of SCN to applied pressure in a uniform temperature bath. It was stated that tip velocity rose while radius decreased with pressure, due to the change in equilibrium melting temperature according to the Clapeyron effect [13], and the initiation of side branches were also facilitated by pressure, owing to the destabilizing effect of pressure on interface. Nevertheless, almost all of those investigations take single equiaxed dendrite as research object, and seldom research on how pressure influences columnar dendrite during directional solidification has been executed.

In this work, a novel experimental apparatus inspired from the apparatus of direct squeeze casting was established to accomplish the in-situ observation of dendritic growth under pressure in directional solidification. The dendritic growth evolution of SCN solidified at ambient pressure was captured and compared with that under pressure of 3.0 MPa, by analyzing dendritic morphology, tip velocity and SDAS qualitatively and quantitatively under the two conditions. Moreover, the corresponding reason behind was discussed.

Experiments Description

In this work, SCN which is a transparent BCC material with a nominal melting point of approximately 58 °C, making it a convenient model material for in-situ observation of dendritic crystal growth, has been selected as the research objective. In order to realize the in-situ observation, a custom experimental setup inspired from the apparatus of direct squeeze casting was designed. The whole experimental apparatus contains five parts, that is, the mould, pressure-controlling system, temperature-controlling system, data acquisition system and observation system. Firstly, the mould, made of stainless steel, contains punch (Φ15 mm in diameter and 56 mm in height) and lower mould (40 mm × 40 mm × 85 mm), forming a cylindrical growth chamber (Φ15 mm in diameter) for SCN. The pressure-controlling system is composed of a digital pressure-controlling system refitted by a tensile test machine and featured by computer close-loop control, which can modulate the applied pressure on liquid SCN accurately, via a pressure sensor in the machine and connected to the punch. The two-way temperature-controlling system controls the temperature of upside and downside of lower mould by corresponding heaters, forming a temperature gradient in the lower mould and thus increasing temperature from bottom to up in the SCN. The pressure and the temperature of

liquid SCN can be measured via corresponding sensors and recorded by a precise data acquisition system manufactured by Integrated Measurement Corporation (IMC, Berlin, Germany). Finally, the dendritic growth of SCN can be observed and recorded through the observation system. The view window is built by two transparent cuboid sapphire, generating a laminar gap with 0.5 mm in thickness, i.e. the observable growth chamber. Along the observation direction, the dendritic growth can be observed intuitively through the view window and captured by a high-speed microscope (NAC Memrecam HX-6), as long as bright light through the sapphire window.

In this work, the dendritic growth of SCN at ambient pressure P_0 was compared with that under $P = 3.0$ MPa. The sequence of present experiment of crystal growth is as follows. At first, the upside-downside temperature of lower mould was set to be 60–51 °C by the temperature-controlling system, forming a temperature gradient in the SCN, and kept for about 15 min to obtain a stable solid/liquid (S/L) interface in appropriate height in the observable growth chamber. Secondly, the pressure was increased to be 3.0 MPa with a speed of 0.02 MPa/s, and then kept for about 15 min to gain another stable S/L interface which increased a bit with elevated pressure. Afterwards, the temperature gradient was modified to be 60–50 °C, accompanied by dendritic growth from bottom to up due to higher undercooling. Finally, the dendritic growth was captured by a high-speed microscope, with the image resolution 1280 dpi * 1280 dpi and the frame rate 50 fps to achieve high definition videos.

Results and Discussion

Based on the experimental setup and method, the dendritic growth evolution of SCN at ambient pressure and higher pressure was captured, making it possible to investigate the effect of pressure in liquid on dendritic growth in directional solidification. Figure 1 shows the evolution of dendritic morphology when solidified at ambient pressure P_0. In the beginning, the S/L interface kept relatively stable at $t = 0$ s, and then some cellular grain germinated from the interface and began to grow with the increase of undercooling in the liquid due to the change of temperature gradient ($t \leq 10$ s). With the processing of growth, the cellular dendrite transformed to columnar dendrite with a few secondary arms sprouted ($t = 10$–20 s), and the columnar dendrite grew higher, with more developed side branches (20–30 s). After $t = 30$ s, the dendrite grew very slowly for a long time, in the last period of which even coarsening happened, and finally the growth nearly stopped at $t = 70$ s.

Figure 2 illustrates the dendritic growth under pressure of $P = 3.0$ MPa, which displays plenty of qualitative differences in morphology evolution, compared with that at ambient pressure in Fig. 1. Firstly, the stable S/L interface rose up, indicating that the melting point of SCN, i.e. the temperature at S/L interface, increased with pressure according to the Clapeyron effect. Secondly, the columnar dendrites grew

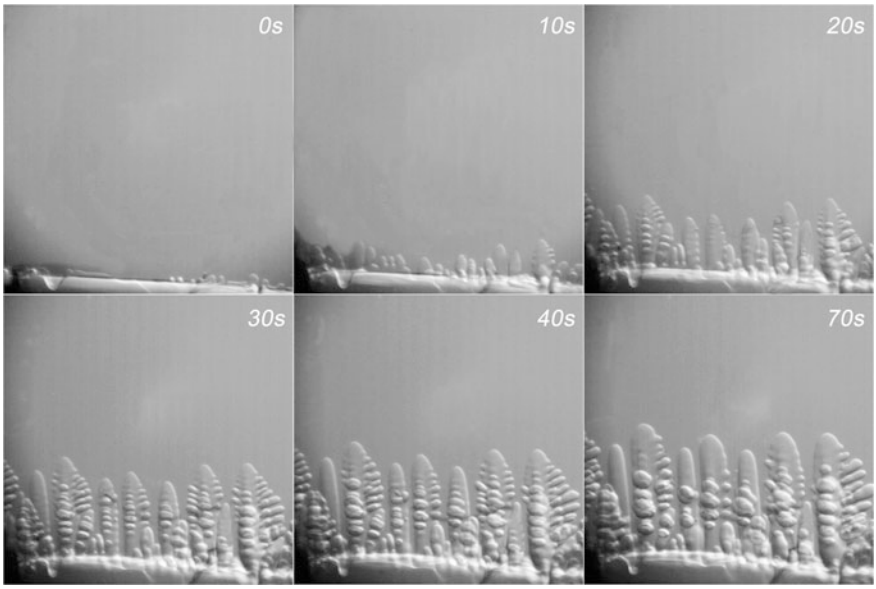

Fig. 1 The evolution of dendritic growth at ambient pressureP_0

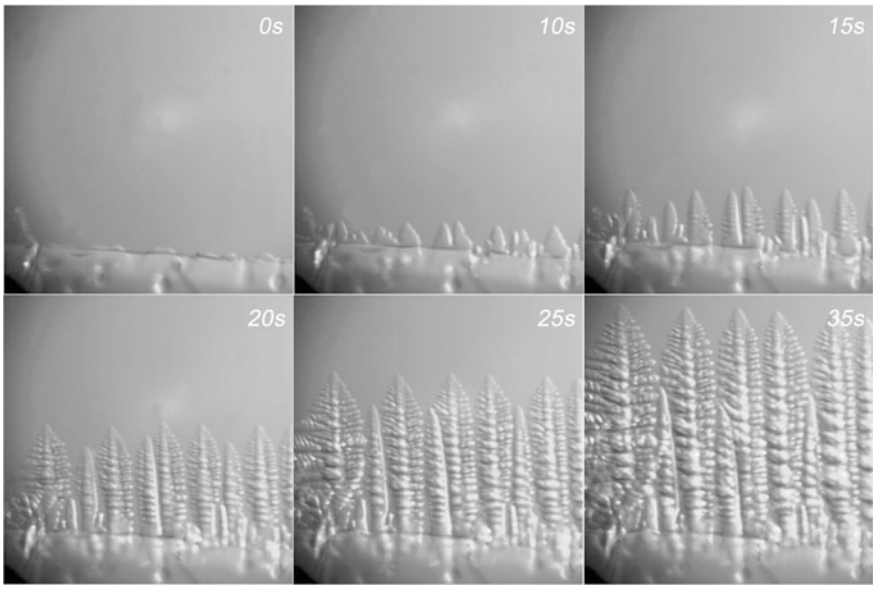

Fig. 2 The evolution of dendritic growth under pressure $P = 3.0$ MPa

much faster than that under P_0, with much higher columnar dendrite at the same time. Thirdly, the dendrites were more developed, with more and slimmer secondary arms and thinner SDAS. Lastly, the impingement of adjacent well-grown dendrites happened, leading to competitive growth between them, with some columnar dendrites growing fast while some in weak growing state.

Besides these qualitative differences in dendrite morphology, the quantitative distinctions were also analyzed by comparing tip velocity and SDAS in the two conditions. Seen from Fig. 3, both the tip velocities under P_0 and P go up initially and then decline. The reason behind is that tip velocity is determined by the undercooling in front of dendrite tip, which is influenced by two factors, declined temperature and rising growth height which increases and decreases the undercooling, respectively. Consequently, under the combined effects of the two factors, the undercooling climbs up at first period and then falls off, leading to tip velocity in the same variation trend. Comparing the two curves, tip velocity under pressure of 3.0 MPa is much higher than that under P_0, with higher maximum and average values. The average tip velocities in the first 35 s are 14.5 μm/s and 29.8 μm/s, respectively, with 100% increase when growing under pressure P. What's more, the SDAS which is an essential parameter in microstructure is 50.3 μm and 30.2 μm, respectively, declining by 40% when solidified under pressure P compared with that under P_0, as shown in Table 1.

Based on the experimental results, it is indicated that increased pressure promotes dendrite growth in directional solidification, elevating tip growth velocity and facilitating the burgeoning and growth of secondary arms, resulting in longer and more developed dendrites and much smaller SDAS. This can be attributed to

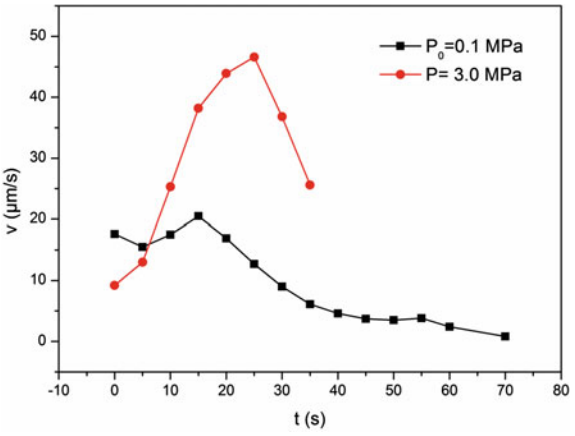

Fig. 3 Tip velocities with time under different pressures

Table 1 Average velocity and SDAS under different pressures

Pressure (MPa)	$P_0 = 0.1$	$P = 3.0$
Average velocity (μm/s)	14.5	29.8
SDAS (μm)	50.3	30.2

the effect of pressure on melting point and the destabilizing effect on S/L interface. The Clapyron effect is shown by the following equation

$$\frac{dP}{dT} = \frac{\Delta s}{\Delta V} = C_c$$

where dT is the change in melting temperature resulting from a change in pressure dP, ΔV is the specific volume change of the phase transition and Δs is the entropy change of phase transition. C_c is the Clapeyron coefficient, representing the melting temperature shift per unit change of pressure, and reported to be 24.5 mK/atm [13], which is about four times of that of pure Mg or Al. In this work, the applied pressure is 3.0 MPa, bringing about a rise of melting point, and thus the undercooling in the liquid SCN, about 735 mK. It is reported that dendritic crystal growth experiments on SCN typically employ undercoolings ranging from 1 K to as low as 50 mK which significantly change the true undercooling of an SCN melt. Consequently, the undercooling resulting from the applied pressure in this work is high enough to modulate the dendritic growth dramatically. Moreover, pressure changes is supposed to destabilize the interface, which promotes the growth of secondary arms.

Conclusions

A custom fabricated apparatus was designed from the design philosophy of direct squeeze casting to realize the in-situ observation of dendritic growth under pressure in directional solidification of SCN. Comparing dendritic growth at ambient pressure and under pressure of 3.0 MPa, qualitative and quantitative distinctions and the reason behind are reveled:

(1) Qualitatively in morphology, increased pressure promotes dendrite growth in directional solidification, elevating tip growth velocity and facilitating the burgeoning and growth of secondary arms, resulting in longer and more developed dendrites and much smaller SDAS.
(2) Quantitatively, the average tip velocities in the first 35 s under P_0 and $P = 3.0$ MPa are 14.5 μm/s and 29.8 μm/s, respectively, with 100% increase when growing under pressure P. Moreover, the SDAS which is an essential parameter in microstructure are 50.3 μm and 30.2 μm, respectively, declining by 40% when solidified under pressure P.
(3) This phenomenon can be attributed to the effect of pressure on melting point and the destabilizing effect on S/L interface, and the undercooling resulting from the applied pressure in this work is high enough to modulate the dendritic growth dramatically.

Acknowledgements This work was supported by the National Key Research and Development Program of China (No. 2016YFB0701204).

References

1. Ghomashchi MR, Vikhrov A (2000) Squeeze casting: an overview. J Mater Process Technol 101(1–3):1–9
2. Masoumi M, Hu H (2011) Influence of applied pressure on microstructure and tensile properties of squeeze cast magnesium Mg–Al–Ca alloy. Mater Sci Eng A 528(10–11): 3589–3593
3. Han Z, Huang X, Luo AA, Sachdev AK, Liu B (2012) A quantitative model for describing crystal nucleation in pressurized solidification during squeeze casting. Scripta Mater 66(5): 215–218
4. Shang S, Han Z, Sun W, Luo AA (2017) A phase field model coupled with pressure-effect-embedded thermodynamic modeling for describing microstructure and microsegregation in pressurized solidification of a ternary magnesium alloy. Comput Mater Sci 136:264–270
5. Pan H, Han Z, Liu B (2016) Study on Dendritic Growth in Pressurized Solidification of Mg–Al Alloy Using Phase Field Simulation. J Mater Sci Technol 32(1):68–75
6. Han Z, Pan H, Li Y, Luo AA, Sachdev AK (2015) Study on Pressurized Solidification Behavior and Microstructure Characteristics of Squeeze Casting Magnesium Alloy AZ91D. Metall Mater Trans B 46(1):328–336
7. Shang S, Hu B, Han Z, Sun W, Luo AA (2017). Macro- and Micro-Simulation and Experiment Study on Microstructure and Mechanical Properties of Squeeze Casting Wheel of Magnesium Alloy. Proceedings of the 4th World Congress on Integrated Computational Materials Engineering (ICME 2017), Ypsilanti, Michigan, 21–25 May 2017
8. Yokoyama C, Tamura Y, Nishiyama Y (1998) Crystal growth rates of tricaprin and trilaurin under high pressures. J Cryst Growth 191(4):827–833
9. Sawada T, Takemura K, Shigematsu K, Yoda S, Kawasaki K (1995) Diffusion field around a dendrite growing under microgravity. Phys Rev E 51(5):R3834–R3837
10. Sawada T, Takemura K, Shigematsu K, Yoda S, Kawasaki K (1998) Effects of gravity on a free dendrite of NH4Cl grown by dynamic pressure control. J Cryst Growth 191(1–2): 225–233
11. Koss MB, LaCombe JC, Chait A, Pines V, Zlatkowski M, Glicksman ME, Kar P (2005) Pressure-mediated effects on thermal dendrites. J Cryst Growth 279(1–2):170–185
12. Kar P, LaCombe JC, Koss MB (2004) Velocity and radius transients during pressure mediated dendritic growth of succinonitrile. Mater Sci Tech-Lond 20(10):1273–1280
13. LaCombe JC, Koss MB, Tennenhouse LA, Winsa EA, Glicksman ME (1998) The Clapeyron effect in succinonitrile: applications to crystal growth. J. Cryst. Growth 194(1):143–148

Modeling of Solute-Dependent Fluidity and Hot Tearing Sensitivity of Conductive Aluminum Alloys

Hengcheng Liao, Qigui Wang, Xiaojin Suo, Zixing Feng and Qin Huang

Abstract Empirical models have been developed to predict fluidity and hot tearing sensitivity of conductive aluminum alloys. An orthogonal test of 4 factors and 4 levels was designed to evaluate the effect of solute content of Si, Mg, Cu and Fe in conductive aluminum alloy on fluidity and hot tearing sensitivity (HTS). Results showed that Si, Mg and Cu elements have positive effect on fluidity and increasing their contents improves the fluidity. The effect of Fe content on fluidity is negative. For HTS, the effect of Si and Mg is negative while Cu and Fe is positive. Multi-element linear/non-linear polynomial regressions are adopted to construct the solute-dependent empirical models for fluidity and HTS. The predicted results based on the empirical models agree well with the verification tests.

Keywords Conductive aluminum alloy · Orthogonal test · Polynomial regression · Fluidity · Hot tearing sensitivity

Introduction

Aluminum and high purity aluminum alloys have been widely used as electrical conductors in power lines and hybrid induction motor applications because of their high specific strength, good corrosion resistance and excellent electric conductivity [1, 2]. As the conductive aluminum alloys currently used in hybrid induction motor components are usually cast, the castability of the alloys becomes critical to their success in induction motor applications.

H. Liao (✉) · X. Suo · Z. Feng · Q. Huang
Jiangsu Key Laboratory for Advanced Metallic Materials, School of Materials Science and Engineering, Southeast University, Nanjing 211189, China
e-mail: hengchengliao@seu.edu.cn

Q. Wang
Materials Technology, GM Global Propulsion Systems, 800 North Glenwood Ave, Pontiac, MI 48340, USA

The Minerals, Metals & Materials Society, *TMS 2018 147th Annual Meeting & Exhibition Supplemental Proceedings*, The Minerals, Metals & Materials Series,
https://doi.org/10.1007/978-3-319-72526-0_34

Fluidity and hot tearing sensitivity (HTS) are two most important index to monitor the castability of an alloy. For the fluidity and hot tearing sensitivity, there are too many affecting factors, and the mechanisms are rigorously complex. Usually, the constituents and element contents of an alloy (or alloy composition) [3–7], amount of eutectic [8–10], crystallization temperature interval [11–13], mushy zone width during solidification and solidification mode [3, 14, 15], and plasticity of solid and liquid [10] are thought to be the main affecting factors as well as the superheat of the liquid melt during casting [16]. Among these factors, the alloy composition is the key as it determines not only the crystallization temperature interval in nature but also the amount of eutectic, mushy zone width and solidification mode to a significant extent. For a given alloy, the thermodynamic and thermo-physical properties of the alloy is very much determined. Certainly, solidification condition is also another key. When the alloy composition is given, the variation of solidification condition can significantly change the amount of eutectic, mushy zone width and solidification mode. It is generally accepted that an alloy with a good fluidity means less solidification shrinkage and lower hot tearing sensitivity. The smaller the crystallization temperature interval is, the better the fluidity and the lower the hot tearing sensitivity. Adding a small amount of alloying elements into pure Al such as Ti, Fe, Zr, Cr, Mn and Cu will slightly decrease the fluidity [4–7]. But when the addition level is beyond certain amount, the fluidity is increased because of the increased amount of eutectic [17]. However, some alloys have a small crystallization temperature interval, but have a high hot tearing sensitivity, such as Ni alloys (IN792 and CM247) [18]. Both Al–Fe and Al–Mn alloys have very small crystallization temperature interval, but the hot tearing sensitivity of Al–Mn alloys are much higher than that of Al–Fe alloys [19]. This indicates hot tearing of an alloy depends not only on the crystallization temperature interval, but also on the linear contraction rate, physical-mechanical properties and inherent solidification characters of the alloy.

To develop a new conductive Al alloy to meet the above requirements for hybrid induction motor components, Mg, Si and Cu should be selected as strengthening elements to possess a good strength. Fe is the common impurity element that should be controlled strictly. Although qualitative influence of these elements on fluidity and hot tearing sensitivity is known well, the quantitative correlations of fluidity and hot tearing sensitivity with element content in conductive aluminum alloys have not been established. An accurate prediction model is also needed. In present study, an orthogonal test is designed to evaluate the effect of solute contents of Si, Mg, Cu and Fe in conductive aluminum alloy on fluidity and HTS and multi-element linear/non-linear polynomial regressions are adopted to construct the solute-dependent empirical models of fluidity and HTS.

Experimental Procedure

Orthogonal Test Design

Mg, Si and Cu are the strengthening elements in conductive aluminum alloys and Fe is an unavoidable impurity. So, Mg, Si, Cu and Fe solute contents are selected as controlling factors. Their levels are listed in Table 1. An orthogonal test (L^{16}) was chosen to carry out the experiments.

Alloying and Casting

The chemical compositions of the test alloys are listed in Table 2, which were measured using ARL-3460 (Flame direct reading spectrometry). The ingots of

Table 1 Factors and its levels in orthogonal test

Factors (wt%)	A	B	C	D
	Mg	Cu	Fe	Si
Level 1	0.2	0	0.15	0.2
Level 2	0.35	0.25	0.25	0.4
Level 3	0.5	0.5	0.4	0.6
Level 4	–	–	–	1.0

Table 2 Composition of the test alloys measured by ARL-3460, wt%

Alloy serial no.	Si	Mg	Cu	Fe
1	0.202	0.198	0	0.151
2	0.405	0.203	0.254	0.252
3	0.611	0.201	0.506	0.404
4	1.030	0.199	0	0.150
5	0.608	0.351	0	0.249
6	1.080	0.349	0.250	0.152
7	0.205	0.350	0.503	0.149
8	0.401	0.353	0	0.403
9	1.040	0.510	0	0.410
10	0.603	0.510	0.251	0.151
11	0.411	0.504	0.510	0.148
12	0.207	0.506	0	0.247
13	0.408	0.202	0	0.153
14	0.204	0.199	0.249	0.397
15	1.030	0.210	0.501	0.250
16	0.610	0.207	0	0.150

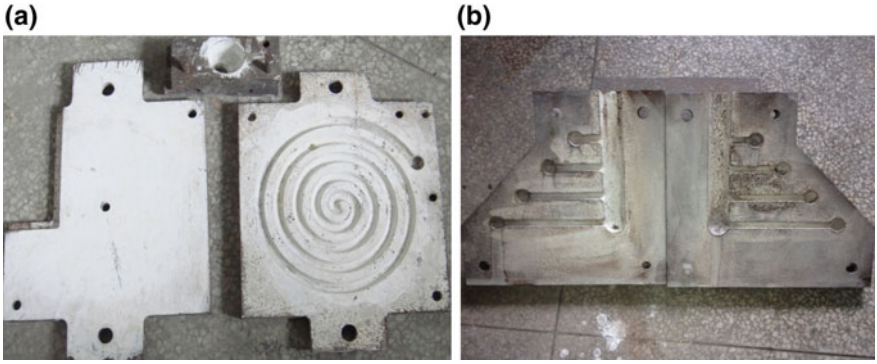

Fig. 1 Metal molds for castability evalution **a** Spiral fluidity test mold **b** HTS test mold

commercially pure aluminum (99.8%), copper (99.8%) and magnesium (99.8%) and Al-12.5% Si were melted in a graphite crucible of 3 kg capacity using an electrical resistance furnace. The melt was held at 760 °C for at least 30 min. After cooling to 720 °C, the melt was degassed using C_2Cl_6 (0.6 wt%). Prior to pouring, the melt was held in vacuum (−0.1 MPa) at 720 °C for 1 h. After processed, the molten aluminum was poured into various preheated metal molds (at 250 °C for about 5 h) including fluidity and HTS test molds.

Fluidity and HTS Tests

The fluidity and HTS of the test alloys were evaluated by casting the samples in the fluidity and HTS molds as shown in Fig. 1. Fluidity was obtained by measuring the final length of the sample solidified in spiral fluidity test mold. HTS was estimated following the method as described in detail in Ref. [20].

Results and Discussion

Significance Analysis of Fluidity and HTS

Orthogonal test results of fluidity and HTS and the statistical analysis are listed in Table 3. Serial No. 9 has the highest fluidity (60 cm length of the spiral sample) and smallest HTS (10.0). Serial No. 14 has the lowest fluidity (38 cm length) and largest HTS (21). K represents the sum of the assessment objective of each factor in the same level, and the subscript indicates the corresponding level; k is the average of K values. “Range” is the difference of the maximum and minimum k values of each factor, and “Range/1%” is the contribution to “Range” per 1% of solute

Table 3 Orthogonal test form of fluidity and HTS, and range analysis

Alloy serial no.	Si (%)	Mg (%)	Cu (%)	Fe (%)	Fluidity (cm)	HTS
1	1 (0.2)	1 (0.2)	1 (0)	1 (0.15)	42	19.5
2	2 (0.4)	1	2 (0.25)	2 (0.25)	46	17.0
3	3 (0.6)	1	3 (0.5)	3 (0.4)	48	16.5
4	4 (1.0)	1	1	1	50	12.0
5	3	2 (0.35)	1	2	49	15.5
6	4	2	2	1	57	11.0
7	1	2	3	1	43	19.5
8	2	2	1	3	45	17.0
9	4	3 (0.5)	1	3	60	10.0
10	3	3	2	1	51	13.5
11	2	3	3	1	49	16.5
12	1	3	1	2	44.5	18.0
13	2	1	1	1	45	16.5
14	1	1	2	3	38	21.0
15	4	1	3	2	52	13.0
16	3	1	1	1	48	14.5
K_1	167.5	369.0	383.5	385.0	Range analysis of fluidity	
K_2	185.0	194.0	192.4	191.5		
K_3	196.0	204.5	192.4	191.0		
K_4	219.0	–	–	–		
k_1	41.88	46.12	47.94	48.12		
k_2	46.25	48.50	48.00	47.88		
k_3	49.00	51.12	48.00	47.75		
k_4	54.75	–	–	–		
Range	12.87(+)	5.00(+)	0.06(+)	0.37(-)		
Range/1%*	16.08(+)	16.67(+)	0.12(+)	1.48(-)		
K1	78.0	130.0	123.0	123.0	Range analysis of HTS	
K2	67.0	63.0	62.5	63.5		
K3	60.0	58.0	65.5	64.5		
K4	46.0	–	–	–		
k1	19.5	16.3	15.4	15.4		
k2	16.8	15.8	15.6	15.9		
k3	15.0	14.5	16.4	16.1		
k4	11.5	–	–	–		
Range	8.0(−)	1.8(−)	1.0(+)	0.7(+)		
Range/1%	10.0(−)	6.0(−)	2.0(+)	2.8(+)		

Range/1%*: The range contribution per 1% of solute element content in the alloy

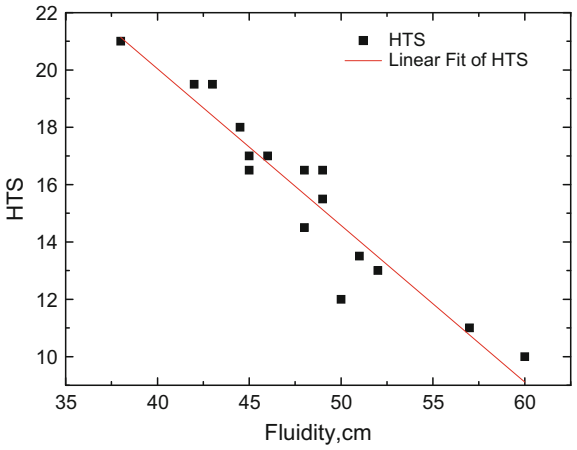

Fig. 2 The relationship between HTS and Fluidity, data from the studied conductive Al alloys

element content in the alloy. Because the selected levels of each factor in this study are not equal, thus "Range/1%" indeed represents the impact of each factor. Large range/1% expresses a high conspicuousness of the factor.

From Table 3, it is seen that Si and Mg have nearly the same impact on fluidity (16.08 and 16.67 of Range/% respectively), much higher influence than Fe (1.48 of Range/%), however Cu has almost no effect (0.12 of Range/%). Si, Mg, and Cu have positive impacts on the fluidity, i.e. the fluidity is improved with the increase of their contents, while Fe has a negative impact. It is also seen that the impact of Si on HTS is the highest (10.0 of Range/%), followed by Mg (6.0 of Range/%), and that Cu and Fe have almost the same but much less influence (2.0 and 2.8 of Range/% respectively). Cu and Fe have positive impacts on HTS, i.e. the HTS increases with the increase of their contents, while Si and Mg have negative impacts, i.e. increasing the contents of Si and Mg decreases the HTS. In fact, the HTS of an alloy is tied closely with its fluidity. As shown in Fig. 2, HTS is decreased linearly with Fluidity. In the view of point of the physical process, the hot tearing formation originates from the insufficient feeding of liquid to the solidifying shrinkage in nature. So, if an alloy has a good fluidity, its HTS is expected to be low too.

As the latent heat of Si is 1.8 kJ/g, 4.5 times of that of Al, the released latent heat during solidification is increased with the Si content and so does the fluidity [21, 22]. With the increase of Si content in the alloy, the degree of superheat is increased if the pouring temperature is kept the same, which is in favor of the flow of alloy melt. Addition of Mg in alloy produces a large constitutional supercooling which impedes the growth of the primary Al dendrites and thus the size of the growing dendrites becomes uniform [23]. The latent heat of Mg_2Si is 1.05 kJ/g, about 2.5 times of Al [24]. The formation of Mg_2Si will slow the solidification rate, namely extending the flow time of alloy melt. So, the fluidity of the alloy is increased with Mg content. Cu and Fe solutes have no significant effect on the fluidity. The fluidity variation due to Cu and Fe content changes is within the range of experimental error.

As shown in Table 3, the k value for HTS is decreased with the Si content, indicating that the HTS is weakened. As the linear shrinkage coefficient of Si is very small, about 0.12 to 0.31 times of Al, the linear shrinkage of the alloy is decreased with the increase of Si content in the alloy. Although the solidification temperature range increases with the Si content, the HTS become smaller due to the obviously reduced linear shrinkage [13]. On the other hand, due to non-equilibrium solidification, the amount of eutectic phases is increased with silicon content, which is expected to improve the feeding ability of the alloy and hence makes HTS smaller. Adding Mg element in the alloy hinders the growth of the primary α-Al dendrites, which would improve the feeding ability of the alloy and thus the HTS is reduced. Increasing Cu content in the alloy increases the linear shrinkage coefficient [25] and thus the HTS. Fe, an impurity element in aluminum alloy, forms needle-like or skeleton-like Al_5SiFe phase with Al and Si at the early stage of the solidification process, which hinders the liquid metal feeding and thus increases the alloy HTS.

Regression Analysis and Model Verification

Based on the results of the orthogonal test, multi-element linear/non-linear polynomial regressions are adopted to construct the solute-dependent empirical models of fluidity and HTS. Four models are evaluated: Model-I, only taking account of the linear impacts of Si, Mg, Cu and Fe solutes; Model II, further considering the interaction of Si and Mg solutes on the basis of Model I; Model III, considering both the linear impacts of Si, Mg, Cu and Fe solutes and the quadratic nonlinear impacts of Si and Mg solutes; Model IV, further considering the interaction of Si and Mg solutes on the basis of Model III. Because of the low significance of Cu and Fe, their quadratic nonlinear impacts on fluidity and HTS and their interactions with Si and Mg are neglected in the polynomial regression models. In order to verify the prediction models of polynomial regressions, another 6 alloys (marked as A, B, C, D, E and F) are prepared using the same method as described above and the fluidity and HTS are measured. Their compositions are listed in Table 4.

Table 4 Compositions of the alloys for verification

Serial no.	Composition measured, wt%			Composition designed, wt%
	Si	Mg	Fe	
A	0.292	0.205	0.101	Al-0.3Si-0.2Mg
B	0.284	0.224	0.105	Al-0.3Si-0.2Mg
C	0.280	0.302	0.173	Al-0.3Si-0.3Mg
D	0.246	0.311	0.104	Al-0.25Si-0.3Mg
E	0.23	0.31	0.116	Al-0.2Si -0.3Mg
F	0.50	0.52	0.16	Al-0.5Si-0.5Mg

Table 5 Verification test data and prediction data by Model I

Alloy	Fluidity, cm			HTS		
	Verification test	by Model I	error (%)	Verification test	by Model I	error (%)
A	44.0	42.3	3.8	18	18.0	0.0
B	44.5	42.5	4.4	18	18.0	0.0
C	45.8	43.6	4.7	17	17.8	4.7
D	45.3	43.3	4.3	18	17.8	1.1
E	43.0	42.6	0.9	18	18.0	0.0
F	49.0	50.0	2.0	16	15.3	4.3

Among four models, the Model I appears to have the highest regression coefficient for both fluidity and HTS. The predicted data by Model I also agrees quite well with the verification test results, only with less than 5% error, as seen in Table 5. This indicates that the simple polynomial regression model can accurately predict the fluidity and HTS. It is also seen from Tables 4 and 5 that Alloys A and B have approximately the same compositions and their verification data of the fluidity and HTS are also the same, indicating a good reliability of the test data.

Conclusions

(1) The effect of Si, Mg and Cu contents on the fluidity is positive, that is, increasing their contents improves the fluidity. The effect of Fe content on fluidity is however negative.
(2) For HTS, the effect of Si and Mg is negative while the influence of Cu and Fe is positive.
(3) The developed multi-element linear/non-linear polynomial regression models can be used to predict alloy fluidity and HTS with a good accuracy based on Si, Mg, Cu and Fe contents.

Acknowledgements This work is supported by GM Research Foundation under contract No. GB1279-NV.

References

1. Karabay S (2008) Influence of AlB_2 compound on elimination of incoherent precipitation in artificial aging of wires drawn from redraw rod extruded from billets cast of alloy AA-6101 by vertical direct chill casting. Mater Des 29(7):1364–1375

2. Karabay S (2006) Modification of AA-6201 alloy for manufacturing of high conductivity and extra high conductivity wires with property of high tensile stress after artificial aging heat treatment for all aluminium alloy conductors. Mater Des 27(10):821–832
3. Flemings MC (1974) Solidification processing. Metall Mater Trans B 5(10):2121–2134
4. Sheshradri M, Ramachandran A (1965) Casting fluidity and fluidity of aluminum and its alloys. AFS Trans 73:221–229
5. Gowri S, Samuel F (1994) Effect of alloying elements on the solidification characteristics and microstructure of Al-Si-Cu-Mg-Fe 380 alloy. Metall Mater Trans A 25(2):437–448
6. Rooy E (1985) Scrap recycling and its impact on the metal castings industry. AFS Trans 93:102–114
7. Crikel J, Pfeiffer W, Sabath G (1986) Effect of zinc, iron and manganese on the properties of AlSisCu3-type alloys. Aluminum 61:9–17
8. Loper C (1992) Fluidity of aluminum-silicon casting alloys-II. AFS Trans 100:576–590
9. Pumphrey W, Jennings P (1948) A consideration of the nature of brittleness at temperatures above the solidus in castings and welds in aluminum alloys. J Inst Met 75:235–256
10. Hu YG, Shao GJ, Yang YT (2008) Effects of Si on hot crack behavior of 6082 alloy. Spec Cast Nonferrous Alloy 28(3):221–223
11. Singer A, Cottrell S (1946) Properties of the Al-Si alloys at temperatures in the region of the solidus. J Inst Met 73:33–54
12. Heck K, Blackford R, Singer R (1999) Castability of directionally solidified nickel base superalloys. Mater Sci Tech 15(2):213–220
13. Zhao J, Chen GY (1985) Study of influence of solidification characteristics of Al-Si casting alloys on the hot tearing. J Dalian Univ Tech 4:31–35
14. Kim J, Loper C Jr (1995) Effect of solidification mechanism on fluidity of Al-Si casting alloys (95–08). AFS Trans 103:521–530
15. Bastien P, Armbruster J, Azou P (1962) Flowability and viscosity. AFS Trans 70:400–409
16. Clyne T, Davies G (1981) Influence of composition on solidification cracking susceptibility in binary alloy systems. Br Foundryman 74:65–73
17. Loper C (1992) Fluidity of aluminum-silicon casting alloys-I. AFS Trans 100:533–538
18. Heck K, Blackford R, Singer R (1999) Castability of directionally solidified nickel base superalloys. Mater Sci Tech 15(2):213–220
19. Pumphrey W, Lyons J (1948) Cracking during the casting and welding of the more common binary aluminum alloys. J Inst Met 74:439–455
20. Liao HC, Liu Y, Lü CL, Wang QG (2015) Effect of Ce addition on castability, mechanical properties and conductivity of Al-0.3% Si-0.2% Mg alloys. Int J Cast Met Res 28(4):213–220
21. Wang J, He S, Sun B (2003) Grain refinement of Al–Si alloy (A356) by melt thermal treatment. J Mater Proc Tech 141(1):29–34
22. Wu KN, Weng YB (2006) Study on novel aluminum alloys for motor rotor material. Electr Tool 5–6
23. Xie Rui (2010) The Effect of element Mg, Cu, Mn on microstructure and mechanical properties of Al-20Si aluminium alloy. Master's thesis, Nan zhou University of Technology
24. Zhang CX, Guan SK, Chen HJ, Zhao HL, Lu GX, Qi XH (2004) Effect of Si on microstructure and properties of Mg-8Zn-4Al-0.3Mn alloy. Mater Mech Eng 28(9):19–22
25. Yu LZ, Li JP, Yang T, Guo YC, Yang Z, Xia F, Wang JL (2011) Effect of Cu addition on casting property of Al-7Si-xCu-0.3 Mg alloys. Foundry 60(4):345–348

Coupling Void Coalescence Criteria in Finite Element Models: Application to Tensile Test

A. Abdelkader and Ch. A. R. Saleh

Abstract Ductile fracture has been described by many models on different scales; namely, continuum, micro, miso and even on atomistic scales. A widely accepted model is the micromechanical phenomological model, Gurson's. Gurson assumes that material is porous with spherical voids. Under deformation, original voids grow and new voids are nucleated. Failure become pronounced in the third stage; coalescence. Coalescence mechanism occurs either by localized shear at ligaments between voids or by their preferential growth parallel to the axis of highest principal stress as reported in literature. Literature includes many void Coalescence models. The model proposed by Ragab is the concerned model in this study. In this work, Finite element analysis FEA is used to model materials obeying Gurson function on a uniaxial tensile test. The coalescence criterions are introduced to the FEA solver, Abaqus via a user subroutine. The onset of coalescence is determined and compared to experimental results.

Keywords Ductile fracture · Porous metals · FE · Void coalescence

Introduction

If a uniaxial tension test is performed on a perfect ductile material (free from inclusions and second phase particles), the plastic deformation process continues by 100% reduction in area at the neck until fracture. However, engineering metals always contain inclusions and second phase particles. Under plastic deformation, these particles act as nucleation sites for internal cavities which grow and finally

A. Abdelkader (✉)
Pressure Vessels Department, Engineering for the Petroleum and Process Industries, Enppi, 1 "A" Ahmed El-Zomor Street, 8th District, Nasr City, Cairo 11361, Egypt
e-mail: Ahmed.abdelkader@enppi.com

Ch. A. R. Saleh
Department of Mechanical Design and Production, Faculty of Engineering, Cairo University, Giza, Cairo, Egypt

The Minerals, Metals & Materials Society, *TMS 2018 147th Annual Meeting & Exhibition Supplemental Proceedings*, The Minerals, Metals & Materials Series,
https://doi.org/10.1007/978-3-319-72526-0_35

coalesce. The nucleation and growth stages occur concurrently during plastic deformation. The coalescence is the final stage where failure becomes pronounced. Void nucleation process is well understood with multiple experimental evidences. Void nucleation models are diverse with multiple basis that provides different results when compared to experimental work due to the stochastic nature of existence. Void growth is observed by metallographic techniques on longitudinal section of fractured specimens as shown by Puttick [1], Park and Thompson [2], and Cox and Low [3].

On the modeling side, Gurson's [4] mechanical model for voided material is a widely accepted model. Gurson introduced a local damage model which is the void volume fraction. Important modifications are due to Tvergaard [5, 6] who introduced adjustment parameters to Gurson model because the model differs significantly from numerical result. Hence, the form of the yield function has become:

$$\overline{\sigma}^2 = \overline{\sigma}_M^2\left(1 + q_3 C_v^2\right) - 2q_1 C_v \overline{\sigma}_M^2 \cosh\left[q_2 \frac{3\sigma_m}{2\overline{\sigma}_M}\right] \tag{1}$$

Where $\overline{\sigma}_M$ is the effective stress of the matrix material, $\overline{\sigma}$ is the macroscopic Mises effective stress, σ_m is the mean stress component, C_v is the void volume fraction, $q1$, $q2$, $q3$ are material parameters.

Coalesence is the last of vital importance [7]. Coalescence comes in different modes. One of them is the internal necking where the ligament between the voids is reduced to a point as observed in a variety of metals [2, 8, 9]. Coalescene models are multiple. This study focus only on verification of coalescence model proposed by Ragab [10]. Ragab's criterion considers the influence of void shape change, strain hardening and softening due to existence of voids in his model. This criterion has the form:

$$\frac{\sigma_1}{\overline{\sigma}_M} \geq \left(1 + \frac{2\lambda_1^2}{b_2/b_1 - 1}\right) \log\left[1 + \frac{1}{2\lambda_1^2}(b_2/b_1 - 1)\right] \times \left[1 - \frac{\pi}{4}\left(\frac{b_1}{b_2}\right)^2\right] (\varepsilon_l/\varepsilon_{uc})^n \tag{2}$$

Where λ_1 is the current aspect ratio of the void, ε_l and ε_{uc} are the strain within the ligament and the average macrospic strain within the unil cell respectively. b_2/b_1 are void geometrical factors as shown in Fig. 1. Void shape evolution were evaluated by Ragab [11]. The evolution equations are summarized in Table 1.

where λ_2 is the current aspect ratio of the matrix material volume confocal with the void. λ_{2i} and λ_{1i} are the initial aspect ratio of the spheroidal matrix material volume confocal with the void and the final aspect ratio of the void respectively and n is the strain hardening exponent.

The objective of this work is to integrate Ragab coalescence criterion into FE software, Abaqus so that the onset of ductile fracture can be checked numerically. The introduced coalescence criterion is then to be applied on modeling a tensile test and compared to experimental results.

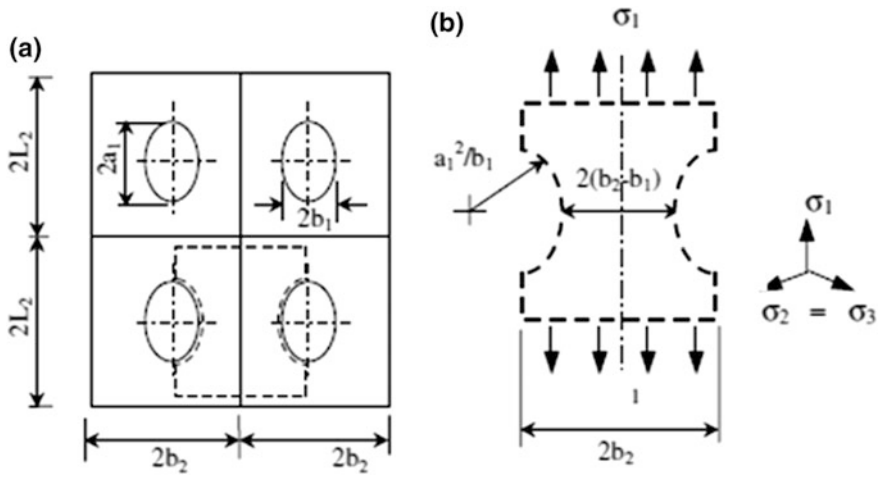

Fig. 1 The representative element of a voided material as simulated by Ragab [8]: **a** array of unit cells each containing an isolated ellipsoidal void and **b** intervoid matrix

Table 1 Void shape evolution equation as presented by Ragab [11]

$\frac{b_1}{b_2} = \left[\frac{6\lambda_2 C_V}{\pi\lambda_1}\right]^{\frac{1}{3}}$	(3)
$\lambda_2 = \lambda_{2i}\ \exp\ \left[\frac{3}{2}\varepsilon_1 - \frac{1}{2} In\left(\frac{1-C_{V0}}{1-C_V}\right)\right]$	(4)
For initially prolate void: $\lambda_{1i} \geq 1$ and $\frac{1}{3} < \frac{\sigma_m}{\bar{\sigma}} < 3$ $\log\left(\frac{\lambda_1}{\lambda_{1i}}\right) = [(-0,535 + 0,0235\sin\varepsilon)\log\lambda_{1i} +]\left(2 - \frac{\sigma_m}{\bar{\sigma}_M} + n\right)(1 - C_V)(1.15\sin\varepsilon_1)$	(5)

Numerical and Experimental Procedures

To check the occurrence of void coalescence according to Ragab's criterion in Abaqus, material point information must be known at the end of each solution increment. An Abaqus utility subroutine reads stresses and strains for every material point instantaneously while Abaqus is running. Having Gurson constitutive equation built in the source code of the software saved the step of integrating the constitutive equation; however the utility routine does not support reading the void volume fraction while the job is being processed. Hence, calculation of the void volume fraction is necessary before proceeding to void coalescence check. Void shape evolution is then evaluated and the occurrence of coalescence criterion could be checked.

The material used in the comparison is dual phase steel (DP600). This steel consists of a ferrite matrix containing islands of martensite. Having dual phases in the matrix promotes the process of porous plasticity as highlighted in the literature

Table 2 Material properties of DP600 employed in the finite element model

C_{vo}	λ_{1i}	εN	UTS (MPa)	Y (MPa)	r	n	K (MPa)
0.00034	1	0.15	650	360	1	0.2	1180

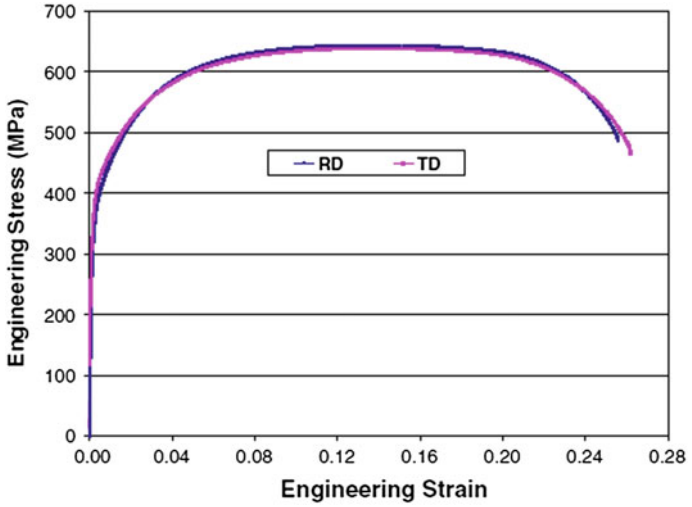

Fig. 2 Engineering stress-strain curve of DP 600 for two samples; RD: rolling direction and TD: transverse direction

review. The mechanical properties and engineering stress-strain curve are determined by Cingara et al. [12] and enlisted and presented in Table 2 and in Fig. 2 respectively.

Where C_{vo} is the initial void volume fraction, λ_{1i} is the initial aspect ratio, n is the strain hardening exponent, ε_N is the nucleation strain, and r is the anisotropic ratio.

The material is assumed to follow the power hardening rule even for the regions of the non-uniform elongation. In other words, the plastic true stress-strain curve is assumed to have a constant slope on the logarithmic scale which is 0.2 in the investigated case.

The material is provided in the form of 1.8-mm-thick sheet. The specimens used are according to ASTM E8 standard with a gage length of 25.4 mm. Strain was continuously measured by Aramis setup as shown in Fig. 3a and b. Aramis continuously capture the image of the specimen and perform image processing to calculate surface strains. When fracture occurs, the mesh is broken and Aramis is no longer able to process the image. Hence, the strains denoted by experimental fracture strains correspond to the strains just before fracture.

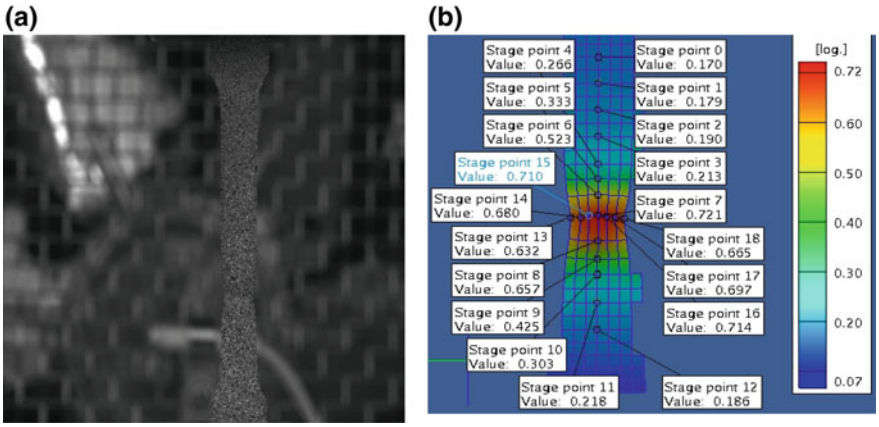

Fig. 3 **a** Image captured by Aramis at the stage point just perior to fracture. **b** Processed image of strain distribution at the stage point prior to fracture

Employing the isotropic properties of the material and the symmetric geometry; only a quarter of the specimen can be used to enable the use of a fine mesh at the quarter of the computational cost as shown in Fig. 4. The constitutive equation of material behavior is Gurson's with Tevergaard modifying parameters. The nucleation model used here is as proposed by Avramovic-Cingara et al. [12] at a thickness strain of 0.15. As introduced earlier; the suitable element for this type of analysis is the first order hexahedral brick element with 8 nodes and reduced integration algorithm. Abaqus hourglassing control is activated for every element to avoid unreal elements straining.

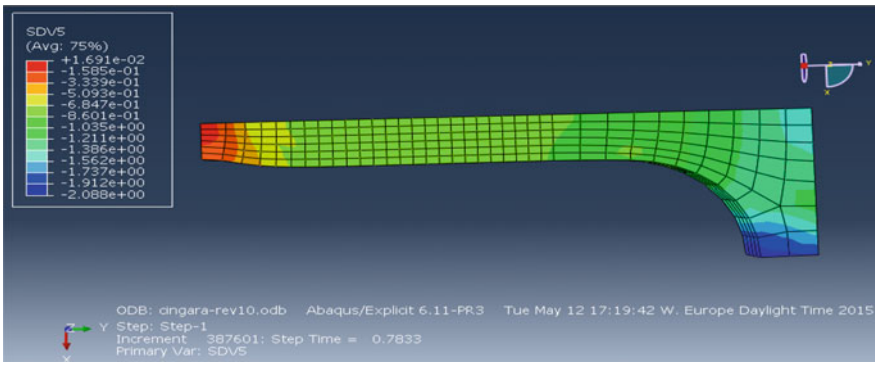

Fig. 4 Tensile test modeling on Abaqus at the onset of coalescence

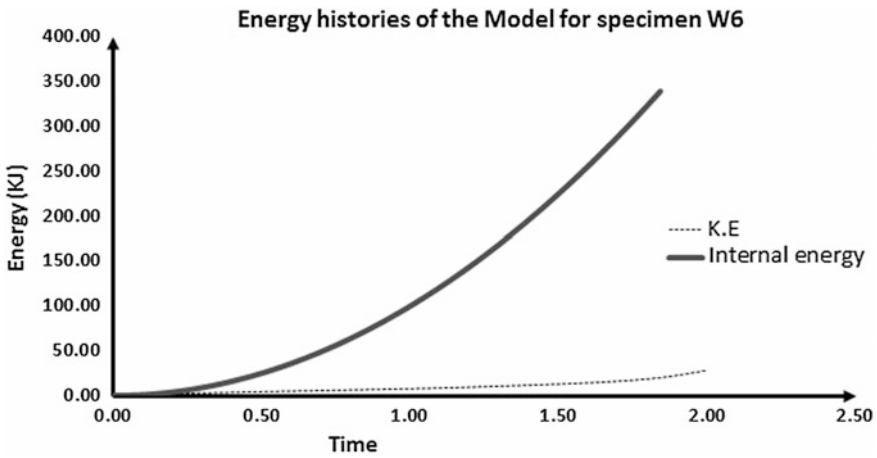

Fig. 5 Energy history for specimen W6 through the solution

Results and Discussion

The analysis step continues until the admitted coalescence criterion is met. Then, the analysis stops. To ensure the insignificance of the inertial forces, the kinetic energy and the total energy are kept monitored. Figure 5 is the plot of system energies that shows that inertial effects are negligible.

After submitting the model for analysis, the subroutines are invoked by Abaqus to calculate void shape evolution, void volume fraction and finally checking for coalescence criteria at each time increment. Necking is identified on the FE model matching experimental results as shown on Figs. 6 and 7.

Coalescence was found to occur according to Ragab criteria at a first principle strain in agreement with experimental results. Figure 8 shows principle strains evolution till coalescence for the most strained point in both experimental and numerical work.

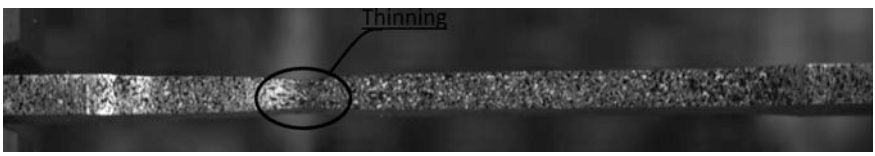

Fig. 6 Image taken by Aramis software at the point just before coalescence

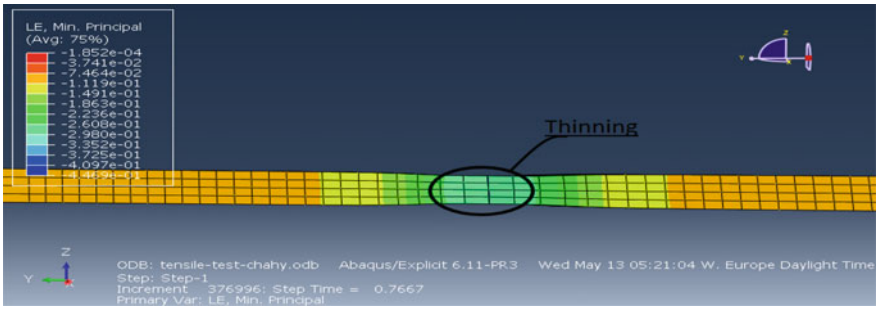

Fig. 7 FE results showing thinning at the point of coalescence

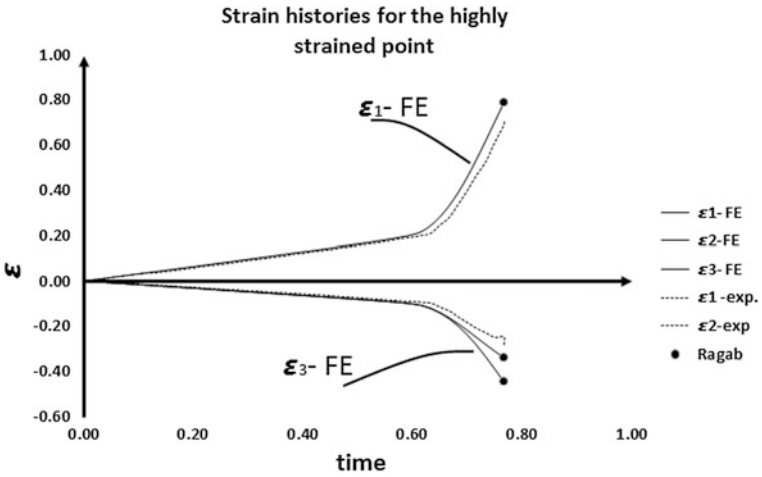

Fig. 8 Strain histories for the highly strained point until fracture/coalescence in both experimental and FE work

Conclusion

In this work, FEA is used to model materials obeying Gurson function as the constitutive equation for material yielding. Ragab's coalescence criterion is introduced to the FEA solver, Abaqus via user subroutines. Material information at every calculation increment is passed through utility subroutine to the Fortran compiler which in turn checks if the introduced coalescence criteria is met. Calculated material information by the Fortran compiler are passed back to Abaqus/CAE (the complete abaqus environment) through the same subroutine. The developed methodology is general and can be applied to any material obeying Gurson yield function. The model is applied to the case of tensile testing of DP600

where comparison between experimental results and numerical model implemented in FEA is held. It was found that Ragab's criterion is in agreement with experimental results.

References

1. Puttick KE (1959) Ductile fracture in metals. Philos Mag 4(44):964–969
2. Park I-G, Thompson AW (1988) Ductile fracture in spheroidized 1520 steel. Acta Metall 36 (7):1653–1664
3. Cox TB, Low JR (1974) An investigation of the plastic fracture of AISI 4340 and 18 Nickel-200 grade maraging steels. Metall Trans 5(6):1457–1470
4. Gurson AL (1977) Continuum theory of ductile rupture by void nucleation and growth: part I —yield criteria and flow rules for porous ductile media. J Eng Mater Technol 99(76):2–15
5. Tvergaard V (1981) Influence of voids on shear band instabilities under plane strain conditions. Int J Fract 17(4):389–407
6. Tvergaard V (1982) On localization in ductile materials containing spherical voids. Int J Fract 18(4):237–252
7. Weck AG (2007) The role of coalescence on ductile fracture. PhD thesis, McMaster University
8. Thompson AW (1987) Modeling of local strains in ductile fracture. Metall Trans A 18 (11):1877–1886
9. Knott J (Sept 1980) Micromechanisms of fibrous crack extension in engineering alloys. Met Sci pp 327–336
10. Ragab AR (2004) A model for ductile fracture based on internal necking of spheroidal voids. Acta Mater 52(13):3997–4009
11. Ragab ARR (2004) Application of an extended void growth model with strain hardening and void shape evolution to ductile fracture under axisymmetric tension. Eng Fract Mech 71 (11):1515–1534
12. Avramovic-Cingara G, Saleh CAR, Jain MK, Wilkinson DS (2009) Void nucleation and growth in dual-phase steel 600 during uniaxial tensile testing. Metall Mater Trans A 40 (13):3117–3127

Design of a New Multi-element Beta Titanium Alloy Based on d-Electron Method

S. Sadeghpour, S. M. Abbasi and M. Morakabati

Abstract A new beta titanium alloy in the Ti-Al-Mo-Cr-V system has been designed using the d-electron method with the aim of activating a combination of different deformation mechanisms. In this regard Ti-3Al-5Mo-7V-3Cr (Ti-3573) alloy has been designed and compared with a commercial Ti-5Al-5Mo-5V-3Cr (Ti-5553) alloy. To evaluate the accuracy of the d-electron theoretical predictions, uniaxial compression tests were performed at room temperature. The deformation mechanism of Ti-3573 was found to be a combination of slip, stress-induced martensitic transformation and mechanical twinning. As a result of the combined deformation mechanisms, the designed alloy showed enhanced compressive strength and ductility in comparison to the Ti-5553 alloy. The results showed that in the case of twinning the prediction by the d-electron method is consistent with experimental observations but regarding the stress-induced martensitic transformation this method should be used with modifications to the d-electron phase stability map.

Keywords Beta Ti alloy · Alloy design · d-Electron method
Twinning · Stress-induced martensite

Introduction

Metastable β Ti alloys are an important category of Ti alloys with a wide variety of mechanical properties due to the occurrence of several deformation mechanisms. Depending on the β phase stability, dislocation slip, twinning and stress-induced martensitic (SIM) transformation can all occur during the deformation of β Ti alloys [1–3]. It has been demonstrated that with increasing stability of the β phase, the deformation mechanism changes from SIM to twinning and then to slip [1, 4].

S. Sadeghpour (✉) · S. M. Abbasi · M. Morakabati
Metallic Materials Research Center, Malek Ashtar University of Technology, Tehran, Iran
e-mail: sinsad64@yahoo.com

The Minerals, Metals & Materials Society, *TMS 2018 147th Annual Meeting & Exhibition Supplemental Proceedings*, The Minerals, Metals & Materials Series,
https://doi.org/10.1007/978-3-319-72526-0_36

When mechanical twinning is the dominant deformation mechanism, β Ti alloys exhibit a high strain hardening rate and large ductility but a low yield strength [5, 6]. In contrast, β Ti alloys with dislocation slip as the dominant deformation mechanism show very low ductility but a high yield strength. It has also been shown that SIM strongly affects the mechanical response of metastable β Ti alloys [7–9]. Thus, control of the deformation mechanisms is considered as a key strategy in the optimization of the mechanical properties of β Ti alloys. Extensive efforts have been made to control the β phase stability in order to control the deformation mechanisms [6–10]. However, for a long time, new optimized compositions have been formulated principally by trial and error methods, with no fundamental physical basis. During the last decade, the design strategy of new β Ti alloys has often been based on theoretical approaches [10, 11], and a particular attention has been paid to the "d-electron method" [12–14]. This theoretical alloy design method has been developed on the basis of the discrete variational Xα (DV-Xα) molecular orbital calculation of the electronic structure of alloys. Two alloying parameters are used in this method, one is the d-orbital energy level of an alloy transition metal (Md) in a given base metal system and the other alloying parameter is known as the bond order (Bo) which correlates well with the electronegativity and the metallic radius of alloying elements.

Firstly, the d-electron method was extensively used in the design of Ti alloys presenting enhanced elastic properties [12, 15, 16]. Recently, it has been shown that the mechanical stability of the β phase is also connected to the electronic parameters Bo and Md [12]. Therefore, this method has been realized to be effective in predicting the plastic deformation mechanisms of β Ti alloys [17–19]. That way $\overline{Bo}$-$\overline{Md}$ maps can be used as a tool to design new Ti alloys exhibiting specific deformation mechanism. The results have shown that a combination of martensitic transformation induced plasticity (TRIP) and twinning induced plasticity (TWIP) effects can improve the mechanical properties [17–19]. Nonetheless, until now this method has only been used for designing simple binary β Ti alloys and very recently for ternary alloys [17, 19]. The present study aims at evaluating the reliability of the d-electron method in predicting the deformation mechanisms of complex multi-element β Ti alloys. On this basis, starting from the well-known Ti-5553 (Ti-5Al-5Mo-5V-3Cr) system, we introduce a new composition with the same alloying elements but differing predicted β phase stabilities to investigate and compare the deformation mechanisms and mechanical properties.

Materials and Methods

Starting with the initial composition Ti-5Al-5Mo-5V-3Cr, the d-electron method was used to design the new compositions, Ti-3Al-5Mo-7V-3Cr (Ti-3573). The details of alloy design procedure are discussed in the following section. An ingot of the designed alloy was melted twice using the vacuum arc melting to ensure

chemical homogeneity. After homogenizing, the ingot was forged and then rolled to 20 mm thick plates. Samples from the ingot were solution-treated at 1000 °C in a preheated box furnace and held for 30 min followed by water quenching to retain a fully β structure at room temperature.

The deformation behavior of the annealed β samples was evaluated using uniaxial compression at room temperature. The compression tests were carried out in an Instron 8502 testing machine on cylindrical specimens with a dimension of $\phi 8 \times 12$ mm at an initial strain rate of 0.7×10^{-3} s^{-1}.

In order to analyze the microstructures, the deformed specimens were sectioned along the compression axis. Standard metallographic techniques were employed to prepare the samples. Specimens for optical microscopy (OM) were etched in a modified Kroll's reagent (6% HF + 18% HNO_3 + 76% H_2O) to reveal the microstructures. Electron backscatter diffraction (EBSD) scans were performed using a field emission gun Zeiss Sigma scanning electron microscope operating at 15 kV with a step size ranging from 0.5 to 0.05 μm.

Results and Discussion

Alloy Design

The Ti-Al-Mo-V-Cr composition is an important alloy system in which several β Ti alloys have been introduced and used in commercial applications [20]. The most popular example is the Ti-5553 alloy that is a high strength β Ti alloy with the chemical composition of Ti-5Al-5Mo-5V-3Cr (wt%). Although the metastable β alloys generally display better cold workability compared to that of α and α + β titanium alloys, the cold workability of the most common high strength β Ti alloys, such as the Ti-5553, is only moderate as a result of their deformation mechanism. This can be considered as a drawback restricting its application to bulk structures. The main idea to improve the mechanical properties of the Ti-5553 alloy is to activate a combination of different deformation mechanisms as a potent approach to enhance the ductility without sacrificing the yield strength.

As mentioned, the electronic $\overline{Bo}$-$\overline{Md}$ maps can be used to predict the deformation mechanism occurring in an alloy and such a map and the locations of the present alloys are shown in Fig. 1a. The area between the M_s and M_d lines corresponds to the occurrence of the SIM transformation. The M_s and M_d correspond to the martensite start temperature and the minimum temperature above which β is stable and does not transform to martensite by deformation, respectively. The critical resolved shear stress (CRSS) for SIM is expected to increase on going from the M_s line toward the M_d line and the SIM transformation will occur most readily near the M_s line. Mechanical twinning is expected to be the dominant deformation mechanism between the M_d line and the borderline between the slip and twinning regions. It can be supposed that in the transition regions, i.e. close to the borderlines

between the deformation mechanisms, two or three deformation mechanisms may occur in combination. Hence, to obtain different combinations of deformation mechanisms, the designed alloy should be targeted to locate close to the M_s, M_d and Slip/Twin lines.

The extension of the d-electron method towards multi-element systems for desired active deformation mechanisms can be achieved by correlating alloying vectors (Fig. 1b). These alloying vectors show the variation in the $\overline{Bo}$ and $\overline{Md}$ values of pure Ti with the Al, Mo, V and Cr content [21]. A linear combination of different alloying vectors (Al, Mo, V and Cr) was used to reach the desired locations of new compositions on the $\overline{Bo}$-$\overline{Md}$ map.

In designing the alloy, the variation of alloying elements was considered in a way to fall in the critical regions on the stability map, i.e. close to the borders. Since the position of Ti-5553 alloy is quite far from the desired region in the stability map (Fig. 1a), the values of $\overline{Bo}$ and $\overline{Md}$ should be changed. In order to get closer to the desired position in the stability map, the $\overline{Bo}$ parameter must be increased or $\overline{Md}$ decreased. As it is evident from Fig. 1b, Al and Mo have almost the highest effect on the $\overline{Bo}$ parameter. Thus, increasing the Mo or/and decreasing the Al content is preferred. Given that the V does not have a significant effect on $\overline{Bo}$, its content was changed to optimize the $\overline{Md}$ value. The Cr content of the new alloy was chosen to be constant and at the same level as in the Ti-5553, in order to avoid unnecessary complexity in the designing procedure.

For the new alloy, the $\overline{Bo}$ and $\overline{Md}$ values were selected such that the alloy locates close to the middle of the twinning region, but close to the M_d line so that the alloy is expected to undergo both twinning and SIM transformation upon deformation. As shown in a previous work [18], an additional line can be drawn on the stability map locating the possible coexistence of TRIP and TWIP effects in a combined

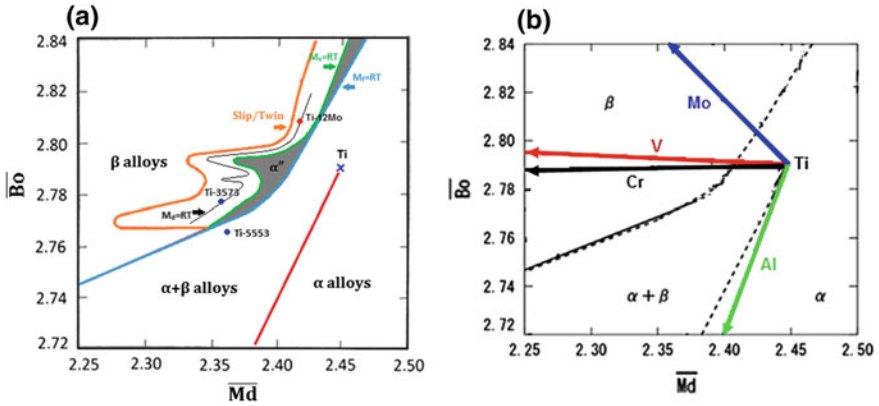

Fig. 1 **a** The Bo-Md phase stability diagram showing the designed alloys in relation to the commercial Ti-5553 alloy **b** d-electron map showing V_{Al}, V_{Mo}, V_V and V_{Cr} alloying vectors as functions of Bo and Md

way. This is the black thin line in Fig. 1. It is obvious from Fig. 1 that the Ti-3573 alloy lies on this line. Therefore, it is expected that this alloy will show a combination of TRIP and TWIP effects. The calculated values of $\overline{Bo}$ and $\overline{Md}$ are superimposed on the stability map (Fig. 1). As can be seen, the designed alloy lies on the Martensite/Twin borders.

Microstructural Analysis

EBSD microstructure of the solution treated alloy shown in Fig. 2a displays equiaxed single phase β grains with an average diameter of 200 μm. Only β grains are visible on the micrograph without any evidence of α″ martensite phase in the matrix indicating that the M_s temperature of the alloy is below room temperature. This observation is in agreement with the prediction of the d-electron method for Ti-3573.

In order to understand the deformation mechanisms of the alloy, interrupted compression tests were performed up to 10% strain and corresponding microstructures were investigated. Figure 2b shows the light optical microstructure after deformation. It can be observed that deformation induced products are appeared in the alloy. To better understand the nature of these deformation products, EBSD examinations were performed on the deformed samples.

The high resolution EBSD maps in Fig. 3 display the deformation microstructure of Ti-3573 after 10% compressive strain. Some wide deformation bands are evident in the deformed β matrix. Figure 3b shows that most of the deformation bands can be indexed as mechanical twins. Figure 3d shows the misorientation profile along the line AB across the deformation band shown in Fig. 3b. It can be seen that the misorientation angle between the deformation band and the matrix is

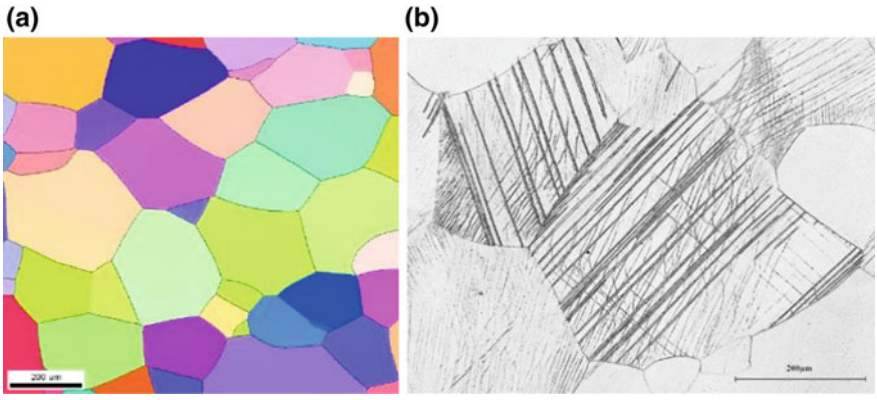

Fig. 2 **a** EBSD maps of the Ti-3573 alloys in solution treated condition **b** optical microstructure of Ti-3573 after the 10% interrupted cold compression test

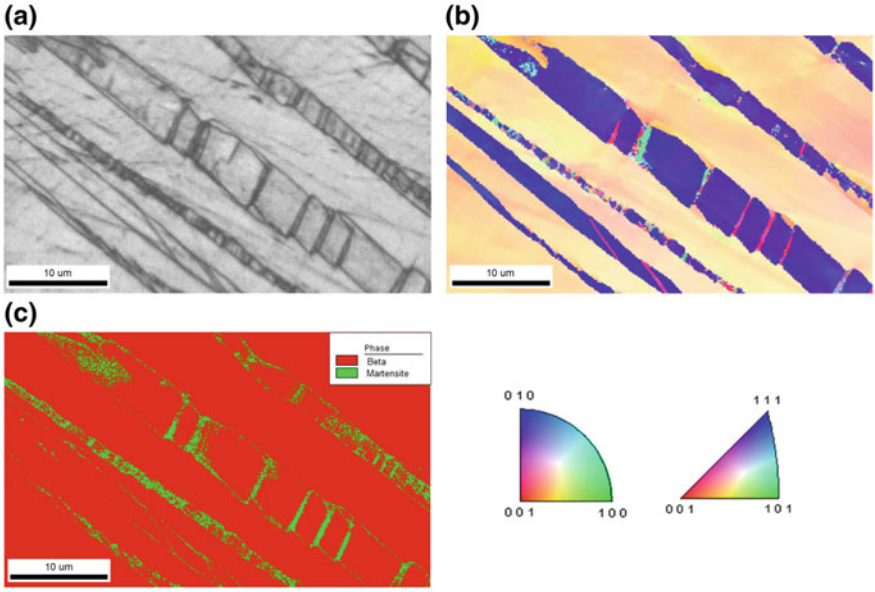

Fig. 3 EBSD maps of the secondary twins and SIM phase inside the primary twins in the Ti-3573 alloy subjected to 10% compressive strain. **a** Image quality (IQ) map, **b** inverse pole figure (IPF) map and **c** phase map

approximately 50.5° around the <110> β direction. This profile proves that the wide deformation bands observed in light optical microscopy (Fig. 2b) are {332} <113> twins. Similar results for some β Ti alloys have been reported in the literature [22–24]. It can be seen that, depending on the orientation, several secondary {332} <113> twins are formed within the primary twins in agreement with observations in earlier studies [24–26]. Figure 3c also indicates that SIM forms inside the primary twins as a secondary deformation product. Such formation of SIM inside the twins has also been reported in the literature [18, 25].

According to EBSD results, Ti-3573 showed α″ SIM after compressive deformation at room temperature. However, based on the stability map in Fig. 1 the formation of SIM is not expected in this alloy. Further, some other Ti alloys such as Ti-10V-2Fe-3Al [27] and Ti-10V-2Cr-3Al [28] showed SIM after cold deformation while the locations of these alloys also lie outside the α″ martensite region. Based on these observations, an expansion of the SIM region on the Bo-Md map is proposed especially in the lower part of the diagram. This suggestion was also made by Ahmed et al. [29] based on their investigation of the compressive deformation behavior of Ti-10V-3Fe-3Al.

Hence, the combination of SIM and twinning were found in the deformed microstructure of the Ti-3573 alloy. This, as previously reported [18], may lead to the enhancement of the ductility of this alloy. A similar combination of TRIP and TWIP effects has been reported in some binary and ternary Ti alloys [17–19].

However, to the best knowledge of the authors, very limited examples have been found showing both TRIP and TWIP effects simultaneously in a metastable β Ti alloy containing more numerous alloying elements.

Mechanical Properties

Figure 4 presents room temperature compressive stress-strain curves of the designed alloy along with those of the reference Ti-5553 alloy. The compressive yield strength was 830 and 930 MPa for Ti-5553, and Ti-3573 alloys, respectively. The yield strength of the designed alloy is higher than that of the Ti-5553 reference alloy and also higher than the reported yield strengths of other metastable β Ti alloys.

In the case of Ti-3573, the stress-strain curve does not exhibit any double yielding phenomenon. Thus, we can conclude that the trigger stress of the martensitic transformation in the Ti-3573 alloy is higher than the elastic limit so that no pseudo-elasticity occurs during the compressive loading. When the triggering stress is low compared to the yield stress, the double yielding phenomenon occurs whereas the stress-strain curve presents no double yielding when the triggering stress is close to or even higher than the yield stress [7, 30]. It is well known that delayed formation of stress-induced martensite will contribute to plastic deformation of the alloy and improve the work hardening [18, 25]. Contrary to that, the early reversible stress-induced martensite activated in the elastic region always causes elastic softening [31].

The failure strain was 30 and 49% for the Ti-5553 and Ti-3573 alloys, respectively. This indicates that the designed alloy has enhanced plastic deformation

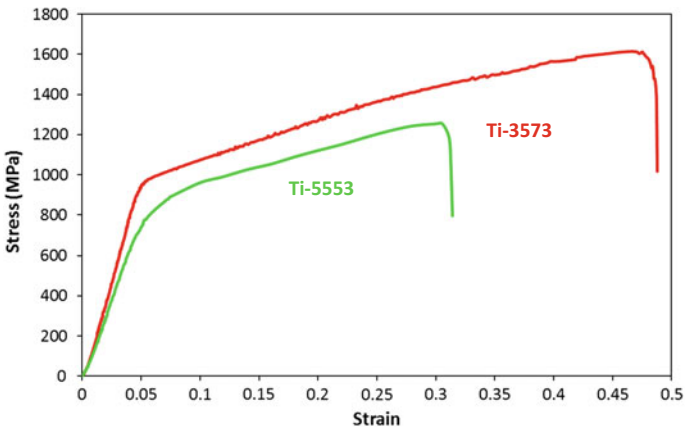

Fig. 4 Compressive stress-strain curves of the Ti-5553 and Ti-3573 alloys at room temperature

ability. The higher compressive properties of the Ti-3573 alloy in comparison to Ti-5553 can be attributed to the delayed SIM formation and the activation of a combination of TRIP and TWIP effects.

Conclusions

A multi-element Ti alloy, Ti-3Al-5Mo-7V-3Cr (in wt%) has been designed using the d-electron method targeting to the composition where several deformation mechanisms could be operative simultaneously. The mechanical properties and microstructural evolution of the designed alloy as seen in uniaxial compression testing were investigated and compared with the behavior of the reference commercial alloy Ti-5Al-5Mo-5V-3Cr (Ti-5553). The main results and conclusions are summarized below.

(1) Increasing the bond order (Bo) and decreasing the d-orbital energy level (Md), i.e. increasing the β phase stability changed the deformation mechanisms from slip/TRIP to slip/TRIP/TWIP.
(2) The combination of SIM, primary and secondary {332} <113> twinning and dislocation slip found as the deformation mechanisms in Ti-3573 resulted in higher strength and ductility.
(3) The d-electron phase stability map successfully predicted the activation of the twinning mechanisms for a multi-element alloy; however, the method needs to be modified regarding the prediction of SIM transformation when several alloying elements are present.

References

1. Hanada S, Izumi O (1986) MTA 17:1409
2. Xing H, Sun J (2008) Mechanical twinning and omega transition by <111> {112} shear in a metastable β titanium alloy. Appl Phys Lett 93:031908
3. Bertrand E, Castany P, Péron I, Gloriant T (2011) Twinning system selection in a metastable β-titanium alloy by Schmid factor analysis. Scr Mater 64:1110–1113
4. Ohyama H, Nishimura T (1995) Effects of alloying elements on deformation mode in Ti-V based b titanium alloy system. ISIJ Int 35:927–936
5. Min XH, Emura S, Nishimura T, Tsuchiya K, Tsuzaki K (2010) Microstructure, tensile deformation mode and crevice corrosion resistance in Ti-10Mo-xFe alloys. Mater Sci Eng A 527:5499–5506
6. Min XH, Emura S, Sekido N, Nishimura T, Tsuchiya K, Tsuzaki K (2010) Effects of Fe addition on tensile deformation mode and crevice corrosion resistance in Ti-15Mo alloy. Mater Sci Eng A 527:2693–2701
7. Bhattacharjee A, Varma VK, Kamat SV, Gogia AK, Bhargava S (2006) Influence of β grain size on tensile behavior and ductile fracture toughness of titanium alloy Ti-10V-2Fe-3Al. Metall Mat Trans A 37:1423–1433

8. Paradkar A, Kashyap BP, Gogia AK, Kamat SV (2009) On the influence of alloy composition on the fracture toughness of two-phase Ti-Al-Nb alloys undergoing stress-induced martensitic transformation. Metall Mat Trans A 40:1604–1610
9. Paradkar AG, Kamat SV, Gogia AK, Kashyap BP (2009) On the validity of Hall-Petch equation for single-phase β Ti-Al-Nb alloys undergoing stress-induced martensitic transformation. Mater Sci Eng, A 520:168–173
10. Friák M, Counts WA, Ma D, Sander B, Holec D, Raabe D et al (2012) Theory-guided materials design of multi-phase Ti-Nb alloys with bone-matching elastic properties. Materials 5:1853–1872
11. Raabe D, Sander B, Friák M, Ma D, Neugebauer J (2007) Theory-guided bottom-up design of β-titanium alloys as biomaterials based on first principles calculations: Theory and experiments. Acta Mater 55:4475–4487
12. Abdel-Hady M, Hinoshita K, Morinaga M (2006) General approach to phase stability and elastic properties of β-type Ti-alloys using electronic parameters. Scr Mater 55:477–480
13. Kuroda D, Niinomi M, Morinaga M, Kato Y, Yashiro T (1998) Design and mechanical properties of new β type titanium alloys for implant materials. Mater Sci Eng A 243:244–249
14. Morinaga M, Yukawa N, Maya T, Sone K, Adachi H (1988) Theoretical design of titanium alloys. In: Sixth world conference on titanium III. Cannes, p 1601
15. Abdel-Hady M, Hinoshita K, Fuwa H, Murata Y, Morinaga M (2008) Change in anisotropy of mechanical properties with β-phase stability in high Zr-containing Ti-based alloys. Mater Sci Eng A 480:167–174
16. Laheurte P, Prima F, Eberhardt A, Gloriant T, Wary M, Patoor E (2010) Mechanical properties of low modulus beta titanium alloys designed from the electronic approach. J Mech Behav Biomed Mater 3:565–573
17. Brozek C, Sun F, Vermaut P, Millet Y, Lenain A, Embury D et al (2016) A β-titanium alloy with extra high strain-hardening rate: design and mechanical properties. Scr Mater 114:60–64
18. Marteleur M, Sun F, Gloriant T, Vermaut P, Jacques PJ, Prima F (2012) On the design of new β-metastable titanium alloys with improved work hardening rate thanks to simultaneous TRIP and TWIP effects. Scr Mater 66:749–752
19. Sun F, Zhang JY, Marteleur M, Brozek C, Rauch EF, Veron M et al (2015) A new titanium alloy with a combination of high strength, high strain hardening and improved ductility. Scr Mater 94:17–20
20. Fanning JC (2005) Properties of TIMETAL 555 (Ti-5Al-5Mo-5V-3Cr-0.6Fe). J Materi Eng Perform 14:788–791
21. Morinaga M, Murata Y, Yukawa H (2007) Molecular orbital approach to alloy design. In: Bozzolo G, Noebe RD, Abel PB (eds) Applied computational materials modeling: theory, simulation and experiment. Springer, USA, pp 255–306
22. Yang Y, Wu SQ, Li GP, Li YL, Lu YF, Yang K et al (2010) Evolution of deformation mechanisms of Ti-22.4Nb-0.73Ta-2Zr-1.34O alloy during straining. Acta Mater 58: 2778–2787
23. Qu L, Yang Y, Lu YF, Feng L, Ju JH, Ge P et al (2013) A detwinning process of {332} <113> twins in beta titanium alloys. Scr Mater 69:389–392
24. Min XH, Tsuzaki K, Emura S, Sawaguchi T, Ii S, Tsuchiya K (2013) {332} <113> Twinning system selection in a β-type Ti-15Mo-5Zr polycrystalline alloy. Mater Sci Eng A 579: 164–169
25. Sun F, Zhang JY, Marteleur M, Gloriant T, Vermaut P, Laillé D et al (2013) Investigation of early stage deformation mechanisms in a metastable β titanium alloy showing combined twinning-induced plasticity and transformation-induced plasticity effects. Acta Mater 61:6406–6417
26. Zhou X, Xa Min, Emura S, Tsuchiya K (2017) Accommodative {332} <113> primary and secondary twinning in a slightly deformed β-type Ti-Mo titanium alloy. Mater Sci Eng A 684:456–465

27. Li C, Wu X, Chen JH, van der Zwaag S (2011) Influence of α morphology and volume fraction on the stress-induced martensitic transformation in Ti-10 V-2Fe-3Al. Mater Sci Eng, A 528:5854–5860
28. Li C, Chen JH, Wu X, Wang W, van der Zwaag S (2012) Tuning the stress induced martensitic formation in titanium alloys by alloy design. J Mater Sci 47:4093–4100
29. Ahmed M, Wexler D, Casillas G, Ivasishin OM, Pereloma EV (2015) The influence of β phase stability on deformation mode and compressive mechanical properties of Ti-10V-3Fe-3Al alloy. Acta Mater 84:124–135
30. Grosdidier T, Philippe MJ (2000) Deformation induced martensite and superelasticity in a β-metastable titanium alloy. Mater Sci Eng A 291:218–223
31. Hao YL, Li SJ, Sun SY, Zheng CY, Yang R (2007) Elastic deformation behaviour of Ti-24Nb-4Zr-7.9Sn for biomedical applications. Acta Biomater 3:277–286

Part XV
Computational Materials Science and Engineering for Nuclear Energy

Effects of Oxygen on the Density of States and Elastic Properties of Hafnium—First Principles Calculations

Yang Zhang, Yajie Wen, Naimeng Liu, Hao Guo, Ye Cui, Dan Chen and Zhongwu Zhang

Abstract Due to its excellent comprehensive properties, Hf has been the preferred material for control rods in the nuclear reactors. There is a very strong influence of even small additions of oxygen element on the mechanical properties of Hf alloy. This work we report results of first-principles calculations of structure stability, density of states and elastic properties including the full set of second order elastic coefficients, bulk moduli and shear moduli, Young's moduli, and Poisson's ratio of Hf as a function of positions and concentration of oxygen atoms. Oxygen atom prefers to occupy octahedral and hexahedral interstitial sites due to the lower formation energy and less lattice distortion. Oxygen content has very weak influence on the density of states. The effects of oxygen content on the elastic parameters were estimated with the conclusion that approximately high oxygen addition decreased elastic and plastic properties.

Keywords Hafnium · First principles calculations · Oxygen content
Density of states · Elastic properties

Introduction

Hafnium (Hf) has good mechanical properties, radiation resistance, corrosion resistance, high melting point and small thermal expansion coefficients, and has been used as control rod material of various types of reactors. Hf is used mainly due to a large neutron absorption cross section of 1.15×10^{-26} m^2 and excellent water corrosion resistance [1]. However, the mechanical properties are also very critical, because it can result in a serious accident if the Hf control rods crack during working.

Y. Zhang · Y. Wen · N. Liu · H. Guo · Y. Cui · D. Chen · Z. Zhang (✉)
Key Laboratory of Superlight Materials and Surface Technology, Ministry of Education, College of Materials Science and Chemical Engineering, Harbin Engineering University, Harbin 150001, China
e-mail: zwzhang@hrbeu.edu.cn

The Minerals, Metals & Materials Society, *TMS 2018 147th Annual Meeting & Exhibition Supplemental Proceedings*, The Minerals, Metals & Materials Series,
https://doi.org/10.1007/978-3-319-72526-0_37

It is reported that small additions of alloying elements (such as O, Fe) and impurities (such as C, N) have a very big effect on the mechanical properties of Hf alloys [1]. Keeping a low level of impurities, specifically oxygen is one of the effective method to avoid cracking during the transformation of Hf tube/plate. Therefore, it is of great significance to investigate the effects of oxygen on the mechanical properties of Hf.

Many efforts have been made to study the effect of oxygen on the microstructure and mechanical properties in alloys [2–5]. It is generally believed that the mechanical properties will decrease with the increase in oxygen content. However, how the oxygen content affects the mechanical properties remains unknown in Hf. In this paper, the stable oxygen interstitial sites were determined by using first-principles method. The effects of oxygen content on the lattice distortion, density of states, and elastic parameters including the full set of elastic coefficients, bulk moduli and shear moduli, Young's moduli, and Poisson's ratio were calculated and estimated. The relationship between the elastic and plastic properties of Hf was also discussed empirically.

Computational Procedure

The calculations were conducted using a planewave pseudopotential method based on density functional theory (DFT) with the generalized gradient approximation (GGA) in the scheme of Perdew–Burke–Ernzerhof [6]. The ultrasoft pseudopotentials were chosen for the interactions between electrons and ionic cores. The Fermi smearing of the electronic occupancy in the calculations was 0.2 eV and the plane wave cut-off energy was set to 340 eV. The Brillouinzone integrations were made using a (4 × 4 × 2) *k*-point mesh according to the Monkhorst-Pack scheme in a 2 × 2 × 2 cell [7]. The following orbital electrons were treated as valence electrons: Hf–$6s^2 5d^2$ and O–2 $s^2 2p^4$. Elastic constants were determined by calculating the variations in energy arising from applied strain.

It is well know that Hf has two kinds of crystal stuctures: HCP and BCC. Hf belongs to HCP crystal strucure in its natural state, and will transform to a BCC crystal structure when the temperature reaches 1742 °C. In this study, we only investigate the HCP phase. In HCP crystal structure, there are eight kinds of interstitial sites which can be occupied by oxygen atom according to Reference [8]: octahedral(OC), tetrahedral (TE), hexahedral (HE), basal octahedral (BO), crowdion (CR), basal crowdion (BC), split dumbbells along *c* axis (SP), and split dumbbells in the basal plane (BS) as shown in Fig. 1. On one hand, we calculated the formation energy and cell parameters for all these eight interstitial sites to determine the stable sites for oxygen atom to occupy. On the other hand, similar to our previous study [9], we construct the structure models with different interstitial oxygen concentration, the concentrations of oxygen atoms used in the calculations

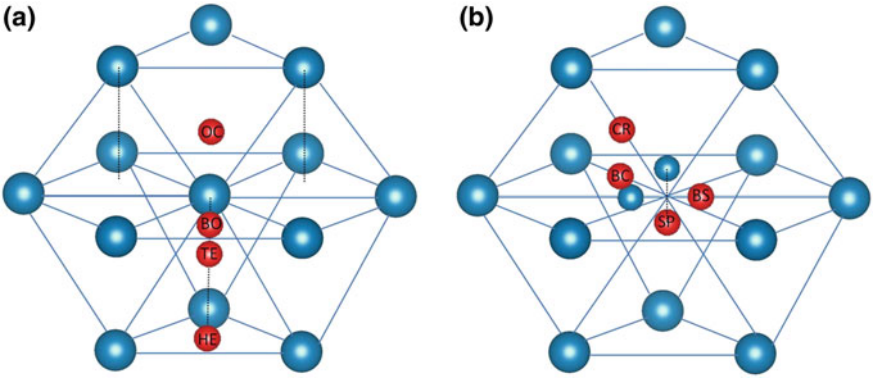

Fig. 1 Schematic of interstitial sites occupied by one interstitial oxygen atom in Hf: **a** octahedral (OC), tetrahedral (TE), hexahedral (HE), basal octahedral (BO); **b** crowdion (CR), basal crowdion (BC), split dumbbells along c axis (SP), and split dumbbells in the basal plane (BS)

are 5.88% (2 × 2 × 2 supercell, 16 Hf atoms + 1 O atom), 4.00% (2 × 2 × 3 supercell, 24 Hf atoms + 1 O atom) and 2.70% (3 × 3 × 2 supercell, 36 Hf atoms + 1 O atom).

Results and Discussion

The formation energy of the addition of an oxygen atom is denfined as:

$$E = E_{\text{def}} - \left(E_{\text{per}} + E_{\text{O}}\right) \tag{1}$$

where E_{def} is the final energy of the unit cell with the addition of an oxygen atom, E_{per} is the final energy of the perfect lattice, and E_{O} is the energy of single O atom, respectively. The formation energy of O_2 molecules was firstly calculated, and then half of the energy was treated as the formation energy of single O atom. The total energy of pure Hf crystal structure in a 2 × 2 × 2 unit cell and a half of O_2 molecules were calculated to be 6541.333 eV and 433.932 eV, respectively. According to Eq. 1, the formation energies with an oxygen atom occupying different interstitial sites in the crystal structure were all calculated and shown in Table 1. The results show that only OC and HE sites are stable, and other sites are all unstable. In general, interstitial elements (O, N, C) prefer to occupy octahedral and tetrahedral sites [10]. Oxygen stable interstitial sites are OC, HE, and CR in α-Ti [8]. The coordination numbers of oxygen atoms for OC and HE cases are eight and six, respectively, and the high coordination numbers make the binding energy between atoms lower and thus more stable. The oxygen atom at BO site will move to OC after geometry optimization, and TE site will relax to HE which is identified with Scotti's results in pure Ti [8]. The change of the cell parameters can reflect the

degree of lattice distortion. Although the positions of oxygen atom at CR, BC, BS, and SP sites do not move too much after geometry optimization, the lattice distortion caused by oxygen atom is very large. For example, the length of Hf–Hf is 3.198 Å in the original cell for BC case, and will increase to 4.509 Å after geometry optimization, which indicates that this kind of oxygen site is unstable due to the large effects on the lattice distortion. A recent research shows that the lattice distortion restrains dislocation motion and causes embrittlement and loss of ductility in Ti alloys [5]. The lattice parameters of all the interstitial sites are shown in Table 1. The values of all the cell parameters for OC site are very close to pure Hf, indicating a very small lattice distortion. The formation energy of OC site is also the lowest, and thus it is the most stable site among all the eight sites. In the following study, we only choose OC site to investigate the effect of oxygen on the lattice distortion, density of states, and elastic properties. The lattice parameters of the models with different oxygen content are shown in Table 2. It is found that oxygen content has a very weak effect on the cell parameters *a* and *b*, while the value of *c* increases slightly with increase of oxygen content. Oxygen atom occupying OC site causes small lattice distortion. From this point of view, it is also demonstrated that octahedral interstitial site for oxygen atom is very stable in Hf crystal structure. The value of *c*/*a* can be used to estimate the ductility for HCP metal, which determines their slip modes [5]. The higher is the value of *c*/*a*, the worse is the ductility. With the increase of oxygen content, the value of *c*/*a* presents a slight increase, indicating that a high oxygen content may weaken the ductility of Hf.

Table 1 The formation energy and cell parameters after geometry optimization for pure Hf and eight kinds of interstitial sites models

Position	After geometry optimization	Formation energy (eV)	*a* (Å)	*b* (Å)	*c* (Å)	α (°)	β (°)	γ (°)
Pure Hf	–	–	6.468	6.468	10.182	90.000	90.000	120.375
OC	stable	−5.780	6.460	6.457	10.285	90.038	89.946	120.001
TE	Relax to HE	−4.091	6.555	6.558	10.223	89.976	90.026	119.712
HE	stable	−5.780	6.599	6.573	10.110	89.989	90.006	119.826
BO	Relax to OC	−4.091	6.454	6.452	10.271	89.998	89.946	119.856
CR	unstable	−5.139	6.422	6.437	10.569	90.119	81.030	119.808
BC	unstable	−4.481	6.287	6.287	9.724	90.014	90.006	104.259
BS	unstable	−4.881	7.646	6.246	9.800	90.010	89.995	127.683
SP	unstable	−4.084	6.554	6.553	10.252	90.046	89.949	119.807

Table 2 The cell parameters of OC interstitial site with various oxygen concentrations

O atom content (%)	*a* (Å)	*b* (Å)	*c* (Å)	α (°)	β (°)	γ (°)	*c*/*a*
0	3.234	3.234	5.091	90.000	90.000	120.375	1.574
2.70	3.234	3.237	5.108	89.998	89.980	120.081	1.579
4.00	3.228	3.228	5.117	89.980	90.024	120.180	1.585
5.88	3.230	3.228	5.143	90.039	89.946	120.001	1.592

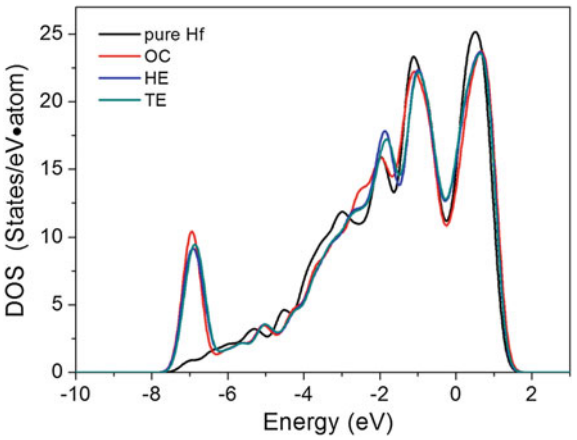

Fig. 2 The density of states (DOS) of pure Hf, and the models of OC, HE and TE interstitial sites

The total density of states of pure Hf, stable OC and HE interstitial sites are shown in Fig. 2, in which TE sites are also shown for comparison. From Fig. 2, one can observe an obvious difference at about −7 eV where the density of states of OC, HE, TE sites is increased significantly, indicating that this peak is completely due to oxygen orbital electronics. The peak positions of different oxygen interstitial sites are very close, and there is no obvious difference between them.

In order to further study the individual effect of Hf and O orbital electronics, the partial density of states (PDOS) of Hf with one oxygen atom occupying OC interstitial site in a 2 × 2 × 2 unit cell are shown in Fig. 3. The O 2s state is located at a much lower energy of about −20.5 eV, and so it is not shown here. Oxygen orbital electronics have very weak contribution near the Fermi level. There is an interaction between O 2p state with Hf orbital electronics at −7 eV, however, the peak here is not observed in pure Hf from Fig. 2, further demonstrating that the

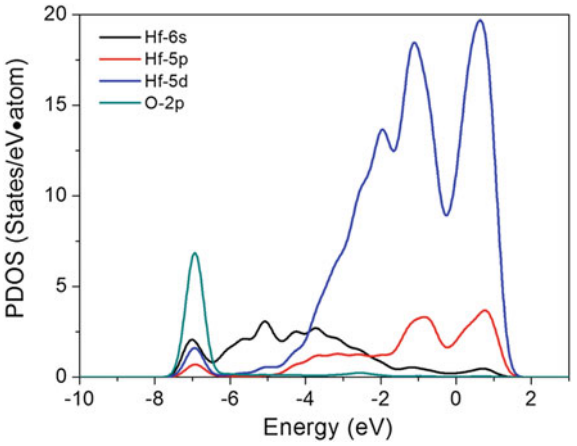

Fig. 3 The partial density of states (PDOS) of O 2p, Hf 6 s, Hf 5p,and Hf 5d at OC site

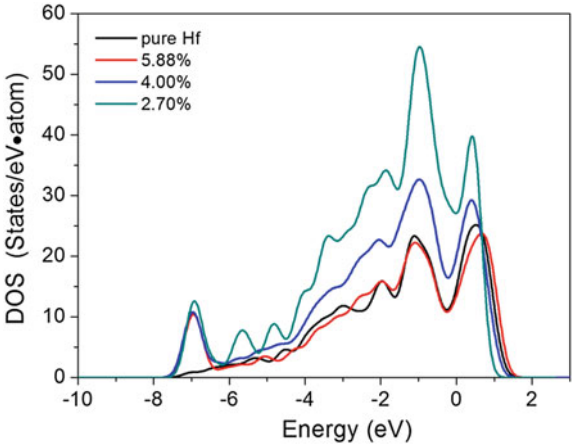

Fig. 4 The density of states (DOS) of pure Hf, and the models of different interstitial oxygen concentration at OC site

orbital hybridization is attributed to oxygen atom. The DOS of pure Hf is compared to those of different concentrations of interstitial oxygen atom at OC site shown in Fig. 4. When oxygen content reaches 5.88%, the pseudogap width is obviously wider than pure Hf, indicating shifts of the bonds type to more covalent [5].

The elastic constants of the crystal reflect the macroscopic mechanical properties of the material under room temperature and static load, and determine the response to stress or strain, which are generally described by Young's modulus, shear modulus, bulk modulus, and Poisson ratio, etc. The calculated elastic constants, bulk modulus B, shear modulus G, Young modulus E and Poisson's ratio γ with various oxygen content at OC site together with the computational and experimental results in the previous works are shown in Table 3. Our results agree with the data in References [11, 12, 14]. To further observe the variation of elastic constants with oxygen content, the values of C_{11}, C_{12}, C_{13}, C_{33} and C_{44} as a function of oxygen concentration are plotted in Fig. 5. The C_{11} decreases with the increasing oxygen content, however, there are no obvious rules observed for other elastic constants. For hexagonal crystal system, mechanical stability can be judged by the relationships of the elastic constants according to the Born criteria: $C_{11} > 0$, $C_{11} - C_{12} > 0$, $C_{44} > 0$ and $(C_{11} + C_{12})C_{33} > 2C_{13}^2$ [11, 13]. If all the Eqs are satisfied, one can conclude that the crystal structure is stable. In our case, mechanical property is stable no matter for pure Hf or Hf with different concentration of oxygen in the OC site.

The value of B/G can be used to estimate the effect of oxygen concentration on the brittle/ductile behavior of Hf using Pugh's criterion, in which the critical value from ductile to brittle transition is 1.75 [5, 15]. A lower value of B/G means that the material is easier to occur brittle fracture. The values of B/G as a function of oxygen content are plotted in Fig. 6. With the increase in oxygen content, the B/G value decreases, indicating that a high oxygen content will deteriorate the ductility.

Table 3 The calculated elastic stiffness moduli with various oxygen content at OC site together with the computational and experimental results in the previous works [11, 12, 14]

Oxygen content	C_{11} (GPa)	C_{12} (GPa)	C_{13} (GPa)	C_{33} (GPa)	C_{44} (GPa)	B (GPa)	G (GPa)	B/G	$\bar{E}$ (GPa)	$\bar{\gamma}$
Pure Hf	208.3	79.6	85.3	224.3	57.6	126.8	62.0	2.05	159.8	0.29
Pure Hf-Cal. [11, 12]	183.0/194.0	70.2/59.0	68.2/68.8	192.5/196.2	52.8/52.7	108.0/108.6	55.9/60.4	1.93/1.80	142.9/152.9	0.28/0.26
Pure Hf-Expt. [12, 14]	181.1/190.1	77.2/74.5	66.1/65.5	196.9/204.4	55.7/60.0	108.7/110.6	56.0/60.8	1.94/1.82	143.3/154.2	0.28/0.27
2.70%	204.0	82.2	83.4	220.8	61.2	125.2	62.0	2.02	159.6	0.29
4.00%	201.2	80.5	76.1	221.1	59.8	121.0	62.1	1.95	159.0	0.28
5.88%	198.3	80.7	74.9	215.6	63.1	119.2	62.4	1.92	159.5	0.28

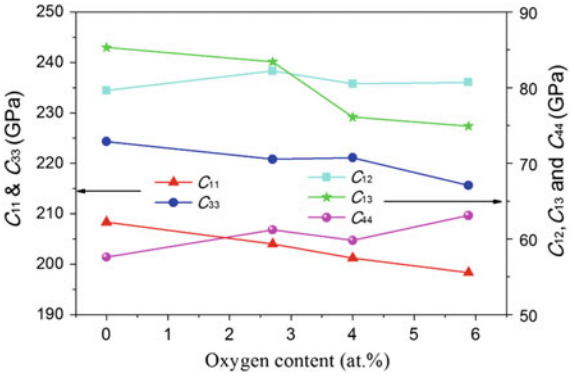

Fig. 5 The values of C_{11}, C_{12}, C_{13}, C_{33} and C_{44} as a function of oxygen concentration

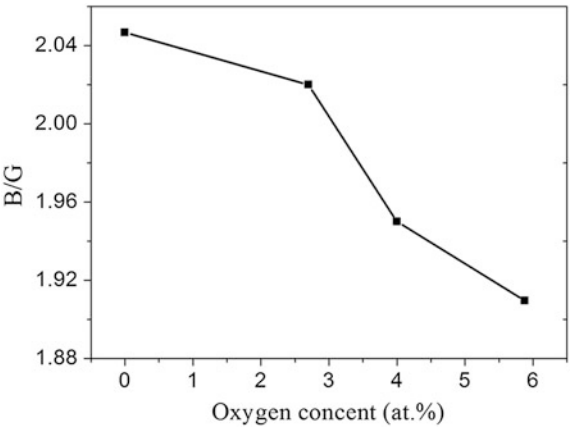

Fig. 6 The value of *B*/G as a function of oxygen concentration

Conclusion

In conclusion, the octahedral site is the most stable oxygen site among all the eight interstitial sites, and the hexahedral site takes the second place. The oxygen atom at other sites will either relax to octahedral site/hexahedral site or make the lattice generate a very large distortion. The addition of oxygen contributes the peak at about −7 eV in DOS, and the increase of oxygen content makes the bonds type more covalent. The calculated C_{11} decreases with the increasing oxygen content, while the values of C_{12}, C_{13}, C_{33} and C_{44} have no obvious rules with the variation of oxygen content. Mechanical property is stable after the addition of oxygen atom according to Born criteria. Oxygen content has little effect on the parameters of shear modulus G, Young modulus E and Poisson's ratio γ. The value of B/G decreases with the increase in oxygen content, demonstrating that the existence of oxygen will bring a bad effect on the ductility of Hf.

Acknowledgements This work was supported by the the International Exchange Program of Harbin Engineering University for Innovation-oriented, the Fundamental Research Funds for the Central Universities (HEUCFJ171005, HEUCFJ171001 and HEUCFP201703), China Postdoctoral Science Foundation funded project (3236310478).

References

1. Bechade JL, Cea-Saclay C (1998) Fabrication and metallurgical properties of hafnium alloys for control rods, Paper presented at the conference of control assembly materials for water reactors: experience, performance and perspectives, Austria, Vienna, 12–15 October 1998
2. Nakai M, Akahori T, Tsutsumi H, Ogawa M (2009) Effect of oxygen content on microstructure and mechanical properties of biomedical Ti–29Nb–13Ta–4.6Zr alloy under solutionized and aged conditions. Mater Trans 50(12):2716–2720
3. Liu Z (1998) Effects of oxygen and heat treatment on the mechanical properties of alpha and beta titanium alloys. Metall Mater Trans A 19A:527–542
4. Li YG, Loretto MH, Rugg D, Voice W (1999) Effect of carbon and oxygen on microstructure and mechanical properties of Ti–25 V–15Cr–2Al (wt%) alloys. Acta Metall 44(10): 2889–2905
5. Kwasniak P, Muzyk M, Garbacz H, Kurzydlowski KJ (2014) Influence of oxygen content on the mechanical properties of hexagonal Ti—First principles calculations. Mater Sci Eng A 590:74–79
6. Perdew JP, Burke K, Ernzerhof M (1996) Generalized gradient approximation made simple. Phys Rev Lett 77(18):3865
7. Monkhorst HJ, Pack JD (1976) Special points for Brillouin-zone integrations. Phys Rev B 13(12):5188
8. Scotti L, Mottura A (2016) Interstitial diffusion of O, N, and C in alpha-Ti from first-principles: analytical model and kinetic Monte Carlo simulations. J Chem Phys 144(8): 084701
9. Zhang Y, Leng Y, Liu J, Ji NJ, Duan XL, Li JQ, Zhao X, Wang JY, Jiang HD (2015) Mechanism of hydrogen treatment in $KTiOPO_4$ crystals at high temperature: experimental and first-principles studies. Cryst Eng Comm 17(20):3793–3799
10. Conrad H (1981) Effect of interstitial solutes on the strength and ductility of titanium. Prog Mater Sci 26:123
11. Hao Y, Zhu J, Zhang L, Ren H, Qu J (2011) Structure phase transition and elastic properties of hafnium: first-principles study. Phil Mag Lett 91(1):61–69
12. Lu Y, Zhang P (2014) Elasticity behavior, phonon spectra, and the pressure–temperature phase diagram of HfTi alloy: a density-functional theory study. Comp Mater Sci 82:5–11
13. Born M, Huang K, Lax M (1955) Dynamical theory of crystal lattices. Am J Phys 23(7):474–474
14. Fisher ES, Renken CJ (1964) Single-crystal elastic moduli and the HCP → bcc transformation in Ti, Zr, and Hf. Phys Rev 135(2A):A482–A494
15. Pugh SF (2009) XCII. Relations between the elastic moduli and the plastic properties of polycrystalline pure metals. Lond Edinb Dublin Phil Mag J Sci 45(367):823–843

Morphological Study of Dispersion Phases in Heterogeneous Waste Form Materials for Efficient Nuclear Waste Containment

K. Patel, M. Riaz, F. Rabbi, R. Raihan and K. Reifsnider

Abstract The efficiency of high-level nuclear waste immobilization by incorporating a host phase within a hollandite material structure can be increased by carefully synthesizing the dispersion phases inside the hollandite matrix. Also, estimation of the leaching rate from these nuclear waste forms is critical. Hence, conformal finite elemental model has been developed to study the effect of morphology of dispersive phases on diffusive nuclear flux. COMSOL Multi-physics is used as a computational tool to solve a Nernst-Plank Equation to study the diffusion leakage flux. A 2D model is built to identify the effect of volume fractions, surface areas, and different shapes of dispersion phase on the exit flux behavior. The results have indicated that there exists an optimum combination of different parameters such as volume fraction, surface area, position with respect to open boundary, and shape of dispersion phases for immobilization.

Keywords Diffusion · COMSOL · Nernst-Planck · Nuclear waste form

K. Patel (✉) · M. Riaz (✉) · K. Reifsnider (✉)
University of Texas at Arlington, Arlington, USA
e-mail: krutarthshailes.patel@mavs.uta.edu

M. Riaz
e-mail: mdriaz.kayser@uta.edu

K. Reifsnider
e-mail: kenneth.reifsnider@uta.edu

F. Rabbi (✉) · R. Raihan (✉)
University of Texas at Arlington Research Institute, Arlington, USA
e-mail: rabbi@email.sc.edu

R. Raihan
e-mail: mdrassel.raihan@uta.edu

The Minerals, Metals & Materials Society, *TMS 2018 147th Annual Meeting & Exhibition Supplemental Proceedings*, The Minerals, Metals & Materials Series,
https://doi.org/10.1007/978-3-319-72526-0_38

Introduction

The fission product, Cs is extremely difficult to immobilize, because of the high thermal power of Cs, its long lifetime, its tendency to form water soluble compounds, and its volatility at elevated temperatures during waste-forms synthesis [1–4]. Safe and reliable storage of high level Nuclear waste like Cs is a primary concern of next generation nuclear energy development and it is critical to understand the characteristics of nuclear spent fuel and how it affects the storage environment. One strategy for immobilizing the Cesium cation is to incorporate it into a ceramic or glass matrix from which it is difficult to remove. Hollandite ceramics have been extensively studied for this purpose and are generally regarded as being more leach resistant than glass [5]. Hollandite is one of the major phases of Synroc, a multiphase ceramic matrix also containing zirconolite and perovskite phases [6] that is being considered as a matrix for immobilizing Cs resulting from enhanced separation of fission product solutions from spent fuel reprocessing [7]. The long-term effects of radiation on waste form solids is a critical concern in the performance assessment of the long-term containment strategy [8].

Hence, A 2D model is built to monitor the effect of volume fractions, surface areas and different shapes of dispersion phases on nuclear waste material. Moreover, A Multiphysics model of heterogeneous microstructure that represents the actual waste form material has been created by a Voronoi tessellation method, so that the critical variables (material and structural) that control the elemental release rate of that material could be identified and controlled. Finally, a comparison between different morphologies of dispersion phases in heterogeneous waste form materials is presented to identify the maximum nuclear waste confinement parameters.

Method of Analysis and Model Set-up

The primary goal of the present research is to set a Multiphysics model of the diffusion of waste phase material out of a heterogeneous waste form material on the as-prepared microstructure, so that the critical variables (material and structural) that control the elemental release of that waste material could be identified and controlled. The basic governing equation in the developed simulation technique is the Nernst-Plank Equation, which describes the transport behavior of chemical species by diffusion, migration and convection present in the waste form material.

$$\boldsymbol{N_i} = -\boldsymbol{D_i}\nabla \boldsymbol{c_i} - \boldsymbol{z_i u_{m,i} F c_i}\nabla \varnothing + \boldsymbol{c_i u} \tag{1}$$

Here, N_i (mol/m^2 s) is the flux of chemical species, i, D_i (m^2/s) is the diffusion co-efficient of the same species, i, ∇c_i (mol/m^3) is the concentration gradient of ion, i, z_i is the valance of the species, F is the Faraday constant, $\nabla\varnothing$ is the electrolyte

potential gradient and u (m/s) is the mass velocity vector. Absence of fluid flow within the geometry of our current problem, renders the velocity term $\boldsymbol{u_i}$ to zero, and since there is no electrical potential applied over the boundaries, the migration term becomes zero. Hence, the leaching of cesium ions will be carried out mainly by the diffusion of the waste species present in the waste form to an exit surface in present case.

Figure 1 shows our representative volume element (in 2D), in which all interior boundary surfaces is specified with zero-flux boundary conditions to ensure identical behavior in all interior directions, and one of the boundaries is kept as "free" to represent outer environment region. F. Rabbi et al. (our previous team) [9] selected a similar kind of representation with different Initial Concentration of different phases. Nernst-Plank Equation Module under Chemical Reaction Engineering Module of COMSOL Multi-Physics has been used throughout the presented study.

Figure 1 represents two different phases of the Cesium waste form with different Cesium diffusion co-efficient as well as initial concentrations. The diffusion co-efficient were maintained to insure the over-all Diffusion co-efficient ratio of 0.1 (i.e. diffusion co-efficient of inclusions materials for Cs: 10^{-9} m^2/s and diffusion co-efficient of matrix materials for Cs: 10^{-8} m^2/s).

The ionic conductivity of Cs in a hollandite structure [10–12] gives us the diffusion co-efficient of the domains here. And based on the Nernst-Einstein relation, the diffusion co-efficient is given by Eq. (2).

$$\sigma = \frac{\boldsymbol{Z_i^2 e^2 C_i}}{\boldsymbol{K_B T}} \boldsymbol{D_i} \tag{2}$$

Three out of four edges of our RVE have been given periodic boundary conditions whereas the remaining boundary was kept "open" (i.e. very low Cs concentration (0.01 mol/m^3)) which facilitates the flow of the chemical species. The observed flow gives us the estimation of elemental boundary flux out of the waste form. Equation (3) describes the periodic boundary conditions, which in turn means

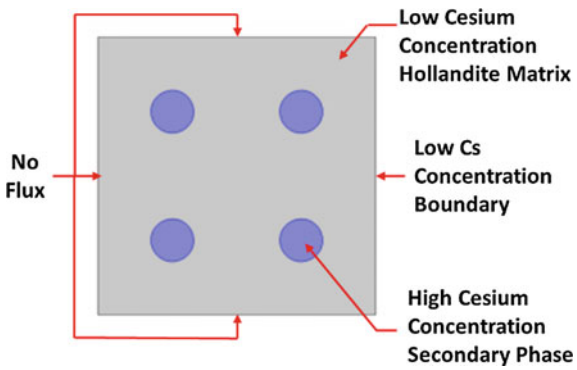

Fig. 1 Two-dimensional RVE used for computational study

that no flux transport occurs out of the system over these boundaries either chemically or electrically.

$$-\boldsymbol{n} \cdot \boldsymbol{N}_i = \boldsymbol{0} \quad \textit{and} \quad -\boldsymbol{n} \cdot \boldsymbol{N}^v = \boldsymbol{0} \tag{3}$$

And the Dirichlet boundary condition has been applied to the open boundary given by the equations in (4).

$$\boldsymbol{C}_i = \boldsymbol{C}_{0\,j} \quad \textit{and} \quad \boldsymbol{V} = \boldsymbol{V}_0 \tag{4}$$

where, $C_{0\,j} = C_{0,\,Cs}$ kept as 0.01 mol/m^3 and $V_0 = 0$ V.

No global (fixed and constant) concentration gradient to drive the diffusion of stored waste material is present in the beginning. Only specific concentrations in the individual storage phase material have been applied, so that the local concentration gradients drive the diffusive flux, i.e., mathematically it is an initial value problem.

Voronoi tessellation techniques have also been used to generate 3D representations of the as-prepared models of the material, and similar kinds of model set-up as explained above were chosen for the analysis. The influence of Grain-Boundaries on the exit flux were analyzed, again with the same simulation procedure.

Results and Discussion

Influence of Volume Fraction on Boundary Flux

Here the volume fraction of stored material/secondary phases is varied while keeping the relative concentration of stored waste phase constant relative to the bulk matrix phase, for cases in which the storage volume consisted of one, four, nine, or sixteen particles. Conspicuously the surface of the storage phase is increasing sharply for those choices, with the smallest area being the largest (single) particle. However, the results also indicate a non-intuitive result. In Fig. 2 the calculations indicate that the sensitivity to morphology details has a kind of "threshold" at a volume fraction of about 0.4, below which there is comparatively little sensitivity of exit flux to the size of the storage phase particles (for a given volume fraction of storage phase). While this is an important design parameter, it could be assumed that a practical storage material would have a minimum of the order of 40% of the storage phase material in most situations.

Influence of Surface Area on Boundary Flux

Figure 3a provides insights onto the released flux when the stored waste phase in one particle (for a given volume fraction of 0.5 in this example), is divided into

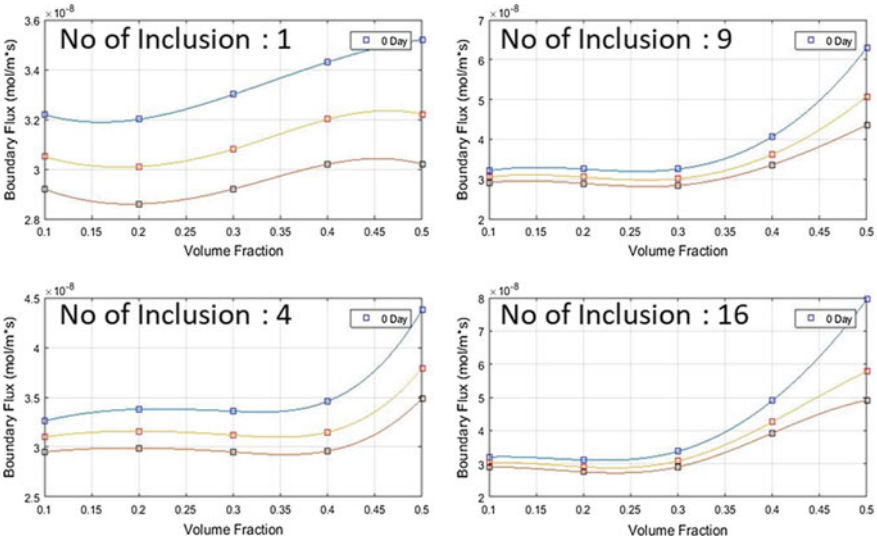

Fig. 2 Boundary flux for various volume fractions of stored waste material when divided into different numbers of particles

multiple particles, calculated at consecutive time periods. The calculation was done for divisions up to 16 particles. The results suggest that increasing the surface to volume ratio of the stored material by distributing the waste in small particles versus a single large one creates more exit flux loss of stored material, especially in the early life of the waste form material for this model scenario.

A similar calculation with increased number of inclusions is shown in Fig. 3b (a situation more likely to apply to a manufactured condition for a heterogeneous manufactured material form). The initial ("Day 0") case produces a quite similar result to Fig. 3a, but the difference diminishes after some time of storage, and over long periods of time the particle size effect becomes a minor parameter.

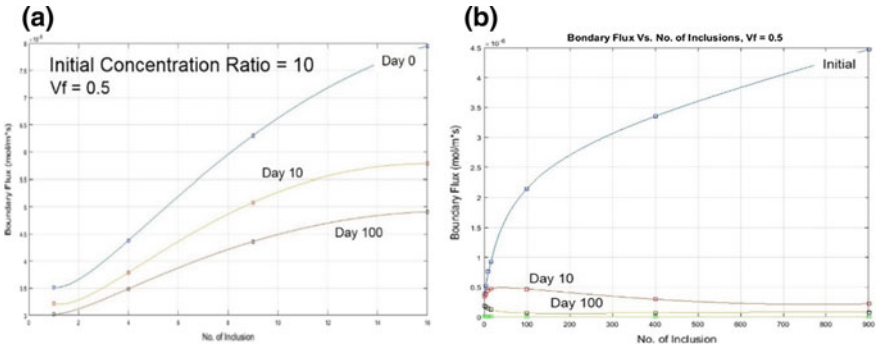

Fig. 3 Predicted elemental flux out of the waste form volume as a function of the number of inclusions for a given volume fraction **a** Small number of inclusions **b** large number of inclusions

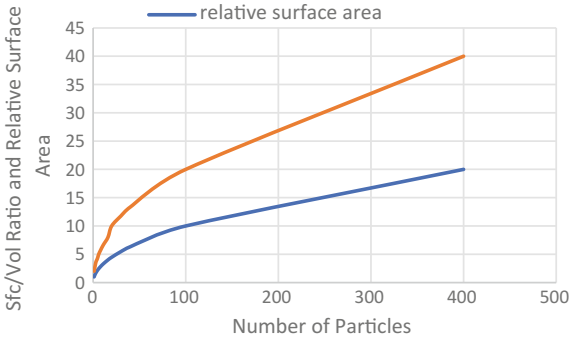

Fig. 4 Obtained relative surface area and surface to volume ratio as a single unit circle is divided into many circles

Separately, the calculation has been done for surface to volume ratio and relative surface area (compared to a unit circle) as a function of the number of times that area is divided, and plotted as the results shown in Fig. 4. We observe quite similar shaped curves as in Fig. 3b and the general curves in Fig. 3a. *We conclude that for an initial period of service, the flux from the waste form is proportional to the surface to volume ratio of the waste storage particle/phase materials.* We also note that after some period, the surface to volume ratio becomes less important, and that its influence continues to diminish after that.

Influence of Shapes on Boundary Flux

The influence of distributed phase shapes on released flux was determined for elliptical and circular particles. An example of those results is shown in Figs. 5 and 6.

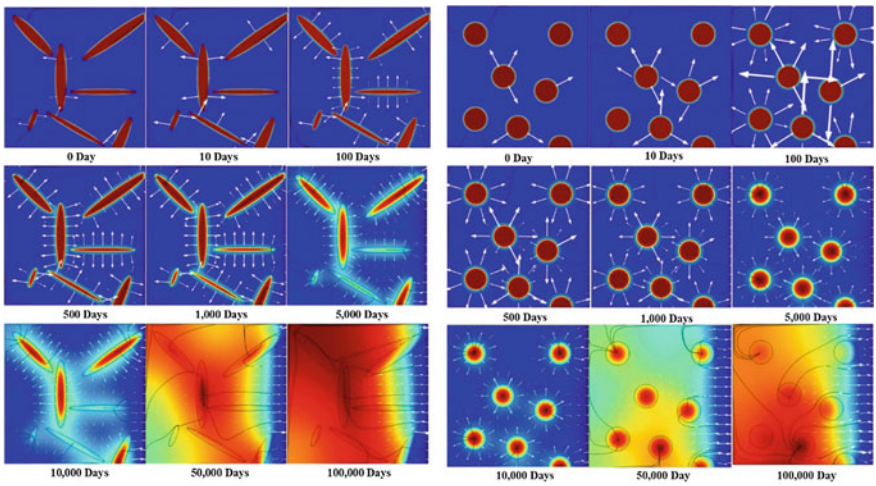

Fig. 5 Variation of flux concentrations and vector magnitudes when the same volume fraction of waste material is configured into elliptical versus circular particles

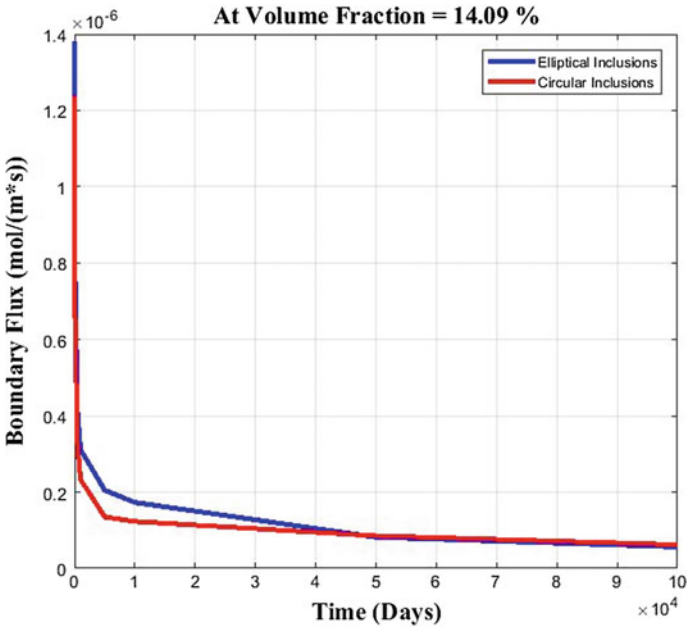

Fig. 6 Variation of exit flux when the same volume fraction of waste material is configured into elliptical versus circular particles

Figure 5 shows the local flux vectors and the global concentration variations as the compared waste forms progress through 100,000 days. First, the local flux vectors in the circular case are larger than for the elliptical particles, but it must be remembered that the total surface area (for fixed volume fraction) of the elliptical particles is much greater than for the circular particles (which have a minimum surface to volume ratio for all shapes). As a result, it also is seen that, for example at 50,000 days, the global concentration is nearly uniform in directions perpendicular to the exit surface normal (i.e. the influence of the individual particle geometry is no longer dominant) while that condition is only reached at 100,000 days for the circular particle case. So, again, this confirms that the major effects of the particle geometry, *when all other variables are held constant*, is the influence on the early rate of loss of the waste material to the external surfaces, which may be important to efforts to control the inevitable peak in the flux that occurs in the early life of the waste forms. Figure 6 shows this result in a plot of the exit flux versus time for the two geometries. The elliptical inclusions have more flux in early life, and less in later life, as we discussed.

Study of Space-Filling and "Real" Microstructures

Figure 7a shows a Hollandite-$Nd_2Ti_2O_7$ waste form material morphology. Calculating the actual flux out of such materials has been facilitated by using as-manufactured microstructures from tomography and renderings generated by other team members; however, it is extremely important that we be able to vary the parameters systematically that control such microstructures with the help of general information from such studies. This was enabled in the present situation by using a Voronoi tessellation method to create space-filling morphology that can be systematically changed. This enables systematic basic studies to establish foundation concepts for waste forms. In other words, it would be great to know if it is better to store waste material in one large volume/storage phase surrounded by the containing phase, or to store it in smaller second phase grains in a heterogeneous solid form.

An example of such a study is given by the comparison shown in Fig. 8. The volume fraction of waste storage phase in all calculations was Vf = 0.5176. As shown in the left image of Fig. 8, the material is distributed in a heterogeneous microstructure (e.g. the dark phases) and in the comparison case it is concentrated in a single spherical (e.g. circular in our 2D study) particle as shown in the right image. Figures 9 and 10 present the released flux results of this study of "real" morphology having contiguous phases, for a short term (5 days) and long term (100,000 days) respectively. From Figs. 9 and 10 one of the conclusions can be drawn is, creating heterogeneous waste forms with material distributed into several small distributed phase (contiguous) regions (for a given volume fraction) results in reductions of released waste material from that volume, by more than an order of

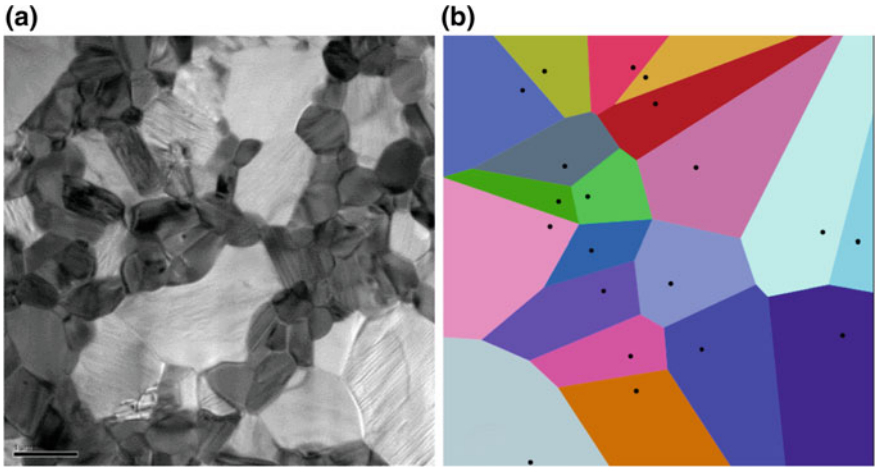

Fig. 7 **a** Heterogeneous morphology of a hollandite-$Nd_2Ti_2O_7$ waste form material made by the present team. **b** Heterogeneous morphology created by a Voronoi tessellation method

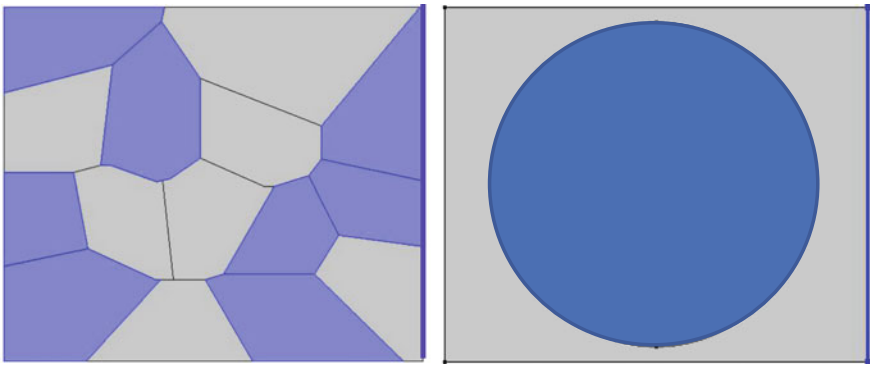

Fig. 8 Segmented heterogeneous morphology (left) compared to a single second phase of storage material (right) as a comparison

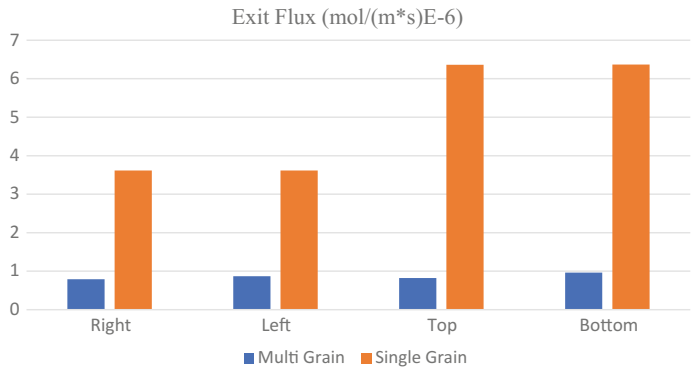

Fig. 9 Exit surface flux on 5th day for heterogeneous multigrain waste form with Vf = 0.5176 compared to single waste grain inclusion, shown in Fig. 8

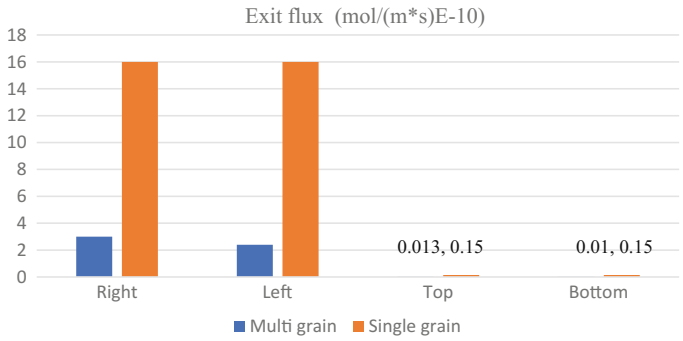

Fig. 10 Exit surface flux on 100,000th day for heterogeneous multigrain waste form with Vf = 0.5176 compared to single waste grain inclusion for all surfaces of the computational morphology, shown in Fig. 8

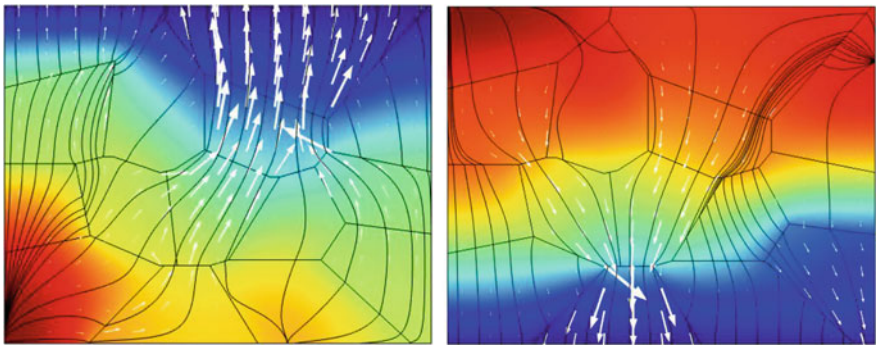

Fig. 11 Exit surface flux paths from top exit surface (left) and bottom exit surface (right)

magnitude in the present example. This is one of the foundation concepts and motivations for heterogeneous waste forms at the fundamental level, and confirmation of that storage method.

Another conclusion is that the morphology matters, i.e., the flux magnitudes for the left, right, top, and bottom open boundary of the single analysis cell are not the same, a difference that can only be driven by the different microstructure that "faces" those respective exit surfaces since all other variables are held constant. In that context, Figs. 9 and 10 also show that the heterogeneous multigrain waste form has an even greater advantage (lower lost storage material) compared to the single particle situation for the long-term storage case than for the short term, again suggesting that the advantage is a bulk effect and not a near-surface phenomenon. One could talk about the near-surface grain effects in that context, but Fig. 10 shows that the difference is larger for long term than for short term, an opposite order from the result suggested by near-surface behavior. Further confirmation of this point is made by the computational results shown in Fig. 11.

Figure 11 compares the exit flux vectors of the case when the exit surface is at top compared to the case when the exit surface is the at the bottom of the computational volume at 100,000 days (advanced condition). For this problem in which the stored material in selected grains must travel down the concentration gradients and around other particles in a disordered microstructure, the paths are not the same, and therefore, the flux is not the same for a given point in time, volume fraction, etc. This is further motivation for developing an understanding and modeling capability for this problem.

Conclusion

We have successfully formulated a 2D conformal model of the functional performance of nuclear waste form materials and used that model to draw conclusions on behavior and performance of those materials. Some of our salient conclusions are summarized below.

Leaching of storage material in these heterogeneous materials is greatly influenced by their morphology details and has a "threshold" at a volume fraction of about 0.4 for our models. Below 40% volume fraction, the exit flux shows very little change with respect to the size of the storage particles. We also conclude that for an initial period of service, the flux from the nuclear waste form volume under study is proportional to the surface to volume ratio of the waste storage particle/phase materials. That effect diminishes and becomes less important at the longer periods of storage time.

Along with the size and surface area, shape of the storage phases is also one of the controlling parameters for elemental flux release out of waste form materials as demonstrated by comparison between circular and elliptical inclusions where the later type has greater total surface area (while keeping other parameters constant) than the prior, and as a result, the global concentration becomes nearly uniform over the considered volume considerably earlier in the case of elliptical inclusions that for circular ones. Hence, carefully synthesized microstructures can result in significantly accelerated or delayed leaching of the stored nuclear waste.

Our results also show that heterogeneous materials with high numbers of grains have exit flux values typically one order of magnitude less than storage phases which contain waste material in a single particle or mass.

We have also developed 3D models, and find consistent results for flux distributions both over short and long periods compared with the 2D model presented in this paper. However, 3D models may be preferred for accuracy and estimation of real world physical values of exit flux. The results will be presented in our subsequent publications. For maximum nuclear waste confinement, heterogeneous structures with higher numbers of grains per unit volume are preferred morphologies.

Acknowledgements The authors are grateful for the support of Nuclear Energy University Program of the US Department of Energy (Award ID: DENE0008260), and the support for the present study by the Institute for Predictive Performance Methodologies at the University of Texas Arlington Research Institute (UTARI).

References

1. Aubin V et al (2004) The stability under irradiation of hollandite ceramics, specific radioactive cesium-host wasteforms. No. INIS-FR–3008. LCAES (UMR CNRS 7574)
2. Vittorio L et al (2004) Cesium release from ceramic waste form materials in simulated canister corrosion product containing solutions. No. INIS-FR–2898. Materials and engineering sciences
3. Xu Y et al (2016) A-site compositional effects in Ga-doped hollandite materials of the form BaxCsyGa2x+yTi8−2x−yO16: implications for Cs immobilization in crystalline ceramic waste forms. Scientific reports 6:27412
4. Amoroso J et al (2014) Melt processed single phase hollandite waste forms for nuclear waste immobilization: $Ba_{1.0}$ $Cs_{0.3}$ $A_{2.3}$ $Ti_{5.7}$ O_{16}; A=Cr, Fe, Al. J Alloy Compd 584:590–599
5. Luca V et al (2007) Cesium release from tungstate and titanate waste form materials in simulated canister corrosion product-containing solutions. J Am Ceram Soc 90(8):2510–2516

6. Muthuraman M et al (1996) Sintering, microstructural and dilatometric studies of combustion synthesized synroc phases. Mater Res Bull 31(11):1375–1381
7. Lutze W, Ewing RC (1988) Radioactive waste forms for the future
8. Ewing RC, Weber WJ, Clinard FW (1995) Radiation effects in nuclear waste forms for high-level radioactive waste. Prog Nucl Energy 29(2):63–127
9. Rabbi F, Brinkman K, Amoroso J, Reifsnider K (2017) Finite element analysis of ion transport in solid state nuclear waste form materials. J Nucl Mater 493:303–309. https://doi.org/10.1016/j.jnucmat.2017.05.039
10. Sato H, Yui M, Yoshikawa H (Sept 2017) Ionic diffusion coefficients of Cs, Pb, Sm, Ni, SeO 4 and TcO 4 in free water determined from conductivity measurements SeOz- and TcO, in free water determined from conductivity measurements, 3131. https://doi.org/10.1080/18811248.1996.9732037
11. Sims DJ, Andrews WS, Creber KAM (2008) Diffusion coefficients for uranium, cesium and strontium in unsaturated prairie soil 277(1):143–147. https://doi.org/10.1007/s10967-008-0722-7
12. Leinekugel-le-cocq AY, Deniard P, Jobic S, Cerny R, Bart F, Emerich H (2006) Synthesis and characterization of hollandite-type material intended for the specific containment of radioactive cesium 179:3196–3208. https://doi.org/10.1016/j.jssc.2006.05.047

Part XVI
Computational Thermodynamics and Kinetics

Compare the Energies of Different Structures in Aluminium Electrochemical Cell

Mohsen Ameri Siahooei, Khirollah Mehrani and Mohammad Yousefi

Abstract The fluoroaluminate molten salts are used in the Hall-Heroult industrial process for the production of aluminum by electrolysis. To better understand the mechanism of the dissolution of alumina (Al_2O_3) in cryolitic melts, we have studied the structure stability of these anions The initial structural models of $[Al_2OF_6]^{2-}$, $[Al_2O_2F_4]^{2-}$, $[Al_2O_2F_6]^{4-}$ and $[Al_2OF_{10}]^{6-}$ were generated using Gauss View Since this study attempts to compare the energies of different oxofluoroaluminum structures, the geometries should be optimized at an accurate level of theory Therefore, geometry optimizations and energy calculations were carried out by B3LYP density functional while several basis sets including 6-31g, 6-311g**, 6-311g** and 6-311 ++g** were used. Furthermore, solvent effect on structural energies was investigated through incorporation of conductor-like polarizable continuum model (CPCM) at B3LYP/6-311++g** level of theory the structure was optimized at different levels by applying CPCM solvent model. Similar calculations were performed for the other complex structures and similar results were obtained for them. Based on the energy values, the following stability order is achieved: $[Al_2O_2F_4]^{2-} < [Al_2OF_6]^{2-} < [Al_2O_2F_6]^{4-} < [Al_2OF_{10}]^{6-}$.

Keywords Fluoroaluminate molten · Hall-Heroult industrial process

Introduction

Chemical and electrochemical reactions taking place at or near the anode and cathode of Hall-Héroult cells are of great practical and theoretical importance. Although not fully understood, in spite of extensive research, enough is known to form a reasonable consistent picture. While the carbon lining of the cell is often called the cathode, the true cathode is the molten aluminium that rests on it.

M. A. Siahooei · K. Mehrani (✉) · M. Yousefi
Department of Chemistry, Science and Research Branch,
Islamic Azad University, Tehran, Iran
e-mail: kh.mehrani@sarbiau.ac.ir

The Minerals, Metals & Materials Society, *TMS 2018 147th Annual Meeting & Exhibition Supplemental Proceedings*, The Minerals, Metals & Materials Series,
https://doi.org/10.1007/978-3-319-72526-0_39

The prebaked carbon blocks are suspended in the electrolyte to form the anode of the cell.

Enthalpies of formation and Gibbs free energy of formation of $Al_6(OH)_{18}(H_2O)_x$(x = 0-6), $Al_2O_3 \cdot 3H_2O$, $Al(OH)_6^{3-}$, $Al(OH)_4(H_2O)^{2-}$ and $Al(OH)^{4-}$ are calculated at B_3LYP/6-31G, 6-31G and B_3LYP/6-311++G(3d2p) levels respectively with Dipole and Sphere solvent model by DFT and ab initio methods.

Especially, in the process of $Al(OH)_3$ crystals precipitating from supersaturated sodium aluminate solution, $Al_6(OH)_{18}(H_2O)_x(x = 0 - 6)$ is the favorable growth unit, $Al(OH)_6^{3-}$ is the structure unit of growth units and $Al(OH)_4(H_2O)^{2-}$ is the minimum growth unit. Using DFT Method [1].

The experimentally well-known alumina solubility in the range of acid to neutral cryolite-base melts has been modeled thermodynamically in terms of several oxyfluoride solutes. For an acidic melt, cryolite ratio (CR) = 0.5, the dominant solute is monoxygen $Na_2Al_2OF_6$. In a less acidic regime, dioxygen $Na_2Al_2O_2F_4$ is dominant, whereas for neutral alumina solubility in the compositions (CR = 3) $Na_4Al_2o_2F_6$ starts to gain importance. The fit of the model to the experimental solubility data is virtually perfect. The values of the equilibrium constants for the formation of the individual solutes are reported [2].

Cryolitic liquids (NaF-AlF_3 binary system) with dissolved aluminum oxide (Al_2O_3) are used for the production of metallic aluminum by the Hall-Heroult electrolytic process. To better understand the mechanism of the dissolution of alumina (Al_2O_3) in cryolitic melts, we have studied the structure stability of these anions in electrolyte.

Theoretical Method

A Gaussian 09 was employed to optimize the geometries and calculate energies. Also, Hyper Chem and Gauss View were used for graphical illustrations.

2, 2—**Selection of the molecular models and structure optimization**.

The initial structural models of $[Al_2OF_6]^{2-}$, $[Al_2O_2F_4]^{2-}$, $[Al_2O_2F_6]^{4-}$ and $[Al_2OF_{10}]^{6-}$ were generated using Gauss View. Since this study attempts to compare the energies of different oxyfluoroaluminum structures, the geometries should be optimized at an accurate level of theory. Former DFT based energy calculations [3] ave confirmed that DFT approach can result in good agreement with experimental data. Therefore, geometry optimizations and energy calculations were carried out by B_3LYP density functional while several basis sets including 6-31g, 6-311g**, 6-311g** and 6-311++g** were used. Furthermore, solvent effect on structural energies was investigated through incorporation of conductor-like polarizable continuum model (CPCM) at B_3LYP/6-311 ++g** level of theory (Fig. 1).

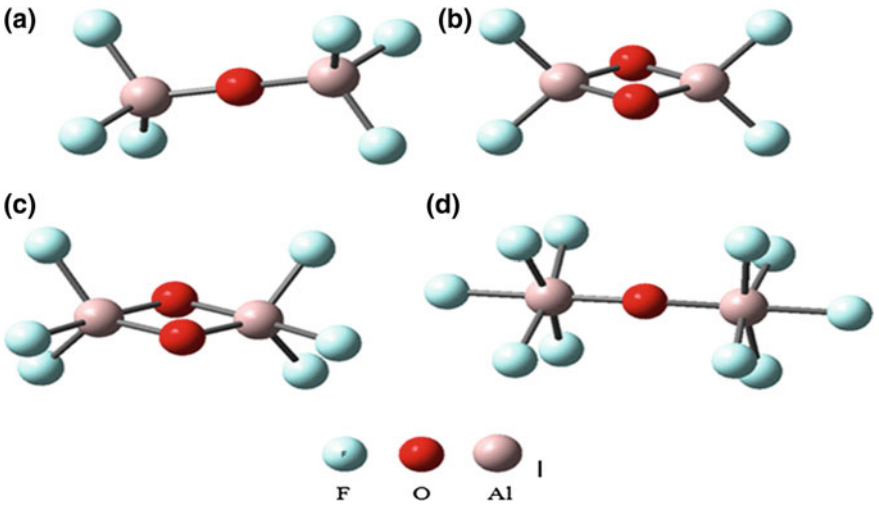

Fig. 1 Geometry optimizations structural models of $[Al_2OF_6]^{2-}$, $[Al_2O_2F_4]^{2-}$, $[Al_2O_2F_6]^{4-}$ and $[Al_2OF_{10}]^{6-}$

For all structures, the initial geometries were supposed to have symmetric configurations and the oxygen atoms were considered as the structural bridges. The noticeable point is that in the $[Al_2OF_6]^{2-}$ complex, the oxygen atom had formed a 110° angle bridge before optimization (Fig. 2) while it forms a 180° bridge, after full optimization and acquiring structural stability. This finding is in good agreement with the results of Zhang et al. [4]. It is noteworthy that $[Al_2OF_{10}]^{6-}$ is unstable in gas phase and it should be concerned in solvent phase. As a consequence, the structure was optimized at different levels by applying CPCM solvent model. Similar calculations were performed for the other complex structures and similar results were obtained for them.

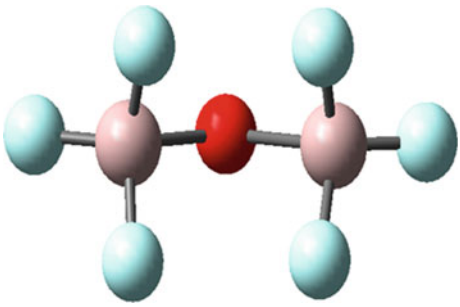

Fig. 2 $[Al_2OF_6]^{2-}$ before optimization

Results and Discussion

The calculated energy values of the four complexes are reported in Table 1.

According to this table, moving from 6-31 g to 6-311 ++g** basis set, i.e. adding polarization and diffusion functions to the basis set, reduces the computed energy and predicts further energy stabilization. Meanwhile, the addition of the second diffuse function has no effect. Based on the energy values, the following stability order is achieved:

$[Al_2O_2F_4]^{2-} < [Al_2OF_6]^{2-} < [Al_2O_2F_6]^{4-} < [Al_2OF_{10}]^{6-}$.

One of the interesting findings of Table 1 is that the solvent affects and stabilizes $[Al_2O_2F_6]^{4-}$ more than any other complex. Also, the solvent stabilizes the $[Al_2O_2F_4]^{2-}$ and $[Al_2OF_6]^{2-}$ complexes by 186.62 and 173.43 kJ mol^{-1} energy compared to the gas phase, respectively. As experiments declare, first $[Al_2OF_6]^{2-}$ complex forms and then $[Al_2O_2F_4]^{2-}$ would generate. Moreover, higher solubility is reported for $[Al_2O_2F_4]^{2-}$ [5]. Our observations verify these statements so that the solvent stabilizes $[Al_2O_2F_4]^{2-}$ more than $[Al_2OF_6]^{2-}$. In order to calculate the chemical shielding tensor of 17O nuclei, GIAO approach was used. The extent of isotropic chemical shielding was calculated by Gaussian package. The chemical shift of oxygen nuclei in $[Al_2O_2F_4]^{2-}$ and $[Al_2OF_6]^{2-}$ complexes was computed to be respectively 35.73 ppm and −7.4 ppm. Robert et al. [6] have experimentally found out that the chemical shift reduces from 25 ppm to 8 ppm, for $[Al_2O_2F_4]^{2-}$ and $[Al_2OF_6]^{2-}$, respectively. The differences between the experimental and theoretical values are attributed to the fact that the theoretical results are associated with gas phase calculations. Also, it should be noted that in the experimental medium, the two species coexist and the chemical shift values in the solvent phase are the average values regarding their simultaneous presence. Therefore, where X represents atomic fraction of oxygen in each complex. Further details and equations are discussed in Ref [7].

Table 1 Comparison the calculated energy values of the four complexes are reported

	$[Al_2OF_6]^2$	$[Al_2O_2F_4]^2$	$[Al_2O_2F_6]^{4-}$	$[Al_2OF_{10}]^{6-}$*
B3LYP/6-31g	−1159.587	−1035.017	−1234.074	−1559.600
B3LYP/6-311g**	−1160.017	−1035.391	−1234.541	−1560.225
B3LYP/6-311+g**	−1160.081	−1035.443	−1234.673	−1560.418
B3LYP/6-311++g**	−1160.081	−1035.443	−1234.673	−1560.418
B3LYP/6-311++g** (CPCM)	−1160.358	−1035.741	−1235.789	

References

1. Zhengping W, Qiyuan C, Zhoulan Y (2005) DFT and ab initio calculation on thermochemistry of $Al_6(OH)_{18}(H_2O)_x(x = 0 - 6)$, $Al(OH)_6^{3-}$, in *Light Metals*. College of Chemistry and chemical engineering
2. Gupta S, Zhang Y (2002) Modeling the solubility of alumina in the NaF-AlF_3 system at 1300 K. Light Metals
3. Levine IN, Learning P (2009) Quantum chemistry. Pearson Prentice Hall Upper Saddle River, NJ
4. Zhang Y, Wu X, Rapp RA (2003) Metal Mat Trans B 34:235–242
5. Wu Z-P, Chen Q-Y, Yin Z-L (2005) Light Metals 1:229–234
6. Robert E, Olsen J, Danek V, Tixhon E, Østvold T, Gilbert B (1997) J Phys Chem B 101:9447–9457
7. Lacassagne V, Bessada C, Florian P, Bouvet S, Ollivier B, Coutures J-P, Massiot D (2002) J Phys Chem B 106:1862–1868
8. Ektefa F, Anafche M, Hadipour NL (2011) Comput Theor Chem 977:1–8

Manganese Influence on Equilibrium Partition Coefficient and Phase Transformation in Peritectic Steel

Huabiao Chen, Mujun Long, Wenjie He, Dengfu Chen, Huamei Duan and Yunwei Huang

Abstract The equilibrium partition coefficient (k) affected by chemical component, phase constitution and temperature is a critical parameter related to solutes distribution during steel solidification. In this study, the effect of Mn on equilibrium partition coefficient and phase transformation was quantitatively analysed. A technique according to the relative amount of δ-Fe and γ-Fe to determine the equilibrium partition coefficients of solutes in L, δ-Fe, and γ-Fe three-phases coexistence zone was proposed. Results showed that Mn promotes the generation of γ-Fe and its effect on peritectic reaction zone is significant. The equilibrium partition coefficients were determined based on the phase change and relative amount of δ-Fe and γ-Fe according to the solidification paths which undergo difference phase coexistence zone. All of k_C^{δ}, k_{Si}^{δ}, $k_{Si}^{\delta+\gamma}$, k_P^{δ}, $k_P^{\delta+\gamma}$, k_S^{δ}, and $k_S^{\delta+\gamma}$ decrease with Mn increasing, while $k_C^{\delta+\gamma}$ increases due to solute Mn promote the generation of γ-Fe forming from peritectic reaction.

Keywords Equilibrium partition coefficient · Phase transformation
Solute interaction · Thermodynamic calculation

Introduction

Solute segregation is one of the most severe defects encountered in steel products. The root cause for it is solute redistribution, and which is closely related to the equilibrium partition coefficient (k) of solutes during solidification. k is a critical parameter showing the potential and diffusion direction of solute segregation in an

H. Chen · M. Long (✉) · W. He · D. Chen (✉) · H. Duan · Y. Huang
College of Materials Science and Engineering, Chongqing University, Chongqing 400044, China
e-mail: longmujun@cqu.edu.cn

D. Chen
e-mail: chendfu@cqu.edu.cn

The Minerals, Metals & Materials Society, *TMS 2018 147th Annual Meeting & Exhibition Supplemental Proceedings*, The Minerals, Metals & Materials Series,
https://doi.org/10.1007/978-3-319-72526-0_40

alloy solidification system [1]. Generally speaking, the lower k is, the more serious segregation it would be [2], such as sulfur and phosphorous, which have a strong tendency to segregation in steel [3]. Obviously, k is a key parameter which affects the solutes redistribution in mushy zone and closely relates to the accuracy of segregation calculation [4].

As we know, k actually depend on chemical components, phase constitution of mushy zone and temperature rather than being constants [5–7]. Ueshima et al. [8, 9] brought in phase transformation from δ-Fe to γ-Fe criterion based on the iron based binary phase diagram and discussed the solutes distribution in δ-Fe and γ-Fe. Zhu et al. [3] pointed out that the peritectic reaction does much effect on the segregation behavior of solutes due to the properties (diffusion and partition) of δ-Fe and γ-Fe are distinctly different. Additionally, You et al. [6, 7] developed a micro-segregation mold which employed temperature-dependence k, the solutes concentration profiles calculated form constants and temperature-dependence k exhibit significant differences. Even so, due to the lack of data, k evaluated from binary or ternary systems was usually assumed as constant and used in the microsegregation [3, 10] and macrosegregation [11, 12] predictions in multi-components steel.

In the previous studies, k of solutes in steel are nearly treated as constants. Besides, as for the phase transformation, from L → δ-Fe to L → γ-Fe, k of solutes in δ-Fe and γ-Fe are simply differentiated based on the peritectic point temperature. However, as the peritectic reaction occurring, the solidification path will undergoes a three-phases coexistence zone of L, δ-Fe, and γ-Fe, in which k of solutes between L, δ-Fe, and γ-Fe ($k^{\delta+\gamma}$) during steel solidification are scanty. Furthermore, He et al. [13] proposed the solute Mn causes a leftward shit of the peritectic point, solute Mn affects the peritectic reaction significantly, while solute Si has less impact on it. Predictably, the effect of Mn on k of solutes in steel is also significant.

In this paper, a thermodynamic calculation model for k of solutes in multi-components steel was established. Due to the harmful elements (S, P) and micro-alloying elements in peritectic steel maintained at low levels, only the solute Mn was selected to investigate the effect on k. The effects of solute Mn on the solidification path and the quantitative evolution of k with the changing of phase fraction were investigated. Furthermore, a technique to determine k of solutes in coexistence zone of L, δ-Fe, and γ-Fe three-phases is proposed. The evolution of k in three-phases coexistence zone and the effect of solute Mn on it are emphatically discussed.

Thermodynamic Model Description

For any multicomponent iron-based alloys, chemical potential of element i in solid (G_i^s) and liquid phases (G_i^L) mush be equivalent when the system reaches equilibrium status [14]. That is,

$$G_i^{0,S} + \mathrm{RTln}\left(\gamma_i^S w_i^S\right) = G_i^{0,L} + \mathrm{RTln}\left(\gamma_i^L w_i^L\right) \quad (1)$$

where w_i is the concentration (wt. pct.) of solute i. γ_i is activity coefficient. G_i^0 is chemical potential in standard state. Superscripts S and L denote solid and liquid phases, respectively. R is the gas constant and T is thermodynamic temperature.

Solving for the concentration ratio from Eq. (1), the formula for equilibrium partition coefficient of solute i is obtained [14]. That is,

$$k_i = \frac{\gamma_i^L}{\gamma_i^S} exp\left[\left(G_i^{0,S} - G_i^{0,L}\right)/RT\right] \quad (2)$$

The equilibrium partition coefficient of solute i between δ-Fe and L (k_i^δ), or between γ-Fe and L (k_i^γ) can be calculated from Eq. (2). As for the three-phases (L, δ-Fe, and γ-Fe) coexistence zone, $k_i^{0,\delta+\gamma}$ can be calculated from Eq. (3) [15].

$$k_i^{0,\delta+\gamma} = \frac{m_\delta}{m_\delta + m_\gamma} k_i^{0,\delta} + \frac{m_\gamma}{m_\delta + m_\gamma} k_i^{0,\gamma} \quad (3)$$

where m_δ and m_γ are mass of δ-Fe and γ-Fe at the same temperature, respectively.

This thermodynamic calculation model of k for steel were processed with the Equilib module of FactSage 6.3, in which the database (FSstel) is selected [16]. Sone more details and the validity about this thermodynamic model are available in our previous production [15]. In this present work, the evolution of k with δ-Fe and γ-Fe fraction for a series samples with different Mn content are quantitatively analyzed basing on the steel solidification path.

Results and Discussion

Phase Diagram and Solidification Path

The main composition of sample series with different Mn content are listed in Table 1. The Fe-C phase diagram of sample S1 and S6 were calculated and shown in Fig. 1, indicating that the effect of Mn on the solidification path is significant. As the results shown, the solidification paths of both sample S1 and sample S6 undergo the coexistence zones of L plus δ-Fe and L plus δ-Fe plus γ-Fe in sequence. However, unlike sample S1, as Mn added into steel, the liquidus and solidus temperature lower, and the inverted triangular zone of peritectic reaction is shifted toward the low-carbon end of phase diagram, which agrees well with the results reported by He [13]. In addition, due to the leftward shift, the three-phases

Table 1 The main chemical composition of selected steels (wt%)

Sample series	C	Si	Mn	P	S
S1	0.1	0.25	0	0.012	0.006
S2	0.1	0.25	0.35	0.012	0.006
S3	0.1	0.25	0.85	0.012	0.006
S4	0.1	0.25	1.35	0.012	0.006
S5	0.1	0.25	1.85	0.012	0.006
S6	0.1	0.25	2.00	0.012	0.006
S7	0.1	0.25	2.35	0.012	0.006

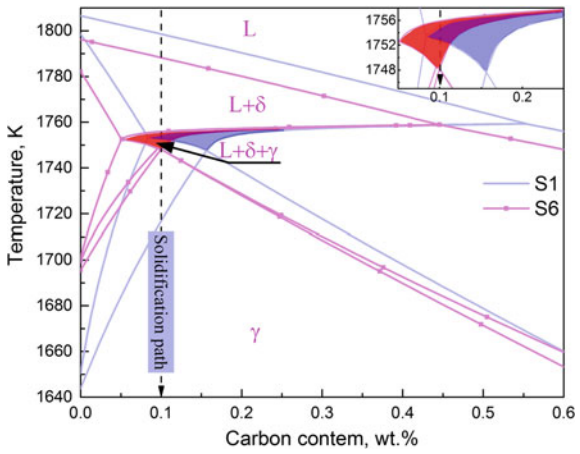

Fig. 1 The phase diagram and solidification path of sample S1 and sample S6

coexistence zone of L, δ-Fe and γ-Fe of S6 is enlarged comparing with that of S1. Therefore, k of solutes in steel should be quantitatively determined basing on the change of phase (L, δ-Fe, and γ-Fe) which is affected by the Mn content in steel.

Equilibrium Partition Coefficient Versus Phase Fraction

The evolution of L, δ-Fe, γ-Fe and k_C during sample S2 solidification are shown in Fig. 2. It is obvious that L begins to transform into δ-Fe since the temperature decrease to 1797 K. In the coexistence zone of L and δ-Fe, C distributes between δ-Fe and L, and k_C^{δ} is almost constant. As the temperature falls below 1755 K, the peritectic reaction (L + δ-Fe → γ-Fe) occurs and the γ-Fe forms, which results in δ-Fe content decreasing, while γ-Fe content increasing. In the three-phases coexistence zone, C distributes between δ-Fe, γ-Fe, and L, and $k_C^{\delta+\gamma}$ increases sharply due to the increasing generation amount of γ-Fe. As the temperature reduces to 1753 K, S2 system solidifies completely.

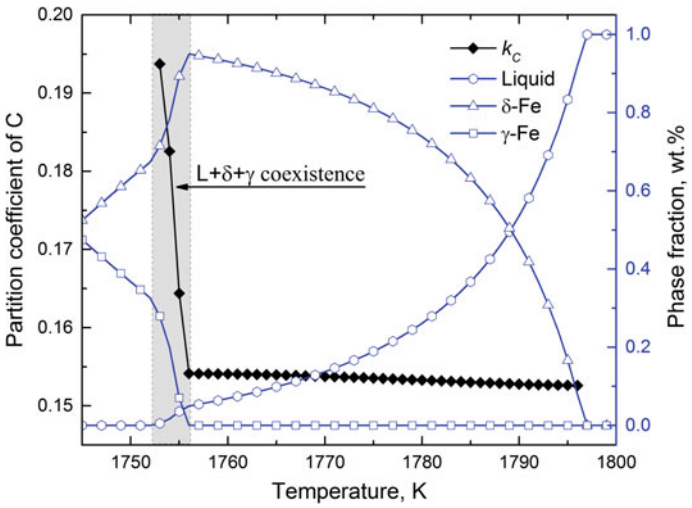

Fig. 2 Evolution of phase fraction of L, δ-Fe, γ-Fe, and k_C in S2 system

The evolutions of k_{Si}, k_{Mn}, k_P, and k_S for S2 system are showed in Fig. 3. As shown in Fig. 3a, k_{Si}^{δ} increases with decreasing temperature. When the temperature falls below from 1796 to 1756 K, k_{Si}^{δ} increases from 0.611 to 0.691, increasing by 13.1%. Obviously, the influence of temperature on k_{Si}^{δ} is not ignorable. In the three-phases coexistence zone, due to the generation of γ-Fe, $k_{Si}^{\delta+\gamma}$ has a slightly reduction with the fact that k_{Si}^{γ} is slightly less than k_{Si}^{δ} [4]. The evolution of k_{Mn} is shown in Fig. 3b. In contrast to solute Si, k_{Mn}^{δ} is increased with decreasing temperature. In the three-phases coexistence zone, $k_{Mn}^{\delta+\gamma}$ increases sharply due to the fact that k_{Mn}^{γ} is greater than k_{Mn}^{δ} [4]. From Fig. 3c and d, it is obviously that k_P, and k_S shows the similar variation trend with phase fraction. Both k_P^{δ} and k_S^{δ} are increased slightly with temperature decreasing, while in three-phases coexistence zone, $k_P^{\delta+\gamma}$ and $k_S^{\delta+\gamma}$ decrease rapidly. This is because k_P^{δ} and k_S^{δ} are roughly around two times of k_P^{γ} and k_S^{γ}, respectively.

Effect of Mn Content on Phase Fraction and Equilibrium Partition Coefficient

The evolutions of k_C in Fe-0.2%C, Fe-0.2%C-1%Mn, and Fe-0.2%C-2%Mn systems are shown in Fig. 4. It is obvious that the addition of Mn will lead to the reduction of k_C either in δ-Fe or γ-Fe, and the extent of the reduction enlarges with increasing the amount of Mn content. This is because the interaction coefficient between solutes C and Mn (ε_C^{Mn}) is negative, which will lead to the activity coefficient of C in

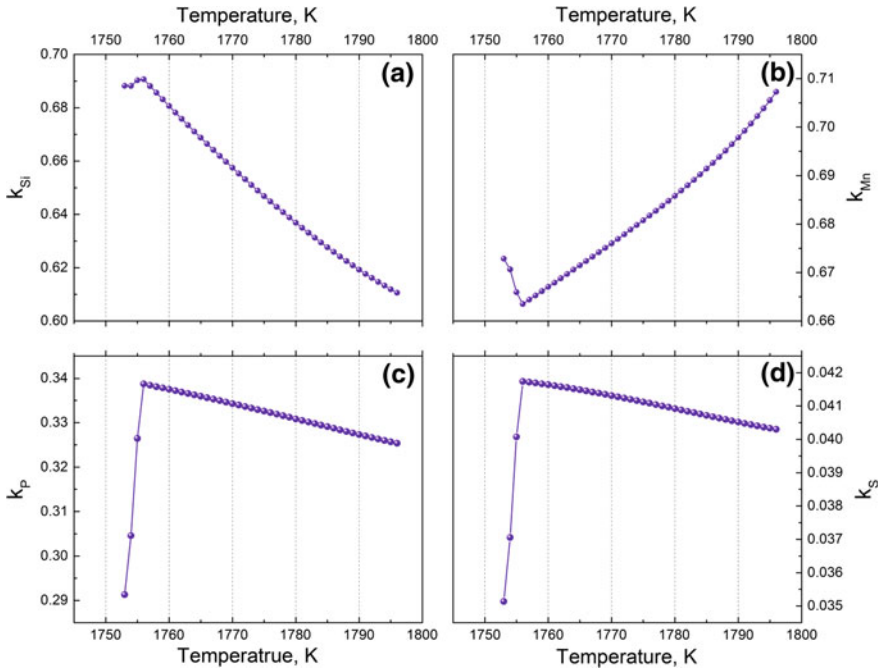

Fig. 3 Evolution of **a** k_{Si}, **b** k_{Mn}, **c** k_P, and **d** k_S in S2 system

L (γ_C^L) decreasing. In order to keep the balance of chemical potential of solute C between liquid and solid phase in the solidification system, the concentration of solute C in liquid will be increasing spontaneously, which result in the reduction of k_C.

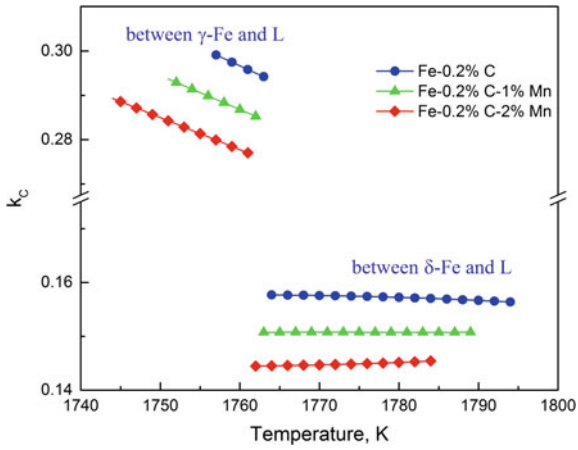

Fig. 4 The influence of Mn on k_C in δ-Fe and γ-Fe

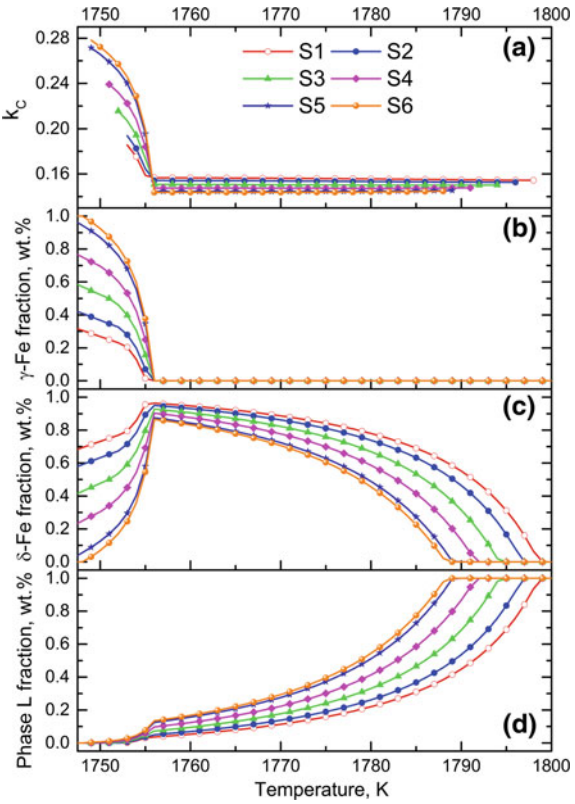

Fig. 5 The influence of Mn content in steel on k_C and phases fraction: **a** k_C, **b** phase fraction of γ-Fe, **c** phase fraction of δ-Fe, **d** phase fraction of L

The evolution of k_C with phase fraction of L, δ-Fe and γ-Fe in samples (from S1 to S6) with different Mn contents are shown in Fig. 5. As the results showing in Fig. 5a, k_C^{δ} in these samples decreases with increasing Mn content. This agrees with the point that the addition of Mn will lead to the reduction of k_C. Instead, in the three-phases coexistence zone, $k_C^{\delta+\gamma}$ increase with increasing the addition amount of Mn. This phenomenon is closely related to the relative amount of δ-Fe and γ-Fe in the three-phases coexistence zone. As the peritectic reaction occurring, showing in Fig. 5a–c, L and δ-Fe transform into γ-Fe, and the generation amount of γ-Fe increases with increasing Mn content. In the three-phases coexistence zone, $k_C^{\delta+\gamma}$ is mainly related to the amount of γ-Fe for these samples. The greater the amount of γ-Fe, the greater the $k_C^{\delta+\gamma}$ is.

As the results showing in Fig. 6, the average values of $k_C^{\delta+\gamma}$, δ-Fe fraction and γ-Fe fraction in three-phases coexistence zone are extracted alone to quantitatively analyze the evolution of $k_C^{\delta+\gamma}$. The Mn addition promotes the generation amount of γ-Fe from the peritectic reaction. Comparing with the interaction of C and Mn (ε_C^{Mn}), the effect of the γ-Fe amount increasing with Mn content on $k_C^{\delta+\gamma}$ is more

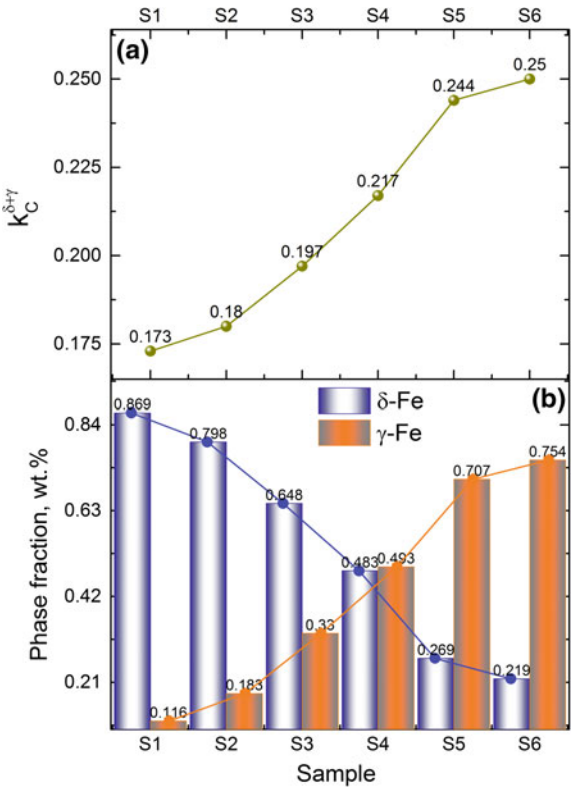

Fig. 6 **a** The evolution of average $k_C^{\delta+\gamma}$, **b** the variation of phase fraction of δ-Fe and γ-Fe in three-phases coexistence zone

significant due to the fact that k_C^{γ} is roughly around two times of k_C^{δ}. And this is the reason why $k_C^{\delta+\gamma}$ increase with increasing Mn content in the three-phases coexistence zone.

The influence of Mn content on k_{Si}, k_{Mn}, k_P, and k_S are shown in Fig. 7. Due to the fact that ε_{Si}^{Mn} is negative, Mn added into steel will leads to k_{Si} decreasing. In contrast to solute Si, k_{Mn} increases with increasing Mn content, which means the self-interaction of solute Mn is positive. The effect of Mn on k_P, and k_S is similar. Both of ε_P^{Mn} and ε_S^{Mn} are negative, which means k_P^{δ} and k_S^{δ} decrease with increasing Mn content. In the three-phases coexistence zone, $k_P^{\delta+\gamma}$ and $k_S^{\delta+\gamma}$ decrease very sharply with the fact that k_P^{γ} and k_S^{γ} are roughly a half of k_P^{δ} and k_S^{δ}. From another perspective, this indicates the effect of phase constitution of mushy zone on k is more significant than the solutes interaction.

The quantitative relation among average k, phase constitution and Mn content in the coexistence zones of L plus δ-Fe and L plus δ-Fe plus γ-Fe are shown in Fig. 8. As the addition of Mn increasing from 0 to 2.0 wt%, the average k_{Si}^{δ} decrease from 0.669 to 0.561, the deviation is 16.1%. And the average $k_{Si}^{\delta+\gamma}$ decrease from 0.719

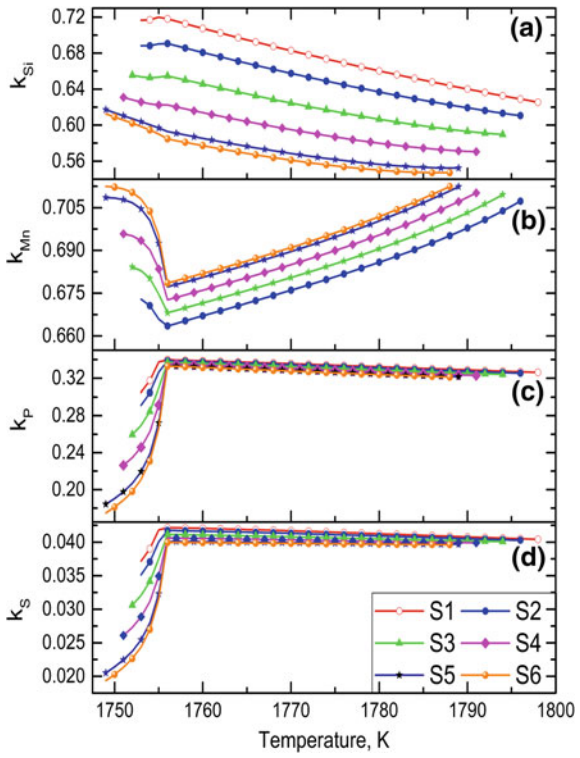

Fig. 7 The influence of Mn content in steel on **a** k_{Si}, **b** k_{Mn}, **c** k_P, and **d** k_S

to 0.602, decreasing by 16.3%. Therefore, the influent of Mn content on k_{Si} is not ignorable. As the addition of Mn increasing from 0.35 to 2.0 wt%, average k_{Mn}^{δ} and $k_{Mn}^{\delta+\gamma}$ increase as low as 1.6% and 5.7%, respectively. The influence of Mn on itself partition coefficient is almost ignorable. It is obvious that the reduction of average k_P^{δ} with increasing Mn content is negligible. However, as the peritectic reaction occurring, the average $k_P^{\delta+\gamma}$ reduces from 0.32 to 0.207 when the addition of Mn increasing from 0 to 2.0 wt%, the deviation is 35.3%, which is very significant. Similar to P, $k_S^{\delta+\gamma}$ reduces by 39.4% when the addition of Mn increasing from 0 to 2.0 wt%. The effect of solute Mn on k is significant in peritectic steel because it promotes the generation of γ-Fe from peritectic reaction.

Peritectic Reaction with Liquid Phase Residual

As mention above, solute Mn in steel promotes the generation of γ-Fe while the peritectic reaction occurs and the effect on k is significant. In the peritectic reaction

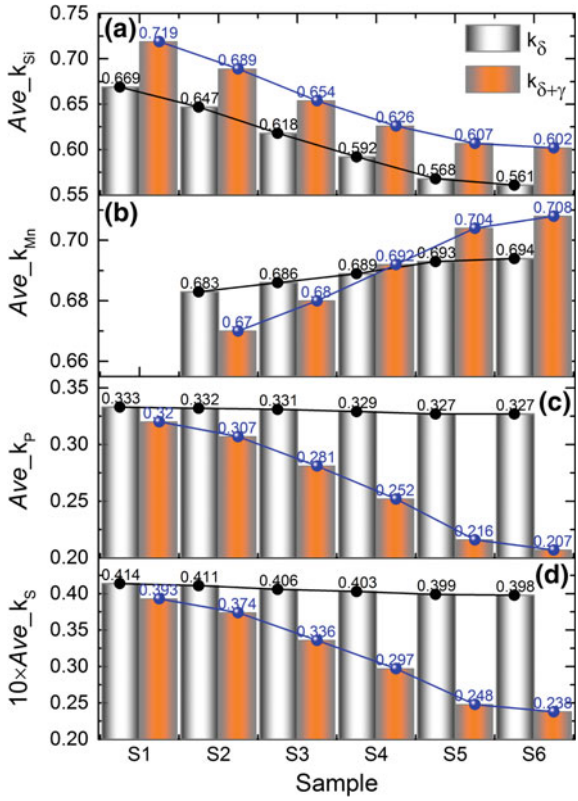

Fig. 8 Average k of solutes in two-phases (δ-Fe and L) and three-phases coexistence zone: **a** Ave_k_{Si}, **b** Ave_k_{Mn}, **c** Ave_k_P, **d** Ave_k_S

zone of samples (from S1 to S6), L and δ-Fe transform into γ-Fe. At the end of the peritectic reaction, L is exhausted and these systems solidify completely. As the Mn content in steel further increasing, the solidification path has a big change. As the results shown in Fig. 9a, after the peritectic reaction in S7 system, phase L is residual and the residual L further transform into γ-Fe with the decreasing of temperature. In short, L plus δ-Fe, L plus δ-Fe plus γ-Fe, and L plus γ-Fe coexist in sequence during the solidification of S7. For this case, k of solutes in steel should be strictly determined according to the solidification path. As the results shown in Fig. 9b, k_C further increases after the peritectic reaction.

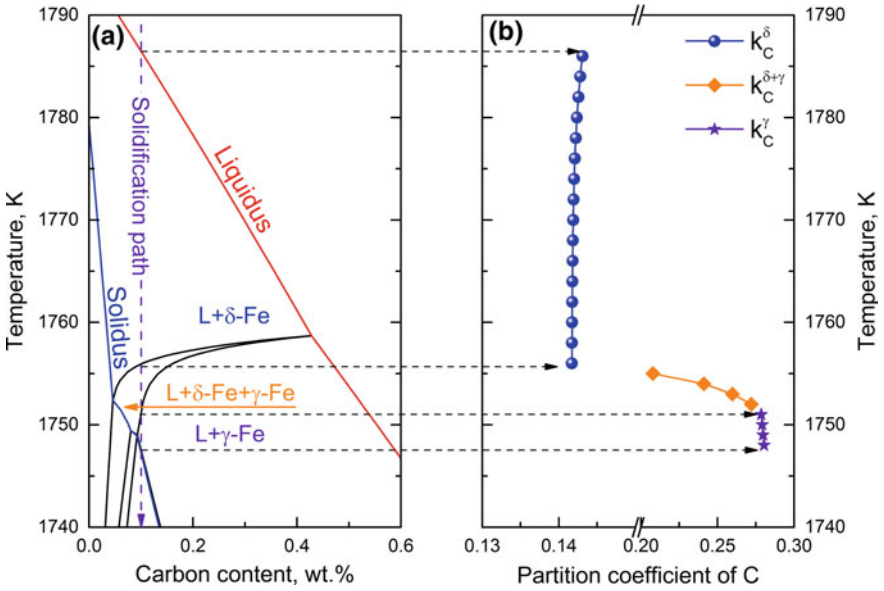

Fig. 9 **a** Solidification path of sample S7, **b** evolution of k_C in sample S7

Conclusions

- Mn addition results in the peritectic reaction zone shifting toward the low-carbon end of phase diagram.
- The solute Mn promotes the generation of γ-Fe from peritectic reaction. k should be strictly determined according to solidification path.
- A technique based on the phase relative amount in the three-phases coexistence zone of L, δ-Fe and γ-Fe to determine k is proposed.
- The effect of phase constitution on k_C, k_P, and k_S is more significant than the solute interaction of Mn, while the effect on k_{Si} and k_{Mn} is weak.

Acknowledgements The authors would like to thank the Natural Science Foundation of China (NSFC) for the financial support (Project NO.: 51504048; 51374260; 51611130062).

References

1. Schneider MC, Beckermann C (1995) Formation of macrosegregation by multicomponent thermosolutal convection during the solidification of steel. Metall Mater Trans A 26(9):2373–2388

2. Sung PK, Poirier DR (1999) Liquid-solid partition ratios in nickel-base alloys. Metall Mater Trans A 30(8):2173–2181
3. Wang WL, Zhu MY, Cai ZZ, Luo S, Ji C (2012) Micro-segregation behavior of solute elements in the mushy zone of continuous casting wide-thick slab. Steel Res Int 83(12):1152–1162
4. Fujda M (2005) Centerline segregation of continuously cast slabs influence on microstructure and fracture morphology. JOM 15(2):45–51
5. Valdes J, Shang SL, Liu ZK, King P, Liu XB (2010) Quenching differential thermal analysis and thermodynamic calculation to determine partition coefficients of solute elements in simplified Ni-base superalloys. Metall Mater Trans A 41A(2):487–498
6. You D, Bernhard C, Wieser G, Michelic S Microsegregation model with local equilibrium partition coefficients during solidification of steels. Steel Res Int 87(7):840–849
7. You D, Bernhard C, Michelic S, Wieser G, Presoly P (2016) On the modelling of microsegregation in steels involving thermodynamic databases. In: Paper presented at IOP conference series: materials science and engineering
8. Matsumiya T, Kajioka H, Mizoguchi S, Ueshima Y, Esaka H (1984) Mathematical-analysis of segregations in continuously-cast slabs. T Iron Steel I Jpn 24(11):873–882
9. Ueshima Y, Mizoguchi S, Matsumiya T, Kajioka H (1986) Analysis of solute distribution in dendrites of carbon-steel with delta-gamma-transformation during solidification. Metall Mater Trans B 17(4):845–859
10. Won YM, Thomas BG (2001) Simple model of microsegregation during solidification of steels. Metall Mater Trans A 32(7):1755–1767
11. Aboutalebi MR, Hasan M, Guthrie RIL (1995) Coupled turbulent-flow, heat, and solute transport in continuous-casting processes. Metall Mater Trans B 26(4):731–744
12. Li J, Wu MH, Ludwig A, Kharicha A (2014) Simulation of macrosegregation in a 2.45-ton steel ingot using a three-phase mixed columnar-equiaxed model. Int J Heat Mass Trans 72:668–679
13. Xu JF, He SP, Wu T, Long X, Wang Q (2012) Effect of elements on peritectic reaction in molten steel based on thermodynamic analysis. ISIJ Int 52(10):1856–1861
14. Battle TP, Pehlke RD (1989) Equilibrium partition coefficients in iron-based alloys. Metall Mater Trans B 20(2):149–160
15. Chen H, Long M, Cao J, Chen D, Liu T, Dong Z (2017) Phase transition of peritectic steel Q345 and its effect on the equilibrium partition coefficients of solutes. Metals 7(8):288–296
16. Bale CW, Bélisle E, Chartrand P, Decterov SA, Eriksson G, Hack K, Jung IH, Kang YB, Melançon J, Pelton AD, Robelin C, Petersen S (2009) FactSage thermochemical software and databases—recent developments. Calphad 33(2):295–311

Mathematical Modeling on the Fluid Flow and Desulfurization During KR Hot Metal Treatment

Chao Fan, Alexis GoSa, Lifeng Zhang, Qingcai Liu and Dayong Chen

Abstract In the current study, the fluid flow and desulfurization in a 160 t KR ladle were simulated using FLUENT combined with user-developed subroutines. The velocity distribution of the hot metal, the motion and distribution of CaO particles, and the desulfurization rate of the hot metal were calculated. With the increase of rotation speed of the impeller, the velocity of CaO particles increased as well, which resulted in the increase of desulfurization efficiency. The desulfurization rate varied at different positions of the ladle, with a higher rate in the higher speed zone and slower in the dead zone. The desulfurization rate increased slightly with growing rotation speed of the impeller. When the particle diameter increased from 1.3 to 2 mm, the desulfurization rate decreased approximately 3 or 4 times.

Keywords Hot-metal pretreatment · KR · Desulfurization · Desulfurizer particle · Fluid flow · Mathematical modeling

Introduction

As demand for high-quality steel increases, high efficiency of hot metal desulfurization has become one of main objectives in the steelmaking process. Sulfur which is harmful in most steel always leads to the crack on the surface of steel when the temperature is very high [1]. Almost all of the sulfur in hot metal can be removed by hot metal pretreatment in the process of steelmaking. Kambara Reactor (KR) desulfurization is widely used as a high efficiency and low cost desulfurization

C. Fan · Q. Liu · D. Chen
Chongqing University, Chongqing, China
e-mail: fanchao@cqu.edu.cn

C. Fan · A. GoSa · L. Zhang (✉)
University of Science and Technology Beijing, Beijing, China
e-mail: zhanglifeng@ustb.edu.cn

The Minerals, Metals & Materials Society, *TMS 2018 147th Annual Meeting & Exhibition Supplemental Proceedings*, The Minerals, Metals & Materials Series,
https://doi.org/10.1007/978-3-319-72526-0_41

method [2, 3]. During KR stirring process, the CaO particles are involved into hot metal by the cross impeller which is rotating at a high speed under the liquid level [4]. The desulfurization reaction between sulfur and CaO particles that occurred in hot metal was investigated by CFD software, because the fluid flow and particles distribution in invisible hot metal internal were invisible only by the experiment. In the current study, the multi-phase flow and the distribution of added CaO particle during KR stirring process were firstly discussed. Then, the characteristics of desulfurization reaction within the metal steel was investigated with the in-house user-developed subroutines. Finally, the effects of rotation speed of the impeller, immersion depth of impeller, and size of CaO particles on the desulfurization reaction were compared.

Models

Calculation Domain and Mesh System

A schematic of calculation domain and meshes of the current model are shown in Fig. 1. In order to simplify the calculation and avoid the convergence problem caused by complex mesh, the bottom of hot metal ladle was regarded as flat which was round in fact. The impeller was cross shape and the diameter of connecting rod was 150 mm. The mesh type was unstructured hexahedral mesh with a total mesh number of about 400,000. The sizes of the 160 t hot metal ladle and the impeller are showed in Table 1 and Table 2, respectively [5].

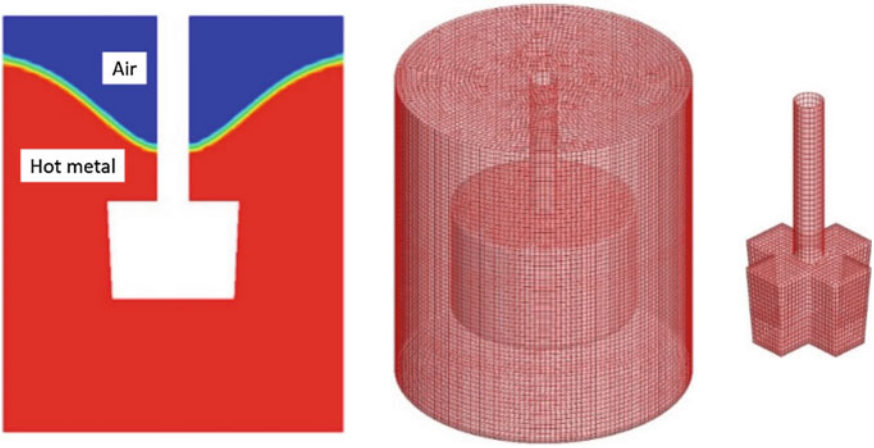

Fig. 1 Schematic of calculation domain and mesh of the current model

Table 1 160 t hot metal ladle size [5]

Diameter of top (mm)	Diameter of bottom (mm)	Height (mm)	Liquid level (mm)
3200	3200	3600	3000

Table 2 Impeller size [5]

	Diameter (mm)	Width (mm)	Height (mm)
Top	1240	470	850
Bottom	1140	390	

Models Used and Boundary Conditions

The turbulence model used in the calculation was standard $k-\varepsilon$ model. In order to obtain the vortex surface distribution, multiphase flow VOF model was used [6]. The desulfurizer particles were added via a discrete phase model (DPM) [7]. The diameter of all the particles was 1 mm. The diffusion of S in hot metal and the desulfurization of CaO particles were performed by solving UDS equations [8].

In the stirring process of KR desulfurization, CaO particles were added into the hot metal to react with sulfur. The main reaction was shown as Eq. 1.

$$CaO(s) + [S] = CaS(s) + [O] \tag{1}$$

According to chemical reaction kinetics, the desulfurization rate can be expressed as Eq. 2 by assuming that the rate-controlling step is the mass transfer of [S] in hot metal.

$$-\frac{d[S]}{dt} = -k \cdot \frac{A}{V_m} \cdot [S] \tag{2}$$

where, k is mass transfer rate, A (m^2) is the interfacial area that can be expressed as the sum of surface area of all particles, V_m is hot metal volume (m^3), and $[S]$ (ppm) is the sulfur concentration in hot metal. The mass transfer rate, k, was obtained by Eq. 3, which was proposed by Nakanishi et al. [9].

$$k = 0.82 \times D_s^{0.5} \times v_t^{0.5} \times \left(\frac{D_t}{2}\right)^{-0.5} \tag{3}$$

where D_s is the diffusion coefficient of S in hot metal (= 2.58 × 10^{-9} m^2/s), v_t is the relative velocity of particle compared with hot metal (m/s), and D_t is the diameter of particles (m). Desulfurization behaviors during KR stirring process were estimated by Eqs. (1)–(3).

Table 3 Materials physical properties [11, 12]

	Hot metal	CaO particle	Air
Density (kg/m^3)	7100	2718	1.225
Viscosity (Pa · s)	0.0065	–	1.789×10^{-5}
Molar mass (g/mol)	56	56	29

The boundary conditions were set as follows:

a. The bottom and side wall of the ladle were non-slip walls;
b. The upper outlet of the ladle was a plane without shear stress;
c. The impeller wall was a rotation wall;
d. The rotation of hot metal and the stirrer were calculated by the multiple reference frame model (MRF) [10].

The properties of materials used in the calculation are shown in Table 3 [11, 12].

Results and Discussion

Flow Field

After the flow was stable, the streamline and the distribution of flow velocity under the condition of the rotation speed was 120 rpm (revolution per minute) are presented in Fig. 2. As the figure shows, the flow of hot metal was divided into two parts of the upper and lower circulation. The flow velocity of hot metal at different

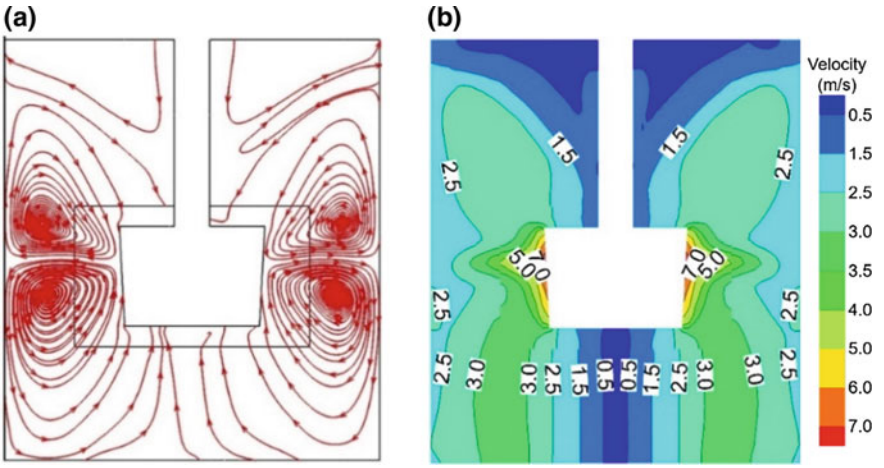

Fig. 2 Predicted velocity field with the rotation speed of 120 rpm

positions is very different. It can be seen that the flow velocity of hot metal is inversely proportional to the distance from the stirring impeller. The flow velocity besides the impeller reaches 7.0 m/s while near the wall it is below 2.5 m/s. The movement of hot metal under the impeller is much worse than other positions. In this paper, the zone in which the flow velocity of hot metal is below 0.5 m/s is defined as dead zone. During the hot metal pretreatment, the dead zone always leads to an increase of sulfur content after the desulfurization is finished.

Distribution of CaO Particles

Figure 3 shows the distribution of 20000 particles at different calculation times after adding into the hot metal, when the rotation speed of the impeller was 100 rpm. It can be seen that under the stirring effect from the impeller, the added particles moved with the hot metal, and at 60 s, the distribution of CaO particles was dispersed well within the hot metal. As the main desulfurizer, the movement and

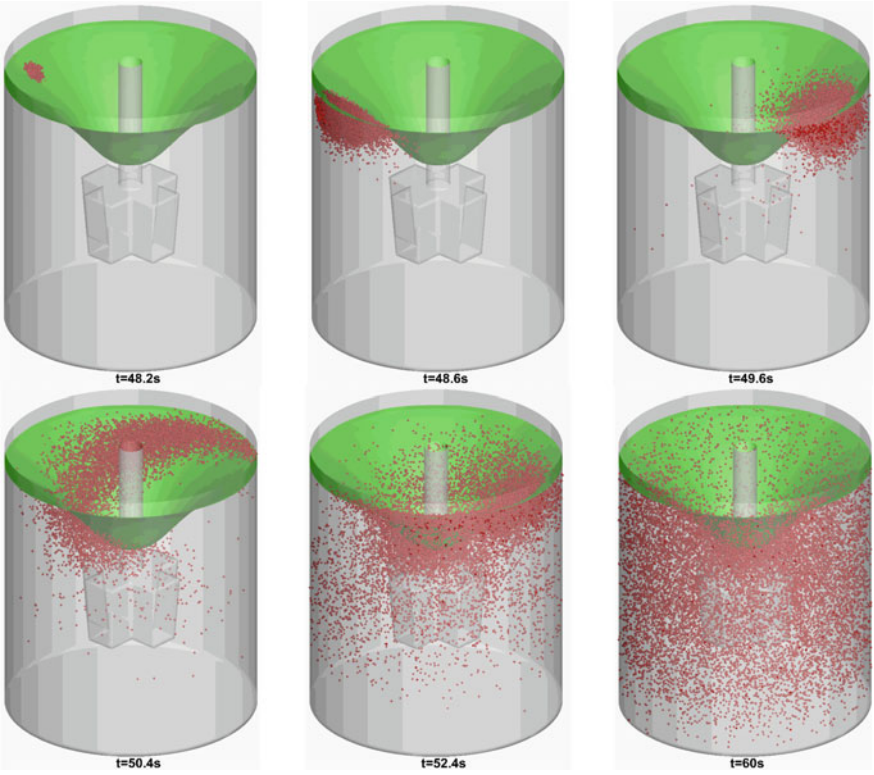

Fig. 3 Predicted particle distribution at different moments

distribution of the CaO particles in the hot metal have significant effect on the desulfurization rate. It is obvious that the CaO particles were moving with hot metal, so the movement situation of CaO particles can be optimized by the optimization of velocity field.

Desulfurization Process

The variation of sulfur content in the hot metal after the injection of CaO particles is shown in Fig. 4, in which the rotation speed of impeller was 100 rpm and the initial sulfur content was 600 ppm. As the figure shows, with the addition of CaO particles, the desulfurization reaction occurred in the hot metal. Figure 5 shows the

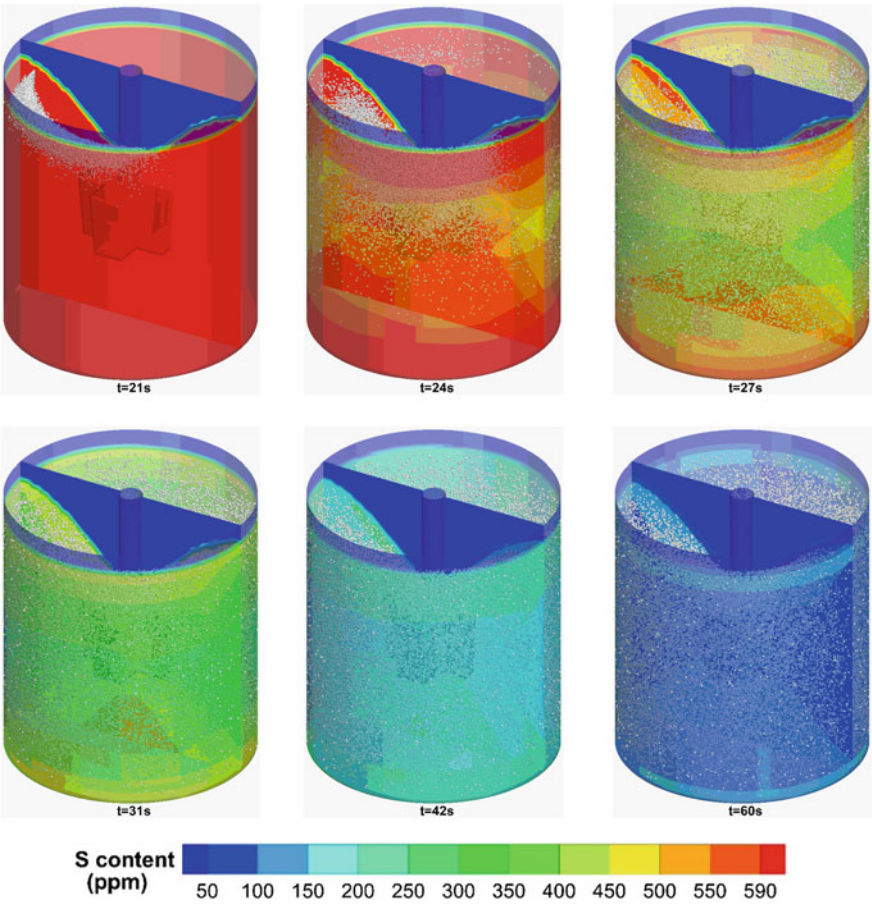

Fig. 4 Predicted sulfur content at different moments

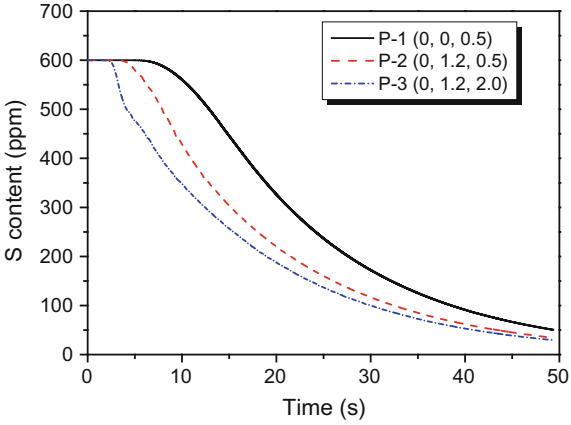

Fig. 5 Predicted change curve of sulfur content at different positions

change of sulfur content monitored in three positions. Obviously, the desulfurization rate at P-3 was much higher than P-1. The reason for this phenomenon is that P-1 is in the dead zone where the flow is the worst in the ladle. On the contrary, P-3 is besides the impeller where the stirring is much stronger than other positions in the ladle. In combination with Eq. (3), it can be seen that the rate of desulfurization was increased due to the high stirring strength near the impeller and the faster rate of hot metal regeneration.

Effect of Parameters on Desulfurization

In this paper, the desulfurization rate under different conditions were simulated, respectively. Figure 6 shows the desulfurization results with different rotation speeds (under the immersion depth of 1.85 m). From the result, it indicated that the

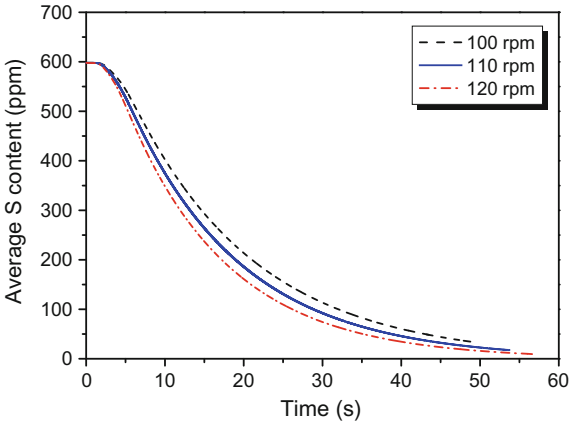

Fig. 6 Predicted change curve of average desulfurization rate with different rotational speed. The immersion depth is 1.85 m

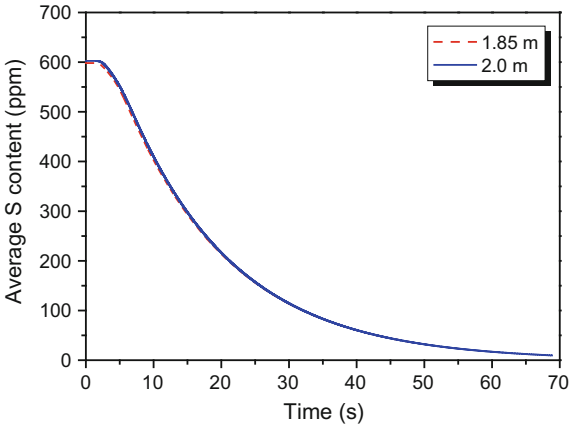

Fig. 7 Predicted change curve of average desulfurization rate with different immersion depths. The rotation speed is 100 rpm

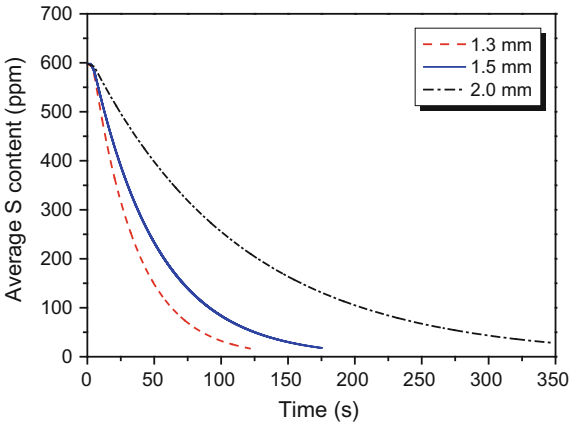

Fig. 8 Predicted change curve of average desulfurization rate with different particle sizes. The rotation speed is 100 rpm. The immersion depth is 1.85 m

desulfurization rate was slightly increased by the increase of rotation speed. That is because the desulfurization rate is not directly effected by the rotation speed, but by the relative velocity of particles compared with hot metal. The increasing rotation speed has a little effect on the relative velocity.

The results of desulfurization rate with different immersion depths and particle sizes are shown in Fig. 7 and Fig. 8, respectively. As Fig. 7 shows, the increasing of immersion depth has no effect on the desulfurization rate. This is because with the increasing of immersion depth, the desulfurization rate of the lower part of the ladle was accelerated, but at the same time the desulfurization rate of the upper part of the ladle was decreased, resulting in no change in the overall desulfurization rate. Figure 8 shows the relationship between the desulfurization rate and particle size. Here, three different diameters of CaO particles were calculated as a contrast. As the

result shows, the desulfurization rate was greatly effected by the particle size. When the particle diameter increased from 1.3 to 2.0 mm, the overall desulfurization efficiency reduced by 3 times mainly due to the surface area reduction of particles.

Conclusions

The KR desulfurization process in hot metal under different conditions were investigated by CFD. The conclusions are summarized as follows.

(1) During KR stirring desulfurization process in the ladle, the flow of hot metal was greatly effected by the rotation speed.
(2) The movement and dispersion of CaO particles were simulated by DPM model. After the desulfurizer was added into the ladle, it can be well dispersed in the hot metal. The desulfurization reaction between the CaO particles and the S in hot metal was also evident.
(3) Desulfurization behavior was simulated using the reaction model. The results obtained show that the increasing of rotation speed and immersion depth have a little effect on the desulfurization rate. It is a significant method to improve the desulfurization rate by controlling the CaO particle size.
(4) The simulation of the KR desulfurization process seems to be feasible and parameter studies give plausible results. Nevertheless, some important phenomena like aggregation of the desulfurizer have not be considered so far. Therefore, it should be careful to analyze simulation results. Further investigations should incorporate these effects in order to achieve more realistic predictions.

Acknowledgements The authors are grateful for support from the National Science Foundation China (Grant No. 51504020 and No. 51404019), Beijing Key Laboratory of Green Recycling and Extraction of Metals (GREM), the Laboratory of Green Process Metallurgy and Modeling (GPM^2) and High Quality steel Consortium (HQSC) at the School of Metallurgical and Ecological Engineering at University of Science and Technology Beijing (USTB); The authors are also grateful for support from Chongqing Key Technology Innovation of Industries (cstc2016zdcy-ztzx20006), Chongqing Social Technology Innovation Foundation (cstc2016shmszx20015), China.

References

1. Yao N, Xing C, Li SX (2011) KR desulfurization effect of hot metal pretreatment. J Mater Metall 10(2):93–95
2. Yang SS, Jia M, Wang H (2009) Brief introduction of KR hot stirring pretreatment process. Bao-Steel Technol 35(1):85–87
3. Huang CY (2013) KR stirring desulfurization process. Met World 1(6):56–59

4. Koichi T, Keita U, Hiroyuki S (2012) Influence of solid CaO and liquid slag on hot metal desulfurization. ISIJ Int 52(1):10–17
5. Gao YL (2012) Numerical simulation of molten iron flow in molten iron desulphurization by KR. Sci Technol Get Rich Guide 1(9):377–378
6. Long P (2013) Numerical investigation on kinetics of desulfurization by mechanical mixing of hot metal. PhD thesis, Huazhong University of Science and Technology
7. Zhang LF, Wang YF, Zuo XJ (2008) Flow transport and inclusion motion in steel continuous-casting mold under submerged entry nozzle clogging condition. Metall Mater Trans B 39(4):534–550
8. Lou WT, Zhu MY (2014) Numerical simulation of desulfurization behavior in gas-stirred systems based on computation fluid dynamics–simultaneous reaction model (CFD–SRM) coupled model. Metall Mater Trans B 45(5):1706–1722
9. Yoshie N, Ikuhiro S, Naoki K (2013) Aggregation behavior of desulfurization flux in hot metal desulfurization with mechanical stirring. ISIJ Int 53(8):1411–1419
10. Cao MJ, Yang FL, Wang HZ (2011) Numerical simulation of turbulent flow in a stirred tank. Drying Technol Equip 9(4):191–199
11. Liu P (2010) KR mechanical desulfurization stirrer inside the fluid flow characteristics. PhD thesis, Northeastern University
12. Stefan P, Philipp G (2002) CFD, a design tool for a new hot metal desulfurization technology. Appl Math Model 26(2):337–350

Part XVII
Coupling Experiments and Modeling to Understand Plasticity and Failure

In-situ Characterization of Microstructural Damage in QP980 Steel

Diyar Salehiyan, Javad Samei and David S. Wilkinson

Abstract During deformation of a steel, retained austenite can transform to martensite through transformation induced plasticity, thereby enhancing elongation to failure. However, obtaining high amounts of retained austenite in the final microstructure is challenging. The quench and partitioning (Q&P) heat treatment has been proposed as a cost-effective solution for stabilization of austenite at ambient temperatures. In this paper, a commercial QP980 steel was investigated by SEM-based in-situ tensile testing to determine micromechanisms of damage during plastic deformation. Results show that ferrite and martensite deform simultaneously and cracks are initiated at both phases. The martensite phase in QP980 steel shows a considerable amount of deformation. However, cracking of the blocky retained austenite happens from a very early stage of necking. X-ray computed tomography shows that most of the damage is found very close to the fracture surface.

Keywords Damage micromechanisms · In-situ tensile test · Q&P steel
X-ray tomography

Introduction

In recent years intensive investigation on advanced high strength steels has been motivated by the need to decrease vehicle weight and fuel consumption without sacrificing occupant safety [1–3]. The quench and partitioning process is one of the most innovative and promising heat treatments leading to the development of advanced high strength steels with an interesting combination of strength and ductility. This heat treatment approach can be applied to a variety of steels to produce microstructures containing carbon depleted martensite, carbon enriched retained austenite, as well as ferrite in the case of partial austenitization [4, 5].

D. Salehiyan (✉) · J. Samei · D. S. Wilkinson
Department of Materials Science and Engineering, McMaster University, Hamilton, ON L8S4L8, Canada
e-mail: salehiyd@mcmaster.ca

The Minerals, Metals & Materials Society, *TMS 2018 147th Annual Meeting & Exhibition Supplemental Proceedings*, The Minerals, Metals & Materials Series,
https://doi.org/10.1007/978-3-319-72526-0_42

Bainite transformation may also occur during quench and partitioning heat treatments because of the proximity of the partitioning temperature to the bainite transformation region [6]. The Q&P heat treatment starts with partial or full austenitization followed by quenching to a temperature between M_s and M_f to produce a specific amount of martensite. The material is then subjected to an isothermal heat treatment at the same or higher temperature which enables partitioning of carbon from supersaturated martensite to untransformed austenite; and finally the material is quenched to room temperature [7, 8].

Carbon enriched retained austenite can exist in the form of either films between martensite laths or blocky retained austenite [9, 10]. Metastable retained austenite can transform to martensite during deformation which provides these steels with high work hardening capacity, formability, and energy absorption. These characteristics make Q&P steels an ideal choice for safety-critical structural parts such as B-pillar reinforcements, cross members, sills, longitudinal beams and bumper reinforcements [11]. Mechanical properties are mainly dictated by the micromechanical behavior of an alloy's constitutive phases. In-situ tensile testing during scanning electron microscopy is one of the most powerful techniques to investigate the microstructural damage behavior of different phases in alloys during deformation. In addition, x-ray computed tomography (XCT) provides information about the damage development process in three dimensions. Combining both techniques gives insight into the ductile fracture process.

Among advanced high strength steels, the most extensive research has been undertaken on microstructural deformation and damage of dual phase steels at different forming conditions [12–18], while the investigation of damage in TRIP-assisted steels is still at an early stage. Indeed, most of the work on these materials has focused more on microstructural transformation during deformation, rather than on ductile damage and fracture. For instance, Wang et al. [11] measured the volume fraction of retained austenite during tensile testing using EBSD. They concluded that finer retained austenite particles are more stable during deformation. Yang et al. [19] investigated the retained austenite transformation behavior at different strains using TEM. They reported that at 12% strain, all the blocky retained austenite had transformed to martensite while most of the film-like retained austenite was still present in the microstructure. Blondé et al. [20] studied the mechanical stability of metastable austenite grains using in-situ synchrotron X-ray diffraction during tensile testing in low-alloyed TRIP steels. They report that grain orientation, carbon content and grain volume are the factors that affect the stability of metastable austenite grains.

The aim of this paper is to turn attention to failure in QP980, by presenting the results of an initial investigation of the micromechanisms of damage using in-situ tensile testing under scanning electron microscopy and X-ray computed tomography.

Experimental Work

The chemical composition of the commercial QP980 steel is listed in Table 1. This steel contains close to 2% Manganese in order to improve the stability of austenite; along with Silicon to suppress carbide precipitation.

The cold rolled sheet has a thickness of 1 mm. In-situ tensile test was carried out using a JEOL 6610 scanning electron microscope and MTII/Fullam SEM Tester stage. The geometry of in-situ tensile test specimens is shown in Fig. 1. Before the in-situ tensile test, specimens were ground, polished to a 1 μm finish and etched with 2% Nitial.

A Bruker SkyScan1172 X-ray tomography scanner was used for quantitative analysis of microstructural damage in a fractured sample at 100 kV using an Al/Cu filter with a pixel dimension of 0.59 μm. Quantitative analysis was carried out using the commercial SkyScan software.

Results and Discussion

Figure 2 presents microstructures of QP980 steel at different local true strains. As shown in Fig. 2a, the microstructure of QP980 steel consists of ferrite (F), martensite (M) and retained austenite (RA). Ferrite is present in the microstructure due to intercritical annealing prior to the quench and partitioning heat treatment of the steel. Retained austenite in QP980 exists in two forms—blocky retained austenite and retained austenite films between martensite laths. Ideally carbide precipitation should not happen during carbon partitioning from martensite to austenite; however, carbide precipitation was not completely prevented and there are carbide precipitates between martensite laths.

Table 1 Chemical composition of QP980 steel

C	Mn	Si	Al	P	S
0.206	1.962	1.474	0.037	0.008	0.002

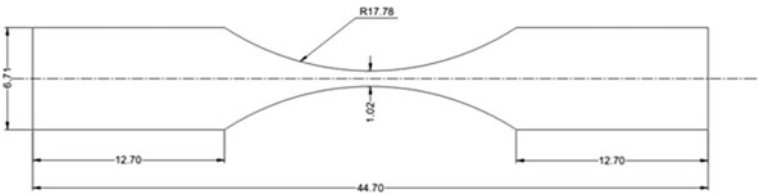

Fig. 1 Geometry of an hour-glass shaped SEM in-situ tensile test specimen (mm)

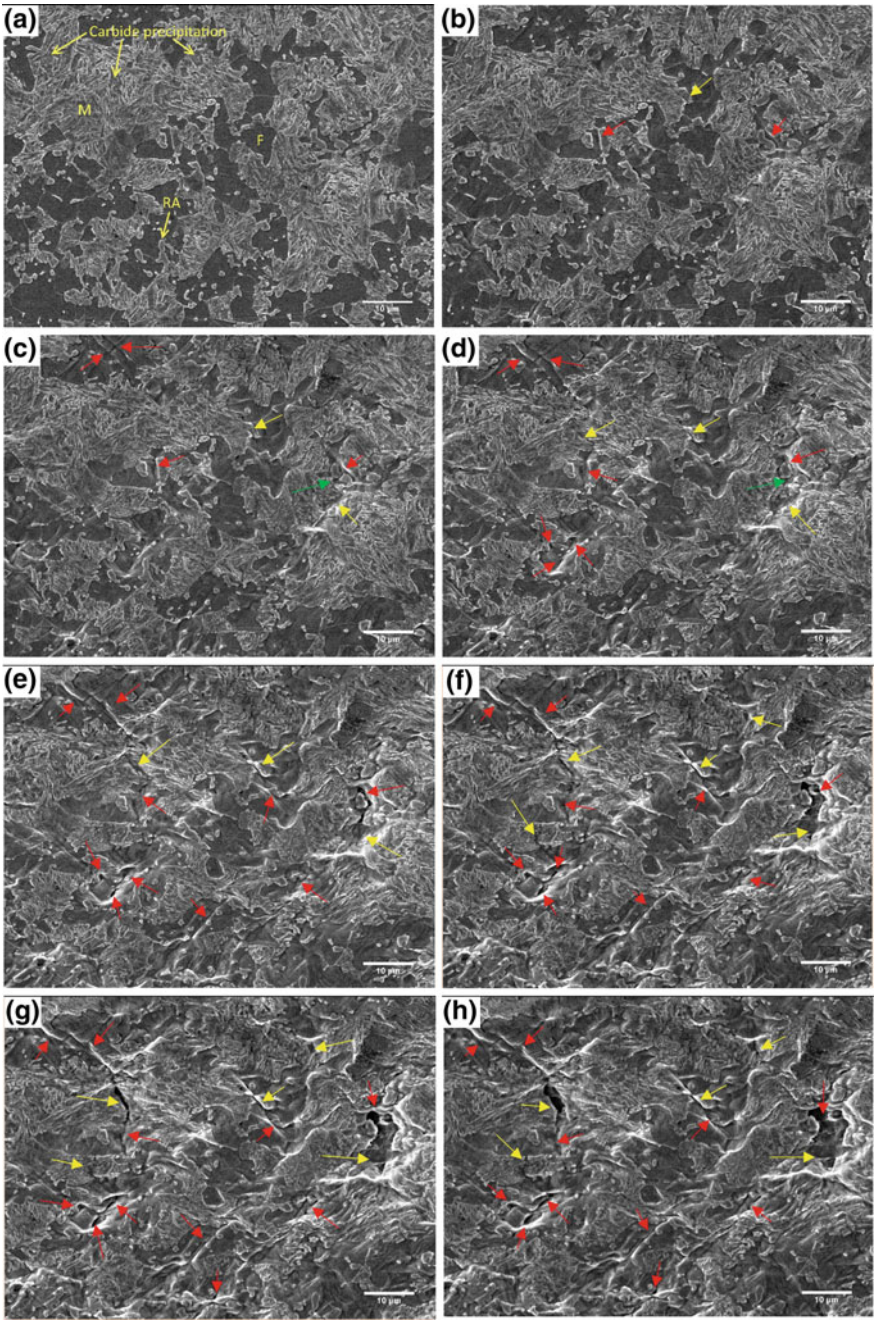

Fig. 2 Scanning electron micrograph of QP980 steel during deformation after local true strain of **a** 0, **b** 0.13, **c** 0.23, **d** 0.35, **e** 0.47, **f** 0.57, **g** 0.63, and **h** 0.69. M: martensite, F: ferrite and RA: retained austenite. Yellow, red and green arrows present sequences of M, F and RA cracking, respectively

As can be seen in Fig. 2, during deformation of QP980 steel, martensite and ferrite deform simultaneously. The high ductility of martensite in QP steels can be attributed to its low carbon content because of carbon migration from martensite to austenite during the partitioning treatment. Furthermore, the existence of film-shape austenite between the martensite lath improves ductility due to transformation induced plasticity (TRIP). As can be seen in Fig. 2c, blocky retained austenite starts to crack as soon as necking commences at a local true strain of 0.23, which suggests that the transformation to martensite can occur during that stage.

According to these SEM images, initiation of voids and micro-cracks occurs in both ferrite and martensite approximately at the same strain levels. However, damage growth is faster in martensite. As shown in Fig. 2h, martensite cracking leads to significant separation such that a large ≈10 μm cavity was formed. Cracks inside ferrite however, remain narrow. As shown in Fig. 2e–h, at higher strain levels during post-uniform deformation, most of microstructural damage occurred by cracks aligned at 45° respect to the loading axis. This can be attributed to the development of a localized shear band leading to enhanced localized deformation; however, further investigation is required to confirm and quantify this hypothesis.

Figure 3 presents a 3D X-ray tomography reconstruction model of the fractured sample. Dimples (green) on the fracture surfaces and voids (red) beneath the

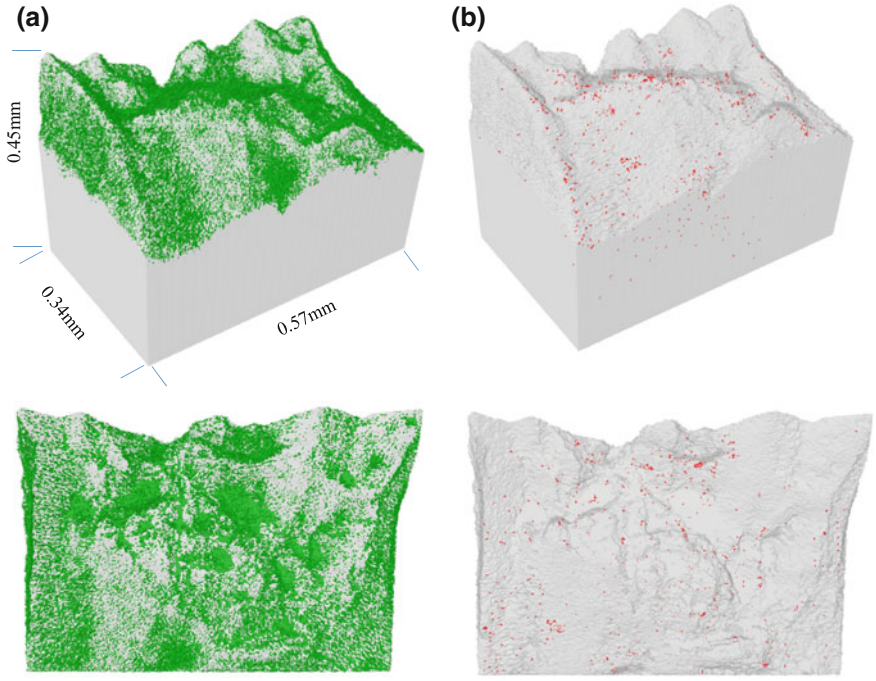

Fig. 3 X-ray tomography models of fractured QP980 steel **a** isometric and top view of dimples (green) on the fractured surface, and **b** isometric and top view of voids (red)

Table 2 Quantitative data for voids > 7 μm^3 and dimples obtained by XCT

	Fraction	Numbers	Mean diameter (μm)
Voids	0.48 vol.%	461	3.45 (largest 50)
Dimples	–	31066	0.85 (all)

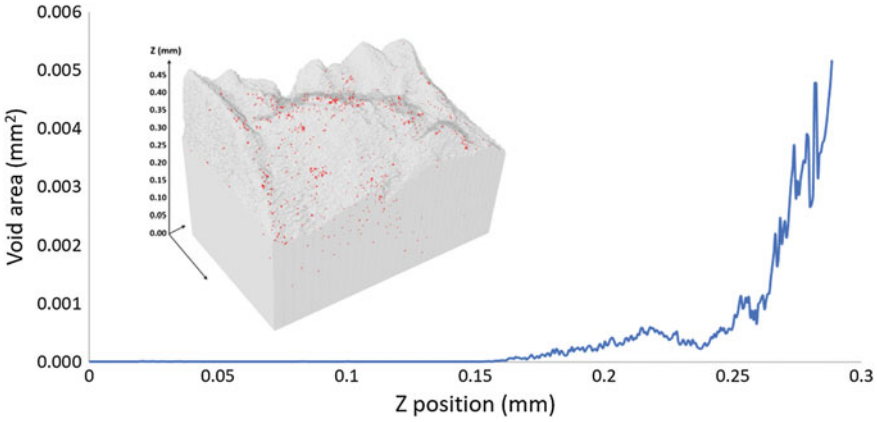

Fig. 4 Increase of void area toward fracture surface

fracture surfaces are shown. Only voids which are larger than 7 μm^3 are displayed in the model and considered in quantitative analysis. The quantitative information obtained from XCT are presented in Table 2. The data is obtained from the parts of materials, which are shown in the 3D models. The mean void diameter is calculated for the largest 50 voids since only the largest voids have an influential role in fracture. However, for calculation of dimple mean diameter all dimples were considered.

As it can be seen in Fig. 3, most voids are located just below the fracture surface. This is in good agreement with the in-situ observations of microstructural damage during tensile tests. As was shown in Fig. 2, intensive nucleation of voids and formation of microcracks occurred at higher localized strains near the fracture surface. The amount of void area along the fractured sample is shown in Fig. 4. As can be seen, there is an exponential increase of microstructural damage toward the fracture surface.

Conclusions

Damage micromechanisms of QP980 steel were investigated using in-situ tension coupled with SEM imaging and X-ray tomography. The following conclusions are drawn from this study:

1. Martensite exhibits a considerable amount of deformation which can be related to its low carbon content due to partitioning process and the existence of film-like austenite between the martensite laths which improves ductility by transformation induced plasticity.
2. Damage occurs in both martensite and ferrite starting at approximately the same strain; however, damage growth is faster in martensite and leads to large cavities.
3. Cracking of blocky retained austenite happens at an early stage of deformation which suggests the possibility of its early transformation to martensite.
4. 3D X-ray tomography investigations confirm that most damage occurs near the fracture surface consistent with previous 2D observations during in-situ tension under SEM.

References

1. Zhong N, Wang XD, Wang L, Rong YH (2009) Enhancement of the mechanical properties of a Nb-microalloyed advanced high-strength steel treated by quenching–partitioning–tempering process. Mater Sci Eng A 506(1):111–116
2. De Moor E, Lacroix S, Clarke AJ, Penning J, Speer JG (2008) Effect of retained austenite stabilized via quench and partitioning on the strain hardening of martensitic steels. Metall Mater Trans A 39(11):2586–2595
3. Zhang K, Zhang M, Guo Z, Chen N, Rong Y (2011) A new effect of retained austenite on ductility enhancement in high-strength quenching–partitioning–tempering martensitic steel. Mater Sci Eng A 528(29):8486–8491
4. Santofimia MJ, Nguyen-Minh T, Zhao L, Petrov R, Sabirov I, Sietsma J (2010) New low carbon Q&P steels containing film-like intercritical ferrite. Mater Sci Eng A 527(23):6429–6439
5. Santofimia M, Zhao L, Petrov R, Sietsma J (2008) Characterization of the microstructure obtained by the quenching and partitioning process in a low-carbon steel. Mater Charact 59 (12):1758–1764
6. Sun J, Yu H, Wang S, Fan Y (2014) Study of microstructural evolution, microstructure-mechanical properties correlation and collaborative deformation-transformation behavior of quenching and partitioning (Q&P) steel. Mater Sci Eng A 596:89–97
7. Bagliani EP, Santofimia MJ, Zhao L, Sietsma J, Anelli E (2013) Microstructure, tensile and toughness properties after quenching and partitioning treatments of a medium-carbon steel. Mater Sci Eng A 559:486–495
8. Santofimia MJ, Zhao L, Petrov R, Kwakernaak C, Sloof WG, Sietsma J (2011) Microstructural development during the quenching and partitioning process in a newly designed low-carbon steel. Acta Mater 59(15):6059–6068
9. Tan X, Xu Y, Yang X, Wu D (2014) Microstructure–properties relationship in a one-step quenched and partitioned steel. Mater Sci Eng A 589:101–111
10. Xu Y, Tan X, Yang X, Hu Z, Peng F, Wu D, Wang G (2014) Microstructure evolution and mechanical properties of a hot-rolled directly quenched and partitioned steel containing proeutectoid ferrite. Mater Sci Eng A 607:460–475
11. Wang L, Speer JG (2013) Quenching and partitioning steel heat treatment. Metall Microstruct Anal 2(4):268–281

12. Avramovic-Cingara G, Saleh CAR, Jain MK, Wilkinson DS (2009) Void nucleation and growth in dual-phase steel 600 during uniaxial tensile testing. Metall Mater Trans A 40 (13):3117–3127
13. Avramovic-Cingara G, Ososkov Y, Wilkinson DS (2009) Effect of martensite distribution on damage behaviour in DP600 dual phase steels. Mater Sci Eng A 516(1):7–16
14. Samei J, Green DE, Golovashchenko S (2014) Metallurgical investigations on hyperplasticity in dual phase steel sheets. J Manuf Sci Eng 136(4):041010
15. Samei J, Green DE, Golovashchenko S (2014) Analysis of failure in dual phase steel sheets subject to electrohydraulic forming. J Manuf Sci Eng 136(5):051010
16. Tasan CC, Diehl M. Yan D, Bechtold M, Roters F, Schemmann L, Zheng C, Peranio N, Ponge D, Koyama M, Tsuzaki K, Raabe D (2015) An overview of dual-phase steels: advances in microstructure-oriented processing and micromechanically guided design. Annu Rev Mater Res 45:391–431
17. Samei J, Green DE, Cheng J, de Carvalho Lima MS (2016) Influence of strain path on nucleation and growth of voids in dual phase steel sheets. Mater Des 92:1028–1037
18. Amirmaleki M, Samei J, Green DE, van Riemsdijk I, Stewart L (2016) 3D micromechanical modeling of dual phase steels using the representative volume element method. Mech Mater 101:27–39
19. Yang X, Xiong X, Yin Z, Wang H, Wang J, Chen D (2014) Interrupted test of advanced high strength steel with tensile split Hopkinson Bar method. Exp Mech 54(4):641–652
20. Blondé R, Jimenez-Melero E, Zhao L, Wright JP, van der Zwaag S, van Dijk NH (2014) Mechanical stability of individual austenite grains in TRIP steel studied by synchrotron X-ray diffraction during tensile loading. Mater Sci Eng A 618:280–287

Part XVIII
Deformation and Damage Mechanisms in High Temperature Ni, Co and Fe-Based Superalloys

Prediction of Incipient Melting Map and γ' Features of Ni-Base Superalloys Using Molecular Orbital Method

M. Mostafaei and S. M. Abbasi

Abstract Experimental nickel-base superalloys based on commercial CM247 LC containing Al and Ta were designed at a constant total Ta + W content (in wt%), on the basis of Molecular Orbital calculation. The γ' solvus, γ/γ' eutectic dissolving temperatures and susceptibility to incipient melting during solution annealing were predicted using this method. Solutioning and aging treatment were carried out following Cannon-Muskegon Corporation indication. For simplifying the model, Md and Bo parameters were replaced by a new electronic parameter (θ) named alloying angle. DSC thermal analysis and quantitative microstructural evaluations showed that a decrease in θ magnitude increases γ' solvus and γ' volume fraction considerably in the solutionized and aged condition. Also an incipient melt fraction (IMF) map versus Al and Ta contents was presented to predict a safe zone from incipient melting point of view during solutionizing treatment. As a result, Al + Ta contents must be less than 6 wt% to reach IMF < 1%.

Keywords Ni-base superalloy · d-electron theory · γ' solvus γ/γ' eutectic · Incipient melting

Introduction

Recently, there has been great progress made in a molecular orbital approach to superalloy design. This approach is based on electronic structure calculations [1, 2]. Nickel-base superalloys contain various alloying elements where each one has a specific role at elevated temperature conditions. There is always an unwanted interaction between alloying elements causing try and error in superalloy design. Nowadays, for decreasing design costs, new phase computation (NEWPHACOMP) is widely used based on molecular orbital models [3–5]. A d-electron concept for alloy design has been constructed on the basis of NEWPHACOMP [6–9]. These

M. Mostafaei (✉) · S. M. Abbasi
Metallic Materials Research Center, Malek Ashtar University of Technology, Tehran, Iran
e-mail: m_mostafaei@mut.ac.ir

The Minerals, Metals & Materials Society, *TMS 2018 147th Annual Meeting & Exhibition Supplemental Proceedings*, The Minerals, Metals & Materials Series,
https://doi.org/10.1007/978-3-319-72526-0_43

models after verifying can be used to predict the γ matrix phase stability or topologically close-packed (TCP) phase formation [10, 11] and to determine microstructural characteristics such as γ' volume fraction [12, 13], γ/γ' eutectic size [14], etc.

The most conventional parameters in molecular orbital model are Md and Bo. Md is d-orbital energy level of each element or metal-d level energy expressed in electron volt (eV). For this reason, the model named the "d-electrons" theory [15, 16]. This Md method, called NEWPHACOMP, has been applied successfully to the design of commercially available alloys with multiple components [17–19]. Experimental studies have shown that decrease in Md led to γ matrix phase stability and reduction in probability of TCP phase formation. Some literatures have reported that a critical Md value should be considered to prevent any TCP phase formation. For instance, the high temperature strength shows the maximum at the Md value of about 0.98 and the Bo value of about 0.67. The creep strength also shows the maximum around this position [20, 21]. The value of Md for each alloy (Md_{avg}) can be calculated according to Eq. (1) as follows [1]:

$$Md_{avg} = \sum_{i=0}^{n} X_i Md_i \tag{1}$$

where X_i is atomic fraction of element i in alloy and Md_i is the Md value of element i. Bo or Bond Order is a criterion for bonding strength between Ni atoms and other alloying elements. Usually γ matrix phase stability increases with decreasing in Bo [22]. The value of Bo for each alloy (Bo_{avg}) can be calculated according to Eq. (2) as follows [1]:

$$Bo_{avg} = \sum_{i=0}^{n} X_i Bo_i \tag{2}$$

where X_i is atomic fraction of element i in alloy and Bo_i is the Bo value of element i. The values of Md and Bo for 1 atomic percent of each element are presented in Table 1. Both the Md and Bo have been increased in new generation of directionally solidified and single crystal superalloys [23]. d-electrons variables were first used by Morinaga et al. [8] over a wide range of Ni-base superalloys and described it as New Phase Computation (NEWPHACOMP) and was developed recently by some researcher [24–26]. Morinaga et al. showed that by adjusting the Md and Bo values in superalloy design, the γ' volume fraction, microstructural characteristics, γ' solvus and other phase transformation temperatures could be predicted [8, 9]. Also Caron [13] developed Morinaga's approaches and predicted volume fraction of γ' and its solvus temperature, but couldn't relate the mentioned properties to the Md and Bo parameters.

In the present work, on the basis of Molecular Orbital method, 6 experimental nickel-base superalloys containing various γ' former elements including Al and Ta were designed based on commercial CM247 LC composition. Using d-electron

Table 1 The values of Md and Bo for 1 atomic percent of elements used in chemical composition of the Ni-base superalloys designed for this study [17]

Element	Md	Bo
Ti	2.271	1.098
Ta	2.224	1.67
Al	1.9	0.533
W	1.655	1.73
Mo	1.55	1.611
Cr	1.142	1.278
Co	0.777	0.697
Ni	0.717	0.514

theory parameters it was tried to give experimental models for prediction of γ' solvus, γ/γ' eutectic dissolving temperatures and occurrence of incipient melting in solution annealed microstructure for Al and Ta-bearing Ni-base superalloys.

Materials and Methods

For designing chemical composition, Al content was increased from 2 to 5.6 wt% to make a wide range of Md values and a tiny change in Bo values, while Ta as a strong Bo raiser was adjusted such that W content decreased and the total Ta + W content (in wt%) became constant in order to prevent TCP phase formation and decrease in solutionizing treatment time [27–29]. Chemical compositions of the studied alloys (wt%) are given in Table 2. All of the data are arranged in ascending order with respect to Al composition.

The alloys were melted and cast in a vacuum induction melting (VIM) furnace under a vacuum environment about 10^{-5} bar and were poured at 1450 °C into an alumina mold. The chemical compositions of the alloys were determined using OXFORD Optical Emission Spectrometer (OES). For microstructural examination, the specimens were polished and etched in solutions composed of 15 mL HCl + 10 mL HNO_3 + 10 mL Acetic acid + 5 drops Glycerol for

Table 2 Chemical compositions of the studied Ni-base superalloys in weight percent. All of the data are arranged into ascending order with respect to Al composition

Alloys	C	Co	Mo	Cr	W	Ta	Ta + W	Al	Ti	Hf	B	Zr	Md	Bo
1	0.07	9.3	0.5	6.2	7.9	3.9	11.8	2.0	0.7	1.4	0.015	0.01	0.869	0.644
2	0.08	9.5	0.5	6.0	6.0	6.2	12.2	2.9	0.6	1.4	0.015	0.01	0.899	0.646
3	0.08	9.2	0.5	6.5	9.1	3.2	12.3	3.5	0.7	1.3	0.015	0.01	0.909	0.647
4	0.07	9.2	0.5	6.1	4.1	8.3	12.4	4.4	0.7	1.4	0.015	0.01	0.942	0.645
5	0.07	9.5	0.5	8.0	9.2	3.1	12.3	5.1	0.7	1.4	0.015	0.01	0.956	0.661
6	0.07	9.1	0.5	6.1	10.1	1.8	11.9	5.4	0.8	1.5	0.015	0.01	0.950	0.643
CM247 LC	0.075	9.2	0.5	8.1	9.3	3.2	12.5	5.6	0.7	1.4	0.015	0.01	0.948	0.638

Table 3 Details of solutioning and aging heat treatment regime performed in the present work

Alloy	γ' solvus (°C) (JMatPro data)	γ' solvus (°C) (DSC data)	Heat treatment regime	
			Solution annealing	Aging
1	880	No data	1204 °C/ 2 h + 1216 °C/ 2 h + 1221 °C/ 2 h + 1232 °C/ 2 h + 1250 °C/ 2 h + AC	1080 °C/ 4 h + 870 °C/ 20 h + AC
2	1020	No data		
3	1050	No data		
4	1191	1206		
5	1180	No data		
6	1190	1218		
CM247 LC*	1220	1200		

*DSC data from Reference [31]

detection of γ' precipitates and γ/γ′ eutectics. In addition metallographic images were observed on an Olympus BX 51 optical microscope (OM) and TESCAN (model VEGA3 XMU/LaB_6 gun) scanning electron microscope (SEM) equipped with energy dispersive spectroscopy (EDS) analysis. Quantitative metallography analyses for γ′ and γ/γ′ eutectic phase volume fraction were performed using ImageJ software.

In order to determine the γ′ solvus temperature, the incipient melting point and solidification range, differential scanning calorimetry (DSC) experiments were carried out in a Mettler Toledo testing apparatus (model TGA/DSC 1 Star), using a heating rate of 10 °C/min from 25 to 1400 °C. The DSC cylindrical samples weighing approximately 100 mg were cut from the as-cast alloys. All DSC tests were conducted in a purged high-purity argon atmosphere using high-purity alumina crucibles. A commercial solutioning and aging heat treatment regime was considered to evaluation of γ' and γ/γ' eutectic dissolution and any incipient melting trace, according to technical datasheet of Cannon-Muskegon Corporation [30]. Details of the heat treatment regime are given in Table 3. γ' solvus temperature calculation was performed using both DSC analysis and JMatPro software data.

Results and Discussion

Alloys Design

Chemical composition in each alloy is defined in d-electron method through parameters such as Md and Bo. Establishing a valid relation between these electronic parameters and microstructural properties could be challenging and complex. For simplifying this correlation, a third parameter named as "alloying angle" or "θ" has been defined as a function of both Md and Bo. Alloying angle may be

calculated graphically in a Md-Bo coordinate system plot. In designing of chemical composition of studied alloys, Al content was increased in a way that θ decreases.

Murata et al. [6], who for the first time calculated "alloying angle", introduced θ as the angle between the line "L" and the line Bo = 0.514 (the Bo value for 1 M of nickel) in a two dimensional Md-Bo coordinate system. The line "L" is drawn from the point "Ni" corresponding to coordinate of 1 M of pure nickel (Md = 0.717, Bo = 0.514) and to the calculated coordinates corresponding to the designed alloys (Fig. 1). They proved that a simple linear relation exists between the γ' volume fraction and θ for around 30 Ni-base superalloys. The graphical method for alloying angle (θ) calculation in this work compared with directionally solidified CM247 LC and some commercial single crystal Ni-base superalloys is illustrated in Fig. 1.

Using of θ parameter provides an easy graphical comparison for designed alloys. θ for each alloy can be calculated mathematically by Eq. (3):

$$\theta(^\circ) = \tan^{-1}\left(\frac{Bo - BoNi}{Md - MdNi}\right) \tag{3}$$

where Md and Bo are Md_{avg} and Bo_{avg} calculated by the Eqs. (1) and (2) respectively. Also Md_{Ni} and Bo_{Ni} are Md and Bo values for Ni (coordinates of the Ni point in Fig. 1). Principally d-electron method is used for equilibrium microstructure, because the molecular orbital model is fundamentally developed for equilibrium conditions. In other words, it is prospected that microstructural evolution of the designed alloys versus θ parameter should be more obvious at solution annealed (homogenized) condition than that in as-cast status.

Before any further discussion about microstructural evolution it should be mentioned that previous studies did not contribute enough to the correlation between d-electron parameters and microstructures [32, 33]. However, the authors intend to find a realistic relationship between them in the current work.

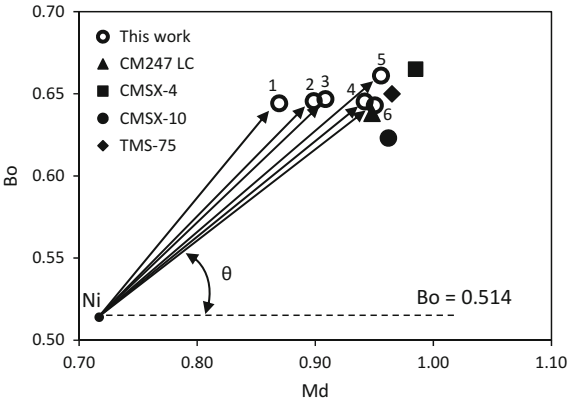

Fig. 1 The graphical method for alloying angle (θ) calculation in this work compared with directionally solidified CM247 LC and some commercial single crystal Ni-base superalloys

Dissolving Temperatures of γ' Precipitates and γ/γ' Eutectics

The as-cast microstructure of designed alloys is presented in Fig. 2. The size and volume fraction of γ/γ' eutectics have increased with decreasing θ parameter due to an intensified elemental segregations and rejection of low partitioning coefficient elements from growing dendrites to the interdendritic spaces. These elements are usually Al and Ta which have high Md values. According to Table 1, Al, Ti and Ta have the highest effect on increasing Md and decreasing θ angle (see Fig. 1). Therefore it may be imagined that there is a systematic relationship between θ and the size or volume fraction of γ/γ' eutectics. Figure 3 illustrates an exponential relation between the measured initial γ/γ' eutectic size and its volume fraction versus θ. The size and volume fraction of γ/γ' eutectics can be estimated inserting calculated θ in Eqs. (4) and (5), respectively, as follows:

$$Vf = 315.8e^{-0.115\theta} \tag{4}$$

$$d = 509.9e^{-0.081\theta} \tag{5}$$

where V_f is the volume fraction of initial (as-solidified) γ/γ' eutectics (in percent) and d is their average diameter (in micron). Equations (4) and (5) are very useful in designing new superalloys. For instance, if the goal is to develop a Ni-base superalloy with only 2% initial γ/γ' eutectics, the corresponding θ angle parameter should be set around 46°. Accordingly, based on Eq. (3) Md should be decreased or Bo should be increased further.

Figure 4 represents the microstructures of the alloys solution annealed according to Table 3. It shows while the alloying angle (θ) decreases the γ' solvus and γ/γ'

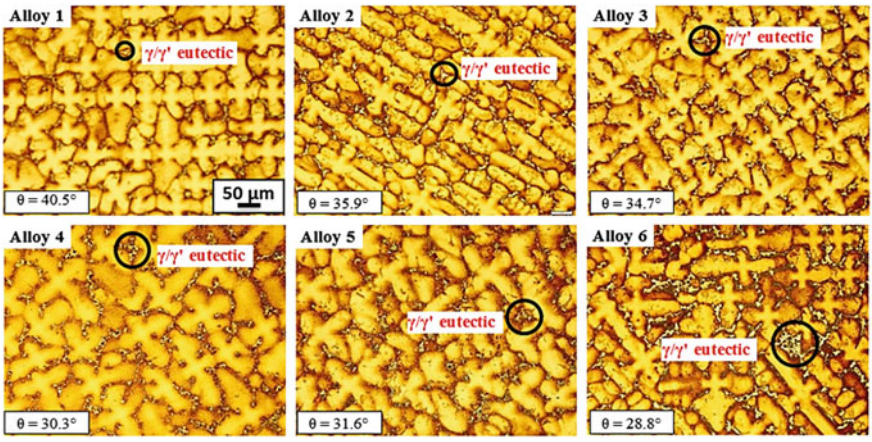

Fig. 2 Comparison of dendritic structure and γ/γ' eutectic phases in as-cast microstructure of designed alloys

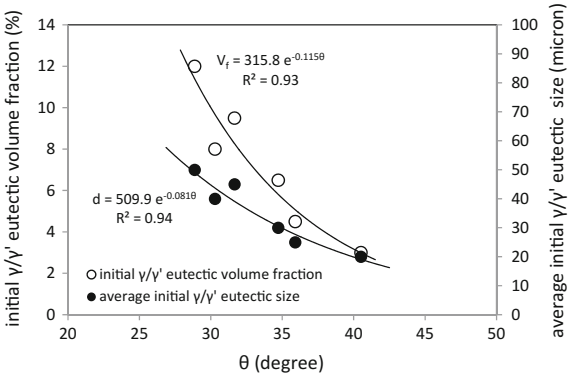

Fig. 3 The exponential relation between the measured initial γ/γ' eutectic size and its volume fraction versus θ

eutectic dissolving temperatures increase. In alloy 1 which has the greatest θ magnitude, the elemental segregations formed during solidification are disappeared completely by solution annealing treatment, so that Interdendritic Grain Boundaries (IGB) are eliminated and Equilibrium Grain Boundaries (EGB) are revealed. This also occurs in alloy 2. The residual IGBs are somewhat visible in alloy 3 and indicates that γ' solvus and γ/γ' eutectic dissolving temperatures are higher than those in alloys 1 and 2. Moreover, no γ/γ' eutectic phase can be tracked in alloys corresponding to θ magnitude between 40.5° and 34.7°. In the same way, in alloys 4, 5 and 6 having lower alloying angle, IGBs are visible clearly and no EGB is formed. As a result, γ/γ' eutectic phases are retained in solution annealed microstructure. As illustrated in Fig. 5, in alloys with higher θ magnitudes, in addition to the greater elimination of elemental segregations, more incipient melting zones are formed during solution annealing. Quantitative analysis of incipient melting areas is discussed more in the following.

DSC heating thermograms for alloys 4 and 6 (Fig. 5) verify the fact that decrease of the alloying angle (θ) increases the γ' solvus and the onset of incipient melting temperatures. For instance, in alloy 6 (θ = 28.8°) the onset temperatures for γ' solvus and incipient melting are about 15 °C and 20 °C higher than alloy 4 (θ = 30.3°), respectively. Calculation of equilibrium γ' solvus temperature using JMatPro package demonstrated a linear relation between γ' solvus temperature versus θ (Fig. 6) and revealed a good agreement with the experimental DSC results too (Fig. 5). According to Fig. 6, the experimental γ' solvus temperature data were regression fitted as a linear function of θ magnitude (see Eqs. (6) and (7)) and then were used to predict γ' solvus temperature ($T\gamma'$) for each designed Ni-base superalloy.

$$T\gamma'\,(^{\circ}C) = -28\,\theta + 2025.1 \tag{6}$$

Inserting Eq. (1) into Eq. (6) results:

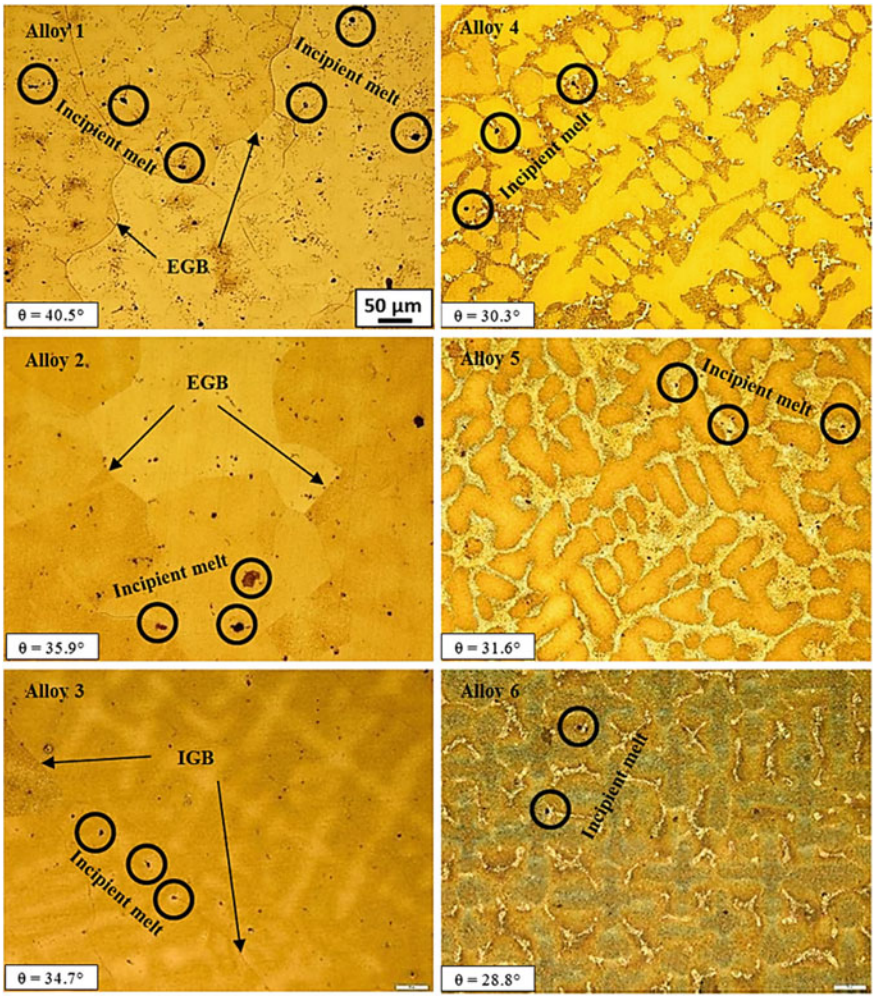

Fig. 4 Microstructure of designed alloys in solution annealed condition showing the variation of retained γ/γ' eutectic and incipient melt areas with change in θ magnitude

$$T\gamma'(^{\circ}C) = -28tan^{-1}\left(\frac{Bo - 0.514}{Md - 0.717}\right) + 2025.1 \quad (7)$$

It should be noted that the data related to coordinates (Tγ' = 1200 °C, θ = 28.24°) in Fig. 7 is from prior author's work [34].

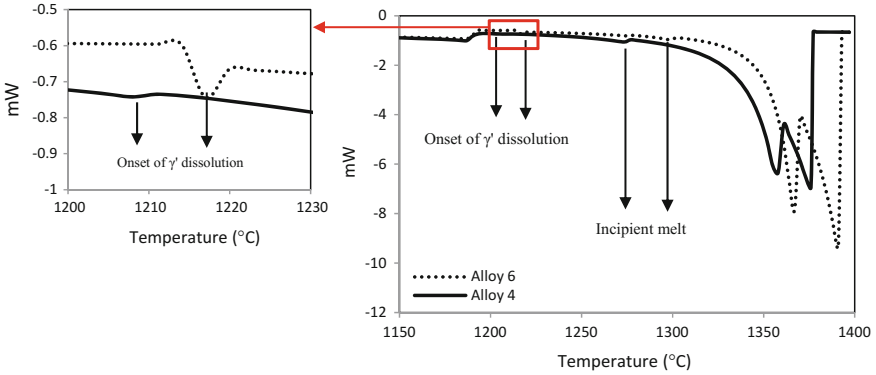

Fig. 5 DSC heating thermograms for alloys 4 and 6 with heating rate of 10 °C/min

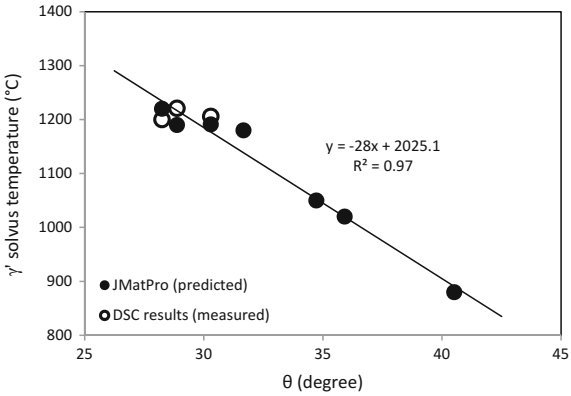

Fig. 6 Linear regression fitting of the both simulated and experimental γ' solvus temperature as a function of θ magnitude

Retained γ/γ' Eutectics and Incipient Melting Formation

Microstructural evaluation of solution annealed alloys reveals a relative decrease in the incipient melt area fraction with decreasing θ magnitude caused by the elevation of incipient melting onset temperature. Also regarding the DSC thermograms depicted in Fig. 5, decreasing the θ magnitude leads to an increase in retained γ/γ' eutectics fraction as a result of inadequate diffusion during solution treatment (see Fig. 7). Hence, in alloys having higher alloying angles (or lower Al content), the interdendritic segregations are eliminated quickly during solution annealing treatment, but it raises the risk of incipient melting formation severely.

Based on quantitative image analysis data of solution annealed microstructures (from several metallographic images at a magnification of 200X as depicted in Fig. 4), variation curves of retained γ/γ' eutectics fraction and incipient melting area percentage as a function of θ angle are drawn in Fig. 8.

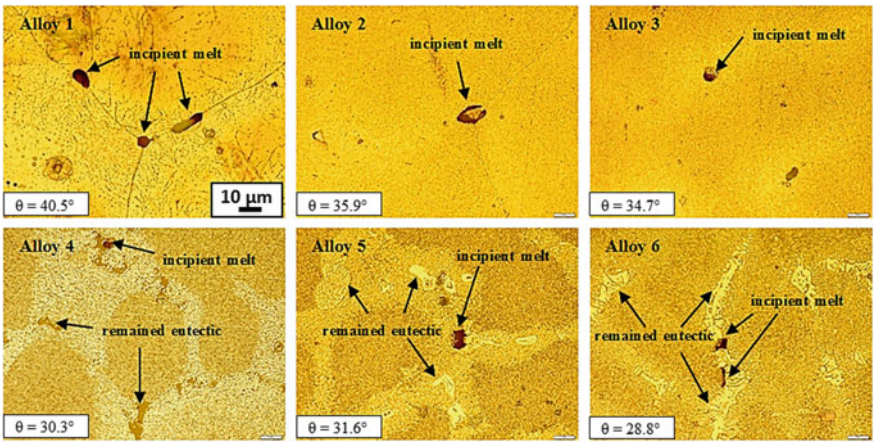

Fig. 7 Simultaneous increase of retained γ/γ' eutectics and incipient melt area fraction with decreasing the θ magnitude resulted from inadequate diffusion during solution treatment

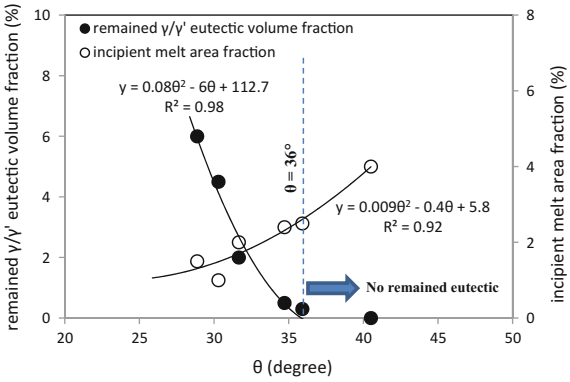

Fig. 8 Variation curves of retained γ/γ' eutectics fraction and incipient melting area percentage as a function of θ angle, based on quantitative image analysis data of solution annealed microstructures

According to this results, the alloying angle around θ = 36° is a critical value for eliminating of retained γ/γ' eutectics. In other words, alloys having an alloying angle more than 36° don't pertain any retained γ/γ' eutectic after solutionizing leading to finer γ' formation during aging step. Consequently, it should be said that with increasing θ resulting from reducing Al content, dissolving temperature of γ/γ' eutectic decreases gradually and accelerates the decomposition of γ/γ' islands and going into matrix solid solution (γ) during solution treatment.

A more accurate investigation of solution annealed microstructures revealed the presence of secondary γ' in low alloying angle alloys as a result of air cooling curve intersecting 1% γ' TTT diagram. In other words, the alloys with lower θ magnitude (higher Al content), have a more supersaturation of γ' former elements in the γ matrix. Therefore after solutionizing treatment followed by a fast air cooling, more nucleation sites (usually in dendrite cores) are present for precipitating of secondary γ'. Figure 9

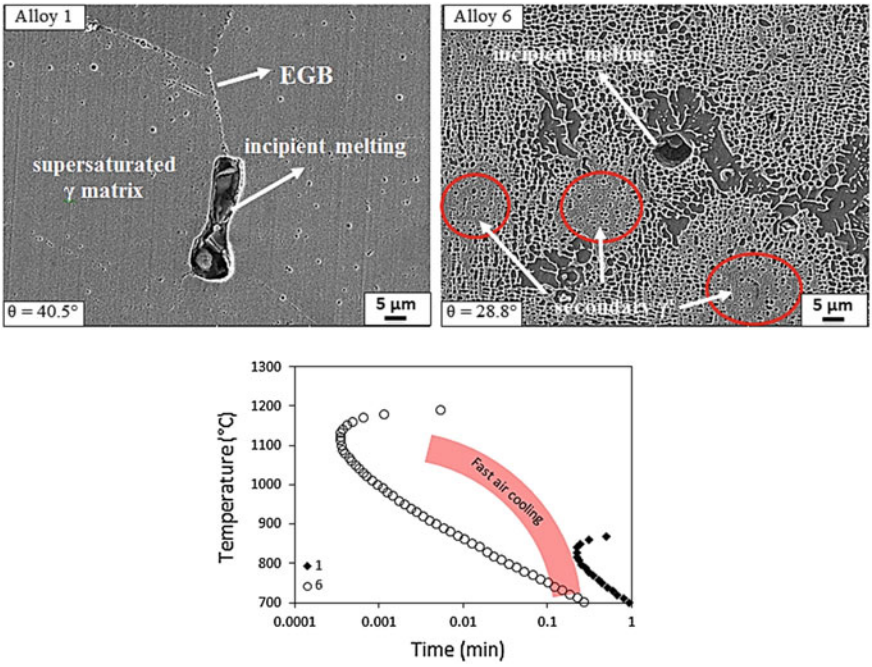

Fig. 9 The solution annealed microstructures of alloy 1 (θ = 40.5°) and alloy 6 (θ = 28.8°) at higher magnification and comparison of 1% γ' TTT diagram for the mentioned alloys

illustrates the solution annealed microstructures of alloy 1 (θ = 40.5°) and alloy 6 (θ = 28.8°) at higher magnification and comparison of 1% γ' TTP diagram for the mentioned alloys. Time-Temperature-Precipitation (TTP) diagram of 1% γ' precipitates for alloys 1 and 6 were calculated using JMatPro software.

To present a practical result from the data of Fig. 8, the positions of six designed alloys (in solution annealed and aged condition) were determined in a two dimensional Ta-Al coordinate system and divided into three zones based on incipient melt area fraction (IMF), as illustrated in Fig. 10:

1. IMF < 1%; the first zone with the Al + Ta content less than 6 wt%. This zone can be considered as a safe zone in designing of superalloys composition.
2. 1.5% < IMF < 2.5%; the second zone with the Al + Ta content between 6 and 9 wt%.
3. IMF > 3%; the third zone with the Al + Ta content more than 9 wt%. This zone can be considered as a dangerous zone in designing of superalloys composition.

Since the new generation commercial Ni-base superalloys contain Al content ranged from 2 to 6 wt% and Ta content ranged between 1 and 9 wt%, the chemical composition of superalloys designed in this work (Al and Ta) was considered in the mentioned range. Therefore, the empirical formula obtained based on experimental data, will be applicable for the many new generated Ni-base superalloys contain Al

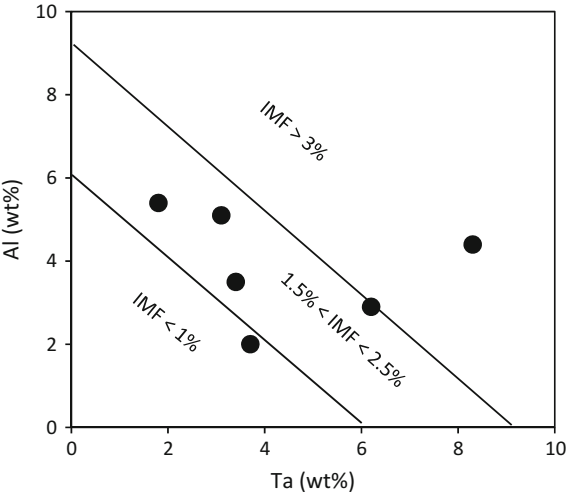

Fig. 10 The positions of the six alloys designed based on CM247 LC superalloy (in solution annealed and aged condition) in a two dimensional Ta-Al coordinate system and its division into three zones based on incipient melt area fraction (IMF)

or Ta. The limitation of the proposed models may be only ignoring of Ti content influences on the related γ' parameters.

Conclusions

- In the present study, an experimental model has been proposed to predict incipient melt area fraction (*IMF*) for Al and Ta-bearing Ni-base superalloys based on d-electrons theory as follows:

$$IMF(\%) = 0.009\,\theta^2 - 0.4\,\theta + 5.8$$

where θ is expressed as follows:

$$\theta(^\circ) = \tan^{-1}\left(\frac{Bo - BoNi}{Md - MdNi}\right)$$

- Changing of Al and Ta contents in a way that θ decreases leads to an increase in γ' solvus from 880 to 1200 °C in the solutionized and aged condition.
- The alloying angle of θ = 36° (Md = 0.899 and Bo = 0.646) is indicated as a critical value for eliminating of retained γ/γ' eutectics. In other words, alloys having alloying angle more than 36° don't pertain any retained γ/γ' eutectic after solutionizing leading to finer γ' formation during aging step.
- To obtain a safe zone in designing Ni-base superalloy compositions (IMF < 1%), sum of Al + Ta contents should be considered less than 6 wt%.

References

1. Wahl JB, Harris K (2012) New single crystal superalloys CMSX-7 and CMSX-8. TMS 2012:177–188
2. Tsao T, Yeh A (2015) The thermal stability and strength of highly alloyed Ni_3Al. Mater Trans 56:1905–1910
3. Morinaga M, Yukawa N (2016) Alloy design based on molecular orbital method. Mater Trans 57:213–226
4. Jintao K, Rui H, Hongchao K, Jinshan L, Xin Z (2015) Alloy design of low-density Nb-Ti superalloy based on d-electrons theory. Eng Rare Met Mater 44:1119–1123
5. Ma SY, Zhang JX (2015) Site preference and alloying effect of Re atoms in the edge dislocation cores in Ni_3Al. Philos Mag Lett 95:253–259
6. Murata Y, Miyazaki S, Morinaga M, Hashizume R (1996) Hot corrosion resistant and high strength nickel-based singlr crytal and directionally-solidified superalloys developed by the d-electrons concept. TMS 1996:61–70
7. Matsugi K, Murata Y, Morinaga M, Yukawa N (1992) Realistic advancement for nickel-based single crystal superalloys by the d-electrons concept. TMS 1992:307–316
8. Morinaga M, Yukawa N, Adachi H, Ezaki H (1984) New phacomp and its applications to alloy design. TMS 1984:523–532
9. Bürgel R, Grossmann J, Lüsebrink O, Mughrabi H, Pyczak F, Singer RF, Volek A (2004) Development of a new alloy for directional solidification of large industrial gas turbine blades. TMS 2004:25–34
10. Hashizume R, Yoshinari A, Kiyono T, Murata Y, Morinaga M (2007) Development of novel Ni-based single crystal superalloys for power-generation gas turbines. Mater High Temp 24:163–172
11. Seiser B, Drautz R, Pettifor DG (2011) TCP phase predictions in Ni-based superalloys: structure maps revisited. Acta Mater 59:749–763
12. Morinaga M, Yukawa H (2004) Recent progress in molecular orbital approach to alloy design. Mater Sci Forum 449–452:37–42
13. Caron P (2000) High γ' solvus new generation nickel-based superalloys for single crystal turbine blade applications. TMS 2000:737–746
14. Matsugi K, Nurata Y, Morinaga M, Yukawa N (1992) Correlation of Ta/W compositional ratios with the high temperature properties of Ni-Cr-Al-Ta-W(-Co) single crystal superalloys. Iron Steel Inst Japan (ISIJ) 78:666–672
15. Hou JS, Guo JT, Yuan C, Guo YA, Li GS, Zhou LZ (2015) Effect of hafnium on the microstructure and creep property of a hot corrosion resistant superalloy. Mater Sci Forum 816:641–647
16. Hisazawa H, Terada Y, Adziman F, Crudden D, Collins D, Armstrong D, Reed R (2017) The effect of Nb/Ti ratio on hardness in high-strength Ni-based superalloys. Metals 7:71–82
17. Morinaga M, Murata Y, Yukawa H (2007) Molecular orbital approach to alloy design. In: Bozzolo G, Noebe RD, Abel PB (eds) Applied computational materials modeling. Springer, Boston, pp 255–306
18. Xu Y, Sha Q, Xia T (2016) Effects of tantalum content on strengthening phase and high temperature oxidation behavior of Co-Al-W superalloy. Chinese J Nonferrous Met 26:302–309
19. Morinaga M, Murata Y, Yukawa H (2005) Alloy design based on molecular orbital method. Mater Sci Forum 475–479:3099–3102
20. Morinaga M, Murata Y, Yukawa H (2006) Alloy design based on the DV-Xα cluster method. In: Adachi H, Mukoyama T, Kawai J (eds) Hartree-Fock-Slater method materials science. Springer, Berlin, pp 23–48
21. Tan X, Liu J, Jin T, Hu Z, Hong HU, Choi BG, Kim IS, Yoo YS, Jo CY (2012) Effect of ruthenium on precipitation behavior of the topologically close-packed phase in a

single-crystal Ni-based superalloy during high-temperature exposure. Metall Mater Trans A 43:3608–3614
22. Hashizume R, Yoshinari A, Kiyono T, Murata Y, Morinaga M (2004) Development of Ni-based single crystal superalloys for power-generation gas turbines. TMS 2004:53–62
23. Yoshinari A, Hashizume R, Murata Y, Morinaga M (2003) Development of the third generation single crystal superalloy for power generation gas turbines. In: Proceedings International Gas Turbine Congress, Tokyo, pp 1–8
24. Smialek J, Garg A, Gabb T, MacKay R (2015) Cyclic oxidation of high Mo, reduced density superalloys. Metals 5:2165–2185
25. Matsugi K, Yamamura S, Xu Z, Choi Y, Sugio K, Sasaki G, Oda N (2015) Compositional optimization of Al-Mn-X alloys and their tensile and corrosion properties. Mater Trans 56:1675–1682
26. Ye YF, Wang Q, Lu J, Liu CT, Yang Y (2016) High-entropy alloy: challenges and prospects. Mater Today 19:349–362
27. Liu C, Shen J, Zhang J, Lou L (2010) Effect of withdrawal rates on microstructure and creep strength of a single crystal superalloy processed by LMC. J Mater Sci Technol 26:306–310
28. Milenkovic S, Sabirov I, LLorca J (2012) Effect of the cooling rate on microstructure and hardness of MAR-M247 Ni-based superalloy. Mater Lett 73:216–219
29. Baldan R, da Rocha RLP, Tomasiello RB, Nunes CA, da Silva Costa AM, Barboza MJR, Coelho GC, Rosenthal R (2013) Solutioning and aging of MAR-M247 nickel-based superalloy. J Mater Eng Perform 22:2574–2579
30. Erickson GL, Harris K, Schwer RE (1985) Directionally solidified DS CM 247 LC optimized mechanical properties resulting from extensive γ' solutioning. In: ASME international gas turbine conference and exhibit, Texas, pp 1–10
31. Mostafaei M, Abbasi SM (2015) Influence of Zr content on the incipient melting behavior and stress-rupture life of CM247 LC nickel base superalloy. J Alloys Compd 648:1031–1037
32. Maeda M, Murata Y, Morinaga M (2003) Degradation of high-temperature oxidation resistance for Ni-based alloys by Re addition and the optimization of Re/Al content. Iron Steel Inst Japan (ISIJ) 43:386–393
33. Matsugi K, Murata Y, Morinaga M, Yukawa N (1993) An electronic approach to alloy design and its application to Ni-based single-crystal superalloys. Mater Sci Eng A 172:101–110
34. Mostafaei M, Abbasi SM (2016) Solutioning and solidification process control in Ta-modified CM247 LC superalloy. J Mater Process Technol 231:113–124

Part XIX
Dynamic Behavior of Materials VIII

Mechanical Properties and Shear Localization of High Entropy Alloy CoCrFeMnNi Prepared by Powder Metallurgy

Bingfeng Wang, Xiaoxia Huang, Yong Liu and Bin Liu

Abstract Mechanical properties of the CoCrFeMnNi high entropy alloy at strain rates (1×10^{-4} s^{-1} to 0.1 s^{-1} and 1×10^{3} s^{-1} to 3×10^{3} s^{-1}) and at temperatures (298.15, 673.15 and 1073.15 K) are investigated. Hat shaped specimens are used to induce the formation of an adiabatic shear band under controlled shock-loading tests. Results indicate that the yield strength of the CoCrFeMnNi high entropy alloy is increasing sensitively with increasing the strain rates. Grains in the boundary of the shear band in the CoCrFeMnNi high entropy alloy are highly elongated along the shear direction, and the core of the shear band consists of nanotwins and ultrafine equiaxed grains. Rotational dynamic recrystallization takes effects on the formation of the microstructures in the shear band.

Keywords High entropy alloy · Powder metallurgy · Mechanical property Microstructure · Shear localization

Introduction

The equiatomic CoCrFeMnNi high entropy alloy is one of the extensively investigated high entropy alloys [1]. It owns a single-phase solid solution with the face-centered-cubic (FCC) structure. Many researchers present a rising interest on the mechanical behavior and the application of the CoCrFeMnNi high entropy alloy.

B. Wang (✉) · Y. Liu · B. Liu
State Key Laboratory for Powder Metallurgy, Central South University, Changsha, People's Republic of China
e-mail: wangbingfeng@csu.edu.cn

B. Wang · X. Huang
School of Materials Science and Engineering, Central South University, Changsha 410083, People's Republic of China

B. Wang
Key Lab of Nonferrous Materials, Ministry of Education, Central South University, Changsha 410083, People's Republic of China

The Minerals, Metals & Materials Society, *TMS 2018 147th Annual Meeting & Exhibition Supplemental Proceedings*, The Minerals, Metals & Materials Series,
https://doi.org/10.1007/978-3-319-72526-0_44

The strength of the CoCrFeMnNi high entropy alloy is relatively low in as-cast state, only around 200 MPa [2]. The compositional segregation of elements and brittle intermetallic are inevitable in the high entropy alloy ingots prepared by vacuum arc melting [3, 4]. Powder metallurgy is an efficient way to prepare high strength CoCrFeMnNi high entropy alloy with homogeneous compositions and microstructures [4]. Mechanical properties of high entropy alloy at strain rates between $1 \times 10^{-4}\ s^{-1}$ and $1 \times 10\ s^{-1}$, have been widely studied, such as strength, ductility and hardness, and serration behavior [1]. Considering another important application of the high entropy alloy requires the study of its mechanical performance and microstructure evolution in dynamic deformation processes such as penetration, impact loading, and shock loading. In these processes the strain rate is beyond $1 \times 10^{3}\ s^{-1}$. Only a few papers report about the research of high entropy alloy under high strain rate (beyond $1 \times 10^{3}\ s^{-1}$). Kumar et al. [5] and Dirras et al. [6] and Wang et al. [7] and Li et al. [8] had used direct impact split-Hopkinson pressure bar to investigate the dynamic mechanical properties of the high entropy alloy.

Adiabatic shear localization, a typical deformation mechanism under high strain rate, usually results in softening or even failure of the material, which had been reported in a number of conventional materials, for instance, tungsten alloys. Elongated subgrains along shear direction can be observed within the shear bands of tungsten heavy alloy [9]. Moreover, elongated subgrains were found to break up into equiaxed micrograins, and this microstructure may be as result of dynamic recrystallization mechanism [10]. Although adiabatic shear localization in various materials had been fully studied, few results are reported in high entropy alloy. Dirras et al. [6] had reported that the dynamic deformation of $Ti_{20}Hf_{20}Zr_{20}Ta_{20}Nb_{20}$ high entropy alloy loaded under dynamic compression condition was strongly localized in macroscopic shear bands along with softening even after yielding.

In the present study, we focus on the equiatomic CoCrFeMnNi high entropy alloy prepared by powder metallurgy. The compressive tests were performed at a wide-range of strain rates and temperatures to explore the plastic deformation and related mechanical behavior. The aims of the paper are as follows: (1) to investigate the mechanical properties of the powder metallurgy CoCrFeMnNi high entropy alloy, especially the effect of the strain rates; (2) to report the microstructure of the shear band in the CoCrFeMnNi high entropy alloy; (3) to discuss the microstructure mechanism for the formation of the shear band.

Materials and Methods

The CoCrFeMnNi high entropy alloy was prepared by powder metallurgy method. The detail of the process was explained in our previous paper [4].

Table 1 Test conditions for the cylinder specimens

Specimen	A	B	C	D	E	F	G	H	I	J
Strain rate (s^{-1})	0.001	0.001	0.0001	0.001	0.05	0.1	1200	1260	2710	2800
Temperature (K)	1073	673	298	298	298	298	298	298	298	298

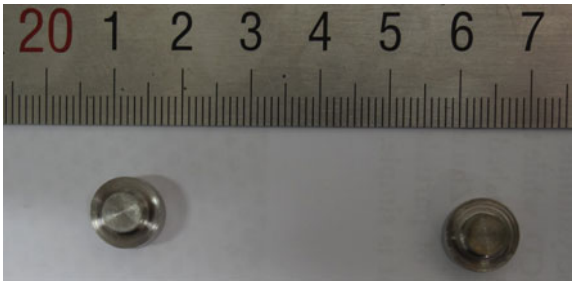

Fig. 1 Picture of the hat-shaped specimens

Cylindrical compressive specimens with 4 mm in diameter or 6 mm in diameter were machined from the sintered specimens by electric discharge machining. Test conditions for the cylinder specimens are listed in Table 1. The loading direction was parallel to the cylindrical axis of these specimens. To ensure uniaxial compressive condition, the end face of the compressive specimens were ground on each side with SiC paper and then lubricated. Quasi-static compressive tests and dynamic compressive tests were performed with the Instron 3369 machine and the split-Hopkinson pressure bar machine, respectively.

The hat-shaped specimen was originally invented by Meyer and Pursche [11], and the narrow shear region was designed to produce an adiabatic shear band due to shear strains concentration. Details of the split Hopkinson pressure bar technique had been introduced in another literature [11]. Figure 1 shows the picture of the hat-shaped specimens for the CoCrFeMnNi high entropy alloy. The thickness of the designed shear region in hat-shaped specimen is about 0.30 mm.

The samples for the investigation were cut from the hat-shaped specimen by line cutting. The etchant for the CoCrFeMnNi high entropy alloy was 25 ml C_2H_5OH + 25 ml HCl + 5 g $CuSO_4.5H_2O$. Optical microscopy was carried out with POLYVAR-MET. Electron probe microanalyses (EPMA) was performed on JXA-8230 electron probe micro-analyzer. The shear band was examined in a Phillips XL30 SEM. A focused ion beam (FIB) instrument was used to accurately prepare TEM samples in the shear band regions. The FIB samples were then characterized by TEM using Tecnai G^2 20 transmission electron microscope operated at 200 kV, and Tecnai G^2 60–300 polar transmission electron microscope operated at 300 kV.

Results and Discussion

The Constitutive Relation of the CoCrFeMnNi High Entropy Alloy

The Zerilli-Armstrong plastic model is one of the common physical based constitutive models. In our present work, the classic Zerilli-Armstrong plastic model for face-centered cubic structure which is used for predicting the strain rate flow behavior of the powder metallurgy CoCrFeMnNi high entropy alloy can be represented as follows [12].

$$\sigma = C_1 + C_2\varepsilon^{n}e^{[T(-C_3 + C_4\ln\dot{\varepsilon})]} \tag{1}$$

where C_1, C_2, C_3, C_4 and n are material constants. Notice that T is deformation temperature. Furthermore, σ is the flow stress, ε is the equivalent plastic strain, $\dot{\varepsilon}$ is the equivalent plastic strain rate.

Figure 2 shows the true strain versus true stress curves of the CoCrFeMnNi high entropy alloy at various temperatures and strain rates. The curves of specimens A–F and specimens G–J are obtained from quasi-static compressive data and dynamic compressive data, respectively. It can be seen that the flow stress decreases with increasing temperature at a strain rate of 1×10^{-3} s^{-1}, and increases with increasing strain rate at ambient temperature. Figure 3 shows the yield strength versus strain rate curves of the powder metallurgy CoCrFeMnNi high entropy alloy as a function of strain rate at ambient temperature. The yield strength distributes from 300 to 700 MPa, and the slope of the lines increases with increasing strain rates, particularly at high strain rate. Therefore, the yield strength increases sensitively with increasing strain rates, especially at dynamic strain rates (beyond 1×10^{3} s^{-1}).

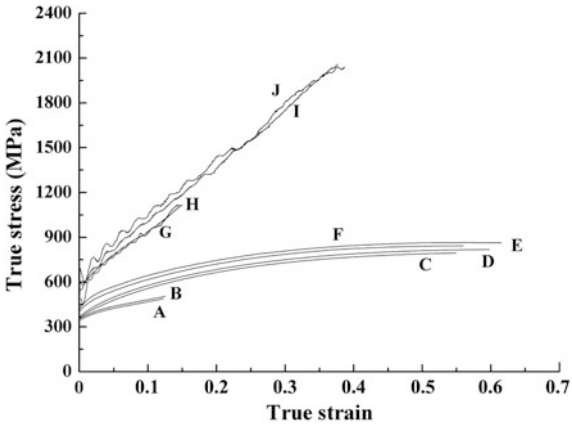

Fig. 2 True strain versus true stress curves of the CoCrFeMnNi high entropy alloy obtained in compressive tests

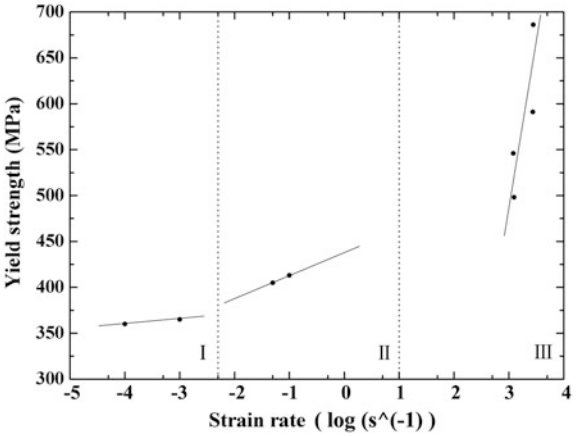

Fig. 3 The yield strength versus strain rate curves of the CoCrFeMnNi high entropy alloy. This plots the logarithm to base 10 of the values on the x-axis

Stress-strain curves are chosen from Fig. 2 to model the flow behavior of the powder metallurgy CoCrFeMnNi high entropy alloy. The value of constants C_1, C_2, C_3, C_4 and n in Eq. (1) is determined by using a MATLAB analysis technique. The constants in the Zerilli-Armstrong plastic model are found to be as follows: $C_1 = 420$ MPa; $C_2 = 1565$ MPa; $C_3 = 3.745 \times 10^{-4}$; $C_4 = 2.975 \times 10^{-4}$; and $n = 0.6536$. Therefore, the constitutive equation based on the Zerilli-Armstrong plastic model can be obtained as follows:

$$\sigma = 420 + 1565\varepsilon^{0.6536} e^{\left[T\left(2.975\times10^{-4}\ln\dot{\varepsilon} - 3.745\times10^{-4}\right)\right]} \quad (2)$$

Figure 4 shows the comparison diagram between theoretical results obtained from Eq. (2) and experimental data showed in Fig. 2. It can be seen that the theoretical results are in a good agreement with the experimental data.

Shear Localization in the CoCrFeMnNi High Entropy Alloy

Figure 5 shows the mechanical responses of the CoCrFeMnNi high entropy alloy during the shear localization process. The obtaining method for the true stress and the true strain and the strain rate is illustrated in our previous paper [13]. The average strain rate is about 4.1×10^5 s^{-1}, and the entire deformation process lasts about 135 μm (Fig. 5a). The true stress and true strain curve of the specimen, demonstrating the deformation process of the equiatomic CoCrFeMnNi high entropy alloy during the shear localization, can be divided into three stages (Fig. 5b). In the first stage (a–b), the true stress increases with the true strain due to strain hardening and strain rate hardening. In the second stage (b–c), thermal softening becomes clearly, and the true stress increases slower than that in the first

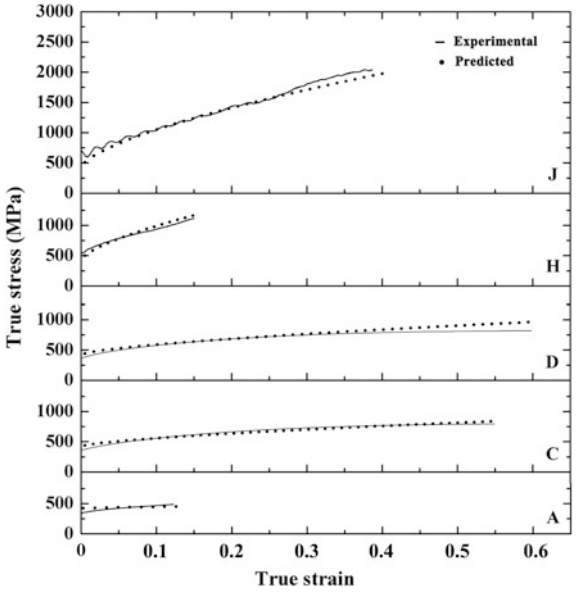

Fig. 4 Comparison between the experimental and predicted stress by the Zerilli-Armstrong plastic model. The solid line and scattered line represent the experimental curves and the theoretical curves, respectively

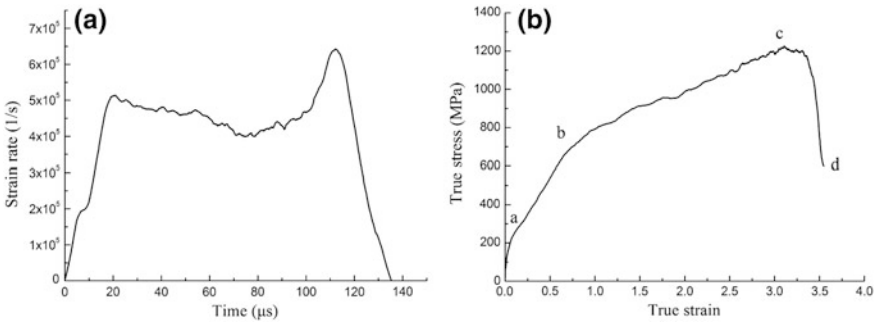

Fig. 5 Mechanical response of the equiatomic CoCrFeMnNi high entropy alloy during the shear localization process. **a** Time—strain rate curve. **b** True strain—true stress curve

stage. Consequently, the true stress for the specimen reaches the maximum value of about 1270 MPa where the strain is about 3. In the last stage (c–d), the true stress sharply decreases with increasing of the strain, and the thermo viscoplastic instability commences at point C. Therefore, an occurrence of the shear localization in the CoCrFeMnNi high entropy alloy needs severe shear deformation.

Fig. 6 The shear section in the specimen revealed by optical micrograph

Figure 6 shows an adiabatic shear band in an equiatomic CoCrFeMnNi high entropy alloy. It can be seen that the shear band is a long and straight band with width about 20 microns inserted in the designed shear zone, which is distinguished from the matrix by boundaries.

Figure 7a shows the region of the line scanning including the matrix, the boundary and the center of the shear band. The corresponding results of the line scanning are shown in Fig. 7b. It can be seen that the five elements contained in the CoCrFeMnNi high entropy alloy distribute homogeneously. There are no elements rearrange within the shear band.

Figure 8 shows the bright field electron micrographs of the shear band. It can be recognized that the boundary of the shear band is characterized by highly elongated cell structures with widths about 0.1 micron and the twin structures about 20 nm in

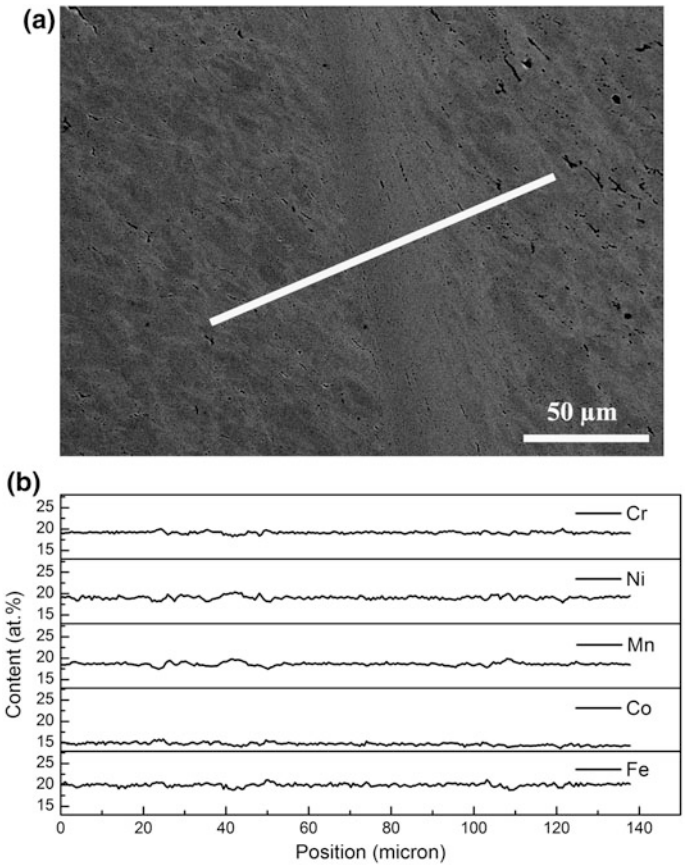

Fig. 7 Electron probe microanalyses of the specimen. **a** Line scanning micrograph. **b** The corresponding results of the line scanning

thickness and 300 nm in length (Fig. 8b), and the core of the shear band consists of ultrafine equiaxed grains with a diameter about 150 nm and nanotwins about 15 nm in thickness and 85 nm in length (Fig. 8c). Both twin structures and elongated cell structures, involving dense dislocation walls and dislocation tangles, are along the shear direction. Figure 8d shows the high-resolution transmission electron micrograph image of nanotwins and its corresponding fast Fourier transforms patterns. The twinning relations are clearly labeled in the Fourier transforms patterns. The twin boundaries are marked by red dashed lines, and the twin angle of 70° is determined. Therefore, nanotwins and ultrafine-equiaxed grains coexist in the shear band. In addition, the high-resolution transmission electron micrograph of the ultrafine grains shows that the local grain-boundary segments tilt about 30°, which indicates that rotational dynamic recrystallization occurs in the alloy as proposed by Meyers et al. [14] (Fig. 8e).

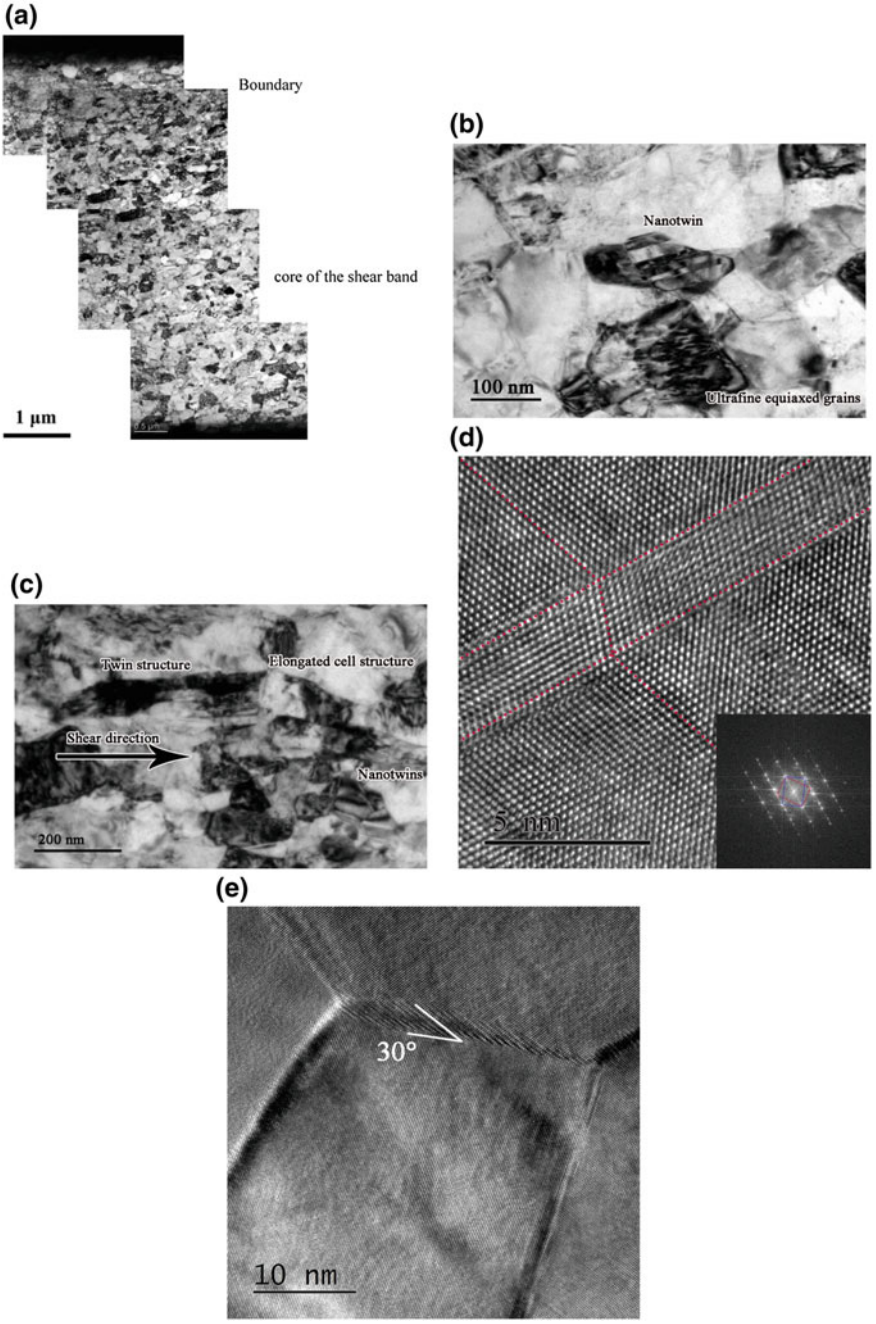

Fig. 8 Microstructure in the shear band of the equiatomic FeCoNiCrMn high entropy alloy. **a** Montage of the bright electron field micrographs across the shear band; **b** the microstructures in the boundary of the shear band; **c** the microstructure in the core of the shear band; **d** the high-resolution transmission electron micrograph image of nanotwins and the insert is the corresponding fast Fourier transforms patterns; **e** the high-resolution transmission electron micrograph of the ultrafine grains

Microstructure Mechanism for the Formation of the Shear Band

Hong et al. [15] and Liu et al. [16] had reported that the twin structures can be destroyed by shear band at large strain when twin density was saturated. Tao et al. [17] also proposed that a grain refinement was induced by transformation of dense dislocation walls and dislocation tangled into sub-boundaries with small misorientations separating individual cells or subgrains, and the sub-boundaries would evolve into highly misorientated grain boundaries. Due to the low stacking fault energy of the CoCrFeMnNi high entropy alloy (about 20 mJ/m^2 [18]), high density of deformation twins are easy to present during plastic deformation of the CoCrFeMnNi high entropy alloy [19]. In this work, the average strain rate for the material in the shear band is about $4.1 \times 10^5\ s^{-1}$ and the maximum strain reached about 3.5. Therefore, during high strain rate deformation, twin structures are generated in the CoCrFeMnNi high entropy alloy, and then destroyed by the shear forces.

The microstructural evolution of the shear band is described as follows. At the beginning of the deformation, the number of deformation twin structures formed along the shear direction. When the twin density is saturated, further twinning becomes difficult to accommodate subsequent strain. Even if twin density is saturated, the volume fraction of twin is still very small. Meanwhile, the grains without twinning can also be elongated into cell structures along the shear direction. Secondly, the twin structures and the elongated cell structures are destroyed into several subgrains by dense dislocation walls due to the strong shear deformation. And then, the subgrains will transform into approximately equiaxed micrograins due to the minimization of the interfacial energy. Finally, the local grain-boundary segments of the micrograins rotate to form high angle grain boundaries. Hence, nanotwins and ultrafine-equiaxed grains coexist in the shear band.

Summary and Conclusions

The equiatomic CoCrFeMnNi high entropy alloy prepared by powder metallurgy has a uniform composition and microstructure. The yield strength of the CoCrFeMnNi high entropy alloy changed from 300 to 700 MPa, increasing with increasing strain rate. The Zerilli-Armstrong plastic model of the CoCrFeMnNi high entropy is obtained.

We also have investigated the adiabatic shear localization in an equiatomic FeCoNiCrMn high entropy alloy. The unstable shear deformation of the alloy emerges after the true flow stress reaches the maximum value of 1270 MPa at the strain about 3. The width of an adiabatic shear band is about 20 microns. In the boundary of the shear band, the twin structures and cell structures of boundaries

are highly elongated along the shear direction. Nanotwins about 15 nm in thickness and 85 nm in length, and ultrafine-equiaxed grains with a diameter about 150 are observed in the core of the shear band.

Acknowledgements This work was financial supported by State Key Laboratory of Powder Metallurgy, Central South University and by National Natural Science of China (No. 51771231, 51671217). The authors would like to express their sincere thanks to Professor M. A. Meyers at University of California, San Diego for good suggestions and helps. The authors would like to express their sincere thanks to Professor Yang Wang and Yu Wang at University of Science and Technology of China, and Professor Xiang Zan at Hefei University of Technology for dynamic testing. The authors also would like to express their sincere thanks to Dr. Yinghong Lin at FEI Co. for preparation of TEM samples.

References

1. Zhang Y, Zuo TT, Tang Z, Gao MC, Dahmen KA, Liaw PK, Lu ZP (2014) Microstructures and properties of high-entropy alloys. Prog Mater Sci 61:1–93
2. He JY, Wang H, Huang HL, Xu XD, Chen MW, Wu Y, Liu XJ, Nieh TG, An K, Lu ZP (2016) A precipitation-hardened high-entropy alloy with outstanding tensile properties. Acta Mater 102:187–196
3. Chen Z, Chen W, Wu B, Cao X, Liu L, Fu Z (2015) Effects of Co and Ti on microstructure and mechanical behavior of $Al_{0.75}$FeNiCrCo high entropy alloy prepared by mechanical alloying and spark plasma sintering. Mater Sci Eng A 648:217–224
4. Liu Y, Wang J, Fang Q, Liu B, Wu Y, Chen S (2016) Preparation of superfine-grained high entropy alloy by spark plasma sintering gas atomized powder. Intermetallics 68:16–22
5. Kumar N, Ying Q, Nie X, Mishra RS, Tang Z, Liaw PK, Brennan RE, Doherty KJ, Cho KC (2015) High strain-rate compressive deformation behavior of the $Al_{0.1}$CrFeCoNi high entropy alloy. Mater Des 86:598–602
6. Dirras G, Couque H, Lilensten L, Heczel A, Tingaud D, Couzinié J-P, Perrière L, Gubicza J, Guillot I (2016) Mechanical behavior and microstructure of $Ti_{20}Hf_{20}Zr_{20}Ta_{20}Nb_{20}$ high-entropy alloy loaded under quasi-static and dynamic compression conditions. Mater Charact 111:106–113
7. Wang B, Fu A, Huang X, Liu B, Liu Y, Li Z, Zan X (2016) Mechanical properties and microstructure of the CoCrFeMnNi high entropy alloy under high strain rate compression. J Mater Eng Perform 25:2985–2992
8. Li Z, Zhao S, Diao H, Liaw PK, Meyers MA (2017) High-velocity deformation of $Al_{0.3}$ CoCrFeNi high-entropy alloy: remarkable resistance to shear failure. Sci Rep https://doi.org/10.1038/srep42742 17 Feb 2017
9. Liu JX, Li SK, Zhou XQ, Zhang ZH, Zheng HY, Wang YC (2008) Adiabatic shear banding in a tungsten heavy alloy processed by hot-hydrostatic extrusion and hot torsion. Scripta Mater 59:1271–1274
10. Liu JX, Li SK, Zhou XQ, Zhang ZH, Wang YC, Yang J (2011) Dynamic recrystallization in the shear bands of tungsten heavy alloy processed by hot-hydrostatic extrusion and hot torsion. Rare Metal Mat Eng 40:0957–0960
11. Meyer LW, Pursche F (2012) Experimental methods. In: Dodd B, Bai YL (eds) Adiabatic shear localization, frontiers and advances, 2nd ed. Elsevier Science Ltd. London, pp 21–110
12. Zerilli FJ, Armstrong RW (1987) Dislocation-mechanics-based constitutive relations for material dynamics calculations. Appl Phys 61:1816–1825
13. Wang BF, Sun J, Wang X, Fu A (2015) Adiabatic shear localization in a near beta Ti–5Al–5Mo–5V–1Cr–1Fe alloy. Mater Sci Eng A 639:526–533

14. Meyers MA, Xu YB, Xue Q, Perez-Prado MT, McNelley TR (2003) Microstructural evolution in adiabatic shear localization in stainless steel. Acta Mater 51:1307–1325
15. Hong CS, Tao NR, Huang X, Lu K (2010) Nucleation and thickening of shear bands in nano-scale twin/matrix lamellae of a Cu–Al alloy processed by dynamic plastic deformation. Acta Mater 58:3103–3116
16. Liu GZ, Tao NR, Lu K (2010) 316L austenite stainless steels strengthened by means of nano-scale twins. J Mater Sci Technol 26:289–292
17. Tao NR, Wang ZB, Tong WP, Sui ML, Lu J, Lu K (2002) An investigation of surface nanocrystallization mechanism in Fe induced by surface mechanical attrition treatment. Acta Mater 50:4603–4616
18. Zaddach AJ, Niu C, Koch CC, Irving DL (2013) Mechanical properties and stacking fault energies of NiFeCrCoMn high-entropy alloy. JOM 65:1780–1789
19. Schuh B, Mendez-Martin F, Völker B, George EP, Clemens H, Pippan R, Hohenwarter A (2015) Mechanical properties, microstructure and thermal stability of a nanocrystalline CoCrFeMnNi high-entropy alloy after severe plastic deformation. Acta Mater 96:258–268

Effect of Phase Transformation on High Temperature Dynamic Flow Stresses of CP-Ti

Sindhura Gangireddy and Steven Mates

Abstract The dynamic mechanical flow stresses of titanium alloys at high temperatures can be strongly affected by phase transformation. Literature documents the flow stresses of the commercial alloy CP-Ti only up to 750 °C. In this study, we investigated the response of commercial alloy, CP-Ti, at very high temperatures of up to 1200 °C while under dynamic loading at strain rates between 1800 and 3500 s^{-1}. Our low temperature data shows good agreement with previous studies, including the dynamic strain aging behavior the material is known to show. For the strain rates in our study, we observe a dynamic strain aging (DSA) peak at around 250 °C, where the thermal softening behavior is milder. The flow curves in the DSA zone are also characterized by a spike in the work hardening of the material. At very high temperatures, we discover a noticeable shift in the softening behavior coinciding with the allotropic transition point at around 880 °C. The data suggests that at this transition point, there is a sharp drop in the flow stresses. The rates of thermal softening are also distinctly different prior and after the transition. Future material models which cover high temperature constitutive response have to consider this effect of phase transformation on the dynamic flow stresses as well.

Keywords High-temperature · Kolsky-Bar · CP-Ti · Dynamic strain aging Phase transformation · Modified Johnson-Cook model

Introduction

Titanium and its alloys have a unique combination of high strength to weight ratio which can be retained at even elevated temperatures, and exceptional corrosion resistance. However, manufacturing titanium alloys has always been problematic due to their poor thermal properties and reactivity with tool materials [1]. The difficulty in machining these materials limits their use in commercial markets where

S. Gangireddy (✉) · S. Mates
Gaithersburg 20878, MD, United States
e-mail: sindhu.g.reddy@gmail.com

The Minerals, Metals & Materials Society, *TMS 2018 147th Annual Meeting & Exhibition Supplemental Proceedings*, The Minerals, Metals & Materials Series,
https://doi.org/10.1007/978-3-319-72526-0_45

rapid manufacturing processes are desired for cost reductions [2]. Understanding the material behavior under the conditions imposed by these processes is highly critical for cost-effective production.

Rapid high temperature forming, high speed machining etc. processes create extreme conditions of high temperatures, rapid heating rates, and rapid loading rates which are hard to study. For this purpose, NIST has developed a new configuration of Split-Hopkinson Pressure Bar (SHPB), capable of reaching heating rates up to 10,000 K/s, loading rates 10,000 s^{-1} with testing temperatures reaching over 1200 °C. Using this equipment, we investigated dynamic flow stresses even beyond the allotropic transition point of 882 °C, up to 1200 °C, at strain rates between 1800 and 3500 s^{-1}. Previous literature on high temperature dynamic deformation has been limited and restricted to below 750 °C. Studies such as Nemat-Nasser [3] well described the thermal softening trends in this temperature range, particularly the presence of dynamic strain aging (DSA) in the temperature range between 23 and 500 °C. We found our low temperature data to agree well with the results of this study, including the DSA peak at around 250 °C for our strain rates. However, we also explored the constitutive behavior beyond the allotropic transition point of 882 °C and discovered that this transformation causes a distinct shift both in the material's strength and the softening rate. In this paper, we will present this high temperature dynamic flow stress data which demonstrates this phenomenon.

Experimental Procedure

Material and Specimen Preparation

Commercial Grade-2 Titanium material was purchased in the form of a 2 mm thick plate and was cut using electrical discharge machining (EDM) to make round compression samples measuring 4 mm in diameter. The chemical composition of the material is given in Table 1.

Table 1 Comparison of the ASTM standard and the chemical composition of the commercial material from spectrographic analysis

Chemical composition (%)	Carbon	Iron	Nitrogen	Oxygen	Hydrogen	Others
ASTM standard[a]	<0.08	<0.3	<0.03	<0.25	<0.015	<0.1
Spectrographic analysis	0.01	0.12	0.008	0.12	19 ppm	

[a]Standard Specification for Titanium and Titanium Alloy Strip, Sheet, and Plate, ASTM B265-13a, page 4

Mechanical Testing

Dynamic compression tests were conducted in Kolsky Bar at strain rates of 1800–3500 s^{-1} and at temperatures of 23–1200 °C in partial vacuum. Samples were resistively heated with high-amperage, low-voltage electric current that was conducted directly through the sample while it sat fixed between the incident and transmission bars. Due to the short heating times (3.5 s in the experiments discussed here), and the small sample cross-section (4 mm diameter) compared to the bars (15 mm diameter), the bars do not undergo significant heating and wave propagation would not be affected, as we have demonstrated in a previous publication [4]. Using an infrared spot pyrometer as a feedback sensor for the PID controller, the heating power is modulated to obtain the set radiance temperature. The temperature uniformity during the heating is monitored through a second pyrometer focused on the other side of the specimen. A thermocouple is also spot welded to obtain the thermodynamic temperature of the specimen before impact. The arrival of the loading wave is timed to occur approximately 30 ms after the heating is turned off. Further details of this heating method, its performance capabilities and assessment of its uncertainties have been described elsewhere [4, 5].

All the specimens were impacted with a 250 mm long striker bar under a gun pressure of 20 psi. The specimen's impedance decreased at higher temperatures, causing greater effective strain rates. As a result, the true strain rate increased from 1800 to 3500 s^{-1} during tests conducted at room temperature to 1200 °C. Titanium has very weak strain rate sensitivity [6], so the effect of this strain rate variation on flow stresses would not be significant. So it would not be unreasonable when such flow stresses are compared in an effort to understand trends in the data. The strain gauge measurements of incident, reflected and transmitted pulses were analyzed to obtain the true stress-true strain curves, which are presented in the results section below.

Results and Discussion

Dynamic Stress-Strain Curves

Figure 1 depicts the dynamic stress-strain curves obtained from Kolsky-Bar testing conducted between 23 and 1200 °C. At the very beginning of a Kolsky-Bar test, the strain rate changes very rapidly and these portion of initial rise of the stress-strain curve is ignored. The data in this plot represents only the portion of the stress strain curves where the strain rate was stable. The temperatures quoted are the initial thermodynamic temperatures measured by the thermocouple just before impact. The curves in Fig. 1 represent the dynamic flow stress of the material during a single, short-duration compression event.

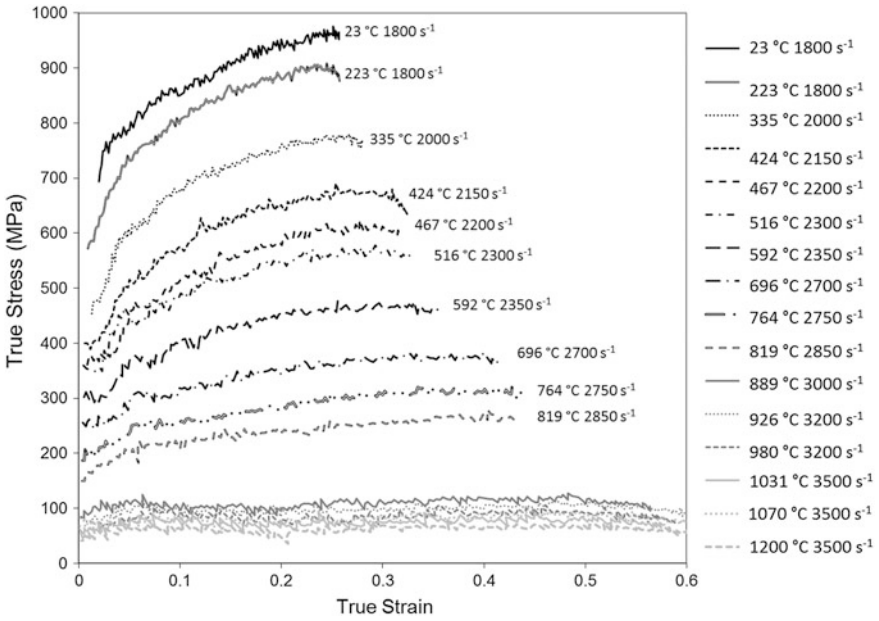

Fig. 1 High temperature dynamic stress-strain curves

During room temperature compression in the Kolsky Bar at 1800 s^{-1}, Fig. 1 shows our dynamic flow stress increasing from about 750 MPa at 0.025 strain to 950 MPa at 0.25 strain. These results are quite comparable to those reported by Gurao [7], at a strain rate of 1500 s^{-1} during dynamic compression in Kolsky Bar at room temperature where the flow stresses increased from 650 MPa at 0.025 strain to 900 MPa at 0.25 strain. Li [8] reported higher flow stresses of 700 MPa at 0.025 strain increasing to almost 1200 MPa at 0.25 strain, but at a higher strain rate of 3000 s^{-1}. Similarly, Wang [9] also have reported even higher flow stresses at a larger strain rate of 4000 s^{-1} on an ultrafine grained ECAP processed material, 800 MPa at 0.025 strain. But this material had a weaker work hardening and the flow stress at 0.25 strain was 1000 MPa, smaller than Li's 1200 MPa at same strain. Huang [10] and Yuan [11] used a tension SHPB at 1400 and 1100 s^{-1} strain rates respectively yielding flow stresses of around 500 MPa at 0.025 strain, much smaller than the above mentioned studies. Nemat-Nasser [3] reported results from compression SHPB at a strain rate of 2200 s^{-1}. Their flow stresses were smaller than even Huang and Yuan at low strains, 300 MPa at 0.025 strain, but due to stronger work hardening the flow stresses at larger strains increased beyond Huang and Yuan's data, to 800 MPa at 0.25 strain. Initial material composition or microstructural differences could have been the cause of the scatter in the room temperature response. Our data also lies within this band of reported values. Table 2 shows the flow stress data from our experiments tabulated along the data from these above literature sources.

Table 2 Room temperature dynamic flow stress comparison

Data source	Test method	Strain rate (s^{-1})	Stress (MPa) at true strain		
			0.025	0.1	0.25
NIST	SHPB compression	1800	750		950
Gurao [7]	SHPB compression	1500	650		900
Li [8]	SHPB compression	3000	700		1200
Wang [9]	SHPB compression	4000	800		1000
Yuan [11]	SHPB tension	1100	500	650	
Huang [10]	SHPB tension	1400	450		700
Nemat-Nasser [3]	SHPB compression	2200	300		800

The literature on high temperature response is more limited and also restricted to about 750 °C. Ahmad [12] study reported flow stresses at 5 test temperatures of 150, 300, 450, 600, and 750 °C. Magargee [13] studied electrically assisted tension testing at 4 temperatures of 25, 74, 249, and 435 °C. Cheng and Nemat-Nasser [14] conducted a more comprehensive study of flow stresses at 8 temperatures between −196 and 725°C. As CP-Ti undergoes allotropic transformation from hcp to bcc crystal structure at 882 °C, we also conducted tests beyond this temperature. The final test matrix composed of 16 different temperatures over a range of 23–1200 °C, designed to cover both alpha and beta phase fields, Fig. 1.

Figure 2 demonstrates the thermal softening trend, i.e. the variation in the dynamic flow stresses as a function of temperature. Here the flow stresses at different plastic strains are plotted against with their corresponding temperatures, including the temperature rise from the initial test temperature due to the adiabatic heating. This thermal softening trend revealed three features:

(a) Below $\alpha \rightarrow \beta$ transus: At low temperatures where CP-Ti is in the alpha phase field, the flow stresses drop significantly with increments in temperature. The trend is almost linear except for a reduced softening rate between room temperature and 500 °C. This deviation appears to peak occur around 250 °C. Similar phenomenon has been reported previously by Nemat-Nasser and Cheng [14] and was attributed to dynamic strain aging (DSA) whose peak temperature varied with the deformation rate. During deformation at a strain rate of 2200 s^{-1}, they also observed a deviation peak around 250 °C, exactly matching the trend we observe. The flow curves from this temperature range also showed a significantly higher work hardening rate (Fig. 3), strengthening the theory that DSA was the cause of this behavior.
(b) At $\alpha \rightarrow \beta$ transus: Between the test conducted at 819 °C in alpha phase field, and the test at 889 °C in the beta phase field, there is quite an abrupt drop. The allotropic transformation which occurs at 882 °C results in hcp α phase to turn to the weaker bcc β phase, which has more number of the available slip systems to accommodate plastic flow. This could be the reason for the discontinuity in the softening trend as seen in the Fig. 2.

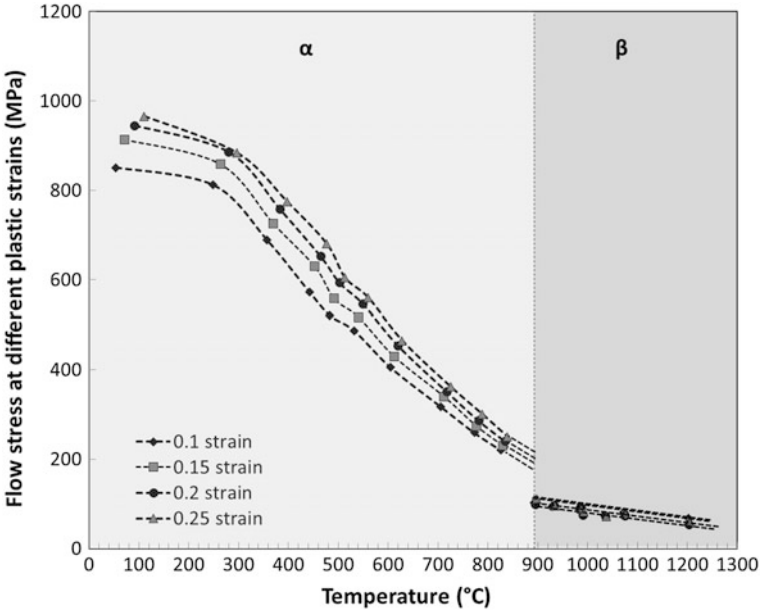

Fig. 2 Thermal softening in the flow stresses at 0.1, 0.15, 0.2, and 0.25 strain with increasing temperature

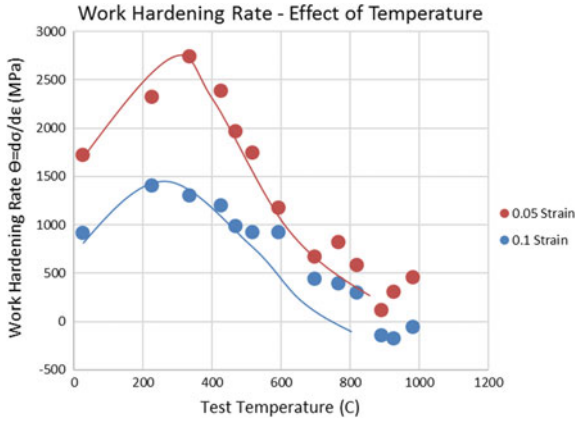

Fig. 3 Rate of work hardening in the flow curves from various test temperatures, showing a peak around 250 °C

(c) Above α → β transus: These high temperatures where CP-Ti is in beta phase field are marked darker grey in Fig. 2. The thermal softening rate here, between 889 and 1200 °C, appears monotonically linear but the slop is significantly milder. This indicates the softening rate is weaker in the beta regime than that seen in alpha regime (light grey on left in Fig. 2).

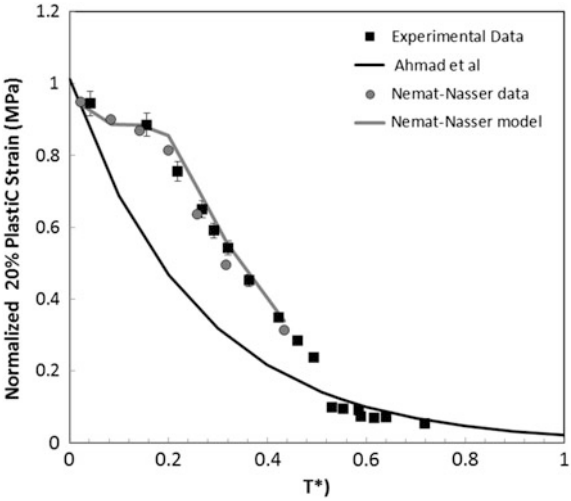

Fig. 4 Comparison of NIST data, normalized flow stresses at 0.2 plastic strain, with Nemat-Nasser's data and their physical model's prediction [3]

At temperatures below beta transus, our thermal softening observations are in good agreement with Cheng and Nemat-Nasser's data (Fig. 4) as well as their physical model, which considered athermal long range, and thermally activated short range barriers for dislocation motion together with evolution of the core atmosphere, and interaction of dislocation and point defects. However, despite the 14 material constants in this complex model, the softening behavior at further high temperatures above the transformation temperature would not be captured by it. In order to cover the constitutive response over this entire temperature range, a different material model or a modification to existing models is necessary and we are attempting to develop such a flow stress equation, which will be presented in a future publication.

Conclusion

This paper explores the dynamic mechanical response of commercially pure titanium (Grade-2) material at very high temperatures much beyond existing literature. The focus is particularly on thermal softening behavior, the variation of flow stresses with temperature. The low temperature softening was similar to existing literature, including the presence of dynamic strain aging in the temperature range of 23–500 °C. High temperature data indicated that allotropic transformation also causes a sharp deviation from a monotonic softening trend. The transformation from hcp to bcc crystal structure at 882 °C had a twofold effect, the former being a sharp drop in the flow stress and the latter being the shift in the softening rate as well. Such constitutive response needs a new modification or model to effectively capture this flow stress trend.

References

1. Rahman M, Wang ZG, Wong YS (2006) A review on high-speed machining of titanium alloys. JSME Int J C Mech Syst Mach Elem Manuf 49(1):11–20
2. Yang X, Richard Liu C (1999) Machining titanium and its alloys. Mach Sci Technol 3(1): 107–139
3. Nemat-Nasser S (1999) Acta Mater 47(13):3705–3720
4. Gangireddy S, Mates SP (2017) J Dynamic behavior mater 3:557
5. Mates SP, Rhorer R, Whitenton E, Burns T, Basak D (2008) A pulse-heated kolsky bar technique for measuring the flow stress of metals at high loading and heating rates. Exp Mech 48(6):799–807
6. Chichili DR, Ramesh KT, Hemker KJ (1998) The high-strain-rate response of alpha-titanium: experiments, deformation mechanisms and modeling. Acta Mater 46(3):1025–1043
7. Gurao NP (2011) Acta Mater 59:3431–3446
8. Li Q (2004) J Mater Process Technol 155–156:1889–1892
9. Wang L (2014) J Mater Sci 49:6640–6647
10. Huang W (2007) Mater Sci Eng A 443:33–41
11. Yuan JM (2000) Int J Solids Struct 39:213–224
12. Sheikh-Ahmad JY (1995) J Eng Mater Technol 117:139–143
13. Magargee J (2013) J Eng Mater Technol 041003-1–041003-10
14. Cheng, Nemat-Nasser (2000) J Acta Mater 48:3131–3144

Shock-Induced Mechanical Response and Substructural Evolution of Ti–6Al–4V Alloy

Yu Ren, Shimeng Zhou, Zhiyong Xue and Chengwen Tan

Abstract The effects of shock stress amplitude on the post-shock mechanical response and substructural evolution of Ti–6Al–4V alloy are investigated within the impact stress range of 6–10 GPa. The reload yield behavior of post-shock Ti–6Al–4V does not exhibit enhanced shock-induced strengthening at an effective strain level even if the shock stress achieves 10 GPa. The residual substructures of post-shock Ti–6Al–4V are examined by transmission electron microscopy. Results reveal that planar slip is the dominant deformation mechanism of this alloy during shock loading pulse. Dislocations tangle and form developed dislocation clusters (planar slip bands) with increased impact stress. The lack of dislocation cells or cell-like structures, high-density twins and additional strengthening phases limits the shock-induced strengthening effect in post-shock materials. However, dislocation multiplication and tangles lead to increased yield strength and strain hardening rate of reloaded materials.

Keywords Ti–6Al–4V alloy · Shock wave loading · Reload mechanical properties · Substructural evolution

Y. Ren (✉) · Z. Xue
School of Energy, Power and Mechanical Engineering,
North China Electric Power University, Beijing 102206, PR China
e-mail: renyuljz@163.com

Z. Xue
e-mail: xuezy@ncepu.edu.cn

S. Zhou
Institute of China Ordnance Industries, No. 52, Yantai 264003, Shandong, China
e-mail: m20909094@163.com

C. Tan
School of Materials Science and Engineering,
Beijing Institute of Technology, Beijing 100081, PR China
e-mail: tanchengwen@126.com

C. Tan
National Key Laboratory of Science and Technology on Materials Under Shock and Impact, Beijing Institute of Technology, Beijing 100081, PR China

The Minerals, Metals & Materials Society, *TMS 2018 147th Annual Meeting & Exhibition Supplemental Proceedings*, The Minerals, Metals & Materials Series,
https://doi.org/10.1007/978-3-319-72526-0_46

Introduction

Microstructural changes such as defect generation and phase transformation may occur during the propagation of shock waves. These changes in microstructure can alter the mechanical properties of metals. Although the preshocked metals usually have a higher yield stress than the original materials, the strengthening effect caused by shock loading is not always stronger than that produced by work hardening in conditional deformation process (such as forging, rolling and extrusion, etc.) at the effective strain [1]. In particular, the extent of strengthening is dramatically affected by the crystal structure, which determines the type, morphology, and density of the defects as a result of the shock-loading pulse [1, 2]. For example, in face-centered-cubic (fcc) metals possessing high stacking fault energy (SFE; >60 mJ m^{-2}) and low Peierls stress such as Ni, dislocations more easily nucleate, travel, and cross slip, thereby tending to form developed dislocation cells resulting in significant strengthening of these materials [2, 3]. Low-SFE (<40 mJ m^{-2}) alloys with the fcc structure (e.g., 304 stainless steel) are characterized by planar dislocation arrays, stacking faults, and twins in {111} planes, which also produce a certain degree of shock-induced hardening effect in these kind of materials [2]. Meanwhile, body-centered-cubic (bcc) materials have fewer operating slip systems and higher Peierls stress than fcc crystals, which means fewer dislocation nucleation and greater resistances to defect motion during shock wave loading. Consequently, the predominant shock-induced substructures in bcc metals (like Ta and Mo) are tangled long straight screw dislocations [4], dislocation loops and debris [4, 5], and a certain amount of twins [4, 6]. Hence, considering the relatively low defect density and fewer interactions of defects, bcc materials commonly do not display enhanced strengthening effect under shock-loading conditions at an effective strain level. However, studies on the shock-induced substructural variation and its influence on the mechanical properties of hexagonal-close-packed (hcp) metallic materials such as pure titanium and its alloys are limited [1, 7].

In this study, the response of commercial Ti–6Al–4V alloy (hereafter denoted as Ti64) with bimodal microstructure to shock wave loading was investigated because of relatively low price and widespread application of this alloy. Bimodal microstructure seems to benefit the fracture resistance of Ti64 under high-strain-rate loading conditions [8, 9]. The effect of shock stress amplitude on the post-shock mechanical properties of Ti64 was revealed through the quasi-static reload compression tests at room temperatures. The substructural evolution of the preshocked alloys was also characterized by transmission electron microscopy (TEM) to display the reasons for changes in the mechanical properties of this alloy.

Material and Experimental Procedure

The Ti64 alloy used was a 30 mm-diameter forging bar stock. The chemical composition (in wt%) is Al 5.82, V 3.84, Fe 0.16, O 0.08, C 0.024, H 0.0014, N 0.023, and balanced Ti. The beta-transus temperature T_β of this alloy determined by differential scanning calorimetry is 1266 K. In order to acquire bimodal microstructure, the forging bars were annealed at 1206 K (60 K below T_β) for 60 min followed by air cooling. Figure 1 shows the optical and TEM microstructures of Ti64 before shock wave loading. The microstructure of the heat-treated Ti64 is composed of the mixture of equiaxed primary α and transformed β. The volume fraction of primary α-phase is about 57%. The TEM image of the heat-treated Ti64 (Fig. 1b) indicates a low dislocation density and the absence of ω phase before shock wave loading. Plate impact specimens (recovery samples) were machined from the center area of the bar stock, such that the impact axis was parallel to the axis of the billet.

Shock recovery experiments were conducted on a 57-mm-diameter and 12.5-m-long single-stage gas gun. Soft recovery target assembly was designed according to Ref. [10]. The shock recovery fixture consists of a 23-mm-diameter and 9-mm-thick recovery sample, stacked behind a 70-mm-diameter and 2.5-mm-thick cover plate. The sample was protected from residual strain and spallation by surrounding an inner momentum trapping ring with outside diameter of 67 mm and supporting with a 10-mm-thick spall plate. The inner momentum trapping ring and spall plate were further concentrically surrounded by an outer momentum trapping rings with outside diameter of 78 mm. The recovery sample and the inner momentum trapping ring were interference fit together. Two trapping rings, cover plate and spall plate were assembled with slip fit. Molybdenum disulfide grease was used during assembly of the trapping tings to remove air gaps in the assembly and to facilitate ring separation during recovery.

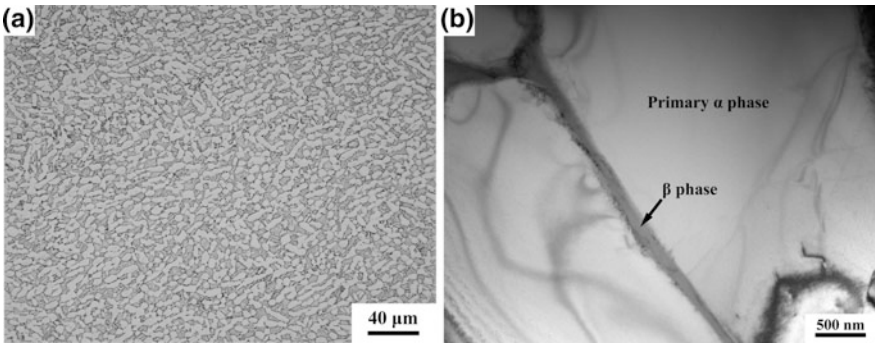

Fig. 1 Microstructure of the Ti64 before shock loading: **a** optical micrograph showing the bimodal microstructure, **b** TEM image showing a low dislocation density in the primary α phase

The Ti64 samples were impacted by flyer plates within the velocity range of 525–843 ms^{-1} to yield impact stresses ranging from 6.24 to 10.34 GPa. All experiments were conducted in symmetrical impact, which means that the recovery assembly and flyer plate were made of the same material (Ti64). The thickness of flyer plates, which was calculated according to Ref. [10], ranged from 4.14 to 4.33 mm to ensure constant pulse duration of 1.5 μs. Impact stress was calculated by $P = \rho_0 U_S u_P = \rho_0 (C_0 + S u_P) u_P$, where, u_P is the particle velocity that is equal to 0.5 times the impact velocity for symmetrical impact, ρ_0 and the shock parameters C_0 and S can be found in Ref. [11]. The impact surfaces of all recovery assemblies and flyer plates were mechanically polished to ensure that the surface roughness was less than 0.8 μm. The planarity of the target assembly to the flyer plate was controlled by adjusting the specimen mount to better than 1 mrad. The impact velocities were measured by an electro-optical system to an accuracy of about 0.5%. After shock loading, the recovery samples were flat and possessed residual plastic strains of 1.6–1.9%, indicating that the influence of lateral release waves on the recovery samples is deemed to be negligible. The residual strain is defined here as the starting sample thickness minus the recovered sample thickness following shock loading divided by the starting sample thickness.

The original material and alloys preshocked at 6.24–10.34 GPa were sectioned from the center area of the heat-treated forging bar and recovery samples respectively into several compression cylinders (4 mm in diameter and 8 mm in thickness) for quasi-static reload compression tests. These reload compression tests were performed at room temperature under a strain rate of 10^{-3} s^{-1} using an MTS 810 hydraulic servo machine. Tests were continuously conducted until the cylinders fractured.

To observe substructure changes of the preshocked alloy, TEM analyses were conducted using a JEOL JEM-2100 system at an accelerating voltage of 200 kV. For TEM observations, thin samples with an initial thickness of 0.5 mm were cut from the recovery samples along the longitudinal (impact) direction, reduced to less than 40 μm thick by mechanical means, then punched into several standard 3 mm-diameter TEM discs, and finally thinned by ion milling.

Results and Discussion

Post-shock Mechanical Response

Figure 2a shows the quasi-static compression stress–strain curves of the post-shock alloys at room temperature in conjunction with the original materials. The reload stress–strain curves of the post-shock alloy have been offset with respect to the original material by the equivalent strains accumulated during the shock-loading process. This expression enables comparison of the strengthening effects imparted

by the propagation of shock waves with those produced by conventional uniaxial stress loading [1, 12]. The shock-induced equivalent strain (ε_{eq}) is defined as [12]:

$$\varepsilon_{eq} = 4/3 \ln(V/V_0) \tag{1}$$

where V and V_0 are the final compressed and initial specific volumes of the material, respectively. The values of V and V_0 can be determined from the shock Hugoniot through the conservation relations [12]. The shock Hugoniot of Ti64 is described elsewhere [11].

In all cases, the reload curves for preshocked Ti64 exhibit a higher flow stress than the original material during room temperature compression tests. However, the post-shock alloys display a lower yield stress than the corresponding flow stress of the original material at the effective strain level, as shown in Fig. 2a. It indicates that shock-loading process cannot improve the strengthening effect of Ti64 even if the impact stress exceeds 10 GPa. Namely, the strengthening effect caused by shock loading is weaker than the work hardening in the conventional deformation process. When the plastic deformation proceeds, the reload curves begin to lie above the original one, indicating more significant strain hardening of the preshocked Ti64 with increased strain. Finally, the reload samples fracture with a fracture strain smaller than the original value (0.53). Fracture strain of preshocked materials ranges from 0.49 to 0.46 and decreases slightly with increased shock stress. The fracture strain is defined as the maximum strain that the specimen endures before it fractures during the compression test.

Figure 2b shows the corresponding compression yield stress and ultimate strength of the post-shock Ti64 as a function of the impact stress at room temperature. The yield stress of preshocked alloys rapidly rises as the impact stress increases. Compared with the original material, the yield stress of Ti64 increases by about 159 MPa after shock loaded to 10.34 GPa. This result suggests that the defect

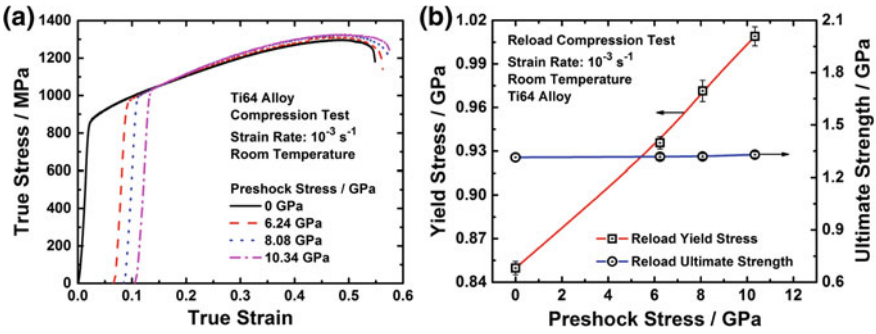

Fig. 2 **a** Typical reload compression stress–strain curves, **b** strength of the post-shock alloy versus shock-loading stress for Ti64 with bimodal microstructure at room temperature under a strain rate of 10^{-3} s^{-1}

type, morphology or density of Ti64 may have been markedly changed during shock loading pulse. On the other hand, the ultimate strength of preshocked Ti64 is hardly changed, implying that the proliferation of defects reaches saturation as the plastic deformation proceeds.

Substructural Evolution

Figure 3 presents the TEM images of dislocation substructure features in Ti64 soft recovered from different impact loads. Compared with the original material (Fig. 1b), the dislocations in the α phase of the 6.24 GPa shocked Ti64 significantly increase in density and become longer and straighter during shock-loading pulse, as shown in Fig. 3a. These dislocations also arrange in parallel to some extent. Thus, the substructure of Ti64 shock loaded at a relatively low impact stress primarily consists of parallel-aligned long and straight dislocations. With increased impact stress up to 8.08 GPa, the dislocation density in the α phase of preshocked Ti64 further increases (Fig. 3b). These dislocations stagger mutually and form a mesh structure, implying more slip system activated at a higher impact stress level. This substructural characteristic is similar to the "planar slip" observed in A-70 Ti shocked to 11 GPa [7]. As seen in Fig. 3c, when the impact stress reaches 10.34 GPa, the density of those long and straight dislocations continuously increases. In some areas, dislocations gather and tangle, and tend to form cluster-like structures, similar to those planar slip bands appearing in Ti64 undergoing the large-strain deformation at quasi-static and dynamic strain-rates [13]. This result indicates that dislocation interaction has fully proceeded within the time of 1.5 μs, confirming the characteristic timescales for shock-induced substructure evolution proposed by Bourne et al. [14]. Namely, the generation and movement of dislocations are faster under shock loading conditions. No twins, developed dislocation cells or cell-like structures are observed in Ti64 with bimodal microstructure even shocked at 10.34 GPa. In addition, analyses on the selected area electron diffraction patterns obtained from the α region in the preshocked materials show the existence of only an α phase, thereby confirming the absence of shock-induced α-to-ω and other phase transformation in Ti64 with at least 10 GPa. This result is consistent with the performance of A-70 Ti [7].

The shock-induced defect substructure directly affects the post-shock mechanical properties of Ti64. Defects multiplication result in the increased yield stress and strain-hardening rate of the reloaded Ti64 at room temperature, as shown in Fig. 2. Dislocations proliferate with increased impact stress, leading to a rapid increase in the yield stress of this alloy as the impact stress exceeds 6 GPa. Nevertheless, the low symmetry and relatively high Peierls stress of the hcp structure restrict further nucleation, traveling, interaction of dislocations, and formation of dislocation cells or cell-like structures in Ti64 under shock-loading conditions. Moreover, the formation of high-density twins and additional strengthening phases such as ω or Martensite phase is suppressed during shock-loading pulse, also bringing about the

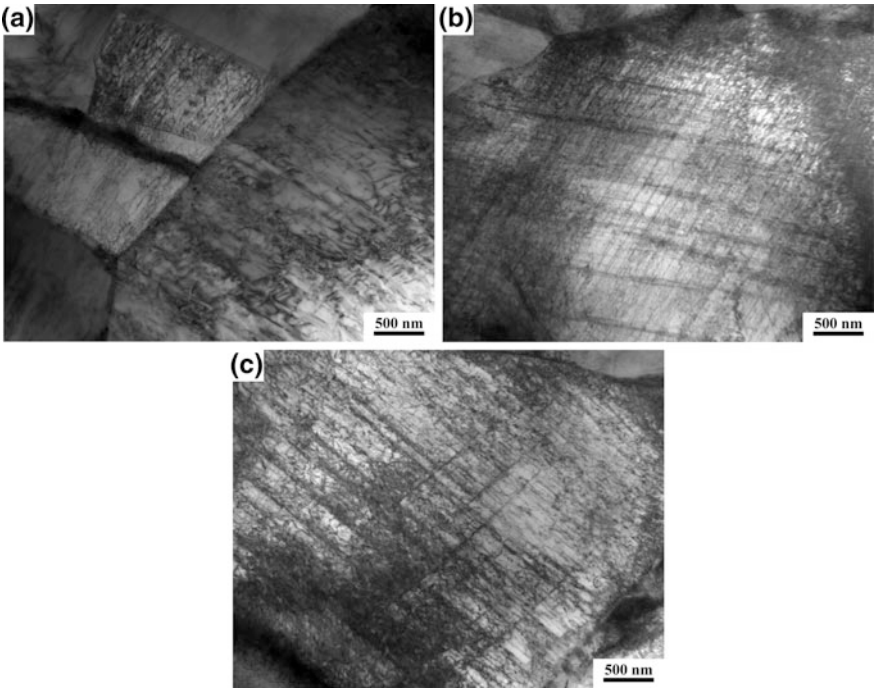

Fig. 3 Bright field TEM images showing dislocation substructures of Ti64 shock loaded to **a** 6.24 GPa, **b** 8.08 GPa, **c** 10.34 GPa

limited strengthening effect. Therefore, Ti64 does not display an enhanced strengthening response at an effective strain level even though the impact stress attains 10 GPa (Fig. 2a). The defects introduced by shock loading hinder the motion of dislocations during reload deformation, resulting in the decreased plastic strain of the preshocked Ti64.

Conclusions

In this study, Ti64 alloy was subjected to shock wave loading and reloaded quasi-statically at room and temperature to investigate the effect of impact stress amplitude on the post-shock mechanical response and substructural evolution of this alloy. Ti64 does not display an enhanced shock-induced strengthening effect compared with the original material at an equivalent strain level at room temperature even if the preshocked stress exceeds 10 GPa. Planar slip dominates the shock-induced plastic deformation process in Ti64. The lack of dislocation cells or cell-like structures, high-density twins and additional strengthening phases such as ω or Martensite phase limits the further strengthening of this alloy through shock

loading. However, dislocation multiplication during shock loading lead to a rapid increase in the yield strength and increased strain-hardening rate of the reloaded materials at room temperature.

Acknowledgements The authors gratefully acknowledge Mingjian Zhang of the Southwest Jiaotong University for his assistance in the plate impact experiments. This work was supported by the Young Scientists Fund of the National Natural Science Foundation of China (grant number: 51501064).

References

1. Bourne NK, Millett JCF, Gray GT III (2009) On the shock compression of polycrystalline metals. J Mater Sci 44:3319–3343
2. Murr LE (1981) Residual microstructure-mechanical property relationships in shock-loaded metals and alloys. In: Meyers MA, Murr LE (eds) Shock waves and high-strain-rate phenomena in metals 1981. Plenum Press, New York, pp 607–673
3. Follansbee PS, Gray GT III (1991) The response of single crystal and polycrystal nickel to quasistatic and shock deformation. Int J Plasticity 7:651–660
4. Gray GT III, Vecchio KS (1995) Influence of peak pressure and structure/property response of shock-loaded Ta and Ta-10W. Metall Mater Trans A 26A:2555–2563
5. Murr LE, Inal OT, Morales AA (1976) Direct observations of vacancies and vacancy-type defects in molybdenum following uniaxial shock-wave compression. Acta Metall 24:261–270
6. Wongwiwat K, Murr LE (1978) Effect of shock pressure, pulse duration, and grain size on shock-deformation twinning in molybdenum. Mater Sci Eng 35:273–285
7. Cerreta E, Gray GT III, Lawson AC, Mason TA, Morris CE (2006) The influence of oxygen content on the α to ω phase transformation and shock hardening of titanium. J Appl Phys 100:013530
8. Lee D, Kim YG, Nam D, Hur S, Lee S (2005) Dynamic deformation behavior and ballistic performance of Ti–6Al–4V alloy containing fine α_2 (Ti_3Al) precipitates. Mater Sci Eng A 391:221–234
9. Liu X, Tan C, Zhang J, Wang F, Cai H (2009) Correlation of adiabatic shearing behavior with fracture in Ti–6Al–4V alloys with different microstructures. Inter J Impact Eng 36:1143–1149
10. Gray GT III (1993) Influence of shock-wave deformation on the structure/property behavior of materials. In: Asay JR, Shahinpoor M (eds) High-pressure shock compression of solids 1993. Springer Science+Business Media, New York, pp 187–215
11. Millett JCF, Whiteman G, Bourne NK, Gray GT III (2008) The role of anisotropy in the response of the titanium alloy Ti–6Al–4V to shock loading. J Appl Phys 104:073531
12. Meyers MA (1994) Dynamic behavior of materials. John Wiley & Sons Inc, New York
13. Follansbee PS, Gray GT III (1989) An analysis of the low temperature, low and high strain-rate deformation of Ti–6AI–4V. Metall Trans A 20A:863–874
14. Bourne NK, Gray GT III, Millett JCF (2009) On the shock response of cubic metals. J Appl Phys 106:091301

The Use of Circumferentially Notched Tension (CNT) Specimen for Fracture Toughness Assessment of High Strength Steels

V. A. Popovich, T. Opraus, M. Janssen, B. Hu and A. C. Riemslag

Abstract The fracture toughness of high strength steels is commonly determined by standard methods using Compact tension (CT) or Single edge notched bend (SENB) specimens. In the past the Circumferentially Notched Tension (CNT) geometry has been reported as a potential candidate for determining the fracture toughness of highly constrained cracks, theoretically approaching plane strain conditions, even for small specimen dimensions. The goal of this study is to develop a more fundamental understanding of the CNT methodology and apply it to high strength S690QT steel. An alternative prefatiguing method was developed and a straightforward relation was established between the Crack Mouth Opening Displacement (CMOD) and the Crack Tip Opening Displacement (CTOD). With the new experimental aspects, it proved feasible to determine upper-shelf CTOD values for S690QT steel, using small CNT specimens ($D = 12$ mm), tested at room temperature with a relative high loading rate. Furthermore, CNT low temperature values were found comparable to those of conventional SENB tests. Hence, the research demonstrates that CNT geometry allows for small scale high loading rate specimen testing, resulting in simple, rapid and cost effective fracture toughness determination.

Keywords Fracture toughness · Circumferentially notched tensile test
High strength steel

Introduction

Most structural applications require the selection of materials with optimum combination of strength, ductility and fracture toughness for effective service performance. Fracture toughness is a property which describes the ability of a material

V. A. Popovich (✉) · T. Opraus · M. Janssen · A. C. Riemslag
Department of Materials Science and Engineering, Delft University of Technology, Delft, The Netherlands
e-mail: v.popovich@tudelft.nl

B. Hu
Allseas Engineering B.V., Delft, The Netherlands

The Minerals, Metals & Materials Society, *TMS 2018 147th Annual Meeting & Exhibition Supplemental Proceedings*, The Minerals, Metals & Materials Series,
https://doi.org/10.1007/978-3-319-72526-0_47

containing a crack to resist fracture and it is considered one of the most important mechanical properties for structural integrity assessment of components.

Fracture toughness ($K_{IC,}$ crack tip opening displacement (CTOD) and J-Integral), is traditionally determined using standardized (ASTM E399 [1], E1820 [2], BS 5762 [3]) Compact Tension (CT), and Single Edge Notched Bend (SENB) test specimens. Unfortunately, these tests are expensive and time consuming. Furthermore, the validity of the tests is governed by two main factors, a minimum required specimen size and a symmetry of the resultant crack front, which are not easy met in actual practical applications.

A practically convenient and cost effective Circumferentially Notched Tension (CNT) specimen is proposed is this work as a potential candidate for determining the fracture toughness of highly constrained cracks. The CNT specimen represents a round bar loaded in tension with a prefatigued notch along its circumference, which contrary to SENB and CT specimen, has no free ends and therefore should provide valid plain strain crack tip loading condition for the smallest possible specimen size [4–7]. Hence, the CNT geometry potentially requires less material, while machining of the specimen is easier and cheaper compared to traditional testing specimens.

In this paper fracture toughness values (CTOD) of high strength steel S690QT were measured at room and low temperature. The CTOD parameter was chosen as theoretically it is based on the physical deformation of the crack faces and it does not have mathematical limitations regarding the level of plastic deformation ahead of the crack tip or elastic unloading associated with crack growth or stress-strain relationship. Ductile to brittle transitional curves determined based on CTOD results for both CNT and SENB geometries were compared and equivalency between the tests is discussed.

A common issue encountered in CNT specimens is a possible development of eccentric pre-fatigue cracks. This matter was assessed by comparing the symmetry of cracks developed using two distinct pre-fatiguing techniques. The first technique is the well-established loading by rotational bending (RB) [6–10], while the second novel technique is designated as compression-compression (C-C) pre-fatiguing. Fracture surface was examined by means of optical and scanning electron microscopy (SEM).

Experimental Details

Material and Sample Preparation

High-strength S690QT steel, a typical steel for offshore application featuring fine grained tempered martensitic microstructure and a yield strength of 760 MPa was used in this work. The samples were cut from a 60 mm thick slab with the composition shown in Table 1. In order to eliminate through thickness microstructural inhomogeneity the samples were taken 10 mm below the surface.

CNT specimens with notch geometry details shown in Fig. 1 were used for fracture toughness measurements. All dimensions of CNT specimens are related to the outer diameter.

Table 1 S690QT composition determined by means of X-ray fluorescence (XRF)

Element	C	Si	Mn	P	Cr	Mo	Ni	Cu	Al	Nb
Wt (%)	0.16	0.2	1.3	0.01	0.36	0.45	0.01	0.081	0.093	0.029

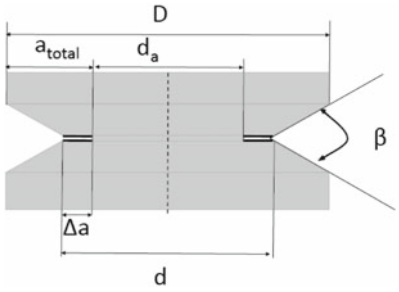

Outer diameter	D	12 mm
Notched diameter	d	8 mm
Ligament diameter	da	6 mm
Diameter ratio	da/D	0.5
Fatigue crack length	Δa	1 mm
Notch depth	a_{mach}	2 mm
Total crack length	a_{total}	3 mm
Length	L	100 mm
Notch angle	β	60 °
Notch radius	ρ	0.2 mm

Fig. 1 CNT notch and pre-crack geometry details

Equivalency tests were performed using sub-sized Single Edge Notched Bending (SENB) specimens with $W = 20$ mm high by $B = 10$ mm thick by 100 mm long with a span of $S = 80$ mm. The specimens were loaded in three point bending according to the AFSuM procedure [11] and BS7448:1991 [12]. All fracture specimens were tested with a through-thickness notch parallel to the rolling direction using an MTS 858 servo hydraulic. All SENB fracture samples were tested with an a_0/W ratio of approximately 0.54. Tests were performed at different temperatures at a loading rate of 2 mm/s.

Pre-fatiguing of CNT Specimens

The fatigue pre-cracking of CNT specimens was performed by two different methods:

- via *Rotational Bending (RB),* which is a conventional way of pre-fatiguing CNT specimens [6–9]. The RB pre-cracking was performed with a "Sincotec 50 Nm four-point rotational bending machine", using a gauge length of 50 mm between the grips. Fatigue pre-cracking was done at a rotational speed of 2000 rpm (33.3 Hz) and a bending moment of 18 Nm, resulting according to [10] in a final stress intensity value of 15 MPa$\sqrt{m}$. A stiff level system, coupled to a load cell, enabled the bending moment to be applied in a so-called displacement controlled manner. During pre-fatiguing, crack development constitutes a reduction in bending stiffness, resulting in a load drop, registered by the load cell. As such, the degree in load drop was used as a means to monitor the internal (and optically hidden) crack extension. A subsequent moment reduction of 5% led to a circumferential crack length of 1 mm for a gauge length of 50 mm. Theoretically,

this pre-fatigue technique should produce symmetrical cracks, due to the interactions of crack length, stiffness and (local) stress intensity.

- via *The Compression-Compression (C-C), method, which is a novel pre-fatigue technique.*

  The C-C method was used to create a circumferential crack extension of about 1 mm, constituting two distinct steps (see schematic in Fig. 2). Firstly, the specimen is given a single compressive load, with a level known to cause a small (compressive) plastic region around the geometrical stress concentration (at the notch root). During subsequent unloading, residual stresses will develop originating from the compressive plastic region. Without external load, the residual stresses are tensile at the notch edge region and become compressive in the centre region. In the second step, the specimen is pre-fatigued in full compression, constituting compressive nominal stress levels in the ligament, normally not causing crack initiation. However, the local residual tensile stresses at the notch root, are cyclically relieved by the nominal compressive fatigue load. This causes a fatigue crack to develop from the notch root, but the crack will arrest when its length has growth through the region with residual tensile stresses. Therefore, the C-C pre-fatigue method is self-regulating (i.e. the crack automatically arrests). If, crack initiation periods would vary at different notch root positions, the C-C prefatigue is still likely to give symmetric crack extensions. The crack extension (i.e. crack arrest) depends on the size of the region with residual tensile stresses, not on the number of fatigue cycles. However, it must be ensured that enough cycles are applied for even the slowest crack extension to reach the moment of crack arrest.

The Compression-Compression fatiguing was performed on a hydraulic MTS 350 kN fatigue testing machine with a single compression load of 72.1 kN, equivalent to a nominal stress level of 89% of the yield strength. Application of 10^5 compressive fatigue cycles was found to give a symmetric crack extension of approximately 1 mm.

Fracture Toughness Testing and Evaluation

Fracture toughness measurements were performed on CNT specimens, at a cross-head speed of 2 mm/min using two universal testing machines, recording the signals of load and Crack Mouth Opening Displacement (CMOD) as raw test data.

Room-temperature tests were performed on an Instron 5500R 100 kN universal testing machine, recording CMOD signals of two Instron extensometers (gauge length 12.5 mm), placed diametrically opposite of each other. Two extensometers were used to reduce potential effects of asymmetric crack growth phenomena.

Low temperature testing was performed on a Zwick 100 kN universal machine, using a Zwick standard clip-on extensometer, which has a non-adjustable gauge length of 20 mm. A thermocouple welded near the specimen notch was used to monitor the test temperature, similar to the AFSuM approach described in [11, 13].

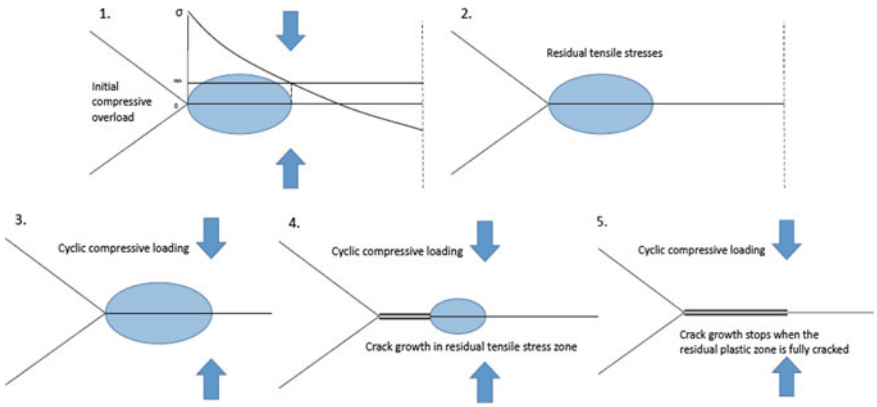

Fig. 2 Schematic depicting Compression-Compression pre-fatiguing process, where blue region indicates the region having a tensile residual stress

For all specimens two extensometers, placed diametrically opposite to each other, have been used. This means that two CODs were directly measured during the test and the largest of the two was used as the critical CTOD. A straightforward relation was established between the Crack Mouth Opening Displacement (CMOD) and the Crack Tip Opening Displacement (CTOD).

Calculation of the critical CTOD from conventional SENB specimens requires a complicated approach, where the hinge effect has to be taken into account [12]. In order to measure the CTOD for a CNT specimen two factors had to be defined: the load at which the critical CTOD is found (maximum load coinciding with fracture initiation occurs) and the linear elastic part of the load-displacement curve. This is important as the measured elastic component is assumed to be the elastic deformation of the bulk material, and all plastic deformation is assumed to be due to crack opening. In cases where the elastic behaviour was not easily visible, as will be shown for most C-C specimens (Fig. 3a), unloading-compliance tests showing pure linear elastic behaviour during the unloading part were used. In order to determine elastic behaviour the Koiter-Benthem compliance function was applied [14], see Fig. 3b.

Results and Discussion

Effect of Pre-fatiguing Method on Room-Temperature Fracture Toughness

Fracture surfaces of rotational bending and compression-compression specimens (see Fig. 4) show the capabilities of both approaches to create a macroscopically centric 1 mm fatigue pre-crack.

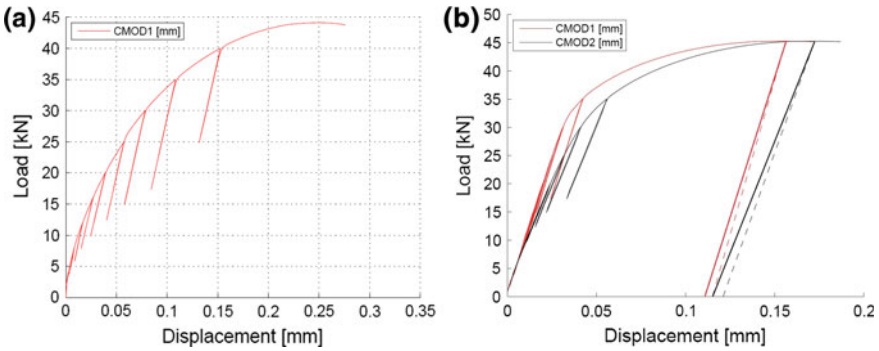

Fig. 3 Unloading compliance tests showing **a** C-C specimens with no distinguishable elastic behaviour **b** elastic behaviour determination based on Koiter-Benthem [14] compliance approach

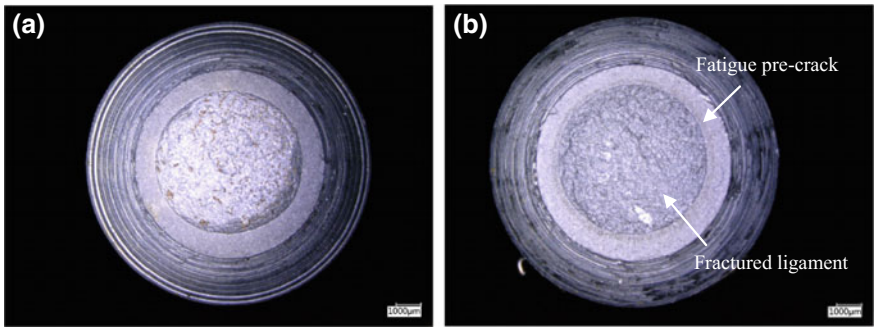

Fig. 4 Fracture surfaces of **a** rotational bending and **b** Compression-Compression samples

When comparing the initial parts of the load-displacement curves for RB and C-C samples, it can be seen (Fig. 5) that RB show almost fully linear behaviour, while the C-C samples do not show any linear behaviour. The other major difference is the average critical CTOD found. For the C-C specimen the CTOD is 0.18 mm, while it is 0.12 for the RB specimen, which is a significant difference of 50%. It should also be noted, that the effect of eccentricities on fracture toughness was found insignificant, as there were no correlations observed. It might be explained by the ductility of the material, which allows to compensate for eccentricity and result in load-line realignment during testing.

Two possible explanations are proposed to explain the different behaviour of C-C specimens, see Fig. 6. The first is the possibility that a certain amount of compressive plastically deformed zone was created after the pre-fatiguing, which possibly influences the tensile behaviour during the fracture toughness tests. The other is based on the principle of the compression-compression approach, where possibly a stress-free crack is created. This would mean that the complete tensile residual stress zone has been cracked and the material at the crack tip is completely undeformed and thus stress-free.

(a)

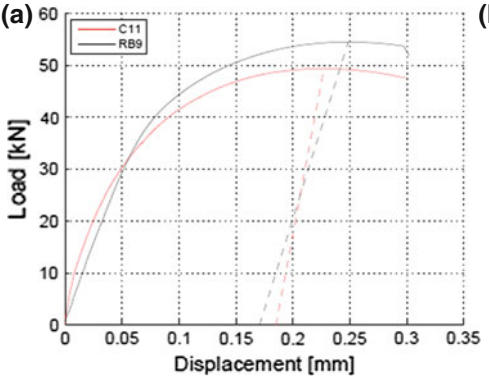

(b)

Sample		Eccentricity, mm	CTOD, mm
Rotational Bending (RB)	1	0.15	0.12
	2	0.15	0.12
	3	0.12	0.12
	4	0.15	0.13
	5	0.21	0.14
Compression-Compression (C-C)	1	0.00	0.19
	2	0.00	0.17
	3	0.20	0.17
	4	0.15	0.21
	5	0.03	0.19

Fig. 5 Comparison of room temperature fracture toughness results for rotation bending (RB) and compression-compression (C-C) CNT samples: **a** load displacement curves for two tests **b** eccentricity and CTOD results

Rotational bending on the other hand, is similar to standard three-point bending fatigue methods, where the crack-tip plastic zone tends to produce compressive stresses in front of a crack. This might explain the substantial difference in CTOD results. These results indicate that tensile stresses influence the fracture toughness behaviour. Hence, the reduced CTOD value, observed for RB samples, might also indicate that the conventional SENB measurements (for room temperature testing) are underestimates, as the pre-fatigue method influences the results. Furthermore, it is known, that the CTOD and ductile tearing criteria are designed primarily to assure that the plastic zone is not large enough to interfere with the boundaries of the specimen and therefore give overestimated results. This observation is further supported by the results of sub-sized SENB (AFSuM), where it was found impossible to determine a reliable CTOD at room temperature because of the so-called material's plastic collapse [11]. Plastic collapse is often regarded in a fracture mechanics context as an extreme situation where a damage-tolerant ductile system reaches its yield strength and fails by gross plasticity before any cracks reach a large enough driving force to grow and/or growth is inhibited because of extreme blunting [15, 16]. This problem does not seem to occur in CNT specimen, because the constraint in the ligament is large enough to allow the material to sustain a far larger stress before failure, and therefore the failure mechanism is dominated by the crack instead of plastic collapse.

Effect of Low Temperature and Equivalency with Conventional SENB Testing

Figure 7 shows ductile-to-brittle transition curves from CNT and SENB specimens. Room temperature fracture toughness tests on sub-sized SENB (AFSuM) samples

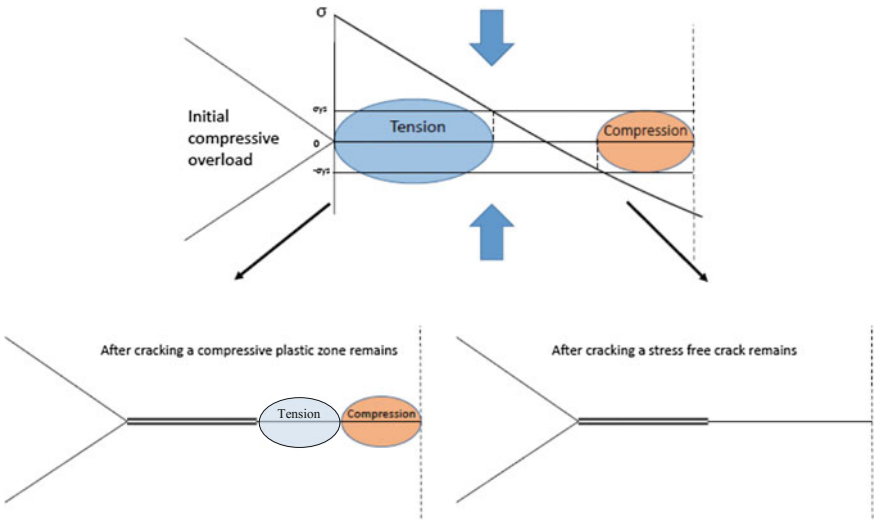

Fig. 6 Schematic depiction of the two possible stress situations at the crack tip for C-C approach

did not measure any fracture behaviour, but, as previously discussed [11], due to yielding through the full height of the ligament, it is rather dependent on plastic materials properties, such as yield strength. Hence it was not possible to determine the equivalency between the CNT and SENB tests performed at room temperature.

While it is clear that the sub-sized SENB specimens will not satisfy most size criteria for upper shelf CTOD, they are adequate for transition and lower shelf values and these lower temperature results showed a valid comparison. It can be seen that the CTOD for the C-C tests appears to be close to the AFSuM fit, contrary to the RB tests. SEM fracture surface of C-C samples (Fig. 8b) shows a mixed mode fracture, while the RB specimen (Fig. 8a) shows a pure ductile failure with voids visible near the fatigue crack front, indicating that plasticity occurred before failure. This observation confirms that the RB specimens did not show a fully brittle failure, as was already indicated from the load-displacement curves. The red line, shown in Fig. 8a, indicates the length of the ductile zone, which was measured to be about 70 μm. This zone is known as the stretch zone width (SZW), and is an indicator for the critical CTOD. The stretch zone width is half the length of the CTOD, meaning the CTOD at the point measured should be 0.14 mm, which is in good agreement with 0.15 mm determined from load-displacement curves.

One possible explanation for these results is the shape (i.e. sharpness) of the crack tip after the two types of pre-fatiguing methods. The C-C should have a very sharp crack tip, due to an absence of a nominal tensile loading, and associated absence of blunting of the crack tip, during pre-fatiguing. However blunting is presumed to happen in the rotational bending process, which possibly explains the difference in room temperature CTODs. When the specimen is cooled to below the ductile-to-brittle transition temperature the absolute shear strength is expected to

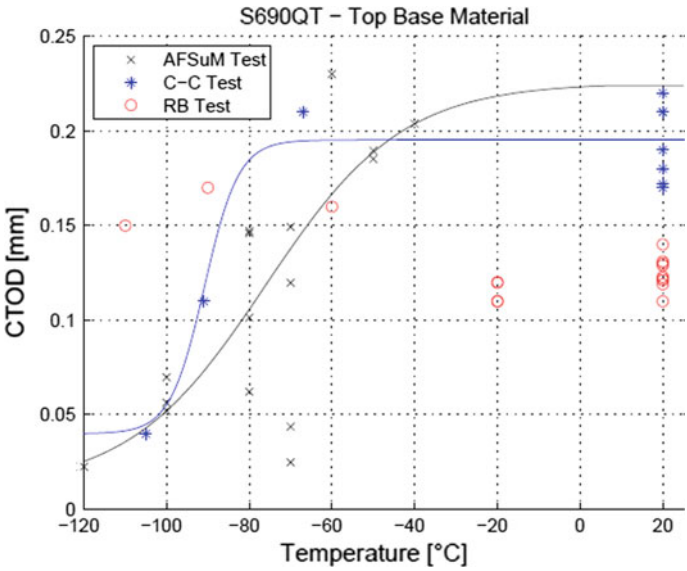

Fig. 7 Ductile to brittle transition curves for steel S690QT measured by two different fracture toughness methods: conventional sub-sized SENB (represented by AFSuM) and CNT (represented by compression-compression (C-C) and Rotational Bending (RB) sample)

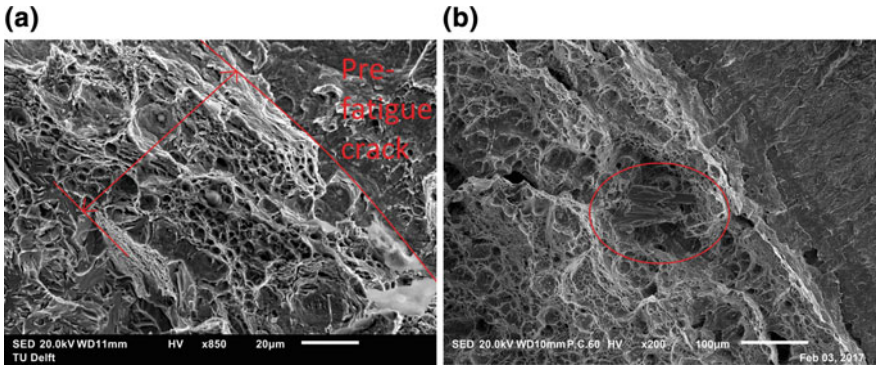

Fig. 8 Room temperature fracture surface showing **a** voids next to the fatigue crack of rotation bending specimen; **b** local cleavage zone in compression-compression specimen

increase up to a level where cleavage mechanisms take over. Instead of reducing the critical CTOD, the slight blunting of the crack tip (RB specimen) would then reduce the stress localisation at the crack tip, allowing it to deform to a higher CTOD level than the sharper C-C specimen.

The general conclusion from these tests is that equivalency between CNT and SENB specimen can be found, with the C-C pre-fatiguing method showing the

most promising results. Room temperature equivalency cannot be proven, as no valid SENB data are available. However adding the room temperature C-C results would allow to fill the missing gap and extrapolate the SENB (AFSuM) curve to a valid upper shelf. Rotational bending pre-fatigued specimens do not follow this curve, which could be caused by the combination of constraint with the more blunted crack tip (i.e. the more pronounced pre-fatigue plastic zone size).

It should also be noted, that the room temperature CTOD results for C-C samples show considerable scatter, which is most likely caused by local brittle zones observed in the material. SEM observations of C-C samples showed that the fracture surface is mostly represented by ductile failure with some areas of local cleavage planes, as shown in Fig. 8b. Brittle failure (cleavage) has a probabilistic nature, which might explain the high scatter in room temperature results. The local brittle zones were not found in the RB specimen.

Conclusions

The following conclusions can be drawn from the results of tests on Circumferentially Notched Tension (CNT) specimens:

- Both Rotational bending (RB) and a new Compression-Compression (C-C) pre-fatiguing methods can lead to centric circumferential cracks in CNT specimens.
- C-C and RB specimens show different load-displacement curves: RB initially shows a clear linear-elastic behaviour, while C-C does not.
- C-C specimens have a room temperature CTOD of 0.18 mm, while RB have 0.12 mm. It is proposed that the difference is caused by a stress-free material condition at the crack tip of the C-C specimen.
- Sub-sized SENB testing gives an underestimation of the upper shelf CTOD, which is believed to be due to the influence of plastic collapse observed at room temperature testing.
- CNT C-C specimens are able to determine a more realistic CTOD for room temperature fracture toughness testing.
- Low temperature fracture-toughness testing showed equivalency between sub-sized SENB and CNT specimens with the C-C pre-fatiguing approach.

Hence, it can be concluded that CNT geometry can be considered a promising option to simplify and improve fracture toughness testing for relatively ductile materials. To substantiate size independency, it is recommended to perform additional tests, on a wider range of specimen sizes. Furthermore, the effect of material types, including different yield strengths, should be investigated. An important finding of this work related to stress free crack with C-C pre-fatiguing should be further experimentally validated by high resolution electron-back scattered (EBSD) measurements.

References

1. ASTM Standard E399 (2009) Standard test method for linear-elastic plane-strain fracture toughness K_{Ic} of metallic materials. ASTM International, West Conshohocken, PA, USA
2. ASTM Standard E1820 (2011) Standard test method for measurement of fracture toughness. ASTM International, West Conshohocken, PA, USA
3. BSI Standard BS5762 (1979) Methods for crack opening displacement (COD) testing, British Standards Institution, London, UK
4. Ibrahim RN, Stark HL (1990) Establishing KIc from eccentrically fatigue cracked small circumferentially grooved cylindrical specimens. Int J Fract 44:179–188
5. Ibrahim RN (1989) The development of a small K_{Ic} specimen and its application to sustained load cracking in aluminum pressure vessels. PhD thesis. Sydney, Mechanical Engineering Department, University of New South Wales
6. Ibrahim RN (1999) An analytical approach for calculating K_{Ic} from eccentrically cracked cylinder specimen. ASME PVP 388:155–161
7. Ibrahim RN, Price JWH (1997) CNT small specimen testing procedure to evaluate fracture toughness, operating pressure equipment, Institute of Metals and Materials of Australia, pp 71–6
8. Singh Raman RK, Rihan R, Ibrahim RN (2006) Metall Mater Trans A 37A:2963–2973
9. Stark HL, Ibrahim RN (1992) Eng Fract Mech 41(4):569–575
10. Tada H, Irwin GR, Paris P (2000) Stress analysis of cracks handbook, Asme Press
11. Walters CL, Voormeeren LO, Janssen M, Wallin K (2013) Validation of the acceptability of 10×20 Mm specimens for fracture toughness determination of high-strength steels, ASME
12. BSI, BS7448 Part 1—1991 (2002) Fracture mechanics toughness tests. Method for determination of K_{Ic}, critical CTOD and critical J values of metallic materials
13. Popovich VA, Richardson IM (2015) Fracture toughness of welded thick section high strength steels and influencing factors. In: TMS 2015 144th annual meeting and exhibition: supplemental proceedings. Cham, Springer International Publishing, pp 1031–1038
14. Benthem JP, Koiter WT (1973) Asymptotic approximations to crack problems, Chap. 3. In: Sih GC (ed) Mechanics of fracture: I. methods of analysis of crack problems, Noordhoff International Publishing, Leyden, The Netherlands, pp 131–178
15. Lanning WR, Javaid SS, Muhlstein CL (2017) Reconciling fracture toughness parameter contradictions in thin ductile metal sheets in tension. Georgia Institute of Technology, USA
16. Scibetta M, Chaouadi R, Van Walle E (2000) Fracture toughness analysis of circumferentially-cracked round bars. Int J Fract 104(2):145–168

A Low-Cost, Laboratory-Scale Method to Identify Regions of Microstructural Changes in Response to Dynamic Loading Conditions

Benjamin Lund and Judith Schneider

Abstract This work outlines the development of a low-cost, laboratory-scale experiment method based on metal cutting techniques to support first-principles modeling of structural material responses under a range of dynamic loadings. The range of strain rates of interest is similar to that experienced in metals in advance of a cutting tool with maximum shear strains up to 4 at maximum shear strain rates up to 10^8 s^{-1}. By characterizing the chips formed at the varying strain rates, regions of microstructural changes can be readily identified and stress versus strain curves of interest can be produced.

Keywords Dynamic material properties · High strain rate testing
Structure-properties-performance under dynamic loading

Introduction

Generation of material databases to support first-principles modeling requires data over the strain rate range from 10^0 to 10^8 s^{-1} [1–5] Data within the strain rate range of 10^3–10^4 s^{-1} is typically obtained using a split Hopkinson bar while higher strain rate data is typically obtained through explosions or ballistic impact testing [6, 7]. The use of different test apparatus can result in discontinuities in material behavior across the range of strain rates, which may be due to either testing apparatus artifacts or microstructural changes. Use of one test apparatus would allow rapid identification of regions of microstructural changes which can be correlated with changes in material behavior.

The range of strain rates of interest to first-principles modeling efforts are similar to that experienced in metals during the cutting process [1, 8]. This provides the

B. Lund (✉) · J. Schneider
University of Alabama in Huntsville (UAH), Huntsville, AL 35899, USA
e-mail: brl0007@uah.edu

J. Schneider
e-mail: jas0094@uah.edu

The Minerals, Metals & Materials Society, *TMS 2018 147th Annual Meeting & Exhibition Supplemental Proceedings*, The Minerals, Metals & Materials Series,
https://doi.org/10.1007/978-3-319-72526-0_48

basis for a low-cost laboratory-scale experiment that utilizes metal cutting techniques to investigate material response over a wide range of strain rates. By studying the response of a metal to varying strain rates, the influence of the microstructural evolution can be studied and understood with respect to damage and failure mechanisms.

Background

In orthogonal machining, the tool has a single, straight cutting edge oriented parallel to the cutting surface and perpendicular to the direction of travel. If the depth of cut is small compared to the width ($w < 20t$), it can be assumed the chip is formed under plane strain conditions [9]. Four types of chips, shown in Fig. 1, occur during metal cutting operations.

The first three types of chips (Fig. 1a–c) were defined by Ernst [11] and Merchant [12, 13] while the fourth type (Fig. 1d) was widely observed as manufacturing technology improved and cutting speeds increased. Type 4 chips are continuous but consist of narrow shear bands of severely deformed material between larger areas of relatively un-deformed material. These chips occur when a narrow band of material in front of the tool is subject to localized adiabatic heating which weakens the material resulting in localized deformation. This localized adiabatic heating and resulting deformation is referred to as shear bands. It is observed that shear bands tend to form at higher cutting speeds and the shear band spacing increases with cutting speed [14, 15]. Mathematical analysis of orthogonal cutting, formulated by Merchant [13] and shown in Fig. 2a, treats the chip as a free body and resolves the forces involved in the cutting process. This model, however, assumes all deformation takes place in a single plane resulting in a constant flow stress and a discontinuity in velocity at the shear plane. Kececioglu [16] attempted to measure stress and strain at high strain rates using a quick-stop device to embed a cutting tool in a workpiece and then obtain images of the chip formation. The size and shape of the plastic zone was estimated based upon the beginning and end of grain deformation. From these results, it was assumed the plastic zone can be represented by a parallel sided model as shown in Fig. 2b. This shear zone model was further refined by Stevenson and Oxley [17, 18].

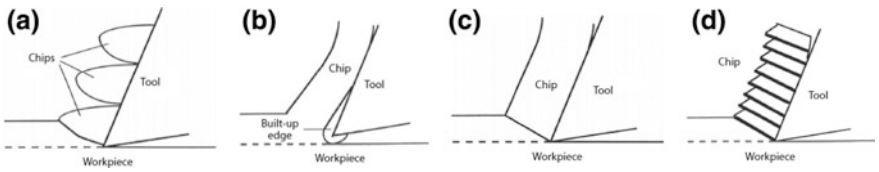

Fig. 1 Basic chip types: **a** type 1, discontinuous, **b** type 3, continuous with built-up-edge, **c** type 2, continuous, and **d** type 4, localized shear [10]

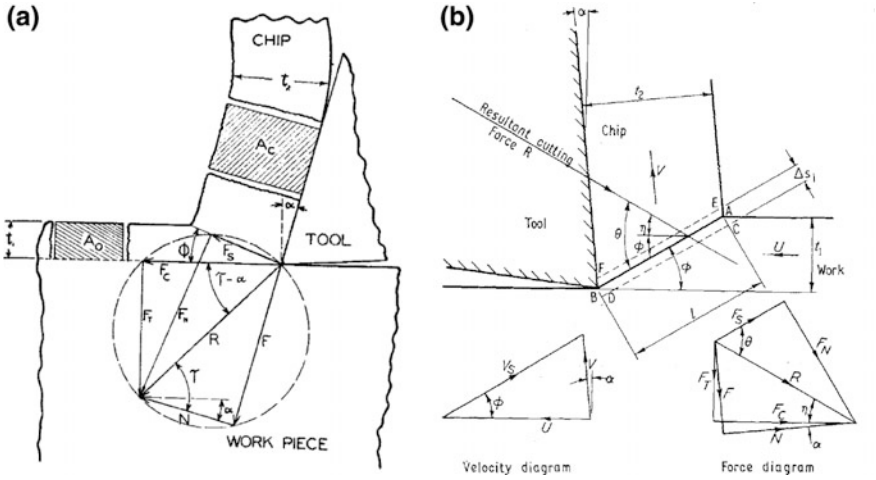

Fig. 2 **a** Merchant's circle diagram of cutting forces [13] and **b** parallel-sided shear zone model of chip formation [17]

The location of the shear zone is dependent upon the shear angle, ϕ, which can be found based upon chip thickness ratio, t_1/t_2, and the rake angle, α, using Eq. 1 [18];

$$tan\phi = \frac{t_1/t_2 cos\alpha}{1 - t_1/t_2 sin\alpha} \tag{1}$$

If the thickness of the shear zone, Δs_1, is known, the strain rate can be calculated using Eq. 2 [18];

$$\dot{\gamma} = \frac{V_S}{\Delta s_1} \tag{2}$$

where V_s is the velocity in the shear plane. The corresponding strain, γ, is calculated using Eq. 3 [18];

$$\gamma = \frac{cos\alpha}{sin\phi \cos(\phi - \alpha)} \tag{3}$$

For type 4 chips exhibiting shear bands, the strain rate is calculated using Eq. 4 [19];

$$\dot{\gamma} = \frac{\cos\alpha}{\cos(\phi - \alpha)} \cdot \frac{U}{\Delta y} \tag{4}$$

where U is the linear cutter velocity and Δy is the shear band spacing.

Shear and normal stresses of the shear plane can be calculated from the normal force, F_N, and the shear force, F_S, on the shear plane and the cross sectional area of the shear plane. To resolve forces, a 3 axis load cell is used to record the cutting force, F_C, and the thrust force, F_T [19].

For type 2 chips, a high speed camera may be used to record the cutting process so that the shear zone thickness, chip thickness and depth of cut can be optically measured. For type 4 chips, the shear band spacing can be measured using optical microscopy after the chip has been mounted, polished, and etched. Use of both methods can be used to validate the equations.

Incorporation of the high speed camera and 3 axis load cell into the test setup allows shear zone thickness, chip thickness, depth of cut, and forces to be measured with respect to time. This data is used calculate stress versus strain plots over the strain rate range of interest.

Experimental Apparatus and Procedure

Initial tests were conducted using a long arm pendulum impactor shown in Fig. 3. The large radius of the long arm allowed approximation of a constant depth of cut over the short specimen length. Figure 3b shows details of the tool, tool holder, and load cell setup mounted on the tip of the pendulum. The long steel pendulum, approximately 0.965 m (38”) in length, hung from the ceiling of a test chamber with a tool holder and tool mounted at the tip to cut chips from steel specimens

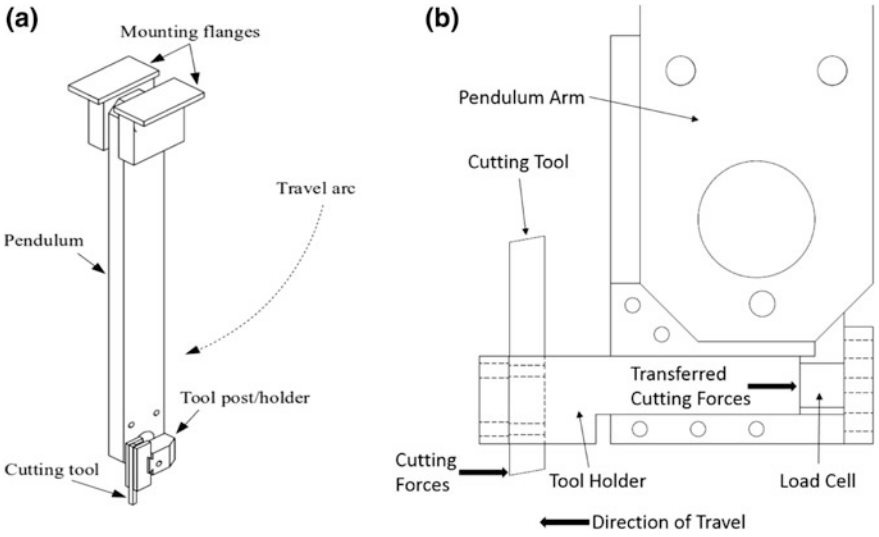

Fig. 3 **a** Pendulum arm and **b** details of the tool holder and load cell mounted at arm tip

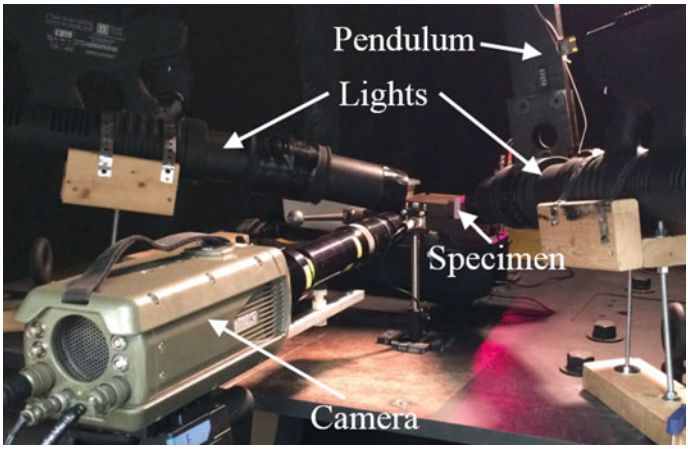

Fig. 4 Overall experimental setup with test specimen clamped in vise

secured in a machinist vise. The jaws of the vise are positioned perpendicular to the pendulum's direction of travel and the vise is secured to a large metal table within the test chamber (Fig. 4). A 15.9 mm (5/8") cutter made from M42 (8% Co) tool steel with a 0° rake angle and a 10° relief angle is mounted in the tool holder on the tip of the pendulum. The pendulum is released, swings downward, and strikes the work piece that is held in the vise. A load cell is located just behind the tool holder to record cutting forces. In order to achieve varying velocities, the pendulum may be released by hand. During initial studies, a single axis load cell was used to demonstrate the proof of concept.

Cutting forces were recorded using a Dytran 1051V6 load cell coupled with a Dytran 4110C line powered constant current power unit/signal conditioner. The load cell is capable of measuring forces up to 22,241 N (5000 lbf) in compression with a sensitivity of 0.232 mV/N (1 mV/lbf). A Thorlabs PDA10A Si Fixed Gain Detector laser trigger is placed in front of the test specimen at a height such that the laser beam is broken only by the tip of the cutter. This allowed calculation of the cutting velocity. Load cell data and trigger pulse are recorded on a Yokogawa DL750 ScopeCorder at a rate of one million samples per second. The trigger pulse is split allowing the pulse width to be recorded by the ScopeCorder and the signal to be delayed by a Berkeley Nucleonics Model 725 Multi-Trigger Digital Delay Generator and used to trigger the high speed camera and load cell data recording.

Digital images of the cutting process were captured with a Phantom V710 high speed camera paired with a K2/SC long-distance microscope lens. The camera records 1280 × 800 pixels at 7500 fps with an exposure time of 5 μs and a field of view of approximately 10 mm. To supply light for the camera, two Megaray MR-175 portable searchlights were used in conjunction with a series of lenses to focus the light onto the test specimen. The searchlights were powered by a Hewlett

Table 1 Experimental cutting conditions

Chip ID #	h_{drop} (m)	$t_{trigger}$ (s)	U (m/s)	t_1 (mm)
17-46	0.965	0.00291	5.457	0.234
17-41	0.965	0.00304	5.229	0.221
17-48	Assisted	0.00306	5.193	0.336
17-42	0.965	0.00308	5.161	0.601
17-44	Assisted	0.00311	5.100	0.202
17-47	0.965	0.00319	4.973	0.262
17-50	0.965	0.00321	4.953	0.682
17-43	0.965	0.00328	4.847	0.209
17-49	0.686	0.00356	4.463	0.514
17-45	0.686	0.00365	4.353	0.168

Packard 6286A DC Power Supply and two Optima YellowTop D34/78 batteries, respectively.

Test specimens of dimensions 41.3 mm by 12.7 mm by 6.4 mm (1.63" by 0.50" by 0.25") were machined from hot rolled 1008 and 1075 steel. The specimens were polished and etched in an attempt to capture the deformation of the grains with the high speed camera. Each specimen was placed in the vice vertically with the thinnest edge against the back jaw. The depth of cut is set by adjusting the height of the tool in the tool holder and shimming the test specimen with shim stock. A water bath is positioned behind the vise to catch and quench the chip.

Results and Discussion

The parent material was metallographically prepared to document the starting microstructure. Standard metallographic procedures were followed to grind and polished the material which was embedded in a phenolic mount. A fine equiaxed grain size was observed for both materials. Phase analysis confirmed the 100% pearlite structure of the 1075 and roughly 10% pearlite composition of the 1008 steel. The average grain size of the 1008 was 16 ± 5 μm and that of the 1075 was 30 ± 10 μm.

To document the microstructure after deformation, metallographic specimens were prepared using the same metallographic procedures to mount and polish chips of the 1075 and 1008 steel. A summary of cutting conditions is given in Table 1. Cutter velocity varied from 4.4 to 5.5 m/s and depth of cut varied from 0.168 to 0.682 mm.

Under the initial test conditions, shear bands did not form in the 1008 but did form in the 1075. This is consistent with the literature that indicates lack of shear

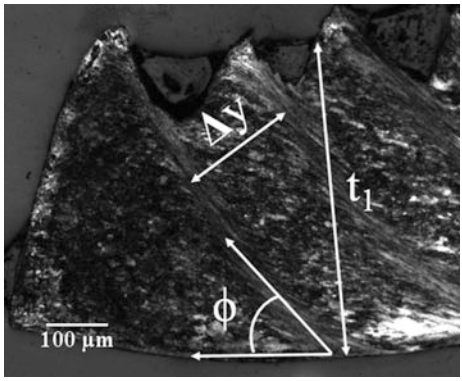

Fig. 5 Measurement locations on 1075 chip

Table 2 Summary of data from 1075 steel

Chip ID #	U (m/s)	t_2 (mm)	γ	$\dot{\gamma}$ (1/s)
17-46	5.457	0.458	2.87	3.6E + 04
17-47	4.973	0.381	2.47	3.1E + 04
17-48	5.193	0.397	2.06	2.7E + 04
17-49	4.463	0.537	2.33	1.2E + 04
17-50	4.953	0.803	2.14	1.1E + 04

band formation in steels with less than ~0.2% C at strain rates up to 10^6 s^{-1} [20, 21]. The 1075 chips were analyzed using Eqs. 3 and 4 with measurements on the chip shown in Fig. 5 and strain and strain rates summarized in Table 2. A maximum strain of 2.87 and maximum strain rate of 3.6×10^4 were achieved at a depth of cut of 0.46 mm and cutter velocity of 5.46 m/s.

In this initial proof of concept study, forces were only obtained in the cutting direction. To fully understand the forces to calculate the shear stress, a 3 axis load cell is needed to resolve Merchant's circle which was shown in Fig. 2 [10, 19, 22]. Once the forces are resolved, a force versus time plot can be made of the cutting process.

Summary

The cutting apparatus used in this study was able to generate strain rates comparable to split Hopkinson bar tests. At the conditions tested, only the 1075 formed primary shear bands which allowed the use of Eqs. 1 and 3. Measuring the secondary shear band thickness along the cutting surface in subsequent tests will allow the use of Eq. 2 to determine shear strain rate. By characterizing the chips formed, metal cutting can be used to evaluate the response of material to varying strain rates using one apparatus. Material response can be obtained ranging from continuous to

discontinuous chip formation. Under the tests, shear bands were not formed in the 1008 but were in the 1075. This is consistent with the literature that indicates lack of shear band formation in steels with less than ~0.2% C at strain rates up to 10^6 s^{-1} [20, 21].

In this initial proof of concept study, forces were only obtained in the cutting direction. To fully understand the forces to calculate the shear stress, a 3 axis load cell is needed [10, 19, 22]. Improved optics, especially lighting, are required to more accurately measure shear zone thickness and to calculate the shear and normal stress on the shear plane. Once these improvements are made to the test fixture, stress versus time and strain versus time plots can be combined to form the stress versus strain response of various metals over a range of shear strain rates.

Acknowledgements Funding was provided through a MDA sponsored Phase I STTR with McConnell Jones Lanier & Murphy LLP for "A Low-Cost, Laboratory-Scale Method to Identify Regions of Microstructural Changes in Response to Dynamic Loading Conditions." The authors acknowledge the support of the Aerophysics Research Center at UAH with the support of Mark Zwiener, Mitch Fleming, and Tony Doll.

References

1. Johnson GR, Cook WH (1983) A constitutive model and data for metals subjected to large strains, high strain rates and high temperatures. In: Proceedings of 7th International Symposium on Ballistics, pp 541–547
2. Bessette GC (September 2004) Modeling coupled blast/structure interaction with Zapotec, benchmark calculations for the conventional weapons effects backfield (CONWEB) Tests. Sandia report (SAND2004-4096)
3. Ferencz RM, DeGroot AJ, Lin JI, Zywicz E, Durrenberger JK, Sherwood RJ, Corey IR (July 2008) ParaDyn implementation in the US Navy's DYSMAS simulation system: FY08 progress report. Lawrence Livermore National Laboratory (LLNL) Technical Report, LLNL-TR-405901
4. SBIR Topic, MDA-073-019 (2014) Hypervelocity intercept modeling with first principle, physics based tools, Contract: HQ0147-14-C-7006
5. Cazamias JU, Schrami SJ (2007) Modeling of non-eroding penetration using ALE3D and Zapotec. Am Inst Phys AIP Conf Proc 955:1281
6. Myers MA (1994) Dynamic behavior of materials, Wiley
7. Reed-Hill RE (2006) Physical metallurgy principles, Pws-Kent series. In: Rittel D, Ravichandran G, Venkett A (eds) Engineering, the mechanical response of pure iron at high strain rates under dominant shear, MSEA, vol 432, pp 191–201
8. Rittel D et al (2007) Thermomechanical characterization of pure polycrystalline tantalum. Mat Sci Eng 447:65–70
9. Fenton RG, Oxley PLB (1968) Mechanics of orthogonal machining: allowing for the effects of strain rate and temperature on tool-chip fraction. Proc Inst Mech Eng 183:417–438
10. Stephenson DA, Agapiou JS (2016) Metal cutting theory and practice, 3rd edn, CRC Press Taylor and Francis Group
11. Ernst H (1938) Physics of metal cutting. In: Mach Metals, ASM, Metals Park, OH
12. Merchant ME (1944) Basic mechanics of the metal-cutting process. ASME J Appl Mech 11: A168–A175

13. Merchant ME (1945) Mechanics of the metal cutting process. I. Orthogonal cutting and a type 2 chip. J Appl Phys 16:267–275
14. Recht RF (1964) Catastrophic thermoplastic shear. ASME J Appl Mech 31:186–193
15. Xie JQ, Bayoumi AE, Zbib HM (1996) A study on shear banding in chip formation of orthogonal machining. Int J Mach Tools Manuf 36:835–847
16. Kececioglu D (1958) Shear strain-rate in metal cutting and its effect on shear flow stress. Trans Am Soc Mech Eng 80:158
17. Stevenson MG, Oxley PLB (1969) An experimental investigation of the influence of speed and scale on the strain-rate in a zone of intense plastic deformation. Proc Inst Mech Eng 184:561–576
18. Stevenson MG, Oxley PLB (1970) An experimental investigation of the influence of strain-rate and temperature on the flow stress properties of a low carbon steel using a machining test. Proc Inst Mech Eng 185:741–754
19. Shaw MC (1984) Metal cutting principles. Oxford University Press, Clarendon
20. Meyers MA, Wittman CL (1990) Effect of metallurgical parameters on shear band formation in low-carbon ($\sim$0.20 Wt Pct) steels. Met Trans A, vol 21a, pp 3153–3164
21. Timothy SP (1987) The structure of adiabatic shear bands in metals: a critical review. Acta Metal 35:301–306
22. Abouridouane M et al (2015) The mechanics of cutting: in-situ measurement and modelling. Procedia CIRP 31:246–251

Part XX
Environmentally Assisted Cracking: Theory and Practice

Environment-Induced Degradation in Maraging Steel Grade 18Ni1700

K. Devendranath Ramkumar, G. Gopi, Ravi Prasad Valluri, K. Sampath Kumar, Trilochana Jena and M. Nageswara Rao

Abstract A high degree of cold working is involved in forming C18Ni1700 maraging steel into products such as flow formed tubes. After the standard aging treatment of 3.5 h at 480 °C, such heavily deformed material acquires a very high strength level with relatively low value of ductility. Such high strength condition, it is apprehended, is also associated with poor resistance to environment-induced degradation. Efforts were made to modify the aging treatment of cold worked C18Ni1700 to arrive at better strength-ductility combination, while still meeting AMS 6520 requirements, and reduced susceptibility to environment-induced damage. The results were found to be encouraging. In addition to normal tensile testing, slow strain rate testing was carried out to assess the susceptibility of the material to environment-induced degradation after different aging treatments. Distinctly lower ductility values were obtained when tested at lower strain rate, strongly suggesting that the material is prone to hydrogen induced damage. Potentiodynamic testing revealed that increasing the aging temperature resulted in major reduction in corrosion rate. Increasing both aging temperature and time resulted in formation of substantial amount of austenite, having an adverse effect on the corrosion rate.

Keywords Maraging steel · Cold work · Flow forming · Slow strain rate testing · Environment-induced degradation

K. Devendranath Ramkumar (✉) · M. Nageswara Rao
School of Mechanical Engineering, VIT University Vellore, Vellore 632014, India
e-mail: deva@vit.ac.in

G. Gopi · R. P. Valluri · K. Sampath Kumar · T. Jena
Defence Research & Development Laboratory, Hyderabad 500058, India

The Minerals, Metals & Materials Society, *TMS 2018 147th Annual Meeting & Exhibition Supplemental Proceedings*, The Minerals, Metals & Materials Series,
https://doi.org/10.1007/978-3-319-72526-0_49

Introduction

18% Nickel maraging steels are distinguished by the unique combination of high strength and excellent fracture toughness. Four different grades of maraging steel are available, covering the yield strength range 1400–2400 MPa—18Ni1400, 18Ni1700, 18Ni1900 and 18Ni2400. All of them contain 18 weight % nickel. The last four digits indicate the yield strength attainable in MPa after heat treatment. A further classification is made based on whether the steels contain cobalt or not. Accordingly one talks of cobalt containing and cobalt free 18% nickel maraging steels. The upper case letter C is used as part of the designation for the former, and the upper case letter T for the latter. Thus T18Nixxxx is the designation for cobalt-free 18% nickel maraging steel, while C18Nixxxx is the designation for cobalt containing 18% nickel maraging steel.

While the high strength attainable after heat treatment is a major attraction for these steels, their susceptibility to environment-induced degradation has been an issue of major concern. High strength steels are well known for their susceptibility to environment-induced degradation and 18% nickel maraging steels with their high strength are no exception. It has been well documented that the susceptibility of 18% nickel maraging steels to stress corrosion cracking increases with increasing yield strength [1]. The slow strain rate testing carried out by Bradhurst and Heuer [2] on three different grades of 18% nickel maraging steel in air and aqueous NaCl solution showed that environment sensitive cracking increased with increasing strength level. Investigations on C18Ni1700 have revealed that ambient air environment, i.e., with no specific corrosive medium surrounding, can cause hydrogen embrittlement in this steel, with yield strength of 1700 MPa [3]. Similar degradation was also reported for T18Ni1700 by Zhang et al. [4]. The authors reported hydrogen assisted cracking in constant displacement tests conducted on samples of this steel in laboratory air environment with a relative humidity of 30%.

Maraging steels are subjected to flow forming for production of thin walled tubes. Cold reductions as high as 80% are involved in flow forming. When the flow formed tubes are subjected to standard aging treatment, they attain a very high strength level. Lee et al. [5], for example, reported yield strength (YS) of 1956 MPa and ultimate tensile strength (UTS) of 1977 MPa on flow formed tubes of C18Ni1700 after aging for 3 h at 480 °C. Based on the foregoing, such high strength level is expected to be associated with a high degree of susceptibility to environment-induced degradation. At such high strength level, the material may exhibit high susceptibility to hydrogen assisted cracking and stress corrosion cracking.

In order to reduce the susceptibility to environment-induced degradation, the avenue available is to reduce the strength while still conforming to AMS 6520C, the governing specification for heat treated components made of 18% nickel maraging steel. According to this specification, the minimum value to be guaranteed for the flow formed tubes made of C18Ni1700 in the aged condition are 1689 MPa YS and

1758 MPa UTS. Thus there is indeed scope to bring down the strength by appropriate choice of aging parameters.

Based on Floreen's suggestion [6], the overaging treatment can be used to reduce the strength. This can be done in two ways—(i) use a higher temperature for aging (ii) increase the time at a given aging temperature. In the present research, studies were carried out on C18Ni1700 material cold worked to simulate the flow forming conditions. In addition to standard aging treatment of 3.5 h at 480 °C, two other treatments involving enhanced aging temperature/time were adopted. Strength reduction resulting from modified aging treatments was evaluated.

Slow strain rate testing was also carried out on samples corresponding to the three different aging treatments. The mechanical properties obtained after standard strain rate testing are compared with those obtained after slow strain rate testing. There were significant differences between the two sets of results, particularly with reference to the percentage elongation values. The results obtained are interpreted in terms of the susceptibility manifested by the material to environment induced degradation.

Material and Experimental Methods

The C18Ni1700 material studied in the present research was produced by double vacuum melting, i.e., by vacuum induction melting followed by vacuum arc remelting. The chemical composition of the alloy in weight percent was 17.88 Ni 4.88 Mo 8.06 Co 0.44 Ti 0.11 Al 0.003 C 0.01 Si 0.02 Mn 0.002 S 0.003 P and balance Fe. The ingot was hot forged to a slab. The slab was then hot rolled to plate with thickness of 7.5 mm. Plate was subsequently subjected to cold rolling to bring down the thickness to 3 mm. Cold rolling was done in two parts. First part was done to bring down the thickness to 4.5 mm. Second part was done to reduce the thickness from 4.5 to 3 mm with rolling direction perpendicular to the direction in the first part. The total reduction by cold rolling works out to 60%.

Three different aging treatments were given to the cold rolled 3 mm thick material—(i) direct aging for 3.5 h at 480 °C (ii) direct aging for 3.5 h at 540 °C and (iii) direct aging for 6 h at 540 °C. The three conditions are designated as M1, M2 and M3 respectively.

Tensile test specimens were machined out from material corresponding to M1, M2 and M3 conditions. The drawing of the tensile test specimen adopted in this study is given in Fig. 1. Tests were carried out at to different cross head speeds—5 mm/min and 0.015 mm/min, corresponding to strain rate of 0.0013 s^{-1} and 1×10^{-5} s^{-1} respectively. For the purpose of the present research, the former is taken as normal strain rate and the latter as slow strain rate. Testing at normal strain rate was done at Micro Labs, Chennai using Instron make universal testing machine. Testing at slow strain rate was done at Defence Research and

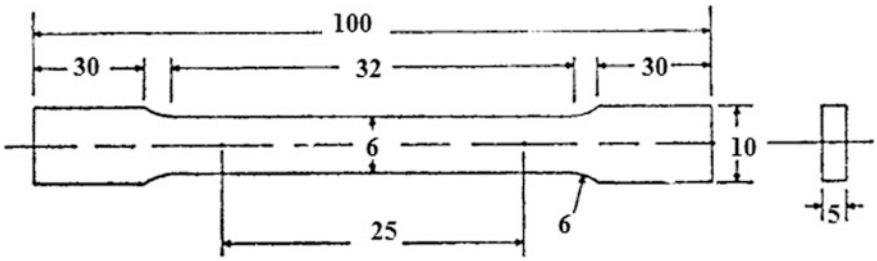

Fig. 1 Drawing of the tensile sample fabricated as per the ASTM E8/8M standard

Development Laboratory, Hyderabad using a 250 kN universal testing machine. At both strain rates, testing was done as per ASTM E8/E8 M. Testing in any given condition was carried out on triplicate number of specimens and the test results reported in the paper are the average values.

Hardness testing in different aged conditions was carried out using Matsuzawa Vickers micro hardness tester. Testing was carried out in conformity with ASTM E-384-16 using a test load of 500 g for a dwell time of 10 s. The hardness values reported in this paper are average of 10 measurements.

Measurements of austenite content were carried out at Advanced Research Centre International, Hyderabad using an X-Ray diffractometer. Cu-K_α radiation with a wavelength of 2.2898 Å was used for the studies. Evaluation was carried as per ASTM E975-13.

Corrosion behaviour in different conditions was characterized by potentiodynamic studies using an electrochemical work station. Dimensions of the samples used were 10 mm × 10 mm × 3 mm. Testing was carried out in a medium of 3.5% NaCl solution using Pt and Ag/AgCl electrodes. Tafel plots were generated and corrosion rates calculated for M1, M2 and M3 conditions. In each condition, testing was carried out on three samples.

Results and Discussion

Figure 2 gives the optical micrographs of the material in M1, M2 and M3 conditions. The lath structure of Fe-Ni martensite was seen in all conditions.

Table 1 gives a compilation of microhardness, results of tensile testing at normal and slow strain rates and austenite content for M1, M2 and M3 conditions.

The microhardness is at its highest (561 HV) when aged for 3.5 h at 480 °C. There was a drop in hardness to 552 HV when aging temperature was increased to 540 °C. There was a further drop in hardness (from 552 to 534 HV) when aging time at 540 °C was increased from 3.5 to 6 h. It is known that aging for 3.5 h at 480 °C results in peak hardness for C18Ni1700. Drop in hardness on increasing the

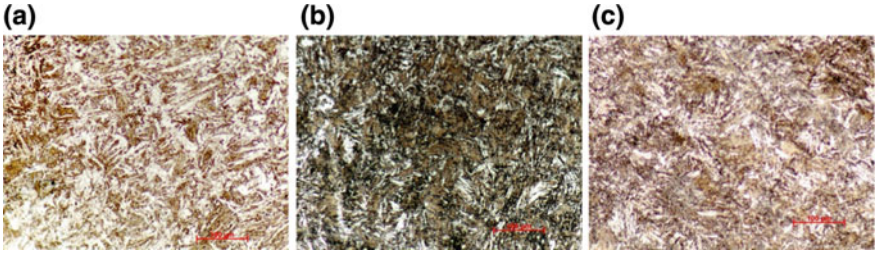

Fig. 2 Optical micrographs in **a** M1 **b** M2 and **c** M3 conditions

Table 1 Tensile test results with normal and slow strain rate for M1, M2 and M3 conditions. Also shown are hardness and % austenite values for the three conditions

Normal strain rate					
Condition	YS (MPa)	UTS (MPa)	% elongation	Hardness (HV)	% Austenite
M1	1769	1852	9	561	1.04
M2	1664	1770	13	552	2.14 ± 0.7
M3	1635	1726	13	534	27.75 ± 0.3
Slow strain rate					
M1	1834	1862	6	561	1.04
M2	1724	1775	8	552	2.14 ± 0.7
M3	1630	1699	10	534	27.75 ± 0.3

aging temperature from 480 to 540 °C and on increasing the aging time from 3.5 to 6 h at 540 °C is to be expected, as increasing amount of overaging sets in.

Austenite content in M1 sample is just about 1%. This is about the level at which austenite is present in the solution treated condition. It is hence believed that aging at 480 °C for 3 h has not resulted in any reversal of austenite. The austenite content in M2 sample is slightly higher (2.14 ± 0.7) and it appears that increasing the aging temperature from 480 to 540 °C, aging time remaining the same, resulted in a small, rather insignificant extent of austenite reversion. It is important to note that an increase in aging time from 3.5 to 6 h resulted in a large increase in austenite level, i.e. rate of austenite reversion goes through a steep increase in the aging time range 3.5–6 h compared to 0–3.5 h. It is documented that at a given aging temperature, austenite reversion occurs initially (in the first stage) at a slow rate [7]. There is a second stage over which it occurs at a fast rate and finally there is a 3rd stage over which the rate falls again, the austenite level approaching a final value, the equilibrium value for that aging temperature. The 0–3.5 h aging at 540 °C appears to fall in first stage and the 3.5–6 h in the second stage.

Similar to the behaviour of microhardness, both the YS and UTS values decrease as one moves from M1 to M2 to M3 condition, be it normal strain rate testing or low strain rate testing. The % elongation values also show the same trend. This is in

line with the conclusions reached earlier. M1 condition largely corresponds to peak aging. Increasing the aging temperature from 480 to 540 °C (M1 → M2), aging time remaining 3.5 h, results in overaging and drop in YS and UTS. Increasing aging time at 540 °C from 3.5 to 6 h (M2 → M3) results in further overaging and further drop in YS and UTS. The drop in strength from M1 to M2 to M3 is accompanied by an increase in ductility, providing further evidence that there is increasing amount of overaging occurring.

The effect of strain rate on the properties will now be examined. For conditions M1 and M2, the UTS value remains unaffected by the strain rate. However, the YS value is significantly higher at lower strain rate.

For all the three conditions, there is drop in % elongation when tested at low strain rate. Loss of ductility has often been used as a measure for the degree of environment-induced degradation. The % loss of ductility works out to 33% for M1, 38.5% for M2 and only 23% for M3. While there is susceptibility to environment-induced degradation in all the three conditions, the conditions M1 and M2 appear to show higher susceptibility compared to M3. This conclusion is also strengthened by the observation that there is an increase in YS at lower strain rate for M1 and M2 conditions. The higher YS and lower % elongation are indicative of a relatively brittle behaviour of the material in M1 and M2 conditions when tested at low strain rate.

The ductility of maraging steel is lower at slow strain rate. This is found to be so in the aged conditions (M1) as well as moderately overaged condition (M2) and highly overaged condition (M3). This embrittlement is believed to be induced by environment. It is believed that hydrogen embrittlement is coming into picture. In the Introduction section, reference was made to the work reported by Venugopal Reddy [3] wherein it was brought out that ambient air environment, with no specific corrosive environment surrounding the material, can cause hydrogen embrittlement of C18Ni1700. The work reported by Soeno and Tagucchi [8] also provides supporting evidence. These authors studied the effect of strain rate on ductility of two grades of maraging steel—17.5Ni–12.8Co–4Mo–1.7Ti and 13Ni–15Co–10Mo–0.2Ti. They reported that the ductilities of these steels, when heat treated to obtain fine and coherent precipitates, increase with increasing strain rate at room temperature. The authors attributed the behaviour to hydrogen embrittlement.

Studies by Venkatanarayana et al. [9] on C18Ni1700 have shown that varying the strain rate over the range 10^{-4}–10^{-1} s^{-1} at room temperature had no effect on % elongation in tensile testing. Material was in solution treated and aged condition, ageing being for 3.5 h at 480 °C. This means that there was no environment-induced degradation occurring in the peak aged condition even at a relatively low strain rate of 10^{-4} s^{-1}. The insensitivity to strain rate observed in their studies is at variance with the embrittlement observed at low strain rates in the present study. The difference is arising because the metallurgical condition in the two studies is not the same. Venkatanarayana et al. [9] studied the material in solution treated and peak aged condition. In the present study the material is in solution treated+cold rolled (60%) and aged condition; M1 condition roughly corresponds to peak aged

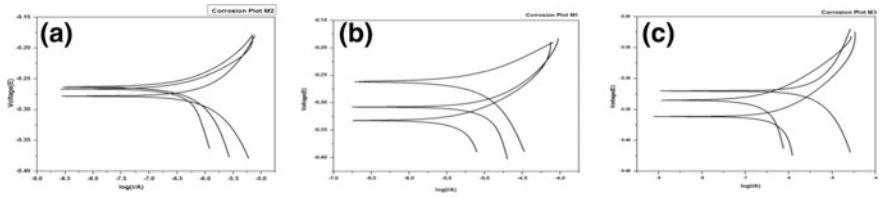

Fig. 3 Tafel plots for **a** M1 **b** M2 and **c** M3 conditions

Table 2 Corrosion potential, corrosion current and corrosion rate for M1, M2 and M3 conditions

Sample condition	Corrosion potential (E)	Corrosion current (A) (10^{-6})	Corrosion rate (mils/year)
M1	−0.29	6.57	9.53
M2	−0.30	3.01	4.15
M3	−0.31	6.90	5.60

condition. The embrittlement observed at low strain rate in the present study is thus believed to be a result of cold work preceding aging. Strength obtained after cold working and aging is higher; this is expected to lead to a higher susceptibility to environment-induced degradation, going by the analysis presented in the Introduction section.

Figure 3 shows the results of potentiodynamic polarization studies in the form of Tafel plots for M1, M2 and M3 conditions. In all the three conditions both anodic and cathodic reactions were observed. Table 2 shows the values of corrosion potential, corrosion current and corrosion rate derived from the plots. It is seen that corrosion rate is highest for the M1 condition. The lowest corrosion rate was obtained for the M2 condition. The M3 condition showed an intermediate corrosion rate. The increase in corrosion rate on moving from M2 to M3 may have to do with large amount of reverted austenite in M3 condition. It was reported that reverted austenite adversely influences the resistance to stress corrosion cracking, during both crack nucleation and propagation stages [10]. Well-developed austenite phase, as is the case with M3 condition, may promote galvanic corrosion, thereby increasing the corrosion rate.

Conclusions

1. Efforts were made to optimize the aging treatment of cold rolled maraging steel plate to obtain improved strength ductility combination and better resistance to environment-induced degradation.
2. M2 condition comes close to meeting the AMS 6520 requirement. The strength values in M3 condition do not meet this requirement.

3. Slow strain rate testing leads to distinct reduction in % elongation values. It is believed that hydrogen embrittlement is responsible for the reduction.
4. Cold working prior to aging results in higher strength after aging and makes C18Ni1700 susceptible to hydrogen induced cracking.
5. There is a drastic reduction in corrosion rate on moving from M1 to M2 condition. Somewhat high corrosion rate in M3 condition may have to do with high amount of austenite present in the microstructure.

Acknowledgements The present work is carried out as part of the execution of contract for acquisition of research services. Devendranath Ramkumar K and Nageswara Rao M are grateful to Director, Defence Research and Development Laboratory for awarding this contract. The authors are grateful to Director, DRDL for according permission to present this work. The authors are indebted to Dr. K Ramesh Kumar, Scientist 'G' DRDO for his guidance and constant encouragement. We also wish to thank A. P. Vardhan, Scientist 'G', Director, Solid Propulsion for their valuable inputs and reviews during the course of this work. The help of Sidharth Dev, senior research fellow, in getting the manuscript ready is thankfully acknowledged.

References

1. Becker WT, Shipley RJ (eds) (2002) Failure analysis and prevention. ASM International, Ohio
2. Bradhurst DH, Heuer PM (1981) Environmental cracking of high strength maraging steels: Part I—Aqueous NaCl solution. Corrosion 37(1):50–55
3. Reddy AV (2004) Investigation of aeronautical and engineering component failures. CRC Press, New York
4. Zhang YP, Shi DM, Chu WY, Qiao LJ, Shi YL, Zheng SL, Wang SB (2007) Hydrogen assisted cracking of T-250 maraging steel. Mater Sci Eng A 471(1):34–37
5. Lee IK, Chou CP, Cheng CM, Kuo IC (2003) Effect of aging treatment on the mechanical properties of C-250 maraging steel by flow forming. J Mater Eng Perform 12(1):41–47
6. Floreen S (1968) The physical metallurgy of maraging steels. Metall Rev 13(1):115–128
7. Naim M, Bahadur S (1986) Effect of microstructure and mechanical properties on the erosion of 18 Ni (250) maraging steel. Wear 112(2):217–234
8. Soeno K, Taguchi K (1981) Effects of test temperature and strain rate on ductilities of 17.5Ni–12.8Co–4Mo–1.7Ti and 13Ni–15Co–10Mo–0.2Ti maraging steels. Trans Iron Steel Inst Jpn 21(9):618–623
9. Venkatanarayana G, Arumugham S, Lakshmanan TS, Prasad Rao P (1996) Effect of temperature and strain rate on tensile behaviour of M250 maraging steel. Mater Sci Technol 12(7):607–609
10. Reddy GM, Rao KS (2015) Microstructure and corrosion behaviour of gas tungsten arc welds of maraging steel. Defence Technol 11(1):48–55

Part XXI
Fatigue in Materials: Fundamentals, Multiscale Modeling and Prevention

Thermal Fatigue Behavior of High Cr Roller Steel

G. Kugler, D. Bombač and M. Terčelj

Abstract In this work thermal fatigue resistance of 1.7C, 11.2Cr, 2.0Ni, 1.2Mo steel for hot working rolls was studied using our newly developed test rig with specially prepared test samples. Tests were carried out in temperature range between 500–700 °C whereas relevant characteristics related to cracks after 200, 500, 1000, and 2500 cycles were obtained. Average length of all cracks, their density, average length of five longest cracks, and relevant microstructural characteristics of tested specimens were determined. It was found that initiation of cracks is strongly related to the cracking and spalling of carbides at specimens surface layer and that cracks growth is related to the characteristics of carbides. For comparison also results for Indefinite Chilled Double Poured roll cast iron are given. Based on obtained results, possible improvements of thermal fatigue resistance of these two materials are discussed.

Keywords Thermal fatigue · Roller steel · Cementite · Graphite · Cracks

Introduction

The surface of hot working rollers is exposed to thermal cycling. During contact with rolled material, roller goes through heating cycle while subsequent water cooling causes cooling cycle. This is then repeated at every turn of work roller, where maximum operating temperatures during hot rolling conditions on the roller bulk surface are in the temperature range 500–700 °C. During cooling stage minimal

G. Kugler (✉) · M. Terčelj
Faculty of Natural Sciences and Engineering, University of Ljubljana, Akereva 12, 1000 Ljubljana, Slovenia
e-mail: goran.kugler@omm.ntf.uni-lj.si

M. Terčelj
e-mail: milan.tecelj@omm.ntf.uni-lj.si

D. Bombač
Department of Materials Science and Metallurgy, University of Cambridge, 27 Charles Babbage Road, Cambridge CB3 0FS, UK
e-mail: db513@cam.ac.uk

The Minerals, Metals & Materials Society, *TMS 2018 147th Annual Meeting & Exhibition Supplemental Proceedings*, The Minerals, Metals & Materials Series,
https://doi.org/10.1007/978-3-319-72526-0_50

temperature reached is between 100–200 °C. The cyclic temperature difference lead to the occurrence of crack networks on the surface layer and the spalling of surface layer material. During hot rolling, thermal stresses experienced by the roller material are comparable or larger than mechanical stresses [1–7].

Main focus of hot working rollers research is study of the influence of used steel, heat treatment, surface improvements [8–10] and crack nucleation and propagation [7, 8]. Thermal fatigue prediction in laboratory is difficult as majority of the tests only achieve similar maximum temperature and they do not reproduce realistic stress states in the material surface layer. Since only a handful of studies exist on the thermal fatigue behavior of roller materials in a wider temperature range comparable to hot rolling, the description of surface degradation mechanisms are not sufficiently understood, although it is accepted that influence of temperature on the mechanisms is significant. In order to fulfill permanent demands of constantly increasing service time of hot working rollers, additional knowledge related to thermal fatigue cracking and degradation mechanisms of cooled roller surface in an extended temperature range is required.

In this study, the thermal fatigue of high Cr steel for hot working rollers at three temperatures (500, 600 and 700 °C) and surface layer degradation mechanisms were investigated using test rig described in detail in reference [7] after 200, 500, 1000 and 2500 thermal cycles. Thermal fatigue resistance was evaluate quantitatively with the average length of all cracks, their density and average length of the seven longest cracks. Microscopy was used to present micrographs explaining crack nucleation and propagation and other surface degradation mechanisms.

Experimental and Modelling

Chemical compositions of the roller steel used in this study is given in Table 1. The material has along a high carbon content also significant amount of other carbide forming elements (Cr, Mo and V). Due to high content of Cr and Mo, transition metal carbides are expected in the microstructure. The initial Vickers hardness was measured as the average of five indentations conducted using a 10 kg load, resulting in hardness of 601 ± 10 HV10. Optical micrographs of the initial microstructure is shown in Fig. 1a with its details depicted in Fig. 1b. The microstructure consists of tempered martensite with primary, eutectic and secondary transition metal carbides with small amounts of MnS inclusions. Eutectic carbides shown in Fig. 1a are

Table 1 Chemical composition of used steel in wt%

C	Si	Mn	Cr	Mo	V	Co	Ni	S	P	B	N
1.65	0.654	0.732	11,279	1.169	0.253	0.017	1.940	0.009	0.017	0.011	0.046

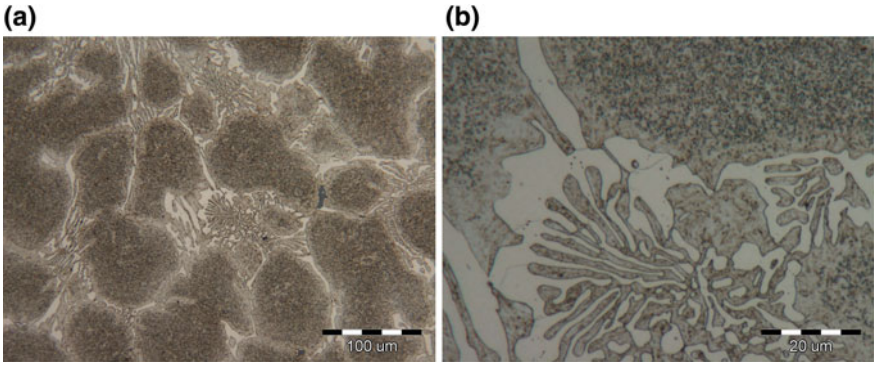

Fig. 1 Microstructure of initial material; **a** eutectic and primary carbide cell structure in the matrix and **b** detail of eutectic carbides

lenticular and spheroidal, while primary carbides are usually on grain boundaries and are ticker and longer compared to eutectic carbides. An average length of lamella of the primary carbide is approximately 50 m with thickness up to 10 μm. An average length of secondary carbides lamella is up to 30 μm with thickness approximately 3 μm. Phase identification from microscopy in combination with a conventional X-ray diffraction (XRD) measurements on a polished sample using a Bruker D8 Advance X-ray diffractometer with position sensitive detector (LynxEye EX) and Cu-Kα radiation (λ = 1.5406 Å) revealed tempered martensite matrix with M7C3 carbides, along smaller amount of M2C carbides. A continuous scanning mode was chosen for XRD with a rate of 0.01° s^{-1} over an angular width of 2θ = 30–120° and a Ni filter was used to obtain a nearly monochromatic X-ray beam. After thermal fatigue testing, the working lengths of each sample were first cut through the middle in an axial direction and one half also in a radial direction for microscopy. Characterization of cracking was focused within the working length of the sample and quantitatively evaluated by (i) average length of all cracks, (ii) density of cracks, (iii) average length of the seven longest cracks. For the observation of surfaces and microstructure, optical microscope (OM, Carl Zeiss AXIO Imager.A1m) and scanning electron microscope (JEOL 5610) were used.

In order to roughly estimate stress conditions within the thermal fatigue specimens, temperatures at the outer surface and inside of the specimen, i.e. 2, 1.1, 0.6, and 0.3 mm from the inner surface, were measured by carefully welding thermocouples within the specimens. These temperatures have been then used in combination with numerical solution of the heat equation to estimate the temperature profile evolution during thermal cycling. Obtained temperature distributions were used for calculation of thermal stresses by simplifying our problem assuming plane stain conditions and elastic deformations. The following equilibrium equation was considered

$$\frac{d\sigma_{rr}}{r} + \frac{\sigma_{rr} - \sigma_{\varphi\varphi}}{r} = 0\,, \tag{1}$$

employing zero stress boundary conditions at inside and outside surfaces of the specimen, i.e. $\sigma_{rr} = 0$ at $r = a$ and $r = b$, respectively. The solution reads as [11]

$$\sigma_{rr} = \frac{E\alpha}{(1-\nu)r^2}\left(\frac{r^2-a^2}{b^2-a^2}\int_a^b Trdr - \int_a^r Trdr\right) \tag{2}$$

$$\sigma_{\varphi\varphi} = \frac{E\alpha}{(1-\nu)r^2}\left(\frac{r^2+a^2}{b^2-a^2}\int_a^b Trdr + \int_a^r Trdr - r^2T\right) \tag{3}$$

$$\sigma_{zz} = \frac{E\alpha}{(1-\nu)}\left(\frac{2\nu}{b^2-a^2}\int_a^b Trdr - T\right), \tag{4}$$

where ν is the Poisson number, α linear expansion coefficient, and E is Young's modulus. Stresses given by these equations (2)–(4) were calculated by solving integrals numerically using Simpson's rule.

Results and Discussion

Figure 2a shows the results of the numerical calculation of temperature profile evolution during one thermal fatigue cycle, i.e. temperature as a function of time at four different radial positions between inner and outer surface of the specimen. The plot of thermally induced radial component of stress as a function of time is shown in Fig. 2b. As can be seen these stresses are the largest during cooling of specimen and they are decreasing with the distance from the inner surface. The same is also true for tangential stresses that are shown in Fig. 2c. Note that they are also given values at both surfaces. As expected they are maximal at the inner surface and minimal at the outer one, and their values are much larger than radial components of stress. Figure 2d shows tangential and radial component of stress along the radius of the specimen at three different times during cooling time interval, where they are the largest. As can be seen, during cooling tensile tangential stresses develop near the inner surface that provoke crack initiation. Tangential stress are decreasing with the distance from the inner surface and are compressive near the outer surface.

Crack Nucleation and Propagation

Cracks initiate and propagate along lenticular carbides as shown in Fig. 3. Crack nucleation is a consequence of tensile stresses on the surface layer due to temperature gradient between the cooled surface and the material inside the sample and differences in thermal expansion coefficients and mechanical properties between the matrix and carbides, where carbides are more brittle in comparison to the surrounding matrix and have lower thermal expansion coefficient. During heating and

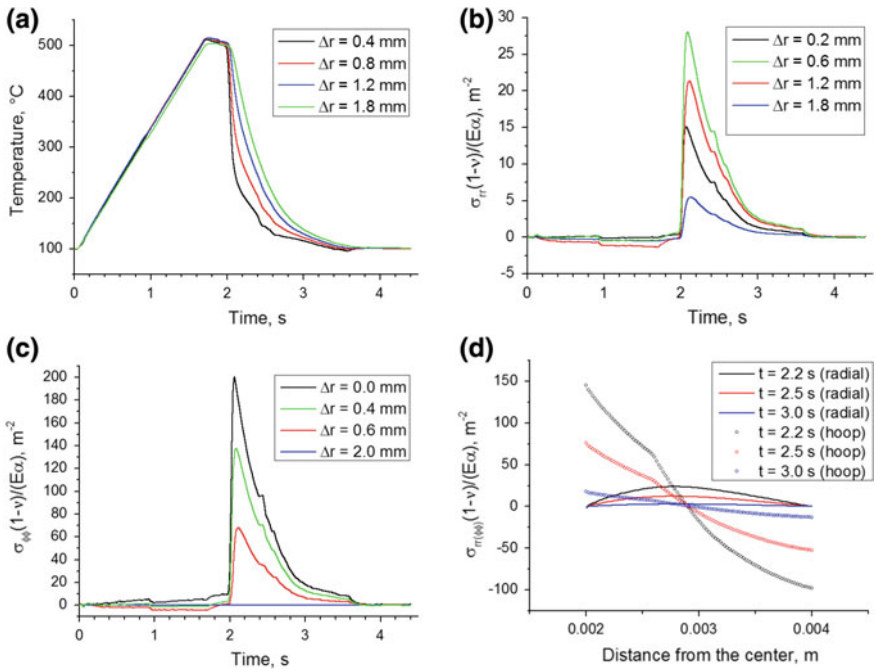

Fig. 2 Results of numerical calculations: **a** temperature, **b** radial stresses, and **c** hoop stresses at various distances from inner surface as a function of time during one cycle. **d** radial and hoop stresses as a function of radial distance from the center during fast cooling at 2.2, 2.5, and 3.0 s

cooling, carbides cannot follow dilatations of the matrix and as a consequence cracks nucleate. Crack propagation depends on the orientation of carbides. As can be seen in Fig. 3, when carbide is oriented perpendicular to the surface, cracks are longer and follow carbide distribution around grain boundaries. However, if initial orientation of the carbide is angular based on the surface, cracks will form enclosed area and cause potential spots for chipping. This can be seen in Fig. 4, where nucleation of angular crack is shown in Fig. 4a and area fully enclosed with cracks in Fig. 4b. Furthermore, from Figs. 3 and 4 follows that crack propagation through the matrix is difficult and preferred crack pathways are carbides. Based on the carbide orientation, shape, position and distribution, several distinctive surface degradation mechanisms were additionally observed. Chipping either occurs after area between carbides and surface is enclosed with cracks as shown in Fig. 4b. Sometimes, carbide lamellae are in a parallel orientation with the surface as shown in Fig. 5a. In the case described, chipping of outer surface layer occurs due to the cracks nucleating parallel with the surface in proximity of the surface. Surface can also degrade at carbides present at the surface when their thickness is large (exceeding 10 μm) as presented in Fig. 5b. Due to difference in mechanical properties and thermal expansion coefficients between the matrix and carbides cracks nucleate at several different position,

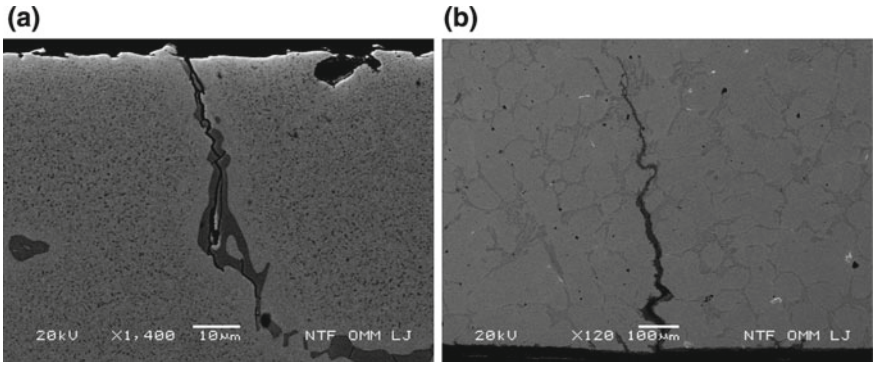

Fig. 3 Cracking along lenticular carbides; **a** at 500 °C and 500 thermal cycles; **b** at 700 °C and 1000 thermal cycles

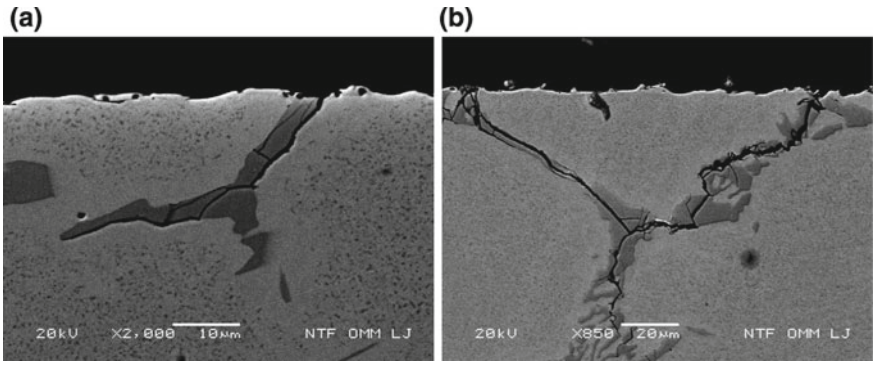

Fig. 4 Angular cracking along carbides; **a** angular crack at 500 °C and 500 thermal cycles; **b** area enclosed by cracks at 700 °C and 1000 thermal cycles

causing breaking of carbide with loss of structural load bearing properties. Similar was also observed for internal cracks, which nucleated at the thicker carbide, and then branch and propagate along thin carbide in vicinity, as shown in Fig. 5c. Interesting observation is depicted in Fig. 5d, where crack propagation was impeded with crack branching along eutectic carbides. Role of eutectic carbides is very important as it impedes crack propagation. However, to be effective it needs to be in vicinity of the surface as can be seen in Fig. 5d and also more globular. If eutectic carbide is lamellar and at the surface it will cause chipping as can be seen in Fig. 5a.

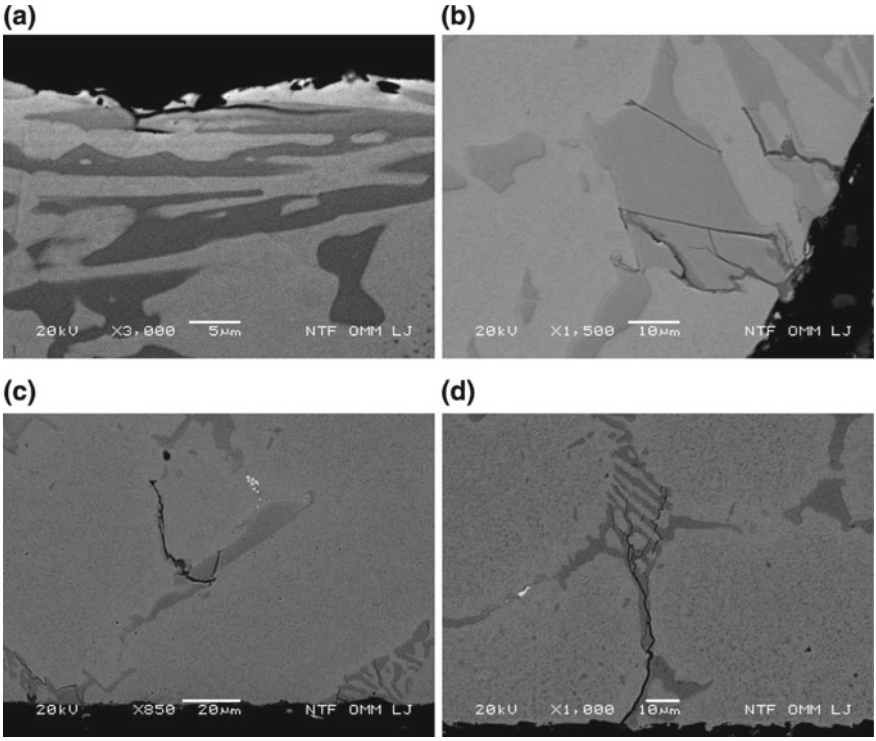

Fig. 5 Crack nucleation and propagation **a** chipping due to cracks in parallel carbides at 700 °C and 500 thermal cycles; **b** crack nucleation in carbide at the surface at 500 °C and 1000 thermal cycles; **c** internal crack nucleated at thick carbide at 600 °C and 500 thermal cycles; and **d** crack branching at eutectic carbide lamellae at 500 °C and 200 thermal cycles

Quantitative Estimation of Crack Propagation

Cracks were quantitatively described through the data analysis of the obtained crack lengths which allowed the determination of the average length of all observed cracks, crack density and the determination of the seven longest cracks observed at each test temperature and number of thermal cycles. The average length of all cracks is shown in Fig. 6a where it can be seen that average lengths increase with temperature and number of cycles. Similar observation can be made also for crack density depicted in Fig. 6b. However, closer inspection of crack density revealed that crack density is not increasing linearly with the number of cycles. In Fig. 6c lengths of the seven longest cracks are depicted in relation to the number of thermal cycles and maximum test temperatures. The average length of the seven longest cracks increases with the tested maximum temperature and number of thermal cycles.

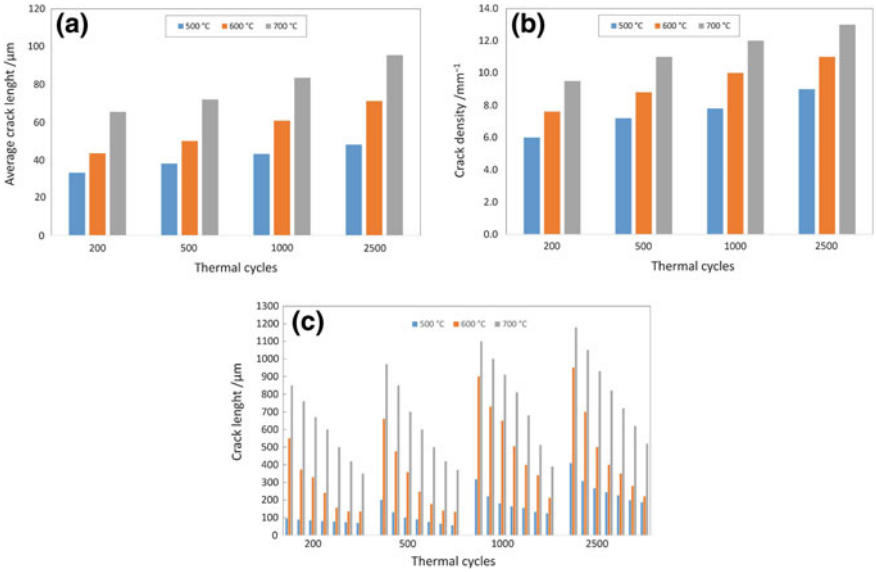

Fig. 6 Influence of maximum test temperature and number of cycles on; **a** average crack length; **b** crack density and **c** lengths of the seven longest cracks

Conclusions

The following conclusions can be reached from present work.

- Numerical calculations reveal that inner surface is subjected to tensile stresses concentrations during cooling part of thermal fatigue cycle since inner surface area cools faster than periphery. These conditions results in crack nucleation and their subsequent growth.
- Degradation of the surface layer progresses through crack nucleation and propagation of surface and internal cracks, their linking and, material spalling and chipping.
- Cracks predominately propagate through primary and eutectic carbides.
- Thick primary carbides are severely cracked, however crack propagation then proceeds through thin eutectic carbides.
- Globular eutectic carbide close to the surface layer serve as unlinked particles in the matrix which impede crack propagation.
- Average length, density and length of the seven longest cracks increase with maximum test temperature and number of cycles.

References

1. Belzunce FJ, Ziadi A, Rodriguez C (2004) Structural integrity of hot strip mill rolling rolls. Eng Failure Anal 11:789–797
2. Goto K, Matsuda Y, Sakamoto K, Sugimoto Y (1992) Basic characteristics and microstructure of high-carbon high speed steel rolls for hot rolling mill. ISIJ Int 32:1184–1189
3. Colas R, Ramirez J, Sandoval I, Morales JC, Leduc LA (1999) Damage in hot rolling work rolls. Wear 230:56–60
4. Garza Montes de Oca NF, Colas R, Rainfort WM (2011) On the damage of work roll grade high speed steel by thermal cycling. Eng Failure Anal 18:1576–1583
5. Pellizzari M, Molinari A, Straffelini G (2005) Tribological behaviour of hot rolling rolls. Wear 259:1281–1289
6. Choi Jin-Won, Kim Donggyu (1999) Mechanisms hot of surface strip rolling deterioration of high-Ni grain roll for hot steep rolling. ISIJ Int 39:823–828
7. Bombac D, Kugler G, Markoli B, M. Terčelj, (2017) Hot work roller surface layer degradation progress during thermal fatigue in the temperature range 500–700°C. Int J Fatigue 104:355–365
8. Fissolo A, Amiable S, Ancelet O, Mermaz F, Stelmaszyk JM, Constantinescu A et al (2009) Crack initiation under thermal fatigue: an overview of CEA experience. Part I: Thermal fatigue appears to be more damaging than uniaxial isothermal fatigue. Int J Fatigue 31:587–600
9. Birol Y (2011) Response to thermal cycling of duplex-coated hot work tool steels at elevated temperatures. Mater Sci Eng A 528:8402–8409
10. Zhu Y, Schwam D, Wallace JF, Birceanu S (2004) Evaluation of soldering, washout and thermal fatigue resistance of advanced metal materials for aluminum die-casting dies. Mater Sci Eng A 379:420–31
11. Kandil A, El-Kady AA, El-Kafrawy A (1995) Transient thermal stress analysis of thick-walled cylinders. Int J Mech Sci 37:721–732

Influence of Cold Spray on the Enhancement of Corrosion Fatigue of the AZ31B Cast Mg Alloy

S. K. Shaha, S. B. Dayani and H. Jahed

Abstract High strength Al 7075 powder was successfully deposited on the AZ31B as-cast dog bone samples. The electro chemical corrosion behavior of AZ31B samples in coated and uncoated condition was examine in 3.5% NaCl aqueous solution at the room temperature. At the same time, the rotating bending fatigue behavior was studied in the similar environmental condition. It is seen that the as deposited cold sprayed alloy obtained lower corrosion resistance compared to the bulk Al 7075 alloy available in the literature, while a significant corrosion resistance was increased in AZ31B alloy with Al 7075 coat. At the same time, the coated sample achieved longer fatigue life compared to the uncoated sample in corrosive environment. The fatigue fracture surface analysis shows that pitting holes were formed at the surface and penetrated up to the coating/substrate interface that basically nucleates the fatigue crack leading to the fatigue fracture.

Keywords Cold spray coating · Magnesium alloy · Al7075 alloy powder Corrosion fatigue

Introduction

Magnesium (Mg) alloys are the lightest engineering material, and are attractive to automotive, aerospace and electronics industries for weight reduction purpose [1]. Because of their chemical reactivity, susceptible to react with oxides, chlorides, and sulfides along with the poor wear, oxidation resistance, low corrosion resistance limits its extensive applications. Many researchers have been reported that the corrosion properties of Mg alloys can be improved by forming protective coatings in cold spray (CS) method [2–8] by utilizing different coating materials, which exhibits better corrosion resistance in particular corrosion fatigue resistance.

S. K. Shaha · S. B. Dayani · H. Jahed (✉)
Department of Mechanical & Mechatronics Engineering, University of Waterloo, 200 University Ave W, Waterloo, ON N2L 3G1, Canada
e-mail: hjahed@uwaterloo.ca

The Minerals, Metals & Materials Society, *TMS 2018 147th Annual Meeting & Exhibition Supplemental Proceedings*, The Minerals, Metals & Materials Series,
https://doi.org/10.1007/978-3-319-72526-0_51

Powders of Aluminium (Al) and its alloys have established as an excellent coating materials which can be deposited effectively on the Mg substrates in CS process [9]. When Al is exposed to air a thin aluminum oxide layer is formed that protect the penetration of oxygen and further oxidation. A significant amount of work has been performed on the CS coatings of Al and its alloys on Mg alloy substrate [2–8]. Tao et al. [10, 11] reported that corrosion is a main cause of weakening the fatigue behavior of AZ91D Mg alloy. They reported that the corrosion properties of the AZ91D can be significantly improved by depositing pure-Al in CS process [10, 11]. Diab et al. [2] investigated the corrosion and corrosion fatigue behavior of pure-Al coatings on extruded AZ31B Mg alloy. A marginal enhancement in fatigue properties at air due to the CS of pure Al, while the corrosion fatigue properties improved significantly. In another study, researchers demonstrated that the pure Al deposited on extruded AZ31B alloy improved its fatigue strength in air by 9% [12]. They concluded that only a small change in the fatigue life of the substrate was achieved because of the low strength of the coating material (pure-Al). Our recent study [13] shows that the fatigue life of the AZ31B cast Mg alloy in laboratory environment increased ~25% by depositing Al7075 powder. At the same time the bonding strength improved significantly. Here, coating material plays an important role in enhancing the fatigue life as Al7075 alloy having high-strength would be a good candidate coating material to improve the corrosion fatigue life of as-cast AZ31B. However, most of the studies focused on the corrosion behavior of CS coatings of pure-Al, and Al/Al_2O_3 or $Al//Mg_{17}Al_{12}$ composites on Mg alloy substrate. A little attention has been paid on the corrosion and corrosion fatigue behavior of the CS Al7075 alloy deposited on the Mg alloy substrate. Therefore, in the present study, the electro chemical corrosion and corrosion fatigue properties of the CS Al7075 alloy on the as-cast AZ31B substrate were investigated in uncoated and coated conditions in 3.5% NaCl solution. Finally, the fracture surfaces in selected condition were examined using scanning electron microscope (SEM), to discuss the fracture mechanisms.

Experimental Details

For this study, as-cast AZ31B Mg alloy was used as a substrate. An Al based wrought alloy Al7075 having higher strength and longer fatigue life than the AZ31B was considered as the coating materials. The CS coating was processed at the Fatigue and Stress Analysis laboratory of the University of Waterloo, Waterloo, Canada, using the Supersonic Spray Technologies (SST) Series P CS system manufactured by Centerline Ltd. First, dog bone shape fatigue samples were extracted from a 300-mm diameter billet of as-cast AZ31B following ASTM: E8/E8 M-11. Then, the sample surfaces were polished up to 600 grid SiC emery paper and rinse with acetone. Details about the coating parameters can be seen in [13].

Microstructural analysis was performed using a SEM (model: FEI Quanta FEG 250 ESEM) equipped with an Oxford EDX.

The electrochemical corrosion behavior of the uncoated and CS Al7075 on as-cast AZ31B samples were conducted in a 3.5 wt% NaCl aqueous solution. The samples were considered as a working electrode while Ag/AgCl in saturated KCl electrode and a platinum plate were set as reference and counter electrode, respectively. The potentials were measured with respect to the Ag/AgCl reference electrode. After that the Tafel fit of the potentiodynamic curve was plotted to calculate the corrosion rate.

The stress controlled fatigue tests were performed using an Instron RR Moore four-point rotating-bending fatigue testing machine in fully reversed ($R = -1$) condition. The tests were conducted at different stress amplitudes between 40 to 145 MPa in both low and high cycle regime. A customized chamber was installed to the fatigue machine to perform the corrosion fatigue test. The chamber allowed a continuous flow of 3.5% NaCl solution onto the specimen gauge section at a constant rate of 40 ml/min during the fatigue testing. For all fatigue teste, a constant frequency of 30 Hz was maintained, and tests were stopped when samples break a parts or reached at 10 million cycles considered as run out/infinite fatigue life. At least two samples were tested for each conditions. The fatigue fracture surfaces were then characterized using SEM.

Results and Discussion

Microstructure

The SEM micrographs with an EDX line scan of the polished cross-section of the coated samples in as-coated material in the surface grinding conditions are illustrated in Fig. 1. As seen in Fig. 1a, the as-coated sample shows almost defects free coatings processed with nitrogen gas environment. The acquired coating thickness in the as-deposition condition was 282 ± 26.11 μm, while the thickness was 122 ± 3.85 μm after grinding of the outer surface for fatigue tests. The EDX line scan (Fig. 1a) near the interface indicates that there was no drastic change in the base alloying elements (Mg/Al). Instead, a gradual change of Mg/Al shows that the interface contains a very thin layer of a Mg and Al mixture. Wang et al. [8] reported that the microstructure of pure Al coatings on the AZ91D Mg alloy using HRTEM. They identified a ~20-nm thick amorphous interlayer zone containing base elements of coating (Al) and substrate (Mg) with a metallurgical bond. It is also noticed that a The magnified SEM image of the interface presented in Fig. 6d shows that the casting defects, such as inclusions and porosities of the AZ31B, were covered by the CS coatings; the coverage of these defects can improve the mechanical properties of the AZ31B [14].

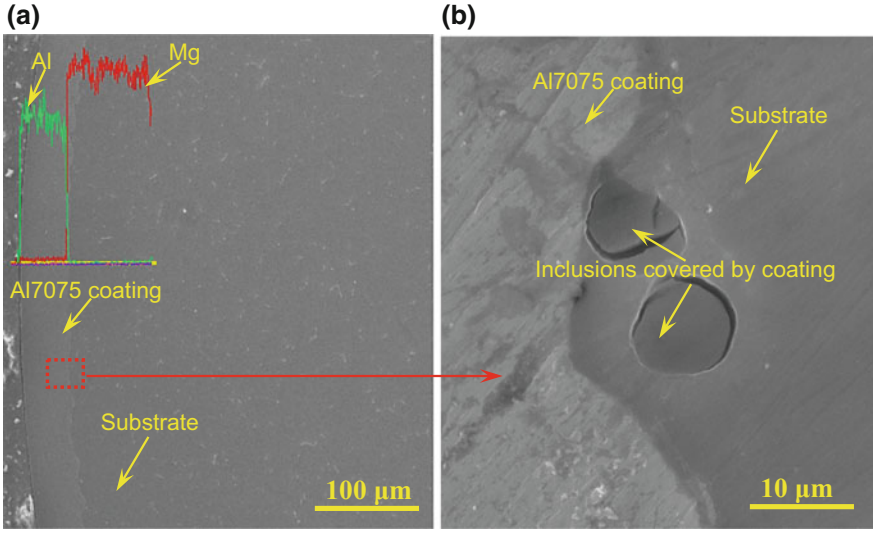

Fig. 1 Cross-sectioned and polished AZ31B magnesium alloy coated with Al7075 alloy EDX line scan in **a** grounded surface for fatigue tests, and **b** a magnified view of the enclosed area to show the casting defects covered by coating

Corrosion Properties

Before starting the potentiodynamic polarisation test, all the samples, uncoated and Al7075 coated AZ31B were immersed in the salt solution for 30 min to achieve the stable state of open circuit potential (OCP). Figure 2 depicts the potentiodynamic polarization curves of the uncoated and coated samples tested in 3.5% NaCl solution. Both curves reveal the same trends. To investigate more closely, the influence of the coatings on the corrosion kinetics of the AZ31B Mg alloy samples, the polarization curves were characterized following the curve-fitting method [15]. The relationship between the measured current density i_{corr} and electrode potential E_{corr} during the potentiodynamic polarisation follows the Butler-Volmer equation as describe in [16]. The evaluated parameters of the electrochemical corrosion test are listed in Table 1.

It is seen that the CS Al7075 shows better corrosion resistance compared to AZ31B Mg alloy. The uncoated AZ31B, i.e. substrate achieved higher value of 7.07 µA/cm^2 for i_{corr}, and lower value of 48 mV/decade, 107 mV/decade and −1.52 V for b_a, b_c and E_{corr}, respectively. In contrast, the CS sample reached half of the substrate current density. It is also noticed that the corrosion rate of the uncoated AZ31B was 1.35 × 10^{-2} mm/year which is two times higher than the CS samples. The change in corrosion rate of CS sample can be attributed by the presence of Mg in the coating material. The presence of Al in coatings form passive layer which basically improve the corrosion resistance of the cold spray sample. However, it is

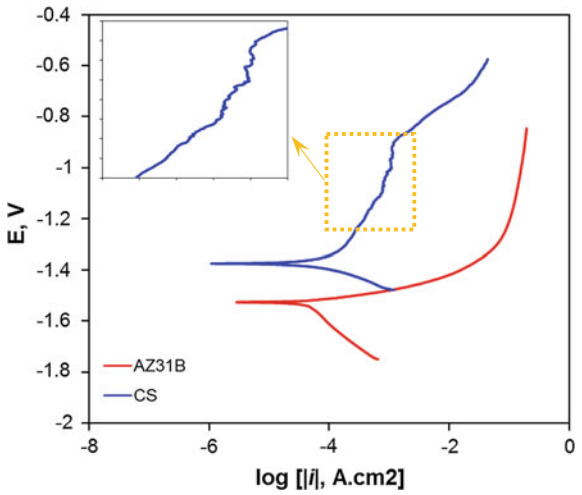

Fig. 2 Typical polarization curves to show the electro chemical corrosion behavior of uncoated AZ31B Mg alloy and coated with Al7075 alloy

Table 1 Tafel fitting results for uncoated and coated with Al7075 of AZ31B alloy specimens

Specimens	E_{corr} (V)	i_{corr} (μA/cm^2)	b_a (mV/decade)	b_c (mV/decade)	Corrosion rate (mm/year)
AZ31B	−1.52	7.07	48	107	1.35×10^{-2}
CS	−1.37	6.29	159	134	0.86×10^{-2}

clearly noticed that a localized corrosion occurs which is confirmed on the polarization curve with the breakdown of the potential (enclosed by yellow dotted line), that may affect the fatigue performance at corrosive environment. The surface morphology of the dog-bone fatigue tested samples before and after corrosion test are shown in Fig. 3. It is evident that the surface of the uncoated sample shows less pits than the CS sample which indicates that the Mg ion goes into the solution and dissolve almost uniformly during corrosion test. In contrast, the CS sample shows localized pits which will be the pathway to penetrate the solution and react with the virgin materials leading to further corrosion. The corrosion resistance of the materials depends on the stability of the passive layer. In CS sample passive layer was not that much stable which can survive for a long time due to the presence of alloying elements specially Mg. Therefore, pits were formed at the CS sample surface.

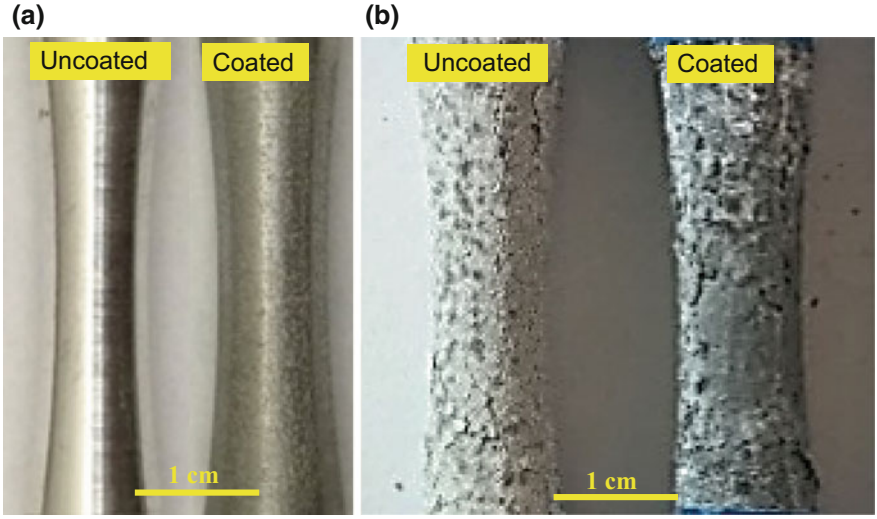

Fig. 3 Image of dog bone samples **a** before and **b** after electrochemical corrosion test samples show the surface morphology

Corrosion Fatigue Behavior

The *S-N* curves of the uncoated and coated samples tested in air and 3.5% NaCl solution at different stress amplitudes are presented in Fig. 4. Generally, the fatigue life at the corrosive environment is always lower than the fatigue life at the air. It is clearly seen that the sample coated with Al7075 alloy tested in air obtained superior fatigue life compared to the other conditions. Compared to the substrate, the Al7075 coat on AZ31B sample achieved about 26% higher fatigue strength at 10^7 cycles. The obtained fatigue strength of CS sample is 92 ± 2.7 MPa, while the fatigue strength of the substrate is 73.4 ± 5.9 MPa. In contrast, the CS sample tested in corrosive environment showed lower fatigue performance in the corrosive environment; even lower than the uncoated sample tested in air. However, it should be worthy to note that the fatigue fracture occurred all stress amplitudes, even at lower stress amplitude of 40 MPa which is half of the compressive yield strength (~90 MPa) and 16% of ultimate strength.

However, the enhancement of fatigue performance in air can be considered as the development of compressive residual stresses in the coating induced during CS process. The high impact velocity and processing carrier gas temperature of CS particles on the AZ31B substrate imposed plastic deformation causing adiabatic share instability on the surface in the vicinity of impacted particle [4, 17]. Spencer et al. [18] During CS, the carrier gas and substrate temperature was 400 °C and 25 °C, respectively. The difference of temperature induced a compressive stress. However, the presence of residual stress in the CS coating, results stress corrosion cracking. As the corrosion resistance of the CS sample is higher than the uncoated

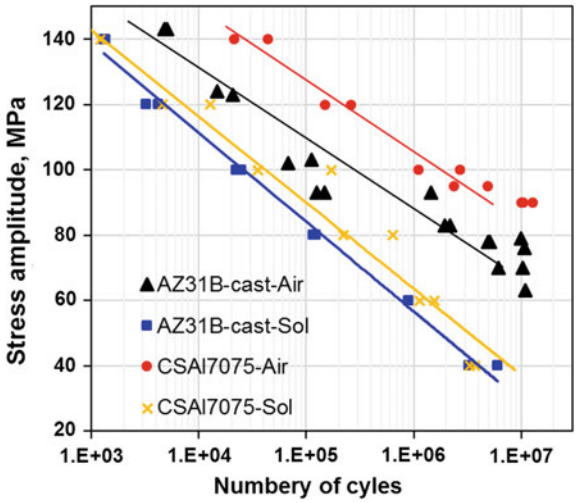

Fig. 4 S-N curves show a comparison of fatigue life between the uncoated and coated AZ31B cast alloy tested in 3.5 wt% NaCl aqueous solution. Note: CS-cold spray, Sol-3.5% NaCl solution

samples, the CS sample shows longer fatigue life compared to the uncoated samples.

Figure 5 depicts the fracture surfaces of the corrosion fatigue tested CS sample after the 3.7 million cycles. It is noticed that the surfaces of the CS sample exhibits deep pits surrounded of the fracture similar to the corrosion tested sample in Fig. 3b. As discussed earlier, the presence of Mg, surface porosity and residual stress are affecting the protective layer results pits are formed. The induced residual stress during coating appeared to be a negative effects on the fatigue life of the CS sample, as the CS sample achieved a shorter fatigue life as compared with the sample tested in air.

Figure 6 displayed the fatigue fracture surfaces of CS samples tested in air and 3.5% NaCl solution at the stress amplitude of 100 MPa. It is seen that there was no interfacial delamination in the fracture surface of the CS sample tested in air.

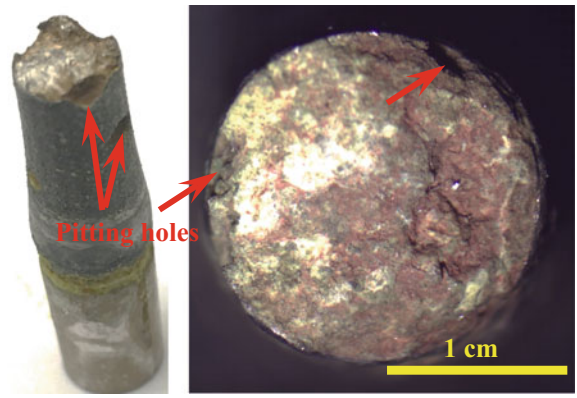

Fig. 5 Picture of corrosion fatigue fracture surface shows pitting holes

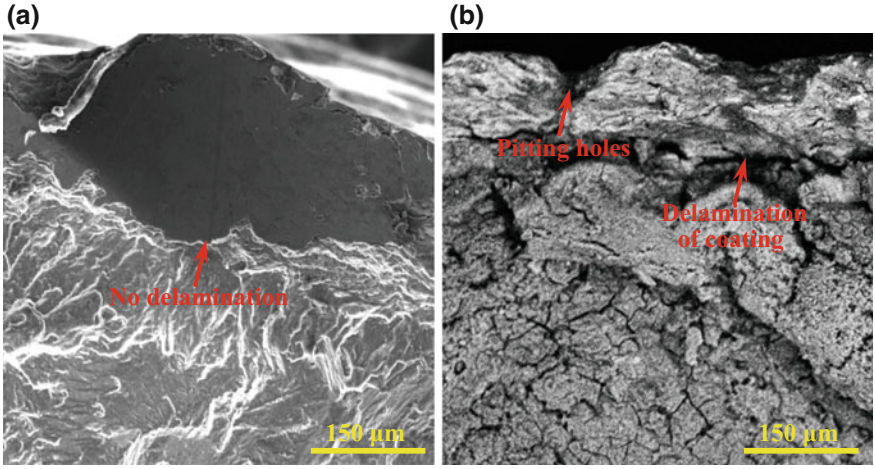

Fig. 6 A comparison of SEM images shows the fatigue fracture surface of the coated samples during fatigue testing at different environmental conditions, **a** in air and **b** in 3.5% NaCl solution. Note: pits were formed at the surface which continued to the interfaces results delamination of coatings

In contrast, the sample tested in NaCl solution shows an interfacial delamination. In CS sample tested in NaCl corrosive environment, the solution penetrated through the deep pits and come in contact to the substrate. As a results a vigorous chemical reaction occurred between the solution and Mg, which delaminated the coatings from the substrate results shorter fatigue life in corrosive environment [19, 20].

Conclusion

The corrosion fatigue properties of a low-pressure CS Al7075 on as-cast AZ31B at were studied in air and 3.5% NaCl solution at room temperature. Based on the results of the study and the above discussion, the following conclusions can be drawn:

- A dense, low-porosity coating of Al7075 was formed successfully on the cast AZ31B Mg alloy.
- The electro chemical corrosion analysis shows that the CS of Al7075 alloy slightly improved the corrosion resistance of as-cast AZ31B. This can be attribute due to the presence of compressive residual stress induced by the CS coating.
- A significant improvement in fatigue strength of the coated samples in was detected; this is due to the compressive residual stress imposed by the CS coating, as well as the higher strength of the Al7075 coating material compared to the AZ31B substrate.

- Compared to the AZ31B substrate, a remarkable improvement in corrosion fatigue properties of the CS Al 7075 coated samples was observed. This is the result of the presence of passive oxide layer on the surface, which improved the corrosion resistance. However, due to the formation of pits, the CS coating create early, which acted as a pathway for NaCl to penetrate into the interface, creating localized pits results an interfacial delamination which causes the premature cracking on AZ31B substrate and hence lower fatigue life of the CS sample in corrosive environment.

Acknowledgements The authors would like to gratefully acknowledge the financial support of the Natural Sciences and Engineering Research Council of Canada (NSERC), Automotive Partnership Canada (APC) program under APCPJ 459269–13 grant with contributions from Multimatic Technical Centre, Ford Motor Company, and Centerline Windsor.

References

1. Karparvarfard SMH, Shaha SK, Behravesh SB, Jahed H, Williams BW (2017) Microstructure, texture and mechanical behavior characterization of hot forged cast ZK60 magnesium alloy. J Mater Sci Technol 33:907–918
2. Diab M, Pang X, Jahed H (2017) The effect of pure aluminum cold spray coating on corrosion and corrosion fatigue of magnesium (3% Al-1% Zn) extrusion. Surf Coat Technol 309:423–435
3. Bu H, Yandouzi M, Lu C, MacDonald D, Jodoin B (2012) Cold spray blended Al+Mg 17Al12 coating for corrosion protection of AZ91D magnesium alloy. Surf Coat Technol 207:155–162
4. Ghelichi R, MacDonald D, Bagherifard S, Jahed H, Guagliano M, Jodoin B (2012) Microstructure and fatigue behavior of cold spray coated Al5052. Acta Mater 60(19):6555–6561
5. Rokni MR, Widener CA, Crawford GA, West MK (2015) An investigation into microstructure and mechanical properties of cold sprayed 7075 Al deposition. Mater Sci Eng A 625(January):19–27
6. Shayegan G et al (2014) Residual stress induced by cold spray coating of magnesium AZ31B extrusion. Mater Des 60:72–84
7. Spencer K, Fabijanic DM, Zhang MX (2009) The use of Al-Al_2O_3 cold spray coatings to improve the surface properties of magnesium alloys. Surf Coat Technol 204(3):336–344
8. Wang Q, Qiu D, Xiong Y, Birbilis N, Zhang MX (2014) High resolution microstructure characterization of the interface between cold sprayed Al coating and Mg alloy substrate. Appl Surf Sci 289:366–369
9. Hassani-Gangaraj SM, Moridi A, Guagliano M (2015) Critical review of corrosion protection by cold spray coatings. Surf Eng 31(11):803–815
10. Tao Y et al (2010) Microstructure and corrosion performance of a cold sprayed aluminium coating on AZ91D magnesium alloy. Corros Sci 52(10):3191–3197
11. Tao Y, Xiong T, Sun C, Jin H, Du H, Li T (2009) Effect of α-Al_2O_3 on the properties of cold sprayed Al/α-Al_2O_3 composite coatings on AZ91D magnesium alloy. Appl Surf Sci 256(1):261–266
12. Kalatehmollaei E, Mahmoudi-Asl H, Jahed H (2014) An asymmetric elastic-plastic analysis of the load-controlled rotating bending test and its application in the fatigue life estimation of wrought magnesium AZ31B. Int J Fatigue 64:33–41

13. Dayani SB, Ghelichi R, Shaha SK, Wang JF, Jahed H (2017) The impact of Al7075 cold spray coating on the fatigue life of AZ31B cast alloy. Surf Coat Technol (Submitted)
14. Xiong Y, Xiong X, Yoon S, Bae G, Lee C (2011) Dependence of bonding mechanisms of cold sprayed coatings on strain-rate-induced non-equilibrium phase transformation. J Therm Spray Technol 20(4):860–865
15. Sabaghi Joni M, Fattah-Alhosseini A (2016) Effect of KOH concentration on the electrochemical behavior of coatings formed by pulsed DC micro-arc oxidation (MAO) on AZ31B Mg alloy. J. Alloys Comp 661:237–244
16. Liu LJ, Schlesinger M (2009) Corrosion of magnesium and its alloys. Corros Sci 51:1733–1737
17. Ghelichi R et al (2014) Fatigue strength of Al alloy cold sprayed with nanocrystalline powders. Int J Fatigue 65:51–57
18. Spencer K, Luzin V, Matthews N, Zhang MX (2012) Residual stresses in cold spray Al coatings: The effect of alloying and of process parameters. Surf Coat Technol 206(19–20): 4249–4255
19. Xiong Y, Zhang M-X (2014) The effect of cold sprayed coatings on the mechanical properties of AZ91D magnesium alloys. Surf Coat Technol 253:89–95
20. Nan Z, Ishihara S, Goshima T (2008) Corrosion fatigue behavior of extruded magnesium alloy AZ31 in sodium chloride solution. Int J Fatigue 30(7):1181–1188

Part XXII
Fracture: 65 Years After the Weibull Distribution and the Williams Singularity

High Temperature Cracking Damage of Calcium Aluminate Cements

John F. Zapata, Maryory Gomez and Henry A. Colorado

Abstract Different formulations of calcium aluminate cements (CAC) with 51 and 71 wt% Al_2O_3, have been exposed to high temperature oxidation environments. Cement paste samples of 0.25, 0.30, and 0.40 water to cement (W/C) ratios were fabricated in this research. Both the raw cement powders and their corresponding samples after hydration were characterized in their microstructure by scanning electron microscopy, X-ray diffraction, Fourier-transform infrared spectroscopy and x-ray fluorescence. Samples were exposed to 500, 800 and 1000 °C in a furnace open to air. Damage occurred while samples were in the furnaces. Damage was analyzed by digital image processing.

Keywords Calcium aluminate cement · Mechanical behavior
Cracking damage · Gibbsite · Cement pastes

Introduction

Calcium aluminate cement (CAC) is a hydraulic cementitious material with uses in high performance applications such as those involving resistance to chemical attack, high early strength, refractory, and resistance to abrasion [1, 2]. Thermal properties of CAC are particularly interesting due to high rate CAC are slow setting

J. F. Zapata (✉) · H. A. Colorado
CCComposites Lab, Universidad de Antioquia (U de A), Calle 70 No. 52-21, Medellin, Colombia
e-mail: johnzap@gmail.com

J. F. Zapata
GISI. Institucion Universitaria de Envigado (IUE), Carrera 27 B # 39 A Sur 57, Envigado, Colombia

M. Gomez
CIDEMAT. Universidad de Antioquia (U de A), Calle 70 No. 52-21, Medellin, Colombia

The Minerals, Metals & Materials Society, *TMS 2018 147th Annual Meeting & Exhibition Supplemental Proceedings*, The Minerals, Metals & Materials Series,
https://doi.org/10.1007/978-3-319-72526-0_52

cements, with a fast hardening. These two characteristics were popular for the fabrication of pre-fabricated parts, although later these materials showed damages which reduced durability in Spain for two main causes [2, 3]: first, for a conversion reaction that produced water and porosity due to the transformation of CAH_{10} in C_3AH_6. Second, for the significant carbonation. There is a lack in research in the fracture and damage problems, as well as in the damage induced by temperature.

The main anhydrous phases in CAC are monocalcium aluminate (CA) and monocalcium dialuminate (CA_2), which in most cases are crystalline phases. The hydration of CA is mainly responsible for early strength development, whereas the hydration of CA_2 contributes after the main reaction of CAC hydration has already exceeded [4, 5].

The hydration of CAC is highly temperature dependent as summarized in Eq. 1, [1–4, 6], producing CAH_{10} as main product at temperatures less than 20 °C, C_2AH_8 and AH_3 at about 30 °C, and C_3AH_6 and AH_3 at temperatures greater than 55 °C. CAH_{10} and C_2AH_8 [7] are known to be metastable at ambient temperature and to convert to the phase more stable C_3AH_6 and AH_3 [7] with consequent material porosity and permeability increase, and the corresponding loss of strength.

$$\left.\begin{array}{rcl} CA + 10H & \xrightarrow{<20°C} & CAH_{10} \\ 2CA + 11H & \xrightarrow{\sim 30°C} & C_2AH_8 + AH_3 \\ 3CA + 12H & \xrightarrow{>55°C} & C_3AH_6 + 2AH_3 \end{array}\right\} \quad (1)$$

According to the phase equilibrium, CAH_{10} and C_2AH_8 are metastable phases which will convert to the stable phase C_3AH_6 over time [8]. The conversion is accompanied with the release of free water which results in a decrease in strength caused by an increase in the porosity. Depending on conditions, the conversion process can last up to several years. This process is summarized in Eq. 2, [8].

$$C_2AH_8 \rightarrow C_3AH_6 + 2AH_3 + 18H \quad (2)$$

Setting and hardening of CAC are primarily due to the hydration of process and phases, which in cement notation are: C = CaO, A = Al_2O_3, F = Fe_2O_3, P = $CaTiO_3$, H = H_2O, CA = $CaAl_2O_4$, CA_2 = $CaAl_4O_7$; CAH_{10} = $CaAl_2O_{14}H_{20}$; C_2AH_8 = $Ca_2Al_2O_{13}H_{16}$; AH_3 = $(Al_2O_3)3(H_2O)$; C_3AH_6 = Ca_3Al_2 $(OH)_{12}$.

In this work, digital image processing was used to quantify the damage by taking into the account factors such as temperature (500, 800 and 1000 °C), the alumina content (51 and 71 wt% alumina content), and the water to cement ratio, (w/c = 0.25, 0.3 and 0.4). This paper contributes in research regarding the damage induced at high temperature, with factors such as the alumina contents, and the water to cement ratio.

Table 1 Chemical composition of raw calcium aluminate cement powders

Samples	Chemical composition (wt%)								
Cement type I and II	Al_2O_3	CaO	SiO_2	TiO_2	Fe_2O_3	K_2O	P_2O_5	ZrO_2	MoO_3
I. CAC 51%	52.12	37.82	5.25	1.87	1.81	0.128	0.108	0.086	0.052
II. CAC 71%	71.09	28.38	0.238	–	–	–	–	–	–

Experimental

Different characterization was used in order to quantify the microstructure of CAC by using scanning electron microscopy (SEM), Fourier-transform infrared spectroscopy (FTIR), fluorescence of X-ray (XRF) and powder X-ray diffraction (XRD).

Two types of powder calcium aluminate cement were investigated. The composition of these powders were obtained in a XRF Thermo spectrometer Model: OPTIM'X. Details of all chemical components are presented in Table 1.

Cement paste samples fabricated with the two types of CAC powder and three water-cement ratio w/c (0.25, 0.3, and 0.4) are summarized in Table 2. Pastes were mixed mechanically while kept at 20 °C. In order to avoid carbonation processes and interaction with environment, cement paste was poured in closed containers to air, and later removed from molds after 28 days of curing.

Sample dimensions were 19 mm diameter and 22 mm height. XRD characterization was done in a X'Pert PRO diffractometer with Cu K_ radiation of 1.5406 A°, Scanning was performed between 2θ of 5 to 70°, step size 0.02°. A JEOL JSM–6490 Scanning electron microscopy (SEM-EDS) was used to observe the microstructure of microstructure for powders and cured cement samples. The samples were heated at 500, 800 and 1000 °C, subjected for one hour, to a heating rate 13.8 °C/min.

Fourier Transform Infrared Spectroscopy (FTIR) measurements were conducted in a Shimadzu IR Tracer-100. Scanning range (cm^{-1}): 400–4100. The test was performed in an ATR FT-IR apparatus.

Table 2 Formulations fabricated for cement paste samples

Samples	Cement type	Temperature (°C)	Curing time (days)	Water/cement (w/c)
1	I, II	20	28	0.25, 0.3, 0.4
2	I, II	500	28	0.25, 0.3, 0.4
3	I, II	800	28	0.25, 0.3, 0.4
4	I, II	1000	28	0.25, 0.3, 0.4

Results and Analysis

The FTIR and XRD tests showed that the main hydrated phases are CAH_{10} (Monocalcium aluminate decahydrate), C_3AH_6 (Katoite), C_2AH_8 (Dicalcium aluminate octahydrate) and AH_3 (Gibbsite). These and other results of the characterization of the raw materials used and the hydrated phases were published in [9].

Figures 1, 2, 3 and 4 shows photographs of calcium aluminate cement samples, subjected to room temperatures: 500, 800 and 1000 °C. Cracks appear for all water cement relationships and higher temperature is greater damage. Another result that can be observed is that the higher the content of lumina, the lower damage is found on samples. For the same temperature but at higher water to cement ratio, more damages is found. This is associated to the higher porosity generated for the higher w/c. Also, a loss of strength can be found due to the phase conversion process driven for the high temperatures exposure, which cal also favor the formation of other more stable phases [4].

CAC pastes with 51 and 71 wt% alumina content and W/C = 0.4 and 0.5, were exposed to 20 °C and were analyzed by SEM and are represented in Fig. 5.

It can be observed in Fig. 5 the regular hexagonal and cubic geometries of the hydrated phases, which mainly correspond to CAH_{10} (Monocalcium aluminate decahydrate), C_3AH_6 (Katoite), and some AH_3 (Gibbsite) [9].

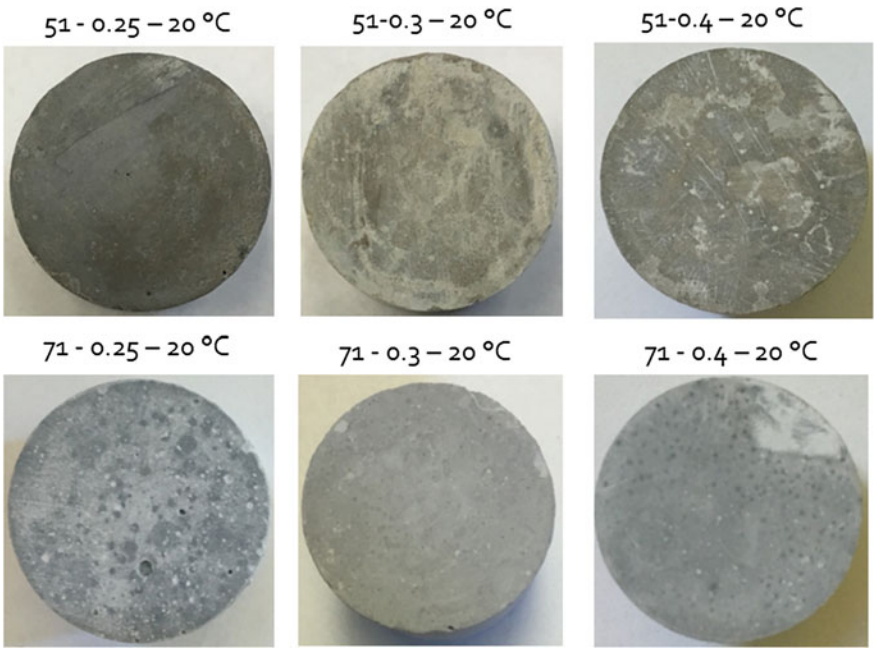

Fig. 1 Images of CAC pastes exposed at room temperature 20 °C

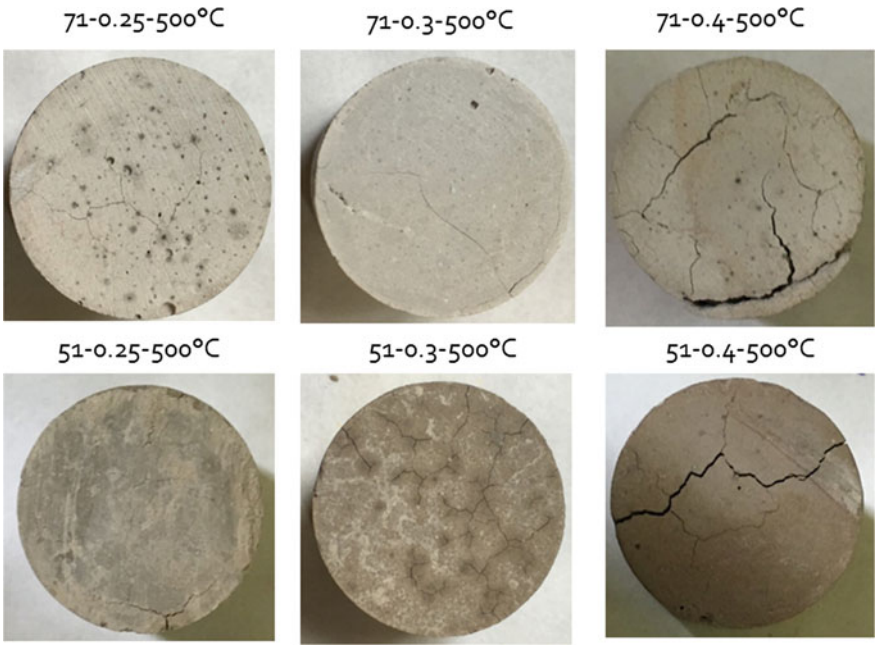

Fig. 2 Images of CAC pastes exposed at high temperature 500 °C

CAC pastes with 51 and 71 wt% alumina content and W/C = 0.25, 0.3 and 0.4, were exposed to 1000 °C for an hour and were analyzed by SEM and are represented in Fig. 6.

Figure 6 shows that at 1000 °C both cements of 51 and 71 wt% alumina content lose their symmetrical shape and most liked its crystallinity. This is because crystalline structures absorb energy or break the bonds generating anhydrous phases or polymorphisms, changing their geometric form to the new amorphous phases shapes [10].

Quantification of Damage to High Temperature and Fracture Analysis for Factors: Alumina Content; Water-Cement Relation (W/C), and Temperature

The quantification of the damage was conducted by digital image analysis of fractured samples according to the alumina content, temperature, and w/c. The cracks length was measured using Image J and data was grouped in just one number, the total crack's length.

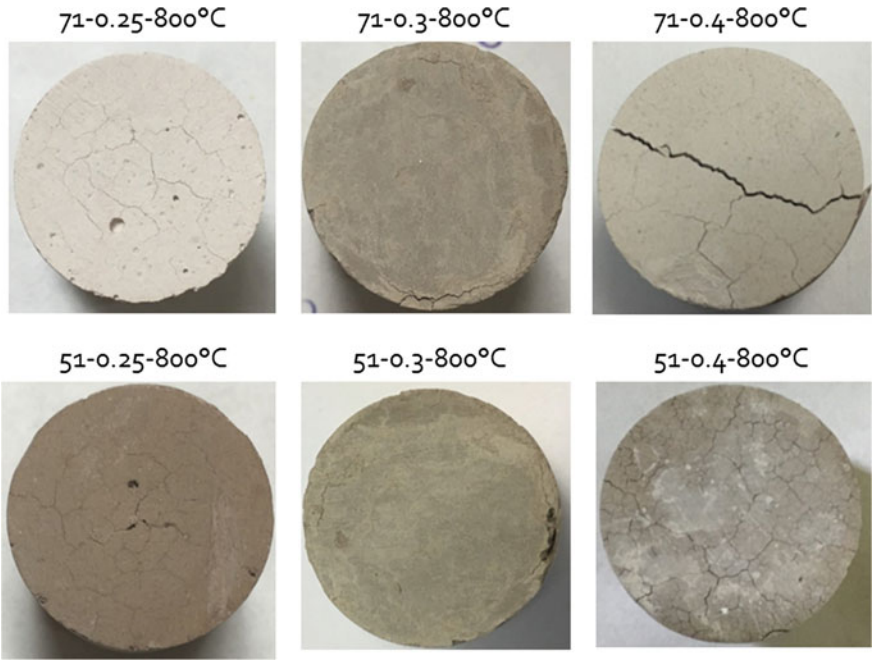

Fig. 3 Images of CAC pastes exposed at high temperature 800 °C

Fracture Analysis for Factor: Alumina Content

Figure 7 shows curves of total crack length for the samples with (a) CAC 51 wt% and (b) 71 wt% subjected to high temperatures 500, 800 and 1000 °C; and for w/c = 0.25, 0.3 and 0.4.

It can be observed that the higher the temperature, the greater the damage in both cements. However, the cement with a lower content of alumina presented a greater damage to a fixed temperature. A connection with the degree of damage and the ratio of water to cement in these two figures is not clear. This suggests that the higher the alumina content the better the behavior of the cement at high temperature, particularly 1000 °C.

Fracture Analysis for Factor: Temperature

Figure 8 shows curves of total crack length for samples of CAC 51 and 71 wt% subjected to temperatures of 500, 800 and 1000 °C. It can be observed that at 500 °C the samples with the greatest damage are CAC 71 wt% for a w/c ratio of 0.4, and CAC 51 wt% for w/c ratio of 0.3. It is not clear direct relationship between the degree of damage, the alumina content, and the ratio of water to cement at this temperature. In addition, at 800 °C the samples with the greatest damage are CAC 51 wt% for w/c

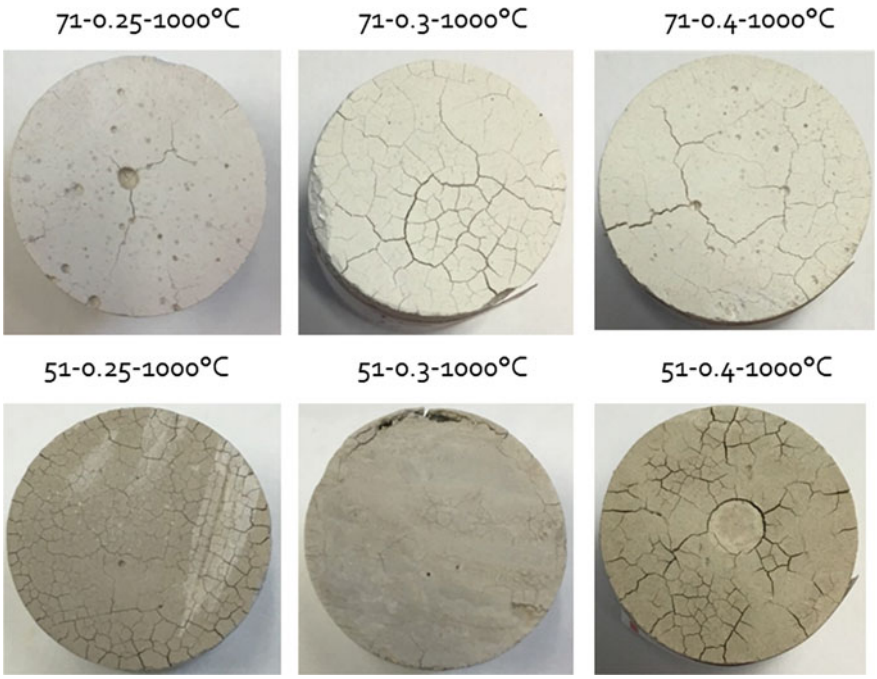

Fig. 4 Images of CAC pastes exposed at high temperature 1000 °C

ratio of 0.4, and CAC 51 wt% for w/c ratio of 0.3. This suggests that at 800 °C the CAC 51 wt% performs better than the CAC 71 wt%. Therefore, it is not clear to establish a direct relationship between the degree of damage, and the ratio of water to cement at this temperature.

On the other hand, at 1000 °C, cement of lower alumina content and lower w/c ratio showed more damage.

Fracture Analysis for Factor: Water to Cement Ratio (W/C)

Figure 9 shows curves of total fracture size (total crack length) for samples of calcium aluminate cement, CAC 51 and 71 wt% subjected to temperatures of 500, 800 and 1000 °C. It is observed that for W/C = 0.25 at 1000 °C and at 800 °C, cement of lower alumina content showed more damage. For W/C = 0.3 at 1000 °C, cement of higher alumina content shows more damage and for 800 °C the least damage occurs. It can also be observed that for W/C = 0.4 at 800 °C, cement of lower alumina content, shows more damage and for 800 °C the least damage occurs.

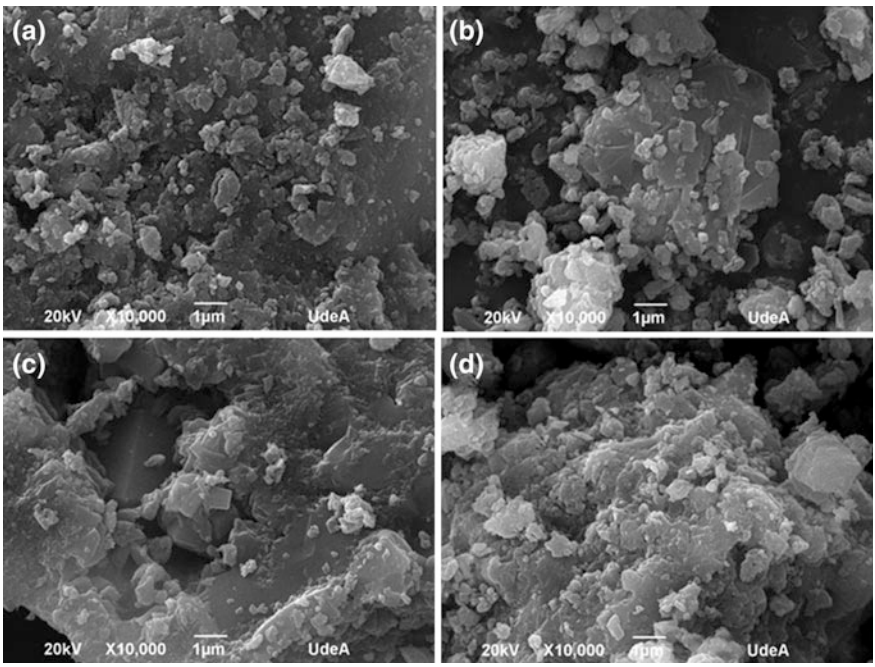

Fig. 5 SEM images for CAC pastes exposed at high temperature (20 °C), 10000X. **a** 51 A-wt%: w/c = 0.4. **b** 51 A-wt%: w/c = 0.5. **c** 71 A-wt%: w/c = 0.4. **d** 71 A-wt%: w/c = 0.5

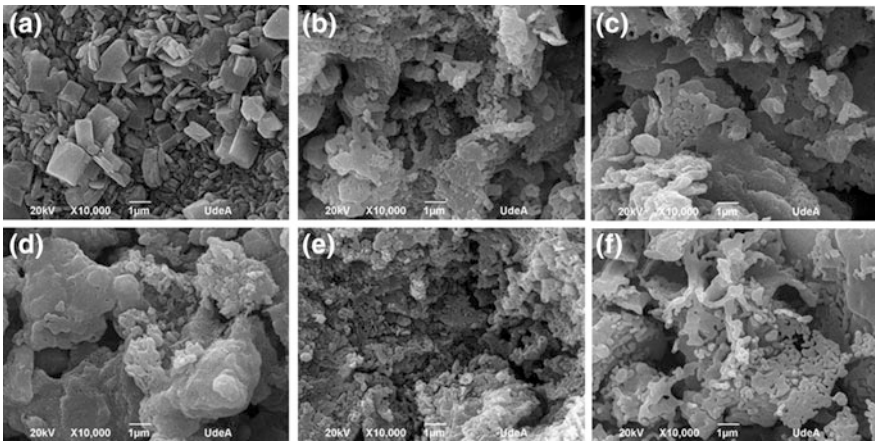

Fig. 6 SEM images for CAC pastes exposed at high temperature (1000 °C), 10000X. **a** 51 A-wt %: w/c = 0.25. **b** 51 A-wt%: w/c = 0.3. **c** 51 A-wt%: w/c = 0.4. **d** 71 A-wt%: w/c = 0.25. **e** 71 A-wt%: w/c = 0.3. **f** 51 A-wt%: w/c = 0.4

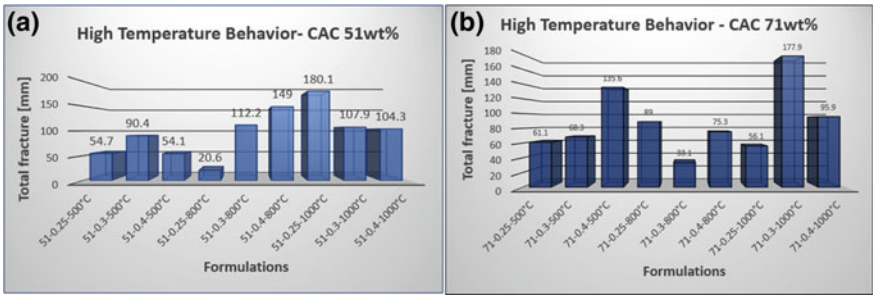

Fig. 7 Damage quantification at high temperature analyzed by the alumina content in two cement formulations: CAC 51–71 wt%

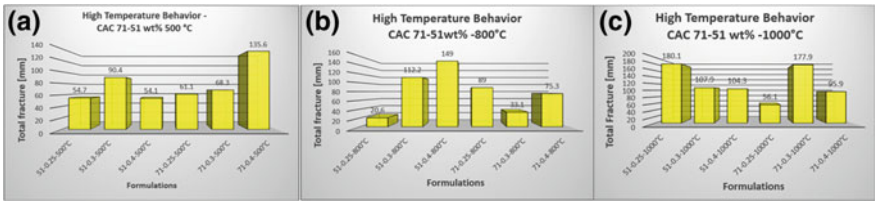

Fig. 8 Damage quantification at high temperature analyzed by temperature at 500, 800 and 1000 °C

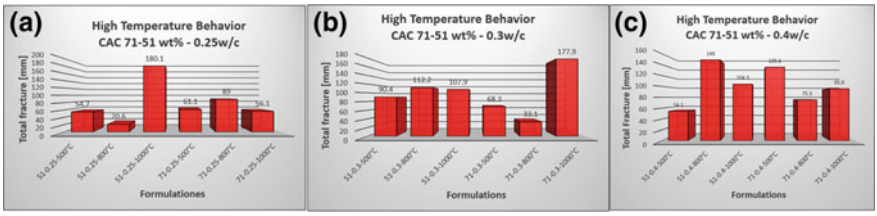

Fig. 9 Damage quantification at high temperature analyzed by water to cement ratio: 0.25, 0.3 and 0.4 w/c

Discussion

Due to Dehydration of the crystalline portion $CAH_{10,}$ the calcium aluminate cement s pastes, readily fracture at 37 °C or higher, increasing the level of damage with increasing temperature. What proves that pure cement paste is not suitable for refractory applications but is the basis for creating refractory ceramics of Mullite, Corundum and Silicon carbide, [11–14], which if they show good resistance behavior at high temperatures up to 1400 °C. As expected at temperatures above

800° C appear the anhydrous phases of the powders due to the release of hydrogen from $CAH_{10.}$

Conclusions

- Materials with higher alumina content have an increased number of cracks. Also, higher w/c contributes to the conversion process propitiating greater number of cracks in these samples.
- At higher temperature and lower w/c there is a greater probability of larger cracks.
- At higher alumina content, the average crack size is higher, which causes that these cements at 1000 °C presented bigger structural problems.
- Calcium aluminate cement pastes exhibit very little refractoriness properties on their own, but when mixed with other minerals it generates highly refractory materials.

References

1. Mangabhai RJ, Glasser FP (2001) Proceedings of International Conference CAC. Edinburgh, UK
2. Yepes SC, Barbudo MÁS (2008) El cemento de aluminato de calcio y sus prefabricados. Universidad de Alicante
3. Bates SCC (1984) High alumina cement concrete in existing building superstructures B.R.E. Londres
4. Bensted J (2002) Calcium aluminate cements. In: Bensted J, Bames P (eds) Structure and performance of cements 2nd edn, London pp 114–138
5. Rivas Mercury JM, De Aza AH Turrillas X, Pena P (2003) Hidratación de los cementos de aluminatos de calcio. Bol Soc Esp Ceram Vidrio 2003(5) 269–276
6. Mangabhai RJ (1990) Proceedings of International Conference CAC. Chapman and Hall, London
7. Matusinović T, Vrbos N, Sipusic J (2005) Rapid setting and hardening calcium aluminate cement materials. Zement-Kalk-Gips Int 1:72–79
8. Midgely HG (1976) Quantitative determination of phases in high alumina cement clinkers by X-ray diffraction. Cem Concr Res 6:217–223
9. Zapata J, Gómez M, Colorado H (June 2017) Characterization of two calcium aluminate cement pastes, in Advances in high temperature ceramic matrix composites and materials for sustainable development: ceramic transactions vol 263, Wiley, pp 493–504. ISBN: 978-1-119-40643-3
10. Valentin A et al (2013) The effect of temperature on the formation of the hydrated calcium aluminate cement structure. Proc Eng 57:99–106
11. Gazulla MF, Gómez MP, Orduña M, Barba A (2006) Physico-chemical characterisation of silicon carbide refractories. J Eur Ceram Soc 26:3451–3458
12. Akpinar S, Altun IA, Onel K (2010) Effects of SiC addition on the structure and properties of reticulated porous mullite ceramics. J Eur Ceram Soc 30:2727–2734

13. Luz AP, Pandolfelli VC (2011) Halting the calcium aluminate cement hydration process. Ceram Int 37:3789–3793
14. Lothenbach B, Pelletier-chaignat L, Winnefeld F (2012) Stability in the system CAO-Al_2O_3-H_2O. Cem Concr Res 42:1621–1634

On the Experimental Evaluation of the Fracture Toughness of Shape Memory Alloys

Behrouz Haghgouyan, Ceylan Hayrettin, Theocharis Baxevanis, Ibrahim Karaman and Dimitris C. Lagoudas

Abstract A methodology for measuring the fracture toughness of shape memory alloys (SMAs) from a single compact tension (CT) nominally isothermal load-load line displacement record is proposed. The methodology uses J-integral as the fracture criterion, relies on the ASTM standards E1820 modified to accommodate the Young's moduli mismatch between the austenite and martensite phases. Finite element analysis (FEA) is employed to validate the methodology while experimental data from CT specimens are interpreted accordingly. The fracture toughness of martensitic equiatomic NiTi at room temperature is much higher than the phenomenological value reported on the basis of linear elastic fracture mechanics.

Keywords Fracture toughness · J-integral · NiTi SMA

Introduction

Shape memory alloys (SMAs) can undergo and recover large strains through a reversible, solid state, diffusionless transformation that can be triggered by mechanical load and/or temperature variations. Depending on the initial state of the material, i.e., austenite or martensite, upon loading, SMAs can go through martensitic transformation or detwinning, respectively. In the former case, SMA may recover the strain upon unloading (pseudoelasticity). In the latter case, the SMA may return to its original shape by increasing the temperature (shape memory). Thanks to these superior properties, SMAs are desirable in a wide range of applications such as biomedical, actuation and vibration damping [1].

B. Haghgouyan · C. Hayrettin · I. Karaman · D. C. Lagoudas
Department of Materials Science & Engineering, Texas A&M University, College Station, TX, USA

T. Baxevanis (✉)
Department of Mechanical Engineering, University of Houston, Houston, TX, USA
e-mail: tbaxevan@central.uh.edu

The Minerals, Metals & Materials Society, *TMS 2018 147th Annual Meeting & Exhibition Supplemental Proceedings*, The Minerals, Metals & Materials Series,
https://doi.org/10.1007/978-3-319-72526-0_53

The successful integration of SMAs into commercial applications requires understanding and practice of fracture mechanics concepts. As discussed in a recent review paper [2], the fracture response of SMAs is rather complex owing to the reversibility of phase transformation, detwinning and reorientation of martensitic variants, the possibility of dislocation and transformation-induced plasticity, and the strong thermomechanical coupling. This complexity is also reflected in the determination of their fracture toughness from specimen that are not prohibitively large.

Fracture toughness values of NiTi SMAs have been reported in few papers [3–10] and nearly identical K_{Ic}-values of ~30 MPa$\sqrt{m}$ has been reported for pseudoelastic NiTi. Most of the published data appears to be determined from test specimens of thickness not large enough compared with the estimate of the plastic zone size in conventional elastic-plastic materials, $1/(3\pi)\cdot\left(K_{Ic}/\sigma_y\right)^2$ [11], i.e., their thickness did not exceed $2.5(K_{Ic}/\sigma_y)^2$, where K_{Ic} is the calculated critical stress intensity factor and σ_y the yield stress of the material. Therefore these tests do not comply with the small yielding condition which is a perquisite for measuring the critical stress intensity factor in conventional elastic-plastic materials. The results measured based on the premise of linear elastic fracture mechanics (LEFM) by using test specimens of sufficient size are as well questionable, since ASTM standards should be interpreted as to require the zone of non-linear deformation close to the crack tip, regardless of the mechanism, to be smaller than a fraction of all the characteristic dimensions of the crack configuration. With respect to SMAs, this restriction leads to a requirement on the size of the stress-induced transformation/detwinning zone, not on the plastic zone size, being small enough for LEFM to be valid. Although the expression $1/(3\pi)\cdot\left(K_{Ic}/\sigma_y\right)^2$ overestimates, by an order of magnitude, the size of the yielding zone in SMAs [12], it underestimates considerably the size of the transformation/detwinning zone, which can be approximated as $1/(3\pi)\cdot\left(K_{Ic}/\sigma_{cr}\right)^2$. In this expression, σ_{cr} denotes either the stress level required for initiation of phase transformation or detwinning of twinned martensite depending on whether the material is in the austenitic or twinned martensitic state at zero load, respectively. For temperatures higher than martensite desist temperature (M_d), σ_{cr} should be understood as the yield stress of austenite. For such a requirement to be satisfied, the SMA specimens may be prohibitively large depending on the ambient temperature.

In the present work, the fracture toughness of NiTi SMA is measured using J-integral as a fracture criterion for which the requirements on specimen sizes are much less strict than those for a valid K_{Ic}-value. The proposed approach relies on the ASTM standards E1820 modified to accommodate the Young's moduli mismatch between the austenite and martensite phases. The experimental data obtained from mode-I testing NiTi compact tension (CT) specimens are interpreted accordingly and the fracture toughness of NiTi SMA is provided.

Methodology

The J-integral is proposed by Rice [13] as a path independent integral over an arbitrary contour surrounding the crack tip:

$$J = \int_{\Gamma} (wdy - T\frac{\partial u}{\partial x}ds) \tag{1}$$

where Γ is an arbitrary path around the crack tip, w is the strain energy density, T is the outward traction vector, u is the displacement vector, ds is the length increment along the contour and x and y are the rectangular coordinates at the crack tip. To enhance the accuracy near the linear elastic regime in experimental measurements of the fracture toughness, the J-integral for non-advancing crack length can be expressed as the sum of elastic and plastic components:

$$J = J_{el} + J_{pl} \tag{2}$$

For conventional elastic-plastic response, the elastic component of J can be considered as the energy release rate, G. Using the relation between G and K, J_{el} can be obtained as:

$$J_{el} = \frac{K^2}{E'} \tag{3}$$

Here $E' = E/(1-\nu^2)$ for plane strain and $E' = E$ for plane stress, where E is Young's modulus and ν is Poisson's ratio. The plastic component of J can be calculated as follows:

$$J_{pl} = \frac{\eta_{pl} A_{pl}}{Bb} \tag{4}$$

where A_{pl} is the plastic area under the load–load line displacement curve, B and b are the specimen thickness and uncracked ligament, respectively and η_{pl} is a function of specimen geometry; $\eta_{pl} = 2 + 0.522(b/W)$ for CT specimen. In view of Eqs. (3) and (4), Eq. (2) yields:

$$J = \frac{K^2}{E'} + \frac{\eta_{pl} A_{pl}}{Bb} \tag{5}$$

The above methodology does not apply as is in SMAs due to the change in the apparent Young's modulus with transformation/detwinning. Instead of using Eq. (3), the following relation as introduced in [14] for elastic-plastic materials is used to calculate the elastic part of the J-value:

$$J_{el} = \frac{\eta_{el} A_{el}}{Bb} \tag{6}$$

where A_{el} is the elastic area under the load–load line displacement curve. η_{el} is a factor that is generally different from aforementioned η_{pl} and will be calculated in

the next section. Using Eq. (6):

$$J = \frac{1}{Bb}(\eta_{el}A_{el} + \eta_{tr}A_{tr}) \tag{7}$$

where $\eta_{tr} = \eta_{pl}$ and A_{tr} is the non-elastic area under the load–load line displacement curve due to transformation. Consequently, determination of η_{el} is the key to the experimental measurement of the J-integral in SMAs. It should be noted that Eq. (7) is developed for stationary cracks. For growing cracks, incremental J-integral evaluation is required. To this aim, J can be written in incremental form as:

$$J^{(i)} = J_{el}^{(i)} + J_{tr}^{(i)} \tag{8}$$

where $J_{el}^{(i)}$ and $J_{tr}^{(i)}$ are the incremental elastic and transformation components of the $J^{(i)}$-value corresponding to the ith step of crack extension. To consider the effect of crack extension, $J_{el}^{(i)}$ and $J_{tr}^{(i)}$ are evaluated from the preceding step as:

$$J_{el}^{(i)} = \left[J_{el}^{(i-1)} + \frac{\eta_{el}^{(i-1)}}{B\,b^{(i-1)}}(A_{el}^{(i)} - A_{el}^{(i-1)})\right]\left[1 - \gamma_{el}^{(i-1)}(\frac{a^{(i)} - a^{(i-1)}}{b^{(i-1)}})\right] \tag{9}$$

and

$$J_{tr}^{(i)} = \left[J_{tr}^{(i-1)} + \frac{\eta_{tr}^{(i-1)}}{B\,b^{(i-1)}}(A_{tr}^{(i)} - A_{tr}^{(i-1)})\right]\left[1 - \gamma_{tr}^{(i-1)}(\frac{a^{(i)} - a^{(i-1)}}{b^{(i-1)}})\right] \tag{10}$$

where $\gamma_{tr} = 1 + 0.76(b/W)$ for CT specimen and γ_{el} will be given as a function of b/W.

Computational Work

Modeling

To determine the η_{el} factor, 2D CT specimen is modeled in Abaqus as shown in Fig. 1a. The mesh consists of four-node bilinear plane strain quadrilateral elements (CPE4) and is refined near the crack tip. A mechanical load P is applied in mode-I at constant temperature. To calculate η_{el}, elasticity is employed as the material model. Consequently, $J = J_{el}$ where J_{el} is as in Eq. (6). Computing J from the contour integral in FEA, one can obtain η_{el} by evaluating A_{el} and using the specimen geometry. Given that the η factor is a function of geometry, we analyzed different crack sizes in the range $0.45 \leq a/W \leq 0.55$ to obtain a relation for η_{el} as a function of remaining ligament, b.

To verify the method, the same problem is solved for a SMA under isothermal loading paths. To this aim, the unified model for polycrystalline SMAs proposed

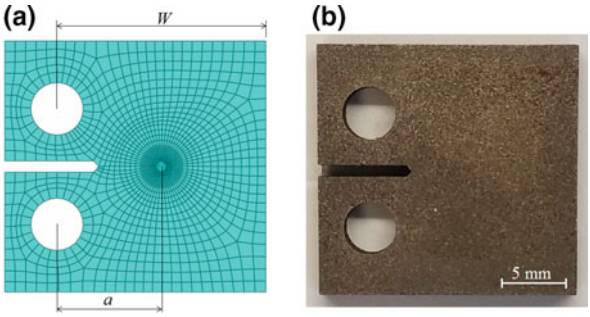

Fig. 1 CT specimen: **a** 2D FE model ($a/W = 0.5$), **b** optical image ($W = 20$ mm)

by Boyd and Lagoudas [15] is included via a user material subroutine (UMAT) in Abaqus. This model is developed within the continuum thermodynamics framework and uses the classical rate-independent infinitesimal strain flow theory for evolution equations governing transformation strains.

Results

J_{el} is computed at each load increment from contour integral in FEA and A_{el} is evaluated from the area under the load–load line displacement response. J_{el} is plotted with respect to A_{el}/Bb for five different crack sizes in $0.45 \leq a/W \leq 0.55$ range as illustrated in Fig. 2a. According to the results, the slope of the linear regression, i.e. η_{el}, decreases by increasing the crack size. To quantify this trend, the η_{el} values are plotted as a function of b/W. A linear relation is observed as illustrated in Fig. 2b and the linear regression yields: $\eta_{el} = 1 + 3.25(b/W)$. Using this, β is calculated for CT specimens as $\gamma_{el} = 8.05(b/W)$.

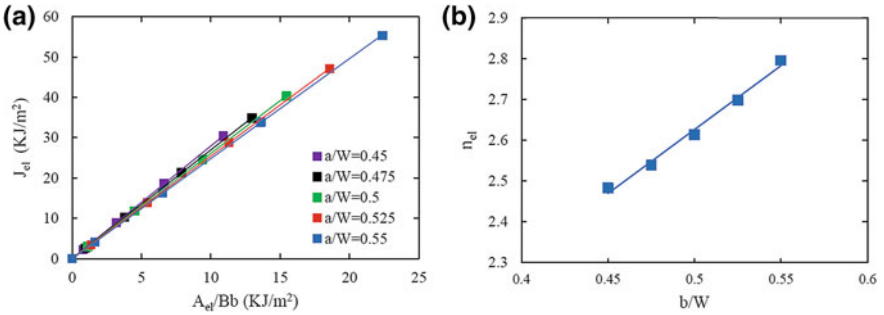

Fig. 2 Computational results of the elastic model with $0.45 \leq a/W \leq 0.55$: **a** J_{el} versus A_{el}/Bb plots used to compute η_{el}, **b** η_{el} as a function of b/W

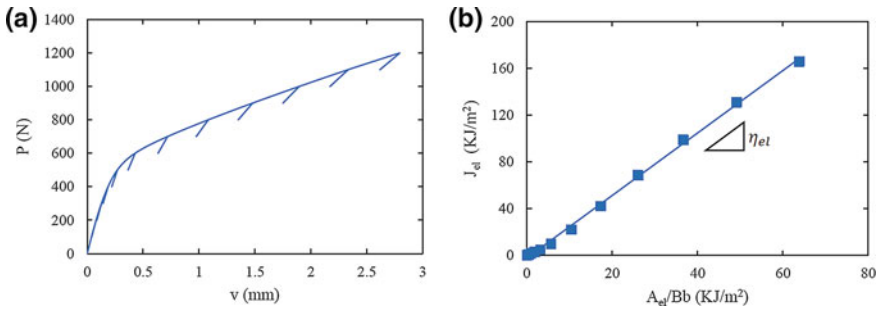

Fig. 3 Computational results of the SMA model with $a/W = 0.5$: **a** load–load line displacement response, **b** J_{el} versus A_{el}/Bb plot used to compute η_{el}

SMA material model is implemented in Abaqus to verify the proposed method. Figure 3a shows the computational load–load line displacement curve. Here the unload/reload sequences are performed during loading using which the elastic and transformation components of A is evaluated. At each load increment corresponding to these unload/reload sequences, J is computed from contour integral in FEA, J_{tr} is obtained as in Eq. (7) and then subtracted from the J leaving J_{el}. Figure 3b plots J_{el} with respect to A_{el}/Bb according which a strong linear relation is observed. η_{el} evaluated from the slope of linear regression agrees with the value obtained using the η_{el} equation.

Experimental Work

Material and Specimen

The material used in this study is equiatomic NiTi manufactured by ATI. According to the differential scanning calorimetry (DSC) results (Fig. 4a), the material is in martensitic state at room temperature. Electro-discharge machining (EDM) is used to cut dog-bone and CT specimens for tensile and fracture tests, respectively. Figure 1b shows the optical image of CT specimen. Tests are carried out at room temperature in servo-hydraulic MTS test frame. For tensile characterization, dog-bone specimen is used. Figure 4b shows the stress-strain response of martensitic NiTi at room temperature. For fracture experiments, specimens are first pre-cracked in fatigue to produce a sharp crack. Pre-cracking is performed under cyclic loading resulting in crack sizes (i.e. notch length plus fatigue crack) within $0.49 \leq a/W \leq 0.53$ range. The fracture tests are carried out in mode-I under displacement control and load–load line displacement records are developed.

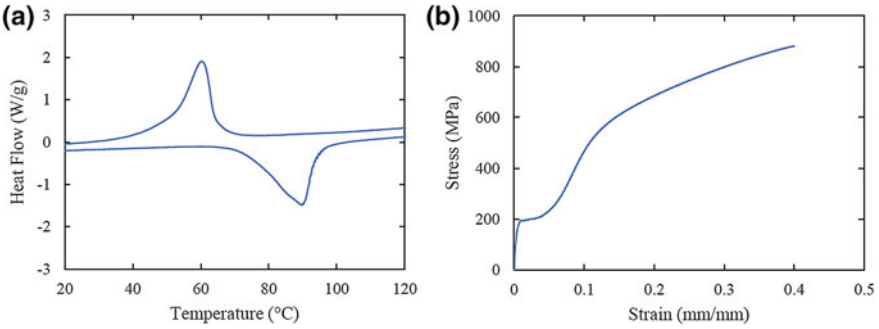

Fig. 4 NiTi characterization results: **a** DSC thermogram, **b** stress-strain response at room temperature

Results

Figure 5a shows the experimental load–load line displacement results for three NiTi CT specimens tested under mode-I at room temperature. In all experiments, the response is linear at the beginning, then it deviates from linearity and reaches a maximum. After the maximum load has reached, the load decreases gradually until the end of the test without any significant load drop, indicating an stable crack extension. To measure the resistance to crack extension, $J - R$ curves are developed. This is a plot of J versus stable crack extension, Δa. J is calculated at each load increment on the load–load line displacement record using Eq. (8) while Δa is estimated using compliance measurements. To determine the initiation toughness, a construction line is first defined using the equation $J = 2\sigma_Y \Delta a$ where σ_Y is effective yield strength and is defined as the average of detwinning stress and tensile strength. Two exclusion lines are then plotted parallel to the construction line intersecting the abscissa at 0.15 and 1.5 mm. All $J - \Delta a$ data points that fall between these two parallel lines are plotted and a power-law regression is fit through as shown in Fig. 5b. Another offset line is then defined parallel to the construction line and intersecting the abscissa at 0.2 mm; the intersection of the 0.2 mm offset line and the power-law regression defines the critical value of J. Based on this procedure, an average J_{Ic} value is obtained as 151 KJ/m^2 for equiatomic martensitic NiTi. This results in an average K_{JIc} of 97 MPa$\sqrt{m}$, where $K_{JIc} = \sqrt{E' J_{Ic}}$ is used to extrapolate the K-based fracture toughness values. This is much higher than the average fracture toughness value obtained on the basis of LEFM, $K_{Ic} = 38$ MPa$\sqrt{m}$.

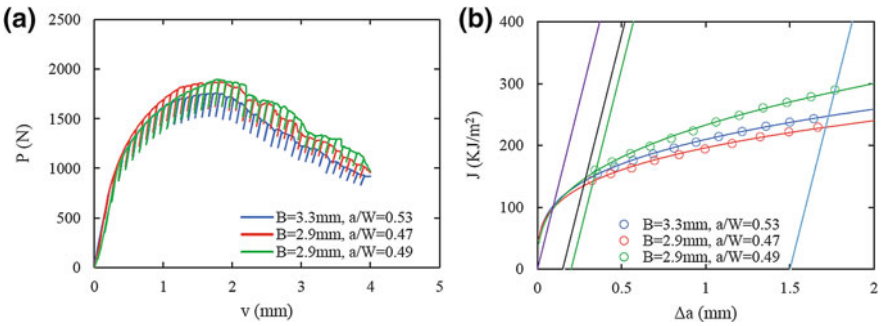

Fig. 5 Experimental results of NiTi CT specimens at room temperature **a** load–load line displacement responses, **b** $J - R$ curves

Summary

In this paper, we developed a methodology to measure the fracture toughness of SMAs using J-integral. The proposed approach differs from the corresponding one used in conventional elastic-plastic materials by accommodating the Young's moduli mismatch in SMAs. FEA is employed to calculate the η-factor required in the formulation. SMA material model is implemented to validate the proposed methodology for SMAs. The methodology is used to interpret the experimental data obtained from testing NiTi CT specimens at room temperature. $J - R$ curves are developed and the fracture toughness J_{Ic} is estimated. It is found that the fracture toughness of martensitic equiatomic NiTi is much higher than the phenomenological value reported on the basis of linear elastic fracture mechanics.

Acknowledgements This material is based upon work supported by AFOSR under Grant No. FA9550-15-1-0287.

References

1. Lagoudas D (2008) Shape memory alloys: modeling and engineering applications. Springer ebook collection/Chemistry and Materials Science 2005–2008. Springer, US
2. Baxevanis T, Lagoudas D (2015) Fracture mechanics of shape memory alloys: review and perspectives. Int J Fract 191(1–2):191–213
3. Holtz R, Sadananda K, Imam M (1999) Fatigue thresholds of ni-ti alloy near the shape memory transition temperature. Int J Fatigue 21:137–145
4. Vaidyanathan R, Dunand D, Ramamurty U (2000) Fatigue crack-growth in shape-memory NiTi and NiTi-TiC composites. Mater Sci Eng A 289(1–2):208–216
5. Robertson S, Ritchie R (2007) In vitro fatigue-crack growth and fracture toughness behavior of thin-walled superelastic nitinol tube for endovascular stents: a basis for defining the effect of crack-like defects. Biomaterials 28:700–709
6. Daly S, Miller A, Ravichandran G, Bhattacharya K (2007) An experimental investigation of crack initiation in thin sheets of nitinol. Acta Mater 55(18):6322–6330

7. Gollerthan S, Young ML, Baruj A, Frenzel J, Schmahl W, Eggeler G (2009) Fracture mechanics and microstructure in NiTi shape memory alloys. Acta Mater 57:1015–1025
8. Maletta C, Sgambitterra E, Furgiuele F (2013) Crack tip stress distribution and stress intensity factor in shape memory alloys. Fatigue & Fract Eng Mater & Struct 36(9):903–912
9. Shafaghi N, Haghgouyan B, Aydiner CC, Anlas G (2015) Experimental and computational evaluation of crack-tip displacement field and transformation zone in niti. Mater Today: Proc 2:S763–S766
10. Haghgouyan B, Shafaghi N, Aydıner CC, Anlas G (2016) Experimental and computational investigation of the effect of phase transformation on fracture parameters of an sma. Smart Mater Struct 25(7):075010
11. Irwin G (1968) Linear fracture mechanics, fracture transition, and fracture control. Eng Fract Mech 1(2):241–257
12. Baxevanis T, Chemisky Y, Lagoudas D (2012) Finite element analysis of the plane strain crack-tip mechanical fields in pseudoelastic shape memory alloys. Smart Mater Struct 21(9):094012
13. Rice JR (1968) A path independent integral and the approximate analysis of strain concentration by notches and cracks. J Appl Mech, 379–386
14. Sumpter J, Turner C (1976) Method for laboratory determination of jc, Cracks and fracture, 3–18
15. Boyd JG, Lagoudas DC (1996) A thermodynamical constitutive model for shape memory materials. part i. the monolithic shape memory alloy. Int J Plast 12(6):805–842

Part XXIII
Frontiers in Solidification Science and Engineering

Inoculation in Lab Scale Low Alloyed Steel Castings

M. Gennesson, D. Daloz, J. Zollinger, B. Rouat, J. Demurger, D. Poirier and H. Combeau

Abstract Several experiments using different inoculant powders (oxides, nitrides, carbides and ferrocerium) were carried out on 42CrMo4 steel in a 50 g induction heated laboratory furnace. The inoculants were selected based on lattice mismatch, thermodynamic stability and relative density. The effects of each inoculant type on the microstructure are discussed in terms of these selection parameters. The addition of materials with a low lattice mismatch tends to refine the grain size, except in the case of ferrocerrium additions. Scanning electron microscope characterization improves understanding of the underlying mechanisms.

Keywords Inoculation · Steel · Cerium

Introduction

Requirements for more homogeneous products is a great concern in steel ingot making. One of the critical processing step to control is the solidification. During solidification, several kinds of defects arise like porosities and chemical segregations. Those chemical segregations are well-known to happen at the microscopic scale. In meter long products like industrial steel ingots, macrosegregation is also a common feature which is defined as "solute composition inhomogeneities at the macroscopic scale", [1]. Macrosegregation is generally provoked by solidification shrinkage, convection, deformation of the mushy zone and/or relative motion between the solid and the liquid phase, [1].

The total density of nuclei in the melt is a possible lever to act on the grain movement, and thus, to modify and improve the macrosegregation pattern in big ingots thus shown in numerical simulations, [2, 3]. Several means have been proposed to

M. Gennesson (✉) · J. Demurger · D. Poirier
Ascométal CREAS, Avenue de France, BP 70045, 57301 Hagondange, France
e-mail: marvin.gennesson@ascometal.com

D. Daloz · J. Zollinger · B. Rouat · H. Combeau
Institut Jean Lamour, 2 allée André Guinier Campus Artem, 54000 Nancy, France

The Minerals, Metals & Materials Society, *TMS 2018 147th Annual Meeting & Exhibition Supplemental Proceedings*, The Minerals, Metals & Materials Series,
https://doi.org/10.1007/978-3-319-72526-0_54

increase the grain density in the melt like modification of the process design with new mold shapes, hot toppings, different pouring rates or electromagnetic stirring, [4–7].

Inoculation is also a common way to have higher grain density in the melt. In the following article, inoculation is defined like the addition/creation of particles inside the melt. The new particles have to promote heterogeneous nucleation, [1]. Inoculation for aluminum alloy and cast irons has been carefully studied, [8, 9]. For the case of low alloyed steels, successful grain refinement has been obtained for rare earth metal, NbC-containing ferroalloy or TiN-containing ferro alloy additions, [10–12]. In all the previous cases, particles are either forming in the melt or contained inside ferroalloys. While reviewing the literature, direct particle additions are rarely found. Recent investigations have shown improved centerline segregation on continuously casted steel with addition of TiN, TiC or ZrN, [13].

This study investigates two different types of inoculation: Ce ferroalloy and pure compound additions. The main goal of this work is to use a small and fast laboratory set-up rather than big castings to select inoculants.

Experiments

Reference Alloys

The reference steel grade in this study is 42CrMo4 (also AISI 4140). 42CrMo4 is a through and surface hardening steel. It is still industrially casted as ingots and its nominal composition is given in the Table 1. 42CrMo4 grade firstly solidifies in α-ferrite up to a solid fraction of 15% and then fully solidifies in γ-austenite.

Cold Crucible Induction Melting Setup

The melting set up is a cold crucible induction furnace as shown in the Fig. 1. The crucible and the coil are made of copper and internally cooled by water. The quartz tube is used to establish a primary vacuum ($\simeq 10^{-3}$ mbar) for cleaning purposes. The quartz tube to control the gaseous atmosphere prevents from adding easily the inoculants after melting. It has been chosen to add the inoculant inside a drilled hole in the base metal. The weight of the sample is 50 g.

When a periodic current goes trough the coil, a magnetic field establishes. The melting of the sample happens thanks to the induced Eddy currents. With this kind of setup, the sample is never fully liquid. The Lorentz forces vertically push

Table 1 Composition of the reference steel (wt%)

Grade	C	Mn	Si	Cr	Cu	Ni	Mo
42CrMo4	0.4	0.7	0.3	1	0.1	0.2	0.2

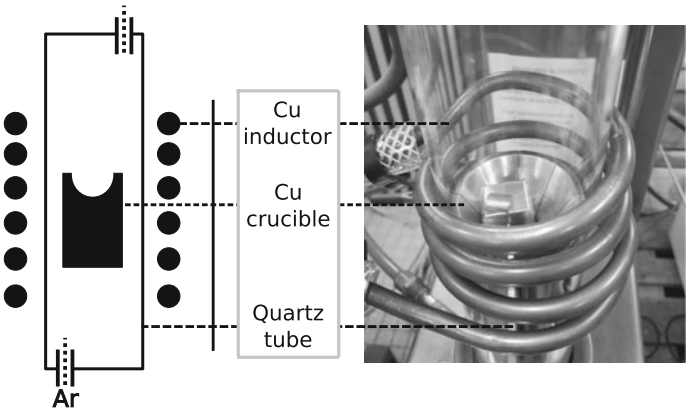

Fig. 1 Induction melting setup composed by a Cu coil, a Cu crucible and a quartz tube linked to a pump and to an argon bottle. A 2D schematic view is drawn on the left of the picture. A photography of the real setup is also given on the right

away the sample from the crucible but one contact point still exists at the bottom of the sample, [14]. Finally, when the coil current intensity is decreased in the coil, the Lorentz forces are not sufficient to push away the droplet. The liquid touches the cold crucible and the solidification begins.

Inoculation Material

The different inoculant powders have been selected according to their density, stability in the melt and misfits with ferrite or austenite. The misfit has been calculated according to the definition of Bramfitt [15]. All the properties of the tested particles are given in the Table 2. $Ce_xO_yS_z$ stands for all the possible particles after ferrocerium addition.

Table 2 Properties of the different inoculant particles (numerically ranked by misfit with α-ferrite)

Formula	Crystal system	Misfit$_\delta$ (%)	Misfit$_\gamma$ (%)	ρ(kg/m^3) [a]
TiN	BCC	4.6	16	5220
$Ce_xO_yS_z$	FCC, BCC, HCP	$0.3 \leq x \leq 6$	$6 \leq x \leq 13$	$5020 \leq x \leq 7130$
CeO_2	FCC	5.6	6.3	7130
β-Si_3N_4	HCP	6.2	0.4	3100
ZrO_2	FCC	7	0.96	6200
α-Al_2O_3	HCP	7.8	6.6	3970
W_2C	HCP	8.1	1.9	17150
HfC	FCC	9.6	8.9	12650
β-SiO_2	FCC	12.1	1.94	2320

[a] Density data are extracted from [17]

As a result of this selection, ferrocerium alloy appears to be a good candidate. Cerium ability to form oxides, sulphides or oxysulphides inside the melt has been known for a very long time, [16]. The composition of the alloy used in this study is Fe-30 wt% Si-20 wt% Ce. This alloy is available as pellets of size 1 mm. The additions were 0.025, 0.05, 0.1 and 0.2 wt% Ce.

Powders of pure compounds (with diameters close to 1 μm) have also been selected and additions of 0.3 wt% were made for pure compounds.

Experimental Characterizations

Cold crucible samples were cut in half along the gravity direction. With such kind of cutting plane, a complete observation of macrostructure (equiaxed, columnar and zone remaining solid during the experiment) is possible. Common metallography (mounting, grinding and polishing) is then applied before etching in a warm super-saturated picric acid solution. This kind of etching allows to reveal primary structure due to selective etching of differences in chemical composition.

In the as cast state, the microstructure is fully martensitic. Solidification grain size cannot be characterized by electron back scattering diffraction technique. Primary phases (α-ferrite or γ-austenite) undergo a solid-state phase transformation during cooling. As cooling rate is high, exhibited microstructure at room temperature is fully martensitic. Microsegregation is the only left record of the primary structure as crystallographic arrangements do not exist anymore.

A ZEISS Axioplan 2 imaging optical microscope with an Axiocam MRc5 camera was used for optical characterizations. A FEI Quanta 650 FEG scanning electron microscope (SEM) with an Electron Dispersive Spectrometer (EDS) was used to perform inclusion characterizations.

Measurements of grain size in the equiaxed zone are performed manually where each grain is outlined with the freehand selection tool in Fiji [18]. A custom macro program is then able to measure all the geometrical features associated with each grain (area, circularity, perimeter, etc.) and colored images are available for visual comparisons.

Results

Solidification Structures

Some of the pure compounds additions like W_2C, CeO_2 and HfC have a small effect on the morphology of the dendritic equiaxed grains. It is not the case for ZrO_2 and to a much lesser extent Si_3N_4, Al_2O_3 and SiO_2. In these cases, the equiaxed area is mixed with large clusters of globular grains and very large dendritic grains (Fig. 2).

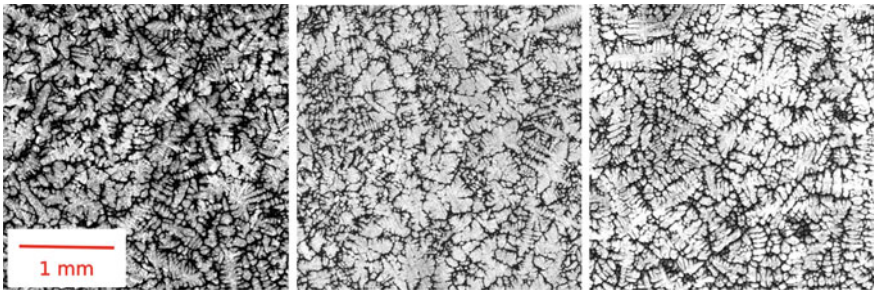

Fig. 2 Example of equiaxed grains after inoculation. From left to right: Reference, 0.3 wt% Al_2O_3, 0.2 wt% Ce

Cerium addition also drastically changes the equiaxed grain morphology. Moreover, columnar grains are likely to develop along the free surface for high cerium addition. In consequence, the equiaxed area tends to be reduced with cerium addition.

Grain Size Measurements

For each samples, 250 grains were measured inside the equiaxed area. Grain size is defined as the square root of the mean value of the measured dendrite areas ($D_{square\ eq} = \sqrt{< A >}$). The results are vividly illustrated in the Fig. 3.

It can be seen than grain refinement is obtained for pure compounds powder that exhibits a low misfit like CeO_2, Si_3N_4 or TiN. The case of grain growth with ZrO_2

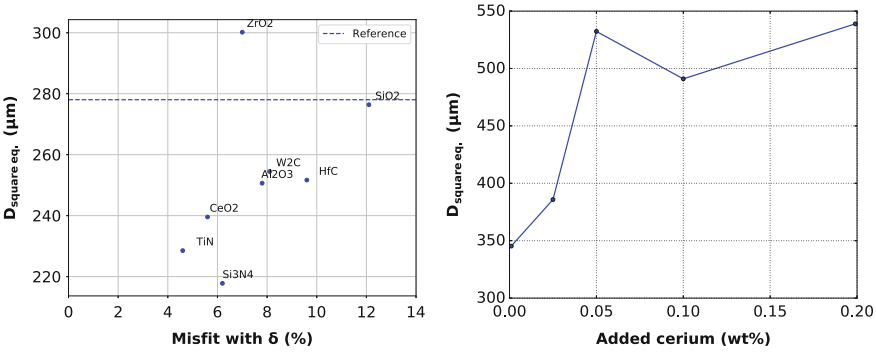

Fig. 3 Mean grain size measurement after inoculation. Pure compound powders inoculated samples are plotted against misfit with ferrite (left). Reference is shown as the blue dotted line. Ferrocerrium inoculated samples are plotted with respect of added cerium (right). Content of added ferrocerium alloy is five times higher

is unexplained in this work. On the other hand, ferrocerium addition provokes grain growth. If the addition is bigger than 0.05 wt%Ce, the final grain size is doubled in comparison to the reference.

SEM Characterizations

All inoculated samples have been undergoing scanning electron microscope investigations. For pure compounds additions, the resulting inclusion distributions are specific to each addition:

- TiN can be found in the equiaxed area in high surface particle density regions. Outside of these rare regions, no particles can be seen.
- Si_3N_4 can be found inside the equiaxed area uniformly dispersed.
- SiO_2 particles are also present in the equiaxed area where they are often found along with MnS inclusions.
- HfC can be present in the equiaxed area where most of them are fully encapsulated inside MnS.
- W_2C particles are only found in the columnar area inside the interdendritic spaces.
- No ZrO_2 and CeO_2 particles have been seen.

For ferrocerium additions, inclusions are mostly cerium sulphides with MnS chunks in the outer shell. They are equally dispersed in the equiaxed zone and globule shaped. The surface density of the cerium sulphides is roughly 200 particles/mm^2 and their mean diameter lies between 1 and 10 μm. Characterization of an etched sample has clearly stated that the particles are not only located inside the interdendritic area. Examples of particles are shown in the Fig. 4.

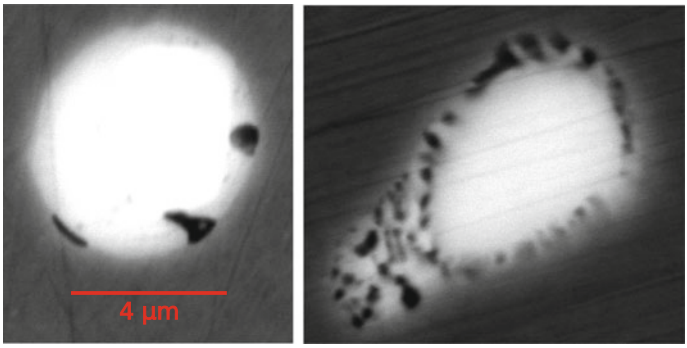

Fig. 4 SEM electron back scattering pictures of cerium sulphide inclusions with MnS chunks (in black) (H=15 kV, *WD* = 11 mm). The scale is the same on both picture

Discussion

Pure Compound Inoculation

Grain refinement has been observed after powder additions for which intensity could be—except for ZrO_2 correlated to misfit values with ferrite. While, it has already been reported in the literature, the misfit with ferrite is not a sufficient parameter to explain the change in morphology observed for some of the cases. As the composition of the reference steel is close to the composition of the peritectic, the misfit with austenite could also be an important parameter. For example, ZrO_2, Si_3N_4 and SiO_2 have a very small misfit with austenite (lower than 2%). After inoculation, their equiaxed structures changed from fully globular to mixed globular/dendritic. The low misfit with austenite could also explain why the grain refinement is more efficient for Si_3N_4 than for CeO_2 or TiN.

There are also other complex effects which could also impact the final grain size. The density of W_2C is very high and could explain why no particles can be found inside the equiaxed area. Si_3N_4 has also a very high solubility limit, [19]. Consequently, it is more likely to dissolve inside the liquid melt. It means that holding time at liquid state could be a crucial parameter. From all these considerations, inoculation success is not only a matter of misfit because it is a complex phenomenon which lies in a combination of several parameters.

Ferrocerium Inoculation

Ferrocerium addition increases grain size and it doesn't agree well with previous results from the literature, [20–22].

In our case, cerium particles can be found inside the equiaxed area and there are not located inside the interdendritic region. It means that they are not forming at a late solidification stage and could help heterogeneous nucleation. Moreover, cerium sulphides have a low misfit with ferrite: 0.8%, 0.4%, 0.4% respectively for CeS, Ce_2S_3 and Ce_3S_4. Finally, their sizes lie in the right range to possibly act as good nucleants. In appearance, all the necessary conditions for inoculation seem to be fulfilled.

Two different phenomena could happen at the same time. The cerium sulphides are complex particles with chunk of manganese sulphides. It is very likely that solute are poisoning the new nucleation sites. This has already been reported in aluminum alloy with high silicon content, [23]. In this case, particles could end up inside the equiaxed grains by engulfment/entrapment. The second effect is that cerium addition could also change the liquid/solid interfacial tension. Previously, it has been reported in the literature that cerium addition decreases the liquid/solid interfacial tension, [10, 24]. This effect could be due to either the presence of solutal cerium

or the decrease in the sulfur and oxygen content in the melt. Liquid/solid interfacial tension affects the dendrite tip velocity and the columnar to equiaxed transition, thus explaining bigger grain sizes and smaller equiaxed areas.

Conclusion

Cold crucible experiments are able to give some preliminary results over pure compound addition. Low misfit pure compounds can be added directly to the melt to reduce the grain size. The best candidates to achieve reduced grain sizes are TiN, Si_3N_4 and CeO_2. As 42CrMo4 base composition is close to the peritectic, misfit with austenite could also be an important parameter. For other additions, other parameters like density and stability in the melt could explain failure.

For cerium addition, unexpected grain growth has been obtained. Cerium sulphides are well dispersed in the equiaxed area and in the 1–10 μm size range and small chunks of MnS are often observed on the outside shell. As those particles exhibit small misfit with ferrite, grain refinement should happen. Solute poisoning of cerium sulphide sites could explain why those sites are not activated. Decreased liquid/solid interfacial tension because of cerium excess and the liquid and/or desulphurization and deoxidation could affect the tip velocity, the columnar to equiaxed transition and the maturation of secondary arms. This could explain the reduced equiaxed area, the increased grain size and the shift in morphology. Further work is needed to improve the understandings on this matter.

Larger 10 kg ingots will be casted with pure compounds addition and ferrocerium to confirm the results. The best candidate will then be selected for a 6.2 tonne industrial casting. The macrosegregation pattern and associated solidification structure will be carefully studied.

Acknowledgements This work was supported by an ASCO Industries/ANRT France under a CIFRE Ph. D. fellowship.

References

1. Dantzig J, Rappaz M (2009) Solidification. Engineering sciences, EFPL Press
2. Kumar A, Založnik M, Combeau H (2010) Prediction of equiaxed grain structure and macrosegregation in an industrial steel ingot: comparison with experiment. Int J Advanc Eng Sci Appl Math 2(4):140–148
3. Lesoult G (2005) Macrosegregation in steel strands and ingots: characterisation, formation and consequences. Mater Sci Eng A 413:19–29
4. Delorme J, Laubin M, Maas H (1977) Solidification of large forging ingots. Casting and solidification of Steel. IPC Science and Technology Press Ltd, Guildford, England, pp 213–276
5. Kumar A, Založnik M, Combeau H, Demurger J, Wendenbaum J (2012) Experimental and numerical studies of the influence of hot top conditions on macrosegregation in an industrial

steel ingot. In: Proceedings of the first international conference on ingot casting, rolling and forging, IRCF, Aachen, Germany IRCF
6. Kermanpur A, Eskandari M, Purmohamad H, Soltani M, Shateri R (2010) Influence of mould design on the solidification of heavy forging ingots of low alloy steels by numerical simulation. Mater Design 31(3):1096–1104
7. Ayata K, Mori T, Fujimoto T, Ohnishi T, Wakasugi I (1984) Improvement of macrosegregation in continuously cast bloom and billet by electromagnetic stirring. Trans Iron Steel Inst Japan 24(11):931–939
8. Quested T, Greer A (2005) Athermal heterogeneous nucleation of solidification. Acta Mater 53(9):2683–2692
9. Elmquist L, Salera S, Diószegi A (2010) Inoculation and its effect on primary solidification structure of hypoeutectic grey cast iron. Int J Cast Metals Res 23(2):124–129
10. Guo M, Suito H (1999) Influence of dissolved cerium and primary inclusion particles of Ce2O3 and CeS on solidification behavior of Fe-0.20 mass %C–0.02 mass%P alloy. ISIJ Int 39(7): 722–729
11. Mizumoto M, Sasaki S, Ohgai T, Kagawa A (2008) Development of new additive for grain refinement of austenitic stainless steel. Int J Cast Metals Res 21(1–4):49–55
12. Ohno M, Matsuura K (2008) Refinement of as-cast austenite microstructure in S45C steel by titanium addition. ISIJ Int 48(10):1373–1379
13. Hu C, Wu K, Trotsan A, Li Y, Isayev O, Hress O, Rodionova I (2016) Effect of microadditives on center segregation and mechanical properties of high-strength low-alloy steels. Metallurgist 60(7–8):888–895
14. Matsuzawa S, Hirata K, Yoshimura T, Yoshikawa G, Miyasaka F (2013) Numerical analysis of cold crucible induction melting employing FEM and MPS method. IEEE Trans Magnet 49(5):1921–1924
15. Bramfitt B (1970) The effect of carbide and nitride additions on the heterogeneous nucleation behavior of liquid iron. Metallurg Trans 1(7):1987–1995
16. Waudby P (1978) Rare earth additions to steel. Int Metals Rev 23(1):74–98
17. Roucan J, Noël-Dutriaux M (1987) Propriétés physiques des composés minéraux. Edition Techniques Ingénieur
18. Schindelin J, Arganda-Carreras I, Frise E, Kaynig V, Longair M, Pietzsch T, Preibisch S, Rueden C, Saalfeld S, Schmid B et al (2012) Fiji: an open-source platform for biological-image analysis. Nat Methods 9(7):676–682
19. Cramb A (2003) The Making. Casting Volume. AISE Steel Foundation, Shaping and Treating of Steel
20. Yanjun L, Qichuan J, Yuguang Z, Zhenmin H (1996) Improvement of the microstructure and mechanical properties of M2 cast high speed steel by modification. J Mater Sci Lett 15(18):1584–1586
21. Fu H, Xiao Q, Kuang J, Jiang Z, Xing J (2007) Effect of rare earth and titanium additions on the microstructures and properties of low carbon Fe-B cast steel. Mater Sci Eng A 466(1):160–165
22. Liu Q, Lu D, Lei L, Qiang H, Fu Q, Zhe Z (2015) Effect of mischmetal on as-cast microstructure and mechanical properties of M2 high speed steel. J Iron Steel Res Int 22(3):245–249
23. Lee Y, Dahle A, StJohn D, Hutt J (1999) The effect of grain refinement and silicon content on grain formation in hypoeutectic Al-Si alloys. Mater Sci Eng A 259(1):43–52
24. Li H, McLean A, Rutter J, Sommerville I (1988) Influence of rare earth metals on the nucleation and solidification behavior of iron and 1045 steel. Metallurg Trans B 19(3):383–395

Phase-Field Modelling of Intermetallic Solidification

Andrew M. Mullis, Peter C. Bollada and Peter K. Jimack

Abstract Many important intermetallic compounds display a faceted morphology during solidification close to equilibrium but adopt a more continuous, dendritic like morphology with increasing departure from equilibrium. We present a phase-field model of solidification that is able to both reproduce the Wulff shape at low driving force and to simulate a continuous transition from faceted to dendritic growth as the driving force is increased. A scaled ratio of the (perimeter)^2 to the area is used to quantify the extent of departure from the equilibrium shape.

Keywords Phase-field modelling · Faceted crystals · Intermetallics

Introduction

Phase-field modelling is widely used to simulate continuous (non-faceted) crystal morphologies, such as dendrites, during growth from the melt. Much less attention has been paid to the growth of faceted crystals as the phase-field rationale of approximating the sharp solid-liquid interface with one that is diffuse does not immediately lend itself to the solidification of such faceted crystals. Despite this, a number of methodologies for simulating faceted morphologies have been proposed [e.g. 1–6].

Much of the interest in simulating faceted crystal growth has been stimulated by the study of Si and Ge due to their importance in the electronics industry. However, the growth of faceted crystals is also important within the light metals industry with regard to structural components. This is not only because Si is used extensively in Al casting alloys, producing a faceted/non-faceted eutectic but also because many

A. M. Mullis (✉) · P. C. Bollada
School of Chemical & Process Engineering, University of Leeds,
Leeds LS2 9JT, UK
e-mail: A.M.Mullis@leeds.ac.uk

P. K. Jimack
School of Computing, University of Leeds, Leeds LS2 9JT, UK

The Minerals, Metals & Materials Society, *TMS 2018 147th Annual Meeting & Exhibition Supplemental Proceedings*, The Minerals, Metals & Materials Series,
https://doi.org/10.1007/978-3-319-72526-0_55

of the most deleterious intermetallics formed due to impurity elements within Al-alloys are strongly faceted (e.g. θ-$Al_{13}Fe_4$ [7]).

It is well established that crystals that grow with faceted morphologies close to equilibrium progressively take on more continuous interface shapes with increasing departures from equilibrium, eventually adopting fully dendritic morphologies. This has been shown for the growth of pure semiconductors [8, 9], the Si phase in Al–Si eutectics [10] and for intermetallic phases [11]. Simulation of this particular aspect of faceted growth has however received very little attention.

Within phase-field the strong anisotropy required to produce faceted growth can be incorporated into the interfacial surface energy [1–3], the kinetic mobility [4, 5] or both [6]. Recent work has tended to favour the kinetic approach, but when considering the faceted to non-faceted transition mediated by high growth velocity this approach is problematic as the tendency towards faceting becomes stronger, rather than weaker, with increasing growth velocity. There is a further problem in that, in the limit of vanishing growth velocity the kinetic anisotropy vanishes, giving rise to isotropic growth. In contrast, faceting introduced via the surface energy has the desirable properties that the faceted morphology is most pronounced at equilibrium and is progressively lost with increasing growth velocity. As such, this approach is a computationally expedient means of studying the faceted to non-faceted growth transition.

In this paper we use a phase-field model of faceted crystal growth mediated by a strong anisotropy in the interfacial surface energy in order to study the transition from faceted to dendritic growth with increasing growth velocity. As far as we are aware, the only previous work to simulate this type of transition using phase-field is [3], and then in the case of thermal growth only.

Phase-Field Model

The equations for the evolution of the phase (ϕ) and solute (c) fields are given by:

$$\dot{\phi} = -M\frac{\delta F}{\delta \phi} \tag{1}$$

$$\dot{c} = \nabla \cdot D\nabla \frac{\delta F}{\delta c} \tag{2}$$

where D and M are the solute diffusivity and kinetic mobility respectively. F is the total free energy for the system, given by:

$$F = \int_{\Omega} G\, d^3x \tag{3}$$

with G being the free energy density given by:

$$G = g(\phi)G_{liq}(c,T) + (1-g(\phi))G_{sol}(c,T) + \omega\left[A(\nabla\phi) + 8\phi^2(1-\phi)^2\right] \quad (4)$$

Here, $g(\phi) = \phi^2(3 - 2\phi)$ is a polynomial that interpolates between the bulk free energies for the liquid (G_{liq}) and solid (G_{sol}) phase respectively at concentration c and temperature T, ω is a scalar that governs the barrier height associated with the double well potential $8\phi^2(1 - \phi)^2$ and A is a function that governs the anisotropy. The most common model for weakly anisotropic materials displaying four-fold symmetry is:

$$A(\nabla\phi) = \frac{1}{2}\delta^2\gamma(\nabla\phi)\cdot\gamma(\nabla\phi)\,,\ \text{with}\ \gamma(\nabla\phi) = [1 + \varepsilon\ \cos 4\theta]\nabla\phi \quad (5)$$

where δ is a measure of the width of the diffuse interface and ε controls the strength of the anisotropy. θ is the angle of the outward pointing normal to the solid-liquid interface, given by:

$$\hat{\mathbf{n}} \equiv \frac{\nabla\phi}{|\nabla\phi|} = \begin{bmatrix}\cos\theta \\ \sin\theta\end{bmatrix} \quad (6)$$

In the simulations reported here we consider the growth of Si crystals from hypereutectic Al–Si at $c = 0.6$ (60 at.% Si). The bulk free energies for the solid and liquid phases are given by:

$$G_j(c,T) = cG_j^{Al}(T) + (1-c)G_j^{Si}(T) + \frac{RT}{\nu_m}[c\ \ln\ c + (1-c)\ln(1-c)] + G_j^{xs}(c,T) \quad (7)$$

Here j labels the phase (either liquid or solid), R is the gas constant and ν_m the molar volume. G^i (i = Al, Si) are the free energy of the pure elements while G^{xs} is the excess free energy on mixing, which are given respectively by:

$$G_j^i = a_j^i + b_j^iT + c_j^iT\ \ln\ T + d_j^iT^2 + e_j^iT^3 + f_j^iT^{-1} + g_j^iT^7 + h_j^iT^{-9} \quad (8)$$

$$G_j^{xs}(c) = c(1-c)\sum_{m=0}^{4}\left(p_j^{(m)} + q_j^{(m)}T\right)(1-2c)^m \quad (9)$$

Equations (7)–(9) are the standard way of representing the thermodynamics of solution phases in CALPHAD. The coefficients a-h and p-q are obtained from version 5.0 of the SGTE solutions database and are based on the thermodynamic assessment contained within [12]. The phase diagram is shown in Fig. 1.

The solution to the above set of equations is obtained using a finite difference implicit scheme with a geometric multigrid solver on an adaptive mesh to achieve

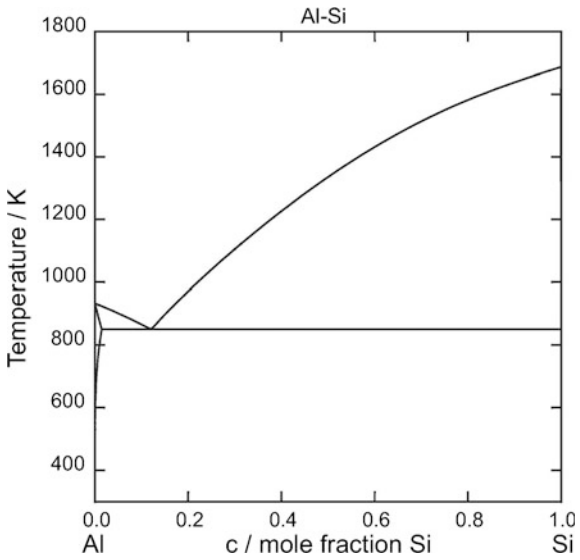

Fig. 1 Phase diagram for the Al–Si system. Simulations here conducted at $c = 0.6$

high a density of mesh elements at the interface. Full details of the computational scheme, applied to the growth of continuous (non-faceted) crystals, are given in [13].

Anisotropy and Modelling of Facets

The effect of the anisotropy function, γ, on the equilibrium shape of the crystal is shown in Fig. 2. Figure 2a shows a polar plot of γ for several values of the anisotropy strength, ε. The corresponding Frank diagram is a contour of γ in $[\phi_x, \phi_y]$ space, where ϕ_x and ϕ_y are the partial derivative of ϕ with respect to x and

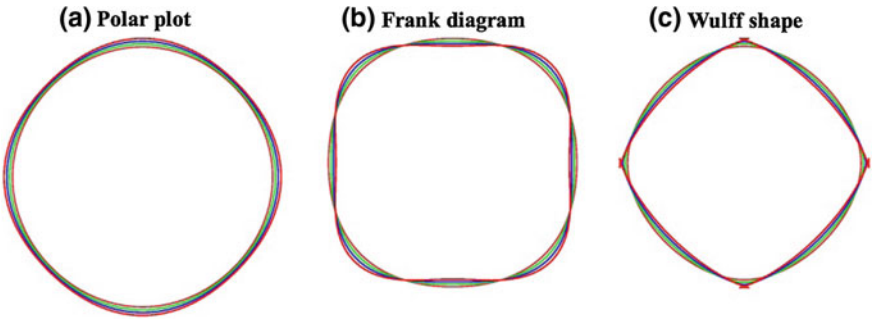

Fig. 2 **a** Polar plot **b** Frank diagram and **c** Wulff shape for a weak 4-fold anisotropy

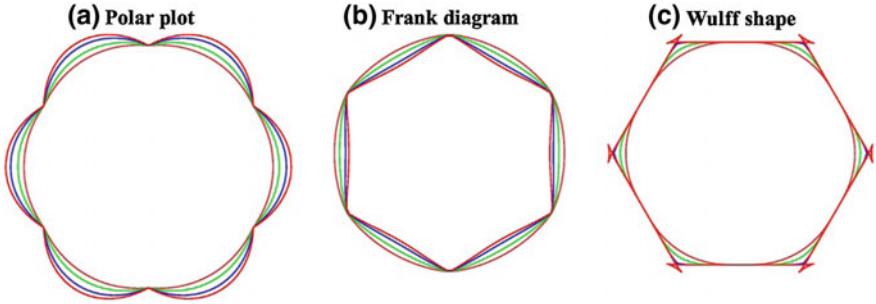

Fig. 3 **a** Polar plot **b** Frank diagram and **c** Wulff shape for a faceted hexagonal crystal

y respectively. An example Frank diagram, corresponding to values of ε used in Fig. 2a is shown in Fig. 2b. From this we can calculate the function $W(t) = [\gamma_x(t), \gamma_y(t)]$, where $[\phi_x = \cos(t), \phi_y = \sin(t)]$ and:

$$\gamma_x \equiv \frac{\partial \gamma}{\partial \phi_x}, \gamma_y \equiv \frac{\partial \gamma}{\partial \phi_y} \tag{10}$$

$W(t)$ is shown in Fig. 2c and is in fact the well-known Wulff shape giving the equilibrium shape of the crystal. For high values of ε it can be seen from Fig. 2c that $W(t)$ develops cusps or 'ears' aligned with the principal anisotropy directions. These correspond to disallowed crystal orientations and indicate that the resulting solidification morphology will develop a sharp vertex during growth. For n-fold symmetry this will occur for $\varepsilon > 1/(n^2-1)$, $\varepsilon > 1/15$ for four-fold growth. However, it is clear from Fig. 2c that the Wulff shape still has curved sides even for $\varepsilon > 1/15$, that is high anisotropy strength per se does not yield a faceted crystal with flat faces.

In fact, as shown in Fig. 3, the condition for flat, i.e. faceted, faces is that polar plot of γ should have concave regions. For six-fold symmetry, as we might require for growth of Si crystals, this is achieved using an anisotropy of the form $(1 + |\varepsilon\cos(3\theta)|)$ and has been adopted within the phase-field code for the simulations reported here. However, the sharp vertices also associated with the Wulff shape for this anisotropy can cause numerical problems, wherein to avoid this we approximate $|\cos(3\theta)|$ by $\sqrt{(\cos 3\theta)^2 + q}$, where q is a small quantity. The effect is to introduce vertices which have a small, but constant curvature. Noting that:

$$\cos 3\theta = \cos^3\theta - 3\cos\theta\sin^2\theta = \frac{\phi_x^3 - 3\phi_x\phi_y^2}{|\nabla\phi|^3} \tag{11}$$

we have the final form of the anisotropy functional as:

$$\gamma = \left\{ 1 + \varepsilon \sqrt{\frac{\left(\phi_x^3 - 3\phi_x\phi_y^2\right)^2 + q^6}{\left(\varphi_y^2 + \phi_y^2 + q^2\right)^3}} \right\} \nabla\phi \tag{12}$$

Results and Discussion

Figure 4 illustrates the crystal morphologies simulated at four different nucleation temperatures; $T_N = 1300$, 1200, 1100 and 1000 K. These are relative to a liquidus temperature at $c = 0.6$ of 1430 K. The progression from essentially flat faceted hexagonal crystal at the lowest undercooling to almost fully continuous six-fold dendrite at the highest undercooling is clear, showing that the proposed model provides an appropriate framework for simulating a faceted to continuous growth transition with increasing driving force. Further detail is given in Fig. 5 in which we show the growth of the crystal at $T_N = 1000$ K at three different instances in time. A pseudo-3D contouring is used in Fig. 5 as this is particularly effective in picking out the solute rich cores evident within the dendrite arms.

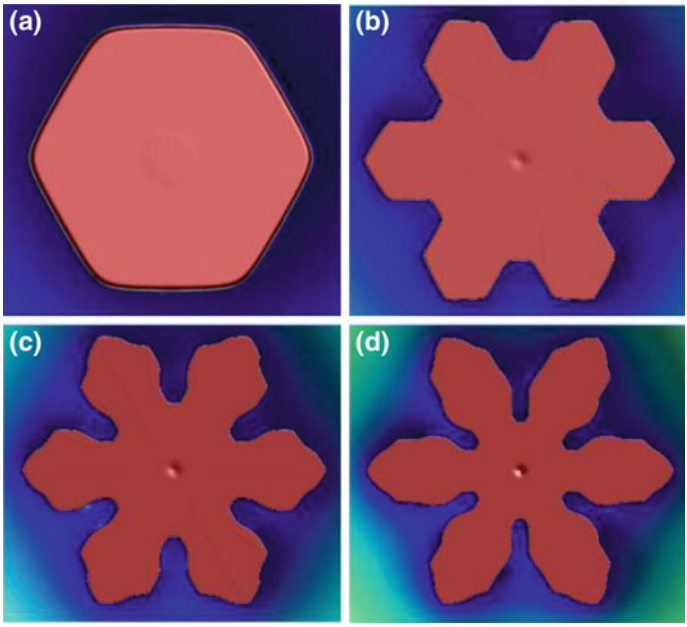

Fig. 4 Crystal morphologies for nucleation temperatures of **a** 1300 K **b** 1200 K **c** 1100 K and **d** 1000 K. All have the same anisotropy function as shown in Fig. 3

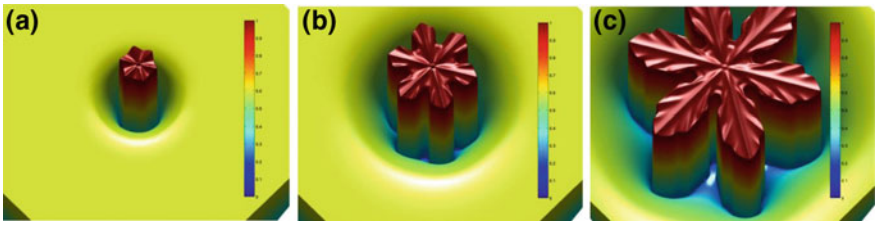

Fig. 5 Three snapshots at different stages in the growth of a crystal with nucleation temperature of 1000 K

In order to evaluate the evolution of the crystal morphology quantitatively as a function of time and undercooling we define Λ as:

$$\Lambda = \frac{Perimter^2}{4\pi \times Area} \tag{13}$$

This measure is invariant under scaling and is normalised so as to equal unity for a circle. Any other closed shape will have $\Lambda > 1$, with a regular hexagon having the value $\Lambda = 6/\left(\sqrt{3}\pi\right) \approx 1.10$. Figure 6 plots (a) Λ and (b) the rate of change of Λ, $\dot{\Lambda}$, both as a function of the maximum extent of growth. Larger values of Λ indicate increasing departure from the hexagonal morphology and hence a crystal with a more dendritic character.

With reference to Fig. 6a it is clear that Λ increases as growth progresses at all undercoolings studied here. From Fig. 6b it can be seen that in all cases $\dot{\Lambda}$ is initially positive but decreasing. This initial transient is as a result of the model using a circular seed to nucleate solidification. This is a deliberate choice so that any subsequent growth of an hexagonal morphology is unambiguously the result of the system selecting such a morphology, not being forced by the initial condition. In the case of the growth of a solid hexagon, Λ will increase from 1.00 to 1.10 and $\dot{\Lambda}$ will decrease monotonically tending asymptotically towards zero. This appears to be the behaviour observed at the highest nucleation temperature (lowest undercooling) of $T_N = 1300$ K. At nucleation temperatures of 1200 K and below, $\dot{\Lambda}$ passes through a local minimum, thereafter increasing rapidly. This corresponds to the point at which Λ initially exceeds 1.10 and as such is the first indication that the resulting crystal morphology will not be a simple regular hexagon. It can be seen from Fig. 6b that all of the minima for different nucleation temperatures lie on a single straight line (in log-linear co-ordinates). Consequently, it would appear that the size of the crystal when it first begins to depart from simple hexagonal can be easily predicted for any given nucleation temperature. It is also clear that the curve for $T_N = 1300$ K has become asymptotic to the line and, as such, is unlikely to display a minimum. This would indicate tha for $T_N = 1300$ K a simple hexagonal crystal will be preserved indefinitely during growth, in line with expectation that close to equilibrium the Wulff shape is recovered.

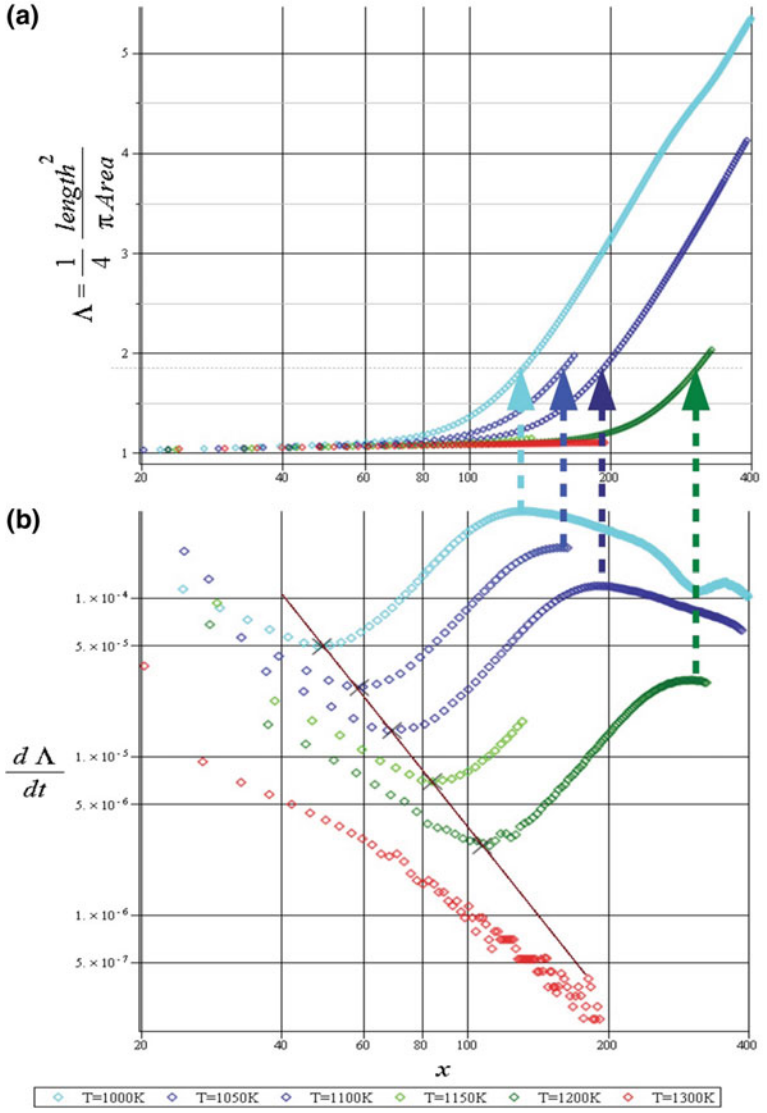

Fig. 6 **a** Scaled ratio of (Perimeter)^2/Area as a function of crystal size for various nucleation temperatures. **b** Rate of change of ratio of (Perimeter)^2/Area

With continued growth, at all nucleation temperatures except $T_N = 1300$ K, Λ subsequently passes through a local maximum. Irrespective of undercooling, this occurs for $\Lambda \approx 1.75$ and corresponds to a morphology which we might loosely describe as a faceted hexagonal star, of which Fig. 4b is an example. This rapid change in Λ (maximum in Λ) seems to be related to the formation of arms along the original locations of the vertices. Thereafter, Λ mostly decreases smoothly, possibly

with subsequent local minima, as evident in the curve for $T_N = 1000$ K. These probably correspond to the formation of the faceted kinks in the dendrite arms, as evident in Fig. 5c.

Summary and Conclusions

A phase-field model for the binary alloy solidification of faceted crystal morphologies has been proposed. It has been demonstrated that not only can the model reproduce the Wulff shape for near equilibrium solidification, but that faceted to dendritic transitions can be simulated at large departures from equilibrium, in agreement with rapid solidification experiments. A scaled ratio of the (perimeter)^2 to the area of the crystal, denoted by Λ, is used as a measure of the departure of the morphology from the equilibrium Wulff shape. The evolution of Λ, and of its rate of change, $\dot{\Lambda}$, as a function of crystal size and undercooling, provides a framework in which the evolution of non-equilibrium crystal shapes may be understood.

Acknowledgements This research was funded by the EPSRC Innovative Manufacturing Research Hub in Liquid Metal Engineering (LiME), Grant No. EP/N007638/1.

References

1. Taylor JE, Cahn JW (1998) Diffuse interfaces with sharp corners and facets: phase field models with strongly anisotropic surfaces. Physica D 112:381–411
2. Eggleston JJ, McFadden GB, Voorhees PW (2001) A phase-field model for highly anisotropic interfacial energy. Physica D 150:91–103
3. Debierre J-M, Karma A, Celestini F, Guerin R (2003) Phase-field approach for faceted solidification. Phys Rev E 68:041604
4. Uehara T, Sekerka RF (2003) Phase field simulations of faceted growth for strong anisotropy of kinetic coefficient. J Cryst Growth 254:251–261
5. Miura H (2013) Anisotropy function of kinetic coefficient for phase-field simulations: reproduction of kinetic Wulff shape with arbitrary face angles. J Cryst Growth 367:8–17
6. Lin HK, Chen HY, Lan CW (2014) Adaptive phase field modelling of morphology instability and facet formation during direction solidification of SiGe alloys. J Cryst Growth 385:44–48
7. Allen CM, O'Reilly KAQ, Cantor B, Evans PV (1998) Intermetallic phase selection in 1XXX Al alloys. Prog Mater Sci 43:89–170
8. Panofen C, Herlach DM (2007) Solidification of highly undercooled Si and Si-Ge melts. Metal Mat Trans A 449:699–703
9. Battersby SE, Cochrane RF, Mullis AM (1997) Highly undercooled germanium: Growth velocity measurements and microstructural analysis, Mater Sci Eng A 226:443–447
10. Liu RB, Herlach DM, Vandyiousse M, Greer AL (2003) Morphologies of silicon crystals solidified on a chill plate. Metal Mat Trans A 35A:1067–1073
11. Xian JW, Belyakov SA, Nogita K, Yasuda H, Gourlay CM (2017) Faceted and Nonfaceted growth of Cu_6Sn_5 crystals. In: Fan Z (ed.) Proceedings of Solidification Processing 2017 (SP17), Brunel University UK, pp 251–254 (ISBN 978-1-908549-29-7)

12. Groebner J, Lukas HL, Aldinger F (1996) Thermodynamic calculation of the ternary system Al-Si-C. CALPHAD 20:247–254
13. Bollada PC, Jimack PK, Mullis AM (2015) Three dimensional thermal-solute phase field simulation of binary alloy solidification. J Comp Phys 287:130–150

Analysis of Formability of Glassy Alloys by Surface Heating Under Convective Conditions

Rahul Basu

Abstract Modification of surface films by focussed energy sources with convective boundary conditions is idealised. The problem is approached by linearizing a coupled set of heat and mass transfer equation. The nonlinearity of the coupled problem introduces many complexities and exact solutions are not available in the general case. This work uses certain transformations not published earlier to obtain tractable solutions and stability benchmarks in terms of macroscopic parameters like the Stefan, Biot and Fourier numbers. Linear ODE's are obtained from the coupled mass and heat transfer equations, which are analysed easily. Evaluation of the properties of the thermal boundary layer and attenuation with imposed fluctuating heat source shows that a regime exists for glass formation. Data from various alloy systems show that glass formability is related to the derived boundary layer thickness and certain non dimensional parameters.

Keywords Glassy alloys · Phase transformations · Heat transfer
Boundary layer

Nomenclature

a	initial size
c	concentration
c_p	specific heat
D	differential operator, Diffusion coefficient
Fo	Fourier number
Bi	Biot number
Ste	Stefan number
h	heat transfer coeff.
a	boundary length
g	temperature concentration gradient

R. Basu (✉)
Adarsha Institute of Technology, Off Intl Airport Road, Kundana,
Bangalore 562110, India
e-mail: raulbasu@gmail.com

The Minerals, Metals & Materials Society, *TMS 2018 147th Annual Meeting & Exhibition Supplemental Proceedings*, The Minerals, Metals & Materials Series,
https://doi.org/10.1007/978-3-319-72526-0_56

K thermal conductivity
k thermal diffusivity
L latent heat
m mass
q source strength
r radial variable
s interfacial position $s = 2\lambda \sqrt{\alpha 12\tau}$
T temperature
t time
z axial coordinate

Greek Symbols

α, κ diffusivity (subscript m for the mass component)
δ Characteristic length
ε porosity
η similarity variable
θ_m non dim temperature
μ small perturbation parameter (not to be confused with chemical potential) τ non-dimensional time
θ non-dimensional temperature
ρ Density

Introduction

In the classic work of Mullins and Sekerka, a 1st order interface is analyzed which moves at constant velocity [1]. The present work is 2nd order in concentration, (first order in time), with a non constant velocity decided by a similarity transformation. Stability criterion on planar interface or spherical converted to planar. Coupled thermal and concentration equations are decoupled through solvus line and an ODE obtained which yields a stability criterion depending on the externally applied Biot and Stefan numbers, whereas the Fourier number is an internally decided parameter decided by the "damping" or similarity number dependent of the diffusivity. Mullins and Sekerka analyzed instabilities as a local phenomenon unaffected by the surrounding diffusive field [1].

Langer started with disturbances in the nucleus or seed crystal, hypothesizing the dissipation of latent heat into an under-cooled melt ahead of the interface [2]. Another aspect which was tackled was the discontinuity imposed on the field solutions due to the moving interface, not discussed in [1]. Eventually any such analysis has to come to grips with this difficult aspect. It was also found that spherical paraboloids or oblate geometries with circular cross sections come out as

solutions of the various diffusive models [2]. Earlier work by Hunt [3] on dendrites shows similar morphologies as those given by Langer [2]. The preferential growth in one direction was clearly a response to the gradient and boundary condition in concentration and temperature. Hunt claimed that theoretical spacing agreed with experiment, based on a spacing selection mechanism that does not depend on marginal stability [4]. It is clear that apart from the arguments propounded in [1], which deal with initial transients and instabilities, the overall field coupled with the boundary conditions imposes a constraint on further growth of the transient nucleus. In order to eliminate separate the effects of time and distance, if these are combined through a similarity transformation, the diffusion equation with coupling terms can be converted to an ODE and then solved.

Analysis

The transformations equations can be written in terms of the coupled mass and thermal diffusive equations, [5]. These solutions for the general case can be derived from first principles as in Eqs. (3) and (4):

Let $\theta = U/r$, then the diffusion equation transforms to the familiar one dim case, the solutions of which can be written:

$$(\theta - \theta_0)/(\theta_1 - \theta_0) = (a/r)\mathrm{erfc}(r - a)/2\mathrm{Sqrt}(Dt). \tag{1}$$

This particular transformed solution can be used to solve several spherical problems, which has been overlooked by several earlier attempts for the spherical case, to model a growing spherical nucleus, [6].

Convective Conditions

For surface temperature decided by convective heat flux, the methodology is to apply a flux balance. Thus

$$\begin{aligned} &h(T - T_0) = K dT/dx. \text{ Where } dT/dX = (Ts - Tm)/l \\ &hl/K(T_s - T_o) = T, \text{ hence } T = BiT_o/(Bi - 1) \text{ where } Bi = hl/K \end{aligned} \tag{2}$$

The thermal equations for heat diffusion can be written as:

$$kD^2T = \rho c_p dT/dt \tag{3}$$

this can be modified to account for remelt as

$$kD^2T + \varepsilon L dc/dt = \rho c_p dT/dt \tag{4}$$

Dividing through and restricting to one dimension with the similarity variable η

$$T'' + \eta/2T' + \left(\varepsilon L/\rho c_p\right) dc/dt = 0, \text{where } \eta = x/(\alpha\tau)^{0.5} \tag{5}$$

The artifice that the thermal gradient dT/dx and concentration gradient dc/dx are linearly connected via the solvus line for melting, where g is the thermal gradient is now applied. Normalized temperature yields the rewritten form (6), using the convective relations explained in (2).

$$\mu\theta'' + .5\mu Fo\theta' + Bi\,\theta = 0 \text{ Forcing function, where } \mu = g\rho c_p/\varepsilon L \tag{6}$$

Assume a solution exp(β η) then $\beta = -Fo/2 \pm \text{sqrt}[Fo^2/4 - Bi/\mu]$

Since μ is small, the discriminant can be negative within the normal range of Bi and Fo (O ~ 1).

From (6), if the second order term is neglected, the equation

$$0.5\mu Fo\theta' + Bi\theta = 0 \tag{7}$$

results (7)

Leading to the "Inner solution"

$$\theta'/\theta = -2Bi/\mu Fo \tag{8}$$

Or

$$\theta(\eta) \sim \exp(-2Bi/\mu Fo)\eta \tag{9}$$

Considering μ as a small parameter, a boundary layer thickness can be found which is related to the Fo term. Approximating it as the distance where the solution attenuates by 1/e, this distance is found to be (μFo/2Bi). This is also known from concepts of the Fourier wavelength, and that attenuation of fluctuations depends on the numerical value of (2Bi/μ).

On the other hand, if μFo is small, a solution of μ θ″ + 0.5 μFo θ′ + Bi θ = 00 depends on μ θ″ + Bi θ = 0 0, which can be expressed in hyperbolic sines and cosines.

The thermal equation is an o.d.e in similarity variables which can easily be solved. The oscillatory properties are decided by the discriminant which depends on the Fourier, Biot, and Stefan numbers. An impinging laser frequency can be matched with resonant frequency of thermal (phase oscillations), thus preventing

nucleation from occurring. Solutions for the planar case are known for Dirichlet conditions and Heat source conditions, [7].

Application to Glassy Films and Amorphous Alloy Formation

Consider $\mu\,\theta'' + 0.5\,\mu Fo\,\theta\ni + 0.5\,Bi\,\theta = 0$ Forcing function, where $\theta = T/Tm$

Using data for Co with applicability to the alloy films of Al-Co-Ce [8]

L for Co = 66 cal/g, Cp = 0.1 cal/gK, ρ = 8.86 gm/cc, [1/Stefan Number] = $L/\rho Cp\Delta T = 0.042$

From the discriminant of $\mu\theta'' + 0.5\,\mu\,Fo\,\theta' + 0.5Bi\,\theta = 0$, (Forcing function), with $\mu = g/\varepsilon Ste$

$Fo^2 = 16\,\varepsilon\,Ste\,Bi/g = 16\,\varepsilon\,0.04\,Bi/g = 0.64\,\varepsilon\,Bi/g$

Take Bi = 0.1, and Fo = 0.2 typical values suggested in Incropera [9], then

$0.04 = 0.064\,\varepsilon/g$, ➔ $\varepsilon/g = 0.625$ ➔ $\varepsilon = 0.625*g$,

Similar calculations may be done easily for other metals using the data in Table 1. where ε porosity, and g = dT/dc slope of solvus line (from the appropriate phase diagram. The metastable or mushy zone is found to be related to the slope of

Table 1 Computed Stefan numbers at fusion

Metal	Latent heat	Melting Pt. Tm	1/Ste	Tg
Co [12]	66	1770	0.042	746
Pd [13]	38.2	1827	0.029	630
Pt [14]	24	2045	0.017	522
Ge [15]	114	1210	0.239	980
Si [16]	430	1685	0.609	1000–1473

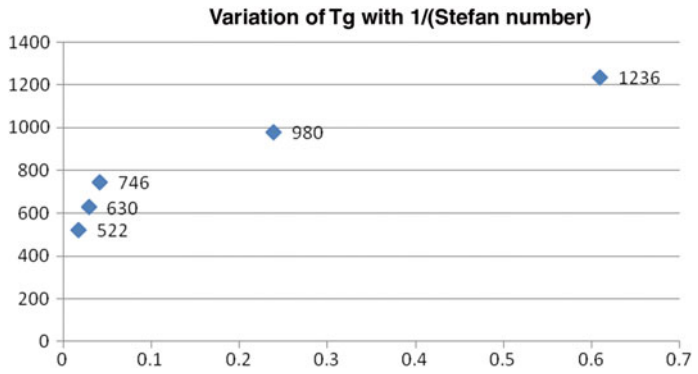

Fig. 1 Graph of 1/Ste (abscissa) vs Tg (ordinate)

the solvus line, and it follows that a deep eutectic would have a larger mushy zone. From (8) the width of the boundary layer is seen to vary as μ or as 1/Ste

Results

Table 1 gives the calculated values for 1/Ste for some metals forming glassy or amorphous alloys. From the phase diagram g can be estimated, the remelt fraction ε is calculated as 0.625 g. This remelt controls the "mushy zone" and thus it is seen that the properties of the mushy zone and the slope of the solvus line can control or dissipate the thermal oscillations near the surface. In fact the formability of glassy alloys is well known to depend on "deep eutectics" [10, 11], thus affecting the width of the mushy zone via "g" from the analysis above. It follows that if the mushy zone is large there is possibility for allowing homogenous nucleation in the liquid and a glassy phase to form [17–19].

Conclusions

Figure 1 clearly shows that the glass formation of Ge and Si lie on a different trend line as compared to the metals Co, Pd, Pt. It may be of interest to note that Ge and Si belong to Group IVA while Co, Pd, Pt belong to VIIIB in the Periodic Table. This particular combination of parameters. **(L/ρcp)** occurring in the Stefan number also has a role to play in the overall values controlling the boundary layer or mushy zone thickness, while the Glass formation temperature Tg is related to the viscosity of the metal/alloy. Although the Stefan number is calculated on the basis of Fusion

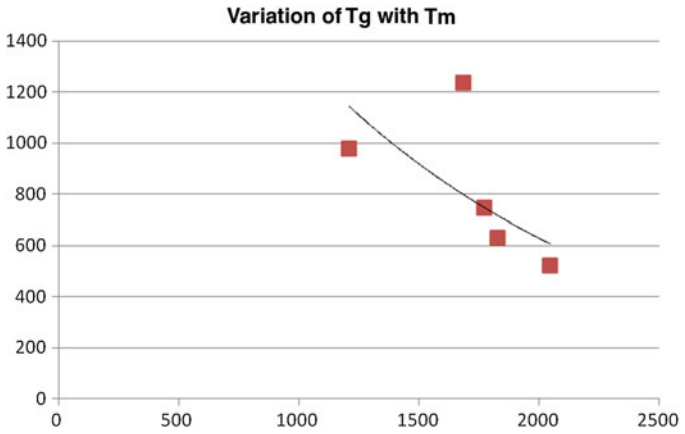

Fig. 2 Graph of Tm (abscissa) vs Tg (ordinate)

temperature, one cannot say there is a linear relation between the Tg and Tm. A plot of these is also attached in Fig. 2. It is possible that there are two separate trends corresponding to the group membership in the Periodic Table. It is suggested that the groups of alloys and glass formers with similar glass forming abilities follow the groupings of the Periodic Table.

References

1. Mullins WW, Sekerka RF (1963) J Appl Phys 34:323–329
2. Langer JS (1980) Rev Mod Phys 52(1):1–30
3. Hunt JD (2001) Sci Technol Adv Mater 2(1):147–155
4. Hunt JD, Lu SZ (1993) Mat Sci Eng A 173(1–2):79–83
5. Luikov AV (1975) Int J Heat Mass Transfer 18:1–14
6. McCue SW, King JR, Riley DS (2003) Proc Roy Soc (A) 459:977–999
7. Carslaw HS, Jaeger JC (1959) Conduction of heat in solids, 2nd edn. Clarendon Press, Oxford, p 276
8. Hoekstra JG, Qader S, Scully J et al (2005) Adv Eng Mater 7(9):805–809
9. Incropera FD, Dewitt DP, Bergmann TL, Lavine AS (2010) Fundamentals of heat and mass transfer, 6th edn. Wiley, NYC
10. Spaepen F, Turnbull D (1974) Scripta Mater 8:563
11. Johnson WL, Na JH, Demetriou MD (2016) Nat Commun 7:10313. https://doi.org/10.1038/ncomms10313
12. Bie L, Li Q, Cao D (2016) Intermetallics 71:7
13. Kajita S, Kohara S, Onodure (2011) Mater Trans 52(7):1349
14. Zhang T, Inoue (2003) Mater Trans 44:1143–1147. https://doi.org/10.2320/mater
15. Mehta A, Shulka RK, Kumar A (2004) J Optoelectron Adv Mater 64:1105
16. Hedler A, Ludwig A, Lamunster K (2004) Nat Mater 3:804
17. Libbrecht K (2005) Rep Prog Phys 68:855–895
18. Granaszy L, Puzsten T, Borszonyi T (2006) Phase field theory of nucleation and polycrystalline pattern formation. In: Handbook of theoretical and computational nano technology. American Scientific Publishers, California, chapter 9 pp 535–572
19. Duwez P (1976) Annu Rev Mater Sci 6:83–117

Study on the Formation and Control of TiN Inclusion in Mushy Zone for High Ti Microalloyed Steel

Tao Liu, Dengfu Chen, Wenjie He, Mujun Long, Lintao Gui, Huamei Duan and Junsheng Cao

Abstract The coarse TiN inclusions can act as potential fracture initiation sites and deteriorate the impact toughness of steels. The experimental observation results indicated that CaS and TiN inclusions precipitated in solidification mushy zone. Meanwhile, it was found that CaS inclusions could act effectively a heterogeneous nucleation substrate for the precipitation of TiN inclusions, and the size of TiN inclusions with CaS core was obviously larger than those TiN inclusions without CaS core. Additionally, the thermodynamic calculation result showed that TiN inclusions began to precipitate at the end of solidification from the dendrites front; moreover, the preexisted CaS inclusions promoted the formation of TiN inclusions. Decreasing sulfur and nitrogen content could significantly reduce precipitation temperature and growth time of CaS and TiN inclusions in mushy zone. Furthermore, TiN inclusions could be prevented from precipitation at the surface of CaS inclusions when the S content of molten steel was below 0.0008 wt%.

Keywords Coarse TiN inclusions · CaS inclusions · Mushy zone Precipitation control

Introduction

Compared with conventional carbon steels, microalloyed steels with a excellently combination of mechanical properties such as high strength, well toughness and weldability have attracted considerable attention, and now this type steels have been

T. Liu · D. Chen (✉) · W. He · M. Long (✉) · L. Gui · H. Duan · J. Cao
College of Materials Science and Engineering, Chongqing University, Chongqing 400044, China
e-mail: chendfu@cqu.edu.cn

M. Long
e-mail: longmujun@cqu.edu.cn

T. Liu
e-mail: cqltao@cqu.edu.cn

The Minerals, Metals & Materials Society, *TMS 2018 147th Annual Meeting & Exhibition Supplemental Proceedings*, The Minerals, Metals & Materials Series,
https://doi.org/10.1007/978-3-319-72526-0_57

considered as the promising engineering materials with wide applications [1, 2]. Those mechanical properties are significantly affected by the characteristics of the non-metallic inclusions in steels, such as their size, shape, distribution, and composition. Most oxides inclusions are mainly generated during steel deoxidation process and solidification process, but sulfide and nitride inclusions tend to form after solidification in microalloyed steels. Coarse sulfide and nitride inclusions in particular are detrimental to the toughness of microalloyed steels [3, 4]. Therefore, it is necessary to modify the inclusions by adding different modifiers into the liquid steel. Calcium treatment is widely used for oxide and sulfide inclusions modification in Al-killed steel to lessen harmful effects and to avoid nozzle clogging in continuous casting. However, insufficient calcium treatment will bring adverse effects and promote the solid calcium aluminates inclusion formations which are hard to be removed. For excessive calcium treatment, redundant calcium will react directly with sulfur to form CaS inclusion. At the same time, the dissolved aluminum and sulfur in molten steel will react with excessive CaO to form oxide-sulfur duplex inclusion, result in a large number of CaS-Al_2O_3 inclusions will form in steels [5, 6]. Either way, those inclusions dispersed in the liquid steel promote heterogeneous nucleation of sulfide and nitride inclusions during continuous solidification, especially in Ti microalloyed steel.

Up to now, TiN particles are frequently used as grain refiner to inhibit prior austenite grain growth at high temperature because of their strong high-temperature stability and low production cost benefits [7, 8]. However, the beneficial potential of TiN particles is usually limited under normal production because of coarse TiN particles formation, as large as several microns, which can act as potent cleavage initiators and deteriorate toughness [9, 10]. Meanwhile, with the wide application of titanium microalloying technology, the surface transverse cracks tendency is increasingly apparent during continuous casting process in Ti microalloyed steel. which result in a severe defect and deteriorate the casting quality [11, 12]. Previous studies [13, 14] reveal that vast coarse nitride inclusions destroy the matrix continuity, the micro-cracks initiate potentially in the interface and then propagate in the matrix. Moreover, a universal conclusion had been drawn, which is that the coarse TiN inclusions (several microns) are mainly generated in liquid steel or mushy zone of solidification [9, 15].

In the present work, the solidification behavior and TiN inclusions precipitation behavior in mushy zone of Ti microalloyed steel were studied via an in situ observation equipment which was confocal laser scanning microscopy (CLSM). Morphology of the inclusions and precipitations were observed using scanning electron microscopy (SEM) and their components were analyzed by energy dispersive spectrometer (EDS). Moreover, the effects of chemical content and pre-existing inclusions on the TiN inclusions precipitated in mushy zone were taken into account simultaneously in the thermodynamic calculation.

Experimental Procedure

The experiments of simulating the solidification process for liquid steel were carried out in a confocal laser scanning microscopy (CLSM, VL2000DX). The detailed schematic of CLSM has been described in previous reference [16]. The experimental specimens were derived from a casting slab at room temperature and machined into 7.5 mm in diameter and 3 mm in height, and then the observed plane was mirror polished and cleaned ultrasonically before the experiment. The chemical composition of the selected steel is listed in Table 1.

Firstly, the cylindrical specimens were heated from room temperature to 1538 °C by a heating rate of 5 °C/s and held 5 min at 1538 °C to ensure they melt completely. Then the specimens were cooled fast to room temperature as a compared specimen via quenching with help of helium gas. As presented in previous research [17], the average cooling rate in the secondary cooling zone is less than 0.5 °C/s. Meanwhile, it is considered that the crack in the slab usually occurs in 1/4 location near the inner arc side. Therefore, in this study, the corresponding cooling rate during solidification was selected as 0.45 °C/s. Thus, to simulate a same thermal history as that in the continuous casting processes, other specimens were heated from room temperature to melt completely and then were cooled to completely solidification with a cooling rate 0.45 °C/s, and then similarly cooled fast to room temperature via helium gas quenching. The start and end temperature of precipitation behavior and solidification behavior were in situ observed and recorded during cooling process. After the in situ observation experiment, morphology and distribution of the inclusions were observed and analyzed using scanning electron microscopy (SEM) and energy dispersive spectrometer (EDS).

Results and Analysis

In Situ Observation of Solidification and Inclusions Precipitation Behavior

The in situ observed results of liquid steel solidification and inclusions behavior during cooling process with a cooling rate of 0.45 °C/s are shown in Fig. 1.

The observation results indicated that some spherical inclusions and irregular inclusions initially floated on the surface of liquid steel before solidification, as shown in Fig. 1a. The solidification process of mushy zone undergone following stages. liquid phase L transformed initially into δ ferrite as shown in Fig. 1b, and

Table 1 Composition of steels investigated (mass fraction, wt%)

C	Mn	P	S	Si	Ca	Cr	Ti	Nb	N
0.16	1.12	0.017	0.002	0.21	0.002	0.05	0.053	0.008	0.0040

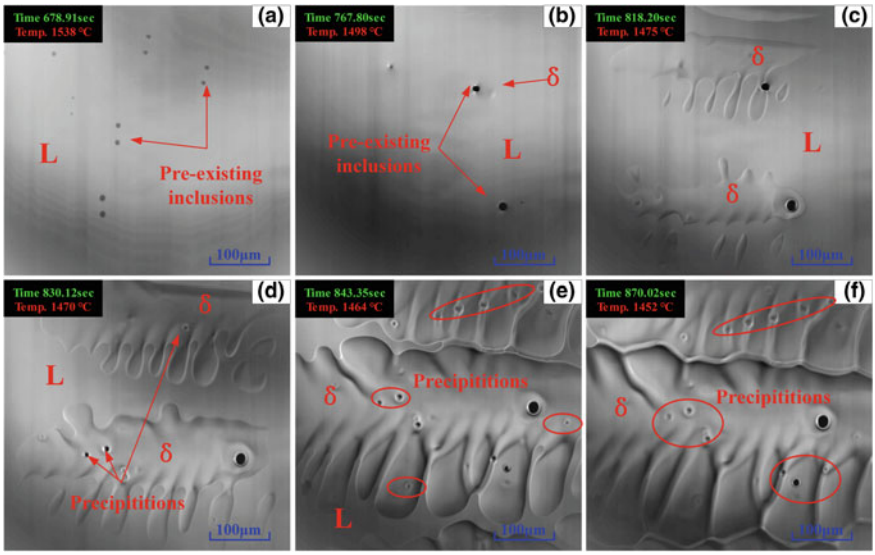

Fig. 1 In-situ observations of solidification and inclusions precipitation behavior

then *L* gradually transformed into the δ phase while the *L* and δ phases coexisted as shown in Fig. 1c. The δ ferrite grains growth continuously and then covered whole field of view when the temperature decreased to solidus temperature as shown in Fig. 1d–f. Meanwhile, the precipitation phenomenon of other inclusions which were different form pre-existing inclusions in liquid steel were not obviously observed during solidification of mushy zone. However, some embossments on the sample surface was observed to precipitate at the end of solidification from the dendrites front, which are shown by the red ellipse in Fig. 1e, and the amount and size of the embossments seem to increase with the continuous decrease in temperature, as shown in Fig. 1f. Since the composition of pre-existing inclusions and precipitations could not be identified in CLSM equipment, the quenching samples of inclusions examination were prepared with standard metallographic techniques and analyzed using scanning electron microscopy (SEM) and energy dispersive spectrometer (EDS).

Morphology and Composition of the Inclusions

After the in situ observation experiment, through the extraction of non-metallic inclusions in samples, it was found that the preexisted inclusions in molten steel were mainly dominated by the oxide inclusions (Al_2O_3, SiO_2), and TiN inclusions was not found in samples of quenching immediately, as shown in Fig. 2a. While many TiN inclusions were observed clearly in the simulating solidification sample.

Moreover, it was also found that some TiN particles precipitated with pure TiN composition in Fig. 2b and some complex TiN particles precipitated based on CaS inclusions or CaS-Al_2O_3 inclusions as the precipitation core in Fig. 2c–d. It means that CaS and TiN inclusions both precipitated in mushy zone, and the precipitation of CaS during solidification was prior to the TiN precipitation. These two kinds of TiN particle size were compared, and found that complex TiN particles size with CaS inclusions or CaS-Al_2O_3 inclusions as the core was significantly larger than the size of pure TiN particles, about lager than 1–3 μm. Since CaS or CaS-Al_2O_3 inclusions completely distributed in the core of TiN inclusions, and not change the contact interface morphology between TiN inclusions and the steel matrix, and it not alleviates the harm of TiN inclusions in mechanical properties. The angular and regular TiN inclusions in steel weaken the continuity of matrix and resulted in micro-crack nucleation under stress concentration during bending and straightening. Therefore, it is vital to control the formation of coarse TiN inclusions regardless of precipitated in CaS core or without CaS core.

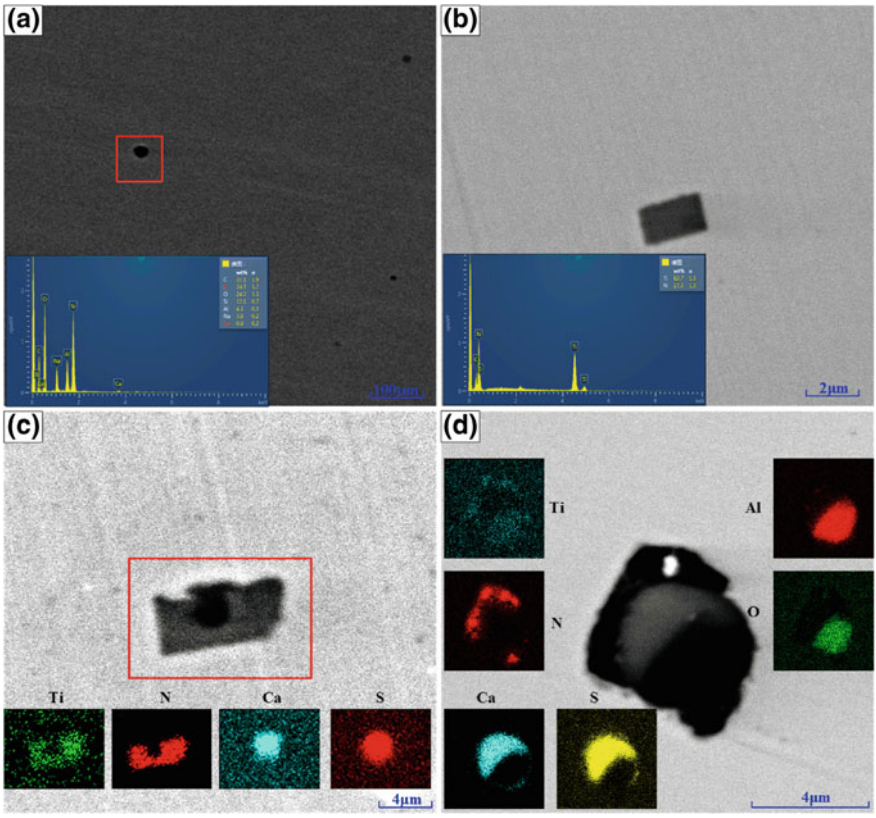

Fig. 2 SEM morphology and EDS results of the core and shell of inclusions: **a** oxide inclusions **b** pure TiN inclusions **c** and **d** complex TiN inclusions

Discussion

Thermodynamic Analysis on the Precipitation of CaS and TiN

The liquidus temperature and solidus temperature of the steel can be calculated according to following equation [18]:

$$\mathrm{T} = 1809 - \sum \Delta T_j \times \mathrm{w}[j] \tag{1}$$

where ΔT_j is the temperature coefficient of j element and w[j] is the mass percentage of j element. The liquidus and solidus temperature of current Ti microalloyed steel were 1513 °C and 1463.5 °C, respectively.

The experimental observation results show that those CaS and TiN inclusions precipitated in mushy zone. The solubility products for CaS and TiN were calculated based on the equilibrium analysis. The solubility constants for titanium nitride and calcium sulfide were described as follows [19]:

$$[\mathrm{Ti}] + [\mathrm{N}] = [\mathrm{TiN}]_{(\mathrm{s})} \quad \Delta \mathrm{G}^{\theta} = -291000 + 107.91\mathrm{T} \tag{2}$$

$$[\mathrm{Ca}] + [\mathrm{S}] = [\mathrm{CaS}]_{(s)} \quad \Delta \mathrm{G}^{\theta} = -530900 + 116.2\mathrm{T} \tag{3}$$

where $\Delta \mathrm{G}^{\theta}$ is the standard Gibbs free energy, J/mol; T is the temperature, K.

The actual change in the Gibbs free energy during the formation of TiN and CaS can be calculated as follows:

$$\Delta \mathrm{G} = \Delta \mathrm{G}^{\theta} + RTln\frac{1}{f_{Ti} * w[Ti] * f_{N]} * w[N]} = \Delta \mathrm{G}^{\theta} - RTln\mathrm{Q}_{TiN} \tag{4}$$

$$\Delta \mathrm{G} = \Delta \mathrm{G}^{\theta} + RTln\frac{1}{f_{Ca} * w[Ca] * f_S * w[S]} = \Delta \mathrm{G}^{\theta} - RTln\mathrm{Q}_{CaS} \tag{5}$$

The actual concentrations of solute atoms during actual solidification process changes due to microsegregation, which results in solute element segregation and enrichment between the dendritic crystals [4]. It can subsequently lead to the great segregation ratios and the concentrations continuous enhancement at the solidification front. The segregation ratio w[j]/w[j_0] of element j can be calculated for the given cooling rate according to the Ohnaka's equations [20]:

$$\frac{w[j]}{w[j_0]} = \left[1 - \left(1 - \frac{\beta k}{1+\beta}\right) f_s\right]^{(k-1)/\left(1-\frac{\beta k}{1+\beta}\right)} \tag{6}$$

$$\beta = \frac{4D_j\tau}{L^2} \tag{7}$$

where $w[j]$ is the mass fraction of solute element j at the solidification front, %; $w[j_0]$ is the original mass fraction of solute j in liquid region, %; k is the equilibrium distribution coefficient of the solute element j; f_s is the solid fraction; D_j is the diffusion coefficient of solute j in solid phase, cm^2/s; and τ is the local solidification time, s; L is the secondary dendrite arm spacing, μm.

The local solidification time τ can be calculated as follow:

$$\tau = \frac{T_L - T_S}{R_C} \tag{8}$$

The secondary dendrite arm spacing L is a function of cooling rate R_C (K/s), which is obtained by the following equation [21]:

$$L = 148 \times R_C^{-0.38} \tag{9}$$

In Ohnaka's segregation model, the Scheil model is obtained for the limiting case when $\beta \to 0$. In the limiting case of when $\beta \to \infty$, it is inconsistent with the lever rule. Clyne and Kurz [22] proposed a modified Eq. (12) to correct β.

$$\beta' = \beta \times \left(1 - exp\left(-\frac{1}{\beta}\right) - \frac{1}{2} exp\left(-\frac{1}{2\beta}\right)\right. \tag{10}$$

In addition, the solidification front temperature T_{L-S} of the mushy region is obtained by the following equation [23]:

$$T_{L-S} = T_0 - \frac{T_0 - T_L}{1 - g\frac{T_L - T_s}{T_0 - T_s}} \tag{11}$$

where T_0 is the melting point of pure iron (1809 K).

The equilibrium constant of CaS and TiN precipitation, which is only related with the temperature $T_{L\text{-}S}$ of solidifying front, can be obtained as follow [24]:

$$K_{TiN} = \exp\frac{\Delta G^\theta}{RT} = 13.01 - \frac{35217.7}{T} \tag{12}$$

$$K_{CaS} = \exp\frac{\Delta G^\theta}{RT} = 5.90 - \frac{19980}{T} \tag{13}$$

where K_{TiN} is the equilibrium constant of TiN; K_{CaS} is the equilibrium constant of CaS.

In this study, Ca, S, Ti and N concentrations change in front of the dendritic crystals were analyzed. The variations of the equilibrium solubility products lgK_{TiN}, lgK_{CaS} and the actual concentration products lgQ_{TiN}, lgQ_{CaS} with solid fraction are calculated and shown in Fig. 3. The actual concentration products lgQ_{TiN}, lgQ_{CaS} increased gradually during solidification. While the equilibrium solubility products

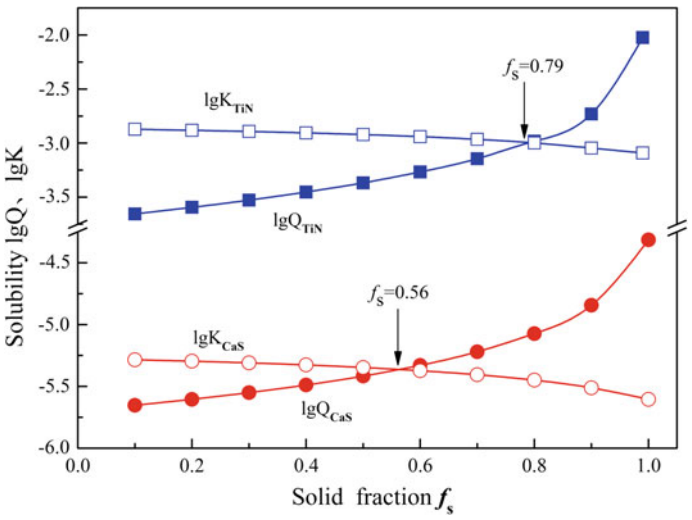

Fig. 3 Variations of equilibrium solubility products and the actual concentration products with solid fraction increasing

lgK_{TiN}, lgK_{CaS} reduced with temperature decreasing. When the solid fraction reached 0.56 and 0.79, CaS and TiN inclusions began to precipitate from the dendrites, respectively. In other words, CaS precipitated before than TiN. In previous inclusions investigations, it has been observed that CaS and TiN can be form in mushy zone during solidification.

Control of CaS and TiN Precipitation Behavior in Mushy Zone

To control of CaS and TiN precipitation behavior in mushy zone, the effect of N and S contents on TiN and CaS precipitation behavior during solidification were researched. The calculation results are illustrated in Fig. 4. As shown in Fig. 4a, initial titanium content w(Ti_0) was assumed to be 0.053 wt%, the solid fraction for the first TiN precipitation was effective delayed from 0.620 to 0.895 when nitrogen content was decreased from 80 ppm to 20 ppm, namely, TiN inclusions would be precipitated at lower temperature with nitrogen content decreasing. Similarly, as shown in Fig. 4b, initial calcium content w(Ca_0) was assumed to be 0.002 wt%, the solid fraction for the first CaS precipitation was effective delayed from 0.278 to 0.795 when sulfur content was decreased from 34 to 8 ppm. Comparing the results of precipitations between TiN and CaS, it reveals that TiN inclusions could be prevented from precipitation at the surface of CaS inclusions when the S content of molten steel was less than 0.0008 wt%. Meanwhile, TiN precipitation was more and

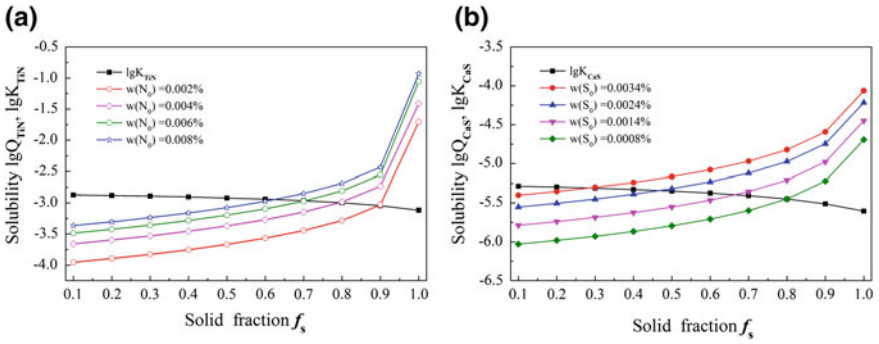

Fig. 4 Effect of N and S content on TiN and CaS precipitation during the solidification: **a** N content **b** S content

more close to the end of solidification with decreasing nitrogen content in steel, and then effectively reduce the growth time of TiN inclusions.

Summary

(1) The experimental results show that CaS and TiN inclusions precipitate in mushy zone of solidification for the current Ti-microalloyed steel, and complex TiN particles size with CaS inclusions or CaS-Al_2O_3 inclusions as the core is significantly greater than the size of pure TiN particles.
(2) The thermodynamic calculation shows that CaS inclusions firstly precipitated when the solidification fraction is higher than 0.56, and TiN particles precipitated when the solidification fraction is higher than 0.79 for the current microalloyed steel.
(3) Decreasing the initial nitrogen content can effectively reduce the TiN precipitation temperature, similarly, reduce the total sulfur content can also effectively delay the precipitation of CaS inclusion during solidification.
(4) The calculation results show that initial sulfur content less than 8 ppm can effectively prevent the TiN inclusions precipitation at the surface of CaS inclusions.

Acknowledgements This work was financially supported by the Natural Science Foundation of China (NSFC, project no. 51374260, 51504048 and 51611130062).

References

1. Chen J (2013) Influence of deformation temperature on γ-α phase transformation in Nb–Ti microalloyed steel during continuous cooling. ISIJ Int 53(6):1070–1075
2. Ralph BHKDK, Bhadeshia RWK (2006) Honeycombe steels (Microstructure and properties), 3rd edn. Elsevier, Amsterdam. 978-0-750-68084-4344; Mater Charact 59(3):348
3. Guo YT, He SP, Chen GJ, Wang Q (2016) Thermodynamics of complex sulfide inclusion formation in Ca-Treated Al-Killed Structural Steel. Metallurg Mater Trans B 47(4): 2549–2557
4. Liu Y, Zhang L, Duan H, Zhang Y, Luo Y, Conejo AN (2016) extraction, thermodynamic analysis, and precipitation mechanism of MnS-TiN complex inclusions in low-sulfur steels. Metallurg Mater Trans A 47(6):3015–3025
5. Holappa L, Hämäläinen M, Liukkonen M, Lind M (2013) Thermodynamic examination of inclusion modification and precipitation from calcium treatment to solidified steel. Ironmaking Steelmaking 30(2):111–115
6. Xu G, Jiang Z, Li Y (2016) Formation mechanism of CaS-bearing inclusions and the rolling deformation in al-killed, low-alloy steel with Ca treatment. Metall Mater Trans B 47(4): 2411–2420
7. Prikryl M, Kroupa A, Weatherly GC, Subramanian SV (1996) Precipitation behavior in a medium carbon, ti-v-n microalloyed steel. Metall Mater Trans A 27(5):1149–1165
8. Yan W, Shan YY, Yang K (2006) Effect of TiN inclusions on the impact toughness of low-carbon microalloyed steels. Metall Mater Trans A 37(7):2147–2158
9. Yan W, Shan YY, Yang K (2007) Influence of TiN inclusions on the cleavage fracture behavior of low-carbon microalloyed steels. Metall Mater Trans A 38(6):1211–1222
10. Strangwood M, Davis CL (2012) Effect of TiN particles and grain size on the charpy impact transition temperature in steels. J Mater Sci Technol 28(10):878–888
11. Ma F, Wen G, Tang P, Yu X, Li J, Xu G et al (2010) In situ observation and investigation of effect of cooling rate on slab surface microstructure evolution in microalloyed steel. Ironmaking Steelmaking 37(3):211–218
12. Dou K, Meng L, Liu Q, Liu B, Huang Y (2016) Influence of cooling rate on secondary phase precipitation and proeutectoid phase transformation of micro-alloyed steel containing vanadium. Met Mater Int 22(3):349
13. Mintz B (2008) Understanding the low temperature end of the hot ductility trough in steels. Mater Sci Technol 24(1):112–120
14. Carpenter KR, Dippenaar R, Killmore C (2009) Hot ductility of Nb-and Ti-bearing microalloyed steels and the influence of thermal history. Metall Mater Trans A 40(3):573–580
15. Zhang LP, Davis CL, Strangwood M (2001) Dependency of fracture toughness on the inhomogeneity of coarse TiN particle distribution in a low alloy steel. Metall Mater Trans A 32(5):1147–1155
16. Shibata H, Arai Y, Suzuki M, Emi T (2000) Kinetics of peritectic reaction and transformation in Fe-C alloys. Metall Mater Trans B 31(5):981–991
17. Long M, Dong Z, Chen D, Zhang X, Zhang L (2015) Influence of cooling rate on austenite transformation and contraction of continuously cast steels. Ironmaking Steelmaking 42(4):1743281214Y.000
18. Maehara Y, Yasumoto K, Tomono H, Nagamichi T, Ohmori Y (1990) Surface cracking mechanism of continuously cast low carbon low alloy steel slabs. Mater Sci Technol 6(9):793–806
19. Jong-Jin P, Jong-Oh JO, Sun-In K, Wan-Yi K, Tae-In C, Seok-Min S et al (2007) Thermodynamics of titanium and oxygen dissolved in liquid iron equilibrated with titanium oxides. ISIJ Int 47(1):16–24
20. Ohnaka I (1986) Mathematical analysis of solute redistribution during solidification with diffusion in solid phase. Trans Iron Steel Inst Jpn 26(12):1045–51

21. El-Bealy M, Thomas BG (1996) Prediction of dendrite arm spacing for low alloy steel casting processes. Metall Mater Trans B 27(4):689–693
22. Clyne TW, Kurz W (1981) Solute redistribution during solidification with rapid solid state diffusion. Metall Mater Trans A 12(6):965–971
23. Ma W-J, Bao Y-P, Zhao L-H, Wang M (2014) Control of the precipitation of TiN inclusions in gear steels. Int J Miner Metall Mater 21(3):234-9
24. Liu Y, Zhang L, Duan H, Zhang Y, Luo Y, Conejo AN (2016) Extraction, thermodynamic analysis, and precipitation mechanism of MnS-TiN complex inclusions in low-sulfur steels. Metall Mater Trans A 47(6):3015–3025

Part XXIV
General Poster Session

Additive Manufacturing of Epoxy Resin Matrix Reinforced with Magnetic Particles

Jose J. Restrepo and Henry A. Colorado

Abstract In this research, polymer composites of epoxy resin matrix with magnetite particles were fabricated by additive manufacturing using the direct ink writing (DIW) technique. Four different formulations of epoxy resin-magnetite powders were fabricated, from which only one showed promising results regarding the dimensional stability and finishing of the printed samples. Four formulations were found to be feasible for the printing process, in which epoxy resin was varied from 32.6 to 41 wt%, while the magnetite powder changed from 67.4 to 69 wt% correspondingly. Compression tests were performed over all printed parts, compressive strength mean values and ductility results are presented. In addition, microstructural characterization was performed by scanning electron microscopy (SEM).

Keywords Additive manufacturing · Direct ink writing (DIW)
Polymer matrix composites · Epoxy resin · Magnetite

Introduction

Additive manufacturing (AM) or 3D printing [1] is a fabrication technique in which a part is produced from a computer 3D model [2] by aggregating (printing) material layer by layer. The shapes are printed directly from computer aided design (CAD) files [3]. The AM has been developed for almost all known materials, from ceramics such as concrete [4], clays [5], biomaterials [6], composites [7, 8], and wood [9].

J. J. Restrepo
CCComposites Laboratory, Universidad de Antioquia UdeA, Calle 70 N°. 52-21, Medellín, Colombia

H. A. Colorado (✉)
Facultad de Ingenieria, Universidad de Antioquia, Bloque 20, Calle 67 No. 53 - 108, Medellín, Colombia
e-mail: henry.colorado@udea.edu.co

The Minerals, Metals & Materials Society, *TMS 2018 147th Annual Meeting & Exhibition Supplemental Proceedings*, The Minerals, Metals & Materials Series,
https://doi.org/10.1007/978-3-319-72526-0_58

Diverse additive manufacturing technologies are now available involving many techniques and materials [3], however, the Direct Ink Writing (DIW) or robocasting [10, 11] technique is one of particular interest because it can be used not only in many diverse materials and compositions, but also everywhere since the technology and its printing raw materials are easy to produce. This investigation contributes to this lack in additive manufacturing data for inexpensive both process and materials, and also uses magnetite as a reinforcement with is a multifunctional material due to its ferromagnetic, pigment, and other versatile properties few explored in polymer matrix composites. Compressive strength, ductility and scanning electron microscopy are presented in this research.

Experimental

Epoxy resin-magnetite composites have been used for the fabrication of samples with additive manufacturing. The magnetite is an inexpensive commercial magnetite powder, less than 3USD/Kg in Colombia. The direct ink writing (DIW) technique was used as the advance manufacturing technique, obtained from the modification of a Maker-R 3D printer apparatus, see Fig. 1a. Samples were made of 10 mm length, 10 mm height, and 40 mm length. Figure 1b shows a typical sample under the printing process.

Four different blends of epoxy resin and magnetite were fabricated with the formulations summarized in Table 1. These formulations were found by trying different combinations and printing them in the machine, thus, only for the compositions shown the mix was feasible to produce a stable shape sample. Therefore, out of this compositions, if more resin is added (more than 41 wt%), the printed sample for the involved materials will most likely collapse. On the contrary, if less

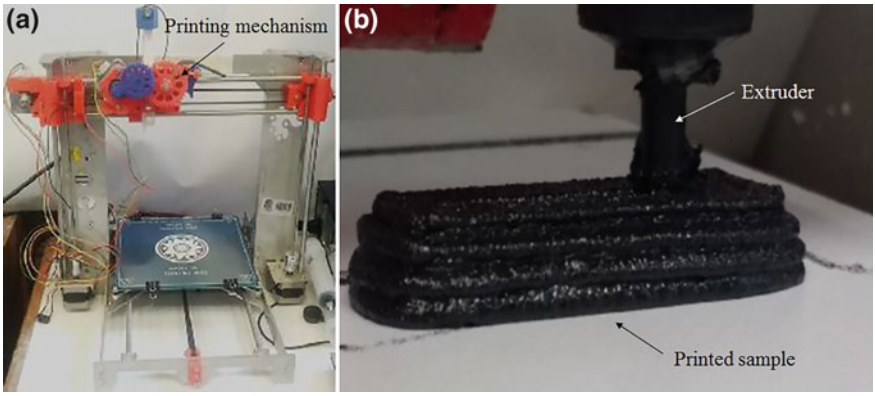

Fig. 1 **a** Direct ink writing machine used in this research, **b** detail of the printing process of epoxy resin with magnetite powder

Table 1 Formulations epoxy resin and magnetite fabricated in this research

Sample	Epoxy (wt%)	Magnetite (wt%)
R33_M67	32.6	67.4
R34_M66	33.6	66.4
R35_M65	35.4	64.6
R41_M59	41	59

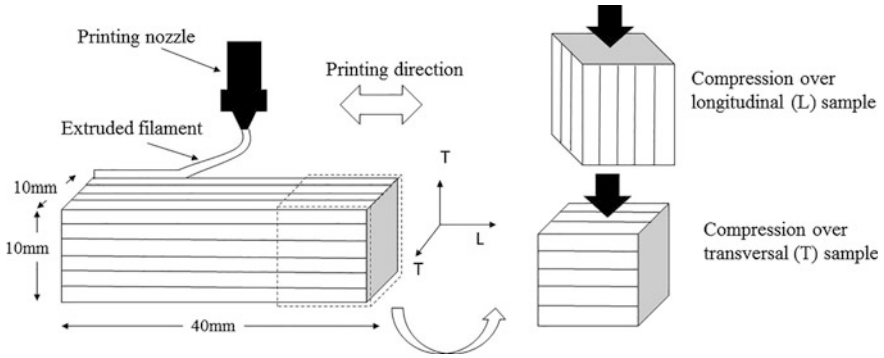

Fig. 2 Representation of samples cut for compression tests from printed samples, longitudinal and transversal samples

resin is added (less than 33 wt%), for the printing system used in this research, the viscosity is too high that will be not flow and thus the printing process will be not possible.

Compression tests were performed over printed samples in a Shimadzu AG250KN universal testing machine at 5 mm/min. Samples for compression were obtained from printed parallelepiped samples as shown in Fig. 2. Two samples type were tested, cube shaped samples cut longitudinally with respect the printing direction, and cube shaped samples cut transversally with respect the printing direction.

Results and Analysis

Figure 3 shows typical defects present in the printed samples. Pores have sizes from 50 to 500 μm, see Fig. 3a. These pores come from the processing itself, since no vacuum processing was done, voids like micro pores naturally appear in the resin for the mixing process and as air trapped in the ceramic powder as well. The particle impregnation by the resin in general was found goo for all sample formations, a typical mix epoxy resin-magnetite powder is shown in Fig. 3b.

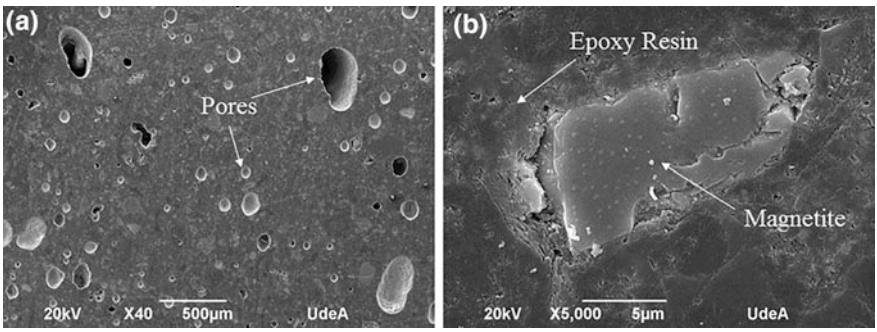

Fig. 3 Typical defects of epoxy resin with magnetite powder in two different magnifications: **a** pores at 40×, **b** magnetite grains at 5000×

Figure 4 shows different cracks generated during the compression tests. In general, samples with less resin had a less catastrophic failure, while samples with more resins showed a more intense failure.

Figure 5a shows typical stress-strain curves under compression for the powder-resin blends fabricated in this research by direct ink writing. These curves correspond to a ductile composite material as expected.

Figure 5b is a representation of the mean compressive strength data, with its corresponding standard deviation, for the different samples fabricated. Each composition represents the summary of 6 compression tests averaging transverse and

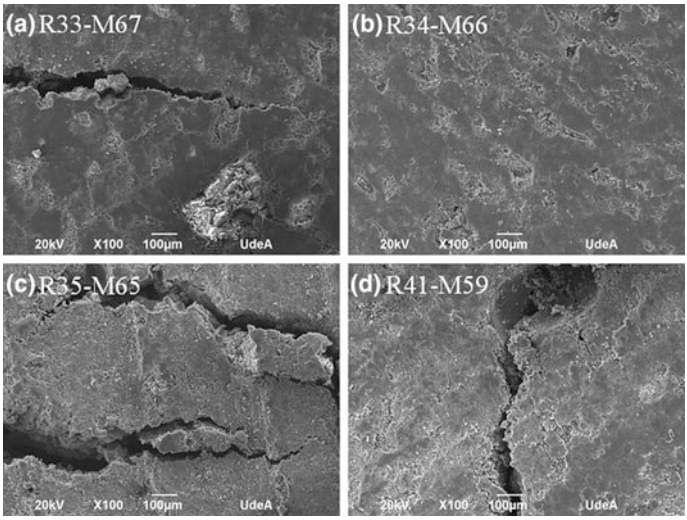

Fig. 4 Typical cracks obtained in the samples under compression loads for **a** R33-M67, **b** R34-M66, **c** R35-M56, and **d** R41-M59

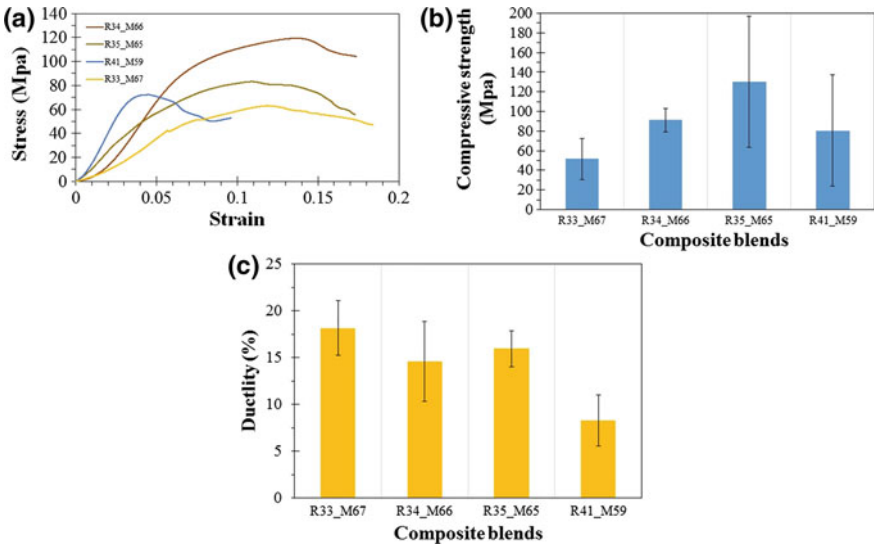

Fig. 5 Compressive strength results **a** typical stress-strain curves obtained under compression test, **b** mean maximum compression strength, **c** ductile mean for samples fabricated

longitudinal direction samples. Clearly, there is a maximum value in compression in curve with a parabolic trend concave downwards, corresponding to the formulation R35-M65. Also, error bars size increased as the resin content increased.

Finally, Fig. 5c is a ductility curve for the same samples under compression loads, fabricated from the mean and standard deviation values of six compression data per composition. From image it is observed that as the resin contents increases, ductility decreases.

Discussion

The direct ink writing process used in this research was successful in producing the epoxy resin with magnetite particles. Since the process was without vacuum, many structural defect appeared, which certainly has a tremendous impact in the compressive strength, ductility and other derived properties not quantified in this investigation. However, this is not at all a negative result for two things. First, the no vacuum means it is a super simple process able to be used elsewhere and with low costs. Second, the compressive values were still very high, in all cases compressive strength was over 20 MPa, and in the main compositions the minimum value was near 80 MPa, which is high in structural applications, such as concrete, where his value corresponds to a high performance concrete. Maximum values were up to 200 MPa, which gives an idea of an optimized composition going near 300 MPa or in the mean values.

On the other hand, ductility shows a trend to decrease as the resin content increase (or as the magnetite powder decreased). This can be associated with two factors: first, the sample porosity could be increased significantly the failure, the crack growing of samples is accelerated with more pores under high loadings. Second, most likely the adhesion strength of resin to particles is not good even the impregnation is acceptable. More investigation is needed in order to quantify and improve these results.

Conclusion

In this investigation were printed successfully epoxy resin with magnetite particles. Upon the trying of many different composition without the use of any other additive, four formulations were successful for the consolidation of stable printed samples, whose results are shown here. Compressive strength and ductility had very compressive values if these composite is used as structural material.

References

1. Gibson I, Rosen DW, Stucker B (2010) Additive manufacturing technologies, vol 238. Springer, New York
2. Zocca A, Colombo P, Gomes CM, Günster J (2015) Additive manufacturing of ceramics: issues, potentialities, and opportunities. J Am Ceram Soc 98(7):1983–2001. https://doi.org/10.1111/jace.13700
3. Travitzky N, Bonet A, Dermeik B, Fey T, Filbert-Demut I, Schlier L, Schlordt T, Greil P (2014) Additive manufacturing of ceramic-based materials. Adv Eng Mater 16(6):729–754
4. Gosselin C, Duballet R, Roux P, Gaudillière N, Dirrenberger J, Morel P (2016) Large-scale 3D printing of ultra-high performance concrete—a new processing route for architects and builders. Mater Des 100:102–109
5. Revelo CF, Colorado HA (2018) 3D printing of kaolinite clay ceramics using the direct ink writing (DIW) technique. Ceram Int (in press)
6. Kumar A, Mandal S, Barui S, Vasireddi R, Gbureck U, Gelinsky M, Basu B (2016) Low temperature additive manufacturing of three dimensional scaffolds for bone-tissue engineering applications: processing related challenges and property assessment. Mater Sci Eng: R: Rep 103:1–39
7. Quan Z, Wu A, Keefe M, Qin X, Yu J, Suhr J, Chou TW (2015) Additive manufacturing of multi-directional preforms for composites: opportunities and challenges. Mater Today 18 (9):503–512
8. Kaisaki DA, Mitra SB, Schultz WJ, DeVoe RJ (1999) U.S. Patent No. 5,856,373. U.S. Patent and Trademark Office, Washington, DC
9. Clemons C (2002) Wood-plastic composites in the United States: the interfacing of two industries. Forest Prod J 52(6):10
10. Lewis JA, Smay JE, Stuecker J, Cesarano J (2006) Direct ink writing of three-dimensional ceramic structures. J Am Ceram Soc 89(12):3599–3609
11. Lewis JA (2006) Direct ink writing of 3D functional materials. Adv Funct Mater 16 (17):2193–2204

Admixture Optimization in Concrete Using Superplasticizers

Andrea Munoz, Sergio Cifuentes and Henry A. Colorado

Abstract The main goal of this paper is to optimize superplasticizer admixtures in concrete in order to reduce the amount of Portland cement in concrete mixtures. There are two main positive impacts of decreasing the amount of Portland cement: first, less cement in concrete reduces the CO_2 that is released into air, so it is more environmentally friendly, and second, less cement reduces the production costs of concrete. Two types of superplasticizers were used with different dosages of admixture. In the first type, dosages were 0.8 and 1.0% (per weight of cement) and in the second type they were 0.9 and 1.1% (per weight of cement). Workability, porosity, compressive strength, granulometry and microscopy tests were conducted for a large number of sample formulations. Compressive strength was tested after 7, 14, 21 and 28 days of curing. The results show the optimal ratio of fine and coarse aggregate, the optimal amount of water, the optimal mixture of cement and aggregates, and the optimal dosage of superplasticizer to increase workability and compressive strength and reduce the cement/water ratio.

Keywords Admixture · Concrete · Environmental · Superplasticizer

A. Munoz · H. A. Colorado (✉)
CCComposites Laboratory, Universidad de Antioquia UdeA, Calle 70 No. 52-21, Medellín, Colombia
e-mail: henry.colorado@udea.edu.co

A. Munoz · S. Cifuentes
Conasfaltos S. A., Medellín, Colombia

H. A. Colorado
Facultad de Ingenieria, Universidad de Antioquia, Bloque 20, Calle 67 No. 53 - 108, Medellín, Colombia

The Minerals, Metals & Materials Society, *TMS 2018 147th Annual Meeting & Exhibition Supplemental Proceedings*, The Minerals, Metals & Materials Series,
https://doi.org/10.1007/978-3-319-72526-0_59

Introduction

Additives that reduce the amount of water in concrete or super-plasticizers (SPs) are now used extensively in order to produce high strength concrete with a low water to cement ratio (W/C) while conserving the necessary conditions for optimum setting and concrete compaction [1]. Most of these super-plasticizers are surfactants with a high surface activity and reactivity due to the fact that their chemical composition involves hydrophilic and hydrophobic groups. Super-plasticizers are high-density molecular polymers that are soluble in water [2, 3].

There are four main types of super-plasticizers widely used in the concrete industry: sulphonated melamine formaldehyde condensate (SMF), sulphonated naphthalene formaldehyde condensate (SNF), modified lignosulphonates (MLS) and lignosulphonate (LS) [4–6].

Several studies involving the effects of super-plasticizer additives on the hydration of cement and their effects on the microstructure of cement paste have been summarized in previous articles [7, 8]. Most of this research agrees that the dispersive action of the SP is due to the adsorption of SP molecules onto the surface of the hydrating cement grains during the initial hydration process. Some explanations [7] are centered on the interactions between Ca ions and the anionic parts of the polymer additives. Additives create crosslinking, which inhibits film-forming properties and changes the crystallization parameters during the cement hardening. The interaction between Ca(OH) and the ionic parts of the additives also plays an important role.

It is accepted that some conventional SPs, such as sulphonated naphthalene formaldehyde condensate (SNF) and modified lignosulphonates (MLS), are absorbed by cement grains through the action of anionic groups (negatively charged). These give the cement grains a negative charge and cause them to electrostatically repel each other. Moreover, three main factors influence the delaying effect of SPs on the cement hydration process [7]:

(a) Superplasticizer molecules already absorbed obstruct the diffusion of water and Ca^{+2} ions at the cement solution interface.
(b) The Ca^{+2} ions produce complexes when reacting with the SP molecules, which inhibit nucleation and precipitation of species containing Ca.
(c) The dispersive action of these admixtures alters the growth kinetics and morphology of the hydration products.

The new generation of SPs centers on synthetic polymers with a base in polycarboxylates. These are typically from a polymerization derived process involving acrylic (CH_2=CH–COOH) and methacrylic (CH_2=C(CH_3)–COOH) acids. Electrostatic repulsion between the cement particles also occurs with these SPs, specifically associated to repulsion between long chain molecules of ether groups. However, more details need to be understood about how these SPs influence the cement paste [7–9].

In this paper, 14 samples were fabricated using the Box-Behnken experimental design, with three factors corresponding to two aggregates and two additives. Diverse characterization including scanning electron microscopy (SEM) and compression and particle-size distribution tests are also presented.

Experimental Method

Ordinary Type I Portland cement was used in this investigation, with some data supplied by the manufacturer, Cementos Argos, summarized in Tables 1 and 2.

Two different aggregate types from the Conasfaltos S.A. company were used in this research. Some characterization data is shown in Table 3.

Two different additives were used following ASTM C 494, which is the Standard Specification for Chemical Admixtures of concrete. Additive S1 based on polycarboxylate was used at 0.8 wt% and 1 wt% of the cement weight, while additive S2 based on naphthalene was used at 0.9 wt% and 1.1 wt% of the cement weight. These additive contents were selected based on the recommendations of the additive manufacturers.

In this research, the Box-Behnken experimental design was used, in which each factor or independent variable is given a typical value of −1, 0, 1. Tables 4 and 5 summarize the method.

Table 1 Chemical information for cement supplied by Cementos Argos

Chemical information	Argos cement data	NTC 321 Tipo I	ASTM C-1157
MgO, max (%)	6.00	7.00	–
SO, max (%)	3.50	3.50	–

NTC 321 is the Colombian standard based on ASTM C 150

Table 2 Physical parameters for cements

Parameters	Argos standard	NTC 121 Tipe I	ASTM C-1157
Initial setting[a], lowest value (min)	45	45	45
Final setting[a], maximum value (min)	420	480	420
Autoclave expansion, max (%)	0.8	0.8	0.8
Water expansion[b], max (%)	0.02	–	0.02
Strength at 28 days[c], min (MPa)	26.0	24.0	28.0
Blaine, min (cm^2/g)	2800	2800	–

NTC 121 is the Colombian standard based on ASTM C 150

[a]Vicat needle tests following NTC 118 (ASTM C191)

[b]Tests on mortar bars after 14 days following NTC 4927 (ASTM 1038)

[c]Compression tests on mortar cubes with standard sand following NTC 220 (ASTM C109)

Table 3 Characteristics of the aggregates used in this research

Property	Fine aggregate	Coarse aggregate
Loose mass (kg/m^3)	1363	1630
Compact mass (kg/m^3)	1541	1693
Apparent specific weight	2.81	2.78
Fineness modulus	3.08	3.62
Organic matter content (NTC 174)	1	1
Sulfate soundness test (NTC 174) (%)	2.8	1,5
Clay lumps and friable particles in aggregate (%) (NTC 174)	0.7	0.67
Carbon and lignite (NTC 174)	0.01	0
Alkali-silica reactivity	Not harmful	Not harmful
Absorption (%)	1.65	1.34
Passing sieve 75 μm (%)	2.7	6.1

NTC 174 is the Colombian standard based on ASTM C 33

Table 4 Factors of the experimental design

Name	Factors	Unit	−1	1
A	Additive S1	%	0.8	1.0
B	Additive S2	%	0.9	1.1
C	Aggregate	Size	Fine	Coarse

Table 5 Experimental design

Sample	A	B	C
1	1	0	1
2	−1	0	1
3	1	0	−1
4	−1	0	−1
5	0	−1	1
6	0	1	1
7	0	1	−1
8	0	−1	−1
9	0	0	1
10	0	0	−1
11	1	0	0
12	−1	0	0
13	0	1	0
14	0	−1	0

Cubic mortar samples of 5 cm^3 were made with a water to cement ratio (W/C) of 0.485, and an aggregate to cement ratio (A/C) of 2.69/1 and 2.73/1 for fine and coarse aggregate respectively. The additives were added to the water. The samples were cured for 7, 14, 21 and 28 days at 23 °C. After 28 days, the samples were submerged in acetone in order to prevent a hydration reaction. Thereafter, samples were dried for 24 h at 55 °C in a regular open furnace.

Compressive strength was tested at 7, 14, 21 and 28 days following the ASTM C 109 standard. Samples cured for 28 days were observed by scanning electron microscopy. For SEM tests, the samples were broken so that the exposed fractured surface could be observed and sputtered in a Hummer 6.2 system (15 mA AC for 30 s), creating a gold film approximately 1 nm thick.

Results and Discussion

Granulometry tests for the aggregates are shown in Figs. 1 and 2. The granulometry tests show a good size distribution due to the small but continuous changes from low to high values for both the fine and coarse aggregates.

Figures 3, 4, 5, 6 and 7 show the effect of additives on the compressive strength. In all cases, the strength increases with an increase in additive content. As a general

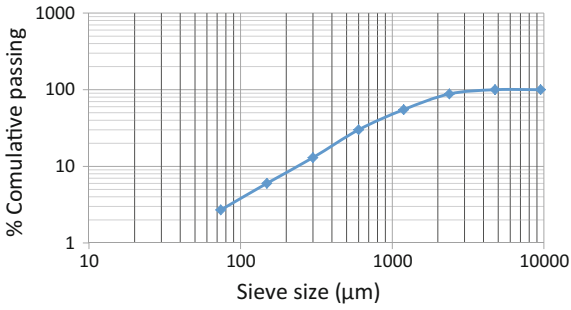

Fig. 1 Granulometry results for fine aggregate

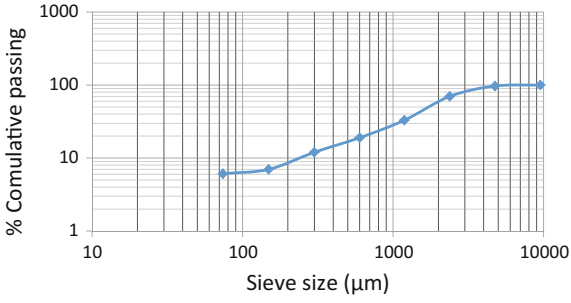

Fig. 2 Granulometry results for coarse aggregate

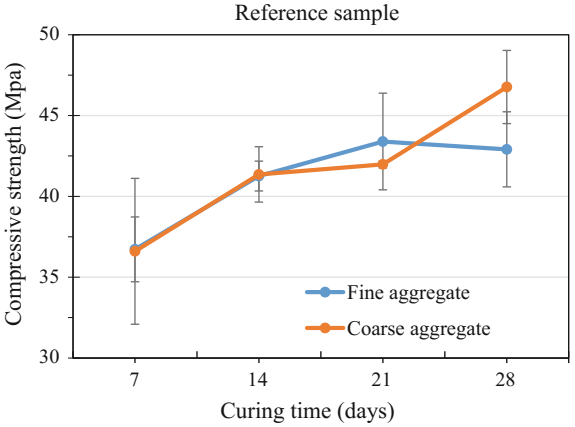

Fig. 3 Compressive strength for the reference samples, without additives

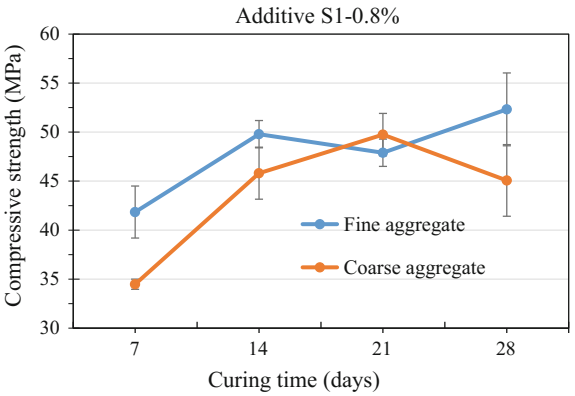

Fig. 4 Compressive strength for samples with 0.8 wt% of S1 additive

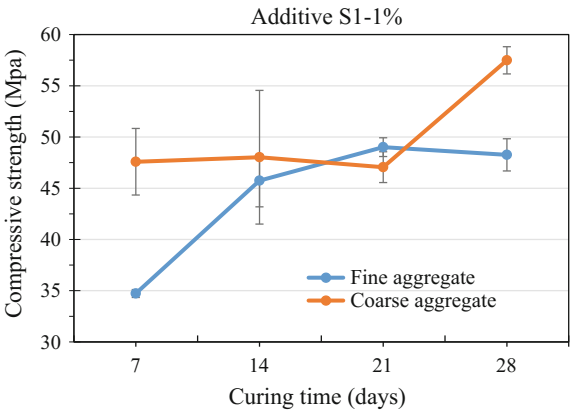

Fig. 5 Compressive strength for samples with 1.0 wt% of S1 additive

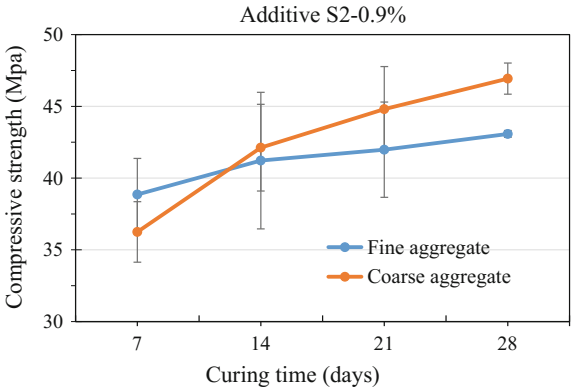

Fig. 6 Compressive strength for samples with 0.9 wt% of S2 additive

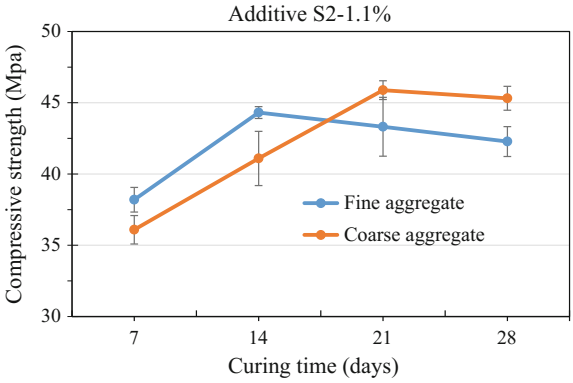

Fig. 7 Compressive strength for samples with 1.1 wt% of S2 additive

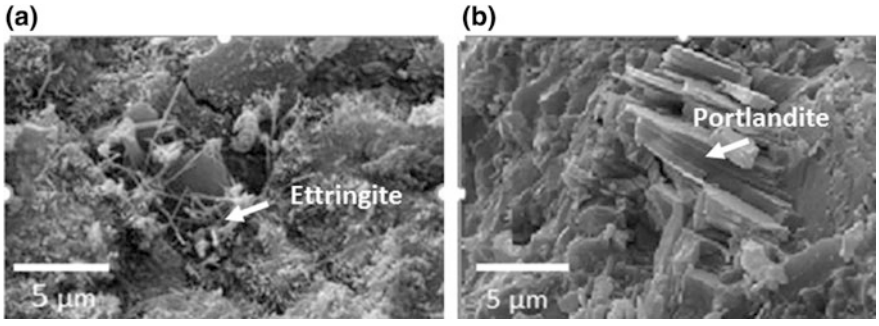

Fig. 8 SEM of samples at 5000× magnification: **a** with coarse aggregate, **b** with fine aggregate

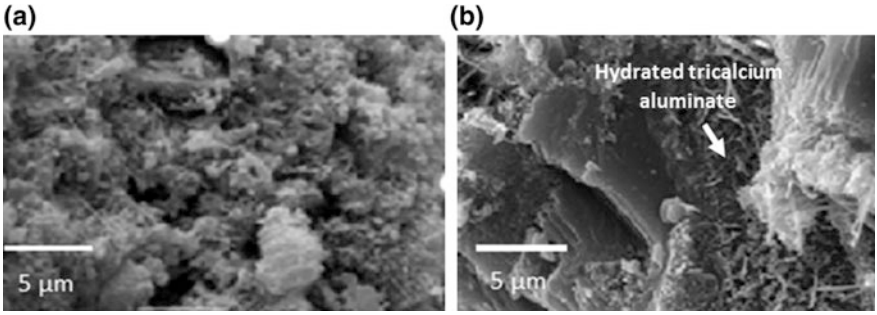

Fig. 9 SEM at 5000× magnification: **a** 0.8% S1 additive, **b** 1% S1 additive

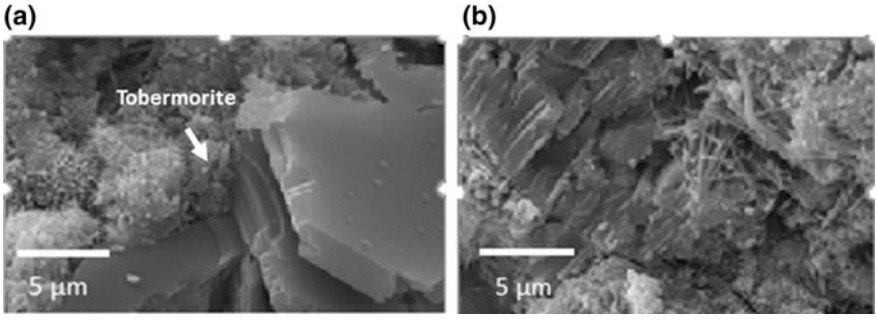

Fig. 10 SEM at 5000×: **a** 0.9% S2 additive, **b** 1.1% S2 additive

trend, additive S1, based on polycarboxylate, produces a bigger increase in strength than additive S2, based on naphthalene. Samples with coarse aggregate show a better performance in terms of compressive strength when compared with fine aggregate based samples. This increase is about 10 MPa.

SEM results are presented in Figs. 8, 9 and 10. These images reveal the presence of tobermorite (C-S-H, $C_3S_2H_3$), portlandite (CH, $Ca(OH)_2$) and ettringite ($Ca_6Al_2(SO_4)_3(OH)_{12} \cdot 26H_2O$) phases. Hydrated tricalcium aluminate (C_3AH_6) was also observed. Additionally, some micro-cracks associated with hydration reactions [10] can be seen in Figs. 8a and 10b.

Summary and Conclusion

The use of superplasticizer (SP) additives can significantly change the setting time of cement paste and change other important properties. In this research, it was shown that when using the additive S1 (based on polycarboxylate) the initial setting time was delayed and the final setting time was increased. When using the additive

S2 (based on naphthalene), no changes in either setting times were detected. In general, both additives improved workability, however, S1 showed a bigger improvement than S2. Moreover, S1 contributes to the increase in compression strength of the hardened cement paste, while S2 does not. Therefore, the results in this investigation confirm that admixtures based on carboxylates produce better properties in cements than similar admixtures based on naphthalene. The combination of these additives (SP) with processed wastes [11, 12] could be used to reduce SP costs making this solution even more suitable for not only high technical and massive structures but also for low volume uses.

Acknowledgements The authors wish to thank Conasfaltos S.A. for its support in this Project.

References

1. Nilson AH (2001) Diseño de estructuras en concreto, Santafé de Bógota. McGraw-Hill Interamericana, S.A., Colombia
2. Roncero J, Gettu R (1998) Aditivos superfluidificantes para hormigones de altas prestaciones. IV Simposio ANFAH, Especialidades Químicas para la Construcción
3. Edmeades RM, Hewlett PC (1998) Cement admixtures. In: Hewlett PC (Arnold) (ed) LEA'S chemistry of cement and concrete, 5th edn, p 589
4. Ramachandran VS, Malhotra VM, Jolicocur C, Spiratos N (1998) Superplasticizers: properties and applications in concrete. CANMETEd, pp 45–48
5. Usher PM, Angles JG, Rixom RM, Ryle RK (1980) Guide to chemical admixtures for concrete. The Concrete Society, London
6. Ramachandran VS, Malhotra VM, Jolicoeur C, Spiratos N (1998) Superplasticizers, properties and applications in concrete. Minister of Public Works and Government Services, Canada
7. El-Gamal Safaa MA, Al-Nowaiser Fawzia M, Al-Baity Asmaa O (2012) Effect of superplasticizers on the hydration kinetic and mechanical properties of Portland cement pastes. J Adv Res 2012(3):119–124
8. Mollah MYA, Adams WJ, Schennach R, Cocke DL (2000) A review of cement-superplasticizer interactions and their models. Adv Cem Res 12(4):153–161
9. Enrique RL (2002) Concreto de Alta Resistencia, 1era. Edición, Instituto de la Construcción y Gerencia, ICG
10. Ortiz JA, Aguado A, Roncero J, Zermeño ME (2009) Influencia de la temperatura ambiental sobre las propiedades de trabajabilidad y microestructurales de morteros y pastas de cemento. Concreto y cemento. Investigación y desarrollo 1(1):2–24
11. Colorado HA, Colorado SA (2016) Portland cement with battery waste contents-Rewas 2016
12. Colorado HA, Garcia E, Buchely MF (2016) White Ordinary Portland Cement blended with superfine steel dust with high zinc oxide contents. Constr Build Mater 112:816–824

Influence of Cold Spray on the Microstructure and Residual Stress of Resistance Spot Welded Steel-Mg

S. K. Shaha, B. Marzbanrad and H. Jahed

Abstract A mixture of Al_2O_3 and pure-Al powder was successfully deposited on weld nugget of the spot weld dissimilar metals Mg and galvanized steel. The cross-sectional microstructure was analyzed using SEM. Also, residual stress was measured through hole drilling and X-ray diffraction methods. The obtained microstructure analysis shows that mixture of Al and Fe with a continuous layer of ~2.7 μm were observed at the interface of weld nugget/coat. At the same time, equiaxed grains were observed near the interface. In contrast, the Zn containing interlayer thickness of ~14 μm with porosity was identified at the interface of the coating on the Zn coated steel. The hardness distribution also revealed that the interface obtained lower hardness compared to the substrate and coating. At the same time, the residual stress also changes through thickness of the coating to the substrate which will improve the corrosion and fatigue properties.

Keywords Resistance spot weld · Steel · Cold spray · Microstructure Residual stress

Introduction

Transportation is one of the major sources of global air pollution. To diminish the emission of CO_2, governments around the world imposed rules to make fuel efficient car. So, automotive companies are intending to decrease the weight of vehicles where light metals and alloys are playing a great rolls. The low weight of the vehicle causes the less fuel consumption and improve the performance of the engine. Therefore, more and more often in vehicles' construction, light materials are successfully used [1–3]. Magnesium (Mg) alloys are the lightest engineering material, and are attractive to automotive, aerospace and electronics industries for

S. K. Shaha · B. Marzbanrad · H. Jahed (✉)
Department of Mechanical & Mechatronics Engineering, University of Waterloo, 200 University Ave W, Waterloo, ON N2L 3G1, Canada
e-mail: hjahed@uwaterloo.ca

The Minerals, Metals & Materials Society, *TMS 2018 147th Annual Meeting & Exhibition Supplemental Proceedings*, The Minerals, Metals & Materials Series,
https://doi.org/10.1007/978-3-319-72526-0_60

weight reduction purpose [4]. However, it is not always possible to use Mg alloys for whole construction, especially in high load bearing components. This problem can be resolved by coupling dissimilar metals. However, the difficulties to make welding between steel and Mg alloys are essentially influenced by their differential melting points, the limited solubility resulting in heterogeneous microstructure, and a considerable differences in thermal and electrical conductivity between these materials [5]. Therefore, the resistance spot welding (RSW) is the most commonly welding processes in the automotive industries. The galvanized Zn layer on the steel is destroyed during RSW, which reduces the corrosion resistance of the steels. At the same time, a significant amount of residual stresses were formed during RSW as well. The presence of residual stress enhances the fatigue crack growth which basically reduces the fatigue performance as well [6–8]. Many researcher has been performed the post welding heat treatment to improve the fatigue performance [9]. However, the localized corrosion resistance is still in question.

Studies [10–18] shows that the cold spray (CS) has a potential to deposit a range of materials on the different substrate. It can refine the microstructure which can alter the mechanical properties. The recent study reported that the Al-Al_2O_3 composite coatings on carbon steel exhibited higher corrosion resistance compared to the substrate. The presence of Al formed a passive layer on the steel, which increased the corrosion resistance [19]. At the same time, the addition of Al_2O_3 ceramic particles formed composite layer with higher hardness compared to the pure-Al. Up-to-date most of the study focused on the corrosion and fatigue performance of the CS on the plain substrate. However, according to the authors' knowledge, there was no study on the effect of CS on resistance weld. Therefore, in this study the change of microstructure and residual stress on effect of CS Al-25 wt % Al_2O_3 on the nugget zone of the RSW galvanized steel were investigated.

Experimental Details

In this study, the RSWed plate of galvanized steel and Mg-alloy was collected from the supplier and used as a substrate. Because of the research interest, the CS was performed on the steel side. The pure-Al and 25 wt% Al_2O_3 powders were mechanically mixed and used as the coating material. The CS coating was performed on the weld nugget and galvanized steel in Stress Analysis laboratory of the University of Waterloo, Waterloo, Canada, using the Supersonic Spray Technologies (SST) Series P CS system manufactured by Centerline Ltd. For the deposition on the weld sample, the surface were polished up to 600 grid SiC emery paper and rinse with acetone. However, for deposition on the steel substrate, the sample was clean in ultrasonic cleaner and wash with acetone. Details about the coating parameters can be seen in [20]. After deposition, the sample were cut and polished following standard metallography procedure. To observe the microstructure of the substrate, the polished samples were etched using 5% natal.

The microstructural analysis was performed using an optical microscope and a scanning electron microscope equipped with an Oxford EDX.

Micro Vickers hardness test was conducted on mounted and polished cross-section samples from the coating surface into the substrate using a LECO DM400LF micro hardness tester, with an applied load of 200 g and a holding time of 10 s. Hardness was measured according to ASTM E384-99 at room temperature.

Residual stress measurements were performed in two methods: (1) hole-drilling and (2) X-ray diffraction. Hole-drilling process was performed using a SINT model: RESTAN hole drilling system (SINT Technologies, Calenzano, Italy), while the Bruker D8 discover were used for X-ray diffraction method. Residual stress was measured on the surface and through thickness. To measure the residual stress along the cross section, the samples were cut, mechanically polished and finally electro polished.

Results and Discussion

Microstructure and Micro-hardness

The SEM micrographs with an EDX line scan of the polished cross-section of the nugget zone coated with pure-Al+Al_2O_3 are illustrated in Fig. 1. The maximum coating thickness in the as-deposited condition was ~150 μm. As seen in Fig. 1a, the as-coated sample shows dense and almost defects free coatings processed with nitrogen gas environment. The black spot in Fig. 1a basically the Al_2O_3 ceramic particles as clearly seen in high magnification image in Fig. 1b. The EDX line (Fig. 1d) scan near the interface (mark by red line in Fig. 1c) indicates that there was no drastic change in the base alloying elements (Fe/Al). Instead, a gradual change of Fe/Al designates that the interface contains a mixer of Fe and Al layer with thickness of*- ~2.7 μm. Wang et al. [16] reported that the HRTEM microstructure of pure-Al coating on the AZ91D Mg alloy obtained similar mixture of Al/Mg at the interface. They recognised an amorphous interlayer zone containing base elements of coating (Al) and substrate (Mg) which formed metallurgical bonding during CS. Figure 2 illustrates the microstructure of the coated base metals (galvanized steel coated with pure-Al+Al_2O_3). The SEM micrograph (Fig. 2a) also show similar dense coating of pure Al reinforced with Al_2O_3. At the same time, interfacial porosities were observed in the base metal coating as marked in Fig. 2b. EDX line scan (marked in Fig. 2c) confirmed that unlike the coating at weld nugget zone, a Zn containing inter layer with a thickness of ~14 μm were observed between the galvanized steel and composite coating. It is also noted that there was no diffusion of Al into the Zn or vise versa. Instead, the Zn melted and squeezed out which created porosity during CS.

Figure 3 shows the microstructure evolution in the weld nugget during CS and the distribution of hardness from the coating surface to the substrate. It is well

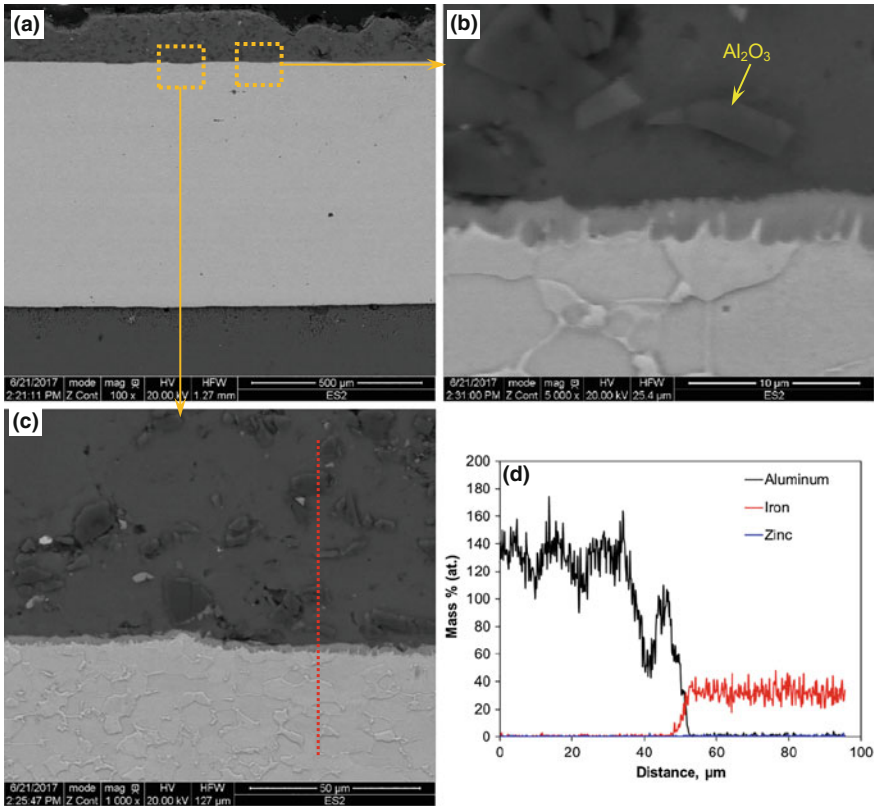

Fig. 1 SEM images of cross-sectioned and polished cold spray of pure-Al with 25 wt% Al_2O_3 on the nugget of resistance weld of steel and Mg at **a** lower magnification, **b**–**c** higher magnification and **d** EDX line scan

established that low carbon martensite are generally formed in the nugget zone of the RSW of galvanized steels [21]. However, due to the CS, a remarkable change in microstructure was identified at the weld nugget zone. It is seen that the interface of the Al/steel shows very fine equiaxed grains with size of ~10.2 μm. Increasing the distance from the interface the grain size further increased to ~13.38 μm. Then, further increasing the distance, the simple ferrite/pearlite phases followed by tempered martensite was observed. Hardness is on of the useful mechanical properties which delivers valuable information about the overall mechanical behaviour of the materials. As seen in Fig. 3, the hardness of the substrate gradually decreased near the interface, from ~247 to ~187 HV, while the obtained hardness on the interface was ~90 HV. Then, the hardness further decreased to ~68 HV as the distance increased from the interface through the coating. In contrast, the hardness of the galvanized steel substrate exhibits lower than the nugget zone while the hardness of the coating layer is about to the same as the coating on the nugget zone.

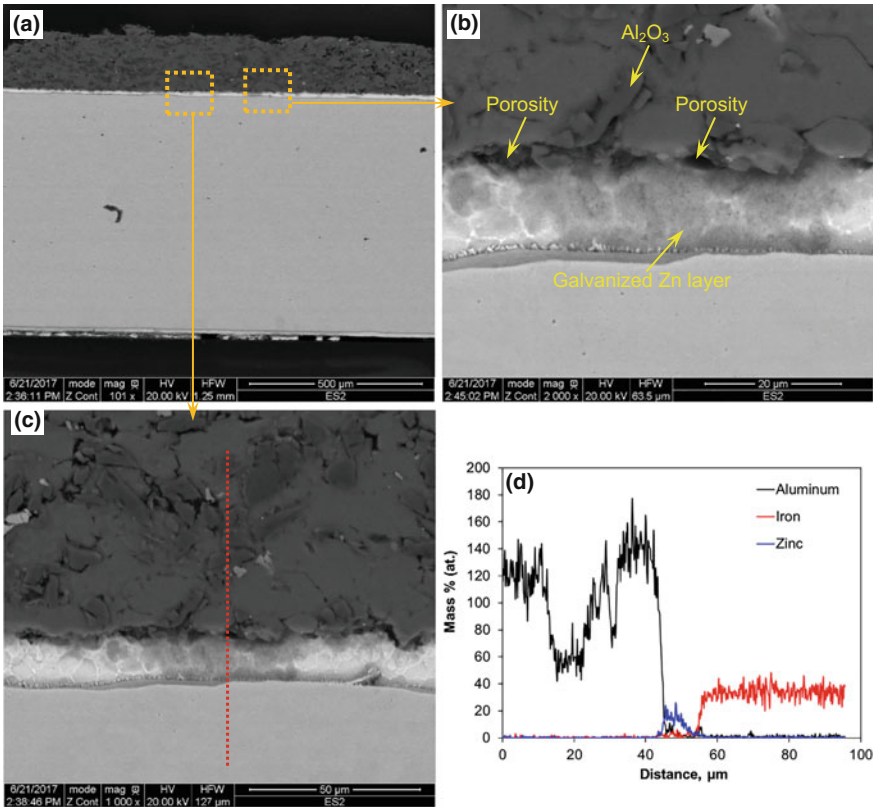

Fig. 2 SEM images of cross-sectioned and polished cold spray of pure-Al with 25 wt% Al_2O_3 on galvanized steel at **a** lower magnification, **b–c** higher magnification and **d** EDX line scan. Note: porosities at the interface

The changes of hardness at the nugget zone can be the effect of microstructural changes due to work hardening near the interface of the substrate, caused by the peening effect of CS. The impact between the particles and the surface of the substrate generate heat along with the carrier gas temperatures, which leads to the transformation of the low carbon martensite to equiaxed grains results a decreased in hardness close to the surface of the substrate and near the coating [22]. However, the hardness of the coating was higher than the hardness of the CS pure-Al (52.05 HV [11]). The hardness of the CS pure-Al+Al_2O_3 composite layer coating near the interface is also higher (~97 HV) than the typical hardness of the bulk Al (~37 HV [22]). The increase in hardness of the pure-Al CS coating can be related to the presence of Al_2O_3 and hammering effect of coating particles during build-up of the coating [13]. The high kinetic energy of the CS powder obtained a remarkable plastic deformation during impact, which also causes work hardening results the generation and interlocking of the dislocations. Thus, CS pure-Al+Al_2O_3

composite coating are usually projected having a dramatically higher hardness than the bulk material [10–12, 23].

Residual Stress

Residual stresses are left behind stresses existing in the materials even when there is no external applied load, which develop mainly due to non-equilibrium changes in metallic component depending on the manufacturing processes like heat treatment, casting, welding, coating etc. Residual stresses can be tensile or compressive subjected to the location and form of changes taking place due to the variance of cooling and heating. The residual stresses in welded joints mostly formed due to differential weld thermal cycles (heating, soaking and cooling at any moment during welding) obtained by the weld metal and area near to fusion zone commonly known as heat affected zone. When the metals are heated for welding, due to thermal expansion and the lower surrounding temperature of the base metal, compressive residual stress is formed in the region of base metal which is being heated for welding. After obtaining the peak temperature, the compressive residual stress gradually drops as the heated metals starts to soften followed by melting. When melting starts, the compressive residual stress near the matting surfaces decrease to zero. At the same time, when metal starts to solidify, it shrinks during cooling results the development of tensile residual stresses. The residual stresses whether they are compressive or tensile type mainly affect the mechanical

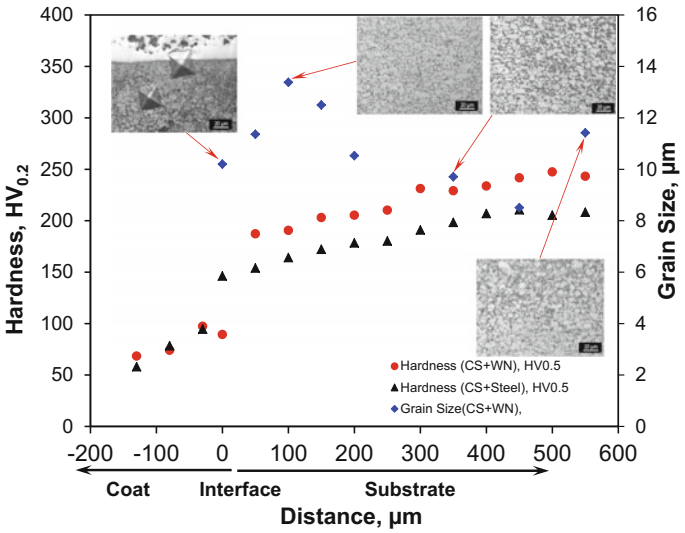

Fig. 3 The distribution of Vickers micro-hardness from the top of the cold spray of pure-Al with 25 wt% Al_2O_3 on nugget of resistance weld of steel and Mg

properties of the joints. As the nature of the residual stresses is additive, their presence in the welds can increase or decrease the tendency of premature failures during external loading. At the same time, the compressive residual stresses reduce the tendency of failure during external tensile loading, since it will reduces the net tensile stresses. In contrast, the tensile residual stress enhances the failure tendency under external tensile stresses as more than 90% failure occurs under tensile loading

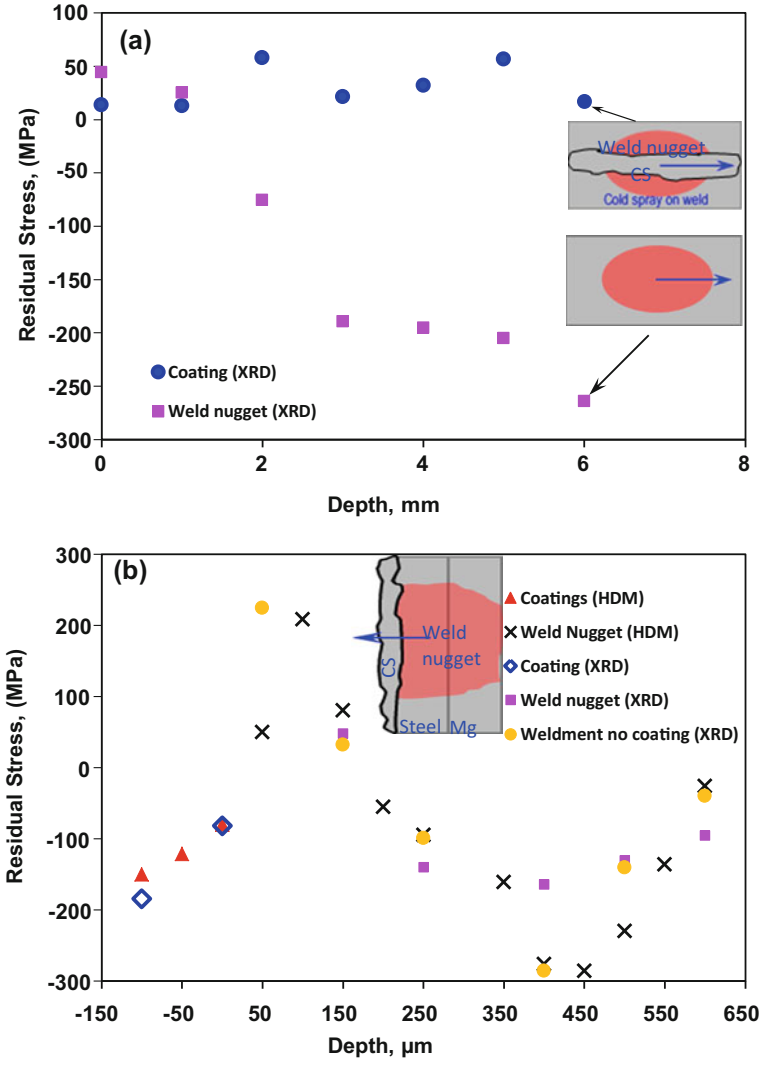

Fig. 4 The distribution of residual stress measured using hole drilling and X-ray diffraction methods of the cold spray of pure-Al with 25 wt% Al_2O_3 on nugget of resistance weld of steel and Mg along the **a** on the surface and **b** through thickness at radial direction as shown schematically

condition by generating and propagating the cracks. Therefore, the tensile residual stresses are undesirable, while the compressive residual stresses are intentionally induced by various method such as shot peening [24, 25].

As seen in Fig. 4, the residual stress distribution in the weld nugget at coated and non-coated area, obtained via hole drilling method (HDM) and X-ray diffraction method (XRD). It is clearly seen that in both methods (HDM, XRD), the trend of the curves are the same. A tensile type residual stress with a magnitude of ~+45 MPa in the surface of the weld sample was measure, which is gradually decreased and transformed to the compressive type of residual stresses with a value of ~−205 MPa along the radial direction (Fig. 4a). In contrast, the coating surfaces obtained a uniform tensile residual stress of ~+10 MPa, which is lower than the nugget surface residual stress. It is also notice in Fig. 4b, that the sub-surface of the nugget obtained a higher tensile residual stress of ~+225 MPa, which is gradually decreased toward the heat affected zone followed by base metal. In contrast, the obtained residual stress at the area coated with pure Al+Al_2O_3 is compressive in nature. The average compressive residual stress in the coating is ~−185 MPa. A similar trend was reported by Ghelichi et al. [12] for the CS coatings of Al7075 on the Al5052 substrate. They concluded that higher carrier gas temperatures fading the peening affect. Thus, tensile residual stresses were observed at the coating surface. As discussed earlier, the presence of compressive residual in coating could be beneficial for improving the mechanical properties and corrosion resistance as well.

Conclusions

A composite layer of pure-Al reinforced with Al_2O_3 particles were successfully deposited on the weld substrate. From the above discussion, it can be concluded that the cold spray refined the microstructure of the substrate which basically changes the hardness at the weld nugget. A remarkable reduction in tensile residual stress was observed at the nugget area. At the same time, the cold spray coating obtained a compressive residual stress of ~−185 MPa, which may improve the fatigue life of the weld materials. Similarly, the presence of Al layer can improve the corrosion resistance at the nugget zone. Therefore, the fatigue and corrosion properties of the welded sample supposed to be evaluated in future.

Acknowledgements The authors would like to gratefully acknowledge the financial support of the Natural Sciences and Engineering Research Council of Canada (NSERC), Automotive Partnership Canada (APC) program under APCPJ 459269 – 13 grant with contributions from Multimatic Technical Centre, Ford Motor Company, and Centerline Windsor. Authors also would like to thank Mr. Siavash Dayani for helping in cold spray process.

References

1. Manzie C, Watson H, Halgamuge S (2007) Fuel economy improvements for urban driving: hybrid vs. intelligent vehicles. Transp Res Part C Emerg Technol 15(1):1–16
2. Manzie C (2010) Relative fuel economy potential of intelligent, hybrid and intelligent-hybrid passenger vehicles. In Electric and hybrid vehicles, pp 61–90
3. Mersky AC, Samaras C (2016) Fuel economy testing of autonomous vehicles. Transp Res Part C Emerg Technol 65:31–48
4. Karparvarfard SMH, Shaha SK, Behravesh SB, Jahed H, Williams BW (2017) Microstructure, texture and mechanical behavior characterization of hot forged cast ZK60 magnesium alloy. J Mater Sci Technol 33:907–918
5. Winnicki M, Małachowska A, Korzeniowski M, Jasiorski M, Baszczuk A (2017) Aluminium to steel resistance spot welding with cold sprayed interlayer. Surf Eng 844:1–8
6. Bae DH, Sohn IS, Hong JK (2003) Assessing the effects of residual stresses on the fatigue strength of spot welds. Weld J 82(1):18S–23S
7. Bae DH, Sohn IS, Hong JK (2003) Assessing the effects of residual stresses on the fatigue strength of spot welds. Weld J Res Suppl 82(1):18s–23s
8. Bae JKHDH, Sohn IS (2003) Assessing effects of residual stress on the fatigue strength of spot welds. Weld J 18–23
9. Park YS, Sohn IS, Bae DH (2014) Fatigue strength assessment including welding residual stress of spot welded joints subjected to cross-tension loads. Int J Automot Technol 15 (5):765–771
10. Bu H, Yandouzi M, Lu C, MacDonald D, Jodoin B (2012) Cold spray blended Al+$Mg_{17}Al_{12}$ coating for corrosion protection of AZ91D magnesium alloy. Surf Coatings Technol 207:155–162
11. Diab M, Pang X, Jahed H (2017) The effect of pure aluminum cold spray coating on corrosion and corrosion fatigue of magnesium (3% Al-1% Zn) extrusion. Surf Coatings Technol 309:423–435
12. Ghelichi R, MacDonald D, Bagherifard S, Jahed H, Guagliano M, Jodoin B (2012) Microstructure and fatigue behavior of cold spray coated Al5052. Acta Mater 60(19):6555–6561
13. Rokni MR, Widener CA, Crawford GA, West MK (2015) An investigation into microstructure and mechanical properties of cold sprayed 7075 Al deposition. Mater Sci Eng, A 625:19–27
14. Shayegan G et al (2014) Residual stress induced by cold spray coating of magnesium AZ31B extrusion. Mater Des 60:72–84
15. Spencer K, Fabijanic DM, Zhang MX (2009) The use of Al-Al_2O_3 cold spray coatings to improve the surface properties of magnesium alloys. Surf Coatings Technol 204(3):336–344
16. Wang Q, Qiu D, Xiong Y, Birbilis N, Zhang MX (2014) High resolution microstructure characterization of the interface between cold sprayed Al coating and Mg alloy substrate. Appl Surf Sci 289:366–369
17. Irissou E, Legoux J-G, Arsenault B, Moreau C (2007) Investigation of Al-Al_2O_3 cold spray coating formation and properties. J Therm Spray Technol 16(5–6):661–668
18. Hassani-Gangaraj SM, Moridi A, Guagliano M (2015) Critical review of corrosion protection by cold spray coatings. Surf Eng 31(11):803–815
19. Bai X, Tang J, Gong J, Lü X (2017) Corrosion performance of Al–Al_2O_3 cold sprayed coatings on mild carbon steel pipe under thermal insulation. Chin J. Chem Eng 25(4):533–539
20. Dayani SB, Ghelichi R, Shaha SK, Wang JF, Jahed H (2017) The impact of Al7075 cold spray coating on the fatigue life of AZ31B cast alloy. Surf Coatings Technol (Submitted)
21. Marashi P, Pouranvari M, Amirabdollahian S, Abedi A, Goodarzi M (2008) Microstructure and failure behavior of dissimilar resistance spot welds between low carbon galvanized and austenitic stainless steels. Mater Sci Eng A 480(1–2):175–180

22. Matli PR et al (2017) Improved properties of Al–Si_3N_4 nanocomposites fabricated through a microwave sintering and hot extrusion process. RSC Adv 7(55):34401–34410
23. Xiong Y, Zhang M-X (2014) The effect of cold sprayed coatings on the mechanical properties of AZ91D magnesium alloys. Surf Coatings Technol 253:89–95
24. Leggatt RH (2008) Residual stresses in welded structures. Int J Press Vessel Pip 85(3): 144–151
25. Edition S (2003) Metallurgy second edition welding metallurgy, vol 822, no 1–3

Part XXV
High Entropy Alloys VI

Development of Oxidation Resistant Refractory High Entropy Alloys for High Temperature Applications: Recent Results and Development Strategy

Bronislava Gorr, Franz Mueller, Hans-Juergen Christ, Hans Chen, Alexander Kauffmann, Ruth Schweiger, Dorothée Vinga Szabó and Martin Heilmaier

Abstract Refractory High Entropy Alloys (HEAs) can be considered as promising materials for high temperature applications because of their high melting point and outstanding high temperature strength. The microstructure of the equimolar alloy Nb-Mo-Cr-Ti-Al consists of a disordered body centered cubic (BCC) phase and a small amount of the Laves phase, while the equimolar alloy Ta-Mo-Cr-Ti-Al exhibits the ordered B2 and several Laves phases in addition to the BCC phase. The experimental studies reveal that these alloys possess a beneficial combination of

B. Gorr (✉) · F. Mueller · H.-J. Christ
Institut für Werkstofftechnik, Universitaet Siegen, Siegen, Germany
e-mail: gorr@ifwt.mb.uni-siegen.de

F. Mueller
e-mail: franz-mueller@uni-siegen.de

H.-J. Christ
e-mail: christ@ifwt.mb.uni-siegen.de

H. Chen · A. Kauffmann · M. Heilmaier
Institut für Angewandte Materialien – Werkstoffkunde, Karlsruher Institut für Technologie (KIT), Karlsruher, Germany
e-mail: hans.chen@kit.edu

A. Kauffmann
e-mail: alexander.kauffmann@kit.edu

M. Heilmaier
e-mail: martin.heilmaier@kit.edu

R. Schweiger
Institut Für Angewandte Materialien – Werkstoff- und Biomechanik, Karlsruher Institut für Technologie (KIT), Karlsruher, Germany
e-mail: ruth.schwaiger@kit.edu

D. V. Szabó
Institut für Angewandte Materialien – Werkstoffprozesstechnik, Karlsruher Institut für Technologie (KIT), Karlsruher, Germany

The Minerals, Metals & Materials Society, *TMS 2018 147th Annual Meeting & Exhibition Supplemental Proceedings*, The Minerals, Metals & Materials Series,
https://doi.org/10.1007/978-3-319-72526-0_61

high temperature strength and corrosion protectiveness. The compressive yield stress of the alloy Nb-Mo-Cr-Ti-Al and Ta-Mo-Cr-Ti-Al at 1200 °C is determined to 100 MPa and 200 MPa, respectively. The oxidation resistance of the alloy Ta-Mo-Cr-Ti-Al in the temperature range between 900 and 1100 °C is comparable to that of multi-phase Ni-based alloys. The main drawback of both alloys is their low ductility at room temperature. Strategies for the future alloy development are discussed.

Keywords High entropy alloys · Refractory metals · Microstructure Mechanical properties · Oxidation resistance

Introduction

The development of high entropy alloys (HEAs) with at least 5 components based on refractory elements has been motivated by high temperature structural applications, particularly aerospace applications. Research on these alloy systems has been mainly driven by Senkov and co-workers [1, 2]. The main incentive has been to develop new materials exhibiting outstanding combination of properties such as high temperature strength, fracture toughness, ductility at room temperature (RT) as well as fatigue and oxidation resistance. Fervent research activities conducted in the field of HEAs during recent years indeed show substantial potential to exceed the service temperature and/or strength of Ni-based superalloys.

Two refractory HEAs, Mo-Nb-Ta-W and Mo-Nb-Ta-V-W, show exceptionally high values of strength that retain reasonable up to around 1700 °C [1]. The compressive yield strength of the alloy Mo-Nb-Ta-V-W, for example, has been determined to 842 MPa at 1000 °C, while the superalloy MAR-M 247® yields a value of only about 350 MPa at the same temperature and applied strain rate [1]. Both refractory HEAs alloys possess a single phase BCC crystal structure. Unfortunately, these materials show a brittle to ductile transition temperature of around 600 °C and their densities are rather high, 12.36 and 13.75 g/cm^3 for the alloys Mo-Nb-Ta-W and Mo-Nb-Ta-V-W, respectively [1]. Thus, in the next series of alloy development, the heavy elements W, Mo and Ta were substituted by the lighter Ti, Hf, and Zr [3]. Though these alloys, retaining still the single BCC phase, became significantly lighter and more ductile, their high temperature strength also decayed substantially. For example, the alloy Hf-Nb-Ta–Ti-Zr exhibited a yield strength of only 295 MPa at 1000 °C [3]. Remarkable ductility in compression ($\varepsilon > 50\%$) and even RT tensile ductility values ($\varepsilon \sim 9.7\%$) were detected for the alloy Hf-Nb-Ta–Ti-Zr [4]. The addition of Cr to these refractory HEAs with reduced density positively increases the yield strength, being e.g. 546 MPa for the alloy Cr-$Mo_{0.5}$-Nb-$Ta_{0.5}$-Ti-Zr at 1000 °C, however, this was accompanied with a simultaneous loss of ductility [5]. These converse effects of the Cr additions on strength/ductility were attributed by the authors to the formation of the Laves phase that is expected from the thermodynamic point of view [6, 7]. Several studies have

clearly proven that the Laves phase is inherently brittle at lower temperatures [8, 9]. In a very recent study, Senkov et al. investigated the microstructure and mechanical properties of the alloy Al-$Mo_{0.5}$-Nb-$Ta_{0.5}$-Ti-Zr [10]. This alloy consists of a nano-scale two-phase microstructure of disordered BCC and coherent, ordered B2 phase. The alloy has an exceptionally high yield strength being superior to the strength of Ni-based superalloys over the whole temperature range from 20 to 1200 °C. It was concluded that the two-phase BCC/B2 nano-structure of the alloy is responsible for its high strength [10]. Furthermore, this alloy possesses sufficient RT ductility in compression ($\varepsilon \sim 10\%$) [11]. Though RT tensile ductility data are completely missing up to date, this alloy represents the first refractory HEA that exhibits simultaneously high strength up to high temperatures and reasonable ductility at RT.

Based on above literature survey, it can be stated that tensile ductility at ambient temperatures of refractory HEAs seems to be the critical challenge rather than sufficient high temperature strength. Low ductility and damage tolerance at RT as well as poor oxidation resistance are well-known shortcomings of refractory metals and their solid solutions in general [12]. It seems therefore a reasonable strategy to search the available literature for potentially ductilizing elements that enhance the RT ductility of refractory elements and refractory metal-based alloys. A first remarkable effect of Re addition on mechanical properties of Mo and W was presented at the Second Plansee Seminar in 1955 already. Geach and Hughes reported that Mo alloyed with 35 at.% Re could be directly cold-rolled in the as-cast condition to reductions of 90% without cracking. The authors explained this behavior by the fact that (coarse) twinning substantially contributed to the overall amount of deformation [13]. Later, Jaffe et al. investigated the effect of Re on the mechanical properties of Mo at room and elevated temperatures. They found that up to 20 at.% Re increased the strength but decreased the (tensile) ductility, while higher Re concentration up to 35 at.% increase both, the tensile strength and the ductility of the alloy at RT [14]. Leichtfried et al. investigated in the most recent study the mechanical properties of powder-metallurgically processed binary Mo-Re-alloys ranging from 5 to 47.5 wt% and concluded that the mechanical properties as determined by impact and low-temperature bend testing were improved essentially in a monotonic way with increasing Re concentration [15].

Similar findings can be stated for the effect of Re in W-based alloys [16]. Klopp et al. found that the W-Re-alloys with high Re contents (Re addition up to 25.6 at.%), which deform initially by twinning, were only slightly more ductile than the dilute alloys (up to 9.05 at.%) which deform entirely by dislocation slip [16]. It should however be noted that the alloy chemistry, in particular the purity, and the microstructure, e.g. the grain size, also have an important impact on alloy ductility [16]. Further, the mechanical properties of Cr have been found to be affected extremely sensitively by Re additions. Generally, Re additions induce solid-solution strengthening of Cr involving a significant increase in the ductile-brittle transition temperature at Re concentrations up to about 10 at.%. This was followed, though, by a dramatic decrease of the ductile-brittle transition temperature at higher Re concentrations [17].

In this paper, the most relevant experimental results on microstructure, mechanical properties and high temperature oxidation behavior of the alloys Nb-Mo-Cr-Ti-Al and Ta-Mo-Cr-Ti-Al will be summarized and discussed in terms of their perspectives and shortcomings. Based on the current experimental observations, the strategy for the future alloy development will be presented.

Experimental Procedures

The alloys Nb-Mo-Cr-Ti-Al and Ta-Mo-Cr-Ti-Al were produced from elemental bulk materials by arc-melting in ~0.6 atm of argon (arc-melter AM 0.5 by Edmund Bühler GmbH). The purities of the starting materials Ta, Mo, Nb, Al were all 99.9%, whereas Cr and Ti had a purity of 99% and 99.8%, respectively. In the alloys, nitrogen impurities were found to be below the detection limit of 5–10 wt. ppm, oxygen content was measured being between 50 and 100 wt. ppm. The prepared buttons were flipped over and remelted more than five times in a water-chilled copper mold to facilitate alloy homogenization. The analysis of nitrogen and oxygen impurities was carried out after the remelting. The alloy microstructure was analyzed by means of a dual beam system Scanning Electron Microscope and Focused Ion Beam (SEM/FIB) of type FEI Helios Nanolab 600 as well a Zeiss Auriga. X-ray diffraction (XRD) measurements were carried out using the X'Pert Pro MPD diffractometer operating in Bragg-Brentano geometry. In order to characterize the microstructures of the alloy Ta-Mo-Cr-Ti-Al, an aberration-corrected (image) transmission electron microscopy (TEM) FEI Titan 80–300 (FEI, Eindhoven) operated at 300 kV and equipped with field emission gun and a Gatan Ultrascan CCD camera (Gatan Inc., Pleasanton, CA) was employed. Quasistatic compression tests were performed at an initial engineering strain rate of 10^{-3} s^{-1} utilizing a Zwick Z100 electromechanical universal testing machine equipped with a vacuum furnace by Maytec. The details of the compression test performance are given in Ref. [18]. Oxidation experiments were carried out in static laboratory air in the temperature range between 900 and 1100 °C. Detailed sample preparation procedures as well as detailed description of oxidation tests can be found elsewhere [19].

Experimental Results: Microstructure, Mechanical Properties and Oxidation Behavior of the Alloy System X-Mo-Cr-Ti-Al (X = Nb, Ta)

A new equimolar alloy system X-Mo-Cr-Ti-Al (X = Nb, Ta) has been proposed as a promising HEA candidate for applications at high temperatures. The alloys should possess the following property combination: (i) a melting point exceeding those of

Ni-based superalloys by at least 200 K, (ii) superior long-term high temperature strength, (iii) oxidation protectiveness at temperatures of at least 1100 °C, and (iv) a density of less than 9 g/cm^3. With respect to the first and second requirements, it seems reasonable that Mo, Nb and Ta can be considered as prime candidates for the new alloy system. Unfortunately, all these refractory elements show a very poor high temperature oxidation resistance, being prone to so-called catastrophic oxidation due to the formation of volatile or solid, non-protective oxides [20]. In order to potentially enable the formation of a protective oxide scale on the metallic surface and, consequently, to ensure the alloy protectiveness, Al and Cr have been added to refractory elements. Both elements, Al and Cr, are essential in promoting the formation of an alumina layer that maintains its protective properties also at temperatures above 1000 °C [21]. In terms of high temperature oxidation, Cr effectively supports the formation of a continuous alumina scale in many alumina-former high temperature alloys [21]. The high density, which is typical of most refractory metals, is undesirable for many practical applications. In order to reduce the density of the new alloy system, Ti has also been added (besides the already mentioned Al).

Figures 1a, b show the microstructures of the alloys Nb-Mo-Cr-Ti-Al and Ta-Mo-Cr-Ti-Al after heat treatment at 1300 °C for 20 h. Experimental results reveal that the alloy Nb-Mo-Cr-Ti-Al after heat treatment (designated as 0 h in Fig. 2a) consists of a disordered BCC-matrix, and a small amount of the Laves-phase Cr_2Nb (C14, hexagonal, <0.5% by volume) located predominantly at grain boundaries (see Fig. 1a). A subsequent heat treatment at 1000 °C for 24 and 72 h leads to the formation of an additional (minor) intermetallic phase Al(Mo, $Nb)_3$ (A15, cubic), see XRD pattern in Fig. 2a designated as 24 and 72 h. Instead, the alloy Ta-Mo-Cr-Ti-Al seems to consist of a phase mixture of a BCC-matrix and its ordered B2-counterpart after heat treatment at 1300 °C for 20 h. However, three Laves-phases, C14, C15 and C36, were also identified (see Fig. 1b and XRD pattern designated as 0 h in Fig. 2b). A subsequent heat treatment of the alloy Ta-Mo-Cr-Ti-Al at 1000 °C does not cause formation of any new phases (XRD, cf. the patterns designated as 24 and 72 h in Fig. 2b). Heat treatment of the alloy Ta-Mo-Cr-Ti-Al performed at 1500 °C reveals, in contrast, only a negligibly small amount of Laves phase precipitated at grain boundaries whereas the grain interior showed no phase contrast (see Fig. 1c).

In order to identify which phases form in the matrix of the alloy Ta-Mo-Cr-Ti-Al at 1500 °C for 20 h, TEM analysis was carried out. Obviously, the heat treatment at 1500 °C amplifies the formation of the ordered B2 phase which seems to precipitate at nano-scale in the BCC matrix, see the respective TEM diffraction pattern (left) and dark field micrograph (right) in Fig. 3. The sample was prepared by FIB subsequent to orientation determination by electron backscatter diffraction (EBSD) in order to adjust a [110] zone axis. B2 super lattice reflections can be easily recognized—additional spots at higher reflection orders are attributed to the Pt protection layer which was deposited prior to the FIB lift-out. Dark field imaging using one of the super lattice reflections, namely (300), reveals spatial irregularities of the ordering. Quantitative analysis of these irregularities is yet difficult to be

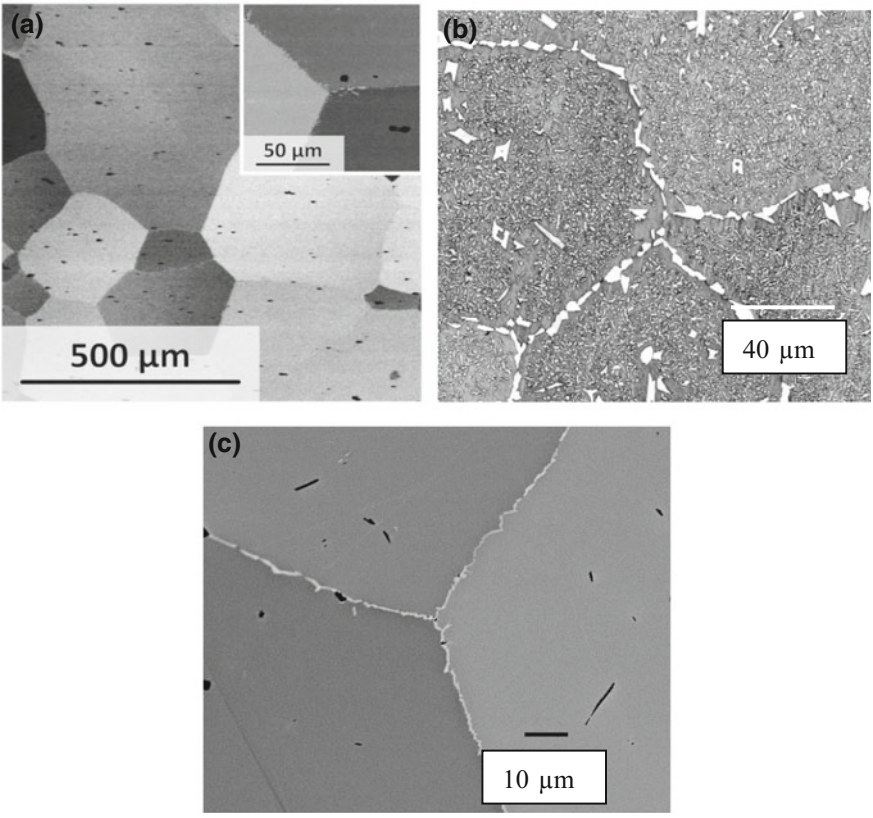

Fig. 1 BSE-image of the microstructure of the refractory HEAs, **a** Nb-Mo-Cr-Ti-Al after heat treatment at 1300 °C for 20 h [18], **b** Ta-Mo-Cr-Ti-Al (heat treatment at 1300 °C for 20 h) and **c** Ta-Mo-Cr-Ti-Al (heat treatment at 1500 °C for 20 h)

performed due to massive internal stress and distortion of the TEM lamella, but the micrograph is clearly indicative for a large amount of nano-scaled B2 phase inherent in the microstructure.

In order to evaluate the potential of the alloys Nb-Mo-Cr-Ti-Al and Ta-Mo-Cr-Ti-Al regarding mechanical properties at temperatures ranging from RT to 1200 °C, compression tests were performed on bulk samples at a strain rate of 10^{-3} s^{-1}. At room temperature, linear elastic behavior without significant plastic deformation was observed for the alloy Nb-Mo-Cr-Ti-Al. In order to clarify whether the matrix, i.e. BCC-phase in the alloy Nb-Mo-Cr-Ti-Al, yields inherently brittle behavior, nanoindentation measurements were carried out at room and elevated temperature. Figures 4a, b show exemplarily SEM-micrographs of a hardness indentation conducted on the BCC-matrix at RT, but essentially the same behavior was also observed for temperatures up to 400 °C. Obviously, the BCC-matrix develops no cracks on indentation—independent of the grain orientation which was

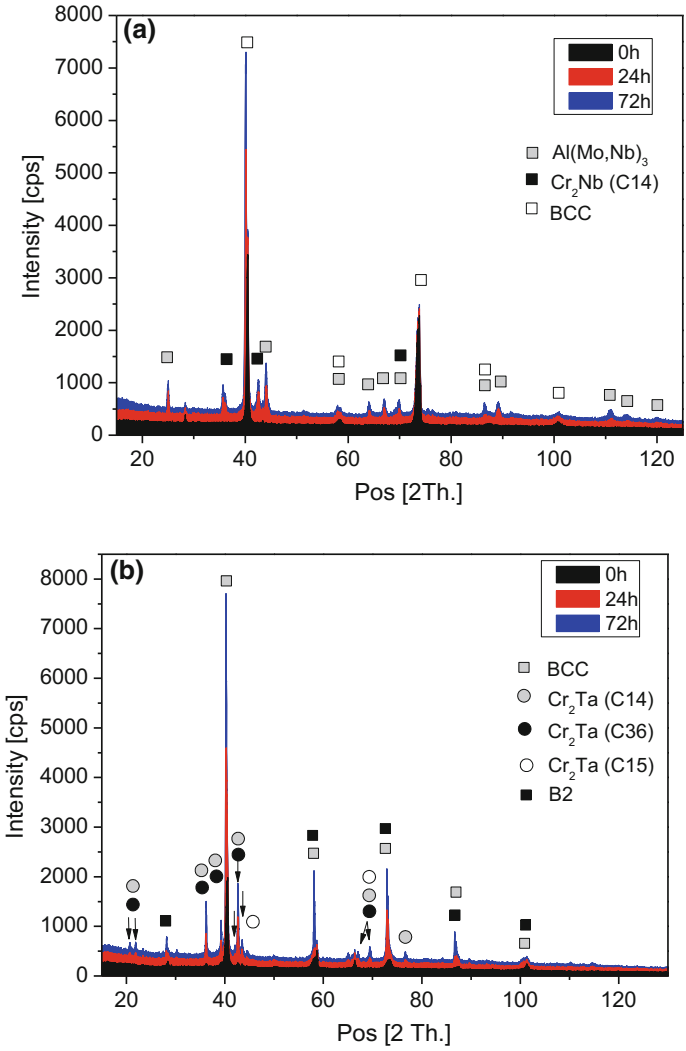

Fig. 2 XRD patterns of the HEAs Nb-Mo-Cr-Ti-Al and Ta-Mo-Cr-Ti-Al after heat treatment at 1300 °C for 20 h (designated as 0 h) and additional heat treatment at 1000 °C for 24 and 72 h (designated as 24 and 72 h); **a** Nb-Mo-Cr-Ti-Al and **b** Ta-Mo-Cr-Ti-Al

probed. Rather, pronounced slip bands are clearly visible near the indent suggesting a potentially ductile dislocation mediated plastic deformation of the BCC-matrix. It is, thus, more likely that the brittle behavior of the bulk samples can be attributed to the presence of the Al(Nb, Mo)$_3$ and Laves-phase at the grain boundaries. Figure 4c shows the compressive stress-strain diagram for the alloy Nb-Mo-Cr-Ti-Al at 800, 1000 and 1200 °C. First indications of plastic deformation were noted for the alloy Nb-Mo-Cr-Ti-Al at 400 °C (not shown here). At 800 °C, yield stress of 980 MPa

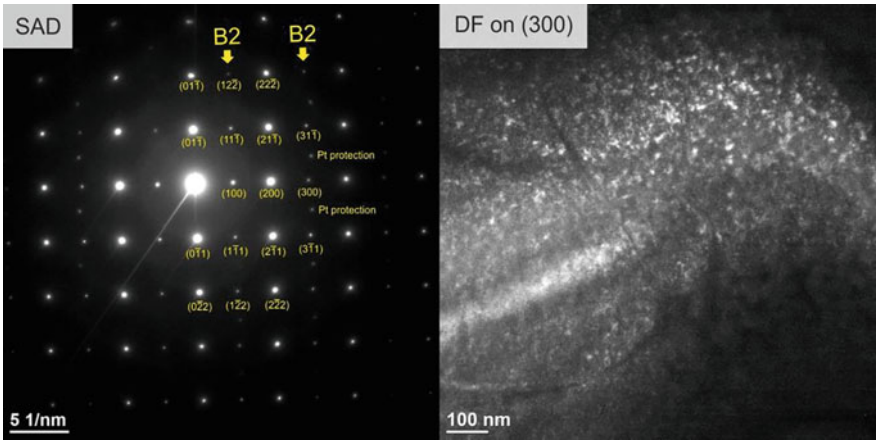

Fig. 3 TEM diffraction pattern and dark field micrograph of the alloy Ta-Mo-Cr-Ti-Al after annealing at 1500 °C for 20 h

was detected and significant plastic deformability with a clear indication of strain hardening was observed before eventual failure at around 13%. At even higher temperatures, dislocation-driven plasticity without indication of internal cracking was reached; at 1200 °C the yield stress drops to 100 MPa [18]. Generally, yield stresses are found to be lower as compared to Senkov's Al-containing HEAs [10]. As discussed above, the combination of BCC/B2-phases building a coherent or semi-coherent nano-scale microstructure shows promise for a higher strength at elevated temperatures [10]. Hence, the alloy Ta-Mo-Cr-Ti-Al in the condition after a heat treatment after 1500 °C for 20 h (see Figs. 1c and 3) may be considered as a proof of concept with a yield stress value of nearly 200 MPa at 1200 °C (not shown here). Even at 1400 °C, the alloy Ta-Mo-Cr-Ti-Al shows notable yield stress of 70 MPa. At RT, the alloy Ta-Mo-Cr-Ti-Al exhibits, however, brittle behavior.

In general, alloys containing a relatively high amount of refractory metals possess poor oxidation resistance as elements such as Mo, Nb or Ta tend to form volatile oxides often causing a fast disintegration of the alloy [20]. The results on the oxidation resistance of the alloy Nb-Mo-Cr-Ti-Al at high temperature have been published in [19, 22]. The alloy oxidizes according to the linear rate law, however, the oxidation rates are rather low. For example, after 48 h of oxidation at 1100 °C, a mass gain of only 8 mg/cm^2 was measured. A discontinuous alumina layer was detected on the alloy substrate. The addition of minor amounts of Si seems to improve the oxidation resistance of the alloy by further lowering the oxidation rates and by supporting the formation of a continuous protective alumina scale [19].

Figure 5a shows thermogravimetric curves of the alloy Ta-Mo-Cr-Ti-Al during exposure to air at high temperatures. Obviously, this alloy oxidizes according to the parabolic rate law indicating the formation of a fully protective oxide layer. This is

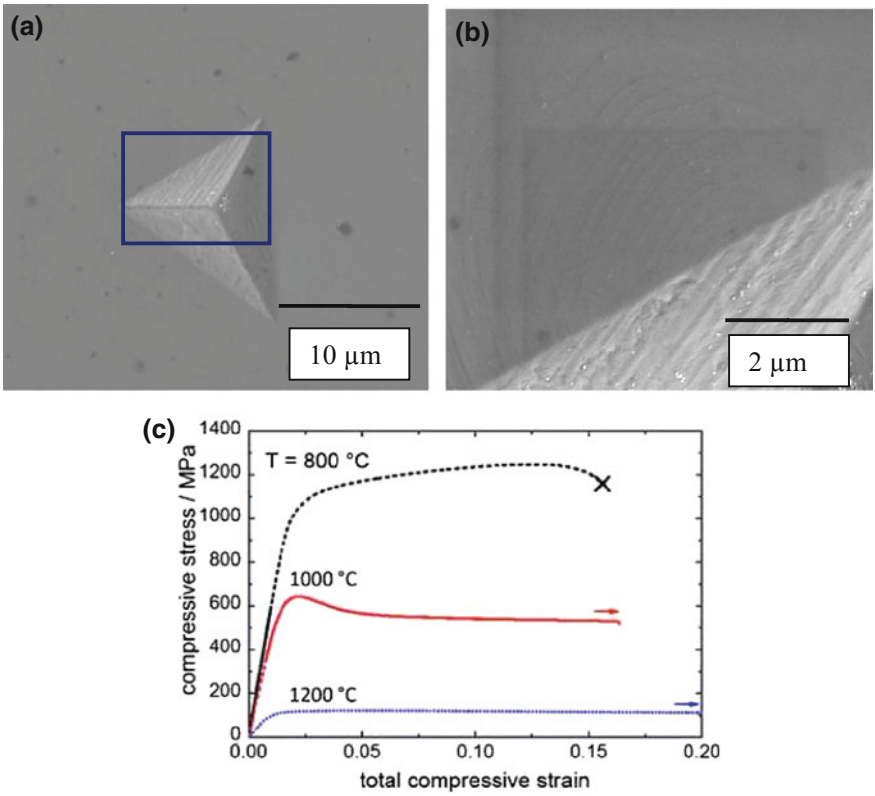

Fig. 4 **a** Hardness indentation in the BCC-matrix of the alloy Nb-Mo-Cr-Ti-Al at RT, **b** Enlarged view of the box shown in **a**, **c** stress-strain dependence of quasistatic compression tests with a strain rate of 10^{-3} s^{-1} of the alloy Nb-Mo-Cr-Ti-Al at 800, 1000 and 1200 °C [18]. Fracture is highlighted by "X". Arrows indicate tests deliberately stopped (without failure)

because underneath coarse particles of rutile, a thin and continuous alumina scale (see Fig. 5b) was observed. Despite the high amount of refractory metals, the alloy Ta-Mo-Cr-Ti-Al exhibits oxidation rates that are comparable to those of Ni-based alloys (see Fig. 5c) [23]. The very good oxidation resistance of the alloy Ta-Mo-Cr-Ti-Al can apparently be attributed to the presence of both elements Cr and Al.

Development Strategy

The relevant properties of two refractory equimolar HEAs, Nb-Mo-Cr-Ti-Al and Ta-Mo-Cr-Ti-Al, have been screened and it can be concluded that these materials show substantial potential for high temperature applications. The first preliminary

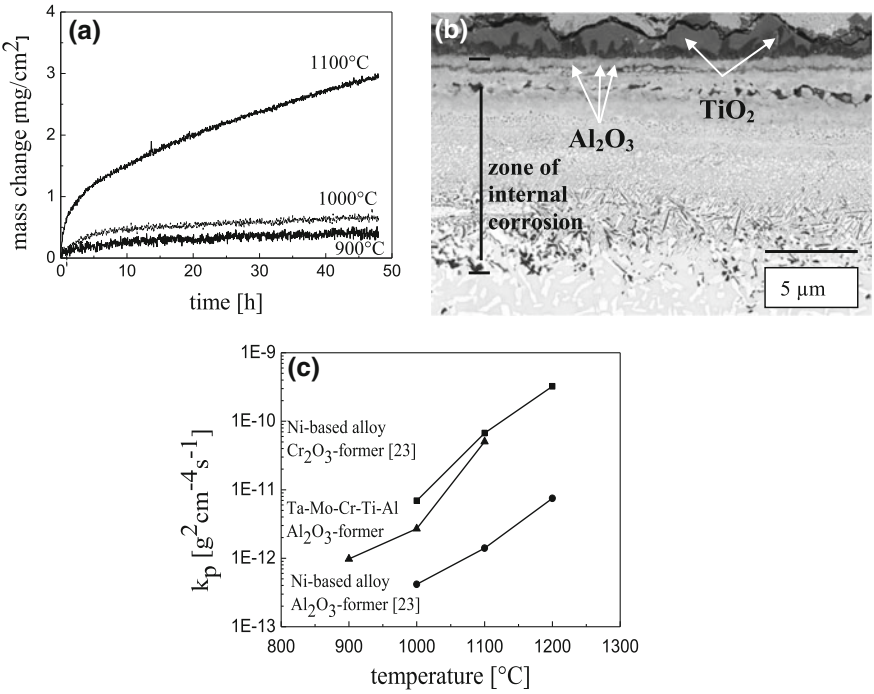

Fig. 5 Oxidation behavior of the alloy Ta-Mo-Cr-Ti-Al in air at high temperatures; **a** Thermogravimetric curves, **b** Cross-section after 48 h oxidation at 1000 °C and **c** Oxidation constants of the alloy Ta-Mo-Cr-Ti-Al compared to those of Ni-base alloys after [23]

results on the mechanical properties of the alloys at room and elevated temperatures show potentials with respect to the high temperature strength, while the low-temperature ductility should be significantly improved. In terms of high temperature oxidation behavior, both refractory metal-based alloys, Nb-Mo-Cr-Ti-Al and Ta-Mo-Cr-Ti-Al, exhibit good to even excellent oxidation resistance. The prime aim of the further alloy development is the successive improvement of mechanical properties of these alloys. The alloy development will be particularly focused on the improvement of low-temperature ductility and high temperature strength while keeping the oxidation resistance on the level already established for the Ta-system (Fig. 5). To improve mechanical properties, three strategies will be pursued in three subsequent steps: (i) the formation of the inherently brittle phases should be suppressed, (ii) a two-phase microstructure with a substantial amount of the second strengthening phase should be established and (iii) the alloy matrix should provide sufficient intrinsic RT ductility.

The first approach primarily aims at the increase of the alloy's intrinsic ductility. This goal will be realized by suppressing the formation of the Laves-phase. Starting from the equimolar alloy composition, the chromium concentration will be progressively reduced related to the concentration of other elements. As mentioned

above, to eliminate Cr entirely seems to be not reasonable because Cr facilitates the formation of the protective alumina scale. The aim is, therefore, to find a suitable balance in the Cr concentration which ensures that Laves-phase will not form on the one hand and the formation of the alumina scale is still possible on the other hand.

The second strategy focuses on an enhancement of the high temperature strength to achieve the level of other refractory HEAs exhibiting two-phase microstructures [10]. Following this approach, the formation of BCC and B2 two-phase microstructure with (preferentially) coherent phase boundaries will be aimed. As shown above, BCC is the major phase in the alloy Nb-Mo-Cr-Ti-Al, while the alloy Ta-Mo-Cr-Ti-Al contains a significant amount of the B2 phase. Through varying the Nb/Ta ratio in a new alloy series Nb-Ta-Mo-Cr-Ti-Al, the formation of both, BCC and B2 phases, is to be expected. Due to different Nb/Ta ratios, the fraction of the B2 phase should be controlled.

The third concept aims at further ductilizing the alloy matrix, i.e. the BCC phase, at RT. This will be done by Re addition. The positive impact of Re on ductility of refractory elements was confirmed for several alloy systems as discussed in *Introduction*. To explore the effect of Re on alloy ductility fundamentally, we will start with alloys Nb-Mo-Cr-Ti-Al and Ta-Mo-Cr-Ti-Al with decreased Cr concentrations, i.e. without Laves phases. Initially, the Re-concentration will be set equal to those of Nb/Ta, Mo, Ti and Al and then gradually decreased to identify the minimal Re-content required to reasonably improve the RT ductility.

In order to establish the fundamental understanding of the alloy behavior, the main attention in our future investigations will be paid on the establishment of the correlation between the alloy chemical composition and its microstructure as well as between the alloy composition/microstructure and its mechanical properties.

Summary

Based on recent experimental results, the following conclusions can be drawn in terms of a potential use of the alloy system X-Mo-Cr-Ti-Al (X = Nb, Ta) for high temperature structural applications:

- The microstructure of the alloy Nb-Mo-Cr-Ti-Al consists of a disordered BCC-matrix, and a small amount of minor phases, Cr_2Nb (C14, hexagonal) and $Al(Mo, Nb)_3$ (A15, cubic). The alloy Ta-Mo-Cr-Ti-Al consists of a mixture of BCC phase, the ordered B2 phase and three Laves-phases.
- The mechanical properties of the alloys Nb-Mo-Cr-Ti-Al and Ta-Mo-Cr-Ti-Al show perspectives, however, they should be significantly improved to satisfy requirements of high temperature applications. In particular, the alloys show reasonable values of high temperature strength, while the low-temperature ductility has to be enhanced significantly. It seems that the Laves-phase(s) contribute(s) to the unacceptable brittleness of the alloys at low-temperatures;

the B2-phase may have, in contrary, a positive effect on high temperature strength.
- Both alloys, Ta-Mo-Cr-Ti-Al in particular, show a surprisingly high level of oxidation resistance at high temperatures due to the formation of a protective alumina scale.

To improve the RT ductiliy, following strategies will be pursued: (i) the formation of the brittle Laves phase will be suppressed by lowering the Cr concentration, (ii) a two-phase microstructure with the second strengthening phase B2 should be established and (iii) a sufficient ductility at room temperature will be provided by addition of potentially ductilizing elements such as Re.

References

1. Senkov ON, Wilks GB, Scott JM, Miracle DB (2011) Mechanical properties of $Nb_{25}Mo_{25}Ta_{25}W_{25}$ and $V_{20}Nb_{20}Mo_{20}Ta_{20}W_{20}$ refractory high entropy alloys. Intermetallics 19:698–706
2. Miracle DB, Miller JD, Senkov ON, Woodward CF, Uchic MD, Tiley J (2014) Exploration and development of high entropy alloys for structural applications. Entropy 16:494–525
3. Senkov ON, Scott JM, Senkova SV, Meisenkothen F, Miracle DB, Woodward CF (2012) Microstructure and elevated temperature properties of a refractory TaNbHfZrTi alloy. J Mater Sci 47:4062–4074
4. Senkov ON, Semiatin SI (2015) Microstructure and properties of a refractory high-entropy alloy after cold working. J Alloy Compd 649:1100–1123
5. Senkov ON, Woodward CF (2011) Microstructure and properties of a refractory NbCrMo0.5Ta0.5TiZr alloy. Mater Sci Eng A 529:311–320
6. Senkov ON, Senkova SV, Woodward CF, Miracle DB (2013) Low density, refractory multi-principle element alloys of the Cr-Nb-Ti-V-Zr system: microstructure and phase analysis. Acta Mater 61:1545–1557
7. Senkov ON, Senkova SV, Miracle DB, Woodward CF (2013) Mechanical properties of low-density, refractory multi-principle element alloys of the Cr-Nb-Ti-V-Zr-system. Mater Sci Eng A 565:51–62
8. Hosoj Y, Wade N, Kunimitsu S, Urita T (1986) Precipitation behavior of laves phase and its effect on toughness of 9Cr-2Mo ferritic-martensitic steel. J Nucl Mater 141:461–467
9. Xia ZX, Wang CY, Zhao YF, Zhang GD, Zhang L, Meng XM (2015) Laves phase formation and its effect on mechanical properties in P91 steel. Acta Metall Sin 28:1238–1246
10. Senkov ON, Isheim D, Seidman DN, Pilchak AL (2016) Development of a refractory high entropy superalloy. Entropy. https://doi.org/10.3390/e18030102
11. Senkov ON, Senkova SV, Woodward CF (2014) Effect of aluminium on the microstructure and properties of two refractory high entropy alloys. Acta Mater 68:214–228
12. Tietz TE, Wilson JW (1965) Behavior and properties of refractory metals. Edward Arnold Ltd, London
13. Geach GA, Hughes JE (1955) The alloys of rhenium with molybdenum or with tungsten having good high-temperature properties, Plansee Proceedings, Pergamon Press Ltd, London
14. Jaffe RI, Sims CT (1958) The effect of rhenium on the fabricability and ductility of molybdenum and tungsten, technical report 156574, Battelle Memorial Institute
15. Leichtfried G, Schneibel JH, Heilmaier M (2006) Ductility and impact resistance of powder-metallurgical molybdenum-rhenium alloys. Metall Mater Trans A 37A:2955–2961

16. Klopp WD, Witzke WR, Raffo PL (1965) Ductility and strength of dilute tungsten-rhenium alloys, technical report NASA TM X-52134
17. Wukusick CS (1964) On the mechanism of the rhenium-alloying effect in group VI-A metals, Report GEMP-314, General Electric Co
18. Chen H, Kauffmann A, Gorr B, Schliephake D, Seemüller C, Wagner JN, Christ HJ, Heilmaier M (2016) Microstructure and mechanical properties at elevated temperatures of a new Al-containing refractory high-entropy alloy Nb-Mo-Cr-Ti-Al. J Alloy Compd 661: 206–215
19. Gorr B, Mueller F, Christ HJ, Mueller T, Chen H, Kauffmann A, Heilmaier M (2016) High temperature oxidation behavior of an equimolar refractory metal-based alloy 20Nb-20Mo-20Cr-20Ti-20Al with and without Si addition. J Alloy Compd 688:468–477
20. Gorr B, Wang L, Burk S, Azim M, Majumdar S, Christ HJ, Mukherji D, Rösler J, Schliephake D, Heilmaier M (2014) High-temperature oxidation behavior of Mo-Si-B-based and Co-Re-Cr-based alloys. Intermetallics 48:34–43
21. Birks N, Meier GH (1983) Introduction to high temperature oxidation of metals. Edward Arnold, London
22. Gorr B, Müller F, Azim M, Christ HJ, Müller T, Chen H, Kauffmann A, Heilmaier M (2017) High temperature oxidation behavior of refractory high entropy alloys: effect of alloy composition. Oxid Met. https://doi.org/10.1007/s11085-016-9696-y
23. Giggins CS, Petitt FS (1971) Oxidation of Ni-Cr-Al alloys between 1000 and 1200 °C. J Electrochem Soc 118:1782–1790

First-Principles Calculations of Stacking Fault Energies in Quinary High-Entropy Alloy Systems

A. M. Scheer, J. D. Strother and C. Z. Hargather

Abstract High entropy alloys (HEAs) are composed of equal or nearly equal quantities of five or more metals that solidify into a single, or sometimes dual, solid solution phase. Due to improved properties in high-temperature and high-stress applications, HEAs have the potential to replace traditional alloy systems in future engineering applications, such as turbine blades and thermal spray coatings. In the present work, first-principle calculations based on density functional theory are used to calculate and rank the stacking fault energies of several quinary HEA systems in order to better understand the slip and deformation behavior of HEA systems. Special quasirandom structures are used to represent the single solid solution with a finite number of atoms and calculations are performed in the Vienna ab initio simulation package within the generalized gradient approximation as implemented by Perdew, Burke, and Ernzerhof. Stacking fault energy calculations are based on the difference between the ground state energy of the perfect HEA structure and the ground state energy of a faulted HEA structure. To validate the calculations, results are compared to experimental data, such as lattice parameter and formation energy, for well-studied HEA system.

Keywords High entropy alloys · FCC · Stacking fault energy
Density functional theory

Introduction

High Entropy Alloys (HEAs) are unique alloys composed of equal or nearly equal quantities of five or more metals in a single phase or dual phase solid solution [1]. HEAs are a relatively new class of materials and have drawn a considerable amount of attention due to the potential possibility to replace traditional engineering alloy

A. M. Scheer (✉) · J. D. Strother · C. Z. Hargather
Department of Materials Engineering, New Mexico Institute of Mining and Technology, Socorro, NM 87801, USA
e-mail: Alexandra.scheer@student.nmt.edu

The Minerals, Metals & Materials Society, *TMS 2018 147th Annual Meeting & Exhibition Supplemental Proceedings*, The Minerals, Metals & Materials Series,
https://doi.org/10.1007/978-3-319-72526-0_62

systems in various applications [1]. The promising qualities of HEAs are: higher resistance to fracture, corrosion and oxidation, and improved ratios between mechanical properties (ductility, strength, and toughness) and weight when compared to conventional alloy systems such as the GTD-111 Ni-base superalloy used as advanced turbine blades [2] and Nitinol (memory shape alloy) used a variety of medical applications [3].

Stacking Fault Energy (SFE) is a critical concept when designing alloys because it is an indicator of the predominant plastic deformation mechanism available in a given HEA system [1]. HEAs containing a high SFE tend to deform by the glide mechanism with minimal transformation and then into partial dislocations, while alloys with low SFE deform by decomposing into partial dislocations more easily [1]. HEAs have the potential to replace traditional alloys because of their improved mechanical properties and potential formability. Being able to calculate and predict the SFE of more face centered cubic (FCC) HEAs will lead to trailblazing knowledge of the failure mechanisms of FCC HEAs.

In order to effectively establish HEAs in engineering alloy applications, creep rates have to be researched and understood. Creep is time-dependent deformation that occurs when temperature and stress remain constant and alloys are in service at elevated temperatures. When creep failure occurs, it is inelastic and irrecoverable [4, 5]. As previously suggested by McLean in 1962 [6], Weertman in 1965 [7], and Barrett and Sherby in 1965 [8], the majority of secondary creep rate models depend on the SFE of the material. Generating computational SFE of FCC HEA systems is an efficient method to get one piece of the puzzle for establishing creep knowledge of HEAs for potential use in engineering alloy applications.

Efficient computational methods for understanding deformation behavior of HEAs have been established in the literature. As first seen in the work of Zaddach et al. [9] density functional theory (DFT) combined with special quasirandom structures (SQS) can be used to obtain the ground state energy of an HEA system. Zaddach et al. [9] also revealed, by studying binary to quinary HEAs experimentally and computationally, that as more elements are added to a system the SFE decreases. Zhang et al. [10] concluded that for ternary and quaternary FCC HEAs, the stacking fault energy can be tuned as a result of local atomic temperature and environment, the origin of negative stacking fault energy in HCP systems, and lattice distortion.

The present work focuses on using first-principles calculations for computational analysis of equiatomic FCC high entropy alloys. The HEA systems investigated are: FeCrCoNiMn, FeCrCoNiCu, and FeCrCoNiAl. The stacking fault energy is calculated for quinary systems directly, and will also be analyzed as an average of the SFE in all constituent ternary systems to investigate if a less computationally expensive option is feasible.

Methodology

The HEA systems studied in the present work are single FCC solid solutions, with equiatomic compositions of the FeCrCoNiMn, FeCrCoNiCu, and FeCrCoNiAl alloys. To represent the single FCC solid solution phase, special quasirandom structures (SQS) are employed [11]. SQSs are created to simulate random dispersion of atom types within the crystal structure using a finite number of atoms. This is done by mimicking the pair correlation functions and bonding behavior of a truly random solid solutions for the first several nearest neighbor shells [1, 12]. In the present work, the atomic positions for 20-atom quinary SQS structure are taken from Gao et al. [1] and Zaddach et al. [9]. The atomic positions for an equiatomic 24-atom ternary SQS structure are taken from Shin et al. [13].

To find the ground state energy of the necessary atomic configurations, in the present work, first-principles calculations based on density functional theory are performed using Vienna ab initio simulation package (VASP) [14]. Calculations are based on the use of the projector augmented wave [15] and generalized gradient approximation as executed by Perdew et al. [16]. The energy cut-off for the plane wave is set to 350 eV, which is about 1.3 times that of the maximum default plane wave cutoff among elements considered, and the SQS structures are non-spin-polarized. During VASP calculations, a combination of the Methfessel-Paxton smearing and Blöchl methods are used. Methfessel-Paxton smearing method [17] computes the forces acting on the atoms. When combined with the linear tetrahedral method in Blöchl's correction for a final single point calculation, an accurate total energy calculation is obtained [18]. Total energy convergence was set to at least 0.5 meV/atom and all degrees of freedom are allowed to relax during calculations. The structures were checked upon completion to ensure the FCC SQS structure was still intact. A gamma-centered k-point mesh of $4 \times 7 \times 7$ is employed.

Three separate sets of quinary 20-atom HEA systems are considered in the present work: FeCrCoNiMn, FeCrCoNiCu, and FeCrCoNiAl. Six 24-atom constituent ternary systems, FeCrCo, CrCoNi, CoNiMn…etc., are also considered. Stacking faults are induced in both the 20-atom quinary and 24-atom ternary systems such that the standard ABCABCABC stacking sequence becomes ABCA**BCBC**AB, where the fault is shown in bold type font. The ground state energies of all systems considered are then calculated using VASP.

To calculate intrinsic SFE in the quinary HEA systems, γ_{isf} the difference of total energies from two different SQS configurations are taken following Eq. 1 [10],

$$\gamma_{isf} = \frac{E_{isf} - E_0}{S_0} \tag{1}$$

where E_{isf} describes the energy of the faulted cell found in the manner is described above, E_0 represents the energy of the primitive cell, and S_0 is the area of the

stacking fault. Equation 1 is applied to the quinary SQS structures: FeCrCoNiMn, FeCrCoNiCu, and FeCrCoNiAl.

The SFEs of the 3 HEA systems are also calculated by averaging the SFE of each of the six constituent ternary systems. A stacking fault in each of the six constituent ternary systems is induced and the SFE for the ternary HEA is calculated following Eq. 2:

$$\gamma_{isf_{average}} = \frac{\left[\left(\frac{E_{isf}-E_0}{S_0}\right)_{ABC} + \left(\frac{E_{isf}-E_0}{S_0}\right)_{BCA} + \left(\frac{E_{isf}-E_0}{S_0}\right)_{CAB} \ldots \text{etc.}\right]}{6} \tag{2}$$

where γ_{isf} is the average ternary SFE, E_{isf} is the energy of the faulted cell found for the individual ternary system, E_0 represents the energy of the individual primitive cell, and S_0 is the individual area of the stacking fault.

Results and Discussion

Before calculating the SFE in HEA systems, the possibility of atomic configuration affecting the ground state energy of the SQS cell is investigated. This was done to ensure that specific pairs or triplets of atoms that were formed within the SQS did not have a significant impact on the ground state energy of the system, which would require additional consideration when calculating the SFEs. Fourteen atomically randomized 20-atom SQS configurations (i.e. AAAABBBBCCCCDDDDEEEE, BBBBCCCCDDDDEEEEAAAA) are considered for the FeCrCoNiMn FCC HEA, where A = Fe, Cr = B, Co = C, etc. The ground state energies are then calculated to understand the behavior of the configuration and their effect on the energy values. Figure 1 represents the data from the investigation of the atomic

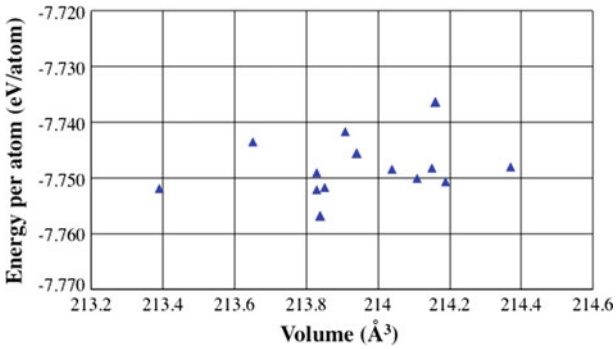

Fig. 1 Energy versus volume based on present data from fourteen different atomic position configurations

Table 1 Statistics of ground state energy from fourteen different SQS configuration calculations

Mean energy per atom (eV)	−7.75
Standard deviation	0.00568
Range (eV)	0.0203

Table 2 Comparison of lattice parameters of the FeCrCoNiMn SQS to known experimental and calculated values in the literature [1, 9]

Lattice parameter	Reference	%diff.
3.50	This work	–
3.54	VASP + SQS [9]	1.11
3.624	Milled [9]	3.11
3.597	Cast [9]	2.70

configuration on ground state energy of the system. The ground state energy of each SQS configuration is plotted versus the volume in $Å^3$ of the cell.

Table 1 establishes a statistical analysis based on the energy values calculated from the fourteen different SQS structures that were presented in Fig. 1. The results show that the average energy per atom of the SQS structures, regardless of atomic configuration, was −7.75 eV/atom, with an extremely tight standard deviation. The statistics in Table 1 lead us to the conclusion that the atomic position of the atoms in the SQS does not significantly affect the results.

To validate the idea that SQSs can be used to accurately represent experimentally investigated HEAs, the lattice parameters from the 14 configurations calculates in the present work are averaged and compared to known values in literature. Table 2 specifies that the average lattice parameter calculated in the present work agree with about 1% error of published values from previously calculated values [1] and within 3% difference from experiments which either cast or milled the FeCrCoNiMn HEA [9]. The differences in the lattice parameters calculated in the present work and previously calculated values from Zaddach et al. [9] could be due to a different treatment of the 3p electrons in Fe, Cr, and Mn from Zaddach's work, and that the present work achieved an additional order of magnitude of energy convergence.

So far, the present work shows that atomic positioning of the atoms does not affect the energy of the system and established a process for obtaining the ground state energy and lattice parameter of quinary SQS HEA systems. The next steps are to apply this methodology to calculate the ground state energy for the faulted and pristine FeCrCoNiMn, FeCrCoNiAl, and FeCrCoNiCu systems. Upon completion of the calculations, the SFE energy will be calculated in two different ways following Eqs. 1 and 2 presented in the methodology section. It is expected that the calculated SFEs will be similar regardless of the calculation method, and that the less computationally expensive technique can be used to report the SFE in a wide variety of equiatomic HEA systems, including higher order systems that are currently computationally prohibitive to study. The complete results from this study will be presented at the 2018 TMS annual meeting associated with this manuscript.

Conclusion

High entropy alloys have the potential to replace traditional alloy systems in future engineering applications such as turbine blades and thermal spray coatings due to their improved properties in high-temperature and high-stress applications. In the present work, an investigation into atomic configuration and the lattice parameter of the FeCrCoNiMn system has been completed. The quinary 20-atom SQS FeCrCoNiMn HEA analysis shows that an ordering of the atom types does not change the ground energy value of the system. This finding helps eliminate redundant possibilities when setting up HEA atomic configurations as well as confirms a process for calculating ground state energy of a HEA system represented using SQS. By implementing VASP + SQS methodology described in the present work, the SFE energy in various HEA systems will be calculated following the two methods described above.

Acknowledgements Calculations performed in this work used the Extreme Science and Engineering Discovery Environment (XSEDE), which is supported by National Science Foundation grant number ACI-1053575, on grant award RF-DMR160006. Start-up funding from New Mexico Institute of Mining and Technology and a generous gift from an anonymous donor were also used to perform this research. The authors would like to thanks J. E. Saal for stimulating discussions related to the research.

References

1. Gao MC, Yeh J-W, Liaw PK, Zhang Y (2016) High-entropy alloys: fundamentals and applications. Springer
2. Reed R (2008) The superalloys: fundamentals and applications. Cambridge University Press, Cambridge
3. Machado LG, Savi MA (2003) Medical applications of shape memory alloys. Braz J Med Biol Res 36(6):683–691
4. Abbaschian R, Reed-Hill RE (2008) Physical metallurgy principles. Cengage Learning
5. Guo Z, Miodownik AP, Saunders N, Schille JP (2006) Influence of stacking-fault energy on high temperature creep of alpha titanium alloys. Scr Mater 54(12):2175–2178
6. Mclean D (1962) Deformation at high temperatures. Metall Rev 7(1):481–527
7. Weertman J (1965) Theory of the influence of stacking-fault width of split dislocations on high-temperature creep rate. Trans Metall Soc AIME 233:2069–2074
8. Barrett CR, Sherby OD (1965) Influence of stacking-fault energy on high-temperature creep of pure metals. Trans Metall Soc AIME 223:1116
9. Zaddach AJ, Niu C, Koch CC, Irving DL (2013) Mechanical properties and stacking fault energies of NiFeCrCoMn high-entropy alloy. JOM 65(12):1780–1789
10. Zhang YH, Zhuang Y, Hu A, Kai JJ, Liu CT (2017) The origin of negative stacking fault energies and nano-twin formation in face-centered cubic high entropy alloys. Scr Mater 130:96–99
11. Zunger A, Wei SH, Ferreira LG, Bernard JE (1990) Special quasirandom structures. Phys Rev Lett 65(3):353–356

12. Zacherl C, Saal J, Wang Y, Liu ZK (2010) First-principles calculations and thermodynamic modeling of the Re-Y system with extension to the Ni-Re-Y system. Intermetallics 18(12): 2412–2418
13. Shin D, van de Walle A, Wang Y, Liu Z-K (2007) First-principles study of ternary fcc solution phases from special quasirandom structures. Phys Rev B 76(14):144204
14. Kresse G, Furthmuller J (1996) Efficient iterative schemes for ab initio total-energy calculations using a plane-wave basis set. Phys Rev B 54(16):11169–11186
15. Blöchl PE (1994) Projector augmented-wave method. Phys Rev B 50(24):17953
16. Perdew JP, Burke K, Ernzerhof M (1996) Generalized gradient approximation made simple. Phys Rev Lett 77(18):3865
17. Methfessel M, Paxton AT (1989) High-precision sampling for Brillouin-zone integration in metals. Phys Rev B 40(6):3616
18. Blochl PE, Jepsen O, Andersen OK (1994) Improved tetrahedron method for Brillouin-zone integrations. Phys Rev B 49(23):16223

Synthesis of FeCrVNbMn High Entropy Alloy by Mechanical Alloying and Study of their Microstructure and Mechanical Properties

P. Ajay Kumar and Chandra S. Perugu

Abstract Traditional alloys are designed on the basis of one or more majority of materials which is Fe-based, Ni-based, and Co-based super alloy for mechanical properties enhancement but results with poor ductility at room temperature. New alloy design of materials requires more alloying elements for improving the material properties consistently. High entropy alloy consists of at least five principal elements with the concentration of each material between 5 and 35 at.% on the basis of maximum configurational entropy at equi-atomic composition with more stable than intermetallic at elevated temperatures. In this paper, FeCrNbVMn alloy phase formed by mechanical alloying. The mechanically alloyed powders were subsequently consolidated by cold pressing and sintered in tube furnace. Analysis of microstructure and mechanical properties were carried out with the help of XRD, SEM, TEM and nanoindetation tests. The bulk sample showed hardness of ~19 GPa at nano scale.

Keywords High entropy alloys (HEA) · Mechanical alloying
Scanning electron microscopy (SEM) · Transmission electron microscopy (TEM)

Introduction

J. W. Yeh introduced the new concept of materials with multicomponent in equi-atomic proportions and these are called as high entropy alloys [1]. High entropy alloys are defined as the ones that possess high configurational entropy and

P. Ajay Kumar (✉)
Department of Materials Engineering, Indian Institute of Science, Bangalore 560012, India
e-mail: ajaymits85@gmail.com

C. S. Perugu
Department of Materials Science and Engineering, University of Wisconsin, Milwaukee, WI 53211, USA

The Minerals, Metals & Materials Society, *TMS 2018 147th Annual Meeting & Exhibition Supplemental Proceedings*, The Minerals, Metals & Materials Series,
https://doi.org/10.1007/978-3-319-72526-0_63

these materials could easily be formed in a multi-component system containing equi-atomic concentration of all the elements. HEA contains at least five principal elements with the concentration of each element being between 5 and 35 at.%. The principle behind this is that the configurational entropy is maximum at equiatomic composition and it increases with increase in the number of elements in the system. This configurational entropy is maximized to form a simple solid solution rather than an intermetallic. Solid solutions with multicomponent elements have been more stable than intermetallic compounds at elevated temperatures due to their large entropy of mixing. Mechanical alloying (MA) is a non-equilibrium process to get a homogenous mixing of alloy compositions in multicomponent system as compared to conventional casting process. It was reported that the solid solubility of mutual soluble components can be increased and supersaturated solid solutions can be prepared by mechanical alloying [2–4]. For insoluble systems, alloys with a degree of solid solubility can be formed under high-energy collision. Thus, powder metallurgy is a promising technique not only for the basic research but also for the industrial application of HEAs. The new combination of HEA alloy is open to explore the high temperature alloy. In this work, we have studied new alloy composition FeCrVNbMn phase formation and its mechanical properties.

Experimental Details

The elemental powders of Fe, Cr, V, Nb, Mn and Nb with particle size (-325 mesh) or diameter ≤ 45 μm and 99.95% purity in equi-atomic (20 at.%) proportion were used as the starting material and tungsten carbide vial (vol. 45 ml) and balls (dia. 10 mm) were used as the milling media. The elemental powders were milled in a planetary ball mill and stearic acid was used as process controlling agent (PCA) in order to avoid excessive cold welding. All the experiments were carried out under argon atmosphere to avoid the excessive contamination from the environment. The milling was carried out with ball to powder ratio of 10:1 and speed was 500 rpm. Milling was conducted for 1, 2, 4, 6, 8 and 10 h. To investigate the phase formation of milled powders x-ray diffraction was performed by Bruker D8 advanced diffractometer (XRD) with Cu kα ($\lambda = 1.5406$ Å) radiation. Scanning electron microscope (SEM) model ESEM Quanta with energy dispersive x-ray spectrometer (EDS) was used to observe microstructural changes and elemental distribution took place during the milling process. Transmission electron microscope (TEM) was used to obtain the microstructural, crystal structure and grain size information of the milled product. The mechanically alloyed powder was subsequently consolidated by cold pressing and sintering in tube furnace at 600 °C followed by nanoindentation studies.

Results and Discussion

XRD Analysis

Figure 1 shows the x-ray diffraction patterns obtained from FeCrNbVMn multi-component alloy powder that was ball milled for different time durations ranging from 0 to 10 h. The XRD pattern obtained from the initial powder mix (i.e. 0 h ball-milled) show many low and high intensity peaks and all the observed peaks are identified to different raw elemental powders used in the mixture. Diffraction peaks related to Nb and V are overlapped with high intensity peaks, whereas Cr, Fe, and Mn related are superimposed with much lower intensity peaks. Diffraction intensity, in general, depends on many factors, such as atomic number, grain size, crystallinity, lattice strain, etc. For the raw powders of this alloy system, Nb is the heaviest element, which endows it with the highest XRD intensity. Drastic decrement of diffraction intensity is observed after 2 h of ball milling. The diffraction peaks of Cr, Fe, and Mn elements can hardly be identified after 2 h ball milling. At this time, only four diffraction peaks can be clearly observed. As the milling duration reaches up to 10 h, the diffraction peaks exhibit no change except for a minor broadening. The disappearance of diffraction peaks and peak broadening can be considered as the beginning of solid-solution reaction and stable formation of bcc solid solution [4, 5]. The intensity decrement and peak broadening are related

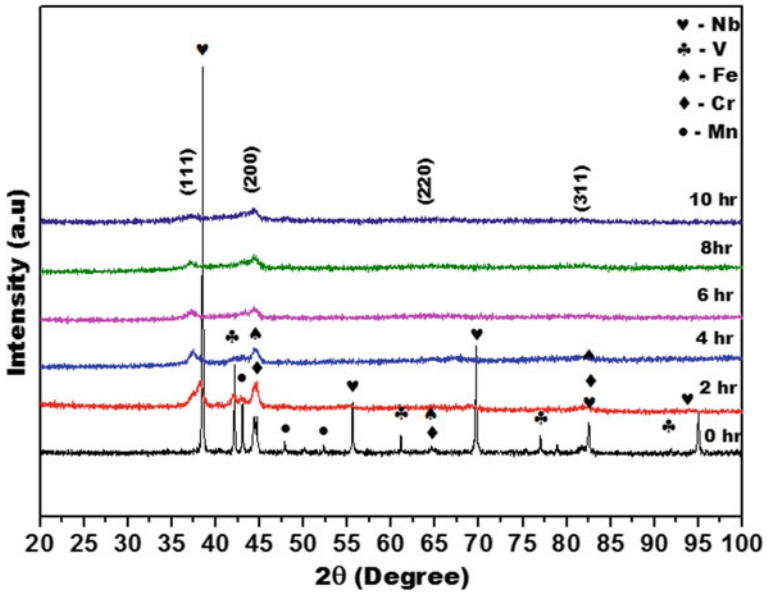

Fig. 1 XRD patterns of ball milled HEA alloy after different duration of time

with the formation of nanocrystalline and high lattice strain induced by mechanical deformation during the MA process [6].

The crystallite size and lattice strain of the metallic powders milled for different durations have been calculated using Scherrer's formula and the x-ray peak broadening after eliminating the instrumental contribution. The crystallite size is greatly refined as the milling duration increases. The 10 h mechanically alloyed powder exhibits a crystallite size of 40 nm. Refinement of the crystal structure is conducted by periodic crushing and cold welding during the milling process. This circulation invokes elemental diffusion and alloying different elements which eventually results in solid solutions for this multicomponent metallic powder. Alloying occurs when the grain sizes of the elemental components decrease down to nanometres range and a substantial amount of enthalpy can be stored in nanocrystalline alloys because of the large grain boundary area [6]. The stored energy serves as the internal driving force to produce solid solution among multicomponent system. Inter-diffusion among the components occurs and the solid solubility is expected to be increases as the milling time is prolonged. No further extension of solid solubility will be achieved until it reaches a super saturation state. The lattice strain of FeCrNbVMn alloy powder increases gradually as the milling time prolongs. The 10 h ball-milled powder exhibits a high lattice strain of 1.06% as calculated from Williamson-Hall method. Generally, the increment in lattice strain is caused by the size mismatch effect among the elements, increased grain boundary fraction and mechanical deformation. As the milling is extended, the grain boundary fraction and mechanical deformation are continuously increased because of the decreased crystallite size. The formation of solid solution among multiple elements increases the size mismatch because of their different atomic radius leads to sluggish diffusion. The increment in lattice strain may also cause by the increased dislocation density produced by severe plastic deformation. The lattice parameter of FCC solid solution alloy is 3.8303 Å.

Microstructure and Phase Analysis

Figure 2 shows the SEM image obtained from the 10 h ball-milled powders and characterized by scanning electron microscopy. The powders were obviously crushed down to refined particles with granular size less than nano meter range as it was ball milled for 10 h. In the milling process, the raw powders were first broken to form much smaller particles. The crushed granules were then cold welded to form much larger ones. This repeated refinement and agglomeration continues for a long time. During this period, the particle size remains almost unchanged, whereas the grain size decreases continuously as milling proceed. The EDS microanalysis results exhibit the chemical homogeneity and equivalent composition as designed after 10 h of ball milling. The average grain size calculated from more than 100

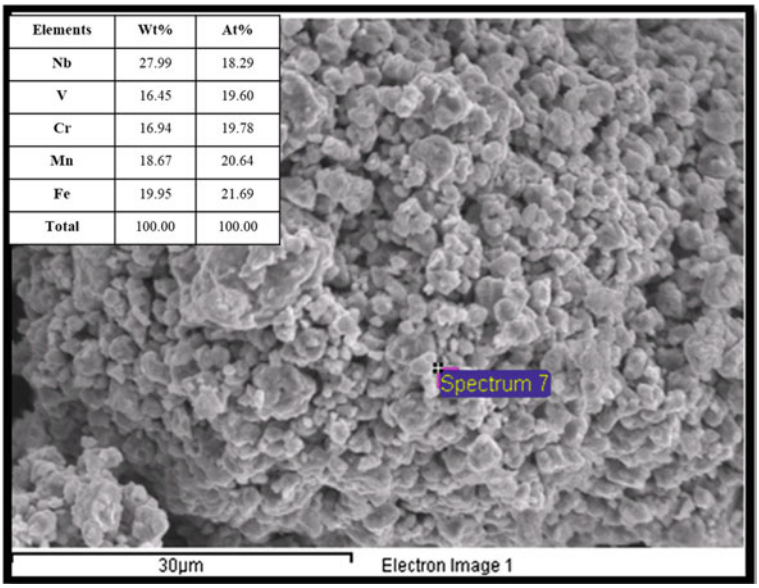

Fig. 2 SEM microstructure of FeCrNbMnV alloy after 10 h of ball milling and EDX analysis

grains is found to be 20 nm. It is to be noted that large fraction of grains is in the range of 10–20 nm and the distribution is nearly uniform. Figure 3 shows the dark field TEM image (Fig. 3a) and corresponding SAD pattern (Fig. 3b) obtained from the 10 h ball-milled powder. The indexed SAD pattern confirmed that the FCC structured solid solution does exist after 10 h of milling.

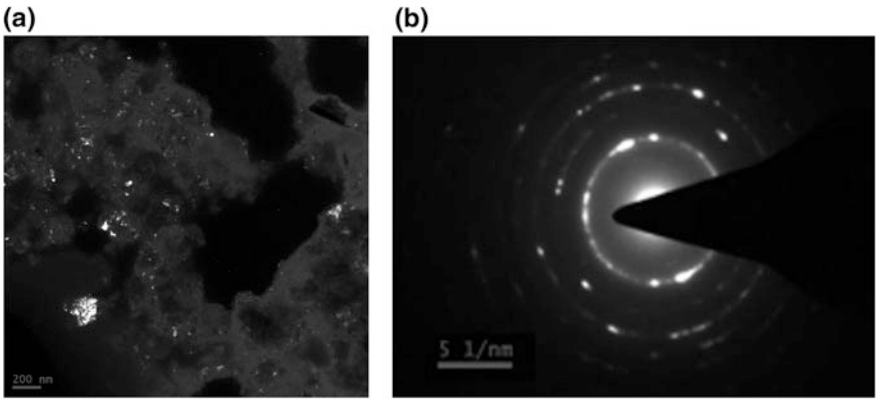

Fig. 3 TEM analysis of HEA alloy after 10 h of milling showing **a** dark field image with crystallite size **b** SAD pattern of polycrystalline nature of FCC solid solution

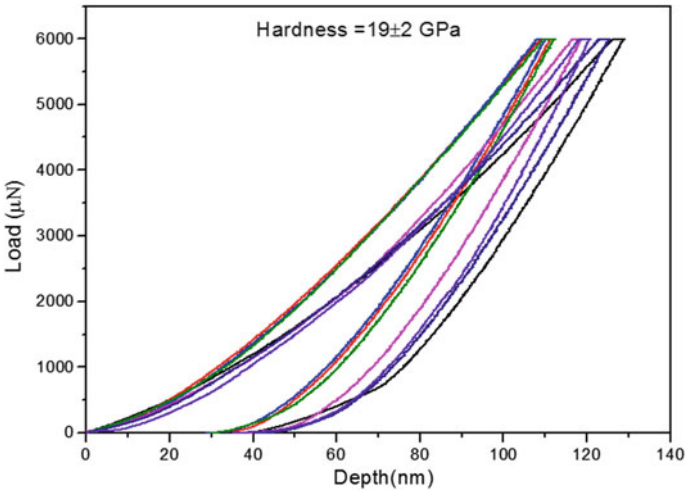

Fig. 4 Load versus depth curves of nano crystalline FeCrVNbV high entropy alloy show the hardness of 19 GPa

Mechanical Properties by Nano Indentation

With the development of nanostructured metals and alloys, instrumented nano indentation seems to be very useful in obtaining the fundamental mechanical properties and for understanding the fundamental material physics. This characterization technique is a very powerful tool, because the tested volume of material is compatible with the microstructure. Load vs depth curves obtained by nanoindentation tests on sintered and consolidated FeCrVNbV HEA showed ~19 GPa hardness for 10 h ball-milled (Fig. 4) which is almost double in rate as compared to the few reported alloy systems. Superior strength of high entropy alloy is attributed to solid solution strengthening and its nanocrystalline nature [7].

Conclusions

FeCrVNbMn multicomponent alloys were successfully prepared by high energy mechanical alloying process in this study. The alloy powders, which are in simple FCC solid solution structure, were synthesized by 10 h ball milling. The particles of the alloy powder are in near spherical structure with uniform size and equiatomic elemental composition. The alloy composition at TEM analysis confirms the nano size particle distribution and FCC solid solution with polycrystalline nature. The bulk sample prepared for nano indentation studies exhibited hardness of ~19 GPa.

Acknowledgements The authors wish to acknowledge Prof. Sundararaman, for giving valuable suggestions to carry out this work.

References

1. Yeh JW, Chen SK, Lin SJ, Gan JY, Chin TS, Shun TT, Tsau CH, Chang SY (2004) Adv Eng Mater 6:299
2. Suryanarayana C (2001) Prog Mater Sci 46:1
3. Murty BS, Ranganathan S (1998) Int Mater Rev 43:101–141
4. Koch CC (1997) Pergamon-Elsevier Science Ltd, pp 13–22
5. Varalakshmi S, Kamaraj M, Murty BS (2008) J Alloys Comp 460:253–257
6. Liang Yu, Chen Y, Hu H, Hsieh CA, Yeh S, Chen SK (2009) J Alloys Comp 48:1768–1775
7. Yeh JW, Chen SK, Gan JY, Lin SJ, Chin TS, Shun TT, Tsau CH, Chang SY (2004) Metall Mat Trans A Phys Metall Mat Sci 35:2533

Part XXVI
Integrative Materials Design III: Performance and Sustainability

Magnesium-Based Metal Matrix Nanocomposites—Processing and Properties

Hajo Dieringa and Norbert Hort

Abstract It is well known that magnesium alloys reinforced with ceramic particles of micro-scale sizes give increased hardness and wear resistance. However, such particles need to be smaller to improve the strength, ductility and creep resistance of alloys. The optimum size of particles for Orowan strengthening is a diameter less than 100 nm. Not only the size of particles, but also their chemical composition and the composition of the alloy are important for the beneficial effect of nanoparticles. The mechanical properties can be tailored with much fewer nanoparticles compared to microparticles, because the interparticle spacing is much smaller. However, with large surface areas compared to their weight and low wettability, any deagglomeration of the nanoparticles in a magnesium melt is difficult to achieve and so requires additional processing, such as by electromagnetic or ultrasound-assisted stirring. This paper presents a short review and some original work on ceramic nanoparticle reinforced magnesium alloys and their properties.

Keywords Metal matrix nanocomposite · MMNC · Mechanical properties
Grain refinement · Orowan strengthening

Introduction

Magnesium-based metal matrix composites (MMCs) have been developed since the early 1980s. Microscale particle reinforcement improves wear resistance, hardness and strength by a certain amount [1, 2]. Short or long fiber reinforcement significantly improves strength [1, 3] and creep resistance [4–6], as well as fatigue

H. Dieringa · N. Hort (✉)
Helmholtz-Zentrum Geesthacht, MagIC – Magnesium Innovation Centre,
Max-Planck-Straße 1, 21502 Geesthacht, Germany
e-mail: norbert.hort@hzg.de

The Minerals, Metals & Materials Society, *TMS 2018 147th Annual Meeting & Exhibition Supplemental Proceedings*, The Minerals, Metals & Materials Series,
https://doi.org/10.1007/978-3-319-72526-0_64

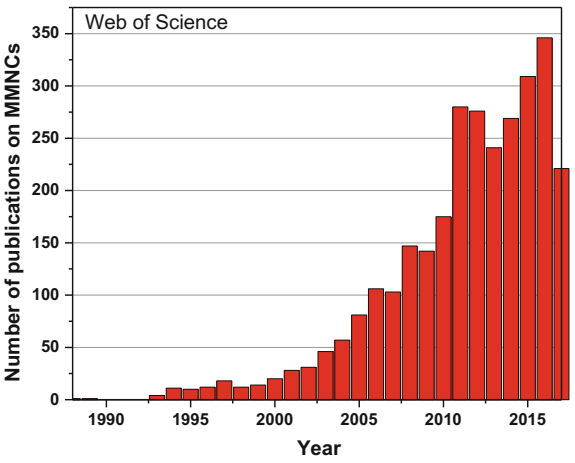

Fig. 1 Number of publications on MMNCs

strength [7, 8]. However, these improvements are possible only with a large amount of reinforcement, i.e. 10–40 vol.%, which also increases the density of the composite and reduces its ductility. Due to much reduced prices, ceramic nanoparticles have been routinely used for reinforcing magnesium-based metal matrix nanocomposites (MMNCs) for several years. Figure 1 clearly shows the increase in numbers of publications on MMNCs since 1988.

A uniform distribution of such small particles can be easily achieved using powder metallurgical processes, but those are usually costly and unsuitable for use in mass production. To distribute nanoparticles uniformly in a light metallic melt is quite difficult to achieve, due to their relatively high surface area and the resulting poor wettability. For this reason stir casting alone does not usually suffice in ensuring a good distribution of nanoparticles. Conventional casting processes that require minimal modifications for distributing nanoparticles are therefore a field of great interest for research and industry. An added external field (electromagnetic, ultrasonic, or mechanical) has to be applied in combination with or subsequent to stirring. This work was done as part of the European Project EXOMET, which ended in 2016. One of the conclusions at the end of the project was that added external fields provide an effective and efficient method of dispersing nanoparticles in light metal melts [9]. Other production processes such as disintegrated melt deposition (DMD) [10, 11] or an evaporation of the melt to increase the concentration of particles [12] have a rather academic background, but are not commercially viable. Reviews with a good overview of metal matrix nanoparticle processing, properties and other aspects can be found in [13–15]. Some of the results of these processes are also mentioned in this paper.

Ultrasound Assisted Stirring

Of the additional fields mentioned above, ultrasonic treatment is ideal as ultrasound waves produce acoustic streaming and cavitation under the ultrasonic probe. This is useful to promote the de-agglomeration of particle clusters and for particle wetting. Acoustic streaming facilitates a vigorous convection, transporting the released particles throughout the melt. This technique has been applied for reinforcing the magnesium alloy Elektron21 with 1 wt% AlN nanoparticles of average diameter 80 nm [16, 17]. Figure 2 shows the nanoparticles, the scale bar length is 200 nm. The particles were added to a vortex of melt produced by stirring followed by ultrasonication for 5 min at 0.3 kW using a HIELSCHER ultrasonic processor UIP1500hd, as shown in Fig. 3, at a frequency of 20 kHz. Two materials, one with and one without AlN nanoparticles were produced using the same processes including stirring and sonication. After sonication the mold and melt were lowered into a water bath, located below the ring furnace. A microstructure investigation, in combination with mechanical testing and creep testing, was performed on the materials. Elektron21 (composition in wt%: Mg-2.8Nd-1.2Gd-0.4Zr-0.3Zn) is one of the most creep-resistant commercially available magnesium alloys, so any further influence of the nanoparticles on its creep behavior was also of interest.

Grain size was slightly reduced by the addition of 1 wt% AlN nanoparticles. As can be seen in Fig. 4a, Elektron21 has a more globular microstructure, whereas the nanocomposite of 1 wt% AlN shown in Fig. 4b appears more dendritic. The hardness was not affected.

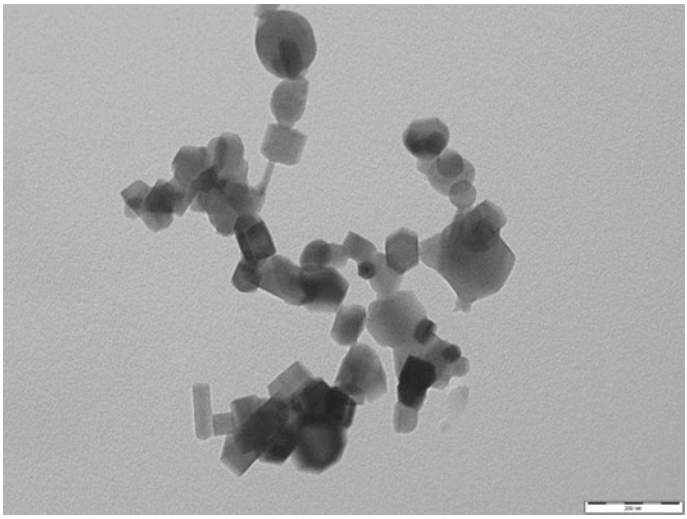

Fig. 2 AlN nanoparticles

Fig. 3 Ultrasonic processor with attached booster and titanium sonotrode

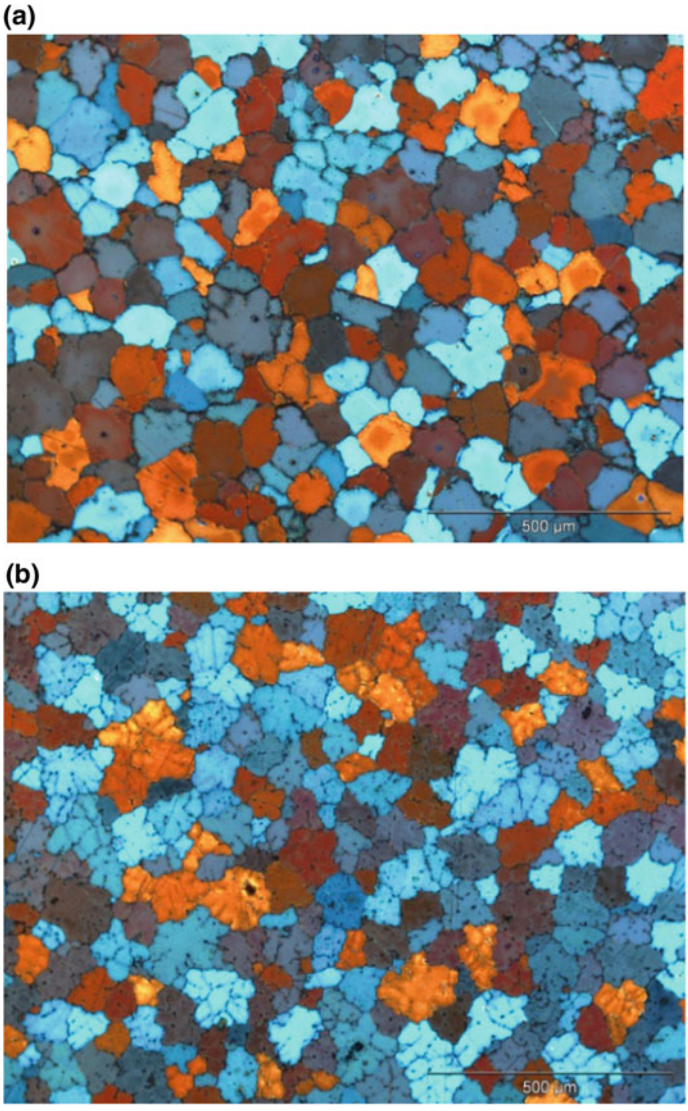

Fig. 4 Optical microscopy of **a** Elektron21 and **b** Elektron21 + 1 wt% AlN nanoparticles [16]

Table 1 Grain size and hardness measurements, the results of compression and tensile tests at room temperature. UCS: ultimate compressive strength; CYS: compressive yield strength; E: elongation at fracture, UTS: ultimate tensile strength; YS: Yield strength [16]

Property	Elektron21	Elektron21 + AlN
Grain size (μm)	80.1 ± 39.4	74.1 ± 32.5
Hardness (HV5)	47.9 ± 2.1	48.1 ± 2.5
UCS (MPa)	316.8 ± 1.5	315.7 ± 0.8
CYS (MPa)	92.4 ± 0.8	88.0 ± 1.0
C (%)	21.6 ± 0.8	22.1 ± 0.6
UTS (MPa)	229 ± 10	226 ± 3
YS (MPa)	115 ± 5	107 ± 3
E (%)	12 ± 3	14 ± 1

The mechanical properties at room temperature under tension and compression are given in Table 1. Both ultimate strength and yield strength under tension and compression are only slightly effected and a little lower with nanoparticles. The ductility was slightly improved.

To determine the properties at higher temperatures, compression creep tests were performed at 240 °C with constant stresses between 70 and 200 MPa. Figure 5a shows the creep curves of both materials from tests at 240 °C and 140 MPa from which the minimum creep rates could be determined.

A summary of all minimum creep rates as a function of applied stresses is shown in Fig. 5b. The stress exponents n can be derived from this plot. It can be clearly seen that the AlN reinforced Elektron21 has a significantly improved creep resistance. At low stresses the minimum creep rate is nearly one order of magnitude lower compared to the unreinforced Elektron21. SEM and TEM investigations showed that the AlN nanoparticles appear in the eutectic region or in magnesium grains close to eutectic region. The nanoparticles seem to strengthen the eutectic region, which ultimately results in creep strengthening of the nanocomposite. The reason for this may be that the particles tend to prevent the material from grain boundary sliding, by strengthening the eutectic and grain boundary regions. After applying the concept of threshold stresses, true stress exponents n_t were found to be 4.2 and 3.3 for the Elektron21 and Elektron21 + AlN respectively. Dislocation climb and glide are the rate-determining deformation mechanisms during creep.

AM60 high pressure die casting (HPDC) alloy was used in another study [18] where nanocomposites were processed similarly to those based on Elektron21 [16]. The optical micrographs in Fig. 6 show that the addition of AlN refined the grain size significantly and the morphology of the grains changed from the dendritic structure in Fig. 6a to the more equiaxed structure shown in Fig. 6b. The grain size measured shows a significant reduction, from 1277.0 ± 301.3 to 84.9 ± 6.2 μm, due to the addition of nanoparticles to the AM60 alloy that was produced in a

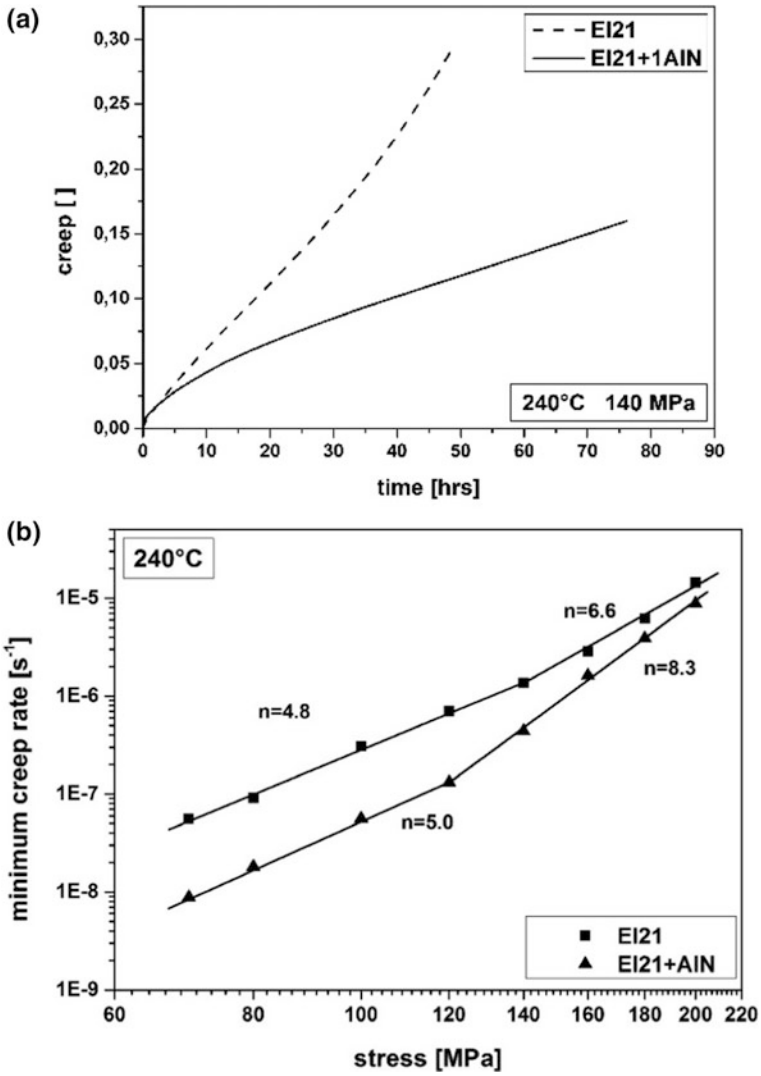

Fig. 5 Creep curves of Elektron21 and Elektron21 + 1 wt% AlN (**a**) and double logarithmic plot of minimum creep rate versus applied stress from tests performed at 240 °C (**b**) [16]

similar manner. Tensile tests were performed at room temperature and it was found that there is an increase of 103% in YS (91.2 MPa compared to 44.9 MPa) and 115% in UTS (235.1 MPa compared to 109.3 MPa). As mentioned, the reinforcement of microparticles or fibers usually lowers the ductility significantly, but in this case the AlN nanoparticle addition more than doubles the elongation to

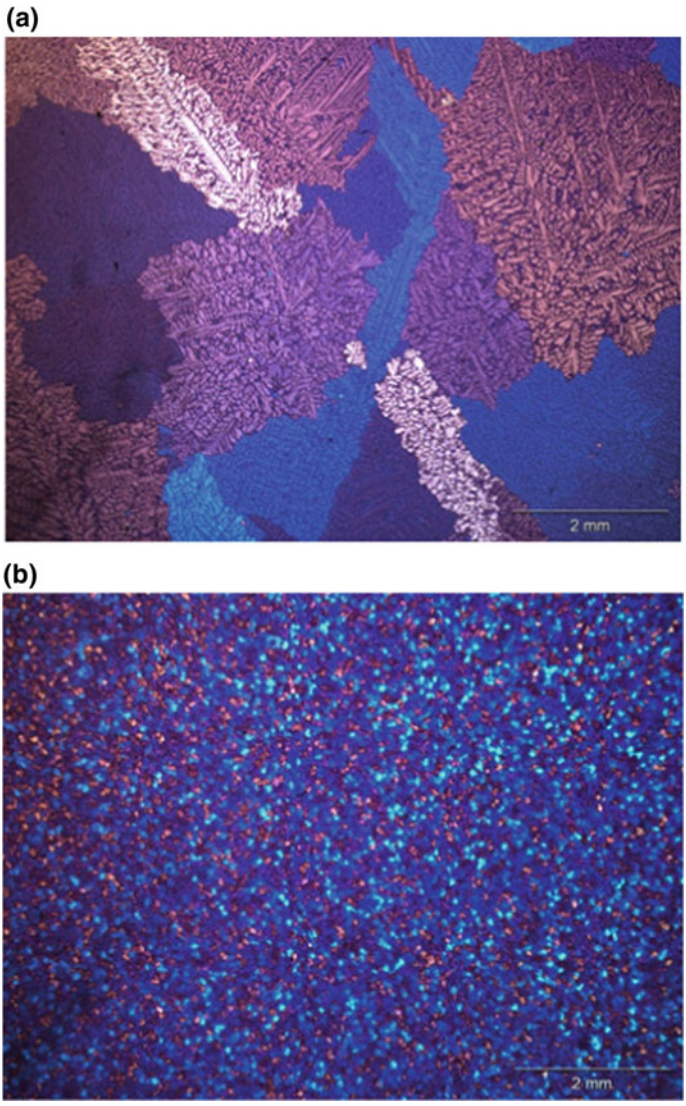

Fig. 6 Microstructure of **a** AM60, and **b** AM60 + AlN [18]

failure. An increase of 140% was observed in the elongation to failure by the addition of AlN nanoparticles (15.4% compared to 6.4%) [18].

It is possible to calculate whether or not the improvement in yield strength of 46.3 MPa can be traced back to grain refinement (Hall-Petch) alone. The improvement in yield strength $\Delta\sigma_{GR}$ is assumed to be:

$$\Delta\sigma_{GR} = k_y\left(\frac{1}{\sqrt{D_{MMNC}}} - \frac{1}{\sqrt{D_0}}\right) \quad (1)$$

The term in brackets is called grain size reduction, where D_{MMNC} and D_0 are respectively the grain sizes of the nanocomposite and the unreinforced alloy, which are processed in the same way. The value of *GSR* is 8.05 × 10^{-2} $\mu m^{-1/2}$ for the as-cast nanocomposite. Taking the grain sizes and k_y to be 530.2 MPa * $\mu m^{1/2}$, the strengthening contribution from grain size reduction according to Eq. 1 is 42.7 MPa for the as-cast nanocomposite. With 8.3 MPa Orowan-strengthening contributing only a small amount to the increase in strength and other mechanisms are negligible. While arithmetic summation of the strengthening effects ends up slightly overestimating the yield strength increase and the quadratic summation method slightly underestimating it, in general the tendency is quite satisfactory [18].

Disintegrated Melt Deposition

DMD is a process for producing monolithic alloys and metal matrix nanocomposites that are based on lighter metals, such as aluminum or magnesium. The mixture of melt and nanoparticles is stirred at a superheated temperature in a graphite crucible under an argon atmosphere. After stirring, the melt is discharged through an orifice at the bottom of the crucible. This is followed by disintegration by two argon jets oriented normal to the melt stream that deposit the melt onto a steel mold. The material produced is thereafter usually heat treated and hot extruded. AZ31 magnesium alloy and its nanocomposites reinforced with 1.0, 1.4, and 3.0 vol.% Al_2O_3 nanoparticles was processed by DMD [19]. Alumina nanoparticles have an average diameter of 50 nm. Tensile tests were performed at room temperature and the resulting mechanical properties are shown in Table 2. Not only yield strength, but also ductility was improved, which can only be explained by grain refinement.

Disintegrated melt deposition (DMD) was also used to produce an alumina particle-reinforced pure magnesium composite [20]. A reinforcement of 1.1 vol.% alumina particles with a diameter of 50 nm was added to the superheated melt (750 °C) and mixed under an argon atmosphere, followed by DMD and hot extrusion at 250 °C. Optical investigation of the microstructural features shows a

Table 2 Mechanical properties and grain size of AZ31 and nanocomposites of it [19]

Material	0.2 YS (MPa)	UTS (MPa)	E (%)	Grain size (μm)
AZ31	204.9	345.3	13.5	4.09
AZ31/1.0Al_2O_3	238.6	384.8	19.5	1.33
AZ31/1.4Al_2O_3	231.0	372.4	17.4	1.12
AZ31/3.0Al_2O_3	245.2	377.0	15.8	3.17

Table 3 Mechanical properties of Mg and Mg+1.1Al_2O_3 [20]

Material	Young's modulus (GPa)	0.2 YS (MPa)	UTS (MPa)	E (%)
Mg	42.8	97 ± 2	173 ± 1	7.4 ± 0.2
Mg+1.1Al_2O_3	52.7	175 ± 3	246 ± 3	14 ± 2.4

Table 4 Mechanical properties from compression tests of Mg-4Zn-3Gd-1Ca and Mg-4Zn-3Gd-1Ca-2ZnO [21]

Material	CYS (MPa)	UCS (MPa)	E (%)
Mg-4Zn-3Gd-1Ca	260.5 ± 2.9	585.4 ± 18.9	12.6 ± 0.3
Mg-4Zn-3Gd-1Ca-2ZnO	355.4 ± 5.0	703.4 ± 39.8	10.6 ± 0.4

significantly reduced grain size of 14 ± 2 μm in the composite compared to 49 ± 8 μm in the pure magnesium. The coefficient of thermal expansion (CTE) is significantly reduced by the incorporation of 1.1 vol.% alumina particles from 28.4 ± 0.3 × 10^{-6} K^{-1} to 25.1 ± 0.3 × 10^{-6} K^{-1}. The mechanical properties are listed in Table 3. Not only strength, but also ductility was significantly improved.

Chen et al. processed an Mg-4Zn-3Gd-1Ca alloy with 2 wt% of ZnO nanoparticles (90–200 nm diameter) using DMD followed by hot extrusion [21]. The mechanical properties from uniaxial compression tests performed at room temperature are shown in Table 4.

Intensive Melt Shearing

Intensive melt shearing applies shear stress to the melt and this can de-agglomerate added nanoparticles in magnesium melts without the use of electromagnetic fields or ultrasound. It is therefore a mechanical process that can be used for mixing ceramic particles into a melt. The melt shearing device used was developed and built at BCAST at Brunel University in the UK, it is shown in Fig. 7.

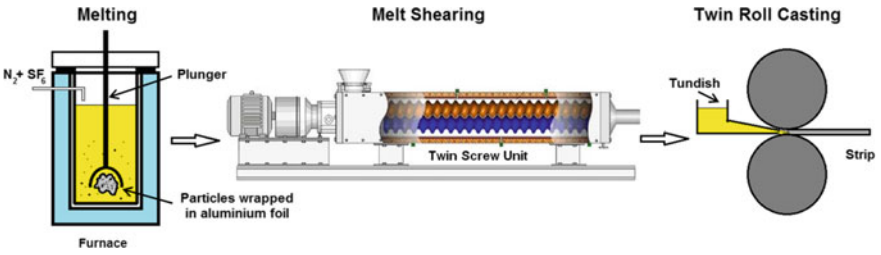

Fig. 7 The devices used for particle addition, melt shearing, and twin roll casting [22]

To study of the influence of CaO (10 μm) and SiC (2 μm) on the mechanical properties of a AM30 wrought alloy, it was melted in a steel crucible to 710 °C and particles were added wrapped in aluminum foil. Three different compositions were used for the present investigation: (i) AM30, (ii) AM30 + 1.5 wt% CaO, and (iii) AM30 + 1.5 wt% CaO + 1.5 wt% SiC. The melt was transferred to a twin-screw melt conditioner (MC) working with a screw rotation speed of 500 rpm for intensive shearing of the melt at 645 °C for 90 s. The conditioned melt was fed into a horizontal twin-roll casting machine with a constant casting speed of 1 m/min. This process was performed at BCAST. Strips with a thickness of 5.5 mm after twin-roll casting were later hot rolled at MagIC, Helmholtz-Zentrum Geesthacht, to sheets with a thickness of 2.25 mm. The strips were first preheated to 400 °C and four rolling passes were performed using a warm-rolling mill, resulting in a 20% reduction in thickness. Tensile tests were performed perpendicular to rolling direction and are shown in Fig. 8. The high yield asymmetry of AM30 was reduced by addition of CaO. The highest UTS was demonstrated by the AM30 reinforced with CaO perpendicular to the rolling direction.

Powder Metallurgical Processes

A powder metallurgical process was chosen for processing SiC reinforced pure magnesium. Two different average sizes of SiC, 25 μm and 50 nm were selected, in order to study the influence of particle size on mechanical property development [23]. Mixtures of the powders were compacted to billets and subsequently sintered in a microwave-assisted process. For the purposes of comparison, pure magnesium was treated in the same way. All the billets were subsequently hot extruded. The properties were examined in a composite with 1 vol.% nm-SiC, a composite with 10 vol.% μm-SiC and a composite with a mixture of both. The results were compared with the pure magnesium sample's properties. The mechanical properties are given in Table 5. A significant increase in UTS and 0.2 YS was reached with only 1 vol.% nm-SiC reinforcement and, surprisingly, the ductility also increased.

Magnesium Evaporation

Chen et al. increased the SiC-nanoparticle concentration by evaporating the alloy [24]. Firstly, an Mg-6Zn ingot with 1 vol.% SiC nanoparticles was produced with an ultrasound assisted stirring process in which the nanoparticles mainly appear at the grain boundaries. This material was again melted and under a pressure of only 6 Torr magnesium and zinc was evaporated. High pressure torsion (HPT) was applied to the material in order to strengthen it by cold deformation. A material with

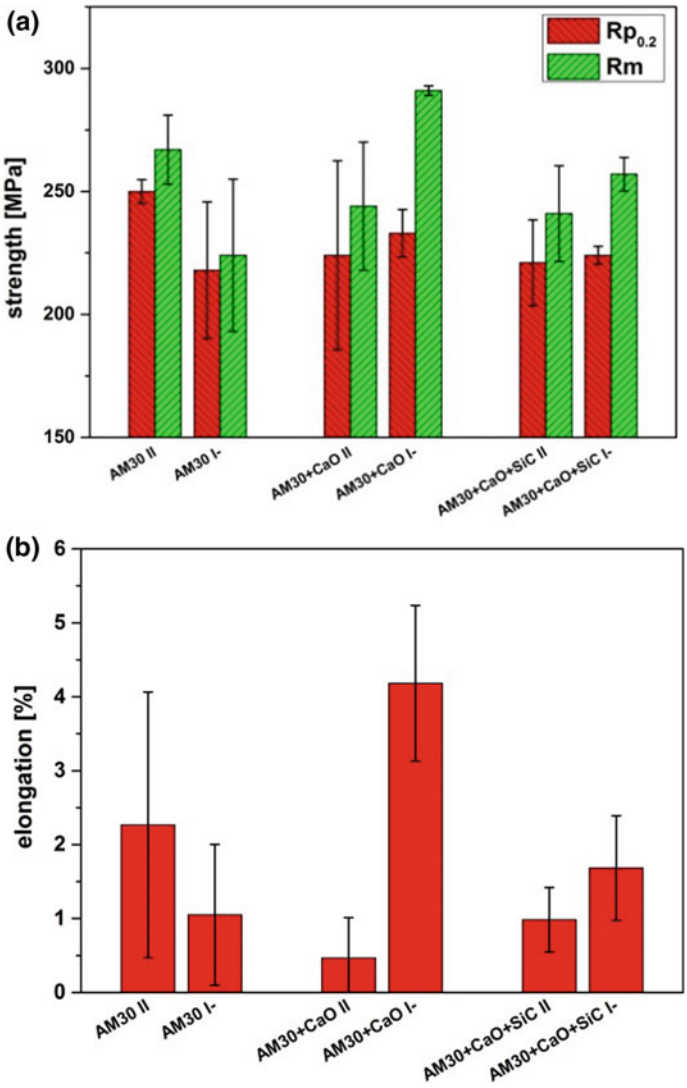

Fig. 8 **a** Tensile strength, and **b** elongation of all materials tested at room temperature [22]

about 14 vol.% nanoparticles in an Mg-2Zn matrix was obtained as a result. For comparison, the same material without the nanoparticles was also processed. An extraordinarily small grain size was achieved by combining ultrasonic assisted casting, evaporation of magnesium and zinc and subsequent HPT. The nanocomposite material achieved a yield strength of 710 MPa. This seems to be the highest ever reported yield strength of a magnesium alloy or composite (Table 6).

Table 5 Mechanical properties of pure magnesium and SiC-composites [23]

Material	0.2 YS (MPa)	UTS (MPa)	E (%)
Pure Mg	125 ± 15	172 ± 12	5.8 ± 0.9
Mg+1% nm-SiC	157 ± 22	203 ± 22	7.6 ± 1.5
Mg+10% μm-SiC	140 ± 2	165 ± 2	1.5 ± 0.8
Hybrid Mg	156 ± 7	185 ± 11	0.6 ± 0.1

Table 6 Mechanical properties of Mg-2Zn and Mg-2Zn+14% SiC processed by alloy evaporation and HPT [24]

Material	Young's modulus (GPa)	0.2 YS (MPa)	Grain size (nm)
Mg-2Zn	45 ± 5	286 ± 35	105 ± 42
Mg-2Zn+14% SiC	86 ± 5	710 ± 35	64 ± 40

Conclusions

Magnesium-based metal matrix nanocomposites have excellent mechanical properties at room temperature and in some cases also improved creep strength compared to their base materials. Processing is more difficult compared to the micrometer-sized MMCs, but the results are often better. Not only is the strength increased, but also ductility. This is attributed to a combination of grain refinement and Orowan strengthening.

References

1. Trojanova Z, Szaraz Z, Labar J, Lukac P (2005) Deformation behaviour of an AS21 alloy reinforced by short Saffil fibres and SiC particles. J Mat Proc Technol 162–163:131–138
2. Mondal AK, Kumar S (2009) Dry sliding wear behaviour of magnesium alloy based hybrid composites in the longitudinal direction. Wear 267:458–466
3. Zhang X, Fang L, Xiong B, Hu H (2015) Microstructure and tensile properties of Mg (AM60)/Al2O3 metal matrix composites with varying volume fractions of fiber reinforcement. J Mat Eng Perform 24:4601–4611
4. Sklenicka V, Pahutova M, Kucharova K, Svoboda M, Langdon TG (2002) Creep processes in magnesium alloys and their composites. Met Mat Trans 33A:883–889
5. Sklenicka V, Svoboda M, Pahutova M, Kucharova K, Langdon TG (2001) Microstructural processes in creep of an AZ 91 magnesium-based composite and its matrix alloy. Mat Sci Eng A 319–321:741–745
6. Viswanath A, Dieringa H, Ajith Kumar KK, Pillai UTS, Pai BC (2015) Investigation on mechanical properties and creep behavior of stir cast AZ91-SiCp composites. J Magn Alloys 3:16–22
7. Ochi Y, Masaki K, Matsumura T, Wadasako M (2007) Effects of volume fraction of alumina short fibers on high cycle fatigue properties of Al and Mg alloy composites. Mat Sci Eng A 468–470:230–236

8. Huang YD, Hort N, Dieringa H, Maier P, Kainer KU (2006) Investigations on thermal fatigue of aluminum- and magnesium-alloy based composites. Int J Fatigue 28:1399–1405
9. Sillekens WH et al (2014) The ExoMet project: EU/ESA research on high-performance light-metal alloys and nanocomposites. Met Mat Trans 45A:3349–3361
10. XingHe T, How WCK, Weng JCK, Onn RKW, Gupta M (2015) Development of high-performance quaternary LPSO Mg-Y-Zn-Al alloys by disintegrated melt deposition technique. Mat Design 83:443–450
11. Hassan S, Gupta M (2002) Development of a novel magnesium-copper based composite with improved mechanical properties. Mater Res Bull 37:377–389
12. Chen L-Y et al (2015) Processing and properties of magnesium containing a dense uniform dispersion of nanoparticles. Nature 528:539–543
13. Dieringa H (2011) Properties of magnesium alloys reinforced with nanoparticles and carbon nanotubes: a review. J Mat Sci 46:289–306
14. Chen L, Yao Y (2014) Processing, microstructures, and mechanical properties of magnesium matrix composites: a review. Acta Metall Sin 27(5):762–774
15. Casati R, Vedani M (2014) Metal matrix composites reinforced by nano-particles—a review. Metals 4:65–83
16. Katsarou L, Mounib M, Lefebvre W, Vorozhtsov S, Pavese M, Badini C, Molina-Aldareguia JM, Cepeda Jimenez C, Pérez Prado MT, Dieringa H (2016) Microstructure, mechanical properties and creep of magnesium alloy Elektron21 reinforced with AlN nanoparticles by ultrasound-assisted stirring. Mater Sci Eng A 659:84–92
17. Daudin R, Terzi S, Mallmann C, Sanchez Martin R, Lhuissier P, Boller E, Pacureanu A, Katsarou L, Dieringa H, Salvo L (2017) Indirect improvement of high temperature mechanical properties of a Mg based alloy Elektron21 by addition of AlN nanoparticles. Mat Sci Eng 688:76–82
18. Dieringa H, Katsarou L, Buzolin R, Szakács G, Horstmann M, Wolff M, Mendis C, Vorozhtsov S, StJohn D Ultrasound assisted casting of an AM60 based metal matrix nanocomposite, its properties and recyclability; submitted to Metals
19. Chen Y, Guo YB, Gupta M, Shim VPW (2013) Dynamic tensile response of magnesium nanocomposites and the effect of nanoparticles. Mater Sci Eng A 582:359–367
20. Hassan SF, Gupta M (2005) Enhancing physical and mechanical properties of Mg using nano-sized Al2O3 particulates as reinforcement. Met Mat Trans 36A:2253–2258
21. Chen Y, Tekumalla S, Guo YB, Gupta M (2016) Introducing Mg-4Zn-3Gd-1Ca/ZnO nanocomposite with compressive strengths matching/exceeding that of mild steel. Scientific Reports 6, 32395
22. Dieringa H, Das S, Eskin D, Fan Z, Katsarou L, Horstmann M, Kurz G, Mendis C, Hort N, Kainer KU (2015) Twin-roll casting after intensive melt shearing and subsequent rolling of an AM30 magnesium alloy with addition of CaO and SiC. Mat Sci Forum 828–829:35–40
23. Wong WLE, Gupta M (2006) Effect of hybrid length scales (micro + nano) of SiC reinforcement on the properties of magnesium. Solid State Phen 111:91–94
24. Chen L-Y, Xu J-Q, Choi H, Pozuelo M, Ma X, Bhowmick S, Yang J-M, Mathaudhu S, Li X-C (2015) Processing and properties of magnesium containing a dense uniform dispersion of nanoparticles. Nature 528:539–548

Part XXVII
Materials and Fuels for the Current and Advanced Nuclear Reactors VII

Investigation of Tin as a Fuel Additive to Control FCCI

Michael T. Benson, James A. King and Robert D. Mariani

Abstract One method to control fuel-cladding chemical interaction (FCCI) in metallic fuel is through the use of an additive that inhibits FCCI. A primary cause of FCCI is the lanthanide fission products moving to the fuel periphery and interacting with the cladding. This interaction will lead to wastage of the cladding and eventually to a cladding breach. Tin is being investigated as a potential additive to control FCCI by reacting with the fission product lanthanides. The current study is a scanning electron microscopy (SEM) characterization of a diffusion couple between U-10Zr-4.3Sn (wt%) and the 4 most abundant lanthanide fission products. As the lanthanides move into the fuel, they are interacting with and breaking down the Zr_5Sn_3 precipitates that formed during fresh fuel fabrication. This reaction produced Ln-Sn precipitates and δ phase (UZr_2), which is conducive to normal fuel operation and increased burnups.

Keywords Metallic fuel · FCCI · Fuel additive

Introduction

Fuel-cladding chemical interaction (FCCI) occurs when the nuclear fuel or fission products react with the cladding material. A major cause of FCCI in metallic fuels during irradiation is fission product lanthanides (Ln), which tend to migrate to the fuel periphery, coming in contact with the cladding. The result of this interaction is degradation of the cladding that will eventually lead to rupture of the fuel assembly [1, 2]. A method of controlling FCCI is needed to extend fuel life. Several methods are being investigated to decrease or prevent FCCI, such as barrier foils, coatings, and additive materials [3–7]. In the additive approach, elements are added to the fuel matrix that will form stable intermetallics with the lanthanides. Criteria were previously developed that identified a set of elements that could be promising

M. T. Benson (✉) · J. A. King · R. D. Mariani
Idaho National Laboratory, P.O. Box 1625, MS 6188, Idaho Falls, ID 83415, USA
e-mail: michael.benson@inl.gov

The Minerals, Metals & Materials Society, *TMS 2018 147th Annual Meeting & Exhibition Supplemental Proceedings*, The Minerals, Metals & Materials Series,
https://doi.org/10.1007/978-3-319-72526-0_65

additives [4]. From this list, Pd [4, 8, 9], In [7], Sb [10], and Sn [3] have been investigated, and each have shown promise as a fuel additive.

Ordinarily, the lanthanides can burn-in as fission products; however, in the case of recycled fuel, they will be present as minor impurities in recycled, as-fabricated fuel [11]. Controlling FCCI in the recycled fuel system is even more important due to the potentially reduced lifetime of the fuel [12]. In this case, as soon as the fuel contacts the cladding due to swelling, there are already lanthanide impurities in the recycled fuel available to initiate FCCI. This will occur at roughly 1–2% burnup. This early form of FCCI in a recycled fuel will occur in accelerated fashion in comparison to the much slower burn-in of fission product lanthanides in a fresh fuel fabricated with clean uranium.

The diffusion couple described in this paper is a continuation of previous work using Sn as a minor additive to control FCCI [3]. In that report, the as-cast and annealed microstructures were investigated, with and without lanthanides present. That characterization was necessary in order to determine the structure of a fresh fuel, and serves as an initial evaluation of the efficacy of a particular additive, in terms of chemical bonding of the additive to the lanthanides over Zr. The drawback with this earlier study is the high temperatures present in the arc melter during fabrication, which may generate high temperature phases that would not be present at reactor temperatures. A diffusion couple, performed at reactor temperature (650 °C), between the fresh fuel and the lanthanides provides a more realistic out-of-pile test of the additive-lanthanide interactions.

Experimental Methods

The alloys, U-10Zr-4.3Sn wt% (71.2U-21.7Zr-7.2Sn at.%) and 53Nd-25Ce-16Pr-6La wt% (52.3Nd-25.4Ce-16.2Pr-6.1La at.%) were fabricated as previously reported [3], and cast into 5 mm diameter pins. All materials, except uranium, were obtained from Alfa Aesar and used as received. The lanthanides were obtained as rods, packaged in Mylar under argon. Uranium was cleaned by submersion in nitric acid, followed by a water wash, then an ethanol wash.

Approximately 3 mm from each pin was cut for the diffusion couple. To prepare the samples for the diffusion couple, the surface was ground flat using SiC grinding paper, followed by polishing with polycrystalline diamond suspensions, starting with 9 μm, then 3 μm, and finally 1 μm. This was performed in air. The samples were transferred into an argon glovebox, and hand polished with polycrystalline diamond suspension, starting with 3 μm, then 1 μm, to remove any oxide layer. The fresh fuel and lanthanide samples were placed together, with polished surfaces in contact and surrounded by Ta foil, in a previously described diffusion couple jig [8]. The jig was tightened to 50 in lbs. The jig was removed from the glovebox and sealed in a quartz tube under vacuum. The tube was then heated to 650 °C and held for 504 h. After the heat treatment, the diffusion couple was quenched in water, then removed from the diffusion couple jig for analysis.

The diffusion couple was mounted in a 31.8 mm diameter phenolic metallographic (met) mount filled with epoxy. The diffusion couple interface was exposed by grinding roughly half the diameter away with SiC grinding paper. The sample was then polished with polycrystalline diamond suspensions, starting with 9 μm, then 3 μm, and finally 1 μm. The polished sample was analyzed with a sputtered coating of approximately 15 nm carbon to control charging of the met mount in the scanning electron microscope (SEM).

The instrument used for this analysis was a JSM-7600f SEM manufactured by the Japan Electron Optics Laboratory (JEOL). The JSM-7600f is a hot field emission SEM equipped with an Oxford Instruments X-Max 20 silicon drift energy dispersive X-ray spectrometer (EDS). The X-ray spectrometer is controlled by Oxford INCA software (v. 4.15, part of the Oxford Microanalysis Suite Issue 18d + SP 4), which also provides image acquisition capabilities.

The SEM was operated at an accelerating voltage of 20 kV and a nominal beam current of approximately 84 nA (which can vary somewhat with column conditions) for these analyses. Prior to analysis, X-ray detector response was verified using a copper target. All of the X-ray spectra were accumulated for 75 live seconds. Spectra were collected over the energy range 0–20 keV, which covers characteristic X-ray energies from all analytes.

Spectra were quantified using so-called "standardless" analysis, which uses a stored library of reference spectra to quantify unknown spectra rather than physical standards. This method is generally accurate to the 0.1–0.5 wt/wt% range, depending on sample and microscope (observation) conditions.

Results and Discussion

Figure 1 shows representative images of the interface between U-10Zr-4.3Sn and the lanthanides. Several features are readily apparent in the large area scans. There is obvious penetration of the lanthanides into the fuel, with only a small amount of fuel moving into the lanthanides. Also apparent is the different zones present in the fuel matrix, extending roughly 100 μm into the fuel. These zones are indicated by the dashed red lines. The locations of the higher magnification images shown in Figs. 2 and 3 are indicated by the red rectangles. Each of these features is discussed in more detail below.

Figure 2 shows magnified images of the interaction zone, with EDS data listed in Table 1. Figure 2a clearly shows the penetration of the lanthanides into the fuel, specifically along the Zr-Sn precipitates. The precipitate has a mottled appearance, with a range of small inclusions present (based on visual inspection). Most of the inclusions through the bulk of the precipitate are small, on the order of 1 μm, so were not analyzed by EDS due to the small size. The small inclusions and mottled appearance likely indicate that the reactions taking place are not complete, and the diffusion couple was quenched too soon. With that stated, there is still useful information in the EDS analysis. Points 1–3 (Fig. 2a, Table 1) are the UZr_2 δ phase,

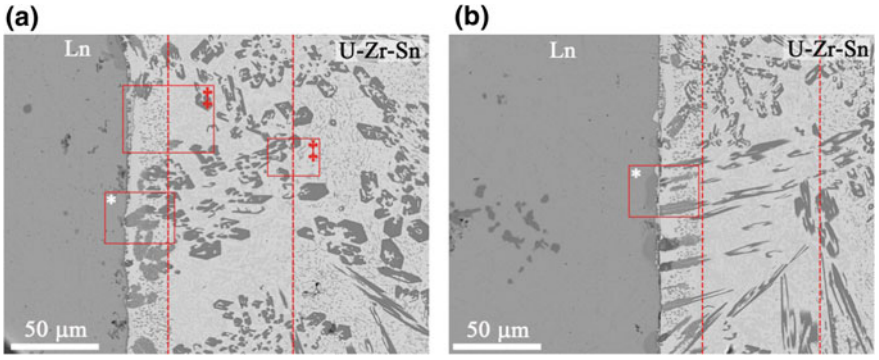

Fig. 1 **a** and **b** SEM BSE images of diffusion zone. The red rectangles indicate the locations for the higher magnification images shown in Figs. 2 and 3. (*) indicates the magnified regions shown in Fig. 2, and (‡) indicates the magnified regions shown in Fig. 3. The dashed red lines indicate the interaction zone boundaries

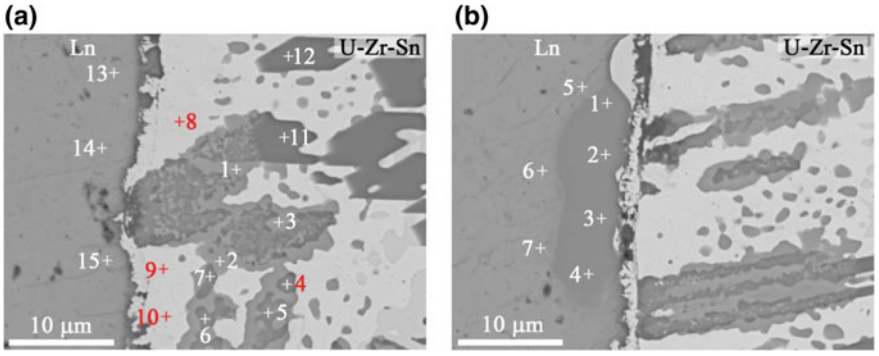

Fig. 2 SEM BSE images of diffusion zone. Magnified region from red rectangle, marked with (*), shown in Fig. 1a, b. Magnified region from red rectangle, marked with (*), shown in Fig. 1b. EDS data listed in Table 1

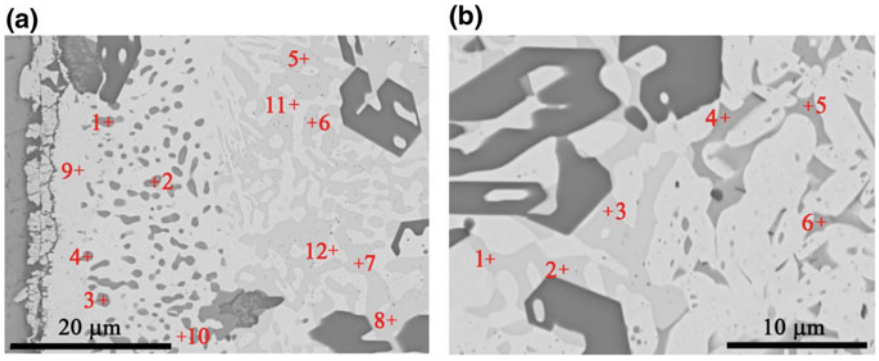

Fig. 3 **a** and **b** SEM BSE images of extended interaction zone in the fuel. Magnified regions from red rectangles, marked with (‡), shown in Fig. 1a. EDS points listed in Table 2

Table 1 EDS data for points shown in Fig. 2. Values in at.%

	U	Zr	Sn	Nd	Ce	Pr	La
Figure 2a							
1	33.6	60.5	1.4	1.0	2.3	0.4	0.7
2	34.9	61.4	0.6	0.6	1.5	0.4	0.7
3	31.2	59.5	2.9	1.8	3.0	0.6	0.9
4	6.1	5.5	34.7	31.5	12.0	1.8	8.4
5	2.5	11.1	33.6	30.4	12.2	2.1	8.1
6	4.1	10.8	32.9	30.1	12.2	2.0	8.0
7	7.5	10.0	31.2	29.6	11.6	2.3	7.8
8	95.3	3.0	0.0	0.0	1.1	0.2	0.5
9	98.1	0.8	0.0	0.4	0.3	0.4	0.0
10	98.1	0.7	0.0	0.4	0.4	0.3	0.1
11	2.4	60.3	37.0	0.0	0.1	0.1	0.1
12	2.4	60.6	37.0	0.0	0.0	0.0	0.0
13	0.1	0.4	0.2	51.4	27.0	3.6	17.2
14	0.1	0.2	0.0	51.5	27.2	3.8	17.2
15	0.0	0.3	0.1	50.8	27.3	4.0	17.3
Figure 2b							
1	0.3	3.4	4.8	64.5	17.3	2.2	7.5
2	0.4	3.2	6.5	63.6	16.8	2.0	7.6
3	0.3	3.0	6.3	63.9	16.9	2.2	7.4
4	0.1	2.9	5.5	64.7	17.3	2.1	7.4
5	0.0	0.4	0.0	50.9	27.4	3.6	17.6
6	0.0	0.2	0.2	51.6	27.2	3.4	17.4
7	0.0	0.2	0.1	51.3	27.3	3.7	17.4

inside what was once a Sn-Zr precipitate. Bands of δ phase are visible in all of the precipitates within the interaction zone. In the Zr_5Sn_3 precipitates (points 11 and 12), there is only small amounts of U present, thus U is moving into the precipitate to bind the Zr released from Zr_5Sn_3 as Ln_5Sn_3 is formed. (Note: Specific phases are inferred from the EDS results.)

Points 4 through 7, Fig. 2a, are primarily Sn and lanthanides, with some Zr and a small amount of U. The Ln/Sn ratio is very close to Ln_5Sn_3. As previously discussed [3], Zr may be substituting into the crystal lattice, creating a $[Zr + Ln]_5Sn_3$ compound. Including Zr into the Ln/Sn ratio in points 5 through 7 indicates a composition of roughly $[Zr + Ln]_2Sn$. While not impossible, a 2 to 1 compound is unlikely since there are no known 2 to 1 compounds between the constituent lanthanides (Nd, Ce, Pr, La) and Sn, based on the binary phase diagrams. Other precipitates in the interaction zone that were analyzed (data not shown) have a range of Zr present, from roughly 4 at.% to above 12 at.%. This could be due to Zr having a high solid solubility in Ln_5Sn_3, or perhaps Zr has not had enough time to migrate out of the precipitate.

Figure 2b shows a region of the interaction zone where constituents in the fuel diffused into the lanthanides. These regions were not present along the entire interaction zone, but were scattered throughout. Curiously, the composition of these regions was very consistent, with a representative example shown in Fig. 2b. The amount of Sn is low, roughly 5 at.%, with a small amount of Zr. The low amount of tin diffusing into the lanthanides is likely caused by the Zr rind, common to U-Zr based alloys, hindering diffusion, and also due to the stability of the Zr_5Sn_3 precipitates. In areas where Sn broke through, diffusion may be kinetically limited, given that the Sn concentration was always roughly 5 at.%. This should be apparent after running a longer diffusion couple.

The lanthanide composition is also very consistent in the regions where tin moved into the lanthanides. Removing the small amounts of U, Zr, and Sn from the EDS points, and normalizing for the lanthanides yields a composition of 70.5Nd-18.9Ce-8.2La-2.4Pr in at.%. This is significantly different from the starting lanthanide concentration, 52.3Nd-25.4Ce-16.2Pr-6.1La at.%. This could indicate a preference for Sn to bind Nd, or could be due to the higher mobility of Ce, Pr, and La due to lower melting points. If the latter were true, a Nd rich region would be expected near the interface on the lanthanide side, with Ln_5Sn_3 precipitates on the fuel side containing a lower concentration of Nd. This is not the case, though. EDS points 13–15 in Fig. 2a, and 5–7 in Fig. 2b, are roughly the same compositions, and are very close to the cast composition of the lanthanides. The Nd content in the Ln_5Sn_3 precipitates on the fuel side also do not support the idea of higher mobility of Ce, Pr, and La over Nd. Normalizing the lanthanide content in points 4–7 (Fig. 2a), and averaging the 4 data points yields a lanthanide content of 57.9Nd-22.8Ce-15.4La-3.9Pr, slightly high in Nd, and a little low in Ce and Pr. Although this is not conclusive, the trend indicates Sn is preferentially binding Nd over the other lanthanides present. A longer reaction time may help clarify this issue.

Figure 3 shows images of the fuel matrix at the beginning and end of the interaction zone indicated in Fig. 1 by the dashed lines, with EDS data listed in Table 2. In Fig. 3a, there is an obvious change in the matrix at roughly 20 μm from the interface, corresponding to the depth of lanthanide diffusion into the fuel. The dark, globular precipitates stop abruptly, with a 2 phase, open matrix structure extending for roughly 75 μm. EDS points 1–4 in Fig. 3a show the globular precipitates to be high in U and Zr, with residual lanthanides present, and no Sn. The structure is δ phase, either with dissolved U or U picked up in the EDS analysis from the surrounding matrix, which is primarily α-U (see EDS points 9 and 10, Fig. 2a, Table 2).

The second region, the two phase open structure, is very low in Zr. The darker areas are a mix of α-U and δ phase, although there is significantly more α-U than δ phase, while the lighter areas are α-U. This zone is likely due to uranium moving into the region, and not a depletion of Zr. Uranium and the lanthanides are immiscible solids, so it appears the movement of lanthanides into the fuel is pushing some of the uranium away from the interaction zone.

Table 2 EDS data for points shown in Fig. 3. Values in atomic %

	U	Zr	Sn	Nd	Ce	Pr	La
Figure 3a							
1	40.7	57.9	0.0	0.0	0.9	0.3	0.3
2	44.1	54.4	0.0	0.0	0.9	0.3	0.4
3	39.4	58.5	0.0	0.0	1.5	0.4	0.2
4	42.9	55.2	0.0	0.0	1.1	0.5	0.3
5	73.9	25.3	0.0	0.0	0.4	0.1	0.3
6	72.6	25.9	0.0	0.0	0.7	0.4	0.4
7	73.8	25.6	0.0	0.0	0.3	0.3	0.0
8	73.8	25.4	0.0	0.0	0.4	0.3	0.1
9	94.8	2.9	0.0	0.0	1.3	0.6	0.4
10	98.0	1.0	0.0	0.0	0.4	0.3	0.3
11	95.5	4.3	0.0	0.0	0.1	0.1	0.0
12	98.5	1.0	0.0	0.0	0.3	0.2	0.1
Figure 3b							
1	72.5	26.4	0.0	0.0	0.5	0.4	0.1
2	72.4	27.0	0.0	0.0	0.4	0.1	0.1
3	72.6	26.8	0.0	0.0	0.3	0.3	0.0
4	40.1	59.4	0.0	0.0	0.3	0.1	0.1
5	40.8	59.0	0.0	0.0	0.1	0.0	0.0
6	41.2	58.5	0.0	0.0	0.1	0.1	0.0

The end of this two phase, open matrix structure is shown in Fig. 3b. EDS analysis indicates the same composition throughout this area (points 5–8 in Fig. 3a, and points 1–3 in Fig. 3b). At the end of this zone, the matrix has the same appearance as the matrix area in the previously characterized U-10Zr-4.3Sn after annealing [3]. The EDS analysis (points 4–6) shows a slightly elevated concentration of U. This was observed previously, and attributed to the small size of the δ phase inclusions, due to depletion of Zr from the matrix, and limitations in the EDS method. The δ phase areas shown in Fig. 3b are on the order of 1 μm, so this explanation is likely the reason for the high U content.

Conclusions

The diffusion couple between U-10Zr-4.3Sn (wt%) and a mix of lanthanides (53Nd-25Ce-16Pr-6La wt%) has been analyzed by SEM. Although a longer reaction time may be needed to fully understand the diffusion (a longer diffusion couple run is in progress), several conclusions are apparent from this investigation.

- The lanthanides aggressively attack the Sn-Zr precipitates. Sn-Zr is decomposing in favor of forming Ln-Sn compounds.
- Uranium is moving into the precipitate to react with the released Zr, forming δ phase, UZr_2.
- Uranium appears to be moving away from the interface, due to the movement of lanthanides into the fuel, and the immiscibility between the lanthanides and uranium.
- Tin moved into the lanthanides, but only in very small amounts. This could be due to the Zr rind that is prevalent in U-Zr fuels, or due to the lack of mobility of Sn while in Zr_5Sn_3 precipitates. In other words, the Sn is inhibited from crossing the reaction front presented by the Sn-Zr compounds, and Sn appears to be the least mobile species in this system.

Acknowledgements The authors gratefully acknowledge the Department of Nuclear Energy, Office of Nuclear Energy, Science, and Technology, under DOE-NE Idaho Operations Office Contract DE-AC07-05ID14517.

References

1. Keiser DD (2006) Fuel-cladding interaction layers in irradiated U-Zr and U-Pu-Zr fuel elements. Tech Rep, Argonne National Laboratory-West
2. Carmack WJ, Chichester HM, Porter DL, Wootan DW (2016) J Nucl Mater 473:167–177
3. Benson MT, King JA, Mariani RD, Marshall MC (2017) J Nucl Mater 494:334–341
4. Mariani RD, Porter DL, O'Holleran TP, Hayes SL, Kennedy JR (2011) J Nucl Mater 419:263–271
5. Lee KS, Kim IY, Lee W, Yoon YS (2015) Metals Mater. Intnl 21:498–503
6. Lo WY, Yang Y (2014) J Nucl Mater 451:137–142
7. Kim YS, Wiencek T, O'Hare E, Fortner J, Wright A, Cheon JS, Lee BO (2017) J Nucl Mater 484:297–306
8. Egeland GW, Mariani RD, Hartmann T, Porter DL, Hayes SL, Kennedy JR (2013) J Nucl Mater 440:178–192
9. Egeland GW, Mariani RD, Hartmann T, Porter DL, Hayes SL, Kennedy JR (2013) J Nucl Mater 432:539–544
10. Xie Y, Benson MT, King JA, Mariani RD, Zhang J. J Nucl Mater, submitted
11. Herrmann SD, Li S (2010) Nucl Tech 171:247–265
12. Mariani RD, Porter DL, Hayes SL, Kennedy JR (2012) Metallic Fuels: the EBR-II legacy and recent advances. In: Poinssot C (ed) ATALANTE 2012, Nuclear chemistry for sustainable fuel cycles, vol 7, pp 513–520

Part XXVIII
Mechanical Behavior at the Nanoscale IV

Mechanical Properties of Rapidly Solidified Ni_5Ge_3 Intermetallic

Nafisul Haque, Robert F. Cochrane and Andrew M. Mullis

Abstract The congruently melting, single phase, intermetallic Ni_5Ge_3 has been subject to rapid solidification via drop-tube processing wherein powders with diameters between 850–150 μm are produced. At these cooling rates (850–150 μm diameter particles, 700–7800 K s^{-1}) the dominant solidification morphology, revealed after etching, is that of isolated plate and lath microstructure in an otherwise featureless matrix. Selected area diffraction analysis in the TEM reveals the plate and lath are a disordered variant of ε-Ni_5Ge_3, whilst the featureless matrix is the ordered variant of the same compound. Microvicker hardness test result shows that mechanical properties improve with decreasing the particle size from 850 to 150 μm as a consequence of increasing the cooling rate.

Keywords Rapid solidification · Intermetallic compound · Plate and lath microstructure

Introduction

Intermetallic compounds have been of widespread and enduring interest within Materials Science over the last 30 years or so. Such compounds are characterised by strong internal order and mixed covalent/ionic and metallic bonding, which gives rise to mechanical behaviour intermediate between ceramics and metals. A range of potential applications such as high temperature structural materials have been proposed for these materials due to good chemical stability and high hardness at elevated temperatures. However, poor room temperature ductility limits formability. Such limitations can be overcome by controlling the degree of chemical ordering present within the intermetallic, with the disordered form typically showing behaviour which is more metallic in character (higher ductility, lower hardness, and lower chemical resistance) than the fully ordered form. Rapid

N. Haque (✉) · R. F. Cochrane · A. M. Mullis
School of Chemical and Process Engineering, University of Leeds, Leeds LS2 9JT, UK
e-mail: pmnh@leeds.ac.uk

The Minerals, Metals & Materials Society, *TMS 2018 147th Annual Meeting & Exhibition Supplemental Proceedings*, The Minerals, Metals & Materials Series,
https://doi.org/10.1007/978-3-319-72526-0_66

solidification of intermetallics is therefore an important area of study as high cooling rates are one means of suppressing ordering. Subsequent annealing of the formed part can then be utilised to restore chemical ordering, and hence the desirable properties of the intermetallic.

In this article we present an analysis of rapidly solidified Ni-37.2 at.%. Ge, which is close to the notional stoichiometry of the Ni_5Ge_3 compound. This is an interesting model system as, being congruently melting, the ordering reaction can be studied without any complicating solute effects. That is, we can be certain that solute partitioning, and hence also solute trapping, is absent.

The phase diagram for the Ni-Ge system has been studied extensively by Ellner et al. [1] and by Nash and Nash [2], in 1971 and 1987 respectively. More recently, further work has been also reported by Liu et al. [3] and by Jin et al. [4]. Ni_5Ge_3 is a congruently melting compound with a homogeneity range for the single phase compound of 34.6–44.5 at.% Ge. The congruent point is towards the Ge-deficient end of this range at 37.2 at.% Ge and 1458 K. Ni_5Ge_3 displays two equilibrium crystalline forms, ε and ε′ [2, 4]. The high temperature ε-phase has the $P6_3/mmc$ crystal structure (Hexagonal, space group 194), while the low temperature ε′-phase has the C2 crystal structure (Monoclinic, space group 5) [4]. The transition between the two occurs either congruently ($\varepsilon \rightarrow \varepsilon'$) at 670 K for Ge-rich compositions or via the eutectoid reaction $\varepsilon \rightarrow \varepsilon' + \delta$ at 560 K for Ge-deficient compositions. No order-disorder transitions are shown on the phase diagram and as far as we are aware it is not known whether the high temperature ε phase orders direct from the liquid upon solidification or in the solid-state at some temperature below the liquidus.

Rapid solidification was affected via drop-tube processing, in which cooling rate is primarily determined by particle size. The main objective of the study is to study the mechanical properties of rapidly solidified drop-tube samples (850–150 μm diameter particles) with respect to increasing the rate of cooling rates.

Experimental Methods

The congruently melting ε-Ni_5Ge_3 compound exists over the homogeneity range of 33.8–43.2 at.% Ge [5]. Single phase ε-Ni_5Ge_3 was produced by arc-melting Ni and Ge together under a protective Ar atmosphere. To ensure homogeneity of the final alloy, the arc-melting process was repeating 8 times with the phase composition of the subsequent ingot being confirmed by XRD using a PANalytical Xpert Pro. Only when the material was confirmed as single phase was rapid solidification processing undertaken.

Rapid solidification was affected by drop-tube processing using a 6.5 m drop-tube. The tube was rough pumped to a pressure of 2×10^{-4} Pa before being flushed with N_2 gas. The rough pump—flush cycle was repeated three times before the tube was evacuated to a pressure of 4×10^{-7} Pa using a turbo-molecular pump. For sample processing the tube was filled with dried, oxygen free N_2 gas at a

pressure of 50 kPa. The alloy sample, of approximately 9.4 g mass was loaded into an alumina crucible which has three 300 μm laser drilled holes in the base. Induction heating of a graphite subsector was used for heating the sample. Temperature determination was by means of an R-type thermocouple which sits inside the melt crucible, just above the level of the melt. When the temperature in the crucible attained 1533 K (75 K superheat) the melt was ejected by pressuring the crucible with ~400 kPa of N_2 gas. This produces a fine spray of droplets which subsequently solidify in-flight and are collected at the base of the tube.

The sample was weighed following removal from the drop-tube and sieved into the size fractions ranges from 850 μm (700 K s^{-1}) to 150 μm (7800 K s^{-1}). For each size fraction the cooling rate, calculated using the methodology described in [6], is shown in brackets.

All of drop-tube powders were subject to XRD analysis to ensure they remained single-phase prior to further analysis. Each sieve fraction was then mounted in transoptic resin and prepared for microstructural analysis using OM (Olympus BX51) and SEM (Carl Zeiss EVO MA15 scanning electron microscope). For such analysis samples were etched for 25 s in a mixture of equal parts of undiluted HNO_3 + HCl + HF. An Oxford Instrument X-Max Energy-Dispersive X-Ray (EDX) detector was used to check the chemical homogeneity of the etched samples. Bright-field imaging and selected area diffraction analysis in the transmission electron microscopy (TEM), using an FEI Tecnai TF20, was used to distinguish between the ordered and disordered variants of each morphology observed. Samples were prepared for TEM analysis using a FEI Nova 200 Nanolab focused ion beam (FIB), with the sections cut being approximately 10 μm × 7 μm and between 55 and 70 nm in thickness. An example of a FIB milled section for the related β-Ni_3Ge compound is shown in [7]. For measurement of micro-hardness of the drop-tube samples a TUKONTM 1202 Wilson Hardness (micro-Vickers) test rig was used with 0.01 kg load. The final measurement of hardness for each sample was based upon an average of at least 10 individual measurements.

Results and Discussion

In drop-tube processing the cooling rate is determined primarily by the ratio of surface area to volume of the droplet, giving a one-to-one relationship between droplet diameter and cooling rate. Therefore a spray with a broad size distribution is used to access a wide range of cooling rates within a single experiment. The process describe in [6] equates the radiative and convective heat flux through the droplet surface with the total heat loss to obtain the cooling rate. However, we make one modification to the method given in [6]. As order/disorder reactions occur in the solid-state, the cooling rates quoted here are given immediately post-solidification, i.e. the effect of latent heat is ignored. The cooling rates for each size fraction are: 850 μm (700 K s^{-1}), 500 μm (1400 K s^{-1}), 300 μm (2800 K s^{-1}), 212 μm (4600 K s^{-1}) and 150 μm (7800 K s^{-1}).

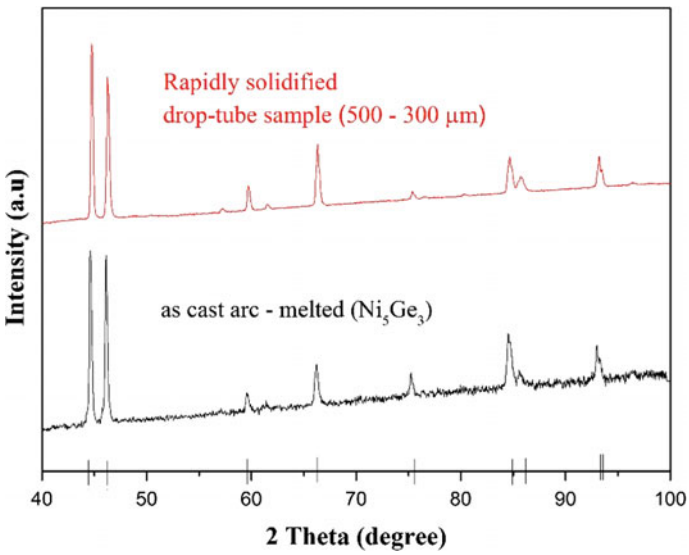

Fig. 1 X-ray diffraction analysis of an arc melted sample prior to drop-tube process (black) and the rapidly solidified drop-tube processed sample 500–300 μm size fraction. Vertical black lines indicate peak position for the ε-Ni_5Ge_3 reference pattern

The starting material for the drop-tube experiments was single phase ε-Ni_5Ge_3, which was confirmed by XRD analysis on a polished surface of the arc-melted ingot. The XRD peaks in Fig. 1 clearly indicate that ε-Ni_5Ge_3 is the only phase present (for reference, the ICCD reference pattern 04-004-7264 for ε-Ni_5Ge_3 is shown on the x-axis). XRD analysis was also conducted on each size fraction of the drop tube powders and again each was confirmed as contains only ε-Ni_5Ge_3. For the sake of brevity, only one example result of this is shown in Fig. 1, that for the 500–300 μm size fraction.

Figure 2a shows a SEM micrograph of a polished and HF etched sample of sieve fraction 500–300 μm in powder form, wherein numerous plate and lath like structures are evident in the sample. Such structure are also observed in the other size fractions considered in this paper. Such structures are common in intermetallic compounds [8–10] and some alloys of iron [10]. A study conducted by Hyman et al. [8] observed that the formation of these lath and plate structure in γ-TiAl during the transformation in the solid state of α dendrites during cooling to $\alpha_2 + \gamma$ mixture lath which is surrounded by γ segregates. McCullough et al. also observed that α_2-Ti_3Al also shows plate and lath morphology which is like ε-Ni_5Ge_3, shares the P63/mmc space group [9].

The contrast between the surrounding matrix material and the plate and lath is interesting in that, as confirmed by XRD analysis, it is not the result of contrast between different phases, the material here being single phase ε-Ni_5Ge_3. An EDX line scan perpendicular to a plate and lath is showed in Fig. 2b. This shows that the

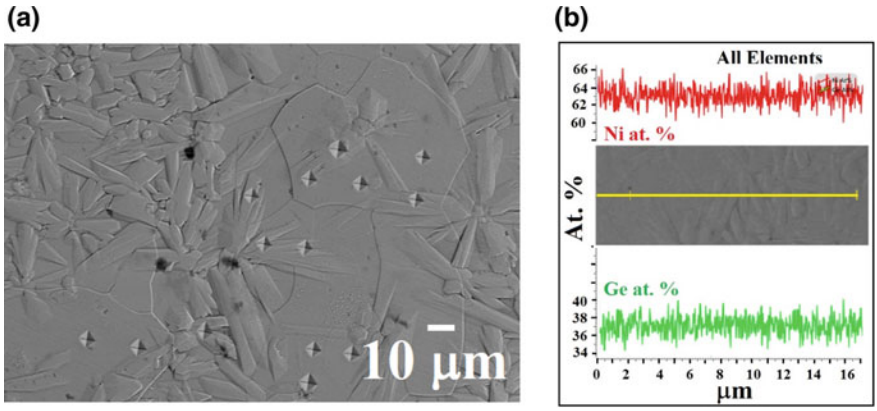

Fig. 2 **a** SEM micrograph of HF etched ε-Ni_5Ge_3 drop-tube particle from the 500 to 300 µm size fraction showing plate and lath structures in a featureless matrix and **b** EDX line scan across a plate and lath trunk showing that the contrast revealed by etching is not the result of solute partitioning

material is chemically homogeneous and that the contrast is therefore not the result of compositional difference between the plate and lath and the surrounding matrix, as might arise from solute partitioning during solidification [11, 12]. We conclude therefore that the contrast revealed by etching does not indicate any relation to phase difference (XRD) nor chemical composition (EDX).

In order to understand the origin of plate and lath morphologies revealed by etching in the rapidly solidified Ni_5Ge_3 drop-tube samples, TEM imaging and Selected Area Diffraction (SAD) analysis has been performed. Figure 3a shows a TEM bright field image of an FIB section of a lath and plate structure and some of the immediately its surrounding matrix material. Selective area diffraction (SAD) identifies two region Figure (a); (i) matrix material that is away from plate

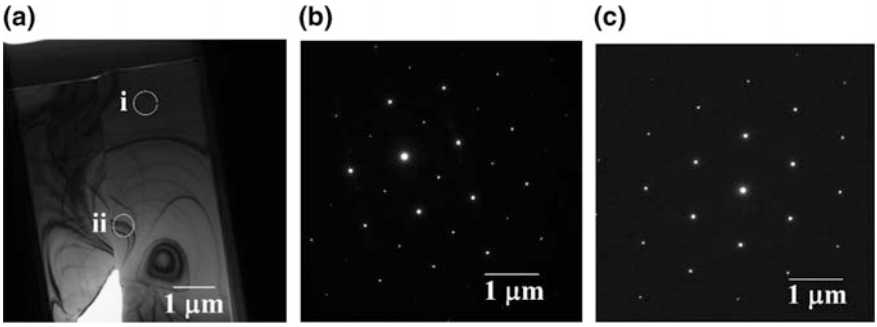

Fig. 3 **a** TEM bright field image of a plate and lath structure and surrounding matrix material in a 500–300 µm size fraction, **b** and **c** selected area diffraction patterns from regions (i) and (ii) identified in the bright field image (i) matrix materials well away from the plate and lath structure, (ii) inside the structure

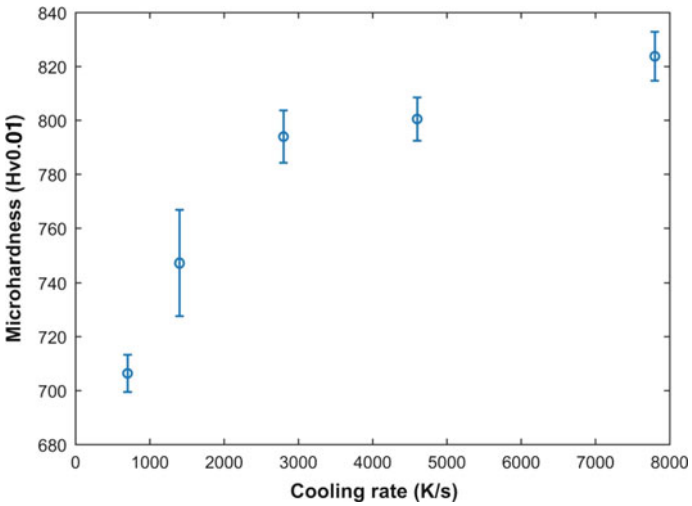

Fig. 4 Micro-hardness value (in Hv0.01) as a function of droplet diameter ranges from 850 to 150 μm

and lath structure, and (ii) inside the plate and lath structure. The SAD results of region (i) and (ii) are shown in Fig. 3b, c respectively. Supper lattice spots are clearly visible in Fig. 3b indicating the matrix material is the chemically ordered structure. On the other hand, the absence of supper lattice spot in Fig. 3c suggest the plate and lath morphology is composed of the chemically disordered material. We conclude that the contrast displayed by etching is because of incomplete chemical ordering, causing the etchant to attack the disordered material and leaving the ordered material unaffected. The lower chemical resistance of the disordered phase has resulted in this type of differential etching between ordered and disordered material to be observed previously in other intermetallic compounds [11, 13].

In order to determine the effect of cooling rate upon mechanical properties, microvicker hardness tests have performed on the plate and lath microstructure contained within all of the sample sizes considered here (850–150 μm). The results of this are shown in the Fig. 4. The maximum hardness, 824 Hv0.01, was observed in smallest size drop-tube sample (212–150 μm diameter particles). Conversely, the minimum hardness was observed in largest drop-tube sample (850–500 μm diameter particles). It can be concluded that the mechanical properties can be altered (hardness increased) by increasing the cooling rate, in the cases studied here from 700 to 7800 K s^{-1}.

The behavior observed here is anomalous and quite contrary to what we would predict. We presume that the plate and lath structures are partially ordered while the matrix material is (near) fully ordered, this being consistent with the TEM results. However, we must suppose that with increasing cooling rate chemical ordering will be suppressed and that consequently the degree of ordering within the partially ordered material will decrease i.e. the plate and lath structures will become more

disordered with increasing cooling rate. However, we would expect that this would cause the microhardness to decrease with increasing cooling rate rather than to increase, as the disordered material because more metallic like with increasing degree of disorder. Many materials will show an increase in strength with rapid solidification due to the Hall-Petch effect, although this does not appear likely here where we are considering microhardness measurements on individual ordered and disordered regions within grains. A possible explanation would be that there is an increase in defect concentration within the lattice due to increased growth velocity at high cooling rate. This may lead to an increase in dislocation density, giving a work-hardening like effect. As such, these results may have significant implications for our understanding of the way in which rapid solidification can be used for the processing of intermetallic materials.

Acknowledgements Nafisul Haque is thankful to the Higher Education Commission (HEC) Pakistan and NED University of Engineering and Technology for financial support.

References

1. Ellner M, Gödecke T, Schubert K (1971) Zur struktur der mischung Nickel-Germanium. J Less Common Met 24:23–40
2. Nash A, Nash P (1987) The Ge−Ni (Germanium-Nickel) system. J Phase Equilib 8:255–264
3. Liu Y, Ma D, Du Y (2010) Thermodynamic modeling of the germanium–nickel system. J Alloy Compd 491:63–71
4. Jin S, Leinenbach C, Wang J, Duarte LI, Delsante S, Borzone G, Scott A, Watson A (2012) Thermodynamic study and re-assessment of the Ge-Ni system. Calphad 38:23–34
5. Nash A, Nash P (1976) Binary alloy phase diagrams. US national bureau of standards monograph series 25. Elsevier, ASM, Ohio, p 35
6. Haque N, Cochrane RF, Mullis AM (2017) The role of recrystallization in spontaneous grain refinement of rapidly solidified Ni3Ge. Metall Mater Trans A 1–8
7. Haque N, Cochrane RF, Mullis AM (2016) Rapid solidification morphologies in Ni 3 Ge: spherulites, dendrites and dense-branched fractal structures. Intermetallics 76:70–77
8. Hyman M, McCullough C, Valencia J, Levi C, Mehrabian R (1989) Microstructure evolution in TiAl alloys with B additions: conventional solidification. Metall Trans A 20:1847
9. McCullough C, Valencia J, Levi C, Mehrabian R (1990) Microstructural analysis of rapidly solidified Ti-Al-X powders. Mater Sci Eng A 124:83–101
10. Broderick T, Jackson A, Jones H, Froes F (1985) The effect of cooling conditions on the microstructure of rapidly solidified Ti-6Al-4V. Metall Trans A 16:1951–1959
11. Haque N, Cochrane RF, Mullis AM (2016) Disorder-order morphologies in drop-tube processed Ni 3 Ge: dendritic and seaweed growth. J Alloy Compd
12. Haque N, Cochrane RF, Mullis AM (2017) Morphology of order-disorder structures in rapidly solidified L12 intermetallics. In: TMS 2017 146th annual meeting and Exhibition Supplemental Proceedings. Springer, pp 729–736
13. Haque N, Cochrane RF, Mullis AM (2017) Morphology of spherulites in rapidly solidified Ni3Ge droplets. Crystals 7:100

Part XXIX
Mechanical Characteristics and Application Properties of Metals and Non-metals for Technology: An EPD Symposium in Honor of Donato Firrao

Production of Cu_2O Powder Using Electrodeposition Method

Shadia J. Ikhmayies

Abstract Cuprous oxide (Cu_2O) has wide-scale applications in gas sensors, solar cells, and lithium-ion batteries. In this work, cuprous oxide (Cu_2O) powder was prepared by electrodeposition method using copper sulphate hydrated $CuSO_4$, where it was dissolved in distilled water. The produced samples were characterized by X-ray diffraction (XRD), and X-ray fluorescence spectroscopy (XRF). X-ray diffractograms revealed the characteristic diffraction peaks of cubic Cu_2O of space group Pn-3 m, in addition to some lines of cubic Cu of space group Fm-3 m. XRF reports showed that the samples are mainly composed of Cu_2O, with impurities mainly including SO_3, P_2O_5, Al_2O_3 and SiO_2.

Keywords Cuprous oxide · Electrodeposition · Powder · XRD
XRF

Introduction

Metal oxides are promising materials that have attracted much attention because of their extraordinary properties in different fields of optics, optoelectronics, catalysts, biosensors and humidity sensors [1]. As a typical p-type semiconducting material, cuprous oxide (Cu_2O) possesses a stable, direct band gap of about 2.17 eV and a higher Hall mobility up to 60 cm^2/V s [2]. It has wide-scale applications of in gas sensors, solar cells and lithium-ion batteries [3, 4] owing to its unique optical and magnetic properties [4–10]. It also has important applications in degrading industrial dyeing wastewater, nitrogen-containing pesticides, and decomposition of water into O_2 and H_2 under visible light [11–15].

To synthesize Cu_2O powder, different experimental routs were used. Among them are electrochemical deposition [16], sol-gel [17], RF reactive sputtering [18] and chemical vapour deposition (CVD) [19]. In this work electrodeposition method

S. J. Ikhmayies (✉)
Faculty of Science, Physics Department, Al Isra University, Amman 11622, Jordan
e-mail: shadia_ikhmayies@yahoo.com

The Minerals, Metals & Materials Society, *TMS 2018 147th Annual Meeting & Exhibition Supplemental Proceedings*, The Minerals, Metals & Materials Series,
https://doi.org/10.1007/978-3-319-72526-0_67

was used because of its simplicity and low cost. The produced powder was characterized using X-ray diffraction (XRD), and X-ray fluorescence spectroscopy (XRF).

Experimental Procedure

Cu_2O powder was prepared by electrodeposition method, where 9.9 gm of copper sulphate hydrated (Assay min 99.5%, chloride Cl max 0.0005%) was fully dissolved in 400 ml of distilled water and a blue solution was produced. The electric circuit is a simple series circuit that consists of a power supply, rheostat, digital multimeter (FLUKE 87), and two rectangular copper electrodes used as a cathode and an anode, and immersed in the solution. For sample (1) which has a mass of 2.4 g, the current in the circuit was maintained at 0.86 A using the rheostat, and sample (4) which has a mass of 5.9 g, was prepared using the same deposition parameters as sample (1), but prepared before about three months. Samples (2) and (3) which have masses 10.5, and 9.0 g respectively, were prepared using a current in the range 1.14–3.0, and 2.0–2.5 A respectively. Samples (1), (3), and (4) were prepared in two days, and directly sent for characterization with sample (1). So it can be said that samples (1), (2), and (3) were characterized after 3–4 days from the date of deposition. When the electric circuit is closed, the color of the cathode started to change to black and dark brown, and dark brown to black precipitate started to accumulate in the bottom of the beaker. After finishing the experiment, the obtained precipitate was leached, and left to dry naturally.

The crystal structures of the as-prepared samples was identified by x-ray powder diffraction (XRD) using SHIMADZU XRD-7000 x-ray utilizing Cu Kα radiation (k = 1.54 Å) with step size and scan speed of 0.01 and 1/min respectively. The measurements were taken in the continuous 2θ mode in the range 10–80 using a current of 30 mA and voltage of 40 kV. The composition of the samples was examined by x-ray fluorescence using SHIMADZU XRF-1800.

Results and Discussion

Figure 1 displays the XRD diffractograms of four as-synthesized samples of the Cu_2O powder prepared by electrodeposition. Diffraction peaks could be readily indexed to the cubic phase Cu_2O with lattice constant $a_0 = 3.61$ Å [20] and space group Pn-3 m (JCPDS: 01-078-2076). In addition, there are some peaks of cubic (Cu) with space group Fm-3 m, identified according to file (JCPDS: 04-0836). Presence of Cu means that not all Cu atoms are oxidized. All Cu_2O peaks were assigned with the corresponding Miller indices as shown in Fig. 1, where they represent reflections from the planes (110), (111), (200), (220), (311), and (222), where the reflection from the (111) plane is the strongest. It is noticed that despite

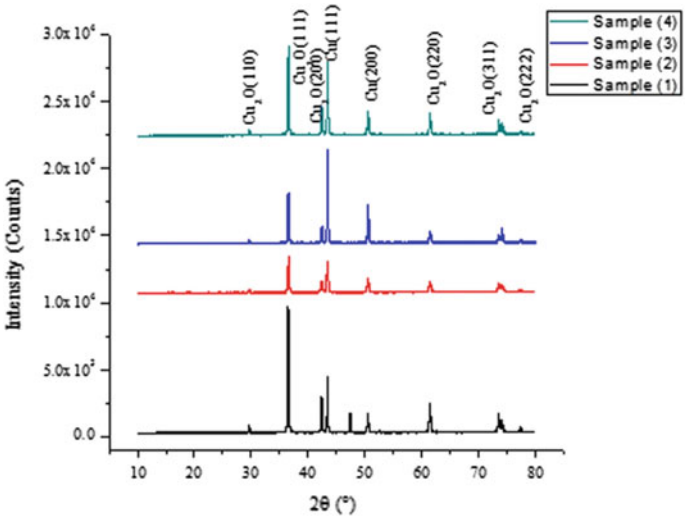

Fig. 1 XRD diffractogram of the produced Cu_2O nanopowder

the higher masses of samples (2) and (3), the lines (111), (110), and (200) of these samples are weaker than those of samples (1) and (4). This may be due to the larger values of current which speed the deposition process, but may slow the rate of crystal growth.

These diffractograms were used to deduce the lattice constant a of cubic Cu_2O crystal lattice. This was done by using the distance of lattice planes (d_{hkl}) from Bragg's law

$$2d_{hkl} \sin \vartheta = \lambda \tag{1}$$

where ϑ is Bragg's angle, 2ϑ is the scattering angle, and λ is the wavelength of the X-ray, which is 1.54 Å for the Cu K_α line. The relationship that connects d_{hkl} with lattice constant a of the cubic structure is:

$$\frac{1}{d_{hkl}^2} = \frac{1}{a^2}(h^2 + k^2 + l^2) \tag{2}$$

where $h, k,$ and l are Miller indices. The plot of d^2 against $h^2 + k^2 + l^2$ (Fig. 2) is used to find the lattice constant a. For this purpose a linear fit was made, and the square root of the slope represents the average value of a, where $a \pm \Delta a = 3.5938 \pm 0.0022$ Å. This value is very close to the accepted value $a_0 = 3.61$ Å.

It is well known that the composition of the samples determines their properties; hence XRF was used to explore the composition of the produced Cu_2O powder. Table 1 lists the XRF report of the four samples. As seen in the table, the

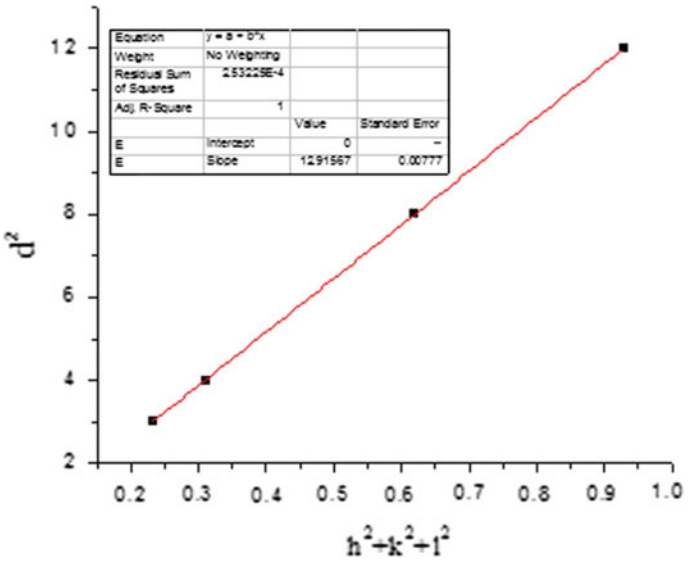

Fig. 2 The plot of d^2 against $h^2 + k^2 + l^2$ with the linear fit. The inset table lists the fit parameters

concentration of Cu_2O in the samples is in the range 96.2–99.4%, and the main impurities are S, P, Si, and Al all incorporated with oxygen. The presence of S is due to the use of the hydrated $CuSO_4$ powder, where the samples were not washed before drying. Si may be liberated from the glass beaker during the deposition process. P and the other impurities (Ru, Fe, and Ni) which have very small concentrations as seen in Table 1, are expected to be included in the hydrated $CuSo_4$, which has purity of just 99.5%. Hence, they have less influence on the properties of the samples.

Table 1 XRF report for the composition of the Cu_2O samples

Sample 1		Sample 2		Sample 3		Sample 4	
Oxide	Concentration %	Oxide	Concentration %	Oxide	Concentration %	Oxide	Concentration %
Cu_2O	96.1854	Cu_2O	97.2513	Cu_2O	98.9089	Cu_2O	99.4462
SO_3	2.5656	SO_3	2.0249	SO_3	0.4487	P_2O_5	0.2462
SiO_2	0.6863	P_2O_5	0.2836	P_2O_5	0.2274	SO_3	0.1767
Al_2O_3	0.4716	SiO_2	0.1755	SiO_2	0.1648	RuO_2	0.0914
Cr_2O_3	0.051	Al_2O_3	0.134	Al_2O_3	0.0971	Fe_2O_3	0.0395
Fe_2O_3	0.0402	RuO_2	0.073	RuO_2	0.0946		
		Fe_2O_3	0.0439	Fe_2O_3	0.0445		
		NiO	0.0138	Cr_2O_3	0.014		

Conclusions

Cu_2O powder was successfully synthesized using the electrodeposition method from $CuSo_4$ aqueous solution. X-ray diffraction patterns (XRD) revealed the presence of the peaks related to cubic Cu_2O of space group Pn-3 m in addition to some peaks related to cubic Cu of space group Fm-3 m. Presence of Cu means that not all Cu atoms are oxidized. Lattice constant was estimated from XRD data and found to be very close to the accepted value. XRF data showed that the percent of Cu_2O is large (96.2–99.4%) in all samples, and the impurities are found with small ratios. The main impurities are due to the use of $CuSo_4$ not washing the samples before dryin.

References

1. Ashokan S, Ponnuswamy V, Jayamurugan P, Subba Rao YV (2015) Fabrication and characterization of CuO nanoparticles: its humidity sensor application. S Asian J Eng Technol (SAJET) 1(1):11–23
2. Ishizuka S, Maruyama T, Akimoto K (2000) Thin-film deposition of Cu_2O by reactive radio-frequency magnetron sputtering. Jpn J Appl Phys 39:L786–L788
3. Lee H-S, Woo C-S, Youn B-K, Kim S-Y, Oh S-T, Sung Y-E, Lee H-I (2005) Bandgap modulation of TiO_2 and its effect on the activity in photocatalytic oxidation of 2-isopropyl-6-methyl-4-pyrimidinol. Top Catal 35:255–260
4. Zhang J, Liu J, Peng Q, Wang X, Li Y (2006) Nearly monodisperse Cu_2O and CuO nanospheres: preparation and applications for sensitive gas sensors. Chem Mater 18:867–871
5. Wanga R-C, Lin H-Y (2010) Simple fabrication and improved photoresponse of ZnO–Cu_2O core–shell heterojunction nanorod arrays. Sens Actuators B 149:94–97
6. Liu W, Chen G, He G, Zhang W (2011) Synthesis of starfish-like Cu_2O nanocrystals through γ-irradiation and their application in lithium-ion batteries. J Nanopart Res 13:2705–2713
7. Das K, De SK (2009) Optical and photoconductivity studies of Cu_2O nanowires synthesized by solvothermal method. J Lumin 129:1015–1022
8. Hafez M, Al-Marzouki F, Mahmoud WE (2011) Single crystalline quasi aligned one dimensional P-type Cu_2O nanowire for improving Schottky barrier characteristics. Mater Lett 65:1868–1870
9. Yue Y, Chen M, Yang J, Zhang L (2012) Stress-induced growth of well-aligned Cu_2O nanowire arrays and their photovoltaic effect. Scripta Mater 66:81–84
10. Liu Y, Zhou H, Li J, Chen H, Li D, Zhou B, Cai W (2010) Enhanced photoelectrochemical properties of Cu_2O loaded short TiO_2 nanotube array electrode prepared by sonoelectrochemical deposition. Nano-Micro Lett 2:277–284
11. Yu Y, Zhang L, Wang J, Yang Z, Long M, Hu N, Zhang Y (2012) Preparation of hollow porous Cu_2O microspheres and photocatalytic activity under visible light irradiation. Nanoscale Res Lett 7:347
12. Hara M, Kondo T, Komoda M, Ikeda S, Shinohara K, Tanaka A, Kondoa JN, Domen K (1998) Cu2O as a photocatalyst for overall water splitting under visible light irradiation. Chem Commun 3:357–358
13. Paracchino A, Laporte V, Sivula K, Gratzel M, Thimsen E (2011) Highly active oxide photocathode for photoelectrochemical water reduction. Nat Mater 10:456–461
14. Xu CH, Han Y, Chi MY (2010) Cu_2O-based photocatalysis. Prog Chem 22:2290–2297

15. Xu HL, Wang WZ, Zhu W (2006) Shape evolution and size-controllable synthesis of Cu_2O octahedra and their morphology-dependent photocatalytic properties. J Phys Chem B 110:13829–13834
16. Khattar HK, Al-Hasnawi SWR, Al-Saady FAA (2015) Electrolytic preparation and characterization of cuprous oxide nano powder. Int J Electr Comput Sci IJECS-IJENS 15 (4):6–12
17. Kumar RV, Mastai Y, Diamant Y, Gedanken A (2001) Sonochemical synthesis of amorphous Cu and nanocrystalline Cu_2O embedded in a polyaniline matrix. J Mater Chem 11(4):1209–1213
18. Armelao L, Barreca D, Bertapelle M, Bottaro G, Sada C, Tondello E (2003) A sol-gel approach to nanophasic copper oxide thin films. Thin Solid Films 442:48–52
19. Ghosh S, Avasthi DK, Shah P, Ganesan V, Gupta A, Saransgi D, Bhattacharya R, Assmann W (2000) Deposition of thin films of different oxides by RF reactive sputtering and their characterization. Vacuum 57:377–385
20. Asharf Shah M, Al-Ghamdi MS (2011) Preparation of copper (Cu) and copper oxide (Cu_2O) nanoparticles under supercritical conditions. Mater Sci Appl MSA 2:977–980

Alumina Feeding System Changes in Aluminum Electrochemical Cell with D18 Technology for Energy Efficiency (Case Study: Almahdi-Hormozal Aluminum Smelter)

Mohsen Ameri Siahooei, Alireza Samimi and Borzu Baharvand

Abstract Aluminum reduction cells have benefited from point feeding technology for a long time, but there are still smelters which are using the old technology of center break and center feed system. Due to several factors this system is no longer approved and there have been a few attempts worldwide to upgrade these cells so as to implement the newer technology by applying mechanical and automation changes. In this paper we will present an attempt which was made in order to retrofit a so-called center break cell to point feeder cell. The results show that this project has decreased the energy consumption and anode effect frequency. Furthermore, there has been a significant increase in current efficiency.

Keywords Efficiency · Energy performance indicator · Manufacturing Normalized statistical distributions

Introduction

Almahdi Aluminium Corporation (AAC), once considered a modern plant, is now concerned with the issue of old reduction cell technology which is far away from currently used technologies. The plant which is located near the city of Bandar

M. A. Siahooei (✉)
Department of Chemistry, Science and Research Branch,
Islamic Azad University, Tehran, Iran
e-mail: m_ameri_s@yahoo.com

A. Samimi
Sharif University of Technology & Arad Aluminum, Tehran, Iran
e-mail: shimi.medeni@gmail.com

B. Baharvand
Research Department, Almahdi-hormozal Aluminum Company,
Bandar Abbas, Iran
e-mail: baharvand_b@yahoo.com

The Minerals, Metals & Materials Society, *TMS 2018 147th Annual Meeting & Exhibition Supplemental Proceedings*, The Minerals, Metals & Materials Series,
https://doi.org/10.1007/978-3-319-72526-0_68

Abbas, has a total number of 240 reduction cells which utilize center break and center feed systems. The amperage of the production line is 175 kA which is about half the amperage of modern cell technology. After the Iranian targeted subsidy plan in 2010 which aimed to replace subsidies on food and energy with targeted social assistance, the price of energy has risen massively. The impact of such noticeable increase on primary aluminium industry was so intense which that it triggered the production section to review and assess its lavish power consumption and search for inexpensive schemes to retrofit its systems and structures.

After the Iranian targeted subsidy plan in 2010 which aimed to replace subsidies on food and energy with targeted social assistance, the price of energy has risen massively. The impact of such noticeable increase on primary aluminium industry was so intense that it triggered the production section to review and assess its lavish power consumption and search for inexpensive schemes to retrofit its systems and structures.

One of the defined R&D projects in AAC was called "Retrofit Upgrade of Center Break Cell Technology to Point Feeding Cell Technology". The project was assigned to an Iranian engineering and consulting company and a group of experienced engineers from AAC [5].

Model

The scope of the project included mechanical and industrial control and automation alterations and optimizations required in order of converting the existing center break reduction cell to a point feeder reduction cell. These modifications are as follow.

Mechanical

Different ideas were developed and different models were tested and compared. In all cases, required mechanical changes were sketched and modelled using SolidWorks™ software and appropriate detailed drawings were developed.

Mechanical changes can be categorized into two groups as follows:

Off-site Mechanical Changes

This group of changes includes those changes which could be applied in the repair shop such as sheet metal work, pneumatic jack installation, pneumatic piping installation and ore hopper adjustments. Due to the fact that the superstructure was designed for a center break reduction cell, a few parts had to be removed such as the ore gate and the center breaker system and a few parts needed to be added to the old superstructure such as point feeder jacks and point breakers.

On-site Mechanical Changes

The main challenge of the project was that some of the main mechanical changes and modifications had to be applied after the reduction cell was set in operation. This meant a working atmosphere with high temperature, intense magnetic field and sometimes hazardous alumina dust. For example, welding process was hindered by the considerable magnetic field inside pot room and special techniques were applied wherever necessary.

Control and Automation

Level one automation system of an aluminum reduction cell consists of the following parts:

- Analog and digital input and output monitoring unit
- Online voltage and current processor of the cell
- Alumina feeding system
- Anode movement system
- Noise detector and control unit
- Metal tapping unit
- Anode changing and beam rising system
- Automatic anode effect termination system
- Level two interconnection unit
- Local panel connection unit.

In order to apply the control philosophy of this system, several modifications were required because the current system was designed based on central breaking and feeding. The new control system utilizes smart methods in different parts especially in the voltage control unit.

Results and Discussion

Improvement of Technology

The aluminium reduction cell's technology of D18 kind from Almahdi Aluminium Company of dubal with 18 pre bak anodes per pot, is designed based on the Kaiser P69. The cells are installed side-by-side.

Studies done on similar D18 technology pots and using the experience and control system from Dubal aluminium production pots, some changes were made to

one of Almahdi's pots. The goal was to improve productivity and reduce the costs through decreasing the energy consumption and improving control and feeding, This article describes these changes and results (Figs. 1 and 2).

Alumina Feed

Normally, the center line of hard crust is broken by cortex breaker jacks. In this method, there is no good control on the added alumina and while loosing much heat from central channel, also during each break large amounts of hard solid crust, entered into the molten bath and disturb the pot's stability. By chaning the feeding system to point feed, Almahdi company was able to increase the height of alumina covering on the anodes, reduce the metal and some changes bath chemistry, thus decreasing waste heat in turn reduced the voltage of pot and specific energy consumption. Also with these changes, the occurrence of anode effects significantly reduced and alumina usage was controlled better which resulted in a significant decrease of sludge on the pot's cathode. Feeding program contains four stages including: base feeding program program, program and an overfeed program with different amounts of alumina feeding in each stage. The algorithm of feeding is shown in Fig. 3.

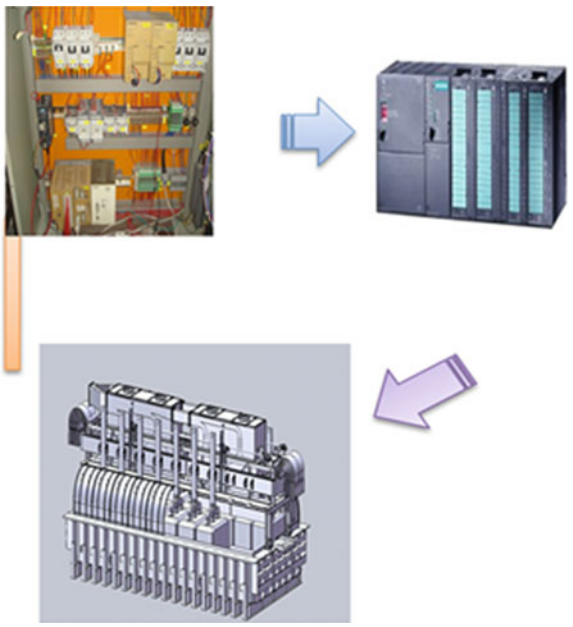

Fig. 1 Programming and upgrade PLCs5 to PLCs7

Fig. 2 Pot with center work (breaker)

Control System

In software system, the local control of present pots, the voltage setting in two different phases is done by anode's motion and failing and central canal feeding which by induction of some changes and covering the algorithm of intelligent feeding control, based on need and anode's simultaneous motion in phase 4 has been shown. In Fig. 3, the process of feeding is sown. To enable compatibility with present level 2 system some changes where necessary in other software parts and also some adjustment in hardware. These changes along with applying the new feeding algorithm, enabled changes in bath chemistry and working conditions as (Fig. 4).

Fig. 3 Pot with point feeder

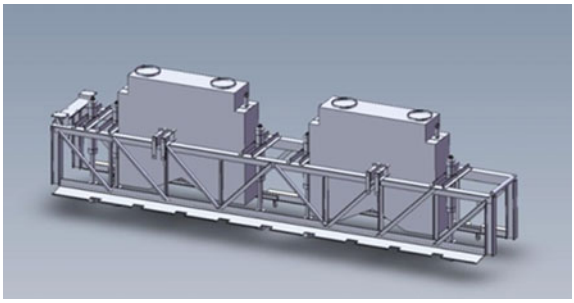

Fig. 4 Simulation and modeling superstructure Almahdi Aluminum Smelter and modified to a point feed cell

Table 1 Compare the operation between center work pot and point feeder pot

Property	Unit	Center work	Point feeder
Time between two feeding	min	60	3
Pot temperature	°C	970	962
Discharge mass	Kg	100	4.4
Anode effect frequency	AE/pot.day	0.75	0.21
Current efficiency	%	90.6	93
Pot voltage	V	4.96	4.56
Power consumption	kWh/t Al	16.4	14.6
CO_2 in the off-gas	%	1.4	0.5
CO in the off-gas	ppm	1650	551

Operating Conditions and Bath Chemistry

By converting to point feeders, 4 small holes along the central line are used and 4.4 kg alumina are added in each feed Crust breaking and feeding is done separately by two compressed air cylinders. The most important advantage of point feeding is that the concentration of alumina in the bath remains almost constant and less fall in of crust occurreds, thus causing the process to work optimally in constant condition and increase the yield of the pots.

The feeding point, should be where the bath has the highest speed. so the best place is the middle channel close to the anodes corners. It should be noted that for point feeding to work optimal a hole in the hard crust must be kept open constantly. Average temperature in the central break feed system is 970 °C. This could be reduced and in the new feeding system to about 962 °C. Excess aluminium fluoride levels of about 8% were achieved average pot voltage is 4.56 V. The height of molten metal could decreased by 4 cm and this helped in reducing the pot's resistance, working average voltage, anode effect frequency and finally energy consumption. With these changes, the current efficiency could be increased by 3%. In Tables 1 a comparison between Almahdi's present pots performance with central feeding and new pot performance with the point feeding system is presented (Fig. 5).

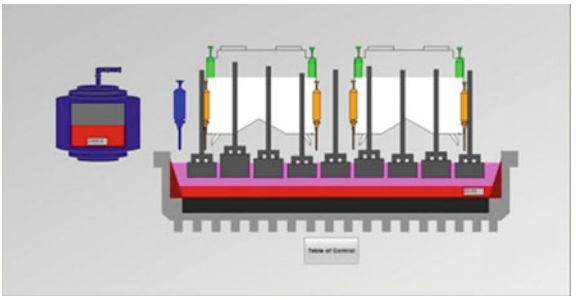

Fig. 5 Pot simulated

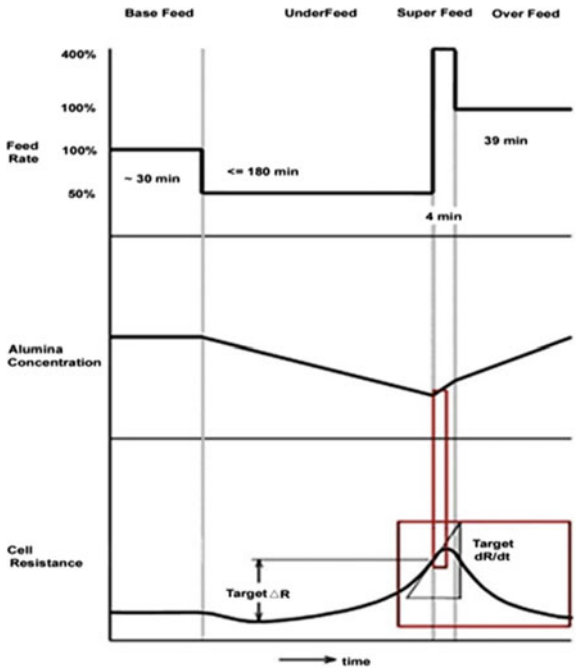

Fig. 6 Adaptive feed control strategy

Conclusion

Almahdi Aluminum Corporation has defined a number of research projects in order to improve the technology and reach a higher efficiency. One of these projects was to improve the ALUMATIC control hardware unit which was a prerequisite for the point feeding retrofit upgrade.

Voltage and current control and monitoring is done via this unit. Also, required mechanical modifications were applied during the project (Fig. 6).

This upgrade was experimentally applied on pots No. 2 and No. 7 along with the replacement of the ALUMATIC hardware with a well-developed hardware called ALUMARAD. This new system uses a SIMATIC S7 PLC unit.

The results confirm the success of the project and the normal conditions of the pot working parameters encouraged the team to expand the project scope. Now, after successful termination of this R&D project, the company is upgrading a section of 30 reduction cells.

The results show that by changing the feeding system to point feed and improve the control of pot through an improved feeding program based on demand-feed, without major changes in current automation system and improvement of some practical condition, the height of molten metal could be decreased by 4 cm. By changes of the additional fluoride aluminium mount setpoint, a bath temperature of

962 °C can reached and a cell voltage about 4.56 V. The specific energy consumption could be lowered from 16.4 kWh/kg- to 14.6 kWh /kg-Al.

It should be note that now 2 executive projects are under way for improve the pot's operational conditions and also for promoting the central control system, recovery of control and pot feeding algorithm by using modern methods which promise the availability of technology and intelligent control of recovery pots through advanced methods and high benefits in aluminium industry in near future.

References

1. Aarons K, Golding C, Clark S (2013) Key considerations for industrial benchmarking in theory and practice
2. Grjotheim K, Kvande H (2006) Introduction to aluminium electrolysis, 2nd edn. Dubai, UAE, pp 325–410
3. Whitfield D, Al-Monien Said A (2009) G Bearne (ed) Development of D18 cell technology at Dubal. Light Metals 2009, pp 477–481
4. Tandon SC, Al-Prasad RN (2003) Crepeau PN (ed) Twenty years of progress at hindalcos-aluminium smelter. Light Metals 2003, pp 379–391
5. Statistical information derived from operational research R&D Almahdi

Hot Ductility of X70 Pipeline Steel in Continuous Casting

Wenxiang Jiang, Mujun Long, Dengfu Chen, Huamei Duan, Wenjie He, Sheng Yu, Yunwei Huang and Junsheng Cao

Abstract Transverse cracks in continuous cast steel may easily form if the hot ductility of the continuous cast steel is poor at the straightening stage. In this paper, the hot ductility of X70 pipeline steel was studied at various temperature from 600 to 1300 °C. The results show that the steel has a good hot ductility (RA above 70%) at 800–1000 and 600–650 °C. And the steel exhibits a hot ductility trough (RA below 80%) at 650–800 °C, which is mainly contributed to the austenite–ferrite transformation. For further understanding the low ductility, the fracture surface was examined by scanning electron microscope, and the second phase particles was examined by energy spectrum analysis. The results indicate that the low ductility of the steel is affected by the equiaxed (Fe, Mn)S precipitate as well as austenite transformation at the third brittle zone.

Keywords Transverse crack · Continuous cast · Hot ductility Transformation

Introduction

The significant economic advantages of transporting gas and crude oil by pipeline necessitates higher quality and higher strength pipeline steels [1], which requires higher quality continuous cast steels. However, the transverse cracks in continuous cast steel has been on of the main problem for decades. It usually forms at the temperatures with low ductility [2]. To prevent cracking during continuous casting process, many studies [3–7] have been performed on hot tensile tests of the susceptible grades of steel. And hot ductility [8, 9] is one of the most important

W. Jiang · M. Long (✉) · D. Chen · H. Duan · W. He · S. Yu · Y. Huang · J. Cao
College of Materials Science and Engineering, Chongqing University, Chongqing 400044, China
e-mail: longmujun@cqu.edu.cn

W. Jiang
e-mail: jiangwenxiang@cqu.edu.cn

The Minerals, Metals & Materials Society, *TMS 2018 147th Annual Meeting & Exhibition Supplemental Proceedings*, The Minerals, Metals & Materials Series,
https://doi.org/10.1007/978-3-319-72526-0_69

information provided by the hot tensile test result, which is evaluated by the reduction of area of the test specimen. Usually, when the reduction of area of the test specimen is below 60% [10], the plastic deformation capacity of continuous cast steel is bad.

The hot ductility is mainly affected by the phase transition, the second phase particle, strain rate and cooling patterns. Mintz [11] has reported that a thin film of ferrite forms around the austenite during cooling, and the ferrite is softer than austenite, all the deformation concentrate on the thin ferrite, which lead to low ductility and ductile intergranular failure. Cardoso et al. [12]. studied the relationship between ferrite content with hot ductility, in order to ensure the good hot ductility (the reduction of area is above 60%), the content of the ferrite should be above 40% in aluminum steel. There are many workers [13] quantitatively studied the austenite transformation based on the thermal expansion method.

In this paper, the hot ductility of X70 pipeline steel was studied at various temperature from 600 to 1300 °C. And the austenite–ferrite transformation at different cooling rate was measured by DIL402C dilatometer. For further understanding the low ductility, the fracture surface was examined by scanning electron microscope, and the second phase particles was also examined by energy spectrum analysis.

Experimental Procedures

The high temperature mechanical property of X70 pipeline steel was measured by the hot tensile test on the Gleeble-1500D thermo-mechanical simulator, and the basic chemical composition of the steel is given in Table 1. Cylindrical tensile test specimens of 10 mm in diameter and 120 mm in length were taken from continuously cast slab. The specimen longitudinal axes parallel to the casting direction. As a preparation for the experiment, a vacuum atmosphere of 1.33×10^{-5} MPa was maintained in the chamber to prevent oxidation of the specimen as well as minimizing the heat convection. The thermal history used in tensile test was described as follows: the specimen was heated at a rate of 20 °C/s up to 1300 °C and held for 60 s at first to take all the micro alloying precipitation into solution, and then cooled at a rate of 1.65 °C/s down to each testing temperature in the range 700–1000 °C and held for 30 s before deformation. At the test temperature, the specimen was stretched at a certain strain rate of 5×10^{-3} s^{-1} to simulate the high temperature deformational behaviors of the strand during the continuous casting process for slab, especially during the unbending operation.

Table 1 Chemical composition of the specimens (mass %)

C	Si	P	S	Mn	Cr	V	Ti	Nb
0.06	0.25	0.0098	0.0016	1.64	0.032	0.035	0.013	0.037

For better understanding the hot ductility which is closely relate to the phase transformation, the dilatometry experiments were carried out with a DIL402C high-resolution dilatometer. Cylindrical specimens 25 mm in length and 4 mm in diameter were employed. The cooling regimen is described as follows; steel samples were heated up to 1000 °C with a heating rate of 5 °C/min, kept for 5 min at this temperature to homogenize; and then cooled to 200 °C with three different cooling rates, including 5, 10 and 20 °C/min. During the process, a stable argon gas flow of 20 mL/min was maintained in the dilatometer chamber to protect the samples from being oxidized. The relative changes in length of the samples were recorded online.

Results and Discussion

Phase Transformation

Figure 1 shows that the relative change of the steel samples length at various cooling rates. It indicates that the relative change of the sample length is a function of temperature and decreases with the decreasing of the temperature because of the contraction in continuous cooling. In the single austenite region (above Ar_3) and the ferrite region (below Ar_1), the relative change of the steel samples length shows a linear change. However, each dilation curve shows an uplift zone, where the austenite transformation takes place. With the increasing of the cooling rates, the uplift zone moves toward low temperatures.

Based on the measured dilation curve (shown as Fig. 1) during continuous cooling, the linear thermal expansion coefficient of the steel can be definitely obtained as:

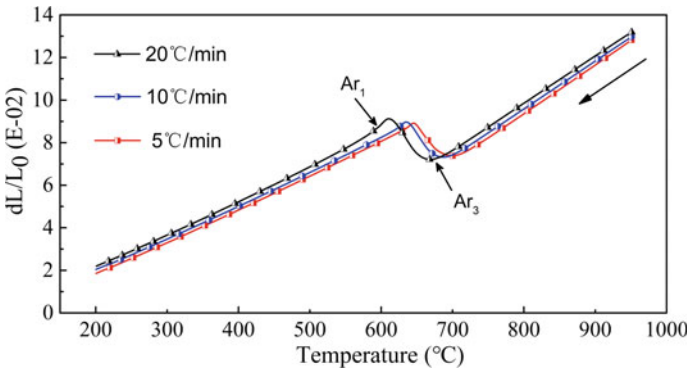

Fig. 1 Dilation curves of X70 pipeline steel obtained at various cooling rates

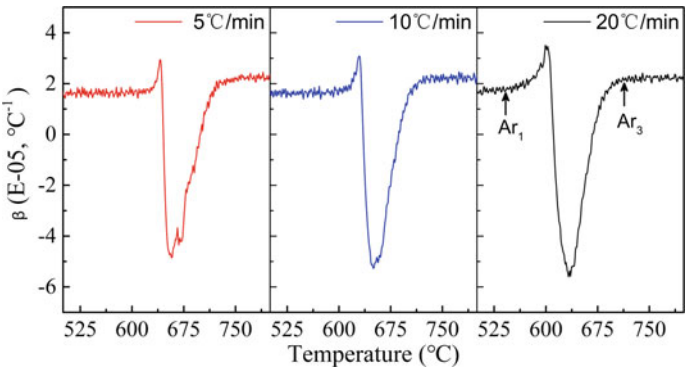

Fig. 2 Thermal expansion coefficient of X70 pipeline steel at different cooling rates

$$\beta = \frac{1}{L_T} \times \frac{\mathrm{d}L_T}{\mathrm{d}T} \tag{1}$$

where L_T and $\mathrm{d}L_T$ are the length and the length change of the sample and $\mathrm{d}T$ represents the corresponding temperature interval.

The critical temperatures of austenite transformation, including the values of Ar_3 and Ar_1, are defined as the points at which the relative change of length first deviate from its initial trend, which could be responded more obvious in the curve of thermal expansion coefficient shown as Fig. 2. The thermal expansion coefficient of the single austenite region and the single ferrite region is basically steady at around 2.24×10^{-5} ($°C^{-1}$) and 1.64×10^{-5} ($°C^{-1}$) respectively with small fluctuation, which fits well with that reported in previous works [14–16]. The critical temperatures of austenite transformation observed in Fig. 2 are summarized in Table 2.

It can be seen that the critical temperatures of austenite transformation, including Ar_3 and Ar_1, decease with the increasing of the cooling rates. In order to predict the critical temperatures of austenite transformation at more wide range cooling rate, an empirical model [17] which was verified is used in the paper. Finally, the regression equations of the model could be written as follows:

$$Ar_3\,(°C) = 798.8 - \exp(4.71 - 4.1/C_R) \tag{2}$$

$$Ar_1\,(°C) = 627.14 - \exp(5.13 - 17.8/C_R) \tag{3}$$

Table 2 Critical Temperatures of Austenite Transformation for X70 pipeline steel

Cooling Rate (°C/min)	5	10	20
Ar_3 (°C)	751.5	721.6	710.5
Ar_1 (°C)	619.3	600	557

where Ar_3 represents the start temperature of austenite transition, and Ar_1 represents the end temperature of austenite transition, C_R means the cooling rate.

Hot Ductility and Fractography

The reduction of area (%RA) is an effective way to evaluate the hot ductility of the fractured specimen. Accordingly, the reduction of area of X70 pipeline steel with the cooling rate of 1.65 °C/s was obtained, and is shown in Fig. 3. However, there is a holding time before tensile test, the holding time could be considered as equilibrium state during the austenite transformation. Therefore, the corresponding critical temperatures calculated by the empirical model (Eqs. 2 and 3) at equilibrium state (the cooling rate is zero) were also marked in Fig. 3.

It could be seen form Fig. 3 that there are two obvious brittle zones, the first brittle zone and the third brittle zone. The first brittle zone of the X70 pipeline steel appears at the place where the temperature is above 1250 °C, which is related to the dendritic segregation [18].

The third brittle zone appears at the temperature range of 650–800 °C. And the start temperature of the austenite formation is exactly 798.8 °C which is also the start temperature of the hot ductility getting bad. The ductility curve of X70 pipeline steel presents best hot ductility at the temperature range from 1150 to 850 °C, in which the ductility value is greater than 80%. To improve surface quality and internal quality of continuous casting steels, the surface temperature of the slab, especially in the area of straightening where great stress occurs, should be controlled in the temperatures avoiding 650–800 °C.

For butter understanding the variation of the hot ductility at different temperatures, especially the bad hot ductility at the temperature range from 800 to 650 °C, the facture surface of the tensile specimens was examined by SEM, and the second phase particles was examined by energy spectrum analysis (EDS), shown as Fig. 4.

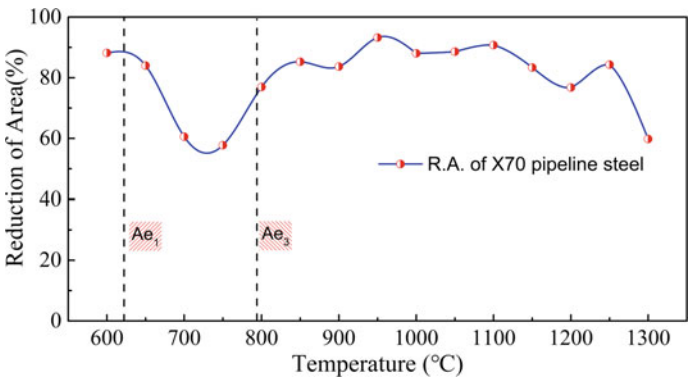

Fig. 3 The hot ductility of X70 pipeline steel at different temperatures

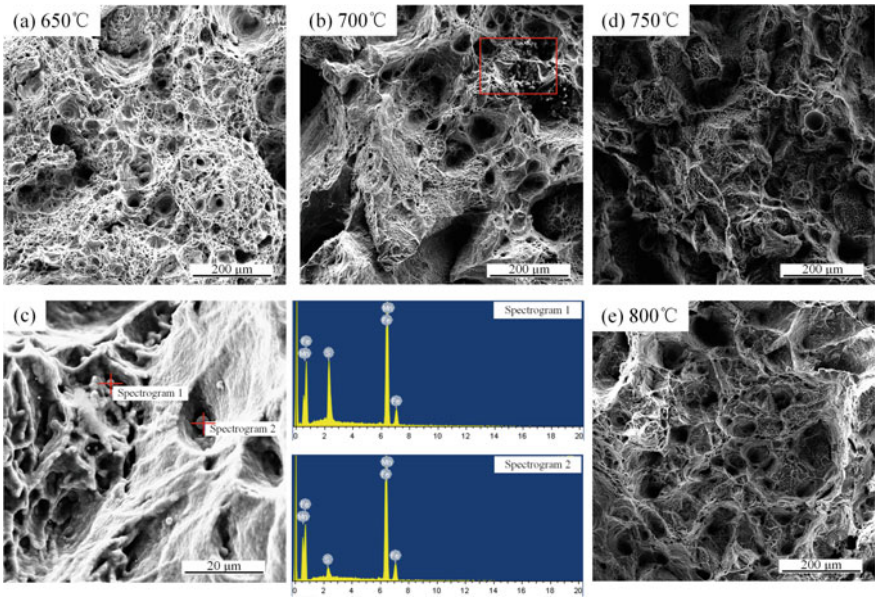

Fig. 4 Electron scanning micrographs, and EDS results of the samples: **a** 650 °C, **b** 700 °C, **c** EDS at 750 °C, **d** 750 °C, **e** 800 °C

As can been seen in Fig. 4a, e, the fracture mode of the X70 steel specimen is ductile failure with dimples. And the smaller and deeper size dimples in Fig. 4a is observed, which means the samples could experience larger plastic deformation before failure, therefore, the hot ductility is good at 650 °C (R.A. of the steel is above 85%). At the temperature of 750 and 700 °C, the intergranular and transgranular fracture were observed, leading to brittle fracture under small deformation, what's more, the EDS results shown in Fig. 4c which is also the area of the red frame in Fig. 4b, indicate that the equiaxed (Fe, Mn)S precipitate makes the ability of the plastic deformation worse.

Conclusions

The hot ductility of the X70 pipeline steel at high temperature was studied, and the main conclusions can be summarized as follows:

(1) The steel has a good hot ductility (RA above 70%) at 800–1000 °C and 600–650 °C. And the steel exhibits a hot ductility trough (RA below 80%) at 650–800 °C.
(2) The low ductility of the steel is affected by the equiaxed (Fe, Mn)S precipitate as well as austenite transformation at the third brittle zone.

Acknowledgements The authors would like to thank the National Natural Science Foundation of China (NSFC) for the financial support (Project NO.: 51374260; 51504048; 51611130062).

References

1. Bott IDS, De Souza LF, Teixeira JC, Rios PR (2005) High-strength steel development for pipelines: a Brazilian perspective. Metall Mat Trans A 36(2):443–454
2. Brimacombe J, Sorimachi K (1977) Crack formation in the continuous casting of steel[J]. Metall Mat Trans B 8(2):489–505
3. Cho KC, Mun DJ, Koo YM, Lee JS (2011) Effect of niobium and titanium addition on the hot ductility of boron containing steel[J]. Mater Sci Eng A 528(10):3556–3561
4. Zhihua D, Dengfu C, Xing LMZ, Jialong S (2013) High temperature mechanical properties for the columnar zone of steel 20CrMnTi[J]. Chin J Mater Res 27(3):273–278
5. Mintz B, Banerjee J (2010) Influence of C and Mn on hot ductility behaviour of steel and its relationship to transverse cracking in continuous casting[J]. Mater Sci Technol 26(5):547–551
6. Kang S, Tuling A, Lau I, Banerjee J, Mintz B (2011) The hot ductility of Nb/V containing high Al, TWIP steels[J]. Mater Sci Technol 27(5):909–915
7. Chown L, Cornish L (2008) Investigation of hot ductility in Al-killed boron steels. Mater Sci Eng A 494(1):263–275
8. Suzuki HG, Nishimura S, Yamaguchi S (1982) Characteristics of hot ductility in steels subjected to the melting and solidification. Trans Iron Steel Inst Jpn 22(1):48–56
9. Suzuki HG, Nishimura S, Nakamura Y (1984) Improvement of hot ductility of continuously cast carbon steels. Trans Iron Steel Inst Jpn 24(1):54–59
10. Suzuki HG, Nishimura S, Yamaguchi S (1979) Characteristics of embrittlement in steels above 600 °C. Tetsu-to-Hagané 65(14):2038–2046
11. Mintz B, Crowther D (2010) Hot ductility of steels and its relationship to the problem of transverse cracking in continuous casting. Int Mater Rev 55(3):168–196
12. Cardoso G, Mintz B, Yue S (1995) Hot ductility of aluminium and titanium containing steels with and without cyclic temperature oscillations. Ironmak Steelmak 22(5):365–377
13. Garcí C, Caballero F, Capdevila C, Alvarez L (2002) Application of dilatometric analysis to the study of solid–solid phase transformations in steels. Mater Charact 48(1):101–111
14. Petrov R, Kestens L, Houbaert Y (2004) Characterization of the microstructure and transformation behaviour of strained and nonstrained austenite in Nb–V-alloyed C–Mn steel. Mater Charact 53(1):51–61
15. Caballero F, Capdevila C, De Andrés CG (2002) Modelling of kinetics and dilatometric behaviour of austenite formation in a low-carbon steel with a ferrite plus pearlite initial microstructure. J Mater Sci 37(16):3533–3540
16. Caballero F, Capdevila C, DE ANDRES CG (2001) A dilatometric study of the austenite/ferrite interface mobility A dilatometric study of the austenite/ferrite interface mobility 30, 2000. ISIJ Int 41(10):1093–1102
17. Long M, Dong Z, Chen D, Zhang X, Zhang L (2015) Influence of cooling rate on austenite transformation and contraction of continuously cast steels. Ironmak Steelmak 42(4):282–289
18. Seol DJ, Won YM, Oh KH, Shin YC, Yim CH (2000) Mechanical behavior of carbon steels in the temperature range of mushy zone. ISIJ Int 40(4):356–363

Ductile Fracture Assessment of 304L Stainless Steel Using 3D X-ray Computed Tomography

A. J. Cooper, O. C. G. Tuck, T. L. Burnett and A. H. Sherry

Abstract Stainless steel manufactured by hot isostatic pressing (HIP) has been shown to exhibit significant differences in ductile fracture behavior when compared to equivalently graded forged steel, due to differences in oxide particle concentration between the two manufacture routes. Herein we analyse and quantify the ductile damage characteristics in the fracture process zone of equivalently graded forged and HIP 304L steel using 3D X-ray computed tomography (CT). Ductile void characteristics have been found to vary in size, shape, and spatial distribution; data which are in agreement with the differences in distribution of initiation particles in HIP and forged steel. Using advanced X-ray CT to characterize ductile damage, experimentally determined data can be employed to calibrate existing well-known ductile failure models, developing both our current understanding of ductile failure as well as a predictive tool to simulate fracture in novel HIP components.

Keywords Hot isostatic pressing · Ductile fracture · X-ray computed tomography · Stainless steel · Finite element modelling

The original version of this chapter was revised: Chapter author name has been updated. The erratum to this chapter is available at https://doi.org/10.1007/978-3-319-72526-0_91

A. J. Cooper (✉) · T. L. Burnett · A. H. Sherry
School of Materials, University of Manchester,
Oxford Road, Manchester M13 9PL, UK
e-mail: adam.cooper@manchester.ac.uk

T. L. Burnett
e-mail: timothy.burnett@manchester.ac.uk

A. H. Sherry
e-mail: andrew.h.sherry@nnl.co.uk

O. C. G. Tuck · A. H. Sherry
National Nuclear Laboratory, Birchwood Park, Warrington WA3 6AE, UK
e-mail: olivia.cz.tuck@nnl.co.uk

The Minerals, Metals & Materials Society, *TMS 2018 147th Annual Meeting & Exhibition Supplemental Proceedings*, The Minerals, Metals & Materials Series,
https://doi.org/10.1007/978-3-319-72526-0_70

Introduction

Near net shape (NNS) manufacture is an emerging route for producing structural components used in the nuclear industry. Of these, hot isostatic pressing (HIP), the consolidation of an alloy powder in a mould under high temperature and pressure, has been shown to be effective for producing complex geometry components without the need for welds; thus reducing costs, accelerating manufacturing time, and improving performance [1–4].

One of the fundamental differences between equivalently graded forged and HIP steels lies in the measured oxygen concentrations in the bulk material, with HIP steels typically exhibiting oxygen concentrations over an order of magnitude greater than those found in equivalently graded forged steels. This increase in oxygen content is thought to arise as a result of metal powder surface oxidation [5] during powder storage and handling, and the oxygen manifests itself in the form of non-metallic oxide inclusions, evenly distributed throughout the HIP'd microstructure. It has been proposed that the finer distribution of oxide particles facilitates the ductile fracture mechanism by acting as additional initiating sites for void nucleation and growth [6–8]; the initial stages of the classical ductile fracture mechanism. This results in reducing the distance over which ductile damage (in the form of voids) is required to grow before resulting in void coalescence with neighbouring voids, thus permitting fracture at smaller levels of plastic strain, and causing an unzipping effect throughout the material microstructure. This difference in ductile failure mechanism is reflected in the measure fracture toughness values ($J_{0.2BL}$) for these the two materials; 1000 kJ m^{-2} and 1750 kJ m^{-2} (reported previously [9]) for HIP304L and F304L, respectively.

Although correlations have been established linking oxygen concentration, oxide particle area fraction on metallographic sections, Charpy impact toughness, and differences in ductile dimple characteristics, thus allowing for the development of this working hypothesis [9–12], it has so far not been possible to obtain 'statistically significant' information regarding the ductile void growth characteristics during failure, on which the developed understanding hinges. SEM offers high resolution to probe ductile void characteristics below the fracture surface of sectioned test specimens, however it can be challenging and inefficient since fractured test specimens often exhibit very few voids on each metallographic plane (shown later); analysis therefore requires numerous sections to be prepared and analysed in order to build up an accurate representation of global damage.

In contrast, three-dimensional X-ray computed tomography (CT) offers the ability to study ductile damage in significantly greater detail than has hitherto been observed experimentally, probing the internal void structure of materials and providing quantitative data on the shape, size, spatial distribution, and volume fraction of voids formed below the fracture surface during ductile failure. Importantly, X-ray CT allows for the collection of data with 'statistical significance', whereby imaged specimens may contain thousands of measureable voids that have been subjected to a known stress state and/or loading conditions. In recent years,

X-ray CT has been employed as a tool to study microvoid coalescence in a variety of alloy systems [13, 14], and quantitative X-ray CT has been shown [15–17] to be a promising tool for the determination of ductile damage parameters to inform the predictive model for ductile failure developed by Gurson, Tvergaard and Needleman [18–20].

The Gurson-Tvergaard-Needleman (GTN) model is one of the more popular classical approaches used to predict ductile failure in materials. It is based on a yield criterion for a porous medium, which assumes the influence of damage (in the form of voids) on plastic flow can be accounted for by averaging the behavior within a discrete material volume element using a homogeneous continuum mechanics approach. The model accounts not only for material strain hardening but also the softening that occurs as a result of the nucleation and growth of voids during plastic flow. The model is able to predict material failure, which is assumed to occur when a critical volume fraction of voids is attained within the volume element. However, the implementation of the GTN model is not straightforward; it contains a number of parameters, some of which are interdependent, that must be appropriately calibrated for the material of interest. These parameters are assumed to be material constants, relating to the microstructural characteristics and nature of damage accumulation; once calibrated against a particular dataset can be used to predict ductile failure in other geometries under different loading conditions. Typically, calibration of the GTN model is achieved iteratively, by estimating parameter values using the results of previous studies, performing a Finite Element Analysis (FEA) of laboratory fracture mechanics tests using these parameters, and comparing the simulation results to the experiment, and adjusting the parameters accordingly. This can be very time consuming, and the varying methods used to adjust the parameters by different researchers can lead to very different parameters for the same material and test conditions [21, 22]. Furthermore, the underlying physical processes involved do not guide the adjustment of parameters; there is a danger that values of the calibrated parameters bare little correspondence to the physical quantities they are meant to represent. Quantitative microstructural analyses are therefore needed to better inform the setting of parameters. Hence, not only can XCT studies improve our comprehension of ductile fracture by providing qualitative information regarding failure mechanisms, but are also able to deliver quantitative data to support the calibration of predictive models.

In this paper, the ductile fracture behaviour of 304L stainless steel is examined using X-ray CT, and we explore various avenues through which the GTN model could be calibrated using the experimental data.

The three-dimensional tomography scans were performed on an instrument capable of resolving voids of only a few microns in size, allowing for an accurate mapping of void populations without the need for laborious metallographic analyses as well as allowing for the analysis of a much larger sample size. Furthermore, the results of the X-ray CT were processed to generate quantitative data for distributions in void size and spacing.

This work expands on previous work, providing additional experimental evidence to highlight the differences in mechanistic ductile fracture between HIP and

forged variants of 304L stainless steel, and employs the use of SEM to study the differences in microstructural damage ahead of and surrounding the crack tip of sectioned failed test specimens. This work also expands on the work by Daly et al. [15, 16], who employed the use of 3D X-ray CT to probe ductile damage in SA508 weld metal in order to improve the calibration of the Gurson, Tvergaard and Needleman [18–20] ductile fracture model, by investigating approaches to approximating the fracture surface of cores which exhibit a large depth of fracture process zone.

Background: Continuum Damage Mechanics Models

The GTN model is an example of a continuum damage mechanics model in which the influence of an initial volume fraction of porosity (f_0), the nucleation and growth of said porosity as well as newly initiated voids, and subsequent coalescence of voids on the load-bearing properties of material elements is simulated. The model is integrated into the constitutive equation of material behaviour within FEA such that the plastic flow potential (Φ) is given by:

$$\Phi = \left(\frac{\sigma_{eq}}{\sigma_f}\right)^2 + 2q_1 f cosh\left(\frac{3q_2\sigma_h}{2\sigma_f}\right) - \left(1 + (q_1 f)^2\right) \tag{1}$$

where σ_{eq} denotes the von Mises equivalent stress, σ_f denotes the matrix flow stress, σ_h denotes the hydrostatic stress and q_1 and q_2 denote material parameters first introduced by Tvergaard who defined $q_1 = 1.5$ and $q_2 = 1.0$ [18, 19].

The void volume fraction f is calculated from the growth rate of initial porosity, $\dot{f}_{gr}$, and the nucleation rate of newly initiated voids, $\dot{f}_{nu}$. The growth rate of the total void volume fraction is derived from the plastic part of the strain rate tensor. The nucleation rate of new voids is related to the equivalent plastic strain rate

$$f = \dot{f}_{gr} + \dot{f}_{nu} = (1 - f)\dot{\varepsilon}^p_{ii} + A\dot{\varepsilon}^p_{eq} \tag{2}$$

where

$$A = \frac{f_N}{S_N\sqrt{2\pi}} exp\left[-\frac{1}{2}\left(\frac{\varepsilon^p_{eq} - \varepsilon_N}{S_N}\right)\right] \tag{3}$$

where the parameter f_N denotes the volume fraction of particles that initiate new voids and ε^p_{eq} is the equivalent plastic strain. The parameters ε_N and s_N define a normal distribution of nucleation strain with ε_N being the mean strain and s_N the standard deviation.

Tvergaard and Needleman [20] included a rapid increase in void volume fraction at high plastic strains to simulate the coalescence phase in the ductile fracture

mechanism. They added a parameter f^* to replace f so that above a critical value, denoted f_c, there is a rapid increase in f^* to account for coalescence and the rapid softening of the material just prior to failure. Below this critical value, f^* is equal to f defined by Eq. (2), i.e.

$$f^{*}(f) = \begin{cases} f & \text{for } f \le f_c \\ f_c + \frac{f_U^{*} - f_c}{f_F - f_c}(f - f_c) & \text{for } f > f_c \end{cases} \tag{4}$$

The void volume fraction f_F is the value of f^* at which final fracture is deemed to have occurred. The parameter $f_u^* = 1/q_1$.

In summary, the primary parameters that require calibration are the following: f_0, f_c, f_F (that describe void growth and coalescence to failure), ε_N, s_N, f_N (that describe void nucleation), q_1 and q_2. Since GTN models are solved using FEA, another parameter, associated with the crack-tip mesh size within the model must also be determined since results are dependent on the resolution of stress and strain fields at the crack-tip. This parameter, the crack-tip mesh size, denoted L_c, is related to the spacing of the large oxide inclusions, since the most prominent voids observed using tomography are likely to initiate at these large oxide particles.

Experimental

Material

The material examined was hot isostatically pressed 304L material, supplied by Areva, and forged 304L stainless steel by Creusot Forge et Creusot Mécanique, Areva (Le Creusot, France). For HIP304L, stainless steel grade 304L powder was heated from ambient temperature to 1123 K (1150 °C) at a rate of 633 K (360 °C) h^{-1} and held at 1123 K (1150 °C) and 104 MPa for a period of 180 min. Post-HIP heat treatment of HIP304L was performed by heating from room temperature to 1343 K (1070 °C) at 633 K (360 °C) h^{-1}, held for 280 min, and water quenched. Forged 304L pipe was subjected to similar heat treatment as the HIP materials (1343 K (1070 °C), for *ca.* 250 min) and water quenched.

The materials' elemental compositions (weight %) and grain sizes are tabulated in Table 1. Grain size measurements were conducted in accordance with ASTM E112-96. [23]

J-R fracture toughness testing was performed on F304L and HIP304L, the experimental details and results of which are presented in a previous study [11]. Specimens selected from the fracture toughness testing for analysis herein were loaded to an applied *J* and crack growth of 742 kJ m^{-2}/ 0.454 mm and 672 kJ m^{-2}/ 0.367 mm, for HIP304L and F304L, respectively. These specimens were selected as they exhibited the smallest degree of crack growth and loaded to the smallest

Table 1 Elemental composition

		Grain size	Cr	Ni	Mo	Mn	Si	C	O/ ppm	N/ ppm
304L	Spec. (%wt.)	–	18.5–20.00	9.00–10.00	–	<2.00	<1.00	<0.035	200	–
	Forged	94 μm	19.40	9.648	0.345	1.654	0.573	0.027	**15**	817
	Powder (%wt.)	–	19.2	9.44	–	1.37	0.74	0.022	110	–
	HIP (%wt.)	27 μm	19.5	9.45	0.01	1.33	0.72	0.022	**120**	840

applied J, in an attempt to assess specimens which were loaded to within the J_{max} validity limit of 738 kJ m^{-2}, as determined using ASTM E1820 [24].

Specimens prepared for metallurgical analysis were sectioned, mounted, ground, and polished in accordance with the recommended procedures in ASTM practice E3-01 [12].

Electron microscopy was performed using an FEI Quanta 650 ESEM and an FEI Sirion SEM, both equipped with field emission guns and Electron Back-Scattered Diffraction (EBSD) detectors, and a Hitachi S-3700 scanning electron microscope equipped with Oxford Instruments INCA X-ACT energy dispersive spectroscopy for semi-quantitative chemical analysis. The SEM was performed under vacuum using a 20 kV accelerating voltage and a spot size of 4.0 nm, at a working distance (WD) of approximately 10 mm.

Tomography Specimen Preparation

Cylindrical core specimens were extracted from failed C(T) specimens (HIP304L and F304L) using electro-discharge machining (EDM). The samples measured approximately 0.5 mm in diameter and 20 mm in length. Three cores were extracted along the ductile tearing zone of each C(T) specimen, and a single core was extracted in a region of the machined notch far from any crack propagation; this was taken in order to detect the presence of any initial voids within the material in order to distinguish between initial porosity and ductile damage. Extraction of the cores from the ductile tearing region was located as central to the specimen as reasonable possible, such that the material under investigation had been subjected to plane strain conditions.

The extraction plan for the cores is shown in Fig. 1.

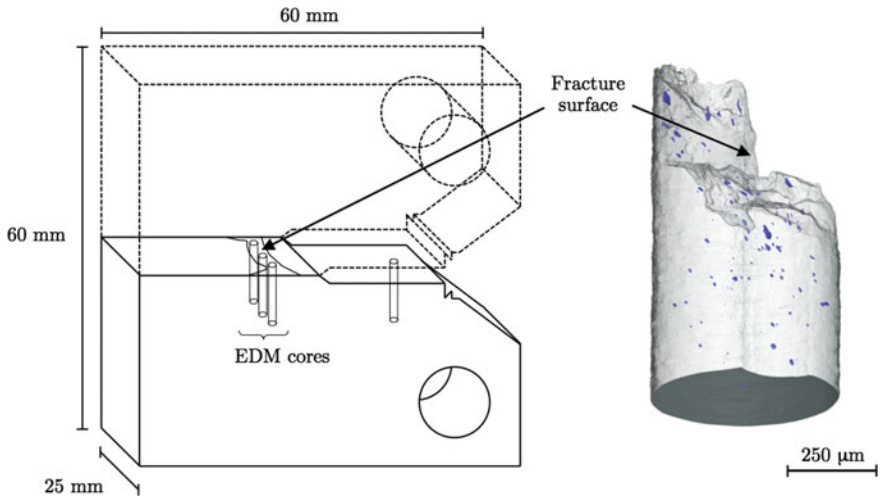

Fig. 1 EDM sample extraction plan. Three samples were extracted for each specimen within the ductile tearing zone (Left (L), Centre (C) and Right (R)) of a failed CT half specimen. A fourth sample was extracted behind the fatigue pre-crack away from any ductile damage

3D X-Ray Tomography

3D rendered X-ray CT was performed on each core using a Zeiss Versa 500 machine with a 4X objective, using 100 kV X-rays and 9 W power. An exposure time of 8 s was used, and an LE3 filter was employed. A final voxel size of 0.75 μm^3 was obtained, for the 4X scans.

Data processing was performed using Avizo® 9.0.0 software. In order to reduce image noise and improve contrast between voids and metal, an edge-preserving smoothing filer was applied to the data. The immediate surface perimeter of the core was cropped by five voxels to remove the very porous surface as a result of EDM machining of the cores, which may contribute to the inaccurate rendering of voids. The procedure used to segment voids and metal in the X-ray CT reconstructed images is detailed by Daly et al. [16]; to which the reader is directed for details. Void segmentation was performed such that any voids in any contact with the fracture surface were assigned to the air surrounding the core. This was to ensure consistency when segmenting voids close to/in contact with the fracture surface. In order to quantify size, shape, and nearest neighbour distances of voids, the spatial coordinates and volumes of each void were extracted. In order to manipulate the data usefully, it is useful to know the spatial location of damage relative to the fracture surface; various methods were explored for this and are detailed in the results section.

Void volume fractions were calculated as a function of distance from the fracture surface, and was determined by calculating the volume fraction of each reconstructed 'slice', where a slice had a thickness equal to that of the voxel resolution, e.g. 0.75 μm.

Results

Table 1 shows the elemental composition of the two materials studied, the specification for 304L, as stated on the material certificate for 304L, is also tabulated. Both of the materials are within specification. The oxygen concentration is not usually specified on materials certificates; however it is clear that the oxygen content in the HIP304L is over an order of magnitude greater than that of F304L. This observation was also made in previous stainless steel studies [9–11].

Figure 2 shows reconstructed CT scans of cores extracted from regions far away from the ductile tearing zone, for (a) F304L and (b) HIP 304L. In both specimens, there appears to be a small volume fraction of particles that are above the 0.75 μm resolution of the CT scans. Because no porosity has previously been observed in these materials [10, 11], it is believed that the particles are non-metallic oxide inclusions. 57 and 74 inclusions were resolved in the HIP304L core and F304L core, respectively. The average radii of the oxide inclusions in the cores were measured to be 2.86 μm and 2.67 μm, for HIP304L and F304L, respectively. It is important to note that there will be a appreciable number of inclusions in the microstructure that are smaller than the resolution of the CT scanner and objective for this particular experimental setup; indeed previous microstructural analyses of similar HIP 316L materials revealed oxide inclusions with radii on the order of 0.3 μm [11], which would be below the resolution of these CT scans.

Figures 3 and 4 show reconstructed CT scans of F304L and HIP304L, respectively, and ductile damage is observed below the fracture surface in each core cores (highlighted blue). It can be seen in Fig. 2 that the voids in the F304L cores display slight elongation in the direction if maximum principal plastic strain, which is not as obvious in the HIP304L specimens. It is thought that this is related to the degree of large scale plasticity surrounding the crack tip, which is significantly more prominent in the F304L cores than HIP304L, and which results in a more heavily deformed crack tip region due to excessive levels of plastic strain. Evidence of much more prominent plasticity in F304L is also shown in the topography of the cores, whereby F304L cores exhibit a fracture surface on a sharp gradient, in contrast to HIP304L which exhibit core topography with comparatively flatter fracture surfaces.

In contrast, the damage below the fracture surfaces of the HIP cores appears largely spherical, with minimal evidence of elongation. Even by eye, there appears to be a greater degree of ductile damage in the H304L cores than in the F304L cores, and damage is localised to a region of approximately 250 μm below the fracture surface.

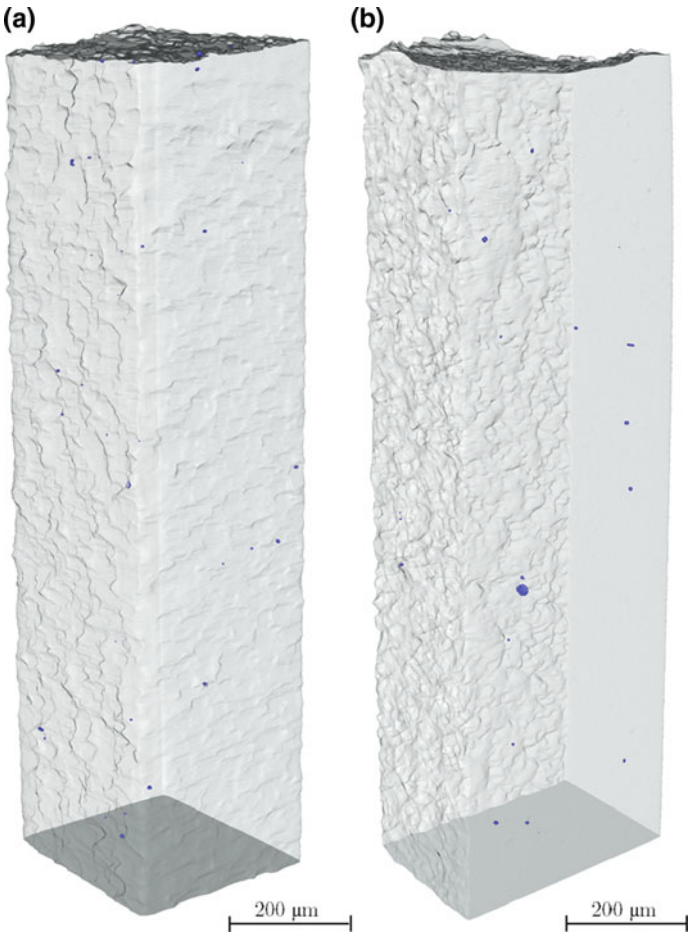

Fig. 2 3D rendered EDM cores extracted from the loading pin region of (**a**) F304L, and (**b**) HIP304L, showing a small volume fraction of initial particles in the microstructure

Further evidence of F304L's higher crack tip deformation is shown in Figs. 5 and 6, which show backscatter electron (BSE) images of sectioned compact tension test specimens, and highlight the various stages of crack growth; moving from right to left, fatigue pre-crack, controlled ductile tearing zone (from which the X-ray CT cores were extracted), followed by the end of ductile tearing and beginning of fatigue post-crack. The BSE images highlight the degree of microstructural damage ahead of and surrounding the crack tip, and a clear definable region of large plastic deformation (plastic zone) can be seen at the crack tip of F304L (Fig. 5) with an approximate radius of *ca.* 500 µm. In contrast, the plastic zone is much more difficult to distinguish in HIP 304L (Fig. 6), partially due to the finer grain size, but also due to significant less crack tip blunting. In both sectioned specimens (Figs. 5 and 6),

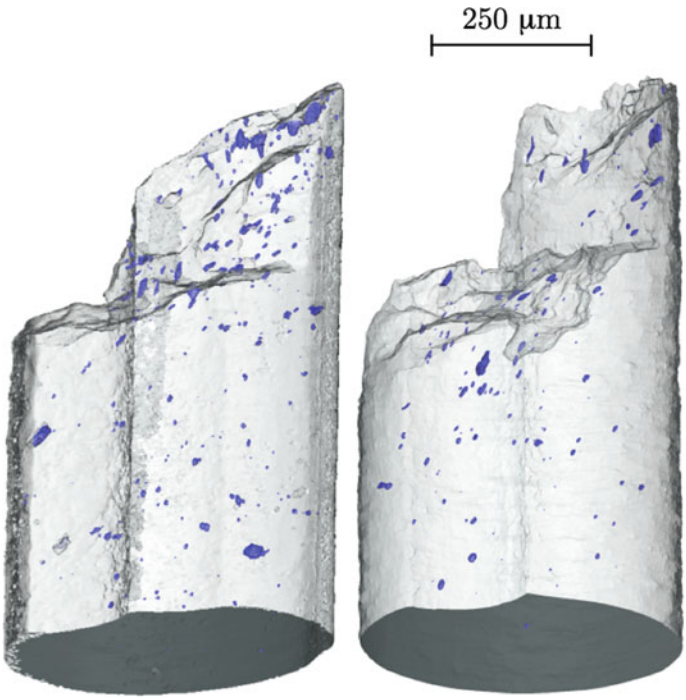

Fig. 3 3D rendered EDM cores extracted from specimen F304L showing a side view (fracture surface at the top) of the reconstructed 4X X-ray CT data

there are clear and significant levels of plastic slip, identifiable by the slip lines orientated within grains.

It can be seen at the crack tip of F304L that there is a region where the material resembles complete plastic flow, whereby individual grains are no longer identifiable, thus indicating the high levels of crack tip blunting which has occurred during loading. This is not as identifiable in HIP304L.

It is interesting to note how few voids are visible in the sectioned BSE images in comparison to the 3D rendered X-ray CT images, which emphasises the 3D nature of the ductile void damage and highlights how sectioning specimens to assess the extent of ductile void damage can be both challenging and misleading. This is not surprising since metallographic sectioning of specimens only reveals ductile damage that is located on the sectioned plane, and it is not possible to determine void sizes accurately since sectioning does not necessarily, and is very unlikely to, occur through the centre of the void. This results in voids appearing smaller than the actual radii they possess.

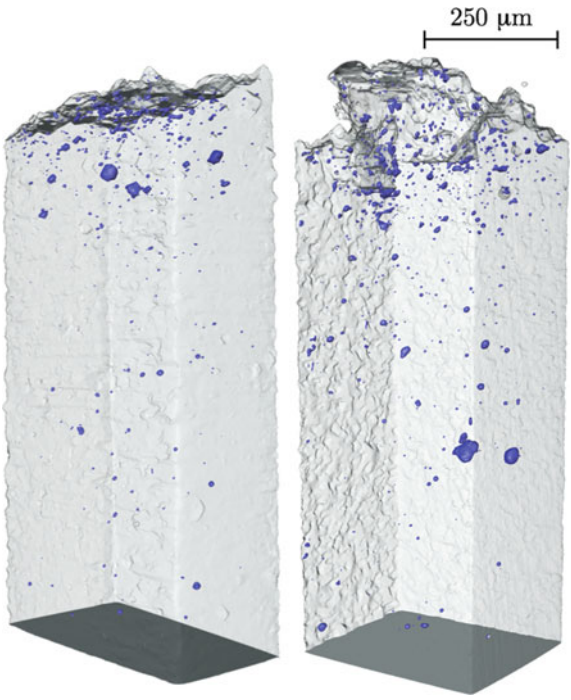

Fig. 4 3D rendered EDM cores extracted from specimen HIP304L showing a side view (fracture surface at the top) of the reconstructed X-ray CT data

Characterising Ductile Damage

The average VVF data for HIP304L and F304L, as presented in Fig. 7, indicate very little difference between the two materials when considering damage represented as VVF; interesting given the materials' appreciable difference in fracture toughness.

It is challenging to quantify any differences in ductile damage of HIP and Forged materials, when representing damage in the form of void volume fractions as a distance below the fracture surface. This is perhaps a reasonable result, since it could be argued that in theory, the two materials should exhibit the same *volume fraction* of damage at failure, since the HIP material exhibits more, finer voids, whereas the Forged material exhibits fewer, larger voids.

This argument is further strengthened when characterizing the average void sizes and the extent of ductile damage in terms of total 'void count', which represents the total number of resolved voids in the material. Total void count has been measured and plotted as a function of distance below the fracture surface, in bins of 50 µm thickness, for HIP304L (Fig. 8) and F304L (Fig. 9). The most notable observation is the much larger total void count for the HIP cores when compared to the Forged cores; the total number of voids observed in the three F304L cores was 1232 whereas the total number of voids resolved in the HIP 304L cores was 5042, an increase in over 300%.

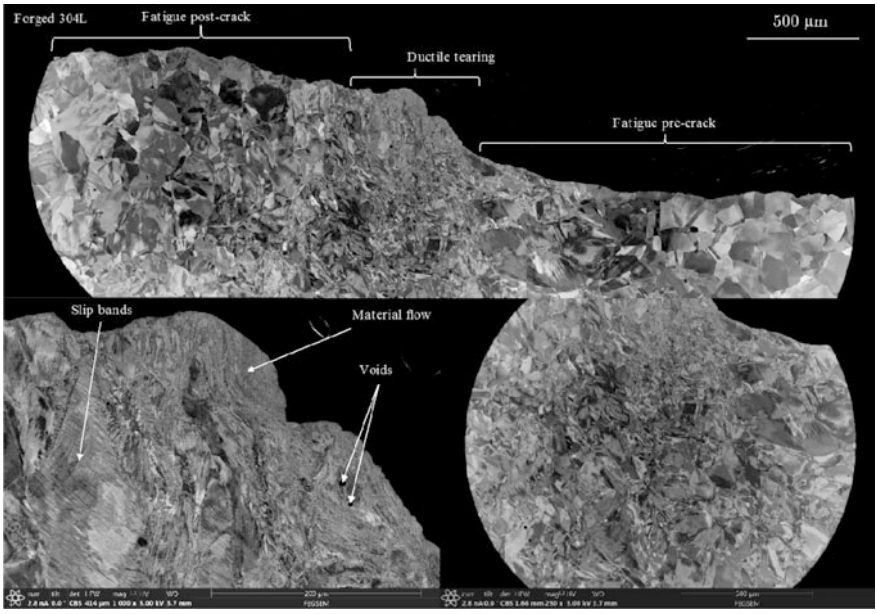

Fig. 5 BSE images of the crack tip of F304L showing the various stages of the fracture process, and the ductile tearing region from which cores were extracted, as well as evidencing various damage features; slip bands, material plastic flow, and ductile voids

We have hypothesised this link previously [11], but this is the first time that the extent of damage associated with ductile failure has been visualized in 3D. In Fig. 6, the damage can be seen to increase drastically as distance approaches the fracture surface, to a peak of 700 voids per 50 µm bin size. At this peak of 700 voids per 50 µm bin size, HIP304L exhibits a total number of voids over an order of magnitude greater than the equivalent distance in F304L, and although we must be careful when analysing data relative to the 'fracture surface', this is in line with differences in oxygen concentration between the two materials of 15 mm and 120 ppm for F304L and HIP304L, respectively. This could be significant, since it is important to remember that the voids we are observing are only voids that have been subjected to plastic strains large enough to cause sufficient void growth to sizes above the resolution of the CT scanner. It is plausible that the same number of voids exist within each bin throughout the entire core, but have not experienced sufficient void growth to permit their resolution in these scans.

We believe the drop-off in void count at distances in close proximity to the fracture surface is associated with voids that have not been selected in the analysis due to being involved with the fracture surface, as detailed in the experimental section. In contrast, this trend is not observed for the F304L cores, and is thought to be due to having insufficient number of voids to resolve such a trend. If enough voids were resolved, by sampling more material, it is thought that the same trend would be observed.

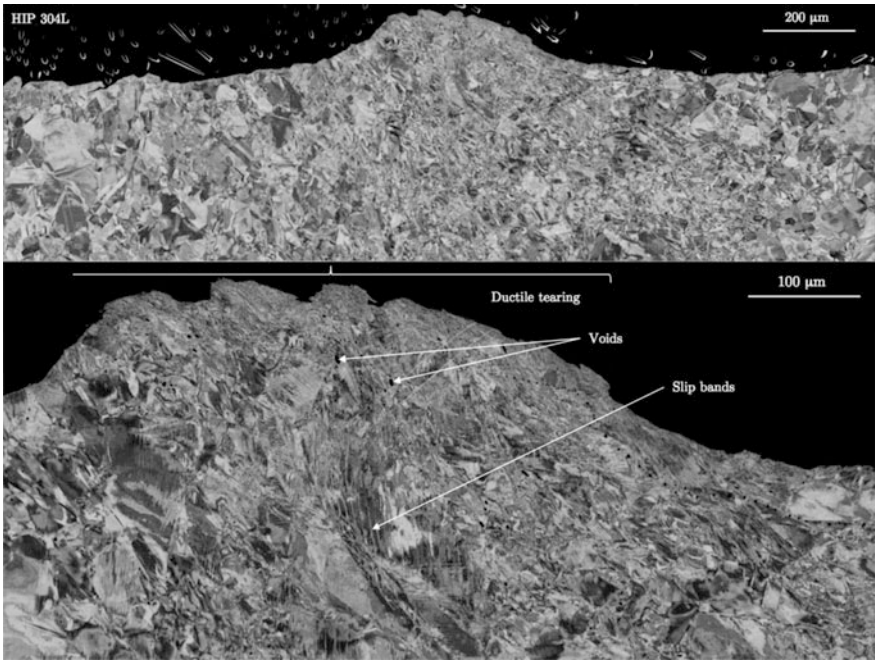

Fig. 6 BSE images of the crack tip of HIP304L showing the various stages of the fracture process, and the ductile tearing region from which cores were extracted, as well as evidencing various damage features; slip bands, material plastic flow, and ductile voids

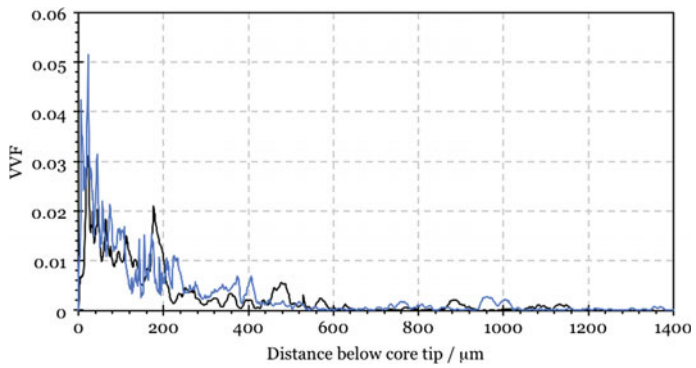

Fig. 7 Average VVF fraction data for HIP304L (blue) and F304L (black) as a function of distance below the core tip

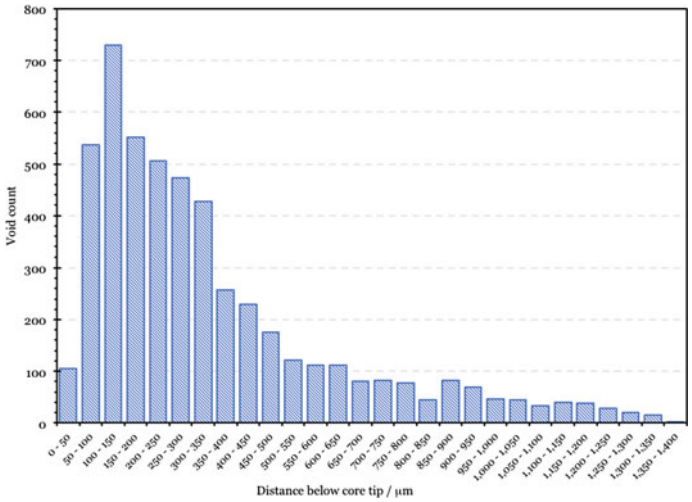

Fig. 8 Total void count of the F304L cores presented as a histogram with bin sizes of 50 µm as a function of distance below the core tip

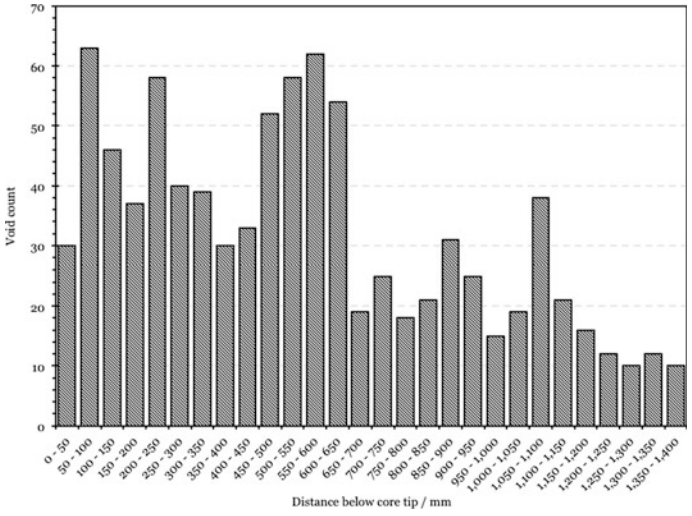

Fig. 9 Total void count of the F304L cores presented as a histogram with bin sizes of 50 µm as a function of distance below the core tip

Discussion

Through using X-ray CT to visualise the extent of ductile damage in fractured compact tension test specimens, various damage characteristics can be extracted and analysed. It has been shown previously that equivalently graded HIP and Forged stainless steel exhibits clear differences in fracture and impact toughness, as well as the number of oxide particles in the microstructure, which act as initiation sites for the nucleation and growth of voids during ductile failure. Whilst the spatial distribution of these initiating particles varies significantly between HIP and forged 304L, the stress strain behaviour of the materials has been previously reported as being comparable exhibiting similar strain hardening behaviour, which indicates that the rate of void growth should be similar for specimens tested under equivalent loading conditions. The rate of void growth can be estimated using various void growth models, such as those proposed by Rice and Tracey [25] and McClintock [17], and indeed Rice and Tracey calculations have been shown to glean comparable results for both HIP and forged 304L [9]. This is significant since it suggests that the ductile fracture mechanism of these two different steels is not governed by the void volume fraction of voids below the fracture surface, and instead is dominated by the inter-particle distance of nucleating voids. This is perhaps intuitive, since the total volume fraction of fewer, larger voids (as seen in the forged specimens) would be expected to equate to the total volume fraction of more, finer voids, at void coalescence and fracture initiation, if said voids are assumed to grow with comparable growth rates.

Indeed, the coalescence stage of failure will occur at different levels of plastic strain for two materials exhibiting different average inter-particle spacing, but the VVF of ductile damage below the fracture surface at each material's respective fracture initiation, providing the materials exhibit similar strain hardening behaviour, should be comparable. Though this has formed the basis of a working hypothesis for recent works, this is the first set of experimental data evidencing how the ductile damage evolves between the two materials during failure. Significantly, if little differences between VVF data are discernible, then significant differences between the void size, distribution, and frequency should be observable in order to explain the differences in fracture and impact toughness previously reported. The total number of resolvable voids was found to be 5042 for HIP and 1232 for F304L, an increase in over 300%. The average void radii were found to be 3.58 μm for HIP304L and 5.46 μm for F304L; a 53% increase in average void size for F304L. Voids in HIP304L were found to be more finely spaced than in F340L, with a reduction in distance on average of 16.34 μm. These significant differences in ductile damage characteristics are representative of the difference in fracture toughness between the two materials.

In principle, it is well within the capability of X-ray CT to accurately characterise the damage that accumulates during ductile failure. It has been shown here that void volume fractions, nearest neighbour distances, and void shapes and sizes, which are all characteristic of ductile failure, can be measured in 3D using X-ray

imaging, and these data can be employed in continuum damage mechanics models such as the GTN model. The GTN model in particular employs the use of void volume fractions to quantify damage at various stages of failure (f_n, f_c, and f_F) as well as an additional void volume fraction parameter associated with the initial porosity in the material (f_0). The challenge here is to assign particular void volume fractions to the various stages of ductile failure (void nucleation, growth, and coalescence) which might be possible through the use of nearest neighbour distance and void shape characteristics. The specimen cores analysed in this work can be thought of as capturing the failure history of the test specimen. Voids that are located remote from the fracture surface (and crack tip), and which reside towards the limit of the plastic zone can be associated with void nucleation, rather than growth and coalescence. These voids are not subjected to sufficiently high plastic strains such as to cause necking and coalescence with neighbouring voids, because they do not have the opportunity due to the failure process at the crack tip. Therefore it might be plausible to assume a region remote from the fracture surface, within which there average void volume fraction can be associated with f_n. Similarly, in regions close to the fracture surface, voids will experience levels of plastic strain sufficiently large enough to result in coalescence with neighbouring voids. These voids, as a result of the necking process, are expected to exhibit non-sphericalness, and it might be possible to assign a probability of coalescence based on void geometry. Finally the void volume fraction of damage associated with failure (f_F) may be characterised using the measured void volume in direct contact with the fracture surface of the cores. The void volume fraction associated with initial porosity (f_0) is associated with porosity (or voids) in the initial unloaded microstructure (i.e. inclusions at which voids form). As shown previously, X-ray CT might not be the most appropriate method to determine this parameter, since the vast majority of non-metallic inclusions in the microstructure will have radii, which are below the resolution of even the most advanced high-resolution CT scanners. Scanning electron microscopy on several sections of material, or indeed through the use of Plasma focused ion beam (FIB), would be the most appropriate methodology to obtain accurate void volume fraction data associated with f_0.

Clearly there are several approaches that could be employed here to separate and assign damage to the various stages of ductile failure, which merits its own separate investigation and sensitivity study. As well as the various stages of failure, the GTN model assumes an inter-particle spacing (implemented into an FE model via the mesh size). This inter-particle spacing can be assumed to be the nearest neighbour distance of voids observed using X-ray CT. It is important to realise here that voids close the fracture surface (and crack tip) will experience sufficiently large plastic strains to grow to sizes detectable by the CT scanner, and thus, decay in number of voids (and increase in nearest neighbour distance) observed as a function of distance below the fracture surface is a result of the stress field (and plastic zone). Because of this, it can be assumed that the small nearest neighbour distance values in close proximity to the fracture surface is actually constant and extends throughout the core. This nearest neighbour distance of voids can be usefully employed as the inter-particle spacing (and mesh size) and would play an important

role in governing the fracture toughness of ductile materials. Significantly, it has been shown here that there are little discernible differences between the damage characteristics when considering void volume fractions as a function of distance from the fracture surface (Fig. 7). By extension of this, it might be expected that the two materials would also exhibit comparable void volume fractions for the various stages of failure, and instead, the fracture mechanism is governed by the inter-particle spacing (nearest neighbour distance), which differs on average by *ca.* 16 μm.

Work remains to accurately assign observed damage to the various stages of failure and develop this approach to calibrate such ductile failure models, but the authors hope to highlight the capabilities of this form of experimental analysis to better understand the mechanisms of ductile failure and by extension, to accurately calibrate existing ductile failure models.

Conclusions

This work has used 3D X-ray computed tomography to probe the fracture behaviour of equivalently graded HIP and forged 304L stainless steel, and for the first time, has revealed the differences in ductile void characteristics in these materials when subjected to severe loading conditions. The work concludes recent investigations into the mechanistic failure of HIP steels when compared to forged steels, and confirms a working hypothesis regarding how fracture toughness is governed by the spatial distribution of non-metallic oxide inclusions, which act as initiation sites for the nucleation, growth, and, crucially, the coalescence of neighbouring voids during ductile failure. The authors also propose the appropriateness of X-ray CT for determination of relevant parameters required to calibrate the GTN continuum damage mechanics model.

Acknowledgements The authors would like to thank the UK EPSRC for funding of this research project.

References

1. Rao GA, Kumar M (1997) High performance stainless steel via powder metallurgy hot isostatic pressing. Mater Sci Technol 13:1027–1031
2. Barre C (1999) Hot isostatic pressing. Adv Mater Process 155:47–48
3. Jeon YC, Kim KT (1999) Near-net-shape forming of 316L stainless steel powder under hot isostatic pressing. Int J Mech Sci 41:815–830
4. Atkinson HV, Davies S (2000) Fundamental aspects of hot isostatic pressing: an overview. Metall Mater Trans A 31:2981–3000
5. Arnberg L, Karlsson A (1988) Influence of powder surface oxidation on some properties of a hiped martensitic chromium steel. Int J Powder Met 24:107–12
6. Thomason PF (1990) Ductile fracture of metals. Pergamon Press

7. Anderson TL, Anderson T (2005) Fracture mechanics: fundamentals and applications. CRC Press
8. Sato Y, Maie T, Kuwana T (1995) Influence of oxygen on the impact toughness and microstructure of steel weld metal. In: Proceedings of the international conference on offshore mechanics and arctic engineering—OMAE 1995, pp 485–490
9. Cooper AJ, Smith RJ, Sherry AH (2017) An assessment of the ductile fracture behavior of hot isostatically pressed and forged 304L stainless steel. Metall Mat Trans A 48:2207–2221
10. Cooper AJ, Cooper NI, Bell A, Dhers J, Sherry AH (2015) A microstructural study on the observed differences in charpy impact behavior between hot isostatically pressed and forged 304L and 316L Austenitic stainless steel. Met Mat Trans A 46:5126–5138
11. Cooper AJ, Cooper NI, Dhers J, Sherry AH (2016) Effect of Oxygen content upon the microstructural and mechanical properties of type 316L Austenitic stainless steel manufactured by hot isostatic pressing. Met Mat Trans A 47:4467–4475
12. Cooper AJ, Dhers J, Sherry AH (2016) Mechanistic studies on type 300 stainless steels manufactured by hot isostatic pressing: the impact of Oxygen involvement on fracture behaviour. V06ATA012
13. Taylor KL, Sherry AH (2012) The characterization and interpretation of ductile fracture mechanisms in AL2024-T351 using X-ray and focused ion beam tomography. Acta Mater 60:1300–1310
14. Hosokawa A, Wilkinson DS, Kang J, Kobayashi M, Toda H (2013) Void growth and coalescence in model materials investigated by high-resolution X-ray microtomography. Int J Fract 181:51–66
15. Daly M, Leonard F, Sherry AH (2014) Application of 3D X-ray tomography to enhance the calibration of ductile fracture models. In: ASME 2014 Pressure vessels and piping conference: American society of mechanical engineers, pp V005T11A7-VT11A7
16. Daly M, Burnett TL, Pickering EJ, Tuck OCG, Léonard F, Kelley R et al (2017) A multi-scale correlative investigation of ductile fracture. Acta Mater 130:56–68
17. McClintock FA (1968) A criterion for ductile fracture by the growth of holes. J Appl Mech 35:363–371
18. Tvergaard V (1981) Influence of voids on shear band instabilities under plane strain conditions. Int J Fract 17:389–407
19. Tvergaard V (1982) On localization in ductile materials containing spherical voids. Int J Fract 18:237–252
20. Tvergaard V, Needleman A (1984) Analysis of the cup-cone fracture in a round tensile bar. Acta Met 32:157–169
21. Bernauer G, Brocks W (2002) Micro-mechanical modelling of ductile damage and tearing: results of a European numerical round robin. Blackwell, Oxford, ROYAUME-UNI
22. Zhang Z (1996) A sensitivity analysis of material parameters for the Gurson constitutive model. Fatigue Fract Eng Mater Struct 19:561–570
23. ASTM E112-96: standard test methods for determining average grain size (1996) ASTM International, West Conshohocken, PA
24. ASTM E1820: standard test method for measurement of fracture toughness (2003) ASTM International, West Conshohocken, PA
25. Rice JR, Tracey DM (1969) On the ductile enlargement of voids in triaxial stress fields∗. J Mech Phys Solids 17:201–217

Thermo-Calc of the Phase Diagrams of the Nb-N System

Shadia J. Ikhmayies

Abstract In this work, Thermo-Calc software was used to produce the temperature-N mass percent phase diagram and Gibbs free energy of all obtained phases for the Nb-N system. Two solid single stable phases were observed which are the fcc δ-NbN_{1-x} and hexagonal β-Nb_2N, in addition to bcc α-NbN solid solution. Mixed solid stable phases obtained are α-NbN + β-Nb_2N and β-Nb_2N + δ-NbN_{1-x}. Gas and liquid phases were observed as single phases and mixed with each other or with solid phases. These phases are interesting and they have several technological applications in superconducting microdevices, microelectronic, catalytic probes, and hard coatings. The different phases and their constituents are thoroughly discussed.

Keywords Phase diagrams · Phase transformation · Gibbs free energy
Phase equilibria

Introduction

Transition-metal nitrides have recently attracted considerable interest in condensed matter physics, solid-state, chemistry, and materials science due to their unique/superior physical properties [1]. They are usually metallic and highly refractory, and exhibit excellent properties such as hardness and elasticity than the corresponding transition-metals themselves [2, 3]. The Nb-N system is one of the alloy systems which are important for hard metal industry. A number of different phases have been identified for this system. These are; bcc α-NbN solid solution, hexagonal β-Nb_2N, tetragonal γ-Nb_4N_3, fcc δ-NbN_{1-x}, hexagonal η-NbN, hexagonal δ-NbN, and some N-rich phases; Nb_5N_6, Nb_4N_5. δ-phase and γ-phase are interesting for the superconducting RF applications [4]. The cubic *δ*-NbN was metastable and the hexagonal-structured NbN was more stable than the cubic

S. J. Ikhmayies (✉)
Faculty of Science, Physics Department, Al Isra University, Amman 11622, Jordan
e-mail: shadia_ikhmayies@yahoo.com

The Minerals, Metals & Materials Society, *TMS 2018 147th Annual Meeting & Exhibition Supplemental Proceedings*, The Minerals, Metals & Materials Series,
https://doi.org/10.1007/978-3-319-72526-0_71

counterpart. In this work Thermo-Calc software was used to predict the temperature-N mass percent phase diagram of the Nb-N system, and Gibbs free energy for the obtained phases. The results are important for superconducting devices and hard metal industries.

Methodology

Thermo-Calc software is computational thermodynamic software that utilizes the procedure of Gibbs free energy minimization to calculate phase equilibria and thermodynamic properties of a chosen system [5]. For a given set of conditions, the computer determines the change in free energy for each possible combination of phases and phase compositions, and it selects the state that makes the total Gibbs free energy minimum. The software is used in conjunction with different thermodynamic databases which contain the descriptions of the Gibbs free energies assessed using the CALPHAD approach. CALPHAD is a phase-based approach to model the underlying thermodynamics and phase equilibria of a system through a self consistent framework [6].

In this work, MAP calculations—a type of the calculations in the Thermo-Calc software—were used to calculate the equilibrium phase diagram of the Nb-N system in the temperature range 300–4000 K. The used database is the TCBIN: TC Binary Solutions v1.1 database and the mass percent of nitrogen had varied from 0 to 100. The calculation type was chosen to be binary phase diagram.

Results and Discussion

Figure 1 displays the temperature against nitrogen (N) mass percent phase diagram of the Nb-N system. The melting temperature of Nb from Fig. 1 is 2748 K (2475 °C), which is very close to the known value T_{melt} = 2750 K (2477 °C) [7]. The stable single phases are seen as white regions in Fig. 1a. They are the three solid phases fcc δ-NbN_{1-x}, hexagonal β-Nb_2N, bcc α-NbN solid solution, the liquid phase, and gaseous phase. There are eight two phase co-existing regions, seen as lined green regions in Fig. 1a. They are bcc α-NbN (BCC-A2) + hexagonal β-Nb_2N (HCP-A3), fcc δ-NbN_{1-x} (FCC-A1) + hexagonal β-Nb_2N (HCP-A3), gas + fcc δ-NbN_{1-x} (FCC-A1), gas + hexagonal β-Nb_2N (HCP-A3), liquid + hexagonal β-Nb_2N (HCP-A3), gas + liquid.

The mixed phase bcc α-NbN (BCC-A2) solid solution + hexagonal β-Nb_2N (HCP-A3) starts from 0 N mass percent at T = 1500 K and extends until 7 N mass percent, where phase boundaries are shown as solid lines. This phase transforms to the single hexagonal β-Nb_2N (HCP-A3) phase, where the transition starts at 6.74 N mass percent for the temperature range 300–2858 K. On the other hand, it transforms to the single phase bcc α-NbN (BCC-A2) solid solution, where the

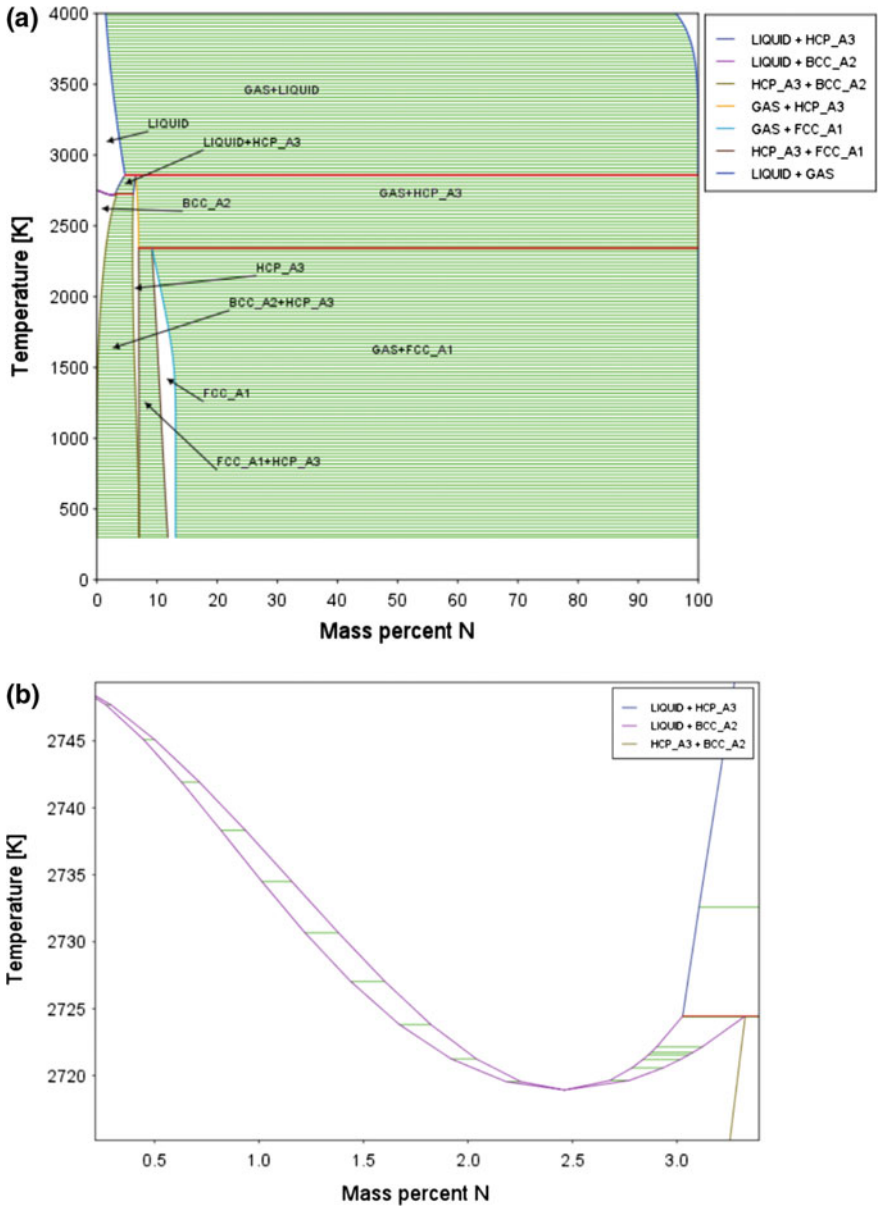

Fig. 1 Temperature against N mass percent phase diagram obtained using Thermo-Calc software (**a**), and an extended narrow range 0–3.5 of the same phase diagram (**b**)

transformation temperature increases with N mass percent until T = 2748 K. The stable bcc α-NbN solid solution phase appears in the region T = 1500–2148 K and N mass percent range 0–3.7, and it is dilute with nitrogen. This phase transforms to

the mixed phase liquid + bcc α-NbN (BCC-A2) solid solution starting from the melting point of Nb at 2748 K until T = 2748 K.

The stable hexagonal β-Nb_2N (HCP-A3) phase is seen in the narrow zone (white colored in Fig. 1a) that appears at 6.74 N mass percent. The two phase boundaries start at 6.74 N mass percent and T = 300 K. they separate and meet at the same N mass percent but T = 2845 K. This means that this phase appears at a certain value or in a narrow range of N mass percent with slight changes in the transformation temperature.

The stable mixed phase fcc δ-NbN_{1-x} (FCC-A1) + β-Nb_2N (HCP-A3) phase starts from 6.74 N mass percent and T = 300 K, and extends until 11.8 N mass percent where the phase fcc δ-NbN_{1-x} (FCC-A1) starts to appear. A strong drop in transition temperature is observed upon increasing nitrogen content, where it drops from T = 2334 K at 7 N mass percent to 300 K at 11.8 N mass percent. The stable phase fcc δ-NbN_{1-x} (FCC-A1) seen in the zone (white colored in Fig. 1a) is restricted in the N mass percent range 9.2–13. It transforms to gas, where this transformation starts at T = 2334 K and 9.2 N mass percent, but the transformation temperature strongly decreases with nitrogen content until 13 N mass percent where it sharply drops to T = 300 K.

With increasing nitrogen content a mixed phase of gas + fcc δ-NbN_{1-x} (FCC-A1) appears, which is restricted in the lined green region in Fig. 1a in the ranges T = 300–2343.6 K and N mass percent 9.12–100. For T = 300 K to T < 1500 K and N mass percent 13–100, the value of x ≈ 0, and the solid phase is fcc δ-NbN (FCC-A1). The gas consists of N_2, N, N_3, and Nb, where the main portion of the gas is N_2, while the other components have approximately zero fractions at low temperatures. But, the fractions of N, N_3, and Nb increase with increasing temperature. In general, the number of moles of the whole gas increases with the N mass percent and temperature, while the number of moles of the phase fcc δ-NbN_{1-x} (FCC-A1) decreases with N mass percent and temperature.

The mixed phase that consists of gas + hexagonal β-Nb_2N (HCP-A3) exists in the temperature range 2343.6–2858.2 K and N mass percent 6.5–7. The gas has the same constitution as before, and concentrations of all components increases with temperature, and with N mass percent. In general, the mole fraction of gas relative to the solid phase increases with temperature and N mass percent, where the rate of increase is larger for higher temperatures. At N mass percent close to 100 and T = 2858.2 K the fraction of the β-Nb_2N (HCP-A3) is very small. The density of N vacancies in β-Nb_2N (HCP-A3) decreases with temperature, and near N mass percent 100 and T ≈ 2858 K the ratio of N vacancies is 0.08.

Between the two single phases; α-NbN (BCC-A2) solid solution and the liquid, there is a mixed phase consists of both of them as shown in Fig. 1b. It extends in the N mass percent range 0–3.3 and T = 2748–2724.5 K. The liquid consists of melted Nb and N atoms. With increasing temperature the whole α-NbN (BCC-A2) solid solution transforms to a stable liquid phase. The white zone in Fig. 1a between T = 2748–4000 K and N mass percent 0–4.7. As mentioned above, it consists of Nb and N, where the mole fraction of N increases with N mass percent, and decreases with temperature.

The lined green region in Fig. 1a between N mass percent 1.58 and 100 in the temperature range 2858–4000 K consists of two mixed phases; gas + liquid similar to those mentioned before. But most of the gas is N_2, with higher fractions of N, N_3, and Nb than before. But as T and N mass percent increase, the fractions of N, N_3, become more than 0.001, and that of Nb of the order of 10^{-12}. The liquid consists mainly of Nb, where the fraction of Nb/N is about 9.5. The white zone in the upper right corner of Fig. 1a is a gaseous phase of the same composition as before and N_2 represents the highest fraction followed by Nb then N.

Figure 2 represents the Gibbs free energy against N mass percent for all observed phases. As the figure shows, for the liquid + gas phase it is restricted in the range $-(4.3 - 2.97)\ 10^5$ J/mol, for the gas + β-Nb_2N (HCP-A3) phase Gibbs free energy is in the range $(-2.97 - 2.42)\ 10^5$ J/mol, and for gas + δ-NbN (FCC-A1) phase its values are in the range $-(2.42 - 8.28)\ 10^5$ J/mol. For the mixed solid phases δ-NbN_{1-x} (FCC-A1) + β-Nb_2N (HCP-A3) and α-NbN (BCC-A2) + hexagonal β-Nb_2N (HCP-A3), Gibbs free energy is restricted in the ranges $-(2.21 - 1.08)\ 10^5$ J/mol and $-(2.36 - 0.623)\ 10^5$ J/mol respectively. The solid single phases δ-NbN_{1-x} (FCC-A1), and β-Nb_2N (HCP-A3) have Gibbs free energy in the ranges $-(1.08 - 2.21)\ 10^5$, $-(0.83 - 0.62)\ 10^5$ J/mol respectively. Finally the solid solution α-NbN (BCC-A2) has phase boundaries which drop with N mass percent. Hence Gibbs free energy for this phase has a minimum value of -2.23×10^5 at 2.47 N mass percent and a maximum of -1.14×10^5 J/mol at 0.0 N mass percent.

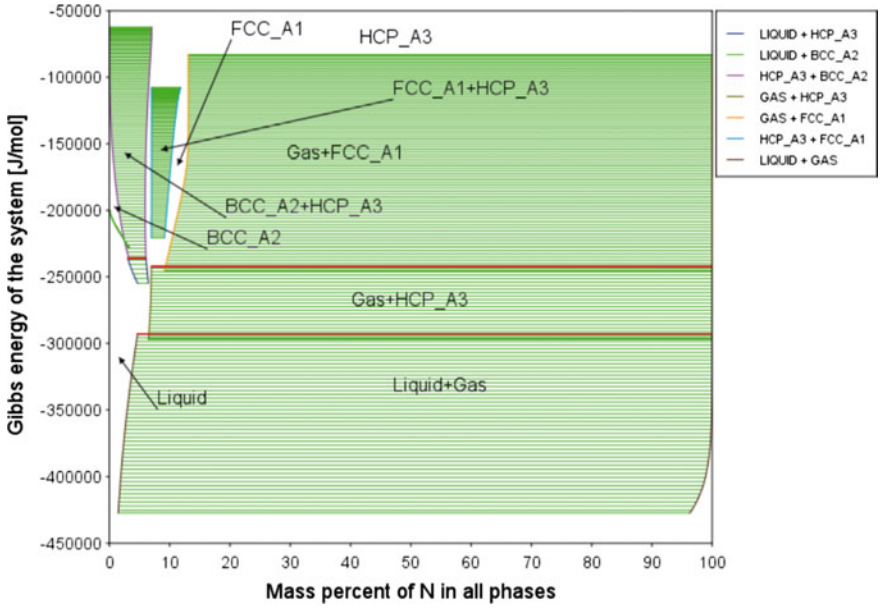

Fig. 2 Gibbs free energy against N mass percent for all phases

Conclusions

Thermo-Calc software was used to produce the phase diagram and Gibbs free energy of the Nb-N system. Three stable solid phases were found as single phases; bcc α-NbN solid solution, hexagonal β-Nb_2N, and fcc δ-NbN_{1-x}. In addition, there two mixed solid phases which are α-NbN + β-Nb_2N, and δ-NbN_{1-x} + β-NbN. Liquid phase is found mixed with solid phases α-NbN and β-Nb_2N, and mixed with gas. The gas phase was found as a single phase at large nitrogen content and high temperatures. The results of this work are important for hard metal industry.

References

1. Zou Y, Wang X, Chen T, Li X, Qi X, Welch D, Zhu P, Liu B, Cui T, Li B (2015) Hexagonal-structured ε-NbN: ultra-incompressibility, high shear rigidity, and a possible hard superconducting material. Sci Rep. https://doi.org/10.1038/srep10811
2. Ihara H, Kimura Y, Senzaki K, Kezuka H, Hirabayashi M (1985) Electronic structures of B1 MoN, fcc Mo_2N, and hexagonal MoN. Phys Rev B 31:3177–3178
3. Bull CL, McMillan PF, Soignard E, Leinenweber K (2004) Determination of the crystal structure of δ-MoN by neutron diffraction. J Solid State Chem 177:1488–1492
4. Eremeev G (2009) Review of RF properties of NbN and MgB_2 thin coating on Nb samples and cavities. In: Proceedings of SRF 2009, Berlin, Germany, pp 159–163
5. Boutwell BA, Thompson RG, Saunders N, Mannan SK, and de Barbadillo JJ (1997) Phase formation modeling of an alloy casting using computational thermodynamics. In: Paper is presented at the 4th international symposium on superalloys and derivatives, Pittsburgh, Pennsylvania, 15–18 June 1997
6. Introduction to Thermo-Calc. In: Thermo-Calc software. http://www.thermocalc.com. Accessed 18 Sept 2016
7. Virginia O, Harry AJ (eds) (2010) Critical melting points and reference data for vacuum heat treating. Vac Furn Ref Ser 1:6. http://solarmfg.com/wp-content/uploads/2011/01/Critical-Melting-Point1.pdf. Accessed 26 Sept 2017

Part XXX
Multi-material Additive Manufacturing: Processing and Materials Design

Development of Novel Squeeze Cast High Tensile Strength Al–Si–Cu–Ni–Sr Alloys

Li Fang, Luyang Ren, Xinyu Geng, Henry Hu, Xieyuan Nie and Jimi Tjong

Abstract The Taguchi method, as a design of experiment (DOE) technique, was used to develop squeeze cast high strength aluminum alloys containing elements of Si, Cu, Ni and Sr. The designed aluminum-based experimental alloys possess four factors: Si, Cu, Ni and Sr contents with three different levels of weight percentages (Si: 6, 9, 12%, Cu: 3, 5, 7%, Sr: 0.01, 0.02, 0.03% and Ni: 0.5, 1, 1.5%). Tensile properties including ultimate tensile strength, yield strength and elongation at failure were selected as three individual responses to evaluate the engineering performance of the designed alloys. An analysis of the mean of signal-to-noise (S/N) ratio implies that the tensile properties of the tested aluminum alloys are influenced significantly by the levels of the alloying elements in the Taguchi orthogonal array. The optimized major element content for the as-cast high strength aluminum alloy are 9% Si, 7% Cu, 0.03% Sr and 1.0% Ni. The percentage contribution of each factor is determined by the analysis of variance (ANOVA). The results indicate that the contents of Si and Ni are the most significant two factors influencing the tensile properties of the experimented alloys.

Keywords Taguchi method · Analysis of variance · Elements Ni, Si, Cu, and Sr · Al–Si–Cu alloy

Introduction

Aluminum and its alloys as lightweight structural materials have been in widespread use, and their commercial applications continue to increase. Especially in the automotive industry, Al–Si–Cu alloy is one of the most widely used material

L. Fang · L. Ren · X. Geng · H. Hu (✉) · X. Nie · J. Tjong
Mechanical, Automotive and Materials Engineering, University of Windsor, Windsor, ON N9B 3P4, Canada
e-mail: huh@uwindsor.ca

The Minerals, Metals & Materials Society, *TMS 2018 147th Annual Meeting & Exhibition Supplemental Proceedings*, The Minerals, Metals & Materials Series,
https://doi.org/10.1007/978-3-319-72526-0_72

because of its moderate properties and relatively low cost. For further expansion of aluminum usage to the area where heavy dynamic loading is required in vehicles, as-cast aluminum alloys with improved properties and their corresponding manufacturing processes become essential. Previous studies have indicated that the transition metal elements as copper (Cu) and nickel (Ni) are found to be effective for improvement of mechanical properties of Al–Si alloy at elevated temperature [1–3]. Studies on Ni-containing aluminum alloys indicated that the Ni presence enabled many complex intermetallic phases to form including $A_{l2}Cu$, Al_3Ni, Al_7Cu_4Ni, Al_9FeNi and $Al_5Cu_2Mg_8Si_6$ in aluminum alloys. The Al_3Ni, Al_3CuNi and Al_7Cu_4Ni phases were found having great contribution to the elevated-temperature properties of Al–Si alloy [4–6]. Also, it has been indicated that the eutectic silicon phases affected the mechanical properties of Al-Si alloys significantly. Since the Si phase is hard and brittle, the coarse Si eutectic reduces mechanical properties of A–Si–Cu alloys [7, 8]. To enhance the strengths of Al–Si alloys, the needle shaped eutectic silicon has to be modified. Alkali element, sodium (Na), alkaline earth element, strontium (Sr), and metalloid, antimony (Sb), were found to affect the nucleation and growth processes of eutectic silicon crystals effectively in Al–Si alloys. Among the three, Sr is by far the most efficient and effective modifier due to the handling difficulty of sodium and the toxicity of the antimony. Sr was demonstrated to be capable of effectively modifying the morphology of eutectic silicon from acicular (plate or needle-like) to fibrous form despite that Sr addition might coarsened the primary silicon in hypoeutectic Al–Si alloys. The results of mechanical properties showed that Sr modification enhanced tensile properties of both hypereutectic and hypoeutectic properties significantly [9–18]. Up to date, however, no extensive research has been performed with the addition of two transition elements (Ni and Cu) and one alkaline earth element (Sr) together in a as-cast alloy to maximize mechanical properties of Al–Si alloys. Past studies failed to systematically and thoroughly design this type of the alloys using an optimization approach.

In this study, a design of experiment (DOE) technique, the Taguchi method, was used to design the chemistry of as-cast Al–Si–Cu alloys with other element additions for maximized engineering performance, which was evaluated by the resultant tensile properties. Unlike traditional full factorial design involving large amount of experiments to identify all possible combinations for a given set of variables, the Taguchi method uses a special design of orthogonal arrays to study all the designed factors with a minimum of experiments at a relatively low cost. Orthogonality means that factors can be evaluated independently of one another; the effect of one factor does not interfere with the estimation of the influence of another factor [19, 20]. With the consideration of the influencing extent of individual element content, the selection of four influential factors, i.e. element additions of Si, Cu, Ni and Sr with three different weight percentages, were selected in the design of experiment. Tensile tests were conducted to determine the mechanical properties such as ultimate tensile strength, yield strength and elongation at failure of the designed

experimental alloys. The results of the factor response analysis were used to derive the optimal levels combinations. The percentage contribution of each factor was determined by an analysis of variance.

Experimental Procedures

Materials

Designed Al–Si–Cu–Ni–Sr alloys were prepared by using commercially pure Al, Si, Cu, Al-20 wt% Ni and Al-10 wt% Sr. Al, Si, Cu, and Al-20 wt% Ni were melt and mixed in an electric resistance furnace to achieve the desired compositions which were verified by an Inductively-Coupled Plasma Atomic Emission Spectrometer based on ASTM E1479-99. The melt was modified by introducing Al-10 wt% Sr for modification of Si eutectic phase, and was kept at 730 ± 10 °C for 30 min for the completion of homogenization and modification, and then the melt temperature was decreased to 650 °C for squeeze casting.

Squeeze Casting

Cylindrical coupons having a diameter of 100 mm and a section thickness of 25 mm were squeeze cast with the prepared melt. The squeeze casting experiments started with the transfer of a metered quantity of the prepared melt (650 °C) into the bottom half of the preheated (300 °C) die set mounted in a hydraulic press. The dies were then closed, with the top half (punch) lowering into the bottom die. An applied pressure of 90 MPa was exerted by the punch on the molten metal and maintained until the entire casting solidified.

Tensile Testing

The mechanical properties of the squeeze cast novel alloys were evaluated by tensile testing, which was performed at ambient temperature on a MTS criterion Tensile Test Machine (Model 43) equipped with a data acquisition system. Following ASTM B557, flat tensile specimens (25 mm in gage length, 6 mm in width, and 4 mm in thickness) were machined from the squeeze cast disks. The tensile properties, including 0.2% yield strength (YS), ultimate tensile strength (UTS), and elongation to failure (E_f), were obtained based on the average of three tests.

Taguchi Design of Experiment

Design of Orthogonal Array and Signal-to-Noise Analysis

For alloy chemistry design, based on the literature survey, four alloying elements, Si, Cu, Ni, and Sr, were chosen with three levels and are listed in Table 1. The experimental layout for the four factors using L9 orthogonal array is given in Table 2. Two sets of the Taguchi experiments were conducted to ensure the reliability of experimental data for signal-to-noise analysis.

In process design, it is almost impossible to eliminate all errors caused by the variation of characteristics. An increase in the variance of multiple characteristics lowers the properties of material. The Taguchi method [11–13] uses signal-to-noise (S/N) ratio instead of the average value to interpret the trial results data into a value for the evaluation characteristic in the optimum setting analysis. To minimize the influence of the error caused by the variation of characteristics, the signal-to-noise

Table 1 Design factors and levels

Level	Factor			
	A Si (wt%)	B Cu (wt%)	C Sr (wt%)	D Ni (wt%)
1	6	3	0.01	0.5
2	9	5	0.02	1
3	12	7	0.03	1.5

Table 2 Designed experiment plans

Experiment	Si (wt %)	Cu (wt %)	Sr (wt%)	Ni (wt%)
1	6 (A1)	3 (B1)	0.01 (C1)	0.5 (D1)
2	6 (A1)	5 (B2)	0.02 (C2)	1 (D2)
3	6 (A1)	7 (B3)	0.03 (C3)	1.5 (D3)
4	9 (A2)	3 (B1)	0.02 (C2)	1.5 (D3)
5	9 (A2)	5 (B2)	0.03 (C3)	0.5 (D1)
6	9 (A2)	7 (B3)	0.01 (C1)	1 (D2)
7	12 (A3)	3 (B1)	0.03 (C3)	1 (D2)
8	12 (A3)	5 (B2)	0.01 (C1)	1.5 (D3)
9	12 (A3)	7 (B3)	0.02 (C2)	0.5 (D1)

(S/N) ratio was employed, which converted the trial result data into a value for the response to evaluate the mechanical properties in the optimum setting analysis. The S/N ratio consolidated several repetitions into one value which reflected the amount of variation present. This is because the S/N ratio can reflect both the average and the variation of the quality characteristics. There are several S/N ratios available depending on the types of characteristics: lower is best (LB), nominal is best (NB), and higher is best (HB). In the present study, alloys mechanical properties were treated as a characteristic value. Since the mechanical properties of novel alloys were intended to be maximized, the S/N ratio for HB characteristics was selected, which was be calculated as follows:

$$S/N_{HB} = -10\log\left(\frac{1}{n}\sum_{i=1}^{n}\frac{1}{\eta_{pi}^{2}}\right) \tag{1}$$

where n is the repetition number of each experiment under the same condition for design parameters, and η_{pi} is recovery rate of an individual measurement at the i_{th} test. After calculating and plotting the mean S/N ratios at each level for various factors, the optimal level, that was the largest S/N ratio among all levels of the factors, was determined.

The proposition for the optimization of mechanical properties with multiple performance characteristics (three objectives) using a weighting method is defined as the Eqs. (2)–(4):

$$Y_{SUM} = Y_P \times W \tag{2}$$

where

$$Y_{SUM} = \begin{bmatrix} \eta_{1c} \\ \eta_{2c} \\ \vdots \\ \eta_{9c} \end{bmatrix}, Y_p = \begin{bmatrix} \eta_{11} & \eta_{12} \\ \eta_{21} & \eta_{22} \\ \vdots & \vdots \\ \eta_{91} & \eta_{92} \end{bmatrix}, w = \begin{bmatrix} w_1 \\ \vdots \\ w_3 \end{bmatrix} \tag{3}$$

and

$$\sum_{i=1}^{2} w_i = 1 \tag{4}$$

where w_1, w_2 and w_3 are the weighting factor of ultimate strength, elongation at failure and yield strength, respectively. η_{jc} is the multi S/N ratio in the jth test, η_{ji} is the ith single response S/N ratio for the jth test; w_i is the weighting factor in the ith performance characteristics.

The objective function was formulated according to the previous optimization criteria:

$$\text{Maximaze} f(X) = w_1 \cdot \eta_{\text{UTS}} + w_2 \cdot \eta_{\text{Ef}} + w_3 \cdot \eta_{YS} \tag{5}$$

The above objective function is presented in an analytical form as a function of input parameters since two strengths and elongation as three characteristics are important properties for cast components. The three characters should be considered as different critical roles by weighting factors. For various engineering applications, required technical specifications can vary due to the presence of differences in loading conditions. For cast components of which strengths have a priority higher than ductility, high weighting factors of ultimate tensile strength and yield strength need to be considered. When cast parts are required to be relatively ductile for energy absorption, elongation at failure becomes more important than strengths and has a high value of the weighting factor. As an example, in this study, for strength-related application, combination of weighting factor as 0.7:0.1:0.2, i.e., ultimate tensile strength ($w_1 = 0.7$) and yield strength ($w_3 = 0.2$), and the elongation at failure ($w_2 = 0.1$), is selected to demonstrate the optimization of strength. The combinations of weighting factors may vary for various application and engineering requirements.

Analysis of Variance (ANOVA)

The purpose of the analysis of variance is to investigate the contribution of each factor (chemical element) with multiple characteristics that significantly affect the mechanical properties. Following the analysis, it is relatively easy to identify the effect order of factors on mechanical properties and the contribution of factors to mechanical properties. In this study, variation due to both the four factors and the possible error was taken into consideration. The ANOVA was established based on the sum of the square (SS), the degree of freedom (D), the variance (V), and the percentage of the contribution to the total variation (P). The five parameters symbol typically used in ANOVA are described below:

1. Sum of squares (SS). SS_P denotes the sum of squares of factors A, B, C, and D; SS_e denotes the error sum of squares; SS_T denotes the total sum of squares.

   The total sum of square SST from S/N ratio was calculated as:

$$SS_T = \sum_{i=1}^{m} \eta_i^2 - \frac{1}{m}\left[\sum_{i=1}^{m} \eta_i\right]^2 \tag{6}$$

where m is the total number of the experiments, and η_i is the factor response at the ith test.

The sum of squares from the tested factors, SS_p, was calculated as:

$$SS_P = \sum_{i=1}^{m} \frac{\left(S_{\eta_{jc}}\right)^2}{t} - \frac{1}{m}\left[\sum_{i=1}^{m} \eta_i\right]^2 \quad (7)$$

where m is the number of the tests (m = 9), j the level number of this specific factor p, t is the repetition of each level of the factor p, and $S_{\eta j}$ the sum of the multi-response S/N ratio involving this factor p and level j.

2. Degree of freedom (D). D denotes the number of independent variables. The degree of freedom for each factor (D_P) is the number of its levels minus one. The total degrees of freedom (D_T) are the number of total number of the result data points minus one, i.e. the total number of trials times the number of repetition minus one. And the degree of freedom for the error (De) is the number of the total degrees of freedom minus the total of degree of freedom for each factor.
3. Variance (V). Variance is defined as the sum of squares of each trial sum result involved the factor, divided by the degrees of freedom of the factor:

$$Vp\ (\%) = \frac{SS_P}{D_P} \times 100 \quad (8)$$

4. The corrected sum of squares (SSp). SSp is defined as the sum of squares of factors minus the error variance times the degree of freedom of each factor:

$$SS_P^{'} = SS_P - D_P V_e \quad (9)$$

5. Percentage of the contribution to the total variation (P). Pp denotes the percentage of the total variance of each individual factor:

$$Pp\ (\%) = \frac{SS_P^{'}}{SS_P} \times 100 \quad (10)$$

Results and Discussion

Tensile Properties and Multi-response S/N Ratios

The mechanical properties of the designed alloys were evaluated by tensile testing. Properties including ultimate strength (UTS), elongation at failure (E_f) and Yield strength (YS) are listed in Table 3.

Since the objectives, i.e., tensile properties, were intended to be maximized, the S/N ratio for HB (higher-is-better) characteristics was used. The S/N ratios of these

Table 3 Tensile properties, S/N ratio and multi-response S/N ratio of the designed alloys

EXP.	UTS (MPa)		Ef (%)		YS (MPa)		S/N ratio (UTS)	S/N ratio (Ef)	S/N ratio (YS)	Multi-response of S/N ratio
	Test 1	Test 2	Test 1	Test 2	Test 1	Test 2				$w_1 = 0.7$ $w_2 = 0.1$ $w_3 = 0.2$
1	243.26	247.59	0.88	0.94	213.79	206.59	47.80	−0.82	46.45	42.67
2	243.93	253.37	0.78	0.79	215.20	213.97	48.02	−2.10	46.63	42.73
3	228.88	232.69	1.93	1.79	146.71	150.28	47.26	5.37	43.43	42.31
4	245.82	246.16	1.21	1.15	170.83	175.86	47.82	1.43	44.78	42.57
5	271.81	281.53	0.83	0.82	229.95	241.55	48.84	−1.68	47.44	43.50
6	291.36	281.93	0.90	0.85	221.29	223.02	49.14	−1.17	46.93	43.67
7	243.04	249.18	1.40	1.55	153.36	150.41	47.82	3.34	43.63	42.53
8	234.00	230.00	0.73	0.79	197.31	183.96	47.31	−2.39	45.59	41.99
9	239.75	250.48	0.99	1.07	184.55	189.39	47.78	0.25	45.43	42.56

Table 4 The factor's mean multi-response S/N ratio for each level with two weighting factors

Level	Mean S/N ratio for case: $w_1 = 0.4$, $w_2 = 0.2$ and $w_3 = 0.4$			
	A Si	B Cu	C Sr	D Ni
1	42.57	42.59	42.78	42.91
2	43.25	42.74	42.62	42.98
3	42.36	42.85	42.78	42.29

tensile properties were given in Table 3, and the multi-responses of S/N ratio using three weighting factor combinations were also concluded in Table 3. The response of each factor to its individual level was calculated by averaging the S/N ratios of all experiments at each level for each factor. With three combinations of weighting factors, the factor's mean multi-response S/N ratios for each level were summarized in Table 4, respectively. For instance, the mean S/N ratio (42.62) for Sr addition at level 2 in Table 4 with the weighting factors of $w_1 = 0.7$, $w_2 = 0.1$ and $w_3 = 0.2$ was the average value of the S/N ratios of experiment No. 2 (42.73), No. 4 (42.57) and No. 9 (42.56) which were listed in Table 3.

Optimal Chemical Composition for Strength Performance

To optimize strength of alloy, the order of the performance characteristics is given as ultimate tensile strength ($w_1 = 0.7$) and yield strength ($w_3 = 0.2$), and the elongation at failure ($w_2 = 0.1$). Figure 1 depicts the multi-response S/N ratios for the certain case of strength optimization.

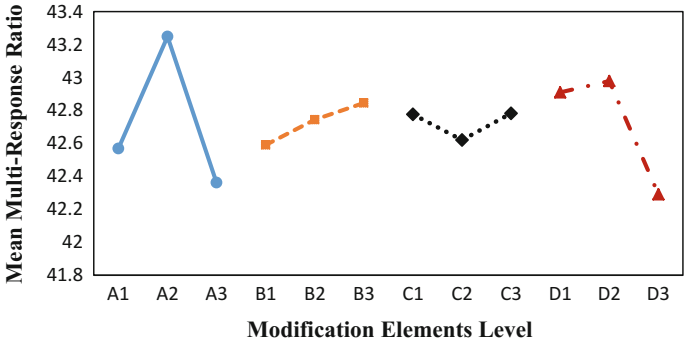

Fig. 1 Multi-response signal-to-noise graph for case: $w_1 = 0.7$, $w_2 = 0.1$ and $w_3 = 0.2$

As show in Fig. 1, the mean S/N ratio for factor A of Si addition increased with the amount of Si from 6% (level 1) to 9% (level 2) and decreased to the low value with further addition of Si up to 12% (level 3). When the relatively high amount of Si was introduced to the alloy with the presence of a low level of Sr addition, the volume of partially modified eutectic Si phase likely increased. They were found to have a plate-like shape, hard, brittle, and reduce mechanical properties of alloys [12]. The effect of the Cu addition (factor B) on the mean S/N ratio of the mechanical properties was also plotted in Fig. 1. The mean multi-response S/N ratio of tensile properties rose when Cu was added. As Cu addition increased from the 3% (level 1) to 7% (level 3), the mean multi-response S/N ratio of tensile properties increased to 37.63. This might be because sufficient Cu addition could form a large amount of the strengthening intermetallic phase. For Sr addition, as increasing from levels 1–2, the S/N ratio decreased slightly. Further addition of Sr led to an increase in the S/N ratio, which suggested that the presence of a high level of Sr benefited the strengths of the designed alloys. Examination of the effect of Ni addition (factor D) revealed that the S/N ratio of the tensile properties slightly increased and then decreased as the amount of Ni addition increased. It was also pointed out [5] that Ni apparently had a little influence on the room temperature strengths of Al–Si–Ni cast alloys with the presence of Sr. Also, the introduction of 3 wt% Cu and 1 wt% Ni together into the Al-13 wt% Si alloy resulted in the formation of γ-Al_7Cu_4Ni instead of δ-Al_3CuNi, which had a limited influence on strength. By selecting the highest value of the mean S/N ratio for each factor, the optimal levels were determined, which were A2B3C3D2; i.e. 9% Si, 7% Cu, 0.03% Sr and 1.0% Ni. To verify the optimal levels of the added elements suggested by the Taguchi method, a confirmation experiment needs to be carried out.

Table 5 Results of the ANOVA for case: $w_1 = 0.7$, $w_2 = 0.1$ and $w_3 = 0.2$

Factors	Degree of freedom (D)	Sum of squares (SS_p)	Variance (V)	Corrected sums of squares (SS_p')	Contribution	Rank
Si (%)	2	2.17	1.08	2.17	43.16%	1
Cu (%)	2	3.35	1.67	3.35	12.26%	3
Sr (%)	2	2.95	1.48	2.95	9.50%	4
Ni (%)	2	2.67	1.33	2.67	35.08%	2
Error		0.00	0.00		0	
Total		11.14			100%	

The Factor Contributions with Combination of Weighting Factors

The contribution of each factor to the tensile properties was determined by performing analysis of variance based on Eqs. (6)–(9). The results of analysis of variance (ANOVA) for case: $w_1 = 0.7$, $w_2 = 0.1$ and $w_3 = 0.2$, is summarized in Tables 5.

Table 5 lists the contribution of the four factors (Si, Cu, Sr and Ni addition) in case: $w_1 = 0.7$, $w_2 = 0.1$ and $w_3 = 0.2$, in which the strengths are in priority, was 43.16%, 12.26%, 9.50% and 35.08%, respectively. The addition of Si had the highest contribution of 43.16%, which indicated that Si had the major influence on the tensile properties of the designed alloys. Ni (35.08%) was ranked as the second highest contributor which had a very close contribution to Si. The addition of Cu had a contribution of 12.26% took the third place while Sr had the lowest contribution of 9.50%.

Conclusions

The Taguchi method with multiple performance characteristics was employed to optimize the addition levels of one metalloid element (Si), two transient elements (Cu and Ni), and one alkaline earth element (Sr) based on defined objectives, i.e., tensile strength, elongation and yield strength. The addition content of Si, Cu, Sr and Ni were chosen as factors and three levels for each factor were considered in the design of experiment. In case of developing an alloy with strengths as priority and maintaining functional ductility level ($w_1 = 0.7$, $w_2 = 0.1$ and $w_3 = 0.2$), an optimum combination of 9% Si, 7% Cu, 0.03% Sr and 1.0% Ni was calculated. All the considered four elements exhibited an effective contribution on the tensile properties of the proposed alloys with a lowest contribution in both the designed cases of around 10% while the content of Si and Ni are the most significant two factors affecting the mechanical properties of alloy with contribution of 43.16% and

35.08% respectively. For applications aiming at improving the strengths of the alloys, Si and Ni content had the major contribution on the tensile properties. As ductility became a priority, Sr and Cu played an important role than Si and Ni. To verify the optimal levels of the added elements suggested by the Taguchi method, a confirmation experiment needs to be carried out.

Acknowledgements The authors would like to take this opportunity to thank the Natural Sciences and Engineering Research Council of Canada, Ford Motor Company of Canada, and the University of Windsor for supporting this work.

References

1. Cho YH, Joo DH, Kim CH, Lee HC (2006) The effect of alloy addition on the high temperature properties of over-aged Al-Si (CuNiMg) cast alloys. Mater Sci Forum 519:461–466
2. Rajaram G, Kumaran S, Rao TS (2011) Effect of graphite and transition elements (Cu, Ni) on high temperature tensile behaviour of Al–Si alloys. Mater Chem Phys 128(1):62–69
3. Pratheesh K, Kanjirathinkal A, Joseph MA, Ravi M (2015) Study on the effects of squeeze pressure on mechanical properties and wear characteristics of near eutectic Al–Si–Cu–Mg–Ni piston alloy with variable Mg content. Trans Indian Inst Met 68(1):59–66
4. Chen C-L, Richter A, Thomson RC (2010) Investigation of mechanical properties of intermetallic phases in multi-component Al–Si alloys using hot-stage nanoindentation. Intermetallics 18(4):499–508
5. Li Y, Yang Y, Wu Y, Wang L, Liu X (2010) Quantitative comparison of three Ni-containing phases to the elevated-temperature properties of Al–Si piston alloys. Mater Sci Eng, A 527 (26):7132–7137
6. Chen CL, Richter A, Thomson RC (2009) Mechanical properties of intermetallic phases in multi-component Al–Si alloys using nanoindentation. Intermetallics 17(8):634–641
7. Wang L, Makhlouf M, Apelian D (1995) Aluminium die casting alloys: alloy composition, microstructure, and properties-performance relationships. Int Mater Rev 40(6):221–238
8. Hu H, Wang Y, Chu Y, Cheng P, Alpas AT (2005) Solution heat treatment of vacuum high pressure die cast aluminum alloy A380. NADCA Trans 22–33
9. Gruzelski JE, Closset BE (1990) The treatment of liquid aluminium–silicon alloys. Foundry Society, Amer
10. Dahle AK, Nogita K, McDonald SD, Zindel JW and Hogan LM (2001) Eutectic nucleation and growth in hypoeutectic Al-Si alloys at different strontium levels. Metall Mater Trans A 32 (4):949–960
11. Heusler L, Schneider W (2002) Influence of alloying elements on the thermal analysis results of Al–Si cast alloys. J Light Met 2(1):17–26
12. Wang G, Bian X, Wang W, Zhang J (2003) Influence of Cu and minor elements on solution treatment of Al–Si–Cu–Mg cast alloys. Mater Lett 57(24):4083–4087
13. Dahle AK, Nogita K, McDonald SD, Dinnis C, Lu L (2005) Eutectic modification and microstructure development in Al–Si alloys. Mater Sci Eng A 413:243–248
14. Shabestari SG, Ghodrat S (2007) Assessment of modification and formation of intermetallic compounds in aluminum alloy using thermal analysis. Mater Sci Eng A 467(1):150–158
15. Cho YH, Lee HC, Oh KH, Dahle AK (2008) Effect of strontium and phosphorus on eutectic Al-Si nucleation and formation of β-Al5FeSi in hypoeutectic Al-Si foundry alloys. Metall Mater Trans A 39(10):2435–2448

16. Timpel M, Wanderka N, Kumar GV, Banhart J (2011) Microstructural investigation of Sr-modified Al–15wt% Si alloys in the range from micrometer to atomic scale. Ultramicroscopy 111(6):695–700
17. Stunova BB (2012) Study of AlSi10 Mg alloy structures after modification by various Sr agents. MM Sci J 318–320
18. Sarada BN, Srinivasamurthy PL, Swetha (2013) Microstructural characteristics of Sr and Na modified Al-Mg-Si alloy. Int J Innov Res Sci Eng Tech 2(8):3975–3983
19. Phadke MS (1995) Quality engineering using robust design. Prentice Hall PTR
20. Ross PJ (1996) Taguchi techniques for quality engineering: loss function, orthogonal experiments, parameter and tolerance design

Part XXXI
Nanocomposites V: Structure-Property Relationships in Nanostructured Materials

Carbon Nanocomposite for Reliable Seal Applications in High-Temperature, High-Pressure, Corrosive Environments

Lei Zhao and Zhiyue Xu

Abstract Achieving a reliable seal in the extremely harsh environments of high pressure, high temperature (HPHT), and corrosive fluids has been highly demanded in various industries, including oil and gas, aerospace, chemicals, and nuclear, etc. Traditional seal materials such as rubber or plastic often fail to achieve reliable sealing due to thermal degradation under hot, wet, and corrosive conditions. Metal-to-metal seals also show limited success due to their low elasticity and weak acid corrosion resistance at HT. This paper presents a novel carbon-based nanocomposite that exhibits a temperature rating higher than 300 °C, filling a technical gap of high-temperature sealing materials in extremely corrosive environments. The composition-microstructure-property relationship and superior seal performance of this novel nanocomposite will be discussed.

Keywords Carbon nanocomposite · Elastic · High temperature
High pressure · Seal · Corrosive resistance

Introduction

Steadily increasing demands from global economic growth and the paucity of easy-to reach reservoirs, has compelled the oil and gas industry to conduct more exploration activities in extremely harsh environments that traditionally were considered economically or technically inaccessible [1, 2]. Most of these new reservoirs, e.g., offshore, heavy oil, geothermal, etc., exhibit extremely high-temperature, high-pressure, or highly corrosive environments that are beyond the rating of most downhole drilling or production equipment [3]. Improving their working temperature or pressure is limited by the seals that confine downhole fluids

L. Zhao (✉) · Z. Xu
Baker Hughes, a GE Company, 14990 Yorktown Plaza Dr, Houston, TX 77040, USA
e-mail: lei.zhao@bakerhughes.com

Z. Xu
e-mail: zach.xu@bakerhughes.com

The Minerals, Metals & Materials Society, *TMS 2018 147th Annual Meeting & Exhibition Supplemental Proceedings*, The Minerals, Metals & Materials Series,
https://doi.org/10.1007/978-3-319-72526-0_73

or gas [4]. Currently, these seals rely on different types of rubber materials that chemically decompose at elevated temperatures or in corrosive fluids [5–7]. In addition, these rubber materials typically fail at even lower temperatures because their mechanical properties degrade with temperature increases [5].

It is true that various types of high-temperature seal solutions, e.g., metal-to-metal (M2 M) seal, graphite seal, glass seal, etc., may be available in other industries [8]. However, these solutions have been proven non-effective in oil and gas exploration because their inorganic materials lack the elasticity and malleability that rubber materials exhibit for unique downhole conditions (i.e., most sealing surfaces are tubular that are high corroded, eroded or deposited with thick scale or wax; they are usually thousands of feet underground and inaccessible to any machining operations) [2–4, 8].

Due to its extreme thermal and chemical stability, carbon is probably one of the most inert materials in nature and one of the most broadly utilized materials for seal applications [8]. However, carbon materials are limited to low and medium pressure ratings (~ 10 MPa). To address this issue, a novel elastic carbon composite (ECC) was developed that successfully incorporates a second metal phase to enhance the mechanical property of the flexible carbon material. Material tests show that this ECC has excellent thermal stability up to 537 °C and dramatically improved mechanical strength up to 100 MPa. Even though this ECC displayed strong corrosion resistance to common downhole fluids (hydrocarbons, brines, weak acids, etc.), it failed to survive in concentrated acid fluids that are required by various industrial sections such as heavy oil recovery and petroleum refineries. In this work, different formulations are discussed, and a new binder phase is described that provides the new ECC with excellent corrosion resistance to concentrated acid, as well as a high-temperature rating greater than 300 °C.

Design of Elastic Carbon Composite

ECC is a composite material, consisting of flexible carbon grain and effective bonding phases. In stark contrast to traditional carbon materials that are typically hard and brittle, the flexible carbon material (due to the presence of nano-sized closed pores) exhibits elasticity for effective sealing (Fig. 1a). Additionally, metallic and other bonding phases are used to bond the carbon grains (forming a bonding phase between the binder material and the carbon grain, the black region in right insert of Fig. 1a) and forming a continuous phase to interlock these grains, enhancing the mechanical strength for the ECC. As shown in Fig. 1b, scanning electron microscopy (SEM) analysis shows that carbon phase (black) and binding phase (white) form a bi-continuous microstructure, resulting in a composite that benefits from the elasticity of the flexible carbon grain and the mechanical strength enhancement from the binding phase.

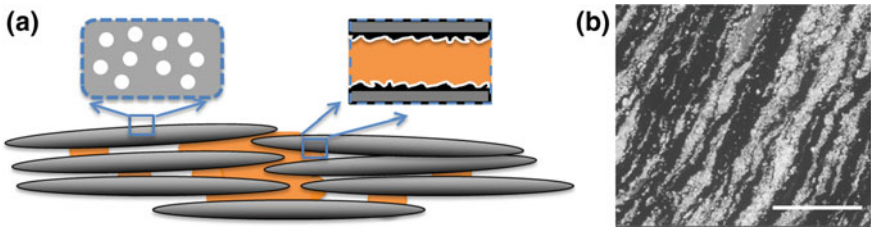

Fig. 1 Schematic illustration of ECC microstructure (**a**) and SEM image of ECC material with scale bar of 200 μm (**b**)

Because carbon is chemically inert to most acids (except HF), to meet the strong acid resistance requirement, the bonding phase must be carefully selected and engineered to survive a highly corrosive environment (concentrated acid in this case). In this work, stainless steel (SS), Inconel, and fluoropolymers (three engineering materials that are broadly utilized for corrosion-resistance applications in oil and gas) are evaluated as potential new binder candidates that could offer strength enhancement and chemical stability in the concentrated acid environment at HPHT.

Experiment Set-up

The mechanical, thermal and acid-resistance properties of the new ECC were fully investigated to ensure reliable performances of the material in high-temperature and extremely corrosive environments. The thermal stability of the ECC was characterized by a thermogravimetric analyzer (TGA) in nitrogen (i.e., a non-oxidizing environment as in the targeted applications) with a heating rate of 20 °C/min. The thermo-mechanical properties of the ECC were measured by dynamic mechanical analysis (DMA) in open air with a heating rate of 4 °C/min. Acid-resistance tests were performed by immersing cylindrical test coupons in a concentrated nitric acid solution (65–70 wt%) for eight days at 65 °C. This test was performed in an autoclave. After the ECC cooled and dried out, it was examined for surface cracks and corrosion. The mechanical properties of the ECC related to sealing are strength, elasticity, as well as malleability, which were obtained via an unconfined compression test. An unconfined compression test, according to ASM E9-09, was performed on cylindrical test coupons that were 12.7 mm diameter and 12.7 mm tall. The compression rate was 0.0211 mm/s, and the measurement stopped after the sample broke.

Results and Discussion

Acid Resistance of ECC

In a previous work, an ECC was developed with a metallic binder for downhole zonal isolation applications. Its corrosion resistance to common downhole fluids was approved by an aging test in tap water, a 3% KCl solution and 15% HCl solution at an elevated temperature, i.e., 93 °C [5]. However, the previous formulation failed the concentrated acid test. To expand the application of this novel material in harsh environments, a new binding phase with increased acid resistance had to be developed.

Corrosion resistance to concentrated acid has always been challenging for metallic materials, especially at elevated temperatures. Except for certain precious metal, e.g., Au, Pt, Ir, etc., most engineering metals or alloys react with acid readily, and the corrosion rate increases dramatically as temperature rises [9]. Under oxidized conditions, a thin oxidation layer may form for certain metal materials (e.g., Al, stainless steel, etc.) as a barrier to prevent further reaction. These anti-corrosion layers, though, are not thermally stable; they dissolve or break easily at elevated temperatures [9]. In this work, stainless steel and Inconel—two of the most broadly utilized corrosion-resistant metals in the oil and gas industry—are selected as bonder material. However, both show unsatisfying corrosion resistance during the acid-corrosion resistance test, as shown in Fig. 2. In concentrated nitric acid at 65 °C, nearly all the stainless steel bonding phase is etched away (40% mass loss), leaving only the graphite phase delaminated into pieces. It is true that Cr in stainless

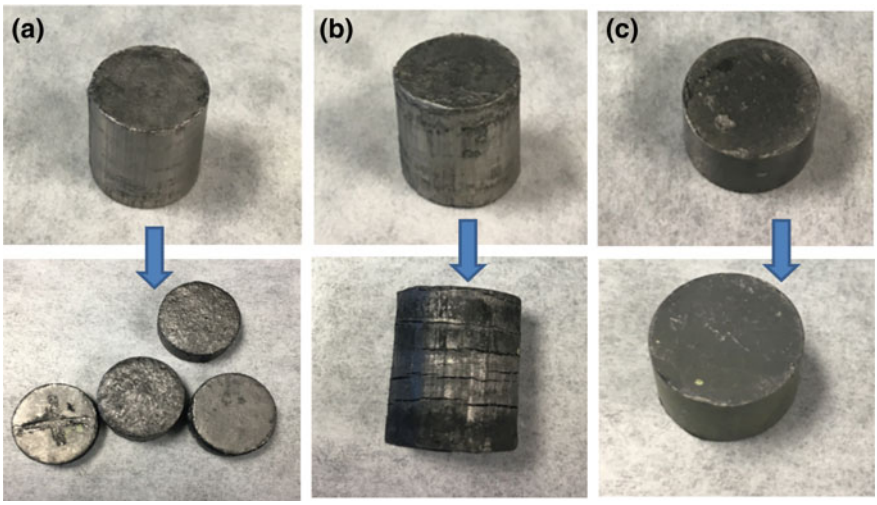

Fig. 2 Images of samples before and after high-temperature aging test in concentrated nitric acid for sample made from stainless steel (**a**), Inconel (**b**) and fluoropolymer (**c**)

steel can form a dense oxidized barrier in concentrated nitric acid to prevent further etching, but, this layer is clearly thermally unstable in tested conditions, as shown in Fig. 2a. Compared with stainless steel, Inconel shows much stronger resistance to concentrated nitric acid at elevated temperatures (~ 2% mass loss), and ECC bonded by Inconel keeps its integrity after an eight-day corrosion test. However, this material could not perform as a reliable seal because cracks formed, weakening the material and causing a pathway for leaks (Fig. 2b).

According to ECC design strategy, the use of precious metal that has proven chemical resistance to acid should most definitely lead to improved performance of the final composite. However, this strategy does not make economic sense from the view of practical application. To address this issue, fluoropolymer—another category of popular engineering materials with proven acid resistance in the oil and gas industry—was tested as a bonding material for ECC, and it showed excellent result during the acid-resistance test. As shown in Fig. 2c, after eight days of aging at elevated temperatures, the ECC coupon made from fluoropolymer showed no visual changes before and after the test, and no weight loss was measured. As illustrated in the ECC microstructure, because the carbon phase and bonding phases are resistant to nitric acid, it is not unexpected for this new ECC to achieve high corrosion resistance.

Mechanical Property of ECC

In a previous work, the mechanical properties and sealing performance of an ECC material made from metal were confirmed through various mechanical tests: 1. A compression test showed that the ECC material had a strong HP rating and high conformability for rough sealing counterparts; 2. A loop test and a hysteresis test confirmed the ECC had sufficient reliable elasticity to be energized for long-term seal applications [2]. Even though the fluoropolymer-bonded ECC passed the acid-resistance test, this novel material was also required to exhibit reasonable strength to replace the previously metal-bonded ECC to seal high-pressure differentials. As shown in the compressive test (Fig. 2), the material strength of the fluoropolymer-bonded ECC could reach 66 MPa, making it a reliable seal for most high-pressure applications. The strength of ECC made from fluoropolymer was similar to Inconel-bonded ECC, and both were lower than those made from stainless steel (Fig. 3).

Based on the microstructure, there are two functions for the binder to improve mechanical strength of overall ECC: first, it forms a bonding phase (intermetallic in this case) between binder material and carbon grains, performing like an adhesive; second, the binder material forms a continuous solid phase, physically interlocking the carbon grains. Iron readily forms carbide with carbon, so SS could also from a strong bonding phase with carbon grains. In contrast, Ni has low reactivity with C, and thus the bonding strength between Inconel and carbon grain is lower. As for fluoropolymer, its molecules has extremely high chemical stability, so no bonding

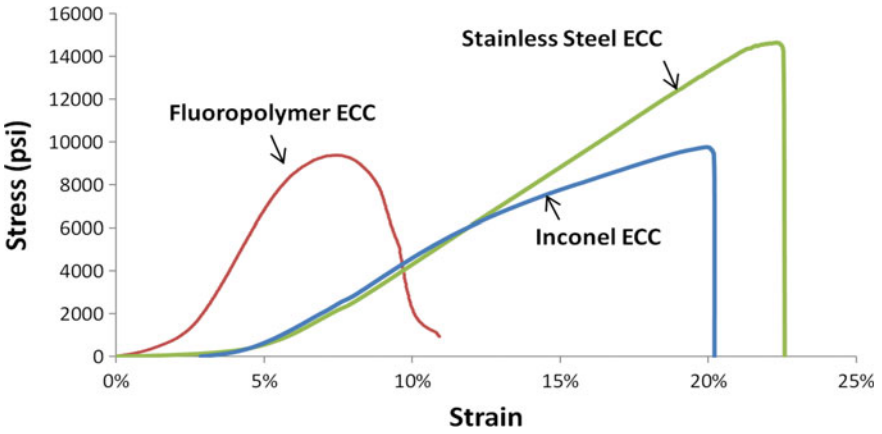

Fig. 3 Unconfined compression stress-strain curves of ECC made from stainless steel (**a**), Inconel (**b**) and fluoropolymer (**c**)

phase is expected to form. Only the interlocking mechanism exists for an ECC made from fluoropolymer and Inconel, and their strength is lower than the SS-bonded ECC. In the current work, the malleability of fluoropolymer we used was lower than Inconel, leading to the reduced malleability of the ECC. However, the malleability was enough for many seal applications.

Thermal Properties of ECC

As discussed previously, the ECC is designed to be an elastic seal solution to replace rubber or plastic seal material beyond their degradation temperature. An ECC made from metal binder has shown thermal stability above 400 °C. However, because most engineering metallic materials fail due to their low resistance to concentrated acid and fluoropolymer is currently the only economic solution, its thermal stability needs to be systematically evaluated for high-temperature applications similar to a metal-based ECC material.

Because inert or a reducing environment is more common in targeted applications (oil and gas extraction and processing), the TGA of the ECC was tested in nitrogen, and no weight loss was observed until 400 °C, as shown in Fig. 4. This test result confirms that an ECC made from fluoropolymer is chemically stable (i.e., no thermal decomposition) at the targeted temperature of 300 °C with large safety margin. This result is expected because the carbon grain and the fluoropolymer have excellent thermal stability. High chemical stability at elevated temperatures means longer life time and good reliability, but does not necessary mean the material can work as a seal in that temperature range. To qualify for sealing, the material should maintain reasonable mechanical strength or elastic modulus at an

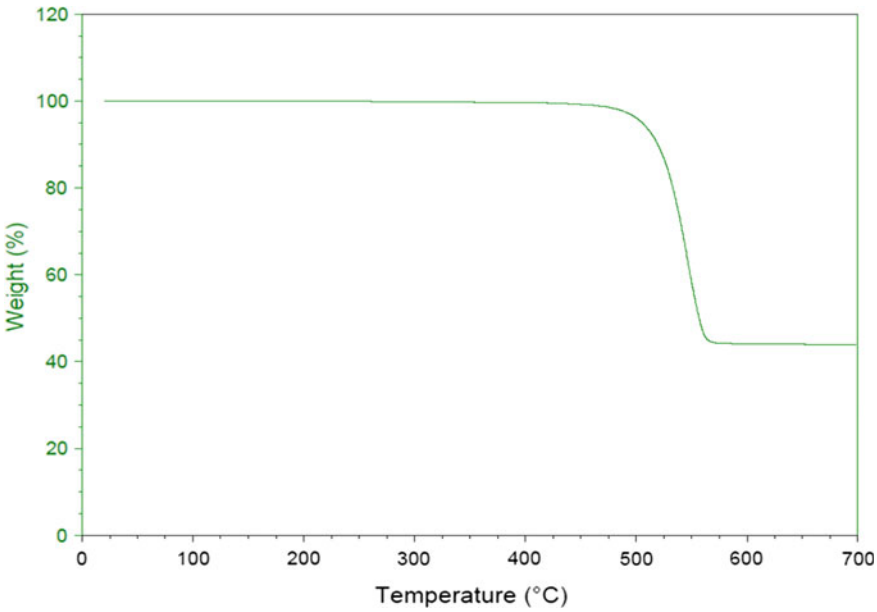

Fig. 4 Thermogravimetric analysis of fluoropolymer-based ECC in nitrogen protection

elevated temperature, otherwise it will be extruded under pressure differential. As matter of fact, mechanical properties of most seal material degrade at a temperature point far below their chemical decomposition temperature. To find the temperature rating of an ECC made from fluoropolymer, a dynamic mechanical analysis (DMA) was performed on this new ECC material to characterize its mechanical degradation with temperature.

As shown in Fig. 5, the storage modulus and loss modulus remained below 220 °C, which means the ECC kept its excellent mechanical property as seal material at elevated temperatures. Above 220 °C, mechanical degradation was observed, i.e., the storage and loss modulus decreased. This decrease can be attributed to the glass transition of fluoropolymer because previous tests confirmed that the mechanical property of carbon grain is basically inert to temperature change. Even though the material became softer, the storage modulus only dropped from 6.96 to 4.48 MPa, which is still high enough to resist extrusion in most of downhole conditions. Between 220–300 °C, the modulus of ECC remained same without further degradation (Fig. 5). Through the TGA and DMA characterization, the ECC exhibited excellent thermal stability, and it could be rated for seal applications up to 300 °C.

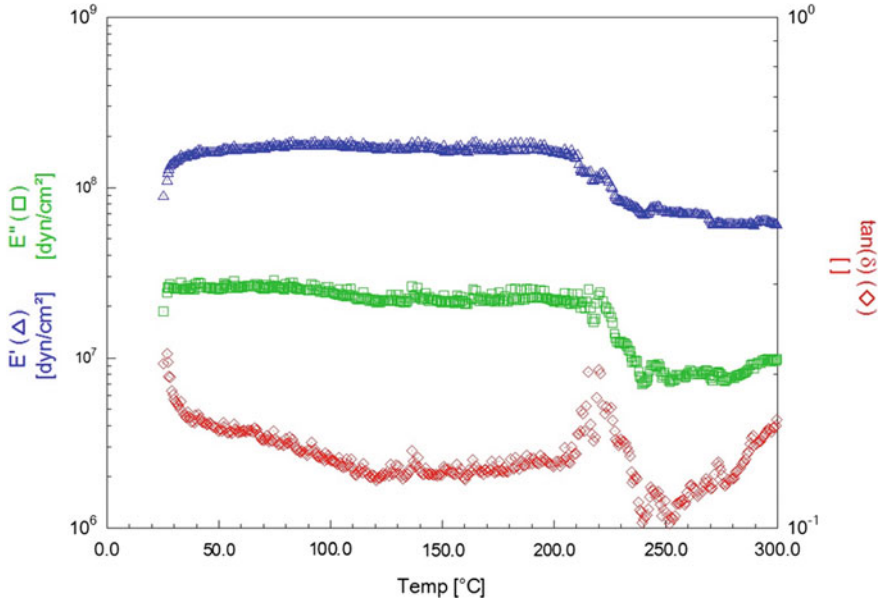

Fig. 5 Dynamic mechanical analysis of fluoropolymer-based ECC in open air

Conclusion

In a previous work, a new elastic carbon composite was successfully developed that showed extremely high thermal stability (over 537 °C) and filled the technical gap of sealing material with a temperature rating over 300 °C in the oil and gas industry. To expand its application in even harsher environments (concentrated acid), different corrosion-resistant engineering materials, i.e., stainless steel, Inconel alloy, and fluoropolymer, were evaluated as binder material to improve the corrosion resistance of final ECC to concentrated nitric acid. The results showed that the corrosion resistance of the final ECC was strongly dependent on its binder phase. Stainless steel and Inconel exhibited limited corrosion resistance to concentrated acid, with Inconel performing relatively better due to the lower corrosion rate of Ni alloys in concentrate acid. In stark contrast to metal binders, the ECC made from fluoropolymer showed excellent corrosion resistance in concentrated nitric acid at elevated temperatures. In addition, thermal analysis showed that it was chemically stable up to 400 °C, and maintained its mechanical strength up to 300 °C for seal applications, even though slight mechanical degradation occurred at the glass transition point of fluoropolymer, i.e., 220 °C. This new technology is expected to help the heavy-oil industry and petroleum refinery industry to maximize recovery, reduce operating cost, and prevent or mitigate harmful environmental impacts.

References

1. DeBruijn G, Skeates C, Greenaway R, Harrison D, Parris M, James S, Mueller F (2018) High-pressure, high-temperature technologies. Oilfield Rev 20:46–60
2. Xu Z, Zhao L, Ganguly P (2017) Elastic carbon composite and its use as ultrahigh temperature packer element. In: Paper presented at the 20th SPE middle east oil and gas show and conference, Manama, Bahrain, 6 March 2017
3. Xu Z, Zhao L, Prieto C (2017) Ultra-high temperature rated elastic carbon composite packer for reliable downhole zone isolation. In: Paper presented at SPE annual technical conference and exhibition, Dubai, UAE, 26 September 2017
4. Zhao L, Xu Z, He P (2017) Impaction and wear-resistant carbon elastic seal for HTHP downhole valve application. In: Paper presented at SPE Kingdom of Saudi Arabia annual technical symposium and exhibition, Dammam, Saudi Arabia, 24–27 April 2017
5. Ito M, Noguchi T, Ueki H, Takeuchi K, Endo M (2011) Carbon nanotube enables quantum leap in oil recovery. Mater Res Bull 46:1480–1484
6. Endo M, Noguchi T, Ito M, Takeuchi K, Hayashi T, Kim Y, Wanibuchi T, Hiroshi J, Mauricio T, Dresselhaus M (2008) Extreme-performance rubber nanocomposites for probing and excavating deep oil resource using multi-walled carbon nanotubes. Adv Funct Mater 18:3403–3409
7. Zeng D, He Q, Hu J, Shi T, Zhang Z, Yu Z, Liu R (2016) Corrosion mechanism of hydrogenated nitrile butadiene rubber O-ring under simulated wellbore conditions. Corros Sci 107:145–154
8. Flitney R (2007) Seals and sealing handbook. Elsevier Science, Amsterdam
9. Cramer S et al (eds) (2006) ASM handbook, vol 13. Materials Park, OH-ASM International

The Dielectric Behavior in Reduced Graphene Oxide/Polymer Composites with a Segregated Structure

Yonghua Li and Mengkai Li

Abstract Novel composites with a segregated structure have been prepared through coating graphene oxide (GO) on poly(vinylidene fluoride) (PVDF) powders and then were hot pressed at 200 °C for 2 h to form composites. During hot-pressing, the graphene oxide was turned into reduced graphene oxide. The resulting composites with graphene as conductive filler formed a two-dimensional conductive network and exhibited a low value of the percolation threshold. The image of GO-coated PVDF powders was observed by scanning electron microscopy (SEM). The dielectric permittivity of the graphene/PVDF composites as a function of frequency with different graphene volume fraction were shown at room temperature. The composite of filler content 0.263 vol.% exhibits higher dielectric constants (225) and smaller loss factor (7.9) at 1000 Hz.

Keywords Graphene oxide · Composite · Dielectric permittivity
Segregated structure

Introduction

A true two-dimensional material, graphene with high surface area (~2600 m^2/g), high thermal conductivity (~5000 W/(mK)), high Young's modulus (~1 TPa) and fracture strength (~130 GPa), make it very attractive for various applications [1]. Graphene/polymer composites have been much attention in the past few years [2–4]. Graphene nanosheets can significantly improve the physical properties of the host polymer at very low content of conductive filler loading. Poly(vinylidene fluoride) (PVDF) is a semicrystalline thermoplastic polymer with remarkable high

Y. Li (✉)
School of Sciences, Harbin Engineering University, Harbin 150001, China
e-mail: yonghuali@hrbeu.edu.cn

M. Li
College of Materials Science and Engineering, Jilin University, Changchun 130012, China

The Minerals, Metals & Materials Society, *TMS 2018 147th Annual Meeting & Exhibition Supplemental Proceedings*, The Minerals, Metals & Materials Series,
https://doi.org/10.1007/978-3-319-72526-0_74

piezo- and pyroelectric coefficients, excellent thermal stability and chemical resistance. Many researchers have recently devoted to the preparation of high-ε' composites based on PVDF. Nan et al. have first reported on the high-ε' PVDF-based composites fabricated with conductive nickel powders filler [5]. The percolation threshold was 17 vol.% and at low frequency the effective ε' of the composites near the threshold increased to 400. Nanocomposites with larger aspect ratio filler dispersed in PVDF matrix have an ultralow percolation threshold. Zhong et al. have reported reduced graphene oxide (RGO)/PVDF composites prepared with a solution casting approach, which displayed a low percolation threshold 0.18 vol.% and a high-ε' of 340 at 100 Hz near the percolation threshold [6]. Our group reported a simple, environmentally-friendly and practical new method to prepare graphene/polymer composites with a segregated structure, GO coated on PVDF particles and then in situ thermal reduction makes electrically insulating PVDF highly conductive, which can effectively prevent the aggregation of graphene and lower graphene content (the percolation threshold 0.105 vol.%) [7]. Dielectric permittivity of the composites incorporated with conductive fillers can be depicted by the percolation power law [8]. Near the percolation threshold, the dielectric permittivity of the composites underwent a significant change of several orders of magnitude. It can be found that the percolation threshold values obtained from conductivities and dielectric permittivity are the same. A low filler content and high-ε' composite is the goal for some researchers are always seeking. However, there has been no report on the dielectric contents of graphene/polymer composites with a segregated structure.

In this work, we report on the dielectric behavior of RGO/PVDF composites prepared through the solution mixing method. The segregated structure composites with various reduced graphene oxide contents exhibit a typical percolation behavior with a low percolation threshold. The RGO/PVDF composites with the ultralow percolation threshold are very prospective in high energy density capacitors and high technology applications.

Experimental

Go following a modified Hummers method from graphite powders [9]. The dried GO was dispersed in deionized water and exfoliated to graphene oxide by ultrasonication for 3 h to obtain a homogeneous suspension. PVDF powders were added into the suspension, and then mildly stirred at 80 °C. The GO sheets were coated on PVDF powders after a large amount of water was evaporated. In order to remove the residual water the obtained composite powders were kept under the vacuum at 80 °C for 24 h and subsequently hot pressed at 200 °C for 2 h to form the thermally reduced GO/PVDF composites. A GO sheet has also been hot pressed at 200 °C for 2 h, where it lost 43% of the original mass. The volume fractions of RGO were obtained based on the mass loss and the density of graphene ($\rho = 2.2$ g/cm^3) [10]. The morphology of GO coated PVDF powders was observed in a scanning electron

microscope (SEM) (JEOL JSM-6700F). Electrical measurements were performed with a Solartron 1260/1296 in frequency ranging from 10^2 to 10^6 Hz. The disk specimens were coated with silver paste prior to electrical measurements.

Results and Discussion

Figure 1 shows the dispersion of GO on PVDF particles. It can be seen that GO nanosheets are randomly dispersed on the surface of polymer particles. There are some polymer particles are almost entirely covered with GO sheets, at the same time a small number of GO aggregates are also present. Figure 2 reveals the optical pattern of composites with the segregated structure after hot pressing. The initial distribution of GO nanosheets remains essentially unchanged on the boundaries between polymer particles. The white regions are polymer matrices and the black lines are RGO conductive paths. RGO sheets don't equably disperse in the whole polymer matrix, those only distribute on the boundary spaces between polymer particles.

Dielectric properties of the composites are measured by using a Solartron 1260/1296 impedance analyzer. The measurements are carried out in the frequency range of 10^2–10^6 Hz. A parallel combination of a capacitor and a resistor is used as the equivalent circuit model to simulate the behavior of the composites. The complex impedance of the equivalent circuit can be denoted as follows [11]:

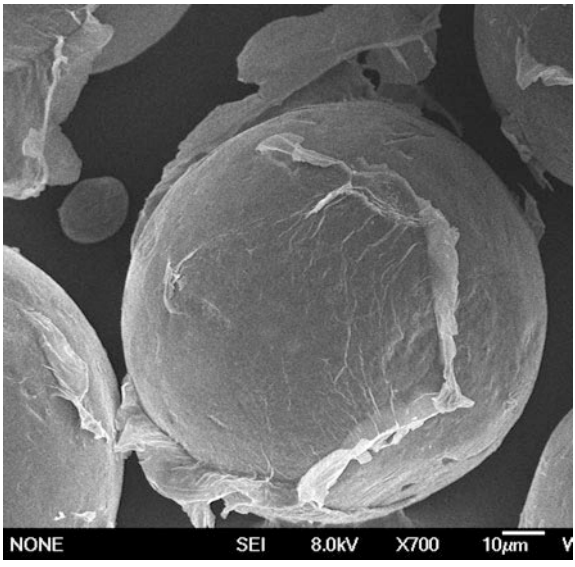

Fig. 1 SEM images of GO-coated PVDF powders

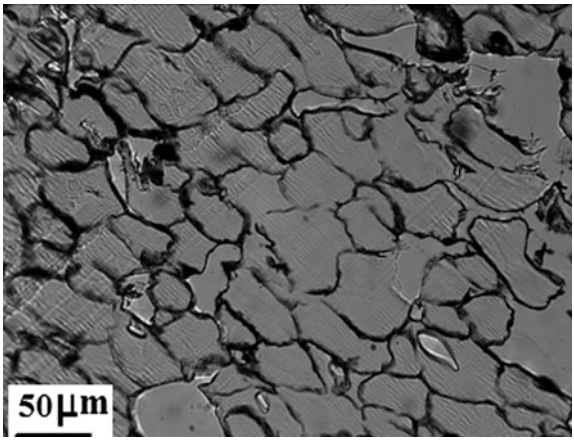

Fig. 2 The optical micrograph of RGO/PVDF composite

$$Z = Z^{'} - jZ^{''} = \frac{1}{\frac{1}{R} + j2\pi fC} \tag{1}$$

where R, f, and C are the resistance of the resistor, the frequency and the capacitance of the capacitor, respectively. The dielectric permittivity $\varepsilon^{'}$, which is also known as the relative dielectric constant, is the real part of the complex dielectric permittivity $(\varepsilon = \varepsilon^{'} - j\varepsilon^{''})$. The loss factor $(\tan\delta = \varepsilon^{''}/\varepsilon^{'})$ is commonly used as a measure of the energy dissipation in a dielectric material. Thus $\varepsilon^{'}$, $\tan\delta$ and the alternating current (AC) conductivity (σ) of the composites can be calculated as follows:

$$\varepsilon^{'} = \frac{Z^{''}}{2\pi fC_0(Z^{'2} + Z^{''2})} = \frac{Z^{''}d}{2\pi fA\varepsilon_0(Z^{'2} + Z^{''2})} \tag{2}$$

$$\tan\delta = \frac{Z^{'}}{Z^{''}} \tag{3}$$

$$\sigma = 2\pi f\varepsilon_0\varepsilon^{''} = \frac{Z^{'}d}{A(Z^{'2} + Z^{''2})} \tag{4}$$

where d and A are the thickness and the surface area of the samples. The dielectric permittivity $(\varepsilon^{'})$, AC conductivity (σ) and loss factor $(\tan\delta)$ of the RGO/PVDF composites as a function of frequency at room temperature are showed in Fig. 3. As expected, dielectric properties of the RGO/PVDF composites reveal a typical percolation transition behavior as the volume fraction of RGO increases. In the studied frequency range of 10^2–10^6 Hz, the dielectric permittivity of pure PVDF material gradually decreases from 9.5 to 7.2 as the frequency increases (see Fig. 3b). It is distinctly observed that the dielectric permittivity of the composites can be

enhanced by filling RGO nanosheets. At low filler content (≤ 0.0986 vol.%), the dielectric permittivity of the composites still exhibits a slow decrease trend along with the increasing frequency and are less than 15 at 100 Hz. When the RGO volume fractions are from 0.267 to 1.61 vol.%, the dielectric permittivity values of composites are from 277 to 940 at 100 Hz and from 225 to 754 at 1000 Hz (see Fig. 3a), which can be well explained by interfacial polarization effect and microcapacitor model [12]. The conductive RGO nanosheets are isolated by insulating PVDF Particles, those form lots of microcapacitor structures throughout the composites. The microcapacitors give rise to a significant increase in the intensity of local electric field, which can further promote the migration and accumulation of charge carriers at the interfaces between the RGO nanosheets and PVDF host. The dielectric constants depended on the frequency should be mainly ascribed to the Maxwell−Wagner−Sillars (MWS) polarization in the low frequency range [13]. MWS interfacial polarization occurs whenever there is an accumulation of charge carriers at an interface between two materials. The free charges in graphene pile up at the interface touch off the strong MWS polarization, and thus lead to the dielectric constant increase. In this context, the permittivity becomes more sensitive to frequency and rapidly decreases with the increasing frequency. The percolation threshold of 0.105 vol.% (t = 1.101) was obtained in the thermal RGO/PVDF composites with a segregated structure [7]. Above the percolation threshold (≥ 0.263 vol.%) the conducting network forms in the PVDF matrix, and the dielectric loss increases markedly with increasing filler content (see Fig. 3c). For composites incorporated with conductive fillers, the dielectric loss is mainly caused by the leakage current in the composites. Higher content of conductive filler could construct more conductive pathways, which leads to more leakage current and dielectric loss. For the conductivity, when the filler contents are below percolation threshold an obvious increase in the conductivity values is observed with the increase of frequency (see Fig. 3d). As the RGO loading exceeds 0.105 vol.%, the conductivity values show typical percolation transition from insulator to semiconductor. At the filler contents higher than 0.105 vol.%, the conductivity exhibits a conducting feature that is hardly affected by the change of frequency.

Figure 4 shows the dielectric permittivity and loss factor of the RGO/PVDF composites as a function of volume fraction of RGO at 10^3 Hz. For the composites incorporated with conductive fillers, by the percolation power law the changes of the dielectric permittivity can be depicted as follows [12, 14, 15]:

$$\varepsilon_{eff} \propto (f_c - f)^{-s} \quad \text{for} f \prec f_c \tag{5}$$

$$\sigma \propto \omega^{u} \quad \text{as} f \to f_c \tag{6}$$

where ε_{eff} is the effective dielectric permittivity of the composite, s is a critical exponent, $\omega = 2\pi f$, u = t/(t + s) is the corresponding critical exponent, f and f_c are the volume fraction of RGO fillers and the percolation threshold, respectively. As can be seen in Fig. 4a, the experimental values of dielectric permittivity of the composite agree with Eq. 5, with s = 0.109 (see bottom-right inset in Fig. 4a). u is

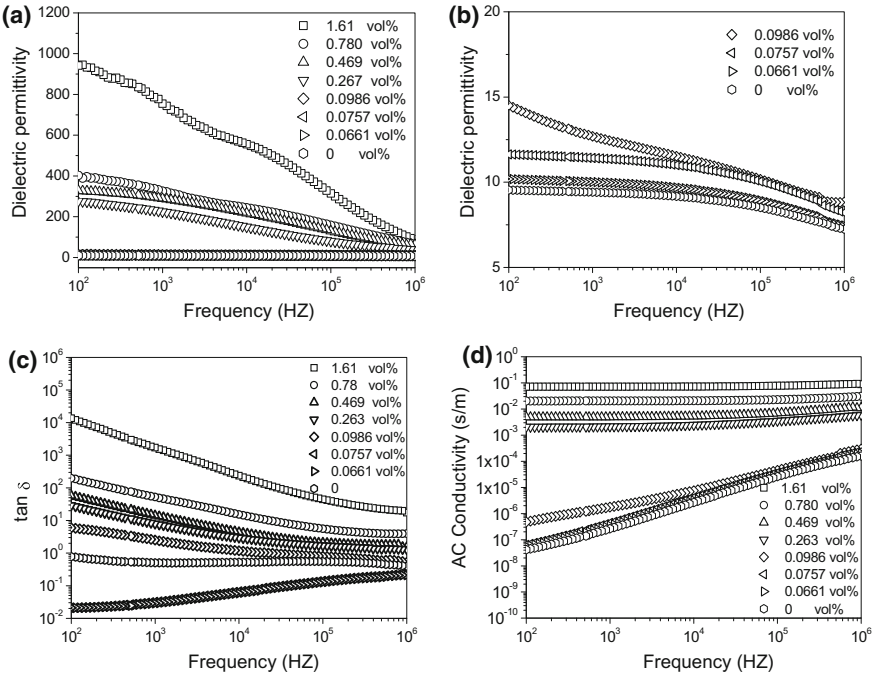

Fig. 3 Dielectric permittivity (ε') (**a** and **b**), loss factor $(\tan\delta)$ (**c**) and AC conductivities (σ) (**d**) of the TRGO/PVDF composites with different volume fraction of RGO as a function of frequency at room temperature

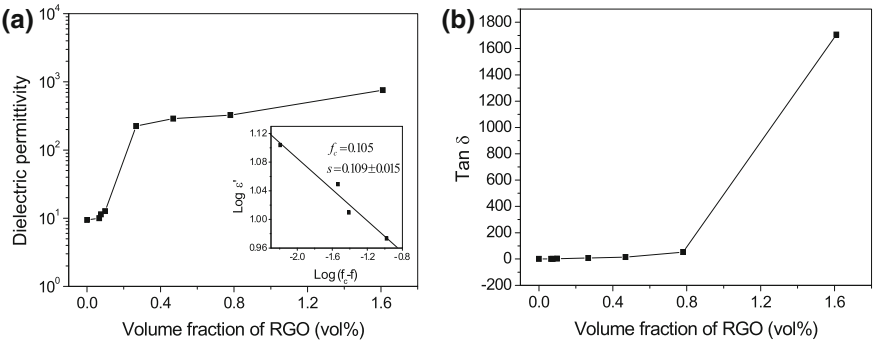

Fig. 4 Dielectric permittivity **a** and loss factor **b** of the RGO/PVDF composites as a function of volume fraction of RGO at 1000 Hz. The insert shows the log–log plot of dielectric permittivity with $f_c - f$ for $f_c > f$

calculated 0.91. The u value is slightly larger than that of Dang et al. reported [16]. From Fig. 4 it is noted that the composite (f = 0.263 vol.%) exhibits higher dielectric constants (225) and smaller loss factor (7.9) at 1000 Hz.

Conclusions

In this study, a new preparation method of RGO/polymer composites with a segregated network structure is demonstrated. The resulting composites with graphene as conductive filler formed a two-dimensional conductive network and exhibited a low value of the percolation threshold. The dielectric properties of the RGO/PVDF composites are measured in a frequency range from 10^2 to 10^6 Hz. A typical percolation transition is observed as the increase of the RGO filler content. The dielectric properties showed a dramatic change as high as several orders of magnitude near the percolation threshold. The RGO/PVDF composite (f = 0.263 vol.%) exhibits higher dielectric constants (225) and smaller loss factor (7.9) at 1000 Hz. This type of RGO/PVDF composites with a low percolation threshold can be potentially applied in high energy density capacitors and high technology applications as novel dielectric materials.

References

1. Zhu YW, Murali S, Cai WW, Li XS, Suk JW, Potts JR et al (2010) Adv Mater 22:3906–3924
2. Kim I-H, Baik DH, Jeong YG (2012) Structures, electrical, and dielectric properties of PVDF-based nanocomposite films reinforced with neat multi-walled carbon nanotube. Macromol Res 20(9):920–927
3. Wang D, Bao Y, Zha J-W, Zhao J, Dang Z-M, Guo-Hua H (2012) Dielectric properties of nanocomposites based on poly(vinylidene fluoride) and poly(vinyl alcohol)-functionalized graphene. ACS Appl Mater Interfaces 4:6273–6279
4. Li YC, Tjong SC, Li RKY (2010) Electrical conductivity and dielectric response of poly (vinylidene fluoride)–graphite nanoplatelet composites. Synth Met 160:1912–1919
5. Dang ZM, Lin YH, Nan CW (2003) Adv Mater 15:1625–1629
6. Fan P, Wang L, Yang J, Chen F, Zhong M (2012) Nanotechnology 23:365702
7. Li M, Gao C, Hongliang H, Zhao Z (2013) Electrical conductivity of thermally reduced graphene oxide/polymer composites with a segregated structure. Carbon 65:371–373
8. Nan C-W (1993) Prog Mater Sci 37:1–116
9. Hummers WS, Offeman RE (1958) Preparation of graphitic oxide. J Am Chem Soc 80 (6):1339
10. Stankovich S, Dikin DA, Dommett GHB, Kohlhaas KM, Zimney EJ, Stach EA et al (2006) Graphene-based composite materials. Nature 442:282–286
11. Wang D, Zhang X, Zha J-W, Zhao J, Dang Z-M, Guo-Hua (2013) Dielectric properties of reduced graphene oxide/polypropylene composites with ultralow percolation threshold. Polymer 54:1916–1922
12. Dang ZM, Wang L, Yin Y, Zhang Q, Lei QQ (2007) Adv Mater 19:852–857

13. He F, Lau S, Chan HL, Fan JT (2009) Adv Mater 21:710–715
14. Wang L, Dang ZM (2005) Appl Phys Lett 87:042903
15. Chiteme C, McLachlan DS (2003) Phys Rev B 67:024206
16. Dang Z-M, Peng B, Xie D, Yao S-H, Jiang M-J, Bai J (2008) High dielectric permittivity silver/polyimide composite films with excellent thermal stability. Appl Phys Lett 92:112910

Part XXXII
Phase Transformations and Microstructural Evolution

Solid State Phase Transformation Mechanism in High Carbon Steel Under Compressive Load and with Varying Cr Percent

Rumana Hossain, Farshid Pahlevani and Veena Sahajwalla

Abstract Low alloyed High carbon steels with duplex (DHCS)s structure of martensite and retained austenite (RA) have considerable potential for industrial application in high abrasion environments due to their hardness, strength and low cost. Using standard compression testing, XRD, nano-indentation, EBSD and TEM, we determined the mechanical stability of RA in DHCS under compressive stress and recognized the phase transformation mechanism, from the macro to the nano level. We found that at the initial stage of plastic deformation both BCT and HCP martensite formation takes place, whereas higher compression loads trigger BCT martensite formation. The combination of this phase transformation and strain hardening is able to increase the hardness significantly. We also investigated the effect of Cr on the transformation behaviour, hardness and mechanical stability of RA with varying Cr contents. Increasing Cr% increased the stability of retained austenite, consequently, increased the critical pressure for martensitic transformation.

Keywords High carbon steel · Solid-state phase stability · Retained austenite Effect of Cr

Introduction

High carbon steel with the martensite and retained austenite (RA) structure is favourable for the extreme operation condition and high abrasion environment due to its high hardness and relatively low cost. The amount and stability of retained austenite in the martensitic steel plays an important role in optimizing the mechanical properties. Changing chemical composition [1], strain partitioning [2], formation of mechanical twinning [3], grain size refinement [4] and martensitic

R. Hossain (✉) · F. Pahlevani · V. Sahajwalla
School of Materials Science and Engineering, Centre for Sustainable Materials Research and Technology, UNSW Sydney, Sydney, Australia
e-mail: r.hossain@unsw.edu.au

The Minerals, Metals & Materials Society, *TMS 2018 147th Annual Meeting & Exhibition Supplemental Proceedings*, The Minerals, Metals & Materials Series,
https://doi.org/10.1007/978-3-319-72526-0_75

transformation [1, 5] due to the solid state compression deformation are linked to the stability of retained austenite and mechanical property of the steel. In this steel, metastable RA transforms to the stable martensite structure when it can pass the required barrier energy. This energy can be achieved through, stress, strain and/or temperature [2, 6]. The strength and ductility of this steel is affected by the phase transformation and strain hardening effect through deformation [7, 8].

Stability of RA is studied by a lot of researcher; however there are few studies in the literature focusing on the stability of retained austenite in the low alloyed high carbon steel, DHCS. The present work is aimed at investigating the mechanical stability of retained austenite grain from macro to nano scale by the standardize compression test on bulk material and nanoindentation technique in individual retained austenite (RA) grains, combined with electron backscattered diffraction (EBSD), X-ray diffraction (XRD), focused ion beam (FIB) milling and transmission electron microscopy (TEM).

Results and Discussion

We investigated 1.0% C DHCS with a mixture of plate and lath martensite and containing ~45–50% retained austenite. Figure 1a shows the EBSD micrograph of the undeformed sample where BCT martensite is shown in red, HCP martensite in yellow and the retained austenite in blue in the phase diagram. The black lines on the maps represent the boundaries, across which misorientation is more than 15°. These EBSD scan were conducted with a pattern binding of 2 × 2, with an integration number of frames of 10 for 25 kV and that the step size chosen was 50 nm. The kernel average misorientation (KAM) of the undeformed steel sample is also presented here which shows higher misorientation in the close vicinity of martensite boundaries.

We designed a standardize compression test in the small sizes (4 mm × 4 mm × 4 mm) samples at room temperature with an Instron 8510 instrument operating at 0.10 mm/min cross-head speed. Figure 1b, c shows the EBSD results for the samples at 2000 and 3500 MPa compression. The results revealed both the transformation of RA to martensite and the generation of smaller martensitic grains. The corresponding XRD patterns revealed that, after deformation, there are variations in the peak intensities and a deformation-induced phase transformation occurred as evidenced by a more prominent BCT α′-martensite peak and a reduced γ-austenite peak. It is worth noting that at moderate compression deformation, both BCT α′-martensite and HCP ε-martensite formation triggered. However, at larger strain due to higher compressive load only BCT α′-martensite formation dominates. More misorientation was observed while the sample was induced to more load. As the compression load increases the misorientation angle becomes high enough to form new grain boundaries which further reduces the misorientation in the microstructure (Fig. 1b2, c2). The sample hardness increases with increasing martensitic volume fractions because the martensitic structures act as a barrier to

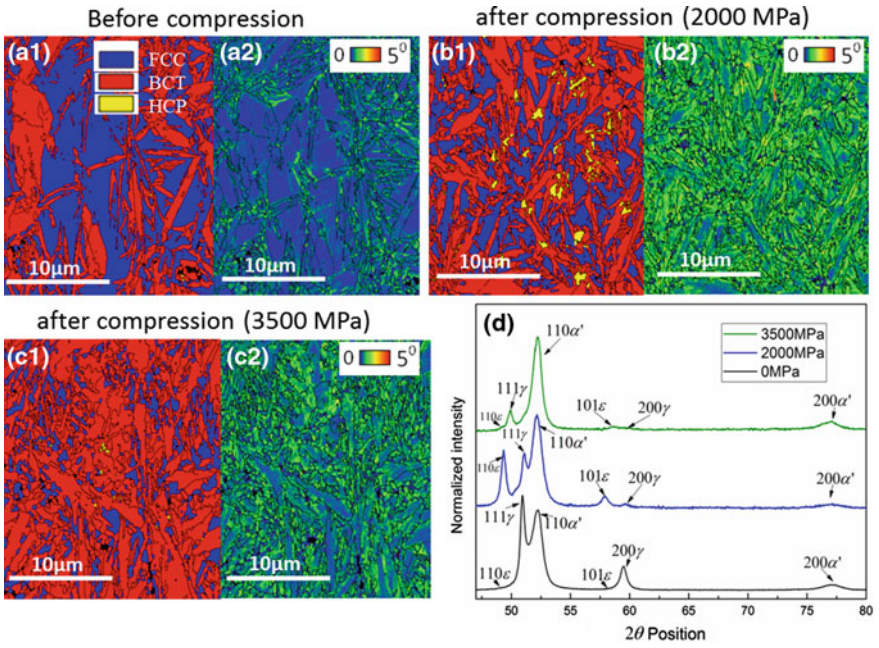

Fig. 1 EBSD patterns of studied materials; Phase map and KAM (**a**) without compression and compressed at **b** 1000 MPa and **c** 3500 MPa. **d** XRD spectrum of sample with and without compression deformation

dislocation movements. Refined grains also can strengthen the microstructure. Before compression deformation the overall hardness measured in the sample was ~7.51 GPa which was increased after compression deformation and calculated to be ~9.76 GPa in a micro Vickers hardness tests performed at 0.2 HV load.

A nano indentation investigation on the individual austenite grain was performed to identify the phase transformation phenomena at the nano level. Nano-indentation tests were carried out in load control mode on a TI 900 Hysitron Tribolab system with a Berkovich three-sided pyramidal diamond tip indenter with a tip radius of 100 nm. It is possible to detect the position of each indent by EBSD micrograph, Fig. 2a shows that after the indentation the austenite grain was transformed to martensite within the close vicinity of the indentation mark and the transformation process was observed by several pop-in as marked with arrows in the P-h curve (Fig. 2b). After using focused ion beam (FIB, XT Nova Nanolab 200, at 30 kV) to prepare the sample a further TEM micrograph and SAD pattern by a Philips CM 200 with a field emission gun reveals clear martensitic transformation due to the indentation load. It is also possible to identify the critical force (Pc) for the martensitic transformation at the nano level due to the indentation. The first pop-in in the elastic plastic regime of the P-h curve shows the critical load for the

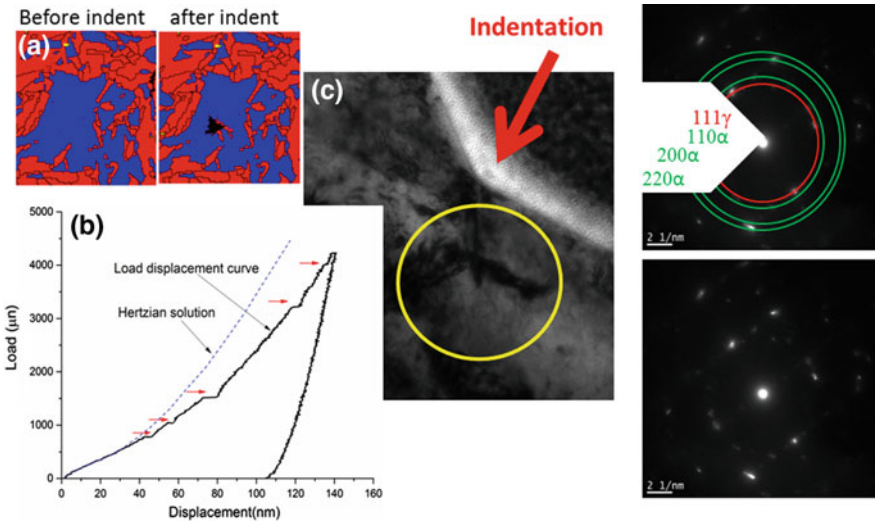

Fig. 2 **a** The EBSD phase map of austenite grain before and after nano-indentation. **b** Nano-indentation load displacement curve of corresponding indent. The red arrows are indicating pop-ins during nano-indentation and blue dashed line represents the calculated Hertzian elastic contact solution. **c** Bright field TEM image and SAD pattern showing existence of α′ martensite and retained austenite at spot

martensitic transformation which is an indicative of the stability of retained austenite at the nano level [5, 9].

Some of the elements within steel have the effect on the stability of the retained austenite, i.e. C, Mn, Cr [5, 10] etc. This research investigated steels with varying chromium contents in chemical composition. To keep the steel cost effective for industrial applications we varied the Cr percentage within a smaller range to design and characterize low cost low alloyed high carbon steel. Chromium addition caused an increase in the eutectoid temperature and a drop in the eutectoid carbon content. Therefore, Manganese content was adjusted to offset these effects. By adding Cr it is possible to prevent the corrosion and oxidation and enhance the higher temperature strength [11]. For this purpose we designed three steel samples with varied Cr% within the range of 0.10–2.5%. The samples selected had similar retained austenite in order to establish the effects of chromium on the solid-state transformation of retained austenite. Nano indentation load displacement curve of individual austenite grains from 3 samples are presented in Fig. 3. The results revealed that the increased Cr% contributed to the higher mechanical stability of the austenite grains; i.e. the sample having lower Cr% (0.1–0.18% Cr) has lower critical load which was ~900 μN and for the higher Cr sample (0.6–0.8% Cr), it was ~6000 μN. At the same nano-indentation load, 8000 μN, the hardness measured 8.3, 7.5 and 6.1 GPa for low (0.1–0.18%), medium (0.6–0.8%) and high (1.8–2.5%) Cr samples within this short range. For the increased Cr% the austenite grain resists more for the transformation process. In the lower Cr sample, the stability of the retained

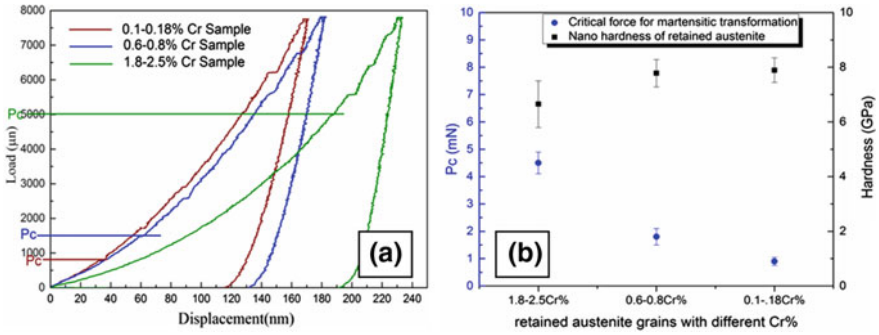

Fig. 3 **a** Load displacement curves by nano indentation in austenite phases for three samples. Pc indicates the critical load for martensitic transformation. **b** The average critical loads for martensitic transformation and corresponding hardness of austenite phases in the samples. This statistics are the summarization of alteast 50 indents on austenite phase for each samples

austenite is less and it transforms more to the martensite. As martensite is harder than the austenite phase, more martensitic transformation leads to elevated hardness. This is the reason behind the hardness variation in the retained austenite with varied Cr%. In this study, the average hardness of retained austenite was calculated 6.95 GPa in sample with 1.8–2.5% Cr; 7.78 GPa in sample with 0.6–0.8% Cr and 7.89 GPa in sample with 0.1–0.18% Cr respectively by the nano indentation investigation. Nevertheless, the actual hardness of austenite should be lower. Martensitic transformation increased the nano-hardness of retained austenite.

In the current study we have described comprehensively the effect of external compressive stress on martensitic transformations and grain size refinement, effect of Cr% on retained austenite stability within a small range. Such understanding is critical for controlling the microstructure, hardness and mechanical stability of DHCS to design it as a low cost low alloyed steel for industrial applications.

Conclusion

In the present work, the mechanical stabilities of metastable retained austenite in high-carbon steel were investigated by using a combination of standardize compression test, nano-indentation, EBSD, FIB and TEM. The results revealed that, it is possible to increase the hardness of DHCS through the combination of phase transformation, grain refinement and strain hardening by compression deformation. The effect of varied Cr% was also described which demonstrated that by increasing the Cr%, the stability of retained austenite was increased, consequently, the critical pressure for martensitic transformation was also increased. This study makes a significant and important contribution to our understanding on DHCS, thereby potentially opens new scopes of applications and replace more expensive high alloy

grade steels. This could increase the usage of cost-effective high carbon steels in industry, with significant flow on benefits for businesses and economies.

References

1. Hossain R et al (2016) Stability of retained austenite in high carbon steel under compressive stress: an investigation from macro to nano scale. Sci Rep 6
2. Ryu JH et al (2010) Strain partitioning and mechanical stability of retained austenite. Scr Mater 63(3):297–299
3. He B, Luo H, Huang M (2016) Experimental investigation on a novel medium Mn steel combining transformation-induced plasticity and twinning-induced plasticity effects. Int J Plast 78:173–186
4. Lee S, Lee S-J, De Cooman BC (2011) Austenite stability of ultrafine-grained transformation-induced plasticity steel with Mn partitioning. Scr Mater 65(3):225–228
5. Hossain R, Pahlevani F, Sahajwalla V (2017) Effect of small addition of Cr on stability of retained austenite in high carbon steel. Mater Charact 125:114–122
6. Bhadeshia H (1981) Driving force for martensitic transformation in steels. Metal Sci 15(4): 175–177
7. Olson G, Cohen M (1982) Stress-assisted isothermal martensitic transformation: application to TRIP steels. Metall Mater Trans A 13(11):1907–1914
8. Zaefferer S, Ohlert J, Bleck W (2004) A study of microstructure, transformation mechanisms and correlation between microstructure and mechanical properties of a low alloyed TRIP steel. Acta Mater 52(9):2765–2778
9. He B et al (2013) Nanoindentation investigation on the mechanical stability of individual austenite grains in a medium-Mn transformation-induced plasticity steel. Scr Mater 69(3): 215–218
10. Qiao X et al (2015) Nano-indentation investigation on the mechanical stability of individual austenite in high-carbon steel. Mater Charact 110:86–93
11. Davis JR et al (1990) Metals handbook: irons, steels, and high-performance alloys. Properties and selection. ASM International

Microstructure Characterization of Aged Heat Resistant Steels

Maribel L. Saucedo-Muñoz, Arturo Ortiz-Mariscal, Victor M. Lopez-Hirata, Jose D. Villegas-Cardenas and Ana Maria Paniagua-Mercado

Abstract The precipitation evolution was studied experimentally and numerically during aging of as-cast heat resistant steel at 700, 800 and 900 °C. Thermo-Calc result showed a good assessment of the non-equilibrium phases for as-cast HK40 steels in comparison to the experimental results. In contrast, the Time-Temperature-Precipitation diagram for the $M_{23}C_6$ precipitation calculated with PRISMA showed a good agreement with the experimental growth kinetics precipitation for the steel after aging at 700, 800 and 900 °C.

Keywords Carbide precipitation · Isothermal aging · As-cast Heat resistant steels

Introduction

Heat-resistant type steels are used usually in the as-cast condition and they were developed to be used at high temperatures of 700–900 °C for prolonged times. This exposure may cause the deterioration of microstructure [1]. For instance, HK40 and HP40 steels are examples of heat resistant steels which have been applied to fabricate different industrial components [2]. These components may failure because of creep damage, metal dusting creep fatigue and the presence of brittle phases, among other causes [3–5]. The microstructure changes usually occurs during heating of these steels [4]. Several works [6, 7] have been conducted to study the microstructure evolution in this steel. Thermo-Calc softwares [8] have been utilized successfully to analyze not only the phase stability in the equilibrium and non-equilibrium (as-cast) conditions, but also the precipitation kinetics in different alloys at the service temperatures. PRISMA software permits to calculate

M. L. Saucedo-Muñoz · A. Ortiz-Mariscal · V. M. Lopez-Hirata (✉)
J. D. Villegas-Cardenas · A. M. Paniagua-Mercado
Instituto Politécnico Nacional (ESIQIE-ESFM), UPALM Edif. 7,
Mexico City 07300, Mexico
e-mail: vlopezhi@prodigy.net.mx

The Minerals, Metals & Materials Society, *TMS 2018 147th Annual Meeting & Exhibition Supplemental Proceedings*, The Minerals, Metals & Materials Series,
https://doi.org/10.1007/978-3-319-72526-0_76

numerically the growth kinetics of precipitation and the precipitation results can be summarized in Time-Temperature-Precipitation TTP diagram. Thus, the purpose of the present work is to analyze microstructural and numerically the formed phase in two heat-resistant steels, HK40 and the precipitation evolution during the isothermal aging at 700, 800 and 900 °C for different times.

Experimental Procedure

The chemical composition of the HK40 steel is shown in Table 1. Specimens of approximately 10 × 10 × 10 mm were cut from the cast ingot. These specimens were aged at 700, 800 and 900 °C for times up to 2000 h in an electric tubular furnace. The as-cast and aged specimens were prepared metallographically, etched with Kalling etchant, and then observed with both light (LM) and scanning electron (SEM) microscopes. Energy-Dispersive X-ray (EDX) analysis was used to determine the chemical composition of some precipitates in the steel specimens. Some specimens were also analyzed by X-Ray Diffraction (DRX) with Cr Kα radiation.

Precipitate size was determined using SEM micrographs with a commercial software installed in a PC. A Thermo-Cal and PRISMA analyses were conducted for the phase formation and precipitation of HK40 [9].

Results and Discussion

Microstructural Characterization of Precipitation

Figure 1 shows the SEM micrographs of the microstructure evolutions for HK40 steel aged at 700, 800 and 900 °C for times up to 1500 h. SEM micrograph of as-cast steel indicates the presence primary carbides in the interdendritic zones and dendrites of the austenite matrix This primary carbides show an interlamellar morphology because they are formed by a eutectic reaction, as will be explained later. XRD diffractogram is shown in Fig. 2 for as-cast steel and it indicates the presence of XRD peaks corresponding to the austenite matrix and M_7C_3 carbides.

The aging process causes the precipitation of secondary carbides in the austenite matrix. These carbides have a cuboid morphology at the beginning of aging and it changes to rectangular plates with aging time. These plates show a crystallographic alignment with the austenite matrix [10]. The size of precipitates increases with aging time and temperature, as shown in Fig. 3. The coarsening process of

Table 1 Chemical composition in wt% of steel

Steel	C	Mn	Si	Cr	Ni	Nb	Ti
HK40	0.40	1.50	1.60	25.00	20.00	–	–

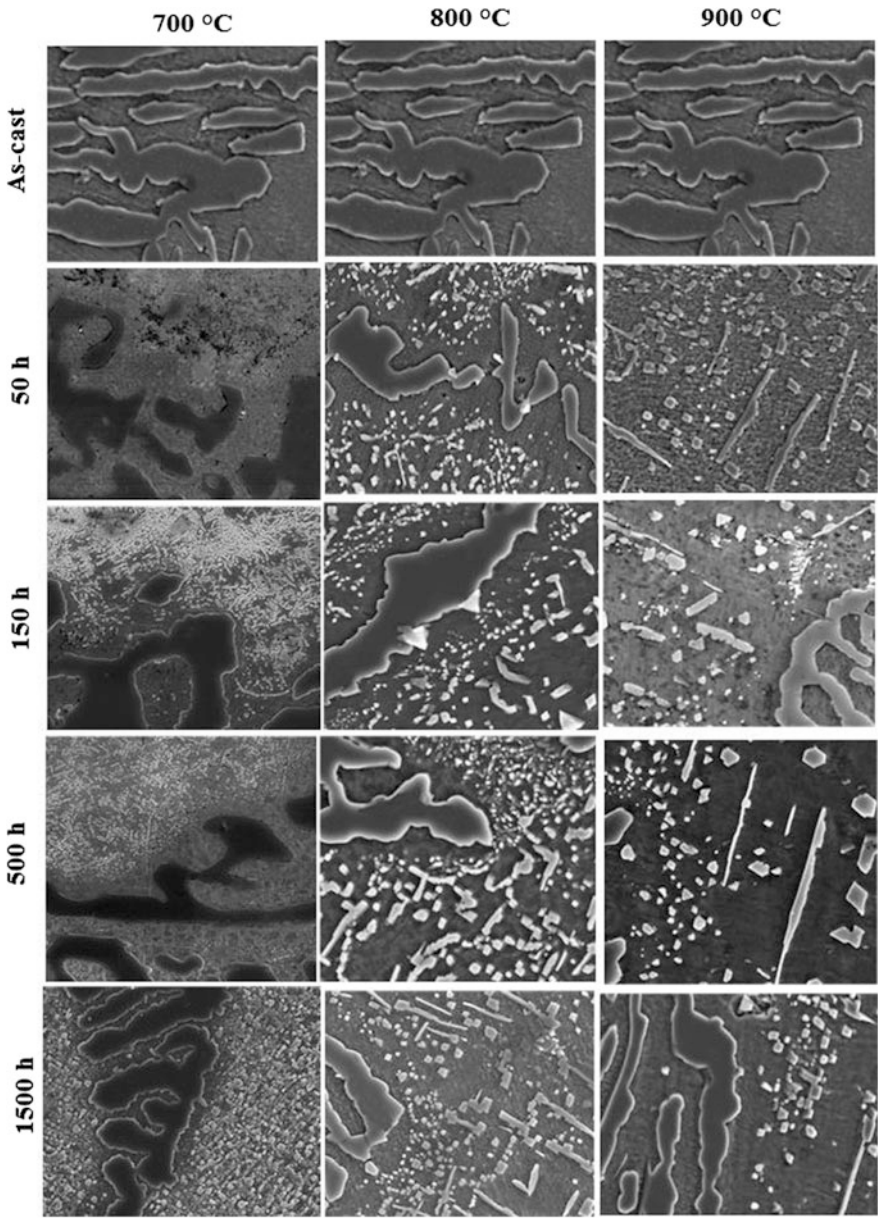

Fig. 1 SEM micrographs of the aged at 700, 800 and 900 °C for different times

secondary carbides is notorious during aging at 800 and 900 °C for long aging times. The decrease in the density of precipitates is clearly observed for these cases. Figure 5 shows the variation of radius to cube versus aging time having a linear

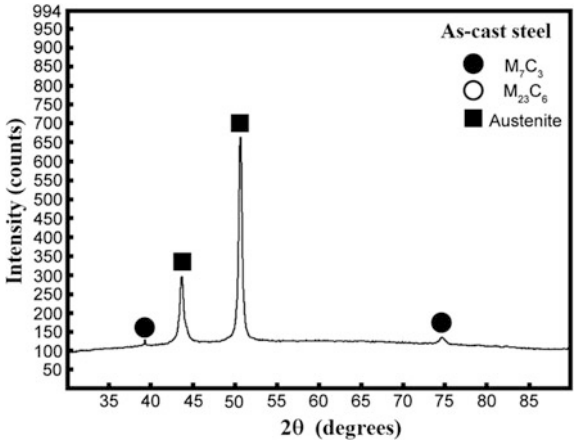

Fig. 2 XRD diffractogram of the as-cast steel

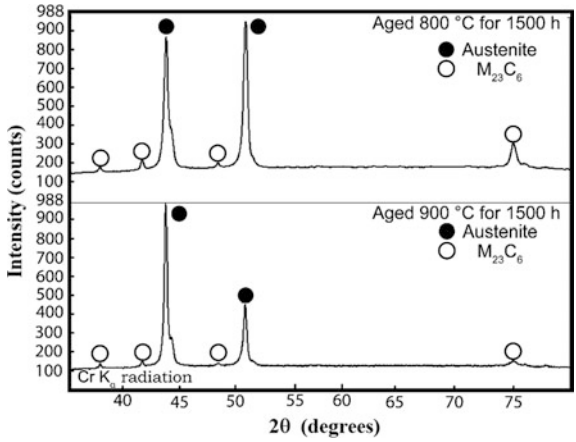

Fig. 3 XRD diffractograms of the steel aged at 800 and 900 °C

dependence which suggests that the coarsening of secondary carbides is a diffusion-controlled process as predicted by the Lifshitz-Slyozov-Wagner theory [11]. The primary carbides are observed to be gradually dissolved with aging time. XRD diffractograms for the specimens aged at 800 and 900 °C for 1500 h, as shown in Fig. 3, which indicates that the precipitates correspond to $M_{23}C_6$ carbides for both specimens.

The EDS-SEM element mapping images of the steel in the condition of as-cast and aged at 700 °C for different times is shown in Fig. 4. This figure shows clearly that the primary carbides are mainly composed of Cr; however, the presence of Mn is also noted. The chemical composition of secondary carbides is not clearly distinguished in Fig. 4. Nevertheless, SEM-EDS analysis reveals that are mainly composed of Cr and Fe.

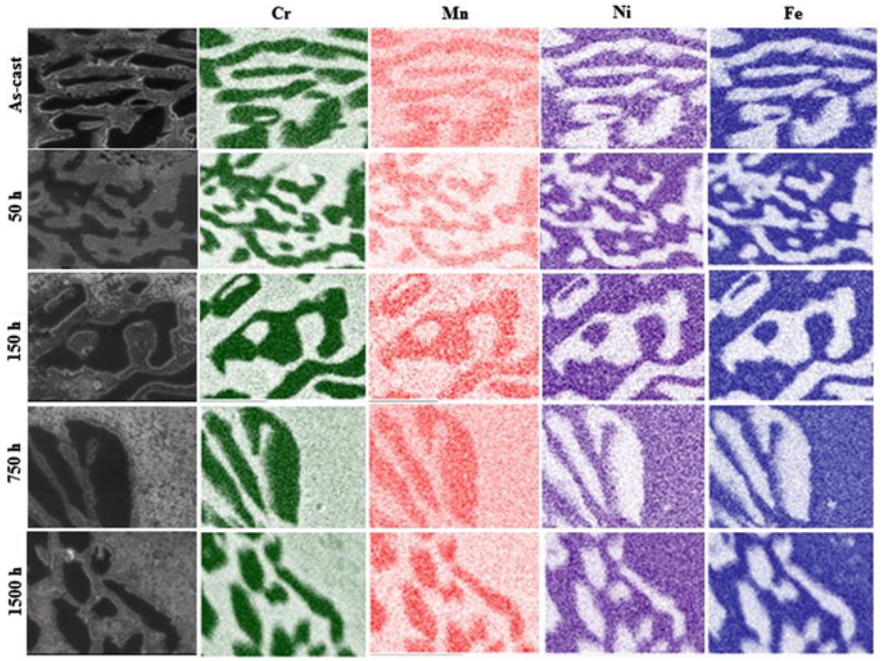

Fig. 4 EDS-elemental mapping for the as-cast steel and aged at 700 °C for different times

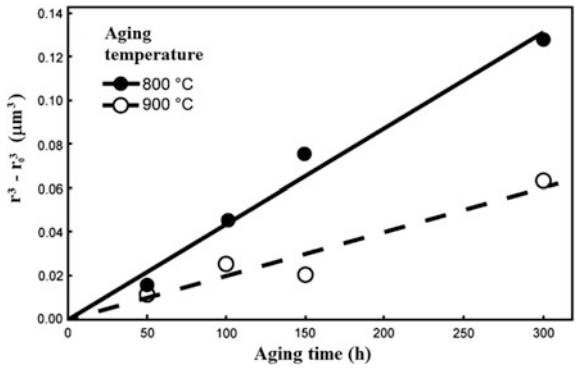

Fig. 5 Plot of r^3 versus aging time for the steel aged at 800 and 900 °C

The previous characterization results point out that the secondary $M_{23}C_6$ carbides are formed by the following precipitation reaction:

$$\gamma \rightarrow \gamma + M_{23}C_6 \tag{1}$$

That is the formation of $M_{23}C_6$ precipitates is useful to increase the creep strength of the steel when is in-service operation at high temperatures.

Thermo-Calc and PRISMA Analysis

The analysis of solidification for the steel was carried out based on the Scheil-Guiliver equation [8]. This analysis permits to determine the non-equilibrium phases formed during the alloy solidification. For instance, Fig. 6 shows the plot of temperature against the mole fraction of all phases. This figure indicates that the first solid phase is the austenite (FCC_A1#1 in Thermo-Calc designation) dendrites and subsequently the primary carbide M_7C_3 is formed following the eutectic reaction: $L \rightarrow \gamma + M_7C_3$. Furthermore, Themo-Calc predicts that the eutectic reaction takes place at approximately 1260 °C which is in good agreement with the literature [6]. The presence of this lamellar microconstituent is also observed in as-cast steel, Fig. 1. Thermo-Calc also shows that the carbides are not only formed by C, but also Mn content is also present which is in agreement with Fig. 4. As the temperature decreases, Fig. 6 shows that the M23C6 can precipitate from the supersaturated austenite matrix. The delta ferrite phase (BCC_A2) can also be present at low temperatures in a low volume fraction. This phase was not detected by XRD analysis of Fig. 2.

Figure 7 shows the equilibrium isoplethic or pseudobinary Fe-Cr phase diagram calculated by Thermo-Calc. This diagram shows clearly that the γ austenite and $M_{23}C_6$ carbides (FCC_A1#1 and M23C6) are the equilibrium phases expected for the steel composition at temperatures between 700 and 900 °C. These phases are consistent with the phases detected in the steel aged at 800 and 900 °C for 1500 h. This also confirms the precipitation reaction, as described previously.

TC-PRISMA [8, 12] enables us to calculate the Time-Temperature-Precipitation TTP diagram of $M_{23}C_6$ carbide precipitation for this steel. The chemical composition of the austenite phase was calculated by Thermo-Calc using the Scheil module. This is very close to that of the real alloy composition. Additionally, the interfacial energy between γ and $M_{23}C_6$ was considered to be about 0.23 J/m^2, according to the literature [12].

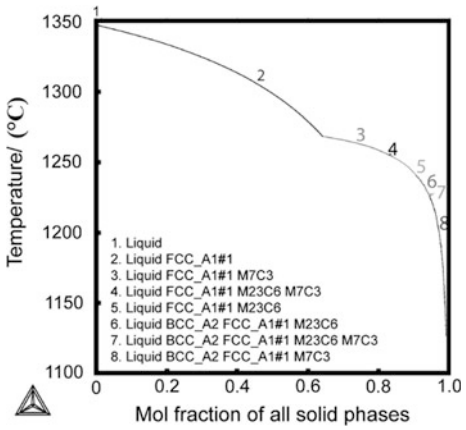

Fig. 6 Thermo-Calc calculated plot of temperature against mole fraction of the all solid phases calculated for the steel

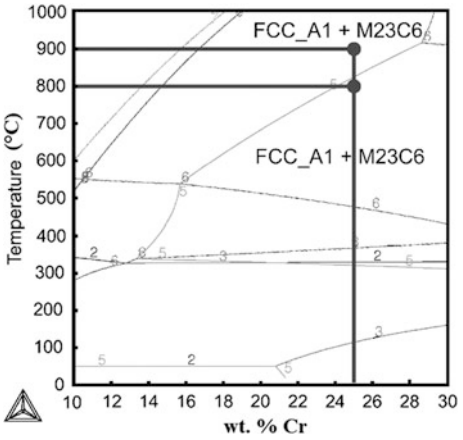

Fig. 7 Thermo-Calc calculated equilibrium pseudo binary Fe-Cr phase diagram of the steel

TC-PRISMA solves numerically the equation of the modified Langer-Schwartz theory [11] which consider that the nucleation, growth and coarsening of precipitates is concomitant. The solution can be completed using the N-model of Kapmann and Wagner [11]. The precipitation was considered to be a homogeneous nucleation process (bulk nucleation). TTP diagram is presented in Fig. 8 which indicates that the nucleation and growth kinetics of M23C6 precipitation in the austenite matrix occurs more rapidly at about 880 °C which is consistent with SEM microstructure of Fig. 1 which shows a faster kinetics of precipitation at about 900 °C than that of the other two temperatures, 700 and 800 °C.

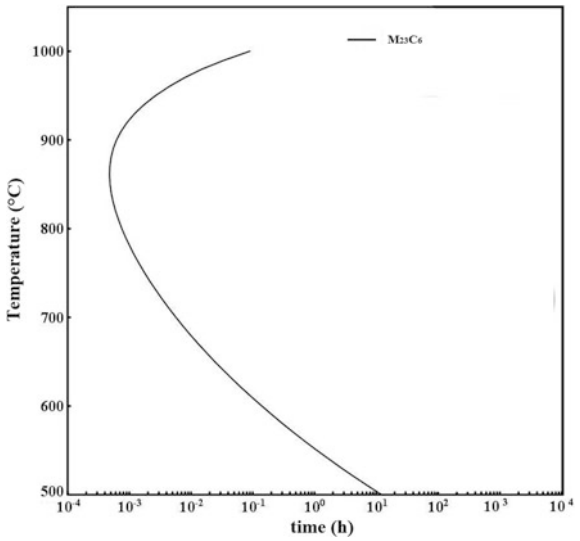

Fig. 8 TTP diagram of $M_{23}C_6$ precipitation for the steel

Conclusions

Thermo-Calc analysis of as-cast HK40 steel assessed correctly the non-equilibrium formed phases. These are mainly M_7C_3 carbides and austenite. Aging treatment at temperatures of 700, 800 and 900 °C for different times promoted the precipitation of $M_{23}C_6$ in the austenite matrix. PRISMA calculated TTP diagram for the $M_{23}C_6$ precipitation is consistent with the SEM observations of the aged steel.

Acknowledgements The authors wish to thank the financial support from SIP-COFAA-IPN and CONACYT.

References

1. Kaya AA (2002) Microstructure of HK40 alloy after high temperature service in oxidizing/carburizing environment, I. Oxidation phenomena and propagation of a crack. Mater Charact 49:11–21
2. Liu J, Jiao D, Luo C (2010) Microstructural evolution in austenitic heat-resistant cast steel 35Cr25Ni12NNbRe during long-term service. Mater Sci Eng A 527:2772–2779
3. Haro S, Lopez D, Velasco A (2000) Microstructural factors that determine the weldability of a high Cr-high Si HK40 alloy. Mater Chem Phys 66:90–96
4. Babakr AM, Al-Ahmrai A, Al-Jumayiah K (2009) Failure investigation of a furnace tube support. J Fail Anal Preven 9:16–22
5. ASTM Standard A351/A351 M–03 (2004) Standard specification for casting, austenitic, austenitic-ferritic (duplex), for pressure-containing parts. ASTM
6. Coreño-Alonso O, Duffus A, Sanchez C (2004) On the effect of σ-phase formation during metal dusting. Mater Chem Phys 84:20–28
7. Almeaida LH, Freitas A, Le May I (2003) Microstructural characterization of modified 25Cr-35Ni centrifugally cast steel furnace tubes. Mater Charact 49:219–229
8. Andersson JO, Helander T, Höglund L, Shi P, Sundman B (2002) Themo-Calc and Dictra. Comput Tools Mater Sci Calphad 26:273–312
9. Thermo-Calc software 2016b/tcfe7.tdb and mobFe2.ddb data
10. Kegg GR, Silcock JM (1972) The shape of M23C6 particles. Scr Metall 6:1083–1086
11. Kostorz G (2001) Phase tranformation in material. Wiley-VCH, Germany, pp 309–408
12. Pellizari M (2010) Thermodynamic modelling for the alloy design of high speed steels and high chromium cast irons. Mater Tech 44:121–127

Sublimation and Self Freezing of Planar Surfaces in Rarefied Atmospheres

Rahul Basu

Abstract A simulation of phase transformations in planar geometries under various boundary conditions is performed. The case of ablation accretion self-freezing under rarefied atmospheres application of external heating is looked at for the ice-water-vapor naphthalene systems. Consideration of ablation is important in applications with space shields in space flight under radiation heat sources along with near vacuum conditions. Recent Noninvasive methods in cryogenic surgery also rely on the production of extreme cold in subcutaneous layers by surface ablation. In this paper sample calculations for water-ice naphthalene give the velocities of the freezing vaporization fronts under various parameter combinations assuming isotropic properties in each phase. It is shown that considerable difference exists between the cases of self-freezing ablation accretion. For instance in the case of water rates of self- ablation without heat sources self-accretion (as in the formation of ice crystals directly from vapor) differ by an order of Magnitude.

Keywords Self-freezing · Sublimation · Ablation · Moving boundary problem

Nomenclature

A,B,C,D,E	Constants
D	Differential operator
a(t),R(t)	Interface position with time
g	Thermal concentration gradient
c	Concentration
K	Diffusivity
k	Conductivity
L	Latent heat of transformation (melting or vapourization)
Q	Heat sink/source strength

R. Basu (✉)
Adarsha Institute of Technology, Off Intl Airport Road, Kundana, Bangalore 562110, India
e-mail: raulbasu@gmail.com

The Minerals, Metals & Materials Society, *TMS 2018 147th Annual Meeting & Exhibition Supplemental Proceedings*, The Minerals, Metals & Materials Series,
https://doi.org/10.1007/978-3-319-72526-0_77

r	Radius
s, r	Coordinates in rectilinear and cylindrical, or spherical coordinates
t	Time
u,v	Temperatures
α	Eigenvalue for the position of interface
μ	Inverse Stefan parameter
ε	Remelt, porosity term
ρ	Density
θ	Non dimensional temperature
Θ	Non dim initial temperature
η	Fourier number (non dimensionalised time/distance)
Fo	Fourier number
Bi	Biot number
Ste	Stefan number (latent heat/sensible heat)
erf	Error function
grad	Gradient function, Ei exponential integral function

Introduction

The ice-vapor and naphtha-vapor sublimation cases which are of theoretical and practical interest are simulated. Sublimation involves a direct transformation from solid to vapor. No liquid phase is produced; the latent heat of sublimation can be estimated by summing the heats for melting, thermal heat to go up to vaporization and the latent heat of vaporization. The cases of self-sublimation without any heat source are also examined.

Practical instances of sublimation exist in space vehicles operating in cold regions of space under near vacuum, production of whiskers and preservation of food and artifacts by treatment in a vacuum. Naphtha is of interest as it is used in experimental flow studies as a tracer, as it sublimes at room temperature. A further interesting feature of Naphtha is the observation that it condenses in the form of needles. This fact prompts the subsequent modeling and simulation of sublimation from a general surface (plane or spherical) and condensation as solid in the form of cylinders. One further difficulty is the determination of the physical constants of heat transfer for Naphtha. The heat and mass transfer analogy is used as one way out of this difficulty, Cho and Goldstein [1]. Naphthalene is used in flow studies and has been described by Haring et al. [2] and de Souza-Mendes [3] with the mass transfer analogy. Naphthalene sublimation has been analyzed with neural and evolutionary models by Curteanu et al. [4], for optimal sublimation rates. Its use has also been reported for electronic cooling to obtain accurate heat transfer rates by Schmidt [5].

As a physical phenomenon, ablation is important in applications for space shields in space flight under radiation and heat sources along with near vacuum

conditions. Naphthalene has found application as a tracer in various experiments. Carbon composites and various allotropes of Carbon have been developed especially for Nano technology. The different structures and allotropes of Carbon allow for much scope and latitude in the design and fabrication of novel products. In this paper, sample calculations for naphthalene give the velocities of the freezing and vaporization fronts under various parameter combinations. It is found that considerable difference exists between the cases of self-freezing, ablation, and accretion. However, the data for diamond is scarce. Diamond films are much sought after for various technological reasons, a model for deposition directly from vapor is therefore of value.

The coupled diffusion equations and are usually solved numerically. In order to study stability, a criterion is developed using the linearised equations. The main controlling factor is the motion of the interface and the energy flux across this boundary, and whether the velocity of movement allows for the flux to be sustained. After linearising, a transform is applied to decouple the concentration (mass) and heat terms, giving an exact as also perturbation solutions in terms of a small parameter using the Stefan number.

The usual coupled equations are given by the heat equation coupled with the remelt terms which add a heat source, and the concentration or mass transfer equation. The decoupling is through a variable $Z = \Theta + \beta C$, the decoupling constant β allows a diffusion equation in Z to be solved, and subsequently, the individual heat and concentration terms can be extracted from this solution.

Equations for the Thermal Mass Coupled Problem

Let α_m = mass diffusivity, α_I = thermal diffusivity in region i, ε = porosity, ρ = density

$$\mathrm{Cp} = \mathrm{sp.heat},\ \mathrm{U} = \mathrm{non-dim\ conc}, \tau = \text{ time}, \alpha\tau/r^2 = \mathrm{Fo} = \mathrm{Fourier\ no}, \alpha_{12} = \alpha_1/\alpha_2 \tag{1}$$

Generic Solutions are given in Paterson [2] as:

$$\text{Linear: } \theta = \text{Constant}^* \operatorname{erf}\{(r + B)/[2\,\mathrm{sqrt}(K(t + E))]\} + \text{constant} \tag{2}$$

$$\text{Cylindrical: } \theta = \text{Constant}^* \mathrm{Ei}[-r^2/(4K(t + B)] + \text{constant} \tag{3}$$

Spherical:

$$\theta = \text{Constant}^* [(K(t + B)]^{0.5}/r \exp(-r^2/(4K((t + B)) - \pi^{0.5}/2\,\mathrm{erfc}(r/2\left(K(t + B)^{0.5}\right) + \text{Constant} \tag{4}$$

Thermal balance across the phase interface boundary requires

$$K_1 d\theta_1/dt - K_2 d\theta_2/dt = \rho L(ds/dt) \tag{5}$$

where s(t) is the interface position.

(Here erf is the error function, Ei the error integral function).

In particular, papers appearing on self-freezing and sublimation are rare.

Sublimation or Ablation of Various Shapes

The sublimation and ablation case is tackled by utilizing the latent heat as the driving force, without any separate heat source or sink in the above equations, i.e. Q is zero, and the sign of L chosen appropriately. Sublimation is important when transformations occur in near vacuum. The shapes of practical interest are the sphere and the plane. The sublimating sphere (directly to vapour, without liquefying first) can be tackled mathematically with appropriate boundary conditions, making use of material constants in the balance equations [5].

An artifice is used to reduce the spherical case to the planar or the one-dimensional case, as given by Crank [6]. Let T = U/r, then the spherical diffusion equation transforms to the familiar one-dimensional case, the solutions of which can be written:

$$(T - To)/(T1 - To) = (a/r)\mathrm{erfc}(r - a)/2\mathrm{Sqrt}(Dt). \tag{6}$$

Since the calculations start at r = a, the boundary condition at r = 0 is avoided.

To is the initial temperature at r > a, and r = a maintained at T1. If one keeps to finite radii and avoids the singularities at the origin, these three scenarios can be represented by these formulae. In the present case, let us look at the spherical case: By means of the transform U = Tr, both the spherical and rectilinear cases can be represented by the erf formula, with the small change that for the spherical case, the erf is divided by r.

The output of the erf and the erf/r functions is

$$T = To + (T1 - To)\ \mathrm{erf}(\eta) \tag{7}$$

$$T = To + (T1 - To)\ (a/r)\ \mathrm{erf}\{(r - a)/2\mathrm{sqrt}(Dt)), \tag{8}$$

These are the equations for the planar 1 D geometry, which are the same for the spherical case with appropriate change in functions. In the computations that follow, Eq. (4) was used without the [erf/r] term as in Eq. (9).

The change of variables θ = Tr allows one to convert the spherical to the rectilinear case. Using typical values for water vapour as: density $\rho = 1.694$ kg/m^3 at 1 bar, diffusivity $K = 2.338 \times 10^{-5}$ m^2/s, conductivity varying from 0.016 to

0.0248 W/m/K, L (latent heat) = 540 cal/gm. With the reaction driven by the heat of sublimation which is 540 + 73.6 + 100 = 713.6 cal/gm, a WOLFRAM calculation was performed.

It was found that for sublimation in the adiabatic case, since the motion of the interface depends only on the latent heat of the solid-liquid-vapour = solid vapour, the velocity is much lower. The solution is extremely sensitive to round off at the 3rd dec. place. Paterson [7] lists several solutions with heat sources. Sublimation, however, could depend on external heat sources or self-driven through the latent heat evolved by a freezing front behind the sublimating interface. In the present simulation, the parameters for the two phases pertain to solid and vapour, not solid and liquid as in melting or freezing.

Heat damage to space shields can be caused by ablation in the vacuum of space and subsequent friction with the atmosphere. Several papers have appeared giving details of ablation for cryosurgery, analysis of ice cores and laser destruction by ablation of space garbage and debris [8–12]. A further point of interest is that mass loss or gain in space vehicles caused by sublimation or accretion would affect the flight trajectories, especially in long distance missions.

In the case of the thermal balance equation for sublimation of ice from a sphere, after transformation to rectilinear coordinates, it is seen that a sign change in L acts to shift the sublimating surface across to the other end of the slab. Here, this depends on the sign of the terms in Eq. (7). For the case of self-sublimation (ice-vapour), the source strength is zero, and the results are given in the following figures. The exact spherical solution has been attempted unsuccessfully by many, and some numerical methods were used by Wu, McCue, Stewartson [13–16]. Nano composite formation with micro spheres applies some of these concepts; Wu [16], while the actual sublimation or accretion occurs under conditions of convective transport. However, due to the difficulties in getting exact solutions, an approximation is applied.

The Case of the Adiabatic Boundary

The inward solidification of a sphere may be considered by transforming to a rectilinear problem by the change of variables mentioned. A similar problem was claimed as unsolvable [13]. Following the notations in [13], which apply to a spherical geometry:

$$du/dt = 1/r^2\, d/dr\left(r^2 du/dr\right) \quad R < r < 1 \tag{9}$$

$$dv/dt = K/r^2\, d/dr\ \left(r^2 dv/dr\right) \quad 0 < r < R \tag{10}$$

where R is the interface, u = v = 0 at the interface (r = R)

BC u = − 1 on r = 1, U = 0 on r = R, dv/dr = 0 on r = 0, V = 0 on R

Initial Conditions v = V at t = 0, R = 1 at t = 0

(u = the solid and v = the liquid phase temperatures).

This particular problem describes inward solidification of a liquid sphere, with zero flux at the origin. The transformed coordinates allow one to visualize the problem in a more intuitive way since the original problem involves a zero derivative at the origin, which if transformed, becomes a planar boundary at the left.

For the generic case, the general solution is a spherical error function, namely spherf(r/2(t)$^{0.5}$)

$$\text{With general solution of the form } U = A + B\ \text{spherf}\left(r/t^{0.5}\right) \tag{11}$$

The boundary conditions given in [10] are satisfied by applying u = − 1 at t = 0, giving

A = − 1

Since u = 0 on r = R (interface), one obtains B in terms of spherf(λ), specifically, **B = 1/spherf(λ)**

Next apply dv/dr = 0 on r = 0.

$$\text{This general solution is } v = C + D\left[\text{spherf}\left(r/(kt)^{0.5}\right)\right] \tag{12}$$

$$dv/dr = -D(kt)^{0.5}/r^2\exp\left(-r^2/4kt\right)) \tag{13}$$

$$\text{At } r = 0,\ \text{the expression is } 0 \text{ if } C = \mathbf{0}, \text{consequently } \mathbf{C = 0},\ \mathbf{and}\ v = D\left[\text{spherf}\left(r/(kt)^{0.5}\right)\right] \tag{14}$$

From the stated boundary conditions, v is constant at all times (given by v = V = C from our solution). The analytical solution to this set of equations is v(r,t) = constant to the left of the interface. We have to now choose the value for the constant. But it is also given that the interface temperature is v = 0 (in reduced coordinates). The temperature is seen to jump from the one given constant from the boundary (v = V) to another at the interface, v = 0. The given conditions are inconsistent in this sense and at the best, the problem is badly posed. Given the adiabatic boundary, the temperature cannot smoothly change from v = V at the adiabatic boundary to v = 0 at the phase interface, with any set of functions satisfying these conditions. v = 0 on r = R, is not physically compatible with the stated condition v = V at t = 0, because the analytical solution for v(r, t) is a constant. Hence either v = 0 or v = V, so *only v = 0 can be chosen to be consistent with the temperature (reduced) at the phase interface.*

Hence D = 0 everywhere along with C = 0. The melting temperature has to remain constant in the molten region. In the absence of sinks, heat cannot dissipate since dT/dx = 0 at x = 0. *Thus v = 0 everywhere*. This problem then has the solution (in the absence or sources or sinks)

$$U = -1 + B\left(\text{spherf}\left(r/2\, t^{0.5}\right)\right),\ B = 1/\text{sph erf}\ (\lambda) \quad R < r < 1 \tag{15}$$

Along with v = 0, 0 < r < R, given R = 1 at t = 0.

In terms of the expansion at r = 0, the Laurent series for the spherical error function is

$$U = -1 + B\left[t^{0.5}/r - \pi^{0.5}/2 + r/4t^{0.5} - r^3/96\, t^{3/2} + 0\left(r^4\right)\right] \tag{16}$$

In other words the solution v = V at t = 0 and v = 0 at r = R cannot be simultaneously satisfied by the same expression for v which is a constant.

In reality, **sources or sinks** must be present to maintain a constant temperature in the diffusive field given by the second order spatial terms with differing boundary conditions. That is to say, a heat addition or subtraction artifice maintains a constant temperature. Sinks or sources affect the shape of the error function curve and one can only get a zero derivative at the boundary this way. Another alternative is to have a uniformly constant temperature. This version of the solution has the temperature at a constant value v = V = C calculated on the *basis of the I.C at t = 0* in the absence of any distributed heat sinks or sources. In the case of ablation or sublimation, if a zero heat flux is applied at the centre, the only possibility is for heat to be dissipated in the mass behind the interface by heating or melting or in this case, sublimation at the surface. Sublimation avoids the buildup of heat behind the surface and thus the phase velocity adjusts itself accordingly to keep a mass and heat balance as in the energy balance equations.

Application to Water and Naphthalene

Data for Naphthalene is used from sources Bonning, David, Chirico [17–19]. The latent heat of sublimation is reported as varying by different sources, a value 131.9 cal/gm is used. Similarly, the conductivity, diffusivity, and density have been taken from the sources [13, 14, 20]. One of the interesting features of naphthalene is its sublimation at room temperature. The morphology of deposited naphthalene has been reported from solution as either needles or plates, Simbrunner [21]. Naphthalene has an interesting structure as a pair of rings and thus the crystal may grow axially or radially, depending on the substrate. Presumably, the same reasoning holds for rarefied atmospheres although the literature is scant. A further interesting fact is that the deposition of vapour to solid (reverse sublimation or accretion) occurs in the form of needles, for naphthalene [19] and for similar compounds like phenytoin, Eheman [22]. In the case of water vapour to solid, the patterns of snowflakes are well-known and occur in the planar direction. For Naphthalene, a vapour to cylinder sublimation model is suggested by the observations. In Librecht, a diagram (Nakaya) [23] portraying the preferred morphology of the crystals growing at various saturations and temperatures indicates that the plates and needles

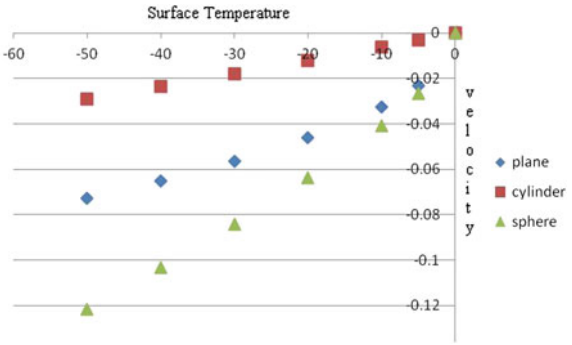

Fig. 1 Combined sublimation plot naphthalene, showing rate versus temperature

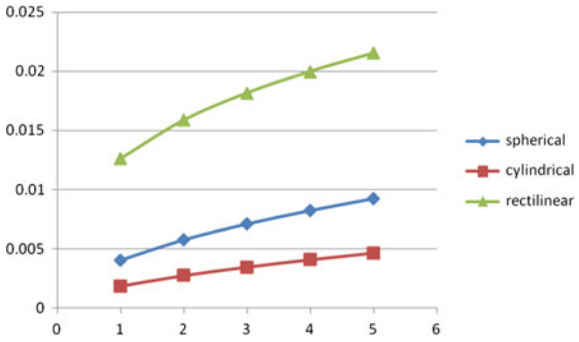

Fig. 2 Combined sublimation plot water-ice, melting temperature versus transformation rate

form alternately. The simulations done here, (termed two-sided Stefan since the parameters vary on both sides of the interface), indicate the velocities of plane and cylinder are closer than those of the spherical morphology. (The order appears to be cylinder-planar-spherical). The data for water and ice are given in Paterson [7]. The rates for water-ice sublimation and naphthalene sublimation as calculated in the present work also show a preference for certain geometries as can be seen from Figs. 1 to 2. It is clear that the difference between the sublimation rates for ice and naphthalene are quite significant, as Naphthalene sublimates easily at room temperature.

Conclusion

Solutions for self-freezing and ablation cases are developed in the rectilinear and spherical case. In the case of adiabatic conditions, (as in insulated space vehicles), sublimation from the surface is very likely, as the frictional heat cannot dissipate inwards. Data for Carbon compounds are not reliable because of the many allotropes in existence, especially of the nano forms. It is found that the preferred morphologies for water-vapour deposition are different from those of Naphtha.

In the special case of pure Carbon, due to the small difference between graphite and diamond one can easily get graphite instead of diamond in the vapour deposits. The difference in heat of combustion for graphite and diamond is only 2 kJ/mole, and similarly, the difference in heat of fusion is also about 2–3 kJ/mole. Further refined calculations should be able to predict the preferred form of the deposited vapour from a sublimate. The equilibrium sublimation rates for ice and naphthalene are found to differ by an order of magnitude (Figs. 1 and 2).

References

1. Cho HH, Goldstein RR (1993) Heat (mass) transfer and film cooling effectiveness with injection through discrete holes-Part 1. ASME 93-WA-58
2. Haring M, Holts A, Bolcs AR, Weigand B (1995) An experimental study to compare naphthalene sublimation with liquid crystal technique in compressible flow. ASME 95-GT-16 Houston TX June 5–8
3. de Souza Mendes P (1991) The naphthalene sublimation technique. Exp Therm Fluid Sci 4:510–523
4. Curteanu S, Smarandoiu M, Haroba D, Leon F (2014) Naphthalene sublimation experiment and optimization based on neuro evolutionary methodology. J Ind Eng Chem 20(4):1608–1611
5. Schmidt RR (2001) Use of Naphthalene sublimation Technique for obtaining accurate heat transfer coefficients. Des Heat Sinks Mater 3:7
6. Crank J (2009) The mathematics of diffusion. OUP, UK
7. Paterson S (1952) Propagation of a boundary of fusion. Glasgow Math Assn Proc 1:42–44
8. Carslaw HS, Jaeger JC (1959) Conduction of heat in solids, 2nd edn. Clarendon Press, Oxford, p 276
9. Arless SG, Milder L, Abboudi M, Wittenberger D, Carroll S (2012) Method of simultaneously freezing and heating tissue for ablation. US Patent 8287526 b2
10. Combs CS, Clemens NT, Danehy AM. Development of naphthalene PLIF for visualizing ablation products from a Space capsule shield. https://doi.org/10.2514/6.2014-1152
11. Combs CS, Clemens NT, Danehy AM (2014) Visualization of capsule reentry vehicle heat shield ablation using naphthalene PLIF. In: 17th International symposium of laser techniques in fluid mechanics, Lisbon Portugal, 7-1
12. Reinhardt H, Kriews M, Miller H et al (2001) Laser ablation inductively coupled plasma mass spectrometry: a new tool for trace element analysis in ice cores. Fresenius J Anal Chem 370:629–639
13. Wu B (2008) Mathematical modeling of nano particle melting or freezing. http://ro.uow.edu.au/theses/787
14. McCue SW, Wu B, Hill JM (2008) Classical two-phase Stefan problem for spheres. Proc Roy Soc A 464:2055–2076
15. McCue SW, King JR, Riley DS (2003) Extinction behavior for two-dimensional inward-solidification problems. Proc Roy Soc A 459:977–999
16. Stewartson K, Waechter RT (1976) On Stefan's problem for spheres. Proc Roy Soc Lond A 348:415–426
17. Bonning B, Laporte JL, DeLeon RT (1996) Thermal diffusivity measurements in naphthalene crystals using photopyroelectric correlation and lock-in techniques. Phys Status Solidi A 153 (2): 367–377

18. David DJ (1964) Determinations of specific heat and heat of fusion by differential thermal analysis. Study of theory and operating parameters. Anal Chem 36(11):2162–2166. https://doi.org/10.1021/ac60217a038
19. Chirico RD, Knipmeyer SE, Nguyen A et al (1993) The thermodynamic properties to the temperature of 700 K of naphthalene and of 2,7-methylnaphthalene. J Chem Thermodyn 25:1461–1494
20. Liedahl DA, Libby SB, Rubenchik A. Momentum transfer by laser ablation of irregularly shaped space debris. Arxiv.org: 1004.0390.pdf
21. Simbrunner C, Schwabegger G, Resel R, Dingemans et al (2014) The epitaxial growth of self-assembled ternaphthalene fibers on muscovite mica. Cryst Growth Des 14(2):442–449. https://doi.org/10.1021/cg400912t
22. Ehemann HMA, Baumgartner R, Kunert B et al (2014) Morphologies of phenytoin crystals at silica model surfaces: vapor annealing versus drop casting. J Phys Chem C 118:12855–12861. https://doi.org/10.1021/jp502330e
23. Libbrecht KG (2005) The physics of snow crystals. Rep Progr Phys 68(4):855–895

Effect of Precipitation on Creep Properties of Ferritic Steels

Maribel L. Saucedo-Muñoz, Arturo Ortiz-Mariscal, Shi-Ichi Komazaki and Victor M. Lopez-Hirata

Abstract The precipitation evolution was studied experimental and numerically during aging of 5Cr-0.5Mo steel at 600 °C. $M_{23}C_6$ precipitation occurred intra- and intergranular during aging. The coarsening of the carbides was observed to occur with the increase in aging time. The hardness decreased with aging time. The creep tests at 600 °C shows that the time-to-rupture decrease with increasing testing stresses. Besides, the creep deformation occurred in a transgranular. Both intragranular and intergranular precipitates coarsened during the creep test.

Keywords Carbide precipitation · Creep · Ferritic steel

Introduction

Ferritic alloy steels are widely employed to fabricate industrial equipment such as, heat exchanger and direct fired heaters tubes [1–3] since they possess good mechanical properties at operation temperatures from 400 to 600 °C for very prolonged and thus the deterioration in mechanical properties, toughness and creep strength, are associated to the long exposure of heating which causes microstructural changes such as, grain boundary segregation and coarsening of precipitates [2, 3]. Ferritic steels are usually used after its heat treating which usually consists of normalizing and tempering. That is, the precipitation process starts from those treatments and it continues during its in-service operation for prolonged times. An example of this type of steel is the ferritic 5Cr-0.5Mo steel [4]. This steel has a microstructure composed of ferrite and carbides which confers good creep strength to the steel. Thermo-Calc and PRISMA [5] commercial software have shown to be

M. L. Saucedo-Muñoz · A. Ortiz-Mariscal · V. M. Lopez-Hirata (✉)
Instituto Politécnico Nacional (ESIQIE), UPALM Edif. 7, Mexico City 07300, Mexico
e-mail: vlopezhi@prodigy.net.mx

S.-I. Komazaki
Research Field in Engineering, Science and Engineering Area, Research and Education Assembly, Kagoshima University, Kagoshima 890-0065, Japan

The Minerals, Metals & Materials Society, *TMS 2018 147th Annual Meeting & Exhibition Supplemental Proceedings*, The Minerals, Metals & Materials Series,
https://doi.org/10.1007/978-3-319-72526-0_78

a powerful tool to analyze the phase stability and precipitation kinetics of different industrial alloys. Thus, it is a good alternative to analyze the precipitation of ferritic steels. Therefore, the purpose of present work is to study the precipitation process in ferritic 5Cr-0.5Mo steel, as well as its effect on the creep behavior.

Experimental Procedure

The chemical composition of 5Cr-0.5Mo steel is shown in Table 1. The steel plate has a thickness of about 16 mm and it was received after austenizing at 950 °C for 8 min then air cooling, and subsequently tempering at 750 °C for 16 min and then again air cooling. This plate was cut to obtain specimens of about 10 × 10 10 mm. Aging treatment was conducted at 600 °C for times up to 7000 h. Both as-received and aged specimens were prepared metallograpically using emery papers and alumina solution, and then etched with Nital etchant to be observed wit optical microscope (OM), and conventional and high-resolution scanning electron microscopes (SEM) equipped with EDS analysis. Vickers hardness of specimens was determined wit 50 g and 12 s. In addition to, a uniaxial creep test was conducted at 600 °C and, 78 and 95 MPa following the standard procedure described in JIS Z2271 [6]. Thermo-Calc and PRISMA softwares [7] were used to evaluate the phase stability and precipitation kinetics at 600 °C.

Results and Discussion

Microstructural Evolution

Figure 1 shows the High-Resolution (HR) SEM micrographs of the microstructure evolutions for 5Cr-0.5Mo steel aged at 600 °C for 0 (as-received), 200 and 2000 h. SEM micrograph of as-received steel, 0 h, indicates the presence of equiaxed ferrite and bainite which was formed during the normalizing process. Besides, inter- and intragranular fine precipitation seems to be present. As the aging progresses, two events are evident: first the disappearance of bainite and the coarsening of intra and intergranular precipitates which also shows a decrease in density number of precipitates [8]. The EDS-SEM microanalysis of some precipitates indicates that the carbides are richer in Cr, but Fe and Mo are also present. The variation of Vickers hardness number, VHN, with aging time is shown in Fig. 2 for the steel. There is a

Table 1 Chemical composition in wt% of the steel

C	Cr	Mo	Mn	Si	Cu	Ni	Nb	V	Ti	S	P
0.096	4.531	0.911	0.351	0.344	0.041	0.117	0.003	0.009	0.003	0.005	0.009

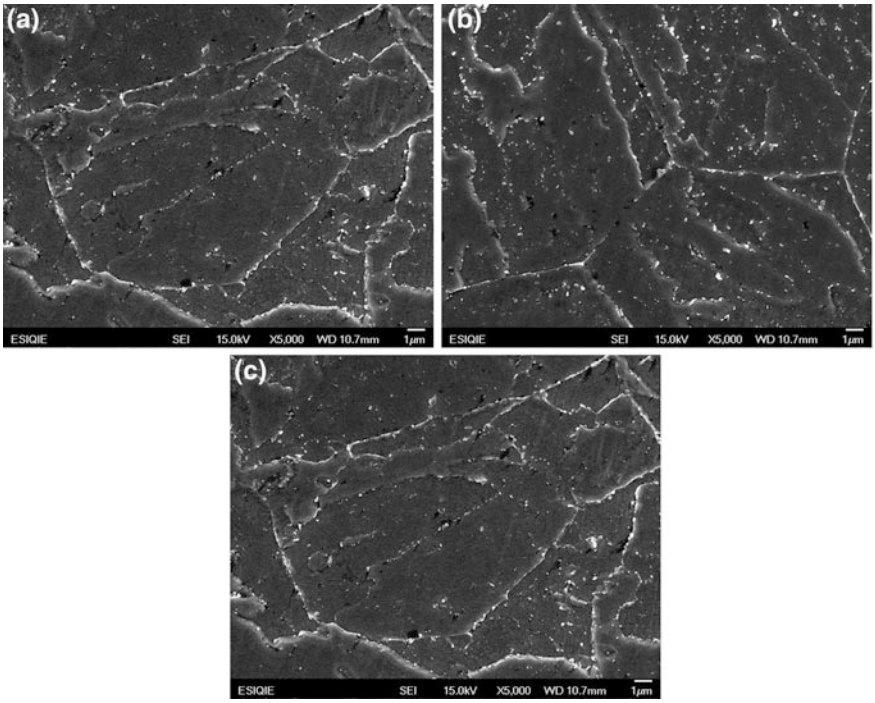

Fig. 1 HR-SEM micrographs of 5Cr-0.5Mo steel in the condition of **a** as-received, and after aging at 600 °C for **b** 200 h and **c** 2000 h

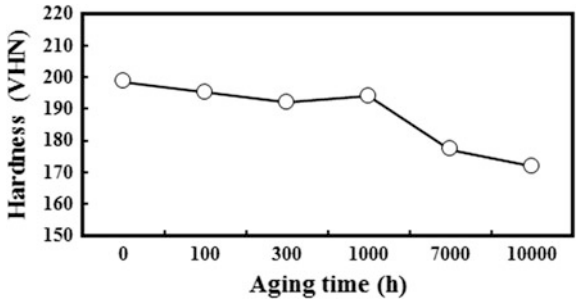

Fig. 2 Vickers hardness versus aging time at 600 °C

decreasing tendency of hardness with time. This can be attributable to the coarsening process of carbides.

The creep curves of the steel creep tested at 600 °C with stresses of 75 and 98 MPa are shown in Fig. 3. These curves show clearly the secondary and tertiary creep stages. The primary stage is not appreciated due to the scale of strain axis. The higher the stress, the shorter time-to-rupture and faster creep strain rate of the secondary stage. SEM micrographs of the creep tested, corresponding to Fig. 3, are shown in Fig. 4a, b.

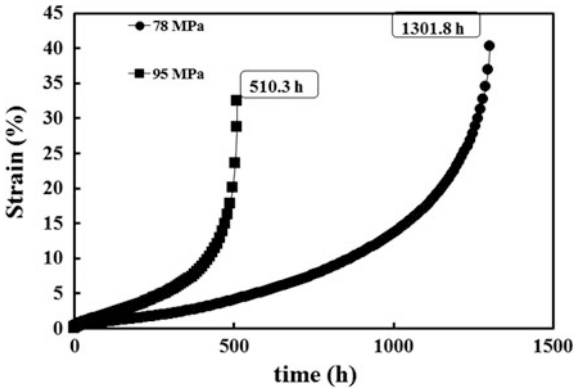

Fig. 3 Creep curve of the steel at 600 °C with stresses 78 and 95 MPa

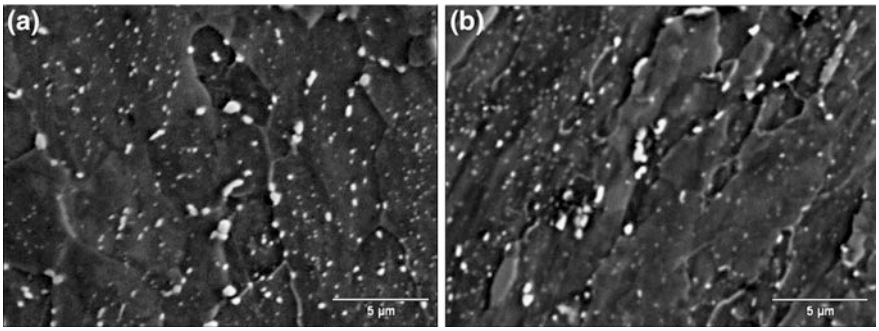

Fig. 4 SEM micrographs of the creep tested specimen at 600 °C with stresses of **a** 78 Mpa and 95 Mpa

These SEM micrographs show that the presence of slightly elongated ferrite grains which suggests that the creep deformation takes place in a transgranular mode. Besides, the existence of both intra and intergranular precipitates can be observed in the tested specimens. Furthermore, the appearance of fracture surface was ductile mode for both tested specimens [9, 10].

The pseudoternary Fe-Cr-Co phase diagram at 600 °C is shown in Fig. 5. This diagram indicates that the equilibrium phases are ferrite and $M_{23}C_6$ for the 5Cr-0.5Mo steel. Nevertheless, several works [4] have pointed out that the first precipitated phase is Fe_3C during aging, and subsequently M_7C_3 carbide and the last precipitated to be formed is $M_{23}C_6$. Thus, the precipitation process was analyzed using PRISMA software. Both inter- and intragranular precipitation were analyzed considering an interfacial energy of 0.2, 0.3 and 0.2 J m^{-2} [7] for the interfaces of ferrite phase with Fe_3C, M_7C3 and $M_{23}C_6$ phases, respectively, and a ferrite grain size of about 100 µm. For instance, Fig. 6 presents the PRISMA calculated Time-Temperature-Precipitation TTP diagram for the precipitation of

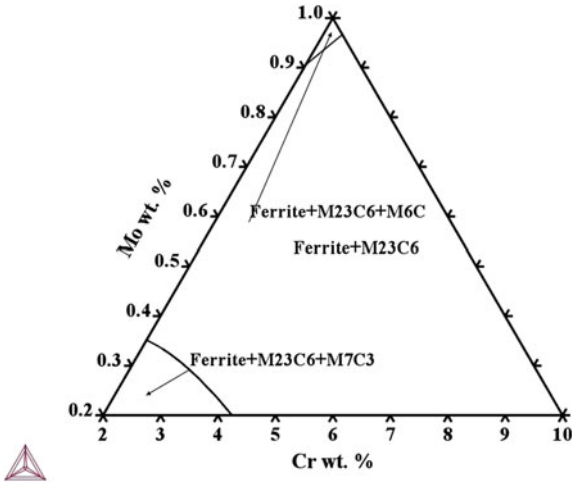

Fig. 5 Thermo-Calc calculated pseudoternary Fe-Cr-Mo phase diagram for the steel

Fe_3C, M_7C3 and $M_{23}C_6$ phases on dislocation, intragranular precipitation. The calculated TTP for intergranular precipitation shows a faster growth kinetics than that for dislocation precipitation. Nevertheless, both TTP diagrams confirm the precipitation sequence described previously. This figure seems to suggest that the Fe3C phase would be the first phase formed, after a normalizing of the steel at a cooling rate of approximately 0.6 °C s^{-1}. This TTP diagram also indicates that the

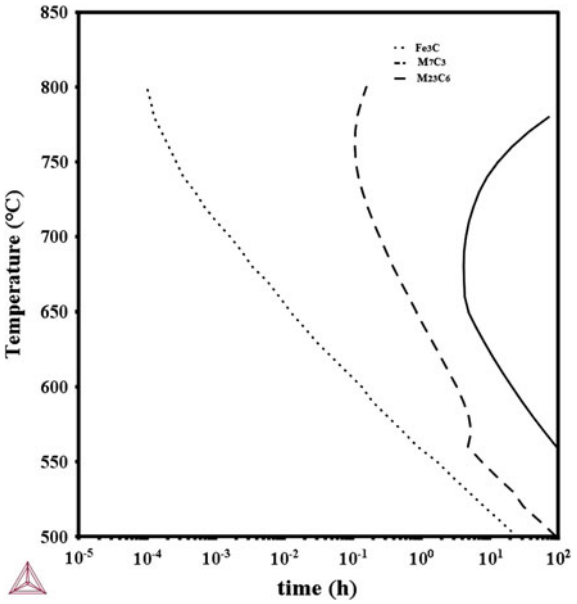

Fig. 6 PRISMA calculated TTP diagram for the steel

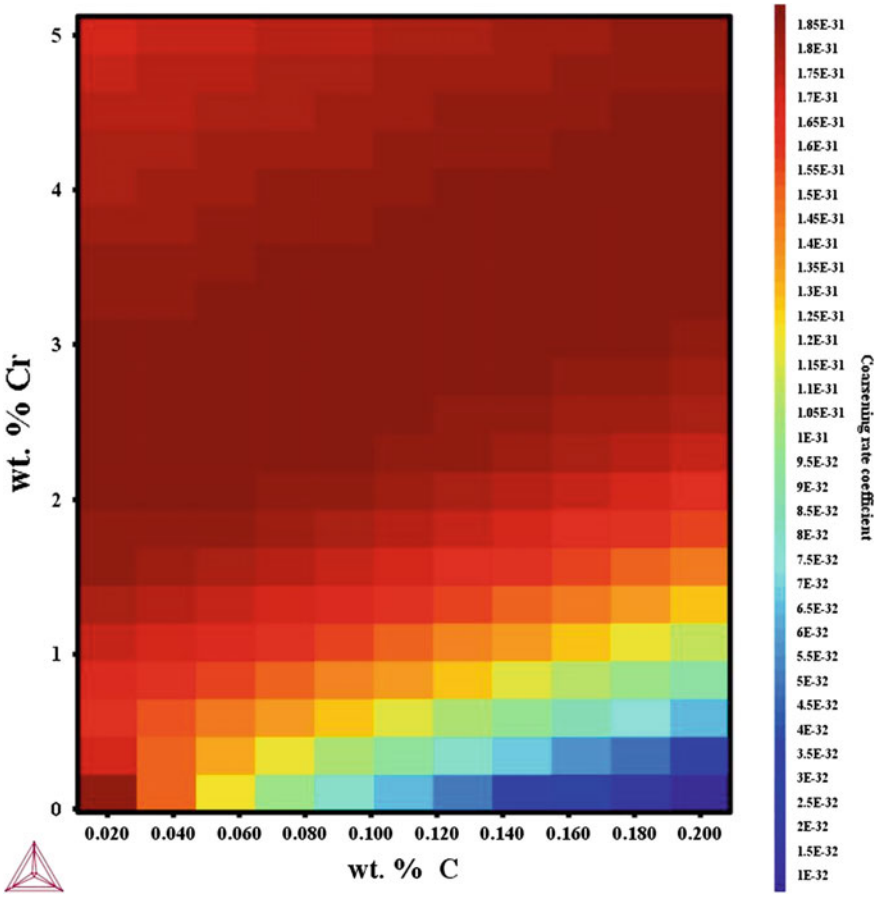

Fig. 7 Thermo-Calc calculated variation of the coarsening rate at 600 °C as a function of Cr and C content of the steel

fastest growth kinetics of precipitation occurs at about 700 °C which is the minimum requested tempering temperature for this steel. That is, the precipitation reaction may be completed after normalizing and tempering to produce fine $M_{23}C_6$ precipitate distribution to exhibit good creep strength.

The Thermo-Calc calculated coarsening rate of $M_{23}C_6$ carbides at 600 °C is shown as a function of Cr and C content of the steel. The higher coarsening rate may occur for C content of about 0.1 wt% with a Cr content of about 3 wt% Cr. This fact suggests that the creep strength of 5Cr-0.5Mo steel will be decreased due to its prolonged exposure at 600 °C (Fig. 7).

Conclusions

This study shows that the precipitation sequence is as follows: Fe_3C to M_7C_3 and finally to $M_{23}C_6$ which starts from the normalizing and tempering treatments. The steel exposure at 600 °C promotes the coarsening of $M_{23}C_6$ carbides which may decrease the creep strength of the steel since the number density of precipitates is decreased. The creep deformation took place in a transgranular way.

Acknowledgements The authors wish to thank the financial support from Kagoshima University, SIP-COFAA-IPN and CONACYT.

References

1. Abe F, Kern T-U, Viswanathan R (2008) Creep resistant steels. Woodhead Publishing, Cambridge, pp 18–64
2. Mitchell DG, Ball CJ (2001) A quantitative X-ray diffraction and analytical electron microscopy study of service-exposed 2.25Cr–1Mo steels. Mater Charact 47:17–26
3. Fujio B (2003) Creep resistance steel. Nature 424:294–296
4. Tan J, Chao YJ (2005) Effect of service exposure on the mechanical properties of 2.25Cr–1Mo pressure vessel steel in a hot-wall hydrofining reactor. Mater Sci Eng A 405:214–220
5. Andersson JO, Helander T, Höglund L, Shi P, Sundman B (2002) Themo-calc and dictra. Comput Tools Mater Sci Calphad 26:273–312
6. JIS Standard, JIS Z 2271: 2010 (2011) Metallic materials—uniaxial creep testing in tension-method of test, Japanese Industrial Standard
7. Thermo-Calc and PRISMA software 2016b/tcfe7.tdb and mobFe2.ddb data
8. Kostorz G (2001) Phase transformation in material. Wiley-VCH, Germany, pp 309–408
9. Tamura M (2013) Larson–Miller constant of heat-resistant steel. Met Mater Trans 44A:2645–2661
10. Viswanathan R (1989) Damage mechanisms and life assessment of high temperature components. ASM International, OH USA, pp 85–110

Microstructural Evolution of a New Beta Titanium Alloy During the Beta Annealing, Slow Cooling and Aging Process

S. Sadeghpour, S. M. Abbasi and M. Morakabati

Abstract A new beta titanium alloy Ti–4Al–7Mo–3Cr–3V (Ti-4733) was developed and its microstructural evolution during the Beta Annealing followed by Slow Cooling and Aging (BASCA) process was investigated. The effect of microstructure on the tensile properties was discussed and compared with the one of the commercial titanium alloy Ti-5553. The results showed that the BASCA heat treatment results in a microstructure with combination of grain boundary α and lamellar α phase colonies formed during the slow cooling and fine acicular α precipitates formed during the subsequent aging. The BASCA-processed specimens exhibited a high elongation and relatively high strength. The fracture mode in BASCA specimens was found to be a combination of ductile and transgranular brittle fracture. Although the alpha phase morphology was similar in both the alloys, the obtained microstructure was generally finer in Ti-4733 than in the Ti-5553 alloy, leading to enhanced tensile properties.

Keywords Beta titanium alloy · BASCA heat treatment · Alpha phase morphology · Tensile properties · Fracture

Introduction

The Ti–Al–Mo–V–Cr composition is an important alloy system in which several β titanium alloys were introduced and used in commercial applications [1]. The most popular example is the Ti-5553 alloy that is a high strength β titanium alloy with chemical composition of Ti–5Al–5Mo–5V–3Cr (wt%). This alloy was primarily designed for high-strength forging applications as an improved version of the Russian alloy VT22 (Ti–5.7Al–5.1V–4.8Mo–1Cr–1Fe) on account of improved properties and deep hardenability over large thickness compared to the VT22.

S. Sadeghpour (✉) · S. M. Abbasi · M. Morakabati
Metallic Materials Research Center, Malek Ashtar University of Technology, Tehran, Iran
e-mail: sinsad64@yahoo.com

The Minerals, Metals & Materials Society, *TMS 2018 147th Annual Meeting & Exhibition Supplemental Proceedings*, The Minerals, Metals & Materials Series,
https://doi.org/10.1007/978-3-319-72526-0_79

The Ti-5553 alloy proved also to be a better alternative than the Ti-10-2-3 alloy in some applications [1]. While the metastable β alloys generally display better cold workability when compared to α and α + β titanium alloys, unfortunately the cold workability of the most common high strength β titanium alloys, such as the Ti-5553, is not too high. This can be considered as a drawback for the Ti-5553 alloy restricting its application to bulk structures. Recently, a new Ti–4Al–7Mo–3V–3Cr (Ti-4733) alloy, which contains almost the same primary alloying elements as the Ti-5553 alloy, was designed through the theoretical d-electron method with the aim of improving the alloy cold workability at room temperature [2]. This alloy was reported to exhibit high compressive strength (~1400 MPa) and excellent compressive deformability (~35%) in the solution treated condition.

High levels of strength can be attained in the β titanium alloys through an aging heat treatment resulting in the precipitation of a fine secondary α phase [3]. In addition to conventional solution treating and aging process, several heat treatment schedules have been designed in β titanium alloys to attain specific goals. For example, a particular processing method including Beta Annealing followed by Slow Cooling and Aging (BASCA) was developed to maximize the fracture toughness while maintaining a relatively high degree of strength in the conventional Ti-5553 alloy [4]. Although the microstructure and mechanical properties of the conventionally solution treated and aged Ti-5553 alloy have been vastly investigated over the past few years [1, 2, 5], the microstructural evolution during the BASCA process has not been studied systematically. The present work aims at studying the microstructural evolution of the Ti-4733 alloy as a result of the BASCA process and comparing it with the one of the conventional Ti-5553 alloy.

Experimental Procedure

The new β titanium alloy Ti–4Al–7Mo–3V–3Cr (Ti-4733) was designed based on the commercial β titanium alloy known as Ti-5553 with the aim of controlling the cold deformation mechanisms. The details of alloy design strategy were presented elsewhere [6]. Ti-4733 and Ti-5553 ingots were melted twice by vacuum arc melting process to ensure chemical homogeneity. The ingots were then forged at 1100 °C and subsequently rolled to a 20-mm thick plate at 750 °C. The chemical composition of the alloys is given in Table 1. The β transition temperature (T_β) of the Ti-4733 and Ti-5553 alloys measured by metallographic method are 860 °C and 870 °C, respectively.

Table 1 Chemical composition of the investigated alloys (wt%)

Alloy	Al	Mo	V	Cr	Ti
Ti-4733	3.9	6.8	3.0	2.9	Balance
Ti-5553	5.2	4.8	4.7	2.9	Balance

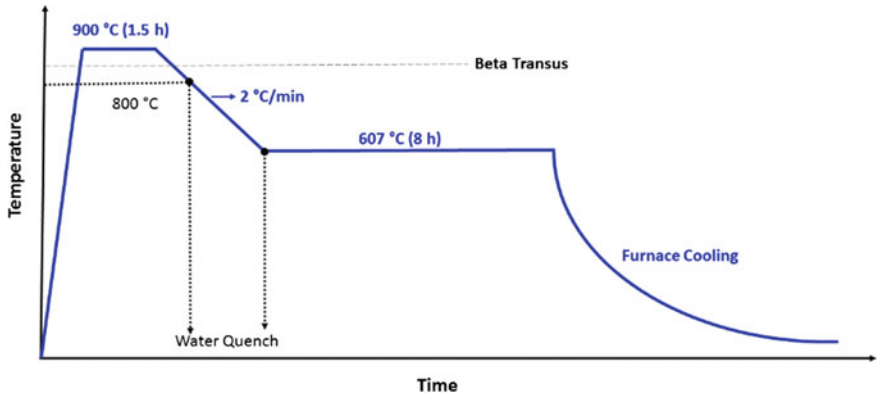

Fig. 1 Scheme of the BASCA heat treatment applied in this study

Samples were cut from both the alloys and the BASCA process was carried out on them. The BASCA parameters were selected according to the original process introduced by Boeing for processing large components of airplanes aiming at improving the part fracture toughness [7]. As seen in the scheme of the BASCA heat treatment in Fig. 1, the samples were heated up to 900 °C and, after holding at this temperature for 1.5 h, slowly (2 °C/min) cooled down to 607 °C. After holding at 607 °C for 8 h, the samples were furnace cooled down to room temperature. To investigate the microstructure evolution during the BASCA process, two specimens were quenched in water after slow cooling down to 800 and 600 °C, respectively (Fig. 1).

The specimens for microstructure observations were polished with 80–3000 grid SiC paper in water, followed by chemical polishing. A modified Kroll's reagent (6 ml HF + 18 ml HNO_3 + 76 ml H_2O) was employed to reveal the microstructures. The microstructural observations were carried out on an optical Olympus microscope and a TESCAN, MIRA3 Scanning Electron Microscope (SEM). The area fraction of the α phase was measured using the Clemex image analysis software. The calculation was performed based on several SEM micrographs from different positions of each sample.

The mechanical properties were evaluated by uniaxial tensile testing of ASTM-E8 standard specimens at room temperature. Flat tensile specimens with gage length 25 mm, width 6 mm and thickness 3 mm were machined along the rolling direction. Tensile tests were carried out on an Instron 8502 testing machine at a constant cross-head speed of 2 mm/min so that the initial strain rate was 1.3×10^{-3} s^{-1}.

Results and Discussion

The SEM micrographs of the two alloys after BASCA process are shown in Fig. 2. The lamellar inter and intra-granular α phases as colonies with different morphological orientations along with discontinuous grain boundary α (α_{GB}), are observed in the BASCA microstructures. Also, there are some fine secondary α (α_s) precipitates with acicular morphology between the primary α colonies.

By comparing the microstructures of the Ti-4733 and Ti-5553 alloys in Fig. 2, it is observed that the BASCA-treated Ti-4733 alloy tends to have more refined microstructure with a lower volume fraction of the α phase compared with Ti-5553 alloy (Table 2). This could be a result of the higher stability of the Ti-4733 alloy.

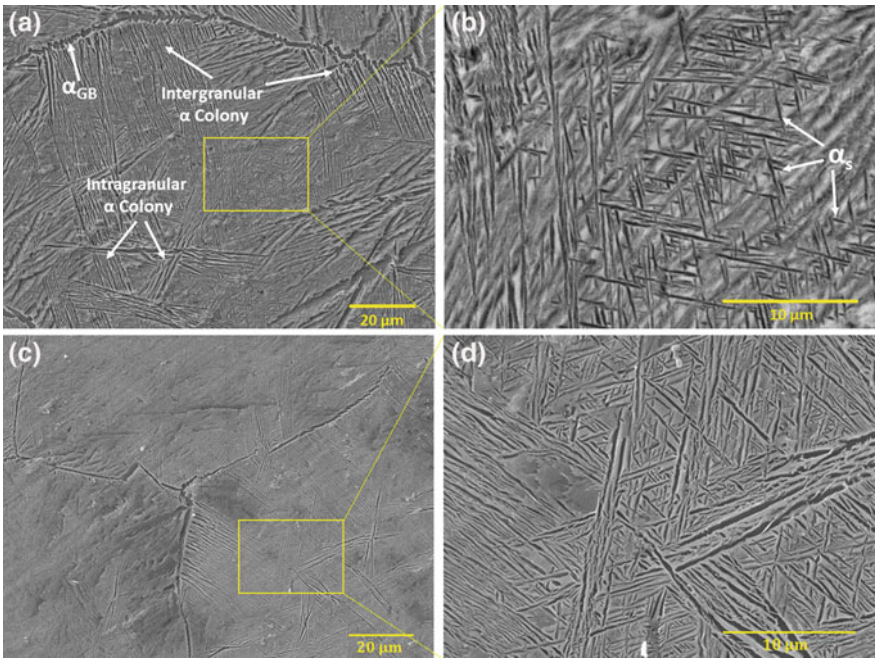

Fig. 2 SEM micrographs of the BASCA specimens for the (**a** and **b**) Ti-4733 and (**c** and **d**) Ti-5553 alloys

Table 2 The volume fraction of the alpha phase in different microstructures

Alloy	Volume fraction (%)	BASCA
Ti-4733	Total α	42.6 ± 1.7
	Secondary α	14.1 ± 1
Ti-5553	Total α	51.9 ± 1.5
	Secondary α	14.4 ± 1.1

To investigate the microstructural evolutions during the BASCA heat treatment, samples from different stages of this process were analyzed. Slow cooling from solution temperature is a critical part of the BASCA process because can result in the formation of large α laths. To observe the effect of a slow cooling rate, specimens were cooled to 800 and 600 °C at a rate of 2 °C/min after annealing at 900 °C. Figure 3 shows the optical microstructure of the Ti-4733 alloy after slow cooling to 800 °C. It can be seen that the β grain boundaries are decorated by globular α precipitates acting as a precursor for nucleation and growth of intergranular α laths. These lamellar side plates form by branching out from α_{GB} globes as shown in Fig. 3b. No lamellar α plates nucleating directly on β/β grain boundaries were detected in the microstructure. In fact, the formation of lamellar α colonies is not possible without the presence of a parent α_{GB}. This observation is in accordance with a previous literature work [8]. These intergranular plates grow in a group resulting in the formation of a colony of parallel α plates. Higher magnification in Fig. 3b shows that α laths are not always present at both sides of the grain boundaries. Such orientation relationships between the α laths and β grains have already been observed in the Ti-5553 alloy [7] and in some α/β titanium alloys [9]. Some intragranular plates also nucleate in the interior of the β grains and grow as a group of parallel plates remaining stacked in a parallel mode within a given packet.

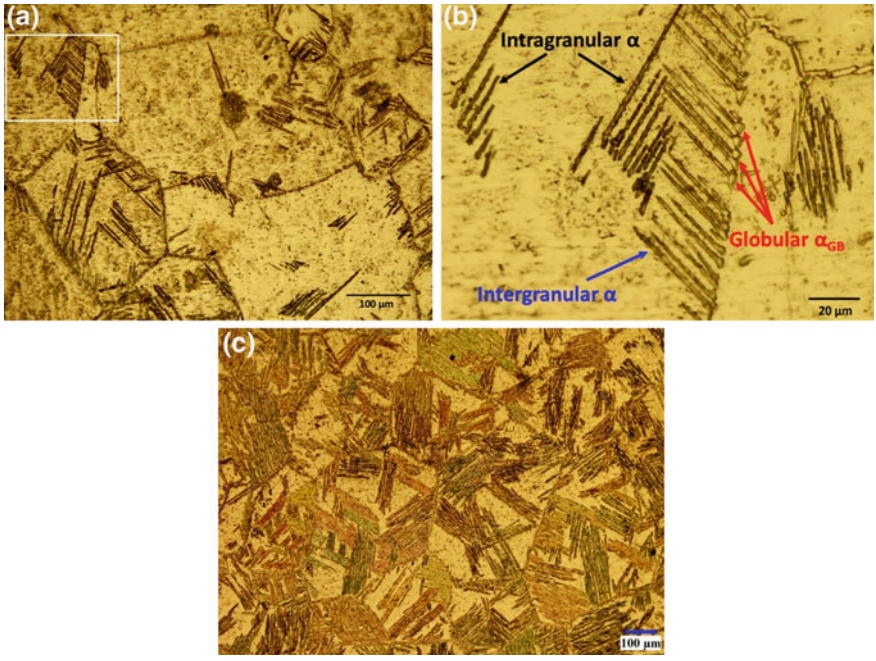

Fig. 3 Optical microstructure of the Ti-4733 alloy after slow cooling (2 °C/min) from 900 °C to (**a** and **b**) 800 °C, **c** 600 °C

At lower cooling rates, laths that nucleate early at higher temperatures coarsen with the temperature reduction. Figure 3c shows the optical microstructure of a sample that was slow cooled from the solutionizing temperature to 600 °C and then water quenched. Its microstructure presents grain boundary α (α_{GB}) and large volumes of intergranular and intragranular α laths. Intergranular α laths are formed in the form of many parallel plates growing towards the grain interior. They have short length and don't form the large colonies observed in common α/β titanium alloys. Intragranular α phases are also observed within the β matrix as plates growing in three preferred orientations. Furthermore, as seen in Fig. 3c, there are some regions within the β grains where no α precipitates are detected, pointing out that the equilibrium volume fraction of α has not yet been achieved by cooling down to 600 °C. Therefore, further aging at this temperature (around 600 °C) can lead to the α precipitation over the entire β matrix. It is important to note that, because of the slow diffusion at low temperatures, the nucleation of secondary α precipitates can only occur with long aging treatments at low temperatures such as 600 °C.

Based on the observations, the sequence of microstructural evolution during the BASCA process can be summarized as follows:

(1) The globular α_{GB} precipitates form at the grain boundaries with starting the slow cooling from the solution temperature.
(2) The intergranular α colonies initially nucleate on the α_{GB} grow inside the grains with a lamellar morphology.
(3) The intragranular α colonies nucleate and grow inside the grains with lamellar morphology.
(4) At the end of the cooling stage, there would be some precipitate free zones inside the grains. With aging at 607 °C for a long time, the α_s precipitates with acicular morphology form in these zones.

According to Fig. 4, in comparison to the conventional solution treatment and aging (STA), the BASCA specimens exhibit higher elongation. This can be attributed to the coarse α-laths (Fig. 3c) resulting from the slow cooling employed in the BASCA process. According to Table 2 it can be seen that a considerable amount of the α phase in the BASCA samples is related to the lamellar α formed during the slow cooling. Although these coarse lamellar α phases can enhance the elongation of the BASCA specimens compared with the STA specimens, but they have a relatively poor hardening effect leading to lower strength levels. Despite the presence of coarse α-laths, the BASCA specimens show a tensile strength higher than 1100 MPa arising from the formation of secondary acicular α phases during the subsequent aging. In fact, the lamellar α phase determines the elongation of the BASCA specimens while the acicular α phase determines their strength. As shown in Fig. 4, the elongation of the Ti-5553 alloy in the BASCA condition is higher than that of the Ti-4733 that arises from its larger lamellar α phase and higher volume fraction of the lamellar α. However, with almost same volume fraction of the α_s precipitates, the strength of the Ti-5553 alloy is lower than that of the

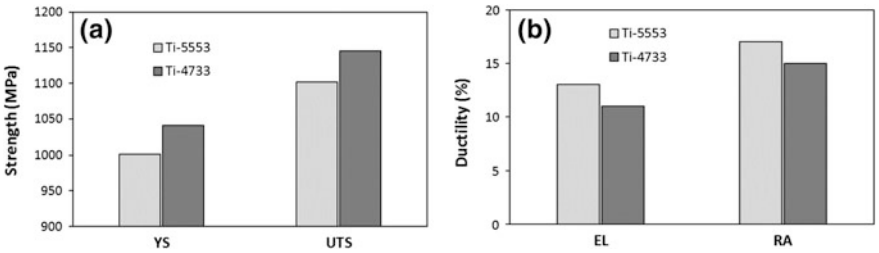

Fig. 4 Tensile properties of the Ti-4733 and Ti-5553 alloys including **a** yield strength (YS) and ultimate tensile strength (UTS), **b** elongation to failure (EL) and reduction of area (RA) after BASCA heat treatment

Ti-4733 because of its larger acicular α_s phase. However, it should be noted that these microstructural features are strongly dependent on the BASCA process parameters. In this study, we used the standard parameters of the Ti-5553 BASCA processing for both the alloys. Therefore, thanks to the optimization of the process parameters for the Ti-4733 alloy we may achieve even better mechanical properties.

In addition, it can be concluded that the Ti-4733 alloy exhibits a better combination of mechanical properties compared with those of the Ti-5553. Meanwhile, the Ti-4733 alloy shows an enhanced cold deformability at room temperature in the single-phase solution treated condition [2]. This indicates that Ti-4733 can be used in applications including not only bulk structures but also plate or sheet products thanks to the achieved strength and ductility.

Figure 5 shows the fracture surface of the BASCA samples after the tensile test. As can be seen, both the alloys exhibit a combination of ductile fracture with deep dimples and transgranular brittle fracture with some cracks (shown with arrows in Fig. 5b). It has been reported [10] that in the lamellar microstructures the cracks are much more liable to initiate at and propagate from the tips of thin microstructures that are the stress concentration regions. The high undulation depth on the fracture surface of the BASCA samples (Fig. 5), indicates the large deflection of crack path. In fact, the higher elongation of the BASCA samples compared with the STA samples arises from the presence of large lamellar α colonies. In general, the size of the lamellar α colonies, thickness of the α lamellae and size of the grain boundary α phase determine the alloy fracture behavior. In the Ti-5553 alloy, the lower stability of the β phase results in the growing of the α colonies, α lamellae and grain boundary α phase.

It is well known that the Ti-5553 alloy exhibits a higher fracture toughness when processed under BASCA conditions in compared to other processing routes, such as the conventional STA [4]. Although the fracture toughness of the samples was not measured in this study, some microstructural features can be useful to qualitatively describe the higher fracture toughness of the BASCA processed samples. It was showed that when the energy needed for the α lamellar fracture is higher than that needed for crossing colonies, the crack changes directions causing crack branching,

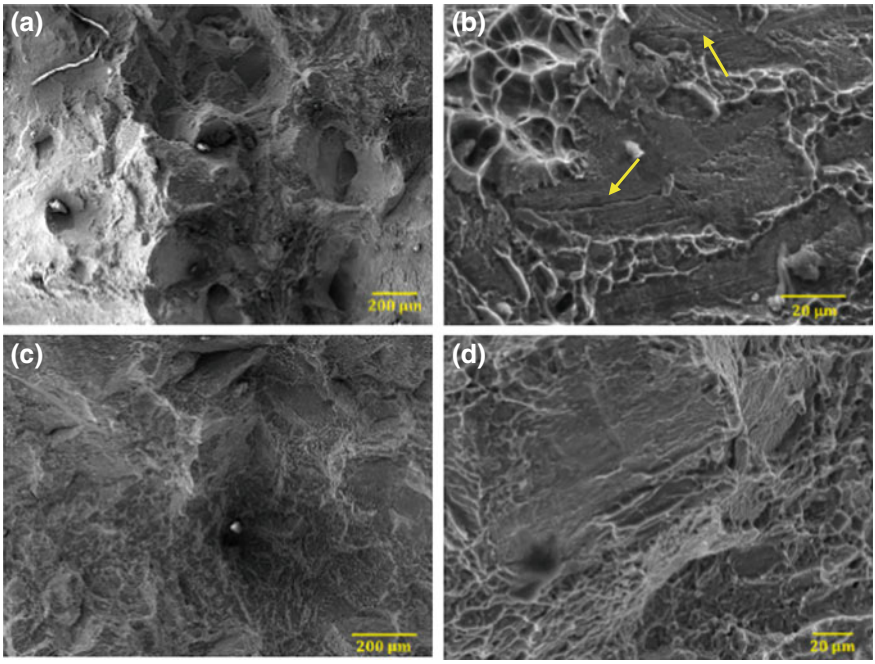

Fig. 5 Fracture surface of the (**a** and **b**) Ti-4733 and (**c** and **d**) Ti-5553 alloys in the BASCA condition

zigzagging and secondary crack creation [11, 12]. This process requires additional energy and can result in increased fracture toughness in the material [10].

The plastic zone of the crack tip is another factor in controlling the fracture behavior. The bigger the size of the plastic zone the higher the fracture toughness. According to Fan et al. [10] larger acicular α precipitates increase the plastic zone at the crack tip. They showed that the nucleation of dislocations from the crack tip across the smaller α phase leads to strain localization. Thus, it would significantly reduce the size of the plastic zone of the crack tip. The fact that the average size of the secondary α precipitates in the BASCA microstructure is much larger than that of the STA microstructures, can be another reason for the higher fracture toughness of the BASCA processed samples.

Generally, the α_{GB} has a critical importance due to its effect on the ductility [13–15]. Two aspects of α_{GB} can affect the fracture behavior of materials, namely its width and continuity [16]. As mentioned before (Fig. 2), there is a significant amount of α_{GB} phase in the microstructure of the BASCA samples. However, this α_{GB} phase exhibits a zigzag and discontinuous morphology as can be observed in Fig. 2. The discontinuity of the α_{GB} arises from the slow cooling during the BASCA process. In fact, during the slow cooling large and isolated globular α_{GB} particles form (Fig. 3b) and, subsequently, lead to a discontinuous grain boundary α phase. The propagation of crack will be more difficult through a discontinuous α

layer compared to continuous α layer. Therefore, despite the presence of large amount of α_{GB}, it doesn't reduce the ductility significantly due to its discontinuous morphology. In addition, the three different and specific morphological aspects of large lamellar α colonies, larger acicular α_s precipitates and discontinuous α_{GB} are the main reasons of the higher fracture toughness in the BASCA microstructures.

Conclusions

In the present study, the microstructural evolution during the BASCA process and its effect on the tensile properties of Ti-4733 were investigated and compared with the ones of the commercial Ti-5553 alloy. The main results can be summarized as follows:

(1) Although both the Ti-4733 and Ti-5553 alloys exhibit similar microstructures after the heat treatment, Ti-4733 revealed more refined microstructures than Ti-5553 resulting in enhanced strength.
(2) The BASCA heat treatment results in a microstructure with combination of α_{GB} and lamellar α phase colonies formed during the slow cooling and fine acicular α_s precipitates formed during the subsequent aging.
(3) The fracture mode in BASCA specimens was found to be a combination of ductile and transgranular brittle fracture.

References

1. Shekhar S, Sarkar R, Kar SK, Bhattacharjee A (2015) Effect of solution treatment and aging on microstructure and tensile properties of high strength β titanium alloy, Ti–5Al–5V–5Mo–3Cr. Mater Des Part B 66:596–610
2. Kar SK, Ghosh A, Fulzele N, Bhattacharjee A (2013) Quantitative microstructural characterization of a near beta Ti alloy, Ti-5553 under different processing conditions. Mater Charact 81:37–48
3. Li C-L, Mi X-J, Ye W-J, Hui S-X, Yu Y, Wang W-Q (2013) Effect of solution temperature on microstructures and tensile properties of high strength Ti–6Cr–5Mo–5V–4Al alloy. Mater Sci Eng, A 578:103–109
4. Briggs R (2004) Tough, high-strength titanium alloys; methods of heat treating titanium alloys. Google Patents
5. Nyakana SL, Fanning JC, Boyer RR (2005) Quick reference guide for β titanium alloys in the 00s. J Mater Eng Perform 14:799–811
6. Sadeghpour S, Abbasi SM, Morakabati M (2015) Deformation-induced martensitic transformation in a new metastable β titanium alloy. J Alloys Compd 650:22–29
7. Nag S (2008) Influence of beta instabilities on the early stages of nucleation and growth of alpha in beta titanium alloys. The Ohio State University
8. Salib M, Teixeira J, Germain L, Lamielle E, Gey N, Aeby-Gautier E (2013) Influence of transformation temperature on microtexture formation associated with α precipitation at β grain boundaries in a β metastable titanium alloy. Acta Mater 61:3758–3768

9. Bhattacharyya D, Viswanathan GB, Denkenberger R, Furrer D, Fraser HL (2003) The role of crystallographic and geometrical relationships between α and β phases in an α/β titanium alloy. Acta Mater 51:4679–4691
10. Fan JK, Li JS, Kou HC, Hua K, Tang B (2014) The interrelationship of fracture toughness and microstructure in a new near β titanium alloy Ti–7Mo–3Nb–3Cr–3Al. Mater Charact 96:93–99
11. Lee D-G, Lee S, Lee Y (2008) Effect of precipitates on damping capacity and mechanical properties of Ti–6Al–4V alloy. Mater Sci Eng A 486:19–26
12. Niinomi M, Kobayashi T (1996) Fracture characteristics analysis related to the microstructures in titanium alloys. Mater Sci Eng A 213:16–24
13. Foltz JW, Welk B, Collins PC, Fraser HL, Williams JC (2011) Formation of grain boundary α in β Ti alloys: its role in deformation and fracture behavior of these alloys. Metall Mater Trans A 42:645–650
14. Lütjering G, Albrecht J, Sauer C, Krull T (2007) The influence of soft, precipitate-free zones at grain boundaries in Ti and Al alloys on their fatigue and fracture behavior. Mater Sci Eng A 468–470:201–209
15. Sauer C, Lütjering G (2001) Influence of α layers at β grain boundaries on mechanical properties of Ti-alloys. Mater Sci Eng A 319–321:393–397
16. Ghosh A, Sivaprasad S, Bhattacharjee A, Kar SK (2013) Microstructure–fracture toughness correlation in an aircraft structural component alloy Ti–5Al–5V–5Mo–3Cr. Mater Sci Eng A 568:61–67

Part XXXIII
Powder Metallurgy of Light, Reactive and Other Non-ferrous Metals

A Review of the Preparation Methods of WC Powders

Yijie Wu, Jie Dang, Zepeng Lv, Shengfu Zhang, Xuewei Lv and Chenguang Bai

Abstract Tungsten carbides, which can be widely used for cutting and drilling tools, chemical catalyst and aerospace coatings, have attracted widespread attentions. However, the cost of conventional processes to produce tungsten carbides can be very high, therefore, there is a permanent effort to synthesize WC powder at low temperature to minimize the production cost. Some novel processing techniques have been developed to partially solve this problem. This paper reviewed the current research trends in preparation of WC containing spark plasma sintering, combustion synthesis, sol-gel and in situ carburization method, chemical vapor reaction synthesis and the spray conversion process, etc. The present review also discussed the potential applications, the feasibility, the advantages and disadvantages of industrialization.

Keywords Tungsten carbide · Preparation · Spray conversion
Combustion synthesis · Catalyst

Introduction

Tungsten carbides, which belong to the group of cemented carbides and refractory carbides have the advantages of high melting point (2600–2850 °C), high hardness, low friction coefficients, high Young's modulus of elasticity, high thermal stability and low thermal expansion coefficient [1]. These properties make tungsten carbide appropriate for various engineering applications such as manufacturing of cutting tools, rock drill tips, tools and dies and general wear parts [2–8]. In addition to such extensive structural applications, WC has been used as the Pt electro-catalyst support for various processes such as the methanol oxidation [9], oxygen reduction reaction [10], hydrogen evolution reactions [11], ethanol electro-oxidation [12], and

Y. Wu · J. Dang (✉) · Z. Lv · S. Zhang · X. Lv · C. Bai
College of Materials Science and Engineering, Chongqing University, Chongqing 400044, China
e-mail: jiedang@cqu.edu.cn

The Minerals, Metals & Materials Society, *TMS 2018 147th Annual Meeting & Exhibition Supplemental Proceedings*, The Minerals, Metals & Materials Series,
https://doi.org/10.1007/978-3-319-72526-0_80

NH_3 synthesis, and also used as catalytic electrode for anodic oxidation of hydrogen in fuel cells [13]. WC erosion resistant coatings for aerospace components are another novel application [14].

Tungsten carbide was first synthesized by H. Moissan in 1893. The industrial production of hard metals based on WC started 20–25 years after the discovery of tungsten carbide. WC in electro-catalysis has been intensively studied since 1970s. Levy and Boudart [15] reported that tungsten carbide revealed Pt-like catalytic activity in several catalytic reactions. This catalytic behavior, which is typical behavior of platinum, was not exhibited at all by tungsten. The surface electronic properties of the tungsten are therefore modified by carbon in such a way that they are resemble to those of platinum. Subsequent investigation demonstrated that Pt-like property is due to the change in the electron distribution in tungsten by addition of carbon [16]. Besides, Transition-metal carbides (for instance, WC) are a potential substitute for Pt because of their low cost, high catalytic activity, selectivity, and good thermal stability under rigorous conditions [17].

In this study, the latest developed preparation methods of tungsten carbide are reviewed. The potential applications, the feasibility, the advantages and disadvantages of industrialization are discussed as well.

Preparation of Tungsten Carbide

The preparation methods can be divided into two-step method and one-step method.

Two-Step Method

As presented in Fig. 1, the first step is to reduce the tungsten containing precursor to tungsten powder, and then to carburize with the carbonized material.

Traditional method is to direct carburize tungsten powder: the W powder is mixed with about 6.3 wt% of carbon black by ball-milling for an extended time, and then carbonized at 1400–1600 °C in a flowing hydrogen atmosphere for 2–10 h [18]. Because the high pure and fine W powder must be produced in the first step, the cost can be very high. Furthermore, the process is cumbersome, ball-milling time consuming and powder produced by this method is not suitable for advanced applications [19]. Because the tungsten powder and carbon black is inadequate contact, the reaction rate is slow. It is switched to tungsten precursor with a highly active as raw material, and carburization with carbon-containing gases, such as CH_4, C_2H_6, C_3H_8, and aromatic compounds [8, 20, 21]. These methods can make the high active tungsten solid fully contact reductant and the carbonization temperature can be reduced. Although the technology is commercialized on a large scale, this process may result in deposition of undesirable amounts of free carbon, and the formation di-tungsten carbide (W_2C), along with the synthesis of WC.

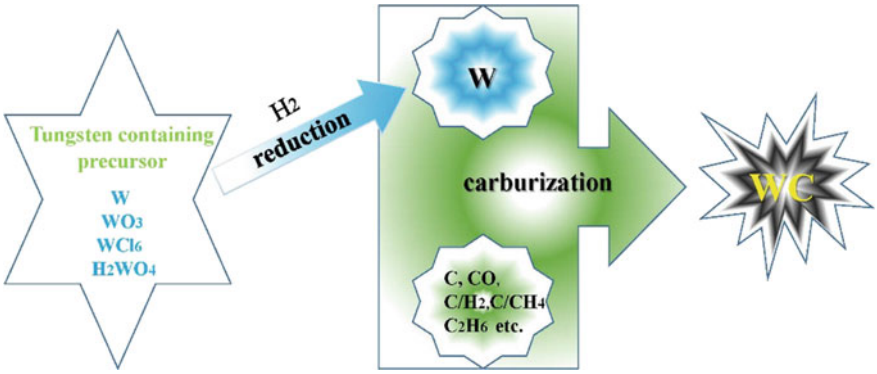

Fig. 1 Two-step method

Table 1 The methods and conditions for the preparation of ultrafine particles WC by two-step processing

Preparation method	Tungsten precursor	Reductant	Reduction temperature (°C)	Carbonization temperature (°C)	Carbon source	Particle size (μm)
Traditional method [18]	W			Carbon black/H_2	1400–1600	1–10
W oxide method [8]	WO_3	H_2/N_2	1400–1200	Carbon black/CH_4	1000–1600	<0.5
Ball milling method [24]	W			Carbon black		0.0072
Halide method [28]	WCl_6	H_2			1400	Ultrafine
Plasma method [28]	WCl_4			H_2/CH_4	Plasma	0.1

In addition, the starting material is again very pure, fine W powder and altogether non-economical. The methods and conditions for the preparation of ultrafine particles WC by two-step processing are shown in Table 1. High-energy mechanical ball milling is the straightforward method for producing nano-sized WC powder. Although milling techniques can be used to produce powders as fine as 10–20 nm, the long duration of processing, contamination, and high-energy expenditure are problems to be solved [22–24]. The spray conversion process is another significant method for synthesis of nano-sized WC powder [25, 26]. Fully dense WC (100%) with a grain size of about 300 nm could be made by sintering at 1750 °C. However, because of the presence of an oxide surface layer, the product contained small amounts of W_2C [27].

One-Step Method

The one-step method is to synthesize WC by using tungsten containing precursor and carbon-containing gas to direct reduction and carburization tungsten carbide. The tungsten-containing precursors were tungsten trioxide [19], tungsten hexachloride [29], tungstenic acid and organic compound [30], Blue tungsten [31], ammonium paratungstate [31]. This process can not only shorten the process but also improve the preparation efficiency of tungsten carbide powder, with a good uniformity and smaller particle size.

(1) *Temperature-programmed reduction method (solid-gas reaction)*

Since tungsten carbide usually has low porosity, the specific surface area is lower than 10 m^2/g. Therefore, many researchers focus on the new synthesis route to obtain higher surface area. Based on the form of carbon resource, the synthesis route can be divided into: solid-liquid reaction, solid-gas reaction, and solid-solid reaction method. In general, tungsten carbide is synthesized by the solid-gas reaction (temperature-programmed reduction) method which uses the reaction between the tungsten oxide (WO_2 or WO_3) and the mixture gas of hydrogen and carbon-containing gases, such as CH_4, C_2H_6, C_3H_8, C_4H_{10} and aromatic compounds [8, 29, 32, 33]. However, Temperature-programmed reduction also has some evident shortages. For example, the products are covered by polymeric carbon resulted from the pyrolysis of excessive carbon-containing gases, and this coke can reduce the surface area and block the catalytically active sites. Moreover, the reaction gas is flammable, and the reaction employs a large amount of flammable gas at high temperature which is very dangerous [34]. Therefore, researchers try to develop new methods to synthesize tungsten carbide under low temperature condition to synthesis high surface area tungsten carbide. Recently, WC was synthesized by a temperature-programmed carburization approach with phosphotungstic acid (PTA) as a precursor and mesoporous silica materials as hard templates, In this method, the WC powder has higher porosity and surface area (BET > 100 m^2/g) but removal of the template generally requires washing with highly corrosive agents such as hydrofluoric acid [35]. Ma et al. [36] successfully synthesized WC with controllable mesoporous structure by hydrothermal synthesis and gas-solid reaction. This mesoporous WC with low carbon content has high surface area (20.4 $m^2\ g^{-1}$), large pore volume (0.074 $cm^3\ g^{-1}$), and large pore-size distribution (centered at about 22 nm). Volatile components enable formation of mesoporous structure and the hydrothermal temperature and ammonium carbonate concentration can control mesopore size. Additionally, the carburization process can be completed at 800 °C for 2 h, the synthesis process is shown in Fig. 2. Cui et al. [37] present a modified replication method to synthesize mesoporous WC with high surface area of 138 $m^2\ g^{-1}$ at a relatively low temperature. The mesoporous WC showed high and stable catalytic activity. In this route PW_{12} as the W source was sealed in the pore channels by compaction under an external pressure to prevent the volatilization of W source during the following reactions with carbon source at a certain

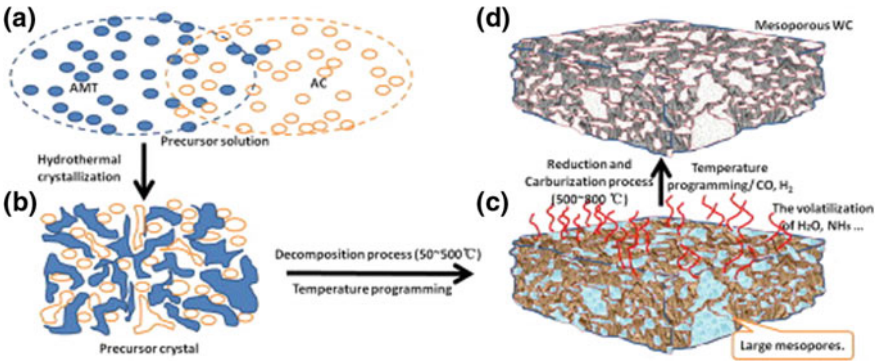

Fig. 2 Schematic illustration of the growth mechanism of mesoporous WC with CO/H_2 mixture as carburization agents: **a** preparation of the precursor solution; **b** crystallization of the precursor crystal; **c** decomposition of volatile components; and **d** carburization [36]

temperature, and WC particles can form only in pore channels which act as a closed micro-reactor.

(2) *Solid-liquid reaction method*

Some researchers have found liquid carbon source can also be employed for the synthesis of tungsten carbide. Giordano et al. [38] and Giordano and Antonietti [39] firstly prepared tungsten carbide by using urea as carbon-source. This specific technique exploits a joint glass of metal orthoesters with urea as a starting reagent, while the output of the reaction could be safely adjusted by the relative composition of the glass. The particles are made as very fine particles with high specific surface area and the BET surface area is about 84 m^2/g [38].

(3) *Solid-solid reaction method*

The large majority of the industrial productions of WC depends on the carbothermal reduction reaction [40, 41]. The current sources of carbon in these methods are non-renewable and include carbon black, coke, asphalt and graphite. These are usually extracted from oil, mined, and their obtainment demands a significant amount of energy [42–45]. WC with higher porosity and surface area (BET > 100 m^2/g) can be synthesized by using the template method [35]. However, removal of the template generally requires washing with highly corrosive agents such as hydrofluoric acid [35]. This leads to an increase in processing costs due to the need for highly selective sacrificial materials and the precautions that must be taken when working with hazardous reagents [46]. Wang et al. [47] proposed a simple approach to fabricate tungsten carbide by using chitosan (a green and renewable biopolymer) as a carbon source. Islam and Martinez-Duarte [46] presented the use of renewable carrageenan (derived from algae) and chitin (derived from disposed shrimp shells) to replace petroleumbased carbon precursors in the synthesis of WC. They mixed these biopolymers with tungsten oxide nanoparticles

to derive a gel-like paste that will serve as carbide precursor. Porous WC was synthesized by heat-treating a biopolymer-tungsten oxide composite (PCP) at 1300 °C for 3 h. The BET surface area was measured as 67.03 m^2/g. The d-spacing was 0.25 nm and is attributed to the t(100) plane of hexagonal WC. The grain size of WC increases from 17.5 nm at 960 °C to 43.3 nm at 1450 °C. In contrast, there is almost no change in grain size with the increase in the dwell time.

Other Methods

Besides those methods, combustion synthesis [22], or self propagating high temperature synthesis (SHS), has also been applied for the synthesis of tungsten carbide. Combustion synthesis, is another attractive technology in carbide fabrication because of its energy efficiency [48]. Won et al. [22] prepared nano-size tungsten carbide powder with a WO_3+M+C+Carbonate system by using alkali halides. X-ray diffraction data and W particle analysis showed that the final product synthesized from a WO_3-Mg-C-$(NH_4)_2CO_3$-NaF system contains pure-phase tungsten carbide with a particle size of 50–100 nm. A small amount of ammonium carbonate activated the carburization of tungsten carbide by the gas phase carbon transportation. Lower synthesis temperature implies lower energy required in the process. Together with the choice of precursors, this makes the process more energy efficient than the traditional methods.

Conclusions

As reviewed above, the present study has focused on the recent research results regarding the processing and characterization of WC powders. The current preparation methods can be divided into two categories, namely two-step method and one-step method. It is obvious that the different preparation routes, tungsten precursors and carbon source can influence the physicochemical properties of tungsten carbides, especially the surface area. By comparing these methods, it is found that one-step method can shorten the process time, improve the preparation efficiency. WC powders prepared by one-step method have high purity and high surface area as well. However, more work is needed to be done in order to reduce the production cost and improve the quality of tungsten carbides. The research trend is to produce tungsten carbides by using the biopolymers as the carbon sources. The potential applications, the feasibility, the advantages and disadvantages of industrialization for these methods were also discussed in this study.

References

1. Kosolapova TIA (1971) Carbides: properties, production, and applications. Chem Commun 49:11133–11148
2. Sternitzke M (1997) Structural ceramic nanocomposites. J Eur Ceram Soc 17:1061–1082
3. Bounhoure V, Lay S, Loubradou M, Missiaen J (2008) Special WC/Co orientation relationships at basal facets of WC grains in WC-Co alloys. J Mater Sci 43:892–899
4. Basu B, Raju GB, Suri AK (2006) Processing and properties of monolithic TiB_2 based materials. Int Mater Rev 51:352–374
5. Einarsrud M, Hagen E, Pettersen G, Grande T (1997) Pressureless sintering of titanium diboride with nickel, nickel boride, and iron additives. J Am Ceram Soc 80:3013–3020
6. Jia K, Fischer TE, Gallois B (1998) Microstructure, hardness and toughness of nanostructured and conventional WC-Co composites. Nanostruct Mater 10:875–891
7. Schubert WD, Bock A, Lux B (1995) General aspects and limits of conventional ultrafine WC powder manufacture and hard metal production. Int J Refract Met Hard Mater 13:281–296
8. Mukhopadhyay A, Basu B (2007) Consolidation–microstructure–property relationships in bulk nanoceramics and ceramic nanocomposites: a review. Int Mater Rev 52:257–288
9. Shi M, Zhang W, Li Y, Chu Y, Ma C (2016) Tungsten carbide-reduced graphene oxide intercalation compound as co-catalyst for methanol oxidation. Chin J Catal 37:1851–1859
10. Zhu H, Sun Z, Chen M, Cao H, Li K, Cai Y, Wang F (2017) Highly porous composite based on tungsten carbide and N-doped carbon aerogels for electrocatalyzing oxygen reduction reaction in acidic and alkaline media. Electrochim Acta 236:154–160
11. Bukola S, Merzougui B, Akinpelu A, Zeama M (2016) Cobalt and nitrogen Co-doped tungsten carbide catalyst for oxygen reduction and hydrogen evolution reactions. Electrochim Acta 190:1113–1123
12. Singla G, Singh K, Pandey OP (2017) Catalytic activity of tungsten carbide-carbon (WC@C) core-shell structured for ethanol electro-oxidation. Mater Chem Phys 186:19–28
13. George M, Baker BS (1975) New materials for fluoro sulfonic acid electrolyte fuel cells. Interim report no 2, 7 March–7 November 1975
14. Garg D, Dyer PN (1989) Tungsten carbide erosion resistant coating for aerospace components. In: MRS proceedings, vol 168
15. Levy RB, Boudart M (1973) Platinum-like behavior of tungsten carbide in surface catalysis. Science 181:547–549
16. Ma Y, Guan G, Hao X, Cao J, Abudula A (2017) Molybdenum carbide as alternative catalyst for hydrogen production—a review. Renew Sustain Energy Rev 75:1101–1129
17. Wu M, Lin X, Hagfeldt A, Ma T (2011) Low-cost molybdenum carbide and tungsten carbide counter electrodes for dye-sensitized solar cells. Angew Chem Int Ed 50:3520–3524
18. Toth LE (1971) Transition metal carbides and nitrides. Academic Press
19. Koc R, Kodambaka SK (2000) Tungsten carbide (WC) synthesis from novel precursors. J Eur Ceram Soc 20:1859–1869
20. Löfberg A, Frennet A, Leclercq G, Leclercq L, Giraudon JM (2000) Mechanism of WO_3 reduction and carburization in CH_4/H_2 mixtures leading to bulk tungsten carbide powder catalysts. J Catal 189:170–183
21. Kanayama N, Horie Y, Nakayama Y (2007) Plasma-carburizing of tungsten with a C_3H_8-H_2 mixed gas. ISIJ Int 33:615–617
22. Won HI, Nersisyan HH, Won CW. Combustion synthesis of nano-sized tungsten carbide powder and effects of sodium halides
23. Fitzsimmons M, Sarin VK (1995) Comparison of WCl_6-CH_4-H_2 and WF_6-CH_4-H_2 systems for growth of WC coatings. Surf Coat Technol 76–77:250–255
24. Fecht HJ, Hellstern E, Fu Z, Johnson WL (1990) Nanocrystalline metals prepared by high-energy ball milling. Metall Trans A 21:2333–2337

25. Zhang Z, Wahlberg S, Wang M, Muhammed M (1999) Processing of nanostructured WC-Co powder from precursor obtained by co-precipitation. Nanostruct Mater 12:163–166
26. Seegopaul P, Gao L (2003) Method of forming nanograin tungsten carbide and recycling tungsten carbide, US
27. Zhao J, Holland T, Unuvar C, Munir ZA (2009) Sparking plasma sintering of nanometric tungsten carbide. Int J Refractory Met Hard Mater 27:130–139
28. Ryu T, Sohn HY, Hwang KS, Fang ZZ (2008) Tungsten carbide nanopowder by plasma-assisted chemical vapor synthesis from WCl_6–CH_4–H_2 mixtures. J Mater Sci 43:5185–5192
29. Hojo J, Oku T, Kato A (1978) Tungsten carbide powders produced by the vapor phase reaction of the WCl_6-CH_4-H_2 system. J Less Common Met 59:85–95
30. Wanner S, Hilaire L, Wehrer P, Hindermann JP, Maire G (2000) Obtaining tungsten carbides from tungsten bipyridine complexes via low temperature thermal treatment. Appl Catal A Gen 203:55–70
31. Medeiros FFP, Oliveira SAD, Souza CPD, Silva AGPD, Gomes UU, Souza JFD (2001) Synthesis of tungsten carbide through gas–solid reaction at low temperatures. Mater Sci Eng A 315:58–62
32. Löfberg A, Frennet A, Leclercq G, Leclercq L, Giraudon JM (2000) Mechanism of WO_3 reduction and carburization in CH_4/H_2 mixtures leading to bulk tungsten carbide powder catalysts. J Catal 189:170–183
33. Decker S, Löfberg A, Bastin JM, Frennet A (1997) Study of the preparation of bulk tungsten carbide catalysts with C_2H_6/H2 and C_2H_4/H_2 carburizing mixtures. Catal Lett 44:229–239
34. Ma Y, Guan G, Hao X, Cao J, Abudula A (2017) Molybdenum carbide as alternative catalyst for hydrogen production—a review. Renew Sustain Energy Rev 75:1101–1129
35. Wu Z, Yang Y, Gu D, Li Q, Feng D, Chen Z, Tu B, Webley PA, Zhao D (2009) Silica-templated synthesis of ordered mesoporous tungsten carbide/graphitic carbon composites with nanocrystalline walls and high surface areas via a temperature-programmed carburization route. Small 5:2738
36. Ma C, Chen Z, Lin W, Zhao F, Shi M (2012) Template-free environmentally friendly synthesis and characterization of unsupported tungsten carbide with a controllable porous framework. Microporous Mesoporous Mater 149:76–85
37. Cui X, Li H, Guo L, He D, Chen H, Shi J (2008) Synthesis of mesoporous tungsten carbide by an impregnation–compaction route, and its NH_3 decomposition catalytic activity. Dalton Trans 6435
38. Giordano C, Erpen C, Yao W, Antonietti M (2008) Synthesis of Mo and W carbide and nitride nanoparticles via a simple "urea glass" route. Nano Lett 8:4659–4663
39. Giordano C, Antonietti M (2011) Synthesis of crystalline metal nitride and metal carbide nanostructures by sol–gel chemistry. Nano Today 6:366–380
40. Barker J, Saidi MY, Swoyer JL (2003) Lithium iron(II) phospho-olivines prepared by a novel carbothermal reduction method. Electrochem Solid-State Lett 6:A53
41. Guo X, Zhu L, Li W, Yang H (2013) Preparation of SiC powders by carbothermal reduction with bamboo charcoal as renewable carbon source. J Adv Ceram 2:128–134
42. Wang J, Risa Ishida A, Takarada T (2000) Carbothermal reactions of quartz and kaolinite with coal char. Energy Fuels 14:1108–1114
43. Czosnek C, Janik JF, Olejniczak Z (2002) Silicon carbide modified carbon materials. Formation of nanocrystalline SiC from thermochemical processes in the system coal tar pitch/poly(carbosilane). J Clust Sci 13:487–502
44. Narisawa M (2008) Silicon carbide particle formation from carbon black and polymethylsilsesquioxane mixtures with melt pressing. J Ceram Soc Jpn 116:121–125
45. Alizadeh A, Taheri-Nassaj E, Ehsani N (2004) Synthesis of boron carbide powder by a carbothermic reduction method. J Eur Ceram Soc 24:3227–3234

46. Islam M, Martinez-Duarte R. A sustainable approach for tungsten carbide synthesis using renewable biopolymers
47. Wang B, Tian C, Wang L, Wang R, Fu H (2010) Chitosan: a green carbon source for the synthesis of graphitic nanocarbon, tungsten carbide and graphitic nanocarbon/tungsten carbide composites. Nanotechnology 21:025606
48. Merzhanov AG (2004) The chemistry of self-propagating high-temperature synthesis. J Mater Chem 14:1779–1786

Influence of Hot Rolling on Mechanical Behavior and Strengthening Mechanism in Boron Carbide Reinforced Aluminum Matrix Composites

Hao Guo, JianNeng Zhang, Yang Zhang, Ye Cui, Dan Chen, Yu Zhao, SongSong Xu, NaiMeng Liu and ZhongWu Zhang

Abstract Boron carbide reinforced aluminum matrix composites are widely used as neutron absorption materials. Here we report that mechanical alloying has been successfully employed to synthesize metal matrix composite powders with Al as the matrix and B_4C, Al_4Gd and Al_4Sm as the reinforcement. The effects of hot rolling on the morphology, mechanical properties as well as the strengthening mechanisms are investigated. Hot rolling results in improving particle distribution and less agglomeration, improving the bonding between particles and matrix and decreasing voids. Thermomechanical processing can increase the density and remove the defects. As increasing rolling deformation to 50%, both YS and UTS of composites are enhanced significantly, showing 25.8 and 27.0% improvement in comparison with composites after sintered, but the elongation changes little. The increase in the yield strength after hot rolling can be attributed to two primary strengthening mechanisms in this work: The coefficient of thermal expansion (CTE) mismatch between B_4C, Al_4Gd and Al_4Sm reinforced particles and Al matrix and the existence of load transfer from Al matrix to the hard reinforced particles.

Keywords Boron carbide · Aluminum matrix composites · Mechanical properties · Strengthening mechanism

Introduction

The development of strong and lightweight aluminum matrix composites have attracted strong interest in these material systems of the aerospace application, military industries and automotive industries, and energy applications [1–6] by

H. Guo · J. Zhang · Y. Zhang · Y. Cui · D. Chen · Y. Zhao · S. Xu · N. Liu
Z. Zhang (✉)
Key Laboratory of Superlight Materials and Surface Technology, Ministry of Education, College of Materials Science and Chemical Engineering, Harbin Engineering University, Harbin 150001, China
e-mail: zwzhang@hrbeu.edu.cn

The Minerals, Metals & Materials Society, *TMS 2018 147th Annual Meeting & Exhibition Supplemental Proceedings*, The Minerals, Metals & Materials Series,
https://doi.org/10.1007/978-3-319-72526-0_81

virtue of their favorable properties. Aluminum matrix composites can be produced by powder metallurgy with various reinforced particulates like oxides, carbides and borides [4–11]. B_4C is one of the most widely used ceramic reinforcements for aluminum matrix composites. Boron carbide (B_4C) is an attractive reinforcement material due to its excellent properties of high hardness, low density, and good interfacial cohesion with aluminum [12, 13]. Boron carbide ceramics also have excellent chemical resistance and high capability for neutron absorption. It has been used in many industrial fields, such as military, engineering and nuclear energy.

The influence of adding B_4C reinforced particles on the mechanical behavior of aluminum matrix composites has been widely studied in the literature [14–16]. The related strengthening in boron carbide reinforced aluminum matrix composites is usually complex due to multiple potential mechanisms, all the mechanisms are associated with the microstructure of composites, which varies greatly with the dispersion and consolidation processes in different studies [17, 18].

In this study, the effects of hot rolling on the morphology, mechanical properties as well as the strengthening mechanisms are investigated. XRD was used analysis the existence of phases, optical microscope (OM) were reveal the microstructure, and scanning electron microscope (SEM) showed the size distribution, morphology of powders and the appearance of fracture.

Experimental

High purity (99.9%) Al powders, 92.5% pure boron carbide particles and Al-Gd, Al-Sm powders were prepared as starting materials. And the average particle size of Al powders was about 10 μm, the average particle size of boron carbide particles was about 10 μm. Aluminum powders were mixed with reinforced particles and 1 wt% stearic acid, then ball milled to produce Al-30%B_4C-1%Gd-1%Sm composites with 30 wt% of boron carbide, 1 wt% Gd and 1 wt% Sm content using a high energy ball milling machine named QM-3SP2. In this work, we used two zirconia vials containing Al_2O_3 balls. The powders were sealed in a zirconia jar together with 600 g Al_2O_3 media balls (6 mm in diameter). Ball milling parameter: the rotation speed was 300 rpm/min and milling time was 8 h, and ball to powder weight ratio was 5:1. To minimize cold welding of Al powders, we used 1 wt% of stearic acid as a process control agent.

Then Milled powders were consolidated into bulk composites with homogeneously distributed B_4C. Milled powders were put into a steel die for hot pressed and sintered. Subsequently milled powders was heated to 570 °C for 2 h and pressed at 20 MPa. The whole process is under high vacuum environment reached 3×10^{-2} Pa. The hot pressed samples were then prepared for hot rolling. The samples were heated at 450 °C for 30 min and then hot-rolled with a thickness reduction of 25% and 50%. Between passes samples were returned to heat to 450 °C for 30 min.

The phase components were analyzed by X-ray diffraction (XRD) with Cu Kα radiation on Rigaku D/max-TTR-III diffractometer with a Cu Target K alpha ray, 40 kV, 150 mA. Optical microscopy (OM) was used to characterize the microstructure. The distribution of the B_4C in the Al matrix, as well as the B_4C powder morphology, tensile fracture morphologies was studied using a scanning electron microscope (SEM). The tensile tests were conducted at room temperature with a strain rate of 1×10^{-3}/s on INSTRON 5565. For each composite, three specimens were tested. The yield strength was used the 0.2% off set plastic strain method.

Results and Discussion

Figure 1 shows the SEM micrographs of the mixture of Al-30%B_4C-1%Gd-1%Sm powders after 8 h milling. In the powder mixtures, the B_4C particles were randomly dispersed. In high energy ball milling processes, it can be seen that particles appear spherical after milled for 8 h, severe plastic deformation happened to Al powder particles, accompanied with reinforced particles damage. And Al particles seem plate like and fragmentary, most particles became smaller, but there still were limited change happened to several big particles.

Microstructure

Figures 2, 3 and 4 shows the microstructures of the Al-30%B_4C-1%Gd-1%Sm composites samples. Figure 2 shows the sintered samples were highly consolidated and no macropore was observed: (a) as sintered at low magnifications, (b) as sintered at high magnifications. Figure 3 shows the 25% hot-rolled samples: (a) 25%

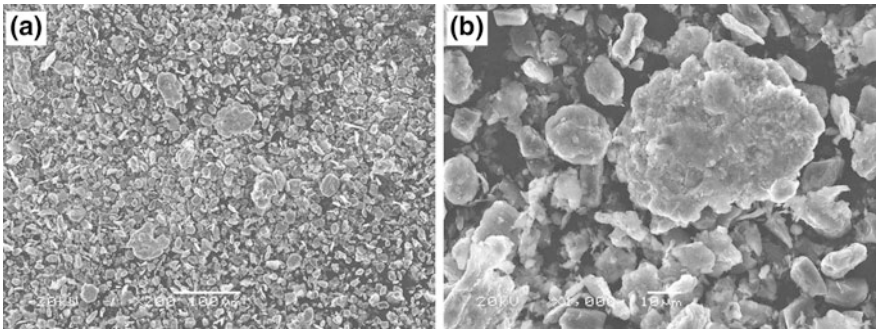

Fig. 1 SEM micrographs of a mixture of Al-30%B_4C-1%Gd-1%Sm powders, milled for 8 h: **a** at low magnifications, **b** at high magnifications

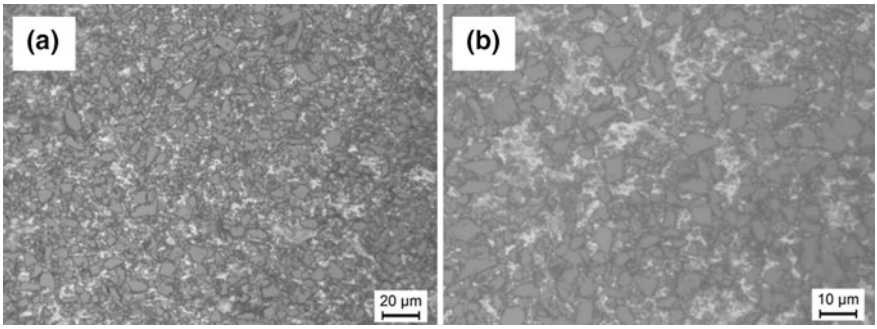

Fig. 2 Microstructures of the samples as sintered: **a** at low magnifications, **b** at high magnifications

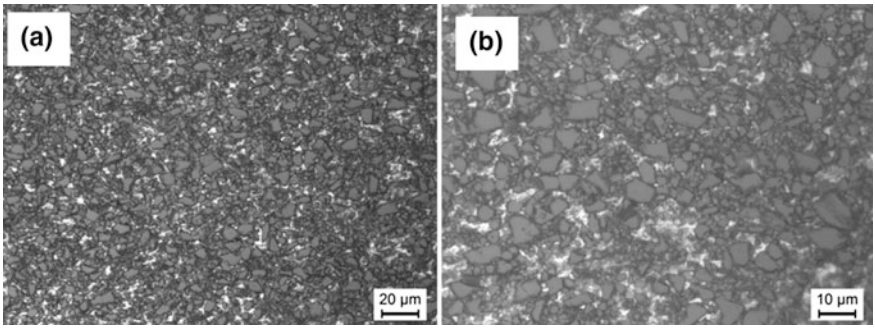

Fig. 3 Microstructures of the samples 25% hot-rolled: **a** at low magnifications, **b** at high magnifications

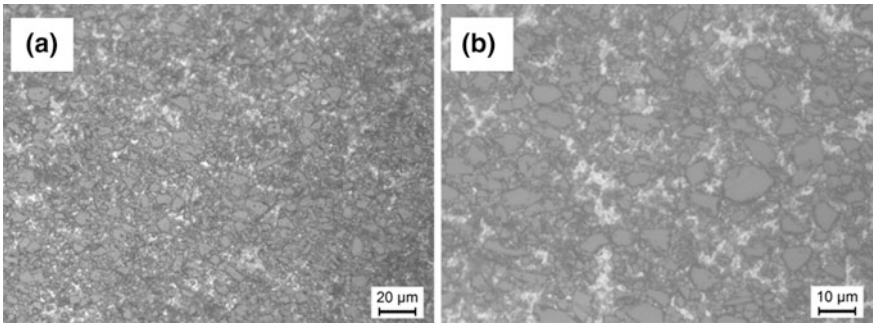

Fig. 4 Microstructures of the samples 50% hot-rolled: **a** at low magnifications, **b** at high magnifications

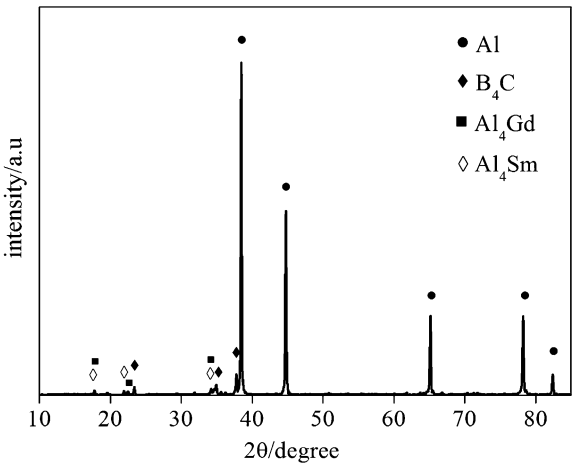

Fig. 5 XRD patterns of Al-30%B_4C-1%Gd-1%Sm composites after sintered

hot-rolled at low magnifications, (b) 25% hot-rolled at high magnifications. Figure 4 shows the 50% hot-rolled samples: (a) 50% hot-rolled at low magnifications, (b) 50% hot-rolled at high magnifications. From the microstructures, hot rolling results in improving particle distribution and less agglomeration, improving the bonding between particles and matrix and decreasing voids. And the density of the composites can reach 96.6% after sintering. Thermomechanical processing can increase the density further to 98.3% and remove the defects.

Figure 5 shows the XRD patterns of Al-30%B_4C-1%Gd-1%Sm composites samples after sintered. It can be seen that Al peaks and B_4C peaks can be detected easily. The intensities of the Al peaks and B_4C peaks are all clear, and it's obviously to be seen that the intensities of the Al peaks are stronger than B_4C peaks, it means that the content of Al much more than the content of B_4C. Meanwhile many small peaks were also observed. It confirmed that there was indeed Al_4Gd and Al_4Sm existed in the composites.

Mechanical Properties

The engineering tensile stress-strain curves of Al-30%B_4C-1%Gd-1%Sm composites with different conditions: after sintered, 25% hot-rolled and 50% hot-rolled are shown in Fig. 6. The average 0.2% offset yield strength (YS) of Al-30%B_4C-1%Gd-1%Sm composites after sintered, 25% hot-rolled and 50% hot-rolled were measured to be 221 MPa, 268 MPa and 278 MPa, respectively. The ultimate tensile strength (UTS) of Al-30%B_4C-1%Gd-1%Sm composites after sintered, 25% hot-rolled and 50% hot-rolled are respectively 278 MPa, 320 MPa and 353 MPa. The elongation of Al-30%B_4C-1%Gd-1%Sm composites after sintered, 25% hot-rolled and 50% hot-rolled are 1.24%, 1.27% and 1.00%, respectively. It is obviously that, as increasing

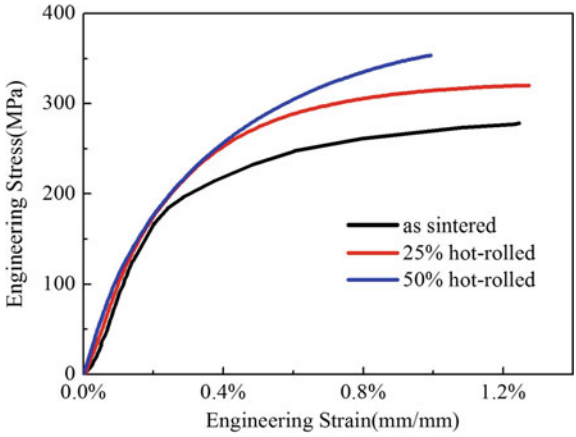

Fig. 6 Tensile properties of the investigated Al-30% B_4C-1%Gd-1%Sm composites

rolling deformation to 50%, both YS and UTS of composites are enhanced significantly, showing 25.8 and 27.0% improvement in comparison with composites after sintered, but the elongation changes little. It is known that rolling can enhance Al matrix strength but sacrifice ductility. Meanwhile, except for Al matrix strength, the composite strength is also related to reinforcing effect of B_4C, Al_4Gd and Al_4Sm reinforced particles. Thermomechanical processing can also remove the defects. All composites exhibited high mechanical properties. This is mainly attributed to fine grain, uniform B_4C, Al_4Gd and Al_4Sm reinforced particles distribution, and good interfacial bonding between B_4C and Al matrix.

Strengthening by Hot Rolling in Al/B_4C Composites

For a successful development of B_4C reinforced aluminum matrix composites, it is necessary to understand the relevant strengthening mechanisms of these composites. There are several modeling methods available for predicting the strength of B_4C reinforced Al composites. In general, the increase in the yield strength of B_4C reinforced Al composites can be attributed to four strengthening mechanism [19]: (1) the coefficient of thermal expansion (CTE) mismatch between B_4C, Al_4Gd and Al_4Sm reinforced particles and Al matrix; (2) The existence of load transfer from Al matrix to the hard reinforcements B_4C, Al_4Gd and Al_4Sm particles in B_4C reinforced Al composites; (3) Orowan strengthening mechanism exists in the B_4C reinforced Al composites; (4) Hall-Petch strengthening mechanism exists in the composites. In this work, Orowan strengthening mechanism and Hall-Petch strengthening mechanism resulting in only a minor strength change between different rolling conditions.

The coefficient of thermal expansion (CTE) mismatch between B_4C, Al_4Gd and Al_4Sm reinforced particles and Al matrix can play an important role in

strengthening. Hot rolling leads to the dislocation density increase around the reinforced particles because of the different coefficient of thermal expansion between reinforced particles and Al matrix. CTE mismatch strengthening can be calculated by [14]:

$$\Delta\sigma_C = \alpha G b \left(\sqrt{\frac{12 f \Delta C \Delta T}{bd}} \right) \tag{1}$$

where α is a constant that is equal to 1.25, G is shear modulus of the pure Al matrix (26.4 GPa), ΔC is the CTE mismatch between the B_4C particle and the Al matrix [16], ΔT is the maximum temperature change during thermomechanical processing, the value $\Delta T = 425$ K was calculated, f is the volume fraction of reinforcement particles, $b = 0.286$ is the magnitude of the Burgers vector, d is the average reinforcement particle diameter. According to the calculation, the $\Delta\sigma_C$ caused by hot rolling under different rolling conditions: after sintered, 25% hot-rolled and 50% hot-rolled are 0 MPa, 39.1 MPa and 39.1 MPa, respectively.

According to the load transfer model in metal matrix composites developed by Kelly and Tyson [17], the load transfer from matrix to the hard reinforcements B_4C particles under an applied external load such as hot pressed process, hot rolling process contributes to the strengthening of the Al matrix. B_4C particles are loaded by the plastically flowed matrix via an interfacial shear stress generated along the B_4C particles surface under tension. If the size of the boron carbide particulate parallel to the load direction l is smaller than a critical length (l_c) given by $l_c = d \cdot \sigma_R / \sigma_m$ [17, 20], where d and σ_R are respectively the size of the boron carbide particulate perpendicular to the load direction and strength of reinforced particles, and σ_m is the strength of Al matrix, reinforced particles will be pulled out. Otherwise, B_4C, Al_4Gd and Al_4Sm reinforced particles will fail by breakage. Since the equiaxed boron carbide particulates and the strength of reinforced particles σ_m is higher than strength of Al matrix, reinforced particles are predicted to fail in the pull-out mode, which agrees well with the Fig. 7. On the fracture surface of the

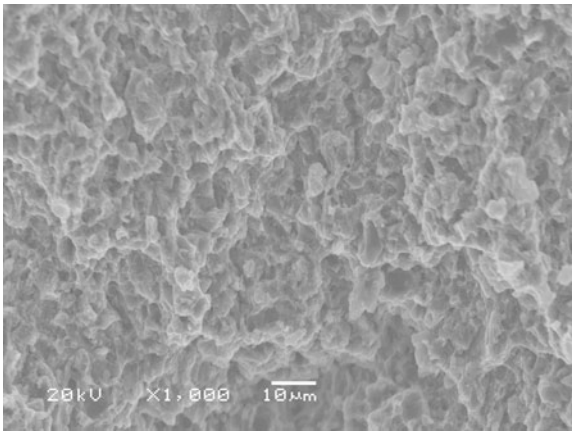

Fig. 7 Tensile fracture morphologies of the samples

composites, pulled-out B_4C particles are observed, suggesting that the load transfer mechanism gives much contribution.

Under the pull-out mode, for the equiaxed boron carbide particulates, a general equation for the load transfer contribution of B_4C, Al_4Gd and Al_4Sm reinforced particles is given in the following expression [21, 22]:

$$\Delta\sigma_{LT} = \frac{1}{2} v_p \sigma_m \tag{2}$$

where v_p is the volume fraction of reinforced particles in the Al matrix. The σ_m of Al matrix is different under different rolling conditions. According to the calculation, the $\Delta\sigma_{LT}$ for composites after sintered, 25% hot-rolled and 50% hot-rolled are 12.9 MPa, 16.6 MPa and 17.8 MPa, respectively.

By the above analysis, difference value between the yield strength of theoretic and experiment values is slight. There is a yield strength difference of 47 MPa between the composites after sintered and 25% hot-rolled, and a yield strength difference of 57 MPa between the composites after sintered and 50% hot-rolled in experiment values. The theoretic values of the yield strength difference are 42.8 MPa and 44.0 MPa, respectively.

SEM Analysis of Tensile Fracture

Figure 7 shows the fracture surface morphology of the Al-30%B_4C-1%Gd-1%Sm composites sample after tensile tests. It can be seen by SEM images that the fracture morphology is including both shallow dimples and brittle fractures. But the dimples are small and shallow. On the fracture surface of the composites, B_4C particles pull-out phenomenon can be detected, suggesting that the load transfer mechanism gives much contribution. However, the observed B_4C particles clusters on the fracture surface acted as crack initiation sites, the interfacial bonding strength between particle and matrix is weak. So the interfacial debonding is the primary cause of Al-30%B_4C-1%Gd-1%Sm composites sample is the cleavage fracture of particle.

Conclusions

In this study, synthesis and characterization of Al-30%B_4C-1%Gd-1%Sm composites by mechanical alloying was investigated. The present work has revealed that: In the powder mixtures, the B_4C particles were randomly dispersed, severe plastic deformation happened to Al powder particles, accompanied with reinforced particles damage. Hot rolling results in improving particle distribution and less agglomeration, improving the bonding between particles and matrix and decreasing

voids. Thermomechanical processing can increase the density and remove the defects.

As increasing rolling deformation to 50%, both YS and UTS of composites are enhanced significantly, showing 25.8 and 27.0% improvement in comparison with composites after sintered, but the elongation changes little. The increase in the yield strength of B_4C reinforced Al composites after hot rolling can be attributed to two primary strengthening mechanisms in this work: The coefficient of thermal expansion (CTE) mismatch between B_4C, Al_4Gd and Al_4Sm reinforced particles and Al matrix and the existence of load transfer from Al matrix to the hard reinforced particles.

Acknowledgements This work was supported by the NSFC Funding (51371062 and U1460102), NSFHLJ (ZD201411). Hao Guo is benefited from the International Exchange Program of Harbin Engineering University for Innovation-oriented Talents Cultivation.

References

1. Casati R, Bonollo F, Dellasega D, Fabrizi A, Timelli G, Tuissi A et al (2014) Ex situ Al-Al2O3 ultrafine grained nanocomposites produced via powder metallurgy. J Alloy Compd 615(Suppl S1):S8–S386
2. Han BQ, Huang JY, Zhu YT, Lavernia EJ (2006) Strain rate dependence of properties of cryomilled bimodal 5083 Al alloys. Acta Mater 54(11):24–3015
3. Wu C, Fang P, Luo G, Chen F, Shen Q, Zhang L et al (2014) Effect of plasma activated sintering parameters on microstructure and mechanical properties of Al-7075/B4C composites. J Alloy Compd 615(Suppl C):276–282
4. Yi C, Chen X, Gou F, Dmuchowski CM, Sharma A, Park C et al Direct measurements of the mechanical strength of carbon nanotube—Aluminum interfaces. Carbon
5. Zhou YT, Zan YN, Zheng SJ, Wang QZ, Xiao BL, Ma XL et al (2017) Distribution of the microalloying element Cu in B4C-reinforced 6061Al composites. J Alloy Compd 728(Suppl C):112–117
6. Ye J, Han BQ, Lee Z, Ahn B, Nutt SR, Schoenung JM (2005) A tri-modal aluminum based composite with super-high strength. Scr Mater 53(5):481–486
7. Zhang P, Li Y, Wang W, Gao Z, Wang B (2013) The design, fabrication and properties of B4C/Al neutron absorbers. J Nucl Mater 437(1):350–358
8. Froumin N, Frage N, Aizenshtein M, Dariel MP (2003) Ceramic–metal interaction and wetting phenomena in the B4C/Cu system. J Eur Ceram Soc 23(15):2821–2828
9. Abdollahi A, Alizadeh A, Baharvandi HR Dry sliding tribological behavior and mechanical properties of Al2024-5wt.%B4C nanocomposite produced by mechanical milling and hot extrusion. Mater Des 55(Suppl C):471–481
10. Han Q, Geng Y, Setchi R, Lacan F, Gu D, Evans SL (2017) Macro and nanoscale wear behaviour of Al-Al2O3 nanocomposites fabricated by selective laser melting. Compos B Eng 127(Suppl C):26–35
11. Kubota M, Cizek P, Rainforth WM (2008) Properties of mechanically milled and spark plasma sintered Al-15at.% MgB2 composite materials. Compos Sci Technol 68(3):888–895
12. Ma Q-C, Zhang G-J, Kan Y-M, Xia Y-B, Wang P-L (2010) Effect of additives introduced by ball milling on sintering behavior and mechanical properties of hot-pressed B4C ceramics. Ceram Int 36(1):167–171

13. Kubota M (2010) Solid-state reaction in mechanically milled and spark plasma sintered Al-B4C composite materials. J Alloy Compd 504(Suppl 1):S319–S322
14. Chen HS, Wang WX, Li YL, Zhang P, Nie HH, Wu QC (2015) The design, microstructure and tensile properties of B4C particulate reinforced 6061Al neutron absorber composites. J Alloy Compd 632(Suppl C):23–29
15. Jiang L, Wen H, Yang H, Hu T, Topping T, Zhang D et al (2015) Influence of length-scales on spatial distribution and interfacial characteristics of B4C in a nanostructured Al matrix. Acta Mater 89:327–343
16. Jiang L, Yang H, Yee JK, Mo X, Topping T, Lavernia EJ et al (2016) Toughening of aluminum matrix nanocomposites via spatial arrays of boron carbide spherical nanoparticles. Acta Mater 103:128–140
17. Chen B, Kondoh K, Imai H, Umeda J, Takahashi M (2016) Simultaneously enhancing strength and ductility of carbon nanotube/aluminum composites by improving bonding conditions. Scr Mater 113(Suppl C):158–162
18. Chen B, Shen J, Ye X, Jia L, Li S, Umeda J, et al (2017) Length effect of carbon nanotubes on the strengthening mechanisms in metal matrix composites. Acta Mater
19. Guo H, Zhang Z (2017) Processing and strengthening mechanisms of boron- · carbide-reinforced aluminum matrix composites. Metal Powder Rep
20. Bakshi SR, Agarwal A (2011) An analysis of the factors affecting strengthening in carbon nanotube reinforced aluminum composites. Carbon 49(2):533–544
21. Sanaty-Zadeh A (2012) Comparison between current models for the strength of particulate-reinforced metal matrix nanocomposites with emphasis on consideration of Hall–Petch effect. Mater Sci Eng A 531(Suppl C):112–118
22. Casati R, Vedani M (2014) Metal matrix composites reinforced by nano-particles—a review. Metals (Basel) 4(1):65–83

Preparation of Titanium Foams with Uniform and Fine Pore Characteristics Through Powder Metallurgy Route Using Urea Particles as Space Holder

Qiu Guibao, Lu Tengfei, Wang Jian and Bai Chenguang

Abstract Titanium powder particles were used as the matrix and powdery urea particles as the space holder to fabricate porous titanium by powder metallurgy technology. And titanium foams with porosity of 42.7–56.2% were prepared successfully. The uniform distribution of the tiny urea particles in the matrix made the titanium foams have homogeneous and connected pore structure. Pore morphology and compressive behavior of the resulting foam have been studied. The pore structure is composed of large pores and small pores distributed on the hole wall, and these small pores are mostly interconnected. Porous regions contained some micro-pores increasing the connectivity of pores. The mechanical behavior was investigated by compressive test, the foams delineated a relatively stable plateau region and the yield strength and Young's modulus vary in the range of 93.85–276.52 Mpa and 1.53–3.21 GPa respectively. The results manifested that the processed foams is an ideal medical implant, impact energy absorbing and filterability material.

Keywords Porous Ti · Pore structure · Mechanical property
Porosity

Introduction

Metallic foams find a variety of applications in the field of lightweight structural materials, impact energy absorbers, filters and biomedical implants due to their excellent physical and mechanical Properties [1]. In recent years, titanium foams have drawn considerable attention due to its high specific strength and stiffness,

Q. Guibao (✉) · L. Tengfei · W. Jian · B. Chenguang
College of Materials Science and Engineering, Chongqing University,
Chongqing 400040, China
e-mail: qiuguibao@cqu.edu.cn

The Minerals, Metals & Materials Society, *TMS 2018 147th Annual Meeting & Exhibition Supplemental Proceedings*, The Minerals, Metals & Materials Series,
https://doi.org/10.1007/978-3-319-72526-0_82

good biocompatibility and excellent corrosion resistance [2], which enhance the potential for the use of Ti in industrial applications. High melting point and excellent corrosion resistance of titanium also make it suitable for high temperature applications such as high temperature heat exchangers [3]. Open cellular titanium foams are also being utilized in bone implants due to their excellent mechanical properties and biocompatibility. The closed cell titanium foams possess higher modulus, strength and good compression performance is a kind of potential structural application materials in the aerospace and naval industries [4]. At the same time, It should be mentioned that titanium foams are difficult to fabricate through liquid metallurgy technology due to the high melting point (1667 °C) and chemical reactivity of the element with atmospheric gases such as oxygen, nitrogen etc. [3]. Therefore, powder metallurgy and pore forming agent technology [5] have been widely used in the preparation of titanium foams in various ways. Amongst them, sintering of powder preformed with a gas blowing agent or solid space holders is most commonly used [6]. The pore forming agent is a temporary filling material which can be removed in the process of preparing titanium foam. Accordingly, the porosity of the foam can be adjusted by changing the amount of pore forming agent, meanwhile the porous titanium with different pore structure can be prepared by selecting different Shapes and dimensions of solid space holders. In the process of preparing titanium foam, various space holders like polymeric materials [7], urea [8], magnesium [9], ammonium hydrogen carbonate [10], saccharose [11], starch [12] have been utilized. Because of its simple operation, good controllability and low cost pore forming agent technology has became an important method for the preparation of titanium foam.

In view of the above, porous titanium was prepared successfully using powdery urea as the solid state space holder in the present work. The pore morphology and compression behavior of the foam have been investigated.

Experimental Procedure

Titanium metal powder (average particle size ~45 μm, 99.5% pure) supplied by Beijing Xing Rong Yuan Technology Co., Ltd., China and urea particles (size: ~165 μm, 99.5% pure) supplied by Chengdu Ke Long Chemical Co., Ltd. were used as the starting materials, the raw materials' Titanium powder was irregular in shape while urea were generally Powdery particles, and the microstructure of urea particles and Ti-powder is shown in Fig. 1a and b (Some of the darker areas of urea are shown to be caused by poor electrical conductivity of urea). In the present study, in order to obtain foam titanium with interconnected structure, the volume fraction of urea was increased from 55 to 70% in this experiment. Titanium powder and urea particles were mixed uniformly in a mortar for 30 min. Moreover, a little zinc stearate (about 0.5 g) was used to improve the

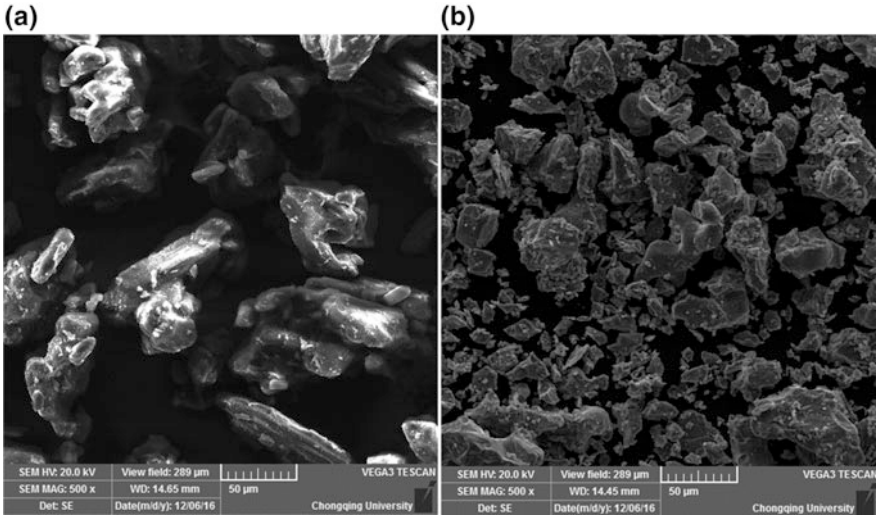

Fig. 1 SEM micrograph showing (**a**) urea particles and (**b**) Ti powder

fluency and lubrication property between the mixing particles and cylindrical die to reduce the friction in the pressing process. Then, the particle mixed was cold compacted in a 16 mm diameter cylindrical die at an applied pressure of 150 MPa for 1 min in order to ensure effective and uniform pressing. And the last step is heating process, the compacted samples were heated up to 450 °C firstly at a constant heating rate of 13 °C/min and held at that point for 60 min with a view to realize the complete removal of urea, and secondly sintered at the temperature of 1200 °C for 1.5 h (The parameters, i.e. the temperature, duration and rate of heating for the urea removal and high sintering treatments, were selected based on previous studies). As described earlier, the level of vacuum in the furnace must be kept at 10^{-3} mbar when removing urea and sintering because of high chemical reactivity of titanium in this experiment. Finally, the samples were taken out from the furnace after which has been cooled to ambient temperature.

The pore structure of Ti samples was determined by scanning electron microscope (SEM) and porosity calculated according to the following equation [13, 14].

$$P = 1 - \frac{\rho^*}{\rho_s} \tag{1}$$

where ρ* represents the density of porous Ti, which can be measured by dividing the whole weight to the whole volume of the sample; ρ_s denotes the density of the solid Ti ($\rho_s = 4.503$ g/cm^3). Meanwhile, the compressive strength was measured by material testing machine at a strain rate of 0.01/s. An average of three observations has been reported in this case.

Results and Discussion

Macroscopic Morphology and Composition Analysis of Titanium Foam

Using the space-holder method, titanium foams with various initial urea particles content (55, 60, 65 and 70 vol.%) were successfully fabricated. The Fig. 2a is the image of titanium foams sintered, and the (b) is its XRD pattern. Visual inspection reveals a good integrity of the sintered samples, which possess obvious pore characteristics. And pores distributed uniformly can be observed from the surface of cylindrical samples. Figure 2b indicates that there is no characteristic peak of other substances in addition to the characteristic peaks of titanium. The result illustrates that the urea (pore forming agent) added in the preparation process had been completely decomposed, and the decomposition products were excluded from the furnace in time,which ensures the purity and non toxicity of the titanium foam products. Meanwhile, it reflects the safety of the titanium implant.

The Pore Structure of Titanium Foam

As shown in Fig. 3, the black part represents the pore areas and the yellow part represents the pore walls (titanium matrix). It is clear from Fig. 3 that the pore area is evenly distributed in the entire section, the macro-pores are connected to each other to form a clear connection structures. From the direction indicated by the arrow in Fig. 3, these pores are actually interconnected to form a larger and longer connection structure. And there is little macro-pore exists alone in the cross section of the foam but these are connected to some extent. It is noteworthy that there are

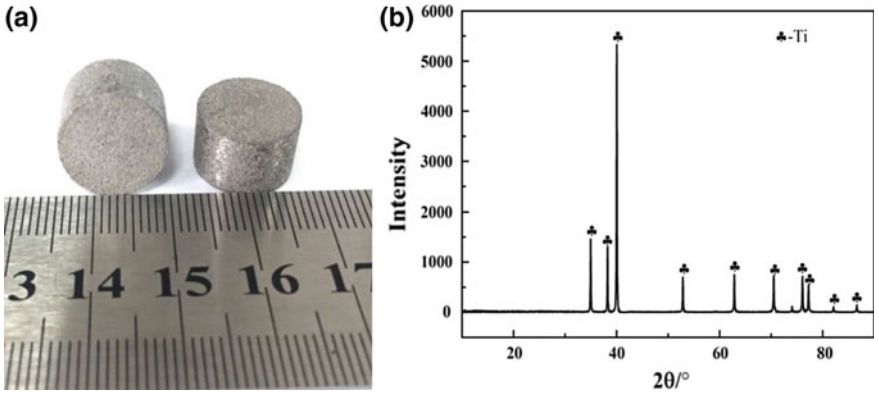

Fig. 2 The image (**a**) and XRD pattern (**b**) of sintered Ti foam with a porosity of 51.67%

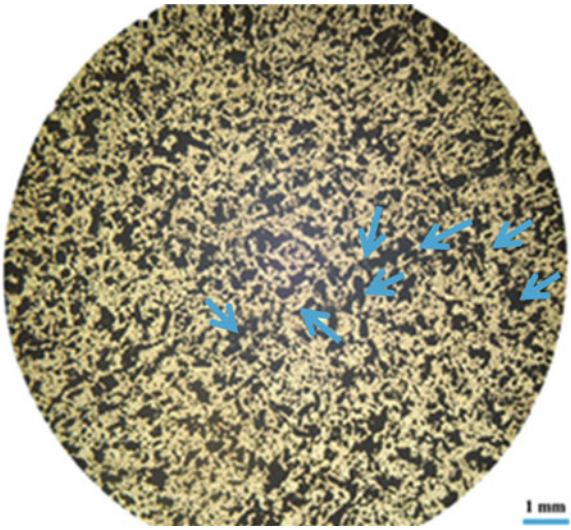

Fig. 3 Optical microscope micrographs showing the pore structure of foam titanium with a porosity of 51.67%

still a large number of small pores in the pore wall, which are also connected to adjacent pores as shown in Fig. 4c. Thus, the above two kinds of connected pore features will enhance the connectivity (permeability) of the foams. Based on pore morphology observation, the pores do not have specific shapes and show the diversity of pore morphology, which makes titanium foams possess diverse pore structures. On the one hand, this result is probably due to powdery urea particles used as pore forming agent. The fine pore forming agents can be more homogeneous with titanium powders than the larger one at the mixing stage because of excellent dispersion characteristics. However, as shown in Fig. 4b, urea aggregation effect results in the presence of some spherical macro–pores in some local areas. This does not affect the uniformity of the foam titanium as a whole shown in Fig. 4a. On the other hand, in the sintering process, the diffusion of titanium atoms and the shrinkage of the matrix are also possible to make the adjacent small pores with thin pore walls fuse into larger pores in partial area after removing the pore forming agent. This combination of pores into a large one through the fusion is also a way to improve the connectivity and diversity of foam titanium. In the pore structure of Fig. 4d, there are also some micro-pores, which is about 1–5 μm in size. Its presence is mainly due to the tiny gaps between titanium particles in the green compact and the incomplete sintering of the titanium powders during the sintering process. From the view of the biomedicine, the micro-pores on the pore walls are also conducive to further improvement of the titanium foams connectivity. The titanium foams were prepared in this experiment with pore size distribution mainly in the range of 50–300 μm. This is beneficial to cell adhesion, growth and differentiation. Furthermore, it can also promote the bone tissue growth and strengthen the connection between titanium foam and bone tissue, the transmission of human tissue fluid and the discharge of metabolites [15, 16].

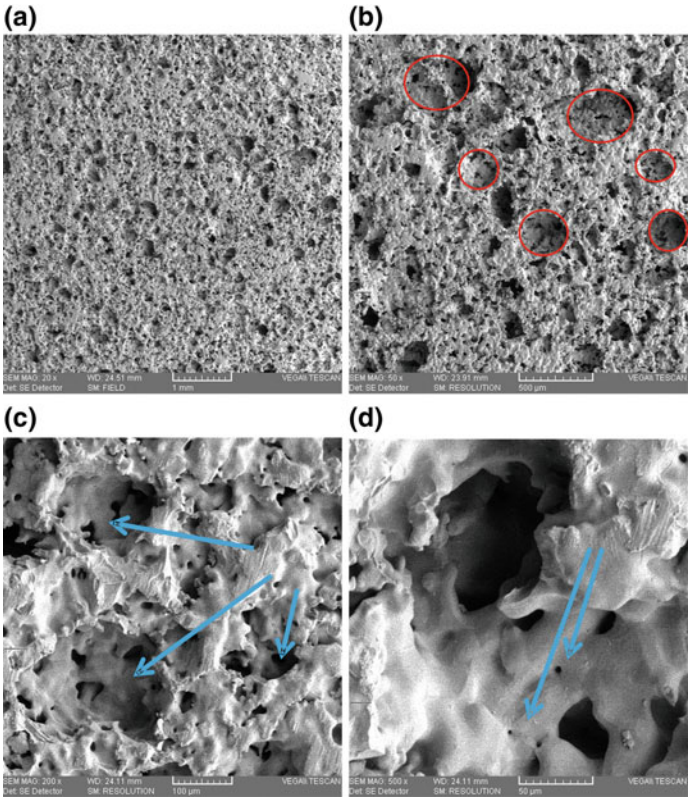

Fig. 4 SEM images showing the pore structure of foam titanium with a porosity of 56.23% under different magnification

Compression Property

A typical true stress–strain diagram of the sintered foam is shown in the Fig. 5. It describes an initial linear stage, followed by plateau-like stage and finally by densification stage which commences at strains between 0.4 and 0.6. It is indicated that the increase of porosity can enhance the compressibility of titanium foams, which means the compressive yield strength and the elastic modulus decreased with increasing porosity. In addition, the presence of the densification stage was delayed. As shown in Table 1, the yield strength values of titanium foams containing porosities in range of 42.71–56.23% were observed to vary between 93.85 and 276.52 Mpa. The Young's modulus was between 1.53 and 3.21 GPa. The elastic modulus of the natural bone of the body is 2–20 GPa, which is close to fabricated titanium foams. Meanwhile, the strength of the titanium foams can completely resist the external force and prevent fracture when implanted into human body. In addition, the stress-strain curve also shows that the titanium foams produced by the

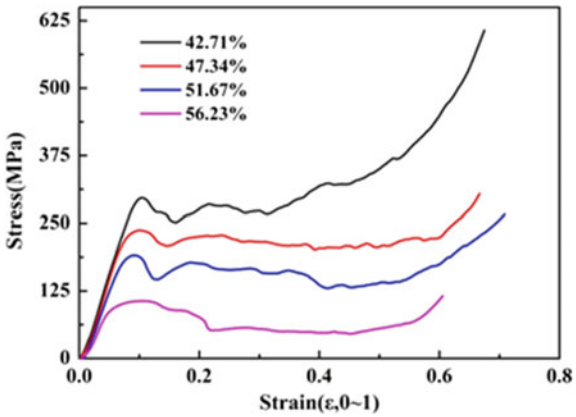

Fig. 5 Stress–strain diagram for the titanium foam

Table 1 Porosity, initial yield strength and modulus of elasticity of porous Ti

Porosity (%)	Initial yield strength (MPa)	Modulus of elasticity (GPa)
42.71	276.52	3.12
47.34	217.64	2.86
51.67	170.22	2.67
56.23	93.85	1.53

experiment has a long and stable plateau stage with high platform stresses (Probably in the range of 70–280 MPa), which makes the titanium foams capable to cushion the external impact [17].

Conclusions

Titanium foams can be successfully fabricated through powder metallurgy route using powdery particles of urea as space holder. The experimental results show that the granular urea can make the titanium foams have uniform fine pore structure and obtain high connectivity due to more connection structure and micro-pores on the pore wall. And the titanium foams consisted of near spherical porous regions of size up to 300 μm, which can meet the requirements of medical implants. Meanwhile, suitable sintering temperature and holding time ensures that the sintered titanium foam has obvious uniform pore characteristics and preferably mechanical properties, which especially makes titanium foam has obvious elastic, plateau and densification stages in compression experiments. So the processed foam has a great energy absorbing capacity with stable plateau stress.

Acknowledgements This research was financially supported by the National Natural Science Foundation of China (grant no. 51174243)

References

1. Metals, Baoji Research Institute of nonferrous (1978) Powder metallurgy porous material
2. Lefebvre LP, Banhart J, Dunand D (2007) Porous metals and metallic foams. In: Proceedings of the fifth international conference on porous metals and metallic foams
3. Dunand DC (2004) Processing of Titanium Foams. Adv Eng Mater 6(6):369–376
4. Lefebvre L-P, Banhart J, Dunand DC (2010) Porous metals and metallic foams: current status and recent developments. Adv Eng Mater 10(9):775–787
5. Zhang YP, Yuan B, Zeng MQ et al (2007) High porosity and large pore size shape memory alloys fabricated by using pore-forming agent (NH 4 HCO 3) and capsule-free hot isostatic pressing. J Mater Process Technol 192–193(10):439–442
6. Ye B, Dunand DC (2010) Titanium foams produced by solid-state replication of NaCl powders. Mater Sci Eng A 528(2):691–697
7. Jee CSY, Guo ZX, Evans JRG et al (2000) Preparation of high porosity metal foams. Metall Mater Trans B 31(6):1345–1352
8. Kotan G, Bor AA (2007) Production and characterization of high porosity Ti-6Al-4 V foam by space holder technique in powder metallurgy. Turk J Eng Environ Sci 31(3):149–156
9. Esen Z, Bor Ş (2007) Processing of titanium foams using magnesium spacer particles. Scr Mater 56(5):341–344
10. Wen CE, Yamada Y, Shimojima K et al (2002) Processing and mechanical properties of autogenous titanium implant materials. J Mater Sci Mater Med 13(4):397
11. Jakubowicz J, Adamek G, Dewidar M (2013) Titanium foam made with saccharose as a space holder. J Porous Mater 20(5):1137–1141
12. Mansourighasri A, Muhamad N, Sulong AB (2012) Processing titanium foams using tapioca starch as a space holder. J Mater Process Technol 212(1):83–89
13. Hu Yunhua, Grainger David W, Winn Shelley R, Hollinger Jeffrey O (2002) Fabrication of poly (α-hydroxy acid) foam scaffolds using multiple solvent systems. J Biomed Mater Res 59 (3):563–572
14. Maspero FA, Ruffieux K, Müller B, Wintermantel E (2002) Resorbable defect analog PLGA scaffolds using CO2 as solvent: structural characterization. J Biomed Mater Res 62(1):89–98
15. Wen CE, Yamada Y, Nouri A et al (2007) Porous titanium with porosity gradients for biomedical applications. Mater Sci Forum 720–725
16. Nicula R, Lüthen F, Stir M et al (2007) Spark plasma sintering synthesis of porous nanocrystalline titanium alloys for biomedical applications. Biomol Eng 24(5):564–567
17. Sharma M, Gupta GK, Modi OP et al (2011) Titanium foam through powder metallurgy route using acicular urea particles as space holder. Mater Lett 65(21–22):3199–3201

Leaching Characteristics of Non Ferrous Metals Recovery from Korean Municipal Solid Waste Incineration Bottom Ash Samples

T. Thriveni, Ch. Ramakrishna and Ahn Ji Whan

Abstract Incineration is an advanced solid waste management for municipal solid waste. Municipal solid waste incineration (MSWI) is an efficient combustion process of the waste disposal/treatment. Municipal solid waste incineration (MSWI) fly ash and bottom ashes are the byproducts of incineration combustion process. In particular, incineration of waste samples (bottom ash) containing valuable nonferrous metals such as copper (Cu), zinc (Zn), lead (pb), nickel (Ni), titanium (Ti), including some heavy metals arsenic (As), chromium (Cr), cadmium (Cd) and mercury (Hg) etc., critical rare metals and rare earth elements. We collected the copper rich four different municipal solid waste incineration bottom ash samples from four different incineration plants from Seoul, Korea. The investigations were carried out at bench scale. For copper extraction, sulfuric acid was used more suitable for high efficiency. In this work, we used LIX extractant for selective extraction of copper from bottom ash samples. Finally, an efficient recovery of the copper was extracted 90% was achieved.

Keywords Leaching · Characteristics · Nonferrous metals · MSWI bottom ash · Recovery

T. Thriveni · Ch. Ramakrishna
Department of R&D Team, Hanil Cement Corporation,
Danyang 395-903, Republic of Korea

A. J. Whan (✉)
Climate Change Mitigation and Sustainability Division,
Carbon Mineralization Center, Korea Institute of Geosciences
and Mineral Resources (KIGAM), 124 Gwahagno, Gajeong-dong,
Yuseong-gu, Daejeon 34132, Republic of Korea
e-mail: ahnjw@kigam.re.kr

The Minerals, Metals & Materials Society, *TMS 2018 147th Annual Meeting & Exhibition Supplemental Proceedings*, The Minerals, Metals & Materials Series,
https://doi.org/10.1007/978-3-319-72526-0_83

Introduction

The increasing amount of municipal waste generated by an increasing consumption of goods has led to the development of methods to combust the waste. This is now a widely utilized waste management method [1]. Incineration of municipal solid waste (MSWI) gives the possibility to recover energy and reduce the waste mass by 70%, as well as the waste volume by 90% [2]. Generally, municipal solid waste incineration (MSWI) produces two main types of combustion ash; bottom ash and fly ash. Bottom ash is the major ash collected at the bottom of the combustion chambers. This ash contains glassy silicate slag, metal objects, pieces of glass, ceramics and minerals with high melting points.

Currently, global municipal solid waste generation levels are reached to 1.3 billion tonnes per year, and it is expected to increase 2.2 billion tonnes per year by 2025 [3]. The annual waste generation from East Asia and the Pacific region is gradually increased. Developing countries faced problems associated with the poorly managed solid waste management system. There are several reports published on the low performance of MSW accessibility of the city due to the lack of properly designed collection route system and poor condition of the final dump site, littering of the corner around the skips which encouraged illegal dumping which leads the environmental and health risks [3]. However, incineration produces large quantities of by-products, among which bottom ash (BA) is the most abundant with respect to the generated volumes [4]. In order to move towards a circular economy, the utilization of bottom ash in building materials as a secondary raw material is preferred over land filling [5, 6].

Municipal solid waste through incineration process, the organic content of the waste is converted into thermal energy which can be used for electrical power generation or district heating. The incineration residue consists essentially of inorganic materials and metals. Thus, the complex chemical reactions of organic compounds, e.g. acids and chelating agents, with metals are prevented. In contrast, the inorganic chemistry of mineralized incineration residues is well understood and can be fairly easily controlled. After incineration, bottom ash undergoes further treatments such as separation of un-burnt materials, removal of ferrous and non-ferrous metals, sieving and washing to produce a recyclable fraction. In addition bottom ash residual fraction having rich in contaminants [7, 8]. Its application is limited, beyond a potential for recovering valuable metals [9]. Furthermore, many researchers have studied the particle size dependency of the potentially toxic elements (PTEs) in the incinerated by-products [10–14].

Various technologies have been investigated to utilize MSWI ashes in different countries [15]. Most of the treatment methods developed to aim at the use of the stabilized ash as a construction material. In some methods the targets of leaching are to extract the metals from the ash and in a few cases to recover specific metal from solution by combining with further treatment, such as solvent extraction and electro winning, as in a process for zinc recovery described by Schlumberger et al. [16]. While many publications deal with the leaching behavior of Municipal Solid

Waste Incinerator Bottom Ash (MSWI-BA), only a few address the technical and economic aspects of metal extraction.

The objectives of the present work were to study the influence of different parameters on the acid leaching yield of valuable and toxic metals from an MSWI bottom ash and to examine the possibility of recovering metals from the corresponding bottom ash by acid leaching after crushing and sieving out certain particle sizes with physical and chemical characteristics of municipal solid waste incineration bottom ash samples and to determine the metallic elements of ambient bottom ash samples surrounding MSWI and investigate their properties. Size-segregated particles were collected around an MSWI in South Korea and leaching behavior with different acid concentrations was measured and to discuss with the suitable conditions for Cu, Zn, Pb, Ni and Ti with other heavy metals leaching efficiency.

Materials and Methods

Materials and Characterization MSWI Bottom Ash Samples

In this study, we chose four different municipal solid waste incineration bottom ash samples from Yangcheon, Mapo, Nowon and Gangnam boilers in South Korea, and the elements concentrations were investigated as shown in Table 1. In order to study of Copper recovery from all different bottom ash samples. After receiving the bottom samples we dried at room temperature for the removal of moisture from that samples. After drying, the bottom ash samples were totally dissolved in HCl and HNO_3 solutions for recovery of Cu leaching.

An XRF analysis was conducted to determine the chemical content of each sample. The XRF analysis was commissioned to the Geoanalysis Center of the Korea Institute of Geoscience and Mineral Resources, R&D Tech-Biz Division. Test conditions were set at 24 ± 3 °C temperature, and 25 ± 5% R.H. humidity. Cu and other metal content analysis was commissioned to the Center for Chemical Analysis at the Korea Research Institute of Chemical Technology and conducted using the ICP-AES test method.

Leaching

To obtain the aqueous phases for the extraction experiments, the ashes were leached in 5M HCl and 5M HNO_3 at an automatic titration instrument. Leaching experiments were carried out at 5 g of solid bottom ash are dissolved in 100 ml of 5 M concentrations of liquid solutions for a time long enough to maximize the metal yield (24 h). The hydrochloric acid was prepared from a concentrated acid of 37% Sigma–Aldrich and 98% nitric acid with distilled water. The leachates were

Table 1 Characteristics and chemical composition of municipal solid waste incinerator bottom ash samples

	Size (mm)	SiO_2	Al_2O_3	CaO	MgO	P_2O_5	Na_2O	Fe_2O_3	SO_3	K_2O	TiO_2	Cl	lg	Total
Yang cheon	+4.75	45.40	7.44	21.90	1.60	6.74	6.25	1.59	1.23	1.42	0.36	0.44	4.06	99.96
	4.75–2.36	26.70	9.18	30.80	1.43	11.00	3.33	2.14	0.87	1.92	0.63	1.06	8.12	99.78
	2.36–1.18	21.40	10.60	33.30	1.21	4.47	3.09	2.71	0.83	2.02	0.93	1.60	15.50	99.83
	1.18-0.6	15.00	9.75	38.20	1.15	4.20	2.91	2.36	0.85	1.64	1.05	1.92	19.20	99.85
	0.6–0.3	11.40	9.91	40.00	1.20	4.88	2.54	2.31	0.93	1.39	1.05	2.10	20.50	99.86
	0.3–0.15	8.47	10.10	40.30	1.25	4.82	2.49	2.21	0.94	1.09	1.16	2.16	23.30	99.93
	−0.15	7.06	9.94	39.60	1.28	3.00	2.40	195	0.94	0.96	1.13	2.08	28.10	99.86
Gang nam	+4.75	47.00	10.60	19.00	1.54	4.74	6.05	2.07	1.24	1.62	0.60	0.39	3.69	99.92
	4.75–2.36	28.40	11.40	29.70	1.35	861	3.15	2.96	0.83	1.87	0.88	0.73	8.49	99.90
	2.36–1.18	28.50	11.60	29.00	1.30	6.57	2.55	3.20	0.64	2.08	1.00	0.78	10.40	99.80
	1.18–0.6	17.40	11.50	36.70	1.24	6.52	2.29	3.44	0.85	1.64	1.12	1.18	14.50	99.88
	0.6–0.3	13.20	11.60	38.30	1.21	6.17	2.04	3.33	0.93	1.25	1.14	1.37	18.10	99.86
	0.3–0.15	8.63	12.00	40.40	1.11	4.18	1.79	2.75	1.01	0.85	1.07	1.56	23.50	99.92
	−0.15	6.98	12.20	41.10	1.02	2.63	1.49	2.08	1.01	0.65	0.90	1.62	27.20	99.90
Nowon	+4.75	40.80	7.15	23.90	1.46	9.51	6.96	0.27	0.43	1.45	0.48	0.33	3.53	97.60
	4.75–2.36	29.20	7.98	30.50	1.43	11.00	4.22	2.92	0.41	1.78	0.85	0.66	7.45	99.97
	2.36–1.18	24.50	10.40	31.70	1.44	7.03	3.93	3.12	0.64	2.15	1.15	0.99	11.50	99.86
	1.18–0.6	15.00	11.20	36.40	1.40	6.04	3.32	3.04	0.76	1.69	1.40	1.31	16.90	99.91
	0.6–0.3	11.10	12.20	37.80	1.29	5.23	2.88	2.76	0.79	1.27	1.46	1.54	20.50	100.03
	0.3–0.15	6.35	12.50	39.30	1.06	3.20	2.37	1.94	0.08	0.87	1.13	1.83	27.50	99.19
	−0.15	4.94	12.20	38.50	0.80	1.59	2.03	1.20	0.69	0.71	0.73	1.91	33.80	99.99

(continued)

Table 1 (continued)

	Size (mm)	SiO_2	Al_2O_3	CaO	MgO	P_2O_5	Na_2O	Fe_2O_3	SO_3	K_2O	TiO_2	Cl	lg	Total
Mapo	+4.75	45.80	10.40	20.30	1.64	4.65	6.17	3.43	0.45	1.34	0.84	0.26	3.50	99.92
	4.75–2.36	31.50	11.40	27.90	1.36	7.63	3.39	3.46	0.60	1.71	1.05	0.50	7.60	99.92
	2.36–1.18	26.40	12.00	30.40	1.39	6.15	2.69	3.72	0.77	1.71	1.25	0.64	11.10	100.01
	1.18–0.6	17.40	11.40	37.10	1.30	5.76	1.95	3.79	1.12	1.40	1.41	0.82	14.90	100.01
	0.6–0.3	10.60	10.50	41.40	1.29	5.26	1.49	3.31	1.29	0.09	1.38	0.95	20.10	99.12
	0.3–0.15	8.61	10.10	42.20	1.29	4.63	1.29	3.18	1.30	0.73	1.44	0.96	22.80	99.94
	−0.15	5.56	9.44	43.80	1.15	2.35	0.95	2.22	1.39	0.50	1.11	0.99	29.20	99.95

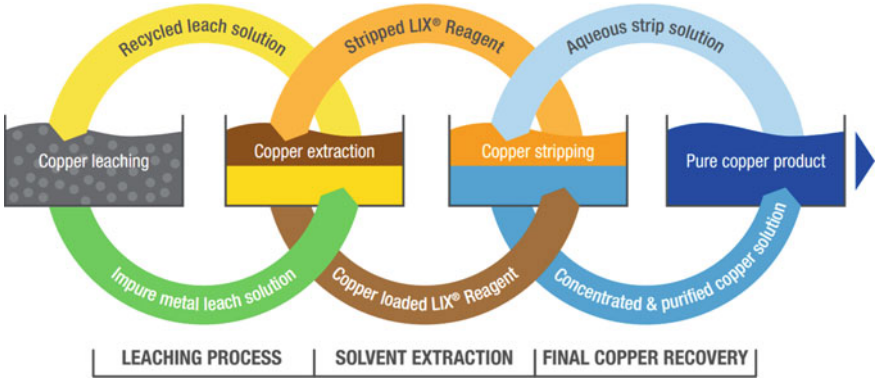

Fig. 1 Copper recovery by leaching and solvent extraction method. *Source* Solvent extraction reagents and application, http://www.cognis.com

collected by filtering process using Whatman filter papers with 0.45 μm pores size and collected an aqueous solutions for measuring total concentrations using inductively coupled plasma atomic emission spectrometry (ICP-AES). In the process of copper recovery from MSWI bottom ash samples was involved in three steps; 1. leaching process, 2. solvent extraction process and finally 3. copper recovery process as shown in Fig. 1 copper recovery involving a process.

Solvent Extraction Studies of Copper

Solvent extraction (also known as liquid-liquid extraction) has been utilized in metallurgy for a long time. It is a very simple technique giving it wide application in hydrometallurgy because it is very easy to handle and low cost chemicals can be utilized for metal recovery from primary and secondary resources. But at the same time it has limitations too. The chemical degradation, third phase formation, sometimes poor selectivity as well as the solubility of certain solvents in aqueous phase create problems. Thus, the extractants need to have following characteristics to be utilized in industrial processing: it should possess low solubility in the aqueous phase and at the same time very high solubility in organic diluents; density/viscosity should be low and stability should be good.

Extraction Procedure

A suitable aqueous (10 ml) of a feed solution containing metal was equilibrated with an equal volume of 1 mol/L LIX 84I (2-hydroxy-5-nonylacetophenoneoxime

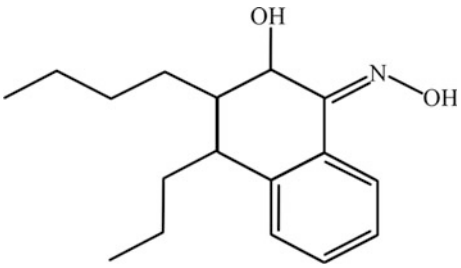

Fig. 2 The chemical structure of the 2-hydroxy-5-nonylacetophenonaoxime (LIX 84I)

shown in Fig. 2) for 20 min in a separating funnel. Initial experiments on the effect of time on metal extraction indicated that 15 min is sufficient to reach an equilibrium reaction. Adding diluted with 1.0 mol/L H_2SO_4 and adjusted the equilibrium pH of the aqueous solution to the desired value. After phase disengagement, the aqueous phase was separated and the metal concentrations were analyzed by ICP-AES. The distribution ratio (D) was calculated as the concentration of the metal present in the organic phase to that part in the aqueous phase at equilibrium. As and when required, the metal concentration in the organic phase was determined after filtration through a 1PS paper and stripping was performed using 1.0 mol/L sulfuric acid solution [17, 18]. The stripping experiments were carried out at ambient temperature (25 °C). Metal concentrations were measured in samples of

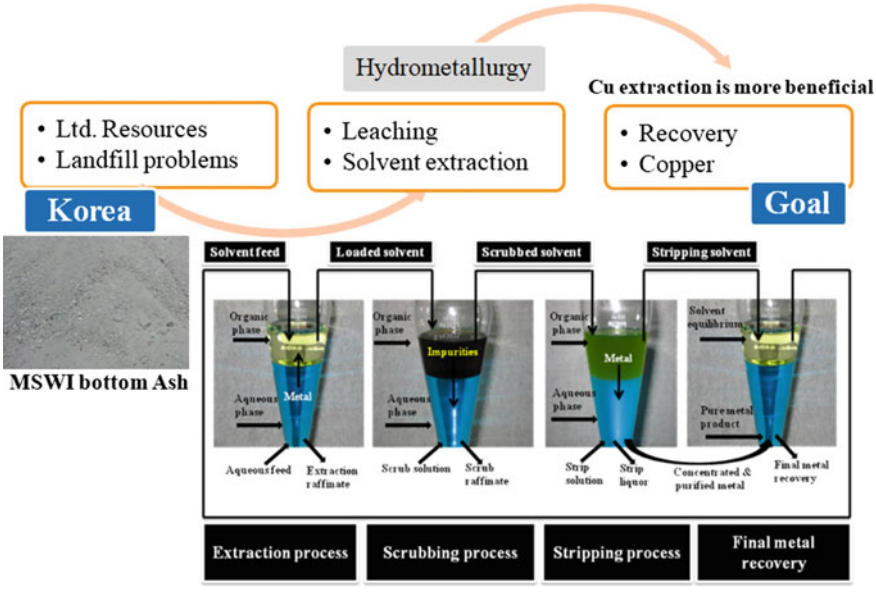

Fig. 3 Copper leaching extractants by solvent extraction method

aqueous phase taken before and after contact with the loaded organic phase and stripping efficiencies were calculated using the mass balances. Figure 3 shows the process of copper recovery from leaching solution by solvent extraction method.

Result and Discussion

Characterization of Bottom Ash and Leachate

In Table 2, shows the chemical composition of the leaching solution of bottom ash samples with 5M HCl and 5M HNO_3. The leaching yield increased with the nitric acid medium when compared to hydrochloric acid. This comparison includes only a few data sets but it is quite clear that the leaching properties of a specific ash needs to be investigated in order to make leaching process optimization possible. It also is shown that the higher leaching of a high acid concentration has to be evaluated against the cost and technical feasibility of using concentrated acid leachates. The physical structure of the bottom ash particles can prevent leaching of metal compounds by enclosing them in for example silicate melt. In addition, it has been observed that the chemical forms of copper present in the ash has a significant influence on how much can be leached out even at low pH [19]. This particular bottom ash seems to have a copper speciation that limits the leachability. Therefore, samples of original and leached bottom ash from the present work are being investigated with respect to the speciation of copper by ICP-AES and the results will be discussed in this paper.

The experiments were performed to determine the number of the solvent extraction stages needed in the mixer-settler system to separate copper from the leaching solution, and to find suitable stripping agents to obtain purified individual

Table 2 Leaching solution analysis with ICP-AES for different municipal solid waste incinerator bottom ash samples (24 h leaching time, liquid to solid (v/w) = 10)

Sample name with size (mm)	Leaching solvent (5 M concentration)	Leaching elements (ppm)			
		Cu	Zn	Zr	Fe
Yangcheon (4.75–2.36)	5M HCl	690	531	1.6	228
Yangcheon (4.75–2.36)	5M HNO_3	908	681	2.2	304
Yangcheon (2.36–1.38)	5M HCl	321	243	0.75	109
Yangcheon (2.36–1.38)	5M HNO_3	665	507	1.6	226
Mapo (4.75–2.36)	5M HCl	425	323	1.0	143
Mapo (4.75–2.36)	5M HNO_3	151	115	0.37	51
Nowon (2.36–1.18)	5M HCl	143	109	0.35	47
Nowon (2.36–1.18)	5M HNO_3	747	568	1.7	253
Gangnam (4.75–2.36)	5M HCl	183	140	0.6	61
Gangnam (4.75–2.36)	5M HNO_3	1536	1169	4.9	522

copper solutions for further treatment. The reactions between extractants and the copper ions are described in Eq. (1) [20, 21].

$$Cu^{2+}_{(aq)} + 2RH_{(org)} \rightarrow R_2Cu_{(org)} + 2H^{+}_{(aq)} \quad (1)$$

The copper extractant is involved in the transfer of one metal ion. However, 10 ml of the copper solution and 1 mol/L LIX 84I is needed to completely extract 87% of copper from the leachate. Considering the fact that co-extraction of other metal ions might occur, 1 mol/L LIX 84I in the organic phases were chosen for the experiments. The kinetics of copper extraction extractions are shown in Table 3. The time required for the distribution ratio of copper to reach equilibrium is less than 1 min for respective systems. A lower phase ratio (O:A) could give more metal concentrated in the organic phase, but it would also result in more operation stages needed. Therefore, the phase ratio (O:A) 1:1 for copper were adopted respectively as operating line for the following investigation using the mixer-settler system. The extraction of copper is found to be 87% roughly extracted in the first two stages.

Copper Stripping

Copper stripping was carried out using sulfuric acid solution based on results from earlier work [18]. The results Table 4, show that in general a higher concentration of the acid solution leads to a better stripping efficiency. When using 0.5 mol/L H2SO4 the efficiency was 80%, and the efficiency increased to more than 95% when the concentration was increased to 5 mol/L. Considering the risk that the equipment would be exposed to corrosion and the cost of the acid, it was decided to use the lower concentration for the stripping.

As presented in Fig. 3, the aqueous feed from filtration was pumped into a mixer settler units for copper extraction with a flow rate 6 mL/min. The counter current flow rate of the organic phase using 1 mol/L LIX 84I in kerosene was 3 mL/min, which is enough to reach the equilibrium. By this arrangement an O:A ratio of 1:1 was achieved. Aqueous samples were taken from each chamber and the metal concentration of those samples and in the aqueous feed was measured. Table 4 shows the extraction results from the aqueous feed, which where more than 80%

Table 3 Separation of Cu and Zn by solvent extraction method from aqueous leachate solution (5 M HNO_3) of gangnam bottom ash (4.75–2.36 mm) sample

Metal name	Feed metal (mg/L)	Metal in aqueous phase (mg/L)	Metal in organic phase (mg/L)	D_E	Extraction (%)
Copper	896	118	778	6.59	86.7
Zink	867	850	17	0.02	>2
Iron	344	–	–	–	–
Lead	13	12.6	0.4	0.03	>3

Table 4 Cu recovery (stripping) from loaded organic phase (LOP) LIX 841 (1.0 mol/L) with 1.0 mol/L H_2SO_4

Metal name	Metal in loaded organic phase (mg/L)	Metal in aqueous phase (mg/L)	Metal in rest loaded organic phase (mg/L)	D_S	Metal recovery or stripping (%)
Copper	778	624.3	153.7	4.06	80.3
Zink	17	13	4	3.25	76.4
Iron	0	–	–	–	–
Lead	0.4	–	–	–	–

copper selectively extracted from the aqueous feed with no other co-extraction besides less than 1% iron in mixer settler stages. The separation factor of Cu/Fe is larger than 1000, indicating that it is feasible to separate those two elements in this system [22]. The concentration of copper in the aqueous phase after mixer settler chambers shown in Table 4.

Conclusions

The results of the present work showed that it is possible to remove the copper from MSWI bottom ash by leaching with nitric acid hydrochloric acid at pH 2. In the present work 80% of the copper was leached. It was also shown that the removed copper metal, can be recovered from the leachate by solvent extraction using the extractant LIX 84I for copper extraction. Metal extraction from the incineration residue of municipal waste is not only environmentally beneficial but also profitable. The overall results indicate that the recovery of copper from MSWI bottom ash using leaching and extraction is feasible up to pilot scale. Since mixer settlers show a near linear scale up behavior these results are promising for further scale up to industrial scale.

Acknowledgements This study was supported by the Energy Technology Development Project [20141010101880] of the Korea Institute of Energy Technology Evaluation and Planning, financed by the Ministry of Trade, Industry and Energy.

References

1. Narayana T (2009) Municipal solid waste management in India: from waste disposal to recovery of resources? Waste Manag 29:1163–1166
2. Wang L, Jin Y, Nie Y, Li R (2010) Recycling of municipal solid waste incineration fly ash for ordinary Portland cement production: a real-scale test. Resour Conserv Recycl 54:1428–1435
3. Hoornweg D, Tata PB (2012) What a waste: a global review of solid waste generation. World bank urban development series knowledge papers, vol 15, pp 1–116

4. Margallo M, Taddei MBM, Hernández-Pellón A, Aldaco R, Irabien Á (2015) Environmental sustainability assessment of the management of municipal solid waste incineration residues: a review of the current situation. Clean Technol Environ Policy 17:1333–1353. https://doi.org/10.1007/s10098-015-0961-6
5. Dutch Ministry of Infrastructure and Environment (2012) Greendeals GD076: sustainable useful application of WtE bottom ash [WWW Document]. http://www.greendeals.nl/gd076-verduurzaming-nuttige-toepassing-aecbodemassen/. Accessed 8 Sept 16
6. Soil Quality Decree (2013) Regeling Bodemkwaliteit, VROM, Den Haag: Ruimte en Milieu. Ministerie van Volkshuisvesting, Ruimtelijke Ordeling en Milieubeheer
7. Chimenos J, Fernández A, Nadal R, Espiell F (2000) Short-term natural weathering of MSWI bottom ash. J Hazard Mater 79:287–299. http://dx.doi.org/10.1016/S0304-3894(00)00270-3
8. Chimenos JM, Fernández AI, Miralles L, Segarra M, Espiell F (2003) Short-term natural weathering of MSWI bottom ash as a function of particle size. Waste Manag 23:887–895. https://doi.org/10.1016/S0956-053X(03)00074-6
9. Tang J, Steenari B-M (2015) Leaching optimization of municipal solid waste incineration ash for resource recovery: a case study of Cu, Zn, Pb and Cd. Waste Manag 48:315–322. https://doi.org/10.1016/j.wasman.2015.10.003
10. Alba N, Gasso S, Lacorte T, Baldasano JM (1997) Characterization of municipal solid waste incineration residues from facilities with different air pollution control systems. J Air Waste Manag Assoc 47:1170–1179. http://dx.doi.org/10.1080/10473289.1997.10464059
11. Chandler RT, Eighmy TT, Hertlen J, Hjelmar O, Kosson DS, Sawel SE, van der Sloot HA, Vehlow J (1997) Municipal solid waste incinerator residues—IAWG (International Ash Working Group). Elsevier
12. Florea MVA, Brouwers HJH (2015) Treatment of incineration by-products for generating new building materials. 19th Ibausil, international conference on building materials (Internationale Baustofftagung). Weimar, Germany, pp 1505–1512
13. Tang P, Florea MVA, Spiesz P, Brouwers HJH (2015) Characteristics and application potential of municipal solid waste incineration (MSWI) bottom ashes from two waste-to-energy plants. Constr Build Mater 83:77–94. https://dx.doi.org/10.1016/j.conbuildmat.2015.02.033
14. Wang K-S, Sun C-J, Yeh C-C (2002) The thermotreatment of MSW incinerator fly ash for use as an aggregate: a study of the characteristics of size-fractioning. Resour Conserv Recycl 35:177–190. https://dx.doi.org/10.1016/S0921-3449(01)00121-5
15. Lam CHK, Ip AWM, Barford JP, McKay G (2010) Use of incineration MSW ash: a review. Sustainability 2:1943–1968
16. Schlumberger S, Schuster M, Ringmann S, Koralewska R (2007) Recovery of high purity zinc from filter ash produced during the thermal treatment of waste and inerting of residual materials. Waste Manag Res 25:547–555
17. Karlfeldt Fedje K, Ekberg C, Skarnemark G, Pires E, Steenari B-M (2012) Initial studies of the recovery of Cu from MSWI fly ash leachates using solvent extraction. Waste Manag Res 30:1072–1080
18. Tang J, Steenari B-M (2015) Solvent extraction separation of copper and zinc from MSWI fly ash leachates. Waste Manag 44:147–154
19. Lassesson H, Fedje KK, Steenari B-M (2014) Leaching for recovery of copper from municipal solid waste incineration fly ash: influence of ash properties and metal speciation. Waste Manag Res 32:755–762
20. Cierpiszewski R, Miesiąc I, Regel-Rosocka M, Sastre AM, Szymanowski J (2002) Removal of zinc(II) from spent hydrochloric acid solutions from zinc hot galvanizing plants. Ind Eng Chem Res 41:598–603
21. Jergensen GV (1999) Copper leaching, solvent extraction, and electrowinning technology. Society for Mining, Metallurgy, and Exploration, Littleton, CO
22. Rydberg J, Cox M, Musikas C, Choppin G (2004) Solvent extraction principles and practice, 2nd edn. Marcel Dekker

Part XXXIV
Surface Engineering for Improved Corrosion Resistance

Anti-corrosion Properties of Rosemary Oil and Vanillin on Low Carbon Steel in Dilute Acid Solutions

Roland Tolulope Loto, Cleophas Akintoye Loto, Bryan Ayozie and Tayo Sanni

Abstract The corrosion inhibition effect of rosemary oil and vanillin (ROV) on low carbon steel in 1 M HCl and H_2SO_4 media was studied through potentiodynamic polarization, weight loss analysis, optical microscopy and IR spectroscopy. Results showed optimal inhibition performance of the compound, but more effectively in HCl solution at 92.57 and 94% compared to 64.57 and 64.55% in H_2SO_4 from both electrochemical test. Identified functional groups of the admixture from IR spectroscopy completely adsorbed on the steel in HCl, but partially in H_2SO_4. Thermodynamic calculations showed chemisorption and physiochemical adsorption according to Langmuir, Freundlich and Temkin isotherm model. Micro-analytical images revealed a well-protected ROV inhibited steel surface in comparison to images from the corroded stainless steel. The inhibition behavior of ROV was determined to be mixed type.

Keywords Corrosion · Inhibitor · Rosemary oil · Vanillin Acid

Introduction

Corrosion inhibition by chemical compounds is of great practical importance, being extensively employed in curtailing wastage of engineering materials and minimizing costs of corrosion control. The use of inhibitors is quite varied often playing an important role in oil extraction and processing industries, heavy industrial manufacturing, water treatment facility etc. to minimize localized corrosion and

R. T. Loto (✉) · C. A. Loto · B. Ayozie
Department of Mechanical Engineering, Covenant University,
Ota, Ogun State, Nigeria
e-mail: tolu.loto@gmail.com

T. Sanni
Department of Chemical, Metallurgical and Materials Engineering,
Tshwane University of Technology, Pretoria, South Africa

The Minerals, Metals & Materials Society, *TMS 2018 147th Annual Meeting & Exhibition Supplemental Proceedings*, The Minerals, Metals & Materials Series,
https://doi.org/10.1007/978-3-319-72526-0_84

unexpected sudden failures. The effectiveness or corrosion inhibition efficiency of a corrosion inhibitor is a function of many factors, including but not limited to fluid composition, mixability water, presence of heteroatoms, molecular structure, flow regime and strength of adsorption with the steel surface. Molecules of natural or organic origin exhibiting a strong affinity for metallic surfaces is the focus of this research toward the development of environmentally tolerant corrosion inhibiting compounds.

Experimental Methods

Low carbon steel (LCS) with a nominal composition 0.8% Mn, 0.04% P, 0.05% S, 0.16% C and 98.95% Fe is the steel test specimen in cylindrical form with dimensions of length, 1 cm and diameter, 1 cm after machining and metallographic preparation. Vanillin and rosemary oil obtained are the organic compounds evaluated for their synergistic corrosion inhibiting properties in combined molar concentrations of 2.96×10^{-3}, 5.93×10^{-2}, 8.89×10^{-2}, 1.19×10^{-2}, 1.48×10^{-2}, 1.78×1^{-2}, in 200 mL of 1 M HCl and H_2SO_4 acid solutions. Polarization measurements were carried out at 30 °C using a three electrode system and glass cell containing 200 mL of the prepared acid solutions at specific concentrations of ROV with Digi-Ivy 2311 potentiostat. Cylindrical LCS electrodes mounted in acrylic resin with an exposed surface area of 0.79 cm^2 were prepared. Polarization plots were obtained at a scan rate of 0.0015 V/s at potentials of −1.25 V and +0.5 V. Measured LCS steel coupons separately immersed in 200 mL of the dilute acid test solution for 240 h at 30 °C were weighed every 24 h to determine the corrosion rate from weight loss analysis. Images of corroded and inhibited LCS surface morphology from optical microscopy were analysed after weight-loss measurement with Omax trinocular through the aid of ToupCam analytical software. Spectral patterns of ROV/1 M HCl and H_2SO_4 solution (before and after the corrosion test) was evaluated and equated to the theoretical IR absorption table to identify the functional groups involved in the corrosion inhibition reactions after exposure to specific range of infrared ray beams from Bruker Alpha FTIR spectrometer between wavelengths of 375–7500 cm^{-1} and resolution of 0.9 cm^{-1}.

Results and Discussion

Potentiodynamic Polarization Studies

The potentiodynamic polarization curves of ROV reaction with LCS in HCl and H_2SO_4 acid solution are shown in Fig. 1a, b. Differences in corrosion rate for specimen A at 0% ROV and specimens B-G at 0.25–1.5% ROV is due to the intermolecular reaction of ROV inhibitor on LCS surface. Current peaks of the

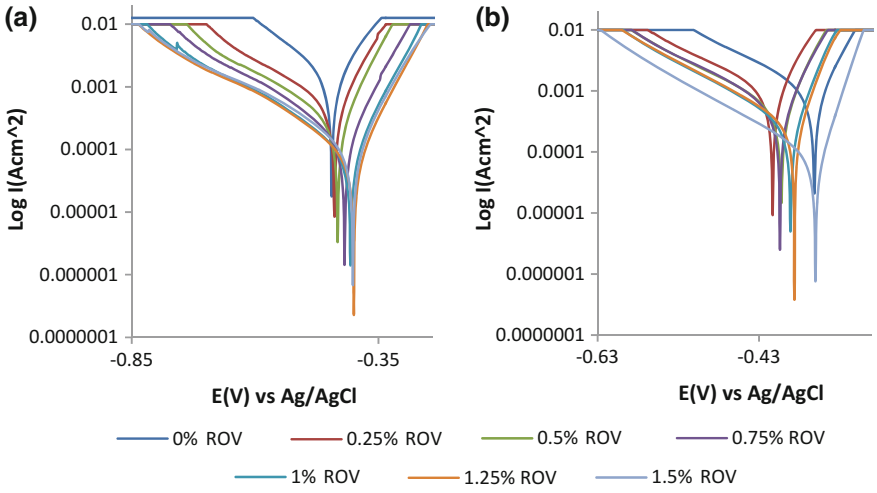

Fig. 1 Potentiodynamic polarization curves for LCS **a** 0–1.5% ROV in 1 M HCl, **b** 0–1.5% ROV in 1 M H_2SO_4

polarization curves in HCl solution (Fig. 1a) decreased significantly with increase in ROV concentration due to precipitation of ROV molecules which eventually shifts the polarization curves in the anodic direction. ROV has no effect on the cathodic Tafel slopes in comparison to anodic Tafel values. The anodic Tafel slope at 0% ROV is as a result of the formation of oxides due to slow electron transfer step (5, 6). Changes in Tafel slope values after 0% ROV is due to changes in the electrode substrate, rate controlling step and influence of potential controlled conditions, thus ROV altered the oxidation electrochemical reactions. LCS was subject to severe alloy degradation in H_2SO_4 solution at 0–0.75% ROV as shown in Fig. 1b. There was a significant improvement in corrosion rate values after 0.75% ROV due to increase in ROV molecules however the maximum inhibition efficiency attained is 60% due to the high current density at the intercept between the anodic and cathodic polarization curves, resulting from the debilitating action of SO_4^{2-}. There is a potential shift in the cathodic direction resulting from the release of excess electrons. After 0.5% ROV the potential shifts in the anodic direction till 1.5% ROV. The anodic Tafel slope values in H_2SO_4 tends to be lower than the values obtained in HCl show due to the strong electrocatalytic nature of LCS at high overpotentials in H_2SO_4.

Weight-Loss Measurement and Optical Microscopy Analysis

Figure 2a, b show the plot of LCS corrosion rate versus exposure time from the acid solutions. Macro images of LCS before corrosion and after corrosion, with and

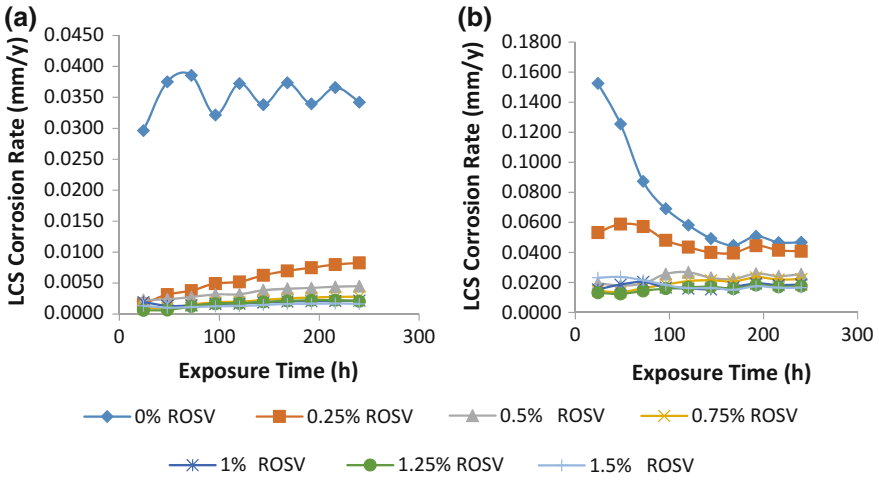

Fig. 2 Graphical illustration of **a** LCS corrosion rate versus exposure time in HCl, **b** LCS corrosion rate versus exposure time in H_2SO_4

without ROV are shown in Fig. 3a–c. Microscopic images of LCS before and after corrosion, with and without ROV are shown from Figs. 4a to 5b. LCS was subject to severe deterioration and corrosion in both acids at 0% ROV (Fig. 2a, b) resulting from the action of sulphates and chloride anions. This caused the formation of porous oxides on the steel (Fig. 3b, c). The corrosion rate at 0% ROV in H_2SO_4 decreased with respect to exposure time until steady state at 144–240 h; however the corrosion rate in HCl solution shifted continually at relatively higher values throughout due to the strong ionization potential of H_2SO_4. As a result of the inability of ROV molecules to effectively stall the surface deterioration of LCS in H_2SO_4 at lower ROV concentrations (Figs. 2a and 5a), transition from active deterioration of the steel surface to the passive state until 1–1.25% ROV. In HCl strong adsorption of ROV molecules after 0.25% ROV result in effective corrosion inhibition of LCS (Figs. 2b and 5b).

ATF-FTIR Spectroscopy Analysis

The spectra diagram (Fig. 6a) for ROV in HCl before corrosion test show peak configurations at wavelength with intensities of 3350.43, 2921.81, 2855.86, 2169.15, 1634.86 and 1458.03 cm^{-1} which refers to amines, amides, alcohols, phenols, alkanes, alkynes, aromatics and nitro compounds functional groups. Only the spectra peaks of 3331.26 and 1631.37 cm^{-1} remained after corrosion inhibition due to chemisorption adsorption of the functional groups at other peaks. The electrochemical action of ROV in H_2SO_4 (Fig. 6b) contrasts its behavior in HCl solution. The spectra peaks before corrosion test which consists of 3353,

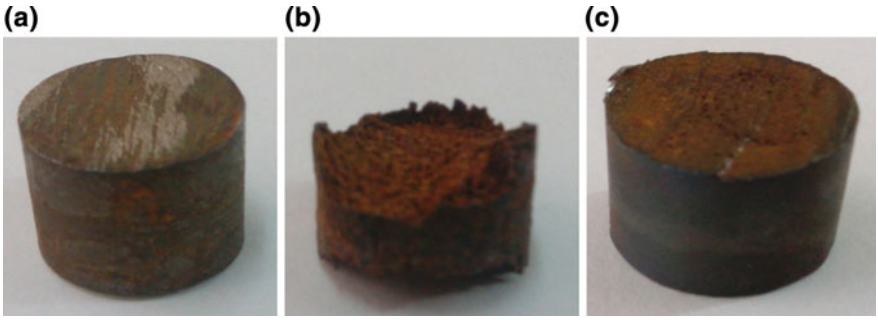

Fig. 3 Macro images of LCS **a** before corrosion, **b** after corrosion without ROV and **c** after corrosion with ROV

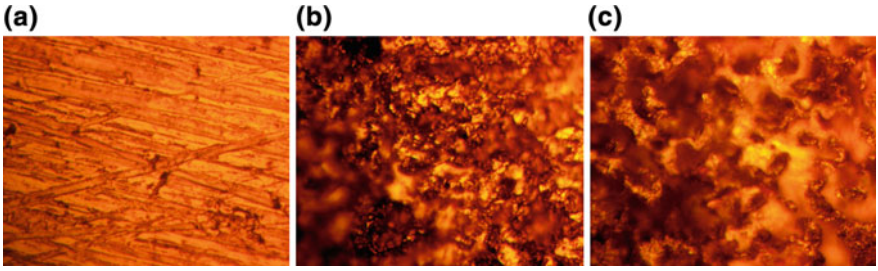

Fig. 4 Micro-analytical image of LCS **a** before corrosion, **b** after corrosion without ROV in HCl, **c** after corrosion without ROV in H_2SO_4

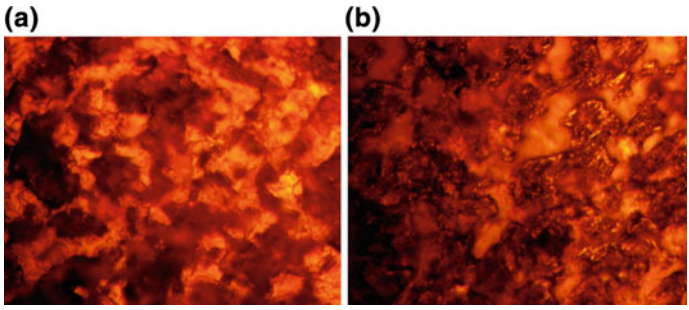

Fig. 5 Micro-analytical image of LCS after corrosion with ROV at mag. $\times 100$ **a** in HCl, **b** in H_2SO_4

2954.05–2852.30, 1460.74, 1376.96, 1168.40, 1052.35 and 721 cm^{-1} (corresponding to alcohols, phenols, amines, amides, carboxylic acids, alkanes, aromatics, alkanes, alkanes, esters, ethers, alkyl halides and aliphatic amines) showed no

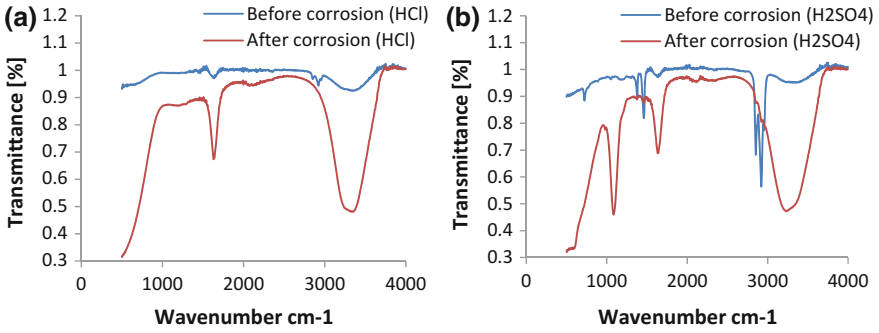

Fig. 6 ATF-FTIR spectra of ROV adsorption on LCS **a** 1 M HCl solution, **b** 1 M H_2SO_4

significant change in wavenumber but only decreased in peak intensity signifying limited adsorption of ROV on LCS.

Adsorption Isotherm

Electrochemical adsorption can be viewed as a replacement reaction of water molecules in the adsorbed layer by ROV molecules within the bulk acid solution. Langmuir, Freundlich and Temkin adsorption isotherm produced the best fit as shown from Figs. 7a to 9b. The plots of $\frac{C_{ROV}}{\theta}$ versus C_{ROV} for ROV adsorption in HCl showed linearity in agreement with Langmuir adsorption isotherm (Fig. 7a) with a correlation coefficient of 0.9999, In H_2SO_4 the plots (Fig. 7b) strongly deviated from ideal Langmuir model with a correlation coefficient of 0.3561. The plots for the Freundlich isotherm which states that adsorbed molecules interact and

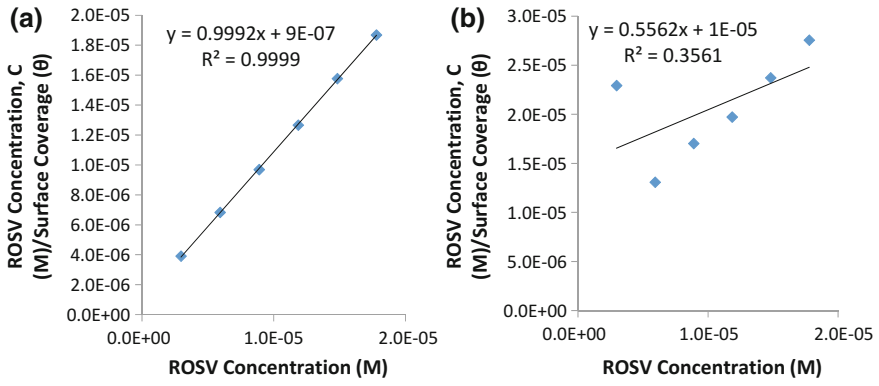

Fig. 7 Langmuir plot of $\frac{C}{\theta}$ versus ROV concentration in **a** 1 M HCl, **b** 1 M H_2SO_4

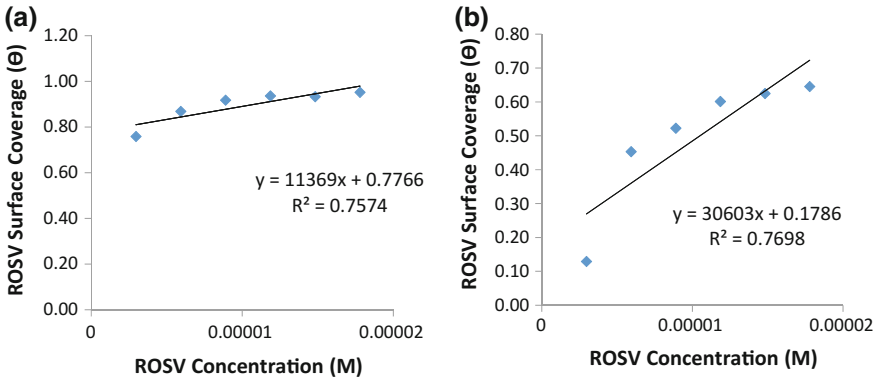

Fig. 8 Freundlich isotherm plot of ROV surface coverage (Θ) against ROV concentration **a** in HCl, **b** in 1 M H_2SO_4

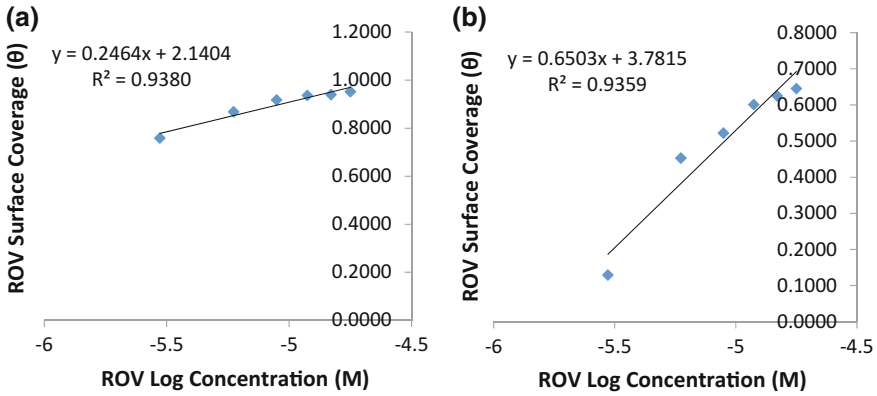

Fig. 9 Temkin isotherm plot of ROV surface coverage (θ) against log ROSV concentration **a** in HCl, **b** in H_2SO_4

influence further adsorption through repulsion or attraction of molecules as the amount adsorbed is the total of adsorption on all sites (9, 10) showed a correlation coefficient of 0.7549 in HCl (Fig. 8a) and 0.7668 in H_2SO_4 (Fig. 8b). Temkin isotherm assumes the heat of adsorption decreases linearly with increase in surface coverage taking into account the indirect interactions of adsorbate-adsorbate molecules on adsorption isotherm. The Temkin isotherm plot for ROV in HCl (Fig. 9a) had a correlation coefficient of 0.9380 while in H_2SO_4 it is 0.9359 (Fig. 9b).

Thermodynamics of the Corrosion Process

The highest and lowest value of ΔG^{o}_{ads} in HCl is value obtained is -44.75 kJ mol^{-1} at 0.25% ROSV and -44.05 kJ mol^{-1} at 1.25% ROSV. These values align with chemisorption adsorption mechanism (12, 13). In H_2SO_4 the values are -39.31 kJ mol^{-1} at 0.5% ROSV and -36.77 kJ mol^{-1} at 0.25% ROSV which is consistent with physiochemical adsorption mechanism.

Conclusion

ROV compound effectively inhibited the corrosion of low carbon steel specimens studied in dilute molar concentrations of HCl acid solution but performed relatively poorly in H_2SO_4 acid due to the electrochemical action of sulphate anions. In HCl the compound chemically adsorbed onto the steel surface through the functional groups within its molecular structure, identified through ATF-FTIR spectroscopy analysis. Physiochemical interaction with the steel occurred in H_2SO_4 solution.

Acknowledgements The author acknowledges Covenant University Ota, Ogun State, Nigeria for the sponsorship and provision of research facilities for this project.

Stainless Steel Corrosion Resistance in 0.5 M H_2SO_4 Using *Cassia fistula* Extract

Olugbenga Adeshola Omotosho, Joshua Olusegun Okeniyi, Cleophas Akintoye Loto, Abimbola Patricia Popoola, Sunday Adeniran Afolalu, Emmanuel Obi, Oluwatobi Sonoiki, Timi Oshin and Adebanji Ogbiye

Abstract A study of the corrosion behavior of stainless steel (SS) in 0.5 M sulphuric acid using *Cassia fistula* leaf extract (*CFLE*) at 30 °C was carried out. The study was conducted by taking the SS samples, in inhibited and uninhibited solutions through linear sweep voltammetry tests, and then subjecting the recorded data from the experiment to analysis, to yield the surface coverage, inhibitor efficiency, inhibition mechanism and adsorption model. The analysed data showed that inhibitor efficiency ranged from 98.59 to 95.25% at 2 and 8 g/L respectively. Surface coverage data for the experiment fitted well to the Langmuir model with a separation factor parameter showing favourable adsorption. Inhibitor adsorption was spontaneous showing overriding physical adsorption, while an anodic inhibition mechanism was displayed. *CFLE* promoted the overriding influence of the chromium oxide passive film on the SS metal surface to forestall the aggressive effect of sulphuric acid.

Keywords Stainless steel · Sulphuric acid · *Cassia fistula* extract Linear sweep voltametry · Anodic slope · Cathodic slope · Inhibition mechanism

Introduction

Stainless steel (SS) finds application in a many industrial facilities because of its corrosion resistance and desirable mechanical and machining properties. It enjoys widespread applications in food, beverage and chemical plants because of its

O. A. Omotosho (✉) · J. O. Okeniyi · C. A. Loto · S. A. Afolalu · E. Obi
O. Sonoiki · T. Oshin · A. Ogbiye
Mechanical Engineering Department, Covenant University, Ota 112001, Nigeria
e-mail: olugbenga.omotosho@covenantuniversity.edu.ng

C. A. Loto · A. P. Popoola
Chemical & Metallurgical Engineering Department, Tshwane University of Technology, Pretoria, South Africa

The Minerals, Metals & Materials Society, *TMS 2018 147th Annual Meeting & Exhibition Supplemental Proceedings*, The Minerals, Metals & Materials Series,
https://doi.org/10.1007/978-3-319-72526-0_85

non-staining properties [1] due mainly to the ability to form a self-healing thin oxide film when abraded. This is made possible by the chromium component of the stainless steel alloy having a very high affinity for atmospheric oxygen; such that chromium oxide is formed immediately the surface is scratched [1–4]. Researchers have therefore been attracted to the study of stainless steel in aggressive media, because when it is exposed to aggressive industrial media like sulphuric acid [5], the thin oxide protective layer is gradually depleted until the alloy is made bare to the corrosive attack of the acid. If this is unchecked, the material loses its thickness, meaning that its effective load carrying capacity is compromised, and thus, cannot support the load it was designed to support [6, 7]. This is followed by catastrophic failure of the component. As a result, there is uncontrollable contamination of the environment especially if the content of the facility is toxic [6]. Other challenges may include the loss of production man hours, litigation, hostility from host communities and disposal problems [4–12]. Thus, because of the versatility of stainless steel in chemical industries, focus is given to its protection from aggressive environments.

The attention of several researchers has increasingly been drawn to the corrosion resistance of stainless steel in acidic environment because of the economic importance of the problem. In the US alone annual direct corrosion cost is put at a whopping 3.1% of Gross Domestic Product (GDP) [13]. In other industrialized countries, corrosion costs to the economy are significant and attempts are being made to nip this environmental menace in the bud [14]. The big loss caused by corrosion can be reduced substantially by utilizing corrosion inhibitors [2–16]. Compounds like molybdates, chromates and phosphates that are inorganic and several organic compounds containing sulphur, oxygen and nitrogen heteroatoms have been studied for their corrosion inhibiting abilities [17–20]. Though the inorganic inhibitors are effective, their tendency to contaminate plant and animal life is the most unacceptable attribute, amongst others that users find disagreeable. In addition, they are expensive, difficult to dispose and often time associated with litigation between plant operators and the community [21–31]. However, respite is offered with the introduction of plant extracts with corrosion inhibiting abilities. Phytochemicals like flavonoids, tanins, terpernoids, alkaloids and saponins contained in most of these plants have been found to be effective in combatting corrosion in acidic media [4, 32, 33]. Thus, effort has been intensified in this direction, because they offer certain benefits amongst which are eco-friendliness, bio-degradability, non-toxicity, availability and affordability. The utilization of plant extracts to retard the degradation of metals in acid media has been published by researchers [4, 6–9, 12, 33]. Previously, we have investigated the effect of *Cassia fistula* plant extract on SS corrosion in HCl [4], while the influence of *Terminalia cattapa* on mild steel in HCl and sulphuric solution was also investigated [33, 34]. The present work captures the continuation of our work on the inhibitive capability of *Cassia fistula* leaf extracts. The study therefore, investigates the corrosion resistance of SS in sulphuric acid environment in the presence of *Cassia fistula* leaf extracts (CFLE). The study is conducted by taking stainless steel samples through linear sweep voltammetry tests to harvest data on electrochemical activity of the plant extract.

Experimental Methods

Stainless steel samples with composition of 15.12 Cr, 11.88 Ni and 67.51% Fe determined by an optical microscope were dimensioned and cut into sizes of 1 × 1 cm (with thickness of 0.3 cm). Each of the metal samples was then treated according to procedures laid down in ASTM G1-03 [35] for pre-experimental cleaning of stainless steel samples. The treated samples were then stored in a dessicator. Afterwards, the treated samples were each connected to an electrical wire on one side, while the other face was exposed to the electrolyte, but the rest of the metal was buried inside a two-epoxy resin system. The electrical wire from the working electrode was connected to the potentiosat whilst, the exposed face, was positioned directly opposite the reference electrode (Ag/AgCl electrode) and the auxiliary electrode (graphite rod) in electrolyte solution inside the three-electrode electrochemical cell assembly manufactured by Princeton Applied Research (model K47). The chemical utilized in this study were of analar grade. The 0.5 M concentration of sulphuric acid used was prepared using double distilled water. *Cassia fistula* fresh leaves obtained from within Covenant University, Ota, Nigeria were taken for identification at the Forestry Herbarium, Ibadan, Nigeria. The sample was assigned voucher FHI No. 110261 at the Forestry Herbarium in Ibadan. The fresh leaves were then dried, under conditioned atmosphere at 21 °C before being milled into a powdery form using a grinding machine. Afterwards, methanolic extract was prepared from the powdered leaves according to procedures stated in previous works [4, 36–38]. *CFLE* concentrations of 2, 4, 6, 8 and 10 g/L respectively were then prepared from the stock solution.

After all connections were made from the corrosion cell kit to the Digi-Ivy potentiostat (model DY2312X050 A0280IR), linear sweep tests were conducted. The open circuit potential (OCP) was obtained prior to commencement of the LSV tests. The monitoring was initiated at a scan rate of 0.1 V/s from an anodic and cathodic potential of +0.5 V and −1.0 V respectively. Parameters like corrosion potential (E_{corr}), charge transfer resistance (R_{ct}), corrosion current density (i_{corr}), and corrosion rate (*CR*) which can be deduced from the Tafel plots of potential versus log i_{corr} was recorded from the databank of the LSV instrument. In order to deduce these parameters the following equations were used:

$$CRA = \frac{3.27 \times 10^{-3} \times i_{corr} \times eq.wt}{d} \tag{1}$$

where i_{corr} = corrosion current density (μA/cm^2), d = density of metallic sample (g/cm^3) and $eq.wt$ = equivalent weight (g). The *CRA* is used in estimating the inhibition efficiency, η (%) and surface coverage (θ), employing Eqs. 2 and 3 respectively [4, 6]:

$$\eta(\%) = \left(\frac{CRA_{solution\ without\ CFLE} - CRA_{solution\ with\ CFLE}}{CRA_{solution\ without\ CFLE}} \right) 100 \tag{2}$$

$$\theta = \left(\frac{CRA_{solution\ without\ CFLE} - CRA_{solution\ with\ CFLE}}{CRA_{solution\ without\ CFLE}} \right) \tag{3}$$

The adsorption studies were conducted by fitting several adsorption models to the experimental surface coverage (θ) data. However, the Langmuir adsorption isotherm had the highest R-value from the test conducted and so it was identified as the isotherm that best described the SS metal-*CFLE* interaction mechanism. Equation 4 is the Langmuir equation in linearized form [39]:

$$\frac{C}{\theta} = \frac{1}{K_L Q_c} + \frac{C}{Q_c} \tag{4}$$

Q_c and K_L are the maximum monolayer capacity (mg/g) and Langmuir isotherm constant. The adsorption studies conducted identified the Langmuir adsorption isotherm as the isotherm with the best experimental data fit for the corrosion system. K_L in the Langmuir expression is associated with R_L in the separation factor expression. Equation 5 depicts the R_L parameter and it is the expression for the separation factor, which is also a dimensionless equilibrium parameter which characterizes the adsorption [40]:

$$R_L = \frac{1}{1 + K_L C_s} \tag{5}$$

The initial concentration and the separation factor are depicted by C_s and R_L respectively.

Results and Discussion

Potentiodynamic polarization plots for the stainless specimens immersed in 0.5 M H_2SO_4 with and without varying *CFLE* concentrations at ambient temperature of 30 °C are presented in Fig. 1. A close scrutiny of the corrosion potential of the

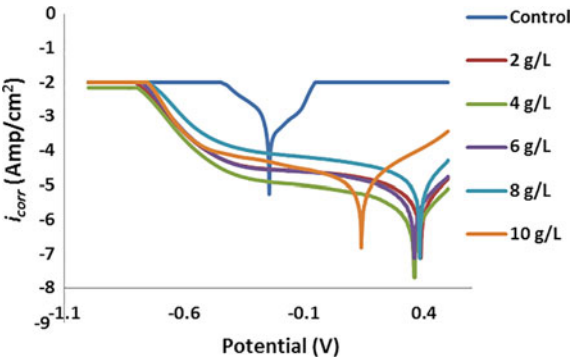

Fig. 1 Plots of potentiodynamic polarization from LSV test-results on stainless steel specimens at 30 °C under the influence of varying *Cassia fistula* leaf extracts concentration

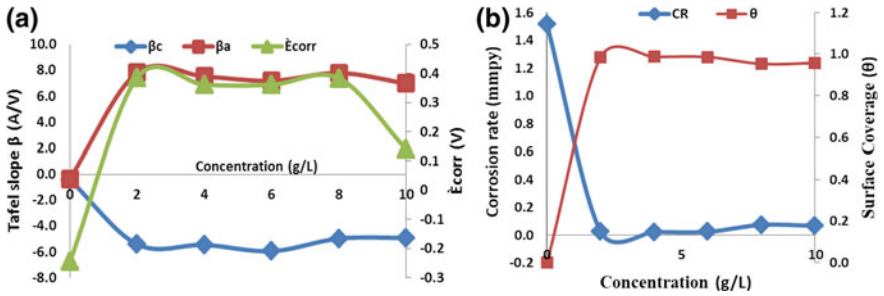

Fig. 2 Plots of **a** Tafel slopes (β_a, β_c) and corrosion potential (E_{corr}) against concentration, **b** corrosion rate and surface coverage (θ) against concentration for SS samples immersed in 0.5 M H_2SO_4 using *Cassia fistula* extract

control specimen, in comparison to the inhibited sample, shows that the potential for the inhibited specimens were more positive at all concentrations. This indicates that the inhibitor was responsible for the anodic reactions on the metal surface. A maximum displacement of 631 mV was obtained from finding the difference between the control and inhibited E_{corr} value. Thus, since a value of 631 mV was greater than 85 mV, the inhibitor is interpreted as having predominantly anodic type inhibitor behaviour [4, 40, 41].

A relationship between the anodic and cathodic Tafel slopes with the inhibitor concentration is shown in Fig. 2a. Figure 2a further represents the variation of the corrosion potential with the inhibitor concentration. It is noted that the anodic and cathodic Tafel slope constants wholly persisted in the anodic and cathodic region as *CFLE* concentration increased. However, a completely anodic behaviour is shown by E_{corr} curve on the graph. The E_{corr} curve for inhibited samples is completely in the anodic region of the graph, while the only E_{corr} value in the cathodic region is for the control sample. This completely agrees with Fig. 1 where the Tafel plots absolutely indicated anodic type inhibitor behaviour by reason of their deviation towards the more positive direction.

In Fig. 2b, a representation of the corrosion rate and surface coverage (θ) against *CFLE* concentration is shown. An indirect relationship exists between corrosion rate and surface coverage. It is noted from the graph that corrosion rate and surface coverage of the inhibited samples reduced and increased respectively as inhibitor concentration changed. However, the reductions and increases did not follow any particular trend. But, the surface coverage was generally high, with a range of 0.95–0.98 for the 4 and 8 g/L *CFLE* concentrations respectively. Generally, surface coverage was high at all *CFLE* concentrations used. This suggests that the inhibitor was effective in covering and protecting the metal surface despite its presence in an acidic media.

In Fig. 3a, where a plot of the inhibitor efficiency against CFLE concentration is presented, it is observed that the inhibitor efficiency generally had high values as concentration changed. However, no particular trend was established. This is clearly in agreement with the surface coverage plots in Fig. 2b. An optimal

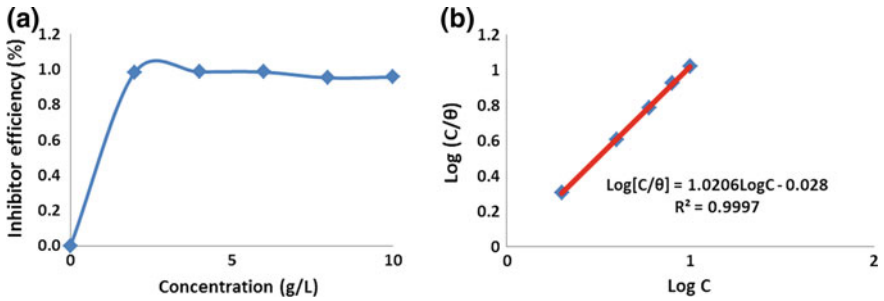

Fig. 3 Plots of **a** inhibitor efficiency against inhibitor concentration (g/L) and **b** Langmuir adsorption isotherm model fitting with experimental data from LSV test on SS samples immersed in 0.5 M H_2SO_4 under the influence of *Cassia fistula* extract at 30 °C

efficiency of 98.59% was attained at CFLE concentration of 4 g/L, while the lowest of 95.25% was at 8 g/L concentration. These two values were very high, depicting the effective of *CFLE*.

The presentation in Fig. 3b shows the fit of the experimental data to the Langmuir adsorption isotherm. Fittings of the experimental data were done to several adsorption models and Langmuir was found to have the highest R-value of 0.99. Thus, the Langmuir adsorption isotherm best described the adsorption of the CFLE extract to the SS metal surface.

Furthermore, the parameters in Table 1 were obtained after a plot of log (C/θ) versus log C was conducted; and the slope and intercept from the graph was compared to Eq. 5. The parameters enable us to establish the degree of favourability of the adsorption process [4, 41–43]. The mode of sorption is classified as; unfavourable if ($R_L > 1$), linear if ($R_L = 1$), favourable if ($0 < R_L < 1$) and irreversible if ($R_L = 0$). Therefore, the adsorption process can be described as favourable since $R_L = 0.995$.

Moreover, the Gibbs free energy ΔG^0_{ad} (of adsorption was deduced by using the expression in Eq. 6 [40–42]:

$$\Delta G^0_{ad} = -2.303RTLog(55.5K_L) \tag{6}$$

R and T are the universal gas constant (8.314 kJ/mol K) and ambient temperature (303 K) respectively. The negative value of −1.05467 kJ/mol obtained by substituting for K_L in Eq. 6 indicates a favourable, but spontaneous, adsorption process

Table 1 Langmuir isotherm linear regression parameters and separation factor

S. no.	Description	Slope	Intercept	Q_C	K_L	R_L	Favourability condition
1	SS_H_2SO_4_*CFLE*	1.0206	0.028	0.978	0.00274	0.948	Favourable

by CFLE on SS. In addition, a prevalent physisorption adsorption process is suggested for the *CFLE* on SS in H_2SO_4 media, since the Gibbs free energy was lower than −20 kJ/mol [4].

Conclusions

This study investigated the corrosion resistance of SS in 0.5 M H_2SO_4 using *CFLE* as a green inhibitor at 30 °C through the linear sweep voltammetry tests. The study established that:

- *CFLE* acts as an efficient corrosion inhibitor for SS in 0.5 M H_2SO_4 at all concentrations, but its efficiency values did not follow a particular trend;
- Optimum inhibitor efficiency of 98.59% was attained at 4 g/L, while the least was 95.25% at 8 g/L;
- The potentiodynamic polarization curve established a predominant anodic inhibition mechanism;
- The surface coverage data fit with several adsorption isotherms yielded the Langmuir isotherm as best, based on r^2 value of 0.9997;
- The separation factor parameter showed a favourable sorption process for *CFLE* on SS;
- The Gibbs free energy of adsorption of −1.054 kJ/mol suggests an overriding spontaneous physisorption process;
- The *CFLE* promoted the influence of the chromium oxide passive film on the SS metal surface.

Acknowledgements The laboratory contribution of Jacob Fademi is acknowledged. The authors also thank the Department of Mechanical Engineering, Covenant University, Ota, Nigeria, for the utilization of laboratory research facilities. Furthermore, the authors wish to appreciate the financial support of Covenant University Center for Research Innovation and Discovery (CUCRID).

References

1. Dewangan AK, Patel AD, Bhadania AG (2015) Stainless steel for dairy and food industry: a review. J Mater Sci Eng 4(5):191–194. https://doi.org/10.4172/2169-0022.1000191
2. Olsson COA, Landolt D (2003) Passive films on stainless steels—chemistry, structure and growth. Electrochim Acta 48:1093–1104
3. Bera S, Rangarajan S, Narasimhan SV (2002) Electrochemical passivation of iron alloys and the film characterization by XPS. Corros Sci 42:1709–1724
4. Omotosho OA, Okeniyi JO, Loto CA, Popoola API, Ajibola OB, Ogbiye AS (2017) *Cassia fistula* leaf-extract effect on corrosion-inhibition of stainless-steel in 0.5 M HCl. In: TMS2017 supplemental proceedings, pp 179–189. Springer International Publishing AG, Cham Switzerland. https://doi.org/10.1007/978-3-319-52132-9_18

5. Omotosho OA, Okeniyi JO, Obi EI, Sonoiki OO, Oladipupo SI, Oshin TM (2016) Inhibition of stainless steel corrosion in 0.5 M H_2SO_4 in the presence of $C_6H_5NH_2$. In: TMS2016: 145 annual meeting and exhibition: supplemental proceedings, pp 465–472. Springer International Publishing AG, Cham, Switzerland. https://doi.org/10.1007/978-3-319-48254-5_56
6. Omotosho OA, Ajayi OO, Ajanaku KO, Ifepe VO (2012) Environment induced failure of mild steel in 2 M sulphuric acid using *Chromolaena odorata*. J Mater Environ Sci 3(1):66–75
7. Omotosho OA, Ajayi OO (2012) Investigating the acid failure of aluminium alloy in 2 M hydrochloric acid using *Vernonia amygdalina*. ITB J Eng Sci 44:77–92
8. Omotosho OA, Ajayi OO, Fayomi O, Ifepe VO (2012) Evaluating the deterioration behaviour of mild steel in 2 M sulphuric acid in the presence of *Butyrospermum parkii*. Asian J Appl Sci 5(2):74–84
9. Omotosho OA, Ajayi OO, Fayomi OS, Ifepe VO (2011) Assessing the deterioration behavior of mild steel in 2 M sulphuric acid using *Bambusa glauscescens*. Int J Appl Eng Res Dindigul 2(1):85–97
10. Okeniyi JO, Omotosho OA, Ajayi OO, Loto CA (2014) Effect of potassium-chromate and sodium-nitrite on concrete steel-rebar degradation in sulphate and saline media. Constr Build Mater 50:448–456
11. Okeniyi JO, Loto CA, Popoola API, Omotosho OA (2015) Performance of *Rhizophora mangle L.* leaf-extract and sodium dichromate synergies on steel-reinforcement corrosion in 0.5 M H_2SO_4-immersed concrete. In: Corrosion 2015 conference and expo. NACE International, Houston, TX, Paper no 5636
12. Omotosho OA, Ajayi OO, Ajanaku KO, Ifepe VO (2012) Environment induced failure of mild steel in 2 M sulphuric acid using *Chromolaena odorata*. J Mater Environ Sci 3(1):66–75
13. U.S. Department of Transportation (2002) Corrosion costs and preventive strategies in the United States. Publication no FHWA-RD-01-156. https://www.nace.org/uploadedFiles/Publications/ccsupp.pdf
14. Committee on Cost of Corrosion in Japan (2001) Report on cost of corrosion in Japan. Japan Society of Corrosion Engineering and Japan Association of Corrosion Control. Extended abstract, Zairyo-to-Kankyo (Corros Eng) 50(11):490–512. http://www.nims.go.jp/mits/corrosion/corrosion_cost.pdf
15. Omotosho OA, Okeniyi JO, Ajayi OO (2010) Performance evaluation of potassium dichromate and potassium chromate inhibitors on concrete steel rebar corrosion. J Fail Anal Prev 10(5):408–415
16. Omotosho OA (2011) Assessing the performance of potassium dichromate and aniline on concrete steel rebar deterioration in marine and microbial media. Res J Appl Sci 6(3):143–149
17. Umoren SA (2009) Synergistic influence of gum arabic and iodide ion on the corrosion inhibition of aluminium in alkaline medium. Portu Electrochim Acta 27(5):565–577
18. Chen WS, Lian JS (2009) Electrochemical destruction of dinitrotoluene isomers and 2,4,6, trinitrotoluene in spent acid from toluene nitration process. J Hazard Mater 161(2–3):1017–1023
19. Khaled KF, AI-Qahtani MM (2009) The inhibitive effect of some tetrazole derivatives towards Al corrosion in acid solution: chemical, electrochemical and theoretical studies. Mater Chem Phys 131(1):150–158
20. Abd El Rehim S, Mohammed AA, Moussa SO, Abdallah SE (2008) The corrosion inhibition of aluminium and its copper alloys in 1.0 M H_2SO_4 solution using linear-sodium dodecyl benzene sulfonate as inhibitor. Mater Chem Phys 112(3):898–906
21. Deepa RP, Selvaraj S (2013) Electrochemical behaviour of *Solanum trilobatum* plant extract on stainless steel in natural sea water environment. Annalen der Chemischen Forschung 1 (3):1–9
22. Scendo M, Trela J (2013) Adenine as an effective corrosion inhibitor for stainless steel in chloride solution. Int J Electrochem Sci 8:9201–9221

23. Obot IB, Obi-Egbedi NO (2010) An interesting and efficient green corrosion inhibitor for aluminium from extracts of *Chromolaena odorata L.* in acidic solution. J Electrochem 40:1977–1984
24. Lebrini M, Robert F, Roos C (2010) Inhibition effect of alkaloids extract from *Annona squamosa* plant on the corrosion of C38 steel in normal hydrochloric acid medium. Int J Electrochem Sci 5:1678–1712
25. Raja PB, Rahim AA, Osman H, Awang K (2010) Inhibitory effect of *Kopsia singapurensis* extract on the corrosion behavior of mild steel in acid media. Wuli Huaxue Xuebao/Acta Physico-Chimica Sinica 26:2171–2176
26. Kasthuri PK, Arulanantham A (2010) Eco-friendly extract of *Euphorbia hirta* as corrosion inhibitor on mild steel in sulphuric acid medium. Asian J Chem 22:430–434
27. Rajalakshmi R, Subhashini S, Leelavathi S, Mary RF (2008) Efficacy of sprouted seed extracts of *Phaseolus aureus* on the corrosion inhibition of mild steel in 1 M HCl. Orient J Chem 24:1085–1090
28. Okeniyi JO, Loto CA, Popoola API (2014) Electrochemical performance of *Anthocleista djalonensis* on steel-reinforcement corrosion in concrete immersed in saline/marine simulating-environment. Trans Indian Inst Met 67:959–969
29. Okeniyi JO, Loto CA, Popoola API (2014) Electrochemical performance of *Phyllanthus muellerianus* on the corrosion of concrete steel-reinforcement in industrial/microbial simulating-environment. Portugaliae Electrochim Acta 32:199–211
30. Hameurlaine S, Gherraf N, Benmnine A, Zellagui A (2010) Inhibition effect of methanolic extract of *Atractylis serratuloides* on the corrosion of mild steel in H_2SO_4 medium. J Chem Pharm Res 2:819–825
31. Okeniyi JO, Oladele IO, Omoniyi OM, Loto CA, Popoola API (2015) Inhibition and compressive-strength performance of $Na_2Cr_2O_7$ and $C_{10}H_{14}N_2Na_2O_8 2H_2O$ in steel-reinforced concrete in corrosive environments. Can J Civil Eng 42:408–416
32. Okeniyi JO, Omotosho OA, Loto CA, Popoola API (2017) Anticorrosion and adsorption mechanism of *Rhizophora mangle* l. leaf-extract on steel-reinforcement in 3.5% NaCl-immersed concrete. In: TMS2017 supplemental proceedings, pp 167–178. Springer International Publishing AG, Cham Switzerland. https://doi.org/10.1007/978-3-319-52132-9_17
33. Omotosho OA, Okeniyi JO, Oni AB, Makinwa TO, Ajibola AB, Fademi EOJ, Obi CE, Loto CA, Popoola API (2016) Inhibition and mechanism of *Terminalia catappa* on mild-steel corrosion in sulphuric-acid environment. Prog Ind Ecol 10(4):398–413I
34. Omotosho OA, Okeniyi JO, Loto CA, Popoola API, Obi CE, Sonoiki OOO (2016) Performance of *Terminalia catappa* on mild steel corrosion in HCl medium. In: AIP conference proceedings, vol 1758, no 030027. AIP Publishing. http://dx.doi.org/10.1063/1.4959423
35. ASTM G 1-03 (2005) Standard practice for preparing, cleaning, and evaluating corrosion test specimens. ASTM International, West Conshohocken, PA
36. Okeniyi JO, Loto CA, Popoola API (2014) Electrochemical performance of *Anthocleista djalonensis* on steel-reinforcement corrosion in concrete immersed in saline/marine simulating-environment. Trans Indian Inst Met 67:959–969
37. Hameurlaine S, Gherraf N, Benmnine A, Zellagui A (2010) Inhibition effect of methanolic extract of *Atractylis serratuloides* on the corrosion of mild steel in H_2SO_4 medium. J Chem Pharm Res 2:819–825
38. Okeniyi JO, Loto CA, Popoola API (2014) Electrochemical performance of *Phyllanthus muellerianus* on the corrosion of concrete steel-reinforcement in industrial/microbial simulating-environment. Portugaliae Electrochim Acta 32:199–211
39. Foo KY, Hameed BH (2010) Insights into the modeling of adsorption isotherm systems. Chem Eng J 156(1):2–10

40. Loto RT, Loto CA, Popoola API (2015) Electrochemical effect of 1, 4-diaminobenzene on the corrosion inhibition of mild steel in dilute acid media. Der Pharma Chem 7(5):72–93
41. Loto RT, Loto CA, Fedotova T (2014) Electrochemical studies of mild steel corrosion inhibition in sulphuric acid chloride by aniline. Res Chem Intermed 40(4):1501–1516
42. Umoren SA, Ogbobe O, Okafor PC, Ebenso EE (2007) Polyethylene glycol and polyvinyl alcohol as corrosion inhibitors for aluminium in acidic medium. J Appl Polym Sci 105 (6):3363–3370
43. Webber TW, Chakkravorti RK (1974) Pore and solid diffusion models for fixed-bed absorbers. Am Inst Chem Eng 20(2):228–238

Synergistic Effect of Benzonitrile and Benzothiazole on the Corrosion Inhibition of 316 Stainless Steel in 6M HCl Solution

Roland Tolulope Loto, Cleophas Akintoye Loto, Alexander McPepple, Gabriel Olanrewaju and Akanji Olaitan

Abstract The synergistic effect of the combined admixture of benzonitrile and benzothiazole (BBZ) on the corrosion inhibition of 316 austenitic stainless steel in 6M HCl solution was evaluated through potentiodynamic polarization, coupon measurement, optical microscopy and IR spectroscopy analysis. Results obtained showed the effective corrosion inhibition performance of the admixture with optimal inhibition efficiency value of 95%. Identified functional groups of alcohols, phenols, amines, amides, carboxylic acids, aliphatic amines, esters and ethers within the compound completely adsorbed onto the steel from analysis of the adsorption spectra while others decreased in intensity due to partial adsorption. Thermodynamic calculations showed the cationic adsorption through chemisorption mechanism according to Langmuir and Freundlich adsorption isotherms. Micro-analytical images showed a badly corroded morphology with corrosion pits in the absence of compounds which contrast the images obtained with the compound. The compound was determined to be mixed type inhibition.

Keywords Corrosion · Inhibitor · Adsorption · Steel

Introduction

Corrosion problems are responsible for a significant percentage of the total costs for most industries worldwide due to the aggressive nature of industrial environments on metallic surfaces of equipment and structures. These problems are associated with operational setbacks, plant shutdowns and equipment maintenance, leading to recurrent partial and even total process shutdown etc. causing in enormous

R. T. Loto (✉) · C. A. Loto · A. McPepple · G. Olanrewaju
Department of Mechanical Engineering, Covenant University, Ota, Ogun State, Nigeria
e-mail: tolu.loto@gmail.com

A. Olaitan
Department of Chemical Metallurgical & Materials Engineering,
Tshwane University of Technology, Pretoria, South Africa

The Minerals, Metals & Materials Society, *TMS 2018 147th Annual Meeting & Exhibition Supplemental Proceedings*, The Minerals, Metals & Materials Series,
https://doi.org/10.1007/978-3-319-72526-0_86

economic losses [1]. Stainless steel corrosion is an electrochemical process, induced by certain electrolytic phenomena in interaction with corrosive environments. These steels are generally corrosion resistant and do perform optimally, however the limit of their corrosion resistance depends on the composition of operating environment and strength of their passive protective films which itself is a product of the alloy composition and metallurgical structure. The continuous exposure of stainless steels to action of acids results in accelerated deterioration of the steels due to breakage of the passive film at specific sites through which aggressive ions penetrate and initiate corrosion in the form of localized attacks [2–4]. Appropriate application of chemical compounds for corrosion inhibition significantly reduces the corrosion effect on the steels [5, 6]. Organic compounds containing heteroatoms in their structure tends to be effective inhibitors as such this study focuses on the synergistic corrosion inhibition properties of benzonitrile and benzothiazole on 316 austenitic stainless steel.

Experimental Procedure

316 austenitic stainless steel (316SS) obtained commercially have a nominal composition shown in Table 1. The steel specimens were machined and abraded with silicon carbide papers before cleansing with distilled water and acetone for weight loss analysis. Measured 316SS specimens were separately immersed in 200 mL of 6M HCl solution for 456 h and weighed 24 h to determine the weight loss and corrosion rate. Potentiodynamic polarization test was performed after mounting the steel specimens in epoxy resin (exposed surface area, 1.33 cm^2) with a three electrode system, glass cell with the electrolyte solution and Digi-Ivy 2311 at a scan rate of 0.0015 V/s between potentials of −0.5 V and +1.5 V to obtain the corrosion rate, corrosion current density, corrosion potential, polarization resistance and inhibition efficiency using the Tafel extrapolation method. Spectral patterns of BBZ/6M HCl solution (before and after the corrosion test) was evaluated and equated to the theoretical IR absorption table to identify the functional groups involved in the corrosion inhibition reactions after exposure to specific range of infrared ray beams from Bruker Alpha FTIR spectrometer between wavelengths of 375–7500 cm^{-1} and resolution of 0.9 cm^{-1}. The inhibiting compounds (benzonitrile and benzothiazole) were purchased from BOC Chemical, USA in the synthesized form.

Table 1 Percentage nominal composition of 304LSS and 316SS

Element symbol	Si	N	Ni	Mo	Cr	Mn	P	S	C	Fe
% composition (316SS)	0.75	0.1	11	3	18	2	0.045	0.03	0.08	65

Results and Discussion

Polarization Studies

The corrosion polarization behaviour of 316SS in 0–1.5% BBZ/6M HCl solution is shown in Fig. 1. Results obtained from the polarization test are presented in Table 2. At 0% BBZ, 316SS severely deteriorated at corrosion rate value of 9.91 mm/year, corresponding to a corrosion potential value of 0.316 V. Addition of BBZ compound (0.25–1.5% BBZ) altered the electrochemical behaviour of 316SS due to the effective inhibiting action of BBZ molecules in counteracting the action of Cl^- ions on the stainless steel surface. The current density reduced sharply after 0% BBZ while the corrosion potential value of 316SS at 0.25% BBZ shifted to a less negative value of 0.231 V signifying anodic inhibition, before alternating within specific ranges at higher BBZ concentration due to the mixed inhibiting properties of BBZ through surface coverage resulting from chemisorption reaction mechanisms. The inhibition efficiency values at from 0.25 to 1.5% are significantly above 90%, which is proportional to the high polarization resistance values. The corrosion rate and corrosion inhibition efficiency results (Table 2) shows changes in BBZ concentration is independent of the corrosion rate results, hence is effective at all concentration studied. The maximum change in corrosion potential value for BBZ corrosion inhibition is 85 mV in the anodic direction thus it is an anodic type inhibitor.

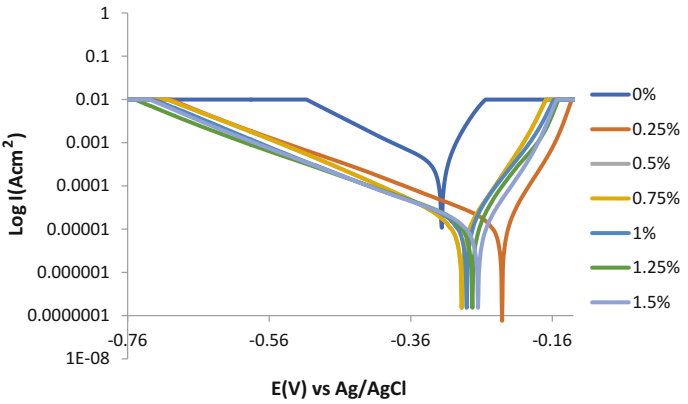

Fig. 1 Potentiodynamic polarization curves for BBZ inhibition of 316SS corrosion in 0–1.5% BBZ/6M HCl solution

Table 2 Potentiodynamic polarization results for BBZ inhibition of 316SS corrosion in 0–1.5% BBZ/6M HCl solution

Sample	BBZ concentration (%)	Corrosion rate (mm/year)	Corrosion current (A)	Corrosion current density (A/cm^2)	Corrosion potential (V)	Polarization resistance, R_p (Ω)	Cathodic Tafel slope, B_c (V/dec)	Anodic Tafel slope, B_a (V/dec)	Inhibition efficiency (%)
0	0	9.91	7.63E−04	9.65E−04	−0.316	33.70	−7.75	0.04	0
1	0.25	0.35	2.67E−05	3.38E−05	−0.231	962.00	−6.32	34.60	96.50
2	0.5	0.27	2.11E−05	2.67E−05	−0.288	1220.00	−7.82	25.30	97.23
3	0.75	0.29	2.24E−05	2.83E−05	−0.254	1150.00	−4.81	31.60	97.06
4	1	0.35	2.69E−05	3.40E−05	−0.281	956.00	−5.87	21.10	96.47
5	1.25	0.30	2.34E−05	2.97E−05	−0.273	1100.00	−6.08	18.80	96.93
6	1.5	0.26	1.99E−05	2.52E−05	−0.265	1290.00	−6.07	28.80	97.39

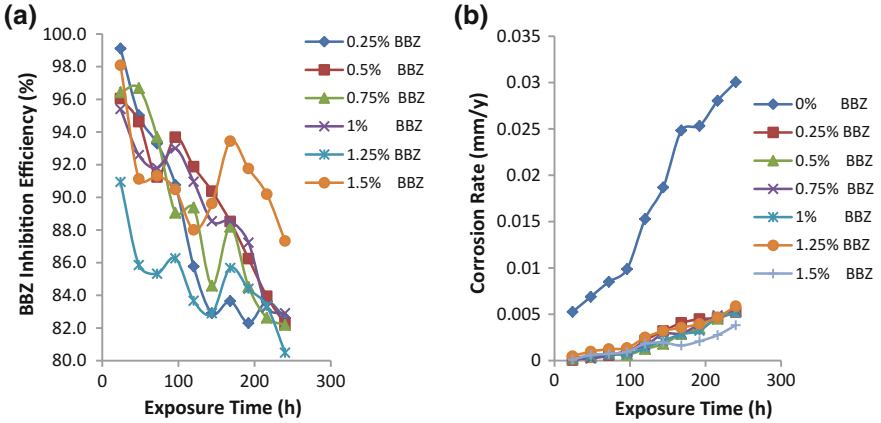

Fig. 2 Graphical plot of **a** BBZ inhibition efficiency, **b** 316SS corrosion rate versus exposure time

Weight-Loss Measurements

Figure 2a, b shows the graphical illustration of BBZ inhibition efficiency and 316SS corrosion rate versus exposure time in the acid media. There is a general decrease in inhibition efficiency corresponding to an increase in corrosion rate during the exposure hours however the corrosion rate of 316SS at 0% BBZ increase exponentially significantly differing from the steel specimens with at specific BBZ concentrations. BBZ compound displayed similar corrosion inhibition characteristics on the corrosion behaviour of 316SS with time basically through adsorption. Its presence in the acid media stifled the oxygen reduction, hydrogen evolution and oxidation reaction mechanism responsible for corrosion. Adsorption of BBZ probably blocked the active sites where the dissolution and release of metal cations into the solution occurs as a result of the action of chloride anions. BBZ belongs to the group of organic compounds consisting of electron rich heteroatoms which are centers of Lewis acid-base interaction with the steel [7]. They act by forming a protective film over the entire exposed area of the steel. The film chemisorbs onto the steel inhibiting the reaction of corrosive anions with the steel [8]. This prevents the passage of metallic cations consisting of Fe^{2+} into the solution.

Adsorption Isotherm

Langmuir and Frumkin adsorption isotherm was applied to describe the adsorption mechanism of BBZ inhibition of 316SS corrosion in 6M HCl solution, as they best fits the experimental results. The negligible deviation of the slopes from unity in Fig. 3a, b is attributed to the molecular interaction among the adsorbed inhibitor

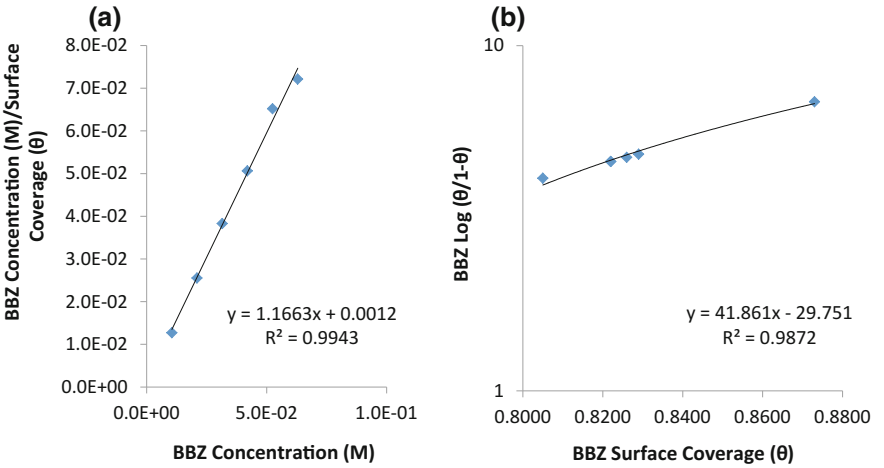

Fig. 3 Adsorption isotherm plots of BBZ adsorption on 316SS surface **a** Langmuir isotherm, **b** Frumkin isotherm

species on the steel surface and changes in the values of Gibbs free energy of adsorption due to changes in surface coverage values. Langmuir isotherm suggests monolayer layer adsorption at specific reaction sites on the steel's surfaces. The adsorptions are identical, equivalent and no lateral interaction between the adsorbed molecules exists [9]. Plots of $\frac{C_{BBZ}}{\theta}$ versus C_{BBZ} (Fig. 3a) perfectly fits with Langmuir isotherm with a correlation coefficient of 0.9943. The Frumkin adsorption isotherm suggests that the steel surface is heterogeneous i.e. lateral interaction effect is not negligible [10]. Plots of log $\left[\theta/(1-\theta)_C\right]$ versus θ in Fig. 3b showed a correlation coefficient of 0.9872.

Thermodynamics of the Corrosion Process

Results shown in Table 3 give supporting evidence of slight deviation from ideal condition of Langmuir and Frumkin isotherm models due to the differential values of Gibbs free energy of adsorption (ΔG_{ads}) with changes in surface coverage (θ) values. The negative ΔG_{ads} values are due to the spontaneity of the adsorption process as a result of the non-homogeneous nature of the steel surface. The values of ΔG_{ads} calculated ranges between -38.70 and -42.22 kJ mol^{-1} indicating chemisorption adsorption mechanism through electrostatic attraction and covalent interaction and bonding.

Table 3 Data obtained for Gibbs free energy, surface coverage and equilibrium constant of adsorption at specific molar concentrations of BBZ

Samples	LCN conc. (M)	Surface coverage (θ)	Equilibrium constant of adsorption (K)	Gibbs free energy, ΔG (KJ mol^{-1})
A	0	0	0	0
B	1.05E−02	0.826	452306.2	−42.22
C	2.10E−02	0.822	220000.4	−40.44
D	3.15E−02	0.822	146667.0	−39.43
E	4.20E−02	0.829	115478.2	−38.84
F	5.25E−02	0.805	78667.1	−37.89
G	6.30E−02	0.873	109159.4	−38.70

ATF-FTIR Spectroscopy Analysis

The spectra diagram for BBZ adsorption and corrosion inhibition of 316SS in 6M HCl is shown in Fig. 4. Peak configuration of BBZ/6M HCl plot (after corrosion) showed significant decrease in wavelength values between 928.04 and 3065.60 cm^{-1} in comparison to the peak configuration of BBZ/6M HCl plot (before corrosion) due to adsorption of the functional groups (identified through comparison of the wavelength numbers within the range of decreased transmittance with the theoretical table of characteristic IR absorptions) on 316SS during the corrosion inhibition process.

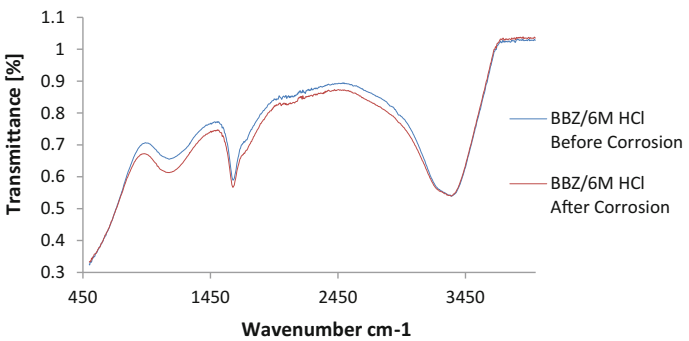

Fig. 4 ATF-FTIR spectra of BBZ adsorption on 316SS 6M HCl solution

Conclusion

BBZ performed effectively in the acid media inhibiting the corrosion of 316 stainless steel. The corrosion inhibition efficiency values of the compound remained generally the same at the concentrations studied with slight deviations as a result of the inhibition reaction of the molecular functional groups and heteroatoms of the compound which influenced the mechanism of the redox electrochemical reactions. Thermodynamic calculations confirm strong chemisorption reaction mechanism and the adsorption aligned with the Langmuir and Frumkin adsorption isotherm. Infrared spectra images confirmed the adsorption of the functional groups resulting in the effective passivation of the steel.

Acknowledgements The author acknowledges Covenant University Ota, Ogun State, Nigeria for the sponsorship and provision of research facilities for this project.

References

1. Garcia-Arriaga V, Alvarez-Ramirez J, Amaya Sosa ME (2010) H_2S and O_2 influence on the corrosion of carbon steel immersed in a solution containing 3M diethanolamine. Corros Sci 52 (7):2268–2279
2. Williams DE, Kilburn R, Cliff J, Waterhouse GIN (2010) Composition changes around sulphide inclusions in stainless steels, and implications for the initiation of pitting corrosion. Corros Sci 52(11):3702–3716
3. Williams DE, Stewart J, Balkwill PH (1994) The nucleation, growth and stability of micropits in stainless steel. Corros Sci 36(7):1213–1235
4. Paroni ASM, Alonso-Falleiros Magnabosco R (2006) Sensitization and pitting corrosion resistance of ferritic stainless steel aged at 800 °C. Corrosion 62(11):1039–1046
5. Trabanelli G (1991) Inhibitors—an old remedy for a new challenge. Corrosion 47(6):410–419
6. Ferreira ES, Giancomelli C, Giacomelli FC, Spinelli A (2004) Evaluation of the inhibitor effect of L-ascorbic acid on the corrosion of mild steel. Mater Chem Phys 83:129–134
7. James OO, Ajanaku KO, Ogunniran KO, Ajani OO, Siyanbola TO, John MO (2011) Adsorption behaviour of pyrazolo [3, 4-b] pyridine on corrosion of stainless steel in HCl solution. Trends AppL Sci Res 6(8):910–917
8. Felicia RS, Santhanalakshmi S, Wilson SJ, John AA, Susai R (2004) Bull Elect 20(12): 561–565
9. Guidelli R (1992) Adsorption of molecules at metal electrodes. VCH Publishers lnc., New York, p 1
10. Hosseini M, Mertens SFL, Arshadi MR (2003) Synergism and antagonism in mild steel corrosion inhibition by sodium dodecylbenzenesulphonate and hexamethylenetetramine. Corros Sci 45:1473–1489
11. George S (2004) Infrared and Raman characteristic group frequencies: tables and charts. Wiley, New York

Corrosion Resistance of Aluminium in 0.5 M H_2SO_4 in the Presence of *Cassia fistula* Extract

Olugbenga Adeshola Omotosho, Joshua Olusegun Okeniyi, Cleophas Akintoye Loto, Abimbola Patricia Popoola, Adeoluwa Oni, Ayomide Alabi and Abisola Olarewaju

Abstract The effect of *Cassia fistula* leaves extract on the corrosion of Al in 0.5 M H_2SO_4 at 30 °C was investigated using gravimetric and electrochemical method. Gravimetric tests were conducted for 32 days in inhibited and uninhibited test solutions, while the potentiodynamic polarization tests were conducted from an anodic and cathodic potential of +0.5 V and −1.0 V respectively, at a scan rate of 0.1 V/s. Result analyses showed that *Cassia fistula* inhibits corrosion of Al effectively and adsorbs according to Langmuir adsorption isotherm. Corrosion rate reduced as inhibitor concentration increased for the gravimetric method, whereas for the electrochemical method it reduced as concentration increased, with exception at 4 and 6 g/L inhibitor concentration. Adsorption was found to be spontaneous for both techniques, while the inhibition mechanism was found to be mixed but predominantly cathodic. *Cassia fistula* boosted thin oxide film surface coverage to hinder attack of the sulphuric acid.

Keywords Aluminium · H_2SO_4 · *Cassia fistula* extract · Potentiodynamic polarization · Tafel slope · Surface coverage · Adsorption

Introduction

The industrial application of aluminium alloy has been on the increase after the discovery of its desirable properties. The challenge of extracting aluminium from its ore, made its early utilization almost impossible. Aluminium and its alloys have the ability to resist atmospheric corrosion in chemical, marine and industrial settings. This high resistance prolongs the useful life of the equipment, reduces maintenance

O. A. Omotosho (✉) · J. O. Okeniyi · C. A. Loto · A. Oni · A. Alabi · A. Olarewaju
Mechanical Engineering Department, Covenant University, Ota 112001, Nigeria
e-mail: olugbenga.omotosho@covenantuniversity.edu.ng

C. A. Loto · A. P. Popoola
Chemical & Metallurgical Engineering Department, Tshwane University of Technology, Pretoria, South Africa

The Minerals, Metals & Materials Society, *TMS 2018 147th Annual Meeting & Exhibition Supplemental Proceedings*, The Minerals, Metals & Materials Series,
https://doi.org/10.1007/978-3-319-72526-0_87

costs considerably and maintains the outward appearance. Thus, because of all these desirable properties ranging from high strength-to-weight ratio to its non-ferromagnetic nature amongst many, aluminium became an economic competitor with immense comparative advantage for engineering applications [1–10]. However, the corrosion resistance of aluminium has been attributed to its ability to form a protective thin oxide film [6, 8, 10]. The exposure of this protective film to acidic environments like pickling, etching, descaling and oil well acidizing operation usually leads to the destruction of the film and eventual attack of the metal. In most cases, engineering metallic parts are simultaneously subjected to chemical exposure/attack and design load situations in service. Eventually, they become unable to support designed load specification, because such attacks reduce the effective thickness of the metal parts. The metal wastage that has occurred ensures that the component is unable to withstand its designed load capacity, because it loses engineering functionality and fails, either gradually or suddenly.

Corrosion prevention and control techniques have been identified as; metallic coatings application, cathodic protection, environmental modification, materials selection, and chemical, organic and green inhibitor utilization amongst others [4–6, 8–19]. Though effective, the use of chemical inhibitors has been associated with negative environmental consequences ranging from contamination of plant and animal life, pollution, disposal burden and litigation from host communities. For these reasons, research focus has shifted from this harmful but effective technique to the use of green inhibitors. They have been recognized as environmentally friendly, litigation free, cheap, affordable and easily disposable [13–16]. Asides from these attributes, they contain compounds with polar functional groups like sulphur, nitrogen, phosphorous and oxygen and a variety of aromatic systems with conjugated double bonds [13–15]. Fundamentally, these surface-assimilative compounds adsorb on the metal surface to stifle the aggressive media harmful reaction. These heterocyclic compounds are chemically and physically adsorptive substances with a very active nature [17]. They are responsible for the corrosion resistant ability displayed by plants.

Since the use of chemical compounds as corrosion inhibitors has become objectionable due to the harmful effects of these compounds on plant and animal life, it is therefore necessary to come up with a new category of corrosion inhibitors with low toxicity, environmental friendliness and great efficiency. Plants have been used by human beings for housing, food, apparel, herbs and corrosion inhibitors [20]. Plant extracts have been used as corrosion inhibitors for more than 80 years [20]. Specifically, for the very first time during acid pickling operation utilizing H_2SO_4, *Chelidonium majus* and some other plants were used [20]. This is because of the unique benefits associated with the use of plants. In this study therefore, which is a continuation of our study on corrosion inhibiting potentials of *Cassia fistula* [21], leaf extract of *Cassia fistula* is utilized as corrosion inhibitor in the Hydrochloric acid corrosion of aluminium alloy using gravimetric and potentiodynamic polarization techniques.

Experimental Methods

Aluminium specimen were cut into 2 cm × 2 cm × 0.3 cm coupons and weighed. Prior to this pre-experimental chemical treatment as per ASTM D2688-94 R99 [22] was conducted on the test sample. Thereafter, they were completely immersed in 100 ml of the test solution in an open container. Before taking the weight readings after each experiment, the metal samples were also subjected to post experimental treatment specified in ASTM G 1-03 [23] for post-experimental treatment. The test solutions consisted of the control and the inhibited test solution (solution containing the *Cassia fistula* leaf extracts). The inhibited solution concentrations were 2, 4, 6, 8 and 10 g/L. The reagents used in this study were of analar grade. Sulphuric acid of 0.5 M concentration was prepared using Double distilled water. The gravimetric tests were conducted for 32 days and the readings were taken every 4 days.

The electrochemical measurements were performed by a Digi-Ivy potentiostat (DY2312X050 A0280IR) equipped with a DY2300 series software. A three-electrode cell is connected to the potentiostat via electrical wire with crocodile clip. The three electrodes are: the working electrode which is the aluminium test sample with exposed surface area of 1 cm^2; the auxiliary electrode (graphite rod) and the reference electrode (Ag/AgCl electrode). Prior to the connection of the aluminium sample potentiostat, the aluminium was chemically treated according to procedures stated in ASTM D2688-94 R99 for pre-experimental treatment of aluminium samples for corrosion monitoring experiment. The treated samples were then embedded in alraldite resin epoxy system with a wire connection protruding out of the system for connection to the potentiostat.

Tafel polarization curves from the linear sweep voltammetry (LSV) test were used to evaluate the corrosion resistance of the aluminium samples. LSV tests was carried out at a scan rate of 0.1 V/s from an anodic potential of +0.5 V and cathodic potential of −1.0 V. The following parameters were obtained from the LSV instrument database: corrosion current density (i_{corr}); corrosion potential (E_{corr}); charge transfer resistance (R_{ct}) and corrosion rate (*CR*). By plotting a graph of potential versus log i_{corr} all the parameters stated earlier could also be estimated from the Tafel plots.

Analyses of Experimental Data

After the completion of the gravimetric tests, the weight loss obtained was employed to calculate the corrosion rate, R_{al}. Weight loss readings were substituted into Eq. (1) below [24–29]:

$$R_{al}(mmpy) = \frac{87.6(W_L)}{T \times A \times \rho} \tag{1}$$

where T, W_L, ρ and A, is the time of immersion (h), weight loss (g), density of mild steel (g/cm^3) and area (cm^2) respectively.

The corrosion rate (R_{LSV}) from LSV tests were deduced from equipment readout using Eq. (2) [21, 24–28]:

$$R_{LSV} = \frac{3.27 \times 10^{-3} \times i_{corr} \times E_W}{\rho} \tag{2}$$

E_W, and i_{corr} are the equivalent weight (g) and corrosion current density (μA/cm^2).

The inhibitor efficiency (IE%) from the weight loss test was estimated using the corrosion rate data. This was done by employing Eq. (3) [8, 24–33]:

$$IE\% = \left(\frac{R_{blank} - R_{CF}}{R_{blank}}\right) \times 100 \tag{3}$$

Also, the surface coverage (θ) of the *Cassia fistula* plant extract was calculated using Eq. (4) [24–28, 32–34]:

$$\theta = \left(\frac{R_{blank} - R_{CF}}{R_{blank}}\right) \tag{4}$$

Results and Discussion

Figure 1 represents the relationship between: corrosion rate and time of the immersion and inhibitor efficiency and concentration. It is observed from Fig. 1a that the corrosion rate of the control system when compared to that of the inhibited sample was higher from the beginning to the end of the experiment. The sulphuric acid ions were in complete control of the entire system and despite the thin oxide film on the aluminium surface. The thin film was broken down by the acidic ions in the solution; this was more evident on 8th day of the experiment. Afterwards, it seemed the corrosion products in the solution formed a barrier on the surface of the metal and reduced the corrosion rate henceforth. However, the values were still higher than the inhibited sample. It is worthy to note that, while corrosion rate values for the inhibited samples were quite low from the beginning to the end of the experiment, it was also closely related in values. The values were marginal and so the deviations of the values were not so evident on the graph. In order to have a clearer picture of what happened, the average corrosion rate values were taken for each inhibitor concentration and the following order was discovered in reducing

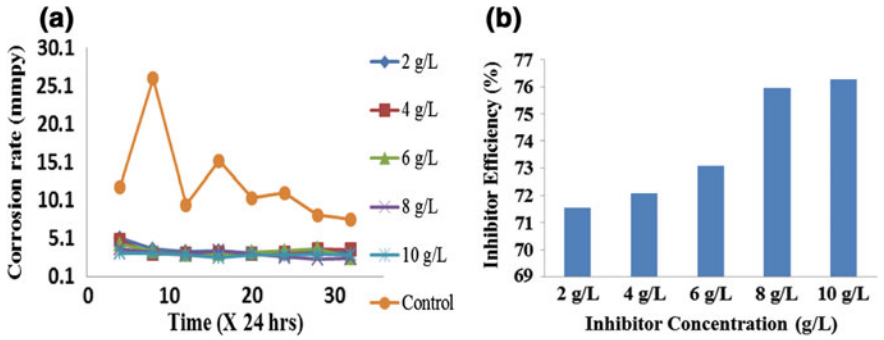

Fig. 1 Plots of **a** corrosion rate against time and **b** inhibitor efficiency against concentration for aluminium sample immersed in sulphuric acid under the influence of *Cassia fistula* leaf extract at 30 °C

order: 2 < 4 < 6 < 8 < 10 < 0 g/L. This completely agrees with Fig. 1b where, it was observed that inhibitor efficiency increased as concentration increased. The highest value of 76.2% was attained at 10 g/L, while the least value of 71.6% was at 2 g/L concentration.

The plot of potentiodynamic polarization (Log i_{corr} vs V) for aluminium samples immersed in 0.5 M sulphuric acid with and without varying inhibitor concentration is shown in Fig. 2a, while Tafel slopes (β_a, β_c) superimposed with the corrosion potential (E_{corr}) against concentration is shown in Fig. 2b. Analysing the corrosion potential of the control specimen, and comparing it with that of the inhibited sample shows that the potential for the 8 and 10 g/L samples were more positive, whereas that of the 2, 4 and 6 g/L samples were less positive. This indicates that the inhibitor influenced the reactions in both anodic and cathodic directions on the metal surface. The maximum E_{corr} displacement in comparison to the control is 67 mV. This value (67 mV) is less than 85 mV [21, 28, 29] and negative. This implies mixed but predominantly cathodic inhibitor behaviour. In Fig. 2a, it was

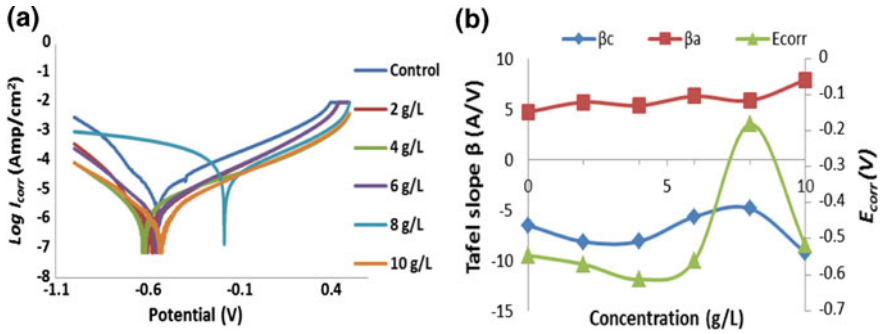

Fig. 2 Plots of **a** potentiodynamic polarization, **b** Tafel slopes and corrosion potential against concentration for Al samples immersed in 0.5 M H_2SO_4 using *Cassia fistula* extract

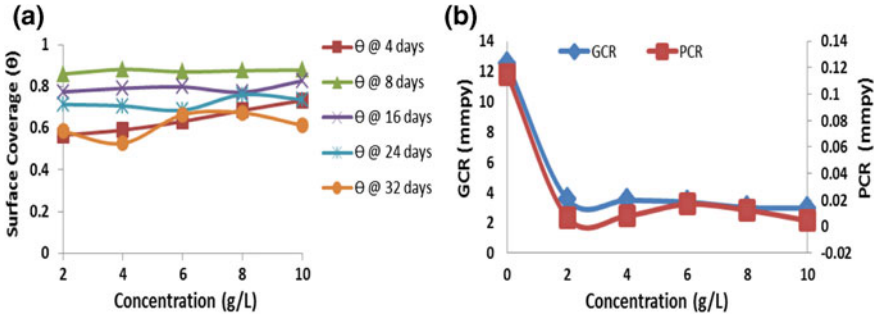

Fig. 3 **a** Plots of dynamic surface coverage as time changes and **b** gravimetric (GCR) and potentiodynamic corrosion rate (PCR) for aluminium sample immersed in 0.5 M HCl under the influence of *Cassia fistula* leaf extract at 30 °C

observed that the anodic and cathodic slope constants wholly lingered in the anodic and cathodic zone as concentration changed. However, it was discovered that, though the E_{corr} values for the 2, 4, 6 and 10 g/L concentration remained in the cathodic zone, the E_{corr} value of the 8 g/L concentration strayed into the anodic region, before moving back into the cathodic zone as concentration increased to 10 g/L. There seems to be an agreement between the trend observed in the Fig. 2a, b, since a predominantly cathodic mechanism was established.

An investigation into the relationship that existed between the surface coverage and concentration as the experimental time increased is presented in Fig. 3a. It is obvious from the plot that surface coverage values for the 8th day was highest across all concentration used. This was closely followed by the 16th and 24th day values. However, the 4th and 32nd day surface coverage values were the lowest. The explanation for the former case could be that the time was too short for surface coverage to build up, while in the latter case, the acidic media aggressive ions had taken over the reaction process in the corrosion process. In the 8th, 16th and 24th day scenario the *Cassia fistula* plant extract were active in enhancing surface coverage of the protective film over the metal surface. This graph simply shows the behaviour of the protective film as the experiment progressed. Figure 3b is a representation of the corrosion rate data for the gravimetric and potentiodynamic techniques against the inhibitor concentration. It is very clear that almost the same behaviour was displayed by the *Cassia fistula* plant extract in both cases. The only slight deviation noticed is at the 2, 4 and 10 g/L inhibitor concentrations. Both curves however show that corrosion rate reduced as inhibitor concentration increased.

The metal-inhibitor adsorption mechanism for the gravimetric and potentiodynamic technique is presented in Fig. 4. Several tests were conducted by fitting experimental data to a variety of adsorption isotherms, and it was found out, for both techniques, that the Langmuir adsorption isotherm best described the mechanism of adsorption. However, a plot of Log (C/θ) versus Log C was conducted to

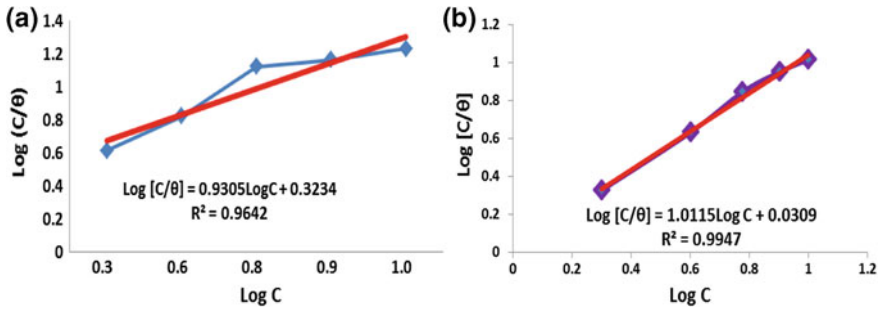

Fig. 4 Plots of adsorption isotherm for **a** gravimetric technique and **b** electrochemical technique for aluminium sample immersed in 0.5 M HCl under the influence of *Cassia fistula* leaf extract at 30 °C

be able to compare that result (shown in the graph in Fig. 4) to the Langmuir equation stated elsewhere [35]. Equation (5) below is the Langmuir equation.

$$\frac{C}{\theta} = \frac{1}{K_{La}Q_c} + \frac{C}{Q_c} \tag{5}$$

Q_c is the maximum monolayer capacity (mg/g), while C is the concentration. The Langmuir adsorption constant obtained from the comparison was further employed in the separation factor equation in which K_{La} had a relationship. Equation (6) is referred to as the separation factor (R_{se}) equation [35] and the equation enables us to ascertain the degree of favourability of the sorption process.

$$R_{se} = \frac{1}{1 + K_{La}C_s} \tag{6}$$

The initial concentration is depicted by C_s. The result of that analysis yielded the K_{La} value. This value was substituted into the separation factor equation to obtain the R_{se} value. Furthermore, the K_{La} value was substituted into Eq. (7) which is the Gibbs free energy equation [35] to obtain the final value of the free energy.

$$\Delta G^0_{ad} = -2.303RTLog(55.5K_{La}) \tag{7}$$

All this analysis produced the data in Table 1 for both techniques. The calculated R_{La} values for the gravimetric and electrochemical techniques showed that the sorption process was favourable based on conditions stated in literature [35] regarding favourable adsorption process ($R_L < 1$). Also, the Gibbs free energy obtained for both techniques indicated that the process was spontaneous. The negative Gibbs free energy value (−12.77 and −18.89 kJ/mol respectively) established a preponderant physisorption process for the adhesion of the *Cassia fistula* leaf extract on the aluminium surface.

Table 1 Langmuir and sorption condition parameters

S. no.	Description	Slope	Intercept	Q_C	K_{La}	R_L	Gibbs (KJ/mol)	Sorption condition
1	Gravimetric	0.9305	0.3234	1.07469	2.877	0.148	−12.77	Favourable
2	Potentiodynamic	1.0115	0.0309	0.987	32.79	0.015	−18.89	Favourable

Conclusions

In this chapter, the investigation of the effect of *Cassia fistula* plant extract on the corrosion resistance of aluminium in 0.5 M H_2SO_4 was conducted employing the gravimetric and potentiodynamic polarization technique. It was discovered that:

- *Cassia fistula* extract acts as a good corrosion inhibitor for Al in 0.5 M H_2SO_4 at all concentrations, with its efficiency increasing as concentration increased for the gravimetric method;
- Inhibitor efficiency for the potentiodynamic technique did not follow a particular trend, however, 10 g/L concentration attained the highest value of 96%, while the least efficiency was 85.22% at 6 g/L;
- The potentiodynamic polarization curve depicted a mixed but predominant cathodic inhibition mechanism;
- The Langmuir adsorption isotherm best described the metal-inhibitor interaction mechanism for both techniques used, based on r^2 value of 0.9642 (gravimetric) and 0.9947 (potentiodynamic);
- The separation factor parameter of 0.148 (gravimetric) and 0.015 (potentiodynamic) showed a favourable sorption process since both values were less than 1;
- The Gibbs free energy of adsorption of −12.77 and −18.89 kJ/mol, for the gravimetric and potentiodynamic technique suggests a preponderant spontaneous physisorption process;
- The *Cassia fistula plant extract* enhanced the effect of the oxide passive film on the aluminium metal surface.

Acknowledgements The laboratory contribution of Thomas Makinwa is acknowledged. The authors also thank the Department of Mechanical Engineering, Covenant University, Ota, Nigeria, for the utilization of laboratory research facilities. In addition, the authors also thank Covenant University Center for Research Innovation and Discovery (CUCRID) for their financial support.

References

1. Patil DB, Sharma AR (2014) Inhibition of corrosion of aluminium in potassium hydroxide solution by pyridine derivatives. ISRN Mater Sci Article ID 154285, 5 pp
2. Prabhu D, Rao P (2013) *Coriandrum sativum* L.—a novel green inhibitor for the corrosion inhibition of aluminium in 1.0 M phosphoric acid solution. J Environ Chem Eng 1(4):676–683

3. Alaneme KK (2011) Corrosion behaviour of heat-treated Al-6063/ SiCp composites immersed in 5wt% NaCl solution. Leonardo J Sci 18:55–64
4. Krishnaveni K, Ravichandran J (2014) Effect of aqueous extract of leaves of *Morinda tinctoria* on corrosion inhibition of aluminium surface in HCl medium. Trans Nonferrous Met Soc China 24(8):2704–2712
5. Bhat JI, Alva VD (2011) A study of aluminium corrosion inhibition in acid medium by an antiemitic drug. Trans Indian Inst Met 64(4–5):377–384
6. Ajayi OO, Omotosho OA, Ajanaku KO, Olawore BO (2011) Failure evaluation of aluminium alloy in 2 M HCl in the presence of *Cola acuminata*. Environ Res J 5(4):163–169
7. Din RU, Bordo K, Jellesen MS, Ambat R (2015) Accelerated growth of oxide film on aluminium alloys under steam: Part II: Effects of alloy chemistry and steam vapour pressure on corrosion and adhesion performance. Surf Coat Technol 276:106–115
8. Ajayi OO, Omotosho OA, Ajanaku KO, Olawore BO (2011) Degradation study of aluminium alloy in 2 M HCl in the presence of *Chromolaena odorata*. J Eng Appl Sci 6(1):10–17
9. Oki M, Oki K, Otaigbe J, Otikor S (2013) Corrosion inhibition of aluminium in HCl by amine modified epoxy resin. J Mater Article ID 479728, 5 pp. https://doi.org/10.1155/2013/479728
10. Omotosho OA, Ajayi OO (2012) Investigating the acid failure of aluminium alloy in 2 M hydrochloric acid using *Vernonia amygdalina*. ITB J Eng Sci 44(1):77–92
11. Orubite KO, Oforka NC (2004) Inhibition of the corrosion of mild steel in hydrochloric acid solutions by the extracts of leaves of *Nypa frutican Wurmb*. Mater Lett 58(11):1768–1772
12. El-Etre AY, Abdallah M, El-Tantawy ZE (2004) Corrosion inhibition of some metals using *lawsonia* extract. Corros Sci 47:385–395
13. Raja PB (2010) Natural products as green corrosion inhibitor for metals in corrosive media. LAP Lambert Academic Publishing
14. Chauhan LR, Gunasekaran G (2007) Corrosion inhibition of mild steel by plant extract in dilute HCl medium. Corros Sci 49(3):1143–1161
15. El-Etre AY (2006) *Khillah* extract as inhibitor for acid corrosion of SX 316 steel. Appl Surf Sci 252(24):8521–8525
16. Ebenso EE, Eddy NO, Odiongenyi AO (2008) Corrosion inhibitive properties and adsorption behaviour of ethanol extract of piper guinensis as green corrosion inhibitor for mild steel in H_2SO_4. Afr J Pure Appl Chem 29:107–115
17. Buchweishaija I, Mhinzi GS (2008) Natural products as a source of environmentally friendly corrosion inhibitors: the case of gum exudates from *Acacia seyal var. Seyal*. Portugaliae Electrochim Acta 26(3):257–265
18. Ajmal M, Mideen AS, Quarishi MA (1994) 2-hydrazino-6-methyl-benzothiazole as an effective inhibitor for the corrosion of mild steel in acidic solutions. Corros Sci 36(1):79–84
19. Bentiss F, Traisnel M, Chaibi N, Mernari B, Vezin H, Lagrene M (2002) 2,5-Bis(*n*-methoxyphenyl)-1,3,4-oxadiazoles used as corrosion inhibitors in acidic media: correlation between inhibition efficiency and chemical structure. Corros Sci 44(10):2271–2289
20. Sanyal B (1981) Organic compounds as corrosion inhibitors in different environments—a review. Prog Org Coat 9(2):165–236
21. Omotosho OA, Okeniyi JO, Loto CA, Popoola API, Ajibola OB, Ogbiye AS (2017) *Cassia fistula* leaf-extract effect on corrosion-inhibition of stainless-steel in 0.5 M HCl. In: TMS2017 supplemental proceedings, pp 179–189. Springer International Publishing AG, Cham Switzerland. https://doi.org/10.1007/978-3-319-52132-9_18
22. ASTM D2688-94 R99 (2005) Standard test methods for corrosivity of water in the absence of heat transfer (weight loss methods). ASTM International, West Conshohocken, PA
23. ASTM G 1-03 (2005) Standard practice for preparing, cleaning, and evaluating corrosion test specimens. ASTM International, West Conshohocken, PA
24. Omotosho OA, Ajayi OO, Ajanaku KO, Ifepe VO (2012) Environment induced failure of mild steel in 2 M sulphuric acid using *Chromolaena odorata*. J Mater Environ Sci 3(1):66–75
25. Omotosho OA, Ajayi OO, Fayomi O, Ifepe VO (2012) Evaluating the deterioration behaviour of mild steel in 2 M sulphuric acid in the presence of *Butyrospermum parkii*. Asian J Appl Sci 5(2):74–84

26. Omotosho OA, Ajayi OO, Fayomi OS, Ifepe VO (2011) Assessing the deterioration behavior of mild steel in 2 M sulphuric acid using *Bambusa glauscescens*. Int J Appl Eng Res Dindigul 2(1):85–97
27. Eddy NO, Momoh-Yahaya H, Oguzie EE (2015) Theoretical and experimental studies on the corrosion inhibition potentials of some purines for aluminum in 0.1 M HCl. J Adv Res 6:203–217
28. Omotosho OA, Okeniyi JO, Oni AB, Makinwa TO, Ajibola AB, Fademi EOJ, Obi CE, Loto CA, Popoola API (2016) Inhibition and mechanism of *Terminalia catappa* on mild-steel corrosion in sulphuric-acid environment. Prog Ind Ecol 10(4):398–413I
29. Loto RT, Loto CA, Popoola API (2015) Electrochemical effect of 1, 4-diaminobenzene on the corrosion inhibition of mild steel in dilute acid media. Der Pharma Chemica 7(5):72–93
30. Ajayi OO, Omotosho OA, Ifepe VO (2011) Acid failure of mild steel in 2 M sulphuric acid in the presence of *Vernonia amygdalina*. J Mater Environ Sci 2:186–195
31. Okeniyi JO (2016) $C_{10}H_{18}N_2Na_2O_{10}$ inhibition and adsorption mechanism on concrete steel-reinforcement corrosion in corrosive environments. J Assoc Arab Univ Basic Appl Sci 20:39–48
32. Okeniyi JO, Loto CA, Popoola API (2014) Electrochemical performance of *Anthocleista djalonensis* on steel-reinforcement corrosion in concrete immersed in saline/marine simulating-environment. Trans Indian Inst Met 67:959–969
33. Okeniyi JO, Loto CA, Popoola API (2015) Corrosion inhibition of concrete steel-reinforcement in saline/marine simulating-environment by *Rhizophora mangle* L. Solid State Phenom 227:281–285
34. Okeniyi JO, Loto CA, Popoola API (2014) *Rhizophora mangle* L. effects on steel-reinforced concrete in 0.5 M H_2SO_4: implications for corrosion-degradation of wind-energy structures in industrial environments. Energy Procedia 50:429–436
35. Foo KY, Hameed BH (2010) Insights into the modeling of adsorption isotherm systems. Chem Eng J 156(1):2–10

Part XXXV
Surface Interactions in Materials

Pt Decorating Effect on CNT Surface Towards Adsorption of SF_6 Decomposed Components

Hao Cui, Xiaoxing Zhang, Dachang Chen, Jiani Fang and Ju Tang

Abstract Carbon nanotubes (CNTs) based sensors are drawn considerable attentions for gas adsorption and sensing due to their large specific surface area. In this paper, the adsorptions of three SF_6 decomposed components (SO_2F_2, SOF_2 and SO_2) on Pt doped CNT are theoretically studied based on density function theory method. The density of state, frontier molecular orbital theory as well as Mulliken population analysis were considered in order to comprehensively understand the adsorbing processes. Results indicated that Pt-CNT has the best sensitivity to SOF_2 owing to their strong chemisorption, followed by SO_2 and the last one comes to SO_2F_2 due to their weak physisorption. Pt dopant that acts as an activated catalytic additive can effectively improve the adsorption ability to gas molecules through providing several active adsorption sites of CNT. Our calculation results would be meaningful not only to explain the sensing mechanism of CNT but also to suggest advanced SWCNTs based sensing materials to be applied in the field of electrical engineering.

Keywords SF_6 decomposed components · Pt · CNT

Introduction

Sulfur hexafluoride (SF_6) in the past decades has received extensive applications in gas insulated switchgear (GIS) and other high voltage devices of the power system owing to its excellent insulating and arcing performances [1]. Even so, in a long-running equipment, SF_6 would be decomposed under partial discharge or partial overheat caused by inevitable insulation defects into several low-fluoride

H. Cui · X. Zhang (✉)
State Key Laboratory of Power Transmission Equipment & System Security and New Technology, Chongqing University, Chongqing 400044, China
e-mail: xiaoxing.zhang@outlook.com

X. Zhang · D. Chen · J. Fang · J. Tang
School of Electrical Engineering, Wuhan University, Wuhan 430072, China

The Minerals, Metals & Materials Society, *TMS 2018 147th Annual Meeting & Exhibition Supplemental Proceedings*, The Minerals, Metals & Materials Series,
https://doi.org/10.1007/978-3-319-72526-0_88

sulfides such as SF_4, SF_3, SF_2 and so on [2]. These would subsequently react in the presence of oxygen and trace water, and form many kinds of typical decomposition products including SOF_2, SO_2F_2, SO_2, H_2S, SOF_4, HF, etc. [3–6], which is bound to deteriorate the performances of SF_6, increasing the potential of system paralysis [7].

Therefore, the online-detection for partial discharge and overheat has become a necessary means to evaluate the operation state of some insulating devices applied in electrical engineering. Through detecting the content of these decompositions, the related insulation defects can be speculated, and it would be much more efficient to take corresponding measures to lower the loss caused by the insulation problems [8]. Carbon nanotubes (CNTs) have aroused considerable attention for gas sensing materials since its first discovery by Iijima and Ichihashi [9], due to their fast response and high sensitivity [10, 11]. The basic sensing mechanism of CNTs sensors is based on the conductivity changes once the gas molecules are adsorbed on such sidewall [12, 13]. However, owing to their strong $sp.^2$ binding in typical geometrical structure, intrinsic CNTs present inactivity with most gas molecules [14]. Thus, in many studies, metals that exhibit good chemical and electronic properties so that response sensitively to changes in their surroundings [15–17] are proposed to decorate the CNTs for the sake of the improvement of sensitivity and selectivity to specific gases, where the metal nanoparticles provide active sites to the interaction with targeted molecules [18].

As a high catalytic activity metal, platinum (Pt) is usually employed as a decoration for CNTs in order to form a high sensitivity complex to certain small gas molecules [19]. To explore its further applications, this paper simulates the adsorption processes of certain SF_6 decomposition products, namely SO_2F_2, SOF_2 and SO_2, on Pt doped CNT (Pt-CNT) based on the first principle theory. The highest occupied molecular orbital (HOMO) and the lowest unoccupied molecular orbital (LUMO) are also introduced to help understand the electronic behavior and the conductivity change during the adsorbing processes. The results show that the Pt-CNT surface displays rather good adsorption performances to the three SF_6 decomposed components, indicating its possibility to be prepared as a novel type of practical sensor utilized in power system.

Calculation Details

All the computations were performed on the $DMol^3$ package of materials studio. Spin-unrestricted DFT in the generalized-gradient approximation (GGA) with the Perdew-Burke-Emzerhof (PBE) was adopted to acquire all the data mentioned below [20]. Brillouin-zone was executed by the Monkhorst-Pack scheme with k-point sampled into $1 \times 1 \times 2$ [21]. The energy tolerance accuracy, maximum force, as well as displacement were set as 10^{-5} Ha, 2×10^{-3} Ha/Å, and 5×10^{-3} Å [22], respectively. The semi-conducting (8, 0) single wall carbon nanotube (SWCNT) was selected with a super cell of 20 Å × 20 Å × 8 Å to acted as the

adsorbed system [23]. One C atom is substituted by Pt atom to form the Pt-CNT. The gas molecules in parallel with Pt-CNT were all geometrically optimized to their most stable structures. To commence the adsorption reactions, the gas molecules were individually approaching the Pt-CNT in diverse orientations with initial distance 2 Å and then relaxed to their most geometric configurations. When successfully completing the calculations, the adsorption distances (D) and adsorption energies (E_{ad}) value can be obtained, in which the adsorption energy of each process were calculated by the following equation [24]:

$$E_{ad} = E_{gas/\mathrm{Pt}-CNT} - E_{gas} - E_{\mathrm{Pt}-CNT} \quad (1)$$

where the $E_{gas/Pt\text{-}CNT}$, E_{gas} and $E_{Pt\text{-}CNT}$ separately represents total energies of the adsorption system, the gas molecule and the Pt doped CNT. Generally, only when the E_{ad} lowers than 0, can relevant reaction occurs spontaneously, while the positive value manifests that this process is not able to happen. Moreover, the more negative this value is, the more possibility this reaction is likely to occur. Additionally, the Mulliken population analysis is considered to evaluate the charge transfer between the gas molecule and adsorbent, results presented by Q_{T}.

Results and Discussion

Optimized Structures of Pt-CNT and Gas Molecule Models

In the optimized Pt-CNT structure (Fig. 1a), the Pt atom obviously protruded out of the tube due to the larger radium of Pt atom than that of C atom. In SO_2 configuration (Fig. 1b), the band length of S–O equals to 1.481 Å and the O–S–O angel to 120.001°. Comparing the SO_2F_2 configuration shown in Fig. 1c with SOF_2 in Fig. 1d, we find that the adding of the O atom causes the shortened distances of S–O and S–F bonds, from 1.462 Å and 1.672 Å to 1.413 Å and 1.613 Å, respectively.

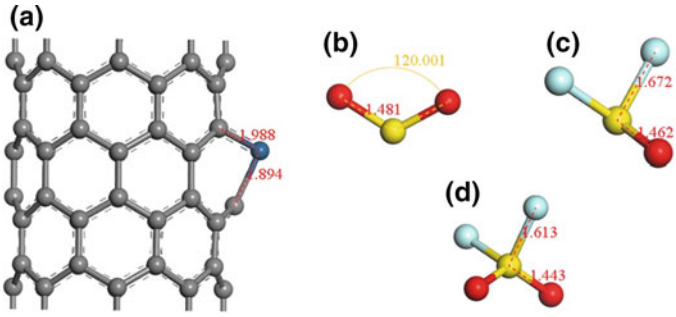

Fig. 1 Optimized structures of Pt-CNT and gas molecules

Adsorbing Configuration for Three Species on Pt-CNT

After adsorbing SO_2, SOF_2 and SO_2F_2 on the sidewall of Pt-CNT, related configurations are shown in Fig. 2. In Fig. 2a where the SO_2 adsorbing system is shown, we can found that SO_2 adsorbed on the Pt-CNT surface with two O atoms oriented, and both O atoms are trapped by the Pt atom with Pt–O bond 2.192 Å. The E_{ad} and Q_T in this system is calculated to be −0.76 eV and −0.449 e, respectively. The negative value for Q_T suggests the electron transferring path from Pt-CNT surface to SO_2 molecule. Referring to the SOF_2 configuration seen in Fig. 2b, it can be seen that owing to the strong adsorption strength of Pt dopant, one F atom is adsorbed on the Pt surface while escaped from the constrained of S atom. At the same time, a new bond between Pt and S atom in the SOF_2 molecule has formed with length of 2.495 Å. After the adsorption of SOF_2, the E_{ad} is −1.41 eV and the Q_T equals to −0.596 eV, suggesting that electron transfers from Pt-CNT to adsorbed molecule as well. Similar to the SOF_2 system, after the adsorption of SO_2F_2 molecule on the surface of Pt-CNT as shown in Fig. 2c, one F atom is also trapped and formed new bond with Pt dopant with length of 2.006 Å, leading to the escape of such F atom from the binding force of S atom. In the meanwhile, the S atom is also trapped by the Pt dopant with the new formed Pt–S bond 2.462 Å. It should be noted that the lengths of newly formed Pt–S and Pt–F bonds in SO_2F_2 system are similar to those in SOF_2 system. In this system, the E_{ad} and Q_T are calculated as −1.66 eV and −0.808 e, respectively.

According to the adsorbing configurations of three system, one can concluded that the Pt doping supplies the CNT surface with good adsorbing ability for these gases, thereby offering its strong adsorption property. Moreover, the Pt-CNT is provided with best adsorption behavior towards SO_2F_2 given the largest values of E_{ad} and Q_T. On the contrary, the Pt doped adsorbent has poorest adsorbing performance towards SO_2 considering the combining analysis of E_{ad} and Q_T. In addition, the adsorbing distance (D) defined as the shortest length from the molecule to Pt-CNT are in order as SO_2F_2, SOF_2 and SO_2, which according with the E_{ad} and Q_T sequences can also confirm the adsorbing ability of Pt-CNT surface towards these three gases. According to the obtained adsorbing parameters, we

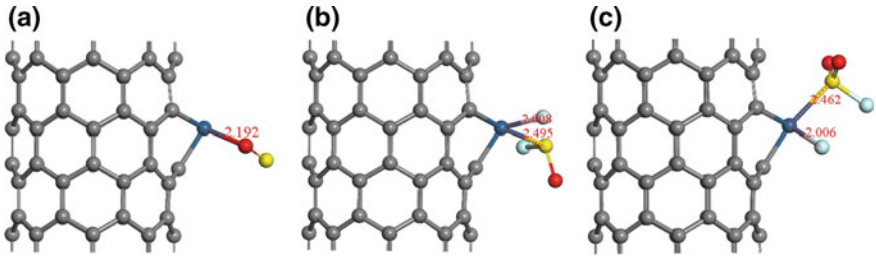

Fig. 2 Adsorption configurations for three systems

comprehensively assume that the adsorption towards SO_2 is physisorption while the adsorption towards SOF_2 and SO_2F_2 can be deemed as chemisorption.

Density of State and Frontier Molecular Orbital Theory Analyses

Density of state (DOS) curve that can obviously provide understanding of electronic behavior for adsorbing system compared with the pure Pt-CNT is important to be plotted. To better understand the change of adsorbing system from the insolated one, the DOS for two system (before and after gas molecules were adsorbed) were figured in the same frame as shown in Fig. 3.

We can find based on these figures that after adsorbing gas molecules, the total DOS peaks are generally improved compared with the pure Pt-CNT ones. At the same time, DOS transfers to a lower or higher region in varying systems, indicating the electron transfer between the gas adsorbate and Pt-CNT. It is just these changes that lead to the increase or decrease in electrical conductivity of proposed sensing material. To further illustrate the change in conductivity, the molecular frontier orbital theory is calculated as shown in Fig. 4. It can be seen that compared with the pure Pt-CNT, the HOMO and LUMO distributions have changed dramatically due to the adsorption of certain gas molecule. We can find from the electron cloud surrounding the Pt dopant in Fig. 4a that Pt is strong hybrid with the carbon nano-support, while the energy gap of Pt-CNT is 0.35 eV. Simultaneously, the change in orbital energies are changed sharply as well after adsorbing gas molecule. The HOMO-LUMO gaps have changed to 0.11 eV for SO_2 system, 0.26 eV for SOF_2 system and 0.50 eV for SO_2F_2 system, respectively as shown in Fig. 4b, c, d. Generally speaking, the increasing gap indicates the decrease for conductivity and conversely, the decreasing gap indicates the increase for conductivity. Therefore, we assume that after the adsorption of SO_2 and SOF_2, the conductivity of Pt-CNT would be increased and, after the adsorption of SO_2F_2, the conductivity of Pt-CNT

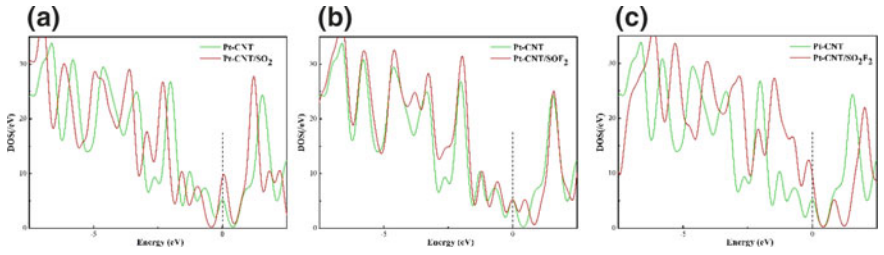

Fig. 3 DOS curves for various adsorbing systems

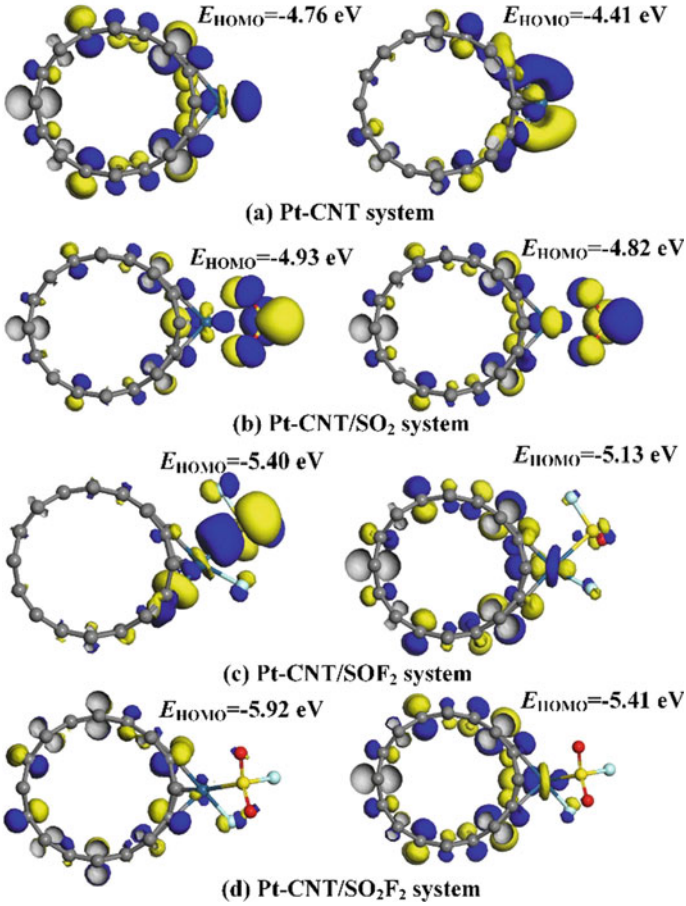

Fig. 4 HOMO and LUMO distributions for varying systems

would be decreased. The conductivity change would be the detecting mechanism for our proposed sensing material to realize the online-detection for SF_6 decomposed components and further, the different changing tendency in conductivity determine the possibility of selective detection for various SF_6 decompositions. Given the adsorption ability and the conductivity change of Pt-CNT towards three gases, we assume that our proposed Pt-CNT can be a good sensing materials for selectively and sensitively detecting of SF6 decomposed species, and thereby realizing the operating state evaluation for SF_6 equipment.

Conclusions

In this paper, the adsorption performance of Pt doped (8, 0) SWCNT to three types of SF_6 decomposed gases were investigated within DFT, for making the material possible as gas adsorbent to guarantee the good insulation state of GIS, and even as sensors employed to evaluate the operation state of such devices.

The calculated results reveal that the Pt decorated CNT has the remarkable sensitivity to SO_2F_2 and SOF_2, and exhibits relatively weak interaction with SO_2. Even though, this Pt decorated surface that exerts good adsorption performance are hopeful to be applied in the field of electrical engineering for the removal of SF_6 decomposed species in GIS. When four types of gas molecule/molecules are adsorbed on the Pt doped surface, its conductivity undergo increase or decrease due to their shrinkages or wideness of energy gap. The conductivity of Pt-CNT would increase after the adsorption of SO_2 and SOF_2, and in SO_2 adsorbing systems, related conductivity increase much more significantly. As a result, Pt decorated CNT provides an enhanced nanostructure for detecting SOF_2 or SO_2F_2 because relevant adsorptions onto the modified surface are desirable and favorable. We believe that such initial investigations can provide our future experiments with a first look into the physicochemical properties of Pt doped CNT, thereby accelerating the practical application of its based material.

References

1. Beyer C, Jenett H, Klockow D (2000) IEEE Trans Dielectr Electr Insulation 7(2):234–240
2. Zhang XX, Liu WT, Tang J, Xiao P (2010) IEEE Trans Dielectr Electr Insulation 17(3):833–838
3. Beyer C, Jenett H, Klockow D (2000) IEEE Trans Dielectr Electr Insulation 7(2):234–240
4. Piemontesi M, Niemeyer L (1996) Presented at the IEEE international symposium on electrical insulation (unpublished)
5. Qiu Y, Kuffel E (2000) IEEE Trans Dielectr Electr Insulation 6(6):892–895
6. Van Brunt RJ, Herron JT (2007) Phys Scr 1994(T53):9–29
7. Braun JM, Chu FY, Seethapathy R (1987) IEEE Trans Electr Insulation 22(2):187–193
8. Kusumoto S, Itoh S, Tsuchiya Y, Mukae H, Matsuda S, Takahashi K (1980) IEEE Trans Power Apparatus Syst PAS-99(4):1456–1465
9. Iijima S, Ichihashi T (1993) Nature 364(6430):603–605
10. Suehiro J, Zhou G, Hara M (2003) J Phys D Appl Phys 36(21):L109–L114
11. Kang H, Lim S, Park N, Chun KY, Baik S (2010) Sens Actuators B Chem 147(1):316–321
12. Zilli D, Bonelli PR, Cukierman AL (2011) Sens Actuators B Chem 157(1):169–176
13. Zhang X, Cui H, Gui Y, Tang J (2017) Nanoscale Res Lett 12(1):177
14. Popov VN (1998) Mater Sci Eng R Rep 24(3):61–102
15. Ruiz A, Arbiol J, Cirera A, Cornet A, Morante JR (2002) Mater Sci Eng C 19(1):105–109
16. Zhang X, Cui H, Dong X, Chen D, Tang J (2017) Appl Surf Sci
17. Zhang X, Cui H, Zhang J, Tang J (2017) Appl Surf Sci 419:802–810
18. Li W, Liang C, Zhou W, Qiu J, Zhou Z, Gongquan Sun A, Xin Q (2003) J Phys Chem B 107 (26):149–154

19. Penza M, Rossi R, Alvisi M, Cassano G, Signore MA, Serra E, Giorgi R (2008) Sens Actuators B Chem 135(1):289–297
20. Avramov PV, Kudin KN, Scuseria GE (2003) Chem Phys Lett 370(5–6):597–601
21. Monkhorst HJ, Pack JD (1976) Phys Rev B 13(12):5188–5192
22. Wang R, Zhang D, Zhang Y, Liu C (2006) J Phys Chem B 110(37):18267–18271
23. Gülseren O, Yildirim T, Ciraci S (2002) Phys Rev B 65(15)
24. Boys SF, Bernardi F (2002) Mol Phys 19(1):553–566
25. Cuong NT, Chi DH, Kim YT, Mitani T (2006) Phys Status Solidi 243(12):3472

Part XXXVI
Thermo-Mechanical Response of Materials with Special Emphasis on In-situ Techniques

"In Situ" Measurement of Electrical Resistivity, Dilatometry and Thermal Analysis of Cast Iron

Primož Mrvar and Mitja Petrič

Abstract The contribution describes the "in situ" measurement of electrical resistivity, dilatometry and thermal analyses of flake and spheroidal graphite cast iron in liquid state, during solidification and in solid state. The shape of graphite formed during solidification influences electrical properties and variations of dimensions of cast irons. The complex "in situ" measurements were performed using in house developed measuring cell. The samples were systematically quantitatively metalographically investigated. It was found that electrical resistivity of lamellar grey cast iron is greater than the electrical resistivity of spheroidal graphite cast iron since the lamellas of graphite interrupt the iron matrix more than the nodules and the conduction electrons are scattered more on interfaces between graphite and metal matrix. The electrical resistivity of the flake graphite cast iron is increasing during solidification and decreasing after solidification. Based on "in situ" obtained results of electrical resistivity, dilatations and temperatures the materials properties were reconstructed.

Keywords Electrical resistivity · Dilatometry · Thermal analysis

Introduction

At materials design someone is always interested in solidification path of material. It is very similar at solidification of different cast irons. Most common tool for solidification monitoring is thermal analysis and in connection with chemical composition it is possible to predict the developed microstructure and also mechanical properties. Beside thermal analysis there are some other techniques to

P. Mrvar (✉) · M. Petrič
Faculty of Natural Sciences and Engineering, University of Ljubljana, Aškerčeva 12, Ljubljana, Slovenia
e-mail: primoz.mrvar@omm.ntf.uni-lj.si

M. Petrič
e-mail: mitja.petric@omm.ntf.uni-lj.si

The Minerals, Metals & Materials Society, *TMS 2018 147th Annual Meeting & Exhibition Supplemental Proceedings*, The Minerals, Metals & Materials Series,
https://doi.org/10.1007/978-3-319-72526-0_89

define solidification and microstructure such as simultaneous thermal analysis (STA), dilatometric analysis and also electrical resistivity measurement [1–3].

After the solidification at cooling or at heat treatment γ—austenite is decomposed into ferrite (α) and graphite (G) or after metastable system into heterogeneous microstructure constituent perlite (α + Fe3C), or mostly by both paths respectively. Knowledge of actual microstructure, which comprises the nodule count, ferrite or perlite fraction in material respectively, is important due to the dependences of the mechanical properties of the casting [4, 5]. In the as-cast state the material has predominantly ferrite-perlite matrix. At the casting manufacture the cooling rate is determined by the local thickness of the casting wall. Final microstructure of material depends mostly of the alloy treatment by nodulizer and inoculant or by the proper choice of the alloy composition. Both measures effect on the course of the solidification and transformation in the solid state, respectively [6].

It's known very well, that transformation in the solid state depends on the microstructure formed in the solidification stage, i.e. of the nodule count. Higher content of impurities or low content of alloying elements effect on the growth and the decomposition of different phases. Low addition of the specific alloying elements, such as Cu, Mn, Sn and Sb, practically lead to the perlite matrix [7–9].

All these reaction mentioned above can be connected with dimensional changes which are the case of this study. Also the electrical resistivity of grey cast iron is changed during solidification and in further cooling in the similar manner. Electrical resistivity of pure metals is rising with higher temperatures because of increased vibration of lattice described as phonons and increased number of lattice defects. During the melting of a metal the electrical resistivity can be increased by the factor 2.2 since the periodicity of the lattice is broken and the conducting electrons are scattered more [10–12]. The theory is similar at resistivity of alloys and beside this the alloying elements have negative influence as well. If there are some other microstructural constituents present in the microstructure they have in most cases negative effect on electrical resistivity since the periodicity of lattice is broken on interfaces which causes electron scattering.

In the case of grey cast irons the situation is very similar. The amount of graphite and the shape of graphite have same influence on electrical resistivity as describe above. In the case of lamellar cast irons the electrical conductivity is higher than in the case of nodular cast iron [13–15].

Experimental

Alloys were prepared in the industrial foundry of the spheroidal graphite cast iron. The basic melt was prepared in the cold-blast cupola. There was one sample used for dilatometric analysis and two for electrical resistivity measurement. Chemical compositions and markings of samples are presented in a Table 1. The sample for dilatation analysis was from spheroidal graphite cast iron (500), and the samples for

Table 1 Chemical compositions of alloys

	C	Si	Mn	S	Cr	Cu	P	Mg
Base	3,95	1,82	0,259	0,048	0,04	0,026	0,031	0,005
500	3,70	2,45	0,27	0,016	0,41	0,58	0,027	0,040
600	3,79	2,54	0,348	0,01	0,039	0,029	0,026	0,045
	Ni	Mo	V	Ti	Sn	Al	Bi	
Base	0,017	0,002	0,004	0,009	0,021	–0,004	0,003	
500	0,026	–	–	–	–	–	–	
600	0,019	0,004	0,004	0,008	0,056	0,007	0,005	

electrical resistivity measurements were from base alloy (Base) and from spheroidal graphite cast iron (600).

The dilatometric analysis was made using the dilatometer with the measuring cell (Fig. 1) which was made by the Croning process, which has been developed from the standard quick-cup probe for the thermal analysis of the cast iron alloys. In the measuring cell two quartz rods have been axially installed, which could move the same way as the analysis sample. The rods are connected with the cores of the induction displacement transducers. The thermocouple is placed in the middle of the measuring cell in the heat center. The induction displacement transducers and the thermocouple were connected through the amplifier with the measuring card of DAQ PAD-Mio16XE-50 and the data was collected to a computer.

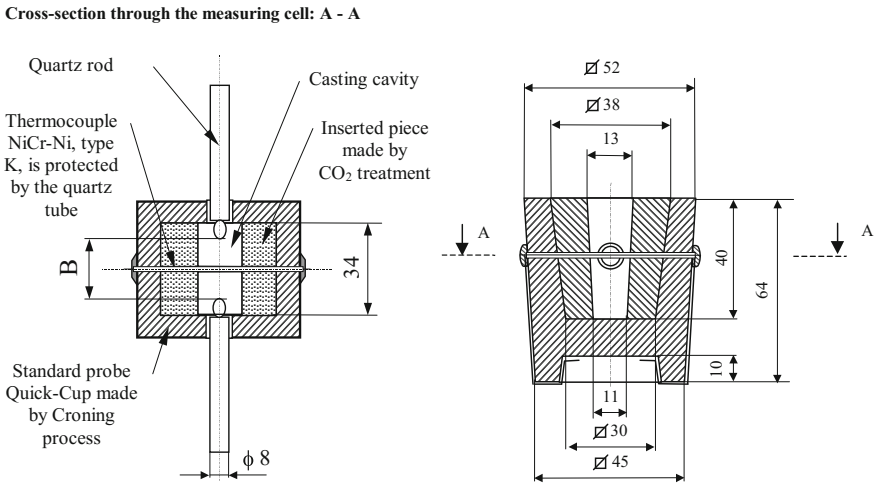

Fig. 1 The dilatation measuring cell for the samples of 12 × 34 mm

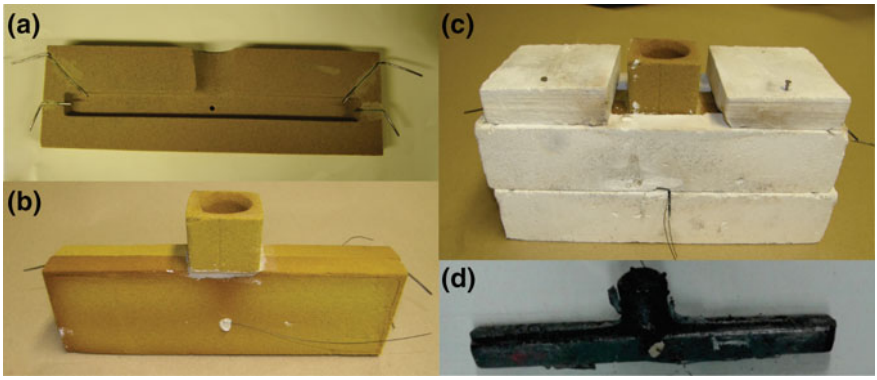

Fig. 2 Half of croning measuring cell with inserted electrodes (**a**), closed measuring cell (**b**), insulated measuring cell prepared for casting (**c**) and casting (**d**)

The electrical resistivity measurements were conducted in a measuring cell presented on Fig. 2. It is made by Croning process and is isolated with calcium silicate brick in order to lower the cooling rates. The casting has a square cross-section with of 330 mm^2 and length of 210 mm. At the ends of casting the two current electrodes were inserted and 20 mm towards the centre the two potential electrodes were inserted in order to measure electrical resistance of the casting by four-probe technique. The four-probe DC technique was used for measuring electrical resistivity as thoroughly described in previous work [3] where iron wires were used as electrodes. Simultaneously the thermal analysis was carried out by K-type thermocouple positioned under the sprue. All the data were captured by National Instruments CompactDAQ NI 9213 and NI 9219 measuring cards.

Acquired data was then plotted in form of curves presenting electrical resistivity versus temperature and/or time. Electrical resistivity (ρ) was calculated according to Eq. 1:

$$\rho = R\frac{S}{l}, \tag{1}$$

where R is measured resistance, S and l are cross-section and measuring length of a sample (170 mm). Cooling curves representing solidification path were plotted as well.

All samples were metallographically examined in order to determine the shape of graphite, size, distribution and portion of graphite and also the matrix. Metallographic observations were done by Olympus BX 61 optic microscope in polished and 2% NITAL etched state. The size and shape of graphite was determined automatically by Analysis 5.0 software.

Results and Discussion

Metallography

Metallographic observations showed the shapes of graphite and pearlite portions in all three samples. Sample of base alloy obtained directly from cupola furnace showed flake shape of graphite or form A. It is also observed that some rosette flake graphite (form B) and undercooled graphite (form D) are present in sample since the melt was not treated and inoculated. Samples of spheroidal graphite cast iron 500 and 600 have mainly nodular graphite, but since the melt was not completely treated before pouring—it was pre-inoculated but it was not in-stream inoculated—the shape of graphite is not perfect form VI but it is degraded to some extent. Microstructures of all three samples are presented in Fig. 3. It can be also seen that in base alloy sample the matrix is nearly 100% pearlitic and in samples of ductile iron is about 80% of pearlite and 20% ferrite.

Dilatometric Analysis

From the dilatometric curve and thermal analysis (Fig. 4) of the sample 500 is noticed, that the eutectic solidification proceeds uncoupled, i.e. the solidification is characterized by the initial contracting due to the precipitation of the austenite dendrites and then of graphite respectively. It is clear that during the austenite precipitation the sample is contracting but when the eutectic reaction starts it starts to expand because of precipitation of graphite. During cooling the sample is contracting again due to thermal expansion coefficient. At the temperatures of eutectoid transformation the sample is expanded again because of transformation of austenite to ferrite and/or pearlite.

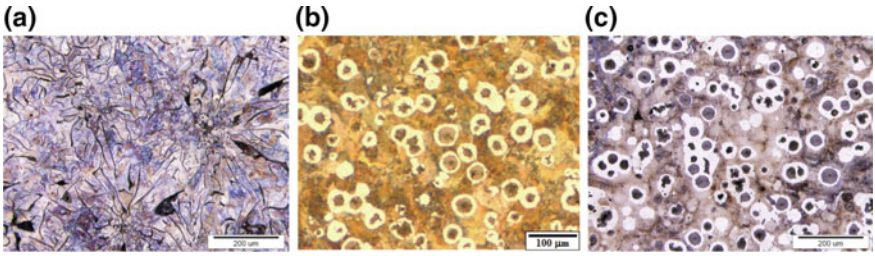

Fig. 3 Microstructures of all investigated samples: base alloy (**a**), 500 alloy (**b**) and 600 alloy (**c**)—etched by NITAL 2%

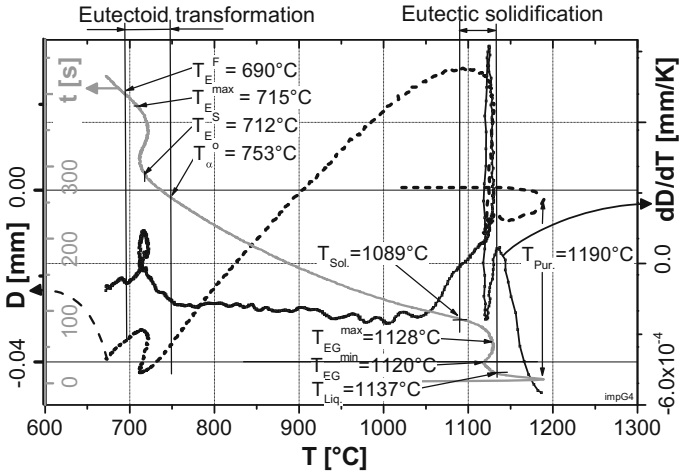

Fig. 4 The dilatation curves and the cooling curve of sample 500

Electrical Resistivity Measurements and Thermal Analysis

As described above the cooling rates were recorded at measurements and electrical resistivity was measured continuously from pouring till 650 °C. Following figures are presenting cooling curves with its derivative curves and curves of electrical resistivity versus time with its derivative curves presented on same diagram in order to correlate cooling curves with change of electrical resistivity. Figure 5 is presenting measurement of sample from basic alloy with flake graphite. One can see that changes and inflection points on cooling curve and its derivative coincide quite well with changes and inflection points on electrical resistivity curve and its derivative (lines in Fig. 5 are annotating the start and the end of solidification). There are some small deviations observed in matching of these points due to measurement where temperature is measured in one point under the sprue where the solidification is the last but electrical resistivity is measured throughout the whole sample and solidification at the ends starts faster.

It is seen that electrical resistivity of base alloy is decreasing during cooling of melt but at the start of solidification it starts to increase. This phenomenon is different from the theory of pure metals due to graphite flakes formation which cause high electron scattering resulting in increased resistivity. When solidification is finished the maximum resistivity is reached and it descends slowly during cooling. Another deflection point on electrical resistivity curve and its derivative is reached at time of app. 400 s which corresponds to 910 °C on cooling curve. This deflection point is believed to be the start of eutectoid transformation since the resistivity is decreasing faster but the mismatch with the temperature is caused by

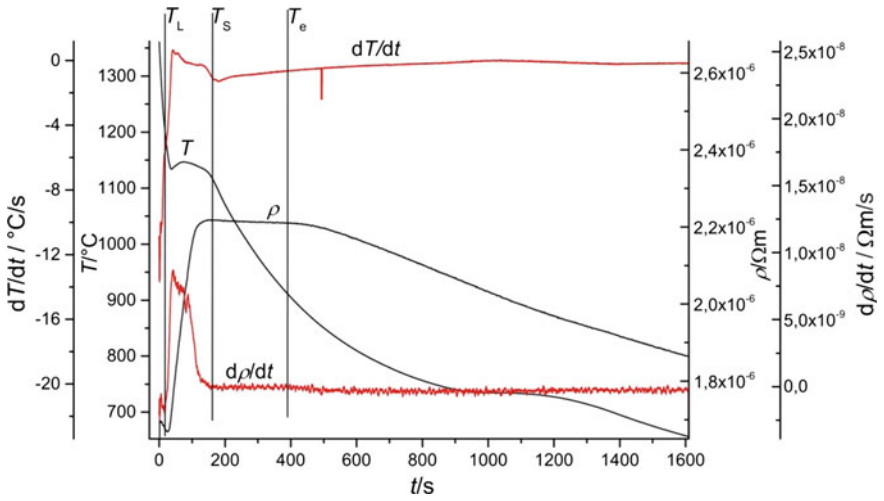

Fig. 5 Diagram presenting cooling curve and electrical resistivity curve with their derivatives of base alloy sample

the reason described above where temperature is measured in one point but the resistivity throughout the whole sample length. According to thermal analysis the eutectoid transformation started at 742.1 °C.

Figure 6 is presenting similar analyses for spheroidal graphite cast irons as Fig. 5 for flake graphite cast iron. One can notice that the curve of electrical resistivity is very different than in case of flake graphite cast iron. The electrical resistivity is not rising during solidification but is decreasing as it is in theory. This is caused by the shape of graphite which is spheroidal and does not interrupt the matrix as much as graphite flakes and does not cause so much of electron scattering resulting in lower resistivity. From the electrical resistivity curve and also from its derivative in Fig. 6 rather difficult to determine exact start and the end of solidification. Similar is with prediction of eutectoid transformation. It is only difficult to see the deflection on resistivity curves at app. 350–400 s when the slope is a little steeper.

For comparison the electrical resistivities versus temperature are given in a Fig. 7. It is clear that the shapes of curves are very distinguished between flake graphite cast iron and nodular cast iron. This is clear confirmation that such measurements are suitable to predict the microstructure of cast irons in terms of shape of graphite which is developed during solidification. It is clear that the drop of electrical resistivity during eutectoid transformation is different for different alloys from where also the state of the matrix can be predicted.

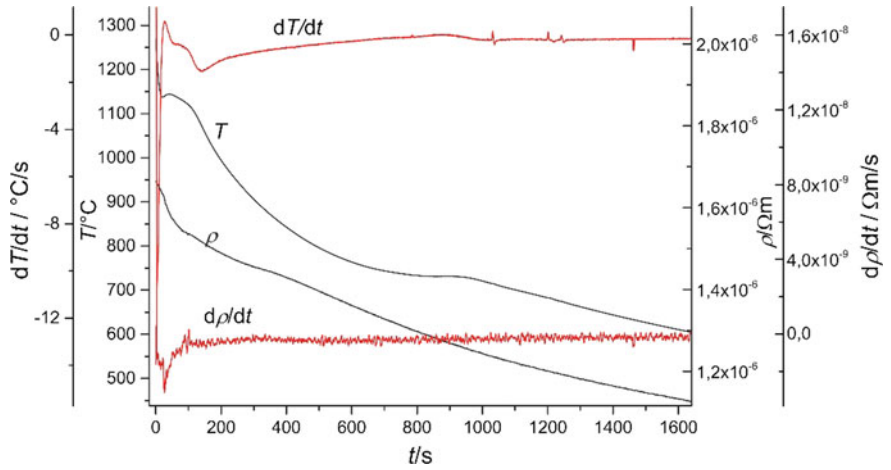

Fig. 6 Diagram presenting cooling curve and electrical resistivity curve with their derivatives of 600 sample

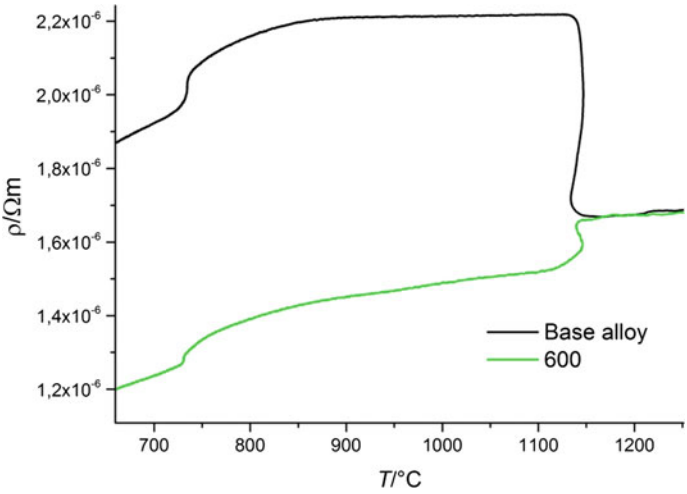

Fig. 7 Comparison of electrical resistivities versus temperature

Conclusions

This paper presents the "in situ" measurements of electrical resistivity and dilatations during solidification and cooling for different cast irons. Results have shown that the electrical resistivity differs for flake graphite cast irons from spheroidal graphite cast irons. The electrical resistivity of flake graphite cast irons is increasing during solidification as a consequence of high electron scattering on flakes. In

spheroidal graphite cast iron it is the opposite way where electrical resistivity is decreased during solidification since the electron scattering is lower at spheroidal graphite which does not interrupt the metal matrix so much.

References

1. Klančnik G, Medved J (2011) Ternary invariant point at 374 °C in the three phase region AlSb-Al-Zn inside the Al-Sb-Zn ternary system. Min Metall Sect B Metall 47(2):179–192
2. Kores S, Vončina M, Kosec B, Medved J (2012) Formation of AlFeSi phase in AlSi12 alloy with Ce addition. Metalurgija 51(2):216–220
3. Petrič M, Kastelic S, Mrvar P (2013) Selection of electrodes for "in situ" electrical resistivity measurements of molten aluminium. J Min Metall Sect B Metall 49(3):279–283
4. Stefanescu D (1993) Ductile iron handbook. American Foundrymen's Society, Inc., pp 1–19
5. Guo X, Stefanescu D (1997) 101st world casting congress. AFS, Inc
6. Hasse S (1996) Duktiles Gußeisen. Schiele & Schön, Berlin, pp 211–216
7. Linares E, Gerval V, Lacaze J (1998) Scr Mater 38:279–285
8. Lacaze J, Ford S, Wilson C, Dubu E (1993) Scand J Metall 22:300–309
9. Kovacs BV (1993) Ductile iron handbook. American Foundrymen's Society, Inc., pp 204–221
10. Markoli B (2008) Structure and properties of materials: electrical and thermal conductivity, insulators, magnets, semi-conductors: intern script, part II. Faculty of Natural Sciences and Engineering, Ljubljana (in Slovenian)
11. Faber TE (1972) An introduction to the theory of liquid metals. Cambridge University Press, New York
12. Sinigoj AR (1999) Basics of electromagnetic. Faculty of Electrical Engineering and Faculty for Computer and Information Science, Ljubljana, p 169 (in Slovenian)
13. Li D, Xu Z, Ma X, Shi D (2015) China Foundry 12(4):239–250
14. (1990) ASM metals handbook, volume 1 properties and selection: irons, steels and high performance alloys. ASM International
15. Nofal A, Waly M, Ahmed A, Agour M (2011) Selection of cast iron grade for stub-anode fixation in aluminium electrolytic cells. Key Eng Mat 457:435–440

Part XXXVII
Ultrafine-Grained Materials X

Mechanical Properties of Ultrafine Grain 2519 Aluminum Alloy

Gbadebo Owolabi, Temitayo Daramola, Nadir Yilmaz, Horace Whitworth and Ahmet Zeytinchi

Abstract The effect of percentage thickness reduction and annealing time on the mechanical properties of cryo-rolled AA 2519 aluminum (Al) alloy was examined. Tensile tests were performed on samples in the longitudinal, transverse and at 45° to the rolling direction. The mechanical properties such as the Yield Strength (YS) and the Ultimate Tensile Strength (UTS) were observed to improve when compared to as-received sample of the 2519 alloy. This is in agreement with the Hall-Petch relationship. The highest variations in these properties were observed in the longitudinal direction, followed by the 45° and the lowest values were obtained in the transverse direction. However, the difference between the mechanical properties in the various directions decreased with an increase in annealing time showing homogeneous distribution of the fine particles.

Keywords Hall-Petch · 2519 Al alloy · Yield strength · Tensile strength Fine particles · Annealing

Introduction

AA 2519 aluminum alloy is a high strength to weight ratio age-hardenable alloy with copper as the principal alloying element. Other minor elements are usually added to increase its resistance to impact load, strength, fracture toughness, and resistance to fatigue failure making it prime candidate for structural applications ranging from ballistic armored vehicles to fuselage components in aircraft [1, 2]. During its service life, it is exposed to several severe and adverse conditions, it is

G. Owolabi · T. Daramola (✉) · N. Yilmaz · H. Whitworth
Department of Mechanical Engineering, Howard University, Washington, DC, USA
e-mail: temitayo.daramola@bison.howard.edu

A. Zeytinchi
Department of Civil Engineering, University of the District of Columbia, Washington, DC, USA

The Minerals, Metals & Materials Society, *TMS 2018 147th Annual Meeting & Exhibition Supplemental Proceedings*, The Minerals, Metals & Materials Series,
https://doi.org/10.1007/978-3-319-72526-0_90

therefore crucial to further improve its reliability and safety while in operation by improving the mechanical properties of the alloy.

One of the most substantial methods used for improving the mechanical properties of aluminum and aluminum alloys is via grain refinement. This is based on the observation that the grain boundaries acts as a pinning point that impedes dislocation movement within the microstructure of an alloy [3]. The grain boundaries acts as barriers to dislocation movement that need greater force to overcome. Grain refinements helps increase the number of pinning points which in turn suppresses the dislocation movement thus strengthening the material. Some of the common techniques used for grain refinement include friction stir processing, accumulative roll bonding, cryogenic rolling, equal channel angular processing, high pressure torsion and repetitive corrugation straightening. In the last couple of decades, processing metals at cryogenic temperature has become a topic of interest [4, 5]. Cryogenic rolling (CR) is considered favorable because the mechanical properties of the bulk metals can be improved for industrial applications through this means. It eliminates the need for large plastic deformation needed in most other methods used in producing nanostructure in metals. In addition, this method helps suppress dynamic recovery at cryogenic temperature and retains the deformation in the strain hardened metal [6, 7].

Several studies on CR process has proven that it is a very productive technique for producing ultrafine grain in aluminum and other metals with improved mechanical properties verified via tensile, impact and hardness tests [8–11]. This study examines the effect of CR and annealing time on the mechanical properties of AA2519 Aluminum alloy. Samples of the CR 2519 alloys were tested in the longitudinal, transverse and at 45° to the rolling direction.

Material and Experimental Method

The materials used in this study is AA2519 Aluminum alloy. The chemical compositions for the alloy is shown in Table 1. A Stanat rolling mill with a single roller of diameter 50 mm was used for the cryogenic rolling.

Samples of dimensions 120 mm × 60 mm × 12 mm of the as received alloy were solution heat treated at 535 °C in a Thermolyne electric furnace for 2 h to help in the homogenization of the grain structure in order to produce equiaxed grains followed by quenching in water. Unidirectional cryogenic rolling was conducted in the longitudinal direction on the heat-treated samples by first immersing and soaking samples in liquid nitrogen for about 20–30 min to ensure uniform

Table 1 Elemental composition of AA2519 aluminum alloy

Composition	Al	Cu	Fe	Mg	Mn	Si	Ti	V	Zn	Zr
%wt	91.5–93.8	5.3–6.4	0.3	0.05–0.4	0.1–0.5	0.25	0.02–0.1	0.05–0.15	0.1	0.1–0.25

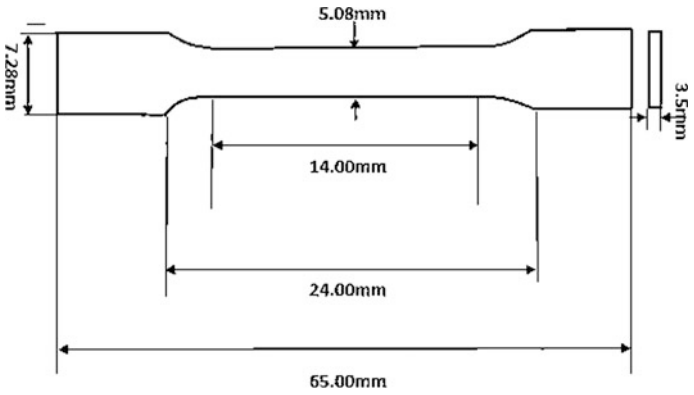

Fig. 1 Geometry of the tensile test sample

temperature along the cross section of the sample. The samples were then cryo-rolled on the Stanat rolling mill. For subsequent passes, the samples were re-immersed in liquid nitrogen for 5 min. The CR process was repeated till the various percentage reductions in thickness (50, 60 and 75%) were obtained. After 50 and 60% reduction in thickness the samples were annealed for 3 min while for 75% reduction in thickness, the samples were annealed for 3, 6 and 9 min all in the Thermolyne electric furnace and aged naturally at room temperature.

Tensile tests were conducted with rectangular tensile test specimens designed according to ASTM E8 standard [12] with the dimensions given in Fig. 1. The machined samples were tested on an Instron 5569A tensile testing machine. The elongation was measured by the displacement of the cross-head.

Results and Discussion

Figure 2 shows the stress-strain curve for different percentage reduction in thickness obtained via cryogenic rolling increases. The figure shows that the mechanical property of the tested samples increase for the 60 and 75% reduction in thickness. The increase in the tensile properties could be attributed to the increase in the number of grain boundaries which help impede dislocation motion during plastic deformation [13]. The tensile properties obtained after 50% reduction in thickness is very similar to the values obtained in the as-received material. This increase was more significant after 60% reduction in thickness with about 40 MPa increase in the Ultimate tensile strength. Further increase is observed after 75% reduction in thickness. The difference increases to about 55% above the value obtained in the as-received material and 15 MPa above its value after 60% reduction in thickness. This is based on the fact that as the reduction in thickness during cryogenic rolling increases, the grains become more refined which leads to an increase in

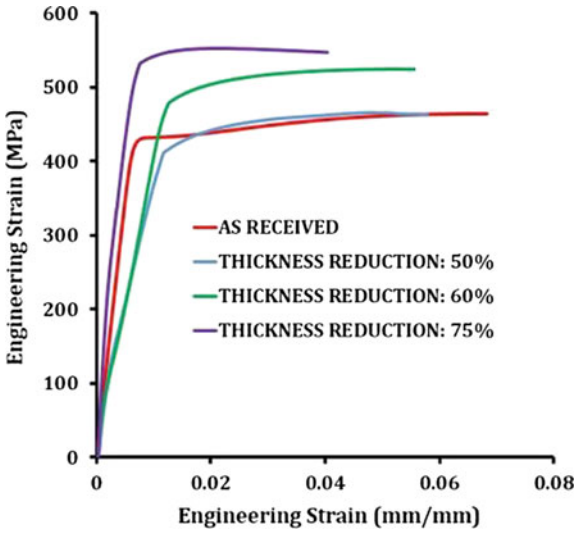

Fig. 2 Effect of percentage reduction in thickness on the mechanical properties of the alloy

crystallographic misorientation of the grains. This serves as an impedance and results in an increase in strength of the material [14, 15]. Secondly since there is always atomic disorder within the grain boundary region, an increase in the number of grain boundaries will facilitate pinning down the mobile dislocation causing restriction to dislocation movement when it crosses grain boundaries. This is in agreement with the Hall-Petch strengthening mechanism [16]. The figure also shows a corresponding decrease in the ductility of the alloy as the percentage reduction in thickness increases from 50 to 75%.

Figures 3, 4 and 5 show the stress-strain curves obtained for the tensile test conducted on the samples that were cryo-rolled with 75% reduction in thickness.

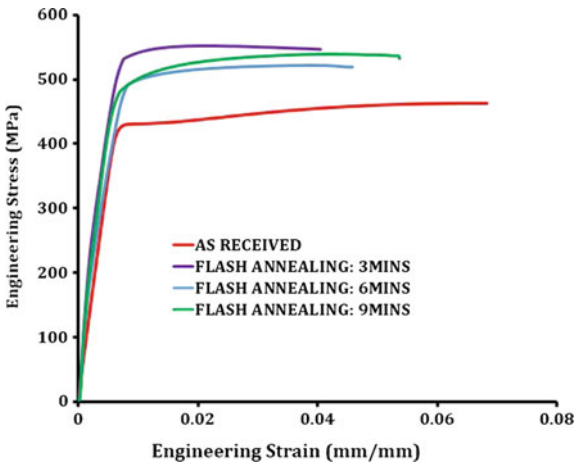

Fig. 3 Stress-strain curve for 2519 Al alloy in the longitudinal direction

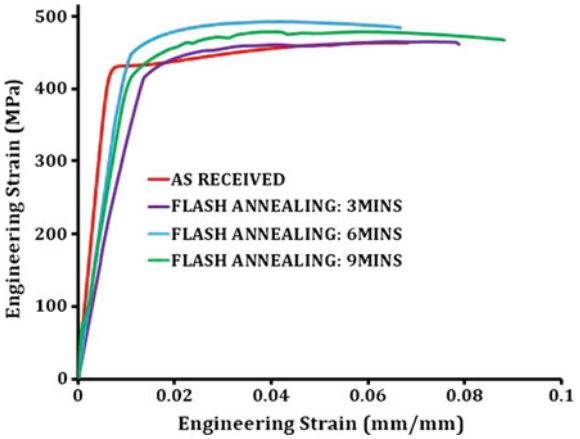

Fig. 4 Stress-strain curve for 2519 Al alloy in the transverse direction

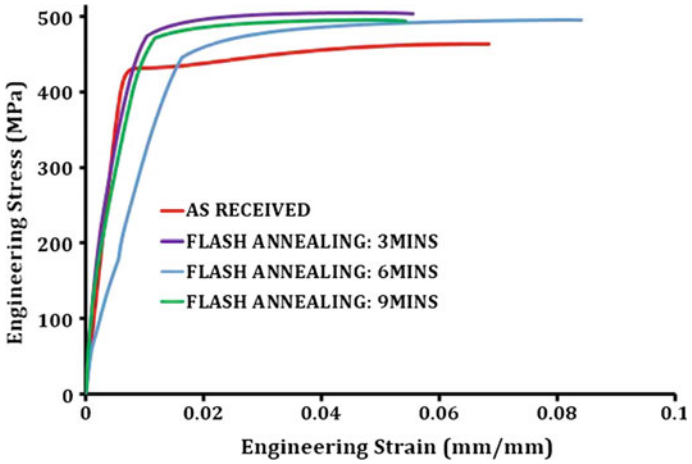

Fig. 5 Stress-strain curve for 2519 Al alloy samples cut at 45° to the rolling direction

The plots shows the effects of flash annealing on the samples for 3, 6, and 9 min in 3 different directions. The annealing time was kept short to avoid appreciable grain growth which might reverse the expected grain size of the alloy to the original size. The directions considered include the longitudinal, transverse and 45° to the rolling direction. The figures show that the anisotropic behavior of the alloy after unidirectional cryogenic rolling. This can be attributed to the fact that the recovery process, grain elongation and the emergence of fine precipitate within the Al matrix have more significant impact in the longitudinal direction as seen in Fig. 3 than in the other directions. Additionally, the grain size for the coarse grain in the as-received material is usually distinctively larger than the grain size of the samples

obtained after cryogenic rolling resulting in an increase the tensile properties of alloy. The maximum UTS of 563.738 MPa was obtained in the longitudinal direction after 3 min flash annealing. This results in an increase of 102.738 MPa when compared to the UTS of the as-received material of 461 MPa. This is due to the suppressed dislocation movement, hindered by additional grain boundaries created during grain refinement produced by the annealing process carried out on the specimen after suppressing dynamic recrystallization within the microstructure of the alloy when it is rolled at cryogenic temperature. It can also be noted from the figures that the ductility, toughness and the energy absorption capability of the alloy before failure increases as the flash annealing time increases.

A comparison between Figs. 3 and 4 shows that the mechanical properties changes more significantly in the longitudinal direction when compared to the transverse direction. An example is the difference in the UTS between 3–6 min annealing time; ranging from 444.23 to 495.15 MPa (approximately 10% increase) in the transverse direction. This may be expected since the grain growth requires lesser energy in the rolling direction during annealing and as such this path is usually more favorable for grain growth. Primary grain elongation is usually along the rolling direction and only minor contraction and expansion occurs in the transverse direction as new equiaxed grains are formed within the grain at the subgrain level [17]. The grain size is therefore not significantly influenced in the transverse direction.

Figure 5 shows the stress strain curve for samples cut at 45° to the rolling direction. In most cases especially at lower annealing time with lesser homogenization, there is more significant variation in the YS showing that the YS is more responsive to variation in grain size obtained since more elongated grains are expected in the rolling direction. As the heat treatment time increases the grain recrystallization commences and the level of homogenization thus increases leading to the proximity seen in mechanical properties in all directions as the grain becomes equiaxed and less lamellar in the longitudinal direction [17]. As annealing time increases it is seen that the UTS between the longitudinal, 45° and transverse gets closer because of the homogenization process. Also precipitate, disturbance in the homogeneity of precipitate and recovery due to annealing dominate over precipitate hardening and softening due to recrystallization effect and this supersedes the softening due to recovery.

Conclusions

In this study, the mechanical properties of cryo-rolled 2519 Al alloys in the longitudinal, 45° and in the transverse direction were examined as a function of the percentage reduction in thickness and annealing time. Based on the results obtained from this study, the following conclusions were drawn.

a. The YS and UTS of cryo-rolled 2519 Al alloy increase with increase in percentage reduction in thickness while there is a corresponding decrease in ductility.
b. Ductility of the cryo-rolled 2519 Al alloy increases as the flash annealing of the alloy increases for the 75% reduction in thickness.
c. The mechanical properties of 2519 Al alloy can be increased significantly through cryogenic rolling with an increase of approximately 100 MPa in the in UTS and YS in the longitudinal direction when compared to other directions (transverse and 45°).

Acknowledgements The authors would like to acknowledge the financial support from the Department of Defense through the research and educational program HBCU/MSI (contract # W911NF-15-1-0457) under the direct supervision of Dr. Joycelyn S. Harrison (Program Manager, AFOSR Complex Materials and Devices Program) and Patricia Huff (HBCU/MI Program Manager, Army Research Office).

References

1. Dursun T, Soutis C (2014) Recent developments in advanced aircraft aluminium alloys. Mater Des 56:862–871
2. Cheung KP (2014) Study of mechanical properties of aluminium-based sheets for structural applications: role of processing parameters. PhD thesis, The Hong Kong Polytechnic University
3. Speidel MO, Hyatt MV (1972) Stress-corrosion cracking of high-strength aluminum alloys. In: Advances in corrosion science and technology. Springer, New York, pp 115–335
4. Markushev M et al (2011) Microstructure and properties of an aluminum D16 alloy subjected to cryogenic rolling. Metally 2011(4):364
5. Konkova T et al (2015) Grain structure evolution during cryogenic rolling of alpha brass. J Alloys Compd 629:140–147
6. Huang YC, Yan XY, Tao QI (2016) Microstructure and mechanical properties of cryo-rolled AA6061 Al alloy. Trans Nonferrous Met Soc China 26(1):12–18
7. Satish DR, Feyissa F, Kumar DR (2017) Cryorolling and warm forming of AA6061 aluminum alloy sheets. Mater Manuf Process 12:1–8
8. Magalhães DC, Hupalo MF, Cintho OM (2014) Natural aging behavior of AA7050 Al alloy after cryogenic rolling. Mater Sci Eng A 593:1–7
9. Yogesha K et al (2016) A Comparative study on tensile and fracture behavior of Al–Mg alloy processed through cryorolling and cryo groove rolling. MMA 5(3):251–263
10. Rao PN, Singh D, Jayaganthan R (2014) Mechanical properties and microstructural evolution of Al 6061 alloy processed by multidirectional forging at liquid nitrogen temperature. Mater Des 56:97–104
11. Koyama M et al (2013) Grain refinement effect on cryogenic tensile ductility in a Fe–Mn–C twinning-induced plasticity steel. Mater Des 49:234–241
12. E8-04 Standard A (2004) Standard test methods for tension testing of metallic materials, annual book of ASTM Standards 3
13. Gashti SO et al (2016) Effect of grain refinement on mechanical and electrochemical properties of ultra-fine grained AA1050 fabricated via ARB process. J Manuf Process 22:269–277

14. Song R et al (2005) Microstructure and crystallographic texture of an ultrafine grained C-Mn steel and their evolution during warm deformation and annealing. Acta Mater 53(3):845–858
15. Soer W et al (2004) Effects of solute Mg on grain boundary and dislocation dynamics during nanoindentation of Al–Mg thin films. Acta Mater 52(20):5783–5790
16. Kato M (2014) Hall-Petch relationship and dislocation model for deformation of ultrafine-grained and nanocrystalline metals. Mater Trans 55(1):19–24
17. Dhal A, Panigrahi S, Shunmugam M (2017) Insight into the microstructural evolution during cryo-severe plastic deformation and post-deformation annealing of aluminum and its alloys. J Alloys Compd 726:1205–1219

Erratum to: Ductile Fracture Assessment of 304L Stainless Steel Using 3D X-ray Computed Tomography

A. J. Cooper, O. C. G. Tuck, T. L. Burnett and A. H. Sherry

Erratum to:
Chapter "Ductile Fracture Assessment of 304L Stainless Steel Using 3D X-ray Computed Tomography" in:
The Minerals, Metals & Materials Society, *TMS 2018 147th Annual Meeting & Exhibition Supplemental Proceedings*, The Minerals, Metals & Materials Society Series,
https://doi.org/10.1007/978-3-319-72526-0_70

The chapter "Ductile Fracture Assessment of 304L Stainless Steel Using 3D X-ray Computed Tomography" originally published with the incorrect author name. O. C. G. Tuck was incorrectly listed as O. G. C. Tuck. The chapter has been updated as well as the table of contents and Author Index.

The update online version of this chapter can be found at
https://doi.org/10.1007/978-3-319-72526-0_70

The Minerals, Metals & Materials Society, *TMS 2018 147th Annual Meeting & Exhibition Supplemental Proceedings*, The Minerals, Metals & Materials Series,
https://doi.org/10.1007/978-3-319-72526-0_91

Author Index

The Minerals, Metals & Materials Society, *TMS 2018 147th Annual Meeting & Exhibition Supplemental Proceedings*, The Minerals, Metals & Materials Series,
https://doi.org/10.1007/978-3-319-72526-0

Subject Index

The Minerals, Metals & Materials Society, *TMS 2018 147th Annual Meeting & Exhibition Supplemental Proceedings*, The Minerals, Metals & Materials Series,
https://doi.org/10.1007/978-3-319-72526-0

D